NLS-29

29th DAE - BRNS NATIONAL LASER SYMPOSIUM

Organized Online by

Raja Ramanna Centre for Advanced Technology, Indore &
Shri Vaishnav Vidhyapeeth Vishwavidyalaya, Indore

February

12-15, 2021

Sponsored by
Board of Research in Nuclear Sciences
Department of Atomic Energy

In Collaboration with

Indian Laser Association

E-Publication

www.ila.org.in/nls29

Preface

The DAE BRNS National Laser Symposium (NLS) is well established, pan-Indian scientific conference of scientists and engineers working in the area of lasers and their applications. The NLS is a national symposium which aims to provide a common platform for researchers working on different aspects of Physics and Technology of lasers as well as applications of lasers in diverse fields such as spectroscopy, biology, laser material processing etc. It provides an opportunity for interaction between experienced scientists and young researchers in the topics of interest such as Physics and Technology of Lasers; Lasers in Nuclear Science and Technology; Laser Materials, Devices and Components; Nonlinear, Quantum and Atom Optics; Ultrafast Lasers and Applications; Lasers in Materials Science; Laser Plasma Interaction; Lasers in Industry and Defense; Laser Spectroscopy and Applications; Lasers in Chemistry, Biology and Medicine; Laser & Fiber Based Instrumentation; and Electronics and Instrumentation for Lasers. The symposium is held under the aegis of Board of Research in Nuclear Sciences (BRNS), Department of Atomic Energy (DAE). All the major Indian laser laboratories and research institutes participate in the National Laser Symposium (NLS). The symposium is held every year at different locations in India so that the researchers and young students of different areas are exposed to modern and technological developments in lasers and related areas.

The current symposium is the 29th in the series which started in the year 1992. Due to prevailing pandemic situation world-wide, this year we have organized the symposium in ONLINE mode so that speakers and participants can join the symposium from their respective work/native place via internet facility, without any physical gathering of people at any place. The 29th DAE-BRNS National Laser Symposium (NLS-29) is organized using **online mode** by Raja Ramanna Centre for Advanced Technology (RRCAT), Indore & Shri Vaishnav Vidyapeeth Vishwavidyalaya (SVVV), Indore, during February 12 to 15, 2021 (for details please check **www.ila.org/NLS-29**). The scientific program of NLS-29 consists of 36 invited talks by leading experts, presentation of research papers and presentation of Ph.D. thesis by research scholars. Just before the NLS-29, on 10th& 11th February 2021, Indian Laser Association (ILA) has

organized two short courses for student participants. In addition, a special session for interactions between Industry and R & D institutes has been organized to promote innovations based on science and technology developed within the country.

In spite of a short time interval between announcement and the date of event, NLS-29 has received a very high response in terms of contributory papers and Ph.D. thesis presentations. After a peer-review process, 146 contributory papers were accepted for the poster presentation in different category of topics. These papers were presented in **online mode** in three dedicated poster sessions during Feb 12-14, 2021. In NLS-29, total 17 Ph.D. theses have been submitted by research scholars and 15 theses were presented in Online mode by Ph.D. scholars. Expert committees were formed to judge the quality of posters and theses presented during NLS-29. The committees selected 10 papers for “Best Poster” award and 5 Theses for “Best Thesis” award. These “Best Thesis” and the “Best Poster” awards were presented by Indian Laser Association (ILA) during the concluding session of NLS-29 on 15th Feb, 2021. In NLS-29, there were 36 invited talks delivered by the experts in different areas of lasers and applications. This constisted of 17 Foreign speakers, 19 Indian speakers. The Keynote address **“Photonics Gone Rogue”** was delivered by Prof. Raman Kashyap, Canada Research Chair on Future Photonics Systems, Ecole Polytechnique de Montreal, Montreal, Canada during the Inaguration Function. There was a session of two special evening talks by internationally renowned scientists: (1) ***“The beginnings of gravitational wave astronomy: current state and future”*** by Prof. Rainer Weiss (Physics Noble Laureate 2017), MIT, USA, and (2) ***“Plasmonic Technologies for Alloyed Hybrid Meta-surfaces”*** by Prof. Martin Olivier, Swiss Federal Institute of Technology, Lausanne (EPFL), Switzerland. These talks were appreciated by most of the participants. There was a separate session for the industry presentation in which information about laser and related products was presented by different vendors.

It is a matter of great pride and honor that **Dr G Satheesh Reddy**, Secretary, Department of Defence R&D and Chairman, Defence Research and Development Organisation (DRDO), Govt. of India, was the Chief Guest at the inaugural function of NLS-29 on 12th Feb, 2021. His gracious online presence and motivating address to the participants and delegates added value to the Symposium. During the inauguration of NLS-29, Shri Debashis Das, Director, RRCAT, Indore and

Shri Purushottamdas Pasari, Chancellor, SVVV, Indore, were special guests who addressed the participants and delegates in online mode. On this occasion of inauguration of NLS-29, Shri S. V. Nakhe, President, ILA, presented the ILA perspective of NLS event. The function was presided by Prof. U. Dhar, Vice Chancellor, SVVV, Indore, who presented his views on symposium and new education policy in his address to participants. During the inaugural session Chief Guest released (virtually) the e-Publication of proceedings of NLS-29 and inaugurated (virtually) the Exhibition Gallery from vendors of lasers and related products. More than 10 industries and vendors displayed their products related information in the exhibition.

Indian Laser Association plays an active role in various ways in planning the NLS. Over the years, the short tutorial courses organized by ILA on laser related advanced topics, preceding the NLS, have become quite popular among the young researchers. This year, two short courses were offered by ILA. These are: (1) "**LASER - A Versatile Tool for Research and Technology Development**" (Course Co-ordinators: Dr. Suprajnya Thakur, Associate Professor, Department of Physics, SVVV, Indore and Dr. Manvendra Kumar, Associate Professor, Department of Physics, SVVV, Indore) and (2) "**Quantum Metrology**" (Course Co-ordinators: Dr. Sendhil Raja S., Head, Advanced Electro-Optics Section, RRCAT, Indore and Dr. Vibhuti Bhushan Tiwari, Head, Atom Optics Lab, RRCAT, Indore). Many young researchers from various parts of country attended these courses which will be beneficial to their future growth.

We express our sincere thanks and gratitude to Dr G. Satheesh Reddy, Secretary, Department of Defence R&D and Chairman, DRDO, who spared his valuable time from his busy schedule to inaugurate NLS-29. We also thank to Shri Debashis Das, Director, RRCAT and to Shri Purushottamdas Pasari, Chancellor, SVVV for their patronage to NLS-29. We are grateful to Prof. U. Dhar, Vice Chancellor, SVVV, Indore for coming forward to host this symposium and for extending the facilities of the institute. We are also thankful to Shri S. V. Nakhe, President, ILA for his whole hearted support to NLS-29 and valuable guidance at every step in organizing the symposium. We are also extremely thankful to all those who have been instrumental and contributed in organizing this symposium. We also

express our sincere gratitude to the members of National Advisory Committee, Symposium Organizing Committee and Local Organizing Committee for their interest, support and valuable suggestions and guidance. We express our sincere thanks and appreciation to all the speakers for accepting the invitation to participate in NLS-29 and sharing the recent developments in their respective research fields. We are also indebted to all the session coordinators, session chairs for conducting the sessions smoothly. Thanks are due to all the referees for the pain taking effort of reviewing the manuscripts and providing the reports to upkeep the standard of NLS at par with other reputed symposia. We also extend our heartfelt thanks and appreciation to the numerous colleagues from RRCAT, Indore and SVVV, Indore for working day-night and providing necessary support for smooth organization of NLS-29.

The e-book of NLS-29 contains the symposium program, abstracts of the invited talks, the contributory papers and the synopses of theses presented. Although all efforts have been made to ensure accuracy, some errors might have crept in which we regret.

On behalf of Symposium Organizing Committee and the Local Organizing Committee, we thank all the delegates and participants for their interest in NLS-29 and having fruitful, scientifically enriching and inspiring interactions during the symposium.

Dr. S. R. Mishra, Convener
Dr. Uttam Sharma, Co-Convener,
Shri Praveen K Agrawal, Secretary
Dr. Nitu Kataria, Co-Secretary

Invited Talks

Keynote Address	Photonics gone rogue *Raman Kashyap*	1
ST-01	Plasmonic technologies for alloyed and hybrid metasurfaces *Olivier J.F. Martin*	2
ST-02	The beginnings of gravitational wave astronomy: current state and future *R. Weiss*	3
IT-01	Pulses and patterns in ultrafast fiber lasers: the dissipative soliton approach *Ph. Grelu, K. Nithyanandan, Z. Wang, S. Hamdi, A. Coillet, P. Tchofo-Dinda*	4
IT-02	Laser welding in fabrication of FBR fuel pins: Metallurgical considerations *S.K. Albert, R Ravikumar, R Lavakumar, Y.V Harinath, T. V. Prabhu*	5
IT-03	Power scaling limits in high power fibre lasers *M.N. Zervas*	6
IT-04	Optical fiber biosensors: Principles and applications *Umesh Tiwari*	7
IT-05	Advancement of speciality fibre optic sensors for in situ monitoring *Sanjeev Raghuvanshi*	8
IT-06	Laser based measurements and perimeter intrusion detection *Aseem Singh Rawat*	9
IT-07	Physics and applications of scattering with extreme light *Donald Umstadter*	10
IT-08	Probing ultrafast dynamics of water at aqueous interfaces with femtosecond two-dimensional heterodyne-detected VSFG spectroscopy *Mohammed Ahmed, Satoshi Nihonyanagi, TaheiTahara*	11
IT-09	Plasma acceleration- What were we thinking in those early days and where are we headed? *Chan Joshi*	12

IT-10	Visualization of charge separation at the in-plane organic heterojunctions using pump-probe microscopy *Sachin Dev Verma*	13
IT-11	Spatiotemporal dynamics of relativistically hot plasmas *G. Ravindra Kumar*	14
IT-12	Making the stories come true: Molecular Laser Isotope Separation to coherent control *Sisir K Sarkar*	15
IT-13	Novel multifunctional organic chromophores for non-linear optical applications *Raavi Sai Santosh Kumar, Chinmoy Biswas*	16
IT-14	Quantum Interference based approach to Nonlinear Optics *Harshawardhan Wanare*	17
IT-15	Flatland Nonlinear Optics *K. V. Adarsh*	18
IT-16	A quantum of science' for the future technologies *Y. B. Kale*	19
IT-17	Multi-GHz burst-mode fiber lasers *F. Ömer Ilday*	20
IT-18	Solid-state lasers for ultrashort pulse generation *Rüdiger Paschotta*	21
IT-19	Spatiotemporal mode-locking in fiber lasers *Frank Wise*	22
IT-20	Advancement in in-situ monitoring and defect detection algorithms for laser powder-bed fusion *Ehsan Toyserkani*	23
IT-21	Towards a predictive model of direct metal deposition *Andrew Pinkerton*	24
IT-22	Post processing of LAM components *Shashank Sharma, J. Ramkumar*	25

IT-23	Functional brain diagnosis with dynamic light scattering imaging approach at broken ergodicity conditions *Igor Meglinski*	26
IT-24	Lasers and nanotechnology in regenerative medicine *Martin J. Leahy*	27
IT-25	Shedding light on radiotherapy: functional optical coherence tomography for radiobiological microvascular imaging *Valentin Demidov, Costel Flueraru, Alex Vitkin*	28
IT-26	Growth of single crystals by various techniques for optical, piezoelectric and communication applications *Binay Kumar*	30
IT-27	Design of wearable devices for underserved populations *Jessica Ramella-Roman*	31
IT-28	Development of high Quality Nonlinear Optical (NLO) single crystals for Second Harmonic Generation (SHG) Applications *Muthu Senthil Pandian, P. Karuppasamy, P Ramasamy*	32
IT-29	Quantitative phase microscopy and nanoscopy using partially spatially coherent laser light: Improvement on image sharpness, phase noise, resolution and speckle free imaging *Dalip Singh Mehta*	33
IT-30	Growth of potential nonlinear optical single crystals by melt and solution growth techniques *N. Vijayan*	34
IT-31	Investigation of Dengue infectivity and dynamics using Förster Resonance Energy Transfer (FRET) *Kamal Kant Sharma, Xin Ee Yong, Sarala Neomi Tantirimudalige, Anjali Gupta, Jan K. Marzinek, Daniel Holdbrook, Xin Ying Elisa Lim,Peter J. Bond, Ganesh S. Anand, Thorsten Wohland*	35
IT-32	Atomic probe of nuclear properties *B. K. Sahoo*	36
IT-33	Dynamical phase transition in mirrorless optical parametric oscillator *Ashok Mohapatra*	37
IT-34	Some of the applications of laser induced breakdown *Alika Khare*	38

IT-35 The advanced LIGO gravitational-wave detector: a discovery machine 39
David H. Reitze

IT-36 Future of gravitational wave detection technology 40
Rana Adhikari

Contributory Papers

Physics and Technology of Lasers

CP-01-236 Development of high average power, high pulsed repetition rate single longitudinal mode dye lasers for selective photo-excitation of Yb isotopes of medical use 41
A. K. Singh, A. Khattar, A.Wahid, J. S. B. Singh, S. K. Maurya, P. R. Mohite, J. S. Dhumal and S. Kundu

CP-01-261 Controlled decoherence in a semiconductor diode laser 45
Neethu K, S. Sivaprakasam

CP-01-369 Determination of gain coefficient and roundtrip resonator losses of Cr:forsterite laser system using a polarization resonator cavity 49
Siba Prasad Sahoo, V.S. Rawat, Jaya Mukherjee, Swarupanand Pradhan

CP-01-396 Energy enhancement in capillary discharge soft x-ray laser operating at 46.9 nm 54
S. Barnwal, S. Nigam, K. Aneesh, M. L. Sharma, Y. B. S. R. Prasad, K. S. Bindra

CP-01-406 Development and characterization of a 40 W narrow linewidth all-fiber multistage amplifier at 1064 nm. 58
Bhuvnesh, C.P. Singh, P.K. Gupta, S. Sahu, P.K. Mukhopadhyay and K.S. Bindra

CP-01-412 Effect of reabsorption losses in Q-switched Yb:YAG laser 62
A. J. Singh, S. Sahu, S. Ahlawat, P. K. Mukhopadhyay, K. S. Bindra

CP-01-418 Development of compact engineered 500 W of single transverse mode all-fiber Yb-doped CW fiber laser 67
Avdhesh kumar, Pushkar Misra, R. K. Jain, Rajpal Singh, V. Bhardwaj, B. N. Upadhyaya, K. S. Bindra

CP-01-422 Parametric study on optimization of double side transversely pumped high power pulsed dye laser amplifier performance 71
Jeetendra S B Singh

CP-01-431	Analysis of core reset in magnetic pulse compression network of metal vapor laser *Dheeraj Kumar Singh, B Dikshit, Jaya Mukherjee, V S Rawat*	75
CP-01-448	DPSSL pumped high repetition rate single longitudinal mode pulsed dye laser *V S Rawat, Paramjit Rana, Siba P Sahoo, S K Mishra, Jaya Mukherjee*	79
CP-01-453	Synthesis and optical properties of RE3+(RE3+= Dy3+, Sm3+ and Eu3+) doped Sr1.99Bi0.01CeO4 phosphors for LEDs applications *G.Subalakshmi, N.P.Rajesh*	83
CP-01-484	Photonic microwave signals generation using optically injected VCSELs under parallel optical injection *E. Jayaprasath, Z. M. Wu, G. Q. Xia*	86
CP-01-490	Development of a laser system for enrichment of Yb176 for medical application *A Wahid, A K Singh, A Khattar, J S B Singh, P K Mohite, J S Dhumal, S K Maurya, S Kundu*	90
CP-01-537	Effect of output coupler reflectivity on the Narrow Band Pulsed Dye Laser Pumped by DPSSL *S K Mishra, Paramjit Rana, Siba P Sahoo, Jaya Mukherjee, V S Rawat*	94
CP-01-542	Development and characterization of a 1 W engineered narrow linewidth all-fiber multistage amplifier system at 1550 nm. *Bhuvnesh, C.P. Singh, P.K. Gupta, P. Hedaoo, S. Sahu, P.K. Mukhopadhyay and K.S. Bindra*	98
CP-01-557	Generation of 50 W of output power at eye safe wavelength of 1600 nm from all-fiber Er-doped fiber laser using MOPA configuration *Ravindra Singh, Avdhesh Kumar, Antony Kuruvilla, Rajpal Singh, B. N. Upadhyaya, K. S. Bindra*	102
CP-01-588	Studies on the high beam quality green and yellow radiation of a 40 W Copper Bromide Laser *G.N.Tiwari, V. K. Shrivastava, R. K. Mishra, S. K. Dixit*	106
CP-01-606	Performance characterization of IGBT based high voltage pulse power supply of CVL MOPA system for long hour operation *R.K. Mishra, Jagdish Kumar, Deepak Naphade, P.K. Agrawal, M.S. Ansari*	110
CP-01-666	Generation of more than 100 W of CW output power from all-fiber Tm-doped fiber laser *Usha Chakravarty, Avdhesh Kumar, Antony Kuruvilla, Aswin Ashok, R. K. Jain,Rajpal Singh, B. N. Upadhyaya, K. S. Bindra*	114
CP-01-667	Studies on second harmonic ultraviolet generation at 255 nm from a low temperature (~500 ˚C) copper vapour laser with different optical resonators *R. Biswal, O. Prakash, S. K. Dixit*	118

CP-01-671 A compact intensity auto-correlator for ultra-short laser pulse width measurement 123

D. Daiya ,R. K. Patidar, S. W. Amalraj, A. Moorti, M. P. Kamath, Sushil Kumar Sharma, N. S. Benerji, K. S. Bindra

CP-01-673 Development of 1.5 kW average power and 30 kW peak power long pulse Nd: YAG laser 127

Sunil Kumar Sharma, M. K. Bairwa, V. Bhardwaj, Bhaskar Paul, Rajpal Singh, Vijay Bhawsar, A. A. Raju, D. Narwat, R.K. Jain, P. Kumar, S. K. Sah, S. Kushwaha, P. Shryner, J. Khanwalkar, R. Arya, B. N. Upadhyaya, K. S. Bindra

Lasers in Nuclear Science and Technology

CP-02-297 $^{98/100}$Mo enrichment by infrared multi-photon dissociation of MoF_6 131

M B Sai Prasad,A. Ghosh, R. C. Das, T. Dwivedi, G. Chakraborty, D. J. Biswas, J. P. Nilaya

CP-02-477 Simulation of transient photo plasma and ion collection dynamics using two-dimensional Particle-in-cell (PIC) methods for laser isotope separation of Ytterbium 135

G.Sridhar, B.Jana, S.Baruah, S.Kundu, S.Sethi

CP-02-597 In-situ laser cutting for repair/replacement of injection valves of emergency core cooling system at KKNPP-2 reactor 139

Basant Kumar Saini ,M. K. Bairwa, R. K. Jain, A. *A. Raju, Rajpal Singh, Benny John, Binu Gopal, Bhaskar Paul, Jata Beshra,Vijay Bhawsar, B. Ekka, Vijay Bhardawj, Vijay Shukla, R. Arya, B. N. Upadhyaya, K. S. Bindra*

CP-02-610 Laser cutting of up to 30 mm thick SS316Lusing 500 W average power pulsed Nd:YAG laser for nuclear field applications 143

M. K. Bairwa, V. Bhardwaj, R. K. Jain, V. Shukla, S. K. Sharma, R. Singh, B. K. Saini,B. Paul, P. Kumar, B. Ekka,Pr. Kumar, J. Beshra, A.A. Raju, S. K. Sah, V. Bhawsar, J. Khanwalkar, R. Arya, B. N. Upadhyaya, K. S. Bindra

Laser Materials, Devices and Components

CP-03-318 Growth of bulk size organic single crystal by a novel immersing ampoule Sankaranarayananan-Ramasamy (ISR) Method for NLO Applications 147

P. Karuppasamy,T. Kamalesh, Muthu Senthil Pandian, P. Ramasamy, Sunil Verma, A. K. Karnal

CP-03-320 Crystal Growth and Characterization of Semi-organic Piperazinium Tetrachlorozincate monohydrate (PTCZ) single crystal for Nonlinear Optical (NLO) applications 151

Z. Nawas Sherif, B. Sahaya Infant Lasalle, T. Kamalesh, P. Karuppasamy, Sunil Verma, Muthu Senthil Pandian, P. Ramasamy

CP-03-336 Bulk growth of Organic non-linear optical Triphenylphosphine Oxide 4-Nitrophenol (TP4N) single crystals by Sankaranarayananan-Ramasamy (SR) method 155

T. Kamalesh, P. Karuppasamy, Muthu Senthil Pandian, P. Ramasamy, Sunil verma, A.K. Karnal

CP-03-364 Investigations on structural, optical, and electrical properties of Neodymium doped rubidium titanyl phosphate single crystal (Nd: $RbTiOPO_4$) 159

Rajesh Narayana Perumal, Arulmani Marimuthu

CP-03-506 Design and analysis of silicon photonic switch matrix for reconfigurable electronic-photonic integrated circuits 162

Mubarak Ali M, Madhupriya G, Indhumathi R, Krishnamoorthy Pandiyan

CP-03-511 Synthesis, crystal growth and characterizations of 2-amino-5-nitropyridinium trichloroacetate (2A5NPTCA): an efficient single crystal for optoelectronic applications 165

V. Sivasubramani, Muthu Senthil Pandian, P. Ramasamy

CP-03-582 A technique for directly cutting type-I SHG plates from as-grown KDP crystal and assessment of its orientation 169

S. K. Sharma, Yashpal Singh, Indranil Bhaumik, A. K. Karnal

CP-03-584 Synthesis of copper doped lithium tetraborate ($Cu:Li_2B_4O_7$) nanoparticles and their characterization for structural and thermoluminescence properties 173

S.Kar, C. Debnath, Sunil Verma, V.S. Tiwari, A.K. Karnal

CP-03-612 Linear and 3rd order nonlinear optical properties of $LiNbO_3$/PMMA nanocomposite 177

Chiranjit Debnath,Sunil Verma, Sujan Kar, V. S. Tiwari, A. K. Karnal

CP-03-620 Growth and investigation of thermo-optic coefficient of cesium triborate single crystals for nonlinear optical application 181

A. Saxena, Ratna Karn, P.A. Darshan, M. Soharab, R. Bhatt, Indranil Bhaumik, B. K. Sajith, A.K. Karnal

CP-03-653 Design and development of monocrystalline AlGaAs/GaAs DBR mirrors with reflectivity exceeding 99% at 1064, 1100 and 1550 nm photonic band 185

Geetanjali Vashisht, Suparna Pal, S. K. Khamari, R. Kamparath, A. Khakha, R. Kumar, C. Mukherjee, V. K. Dixit, T. K. Sharma

CP-03-670 Detection of refractive index inhomogeneity in large size Neodymium (Nd)-doped phosphate glass slabs using a small size laser beam 189

Sanjiv Kumar Tiwari, Sarvendra Singh, Y. Pavan Kumar, Rishipal, G. Muralidharan, A. K. Biswas, M. P. Kamath, N. S. Benerji and K. S. Bindra

Nonlinear, Quantum and Atom Optics

CP-04-217 Nonlinear optical study of differently coloured, free-flowing, dye-based fountain pen inks. 193

Ajay A R, Aji Alexander,Reji Philip

CP-04-252 Synchronization and inverse-synchronization of self-pulsating non-symmetric coupled diode laser system 197

Prachi, S. Sivaprakasam

CP-04-294 Potential Energy distribution study and molecular properties of 1,3-Diphenyl Propenone 201

Revathi H,M. Thirumalaikumar, S. Sampathkrishnan,, C. Charanya, N. Balamurugan

CP-04-312 QPM grating structure for simultaneous RGB generation for projection display applications 205

Indhumathi Ravi Rajan, Mubarak Ali Meerasha, Madhupriya G, Shanmugam Boomadevi, Krishnamoorthy Pandiyan

CP-04-322 Nonreciprocal light propagation in novel photonic crystal/metal hybrid structure 210

Nikhil P P, K Chandrasekharan

CP-04-325 Optical response of anatase TiO_2: The role of exact exchange on predicting exciton binding energy 214

Sruthil Lal S B,D Murali, Matthias Posselt, Alok Sharan

CP-04-342 Decoherence in lambda and ladder systems 218

K. Yadav, A. Wasan

CP-04-359 The third order nonlinear optical exploration in novel Heterocyclic Schiff Base Dye: Z- scan measurements 222

Mohd Mehkoom, S. M. Afzal, Salman A. Khan

CP-04-382 Loading a magneto-optical trap in UHV using a Rb atomic beam source 226

Kavish Bhardwaj, S. P. Ram, S. Sarkar, V. B. Tiwari, S. R. Mishra

CP-04-385 Launching of laser cooled Rb atoms in atomic fountain geometry 229

S. Singh, B. Jain, S. P. Ram, V. B. Tiwari, S. R. Mishra

CP-04-387 Trapping of laser cooled atoms in time averaged adiabatic potentials 233

S. Sarkar, S.P.Ram, Kavish Bhardwaj, V. B. Tiwari, S. R. Mishra

CP-04-388 Studies on optimization of optical pumping of cold ^{87}Rb atoms using Stern-Gerlach (SG) technique 237

Vivek Singh, V. B. Tiwari, S. R. Mishra

CP-04-503 Quantum entanglement between atoms using quantized light 241

S. Kannan, Sudheesh Chethil

CP-04-617 Design and Development of mirror MOT Atom Chips for Cold Atom Interferometry 244

Hriday Dath, Radhika V. N., Harikrishnan A, , Rekha A. R., J Krishnakumar, Hemachandran S

CP-04-627 Generation of entangled photon-pair through difference frequency generation using Type 0 Quasi Phase Matched LiNbO3 248

Adithya Ramesh, Eswara Prasath, Srikrishna V

CP-04-645 Phenomenal optical limiting action from gold and silver through Au@Ag core- shell nanostructures 252

Shiju E,Abhijith T, D. Narayana Rao, K. Chandrasekharan

CP-04-665 Broadband nonlinear optical studies of a Novel Phthalocyanine using MHz and kHz femtosecond pulses 256

Dipanjan Banerjee, K S Srivishnu, Jagannath Rathod, L. Giribabu, S. Venugopal Rao

Ultrafast Lasers and Applications

CP-05-293 Photonic and electronic state nonlinear interactions in $BaTiO_3$ based Microcavity 260

Jitendra Nath Acharyya,D. Narayana Rao, G. Vijaya Prakash

CP-05-295 Linear and nonlinear optical excitons in primary cyclic ammonium based inorganic-organic hybrid semiconductor series 264

Kshetra Mohan Dehury,Prof. G. Vijaya Prakash

CP-05-327 Effects of high repetition rate ultrafast laser pulses on spatial self-phase modulation 268

Soumyodeep Dey, Prem B. Bisht

CP-05-409 All-normal dispersion Ytterbium doped fiber laser mode locked by nonlinear multimode interference based saturable absorber 272

Pradeep K Gupta, C P Singh, P K Mukhopadhyay and K S Bindra

CP-05-565 Volumetric propagation studies of ultrashort pulsed beams in nonlinear dispersive and aberrated optical systems 276

A K Sharma

CP-05-566 Ultra-fast lattice dynamics in GaP/Ge(111) heterostructure measured with time-resolved x-ray diffraction 280

R. Rathore,H. Singhal, R. Roychowdhury, V. K. Dixit, T. K. Sharma and J. A. Chakera

CP-05-586 Complete temporal reconstruction of attosecond pulse trains from high-harmonic generation in an argon filled cell 283

Mukund Kumar, Ajmal Ansari, Himanshu Singhal, Juzer Ali Chakera

CP-05-603 Measurement of refractive index and absorption coefficient of 3, 4, 5 -Trinitro 1-H Pyrazole using terahertz time-domain spectroscopy 288

Rajesh Koalla, Chandan Ghouri, Shivanand Mangali, Naveen Periketi, A.K. Chaudhary

CP-05-649 Anisotropic non-wetting metallic surfaces engineered via femtosecond Laser micromachining 292

Md Abu Taher,Sri Ram G Naraharisetty, D Narayana Rao

Lasers in Materials Science

CP-06-283 Estimation of precise concentration of n and np compound fertilizers sample with laser interaction technique 297

Pooja Baikar,Arpit Rawankar, Vaibhav Kshirsagar, Santosh Jagtap

CP-06-288 Bioreduction potentials of Cynadon Dactylon for ecofriendly silver nanospheres 301

N Venkateswara Reddy, L. Jyothi, T. Sreekanth, N. Sri Ram Gopal and Narayana Rao Desai

CP-06-307 Perfect absorption in a pulsed laser deposited sub-wavelength thick indium tin oxide thin film via Kretschmann-Raether geometry 305

Sumit Goswami, Ashwini Kumar Sharma

CP-06-334 Nanosecond laser texturing with in-situ glass particle deposition on steel mesh for oil water separation 309

Sunita Ahlawat, Amarjeet Singh, P. K. Mukhopadhyay, Rashmi Singh, K.S. Bindra

CP-06-353 Simulation studies of photonic nanojets and photonic nanojet assisted nano-structuring on metallic substrates 313

Bijoy Sugathan,J. Padma Niaya, V.P. Mahadevan Pillai, D.J. Biswas

CP-06-517 Suppression of stress corrosion cracking susceptibility of shear cut surface of 304L stainless steel through laser shock peening 317

Ram Kishor Gupta, A. K. Rai, D. C. Nagpure, R. Biswal, P. Ganesh, S.K. Rai, K. Ranganathan, K. S. Bindra, R. Kaul

CP-06-546 Oxygen vacancies effect on ferroelectric and dielectric properties in Sr0.5Ba0.5Nb2O6 Ceramic for Micro-positioner 321

S. Karmakar, Rachna Selvamani, S. M. Gupta, V. S. Tiwari, A. K. Karnal,

CP-06-549 Pulsed laser deposition assisted fabrication and characterization of bio-inspired plasmonic nanostructures for efficient absorption of broadband optical radiation 325

U. Chakravarty, Jai Khare, M.P. Joshi, C. Mukherjee, Rashmi Singh

CP-06-555 Microwave-assisted preparation of green-emissive carbon dots for potential temperature sensing and pH sensing applications. 329

Shivanand H Nannuri,Santhosh C, Sajan D. George

CP-06-611 Optical properties in CZF ferrofluids 333

Arkilang Challam, Mahender R, Md. Sharif C, Ashok Vudayagiri, R.Singh

CP-06-648 Characterization of aerosol assisted CVD Grown Ni:ZnO thin films 337

Vipin K. Kaushik, Shweta Tiwari, Gourang Vani,

CP-06-707 Effect of melt pool geometry on laser polishing of Laser Additive Manufactured SS 304 341

Ambar Choubey, A.N. Jinoop, Sabir Ali, S.K. Mishra, C.P. Paul, K.S. Bindra

Laser Plasma Interaction

CP-07-338 DSMC study on reduction of atomic vapour Doppler width for LIS 345

Tarang Garg,Sudarshan Baruah, G. K. Sahu

CP-07-349 Study of laser polarization dependant JxB acceleration in relativistic ultrashort laser 349

foil interaction

Tirtha Mandal,V. Arora, A. Moorti, A. Uphadhyay, J.A. Chakera

CP-07-350 Study of fast electron transport in ultrahigh intensity laser matter interaction by 2D imaging of Cu K_α x-rays 353

Tirtha Mandal,V. Arora, A. Moorti, J.A. Chakera

CP-07-379 Tunable electron beams from laser wakefield acceleration by controlled injection 356

S. Mishra,B.S. Rao, A. Moorti, J.A.Chakera

CP-07-394 X-ray spectral measurements from laser plasmas using a gated Micro-channel plate detector 360

A. Kumar,S. Barnwal, M.L.Sharma, A. Singh, S. Jain, A.P. Kulkarni, S. Nigam, Y.B.S.R. Prasad, N.S.Benerji, K.S.Bindra

CP-07-397 Study of spatio-temporal reshaping of ultrashort laser pulse due to plasma defocusing 364

Ajmal Ansari,Mukund Kumar, Himanshu Singhal, Juzar Ali Chakera

CP-07-629 Stimulated Raman and Brillouin scattering processes in magnetized doped semiconductors: A comparative study 368

Jaivir Singh, Arun Kumar, Sunita Dahiya, Navneet Singh, Manjeet Singh

CP-07-635 Energy dependent study of confined laser generated air plasma 372

D. P. S. L. Kameswari,Nagaraju Guthikonda, S. Sai Shiva, P. Prem Kiran

CP-07-654 Laser-Plasma Accelerated Proton Beam Focussing Optics using High Voltage Pulsed Power Solenoid 376

M. Tayyab, S. Bagchi, A. Moorti, J. A. Chakera, M. L. Sharma, K. Aneesh, S. Nigam

Lasers in Industry and Defence

CP-08-380 Development of UHV compatible SS 316L-Kovar welding joint using fiber coupled pulsed Nd:YAG laser for accelerator applications 380

Vijay Bhardwaj, Pawan Kumar, Prabhat Kumar, Mahendra Kumar Bairwa, Rajpal Singh, B. K. Sindal, D. P. Yadav, B. N. Upadhyaya, K. S. Bindra

CP-08-615 Development of 0.9 J pulse energy microsecond pulse Nd:YAG laser and its application to cutting of MEMS devices from ceramic substrate 384

Vijay Shukla,Bhaskar Paul, M. K. Bairwa, V. Bhardwaj, Rajpal Singh Dipen Vachhani, Rahul Shukla, K.K. Pant, C.B. Panwar, D. Narwat, R. Arya, B. N. Upadhyaya, K. S. Bindra

Laser Spectroscopy and Applications

CP-09-304 Theoretical estimation of isotopic concentration of Yb-176 produced through three-step resonant photoionization method 388

Biswajit Jana,Biswaranjan Dikshit

CP-09-316 Simulation of optical emission spectra of Hastelloy plasma for laser-induced 392

	breakdown spectroscopy applications *M.S. Suryan Sivadas,Lekha Mary John, K. K. Anoop*	
CP-09-344	Quantitative Elemental Analysis of copper alloy using laser-induced breakdown spectroscopy *Lekha Mary John,K. K. Anoop*	396
CP-09-356	Concentration dependent optical studies of Nd^{3+}-doped P-Ba-La glasses for future photonic applications *P.Ramprasad , C.K. Jayasankar*	400
CP-09-401	Three-Step Lithium photoionization by optogalvanic spectroscopy *V. K. Saini ,G. N. Tiwari, S. K. Dixit*	404
CP-09-415	Automation of delay scan photoelectron spectroscopy experiments *H. R. Bundel, Shradha Tiwari , Himanshu Singhal, Mukund Kumar, J. A. Chakera, Viraj Bhanage*	408
CP-09-424	Improving the Signal-to-Noise Ratio of Atomic Transitions in LIBS Using Two-dimensional Correlation Analysis *Linga Murthy Narlagiri,S. Venugopal Rao*	412
CP-09-449	Assessment of hand sanitizers using vibrational spectroscopy methods *Soumyabrata Banik,Sindhoora Kaniyala Melanthota, Krishna Kishore Mahato, Anjana Anandan Vannathan, Sib Sankar Mal, Nirmal Mazumder*	416
CP-09-451	Development of a time-of-flight mass spectrometer for isotope selective photoionization of medical isotopes *A. U. Seema, D. Biswal , R.C. Das, Asawari. D. Rath*	421
CP-09-462	Elemental identification and alloy classification by laser-induced breakdown spectroscopy *Supriya K, Megha Mohan, Balakrishna Prabhu B. N., K. K. Anoop*	425
CP-09-464	Studies on Raman spectroscopy of pure ghee and vanaspati *A. Dalal, A. Srivastava, Alka, N. Kumar, H. Krishna, S. K. Majumder*	429
CP-09-466	Raman spectroscopy for monitoring temperature-induced changes in mustard oil *A. Srivastava, A. Dalal, H. Krishna, S. K. Majumder*	433
CP-09-470	Precise determination of laser wavelengths pertaining to three-step selective photoionization for enrichment of ^{176}Yb and qualification of process selectivity *D. Biswal.,A. U. Seema, R. C. Das, D. R. Rathod, A. K. Singh, A. Khattar, J. S. B. Singh, A. Wahid, P. R. Mohite, S. K. Maurya, J. S. Dhumal, J. Thomas, Asawari. D. Rath, S. Kundu*	437
CP-09-475	Trace elemental detection in liquid sample using Laser Induced breakdown spectroscopy and its application in environmental field *Keerthi K, Anish Kumar Warrier, Sajan D. George, Suresh D. Kulkarni, Santhosh C., Unnikrishnan V. K.*	441

CP-09-488 Speckle Interferometry to determine thickness of PVA doped Graphene Oxide of film 445

Athira A, Alok Sharan

CP-09-520 Vortex Beam based Micro-Raman Spectroscopy of optically Trapped Functional Erythrocytes 449

Ghanashyam C,Santhosh Chidangil and Aseefhali Bankapur

CP-09-550 Development of a combined LIBS-Raman spectroscopic system for rapid characterization of plastics 453

Adarsh U.K.,Bhoje Gowd E, Aseefhali Bankapur, Santhosh Chidangil, Unnikrishnan V.K.

CP-09-561 Optical and spectroscopic properties of Sm^{3+} ions doped fluoroborosilicate glasses for photonic device applications 457

Megala Rajesh, B Deva Prasad Raju,

CP-09-579 Laser spectroscopy of TaC in jet-cooled beam 461

Sheo Mukund,Soumen Bhattacharyya, S.G. Nakhate

CP-09-596 Detection of antioxidant compounds using surface enhanced Raman scattering spectroscopy 464

Sweta Sharma,Aarti Jaiswal and K. N. Uttam

CP-09-605 Confocal Raman Micro-spectroscopic Investigation of Phytochromes present in the petals of different Cultivars of Bougainvillea Flowers 468

Aradhana Tripathi,Aishwary Awasthi, Sweta Sharma and K N Uttam

CP-09-621 Laser Interferometry for distance measurement: Demonstration in laboratory 472

Sreelekshmi C A,Hriday Dath, B. V. S. Shravan, Dr. Radhika V. N., Dr. Umesh Kadhane, J. Krishnakumar, S. Hemachandran

CP-09-640 Influence of solvents on the kinetics of ground-state bleaching and vibrational levels of the first excited state, and excited-state absorption of IR800 dye. 476

Sajin Ponnan,Desai Narayana Rao and Sri Ram G Naraharisetty

CP-09-641 THz- TDS As a diagnostic tool for monitoring the water content in different coloured Indian Almond (Catappa) leaves 479

Nagaraju Menchu,Chandan Ghorui, Damarla Ganesh, Prof. Anil Kumar Chaudhary

CP-09-664 Synthesis and spectroscopic characterization of orange-red emitting Sr2Sb2O7:Eu3+ Phosphor for white light emitting diodes 483

Anns George, P R Biju

Lasers in Chemistry, Biology and Medicine

CP-10-278 Influence of nanosecond laser induced micro-grooved stainless steel on cellular behaviour 487

Sunita Kedia,A. G. Majumdar, M. Subramanian, A. K. Sahu, J. P. Nilaya

CP-10-280	Pulsed Laser Deposition of Zirconia thin film on Ti6Al4V Bio-alloy to improve tribological properties *Sunita Kedia, J. P. Nilaya*	491
CP-10-281	Picosecond laser nano-pitting on stainless steel by micro-particle lens array to improve hydroxyapatite growth *Sunita Kedia,A. K. Sahu, J. P. Nilaya*	494
CP-10-282	Infrared laser assisted deactivation of bacteria and virus samples *Tatsat Dwivedi,M. B. Sai Prasad, J. Padma Nilaya, Vandan Nagar, A.V.S.S.N. Rao, R. Shashidhar, S. K. Ghosh*	498
CP-10-373	Study of the effects of short term hyperglycemic exposures on human red blood cells *Yashveer Singh,Aniket Chowdhury, Raktim Dasgupta, Shovan Kumar Majumder*	502
CP-10-434	Raman spectroscopy based detection of microalbuminuria: A feasibility study *Rashmi Shrivastava,Jyoti Kumawat, Amrita Srivastava, Nitin Kumar, Hemant Krishna, Shovan K. Majumder*	506
CP-10-481	Studies on photo stabilityof Rhodamine 110 (Rh 110) in aqueous binary solvents *Ayentika Sen, A. Wahid, A. Singh, Asawari D. Rath, S. Kundu*	510
CP-10-570	Evaluation of an indigenously developed Ultraviolet-C light based wide area disinfection device for inactivation of SARS-CoV-2 virus and pathogenic bacteria *Khageswar Sahu , Vijay Kumar, M Aswin Kumar, Madhuri Taranikanti, Srinivas M, Shankar V. Nakhe and Shovan Kumar Majumder*	514
CP-10-581	Investigation of Phytochromes present in the petals of different cultivars of bougainvillea flowers by laser induced fluorescence spectroscopy *Chhavi Baran, Rahul Uttam, Sweta Sharma and K N Uttam*	518
CP-10-732	Raman spectroscopy for dissolution testing of paracetamol tablets: an exploratory study *V. Kumar, R. Shrivastava, J. Kumawat, N. Kumar, S. Maru and S. K. Majumder*	521

Laser and Fiber based Instrumentation

CP-11-392	Investigation on rectangular dark pulse in mode-locked fiber laser *Nitish Paul,C.P. Singh, P.K. Gupta, P.K. Mukhopadhyay and K.S. Bindra*	525
CP-11-435	Numerical studies on propagation characteristics of dark pulses in optical fiber *Meghna Mukhopadhyay,Afreen Khursheed, Bhupendra Singh Kirar*	529
CP-11-508	Intensity referencing in fibre optics based temperature Sensing *V.K. Dubey, Piyush Saxena, Vivek G., Inderjeet Singh, Jitendra Kumar, Om Prakash, S.K. Dixit, R. Arya, S.V. Nakhe*	533

CP-11-509 Triggering and synchronisation of spark gap switches using optical beam delivery System 536

Ritu Agarwal, Amitava Roy, Archana Sharma

CP-11-525 Design of optical interface module for fiber delivered DPSSGL beam to pump dye laser amplifier 540

A. Khattar,A.K. Singh, S. Kundu

CP-11-573 Inscription of long period fiber grating near phase matching turning point by frequency doubled copper vapour laser 544

R. Mahakud, J. Kumar, S. Chaube, V.K. Srivastava, S. Kumar, U. Kumbhakar, O. Prakash, S. K. Dixit

CP-11-592 Studies on the thermal behaviour of different resonant modes of a long period grating 548

V. K. Srivastav, R. Mahakud, J. Kumar, S. Kumar, U. Kumbhkar, O. Prakash, S. K. Dixit

CP-11-594 High temperature chirped FBG fabrication by thermal stretching of regenerated FBG 552

J. Kumar,R. Mahakud, S. Kumar, U. Kumbhkar, O. Prakash, S. K. Dixit, S. V. Nakhe

CP-11-607 Development of automated polarization phase shifting laser Fizeau Interferometer for flatness measurement of polished optical surfaces 556

Y. Pawan Kumar, Sarthak Gupta, Siddesh Pai, Deepak Daiya, Inderjeet Singh, Rishipal, A. K. Biswas, Sarvendra Singh, M. P. Kamath, Rajiv Jain, P. Saxena, N. S. Benerji, K.S. Bindra

CP-11-633 Design and Simulation of MOEMS Mach-Zehnder Interferometer 560

Ashish Singh Bais, J. T. Andrews

CP-11-644 Initial lab test results of Magneto-Optic Current Sensor diagnostic developed for plasma current measurement in tokamaks 564

Santosh P. Pandya, Kumudni Assudani, Praveenlal E. V., Lavkesh T. Lachwani, Sameer Kumar Jha, M .V. Gopalakrishna and Surya Kumar Pathak

CP-11-661 Investigation of gamma radiation response of multimode graded index fiber in visible region for distributed dosimetry applications 569

S. Chaubey, M. K. Saxena, J. Kishore, T. K. Sahu, G. Haridas, O. Prakash, S. K. Dixit

Electronics and Instrumentation for Lasers

CP-12-186 Implementation of position measuring system for Hall probe alignment in undulator magnetic field measurement 573

Saif Mohd Khan,Mona Gehlot, G. Mishra

CP-12-264 Design and analysis of 2x1 photonic temporal multiplexer using SOI ring resonator for switching and logical applications 577

Madhupriya G, Mubarak Ali Meerahsa, Indhumati Ravirajan, Krishnamoorthy Pandiyan

CP-12-284 Non Contact method for respiration rate measurement with optical interferometry 581

Anu Singh,Saurabh Mehta, Arpit Rawankar

CP-12-516 Development of EPICS based control system for Nd:Glass laser amplifier 585

Hitendra Singh Chouhan,O.P. Joshi, Bhupinder Singh, M.S. Ansari

CP-12-577 Development of a wavemeter based cavity stabilization system for the high repetition rate SLM OPO 589

C. S. Rao, P. Chakrabarthy, N. Kawade

CP-12-651 Microcontroller based control for driving multiple direct digital synthesizers 593

Sasikumar.K.K, BVS. Shravan, Radhika.V.N, Rekha.A.R, Krishnakumar.J

CP-12-669 Programmable power supply for laser based welding system 596

Vijay Bhawsar, Sudheer Kushwaha, Shryner Penumala, Jagriti Khanwalkar, B.N. Upadhyaya, R. Arya

CP-12-696 Static mode performance testing of a streak tube 601

Jankee Upadhyay, Sudhir Kumar, Piyush Saxena, and R. Arya

CP-12-729 Development of control software for cold atom interferometry experiments 604

Ayukt Kumar Pathak,Shradha Tiwari, P P Deshpande, Viraj Bhanage

Theses Abstract

TH-073 Laser drilling and welding of advanced engineering materials: An experimental investigation 608

Suman Chatterjee

TH-081 Studies on electron beam and laser surface melting and welding of INCONEL 718 616

Sumit Kumar Sharma

TH-112 Efficient Terahertz (THz) generation from some indigenously grown organic nonlinear crystals and designing of band pass filters for spectroscopy of high energy materials. 618

Ganesh Damarla

TH-146 A study of nonlinear optical properties of metamaterials 622

Dheeraj Dulhani

TH-161 Magneto-optical transport studies on ultra-low disordered semiconductor quantum wells grown by MOVPE 626

Subhomoy Haldar

TH-187 Ultrafast molecular dynamics and third-order nonlinear optical properties of novel organic, inorganic and energetic materials 630

Katturi Naga Krishnakanth

TH-188 Rigid, flexible SERS substrates fabricated using femtosecond laser pulses for explosives detection 634

Moram Sree Satya Bharati

TH-189 Dynamics of confined laser induced/ablative plasmas and shock waves 639

Nagaraju Guthikonda

TH-213 Linear and nonlinear optical exciton probing in inorganic-organic hybrid semiconductors 644

Mohammad Adnan

TH-222 Studies on electromagnetically induced transparency in ^{87}Rb atoms 648

Charu Mishra

TH-231 Study and characterization of laser based particle assisted surface nanostructuring and cleaning 652

Bijoy Sugathan

TH-249 Structural and optical characterization of pulsed laser deposited mos_2 and ws_2 layered thin films and quantum dots 656

Gobinda Pradhan

TH-268 Study of spectral beam combination techniques for high power, pulsed, dye laser applications 659

Paramjit Rana

TH-301 Optical spectroscopy based urine analysis for disease diagnosis 664

Surjendu Bikash Dutta

TH-338 Raman and time-domain photoacoustic and terahertz spectroscopy of some inorganic, organic and high energy materials 667

Archana Kumari

TH-370 An Insight into the Optical Nonlinearities of Certain Au/Ag Based MetalMetal/Organic Core Shell Nanostructures and Nanohybrids 671

E. Shiju

Program Schedule 674

ILA Best Thesis Awards 681

ILA Best Poster Awards 682

List of ILA Exhibitors 683

Committee Details 684

Invited Talks

Photonics Gone Rogue

Raman Kashyap
The Fabulas Laboratory
Department of Engineering Physics and the Department of Electrical Engineering
Polytechnique Montreal
Montreal, Canada

Abstract

Random events occur in nature all the time. There is great scientific interest in them as they are the vectors of change in the weather, spread of disease, exhibit glassy magnetic behavior, instabilities, turbulence, symmetry breaking, the formation of rogue waves, initiating chaos, and leading to observations of localization in the solid state.

Photonics is an interesting platform to study these effects to provide insights on these various observations within the confines and convenience of a laser laboratory. The onset of chaos and lasing has thus become an important tool in the study of random behavior, such as through nonlinear Brillouin, Raman, and Rayleigh scattering as well as through scattering in lasing media.

The Fabulas laboratory has been engaged in the fabrication of devices such as Random lasers, Rogue gratings as analogues of natural events, and have recently demonstrated random number generation (RNG) at Tbs^{-1}, a world record, through light scattering. This presentation will introduce recent research at Polytechnique Montreal on ultrafast RNG, localization of light, and how the removal of randomness can result in high quality, well behaved, state-of-the-art lasers.

Plasmonic technologies for alloyed and hybrid metasurfaces

Olivier J.F. Martin
Nanophotonics and Metrology Laboratory, Swiss Federal Institute of Technology Lausanne (EPFL)

Abstract

After a general introduction to plasmonics, the optics of metal nanostructures, I will describe different technologies used for the fabrication of metal nanostructures with well-controlled features down to about 10 nm. Only a few plasmonic metals, such as gold, silver or aluminum, produce strong optical resonances, thus limiting the spectral range where plasmonics can be used. To extend that range, we recently developed a technology for the fabrication of Au-Ag alloyed nanostructures with well-controlled shapes that can be combined into metasurfaces to produce lenses or holograms. The working principle of these metasurfaces consists in engineering the phase associated with light scattered from metallic nanostructures to mimic the effects of gratings, lenses or phase plates.

While the metal dictates the wavelength range where plasmonic effects can occur, the dimensions and the shape of the nanostructures control the type of optical resonances that can be supported by a given nanostructure assembly. These optical resonances can be divided in essentially two families: electrical and magnetic modes. At optical frequencies, it is believed that electrical resonances always dominate the response of the system, which has led to some confusion on the so-called magnetism at optical frequencies. I will however demonstrate that it is possible to produce plasmonic systems that radiate purely magnetic light. Finally, I will share some recent results on hybrid nanostructures that combine plasmonic elements with dielectric resonators and show how they can be utilized for sensing.

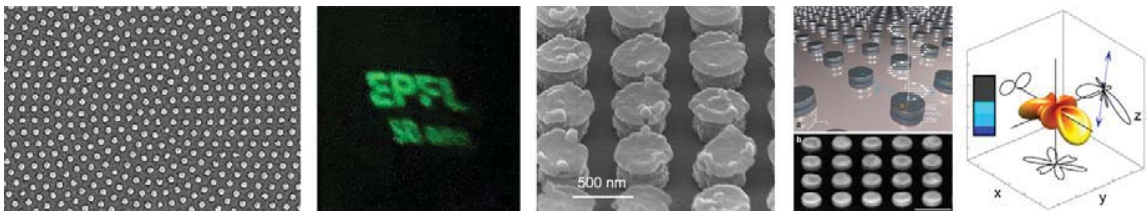

The beginnings of gravitational wave astronomy: current state and future

R. Weiss
MIT on behalf of the LIGO Scientific Collaboration

Abstract

The first detection of gravitational waves was made in September 2015 with the measurement of the coalescence of two ~30 solar mass black holes at a distance of about 1 billion light years from Earth. After an introduction about the field and some of the technology, the talk will provide a review of more recent measurements. Many more black hole events have been detected as well as the first detection of the coalescence of two neutron stars and the beginning of multi-messenger astrophysics. The talk will end with a discussion of some prospects for the field.

Pulses and patterns in ultrafast fiber lasers: the dissipative soliton approach

Ph. Grelu(1), K. Nithyanandan(1,2), Z. Wang(1,3), S. Hamdi(1), A. Coillet(1), P. Tchofo-Dinda(1)
(l) Laboratory ICB UMR 6303 CNRS, Photonics Department, Université Bourgogne—Franche-Comté (UBFC) 9 Av. Savary, F-21000 Dijon, France,
philippe.grelu@ubfc.fr
(2) Current institution: Indian Institute of Technology Hyderabad, Kandi, Sangareddy Telangana 5022285
(3) Current institution: The Institute of Optics, University of Rochester, Rochester NY 14627, USA

Abstract

Schematically, the presentation is divided in two parts. The first part is intended to the broader audience of laser physicists: after briefly recalling some properties of ultrafast fiber lasers, I present the concept of a dissipative optical soliton, and its related principal dynamical features [1,2]. This concept is especially relevant to interpret the dynamics of mode-locked lasers in general, and fiber lasers in particular, the latter being prone to displaying a greater diversity in terms of ultrafast nonlinear dynamics. As a vivid application, we use the concept to understand the generation of ultrashort laser pulses within laser cavities possessing a marked normal dispersion regime, which is counterintuitive when referring to the balance between nonlinearity and dispersion required for conventional optical solitons. The second part of the presentation aims at presenting some advanced characterization features for complex ultrafast dynamics, which currently drive substantial fundamental interest. We first investigate the properties of dissipative soliton molecules, which are self-assembled compact optical pulse patterns that manifest in various states, such as stationary, oscillating or vibrating soliton molecules, in (distant) analogy with the properties of matter molecules [3,4]. The experimental method to characterize the relative motions within a few-picosecond- duration soliton molecule is explicated [5]. Finally, I present the paradoxical generation of chaotic ultrafast pulses, also termed noise-like pulses, which result from a puzzling interplay between localization and pulse breakup [6]. These chaotic pulses are interpreted as incoherent dissipative solitons, illustrating further that ultrafast pulse generation extends well beyond the concept of mode locking [7].

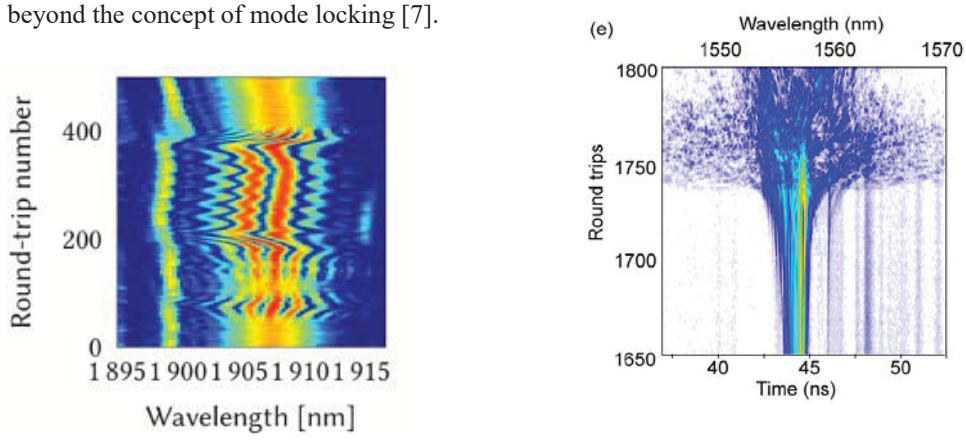

Figure: Real-time spectral recording of ultrafast laser dynamics using dispersive Fourier-transform. (Left) Unstable vibrating soliton molecule. (Right) Buildup of an incoherent dissipative soliton.

Reference

[1] Ph. Grelu and N. Akhmediev, "Dissipative solitons for mode-locked lasers," Nat. Photonics **6**, 84 (2012).
[2] Ph. Grelu, "Solitons and dissipative solitons for ultrafast lasers," in Handbook of Laser Technology & Applications, 2nd Edition, C. Guo (Ed.) Taylor & Francis (March 2021).
[3] K. Krupa, K. Nithyanandan, U. Andral, P. Tchofo-dinda, and Ph. Grelu, PRL **118**, 016613 (2017).
[4] G. Herink, F. Kurtz, B. Jalali, D. Solli, and C. Ropers, Science **356**, 50 (2017).
[5] Z.Q. Wang, K. Nithyanandan, A. Coillet, P. Tchofo-dinda, and Ph. Grelu, Nature Comm. **10**, 830 (2019).
[6] M. Horowitz, Y. Barad & Y. Silberberg, Opt. Lett. **22** 799 (1997).
[7] Z.Q Wang, K.Nithyanandan, A. Coillet, P. Tchofo-Dinda & Ph. Grelu, Phys. Rev. Res. **2** 013101 (2020).

Laser Welding in Fabrication of FBR fuel pins: Metallurgical Considerations

S.K. Albert, R. Ravikumar, R. Lavakumar, Y.V. Harinath* and T.V. Prabhu
Indira Gandhi Centre for Atomic Research, Kalpakkam 603 102
**Water & Steam Chemistry Division, BARC, Kalpakkam 603102*

Abstract

Mixed Oxide (MOX) of Uranium and Plutonium is the fuel currently used for most of the FBRs and metallic fuels (alloy of U-Pu or U-Pu-Zr) are being considered for the future FBRs. For MOX and other ceramic fuels like carbides, fuel pins are made from austenitic stainless steels while for metallic fuels, ferritic steels like Grade 91 steel are being considered. Welding of clad tube with end plug is a critical fabrication step in the production of fuel pins and traditionally Gas Tungsten Arc Welding (GTAW) process is employed widely for this application. However, in recent times, laser welding is replacing GTAW process and fuel pin fabrication for Prototype Fast Breeder Reactor (PFBR) involves use of laser welding for joining of clad tube made of Alloy D9 (15Cr-15Ni-2Mo-Ti stainless steel) with end plugs made of 316LN SS. Recently, an improved version of Alloy D9, (Alloy D9I or IFAC-1) with controlled addition of Si and P and having better resistance to void swelling than Alloy D9 has been developed and trials are in progress to develop procedures welding of clad tubes of this new alloy with 316LN SS plugs using both GTAW and laser welding processes. Similarly, development of procedure for welding of clad tubes of Grade 91 steel with end plugs made of the same steel using laser welding process is also in progress. In the former, susceptibility of the joint due to absence of delta ferrite in the fusion zone is a concern while in the latter, possible reduction in the mechanical properties due to presence of delta phase is a concern! Work that is in progress in IGCAR to develop laser welding procedures for these two types of fuel pins are presented and discussed in this paper.

Power Scaling Limits in High Power Fibre Lasers

M.N. Zervas[1,2]
[1]Optoelectronics Research Centre, University of Southampton, Southampton SO17 1BJ, UK
[2]Advanced Laser Lab, ORC/TRUMPF Lasers UK, Southampton, UK.
*mnz@soton.ac.uk

Abstract

Transverse mode instability (TMI) is compared to thermal lensing (TL) power threshold and used to derive power scaling limits in high power fiber amplifiers. The TMI power threshold is shown to be ~65% of the TL one and dominates power scaling. In addition to commonly used limiting effects, we introduce a bend-induced mechanical reliability criterion which limits the maximum allowable cladding diameter to ~600μm. This also results in the introduction of a critical pump brightness, the minimum required pump brightness at which the maximum signal power is achieved. The maximum achievable power depends primarily on the choice of pumping wavelength, amplifier gain and heat coefficient. Maximum signal powers of ~28kW to ~38kW, for diode pumping (λp=976nm), and ~35kW to ~52kW, for tandem pumping (λp=1018nm), are predicted for single-mode fiber amplifiers operating at signal wavelength λs=1070nm, when the amplifier gain is increased from 10dB to 20dB. For an amplifier gain of 10dB, the maximum achievable signal power varies from 85kW to 25kW for tandem pumping, and 35kW to 20kW for diode pumping, when the heat coefficient varies from 1% to 15% and 5.5% to 20%, respectively. The corresponding critical pump brightness varies from ~0.50 W/(μm2 sr) to ~0.14 W/(μm2 sr) for tandem pumping, and ~0.25 W/(μm2 sr) to ~0.13 W/(μm2 sr) for diode pumping.

Optical Fiber Biosensors: Principles and Applications

Dr. Umesh Tiwari
CSIO, Chandigarh

Abstract

Development of biosensors is driven by the sustained requirement of sensitive, rapid, and real time monitoring techniques in a broad range of areas, e.g. defense, medical, environmental, pharmaceutical, bioprocessing, or food technology. Optical fiber based biosensors are useful for the analysis of a wide range of analytes, including glucose and other clinically important markers in medical diagnosis, food safety, quality control and environmental monitoring. During a sensing signal transmission via optical fiber, there are less electro and magnetic interference, and less influence of ionization radiation and the ability to measure ultra-high speed events. Fiber grating based biosensors is emerging as an efficient, non-destructive and selective technique for the detection of organic and biological species. Here, various sensing techniques based on Enzyme Immobilization on optical fiber for sensitive and selective detection of various analytes will be presented. The presented research demonstrates the developed of a long period fiber grating based sensor for the label free quantitative estimation of Triacylglyceride concentration by the successful covalent immobilization of lipase enzyme directly on the optical fiber. In a recent invention we have realized a new alternative and far-less complicated strategy to immobilize the biorecognition protein (an antibody) over the surface of an optical fiber. A fiber was first gold coated, followed by its modification with MoS2 nanosheets. The nanosized MoS2 covering on the optical fiber should provide a larger surface area over the optical fiber to design an analysis zone. Exploiting the well-known hydrophobic feature of the MoS2 nanosheets, a biorecognition protein (anti-BSA antibody) was interfaced on to the optical fiber.

Advancement of Speciality Fibre Optic sensors for In Situ monitoring

Sanjeev Raghuvanshi
IIT, ISM Dhanbad

Abstract

Non-contact type of measurement with the help of optical technologies in the field of sensing and instrumentation has become a revolutionary idea in the present scenario. The advanced feature of optical fiber/waveguide, such as exceptional sensitivity, safety, and accuracy toward the external environment has made the research arena inevitable and forced us to develop new ideas. This property has a given way to a unique variety of optical sensors which are free from electromagnetic interference. In parallel to these advantages, optical sensor technology has perfect coordination between the optoelectronic and fiber optic communication industry. The current scenario observes an improved quality of optical sensors, thereby increasing the possibility of replacing traditional sensors. Presently numerous research work is undertaken using fiber optic sensors with different interrogation techniques. Consequently, optical sensors with material technology have also opened a new field for sensing platforms. The present research work focuses on the theory, simulation, design, analysis, and development of refractometric based optical sensors based on modified fiber Bragg grating (Nano-material coated novel structure) and Surface Plasmon Resonance (SPR) sensing structure (thin-film multilayer structure, power-coupling structure: prism, optical fiber), to improve power-coupling for high-sensitivity applications. The proposed talk is aimed to provide an insight on recent advancement of Speciality Fibre Optic sensors for In Situ monitoring**".**

Laser based Measurements and Perimeter Intrusion Detection

Aseem Singh Rawat
LPTD, BARC, Mumbai

Abstract

Laser based measuring instruments have distinct advantage of being non-contact, non-destructive and fast in nature. They can be used for on-line monitoring and process control. There are various optical techniques which are used for measurement of different parameters of an object or in a process. Laser being coherent in nature is the most appropriate tool for implementing the optical techniques. In this talk, optical triangulation technique and interference based technique for vibration measurement, shadow pulse technique for diameter measurement and time of flight technique for flow visualisation will be discussed. Laser based technique for perimeter intrusion detection has been used for security of critical installations of large periphery. The talk will cover Mach-Zehnder interferometer based perimeter intrusion detection system using single mode fibre optic cables.

Physics and Applications of Scattering with Extreme Light

Donald Umstadter
Extreme Light Laboratory
University of Nebraska-Lincoln

Abstract

I will discuss the results of recent experiments on the physics and applications of nonlinear relativistic scattering of intense laser light with electron beams and plasma. Applications of compact laser-driven electron accelerators and x-ray sources are also discussed.

1. W. Yan, C. Fruhling, G. Golovin, D. Haden, J. Luo, P. Zhang, B. Zhao, J. Zhang, C. Liu, M. Chen, S. Chen, S. Banerjee, and D. Umstadter, "High-order multiphoton Thomson scattering," *Nature Photonics*, **11** (8), 514-520 (2017).
2. G. Golovin, W. Yan, J. Luo, C. Fruhling, D. Haden, B. Zhao, C. Liu, M. Chen, S. Chen, P. Zhang, S. Banerjee, D. Umstadter, "Electron Trapping from Interactions between Laser-Driven Relativistic Plasma Waves," *Physical Review Letters* **121**, 10, 104801. (2018).
3. C. Fruhling, G. Golovin, and D. Umstadter, "Attosecond electron bunch measurement with coherent nonlinear Thomson scattering," *Physical Review Accelerator and Beams* **23**, 072802 (2020).
4. D. Haden, G. Golovin. W. Yan, C. Fruhling, P. Zhang, B. Zhao, S. Banerjee, D. Umstadter, "High energy X-ray Compton spectroscopy via iterative reconstruction," *Nuclear Instruments and Methods in Physics Research Section A* **951**, 163032 (2020).

Probing Ultrafast Dynamics of Water at Aqueous Interfaces with Femtosecond Two-Dimensional Heterodyne-Detected VSFG Spectroscopy

Mohammed Ahmed, Satoshi Nihonyanagi and Tahei Tahara
Molecular Spectroscopy Laboratory, RIKEN, Japan
RIKEN center for Advanced Photonics (RAP), RIKEN, Japan

Abstract

Aqueous interfaces play important roles in the interfacial chemistry relevant to atmospheric aerosol, electrochemistry, "on-water" catalysis, biological membrane processes and applied sciences. Nevertheless, molecular-level understanding of aqueous interfaces is at its infancy due to the lack of suitable surface-selective technique that can probe interfacial water molecules, having a typical thickness of a few nanometers. Vibrational sum frequency generation (VSFG) spectroscopy has inherent surface-selectivity, and it is a powerful tool to study the aqueous interfaces[1]. In particular, phase-resolved heterodyne-detected VSFG (HD-VSFG) spectroscopy developed by our group[2] provides the accurate vibrational spectra of interfacial molecules that can compared to the IR/Raman spectra in the bulk. Moreover, the sign of the HD-VSFG spectra provides information about the net orientation of interfacial molecules. Recently, by combining femtosecond IR excitation (pump) with HD-VSFG (probe), we realized time-resolved- (TR-)[3] and two-dimensional (2D-) HD-VSFG[4] techniques which can measure the ultrafast dynamics of interfacial molecules in the femtosecond time scale. 2D HD-VSFG is an interface analogue of 2D IR, and it has been successfully applied for clarifying the ultrafast dynamics at aqueous interfaces[5].

In this talk, I will present our recent 2D HD-VSFG study[6] on the femtosecond hydrogen-bond dynamics of water at oppositely charged hydrophobic ion/water interfaces. The obtained results unfold the existence of energetically isolated distinct water structures at the aqueous interface, which relies on the sign of charge of the hydrophobic ion on the water surface.

References:

1. Y. R. Shen, V. Ostroverkhov, *Chem. Rev*., **2006**, 106, 1140.

2. S. Nihonyanagi, J. A. Mondal, S. Yamaguchi, T. Tahara, *Annu. Rev. Phys. Chem.,* **2013**, 64, 579.

3. S. Nihonyanagi, P. C. Singh, S. Yamaguchi, T. Tahara. *Bull. Chem. Soc. Jpn.*, **2012**, 85, 758.

4. P. C. Singh, S. Nihonyanagi, S. Yamaguchi, T. Tahara. *J. Chem. Phys.,* **2012**, 137, 094706

5. S. Nihonyanagi, S. Yamaguchi, T. Tahara, *Chem. Rev.,* **2017**, 117, 10665.

6. M. Ahmed, K. Inoue, S. Nihonyanagi, and T. Tahara, *Angew. Chem. Int. Ed.,* **2020**, 59, 9498.

Plasma Acceleration- What were we thinking in those early days and where are we headed?

Chan Joshi
UCLA, U.S.A.

Abstract

The concept of particle acceleration using collective field generated by charge separation of ions and electrons in a plasma, predated the now famous Tajima and Dawson paper. The many avatars of this concept had had a modest success, until Dawson proposed using a relativistic plasma wave to accelerate electrons. The initial response to this paper was either total disbelief or skepticism. It was in this climate that the UCLA- Laser-Plasma Group (later came to be known as the UCLA-Plasma Accelerators Group), started the first experimental program to demonstrate the most audacious prediction of this idea- that plasma waves could support 1 GeV/cm accelerating gradients. I will discuss what we were thinking in those early days and how a supportive high-energy physics community and funding agency were patient and instrumental in conclusive demonstration of acceleration of externally injected electrons by a relativistic plasma wave. Thereafter the plasma acceleration field rapidly spread worldwide as CPA lasers became commonplace. These lasers and GeV class charged particle beams provided by SLAC enabled rapid progress of the field that included high gradient acceleration of both electrons and positrons, acceleration of narrow energy spread beams containing a significant charge and high efficiency of energy extraction from wakes. I will describe our ongoing efforts aimed at demonstrating a single stage of a multi-stage electron arm of a future collider that will provide spin polarized electron bunches from a plasma accelerator for the first time. As for the ultimate goal of building an ee+ plasma-based linear collider, many basic problems still remain providing an opportunity for young scientists to enter and make their mark on this field.

Visualization of charge separation at the in-plane organic heterojunctions using pump-probe microscopy

Sachin Dev Verma
Department of Chemistry
IISER Bhopal
E-mail: sdv@iiserb.ac.in

Abstract

Organic compounds showing semiconducting properties opened up the way for their application in organic photovoltaics (OPVs). Lower cost, facile solution processing, flexibility, and large-area printing production make OPVs promising contender for next generation technology platform to match the increasing demands for renewable energy. The functionalities of organic semiconductor depend on their capability to carry and transport charges (electron and holes) and neutral excitons (electron hole pairs). Charge separation and transport in organic photovoltaic cells governs the overall efficiency, understanding the underlying mechanism could facilitate the efficiency optimization. Charge separation occurs at the donor-acceptor heterojunction where excitons dissociate into free charges. Subsequently, before being captured or lost, electrons and holes transport through the respective acceptor material. Understanding of the charge separation and transport at ultrafast timescale and molecular length-scale shall provide us with proficient schemes for molecular design and device architecture to achieve unprecedented efficiencies. In this talk, I shall discuss direct visualization of charge separation and transport at the in-plane organic heterojunctions with ultrafast timescale and molecular length-scale by employing pump-probe microscopy.

Spatiotemporal Dynamics of Relativistically Hot Plasmas

G. Ravindra Kumar
Tata Institute of Fundamental Research, Mumbai 400 005
Email: grk@tifr.res.in

Abstract

The dynamics of relativistic electrons accelerated in a solid by a high intensity, femtosecond laser are of utmost importance for target heating and many secondary processes like hard x-ray and ion emission [1]. Equally important are strong shocks and giant magnetic fields created by these electrons. Our group has recently adapted an existing technique to develop a novel diagnostic for sub-picosecond monitoring of transverse plasma motion and shock propagation. I will present the first results from these studies [2] and examine plasma motion, generation of megagauus magnetic fields and their turbulent evolution [3,4].

Experiments mentioned above have been performed with a high contrast, 150 TW femtosecond CPA laser system at TIFR. *This work is a collaboration with Institute for Plasma Research, Gandhinagar and IIT Delhi in India and RAL and York University in the UK.*

References:

[1] M. Shaikh et al., Phys. Rev. Lett. **120**, 065001 (2018)

[2] K. Jana et al., submitted (2021)

[3] G. Chatterjee *et. al.*, Nature Commun. 10.1038/NCOMMS15970 (2017)

[4] A. Das *et. al*, Phys. Rev. Res. **2**, 033405 (2020)

Making the Stories Come True: Molecular Laser Isotope Separation to Coherent Control

Sisir K Sarkar
Bhabha Atomic Research Centre and Savitribai Phule Pune University

Abstract

Chemistry is A + B → C + D, substances and their transformations. Change symbolized by the arrow (→) in the equation, is always of real value, whether it is the chemistries of material synthesis, food preparation, explosives, dyes or metallurgy. One of the most fundamental problems in chemistry is understanding how chemical reactions occur: that is, how reagents make their journey to products. But all along it has been easy to focus on the before and after, on the reactants and products, on the noun and not on the verb. But there is a change in the chemistry today, for the arrow is now well on its way to being understood.

The present narrative will examine the evolution of the field of Chemical Dynamics in the Department of Atomic Energy. Based on the basics of reaction kinetics we began answering the above queries and then gradually move on to relatively young but already very busy area of coherent control of chemical processes. During this journey we pursued and recount chronologically a few contemporary stories, namely laser isotope separation, ultrafast photochemistry and spectroscopy which are the jewel in the crown of Chemical Sciences.

Control science has already taken observational science one step further, mastering the complexity of materials and chemical change and replacing serendipity with intention. Presently we are in the process of demonstrating that the arrow in the chemical process can now be bend to direct the reaction to the targeted products - helping them to break their chains of bondage - a happy ending.

Novel multifunctional organic chromophores for non-linear optical applications

Raavi Sai Santosh Kumar and Chinmoy Biswas
Department of Physics, Indian Institute of Technology Hyderabad, Kandi, Sangareddy, 202285, Telangana
E-mail: sskraavi@phy.iith.ac.in

Abstract

Tetrathiafulvalene (TTF) molecules and their derivatives have been the focus of recent attention owing to the presence of abundant π-electrons, strong intramolecular charge transfer (ICT) properties making them attractive for various organic electronics and optoelectronic applications. In this work, a comprehensive investigation is presented on the photophysical and third-order nonlinear optical (NLO) properties of two thioalkyl substituted tetrathiafulvalene molecules (referred here as, G1 and G3) to understand their utility as photosensitizers for dye-sensitized solar cell (DSSC) and optoelectronic applications. Both steady-state and time-resolved (in fs–ns time regime) absorption and photoluminescence (PL) spectroscopy techniques were employed to comprehend the excited state properties of the molecules in solution as well as thin-film deposited on both glass and mesoporous TiO_2 layers. The spectroscopy measurements in solution and thin-film deposited on glass provided the excited state properties of dye molecules. Time-resolved PL measurements at the dye-TiO_2 interface provided initial evidence of electron injection by fast PL quenching decay dynamics for both the molecules. Detailed target analysis of the femtosecond transient absorption spectroscopy (TAS) data of the dye-TiO_2 sample revealed a multi-step ultrafast electron injection for both molecules, the fastest injection component being 373 fs and 314 fs for G1 and G3 molecules respectively. The ultrafast NLO properties of G1 and G3 were studied using the Z-scan technique with 800 nm, ~70 fs laser pulses. The open aperture measurements showed three-photon absorption with magnitudes of coefficients, 4.7×10^{-5} cm^3/GW^2 and 5.2×10^{-5} cm^3/GW^2 and the closed aperture measurements provided second-order hyperpolarizability (γ) values of 3.53×10^{-31} esu and 4.15×10^{-31} esu for G1 and G3, respectively. Additionally, the onset of optical limiting was estimated to be $5.8 \times 10^{-3}\ J/cm^2$ and $5.7 \times 10^{-3}\ J/cm^2$ for G1 and G3 molecules respectively. The TAS and NLO measurements on these molecules establish the multifunctional aspects of G1 and G3 molecules for solar-conversion devices and optoelectronic applications.

References

1. L. Giribabu, N. Duvva, S. P. Singh, L. Han, I. M. Bedja, R. K. Gupta, et al., "Stable and charge recombination minimized π-extended thioalkyl substituted tetrathiafulvalene dye-sensitized solar cells," Materials Chemistry Frontiers, vol. **1**, pp. 460-467, 2017.
2. S. S. K. Raavi and C. Biswas, "Femtosecond Pump–Probe Spectroscopy for Organic Photovoltaic Devices," digital Encyclopedia of Applied Physics, pp. 1-49, 2003.
3. Chinmoy Biswas, N. K. Katturi, N. Duvva, L. Giribabu, V. R. Soma, and Sai Santosh Kumar Raavi, "Multistep Electron Injection Dynamics and Optical Nonlinearity Investigations of π-Extended Thioalkyl-Substituted Tetrathiafulvalene Sensitizers," J. Phys. Chem. C, vol. **124**, pp 24039–24051 (2020).

Quantum Interference based approach to Nonlinear Optics

Harshawardhan Wanare
IIT, Kanpur

Abstract

The nonlinear optical response as captured by the perturbative description in the conventional optical polarization $P_i = \epsilon_o \left(\chi_{ij}^{(1)} E_j + \chi_{ijk}^{(2)} E_j E_k + \chi_{ijkl}^{(3)} E_j E_k E_l + \cdots\right)$ is quite inadequate in describing a whole range of nonlinear optical behaviour. Numerous counter-intuitive optical phenomena have come to fore in the past few decades. All these are macroscopic manifestations of quantum interference effects such as: Coherent Population Trapping (CPT), Electromagnetically Induced Transparency/Absorption (EIT/A), Lasing Without Inversion (LWI), Electromagnetically Induced Anisotropy (EIAy), giant refractive index, nonlinear wave mixing at low light levels etc. Each of these arise from interference of electronic excitation through multiple pathways in atoms in the presence of light. We propose a closed-loop decomposition based approach that is all encompassing, which essentially tracks a hierarchy of electronic excitation pathways and their interplay. The governing currency in this approach is the phase accumulated along excitation pathways rather than the traditional approach based merely on the strength of light. These quantum interference effects can either enhance or suppress the nonlinear multiphoton processes and thus dominate the macroscopic outcomes even at extremely low light levels. Further, we propose a new classification for nonlinear optical response that captures this atomic-interference based criteria to classify all light-atom multilevel nonlinear optical response.

Reference

A. Kani and Harshawardhan Wanare, Anisotropic nonlinear optics based on quantum interference, Europhysics Letters, Vol. 120, 33001 (2018).

Flatland Nonlinear Optics

K. V. Adarsh

Department of physics, Indian Institute of Science Education and Research, Bhopal-462066, India

Email: adarsh@iiserb.ac.in

Abstract

Graphene, the first atomically thin 2-dimensional (2D) layered material has revolutionized the research in fundamental and applied science for exploring broad range of electronic, optoelectronic, and quantum phenomena. The fundamental limitation of graphene is its zero bandgap that can be overcome by 2D transition metal dichalcogenide (TMDC) with a sizeable bandgap. In addition to bandgap tunability, atomically thin transition-metal dichalcogenides show strong optical nonlinearity with great potential for various applications like second harmonic generation, optical limiting, and switching. First part of this presentation discusses the new insights into the excited state properties of both few-layer and monolayer MoS_2 through spectrally and temporarily resolved femtosecond differential absorption (DA) measurements for different photon fluences. We demonstrate an unusually broad differential absorption over a broad spectral range, spanning more than 300 nm in the electronic and optical bandgap region at photon fluences in the nonlinear regime (above Mott density), manifestation of 1.2 eV giant bandgap renormalization and vanishing exciton resonance. Further, we fully characterize the transient redshift followed by an anomalous blueshift of exciton energy as a function of the photogenerated carrier density, using a phenomenological model similar to Lennard-Jones potential with modified exponents. In the second part, taking few-layer ReS_2 as a model system, we propose and experimentally demonstrate thermalization time as a new degree of freedom to manipulate the ultrafast third- order nonlinear optical response. We experimentally verify this concept by realizing saturable to reverse saturable absorption in our single colour pump-probe Z-scan setup as a function of thermalization time.

A quantum of science' for the future technologies

Dr. Y. B. Kale
University of Bermingham,
UK

Abstract

Ultra-cold atoms are the ideal candidates for the realization and for the translation of quantum concepts into their real-world applications. This results in highly sensitive, more accurate and resilient quantum sensors such as Quantum Gyroscopes and Optical lattice clocks. While planning to take such sensors 'out of the lab' environments new methodologies needs to be developed. The SWAP (size, weight and power) criteria should be such that the sensitivity and accuracy of such sensors need not to be compromised.

Such a field-deployed quantum sensors are not only deciding the future of the fields such as navigation, time keeping, and geodesy but also playing crucial role in addressing physics problems such as tests of general theory of relativity, variations in the dimensionless fundamental constants and accurate measurement of gravitational red shift. They have potential to support light interferometers (such as LIGO) in the detection of Gravitational Waves (GWs).

Multi-GHz Burst-Mode Fiber Lasers

F. Ömer Ilday
Uni. Bilkent, Ankara, Turkey

Abstract

Ultrafast lasers allow thermal damage-free ablation irrespective of the material type. However, this is a slow and inefficient process, because enough time has to pass between subsequent pulses for the material to cool down to avoid heat buildup. We recently demonstrated ablation-cooled laser-material, whereby ultrafast pulses are sent so quickly one after another (within 100's picoseconds of each other) that there is insufficient time for heat to diffuse away from the processing region [1,2]. In this regime, the interaction of the pulses with the target material is no longer isolated, but rather, many thousands of pulses interact collectively with the material. Further, the ablation rate increases by orders of magnitude and consequently the ablation process becomes the dominant heat removal mechanism and the rest of the target material remains cool and without damage.

Utilization of the ablation-cooled regime requires multi-GHz repetition rates, which would normally require kW levels of average power for a modest pulse energy of 1 μJ. In response to this challenge, circa 2011, we started developing the first fiber laser-amplifiers that implemented the commonly used master-oscillator power-amplifier (MOPA) architecture, but these MOPAs operated in the so-called burst-mode operation. In this mode, the laser produces a temporally closely spaced group of pulses, a burst, which is then repeated at a relatively low rate. This way, GHz-level repetition rates can be achieved within the burst. By keeping the burst repetition rate low, the overall average power of the laser system can be lowered indefinitely. The first burst-mode lasers employed pulse pumping of the amplifier just before the arrival of each burst to avoid amplified spontaneous emission between the bursts. This way, burst repetition rates of 1-50 kHz or burst-on-demand operation was possible. Following developments that made generation of high average powers much easier, we have moved on to burst repetition rates that exceed 100 kHz, for which pulsed pumping is not necessary, thus significantly simplifying the laser design [3]. Looking forward, radically different laser designs appear to be possible, designs that do not use the MOPA architecture.

[1] C. Kerse, H. Kalaycıoğlu, P. Elahi, B. Çetin, D. K. Kesim, Ö. Akçaalan, S. Yavaş, M. D. Aşık, B. Öktem, H. Hoogland, R. Holzwarth, and, F. Ö. Ilday, "Ablation-cooled material removal with ultrafast bursts of pulses," Nature 537, 84-88 (2016).

[2] P. Elahi, H. Kalaycioglu, Ö. Akçaalan, C. Ertek, K. Eken, F. Ö. Ilday, "High-power Yb-based all-fiber laser delivering 300-fs pulses for high-speed ablation-cooled material removal," Opt. Lett. 43, 535-538 (2018).

[3] H. Kalaycioglu, P. Elahi, F. Ö. Ilday, Ö. Akcaalan, "High-repetition-rate ultrafast fiber lasers for material processing," IEEE J. Sel. Topics Quantum Electron. 24, 8800312 (2018).

Solid-state Lasers for Ultrashort Pulse Generation

Dr. Rüdiger Paschotta

RP Photonics Consulting GmbH, Waldstr. 17, 78073 Bad Dürrheim, Germany
Paschotta@rp-photonics.com

Abstract

Various kinds of laser gain media are suitable for ultrashort pulse generation – in particular, solid-state bulk media, glass fibers and other waveguide media, semiconductors and laser dyes. Much of the ultrafast laser pulse sources used today are based on solid-state bulk lasers, although fiber-based devices gain a growing share.

The talk will explain the basic principles of producing ultrashort pulses in such lasers, particularly with the technique of passive mode locking, which is most often implemented with semiconductors saturable absorber mirrors (SESAMs). While in the picosecond pulse duration domain a saturable absorber can be the dominant optical component for providing pulse shaping, a more refined approach is required for the femtosecond pulse duration regime, where chromatic dispersion and the Kerr nonlinearity become important. These influences profoundly change and limit the fundamental role of the saturable absorber, although that component still remains essential. Only, in some cases it can be replaced with an artificial saturable absorber, e.g. based on nonlinear self-focusing.

In comparison with fiber-based devices, bulk laser devices exhibit a far lower impact of optical nonlinearities. Therefore, they can be realized based on relatively simple operation principles and achieve far better performance in terms of pulse energy and peak power. In particular, mode-locked thin-disk lasers are suitable for pulse energies of tens of microjoules and multi-megawatt peak powers. The pulse quality, judged with different criteria in the time and frequency domain, is also often superior. On the other hand, fiber-based devices have advantages in the regime of high average output power in combination with moderate peak powers, as is possible particularly for operation with very high pulse repetition rates.

Basic operation characteristics of a passively mode-locked bulk lasers can often be well described with a couple of simple equations, not necessarily requiring computer support for evaluation. This is much in contrast to fiber devices, where the complicated nonlinear dynamics can usually not be explored without detailed computer simulations. Nevertheless, computer simulations can be useful also for bulk lasers, for example for exploring performance limits in terms of peak power or pulse duration, and for exploring the impact of various details on such limits.

Spatiotemporal Mode-Locking in Fiber Lasers

Frank Wise
Department of Applied Physics
Cornell University, Ithaca, NY, USA
Email: frank.wise@cornell.edu

Abstract

Mode-locked lasers are the foundation of the field of ultrafast science and still attract significant scientific interest. Until 2017, all mode-locked lasers essentially operated in a single transverse mode of the laser cavity. In the past few years, the first demonstrations of locking of multiple transverse and longitudinal modes of a fiber laser have appeared [1]. The existence of many different 3-dimensional (spatiotemporal) lasing states opens opportunities for future scientific investigation. Complete spatiotemporal control of the electric field produced by a laser may eventually be possible and would impact applications. Generation of ultrashort pulses in multiple modes may also provide a new route to power scaling in lasers. Basic features of multimode or spatiotemporal mode-locking will be presented along with first steps toward a theoretical treatment [2].

1. L. G. Wright, D. N. Christodoulides, and F. W. Wise, *Science* **358**, 94 (2017).
2. L. G. Wright *et al.*, *Nature Physics* **16,** 565 (2020).

Advancement in in-situ monitoring and defect detection algorithms for laser powder-bed fusion

Ehsan Toyserkani
University of Waterloo, Canada

Abstract

Metal additive manufacturing (AM) has becoming a key player in metal manufacturing. For many years, AM has been known as a platform providing customization, prototyping and low volume manufacturing. However, in recent years, AM has positioned itself to deploy for mass production, without compromising the economies of scope. This readiness and willingness to embrace AM for series production by industry has opened up many R&D opportunities. Like all conventional techniques, quality assurance procedures/tools (either online or offline) are of the utmost importance to aid manufacturers in quality management and certification when it comes to serial production.

This talk aims to present the recent advancement in in-situ monitoring of laser powder-bed fusion (LPBF) and investigate the feasibility of applying in-situ monitoring to LPBF for the detection of disturbances and defect in the LPBF process. This feasibility study will facilitate identifying correlations between physical defects created in printed parts and signals collected from on-axis and off-axis photodiodes that monitor emitted light from the melt pool. Statistical-based approaches and/or artificial intelligence algorithms can be used to deploy the proposed hardware/software to a reliable quality assurance platform required for series production. This talk will address some of these approaches at high level as well as preliminary results obtained from analysis of data collected by the commercially available melt pool monitoring system.

Towards a Predictive Model of Direct Metal Deposition

Andrew Pinkerton
University of Lancaster, UK

Abstract

The moving melt pool is the core of the Direct Metal Deposition (DMD) process, affecting all parts of the process including rate of mass addition, final track geometry and microstructure. Two factors that have significant effect on the melt pool are the laser absorption factor and the melt pool geometry. The former is governed by many factors and while some, such as laser wavelength and materials, can be carefully controlled, others such as temperature and condition of the surface where the beam is absorbed cannot. The latter is known to be affected by flow driven by surface-tension gradient, the magnitude of which can be quantified via the Marangoni number.

By comparing MAPLE simulations with experimental results for melt pool size obtained using an IPG 2kW fibre laser, the paper examines the usual assumption that absorption can be taken as a constant value and the melt pool can be considered as defined by conduction only. It goes on to show how quantification of the factors could be applied to improve the accuracy of modelling the process, particularly in the absence of flow simulation.

Post processing of LAM components

Shashank Sharma and J. Ramkumar
Dept of Mechanical Engineering, IIT Kanpur, Kanpur

Abstract

Laser-based additive manufacturing of metallic components are known to produce a part with very high surface roughness, posing a limitation to industry utilization of as-built parts. In-situ laser remelting/polishing of metal AM have the ability to significantly reduce surface roughness, at the same time alleviating the need for post-processing thereby increasing the overall efficiency of metal AM. In laser polishing, re-melting of the laser-irradiated area produces a thin layer of melt, and the displacement of molten material under the influence of surface tension eliminates the micro-asperities rendering a polished surface. Thus, the understanding of melt hydrodynamics, in laser polishing becomes essential for its better industry utilization. In this talk, a 2D longitudinal (along with the laser scan) geometry with its top surface having Rz= 15 μm was build using fractal functions to analyse melt pool dynamics and relevance of capillary, thermo-capillary forces and recoil pressure during surface roughness reduction. The simulations were carried out with different laser power and scanning speed, which reveals three regimes in laser polishing: shallow surface melting, suppression of surface asperities and surface over melting. Lastly, with the focus towards the use of laser polishing in metal additive manufacturing, an experimental and numerical study of laser polishing of additively manufactured Inconel718 substrate has been discussed.

Functional brain diagnosis with dynamic light scattering imaging approach at broken ergodicity conditions

Igor Meglinski
College of Engineering and Physical Sciences, Aston University, Birmingham, UK
E-mail: i.meglinski@aston.ac.uk

Abstract

The majority of biological tissues are the highly heterogeneous media composing mixture of static and dynamic structural inclusions. The presence of static areas exhibit non-ergodic features providing systematic uncertainty in the quantitative interpretation of the measurements of dynamic light scattering (DLS). In fact, a number of various DLS-based techniques are extensively used for monitoring, imaging and quantitative assessment of blood flows in biological tissues, whereas the issues associated with the non-ergodicity are typically ignored. Based on the simple phenomenological model we present a justification for the applicability of DLS-based imaging technique for monitoring of blood flows within biological tissues under the formally broken ergodicity conditions [1]. In addition we introduce a time-space Fourier Kappa-Omega filtering approach for stabilization of fast dynamic brain images *in vivo* [2].

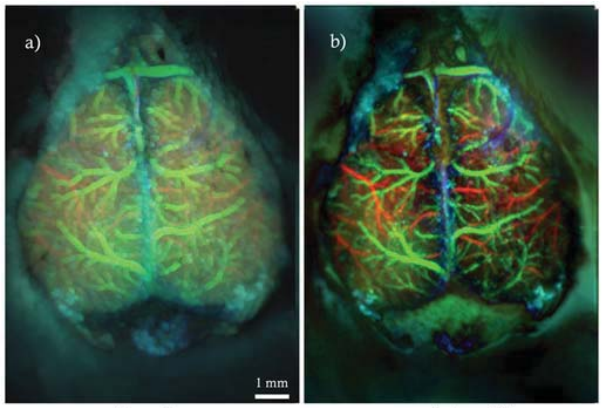

Fig.1. Brain images before (a) and after (b) the application of a time-space Fourier Kappa-Omega filtering approach [2].

References

[1] A. Sdobnov, et. al., "Blood flow visualisation under non-ergodic conditions using laser speckle contrast imaging", *Optics & Spectrosc*opy, 128(6), 778 – 786 (2020).

[2] G. Molodij, et. al., "Time-Space Fourier κω' Filter for Motion Artefacts Compensation during Transcranial Fluorescence Brain Imaging", *Phys. Med. Biol*., 65(7), 075007 (2020).

Lasers and Nanotechnology in Regenerative Medicine

Martin J. Leahy
School of Physics, National University of Ireland, Galway, Ireland

Abstract

Regenerative medicine promises to reverse blindness, lameness, organ failure and many other diseases, often by introducing stem cells to the affected site. However, they have not yet fulfilled their potential, partly because we don't know where stem cells go and what they do deep inside organs of real living humans. We recently identified a general limit of medical imaging which encapsulates the challenge; current technologies do not allow visualization of objects more than 200 times smaller than the depth. For example, cells more than c. 1 mm into typical human tissues like the skin cannot be imaged by any technology. The TOMI lab won a €6M EU H2020 grant to develop technologies to see deeper and smaller and with greater sensitivity than ever before. We go beyond the depth/resolution limit by demonstrating nanosensitive OCT to follow structural changes in cells and tissues at the nanoscale.

Using a unique star-shaped gold nanoparticle made in Galway, which resonates in the low scattering and absorption window, allows us to see deeper and with greater sensitivity than ever before. The combination of long wavelength (1064 nm), tip field enhancement and energy transfer make this particle the brightest ever made. We combine this with photoacoustic imaging, so that we can use diffuse light to illuminate the tissue and ultrasound which is not scattered, to see where it was absorbed. A key Leahy patent will allow photoacoustic images to be calibrated for the first time, allowing quantitative measurements of stem cell concentration, blood oxygen etc. The particle is magnetized so that is also visible in MRI. We will demonstrate this enhanced imaging in Cambridge during stem cell therapy for osteoarthritis of the knee.

Shedding light on radiotherapy: functional optical coherence tomography for radiobiological microvascular imaging

Valentin DEMIDOV[1], Costel FLUERARU[2] and Alex VITKIN[1]
[1]*Department of Medical Biophysics, University of Toronto, Canada*
[2]*Information Communication Technology, National Research Council, Canada* Email: vitkin@uhnres.utoronto.ca

Abstract

Radiation therapy (RT) is widely used for cancer treatment and for managing other pathologies, alone or in combination with other therapies. Recent RT advances have sparked renewed interest in delivering higher dose in fewer fractions compared to conventional RT schedules (small daily doses over several weeks). The emerging higher-dose / fewer fractions regimes potentially invoke both cellular and microvascular damage mechanisms [1]. Microvasculature may thus represent a sensitive functional biomarker of RT early response. However, it is difficult to measure in vivo directly and non- invasively, and its time course, dose dependencies, and overall importance in tumour control are yet to be determined [2]. We used functional optical coherence tomography based on the speckle variance approach for quantitative longitudinal in vivo imaging in preclinical models of human tumour xenografts subjected to 10, 20 and 30 Gy single-shot radiation doses. This yielded a detailed 3D temporal assessment of vascular remodeling following RT. Immediate (minutes to tens of minutes) and early (days to weeks) RT responses of microvascular supply, as well as tumour volume and fluorescence intensity, were quantified and demonstrated robust and complex temporal dose-dependent variations [3]. The resultant trends were compared to theoretical models proposed in the literature [2]. This presentation will summarize the study, discuss implications, and outline the next steps [4,5] in this "shedding light on radiotherapy" research program.

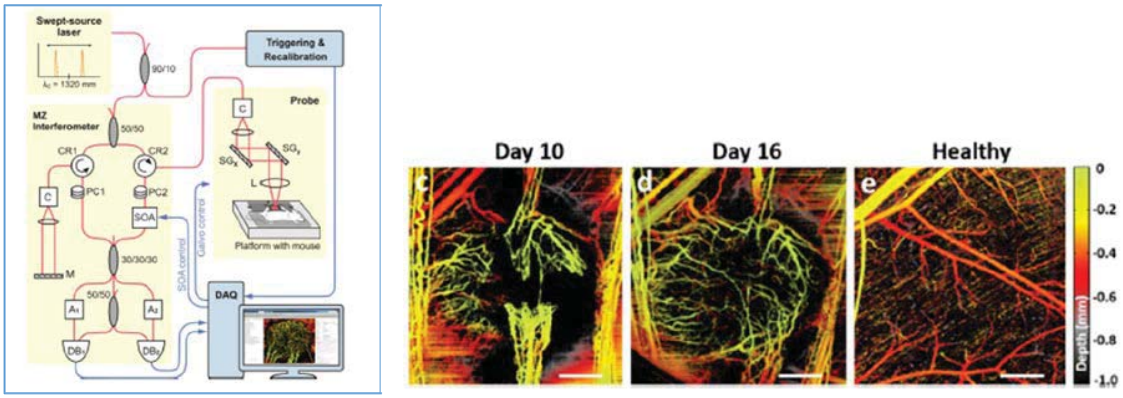

(a) (b)

Figure 1: (a) OCT system schematic (from [5]). (b) 3D cancerous and normal vasculature images of human pancreatic tumours grown in mice; both preparations were irradiated to different dose levels and followed longitudinally for up to 5 weeks (from [3]).

REFERENCES

[1] M. Reyngold et al, Radiation Oncology 14:95 (8), 2019.

[2] S.V. Kozin et al, J. Natl. Cancer Inst. 104 809-905, 2012.

[3] V. Demidov et al, Sci. Reports 8:38 (12), 2018.

[4] A. Maslennikova et al, Sci Reports 7:16505 (10), 2017.

[5] V. Demidov et al, Biomed. Opt. Express 10 4207-19, 2019.

Growth of Single Crystals by Various Techniques for Optical, Piezoelectric and Communication Applications

Binay Kumar
Crystal Lab, Department of Physics & Astrophysics, University of Delhi, Delhi-110007
Email: bkumar@physics.du.ac.in

Abstract

Crystals have always been have great attraction for their various properties and applications. Nature has given us many important crystals which have significant, but fixed, properties. We need to grow crystals of new synthesized materials of required properties in the laboratory under controlled conditions for specific applications.

In the present talk our recent results in respect of growth of single crystals of some important class of materials, particularly piezoelectric and NLO, by different growth techniques, like solution [1] and flux [2] methods, will be presented. A detailed discussion will be given on our recent modifications in Czochralski technique for growing large organic crystals of low melting temperature and high vapour pressure [3]. The quality of these crystals will be compared with the same crystals grown by conventional solution technique. Further, it will be demonstrated that these CZ grown crystals can be used in various devices.

Two important classes of applications viz (i) piezoelectric energy harvesting [4] and (ii) patch antenna for GHz communication [5] will also be discussed. Different grown single crystals are used to demonstrate the piezoelectric energy harvesting and pressure sensor applications. In energy harvesting, it has been shown that the higher output energy can be obtained with enhanced piezoelectric charge coefficient in crystals as compared to its ceramic and nanocrystalline form. In communication applications, it has been demonstrated that the generated GHz frequencies can be tuned with dimensions and doping of the organic crystals.

1. Effect of sunset yellow dye on morphological, optical, dielectric, thermal and mechanical properties of KDP crystal, Binay et al. Arabian Journal of Chemistry 13 (2020) 5750–5764.
2. True-remanent, resistive-leakage and mechanical studies of flux grown 0.64PMN-0.36PT single crystals, Binay et al. Arabian Journal of Chemistry 13 (2020) 2596.
3. Modified CZ technique for the growth of organic crystals having low melting point and high vapour pressure, Binay et al. Journal of Crystal Growth 535 (2020) 125534
4. Tb-doped ZnO:PDMS based flexible nanogenerator with enhanced piezoelectric output performance by optimizing nanofiller concentration, Binay et al. Ceramics International 46 (2020) 24120.
5. Modified low temperature Czochralski growth of xylenol orange doped benzopheone single crystal for fabricating dual band patch antenna Binay et al. Journal of Crystal Growth, 450 (2016) 74.

Design of wearable devices for underserved populations

Jessica Ramella-Roman
Department of Biomedical Engineering and Herbert Wertheim College of Medicine
Florida International University, USA

Abstract

The use of wearable devices is changing the way patients manage chronic health conditions. Wearables allow for continuous monitoring providing useful data towards the management of chronic disorders such as diabetes and cardiovascular disease which are disproportionately present in minorities. Compared to Caucasians, African American are 30% more likely to die of cardiovascular diseases, while Hispanic and Latino are 65% more likely to be diabetic. These groups have also significant higher rate of obesity. The design of wearables devices, and particularly optics-based devices, must consider this diversity. In this talk we will discuss the development of optical wearable devices targeting blood pressure, heart rate, and heart variability and glucose monitoring with particular emphasis on minorities and obese individuals. We will also propose new strategies to overcome these limitations with the goal of designing more inclusive wearable devices.

Development of High Quality Nonlinear Optical (NLO) Single Crystals for Second Harmonic Generation (SHG) Applications

Muthu Senthil Pandian*, P. Karuppasamy, P. Ramasamy
SSN Research Centre, SSN Institutions, Chennai-603 110, Tamil Nadu
*E-mail: senthilpandianm@ssn.edu.in

Abstract

Gravity driven concentration gradient is used in the Sankaranarayanan-Ramasamy (SR) unidirectional solution crystal growth method. TGS, GPI, KAP, SSDH, DGZCD, DGBCM, 2AP4N, benzophenone and many more crystals have been successfully grown by SR method. Longest benzophenone crystal having dimension of 1350 mm length and 55 mm diameter was grown for the first time by this method. The physical properties and crystalline perfection of the SR method grown crystal are compared with the conventional method grown crystals. The quality of the SR method grown crystals has been improved by several modifications made in SR method. The impurity segregation cannot be avoided in the existing SR method. So Rotational Sankaranarayanan - Ramasamy (RSR) method was introduced for growing good quality, unidirectional single crystals. The effect of rotation on unidirectional crystal growth method (RSR) has been investigated for the first time. The organic nonlinear optical 2-aminopyridinium 4-nitrophenolate 4-nitrophenol (2AP4N) crystals have been grown by (i) conventional slow evaporation, (ii) SR method and (iii) RSR method. The grown crystals were subjected to various studies like HRXRD, laser damage threshold, chemical etching, Vickers microhardness, birefringence, UV-Vis NIR, dielectrics and piezoelectrics properties. The RSR method grown crystals show excellent optical, mechanical, dielectric and higher laser damage threshold capability compared to the conventional and normal SR method grown crystals.. The unidirectional crystal growth method is ideally suited for crystal growth along device relevant direction to obtain large size crystals, such as for obtaining SHG oriented crystals with minimum wastage. Using this methodology, large size type-I and type-II phase matching (PM) angles oriented elements have been obtained successfully. In addition, the unidirectional solution crystallization usually occurs at around room temperature, therefore much lower thermal stress is expected in these crystals as compared to crystals grown at high temperatures. Successful development of this unidirectional method will provide the technology to produce crystals with a yield close to 100% and easy scaling-up process.

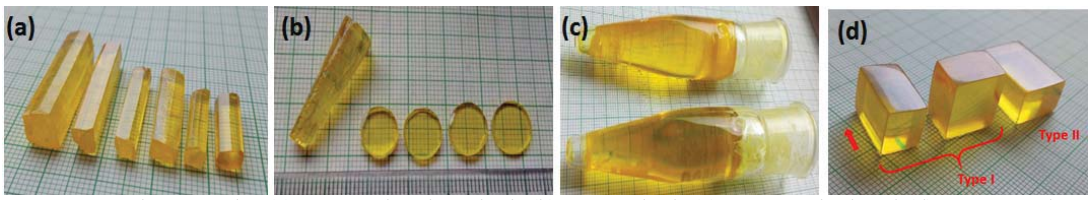

2AP4N crystals grown by (a) Conventional method, (b) SR method, (c) RSR method and (d) Type-I and type-II SHG elements

References

P. Karuppasamy, T. Kamalesh, M. Senthil Pandian, P. Ramasamy, S. Verma, *J. Cryst. Growth*, **2019**, 518, 59-72

Quantitative phase microscopy and nanoscopy using partially spatially coherent laser light: Improvement on image sharpness, phase noise, resolution and speckle free imaging

Dalip Singh Mehta
Bio-photonics and Green Photonics Laboratory, Department of Physics,
Indian Institute of Technology Delhi, Haz-Khas, New Delhi-110016, India

Abstract

Recently there has been enormous advancement in the development of quantitative phase microscopic (QPM) techniques of biological cells and tissues. QPM has become most indispensable technique presently in biology as it provides label-free high contrast images of transparent cells and tissues. QPM is used to quantify various biophysical parameters such as, sample thickness, refractive index (*n*), cell dry mass, Hb concentration, dynamic cell membrane fluctuations etc. These parameters can be determined by means of measuring the phase map of the light field interrogating with sample via interferometric techniques along with solid state area detectors and with the use of suitable computer algorithms. Precise determination of these parameters depends on the accuracy in phase measurement with reduced spatial phase noise and high temporal phase stability. Most of the QPM techniques are employed using highly coherent light like lasers as source. This is due to the remarkable properties of lasers, such as, high spatial and temporal coherence, high brightness, directionality and high color purity. Due to lasers long coherence length it is very easy to realize an interferometric microscope. But the key problems encountered in these techniques include the occurrence of spurious fringes due to multiple reflections from optical components, strong speckle noise and inhomogeneous illumination. This is due to high spatial and temporal coherence properties of laser light. All these factors affect the accuracy in phase measurement and lead to poor image quality.

By means of using partially spatially coherent monochromatic light in QPM we achieved uniform illumination, speckle free-images, very high spatial phase sensitivity, high space bandwidth product and high accuracy in phase measurement. Further, upon using QPM with partially spatially coherent monochromatic light both common path holographic system as well as off-axis holographic systems are implemented. We find that apart from obtaining very high spatial and temporal phase stability, significant improvement on image sharpness, phase noise, resolution and speckle free imaging is also obtained. Experimental results of various biological cells, such as Hela cells, sperm cells, microphases, liver cells and industrial samples will be presented and discussed. We show that the most suitable light source for QPM is partially spatially coherent monochromatic light source which guarantees an order of magnitude higher spatial phase sensitivity compare to coherent light. We have also integrated with the QPM system a total internal reflection fluorescence (TIRF) based nanoscopic system for obtaining fluorescence images of the aforementioned samples simultaneously.

Growth of Potential Nonlinear Optical Single Crystals by Melt and Solution Growth Techniques

N Vijayan
CSIR-National Physical Laboratory, Dr KS Krishnan Marg, New Delhi – 110 012.
E mail: nvijayan@nplindia.org

Abstract

Nowadays, due to enormous developments in advanced science and technology, single crystals are getting more attention because of its numerous applications in different sectors. The rapid development of optical communication system has led to a demand for nonlinear optical (NLO) materials of high performance for use as components in optical devices such as second harmonic generators, electronic modulators and fibre optic technologies etc. In order to satisfy the above said demands, one can find the growth of potential NLO materials by different techniques. In CSIR-NPL, we have grown variety of nonlinear optical single crystals by slow evaporation solution growth and melt growth techniques. In general, solution growth method is more suitable for those materials, which suffer from decomposition at high temperatures and which undergo phase transformations below the melting point. At the same time, for making different components for different applications, one can go for bulk size single crystals which could be possible either by Czochralski or Bridgman techniques. Lithium niobate, benzimidazole, ethyl p-aminobenzoate, 4-nitrophenolate 4-nitrophenol dehydrate etc single crystals have been grown by the above said methods and different characterization analyses have been performed. The observed results will be presented in detail.

Investigation of Dengue infectivity and dynamics using Förster Resonance Energy Transfer (FRET)

Kamal Kant SHARMA[1], Xin Ee YONG, Sarala Neomi TANTIRIMUDALIGE[1], Anjali GUPTA[1], Jan K. Marzinek[1,3], Daniel HOLDBROOK[1,3], Xin Ying Elisa LIM[2], Peter J. Bond[1,3], Ganesh S. ANAND[1], Thorsten WOHLAND[1]

[1]*Department of Biological Sciences, National University of Singapore, 14 Science Drive 4, Singapore 117543, Singapore*

[2]*Duke-National University of Singapore Graduate Medical School, 8 College Road, Singapore 169857, Singapore*

[3]*Bioinformatics Institute (A*STAR), 30 Biopolis Sreet, #07-01 Matrix, Singapore 138671, Singapore*

E-mail: dbskks@nus.edu.sg

Abstract

Dengue is a mosquito-borne virus with dire health and economic impacts. Among its five serotypes, Dengue 2 (DENV2) is the most virulent strain responsible for an estimated ~400 million infections per year. Interestingly, it is also for strains of this serotype that large scale conformational changes, called "breathing" have been observed. Although, the structure of these morphologies have been solved to 3.5 Å resolution the dynamics of viral envelope are still elusive. Here, we combine single molecule fluorescence and mass spectroscopy and computational studies to provide insights into DENV2 structural dynamics. Using amide hydrogen/deuterium exchange mass spectrometry (HDXMS), we captured DENV2 Envelope-protein motifs that undergo either temperature or divalent-ions dependent conformational changes. While using time resolved Förster Resonance Energy Transfer (trFRET), we measured the extent of such conformational changes. Furthermore, using FRET fluctuation spectroscopy (FRET-FCS), we delineated intrinsic fluctuation dynamics of virus in ~0.9 ms and ~2.3 ms range and correlated virus dynamics to the virus infectivity. Our results show that the DENV structural dynamics but not the virus morphologies are correlated to virus infectivity. In addition to whole virus, we also investigated inter and intra dynamics of dengue capsid protein by using single molecule fluorescence methods. Both, virus and RNA chaperone protein structure and their related dynamics are important determinants in viral activity and their knowledge can open new path in vaccine design.

KEY WORDS: Dengue virus morphology and conformation, virus dynamics, fluorescence, FRET-FCS, smFRET, RNA Chaperone

Atomic probe of nuclear properties

B. K. Sahoo,
Physical Research Laboratory, Ahmedabad

Abstract

Accurate description of nuclear structures in the atomic systems is a long-standing problem of nuclear theory. Owing to strong interplay between the strong and electromagnetic interactions within the atomic nucleus, it still remained to be a challenge to accommodate them adequately in a well defined theory to explain the experimental findings. Traditionally, various models were being used to offer ballpark figures of many physical quantities such as nuclear charge-radii and moments, among which nuclear shell-model is the most popular one. With the advent of high-performance computing facilities, development of state-of-the-art nuclear many-body methods are in progress whose validities need to be corroborated. On the other hand, the combined relativistic atomic calculations with high-precision measurements of isotope shifts and hyperfine structure constants can offer very reliable values of nuclear charge-radii and moments, respectively. Reproducing these values by ab initio nuclear calculations can test the potential of the employed nuclear methods. In this talk, some of these aspects will be highlighted by demonstrating the recently reported results from the combined studies of experiments, atomic calculations and nuclear calculations.

Dynamical phase transition in mirrorless optical parametric oscillator

Ashok Mohapatra
NISER, Bhubaneshwar

Abstract

In this talk, I will give a brief overview of mirrorless optical parametric oscillator (MOPO) observed in thermal atomic vapor using double-Lambda system. MOPO is a system where the new light fields are spontaneously generated due to intrinsic feedback of the counterpropagating driving fields interacting with the nonlinear medium through the wave mixing process. There is a first order phase transition of the atoms being in the classical statistical mixture to a quantum superposition of its hyperfine states which leads to a bistable state in the lasing threshold of the MOPO. Experimental demonstration of this phase transition in such a non-equilibrium system will be discussed in detail.

Some of the Applications of Laser Induced Breakdown

Alika Khare
Department of Physics
Indian Institute of Technology Guwahati, Guwahati 781039, India
Email: alika@iitg.ac.in

Abstract

Laser induced breakdown alternatively laser induced plasma (LIP) is coming up as a versatile tool with high precision and fine control in many sectors. It is being used extensively in material processing with a high degree of precision. It is also foreseen as a source of coherent X –Rays and higher harmonics generation as well as a source of highly energetic electrons/ions and neutral beams. Whenever a high power laser is focused on a medium, it results into the formation of high density high temperature transient plasma of the constituent atoms and molecules of the medium. If the medium happened to be a solid target than the material from the target with in the focal region is ablated out along with the formation of the plasma. The plasma emits its characteristics emission which forms the basis of Laser induced breakdown spectroscopy (LIBS), an upcoming powerful tool to identify the chemical composition of any system in any format. LIP of solid comes out with solid density and expands in the surrounding medium. In case surrounding medium is vacuum or a low pressure gas, then the expansion is very rapid and constituent ions and atoms can be deposited by placing a suitable substrate in front of it rendering the formation of thin film. This technique of deposition is termed as pulsed laser deposition (PLD). Pulsed Laser Deposition (PLD) technique has been observed to be very successful for the synthesis of variety of thin films with very high accuracy in a simple and single step manner which could be complicated via other techniques. The material ablated from the solid target in the focal region forms a tiny cavity. On careful scanning of laser or the sample results into the formation of microchannel. With a programmable movement of the sample, any shape of the microchannel can be designed with a required aspect ratio. Again it's a single step, fast and simple technique. In the recent years, pulsed laser ablation in liquid (PLAL) has paved a new way of synthesizing the nano particles (NP) of any material. This technique is also a single step, simple, devoid of involvement of any hazardous chemicals, free from contamination and very versatile. The characteristics of NP can be easily tuned by controlling the laser parameters and the surrounding liquid. The confinement of laser produced plasma by the surrounding liquid causes highly transient extreme pressure and temperature which prefers the growth of metastable phases which are normally not possible via other routine chemical roots. In the present talk, some of the above applications of Laser induced plasma shall be highlighted.

The Advanced LIGO Gravitational-wave Detector: A Discovery Machine

David H. Reitze
LIGO Laboratory
Research Professor of Physics, Caltech, USA

Abstract

The recent by gravitational-wave detectors have revolutionized astronomy and established gravitational waves as a powerful new way of probing the most extreme and highest energy astrophysical events in the universe. In this talk, I'll present an overview of Advanced LIGO and how it is capable of detecting changes in the space-time at an unprecedented sensitivity of less than 1 attometer. I'll also briefly discuss plans for improving Advanced LIGO and technological challenges being addressed.

Future of Gravitational Wave Detection Technology

Rana Adhikari
LIGO Laboratory, California Institute of Technology, Pasadena, California 91125, USA

Abstract

The laser interferometer gravitational-wave detectors, such as LIGO, KAGRA, and Virgo use a variety of precision measurement techniques to enable the measurement of displacements a billion times smaller than the diameter of an atom. The future detectors in the U.S., India, and elsewhere will require the introduction of new materials and measurement techniques taking advantage of the worldwide push towards quantum computers and quantum engineered materials. I will describe a few of these open R&D problems and their potential astrophysical impacts.

Contributory Papers

Development of high average power, high pulsed repetition rate single longitudinal mode dye lasers for selective photo-excitation of Yb isotopes of medical use

A. K. Singh*, A. Khattar, A.Wahid, J. S. B. Singh, S. K. Maurya, P. R. Mohite, J. S. Dhumal, and S. Kundu

Tunable laser Section, BTDG, BARC, Mumbai - 400085

*Email: anilks@barc.gov.in

Abstract:

This paper presents our results on the development of high average power, high pulse repetition rate single longitudinal mode (SLM) pulsed dye lasers for selective photo-excitation of ^{176}Yb, ^{174}Yb and ^{168}Yb isotopes. These isotopes are precursors for producing ^{177}Lu, ^{175}Yb and ^{169}Yb, respectively which are used in nuclear medicine. The developed pulsed SLM dye lasers have shown very good optical to optical conversion efficiency, narrow linewidth (< 80 MHz) and excellent wavelength stability of ±41 MHz over the test period (~1.25 hr).

Introduction:

Narrow linewidth pulsed dye lasers have been proven as a versatile tool for many applications in the science and technology. One of the important applications where narrow linewidth pulsed dye lasers are extensively used is Atomic Vapor Laser Isotope Separation (AVLIS) to enrich a particular isotope of interest from the natural material. In order to get efficient selective photo-ionization, the used lasers should have certain specific properties such as precise tunability, narrow linewidth, high wavelength and linewidth stability, high fluence, high pulse repetition rate (PRR) and good beam quality. All these properties along with high efficiency are easily obtained in the pulsed dye lasers which make them an attractive tool for the AVLIS process.

In recent past, AVLIS technology has gained significant attention of researchers for achieving high enrichment of isotopes for variety of applications owing its high selectivity, high energy efficiency, capability to enrich a middle isotope of material which has many isotopes. For example, enrichment of ^{150}Nd isotope [1] for experiments of neutrino mass detection, enrichment of ^{167}Er [2], ^{149}Sm [3] and ^{157}Gd [4] for burnable poisons in nuclear reactors, separation of ^{91}Zr and ^{107}Pd isotopes from nuclear waste [5, 6], high enrichment of ^{176}Lu [7], ^{176}Yb [8], ^{168}Yb [8], ^{102}Pd [9] for medical applications have been successfully demonstrated using this technology.

As per the reported three photon three step selective photo-ionization scheme [8], linewidth of the lasers used in first and second stage photo-excitation should be (< 300 MHz) [8] while linewidth of the 3rd stage excitation (ionizing) laser could be of relatively broader (~few GHz to 10 GHz). Generation of lasers with linewidth ≤ 300 MHz is possible only if the laser is operating in a SLM. Therefore, we have developed copper vapor laser pumped SLM pulsed dye lasers with linewidth <100 MHz for the first step and the second step excitations with the aim to achieve high selectivity for the desired isotope.

Experiment:

The developed dye laser oscillators operate in transversely pumped configuration in which direction of dye solution flow, pump beam incidence and dye laser output are mutually orthogonal. Here, pump beam is the green component from a copper vapour laser (CVL) master oscillator power amplifier (MOPA) chain operating at 6.25 kHz PRR. Pump pulses are stretched in time with pulse duration ~100 ns (base to base). Pump beam is delivered via an optical fiber of core radius 600 μm and numerical aperture (NA) equal to 0.12. Output beam of the fiber was first collimated using a custom designed lens assembly and then focused by a cylindrical lens of focal length 50 mm to achieve a pump beam size of 10 mm x 0.5 mm in the dye cell. To generate dye lasers at wavelengths corresponding to the first step excitation (~555 nm) and the second step excitation (~581 nm) Rh110 and Rh6G dye solutions in a binary solvent (80% water + 20% n−propanol) have been used, respectively. The concentration of Rh110 and Rh6G solutions were, 0.65 and 0.68 mM, respectively. A typical top view photograph of the developed SLM dye laser oscillator for 1st step excitation is shown in Fig.1. Design of the dye laser oscillator for 2nd step excitation is same as shown in Fig. 1 except the change in dye solution. The dye laser oscillator is consisting of an output coupler (reflectivity: 4%), a dye cell (channel cross-sectional area: 10 mm x 0.3 mm), a dual prism beam expander (expansion factor: 40X), an intra-cavity etalon (free spectral range [FSR]: 17 GHz and finesse: 17) and a holographic plane grating in littrow configuration (groove density: 3000 gr/mm). There is a provision of course and fine tuning in grating and etalon. Coarse tuning is achieved by stepper motors while fine tuning is achieved by piezoelectric transducers (PZT). In this oscillator output coupler has been mounted on a linear micro-meter drive to control laser cavity length. In addition, a PZT has been also attached to the output coupler mount for fine tuning of the laser cavity length. The PZT along with the electronic servo control is used to stabilize the wavelength of the output laser beam. All these components have been mounted on a type 304 stainless steel base plate. It is known that wavelength of the laser is very sensitive to the effective cavity length which varies with temperature and mechanical vibrations. Effects of mechanical vibrations have been mitigated by keeping the oscillator base plate on a vibration free table and properly designing the base plate. The effects of temperature have been minimized by maintaining dye solution temperature stable within ± 0.1^{o}C and base plate temperature with ± 0.05^{o}C. Temperature of the base plate is maintained using a variable current heater source with is wrapped around the periphery of the base plate.

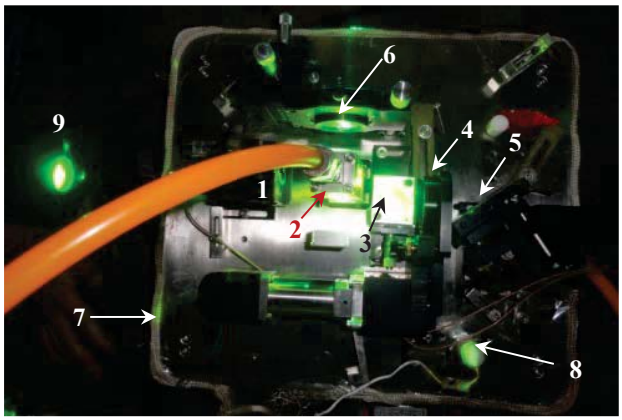

Figure 1 Top view photograph of the actual developed DL oscillator operating near ~555 nm).Components of the oscillator are- [1] Output coupler [2] Dye cell [3] prism beam expander [4]Solid Etalon [5] Holographic plane grating [6] Cylindrical lens for focusing pump beam [7] Insulated heater wire [8] RTD base temperature sensor [9] Laser power meter.

Results and discussion:

The duration of the output DL pulse was measured to be ~65 ns (base to base). Threshold pump power for onset of lasing in this SLM-DL oscillator is ~2.5 W. The variations of the optical to optical conversion efficiency and output power with the pump power for the developed SLM dye laser oscillator operating near ~555 nm is shown in Fig. 2. Our results reveal that the conversion efficiency as well as the total output power of the oscillator increases with the pump power. However, the rate of change in conversion efficiency is high for pump powers in the range of 3 to 6 W and it decrease for pump power (≥ 6 W). The observed slowdown of the rate of change in efficiency with increasing pump power could be due to increase in signal re-absorption by ground state absorption (GSA) and excited state absorption (ESA) processes. The tuning curve of this DL laser oscillator (Rh110 dye solution) under multimode condition (without intra-cavity etalon) at pump power equal to 5.12 W is depicted in Fig. 3. The tuning curve reveals that maximum efficiency of the developed DL oscillator will be in the wavelength range of 543 nm to 547 nm. Therefore, it is expected that SLM-DL efficiencies and output power levels shown in Fig. 2 may further increase if this laser will be operated near 545 nm. Although, we have developed laser near 581 nm, the data only related to the laser operating near 555 nm is presented here due to constraints of the space.

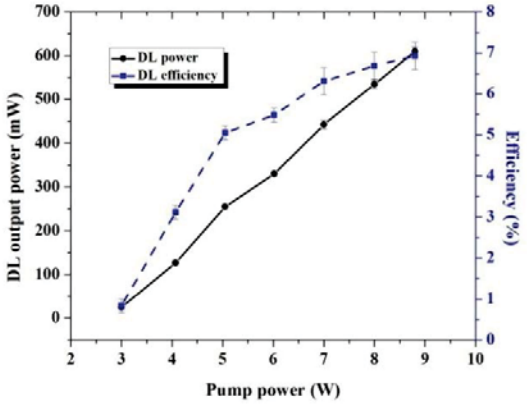

Fig. 2 Variation of the SLM-DL oscillator power and efficiency with pump power at the wavelength of ~555 nm.

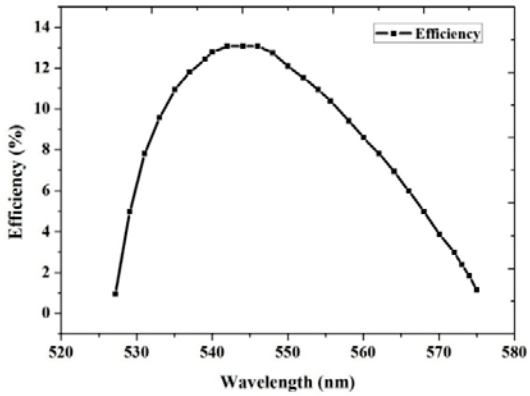

Fig.3 Tuning curve of the DL oscillator in broadband mode (without intra-cavity) @ 5.12 W pump power.

A typical fringe pattern of the output laser beam (~555 nm) transmitted through a Fabry perot etalon (FSR: 4.5 GHz, finesse: 25) and imaged in a CCD plane is shown Fig. 4. It is clearly observable from this figure that the transmitted beam forms distinctly sharp single peak fringes of different orders, indicating that the dye laser oscillator is operating in single longitudinal mode (SLM). Similar, fringes were also formed corresponding to the developed SLM-DL oscillator operating near 581 nm.

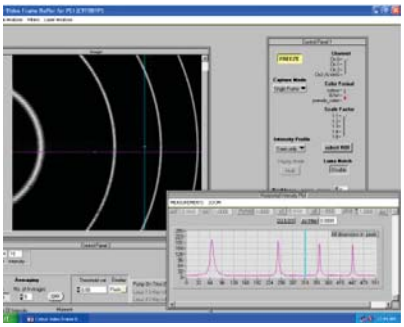

Figure 4 Fringe pattern of the DL output beam transmitted through an etalon of 4.5 GHz FSR.

One of the most challenging tasks in the development of a SLM dye laser is maintaining the SLM operation and wavelength stability over long time durations. Stabilities of the laser wavelength and linewidth under wavelength locking condition have are

shown in Fig. 5 which clearly reveals that the developed SLM-dye laser oscillator has an excellent wavelength and linewidth stability. During the test period of ~1.25 hr wavelength remained stable within ± 42 fm (± 41 MHz). Here, mentioned wavelength fluctuation range is the 3σ value of fluctuations about a set wavelength value. In addition, the mean value of laser linewidth was ~60 MHz while maintaining linewidth values ≤ 80 MHz during the entire test period.

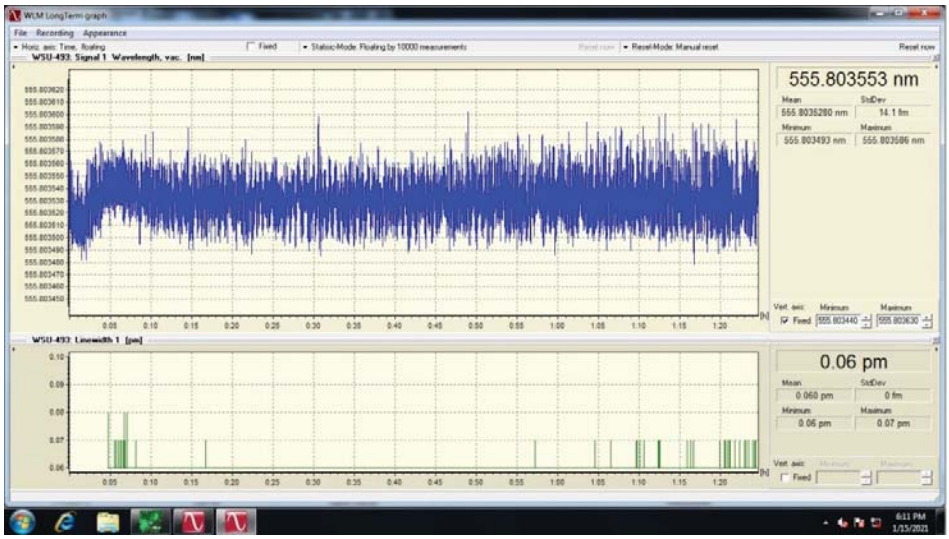

Figure 5 Wavelength and linewidth stability of the developed SLM dye laser oscillator with time.

Conclusion:

We have developed CVL green beam pumped SLM dye lasers operating at 6.25 kHz prf. for selective photo-excitation of Yb isotopes of medical interest (^{176}Yb,^{174}Yb and ^{168}Yb). The developed SLM dye lasers are efficient with excellent wavelength and linewidth stability. The laser linewidth and wavelength fluctuations are significantly lower than the isotope shifts between the target isotopes (^{176}Yb, ^{174}Yb &^{168}Yb) and their corresponding most interfering isotopes. Therefore, it is expected to get high selectivity in excitation of the targeted isotopes.

Acknowledgements: Authors would like express their sincere gratitude towards Dr. (Smt.) Archana Sharma, AD, BTDG for her constant encouragement and support for this research work. Authors would also like to acknowledge support from P. Chakraborty & N. O. Kawade of L&PTD, BARC for providing wavelength mechanism.

References:

1. A. P. Babichev et al., *Quantum Electronics, 35 (10)879-890 (2005).*
2. Haynam et al., *U. S. Patent, No. 5,443,702, Aug. 22 (1995).*
3. A. U. Seema et al., *Appl. Phys. B 118:505–510(2015).*
4. Hideaki Niki et al., *Journal of Nuclear Science and Technology, Vol. 43, No. 4, p. 427–431 (2006).*
5. Takashige Fujiwara et al., *Scientific Reports, 9:1754, 1-12(2019).*
6. Locke C. R., Kobayashi T., Appl. Phys. B 123, 240 (2017).
7. A. B. D'yachkov et al., *Quantum Electronics, 42, (10), 953-956, (2012).*
8. H. Park, *Journal of Nuclear Science and Technology, Supplement 6, 111–116, (2008).*
9. V. I. Derzhiev et al., *Quantum Electronics,33 (6) 553-558 (2003).*

Controlled decoherence in a semiconductor diode laser

Neethu. K and S. Sivaprakasam
Department of Physics, Pondicherry University, Pondicherry – 605014
Email: neethukpgm@gmail.com, prakasam.phy@pondiuni.edu.in

Abstract:

Diode lasers are known to exhibit coherence collapse when subjected to a delayed optical feedback obtained from an external cavity mirror. The quantum of delay is found to influence the coherence properties and the same is numerically investigated. Multimode extension of the well known Lang-Kobayashi model is adopted for the study. The investigations reveal that the delay with which optical feedback is provided to the laser, has a direct bearing on the coherence property of the diode laser. Analysis of the output dynamics established that the coherence property diminishes with an increase in external cavity length.

Introduction:

Diode lasers constitute an integral part of optical communications. However, all the secure online transactions use electronic coding techniques such as RSA techniques. To enable an integrated optical secure information exchange, which is termed as secure optical communications, chaotic diode lasers are essential. An effective implementation of secure optical communication needs an in-depth understanding of semiconductor diode lasers' dynamics subjected to an optical feedback (SLDOF). Diverse dynamics like chaos, nonlinear effects, etc. exhibited by the semiconductor laser diodes in the presence of external feedback captivated the research community's minds for the past two decades[1]. SLDOF has become the backbone of secure communication, message encoding and decoding and chaos communication. A schematic of SLDOF is shown in figure 1 in which a fraction of output light from semiconductor laser is fed back by an external optical mirror.

Model:

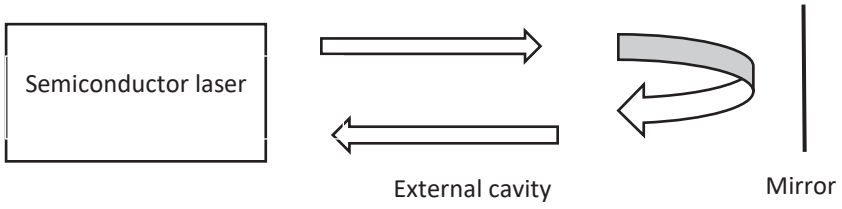

Figure 1. Schematic Diagram of semiconductor diode laser with external optical feedback

In the past, theoretical works on the diode laser output dynamics focused mostly on single-mode laser diodes. Recent works changed the focus to find a multimode model as the practical diodes are found to support multimodes when subjected to an optical feedback[2,3]. Multimode extension of Lang-Kobayashi model[4] proposed by Buldú, García-Ojalvo, and Torrent[5] is adapted for our study. The rate equations are

$$\frac{dE_m(t)}{dt} = \frac{1}{2}(1+i\alpha)(G_m(N) - \frac{1}{\tau_p})E_m(t) + \kappa E_m(t-\tau_{ext})\exp(-i\omega_{0m}\tau_{ext}) \quad \text{.....(1)}$$

$$\frac{dN}{dt} = \frac{J}{e} - \frac{N(t)}{\tau_n} - \sum_m G_m(N)\left|E_m(t)\right|^2 \quad \text{.....(2)}$$

where, mode-dependent gain coefficient $G_m(N)$ chosen as having parabolic profile and its maximum is centered at m_c(central mode) and is given by

$$G_m(N) = \frac{g_0(N - N_{th})}{1 + \varepsilon \sum_m \left|E_m(t)\right|^2} \left[1 - \left(\frac{(m_c - m)\Delta\omega_L}{\Delta\omega_g}\right)^2\right] \quad \text{.....(3)}$$

Longitudinal mode spacing $\Delta\omega_L = \frac{2\pi}{\tau_{in}}$; Feedback rate $\kappa = \frac{(1 - r_2^2) r_{ext}}{r_2 \tau_{in}}$

Nominal frequency of the m^{th} mode $\omega_{0m} = \omega_c \pm (m_c - m)\Delta\omega_L$

$E_m(t)$ is the slowly varying complex electric field of m^{th} longitudinal mode generated by the laser and *N(t)* is the corresponding carrier density with the carrier density at lasing threshold is N_{th} = 1.5×10^8. *J is* the injection current. G_m is the gain of the m^{th} mode and $g_0 = 12\times10^3 s^{-1}$ is the linear gain coefficient. ε is the gain saturation coefficient and *e* is the electronic charge. α = 3.8 is the linewidth enhancement factor. τ_p = 2ps is the photon life time and τ_n = 2ns is the carrier life time. τ_{in} = 8ps is the internal cavity round trip time. r_{ext} is the reflectivity of external cavity mirror . τ is the external cavity round-trip time which is a variable parameter in our study. We have analyzed single, three, and five active modes for comparison purposes.

The key variable in the dynamical studies are the reflectivity of the external mirror (r_{ext}) and external cavity time delay(τ). Famous work by Tkatch and Chraplyvy identified five regimes of operation as a function of feedback power ratio and cavity length[6]. In these regimes, regime-IV was identified as coherence collapse regime. Laser, a device known for its coherence properties, is rendered chaotic due to the external optical feedback and is notionally identified as coherence collapse. In this regime, the inherent laser line-width would have increased, and thus the coherence property has got reduced. In the past, works have focused on the dynamical properties of short cavity limit and long cavity limits and an understanding on the effect of continuous variation of external cavity delay is still evading. Recent work by Deb Kane and co-workers[7] has shed some light in this direction, using a travelling wave model, in which a de-coherence element was introduced within the external cavity and the laser dynamics was studied as a function of the de-coherence strength. In this work, we intend to find the cavity length effect in deciding the coherence property of semiconductor laser diode with optical feedback by changing the external cavity round trip time.

Results:

Using equations (1) and (2), we simulated the laser output at different external cavity lengths and external cavity reflectivities. Laser output intensity (L) is plotted against the drive current (I) and the standard L-I curve is obtained. The laser threshold is calculated from the L/I curve, and the normalized threshold is plotted as a function of external mirror reflectivity (r_{ext}). It is a known effect that, as the external feedback increases, the threshold will get reduced. But the de-coherence factor is expected to suppress this reduction in threshold. Figure 2 shows the corresponding results.

We have examined how much the threshold is getting reduced as we increase the external cavity round trip time τ. By varying τ , we could change the cavity length and is varied as 0.6ns,1ns,4ns, and 5ns and the comparison is shown in Figure 2 in which Figure 2(a), 2(b) and 2(c) represents single-mode, 3-mode, and 5-mode case respectively.

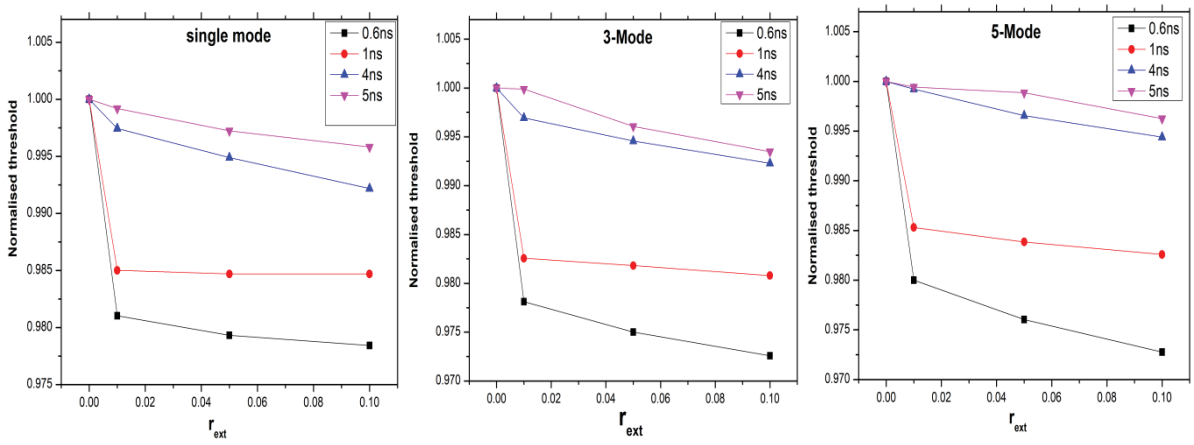

(a) (b) (c)

Figure 2: Normalised threshold of the diode laser subjected to an optical feedback at different external cavity reflectivities for (a) single mode, (b) three mode and (c) five mode

In every case, the threshold is lowered as the external cavity feedback (r_{ext}) increases. But as the τ increases from 0.6ns to 5ns, the threshold reduction, from no feedback (r_{ext}=0) to r_{ext}=0.1, is found to be diminishing. Thus it is evident from the graph that threshold reduction caused by the feedback rate is getting overpowered by the de-coherence factor, which is contributed by the increasing of cavity length. De-coherence effect by the cavity length is predominant over multimode effect. We calculated the power spectra for the relevant time evolutions and the results are shown in figure 3.

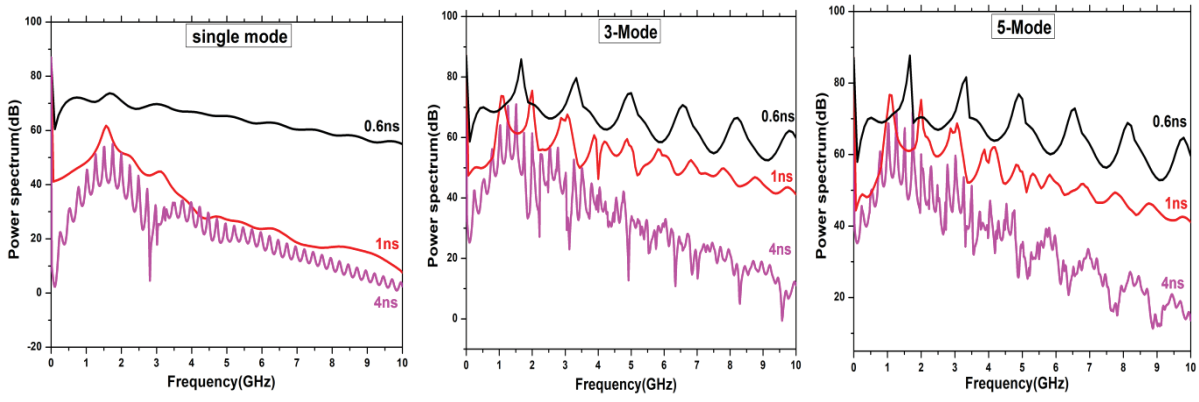

(a) (b) (c)

Figure 3: Power spectra of the laser output. (a) single mode, (b) three mode and (c) five mode

In figures 3(a), 3(b) and 3(c) the power spectra of the laser operated at single mode (fig. 3a), three mode (fig. 3b) and five mode (fig. 3c) cases are shown. In these figures, the power spectra for external cavity delays of 0.6ns, 1ns and 4ns are shown. In the single-mode case (fig.3a), the spectrum has a distinct peak if the delay is 0.6ns, and the peak corresponds to the relaxation oscillation frequency of the laser. When the cavity delay is increased, high frequency components arise and their presence become dominant for a larger external cavity delay of 4ns. This is becauseof the de-coherence effect and thus becomes broader with an increase in the cavity length. So, we can argue and conclude that as the cavity length increases, the coherence property of laser output decreases. A similar result is obtained in the case of three mode and five mode lasers. It can be seen from fig. 3b and 3c, that for a shorter cavity length (0.6ns) harmonic components of frequency arises which is the resultant of the presence of multimode. For the higher cavity lengths, (1ns and 4ns) the power spectra has reduced in its strength alongwith the presence of high frequency oscillations. Thus it is established that, if we increase the external cavity length, de-coherence sets in.

Conclusion:

The effect of cavity length on the coherence property of the semiconductor laser with optical feedback is analyzed. Threshold reduction is suppressed with the increase in the cavity length, which is a strong indication of the decrease of coherence. Power spectra exhibits higher frequency components as the external cavity time delay is increased which gives additional proof for the de-coherence effect in the laser output dynamics. Thus, we report a change over from coherence to de-coherence of a diode laser subjected to an optical feedback as the feedback delay is increased and the same is observed significantly in a higher modal laser and the quantification of coherence is a study of near future.

References:

1. M. Sciamanna and K. Alan Shore, *Nature Photonics,* **9**, 151 (2015).
2. C. Masoller, M. S. Torre, and P. Mandel, *Physical Review A*, **71**, 013818 (2005).
3. C. Serrat, S. Prins, and R. Vilaseca, *Physical Review A*, **68**, 053804 (2003).
4. R. Lang and K. Kobayashi, *IEEE Journal of Quantum Electronics,* **16**, 0347 (1980).
5. J. M.Buldú, J. García-Ojalvo, and M. C.Torrent, *IEEE Journal of Quantum Electronics*, **40**, 640 (2004).
6. R. Tkach, andA. Chraplyvy, *Journal of Lightwave Technology*, **4**, 1655 (1986).
7. M. Radziunas, D. Little and D. Kane, *Optics Letters*, **44**, 4207 (2019).

Determination of gain coefficient and roundtrip resonator losses of Cr:forsterite laser system using a polarization resonator cavity

Siba Prasad Sahoo[*1,2], V. S. Rawat[1,2], Jaya Mukherjee[1], Swarupananda Pradhan[1,2]
[1]*Homi Bhabha National Institute, Anushaktinagar, Mumbai 400094*
[2]*Beam Technology Development Group, Bhabha Atomic Research Centre, Trombay, Mumbai 400085*
Email: sibaps@barc.gov.in

Abstract

The gain coefficient and roundtrip resonator losses of Cr:forsterite laser system is determined using Findlay-Clay analysis in which a polarization-based resonator cavity is used. The cavity geometry allows us to measure the threshold pump energy of the cavity for different reflectivity values of the output coupler accurately, as the cavity alignment can be preserved during the experiment. In this work a confocal resonator cavity is used in which the Cr:forsterite crystal is pumped by a 10 Hz Nd:YAG laser system. The small-gain coefficient of the Cr:forsterite laser system at threshold and roundtrip resonator losses of the cavity are determined to be 0.049 cm^{-1} and 12 % respectively.

1. Introduction

The gain coefficient and roundtrip resonator losses of a laser resonator cavity play an important role in the design and optimization of a laser system. Depending upon the roundtrip resonator losses and small-signal gain of the system, the reflectivity of the output coupler has to be chosen for optimum extraction of the laser power. In most of the solid-state lasers, the small-signal gain coefficient is one order less than that of the dye lasers. Hence the knowledge of the gain coefficient will help in designing a laser resonator cavity with various intracavity elements for optimal performance. The roundtrip resonator losses and gain coefficient of a laser system are measured by Findlay-Clay analysis in which the threshold input pump energy was measured at different values of the output coupler reflectivity [1]. Conventionally, various output coupler mirrors of different reflectivity are used in this measurement, where output coupler mirrors are required to be changed. Thus, the resonator cavity has to be realigned after each replacement and optimum alignment of the resonator cavity is difficult to be assured each time. It leads to inconsistency in the measurement. We have developed a polarization-based laser resonator cavity in which the reflectivity of the output coupler can be continuously varied without misalignment of the laser cavity. Using this resonator cavity, we have measured the small-signal gain coefficient and roundtrip resonator losses for a Cr:forsterite laser system. Chromium doped forsterite (Cr4+: Mg2SiO4) is a tunable solid-state laser crystal in the near-infrared (NIR) region which has immense applications in the field of optical coherence tomography (OCT), biophotonics, nonlinear microscopy, telecommunication, super-continuum generation, and spectroscopy.

Experimental setup:

The complete design and characterization of the polarization-based Cr:forsterite laser resonator is described in detail elsewhere [2]. The experimental setup is shown in Fig. 1 in which the Cr: forsterite crystal is pumped by

the fundamental frequency (1064 nm) of a Q-switched Nd:YAG laser having a pulse repetition rate of 10 Hz.

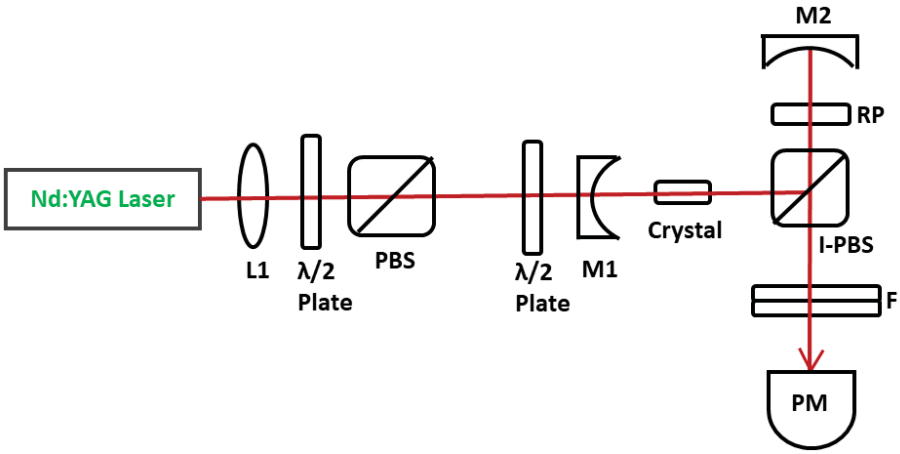

Fig. 1. Schematics of the experimental setup of Cr:forsterite laser resonator. L1: 1000 mm focal length lens; PBS: polarizing beam splitter, M1, M2: concave mirrors, roc:100 mm, R: 99% @1150-1350 nm, T: 90% @1064 nm; I-PBS: intracavity polarizing beam splitter; RP: retardation plate; PM: power meter; F:1064 nm filter;

The laser crystal has dimensions of 5 mm x 5mm x 12 mm which is cut with both *a* and *b* axes parallel to the end-face edges with end faces having single-layer anti-reflection (AR) coating. The crystal has an absorption coefficient of 1.47 cm^{-1} at 1064 nm for polarization along *b*-axis (E∥b) and a figure of merit (FOM) of 17. The FOM is defined by the ratio of absorption of the crystal at pump wavelength (1064 nm) to absorption at the peak lasing wavelength (1236 nm). The laser resonator cavity consists of two high reflecting concave mirrors (M1 and M2) in confocal geometry, an intracavity polarizing beam splitter cube (I-PBS), and a retardation plate (RP). The high reflecting concave mirrors have a radius of curvature of 100 mm, the reflectivity of > 99% at 1150 -1350 nm, and the transmission of 90% at 1064 nm. The pump polarization is made collinear with *a*-axis of the crystal by using a half-wave plate (λ/2 plate) placed before the crystal and the beam emerging from the crystal was vertically polarized. The reflectivity of the output coupler is varied using the retardation plate placed in between the I-PBS and mirror M2. The intracavity beam reflected from the I-PBS oscillates in between the resonator mirror M1 & M2 and the laser output is obtained through the transmission part of the I-PBS along the orthogonal direction. The state of polarization of the laser beam as well as the laser output energy can be controlled by changing the angle of the retardation plate. The output laser beam from the resonator cavity is isolated from the residual pump beam by passing through two 1064 nm filters (F) and its energy is measured with a pyroelectric power meter (PM).

Calculation of roundtrip resonator losses and small-signal gain coefficient

The photon flux inside a laser resonator cavity rapidly builds up from the ambient noise after initiation of the pump source at the expense of the gain of the system. The laser threshold condition in the steady-state is given by [3]

$$2g_0 l = \delta - lnR \approx \delta + T \quad (1)$$

where, $2g_0 l$ is the total gain of the system, g_0 being the small signal-gain coefficient, and l is the length of the crystal. δ is roundtrip resonator losses which include absorption, Fresnel reflection, and scattering losses caused

by different optical elements of the resonator cavity mostly due to the crystal and high reflecting mirror. R is the reflectivity and T is the transmission of the output coupler. Beyond the threshold, the steady-state is again reached when the absorption is balanced by the sum of the spontaneous emission and stimulated emission. In this steady-state, the fraction of the intracavity energy transmitted through the output coupler as cavity output energy is [3]

$$E_{out} = A\left(\frac{1-R}{1+R}\right) I_s \left(\frac{2g_0 l}{\delta - lnR} - 1\right) \quad (2)$$

where A being the effective cross-sectional area of the crystal. Is is the energy density inside the laser resonator.

For a four-level laser system, the small-signal gain coefficient (g_0) as a function of input pump energy (E_{in}) is given by

$$g_0 = \frac{\sigma \tau_f E_{in}}{h\upsilon V} \eta_t \eta_a \eta_p \eta_B = \frac{\sigma \tau_f E_{in}}{h\upsilon V} \eta \quad (3)$$

where η_t, η_a η_p, and η_m are the efficiencies of energy transfer to gain medium, absorption of the pump beam, photon energy transfer, and pump beam overlap in the crystal respectively. η is the total efficiency of the system, σ is the absorption cross-section of the crystal, V is the volume of the gain medium, τ_f is the fluorescence lifetime of the crystal and ν is laser frequency.

Using Eq. (3) in Eq. (2) with the assumption $2(\frac{1-R}{1+R}) = -lnR$, the cavity output power becomes

$$E_{out} = \sigma_s (E_{in} - E_{th}) \quad (4)$$

where $\sigma_s = \left(\frac{-lnR}{\delta - lnR}\right)\eta$ is the slope efficiency of the laser, and E_{th} is the input threshold pump energy is given by

$$E_{th} = \left(\frac{\delta - lnR}{2}\right) \frac{Ah\nu_l}{\eta \sigma \tau_f} \quad (5)$$

Eq. (5) can be written as

$$-lnR = \frac{2\eta}{AI_s} E_{th} - \delta \quad (6)$$

Comparing Eq. (1) with Eq. (6), the total resonator losses (δ) and the small-signal gain coefficient (g_0) of the system are found out from the linear plot of E_{th} vs -lnR.

Results and Discussion:

The threshold pump energy of the resonator cavity is measured for different values of the output coupler reflectivity simply by rotating the retardation plate. The reflectivity of the output coupler is measured and calibrated at the laser peak wavelength using Jones calculus [2]. The polarization-based laser cavity provides an accurate method of measuring the threshold pump energy for different values of the output coupler reflectivity without disturbing the cavity alignment, unlike the conventional method of changing the output coupler. Fig. 2 shows the variation of the input threshold pump energy (E_{th}) versus -lnR which from which a linear graph was obtained with the equation

$$y = 0.182\,x - 0.12 \quad (7)$$

From equation (7), the roundtrip resonator losses (δ) was found to be 0.12 and from the slope of the straight line, the small-signal gain coefficient can be calculated as a function of input pump energy as,

$$g_0 = \frac{2\eta}{2lAI_s} E_{in} \quad (8)$$

which gives g_0 = 0.076 x E_{in} (cm^{-1}). The small-signal gain coefficient (g_0) of the system at the cavity threshold pump energy of 0.65 mJ is 0.049 cm^{-1}.

The absorption coefficient of the crystal at 1064 nm is 1.47 cm^{-1} and a figure of merit (FOM) is 17. This gives the absorption of the crystal at the laser peak wavelength (1236 nm) is 0.086 cm^{-1} which is 10.3 % for 12 mm length of the crystal. The roundtrip resonator losses of the system is 12% which includes 10. 3% absorption losses in the crystal itself.

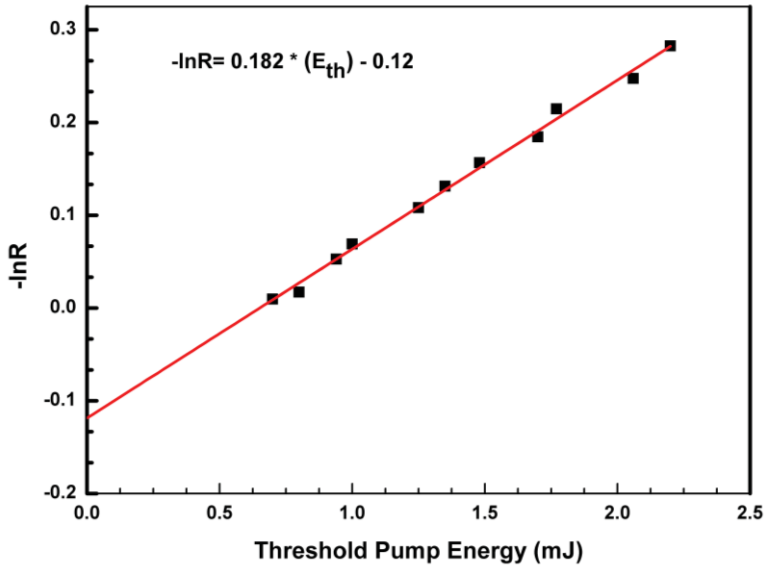

Fig. 2. Threshold pump energy (E_{th}) as a function of the output coupler reflectivity (-lnR).

Conclusi

The small-signal gain co-efficient and the roundtrip resonator losses of a Cr: forsterite laser system are determined from the variation of threshold pump energy with the output coupler reflectivity using Findlay-Clay analysis. A polarization-based confocal resonator cavity is used to change the reflectivity of the output coupler continuously without misalignment of the laser cavity. This method provides precise measurement of threshold pump pulse energy for different output coupler reflectivity. The small-signal gain coefficient at the threshold is determined to be 0.049 cm^{-1} whereas the roundtrip resonator losses is measured to be 12% for this Cr:forsterite laser cavity.

Acknowledgment:

The authors would like to express their sincere gratitude to Dr. Archana Sharma, AD, BTDG for her interest and encouragement in this work.

References:

1. D. Findlay and R. A. Clay (1966), The measurement of internal losses in 4 level lasers, Phy. Lett. 20 (1966) 277-278.
2. Siba Prasad Sahoo, S. Pradhan, Jaya Mukherjee, and V.S. Rawat, Studies of temporal characteristics of all-solid-state, gain-switched Cr:forsterite laser, Optik 227 (2021) 166024.
3. Walter Koechner and Michael Bass, Solid-State Lasers, Springer-Verlag New York Inc. (2003).

Energy enhancement in Capillary Discharge Soft X-ray Laser operating at 46.9 nm

*S. Barnwal[1], S. Nigam[1], K. Aneesh[1], M. L. Sharma[1], Y. B. S. R. Prasad[1], K. S. Bindra[1,2]

[1]Laser Technology Division, RRCAT, Indore, M.P., 452013

[2]Homi Bhabha National Institute, Anushakti Nagar, Mumbai, 400094, India

*Email: sbarnwal@rrcat.gov.in

Abstract

Experiments were carried out to enhance the energy of existing soft X-ray laser operating at 46.9 nm generated from fast capillary discharge scheme. The energy of this laser depends upon several parameters which needs to be optimized carefully to get enhancement in the laser energy. The energy of this soft X-ray laser pulse was enhanced significantly from existing ~ 2 μJ to ~ 50 μJ as a result of these optimization. Some of the laser shots have also shown energy up to ~ 70μJ which is ~ 35 times the previously recorded energy.

Introduction

Coherent soft X-ray light sources have played pivotal role in carrying out new scientific discoveries, research breakthroughs and technological advances after the invention of lasers. These soft X-ray laser sources can be potentially applied in a very wide spectrum of areas in science as well as technology. Their utilization becomes even more promising when they are easily accessible to larger scientific community in very compact sizes such as small table-top versions[1]. Soft X-ray lasers generated from fast capillary discharge scheme provides one of such promising alternative[2]. Argon based Capillary discharge soft X-ray laser operating at 46.9 nm have been successfully used worldwide in various applications like nano-imaging[3,4], interferometric lithography[5], dense plasma diagnostics[6] etc. Such applications demand sufficient energy in the soft X-ray laser pulse. In Capillary Discharge X-ray Laser laboratory at RRCAT, 46.9 nm soft X-ray laser has already been developed and characterized for its various parameters[7,8]. Now, efforts are going on to increase the energy of this laser in order to use it for various applications. The energy of this laser pulse has been enhanced from ~ 2 μJ to ~ 70 μJ as a result of several changes and optimization which forms the basis of this report. However, before going into the details of the experiments carried out in this direction, it would be worth to briefly describe the principal mechanism behind soft X-ray lasing from fast capillary discharge and the structure of Capillary Discharge Soft X-ray Laser system.

Mechanism for generation of soft X-ray lasing

Capillary Discharge soft X-ray Laser system generates soft X-ray lasing in plasma produced by passing fast electric discharge current through a pre-ionized gas inside a capillary tube made of alumina. The capillary tube is generally few tens of centimeters long and has inner diameter of few millimeters. Capillary is initially filled up to a pressure typically 0.1 - 0.4 mbar with a gas suitable for soft X-ray lasing. This gas is pre-ionized initially by a pre-pulse current of few tens of ampere with duration of few tens of micro-seconds. The pre-ionized gas is subjected to discharge current of high amplitude typically ~few tens of kilo-amperes (kA) passing in a very fast time scale of few tens of nanoseconds (ns) leading to a high dI/dt in the range from ~ 10^{11} A/s to 10^{12} A/s. Such a high and fast discharge current rapidly generates high magnetic field in the azimuthal direction

which in turn gives rise to strong Lorentz force acting in radially inward direction on the charged species of plasma. This radial force rapidly compresses (~ 10 times) the entire column to a hot and dense plasma column, named as Z-pinch. Suitable density and temperature of this Z-pinch can generate required population inversion in inner shells of selected ionization state of lasing species for possible soft X-ray lasing. Initial pre-ionization of gas is very essential in order to achieve uniform and efficient compression throughout the length of Z-pinch plasma and also to inhibit growth of instabilities during pinch formation. If argon gas is used to fill the capillary with suitable pressure initially and subjected to suitable discharge current, population inversion can be achieved in 3s - 3p energy levels of Ne-like Ar (Ar^{8+}) ion at the pinch formation. The associated transition leads to generation of soft X-ray lasing at 46.9 nm coming out of capillary exit end. This soft X-ray laser requires an optimum plasma density of 10^{18} to 10^{19} /cc and optimum temperature of 60 to 80 eV at the Z-pinch formation.

System description of Capillary Discharge soft X-ray Laser

Figure 1 shows a photograph of the present Capillary Discharge X-ray Laser system in our laboratory. Requirement of fast and high current discharge has been fulfilled by indigenously designed and developed powerful pulsed power setup with a Marx-generator as primary driver[9]. It was further upgraded replacing Marx-generator by a Tesla-transformer to charge a water-capacitor (filled with De-ionized water as dielectric) up to typically a voltage of few hundreds of kilo-volts in about 3 μs time. This capacitor is connected to the argon filled capillary through a pressurized spark-gap switch. After the capacitor is charged to the desired voltage, the self breakdown of the switch allows the capacitor to discharge its energy rapidly (~ few tens of ns time) through argon filled in the capillary. This drives the required discharge current through the capillary. Few μs before passing the main discharge current, argon gas is pre-ionized by passing long lasting few tens of ampere pre-pulse current through it. The emitted soft X-ray laser (46.9 nm) from the capillary exit end requires sufficient vacuum (> 10^{-4} mbar) to be maintained in order to avoid its absorption. An orifice of 1 mm diameter is placed just after the exit end of capillary for differential vacuum pumping which ensures required gas pressure (0.1 - 0.4 mbar) in the capillary.

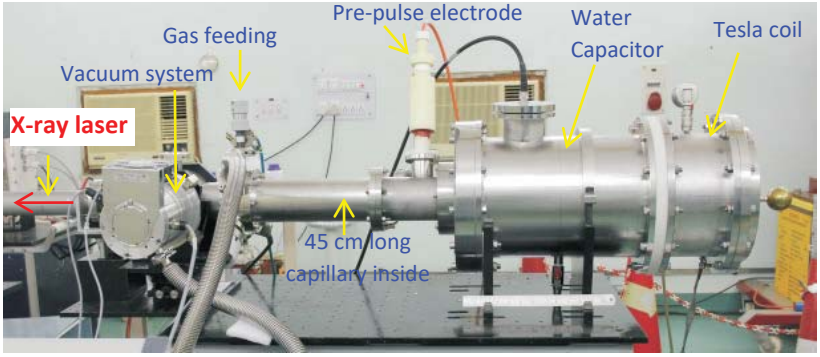

Fig.1 Capillary Discharge X-ray Laser System

Experiments and Results

The soft X-ray laser is achieved from the system when suitable lasing conditions i.e. density and temperature are reached in the argon Z-pinch plasma. The lasing conditions depend upon optimization of various parameters of the system which are main discharge current, its duration, pre-pulse current and its timing

with respect to the main current, initial argon gas pressure, capillary inner diameter and capillary length. Initially, optimization was carried out with a capillary of 15 cm length and 2.8 mm ID. The temporal, spatial and spectral studies were already carried out to ascertain the various properties of this soft X-ray laser e.g. laser pulse duration, its divergence, wavelength, spatial coherence, energy etc. Various detectors like Vacuum diode, Quadrant Vacuum diode and Micro-channel plate (MCP) coupled with phosphor screen were used as X-ray diagnostics in these studies. The energy of this laser was measured to be ~ 2μJ at a discharge current of ~ 26 kA for a capillary of 15 cm length and 2.8 mm ID. This was measured using calibrated vacuum diode detector after heavy attenuation of laser beam by 2.4 μm thick Al foil.

Now, efforts were made to get further increase in the energy of this soft X-ray laser pulse by increasing the length of the gain medium i.e. column length of argon plasma. Accordingly, capillary length was increased to ~ 20 cm to serve the purpose. Capillaries of different inner diameters e.g. 2.0 mm, 2.8 mm and 3.2 mm were explored with this length. It was found that 3.2 mm ID was more favourable for higher laser output. Now, discharge current was varied in the range from 25 to 40 kA with quarter period of current ($T_{1/4}$) to be 45 ns for a capillary of length 20 cm and 3.2 mm ID. Pre-pulse conditions and gas pressures were also varied and optimized for higher laser output. As a result of these optimization, energy in the laser pulse could be enhanced to ~ 10 μJ at a discharge current of ~ 40 kA. Now, keeping the capillary ID to be 3.2 mm, the capillary length was further increased to ~ 45 cm to get substantial increase in the plasma column length. Such a long plasma column led to a significant increase in the inductance of the discharge path which affected the discharge current itself . As a result, the quarter period of the discharge current was now increased to ~ 90 ns. With this changed duration, the amplitude of discharge current was varied in the range from 25 to 35 kA. The gas pressures and pre-pulse conditions were tuned for higher laser output at each discharge current amplitude. These optimization finally led to a significant increase in the laser output. The energy of the laser pulse measured under the optimized conditions was ~ 50 μJ. Some of the laser shots have also shown ~ 70 μJ of energy (as shown in Fig. 2) recorded in the single soft X-ray laser pulse. This is nearly ~ 35 times higher than what was measured previously (~ 2 μJ). Experiments were also carried out with capillary of 4.0 mm ID and 45 cm length at 35 kA

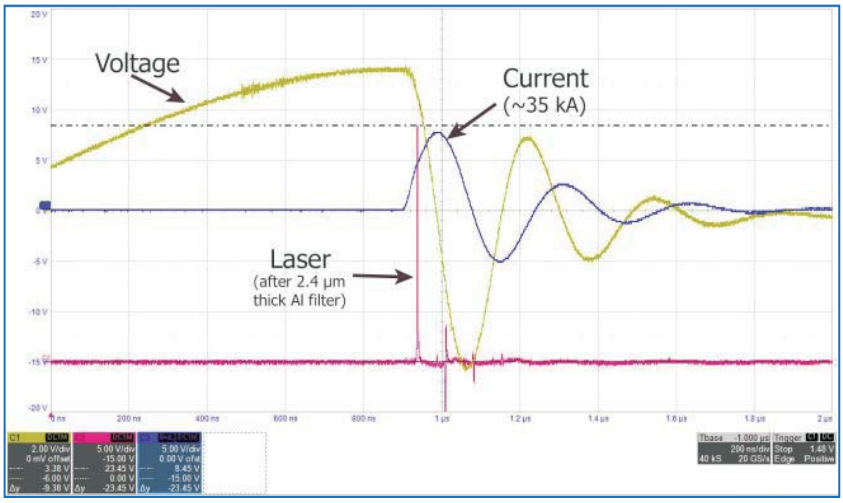

Fig.2 Temporal profile of Voltage, Discharge current and soft X-ray laser pulse in optimized conditions

discharge current in order to explore further enhancement in energy. However, no further enhancement could be observed in the energy even after optimization of other parameters. Experiments are presently underway to investigate the plasma dynamics in order to explore ways for further enhancement of laser energy.

Conclusion

The output of Capillary Discharge soft X-ray Laser operating at a wavelength of 46.9 nm was enhanced ~ 35 times by optimizing various experimental parameters. Under the optimized conditions, the maximum energy of the laser was measured to be ~ 70μJ.

References

1. J. J. Rocca, *Rev. Sci. Instrum.* **70**, 3799 (1999)
2. J. J. Rocca et al, *Phys. Rev. Lett.* **73**, 2192 (1994)
3. I. Kuznetsov et al, *Nat. Commun.* **6**, 6944 (2015)
4. C. A. Brewer et al, *Opt. Lett.* **33**, 518 (2008)
5. M. C. Marconi and P. W. Wachulak, *Prog. in Quant. Elect*. **34**, 173 (2010)
6. J. Filevich et al, *Opt. Lett.* **25**, 356 (2000)
7. S. Barnwal et al, *Appl. Phys. B* **117**, 131 (2014)
8. S. Barnwal et al, *Appl. Phys. B* **122**, 169 (2016)
9. S. Nigam et al*, IEEE Transaction on Plasma Science* **47**, 2696 (2019)

Development and characterization of a 40 W narrow linewidth all-fiber multistage amplifier at 1064 nm.

Bhuvnesh[1,2], C.P. Singh[1], P.K. Gupta[1], S. Sahu[1], P.K. Mukhopadhyay[1] and K.S. Bindra[1]

[1]Laser Technology Division, Raja Ramanna Centre for Advanced Technology, Indore-452013.

[2]E-mail: bhuvneshk@rrcat.gov.in

Abstract: In this paper we present development of an amplifier system at 1064 nm generating 40 W narrow linewidth (< 2MHz) output. Amplification of a narrow linewidth fiber coupled seed laser diode of 20 mW power is carried out in multi-stage all-fiber configuration. Linewidth of the amplified output was measured by delayed self-heterodyne technique based setup. There is no contribution of pump or amplified spontaneous emission in the amplified out and pump to signal conversion efficiency is ~65%.

Narrow linewidth lasers are key source of light in many practical applications such as precise interferometric measurement, metrology, high resolution spectroscopy, wavelength conversion, gravitational wave detection etc [1-3]. Usually, the power level of laser systems required for above mentioned applications is more than ~ 1 W. Oscillators generating stable single longitudinal mode and narrow spectral linewidth (<5 MHz) and delivering such high power need complex designing and system become cumbersome. Amplification of a low power seed source is a better option to make high power laser systems. Amplifier can be made from solid state gain medium or doped fiber. Fiber especially all- fiber configuration is preferred as fiber based laser systems possess several advantages over the solid-state counter parts like diffraction limited beam quality, easy removal of dissipated heat, large gain bandwidth and misalignment free turn-key operation etc. [4]. In recent time, with the advancement in photonics technology, development of fiber and fiber optic components, optical fiber based laser systems are replacing conventional bulk laser systems in almost all the applications. Due to extremely small core diameter and longer length of the optical fiber, nonlinear effects particularly generation of stimulated Brillouin scattering (SBS) and amplified spontaneous emission (ASE) become much significant and require special attention during amplifier design.

Here we report the multi-stage Ytterbium (Yb)-doped all-fiber amplifier developed in our lab for amplification of a narrow linewidth (< 2 MHz) seed signal from a fiber coupled semiconductor laser diode at 1064 nm. Process of amplification requires optimization of many parameters like gain fiber length, pump power, signal strength, ASE level etc. The amplifier design presented here is based on the simulation studies carried out using open-source software [5]. The contribution from ASE was minimized by increasing the power gradually through multistage amplification and optimization of gain fiber length using proper simulations. The problem of nonlinear effects specially SBS was reduced by increasing the core diameter of fiber for successive stages which helps in increasing the threshold for non-linear effects. The amplifier generates ~40 W of CW power with spectral width less than 2 MHz without any significant contribution from ASE or SBS.

Schematic of the amplification scheme is shown in Fig 1, which consists of seed, pre-amplifier stage and amplifier stages (1 & 2). Seed source is a commercial single frequency laser diode (Eagleyard Photonics, Mode: EYP-DFB-1064) with linewidth of < 2 MHz at 1064 nm with output power ~20 mW. Seed source is input to the pre-amplifier stage which consists of ~85 cm long Yb-doped non-polarization maintaining SMF (Core active: Yb-164 with core diameter ~ 6 μm). The active fiber is pumped in core by an FBG stabilized laser diode (LD) at

976 nm using WDM1 (980/1060). Another WDM2 (980/1030) is spliced between the pump diode and 980 nm port of WDM1 for the protection of the pump laser diode from ASE. Seed source is spliced to 1060 nm port of WDM1 through a fiber isolator to avoid any unwanted feedback towards the seed source which can disturb its linewidth.

Output of the pre-amplifier is spliced to input of amplifier stage 1 through a fiber isolator. Amplifier stage 1 consists of a 2.5 m long Yb-doped double clad (DC, core diameter ~ 20 µm) fiber (Nufern, LMA-YDF-20/130-VIII) which is pumped in clad by two multi-mode fiber coupled laser diodes (JDSU, 9W) at 976 nm wavelength through a multi-pump combiner (MPC) with signal feed through. The output of amplifier stage 1 is spliced to the input of amplifier stage 2.

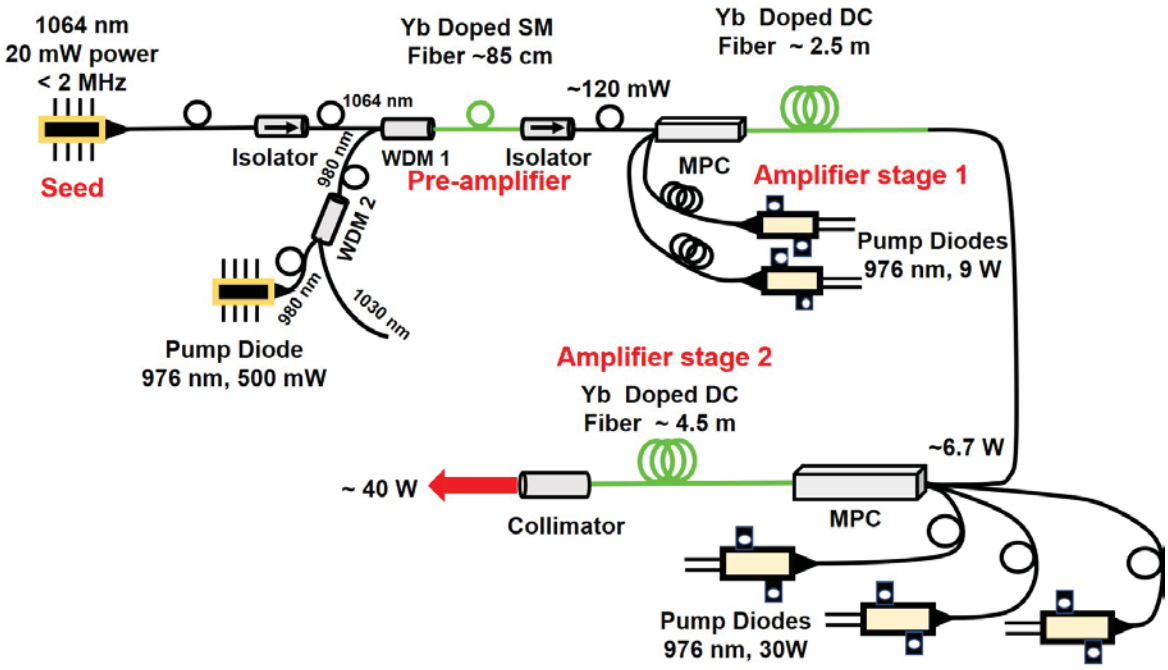

Figure 1 Amplification Setup.

Amplifier stage 2 is based on a 4.5 m long Yb-doped DC fiber (Nufern, LMA-YDF-20/130-VIII, core diameter ~20 µm) pumped in clad by three water cooled multi-mode laser diode (DILAS, 30W) connected in series through an MPC with signal feed through. Output port of amplifier stage 2 is spliced to a fiber coupled collimator. Output power was measured by placing a power meter (Ophir) after the collimator.

For measuring such narrow linewidth, a delayed self-heterodyne measurement (DSHM) setup was developed in the lab [6]. Schematic of the DSHM setup is shown in Fig 2. DSHM technique provides better resolution than most of the commercially available setup for linewidth measurements. For linewidth measurement, a part of amplifier output is coupled to input fiber of DSHM setup. In this setup laser beam to be characterized is divided into two equal parts with the help of a 50:50 fiber coupler (FC). In one of the arms of FC, a fiber coupled acousto-optic modulator (AOM, Gooch & Housego) operating at 200 MHz RF is spliced as a frequency shifter. In the other arm, a long length (~2 km) of non-polarization maintaining fiber pool is spliced to introduce delay

t_0 of ~10 µs between two beams travelling in two arms which is an order of magnitude larger than the coherence time of the laser, so that the signal in two arms becomes uncorrelated. This situation is similar to optical mixing of two separate laser signals both having same linewidth and their central frequencies are shifted by 200 MHz. Another 50:50 coupler is used to allow optical mixing of the beam coming from two arms. A part of the combined signal after second coupler is detected by a fast photodiode (Thorlabs, DET10A) with a rise time of ~1 ns. The photocurrent from photodiode was analyzed using an electrical spectrum analyzer (Keysight MXA SA N9020A, 10 Hz - 3.6 GHz) to know the frequency spectrum of combined signal. The linewidth can be easily estimated as half of FWHM (3 dB fall on log scale) in the frequency spectrum. The detection setup is characterized using a source of known linewidth.

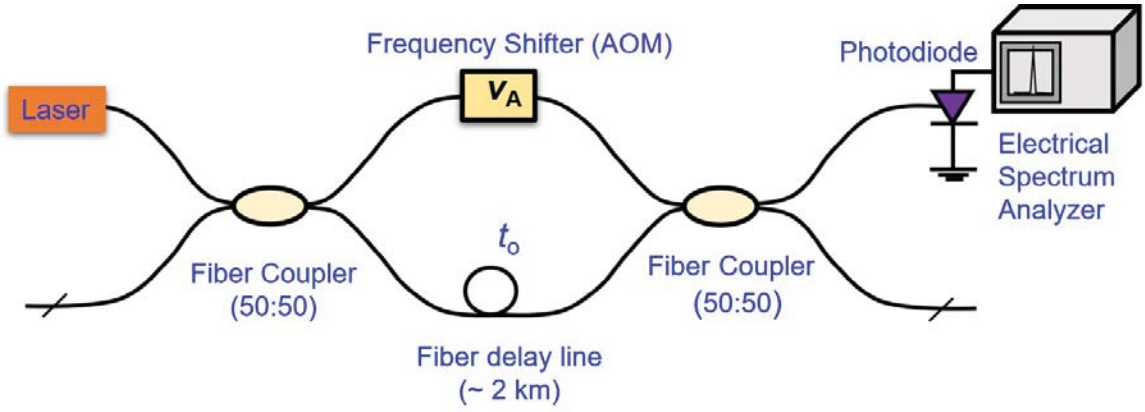

Figure 2 Schematic of delayed self-heterodyne detection technique.

Using pre-amp, output power was scaled almost linearly from ~20 mW (from seed source) to ~150 mW with increase in the pump power. From Amplifier stage 1, power was scaled from ~120 mW (Pre-amp output) to a level of ~6.7 W almost linearly when operated at maximum current ratings of pump diodes (11.5 A). Fig 3(a) shows the variation of output power from amplifier stage 2 with total pump power. Amplifier output increases almost linearly with increase in the pump power. Maximum 42 W output power at 1064 nm was achieved at 65 W pump power giving rise to ~65% pump to signal conversion efficiency.

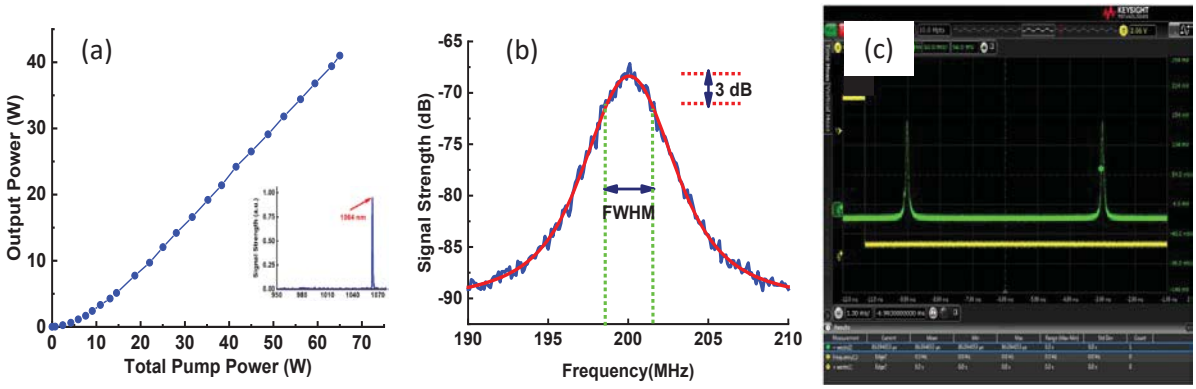

Figure 3 Variation of output power with pump power after the amplifier stage 2 (a), frequency spectrum of amplifier 2 output at ~40 W level (b), FPI measurement on final stage output (c).

Optical spectrum shown in the inset of Fig 3 (a) clearly exhibits amplifier output at 1064 nm without any contribution from pump and ASE. To confirm single frequency and stability of the amplifier output, output was characterized with scanning Fabry-Perot interferometer (FPI), (FSR 1 GHz, Finesse: 300). Fig 3(c) shows the FPI measurement carried out and single frequency operation is clear from figure.

Linewidth of the seed source at 120 mA of diode current (output ~20 mW) was measured using DSHM setup. Linewidth of the signal was measured ~ 1.5 MHz at ~ 20 mW. Linewidth after pre-amp stage and amplifier stage 1 was measured around ~1 MHz and ~ 1.6 MHz respectively. Fig 3(b) shows the frequency spectrum of output at ~40 W level. Linewidth was measured ~ 1.7 MHz after amplifier stage 2 at ~ 40 W of power level.

In conclusion, we have developed an all-fiber amplifier using Yb-doped gain fiber for amplification of the single frequency narrow linewidth seed source at 1064 nm. Power was amplified from 20 mW to ~40 W output power in three stages at 1064 nm without any significance contribution from pump and ASE. For characterization of the linewidth, DSHM setup developed in the lab was used. Linewidth was measured at different pumping power levels in both pre-amplifier and amplifier stages. We observed that there is no appreciable change in the laser linewidth during amplification and measured linewidth is ~1.7 MHz. Further power scaling up to 100 W, second harmonic generation and experiments with narrow linewidth laser system will be carried out in future.

References

1. S. Huang, T. Zhu, M. Liu and W. Huang, Sci. Reports 7:41988 (2017).
2. D. M. Baney and W. V. Sorin, Fiber optic test and measurement Ed. D. Derickson, Prentice Hall, pp. 169-219, (1998).
3. G.P. Agarwal, Nonlinear Fiber Optics, 3rd ed. Academic Press, San Diego, (2001).
4. C. Jauregui, J. Limpert and A. Tünnermann, Nat. Photon 7, 861 (2003).
5. “Fiber Lasers and Amplifiers Design Toolbox” version 1.9.0.0 by Luke Rumbaugh available on Mathworks.
6. T. Okoshi, K. Kikuchi and A. Nakayama, Electron. Lett. vol. 16(16), 630 (1980).

Effect of reabsorption losses in Q-switched Yb:YAG laser

A. J. Singh, S. Sahu, S. Ahlawat, P. K. Mukhopadhyay, K. S. Bindra
Advanced Diode Pumped Laser Laboratory, Laser Development & Industrial Application Division,
Raja Ramanna Centre for Advanced Technology, Indore
Email: ajsingh@ rrcat.gov.in

Abstract: In this work, effect of reabsorption losses on the performance of acousto optically Q-switched diode pumped Yb:YAG laser operating at 1030 nm were studied. It was observed that due to reabsorption losses, laser system acts like a hybrid Q-switched laser consisting of an active and passive Q-switch element in cavity and influences the Q-switching process. It was found that output pulse repetition rate and pulse duration changes in a periodic manner with the pump power and output pulse repetition rate becomes submultiple of active Q-switch modulation frequency.

Diode pumped ytterbium ion (Yb^{3+}) doped YAG crystal has attracted much attention as a gain medium due to its unique spectroscopic properties such as a longer upper laser level state lifetime (0.95 ms), broad absorption band width (~18nm) and a very low quantum defect (8.6%) [1] that results ~3 times less heat generation and smaller thermal loading in pumped crystal in comparison to commonly used neodymium (Nd^{3+}) doped materials based laser systems [2]. Further, owing to simple band structure of Yb^{3+} doped laser material, which consists of two electronic manifold levels, it is favourable to have no effects of up-conversion and concentration quenching which make it suitable for Q-switching process [3]. However, Yb:YAG is a quasi-three-level laser crystal, in which Yb^{3+} ion has only two Stark splitted manifolds: the ground $^2F_{7/2}$ state with four sub-levels, and the excited $^2F_{5/2}$ with three sub-levels which results in a quasi-three-level laser transition [4]. At room temperature, the fractional thermal population of the terminal level of 1030 nm transition is ~5% and hence requires higher pump power to achieve population inversion [5]. This becomes particularly significant for Q-switching operation as the crystal needs to be pumped several times higher the threshold inversion which in turn increases the local temperature of the crystal and population at the terminal level leading to significant reabsorption losses at the lasing wavelength. For a quasi-three level laser, reabsorption loss decreases with the intracavity intensity and if the initial value of re-absorption loss is sufficient high, it can lead to self Q-switching hence it acts like as a saturable absorber [6]. Thus an acousto-optic (AO) Q-switched Yb:YAG laser acts like a hybrid Q-switched system with active and passive Q-switching simultaneously.

In this work, we studied the effect of reabsorption loss on pulse repetition rate of acousto optically Q-switched diode end pumped Yb:YAG laser in a compact linear cavity. Considering the reabsorption loss of quasi three level Yb:YAG laser crystal as a saturable absorber, it was observed that output pulse repetition rate varies with the pump power as well as AO Q-switch modulation frequency and output pulse train is in submultiple of modulation frequency. Further, laser rate equations for actively Q-switched laser including passive Q-switch terms were numerically analysed and confirm the experiment results.

Experimental setup:

The schematic of the experimental setup is shown in Fig.1 (a). Laser resonator was a compact linear plane-plane cavity. The pump source used was a fiber coupled laser diode at 940 nm with a maximum output power of 50 W at 20°C. The fiber has a core diameter of 200 μm and the numerical aperture of the 0.17. The

output beam from the fiber was collimated and then focused on the gain medium to a spot diameter of ~270 μm using two plano-convex lenses (L1 and L2) of focal length 30.0 mm and 50.0 mm respectively. The gain medium was a 3mm long Yb:YAG crystal with 5 at.% doping concentration and was placed at the focused pump spot location. Yb:YAG crystal was wrapped by indium foil and mounted in a cooper block which was maintained by circulating water at a temperature of ~20^{o} C by using a chiller unit. The input mirror, M1, was a plane mirror which was coated for highly reflecting (R>99.5%) for lasing wavelength at 1030 nm but highly transmitting (T>95%) at the pump wavelength at 940 nm for efficient pumping. The plane output mirror M2 was partially reflecting (R~80%) at the fundamental wavelength to couple out the laser beam.

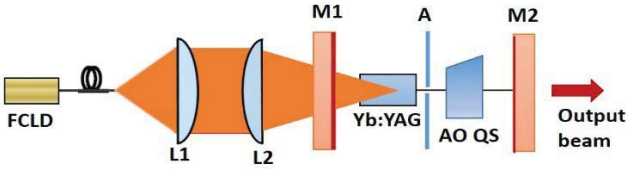

Fig. 1. Schematic of the experimental setup for AO Q-switched Yb:YAG Laser

For pulse operation, an acousto optic Q-switch (AO QS) modulator with operating frequency of 24MHz was positioned in between laser crystal and output mirror M2. An aperture (A) of size 1mm was placed after Yb:YAG laser crystal to block the unabsorbed pump power in the crystal. The geometric length of the cavity was kept to be ~14cm. Laser diode, laser crystal and AO-QS were cooled at 20^{o}C by flowing water using a chiller unit. The generated output beam was coupled out through mirror M2. Output power and temporal pulse profile was monitored with the help of power meter and photodiode respectively.

Results and discussion:

Laser was operated by varying AO Q-switch modulation frequency from 10 kHz to 30 kHz using a TTL signal to AO Q-Switch RF driver and corresponding output power, pulse width and repetition rate was measured for different input pump power. Figure 2(a) shows the variation of output pulse repetition rate with input pump power for different AO Q-switch modulation frequency. Lasing threshold was measured to be ~22 W. From figure 2(a) we observed that for AO Q-switch modulation frequency of 10 kHz, on varying the pump power beyond threshold to 25.5 W, output pulse repetition rate was measured to be 5 kHz and on further increasing the pump power output

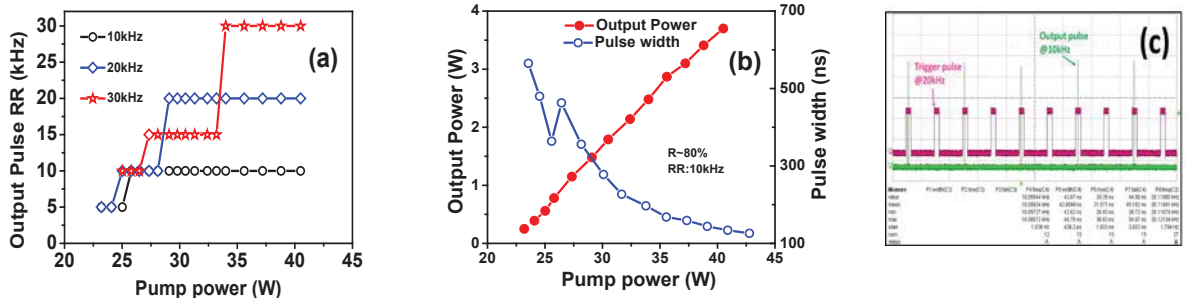

Fig. 2. (a) Variation of output pulse repetition rate with incident pump power (b) Variation of Average output power and pulse width with pump power for 10 kHz AO Q-switch modulation frequency (c) Oscilloscope trace of output pulse train

pulse repetition rate becomes 10 kHz. Also, it was observe that for higher AO Q-switch modulation frequency 30 kHz, output pulse repetition rate varies from 10 kHz to 30 kHz on increasing the pump power. This variation in output pulse repetition rate is attributed to reabsorption losses in Yb:YAG laser crystal which are saturable in nature. Hence it can be considered that system acts like a hybrid Q-switched laser system containing an active (AO QS) as well as passive Q-switch element. At low input pump power reabsorption losses are unsaturated due to lower intracavity intensity and hence during one cycle of AO QS modulation frequency accumulated population inversion in gain medium is insufficient to overcome the overall system loss. Hence hybrid Q-switching system

requires two or more cycles to achieve the population inversion for pulse build up and consequently output pulse repetition rate reduces to submultiple of modulation frequency of AO Q-Switch. At high pump power, accumulation of population inversion within one cycle of the AO Q-switch modulation frequency is sufficient to overcome the threshold and output pulse repetition rate follows the AO QS modulation frequency. Fig. 2(b) represents the variation of the output average power and pulse duration (FWHM), when AO Q-switch modulation frequency was set to 10 kHz. From this graph we observed that as laser crosses the threshold, output power increases almost linearly with the input pump power. ~3.7 W of maximum average power at 40.5 W of input pump power was obtained. On the other hand, on varying the pump power, initially, pulse duration decreases rapidly then increases and again decreases gradually with pump power. For 10 kHz modulation frequency, in between pump power of ~25.5 W and 26.5 W pulse duration increases, as in this pump power interval output pulse repetition rate switches from 5 kHz to 10 kHz as that of modulation frequency and hence a lower gain at higher modulation frequency leads to rise in pulse duration [5]. On further increasing the pump power, output pulse duration gradually reduces due to high gain. At maximum operating pump power, a minimum ~125 ns duration with 10 kHz pulse repetition rate was recorded. Fig. 2(c) shows oscilloscope trace for recorded pulse train of the output pulses (green) at 20 kHz modulation frequency (pink) of AO Q-switch for 26W of pump power. It is clear from the fig (2) that the output pulse repetition rate is 10 kHz as output pulse is appeared after two cycle of the modulation frequency. It shows that during one cycle of modulation frequency reabsorption losses are not saturated and corresponding pulse is missed out. However on increasing the pump power, output pulse repetition rate approaches to that of modulation frequency 20 kHz. Further it was seen that, at high repetition rate of 30 kHz, two consecutive pulses get missed and hence we get output pulse train at 10 kHz. On increasing the pump power, output repetition rate increases to 15 kHz and finally becomes 30kHz as shown in fig 2(a).

Also, we have numerically analysed the rate equations for actively Q-switched Yb:YAG laser considering the reabsorption losses as a passive Q-switch element in the cavity. For a hybrid Q-switched laser consisting of an active and passive Q-switch rate equations for cavity photon density $\phi(t)$, the population inversion density of the gain medium n(t) and the population density of the saturable absorber for absorbing state $n_s(t)$ are given by [7]:

$$\frac{d\phi}{dt} = \frac{\phi}{t_r}\left\{2\sigma ln - 2\sigma_s l n_s - \ln\left(\frac{1}{R} + \delta_a(t) + L\right)\right\} \quad \ldots\ldots\ldots (1)$$

$$\frac{dn}{dt} = R_p - \frac{n}{\tau_f} - 2\sigma c\phi n \quad \ldots\ldots\ldots (2)$$

$$\frac{dn_s}{dt} = \frac{n_{s0} - n_s}{t_s} - c\sigma\phi n_s \quad \ldots\ldots\ldots (3)$$

Here, t_r is the intracavity photon round-trip time; σ, l, and τ_f are the stimulated emission cross section, the length, and the spontaneous decay time of the gain medium, respectively. σ_s and τ_s are the absorption cross section, and the recovery rate of the passive Q-switch; R is the reflectivity of output coupler mirror; L is the cavity loss; R_p is the pump rate; c is the speed of light in vacuum; n_{s0} and n_s is the population densities in ground and excited state of saturable absorber and δ_a is the time dependent loss function for active Q-switch.

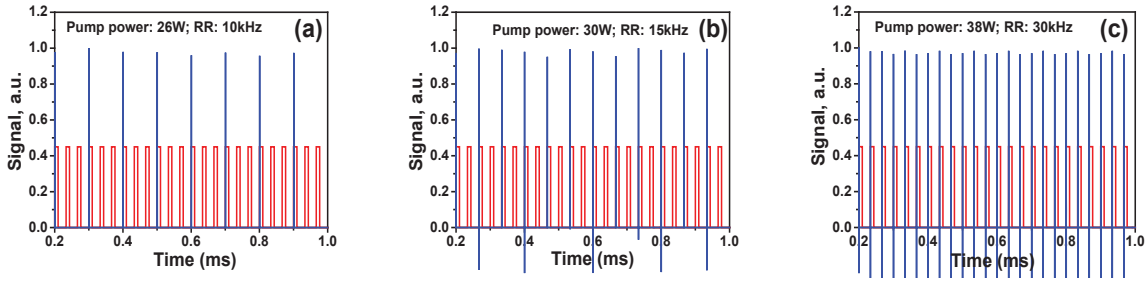

Fig 3. Numerically analyzed output pulse train at different pump power (a) 26W (b) 30W and (c) 38W for AO Q-switch modulation frequency of 30 kHz.

Fig. 3 represents the numerically solved pulse train for varying input pump power for a fixed modulation frequency of active Q-switch of 30 kHz. We observe from fig.3 that at low input pump power of 26W, repetition rate for output pulse train is 10 kHz. For low pump power, intracavity pulse energy is not much enough to saturate the loss during two cycle of modulation frequency hence two pulses are missed out and hence pulse repetition rate is submultiple of modulation frequency. As we increase the pump power upto 30W, pulse energy increases and output pulses after one cycle of modulation frequency are come out with a repetition rate of 15 kHz. Further at higher pump power for 38 W, pulse repetition rate follows the modulation frequency due to higher pulse energy which saturates the losses within one cycle of modulation frequency. These numerically analysed results are in well accordance with the experimental results and confirm the saturable nature of quasi three level Yb:YAG laser crystal due to reabsorption loss. Therefore an actively Q-switched Yb:YAG laser exhibits the behaviour of hybrid Q-switched laser for a certain pump power and modulation frequency of active Q-switch, however at moderate pump power, laser works as a purely active Q-switched laser

Conclusions:

In conclusion, considering the reabsorption losses for quasi three level Yb:YAG laser crystal, the performance of acousto-optic Q-switched Yb:YAG laser operating at 1030 nm were studied. Laser system acts like a hybrid Q-switched laser consisting of an active and passive Q-switch element in cavity. Laser was operated for various modulation frequencies of acoustic optic Q-switch and pulse characteristics were observed. It was found that output pulse repetition rate and pulse duration changes in a periodic manner with the pump power due to saturable nature of reabsorption losses. Further output pulse repetition rate becomes submultiple of Q-switch modulation frequency and laser output pulse can be get at low repetition rate even though for higher modulation frequency of AO Q-switch at an optimum pump power.

References:

[1] G. L. Bourdet, Applied Optics 39(6) (2000)

[2] T. Y. Fan, IEEE J. Quantum Electron 29, 1457–1459 (1993).

[3] D. S. Sumida, T. Y. Fan, Optics Letters, 20, 2384–96 (1995)

[4] R. J. Beach, Optics Communications 123, 385-393 (1995)

[5] W. Koechner, 6th ed. Berlin: Springer (1999).

[6] P. K. Gupta, A. J. Singh, S. K. Sharma, P. K. Mukhopadhyay, K. S. Bindra, S. M. Oak, Review of Scientific Instruments, 046110 (2012)

[7] A. E. Siegman, Lasers, University Science, Chap. 26 (1986).

Development of compact engineered 500 W of single transverse mode all-fiber Yb-doped CW fiber laser

Avdhesh Kumar *, Pushkar Misra, R. K. Jain, Rajpal Singh, V. Bhardwaj, B. N. Upadhyaya, K. S. Bindra
Laser Technology Division, Raja Ramanna Centre for Advanced Technology, Indore-452013, India
*E-mail: avdhesh@rrcat.gov.in

Abstract: In this article, we report on the development of a compact engineered version of 500 W of all-fiber Yb-doped CW fiber laser (YDFL) with single transverse mode (~LP_{01}) output using single-end pumped oscillator configuration. In this single-end pumping configuration, an optical-to-optical slope efficiency of ~75% has been achieved and output beam is nearly diffraction limited with beam quality factors of M_x^2 ~ 1.3 and M_y^2 ~ 1.24. The generated laser signal has a peak at 1080 nm with a 3 dB FWHM linewidth of ~ 1.28 nm. This laser has potential application in cutting, welding and additive manufacturing.

Introduction: High power, multi-kilowatt, Yb-doped CW all-fiber lasers have been demonstrated with laser output signal having nearly diffracted limited beam quality[1]. High power Yb-doped CW all-fiber lasers have been established to have a superior position in multi-kilowatt laser class and surpass others in terms of high wall-plug efficiency, single-mode of operation, compactness, robustness, no misalignment sensitivity and efficient heat dissipation due to large surface area to volume ratio along with all-fiber integration for fiber optic beam delivery. There are two major configurations for generating high power output from fiber lasers, namely; (a) oscillator configuration, and (b) master oscillator power amplifier (MOPA) configuration, which amplifies seed signal from oscillator stage. Zeng et. al.[2] have recently demonstrated near-single-mode 3 kW CW laser power at 1080 nm based on bi-directional pumped monolithic fiber oscillator configuration with optical-to-optical conversion efficiency of 78.4%. The Yb-doped fiber used by Zeng et al. has core/clad diameter of 20/400 μm at both the ends and 30/600 μm in the middle. Yang et al.[3] have reported a maximum output power of 5.2 kW from bi-directional pumped monolithic fiber laser oscillator in fiber core/clad diameter of 25/400 μm with optical-to-optical conversion efficiency of 63%. In MOPA configuration, Yu et al.[4] have demonstrated 3.15 kW of output power with an optical-to-optical conversion efficiency of 75.1% at 1080 nm. Beier et al.[5] have demonstrated 4.3 kW of single transverse mode output power with 90% slope efficiency using amplification of seed of 10 W power at 1067 nm in a 23 μm core diameter optical fiber. Multi-kilowatt Yb-doped all-fiber laser with its high end superiority finds multiple applications in the field of material processing such as laser additive manufacturing, rock and concrete drilling in natural gas and oil exploration, defence, etc. High power CW fiber lasers have become dominant in directed energy weapons. Major challenges faced in the development of multi-kilowatt all-fiber laser systems are: (a) availability of high power compatible components like fiber coupled pump diodes, fiber optic pump & signal combiner and fiber Bragg gratings, (b) minimization of splice loss (c) hotspots in recoated splice joints, (d) efficient heat removal from all fiber components and gain fiber, (e) suppression of self-pulsing, (f) nonlinear effects, (g) transverse mode instability (TMI), and (h) phenomena like fiber fuse effect and photodarkening.

In this direction, we are working on the research and development on high power Yb-doped all-fiber laser systems at RRCAT. We have already demonstrated table-top 700 W output power from Yb-doped all-fiber laser system at 1080 nm with a 3 dB FWHM linewidth of ~ 1 nm[6]. In an attempt to make compact engineered systems for material processing applications, engineered prototype module of 250 W single transverse mode all-

fiber Yb-doped CW fiber laser system[7] pumped at 976 nm has already been performed. Now, we have performed development of compact engineered module of all-fiber 500 W Yb-doped CW fiber laser system pumped at 915 nm. In this design, pumping wavelength of 915 nm was selected to minimize effect of variation in pump wavelength with change in diode temperature and diode pump current, since absorption peak of Yb-doped fiber at 915 nm is very broad as compared to sharp absorption peak at 975 nm. The use of the pump wavelength at 915 nm also results in reduced heat load in the starting pump section of the gain medium as compared to pumping at 975 nm, but requires increased gain fiber length. Compact thermal packaging of fiber lasers with reliable operation is also a challenging task due to requirement of efficient heat removal from various fiber laser components and splice joints. Major problems faced in the development of all-fiber laser system are minimization of splice loss, reliable re-coating at each splice joint, efficient removal of heat load from thin polymer coated double-clad fibers, selection of compatible fibers for pump combiner and gratings.

Experimental Details: Schematic of 500 W of Yb-doped CW all-fiber laser system is shown in figure 1. In this all-fiber laser setup, a Yb-doped double-clad (DC) fiber has been used as the gain/active medium having core/clad diameter of 20/400 µm and outer clad diameter of 550 µm. Numerical apertures of the core & inner clad are 0.075 and 0.46, respectively. Inner clad geometry is of octagonal shape to avoid excitation of skew modes. Yb-doped double-clad fiber has a cladding absorption of 0.4 dB/m at 915 nm. Yb-doped fiber section of 35 m length has been used for efficient absorption of the pump beam providing a total pump absorption of 14 dB (~96%). A diode pump module of six fiber-coupled laser diodes at 915 nm wavelength has been made for pumping of Yb-doped double clad fiber. Each fiber coupled diode provides a maximum output power of 158 W. This diode-pump module has been spliced with (6+1) x1 fiber optic pump and signal combiner.

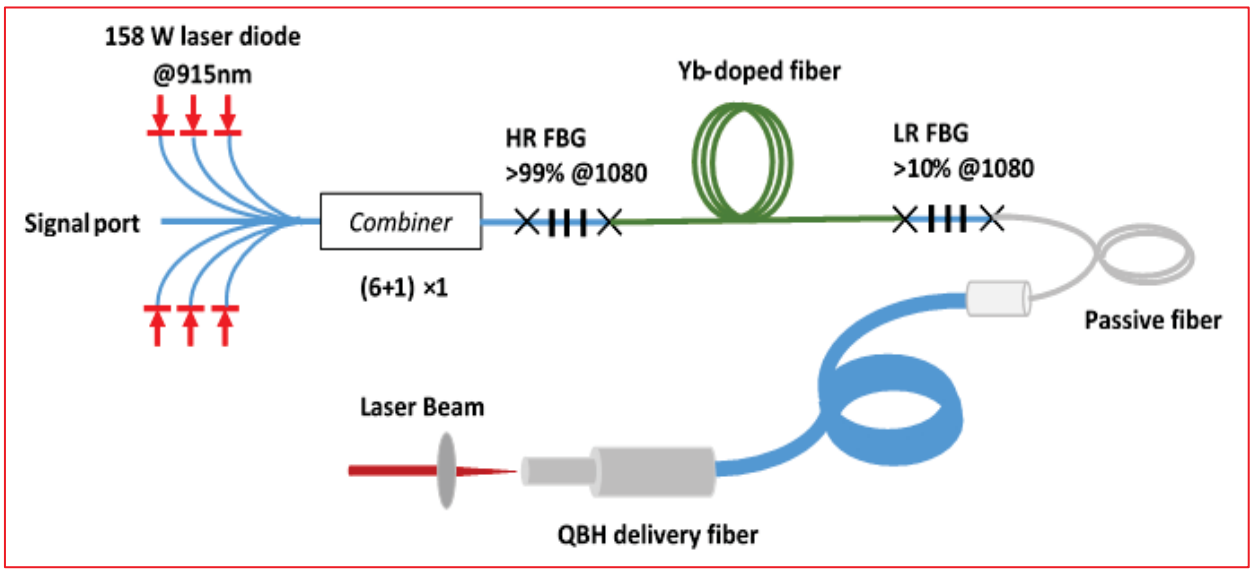

Fig. 1: Schematic of 500 W of all-fiber Yb-doped CW laser system.

The output end of fiber optic pump combiner has a core diameter of 20 µm and inner clad diameter of 400 µm. The combined output power available from six pump laser diodes (maximum current) at the output end of fiber optic pump combiner is ~900 W. The output end of fiber optic pump combiner has been spliced to the input end

of highly reflecting (HR ~99%) fiber Bragg grating (FBG) at 1080 nm and the output end of FBG has been carefully spliced to the octagonal shape Yb-doped DC gain fiber. This fiber Bragg grating is written in a compatible double-clad fiber and it has a peak reflectivity at 1080 nm with a 3 dB FWHM bandwidth of 2 nm. The other end of octagonal shape Yb-doped DC gain fiber has been spliced to another low reflectivity (LR) output coupler (OC) FBG of ~10% reflectivity at 1080 nm and 3 dB FWHM bandwidth of 1 nm. Laser resonator is formed between HR FBG and OC FBG. The output end of OC FBG has been spliced to a 20 m long quartz block head connectorized 20/400 μm fiber optic cable for remote material processing application. Figure 2 (a) shows cross-section of Yb-doped double clad fiber used in the set up and Fig. 2(b) shows a typical splice joint of double clad fiber with fiber Bragg grating.

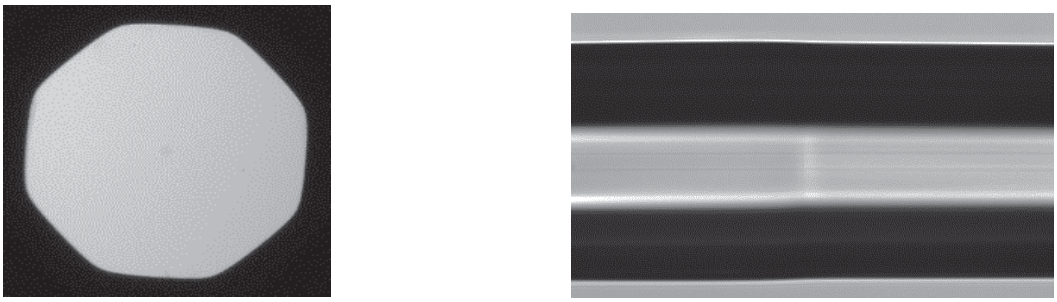

Fig. 2: (a) Cross-section of Yb-doped double clad fiber used in the set up, and (b) a typical splice joint of double-clad fiber with fiber Bragg grating.

Figure 3 shows a view of the compact prototype version of 500 W Yb-doped all-fiber CW fiber laser system and its chiller unit. All the components of fiber laser like pump diodes, gain fiber, FBGs, optic pump combiner and power supply to pump diodes are carefully packaged in a single cabinet. Pump laser diodes used in the set-up have electrical to optical slope efficiency of ~40%, hence these diodes have been mounted on water cooled heat sink for better performance. Further, any irregularity in splice joints or any trap of dust during splicing degrades the quality of joints, hence becomes a source of power loss and it has been observed that when the temperature of splice joint reaches above 80^{o} to 90^{o}C, the joints get burnt. Fiber components likes pump combiner and FBGs have been mounted on water cooled heat sink for their reliable operation. Figure 4 shows variation of laser output power as a function of input pump power. It shows that there is no saturation in the output power due to any thermal or nonlinear problems, which indicates possibility for further scaling of output power with increase in input pump power. At an input pump power of 703 W, 529 W of laser output power has been achieved with an optical-to-optical slope efficiency of 75%. Output beam profile has been measured by using NanoScan v2 beam profiler and beam quality of M_x^2 ~ 1.3 & M_y^2 ~1.24 has been measured. This laser system has been operated continuously for more than 3 hrs. for testing purpose and 1hr./day for a month time and the output from the laser was found to be stable within 1.5%. Fig. 5 shows stability of laser output power with time. Figure 6 shows laser output spectrum with a peak at 1080 nm and FWHM linewidth of ~ 1.28 nm at 500 W of output power.

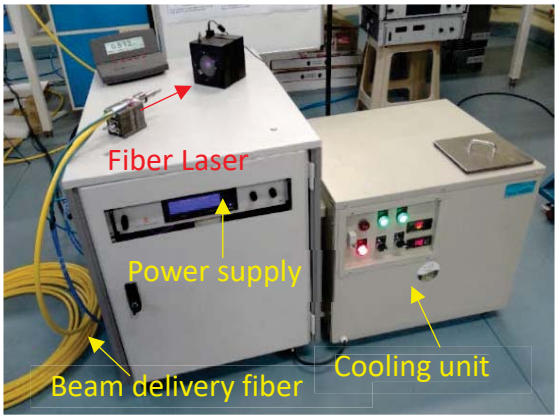

Fig. 3: Compact prototype *version of 500 W of all-fiber Yb-doped CW fiber laser system.*

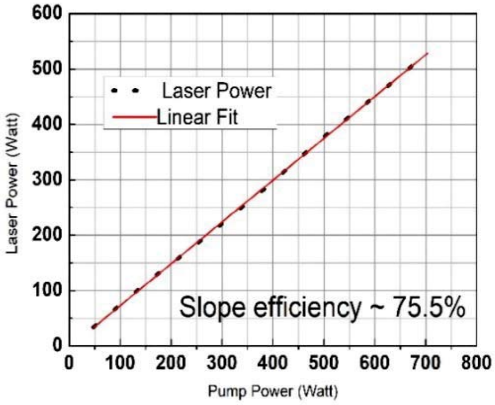

Fig. 4: Variation of laser output power as a function of input pump power for 500 W Yb-doped CW fiber laser system.

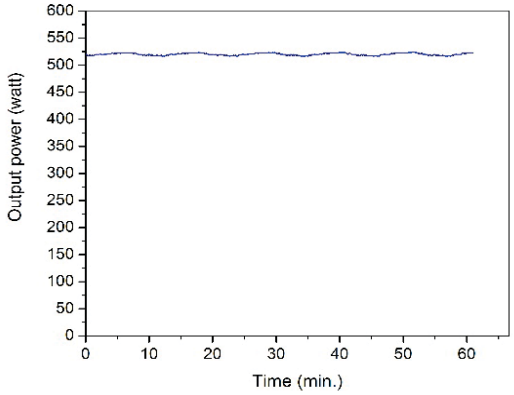

Fig. 5: Output power stability for one hour of continuous operation.

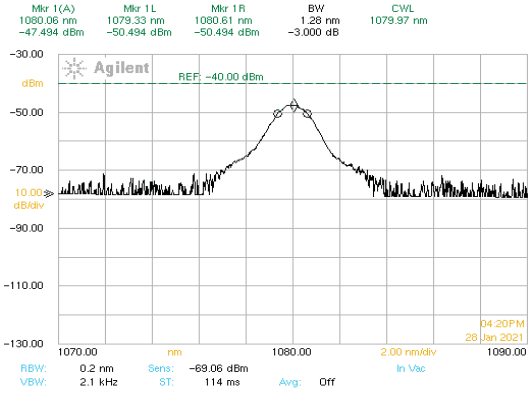

Fig. 6: Laser output spectrum at the maximum output power of 500 W.

Conclusion: In conclusion, development of a compact engineered version of 500 W of all-fiber Yb-doped continuous wave (CW) fiber laser with nearly diffraction limited output beam using single-end pumped all-fiber oscillator configuration and 915 nm pump wavelength has been carried out. Laser output power is stable within 1.5% over 1 hr. of continuous operation. An optical-to-optical slope efficiency of 75.5% has been achieved. The output signal has a peak at 1080 nm with a 3 dB FWHM linewidth of ~ 1.28 nm. This laser has potential application in cutting, welding and additive manufacturing.

References:

1. URL: <http://www.ipgphotonics.com>.
2. Lingfa zeng et al., *Optics Letters*, Vol. **45**, No. 20/15 October 2020.
3. Baolai Yang et al., *Laser Phys. Lett*. **15**(2018) 075106.
4. Hailong Yu et al., *Appl. Opt.*, Vol.**54**, No. 14, 4556-4560 (2015).
5. F. Beier et al., *Optics Express*, Vol. **25**, No. 13, 14892-14899 (2017).
6. Pushkar Misra et al., *DAE-BRNS National Laser Symposium-2018*, Indore.
7. Avdhesh kumar et al., *DAE-BRNS National Laser Symposium-2020*, Chennai.

Parametric Study on Optimization of Double Side Transversely Pumped High Power Pulsed Dye Laser Amplifier performance

J.S.B. Singh

Tunable laser Section, BTDG, BARC, Mumbai - 400085

Email: jeetu@barc.gov.in

Abstract: In order to maximize the efficiency of pulsed dye laser (DL) amplifier pumped by excitation source like copper vapor laser (CVL) or frequency doubled diode pumped solid state laser (DPSSL), optimization of dye concentration, gain length for given pump and signal intensity is essential. The model based on laser rate equations predicts the optimum dye concentration and gain length for given pump and signal intensity, and calculates power extraction efficiency for transversely pumped double side amplifier.

1. Introduction : The most common practice for achieving high power narrow band DL system is to use a narrow band low power oscillator followed by high power pulsed amplifier chains[(1)]. Theoretical modelling of such system specifically amplifier is highly essential to design high power DL facility. The model aims to study effects of several parameters like pump intensity, signal intensity to amplifier, ground state absorption (GSA) and excited state absorption (ESA) at signal wavelength, dye concentration, etc on dye amplifier extraction efficiency. Similar kind of work has been reported by A. Sugiyama et al.[2], where they have considered ASE in rate equation and modelling of amplifier was done only for single side pump configuration. R. Hargrove and T. Kan [3] reported an extensive experimental work on double side pumping configuration but with low signal power (ESA was not considered). A very little information is available about work on double side pumped pulsed dye laser amplifier at high average pump power. The important assumptions made in the model are as follows: (a) the pump intensity across the beam on pump window and, signal intensity across the beam on signal window to be uniform, b) gain loss due to ASE is negligible; (c) signal beam size completely overlaps with the gain volume created by pump and (d) no triplet state effects. The cross sections data and excited state life time used in the model are taken from ref [2].

2. Numerical Solution: To solve numerically, the area (1 mm X 10 mm) of pump window is divided into 100 grids and signal window (1 mm X 1 mm) is divided into 40 grids respectively (fig-1). Calculations vary by less than 1 % when grids value exceeds 100 (along X-axis) and 40 (along Y-axis) and, hence further refinement of gain volume was not considered. The error in the calculation mainly depends on accuracy of cross sections value and assumptions used to simplify the equations. Equations (3) to (7) are solved numerically using finite difference method with indexing of zone, N_1, I^l, I^{P+} and I^{P-} are obtained at 40 X 100 locations inside gain region. Boundaries conditions are suitably applied before each calculation. Equation (6) gives signal intensity values from which signal output power, P^l could be obtained as

$$P^l = I^l * (Rh\nu^l \Delta t^l H^l W) \qquad (1)$$

Where R is the pulse repetition frequency (prf), h: Planck constant, ν^l: signal frequency, Δt^l: pulse duration of signal pulse (55 ns), H^l: height of the signal beam, and W: Width of the gain medium.

The energy extraction efficiency is given by, $e = (P^{out} - P^{in})/P^{pump}$ (2)

Where, P^{in}, P^{out}, and P^{pump} are the average values of dye-laser input power, amplifier output power, and the pump laser power, measured with power meter.

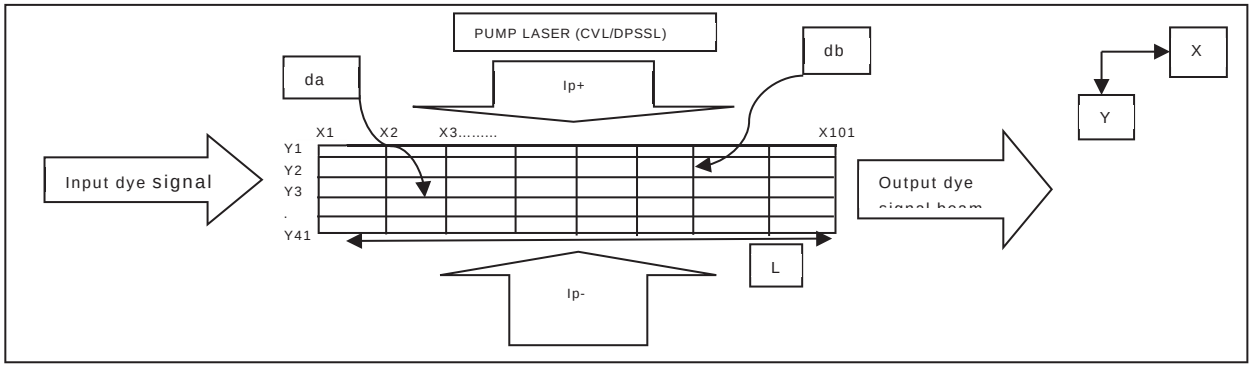

Figure-1: Schematic of transversely pumped dye amplifier, L: length of active medium, X and Y arrows are directions for signal and pump propagation inside gain medium respectively. da and db are grid elements along x-axis and y-axis respectively.

3. Equations used for the computation:

$$\frac{\partial N_1}{\partial t} = N_0\,\sigma_{01}^{p} * (I_{p+} + I_{p-}) - N_1/\tau - N_1\,\sigma_e^{l} I^{l} - N_1\,\sigma_{1N}^{l} I^{l} - N_1\,\sigma_{1N}^{p}(I_{p+} + I_{p-}) + N_0\,\sigma_{01}^{l} I^{l} \quad \text{.....(3)}$$

$$N_1 + N_0 = N_T \quad \text{..... (4)}$$

Setting LHS= 0 in eq. 3 for steady state condition and rearranging gives N_1

$$N_1 = \frac{N_T * [\sigma_{01}^{p}(I_{p+} + I_{p-}) + \sigma_{01}^{l} I^{l}]}{\left[\frac{1}{\tau} + (\sigma_e^{l} I^{l} + \sigma_{1N}^{l} I^{l}) + \sigma_{01}^{p}(I_{p+} + I_{p-}) + \sigma_{1N}^{p}(I_{p+} + I_{p-}) + \sigma_{01}^{l} I^{l}\right]} \quad \text{..... (5)}$$

$$I^{l}(x_i, y) = I^{l}(x_{i-1}, y) * exp \int_{x_{i-1}}^{x_i} \{N_1(x_i, y)(\sigma_e^{l} - \sigma_{1N}^{l}) - N_0(x_i, y)\sigma_{01}^{l}\} da \text{..(6),}$$

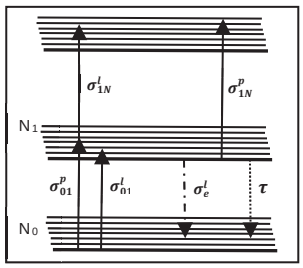

Fig. 2: Energy level diagram

For i=2 to 101.

$$I^{p+}(x, y_j) = I^{p}(x, y_{j-1}) * exp \int_{y_{j-1}}^{y_j} -\{N_1(x, y_j)\,\sigma_{1N}^{p} + N_0(x, y_j)\,\sigma_{01}^{p}\} db \text{.. (7),}$$

For j=2 to 41.

$I_{sat} = \frac{1+\sigma_{01}^{p} Ip\,\tau}{(\sigma_{01}^{l}+\sigma_e^{l})*\tau}$ …. (I_{sat}: Saturation intensity)……..(8)

N_1, N_0 *and* N_T : Population density of first excited state, ground state and total respectively.

σ_e^{l}, σ_{1N}^{l} *and* σ_{1N}^{p} : Stimulated emission cross-section, ESA at signal wavelength and pump wavelength respectively.

$\sigma_{01}^{l}, \sigma_{01}^{p}$: Ground state absorption cross-sections at signal wavelength and ground state absorption at pump wavelength (532 nm) respectively. τ**:** Spontaneous decay life time of first excited state.

I_{p+} : Pump intensity in positive y-direction. Although, I_{p-} (pump intensity in negative y-direction) is not written but expression is identical to that of I_{p+} and has been used in the model. I^{l}**:** Laser intensity at signal wavelength**.**

4. Experimental set-up: A CVL-master oscillator power amplifier system was used to pump DL oscillator and amplifier chain. Only green (510.6 nm) component was used to pump a grazing incidence grating-type dye laser oscillator and DPSSL (532 nm) was used to pump amplifier. The amplifier cell (material: fused silica) had a gain volume of 1 mm X 1 mm X 10 mm. A combination of 2 spherical lenses and 2 cylindrical lenses were used to focus optical fibre delivered pump beam to approximately a 1 mm X 10 mm strip on the cell surface of amplifier. Rh6g dissolved in ethanol with concentration of 0.27 mM in amplifier was used. The concentration used in this experiment corresponds to high absorption of pump power. The input and amplified output power were measured with an Ophir make thermopile based power meter, L-30A. Wavelength of signal beam was measured with Angstrom make WS-6 model.

5. Results and discussions: Two DPSSL units were used to pump main-amplifier from opposite sides of dye cell. Each pump had an average 34 W of power, measured before dye cell pump window. The input signal was precisely time synchronized with the arrival of pump pulse on the dye cell. Dye oscillator was tuned to design wavelength of 583 nm.

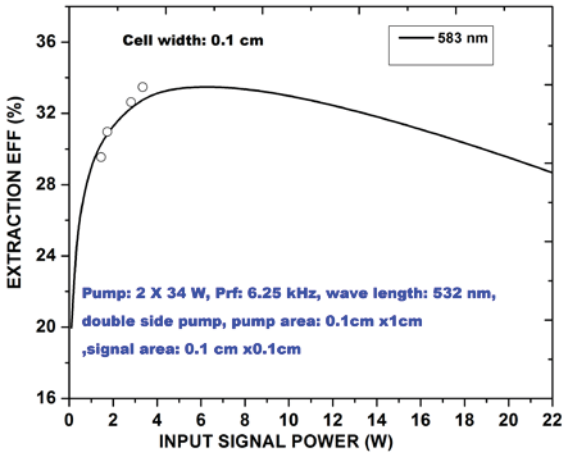

Fig.3: Computed extraction efficiency versus input signal power. Experimental data points are shown by bubble dots.

Fig.3 shows the variation of *amplifier-efficiency* on input signal power. At lower signal power, efficiency increases very rapidly indicates that signal power is insufficient to extract gain available with the given pump intensity. After (saturation power) 3.41 W, rate becomes slower thereafter it falls gradually. The fall in *amplifier- efficiency* at high signal power is basically due to (a) significant ESA at higher power at signal wavelength and (b) higher GSA at signal wavelength[5]. It may be noted that the model results are in close agreement with the experimental results near the operating region**.**

5.1. Optimization of dye concentration and dye cell length for 1 mm width cell

(a) Dye concentration: In order to check dependence of dye amplifier extraction efficiency with dye concentration for case of 1 mm cell width. Pump intensity and signal intensity are kept constant and, extraction efficiency is computed for dye concentration ranging from 0.07 to 0.77 mM in step of 0.1 mM. The result of the computation is shown in fig. 4. Efficiency reaches maximum value around 0.27 mM but gain will be highly non-uniform across cell width. For lower dye concentration, ground state density will be less; therefore population inversion will be less resulting in low efficiency. With higher concentration, absorption of signal photon due to GSA and ESA leads to drop in efficiency at signal wavelength [4]. In addition, low gain (due to pump attenuation) seen by the central part of the signal beam could also lead to drop in efficiency.

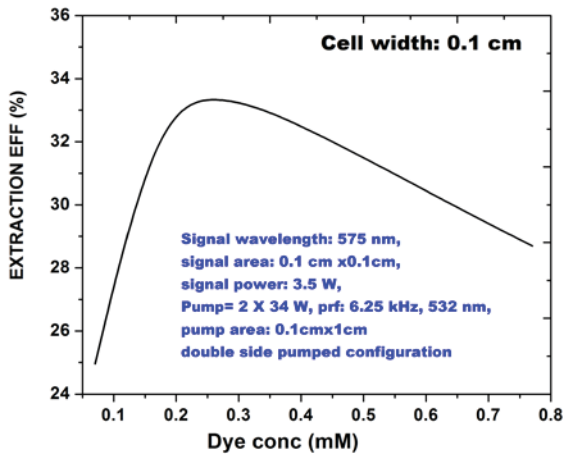

Fig4: Computed extraction efficiency vs. dye concentration, dye cell length fixed at 1cm.

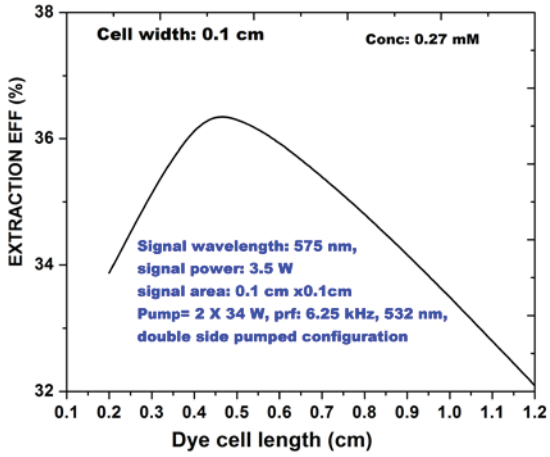

Fig.5: Computed extraction efficiency of dye amplifier for varied dye cell length. Signal intensity was fixed.

(b) **Dye cell length**: To determine optimum dye cell length; dye cell length is varied from 0.2 cm to 1.2.cm in steps of 0.2 cm and corresponding efficiency is computed while keeping signal intensity and dye concentration constant. The result of the computation is shown in figure5. On smaller gain length, fall in efficiency is attributed to shorter gain length as gain is exponential in this regime. And, on larger gain length, fall in efficiency is due to higher GSA and ESA at higher signal intensity as it propagates along gain length[(5)] and drop in pump intensity.

6. Conclusions: The model predicts that in case of 1 mm cell width, maximum efficiency will occur for dye concentration around 0.27 mM. And, efficiency is maximum for dye cell length of 0.5 cm at dye concentration of 0.27 mM. The model results are in close agreement with the experimental observations for figure-3. A fitting factor of 1.049 is used for obtaining best fit with the experimental data, because exact pump area and signal area on dye cell surface could not be obtained accurately. The model result would be useful in setting up pump distribution, dye concentration and designing dye cell geometry for high power DL facility.

Acknowledgment: Author is grateful for experimental support by TLS members of ATLAF-BTDG.

7. References:

1. L. G. Nair, *dye laser, Prog. In quantum electron, 7,153(1982).*
2. Akira Sugiyama et al., *Applied optics, Vol-36, P.5849-5853(1997)*
3. R. S. Hargrove and T. Kan, *IEEE J. Quantum Electron, Volume-16(10), P: 1108-1113 (1980).*
4. Marcelo G. Destro and Jos W.Neri, *Applied optics, Vol. 31, P. 7007-7011(1992).*
5. K. Dasgupta and L. G. Nair, *IEEE Journal of Quantum Electronics, Vol. 26(1), P. 189-192(1990).*

Analysis of core reset in magnetic pulse compression network of metal vapor laser

[*]Dheeraj K Singh[1, 2], B Dikshit[1, 2], Jaya Mukherjee[2], V S Rawat[1, 2]

[1] *Homi Bhabha National Institute, Anushaktinagar, Mumbai, India*

[2]*Laser and Plasma Technology Division, Bhabha Atomic Research Centre, India*

Email: [*]dheeraj@barc.gov.in

Abstract

All solid-state pulse power supply uses magnetic pulse compression circuit (MPC) to reduce the rise time of the voltage pulse applied across the Metal vapor Laser (MVL). In high repetition rate MVL, proper reset becomes extremely important because of tight timing and low jitter requirement. At low repetition rate, resetting of magnetic switch is easy as the oscillation in LC circuit in MPC dies out before the next pulse. However, as the repetition rate increases there is very little time for reset dynamics to take place before the next pulse. Thus, at high repetition rate, understanding of MPC dynamics becomes important for parameter optimization to get desired performance from MPC. In this paper we have presented detailed dynamics of high repetition rate MPC. We have shown how MPC oscillation affects the B-H curve of the magnetic switch. An experimentally validated simulation model is developed for detailed analysis of dynamics of MPC and to observe other implications like effect of reset on jitter in output of MPC.

Keywords: - Magnetic Pulse Compression; Core reset; Pulse Power Supply; Magnetic Switch; Copper Vapor Laser.

Introduction

In order to increase the high energy state electrons i.e., population inversion, in copper vapor Laser (CVL), electrical discharge is applied. As the upper energy level has very short life time (<100ns), the pulse discharge needs to have sharp rise time of less than 100ns [1, 2]. This requirement of low-rise time voltage pulse is accomplished using magnetic pulse compression circuit. MPC is an L-C circuit with capacitor used for storing energy and saturable inductor acts as switch [3]. The switching operation is performed by inductor by virtue of variation in inductance due to non-linear B-H characteristics of ferromagnetic core of the Inductor. During unsaturated state it acts like an open switch and in saturation state it acts like a closed switch [3, 4]. In MPC stages, capacitor value is fixed in each stage and inductance value is reduced to reduce the rise time with maximum power transfer in successive stages.

At high repetition rate understanding of MPC dynamics becomes important for parameter optimization to get desired performance from MPC. Reset is used in magnetic switches to ensure constant ΔB variation in each pulse and quickly die out the oscillations set inside the MPC [4, 5]. As laser is a dynamic load without proper reset there will be ΔB variation due to load variation. As CVL is generally operated in MOPA configuration, jitter constraint becomes even tighter [1]. Therefore, understanding of reset dynamics and then application of proper reset current becomes crucial. In this paper a detailed analysis of the reset dynamics has been shown. Behavior of magnetic switches due to oscillation in MPC is presented using derived B-H curve with hysteresis.

Description of Laser power supply

Circuit diagram of pulse power supply is presented in fig 1. The detailed description of the pulse power supply is presented in reference 6, 7. The output of pulse power supply is 13 kV voltage pulse with rise time of ~80ns.

CVL acts as load offering impedance of ~25 ohm. The details of simulation of power supply are presented in reference 7. In simulation model a fixed resistive load is used and all the components are assumed ideal.

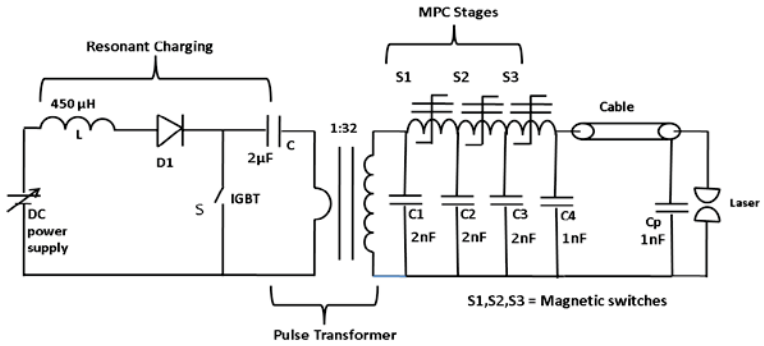

Fig 1 Circuit diagram of Pulse power supply

The B-H curve of the switches is simulated using following equation and Jules Atherton model [8, 9, and 10]

$$B = \frac{\int V dt}{N A_e} \text{ and } H = \frac{IN}{l_e} \qquad \text{eq (1)}$$

Where *N* is the number of winding turns, *Ae* is the effective cross-section area that is the actual area of the magnetic material in the core excluding the area of the insulation and *le* is average magnetic path length. The B and H value calculated using simulated voltage and current waveform is used to draw B-H curve. Three Ni-Zn ferrite cores of dimension 150/100/15 mm are used for each switch with primary and secondary turns of 48/4, 13/4 and 4/4 respectively for S1, S2 and S3. The purpose of adding hysteresis in the B-H curve is to see the effect of MPC dynamics on B-H curve. Hysteresis is added using Jiles Atherton method for nonlinear inductor in simulation model with the parameters value as shown in table 1.

Table 1 Jiles Atherton parameter for Hysteresis simulation

Parameter	S1	S2	S3
Number of primary / reset turns	48/4	13/4	4/4
Effective length	.471m	.471m	.471m
Effective cross-sectional area	.002250m^2	.002250m^2	.002250m^2
Anhysteric B-H gradient	.003mT/A	.003mT/A	.003mT/A
Flux density point on Anhysteric B-H curve (T)	0.2	0.2	0.2
Corresponding field strength	150	100	100
Coefficient for reverse magnetization	0.5	0.4	0.2
Bulk Coupling Coefficient	15	15	20
Inter domain coupling factor	1e-9	1e-9	1e-9

Fig 2 shows the B-H curve for all the three switches. It can be seen that even with fixed load there is oscillation in MPC stages. This can be attributed to inherent nature of L-C circuit. If the load is dynamic than frequency and amplitude of this oscillation will be dynamic. A high frequency oscillation formed between C3 and C4 due to low inductance of S3, current and voltage on S3 oscillates with high frequency which is reflected in the B-H curve of S3. Whereas there is roughly no oscillation in the B-H curve of S1. In S2 few oscillations are there due to oscillating voltage on C 3. Thus, proper resetting of switch S3 is extremely important due to its high frequency oscillation.

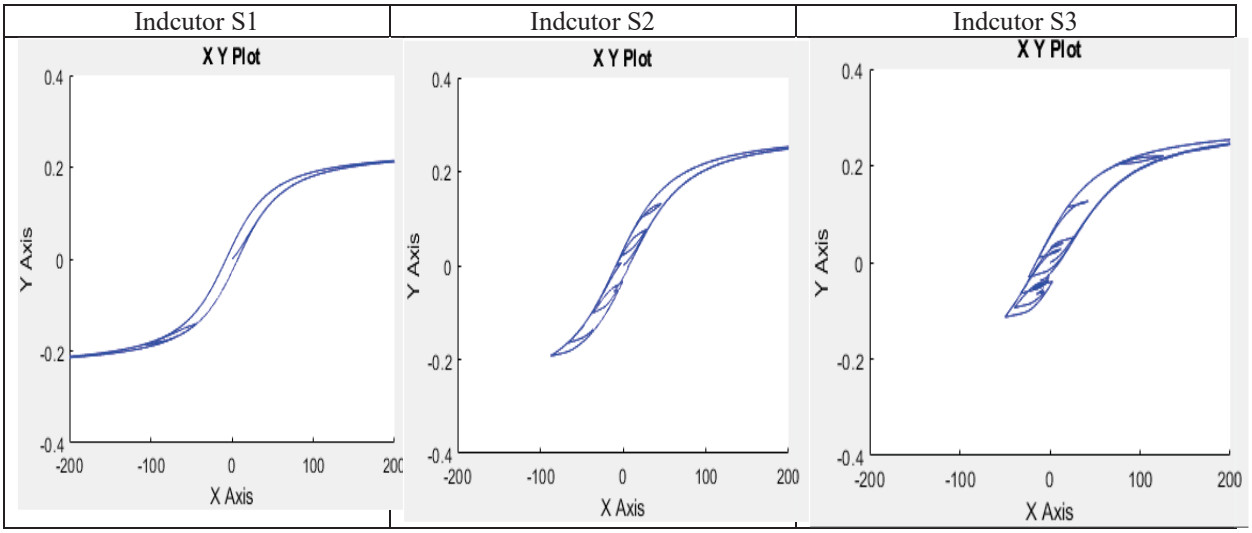

Fig 2 B-H Curve of 3 stages of MPC

Reset in MPC switches

As we know that the dynamics of the MPC involves load impedance. So varying load impedance will change the dynamics of the MPC. We have plotted B field (switch S3) as a function of time for different load impedance of 15/25/35/45 ohm, as shown in fig 3. It can be seen there is significant variation in simulated B field for third stage switch due to load variation. Copper vapor laser is a dynamic load, its impedance varies with time. So, it can be deciphered that the load variation will lead to jitter in the system as per the equation 2.

$$\frac{1}{2}Vt = NA\Delta B \qquad \text{eq (2)}$$

Where *t* is the saturation time of magnetic switch, N is number of turns, A is core area, ΔB is flux density swing and V is voltage applied voltage. As it has been shown that load variation causes variation in B w.r.t time. So ΔB variation available for different pulse will be different and hence it will contribute to jitter.

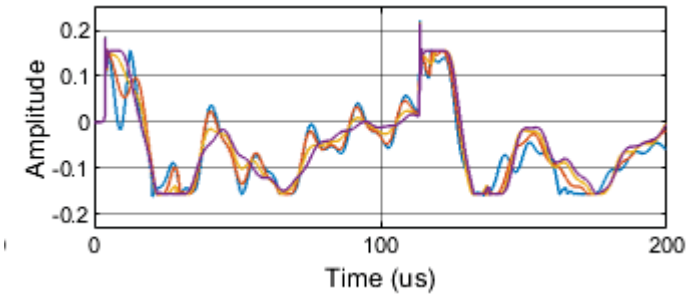

Fig 3 Magnetic Field variation (Tesla) with load impedance of 15/25/35/45ohm for S3 switch

Reset becomes important for MPC stage used in Pulse power supply of dynamic loads like CVL. We have Simulated the B field variation of S1 with time for different values of reset current of 0/0.5/1/1.5. It can be seen that with high reset current, B_{-s} (negative saturation) is quickly reached. As the oscillation in B field quickly damps out, So B_{-s} remains at same value before appearance of next pulse

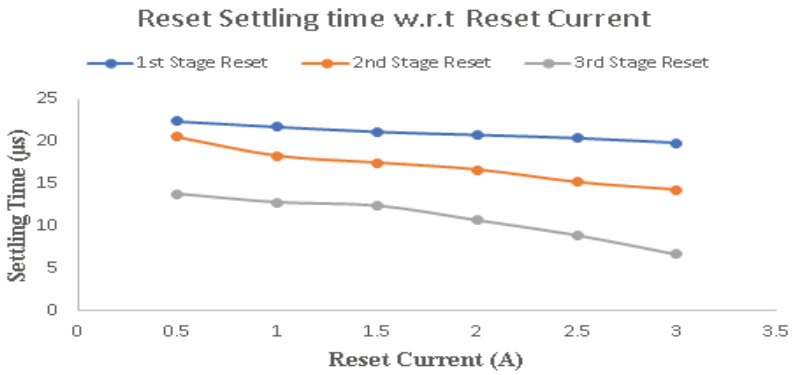

Fig 4 Settling time variation with reset current

Conclusion

A detailed analysis of reset dynamics of MPC is presented. It is shown that load plays a significant role in reset dynamics and influences the MPC parameters. Proper resetting of each switch is important to avoid flux swing variation leading to jitter. As S3 experiences high frequency oscillations it's resetting becomes extremely important.

Acknowledgement: - The authors would like to express their gratitude to Dr Archana Sharma, AD, BTDG for his support and encouragement in this work.

References

1. Metal Vapor Laser; C E Little; John Wiley and Sons [1999].
2. All solid-state pulsed power supply for copper vapor laser; D V Ghodke and K Muralikrishnan, RRCAT Newsletter, vol-22, Issue-I [2009].
3. Introduction of the Magnetic Pulse Compression, Fundamental Review and Practical Application; Jaegu Choi, Journal of electrical engineering and technology Vol. 5, No. 3, pp.484~492, [2010].
4. Core reset consideration in magnetic pulse compression network; D M Barrett, Digest of Technical Papers, Tenth IEEE International Pulsed Power Conference, [2002].
5. Analysis of temporal jitter in a copper vapor laser system; D Durga Praveen Kumar; Review of Scientific Instruments 83, 025105 [2012].
6. Dependence of phantom current in a metal vapor laser on electrode geometry; Dheeraj Kumar Singh, B Dikshit, S Mishra, R Vijayan, A Nayak, Jaya Mukherjee, V S Rawat, Laser Physics, Vol 30, Issue 11, [2020]
7. Exploration of Jitter in Solid State Switch Based Pulse Power Supply of Copper Vapor Laser; Dheeraj Kumar Singh, B Dikshit, N O Kawade, J Mukherjee, V S Rawat, Journal of Russian Laser Research, Vol 41, Issue 6 [2020]
8. Simulation of 3 stage MPC using custom characteristics of magnetic core; Jaegu choi, Takao Namihira, et al, IEEE Transactions on Dielectrics and Electrical Insulation Vol. 14, No. 4, [2007].
9. Extraction of Jiles and Atherton parameters of ferrite from initial magnetization curves; Jacek Izydorczyk, Journal of Magnetism and Magnetic Materials 302, 517–528 [2006].
10. Ferromagnetic Hysteresis; D C Jiles and D L Atherton, IEEE Transactions on Magnetics, VOL. MAG-19, No. 5, [1983].

DPSSL Pumped High Repetition Rate Single Longitudinal Mode Pulsed Dye Laser

V S Rawat[1,2]*,Paramjit Rana[1,2], Siba P Sahoo[1,2], S K Mishra[1], Jaya Mukherjee[1]
ATLAF, BTDG
[1]*Bhabha Atomic Research Centre, Mumbai – 85 INDIA*
[2]*Homi Bhabha National Institute, Anushaktinagar, Mumbai – 94 INDIA*
*Email: vrawat@barc.gov.in

Abstract:

The green beam of high repetition rate DPSSL has been used as pump source for the single longitudinal mode (SLM) pulsed dye laser. The time averaged bandwidth of nearly 250 MHz has been obtained with pulse repetition rate of 9 kHz. The SLM has been obtained in the Littrow configuration with solid etalon of 5 mm thickness and finesse of 19. The SLM dye laser pulse duration was measured to be nearly 35 ns at FWHM with rise time of nearly 12 ns. About 140 mW output power was obtained in single mode dye laser with conversion efficiency of ~ 2.2%.

Introduction:

Single longitudinal mode (SLM) tunable lasers are prerequisite for many high resolution spectroscopic measurements. For several spectroscopic applications variety of tunable laser sources has been developed with specific properties appropriate for the requirement of individual application. The narrow linewidth as well as high power is needed predominantly for the industrial use of SLM dye lasers in the field of isotope separation [1 – 5]. A tunable single mode dye laser is a source of highly coherent electromagnetic radiation, which has high directionality with extremely high spectral purity in the range of 10^{-7} to 10^{-6}. The narrow linewidth can be easily obtained by operating a dye laser in a single longitudinal mode (SLM) while the high power could be achieved by pulse operation of the tunable dye laser system.The main requirements of a pump source for the laser dyes are: adequate absorption in the dye solution, intensity larger than the pump saturation intensity of the fluorescent dye and suitable temporal characteristics of pump laser system. The second harmonic from a Nd:YAG laser is widely used for pumping the dye lasers. The diode pumped solid state laser (DPSSL) meets all these requirements of pump laser source for laser dyes. As the Nd:YAG lasers can be operated from few Hz to high repetition rate of few tens of kHz which seems to be an ideal pump source for pulsed dye lasers. The easiest design of tunable laser is the incorporation of holographic grating in Littrow mode and followed by an output coupler and the wavelength tuning is obtained with rotation of the grating with respect to the cavity axis for this Littrow configuration [3]. The Littrow configuration generates relatively broader linewidth in comparison to the grazing incidence grating (GIG) configuration, which can be further narrow down by insertion of one or more intra-cavity F P etalons. In this paper we are presenting a DPSSL pumped SLM dye laser operating at 9 kHz pulse repetition rate by using F P Etalon of 5 mm thickness.

Experimental Setup:

The SLM dye laser consists of all glass dye cell, one dimensional prismatic beam expander, holographic grating in Littrow, Fabry Perot etalon and an output coupler. The high flow velocity of dye solvent is necessary to eliminate the thermal effects in the SLM dye lasers. The converging straight diverging flow geometry of dye cell with flow cross sectional area of 16x0.5 mm^2 at the interaction zone has been utilized for providing the gain medium for the SLM dye laser. The laser grade rhodamine19 dye was dissolved in ethanol with molar concentration of 0.75 mM and circulated through the dye cell using a dye flow system whose flow velocity was controlled using variable frequency drive (VFD). The dye solvent was cooled using a heat exchanger coil submerged in the dye reservoir and demineralized water (DM) is circulated through the heat exchanger coil at a temperature of $19^{O}C$ whose temperature is controlled within ± 0.1 ^{O}C. The typical Littrow cavity with prismatic beam expender and FP etalon used for generation of SLM is shown in fig 1. The

Littrow cavity comprises a holographic grating of 3300 lines/mm groove density which retro reflect the first order from the holographic grating. On rotation of holographic with respect to resonator axis a coarse tuning to the SLM dye laser was achieved. The holographic grating is mounted in a precision kinematic mounts with resolution of 0.1 arc sec. A one dimensional double prismatic beam expander with magnification of nearly 25 was inserted in between the dye cell and the FP etalon. A converging straight diverging glass dye cell which provides the compulsory gain to the SLM dye laser has been placed in between the beam expander and an output coupler of 4% reflectivity. The dye cell was kept at an angle of nearly 6^{O} with respect to the resonator axis to avoid the parasitic oscillations in between the two glass surfaces of the dye cell due to Fresnel reflections. The holographic grating at Littrow angle of incidence provides feedback to the wavelength with small pass band for this SLM dye laser, which restricts the dye laser oscillation into 4 to 5 longitudinal modes. The actual grating pass band is smaller than the theoretically calculated value due to mode competition effects as well as more number of round trips during available pulsed gain. The solid Fabry Perot etalon of 5 mm thickness and finesse of ~ 19 compels the cavity to oscillate in one axial mode.The insertion of the etalon in the expanded beam reduces the degree of walk off problems significantly. The solid etalon is held in a precision kinematic mirror mount, which offers fine tuning to the SLM dye laser. The tilt angle of the etalon mount is controlled by PZT cascaded with stepper motor to provide larger tilt angle. The PZT precisely controls the tilt angle of the etalon which enables fine tuning to the SLM dye laser. The tilt angle of the etalon can independently tune the SLM dye laser in the range of few GHz for the fixed position of the grating angle. The cylindrical lens of focal length of 50 mm was placed on a precision translational stage to precisely position the gain line inside the SLM dye laser resonator cavity. The cylindrical lens mount was equipped with rotational control for retaining the gain line along the resonator axis. The pump beam, dye beam and the flow of dye solution are mutually perpendicular to each other.

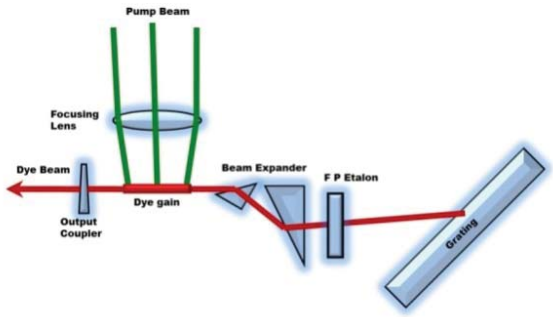

Fig 1: Typical Littrow cavity with FP Etalon for generation of single mode dye laser pumped by high repetition rate DPSSL.

The DPSSL operating at pulse repetition rate of 9 kHz was used as a pump source for the present studies. A diode pumped Nd:YAG laser operated with acousto-optic Q–switch in the linear coupled cavity configuration having switching frequency of 9 kHz was utilized for generating pump wavelength at 532 nm in the intra cavity frequency doubling configuration with KTP crystal. This laser can be operated with the maximum average power of nearly 65 W, pulse duration ~ 45 ns, rise time of ~ 25 ns, jitter of ± 2.8 ns, pointing stability ± 2.8 μ-rad and beam diameter of nearly 2.5 mm. This solid state pump laser was designed and developed indigenously by RRCAT [6]. A telescopic arrangement using a combination of a concave and convex lens with magnification of nearly 6.5 was utilised to increase the beam diameter of the DPSSL beam from 2.5 mm to approximately 16 mm to meet the required gain length at the dye cell. On increasing the beam diameter of the DPSSL laser reduces the beam divergence correspondingly and the expended beam was line focused on the dye cell. About 6.5 Watts average power at the dye cell from DPSSL green beam of 532 nm was used for pumping the SLM dye laser. The pump beam provides necessary gain to the SLM dye laser. Nearly 140 mW of

single mode output power was obtained with conversion efficiency of ~ 2.2 %. The fig 2 shows the single mode dye laser fringes obtained from the F P Etalon of 7.5 GHz free spectral range (FSR) and finesse of 30. The F P etalon used for measurement of SLM dye laser bandwidth has instrumental bandwidth of ~ 250 MHz. The fringe from F P Etalon confirms the single mode oscillation inside the SLM dye laser cavity pumped by the green beam of DPSSL. The single mode oscillation of dye laser was further ensured using a laser wavelength meter. A small portion of the dye laser output power was coupled to an optical fiber of core diameter 62.5 µm and fed to laser wavelength meter (WS – 7L Angastrom make), which also confirms the single mode operation with bandwidth of nearly 0.2 pm (~169 MHz) as shown in fig 3. The SLM dye laser pulse duration was measured using fast photo diode followed by the oscilloscope; it was measured to be nearly 35 ns at the full width half maximum (FWHM). The SLM dye laser pulse rise time was measured to be nearly 12ns as shown in fig 2.

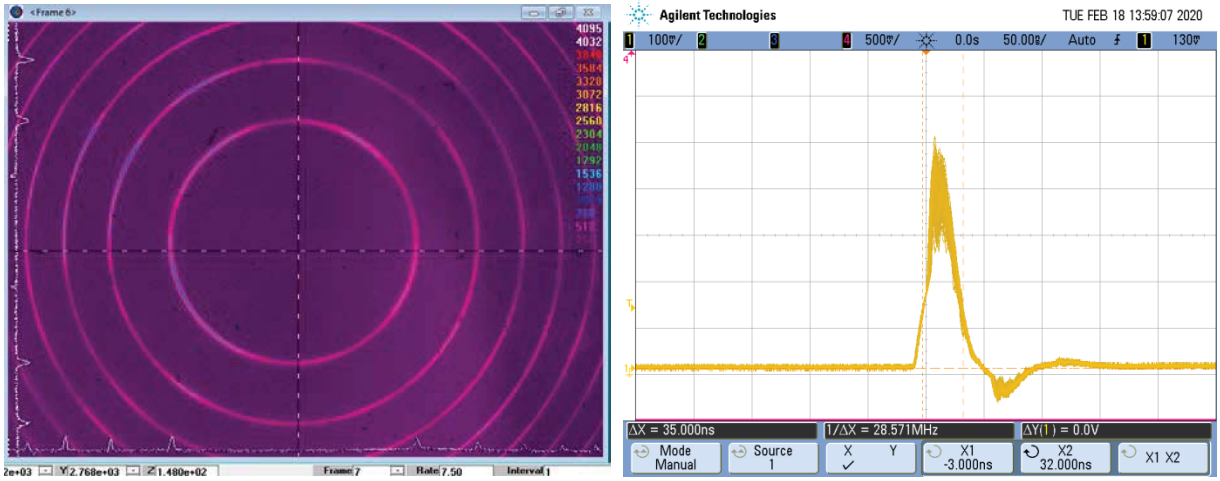

Fig 2: SLM dye laser fringes with FP etalon of 7.5 GHz FSR and Dye laser pulse duration of ~35 ns and rise time of ~12 ns.

The SLM dye laser wavelength was monitored by laser wavelength meter as shown in fig 3. The free running wavelength variation around mean value and bandwidth with time in seconds has been recorded using Angstrom make precision wavelength meter (WS - 7L) with absolute accuracy of $2x10^{-8}$and acquisition time of few milli seconds. The variation of wavelength around the mean value for free running SLM dye laser is measured to be ± 25 MHz as shown in the fig 3. During this entire period the bandwidth of the SLM dye laser was also logged by the wavelength meter and recoded with time. The SLM dye laser was tuned coarsely by the stepper motor attached with the grating while the fine tuning was achieved by PZT movement of the solid etalon.

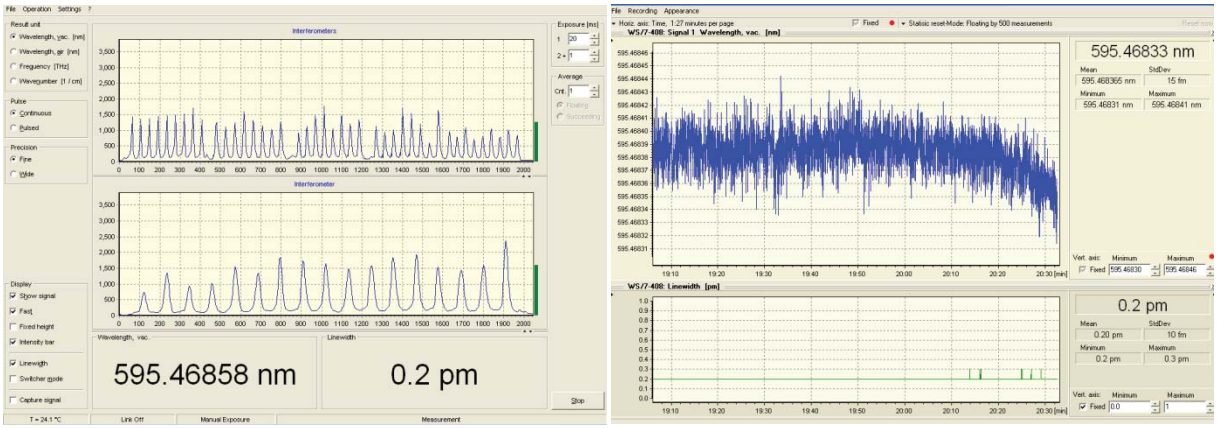

Fig 3: Wavelength and bandwidth measured by the laser wavelength meter, free running SLM dye laser wavelength

Conclusion:

The green beam of DPSSL operating at 9 kHz pulse repetition rate has been utilized for pumping the SLM dye laser and bandwidth of nearly 170 MHz has been obtained from Littrow cavity with solid FP etalon of thickness of 5 mm. The dye laser pulse duration was measured to be nearly 35 ns at FWHM with rise time of nearly 12 ns. The single mode oscillation was confirmed with FP etalon of FSR 7.5 GHz as well as laser wavelength meter (WS – 7L). The wavelength variation around the mean value is ± 25 MHz for free running SLM dye laser monitored by laser wavelength meter.

References:

[1] F J Duarte (Ed.),"High power dye lasers", Springer-Verlag, 1991.

[2] F J Duarte, "Tunable laser Optics", Elsevier Academic Press, 2003.

[3] V S Rawat, Jaya Mukherjee, L M Gantayet, Progress in Quantum Electronics, 43, 31 – 77, 2015.

[4] T W Hansch, Appl. Opt., 11, 895 – 898, 1972.

[5] I L Bass, R E Bonanno, R P Hackel, P R Hammond, "Appl. Opt., 31, 6993 – 7006, 1992.

[6] S K Sharma, RRCAT Newsletter, Vol. 32, Issue 2, 2019.

Acknowledgement:

The author sincerely thanks to the AD BTDG for supporting this research activity. The author would like to acknowledge the laser team members, Rajasree V, Anil Nayak, Dheeraj K Singh, S Mandal, B V Ganawane for providing required help during this experiment. The team members of LDIAD, RRCAT, Indore for providing the DPSSL laser for this study are greatly acknowledge.

Synthesis and Optical properties of RE^{3+}(RE^{3+}= Dy^{3+}, Sm^{3+} and Eu^{3+}) doped $Sr_{1.99}Bi_{0.01}CeO_4$ phosphors for LEDs applications

G.Subalakshmi[a], Rajesh NarayanaPerumal [b,c]

[a]*Assistant Professor, Theivanai Ammal College for Women, Villupuram-605602.*
[b]*Center for Radiation Environmental Science and Technology, SSN College of Engineering, Kalavakkam - 603 110, India.*
[c]*Department of Physics, SSN College of Engineering, Kalavakkam - 603 110, India.*

Abstract:

The$Sr_{1.99-x}Bi_{0.01}CeO_4$:x$RE^{3+}$ (RE^{3+}= Dy^{3+}, Sm^{3+} and Eu^{3+}, x= 0 and 0.03) single doped phosphors synthesized by solid state techniqueand their structureanalysed by X-ray powder diffraction technique (XRD).The results shows that the Dy^{3+},Sm^{3+}, Eu^{3+}, ions are effectively studded into the host lattice site without changing the structure of the host. The position of the diffraction peaks shift towards higher values as the doping content is introduced in the lattice effecting lattice distortion in the host. The deviation in the peak position may be accounted for the substitution of rare earth ions in the host, causing shift due to their difference in atomic radii.

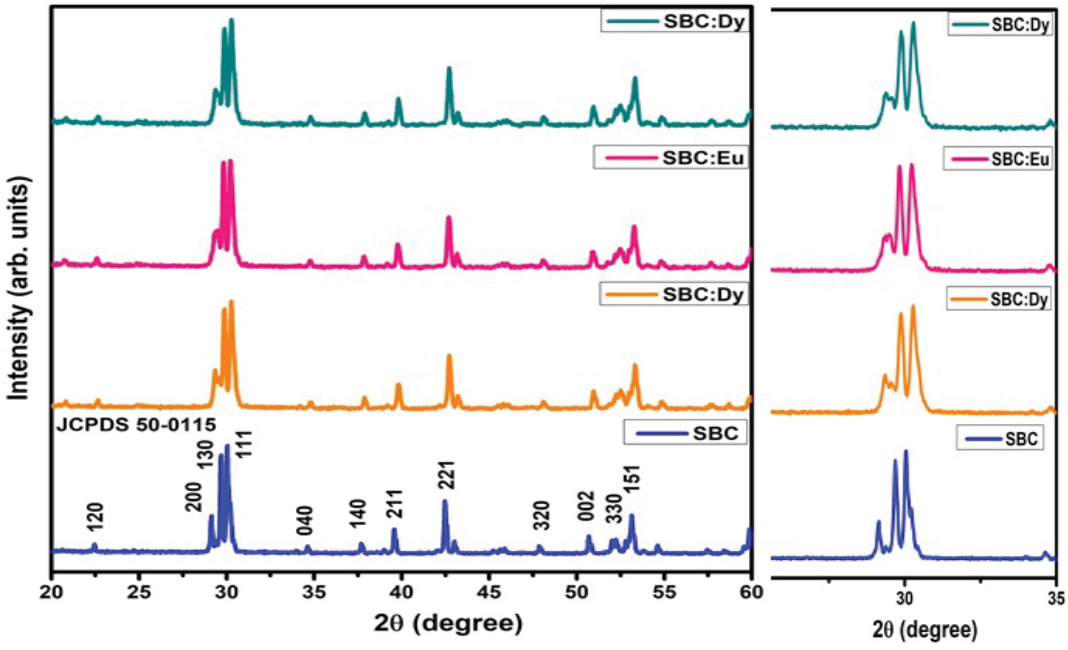

Fig. 1

The luminescence and energy transfer properties of the $Sr_{1.99-x}Bi_{0.01}CeO_4$:x$RE^{3+}$ have been investigated for single, co-doped and tri-doped phosphors under each of the 387 nm(Dy^{3+}: $^6H_{15/2}\rightarrow{}^4I_{13/2}$), 409

nm (Sm^{3+}: $^6H_{5/2}\rightarrow{}^6P_{3/2}$) and 466 nm ($Eu^{3+}$: $^7F_0\rightarrow{}^5L_6$) excitation levels wherein the mean emission values reportedly seem to be 572, 651 and 615 nm respectively

The excitation (λ_{emi}= 572 nm, $^4F_{9/2}\rightarrow{}^6H_{13/2}$) and emission ($\lambda_{ex}$= 387 nm, $^6H_{15/2}\rightarrow{}^4I_{13/2}$) spectra of SBC:Dy are shown in Fig.2. The excitation spectra consist of three bands that correspond to transitions from the ground level ($^6H_{15/2}$) to higher level at 387 nm ($^6H_{15/2}\rightarrow{}^4I_{13/2}$), 425 nm ($^6H_{15/2}\rightarrow{}^4G_{11/2}$) and 454 nm ($^6H_{15/2}\rightarrow{}^4I_{15/2}$). The emission spectra are monitored at 387 nm excitation wavelength, observed the peaks at 467, 572 and 644 nm correspond to $^4F_{9/2}\rightarrow{}^6H_{15/2}$ (magnetic-dipole transition), $^6H_{13/2}$ (electric-dipole transition) and $^6H_{11/2}$, respectively due to their $4f^5$-$4f^5$ transitions level of rare earth elements.

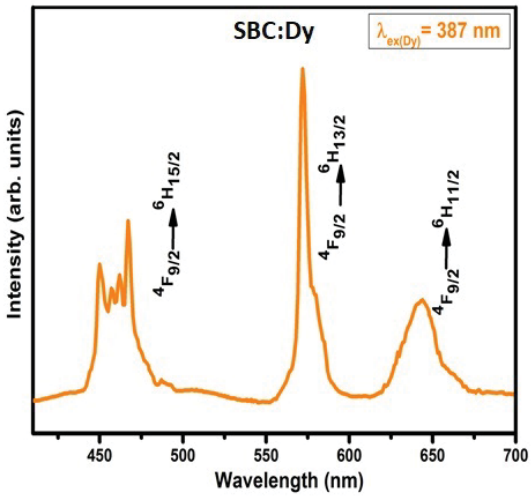

Fig. 2

Fig. 3 displays the excitation and emission spectra of SBC: Sm^{3+}host. High intense emission peak observed at 651 nm has been taken to analyse the excitation spectrum. In excitation spectra monitoring, peaks are attributed to $^6H_{5/2}\rightarrow{}^6P_{3/2}$ (409 nm) and $^6H_{5/2}\rightarrow{}^4I_{13/2}$ (470 nm). Further, intense 409 nm peak taken to monitoring emission spectra, ascribes to$^4G_{5/2}\rightarrow{}^6H_{5/2}$ (at 564 nm, magnetic-dipole transition), $^4G_{5/2}\rightarrow{}^6H_{7/2}$ (at 608 nm, partly electric-magnetic-dipole transition), $^4G_{5/2}\rightarrow{}^6H_{9/2}$ (at 651 nm, electric-dipole transition) and $^4G_{5/2}\rightarrow{}^6H_{11/2}$ (at 713 nm).

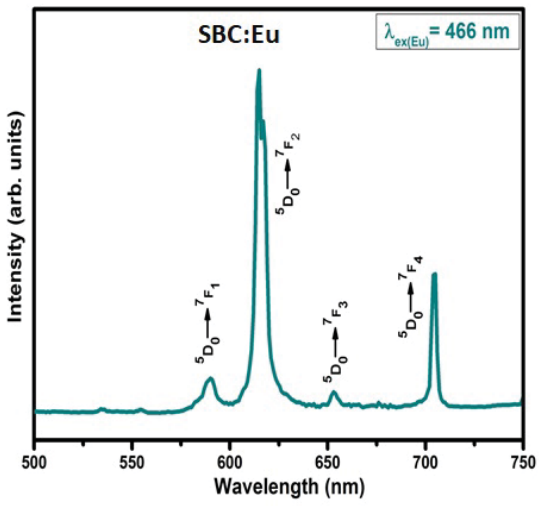

Fig. 3

The chromaticity coordinates and decay time of the synthesized materials are also examined. The results show that the CIE chromaticity coordinates are gives orange, red emission and it is optimum potential candidate for LEDs applications.The estimation of correlated color temperature (CCT) is made as per the following formula:

$CCT=-449n^3+3525n^2-6823.3n+5520.33$

$n=(x-x_e/y-y_e)$ mentions the reciprocal slope and ($x_e=0.332$, $y_e=0.186$) fixes the epicentre and CCT of single doping to be 4739 K, 1914 K and 1666 K indicating Dy^{3+}, Sm^{3+},Eu^{3+} ions respectively. The CCT result shows the synthesized phosphors recommendable for warm LEDs applications.

Keywords: Phosphor; Oxygen evolution; Rare earth elements; CIE colour co-ordinates;

Photonic microwave signals generation using optically injected VCSELs under parallel optical injection

E. Jayaprasath[1, 2], Z. M. Wu[2], and G. Q. Xia[2]

[1]School of Computer Science and Electronic Engineering, Bangor University, Bangor, LL57 1UT, UK

[2]School of Physical Science and Technology, Southwest University, Chongqing 400715, China

Email: ejayaprasath@gmail.com

Abstract: Generation of photonic microwave signals is experimentally studied in a vertical-cavity surface-emitting laser subject to parallel optical injection. Based on period-one dynamics, we study the influence of injection power on the generated microwave frequency and power. We find that microwave frequency can be broadly tunable and there exist hysteresis loops in the microwave frequency over continuous scanning of injection power for a fixed detuning frequency. The results show that the hysteresis loop width in microwave frequency is noticeable for injection power variation.

Introduction: Microwave photonics sources have attracted considerable attention because of their potential applications in radio-over-fibre (RoF) system, signal processing, wireless access networks, and many other applications[1]. Photonic methods have the advantages of improved performance in terms of signal quality, bandwidth, frequency coverage, and low power consumption[2]. Period one (P1) dynamics based photonic microwaves has many distinguishing characteristics[3], such as a broadly tunable microwave frequency far from its relaxation resonance frequency[4]. It is demonstrated that the photonic microwave generation based on P1 oscillation in distributed feedback (DFB) lasers subject to optical injection can produce up to 100 GHz[5] with a tuning range of several tens of gigahertz[6]. A tunable very high frequency, 120 GHz, microwave signal has been obtained using dual-beam optically injected DFB semiconductor laser[6]. In recent years, the generation of photonic microwave signals using VCSELs has drawn a great deal of attention[7-10]. Theoretical investigation shows that the dual-beam injection can generate stronger microwave signal in the multi-transverse-mode VCSEL than in the single-transverse-mode VCSEL[7], and later this has been experimentally confirmed[8]. Recently, tunable photonic microwave generation based on P1 oscillation using single-transverse-mode VCSEL has been demonstrated[9] and for a fixed injection power, the existence of two local maximum microwave powers at the two detuning frequencies has been theoretically explained[10]. Considerable experimental study on the microwave generation using optically injected single-transverse-mode VCSELs is needed to understand the microwaves in photonic systems. In this work, we report our experimental investigation on the generation of photonic microwave signal based on P1 dynamics in a single-transverse-mode VCSEL subject to parallel optical injection. We have examined the response of generated microwave signal frequency and the power over continuous increase and decrease of injection power for a fixed detuning frequency. We observe the hysteresis loop in the microwave frequency for varying injection power and the loop width found to be wider for the variation of injection power.

Experimemtal setup: The experimental schematic of an all-fibre setup for photonic microwave generation in an optically injected VCSEL is shown in Fig. 1. A commercial single-transverse-mode VCSEL (RayCan Co.) operating at 1550-nm is used in the experiment. As shown in Fig. 1, the output from a tunable semiconductor

laser (TSL) is injected into VCSEL by traveling through a variable attenuator (VA), a polarization controller (PC), and an optical circulator (OC). The injection power (P_i) is measured at port 2 of the OC. The output of VCSEL is split into parts for the detection. One part is detected by a 50 GHz bandwidth high-speed photodetector (PD) and recorded by an electrical spectrum analyser (ESA) to test the generated microwave signal; another part is sent to an optical spectrum analyser (OSA) with resolution of 20 MHz to analyse the optical spectrum distribution.

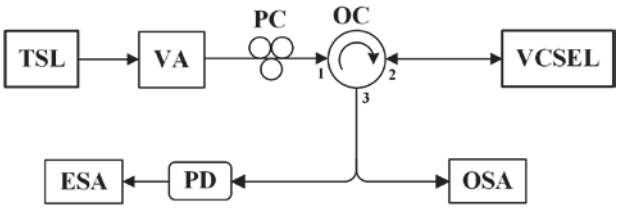

Fig. 1. Experimental setup. VCSEL, vertical-cavity surface emitting laser; TSL, tunable semiconductor laser; VA, variable attenuator; PC, polarization controller; OC, optical circulator; PD, photodetector; ESA, electrical spectrum analyser; OSA, optical spectrum analyser

Results and discussion: The focus of this work is to generate photonic microwave based on P1 dynamics in optically injected VCSEL. In this experiment, the injected light is from TSL. The detuning frequency (Δf) is defined as f_{TSL}-f_{VCSEL}, where f_{TSL} is the frequency of TSL and f_{VCSEL} is the frequency of parallel polarization of the fundamental mode in the solitary VCSEL.

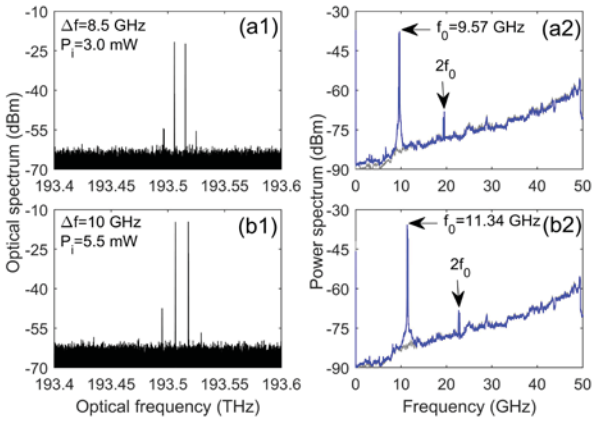

Fig. 2. Experimental optical spectra (left) and power spectra of the P1 oscillation of VCSEL at detuning frequency and injection power of (a) (8.5 GHz, 3 mW) and (b) (10 GHz, 5.5 mW)

Fig. 2 shows the experimental optical spectra (left column) and power spectra (right column) of the total VCSEL output under Pl oscillation for the two set of injection parameters of (Δf , P_i) = (8.5 GHz, 3 mW) and (10 GHz, 5.5 mW). The grey curves in right column of the Fig. 2 correspond to the noise of floor of ESA. Under the injection parameter of (8.5 GHz, 3 mW), the VCSEL emits in P1 oscillation of a fundamental frequency f_0 of 9.57 GHz which is indicated in Fig. 2(a2). For the P1 oscillation, it can be seen that the VCSEL is injection-locked to the regeneratively amplified field component at injection laser frequency (Fig. 2(a1)) and contains relaxation-oscillation generated sidebands separated by the fundamental microwave frequency of f_0[3]. As can be seen in Fig. 2(a2) that the beating between a second strongest sideband and regenerated mode induces second

harmonic at $2f_0$[9], and observed with a power suppression of 30 dB as compared with f_0. As shown in Fig. 2(b), the generated photonic microwave frequency increase to 11.34 GHz for Δf =10 GHz and P_i=5.5 mW condition, which indicates that the detuning and injection power affects the generated photonics microwave signals.

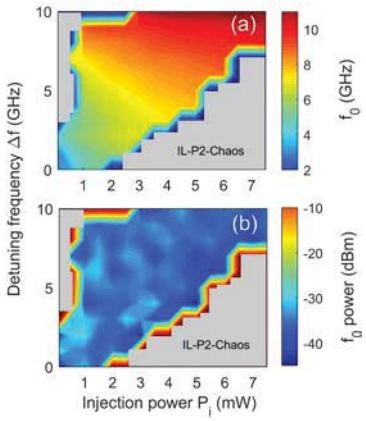

Fig. 3. Experimental magnitude of peaks in power spectrum at (a) fundamental photonic microwave frequency f_0 and (b) the respective microwave power in the injection parameter space of Δf and P_i

The magnitude of peaks in power spectrum at generated microwave frequency f_0 and its respective power in the parameter space of detuning frequency Δf and injection power P_i is shown in Fig. 3. A large region of P1 oscillation is observed in the (Δf, P_i) space, which is just above the Hopf bifurcation boundary. In the embedded grey region, the VCSEL emits injection-locking (IL), period-two (P2), and chaotic dynamics are observed. Fig. 3(a) indicates the generated microwave frequency f_0 has an effect over detuning frequency and injection power. When P_i is gradually increased, f_0 also increases due to the results of competition between red-shifting of the cavity resonance and injection pulling effect. The microwave power variation in (Δf, P_i) space is shown in Fig. 3(b). As evident from Fig. 3(b) that, in the P1 state region (blue area) the microwave power fluctuates within 20 dB, which is almost a stable fluctuation. The microwave tunability with a constant power is an advantage of P1 based photonics microwave sources.

We now analyse in Fig. 4 the variation of generated photonic microwave frequency f_0 and its power over injection power for detuning frequency Δf =10 GHz. As seen in Fig. 4(a), f_0 gradually increases (red curve) with increasing P_i from 2.4 mW to 7.5mW. Increasing injection power enhances the P1 oscillation and increases the oscillation frequency. While decreasing P_i from the higher to a lower value, the microwave frequency bound to decrease (blue curve in Fig. 4(a)). The dependence of f_0 on the injection power is not smooth due to the minor variation of detuning frequency during the injection power variation. Besides, the results show that a clockwise switching arises in f_0 variation and there exists a hysteresis loop with a considerably wider width by scanning injection power. The clockwise switching can be due to a delicate balance between the different optical intensities in the VCSEL, such as injected light, the reflected, and the average intensity within the cavity[11]. A detuning frequency Δf=10 GHz is considered, which will have an effect in contributing less injection power, hence clockwise switching (from high to low state) appears in f_0 variation. Along with the microwave signal generation, this hysteresis loop, therefore, offers for additional applications including microwave frequency switching. The variation of microwave power as a function of injection power is shown in Fig. 4(b). The result shows that the microwave power is completely not affected over P_i, and the power fluctuation is within 10 dB.

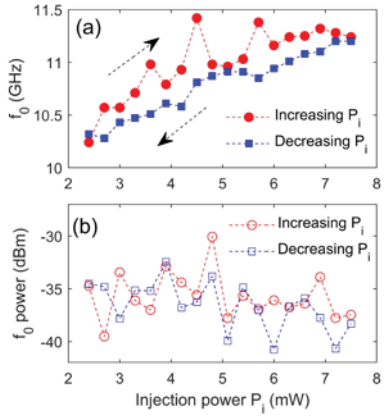

Fig. 4. Photonic microwave frequency f_0 (a), and the power (b), characteristics as the function of injection power P_i for Δf =10 GHz. The red curve and blue curve are data obtained with increasing and decreasing P_i, respectively.

Conclusion: To conclude, we have experimentally investigated the generation of photonic microwave signal based on the period-one oscillations in a single-transverse-mode VCSEL subject to parallel optical injection. We have focused our investigation on the effect of injection power on the generated microwave fundamental frequency and its power. For increasing the injection power, P1 oscillation enhances and increases the microwave frequency. The microwave power fluctuates within 20 dB over injection power. We have also examined the response of generated microwave signal frequency and the power over continuous increase and decrease of injection power for a fixed detuning frequency. We found that there exist hysteresis loops in the microwave frequency over continuous scanning of injection power for a fixed detuning frequency. Along with the tunable microwave signal generation, our results indicate that the emergence hysteresis loop in a microwave will offer additional applications including photonic microwave frequency switching.

References

1. J. Capmany et al., *Opt. Exp*. **21**, 22862 (2013).
2. K. Otsubo et al., *IEEE J. Sel. Top. Quantum Electron*. **15**, 687 (2009).
3. X. Q. Qi and J. M. Liu," *IEEE J. Sel. Top. Quantum Electron*. **17**, 1198–1211 (2011).
4. S. C. Chan et al., *Opt. Exp*. **15**, 14921 (2007).
5. S. C. Chan et al., *Opt. Lett*. **31**, 2254 (2006).
6. Y. S. Juan and F. Y. Lin, *IEEE Photon. J*. **3**, 644 (2011).
7. A. Quirce et al., *J. Opt. Soc. Am. B* **29**, 3259 (2012).
8. H. Lin et al., *J. Opt. Soc. Am. B* **34**, 2381 (2017).
9. S. Ji et al., *Opt. Exp*. **25**, 19863 (2017).
10. A. Valle et al., *IEEE Photon. Technol. Lett*. **30**, 1266 (2018).
11. A. Hurtado et al., *Opt. Exp*. **17**, 23637 (2009).

Development of a laser system for enrichment of Yb^{176} for medical application

A Wahid*, A K Singh, A Khattar, J S B Singh, P K Mohite, J S Dhumal, S K Maurya & S Kundu

ATLA-Facility, BTDG, Bhabha Atomic Research Centre, Trombay, Mumbai-400085
Email: awahid@barc.gov.in

Abstract: Enriched Yb^{176} can be used as a source for the production of Lu^{177} in a reactor. Three narrow-band dye laser (DL) systems have been developed to carry out laser based separation to enrich the stable Yb^{176} isotope. With this laser system, we have achieved enrichment more than 97% of Yb^{176}.

1. Introduction

Over the last decade Lu^{177}has earned considerable recognition in the verity of therapeutic procedures. Despite being late entrant in radionuclide therapy, Lu^{177} has established its potential to be used in Targeted Radionuclide Therapy (TRT). There is a steady expanding list of Lu^{177} labeled radiopharmaceutical that has given an impetus for routine production of Lu^{177}. There are two production routes, named as "direct" & "indirect" through which one can obtain Lu^{177} in a reactor. The direct production route is based on absorption of thermal neutrons by Lu^{176} (n,γ) to yield Lu^{177}whereas indirect production route is rely on absorption of thermal neutron by Yb^{176} (n,γ) to yield Lu^{177}. Each route has specific advantages & disadvantages. Despite having few drawbacks in "indirect" route, there are tremendous prospects associated with the use of No Carrier Added (NCA) Lu^{177} in TRT [1]. Hence, this route is being aggressively pursued world-wide. Natural Ytterbium (abundance of Yb^{176} is 12.73%) is not a good choice for production of Lu^{177}due to co-production of Yb^{169} & Yb^{175} which effectively reduces the specific activity of Lu^{177}. In view of these considerations, enriched Yb^{176} is the only interesting option left to us. We aimed to develop DL system for Laser Isotope Separation technology to enrich Yb^{176}. A 3-step (in visible range) selective photo-ionization scheme, which was proposed in [2] has been characterized with large transitional isotope shift between Yb^{176} & neighboring isotopes [3], and thus it is easier to obtain sufficiently high selectivity of Yb^{176}. Therefore, above photo-ionization scheme is considered for development of our laser facility. The stringent parametric requirements of DL systems, imposed by photoionization scheme, are successfully achieved by three narrowband tunable DL systems pumped by green component (~510.6 nm) of Copper Vapor Laser (CVL) & Diode Pumped Solid State Green Laser (DPSSGL) systems. We have used two SLM DL systems at 12.5 kHz with spectral-width < 80 MHz & frequency stability (with active frequency stabilization) ± 40 MHz for first & second transitions. With our own laser system, we have managed to produce enrichment of Yb^{176} more than 97 %.

2. Pump laser

Pump lasers with high peak power at high pulse repetition rate (~ multi-kHz) & low temporal jitter are pre-requisite for pumping DL. These specifications of pump laser to a great extent are realizable with CVL & DPSSGL, and therefore considered as efficient pump source for generating DL in green-yellow region. We have arranged CVLs in two different MOPA configurations to excite oscillators & first stage amplifiers of DL systems separately. Type-I MOPA with temporally stretched output, which consisted of one master oscillator & two amplifier stages. The

optical pulse was temporal stretched at final stage by using an active ring cavity, known as Optical Pulse Stretcher (OPS) [4] which utilizes a beam splitter with R:T = 55:45. It provided ~ 30W of green beam (λ ~ 510.6 nm) at 6.25 kHz with pulse width ~ 60 ns (FWHM). Whereas, Type-II MOPA with unstretched output contained one master oscillator & three amplifier stages. The generated green beam power was ~ 45W at 6.25 kHz with pulse width ~30 ns (FWHM). Type-I & Type-II MOPA configurations are shown in figure 1 & 2 respectively.

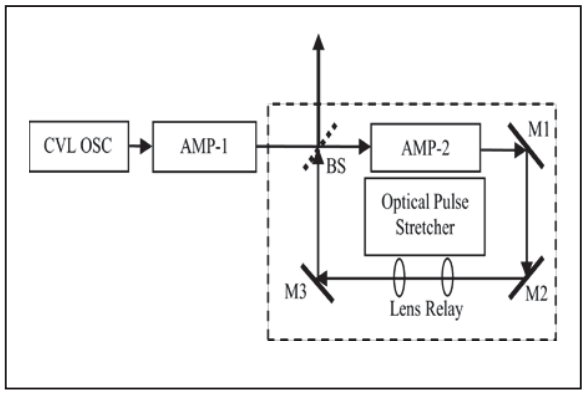

Figure 1: Configuration of Type-I CVL MOPA with OPS.

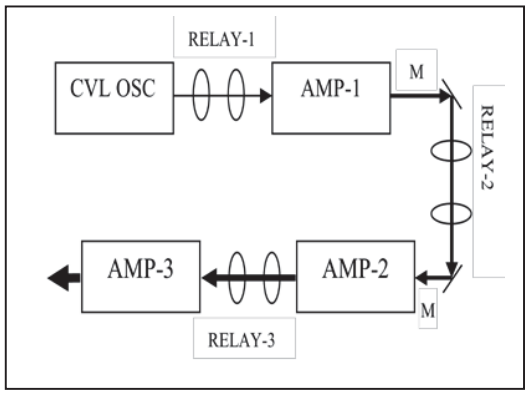

Figure 2: Configuration of Type-II CVL MOPA.

Four Q-switched DPSSGLs, triggered at 6.25 kHz PRR were used for excitation of second amplifier stage of λ_3 MOPA to scale up the avg. power so as to ionize Yb^{176} with good efficiency. The avg. output power of one unit of DPSSGL was ~ 36-40W at λ ~ 532 nm with pulse width ~ 37 ns (FWHM).

3. Dye laser

The three-step photo-ionization scheme is currently being pursued for demonstration of enrichment of Yb^{176} is based on three tunable DL systems (see fig.3) named as λ_1, λ_2 & λ_3. Each of DL system has been arranged in MOPA configuration. In present scheme, two amplifiers for λ_3 & one amplifier for each λ_1 & λ_2 were used. All three DL master oscillators were transversely pumped by green component (λ ~ 510.6 nm) of multiplexed output (12.5 kHz) of Type-I MOPA. Two optical fibers (core size: 600μm & NA: 0.12) were deployed to bring the pump beam for generation of λ_1 & λ_2. The required spot size (10mm X 0.5mm) was achieved by custom designed optical system & a cylindrical lens of focal length 50 mm. With the use of stretched pump pulse, the pulse width of DL oscillator output was found as close as pump laser of next amplifying stage; and thereby achieving good efficiency at amplifier. It also helped to narrow down the spectral width of DL output due spectral narrowing (no of passes travelled by DL pulse inside cavity ~70-80) & thus it has limited the possibilities of non-selective excitation & improves the selectivity of the desired isotope. All three first amplifier stages likewise were pumped by green component of multiplexed output Type-II MOPA while second amplifier stage of λ_3 MOPA was excited by four DPSSGLs.

Two SLM DLs have been designed & developed according to [5]. The laser cavity was made of output coupler (OC), holographic diffraction grating (3000 lines-mm^{-1}) for first order Littrow operation in visible region,

intra-cavity two prism (made of SF11) beam expander & a solid Fabry-Perot (F-P) etalon. The intra-cavity beam expander expands the beam a factor of ~ 40 to illuminate grating completely; thereby maximizing its dispersion. We have used AR coated prisms to reduce the reflection loss. An etalon with free spectral range (FSR) ~17 GHz & fineness ~ 17 was inserted into the cavity to force lasing into a single longitudinal mode. The cavity was placed on a massive stainless steel base plate which was heated to maintain a specific temperature. For long time operation, we stabilized the laser wavelength by maintaining the temperature of solvent & base plate to accuracy 0.1 degree; after reaching the set temperature, wavelength was locked by active feedback frequency stabilization system that was consisted of PZT attached to the OC. The frequency stabilization system was automatically controlled by using PC & homemade software.

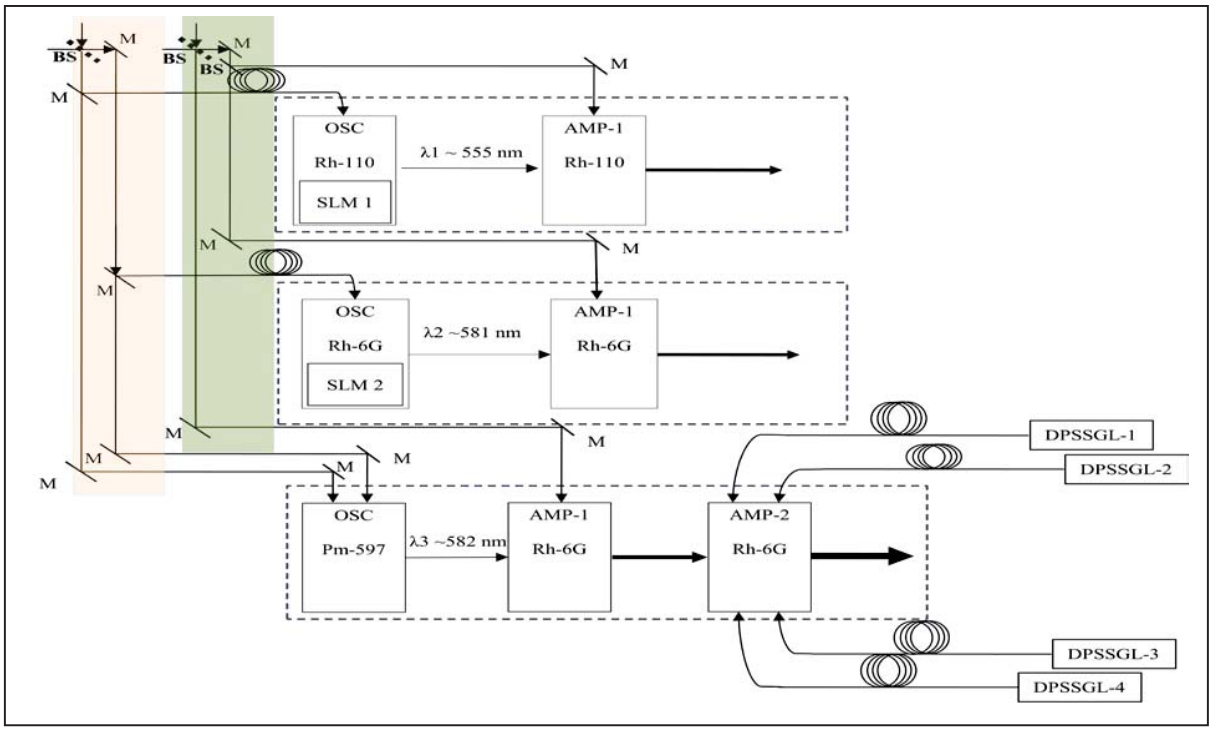

Figure 3: Block diagram of DL MOPA systems pumped by CVL-MOPA & DPSSGL.

The choice of laser dye for SLM oscillators, was made based on following criteria *i)* it should be efficient at process wavelength, *ii*) it should have low quantum of yield of photo-degradation, & *iii*) it should be water-soluble as water based solvent is preferred due to excellent thermo-optical properties of water. Rh-110 in binary solvent (water**:** n-propanol = 4:1 (v:v)) was used in λ_1 (~ 555 nm) oscillator, and the avg. output of SLM radiation was 0.8 W (at pump power 12W), with spectral width < 80 MHz & pulse width ~ 30 ns (FWHM). The oscillator beam was given shape by aperture & focused to subsequent amplifier by using appropriate lens combination. The average signal power reaching to subsequent amplifier was ~ 0.4W after suffering losses due to beam shaping & sizing. For an avg. pump power of 8W at amplifier, the λ_1 MOPA output was 1.2W. Rh-6G in binary solvent was used in oscillator for generation of λ_2 (~ 581 nm), and the avg. SLM output was ~ 0.6W (at pump power 12W) with spectral width & pulse width similar to λ_1. For avg. pump power of 30W at amplifier, λ_2 MOPA output was 4W. To

generate λ_3 wavelength, a narrow-band DL resonator was configured in Grazing Incident Gating (GIG) with holographic diffraction grating (2400 lines-mm^{-1}) which was used as a prime dispersive element for narrow band laser operation along with intra-cavity prism beam expander (M~20). Pyrromethene 597 (Pm-597) along with DABCO as an additive dissolved in HPLC grade ethanol was used as a gain medium for λ_3 ~ 582 nm. The avg. output power was 1.8W (at ~18 W pump power) with spectral width ~ 3.0 GHz & pulse width ~ 30 ns (FWHM). Signal beam was further amplified by the two more amplifying stages. Both amplifiers contained Rh-6G in binary solvent as a gain medium. For an avg. pump power of 35W, the avg. output of first amplifier stage was 7W. While, the total generated output power of λ_3 MOPA was 50W after final amplifier at pump power ~140W (from 4 independent but temporally synchronized output of DPSSGLs).

4. Experiment & Results

After generation of three DL MOPA outputs, they are combined spatially & temporally by using beam combiner optics which consisted of dichroic combiner & cube polarizer. Small part of composite beam was sampled & brought to time of flight (TOF) mass spectrometer with optical fiber for qualification of laser wavelengths. The wavelengths of laser were adjusted to maximize the selectivity of Yb^{176} and selectivity more than 99.5% was obtained in TOF when wavelengths were set on the resonance of Yb^{176}. During the process, we kept our laser intensities low to avoid power broadening effect. After the wavelengths of the laser had been precisely tuned, the composite single beam was sent into the separation chamber for selective ionization of Yb^{176}. After accomplishment of separation experiment, we have analyzed the isotopic abundance of the enriched Yb^{176} & found more than 97%.

Conclusions

We have developed narrowband tunable DL systems pumped by CVL & DPSSGL for enrichment of Yb^{176}. Two SLM DLs were developed for this purpose. We have succeeded producing enriched Yb^{176} with abundance more than 97%. Concerning the laser facility, other isotopes of Ytterbium (*Yb*) can also be enriched.

Acknowledgements: Authors thank Dr. (Smt.) Archana Sharma, AD, BTDG & Head ATLA Facility for her interest, constant encouragement & support in this work. Authors would also like to acknowledge sincere support towards P. Chakraborty & N. O. Kawade of L&PTD, BARC for providing wavelength locking unit.

Reference:

1. Ashutosh Dash et al., Nucl. Med. Mol. Imaging 49:85-107, 2015
2. Hyunmin Park et al. J Korean Physical Society 49(1):382-386, 2006
3. B.B. Krynetskii et al.; J Appl. Spektrosk. 54: 338, 1991
4. J Singh et al.; "Stretching of Copper Vapour Laser Output Pulse by an Active Optical Pulse Stretcher-Simulation and experimental Validation" DAE-BRNS NLS-28
5. A. F. Bernhardt et al., Appl. Phys. B:141-146,1981

Effect of output coupler reflectivity on the Narrow Band Pulsed Dye Laser Pumped by DPSSL

S K Mishra[1*], Paramjit Rana[1, 2], Siba P Sahoo, Jaya Mukherjee[1], V S Rawat[1,2],
ATLAF, BTDG
[1]*Bhabha Atomic Research Centre, Mumbai – 85 INDIA*
[2]*Homi Bhabha National Institute, Anushaktinagar, Mumbai – 94 INDIA*
*E-mail: smishra@barc.gov.in

Abstract:

The green beam of DPSSL has been utilized to pump the narrow band grazing incidence grating (GIG) dye laser cavity at pulse repetition rate of 9 kHz. The effect of output coupler reflectivity on tuning range and bandwidth of the dye laser has been studied. On increasing the feedback to the GIG cavity the tuning range increases and bandwidth decreases.

Introduction:

The organic dye lasers are used for several applications such as atomic spectroscopy, determination of isotope shifts in atomic transitions, resonance ionization mass spectroscopy, laser isotope separation processes, atmospheric and LIDAR applications [1,2]. All these applications demand a narrow spectral width as well as wide tunability of laser radiations. The wide tunability of the entire spectral range from ultra violet to infrared can be obtained by judiciously selecting the laser dyes. They are capable of emitting in the broad spectral range of few hundreds of nm, hence a single laser dye as the active medium can generate continuously tunable source of light over a large spectrum.The harmonics of Nd:YAG laser has been widely used for pumping the dye laser system with pulse repetition rate from few Hz to few tens of kHz range by several groups around the globe [3,4].

In this paper we are presenting the effect of output coupler reflectivity on the performance of the narrow band grazing incidence grating (GIG) pulsed dye laser pumped by green beam of DPSSL operating at high repetition rate of 9 kHz. The Q-factor of the cavity was tailored by suitably optimized output coupler reflectivity and grating resolution in various configurations. The grating resolution and quality factor of the cavity were varied to obtain the narrowband output from the DPSSL pumped GIG dye laser. The effect of the slow rise time of the pump laser of DPSSL on the tuning rangeand spectral narrowing of pulsed dye laser has been investigated and presented here for the GIG configuration. Compactness, superior operational efficiencies and rapidly evolving solid state laser technology enhances the interest and applicability of the present study. The diode pumped solid state laser (DPSSL) was as a pump source used for the GIG pulsed dye laser.This solid state pump laser was designed and developed indigenously by RRCAT [5].This DPSSL can be operated with the maximum average power of nearly 65 W, pulse duration ~ 45 ns, rise time of ~ 25 ns, jitter of ± 2.8 ns, pointing stability ± 2.8 μ-rad and beam diameter of nearly 2.5 mm.

Experimental Setup:

The narrow band dye laser resonator cavity configurations utilizes holographic grating in grazing incidence angle for obtaining necessary resolution. These resonator cavities often use one dimensional prismatic beam expender for increasing the grating resolution by illuminating more number of grooves in the grating. In this configuration a full length of the grating was illuminated so that it can generate narrow bandwidths. A plane mirror was used to reflect back the diffracted beam from the holographic grating. The wavelength tuning is

achieved by rotating the plane mirror around the grating. The experimental setup of narrow band grazing incidence grating (GIG) dye laser cavity configuration is shown in fig 1.

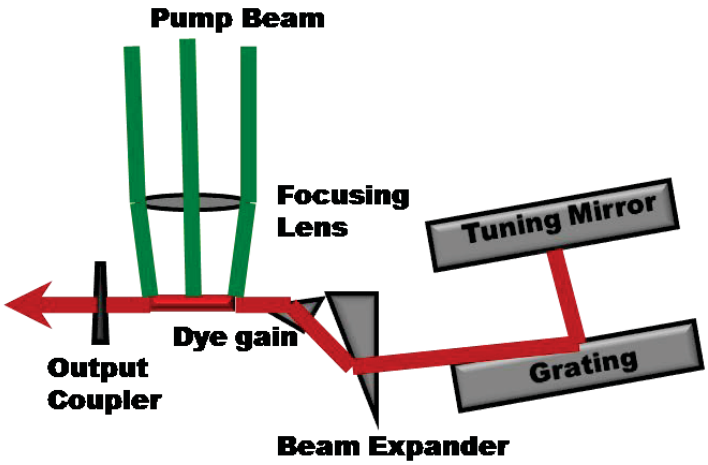

Fig 1: Experimental setup of DPSSL pumped narrow band tunable dye laser of grazing incidence cavity

The green beam from the DPSSL is expanded to nearly 16 mm from 2.5 mm with suitable magnifierand line focused on the dye cell along the 16 mm side using a cylindrical lens. The cylindrical lens of focal length 50 mm was placed on a translation stage with axis of rotation enabled for precise positioning of the line focused pump beam on the dye cell. The axis of rotation in the cylindrical lens provides a precise control of the gain line along the optical axis of the resonator. The GIG cavity build around the indigenously developed fused silica converging straight diverging dye cell utilized a holographic grating of 15 mm width and 65 mm length having groove density of 2400 lines/mm. This grating was inclined at nearly grazing incidence angle of 81^{O} with respect to the beam emerging from the beam expander in the resonator axis. The diffracted first order from the holographic grating is retro-reflected by a rectangular mirror of 15 mm width 65 mm length having nearly 99% reflectivity and uncoated quartz wedge type output coupler having reflectivity of 4%.A prismatic beam expander to provide one dimensional magnification of nearly 22 was inserted in between the dye cell and holographic grating. The pump beam direction and the dye flow direction were mutually orthogonal to each other; they were transverse to the gain axis of the dye laser resonator cavity.The rhodamine 19 laser dye dissolved in high purity ethanol with a concentration of 0.5 mM was circulated through the dye cell using dye flow system whose flow velocity is controlled using variable frequency drive (VFD) [6].The dye solvent was circulated through the dye cell at a flow rate of nearly 1.5 lpm. The dye solvent is cooled using a heat exchanger coil immersed inside the dye reservoir of 3 litre capacity. Demineralised water is used to circulate through the heat exchanger coil at a temperature of $20^{O}C$ which cools the dye solution in the dye reservoir.The narrow band dye laser output parameters were analysed using laser wavelength meter(WS – 7L). A part of the dye laser output beam was coupled to the multi-mode optical fiber of core diameter 62.5 μm and fed to the laser wavelength meter which measures the wavelength as well as bandwidth of the dye laser.The dye laser time averaged bandwidth was measured to be nearly 4.5 GHz by wavelength meter as well as Fabry Perot etalon of free spectral range of 0.25 cm^{-1} and finesse of 30.The tuning range of ~7 nm was obtained for this narrow band GIG dye laser from 557 nm to 564 nm with peak wavelength of nearly 560 nm. The dye laser output beam accompanied with a large amount of amplified spontaneous emission (ASE) for this GIG cavity. To study the effect of reflectivity of the output coupler on the tuning range the reflectivity of output coupler was increased from 4% to higher value of

reflectivity in the range of 20% to 70%. The reflectivity of the output coupler of DPSSL pumped GIG laser dye laser was changed by keeping other parameters the same such as incidence angle of grating, magnification of one dimensional prismatic beam expender and pump pulse energy of nearly 0.5 mJ. The tuning range as well as bandwidth of this dye laser was measured using laser wavelength meter. The tuning range with three different values of output coupler reflectivity namely 20%, 40% and 70% were plotted and shown in fig 2.

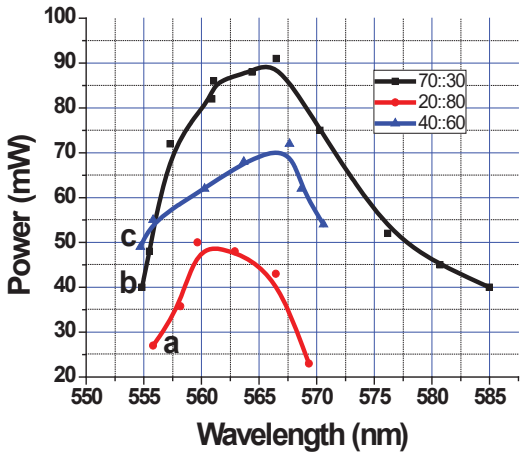

Fig 2: Tuning range of DPSSGL pumped GIG dye laser with output coupler's reflectivity a: 20% (Red), b: 70% (Black) and c: 40% (Blue)

The tuning ranges of the DPSSL pumped GIG dye laser increases with increasing reflectivity of the output coupler. The tuning range is increased from 7 nm to 30 nm on increasing output coupler reflectivity from 4% to 70% respectively as shown in fig 2. On increasing the reflectivity of the output coupler of this GIG dye laser increases the output power from 40 mW to 90 mW for the fixed pump power of nearly 4.5 Watts at peak wavelength of the dye laser. The bandwidth of the dye laser decreased to 3.5 GHz from 4.5 GHz on increasing the reflectivity of the output coupler of the dye laser from 4% to 70%. The decrease in the bandwidth on increasing output coupler reflectivity was due the more number of available cavity round trips for the dye laser beam before emerging from the GIG cavity.

For comparison this GIG dye laser cavity with 4% output coupler was pumped by the green (~510 nm) beam of the CVL with the same pump power of 4.5 Watt operating at the same pulse repetition rate of 9 kHz. The CVL beam has pulse duration of 30 ns and a rise time of ~ 8 ns. The CVL beam was line focused on the dye cell with a combination of spherical and cylindrical lenses. The cylindrical lens of focal length of 50 mm was replaced by 100 mm focal length cylindrical lens and remaining cavity parameters were kept the same for the CVL pumping. The bandwidth of CVL pumped narrow band dye laser was measured to be nearly 2.5 GHz and tuning range of nearly 25 nm was obtained. The poor performance of DPSSL pumped GIG dye laser with 4% reflectivity output coupler was due to larger rise time which is nearly three times higher than the CVL pump beam and the poor beam divergence. The typical pump pulse of DPSSL and the corresponding dye laser is shown in fig 3.

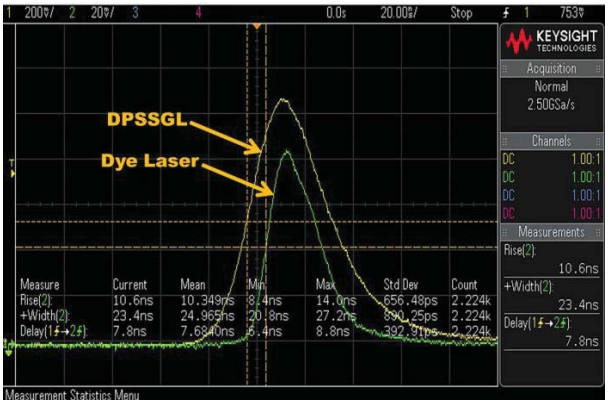

Fig 3: The typical Nd:YAG green pump pulse and the dye laser pulse for narrow band GIG cavity

The dye laser pulse duration and DPSSL pulse durations were measured using fast photodiode (FDS100) followed by an oscilloscope.Both the pulse durations were measured at full width half maximum (FWHM) of their respective pulses.

Conclusions:

The tunability of the narrow band GIG dye laser pumped by the DPSSL increases from 7 nm to 30 nm with increase in the reflectivity of the output coupler from 4% to 70 % respectively for the GIG dye laser cavity. The bandwidth narrowing of GIG dye laser pumped by green beam of DPSSL was achieved on increasing the reflectivity of the output coupler. This decrease in the bandwidth was due to more number of round trip for the cavity photons in the increased cavity decay time due higher reflectivity of output coupler. This dye laser was pumped by the same average power of CVL operating at 9 kHz pulse repetition rate to study the effect of pulse rise time on the dye laser bandwidth and tuning range. The bandwidth obtained with CVL pumped GIG dye laser was nearly 2.5 GHz, which was nearly 28 % less than DPSSL pumped GIG dye laser with higher reflectivity of OC. This narrowband dye laser pumped by DPSSL has application potential in various fields of spectroscopy and diagnostics due to its compactness and superior operational performance.

Acknowledgement:

The author sincerely thanks to the AD BTDG for supporting this research activity. The author would like to acknowledge the laser team members, Rajasree V, Anil Nayak, Dheeraj K Singh, S Mandal, B V Ganawane for providing their help and support during this experiment. The team members of LDIAD, RRCAT, Indore for providing the DPSSL laser for this study are greatly acknowledge.

References:

[1] F J Duarte, “Dispersive dye lasers” High power dye lasers, Springer Verlag Berlin, Heidelberg New York, 1991.

[2] V S Rawat, Jaya Mukherjee, L M Gantayet, Progress in Quantum Electronics, 43, 31 – 77, 2015.

[3] G K Mishra, A Kumar, S K Sharma, A J Singh, O Prakash, P K Mukhopadhyay, K S Bindra, S K Dixit, S V Nakhe, Laser Phys. 25, 055001, 2015.

[4] G K Mishra, A Kumar, O Prakash, R Biswal, S K Dixit, S V Nakhe, Laser Phys. 26, 015003, 2016.

[5] S K Sharma, RRCAT Newsletter, Vol. 32, Issue 2, 2019.

[6] V.S.Rawat, N Kawade, G.Sridhar, S.Singh, L.M.Gantayet, *Pramana Journal of Physics*, Vol. 82, No. 2, 203 – 210, 2014.

Development and characterization of a 1 W engineered narrow linewidth all-fiber multistage amplifier system at 1550 nm.

Bhuvnesh[1,2], C.P. Singh[1], P.K. Gupta[1], P. Hedaoo[1], S. Sahu[1], P.K. Mukhopadhyay[1] and K.S. Bindra[1]

[1]*Laser Technology Division, Raja Ramanna Centre for Advanced Technology, Indore-452013*.

[2]E-mail: bhuvneshk@rrcat.gov.in

Abstract: In this paper we present development of an engineered all-fiber amplifier system at 1550 nm generating 1 W narrow linewidth (< 1MHz) output. Amplification of a narrow linewidth fiber coupled seed laser diode at 1550 nm of 10 mW power is carried out in multi-stage configuration. Output power is stable and there is no contribution of pump or amplified spontaneous emission in the amplified output. Pump to signal conversion efficiency is ~15%.

Narrow linewidth lasers at 1550 nm has aroused wide attention around the world as this wavelength is relatively safe to human eye and since narrow linewidth lasers have longer coherence length so they find applications in long distance coherent-detection systems like measuring velocity of projectile (defense applications), metrological measurements like wind velocity, free-space telecommunication, ranging (LIDAR) etc [1,2,3]. Usually, high power laser systems are used for coherent detection as this ensures a longer transmission distance and better signal to noise (SNR) ratio. Generation of high power narrow linewidth single longitudinal mode output directly from oscillators is difficult as it require a complex design and system become bulky. So better approach is to use MOPA (Master Oscillator Power Amplifier) configuration. In MOPA configuration a low signal strength seed source with narrow linewidth is amplified to generate high output power. All-fiber based amplifier systems are preferred as there are several advantages of using fiber over conventional solid-state counterparts like better heat removal, beam quality, misalignment free operation, compact design etc [4]. Since this wavelength is used in tele-communication/internet, there has been tremendous technological advancement in fiber components for 1550 nm. As a result, almost all the components used for making an amplifier are easily available. This also facilitate making an all-fiber amplifier system at 1550 nm. As fiber core diameter of optical fiber is extremely small and due to longer interaction length, nonlinear effects particularly generation of stimulated Brillouin scattering (SBS) and amplified spontaneous emission (ASE) become much significant and require special attention during amplifier design [5]. Another problem associated with 1550 nm amplifier is the strong heating of Erbium/ Ytterbium (Er/Yb) co-doped fibers which causes fluctuation in output power and sometime damage the active fiber [6]. The Er/Yb co-doped fibers are used because of low absorption cross section of Er near 980 nm. This heating is due to large quantum defects and excitation mechanism.

In this paper we report the multi-stage Er/Yb co-doped all-fiber amplifier, developed in our lab for amplification of a low power narrow linewidth (< 1 MHz) seed signal from a fiber coupled semiconductor laser diode at 1550 nm. Amplification process requires many parameters optimization like gain fiber length, pump power, signal strength, cooling arrangements, ASE level etc. The generation of ASE was minimized by increasing the signal power gradually using multistage amplification process and gain fiber length optimization for each stage using proper simulations. The problem of nonlinear effects was reduced by increasing the core diameter of fiber with power scaling (this helps in increasing the threshold for non-linear effects). The amplifier design presented here is based on the simulation studies carried out using open-source software [7]. The problem of heating was

minimized through proper cooling arrangements of active fiber and other components. The amplifier generates ~1 W of CW power with spectral width less than 1 MHz without any significant contribution from ASE or SBS.

Schematic of the amplification scheme is shown in Fig 1, which consists of three parts: seed source, pre-amplifier stage and amplifier stages. Seed source is a commercial fiber-coupled single frequency laser diode (Eblana Photonics, Mode: Model EP 1550-0-NLW-B-800FM) with specified linewidth of ~800 kHz at 1550 nm with output power ~10 mW. Seed source is input to the pre-amplifier stage. This pre-amplifier stage is required to enhance the signal strength for amplifier stage otherwise ASE will be generated which can damage the optical components. Pre-amplifier stage consists of ~75 cm long Er-doped non-polarization maintaining single mode fiber (SMF) with core diameter ~ 9 µm. The active fiber is pumped in core by an FBG stabilized laser diode (LD) at 976 nm using a wavelength division multiplexer (WDM) through its 980 nm port. A pump protection filter (PPF) is spliced between pump diode and 980 nm port of WDM to protect the pump diode from ASE which can damage it. Seed source is spliced to 1550 nm port of WDM through a fiber coupled isolator to avoid any unwanted feedback towards the seed source which can disturb its linewidth and can cause damage to it.

Output of the pre-amplifier stage is input to amplifier stage. The amplifier stage consists of an active multiple pump combiner (MPC) having two pump ports and a signal port at one side and an active fiber of ~1m length at the other side. Active fiber is Er / Yb co-doped double clad (DC, 10/120) fiber which is pumped in clad by a water cooled multi-mode fiber coupled laser diode (JDSU, 9W) at 976 nm wavelength through pump port of MPC. The signal port of MPC is spliced to pre-amp output through a fiber coupled isolator. The output of amplifier stage is spliced to the fiber coupled collimator with beam size ~ 3 mm. Power meter (Ophir) is placed after collimator for power measurement. The amplifier setup was assembled in a portable enclosure to make it ready for field applications. Photographs exhibiting internal and external views of the developed engineered version of the amplifier setup are shown in Fig 2 (a) and (b) respectively.

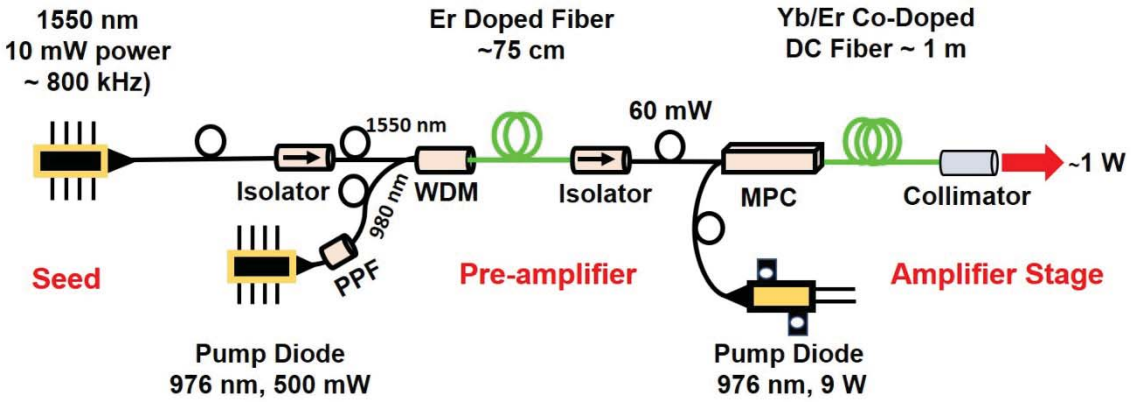

Figure 1 Amplification Setup.

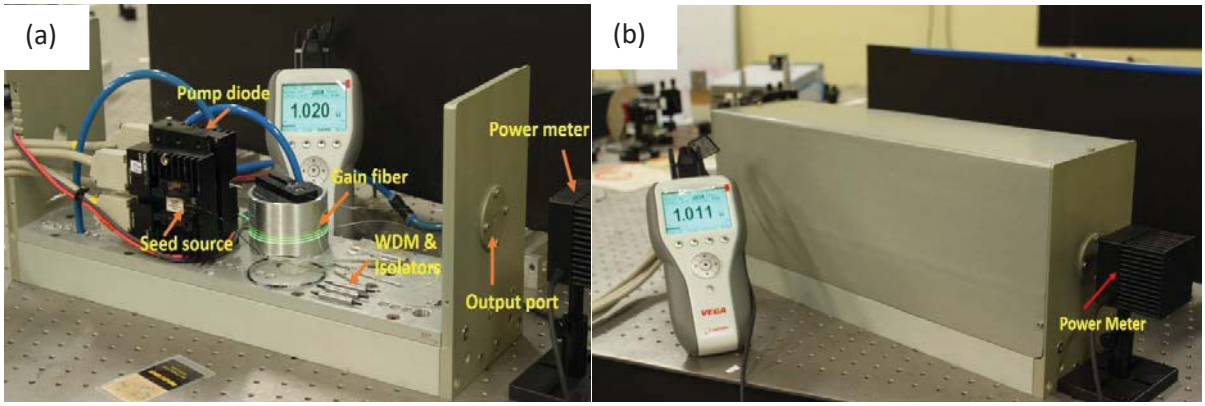

Figure 2 Internal (a) and external (b) view of the developed amplifier setup.

Fig 3(a) shows the variation of amplified power output with pump power. The amplifier output increases almost linearly with increase in the pump power. Maximum 1 W output power at 1550 nm was achieved at 7 W pump power giving rise to ~15 % pump to signal conversion efficiency. To check the repeatability of amplifier output, amplifier was operated many times. Fig 3(b) shows the typical run of amplifier for one-hour duration. It is clear from the figure that amplifier output is stable with fluctuations within ±0.1 %. Optical spectrum shown in the Fig 3 (c) clearly exhibits amplifier output is peaked at 1550 nm without any contribution from pump and ASE.

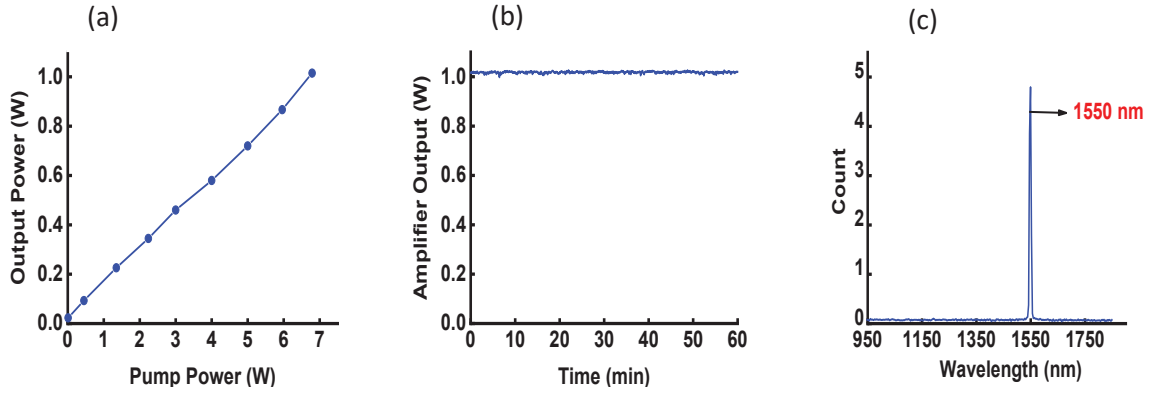

Figure 3 Variation of output power with pump power after the amplifier stage (a), Stability of amplifier output at ~ 1 W level (b), Wavelength spectrum of amplifier output at ~1 W level (c)

In conclusion, we have developed an engineered all-fiber amplifier using Er/Yb co-doped gain fiber for amplification of the single frequency narrow linewidth seed source at 1550 nm. Power was amplified from ~ 10 mW to ~ 1 W output power in multiple stages at 1550 nm without any significance contribution from pump and ASE. For characterization of the linewidth, Delayed Self-Heterodyne Measurement technique based linewidth detection setup at 1550 nm is under development. Further power scaling up to 5 W level and experiments with narrow linewidth laser system will be carried out in future.

References

1. Zhang, X.; Diao, W.; Liu, Y.; Zhu, X. Eye-Safe single –frequency single-mode polarized all-fiber pulsed laser with peak power of 361W. Appl. Opt. 2014, 53, 2465–2469.
2. Jeong, Y.; Sahu, J.K.; Soh, D.B.S.; Codemard, C.A.; Nilsson, J. High-power tunable single-frequency single-mode erbium:ytterbium codoped large-core fiber master-oscillator power amplifier source. Opt. Lett. 2005, 30, 2997–2999.
3. Philippov, V.; Codemard, C.; Jeong, Y.; Alegria, C.; Sahu, J.; Nilsson, J. High-energy in-fiber pulse amplification for coherent lidar applications. Opt. Lett. 2004, 29, 2590–2592.
4. C. J. Koester and E. Snitzer, "Amplification in a fiber laser", Appl. Opt. 3 (10), 1182 (1964),
5. R. Y. Chiao et al., "Stimulated Brillouin scattering and coherent generation of intense hypersonic waves", Phys. Rev. Lett. 12 (21), 592 (1964).
6. M. E. Fermann et al., "Efficient operation of an Yb-sensitised Er fiber laser at 1.56 μm", Electron. Lett. 24, 1135 (1988).
7. "Fiber Lasers and Amplifiers Design Toolbox" version 1.9.0.0 by Luke Rumbaugh available on Mathworks

Generation of 50 W of output power at eye safe wavelength of 1600 nm from all-fiber Er-doped fiber laser using MOPA configuration

Ravindra Singh*, Avdhesh Kumar, Antony Kuruvilla, Rajpal Singh, B. N. Upadhyaya, K. S. Bindra
Laser Technology Division, Raja Ramanna Centre for Advanced Technology, Indore-452013, India.
*E-mail: ravindrasingh@rrcat.gov.in

Abstract: Generation of high output power from Yb-free Er-doped fiber laser is difficult and challenging due to low Er^{3+}-ion absorption cross-section and formation of clusters that leads to development of unbleachable loss at high Er^{3+}-ion concentrations. Hence, usually the efficiency is very low in double-clad Er-doped fiber lasers. In this work, generation of 50 W of output power at 1599.9 nm has been carried out with 24.35% slope efficiency using an all-fiber MOPA configuration of Er-doped large mode area optical fiber by pumping with readily available low cost 976 nm diodes. From the all-fiber Er-doped fiber laser oscillator, an CW output power of 5 W has been generated, which has been further amplified using a single amplifier stage to generate an output power of 50 W. Laser output spectrum is peaked at 1599.9 nm eye-safe wavelength with an FWHM linewidth of ~1.7 nm.

1. Introduction:

Fiber lasers offer several advantages over bulk lasers such as higher efficiency, compactness, better beam quality, and higher brightness along with an excellent heat dissipation ability due to the large surface area to volume ratio[1]. An all-fiber configuration provides robust misalignment free pumping arrangement and resonator, wherein the fiber laser components are made of fibers, which are all spliced and there are no mechanical misalignment problems in comparison to bulk lasers where mirrors are held on separate mounts. So, all-fiber format is of great interest for actual industrial applications. In recent years, fiber lasers have seen an excellent growth in higher output powers and widespread wavelength range. Also, the concept of clad pumping has played a crucial role in power scaling of fiber lasers. It allows efficient coupling from poor beam quality laser diodes and absorption of high pump power in the gain fiber having small core area doped with rare-earth ions. The small core size is necessary to have laser output with good beam quality. With doping of different rare earth ions in the core of the fiber, a varied range of lasing wavelengths are possible in the visible and near-infrared regions. The most widely used doping ion is erbium (Er), which is used to realize erbium-doped fiber amplifiers (EDFAs) for telecommunication networks[2]. The emission of laser radiation from Er-doped fiber lasers in the spectral range of 1500-1700 nm is attractive for many applications as it falls in the eye safe region. The maximal tolerable exposure to human eye near 1550 nm wavelength region depends on the pulse width and is about three to four orders of magnitude higher than that for 1000 nm wavelength region[3]. Important applications include free space communication, LIDAR, sensing, directed energy, etc. For these applications, 1000 nm wavelength region is not suited, since propagation loss in the atmosphere is substantially higher as compared to other bands at longer wavelengths.

Power scaling of Er-doped fiber laser is challenging due to low Er^{3+}-absorption cross-section and increase in unbleachable loss with increase in Er^{3+}-ion concentration because of clustering effect of Er^{3+}-ions, which impedes the manufacturing of efficient double-clad fibers. In recent years, significant success has been obtained in power scaling of Er-doped fiber lasers and amplifiers. Several approaches have been used to

increase the laser efficiency near 1550 nm wavelength. One of the approaches is co-doping of Er-doped gain fiber with Yb^{3+}-ions. But, co-lasing near 1000 nm wavelength in Er-Yb co-doped fibers[4] and low electrical-to-optical conversion efficiency prevents their pervasive use. Another approach to achieve high output power near 1550 nm is core-pumping of Er-doped fiber with a 1480 nm Raman laser. The simplest, and the most efficient approach in terms of electrical-to-optical conversion efficiency is clad-pumping of Yb-free Er-doped fibers with readily available low cost 976 nm pump diodes. A maximum of 656 W of output power at 1601 nm directly from 146 μm core diameter Er-doped fiber laser oscillator has been recently demonstrated by Lin et al[5]. Further, by using non-polarization maintaining Er-doped photonic crystal fiber having hexagonal shaped core of 40 μm diameter in the amplifier stage, 70 W of output have been reported[6]. However, the most common approach is the use of master-oscillator-power-amplifier (MOPA) set-up.

A seed input to Er-doped fiber amplifier has also resulted in 75 W of output power and slope efficiency of 40% using an optimum fiber design [7]. In this report, power scaling of the Er-doped fiber amplifier with clad-pumping at 976 nm has been presented based on the optimization of chemical content and the geometrical parameters to limit the clustering effects in Al_2O_3-P_2O_5-SiO_2 glass matrix. The fiber had a core diameter of 34 μm. Further, power scaling of Er-doped power amplifier up to 100 W level with pumping at 976 nm based on this optimized fiber cladding has also been reported[8]. The above high power laser configurations are altogether based on master oscillator power amplifier (MOPA) topology utilizing low seed powers near 1550 nm either made on their own or by using a commercially existing seed source. In this paper, we have carried out generation of 50 W of CW output power with a slope efficiency of 24% from an all-fiber Yb-free Er-doped fiber laser using MOPA configuration with pumping by low cost readily available 976 nm pump diodes and Er-doped fiber in small core diameter of 25 μm.

3. Experimental details:

The experimental set-up consists of two stages, as shown in Fig. 1. The first stage is a master oscillator, which contains of a large mode area (LMA) Er-doped double-clad active fiber with a core diameter of 20 μm, inner clad diameter of 125 μm, and outer clad diameter of 250 μm. This double-clad fiber has an octagonal shape of the inner cladding to avoid excitation of skew modes by breaking the cylindrical symmetry. Numerical apertures (NA) of core and inner cladding are 0.09 and 0.46, respectively. The absorption of the pump beam at 975 nm for inner clad launching is 1 dB/m. A length of 10 m of Er-doped fiber was selected as the gain medium to have an effective pump absorption of ~10 dB. The Er-doped fiber has been spooled on a water cooled aluminium mandrel to increase heat conductivity from the active fiber surface. The backword pumping scheme is selected for the purpose of pumping of doped fiber. A diode of 70 W output power at 976 nm with pigtail fiber core diameter of 100 μm and 0.22 NA was selected to pump the Er-doped fiber using a multimode fiber optic pump combiner. This diode is mounted on water cooled heat sink to maintain its temperature at 20°C for the entire range of pump operation. Fiber pigtail of the pump diode has been fusion spliced with one of the pump input ports of multimode pump combiner using a fusion splicing machine. Maximum transmission of ~88% was achieved through pump combiner with optimized splice joint. A loss of 12% can be accounted for mismatch between both the fibers of diode pigtail and pump combiner fiber input port along with pump combiner insertion loss from pump input port. Output port of the pump combiner has a core/inner clad diameter of 100/125 μm and an NA of 0.15/0.46. Further, the output signal port of the fiber optic pump combiner has

been spliced with the EDF and a high reflectivity (~99%) fiber Bragg grating (FBG) mirror in series, respectively. This fiber Bragg grating mirror is written in a compatible double-clad fiber and has a peak reflectivity at 1600 nm with a linewidth of 0.2 nm. The 10% reflectivity FBG is spliced at the signal input port of the pump combiner and this also works as output port.

The oscillator is pumped up to 50 W and the maximum output power from the oscillator after the isolator is 5 W. Further, the output power from oscillator was fed to the amplifier stage. In order to separate the oscillator stage from the amplifier stage, a polarization insensitive isolator has been spliced in series to prevent any backward propagating signal causing any damage to the other fiber components in oscillator stage. For the amplifier stage, four pump diodes of 70 W output power at 976 nm were spliced with four pump input ports of a (6+1)x1 pump combiner. The output of the pump combiner was then spliced with another 20 m long EDF having core/inner cald diameter of 25/125 µm and NA of 0.08/0.46. The total combined pump power for the amplifier stage is 220 W.

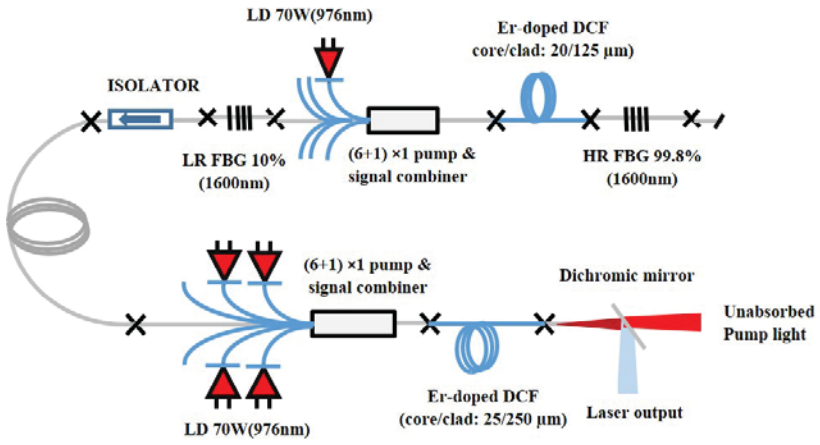

Fig.1: *Schematic of 50 W Er-doped CW fiber laser set up.*

The power supply unit provides voltage variations in the range of 0-15 V and current variations in the range of 0-100 Amp for pump diode operation. A dichroic mirror with high transmission in a broadband from 960-980 nm and high reflectivity in the range of 1500-1600 nm for 45° angle of incidence has been used to filter out the un-absorbed pump power. Laser output power was measured using a thermopile based power meter and the output spectrum was measured using an Agilent make optical spectrum analyser having a minimum resolution of 0.06 nm. A maximum output power of 53 W was achieved at the maximum input power of 220 W. This development required optimization of splice joints of different fiber components such as FBG, Er-doped fiber, isolator, pump combiner and efficient heat removal from different fiber components. Power supply units have been used to control and operate fiber-coupled laser diodes in series.

4. Results and discussion:

Figure 2 shows the variation of laser output power from the amplifier as a function of input pump power. A maximum output power of 53 W has been achieved at the maximum input pump power of 220 W with a slope efficiency of 24%. This graph shows that the output power varies linearly with increase in input pump power and there is no saturation in the output power even at the maximum input pump power. This indicates

that output laser power is limited by the input pump power and there is further scope for power scaling in the same set-up. Figure 3 shows measured output spectrum at the maximum output power of 53 W. The linear fitting of the graph shows a slope efficiency 24.35%. The output spectrum is peaked at 1599.9 nm with a spread from 1599.4 nm to 1601.1 nm and FWHM linewidth ~1.7 nm. Further, laser output is emitted from 25 µm core diameter of the Er-doped fiber in a full cone angle of 120 mrad.

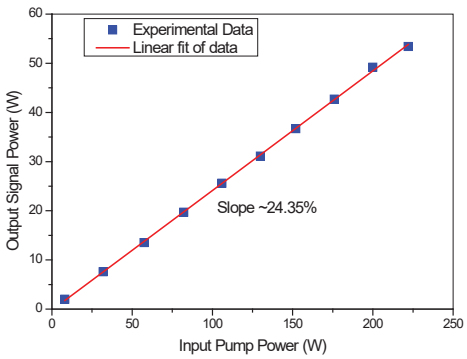

Fig. 2: Laser output power vs input pump power.

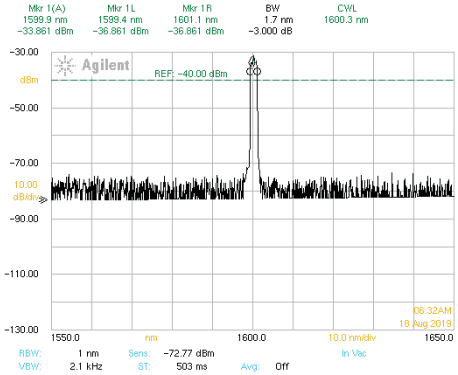

Fig. 3: Er-doped CW fiber laser output spectrum.

The calculated value of V-number of the fiber is 3.6, which suggests that the active fiber possibly will provide guidance of a total of six numbers of fiber modes. In such a case, fiber laser will be slightly multi-moded.

5. Conclusion:

In conclusion, we have carried out generation of 50 W of output power from an all-fiber MOPA configuration of Er-doped large mode optical fiber having a core diameter of 25 µm using readily available high power pump diodes at 976 nm and Er-doped fiber. A slope efficiency of 24.35% has been achieved. The output spectrum is peaked at 1599.9 nm with FWHM linewidth of 1.7 nm. The total output power as well as the optical-to-optical conversion efficiency can be further improved by increasing the output power from the oscillator and by pumping higher power in the amplifier stage. Also, Further power scaling is possible by using a second amplifier stage and an Er-doped fiber having larger core size. This work will be useful in development of laser for eye-safe applications.

References:

1. M.J.F. Digonnet, *Rare Earth Doped Fiber Lasers and Amplifiers*. 2nd ed. USA (Marcel Dekker, Inc. 1993).

2. G.P. Agarwal, *Fiber-Optic Communication Systems*. 3rd ed. USA (John Wiley & Sons, Inc. 2002).

3. B. Danker., *Handbook of Solid-State Lasers, Chapter 13,* 1st ed. UK (Woodhead Publishing 2013).

4. Y. Jeong et. al, *OFC/NFOEC Technical Digest* (Optical Fiber Communication Conference 2005).

5. Lin et. al, *Opt. Lett.* 43, 3080 (2018).

6. V. Kuhn, *Opt. Lett.,* 36, 3030-3032 (2011).

7. Leonid V. Kotov, *Opt. Lett.*. 38, 2230-3032 (2013).

8. Leonid V. Kotov, *Proc. of SPIE* Vol. 8961 (2015).

Studies on the high beam quality green and yellow radiation of a 40 W Copper Bromide Laser

G. N. Tiwari[*a], V. K. Shrivastava[a], R. K. Mishra[b], S. K. Dixit[a]

a. Fiber Sensor & Optical Spectroscopy Section, b. Laser Power Supply Division

Raja Ramanna Centre for Advanced Technology, Indore-452013

*E-mail: gnt@rrcat.gov.in

Introduction:

The copper bromide laser (CBL) is a prominent laser belonging to the class of copper halide lasers [1, 2], which is developed to overcome the problems of pure metal copper vapor laser (CVL). Copper lasers are being used for applications such as nonlinear frequency conversion, pumping of solid-state laser materials and micromachining applications etc. For best results, these applications require a laser of high beam quality. Due to the high gain and short gain duration, copper lasers require operation of the laser with unstable resonator of high magnification to obtain output of high beam quality. With unstable resonator, the beam quality of laser evolves in a stepwise fashion from the highly divergent Amplified Spontaneous Emission (ASE) to low divergence and finally near diffraction limited output as the radiation completes successive number of round trips [3]. If the beam emerging from the cavity is imaged by a lens on its focal plane, the diameter of the focused spot would become smaller as successive transits take place. Thus the total output of the laser is composed of ASE and HBQ components. Spatial filters are configured outside the resonators to filter out the highly diverging ASE component from the beam to obtain HBQ component only. In literature, there are several reports on the beam quality characterization of elemental CVLs, and copper hybrid (Cu-Hy- BrID) and kinetically enhanced (KE)-CVLs but until now, little similar effort has been applied to the CBL [4].

The CBL emits radiation at two wavelength 510.6 nm (green) and 578.2 nm (yellow). The gain and gain duration is different for its spectral components and it is expected that these spectral components would have different response to resonator magnifications. In this paper, we are reporting our results of variation of total power, HBQ component of green and yellow wavelengths along with their divergences under different magnifications of the unstable resonator.

Experimental Details:

The study was performed on an indigenously developed CBL [5] with confocal positive branch unstable resonator of magnifications 12.5, 50 and 100. Gas mixture of Neon and Hydrogen was used as the buffer gas. The buffer gas pressure, repetition rate and electrical input power was kept constant for all the measurements. The laser power was measured by a laser power meter (Gentec,TPM-300). A dichroic mirror was used to separate green and yellow wavelengths of the laser output. The average laser power was 40 W with a plane-plane resonator.

Experimental setup for study of the output characteristics of CBL with confocal positive branch unstable resonator (PBUR) is shown in figure 1. The PBUR consisted of a concave mirror (M_1) of focal length (f_1) and a small diameter (3 mm) button convex mirror (M_2) of focal length (f_2). The focal length of the concave mirror M_1 was kept constant at 250 cm while that of button mirror M_2 was changed to 20, 5 and 2.5 cm for obtaining resonator magnification ($M = f_1/f_2$) of 12.5, 50 and 100 respectively and in each case, the resonator length was

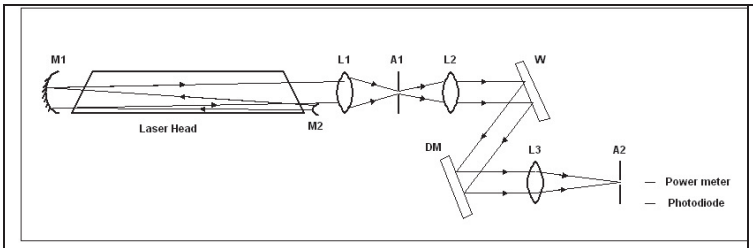

Figure 1: Experimental set up, M1: Concave mirror, M2 button convex mirror, L1-L3 convex lens, A1 spatial filter to remove ASE from total output beam, W optical wedge, DM dichroic mirror, A2 aperture (200μm)

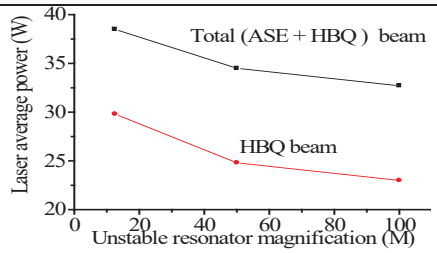

Figure 2: Variation of laser average power for total and HBQ beam with resonator magnification

close to the value given by (f_1-f_2). Both mirrors, M_1 and M_2, are dielectric coated high reflecting mirrors and the output is taken as overfilled collimated radiation past the button mirror M_2. The output obtained past the button convex mirror was spatially filtered with a combination of lens L_1 (focal length = 1m) and an aperture (spatial filter) A_1 of appropriate size placed at focal plane of lens L_1. The aperture was mounted on a precision XYZ translation stage and placed in such a way that it passed the visually seen high intense quality beam completely through it and removed the haloes which are due to ASE component. This optical arrangement removed the highly diverging ASE component from the laser beam and HBQ component was obtained as the output. The focal length of lens L_1 was kept same but the size of the aperture A_1 was ($Ø_{A1}$ 1 mm for 12.5, 0.8 mm for 50 and 0.5 mm for 100) different for different magnifications of unstable resonator. The power in ASE was estimated by deducting the power after spatial filter from the power obtained without spatial filter. Spectral power was measured by placing the dichroic mirror (not shown in the figure 1), after the lens L_2 and was removed while doing divergence measurement.

Results and discussion:

Figure 2 shows the laser average power comprising of both green and yellow spectral components, for the total beam (ASE +HBQ) and HBQ beam only. It shows that average output power was decreased as M was increased from M =12.5 to 100. For total beam, average power of 38.5 W for M =12.5 was reduced to 32.8 W for M = 100, a decrease by 14.8%. This reduction in average power with increase of resonator magnification M is due to reduced feedback ($1/M^2$). It is also observed that for HBQ beam, average power of 29.8 W for M=12.5 was reduced to 23.0 W for M = 100, a decrease by 22.8%. It is observed that spatial filter used to remove the ASE reduces the HBQ power for M =12.5 by 22.6%, for M=50 by 28.1% and for M=100 by 29.9%. This reduction in average power of HBQ beam is due to increase in ASE content with increase of resonator magnification M due to reduced feedback.

Figure 3 shows the variation of laser average power for green and yellow spectral components in total laser beam with unstable resonator magnification M. It shows that both green and yellow components decrease with increase in resonator magnification M. This decrease in output power of spectral components is due to reduced feedback. The green output which was 24.0 watt at M =12.5 was decreased to 21.9 watt at M =100, a decrease by 8.8%. The yellow output which was 14.5 watt at M =12.5 was decreased to 10.9 watt at M =100, a decrease by 24.8%. Figure 4 shows the variation of laser average power for green and yellow components in HBQ beam with unstable resonator magnification M. It shows that both green and yellow components decreases with

increase of resonator magnification M. The green output which was 18.0 watt at M =12.5 was decreased to 15.1 watt at M =100, a decrease by 16.1%. The yellow output which was 11.8 watt at M =12.5 was decreased to 7.9 watt at M =100, a decrease by 33.1%. It can be concluded from Fig. 3 and 4 that effect of resonator magnification is more pronounced on the yellow spectral output as compared to green spectral output. Figure 5 shows the variation of green to yellow power ratio in total laser beam and HBQ beam with unstable resonator magnification M. It shows that green to yellow power ratio was increased as M was increased for both total and HBQ beam. For total beam, this ratio was 1.66 for M=12.5, which was increased to 2.01 for M = 100. For HBQ beam, this ratio was 1.53 for M=12.5, which was increased to 1.91 for M = 100. For M = 12.5, the spatial filter used to remove ASE, reduces the green power from 24.0 watt to 18.0 watt, which corresponds to a transmission of 75 %. The same spatial filter reduces the yellow power from 14.5 watt to 11.8 watt, which corresponds to a transmission of 81.4 %. For M = 50, the spatial filter used to remove ASE, reduces the green power from 22.3 watt to 15.6 watt, which corresponds to a transmission of 70%. The same spatial filter reduces the yellow power from 12.2 watt to 9.2 watt, which corresponds to a transmission of 75.4 %. For M = 100, the spatial filter used to remove ASE, reduces the green power from 21.9 watt to 15.1 watt, which corresponds to a transmission of 68.9% . The same spatial filter reduces the yellow power from 10.9 watt to 7.9 watt, which corresponds to a transmission of 72.5 %. This shows that for each unstable resonator magnification M, the effect of spatial filter A_1 is more pronounced on green spectral output as compared to yellow spectral output. This is due to lower beam divergence of yellow as compared to green. This shows that unstable resonator magnification used to improve the beam quality and spatial filter used to remove the ASE affects its spectral components differently.

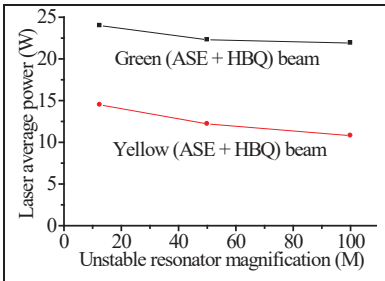

Figure 3: variation of laser average power for green and yellow in total laser beam with unstable resonator magnification M

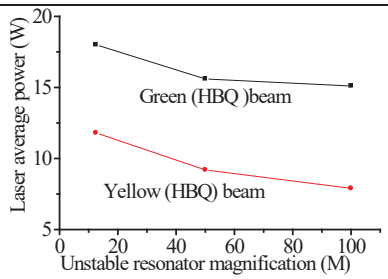

Figure 4: variation of laser average power for green and yellow in HBQ beam with unstable resonator magnification M.

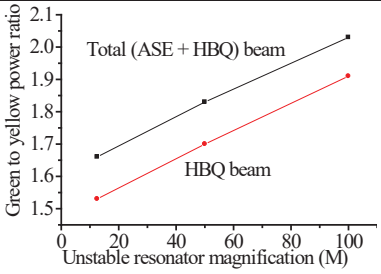

Figure 5: variation of green to yellow power ratio in total laser beam and HBQ beam with unstable resonator magnification M.

A qualitative estimation of the beam quality of the HBQ output beam for each magnification of unstable resonator was made separately for green and yellow spectral output by power in bucket measurement. The HBQ output obtained past the spatial filter was again collimated with another convex lens L_2 of same focal length and 4% of this collimated output beam was taken by reflection from an optical wedge, which was again focused by another convex lens L_3 of 1 meter focal length. A dichroic mirror (DM) was used to separate green and yellow wavelengths. The beam was allowed to pass through a pin hole of diameter 200 μm placed suitably in the path of the beam. The power before and after the pinhole was noted. At M =12.5, the fractional power contained in 0.2 mrad divergence angle is ~16% for green component and 21% for yellow component. At M = 50, the fractional power contained in 0.2 mrad divergence angle is 84.6% for green component and 89.2% for yellow component. Similarly at M =100, the fractional power contained in 0.2 mrad divergence angle is 90.1% for

green component and 93.6% for yellow component. It can be concluded from the data that the beam quality of the laser output beam (both green and yellow components) improves with increase of magnification of the unstable resonator. It also suggest that for each magnification, the beam quality of yellow component is better than that of green component.

Conclusion: The total output power, which consists of amplified spontaneous emission (ASE) and high beam quality (HBQ) parts, of an indigenously developed copper bromide laser with confocal positive branch unstable resonator was studied for green and yellow spectral components of the output as a function of magnification of the resonator. It is observed that magnification of the unstable resonator, which governs the beam quality and the spatial filter, which removes the ASE, do not affect the green and yellow components of the laser output in similar ways. It is observed that the total power and HBQ power of the laser output reduced for both green and yellow components as magnification of the resonator increased from 12.5 to 100 but at each magnification, the ASE percentage in green component was more than that of yellow component. It is also found that the divergence of the laser output beam for both green and yellow components reduced with increase of magnification of the resonator but at each magnification, the divergence of green component was more than that of the yellow component.

Acknowledgements:

The guidance of Dr. Rajeev Khare, ex-head, optical spectroscopy lab, during the course of present work, is duly acknowledged.

References:

[1] D. N. Astadjov, N. V. Sabotinov and M. K. Buchkov, *Opt. Commun*. **56(4)**, 279 (1985)

[2] D. N. Astadjov, K.D. Dimitrov, D.R. Jones, V.K. Kirkov, C.E. Little, N.V. Sabotinov, N.K. Vuchkov, *IEEE J. Quantum Electron*. **33(5)**, 705 (1997)

[3] M.J.Mithford, D.J.W.brown, D.W.Coutts and J.A.Piper, *IEEE Journal of Quantum electronics*, **31(5)** 898 (1995)

[4] P.G.Foster,P.E.Davis,D.Mecoy and J.Munch; *IEEE Journal of Quantum electronics*, **37(12)** 997(2001)

[5] G.N.Tiwari, R.K.Mishra, R.Khare and S.V.Nakhe ; *Pramana -J. Phys,***82(2)**, 217 (2014)

.

Performance characterization of IGBT based high voltage pulse power supply of CVL MOPA system for long hour operation

R.K. Mishra[1], Jagdish Kumar[1], Deepak Naphade[1], P.K. Agrawal[1,2] and M.S. Ansari[1,2]

[1]Laser Power Supplies Division, Raja Ramanna Centre for Advanced Technology, Indore – 452013

[2] Homi Bhabha National Institute, Anushakti Nagar, Mumbai – 400094, India

Email: rkm@rrcat.gov.in

Introduction:

Copper Vapour Laser (CVL) systems are operated for long hours in Master Oscillator Power Amplifier (MOPA) configuration for its use in many strategic and industrial applications to obtain high average laser power with good beam quality. CVL MOPA systems can have two or more CVL which are electrically excited and have pulse repetition rate from 5 kHz to 20 kHz. The voltage magnitude of voltage excitation pulse depends on length of CVL tube and rise time should be less than 100 ns [1]. Continuous operation of CVL MOPA system requires precise synchronization of individual CVLs in the order of 10 ns which depends on pulse to pulse timing jitter and long time drift of individual power supply.

The pulse to pulse timing jitter is very critical in IGBT based high voltage pulse power supply due to presence of magnetic pulse compression (MPC) stages [2]. The MPC stages are used to compress the input voltage pulse to achieve desired output voltage pulse. The design of MPC stages are based on voltage-time product and hence change in input voltage will result in variation in propagation delay time for output pulse. Thus the design of MPC stage is the dominant factor in deciding the overall voltage stability at the input storage capacitor to achieve lowest timing jitter. The pulse width (FWHM) of CVL is around 40 ns and jitter value of 10 ns is sufficient to achieve good power stability in MOPA configuration.

Drift is a critical parameter for long time synchronization. It is a slow phenomenon and mainly depends on temperature coefficient of the components used in the power supply. For auto-synchronization of CVLs in MOPA configuration, CVL system is operated in closed loop to achieve power stability in MOPA beam [3]. When CVL system is operated in open loop, manual corrections are to be carried in delay generator at different interval to synchronize and maximize output power [4].

This paper reports the performance of CVLs in MOPA configuration for continuous run of ~ 35 hour in an open loop. Various parameters like power stability, delay corrections, propagation delay time of individual laser, temperature rise in power supply, and jitter during operations at various instant are reported.

Methodology:

The block diagram of CVL MOPA system experimental set up is shown in figure 1. A delay generator having four channels BNC make, model 575 with resolution of 250 ps is used. The rectangular pulse having pulse width of 5 μs and repetition rate of 6.5 kHz is generated by delay generator. The electrical output pulse from delay generator is converted into an optical pulse by using HFBR-1402 transmitter. An optical output from delay generator is fed as input trigger pulse to optical receiver card mounted on timer unit of pulse generator.

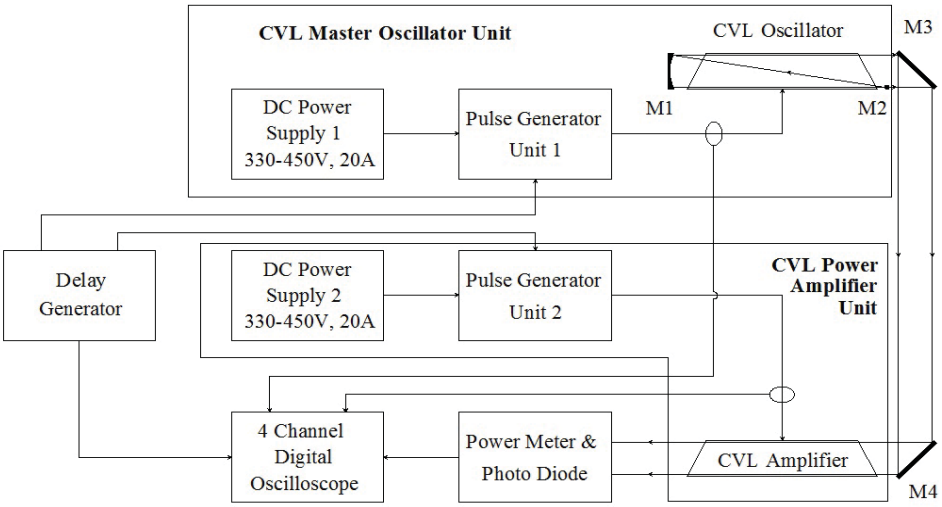

Figure-1: Block diagram of CVL MOPA experimental set up

The CVL power supplies for oscillator and amplifier are solid state pulse power supply based on semiconductor device insulated gate bipolar transistor (IGBT) and MPC as reported earlier [5]. Major components of IGBT and MPC based pulse generator unit are oil dipped which serves as insulator and coolant. The transformer oil is circulated and cooled through shell and tube type oil to water heat exchanger and the outlet oil temperature is monitored to correlate with drift. The oil temperature is measured by using PT100 temperature sensor.

The CVL used for oscillator and amplifier are recrystallized alumina tube of 4.7 cm internal diameter and 150 cm length. Resonator for oscillator is unstable resonator using concave mirror M1, ROC 300 cm and button convex mirror M2, ROC 5 cm. Two plane mirrors M3 and M4 are used to bend the CVL oscillator beam by 90° each and feed it to amplifier. The output power of amplifier is monitored on Gentec make laser power meter TPM300. Partial reflected CVL MOPA beam is fed to bi-planar photo tube Hamamatsu R1193U-52 to monitor optical pulse shape. Four channel digital oscilloscope of Keysight DSO9104 is used to monitor various parameters of experimental set-up. Oscillator and amplifier current pulse is monitored to measure propagation delay time to optimize delay for precise synchronization.

Results & Discussion:

The CVLs were operated by flowing neon buffer gas at 0.8 atm - lt / hr and maintaining tube pressure of 25 mbar. The temperature of water chiller unit is set at 20 °C for cooling. The variable DC power supply was initially operated at 340 V for both oscillator and amplifier with load current of 16.4 A at 7:30 AM. After half an hour it was increased to 360 V, 17.5 A. Again after half an hour, the DC voltage was increased to 375 V and corresponding load current was 18.2 A in both oscillator and amplifier. The optimized operating point is 390 V. For continuous run, both the power supplies were operated at nominal DC input voltage of 375 V. The power supply was turned OFF at 4:30 PM on next day i.e. 33 hours of continuous operation was performed.

The average laser output power of CVL MOPA from amplifier for continuous run of 33 hours is plotted in figure 2. From the plot, the warm up time of laser was 55 minutes. After one hour, MOPA power of 3.6 W was obtained with delay of 120 ns between oscillator and amplifier. The delay setting is adjusted manually to

synchronize both lasers to maximize output power. The delay setting was adjusted at 75, 90, and 120 minutes to obtain output power of 23, 38, 48 W respectively. The delay was adjusted to 32 ns after 2.5 hour of operation and the power obtained was 49 W. Thereafter delay was unchanged for 11 hour and power also remained within 2% of 50 W. Again the delay was adjusted at 13.5 and 26.5 hour of operation to 50 and 38 ns respectively to maintain power within 2% of 50 W.

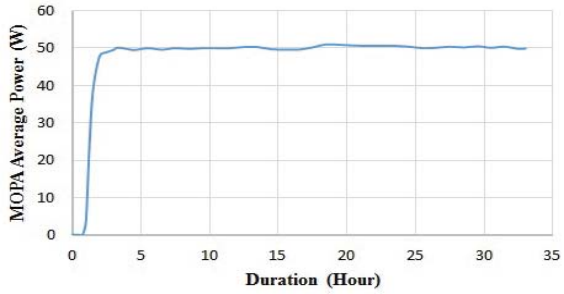

Figure-2: Average laser power of CVL MOPA

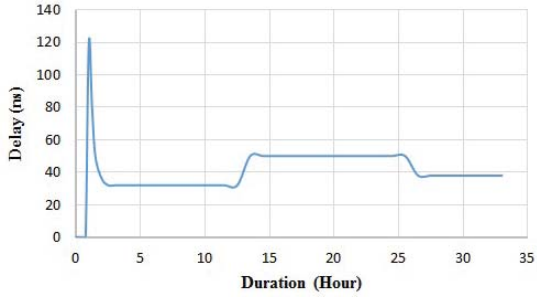

Figure-3: Delay setting for optimized synchronization

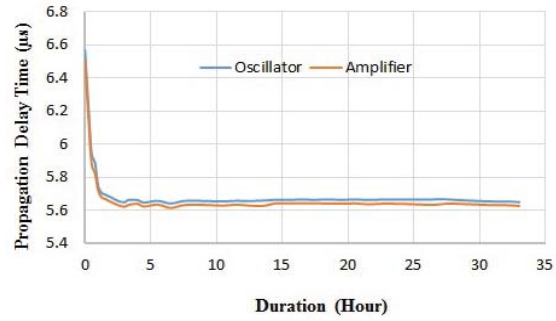

Figure-4: Propagation delay time of oscillator and amplifier current pulse

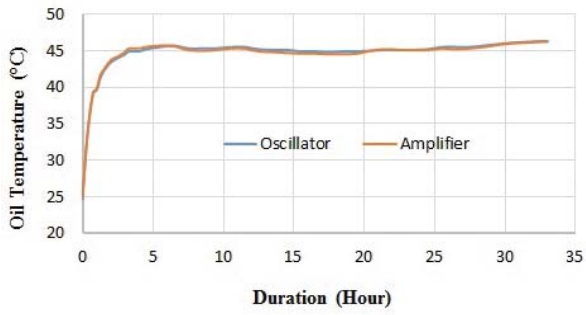

Figure-5: Oil temperature of pulse generator unit of oscillator and amplifier

The delay generator setting with time for optimized synchronization of MOPA beam is shown in figure 3. It was observed that delay setting after initial operation of 2.5 hour remained stable and MOPA power stability also remained within 2% of 50 W for entire duration. After achieving stability in delay setting, it was changed twice in entire duration, once during night at 9 PM and then in the next day morning at 10 AM. The change in delay setting was carried to maintain MOPA power at 50 W.

The pulse propagation delay time of oscillator and amplifier is measured with reference to input trigger pulse by monitoring the laser tube current of oscillator and amplifier. The propagation delay time of oscillator and amplifier with time is shown in figure 4. The propagation delay time of oscillator and amplifier pulse remained within 0.2% of value obtained after initial run of 2.5 hour. The pulse propagation time of oscillator measured initially, after 2.5 hour and finally was 6.567 µs, 5.656 µs and 5.649 µs respectively. Similarly for amplifier these parameters were 6.505 µs, 5.631 µs and 5.625 µs. The slight difference between the two is due to parameter variation of components during fabrication & assembly and also due to oscillator beam path length.

The temperature rise in transformer oil is measured at the outlet of MS tank of pulse generator unit for oscillator and amplifier is shown in figure 5. The oil temperature variation was ~ 5% for both oscillator and amplifier after initial 2.5 hour of operation. The oil temperature of oscillator and amplifier were measured during starting, after

2.5 hour and before shutdown and was 24.7 °C, 44 °C and 46.3 °C respectively and were approximately same for both the systems. The timing jitter of MOPA pulse measured at different instant varied between 6 ns to 8 ns as shown in figure 6. The variation in MOPA pulse average power with change in delay is shown in figure 7.

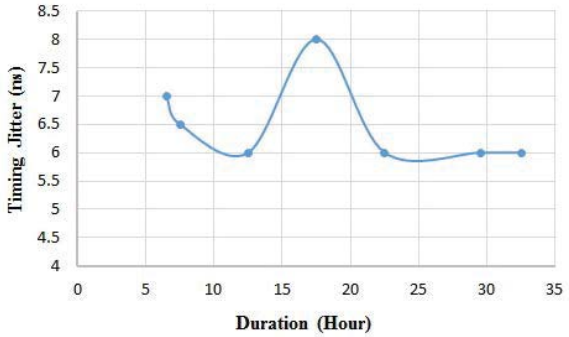

Figure-6: Timing jitter of MOPA pulse

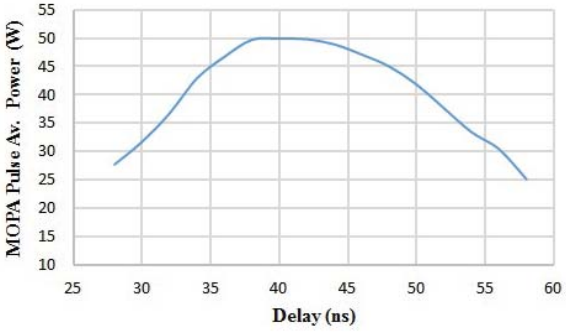

Figure-7: MOPA pulse power variation with delay

The experiment was carried in open loop mode and various parameters were measured initially at 15 minutes interval for 90 minutes, then interval was increased to 30 minutes for next 2.5 hour, thereafter every 1 hour. The parameters were measured so that delay is manually set for optimized synchronization. The manual intervention in delay setting was minimal to achieve good power stability as both the power supplies for oscillator and amplifier were fabricated with same lot of components which has resulted in symmetry. The symmetry has reflected in operating point of power supply, propagation delay time and oil temperature rise of pulse generator. The delay change after 13.5 hour and 26.5 hour of operation can be attributed to slight drift in propagation delay time of amplifier as seen in figure 4 which was corrected to maintain power at 50 W.

Conclusion:

Two copper vapour lasers were operated in oscillator amplifier configuration pumped by high voltage IGBT based pulse power supply in an open loop mode. For precise synchronization and to get maximum power, delay was adjusted between oscillator and amplifier. The timing jitter measured of MOPA pulse was within 6 ns to 8 ns and MOPA power was 50 W, ± 2% obtained after 2.5 hour of operation and remained within the band for entire duration of 33 hours. The pulse propagation delay time and oil temperature rise remained within 0.2% and 5% of 6.656 µs and 44 °C respectively after 2.5 hour of operation.

Acknowledgement:

The authors would like to acknowledge all the team members of LPSD for their active support during the performance testing of high voltage solid state pulse power supply with CVL for long hours of operation.

References:

1. C.E. Little, *Metal Vapor Lasers: Physics, Engineering and applications,* John Wiley & Sons, (1999)
2. R.K. Mishra, D.V.S. Raju, and S.V. Nakhe, *Review of Scientific Instruments,* **86**, 116107 (2015)
3. Anil S. Nayak, Devendra Bhale, Rajasree Vijayan, D.K. Singh, and V.S. Rawat, *Sadhana*, **44:8**, 2019
4. R.K. Mishra, S.K. Agrawal, D.V.S. Raju, G.N. Tiwari, P.K. Agrawal and S.V. Nakhe, *DAE-BRNS National Laser Symposium (NLS-25)*, KIIT University, Bhubaneswar, Dec 2016, Proc. on CD.
5. R.K. Mishra, S.V. Nakhe, G.N. Tiwari, and J.K. Mittal, *Pramana - Journal of Physics,* **75(5)**, 967 (2010)

Generation of more than 100 W of CW output power from all-fiber Tm-doped fiber laser

Usha Chakravarty [*1], Avdhesh Kumar[1], Antony Kuruvilla[1], Aswin Ashok[2], R. K. Jain[1], Rajpal Singh[1], B. N. Upadhyaya[1], K. S. Bindra[1]

[1]*Laser Technology Division, Raja Ramanna Centre for Advanced Technology, Indore-452013*

[2] *International School of Photonics, Cochin University of Science & Technology, Cochin-682022*

[*]E-mail: ushac@rrcat.gov.in

Abstract: In this paper, we report on the development and study of an all-fiber high power Thulium-doped CW fiber laser at ~1940 nm. An output power of ~117 W at 1940 nm has been generated with a slope efficiency of ~49%. Investigation of self-pulsing in high power Tm-doped all-fiber laser has also been performed and analyzed for three different lengths of the gain fiber. Experimental results show that due to higher absorption at wavelengths below ~2000 nm, re-absorption in a longer fiber length results in self-pulsing behavior in laser output. These high peak power random self-pulses needs to be suppressed to avoid catastrophic damage of gain fiber and generate high laser output power. This high power Tm-doped fiber laser is promising for medical field applications and plastic welding.

Introduction: In recent times, Tm-doped fiber lasers (TDFL) operating at eye-safe wavelength near 2000 nm have been a field of intense research and development because of its diverse path breaking applications in the area of medicine, material processing of polymers, gas detection, light detection and ranging (LIDAR), remote sensing, laser spectroscopy and optical communications[1,2]. TDFLs possess an appealing possibility for power scaling in the 2000 nm wavelength range by pumping near 790 nm, which is readily available from AlGaAs diode lasers. The cross-relaxation process overcomes the quantum efficiency of TDFL allowing the laser efficiency to reach well above the Stokes limit of the TDFL when pumped at 790 nm[1]. There are several reports on the development of high power Tm-doped fiber lasers. Ehrenreich et al. have already reported generation of 1 kW CW output from an all-fiber Tm-doped fiber laser using two-stage power amplifier with 53.2% slope efficiency[3]. Most of these reports are related with generation of output wavelengths near 2000 nm, which are suitable for industrial applications. However, for medical applications such as ablation of urinary tissues and lithotripsy, output at 1940 nm is preferable due to high absorption in water near this wavelength[3-5]. For medical applications, TDFLs have better edge over currently used most popular 2100 nm Ho:YAG lasers due to better beam quality, no misalignment issues, lower thermal damage to a tissue and are more compact. To achieve laser operation below 2000 nm from TDFL is challenging due to high absorption of gain fiber at lower lasing wavelength regime of TDF. The highest CW output power reported directly from the oscillator at 1940 nm with 1567 nm pumping with Erbium-doped fiber lasers is 415 W[6]. Recently, there is report on generation of 70 W of all-fiber Tm-doped fiber laser at 1940 nm pumped by 793 nm laser diodes[7]. This is the highest reported power at 1940 nm using 793 nm laser diodes directly from the oscillator. In all these reports, there is no mention of observation of self-pulses in laser output and the mitigation of self-pulses to achieve higher output powers.

Also, there are very few reports on the self-pulsing phenomenon in TDFL even at very low level of pump powers of few watts[8,9]. In this paper, we report on generation of ~117 W of CW output power from Tm-doped

fiber laser at 1940 nm in all-fiber configuration using 793 nm pump wavelength with a slope efficiency of ~49%. To the best of our knowledge, this is the highest reported power at 1940 nm in the oscillator configuration using 793 nm pump diodes. Experimental study on self-pulsing behavior in TDFL at high power levels has also been carried out, which is detrimental in generation of high output powers from TDFL.

Experimental setup: Figure 1 shows a schematic of all-fiber TDFL for the generation of more than 100 W of output power at 1940 nm. The laser cavity comprises of commercially available large mode area Tm-doped fiber (TDF) with core and cladding diameter of 25/400 µm and corresponding numerical apertures of 0.10/0.46 (Nufern LMA-TDF-25P/400-HE). The pump signal absorption at 793 nm is 2 dB/m. To achieve more than 100 W of CW power from TDFL, the length of the TDF was first optimized. For the experiment study, three different lengths of TDF were selected, i.e., 8 m, 6 m, and 4 m. For pumping the TDF, six number of fiber pig-tailed diode lasers at 793 nm with fiber core/clad diameter of 105/125 µm and NA of 0.22 were used. To combine the total output from all the six laser diodes, a multimode pump combiner (PC) is used, which has six pump input ports, one input signal port and one output port. The insertion loss of pump through pump combiner is ~0.17 dB. The six pump input ports of the PC are having matching core and clad diameters of 105/125 µm with core NA of 0.22. The signal port is having core and clad diameter of 10/125 µm. The output port of the PC is compatible with active fiber and has core and clad diameter of 25/400 µm. Two fiber Bragg grating mirrors (FBG), with 99.8% reflectivity and other with 10% reflectivity at the center wavelength of 1940 nm have been used to form the linear cavity with the gain fiber. The output port of the PC is spliced with the highly reflecting fiber Bragg grating mirror (HR-FBG) at 1940 nm with FWHM linewidth of 3 nm. The output end of the HR FBG is spliced with the TDF, which in turn is spliced with the 10% reflectivity FBG mirror (OC-FBG) at 1940 nm with the FWHM linewidth of 1 nm. The LR FBG also acts as the output coupler, as the output signal is taken from this end. The output end of OC FBG is spliced with a 2 m long compatible passive fiber and an end cap is attached at its output end, which is core-less silica fiber. The presence of end cap reduces the power density at the exit fiber end, hence prevents damage of the fiber ends at the high output power. The length of the end-cap must be carefully chosen to maintain beam quality decided by the core of the doped fiber. The maximum length of the end cap without affecting the beam quality is given by,

$$L_{\max} = \frac{d}{2n.NA} \tag{1}$$

Where, d is the diameter of the end cap, n is the refractive index of the silica end cap at the operating signal wavelength, and NA is the numerical aperture of the core of the TDF. The length of the silica end cap spliced with the TDF is ~1.38 mm. For build-up of population inversion and to prevent spurious lasing between the two fiber ends, end cap was cleaved at an angle of 10°.

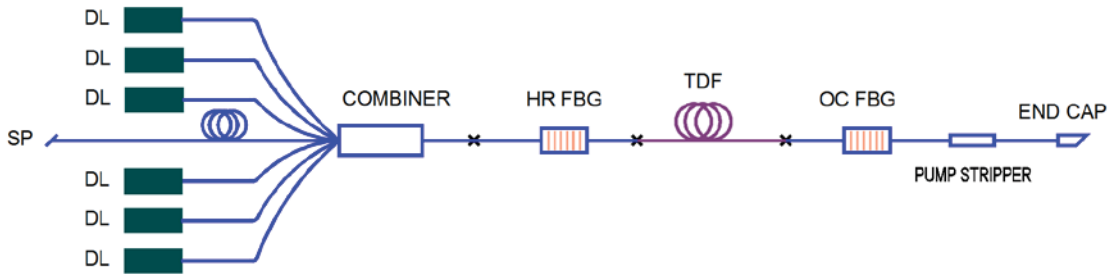

Figure 1: Schematic of the high power Tm-doped all-fiber CW fiber laser in forward pumping configuration.

Results and Discussion:

Figure 2(a) shows the variation of output power at 1940 nm as a function of the launched input pump power, when TDF of 4 m length has been selected for laser up. At the launched pump power of 260 W at 793 nm, total output power of ~138 W was obtained including leakage pump and signal at 1940 nm. When pump power at 793 nm was separated from the signal power at 1940 nm by using high index polymer pump stripper, signal power of ~117 W was obtained. The slope efficiency is ~49% and optical to optical conversion efficiency is ~45%. The slope efficiency in this case is greater than the quantum efficiency limit of 40% of TDFL. This is attributed to the cross-relaxation process occurring in highly doped TDFL, which supports the conversion of one pump photon into two laser signal photons[3]. The enhancement factor in the power due to the cross-relaxation in our case is ~1.2. Maximum achievable pump power from the six diodes is 290 W, but pump power was limited to 260 W due to rise in temperature of the high index pump stripper above 100°C, which may cause burning and damage of the oscillator. There is a slight roll-off of the laser power at higher pump power due to temperature rise at the splice joints. So, a better thermal management is required to remove the roll-off of the signal power. Figure 2(b) shows the spectrum of TDFL at 1940 nm with FWHM linewidth of ~1 nm decided by the FBG mirrors.

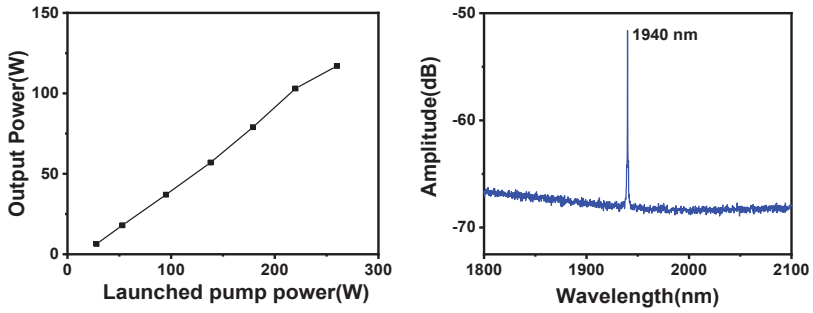

Figure 2: (a) Variation of output power vs input pump power, (b) spectrum of the laser output signal.

When 8 m length of Tm-doped fiber was selected to have efficient pump absorption of 16 dB (97.5%), repetitive damage of the gain fiber was observed. In order to analyze reasons for damage of the gain fiber, a photoreceiver was used to observe time dependent variation of laser output. Since TDF was pumped using CW diodes, a CW output signal was expected, but unexpectedly output contained irregular self-pulses. Figure 3(a) shows the observed self-pulsing behaviour with 8 m length of TDF used in the experimental configuration shown in Fig. 1 and Fig. 3(b) shows the expanded single pulse from train of random self-pulses of nano-second duration. These self-pulses of nanosecond duration raise the peak power density to reach the bulk damage threshold of silica fibers and in the presence of these self-pulses catastrophic damage of doped-fiber was observed repeatedly. Figure 3(c) shows the spectral behaviour of the signal generated from 8 m fiber. It can be seen that signal is generated at above 2000 nm rather than 1940 nm inspite of the fact that the FBG's used in the cavity are at 1940 nm. This result signifies that along the long length of the gain fiber, signal at 1940 nm is re-absorbed and higher wavelengths above 2000 nm are generated. Re-absorbrpion of signal at 1940 nm results in self-pulsing and lasing at longer wavelength region of TDFL. Similar phenomenon was also observed when 6 m length of TDF was selected. With 4 m length of TDF providing pump absorption of 10 dB (90%), no self-

pulsing was observed and CW lasing at the expected wavelength of 1940 nm was also observed at which FBGs were used in the laser set up. Thus, 4 m length of TDF was found to be optimum for lasing at 1940 nm.

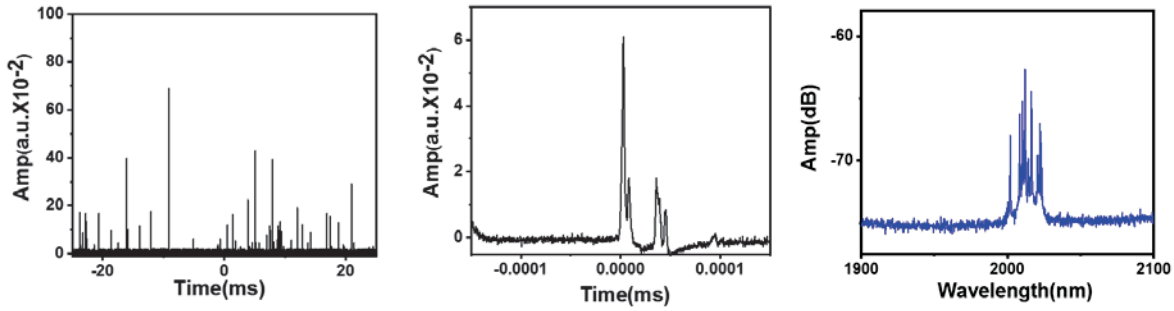

(a) **(b)** **(c)**

Figure 3: (a) Self-pulsing behaviour of 8 m length of TDF, (b) single self-pulse of nano-second duration, and (c) spectrum of output signal generated from 8 m length of TDFL.

Conclusion: In conclusion, a CW output power of ~117 W at eye-safe wavelength of ~1940 nm has been generated using an all-fiber oscillator configuration of Tm-doped fiber laser with a slope efficiency of ~49%. An investigation of self-pulsing behavior in all-fiber Tm-doped fiber laser has been performed using three different lengths of the gain fiber with different values of pump power absorption. Occurrence of random self-pulses with long length of Tm-doped fiber is due to higher re-absorption at the signal wavelength of 1940 nm. For signal generation at ~1940 nm, optimum length of TDF needs to be selected. This high power Tm-doped fiber laser at 1940 nm has potential application in medical field and plastic welding.

References:

1. S.D. Jackson, *Nature Photonics 6, 423 (2012).*
2. Z. Y. Hu, P. Yan, Q. Liu, E. C. Ji, Q. R. Xiao*, Appl. Phys. B 118,101(2015).*
3. T. Ehrenreich et al., *Proc. SPIE, vol. 7580, 758016(2010).*
4. Fried, N. M., *Lasers Surg. Med. 37, 53–58 (2005).*
5. Lei, C., *J. Remote Sens., 16, 192–206(2012).*
6. M. Meleshkevich et al., *2007 European Conference on Lasers and Electro-Optics and the International Quantum Electronics Conference, Munich, 1, (2007).*
7. A. Grzegorczyk et al., *Photonics Letters of Poland, Vol. 11, 81-83 (2019).*
8. Yulong Tang et al., *J. Opt. Soc. Am. B ,Vol. 27, No. 2(2010).*
9. Ashraf F. El-Sherif et al*., Optics Communications 208,381–389(2002).*

Studies on second harmonic ultraviolet generation at 255 nm from a low temperature (~500 ^{o}C) copper vapour laser with different optical resonators

R. Biswal*, O. Prakash[a] and S. K. Dixit[a]

Fiber Sensor and Optical Spectroscopy Section, Laser Group
Raja Ramanna Centre for Advanced Technology, Indore-452013
[a]Homi Bhaba National Institute, Anushakti Nagar, Mumbai-400094
**E-mail: rbiswal@rrcat.gov.in*

Abstract: This paper presents, for the first time, a study on the second harmonic ultraviolet (UV: $\lambda \approx 255.3$ nm) generation from a low temperature CVL with different optical resonators (plane-plane resonator and unstable resonators of magnifications 12.5, 50 & 100). With a type-I, critically phase matched β-BBO crystal as the harmonic generator and different pump average powers (≤ 10 W), the variation in UV average output powers and its conversion efficiencies were studied and found to vary from 0.3 to 2 W and 3 to 26% respectively for the different resonators employed. The experimental results were analysed in light of the beam quality attributes of the pump beams vis-à-vis limiting thermal and walk-off effects associated.

1. Introduction

High pulse repetition rate (~kHz), ns pulse-duration coherent ultraviolet (UV) radiations at $\lambda \sim 250$ nm find applications in manufacturing of photonic components, UV-photolithography, machining of semiconductors, glass/ceramics & polymers as well as photo-excitation studies of elements [1-4]. Among the limited choice available, the UV sources based on second harmonic of copper laser radiation ($\lambda \approx 510.6$ nm) are advantageous owing to its higher repetition rate and excellent spatio-temporal beam quality attributes as compared to that of excimer lasers and frequency quadrupled solid state lasers. Further, between the two temperature (~500 ^{o}C & ~1500 ^{o}C) variants of copper vapour laser (CVL), the low temperature variant has advantages of faster start-up (~4X), higher rep. rate (~20 kHz vs. ~5 kHz), higher efficiency (~2X) and superior beam quality characteristics which enhances its scope of applicability[1,2]. Till date, extensive studies on the second harmonic UV generation of conventional high temperature CVLs are well reported [1,2,5]. However, sufficient attention has not been paid on the second harmonic generation process of the low temperature variant CVLs, apart from a few reported studies [6-9]. Moreover, the UV generation process with different optical resonators of the low temperature CVL is missing in the literature. The conditions of the second harmonic UV generation with different optical resonator in the low temperature CVL are expected to be different from that of the conventional high temperature CVL owing to its relatively lower operating temperature, higher repetition rate and spatio-temporal laser gain characteristics.

In view of the above, this paper presents, for the first time, an experimental study on the second harmonic UV generation of the radiations from an in-house developed high repetition rate (~20 kHz) low temperature CVL (Cu-HBr laser) with different optical resonators [plane-plane resonator (PPR) and positive branch unstable resonators (PBURs) of magnifications (M) 12.5, 50 & 100)] in a type-I, critically phase matched β-BBO crystal. With the variation of pump average power limit of 10 W, variation of the UV average powers/conversion-efficiencies were from 0.3 to 2 W / 3 to 26% respectively. The experimental results were analysed in terms of the measured beam quality attributes of the pump beams as well as associated thermal & walk-off effects.

2. Experimental arrangement

Fig. 1 shows the schematic of the experimental arrangement for studying the second harmonic process of the in-house developed Cu-HBr laser for different resonators fitted with an intra-cavity cube polarizer (BSP).

For PPR (configuration A), the mirrors M_1 & M_2 were high reflecting plane mirror (R~99%) & fused silica blank (R~7%) respectively with overall cavity length (L_R) of 250 cm. For confocal PBURs (configuration B) of different magnifications [$M = |F_1/F_2|$, where F_1 (250 cm) & F_2 were focal lengths of mirrors M_1 (concave) & M_2 (convex) and were separated by a distance $L_R = F_1 - |F_2|$], the value of F_2 was changed to -20 cm, -5 cm & -2.5 cm corresponding to values of M as 12.5, 50 & 100 respectively.

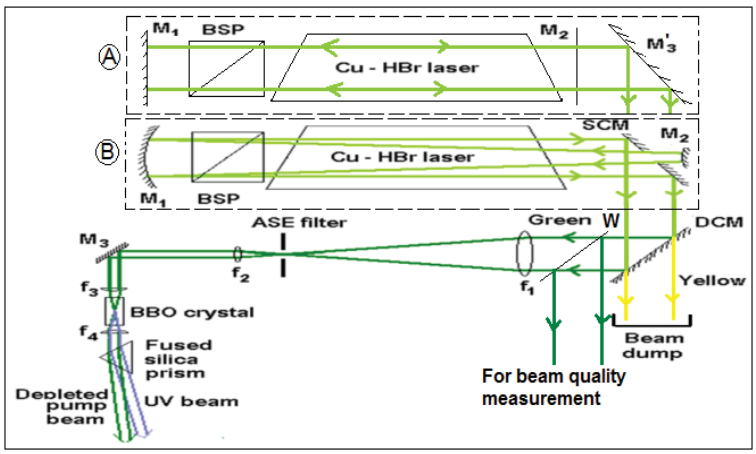

Fig.1 Schematic of the experimental set up for second harmonic UV generation from the low temperature CVL (Cu-HBr laser) fitted with different resonators (A) PPR and (B) PBURs

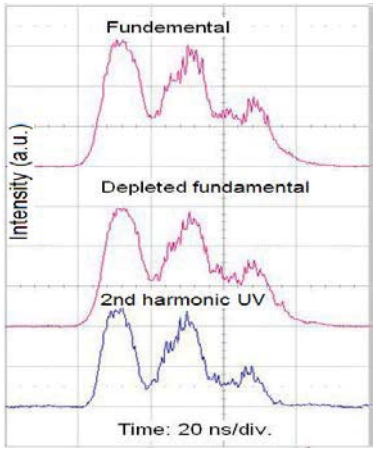

Fig. 2 Typical *temporal intensity profiles of the pump and second harmonic UV beams (PBUR M=50)*

The experiment was carried out sequentially for each resonator, where only the green (510.6 nm) component was selected by using a suitable high reflecting dichroic mirror (DCM) out of the total green & yellow. The selected beam was then compressed by 10 times to about 2.5 mm using a telescopic lens pair (f_1, f_2 = 100, 10 cm) and ASE was filtered out at the common focal plane with an aperture (diameter: ~1.5 mm for PPR & ~0.5 mm for PBURs). The ASE filtered, collimated beam was line focused, by a cylindrical lens (f_3) of focal length 4 cm, on a β-BBO crystal (6 x 4 x 10 mm^3, cut angle = 47^0) which was tilted suitably to match the type-I phase matching angle (~51^o) of the green beam. The crystal was mounted on 5-axis micro-positioner. The depleted green beam and generated UV beam were then collimated using a fused silica cylindrical lens (f_4 =10 cm), which were separated using a fused silica prism. Average UV power was monitored using a power meter (Gentech, TPM 300) while the wavelength of the radiations (fundamental green, depleted green & generated UV) as well as their temporal profiles were monitored using a three synchronized bi-planner photo diodes (Hamamatsu, R1193U-51) & a 500 MHz oscilloscope (Lecroy:Waverunner-6050A) respectively (Fig. 2). For each resonator used, the experiment was carried out with different pump beam powers (≤ 10 W, to prevent the crystal damage) which was varied using the beam splitter M_3 whereas the fundamental beam-quality attributes (divergence, pointing instability etc.) were monitored by sampling out the beam using an optical wedge (W) in similar manner as described elsewhere [ ].

3. Results and discussions

Figs. 3a and 3b show the variation of the UV average output power ($P_{2\omega}$) and UV conversion efficiency ($\eta_{2\omega}$) as a function of pump beam average power (P_{ω}) for PPR and PBURs of M= 12.5, 50 & 100. It is observed that both $P_{2\omega}$ and $\eta_{2\omega}$ increases with increase of P_{ω} for all the resonators. However, the degree of increase of $P_{2\omega}$ are from 30 mW to 300 mW & from 31 mW to 700 mW with corresponding variations in P_{ω} from 3 to 10 W and 1.9 to 9.2 W respectively. On the other hand, for PBURs of M = 50 & M=100, the variations in $P_{2\omega}$ are from 80 mW to 2.05 W & from 81 mW to 1.7 W with corresponding variations in P_{ω} from 1.6 W to 8.2 W & 1.4 W to 6.3 W respectively. Similarly, for PPR & PBUR M=12.5, $\eta_{2\omega}$ increases from 1% to 3% & 1.63% to 7.61% respectively, for corresponding increase in P_{ω}. However, for PBUR M = 50, as P_{ω} increases upto 6.6 W, $\eta_{2\omega}$ increases almost linearly upto 22% (1.43 W UV) and thereafter its slope slows down. At maximum used value of P_{ω} of 8.2 W, $\eta_{2\omega}$ is about 25%. On the other hand, for PBUR M = 100, the slope of the graph slows down at P_{ω} of about 4.6 W [1.01 W UV & $\eta_{2\omega}$ ~ 22%] though $\eta_{2\omega}$ is ~ 26% at the maximum UV power of 1.7 W.

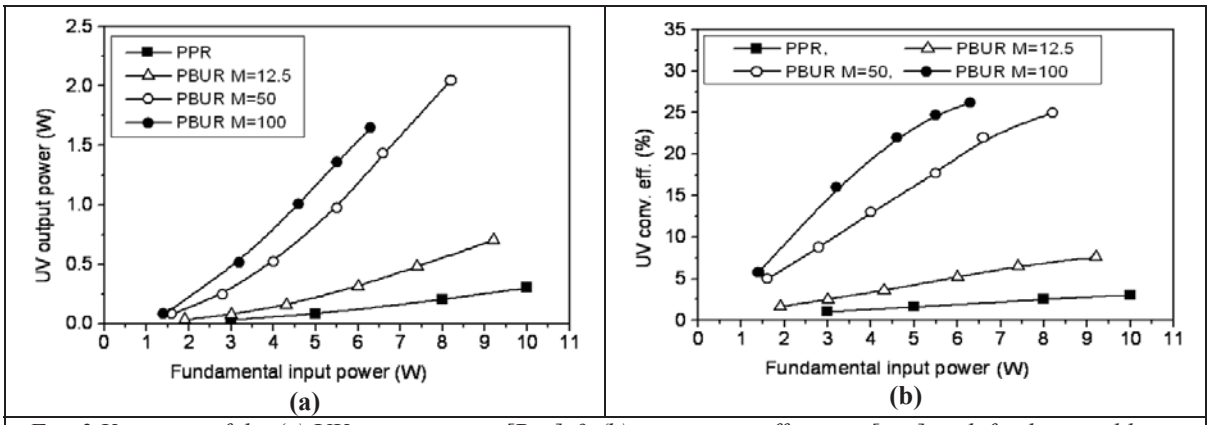

Fig. 3 Variation of the (a) UV output power [$P_{2\omega}$] & (b) conversion efficiency [$\eta_{2\omega}$] with fundamental beam input power [P_{ω}] for different resonators

Further, to characterize the second harmonic UV conversion processes on a uniform scale (independent of fundamental power/intensity), conversion coefficients $C_{2\omega} = \eta_{2\omega}/P_{\omega(p)}$, where $P_{\omega(p)}$ is the peak power of fundamental, were evaluated which act as figures of merit for deciding the efficacy of the UV conversion processes. Fig. 4 shows the variation of the conversion coefficient for different input powers and resonators used. It is noticed that $C_{2\omega}$ is almost constant with values of ~ 0.35 x 10^{-5} W^{-1} for M = 1, ~0.85 x 10^{-5} W^{-1} for M = 12.5. However, for PBUR M=50 & 100, it increases with P_{ω} and attains maximum value & then falls. For PBUR M=50, $C_{2\omega}$ is at maximum value of ~3 x 10^{-5} W^{-1} [P_{ω} = 6.6 W, $P_{2\omega}$ = 1.43 W] and then falls to ~2.74 x 10^{-5} W^{-1} at P_{ω}= 8.2 W [$P_{2\omega}$=2.05 W]. On the other hand, for PBUR M =100, the variation is quite high. With the increase of P_{ω} from 1.4 W, $C_{2\omega}$ increases from ~3.27 x 10^{-5} W^{-1}, attains maximum of ~3.96 x 10^{-5} W^{-1} at P_{ω} = 3.2 W [$P_{2\omega}$ = 512 mW] and then decreases monotonically to ~3.29 x 10^{-5} W^{-1} at P_{ω}= 6.3 W [$P_{2\omega}$= 1.65 W].

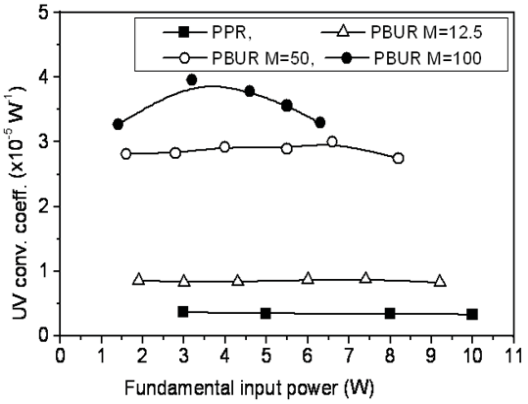

Fig. 4. Variation of the UV conversion coefficients with fundamental powers for PPR and PBURs

Table 1: Attributes of fundamental laser beam with different resonators used

Optical resonator	θ (μrad)	δ (μrad)	τ (ns)	P_ω (W)	$I_{\omega(p)}$ (MW/cm^2)
PPR (M≈1)	~1500	±30	~60	10	~0.62
PBUR M=12.5	~268	±25	~55	9.2	~3.47
PBUR M=50	~118	±19	~50	8.2	~7.72
PBUR M=100	~89	±15	~44	6.3	~8.94

The observed experimental trends can be understood as follows. For perfect phase matching conditions, $P_{2\omega} \propto [P_\omega \,.\, I_\omega] \propto (L^2 P_\omega^2)/(h.f.\theta)$ and $\eta_{2\omega} \propto I_\omega$ where L = interaction length of the crystal [$=\sqrt{L_a L_p} = \sqrt{aL_p/\rho}$], h = beam height at the focus (= 2.5 mm), f = focal length of the cylindrical focusing lens f_3 (= 4 cm), θ = divergence of the pump laser beam, a = laser spot size on the crystal [$=mf_3.\theta$, m is beam compression factor (=10)], ρ = walk-off angle of the crystal (=4.8°), L_a = aperture length of the crystal (≈ a/ρ) and L_p= physical length of the crystal [10]. For a given pump power, as the resonator M increases, θ as well as the spot size (width of spot) decreases (Table 1) and hence I_ω increases. This leads to increase in $P_{2\omega}$ and $\eta_{2\omega}$ as M is increased from 1 (PPR) to 50 (UR). For example, at typical constant pump power of 5 W, the pump spot width on the BBO crystal (=10 $f_3.\theta$) were estimated to be ~600 μm, ~107 μm , ~47 μm and the corresponding values of I_ω are ~0.31 MW/cm^2, ~1.9 MW/cm^2, ~4.7 MW/cm^2 for pump laser beam with resonator M=1, 12.5, 50 respectively. The increase in slope of $P_{2\omega}$ *vs.* P_ω *and* $\eta_{2\omega}$ *vs.* P_ω curves as M is increased from 1 to 50 is again due to the fact that $\partial P_{2\omega}/\partial\theta \propto 1/\theta^2$ and $\partial\eta_{2\omega}/\partial\theta \propto 1/\theta^2$. For M = 100, the pump beam width and intensity on the crystal are ~36 μm & ~7.1 MW/cm^2. It is clear that moving from M= 50 to 100, there is no major change in spot size at crystal due to almost diffraction limited divergence values (1-1.3 DL) in both the cases. Also, the spot sizes are very small (10s of microns) and the peak intensities are high. Hence, the second harmonic process is adversely affected due to increased beam walk-off, limited angular acceptance (~0.38 mrad-cm) and increased dephasing between fundamental and generated beams in the crystal. Hence the frequency conversion performance of M = 50 and 100 are very close. These arguments are evidenced by the fact that for PPR and PBUR M=12.5, $C_{2\omega}$ is almost constant within the pump power limit employed. However, for PBUR M=50 & M=100, reduction of $C_{2\omega}$ beyond certain UV/visible-pump power levels are in line with the thermal dephasing caused due to the absorption of radiations [11]. For the associated wavelengths in the present case for the BBO crystal employed, the corresponding critical powers are estimated to ~5.6 W & ~0.7 W respectively for the fundamental and the 255 nm UV beam [8].

4. Conclusions

In conclusion, an experimental study on the second harmonic UV generation from a high repetition rate (~20 kHz) low temperature CVL (Cu-HBr laser) was carried out with different optical resonators such as PPR and PBURs of M=12.5, 50 & 100 using β-BBO nonlinear crystal. With the variation of pump average power limit of 10 W, variation of the UV average powers/conversion-efficiencies were from 0.3 to 2 W / 3 to 26%

respectively. The experimental trends were explained in terms of the beam quality attributes of the pump beams as well as associated thermal dephasing & walk-off effects.

Acknowledgements: The authors acknowledge power supply support from CVL electronics laboratory of LPSD.

References

[1] C. E. Little *ed*., *Metal Vapour Lasers: Physics, Engineering and Applications* (Wiley, New York: 1999).
[2] C. E. Little and N. V. Sabotinov *eds*. *Pulsed Metal Vapour Lasers* (Kluwer Academic: 1996).
[3] R. Kashyap *ed., Fiber Bragg Gratings* (Academic Press, San Diego, CA: 1999).
[4] O. Prakash, J. Kumar, R. Mahakud, S. K. Dixit, S. V. Nakhe, *IEEE Phot. Tech. Lett.* **26(1)**, 93 (2014).
[5] O. Prakash, S. K. Dixit, R. Bhatnagar, *IEEE J. Quant. Electron.* 38, 603 (2002).
[6] A. A. Isaev, D. R. Jones, C. E. Little, G. G. Petrash & K. I. Zemskov, *Opt. Comm.* 132, 302 (1996).
[7] N. Huot, C. Jonin, N. Sanner, E. Baubeau, E. Audouard and P. Laporte, *Opt. Commun.* 211, 277 (2002).
[8] R. Biswal, P. K. Agrawal, S. K. Dixit, S. V. Nakhe, *Appl. Opt.* 54(32), 9613 (2015).
[9] R. Biswal, P. K. Agrawal, G. K. Mishra, O. Prakash, S. K. Dixit, S. V. Nakhe, *Proc. NLS-2015, CP.1.21*
[10] R. W. Boyd, *Nonlinear Optics* (3rd ed.), (Academic Press, San Diego, CA : 2009).
[11] M. Takahashi, A. Osada, A. Dergachev.. T. Shimizu and N. Sarukura, *Jpn. J. Appl. Phys.* **49**, 080211 (2010).

A Compact Intensity Auto-Correlator for ultra-short laser pulse width measurement

D. Daiya[a,b,*], R. K. Patidar[a], S. W. Amalraj[a], A. Moorti[a, b], M. P. Kamath[a], Sushil Kumar Sharma [a], N. S. Benerji [a] and K. S. Bindra[a,b]

[a]*Raja Ramanna Centre for Advanced Technology, Indore 452013, India*

[b]*Homi Bhabha National Institute, Training School Complex, Anushaktinagar, Mumbai 400094, India*

*Email: deepakd@rrcat.gov.in

Abstract: Design, development and characterization of a compact (palm size) and simple second order autocorrelator for measurement of ultra-short laser pulse width is presented. It consists of only three optical elements and can be directly mounted on a CCD camera (as c-mount camera lens) for recording single shot autocorrelation trace. The optical components and opto-mechanical design used in the autocorrelator are fabricated in-house. A graphical user interface has also been developed, which online monitor's the autocorrelation trace, calculates the pulse width, perform statistical analysis for multiple measurements and save the data. The device was successfully used for measurement of ~ 100 fs duration laser pulses.

1. Introduction

Femto-second class, ultra-short lasers are being operated routinely in many laboratories, industries, hospitals etc. owing to their distinct applications in various streams of science and technology [1-2]. Many methods have been invented for the complete spatio-temporal characterization of ultra-short laser pulses, e.g., Frequency Resolved Optical Gating (FROG) [3], Spectral Phase Interferometry for Direct Electric-filed Reconstruction (SPIDER) [4], interferometric autocorrelation [5] etc. However, temporal characterisation viz. measurement of full width at half maximum (FWHM) is required to be routinely monitored of such lasers for day to day performance, and therefore second order intensity autocorrelator is an important diagnostic. In this paper, we propose a compact and simple design of a second order autocorrelator consisting of only three optical elements, which can be directly mounted on a CCD camera for recording single shot autocorrelation trace. A graphical user interface has also been developed and used for online acquisition, calculations, and saving the measurement data on laser pulse duration.

2. Opto-mechanical design and GUI

The basic optical layout of the developed autocorrelator is similar to GRENOUILLE, a FROG variant. However, the requirement of thick crystal, cylindrical lenses could be omitted for only autocorrelation measurements. As shown in the Figure 1, it consists of three optical elements: a bi-prism, a second harmonic generating (SHG) crystal and an optical filter. The bi-prism splits the laser beam into two halves with some angle between them (in xz-plane), which depends on the base angle of the bi-prism. The SHG crystal is placed at a location where these two angled beams overlaps to generate time correlated SHG signal along x-axis (delay axis) and hence mimicking as a single shot autocorrelator. A pictorial representation of a typical autocorrelation trace recorded for an ultra-short laser pulse is also shown on the screen (detector) which could be CCD camera.

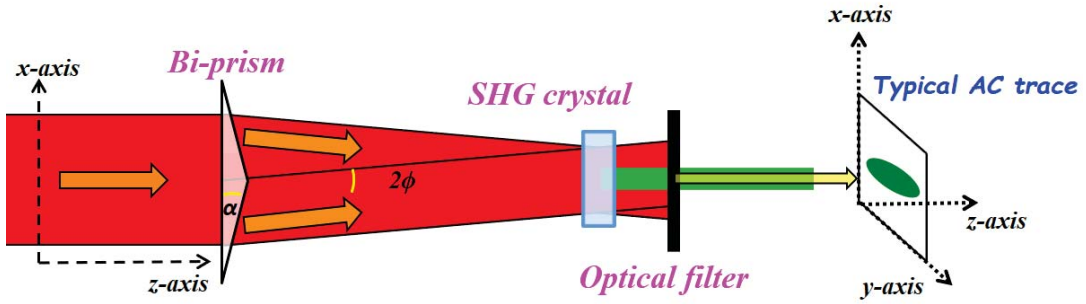

Figure 1: Optical layout of the autocorrelator and pictorial representation of a typical autocorrelation trace

The FWHM laser pulse width (τ_p) can be estimated by multiplying calibration factor ($\tau_{calibration}$) and FWHM width of the recorded trace along x-axis (Δx). The calibration factor is given by $ksin\phi/c$, where, k is a constant depending upon the shape of the laser pulse (1.414 for Gaussian pulse and 1.31 for $sech^2$ pulse), c is the speed of light and ϕ is the half angle between the two beamlets. The half angle ϕ between the beamlets is related to bi-prism's base angle (α) and refractive index (n) as- $\phi = (n-1)\alpha$, hence, the calibration factor of the device can be altered by replacing the bi-prism with different base angle. In this way, the pulse width is estimated by recording the autocorrelation trace using a camera and measuring its width.

All the three optical elements are mounted using three different circular aluminium housing, having threads for locking and inter element coupling. Two different views (3D and top) of complete mechanical assembly with optical arrangement are shown in the Figure 2. The complete structure is in the form of a cylindrical tube, having clear circular aperture of 20 mm and total length about 60 mm. A provision is also made in the assembly to adjust distance between the bi-prism and the SHG crystal to maintain the beam overlap position inside the crystal, which otherwise shifts due to replacement of the bi-prism with different angle. This tube can be mounted onto a CCD camera (as a c-mount camera lens), serving as standalone device with size of a mini camera to capture and estimate pulse width of ultra-short laser pulses.

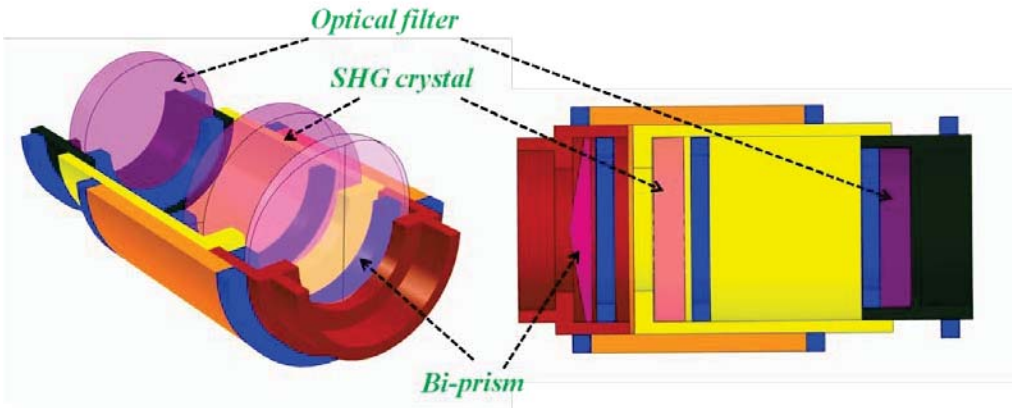

Figure 2: 3D view and Top view of autocorrelator *with complete mechanical assembly with optical arrangement*

Two bi-prisms of diameter 30 mm were fabricated at Optical Design & Development Laboratory of RRCAT, with base angles 10^o and 6^o, resulting into calibration factor of 0.38 fs/μm and 0.23 fs/μm respectively. A 30 mm diameter and 5 mm thick KDP crystal, grown at Crystal Growth Laboratory, RRCAT and cut for SHG phase matching at 1054 nm wavelength, was used. To block the unconverted fundamental signal at 1054 nm, a KG-5 optical filter was used. Photographs of the autocorrelator developed are shown in the Figure 3.

Figure 3: Photographs of the autocorrelator developed in the laboratory

To capture the autocorrelation trace, a CCD camera (Make: Imaging Source, Model: DMK 41BU02) was used. A graphical user interface (GUI) is also developed to capture the camera image and online processing to estimate laser pulse width. Screen shot of the developed GUI is shown in the Figure 4. The captured trace is first filtered using a Gaussian filter; thereafter lineout along horizontal direction (averaged along vertical direction) is taken to estimate laser pulse width using the calibration factor. The calculated value, measured using each captured image, is then plot against the shot number. The statistics of the pulse measurement is also displayed in the GUI, showing minimum value, maximum value and average value of the pulse width measurement along with standard deviation. There is also provision to save the recorded image for offline measurements.

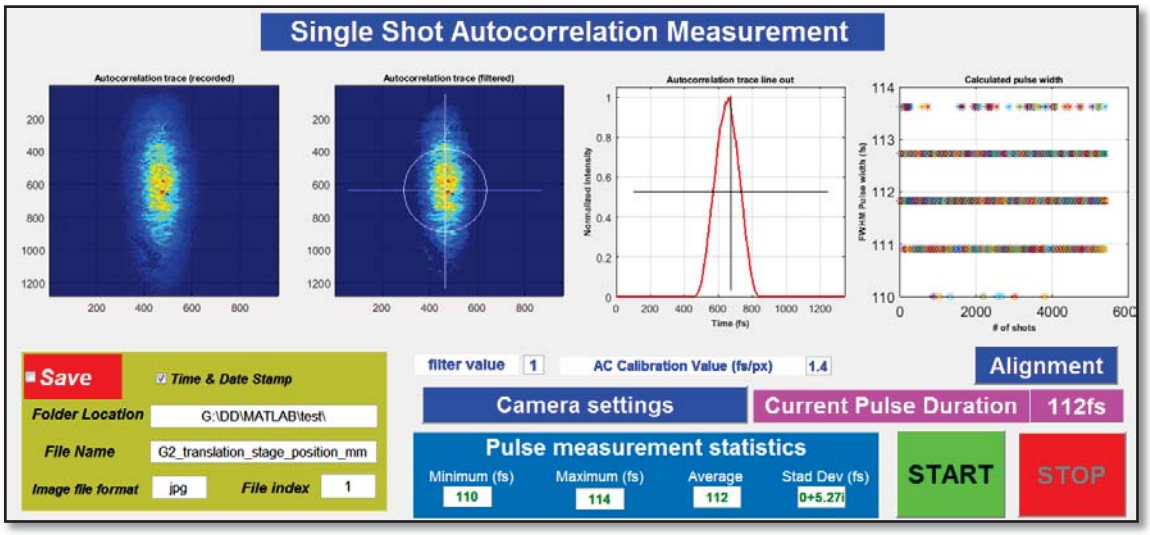

Figure 4: Screenshot of the graphical user interface developed to capture and analysis single shot autocorrelation trace for ultra-short laser pulse width estimation.

The developed autocorrelator can measure pulse duration in the range of 50 fs to 1000 fs for laser wavelengths in the range of 900 nm to 1100 nm. The device was used for measurement of laser pulse from a mode locked fs

laser source (Make: Coherent, Model: Chameleon Ultra II) delivering ~100 fs laser pulses at 80 MHz repetition rate.

A few initial measurements with the developed device matches with the values measured with the other autocorrelator developed in the laboratory.

3. Conclusion

In conclusion, a miniaturized second order autocorrelator has been designed and developed for the estimation of pulse width of ultra-short laser pulses. The autocorrelator is consists of only three optical elements and it is of palm's size. The bi-prism and SHG crystal used in the autocorrelator, and opto-mechanical housing are developed and fabricated in-house. A GUI is also developed for capturing and online estimating the pulse width. Finally, it is used for measurement of ~ 100 fs duration laser pulses.

References

1. "Ultrashort Laser Pulse phenomena", J. C. Diels, W. Rudolf, Academic Press (2006).
2. "Opportunities in intense ultrafast: Reaching for the Brightest Light", The National Academic Press, ISBN 978-0-309-46769-8, DOI 10.17226/24939.
3. P. O'Shea, M. Kimmel, X. Gu, and R. Trebino, *Opt. Lett.* **26**, 932 (2001).
4. M. E. Anderson, A. Monmayrant, S. P. Gorza, P. Wasylczyk, and I.A. Walmsley*, Laser Phys. Lett.* **5(4),** 259 (2008).
5. S. Toenger, R. Mäkitalo, J. Ahvenjärvi, P. Ryczkowski, M. Närhi, J. Dudley, and G. Genty, *J. Opt. Soc. Am. B* **36**, 1320 (2019).

Development of 1.5 kW average power and 30 kW peak power long pulse Nd: YAG laser

Sunil Kumar Sharma[1*], M. K. Bairwa[1], V. Bhardwaj[1], Bhaskar Paul[1], Rajpal Singh[1], Vijay Bhawsar[2], A. A. Raju[2], D. Narwat[2], R. K. Jain[1], Pawan Kumar[1], S. K. Sah[2], Sudheer Kushwaha[2], P. Shryner[2], J. Khanwalkar[2], R. Arya[2], B. N. Upadhyaya[1], K. S. Bindra[1]

[1]*Laser Technology Division, Raja Ramanna Centre for Advanced Technology, Indore-452013, INDIA*

[2]*Laser Electronics Division, Raja Ramanna Centre for Advanced Technology, Indore-452013, INDIA*

[*]*E-mail: sksharma@rrcat.gov.in*

Abstract: Development of 1.5 kW average power and 30 kW peak power long pulse Nd:YAG laser using three ceramic reflector based double lamp pump chambers in a single resonator has been carried. Laser pulse duration can be varied in the range of 4-40 ms and pulse repetition rate in the range of 1-100 Hz. An electrical to laser conversion efficiency of 5% has been achieved. Design of laser resonator has been optimized to achieve a beam quality factor M^2~69, which is good enough for beam delivery through 400 μm core diameter, 0.22 numerical aperture (NA) optical fibers for laser cutting and welding of thick stainless steel plates remotely.

Introduction: High average power and high peak power long pulse Nd:YAG lasers are useful in large depth cutting and welding of metals and alloys with minimum heat affected zone, shrinkage and distortion. As the output power from a single rod is limited due to thermal its fracture limit, multi-rod and oscillator-amplifier configurations are normally used for power scaling. In the case of oscillator-amplifier system, mode matching telescopes and spatial filters are required in laser set up, which results in a complicated structure and efficiency is also poor[1]. As compared to oscillator-amplifier system, multi-rod resonator design is simple and more efficient. In the case of multi-rod resonator, number of rods are kept in a single resonator in rod imaging configuration, thus, the length of resonator becomes very long and precise alignment of Nd:YAG rods is necessarily required to achieve safe and stable operation. Further, discrete unstable regions may also exist in the resonator, if the resonator is not optimally designed. Discrete unstable regions results in a sudden drop in output power in a particular range of input pump power. Thus, it is important to select rods and pump chamber to have similar thermal lensing from all the rods used in the resonator. Driedger et. al.[2] and Kumkar et. al.[3] have have analysed muti-rod resonator configuration in detail. Jiang et. al. have reported development of 2026 W of average output power with an electro-optical conversion efficiency of 3.49%[4]. In most of the reports on high average power long pulse lamp pumped Nd:YAG lasers, a maximum electrical to laser conversion efficiency in the range of 3-4% and pulse energy below 100 J is reported. In this work, we have generated 1.5 kW average output power with 5% electrical to laser conversion efficiency and a maximum pulse energy of 680 J at 40 ms pulse duration, which is on higher side for similar systems reported in literature.

Experimental Set-up

Figure 1 shows schematic arrangement of three rod resonator. The laser consists of three pump chambers (PC1, PC2 and PC3). Each to couple the Flash lamp beam to the Nd:YAG rod in L-shape resonator. All the three pump chambers have the same geometry and each pump chamber consists of an Nd:YAG rod of 8 mm diameter, 160 mm length, [111] orientation, and 1.1 at.% Nd^{3+}-doping concentration. The cylindrical Nd:YAG rod surfaces have a fine ground barrel finish to minimize the optical loss caused by the gallery modes

that occur within the round crystal surface. One rod and two Kr-filled flashlamps have been placed in a close coupled yellow glazed diffuse ceramic reflector. Flashlamps have a bore diameter of 8 mm and arc length of 136 mm. A maximum of 10 kW average power is pumped in each pump chamber and 5 kW in each flashlamp. The diffusive ceramic reflector distributes the pump beam uniformly through the crystal rod to have uniform pumping. Lamp and rod are separated by 10% samarium doped glass filter plates, so that unwanted UV radiation from flashlamp is absorbed by samarium filter, which then emits in the pump band of Nd:YAG rod and results in lower thermal load and enhancement in optical conversion efficiency. Six number of 5 kW power supplies have been used to separately trigger and pump the six flashlamps. However, a single power supply controller has been used to operate all the six power supplies in synchronization to simultaneously pump all the rods in the resonator. Identical water cooling units operating at 22°C have been used for all the three pump chambers to achieve similar thermal lensing for each rod.

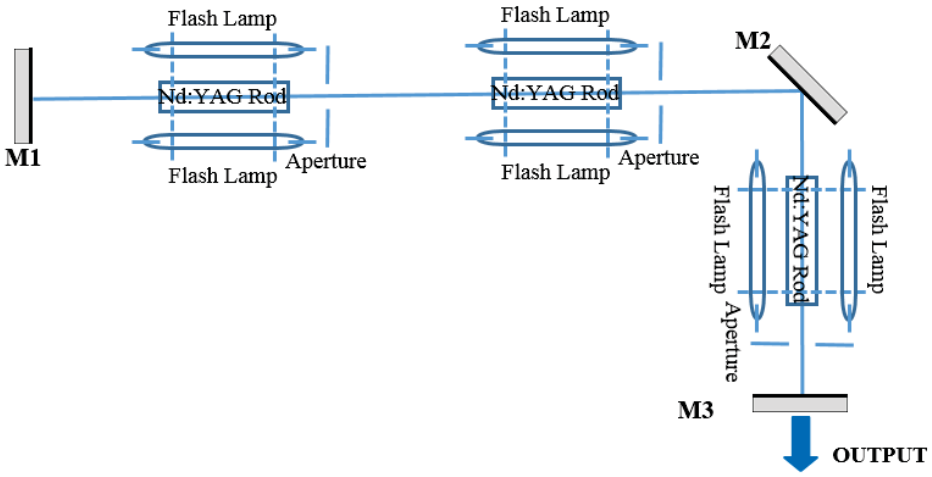

Fig. 1: Schematic of the experimental setup.

Three apertures of 7 mm diameter have been placed close to the outer faces of the pump chamber rods to avoid their damage from the back reflected beam at a narrow angle. A plane-plane L-shape laser resonator has been designed in rod imaging configuration with d:2d:2d:d separation of principal planes of the rod. The rear mirror M1 is plane with high reflection coating at the fundamental wavelength of 1064 nm (R>99.7%) and mirror M2 is also a plane mirror with high reflection coating at the fundamental wavelength at 45° angle to reflect the fundamental wavelength beam. The output coupler mirror M3 is a plane mirror with 20% reflectivity at the fundamental wavelength to couple out the infrared beam. L-shaped resonator design was selected to accommodate laser resonator on optical table of 1.5 m length. The total physical length of the resonator was optimized to 210 cm with 35 cm : 70 cm : 70 cm : 35 cm rod imaging distances from rear mirror to PC1, PC1 to PC2, PC2 to PC3 and PC3 to output coupler mirror distances. Laser output characteristics were studied for different values of *d* in the range of 20 cm to 40 cm. However, a distance of 35 cm was found to be optimum to achieve good beam quality and efficient operation over the whole range of average input pump power from 0-30 kW. Figure 2 shows a table-top view of 1.5 kW average power Nd:YAG laser.

Figure 3 shows variation of average laser output power at 1064 nm as a function of average electrical input pump power. With three rod resonator, a maximum average output power of 1510 W was achieved with

maximum pulse energy of 680 J at 40 ms pulse duration, leading to a peak power of 17 kW. However, at lower pulse duration of 4 ms, a maximum pulse energy of 121 J was achieved leading to a peak power of ~30 kW.

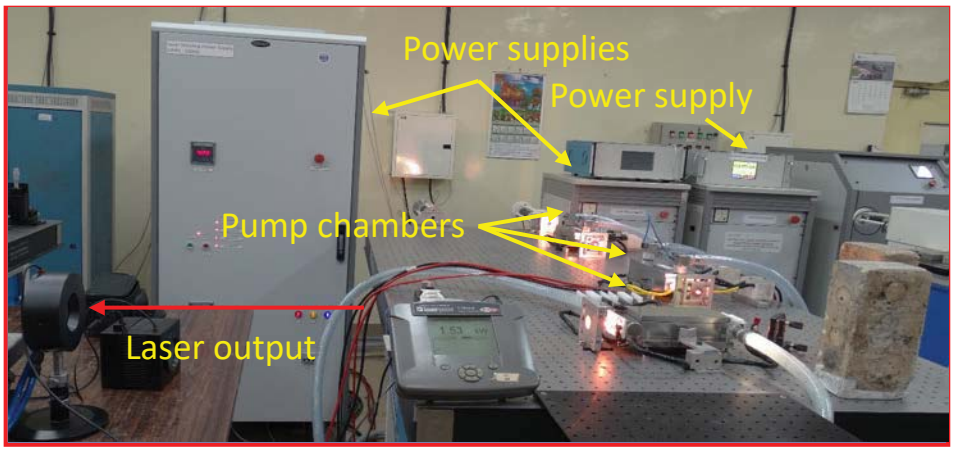

Fig. 2: Table-top view of 1.5 kW average power ms pulse Nd:YAG laser.

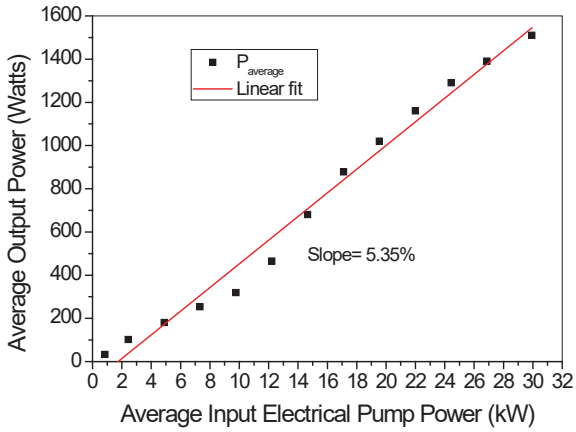

Fig. 3: Variation of average output power with average electrical input pump power.

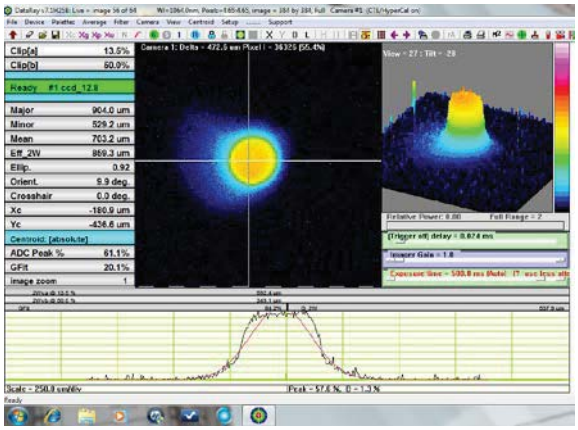

Fig. 4: 2D and 3D spatial beam profile of 1.5 kW average power Nd:YAG laser.

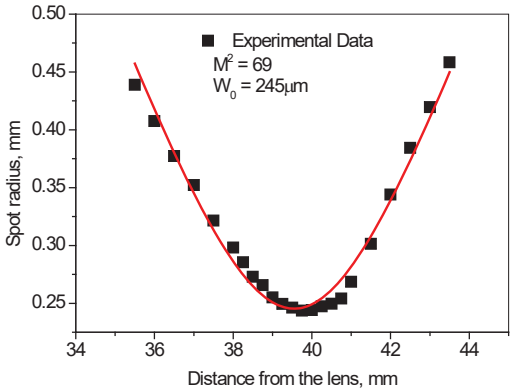

Fig. 5: Plot for M^2 measurement.

Figure 4 shows 2D and 3D spatial profiles of laser output beam, which shows that there is uniform flat top intensity over the beam cross-section. Beam quality was measured using a Wincam beam profiler by measuring beam diameter at different points away and before the focus position of the lens. Figure 5 shows plot and fit for M^2 measurement with a measured value of $M^2 \sim 69$. Experiments for beam delivery through optical fiber for remote material processing applications is underway.

Conclusion: In conclusion, we have designed and developed a high efficient long pulse Nd:YAG laser with maximum average output power of 1510 W and maximum pulse energy of 680 J at 40 ms pulse duration. An electrical to laser conversion efficiency of 5.35% has been achieved. Laser output power varies linearly with the input pump power for the whole range of pump power from 0-30 kW. Measured value of M^2 was found to be 69, which is good enough for beam delivery through 400 μm and 0.22 NA optical fiber. This laser will be useful in large depth cutting and deep penetration welding applications.

References:

1. R. J. St. Pierre et al., IEEE J. Quantum Electorn. **3**, 64-70(1997).
2. Jiang et. al., Proceedings of SPIE Vol. 8312, 83120B (2011).
3. Driedger K. P. et al., IEEE Journal of Quantum Electronics, **24**(4):665-673(1988).
4. Kumkar M et al., Optics and Laser Technology, **24**(2): 67-72(1992).

$^{98/100}$Mo Enrichment by Infrared Multi-photon Dissociation of MoF_6

M. B. Sai Prasad, A. Ghosh, R. C. Das[1], T. Dwivedi, G. Chakraborty, D. J. Biswas[2], J. P. Nilaya*[1]
Laser and Plasma Technology Division,
[1] Homi Bhabha National Institute, BARC, Mumbai-85.
[2] Former RRF, L & PTD
Bhabha Atomic Research Centre, Mumbai-400085
*Email: jpnilaya@barc.gov.in

Abstract

The importance of $^{98/100}$Mo in producing ^{99m}Tc, a radio tracer that is in ever increasing demand, is very well known. We present here our results of experiments carried out to enrich $^{98/100}$Mo by the process of multi-photon dissociation of MoF_6 under cooled conditions (-58°C). Selective excitation of the combination mode ($\nu_3+\nu_5$) lying in the 1050 cm^{-1} region and accessible by the 9 μm band emission lines of a CO_2 laser yielded a maximum enrichment factor of ~1.12 for the case of ^{100}Mo when irradiated with the 9P(10) line that is near-resonant to $^{92}MoF_6$. Efforts to increase the same by increasing the coupled energy into the medium are being explored.

Introduction

The radio-isotope currently in utmost demand for medical imaging is ^{99m}Tc that is obtained through the β decay of ^{99}Mo which itself can be a fission product or formed through neutron capture by ^{98}Mo in a reactor. ^{99m}Tc can also be produced by photoneutron reaction (γ, n) or proton beam induced reaction in an accelerator (p,2n) from ^{100}Mo. Enriching any of these isotopes of Molybdenum is thus of great value in this connection. Molybdenum has seven stable isotopes ranging from 92 to 100 amu in mass, and 9% to 24% in natural abundance (Table 1). In case of MoF_6 molecule, its each vibrational band consists, therefore, of seven overlapping isotopic bands that may differ appreciably in frequency. Out of the six fundamental vibrational modes of MoF_6[1], the ν_3 IR active vibrational mode lies in the mid IR region (741 cm^{-1}) and hence molecular laser isotope separation based on selective excitation of this vibrational mode and separation through IR multi-photon dissociation (MPD) process has been attempted in the past wherein the coherent sources employed have been para-H_2 Raman laser[2] and FEL[3]. The combination mode ($\nu_3+\nu_5$) lying in the 1050 cm^{-1} region is accessible by the 9 μm band emission lines of a CO_2 laser and the same has also been exploited for enrichment studies with a slightly better outcome[4]. The low absorption cross-section of the combination mode is offset by the significantly high energy

Isotope	Natural Abundance (%)
^{92}Mo	14.65
^{93}Mo	Synthetic
^{94}Mo	9.19
^{95}Mo	15.87
^{96}Mo	16.67
^{97}Mo	9.58
^{98}Mo	24.20
^{99}Mo	Synthetic
^{100}Mo	9.74

Table 1. Isotopes of Mo and their natural abundances.

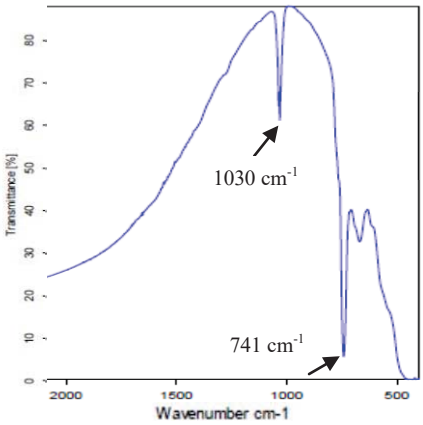

Figure 1. FTIR spectrum of natural MoF_6.

achievable by a CO_2 laser. To be noted that at room temperature, only ~1% population resides in the ground state and is thus available for selective laser excitation. The heavily populated higher energy levels cause hindrance as non-selective excitation from these levels results in scrambling of selectivity. The isotope shifts are small between successive mass numbers (~1 cm^{-1}) which is further obscured by the spectral interference due to hot bands and therefore, laser-based excitation, be it para-H_2 Raman laser[3] or CO_2 laser[4] is not very selective but nevertheless, alters the isotopic ratios of all the isotopes in a rather predictable manner. While the lighter isotopes were enriched and heavier ones depleted in the un-dissociated MoF_6 in reference 3, the effect of laser emitting on various transitions on the resulting enrichment was investigated in reference 4 yielding similar result. In this communication we present the results of our experiments of IRMPD of MoF_6 by targeting the combination mode ($\nu_3+\nu_5$) utilising the emission of a CO_2 laser with the experiments having been carried out both at room temperature and under cooled conditions (-58°C). This study clearly reveals an improvement in the selectivity, and, in turn, in the separation factor under cooled conditions.

The Sample

FTIR spectrum of natural MoF_6 sourced from RMP, Mysuru established the presence of MoF_6 in the form of an intense peak at 741 cm^{-1} corresponding to the ν_3 fundamental vibrational mode, although presence of an impurity too at 1030 cm^{-1} was seen and identified as silicon tetra fluoride (SiF_4) (Figure 1). Since this absorption is far removed from that of the combination mode of ($\nu_3+\nu_5$) lying in the region of 1050 cm^{-1}, no attempt was made to purify the sample. The isotopic ratio in the sample prior to irradiation was measured by Thermal Ionisation Mass Spectrometer (TIMS) and found to match with the natural isotopic abundance of MoF_6. Due to its highly corrosive nature (due to the formation of HF vigorously in presence of moisture) and strong surface adsorption, containment of MoF_6 proved to be very challenging. A Monel cylindrical reaction cell (1inch diameter, 10 cm long) was fabricated (Figure 2), vacuum sealed at the two ends by ZnSe AR coated windows and passivated for use with MoF_6. Usage of special Perfluoro elastomer o-rings for sealing ensured the leak rate to be better than 10^{-9} mbar-lit/sec, repeated baking, degassing, and passivating with F_2-He mixture followed by recurrent exposure to MoF_6 brought down the rate of loss of MoF_6 to within acceptable limits.

Experiments and Results

A 100 Hz, line tunable TEA CO_2 laser (Impact 300 Light Machinery, Canada), capable of delivering up to ~2 J/pulse on the required line of the 9 µm band with a ~200 ns gain switched spike followed by a tail was made use of as the coherent source for selective excitation. The initial IRMPD experiments were carried out at ambient temperatures. The vapour pressure of MoF_6 at room temperature being ~600

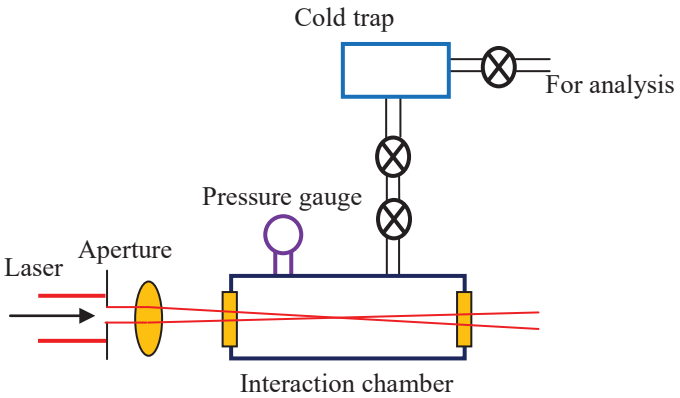

Figure 3. Schematic diagram of the experimental set-up.

mbar, at typical operating partial pressure of few mbar MoF_6 for IRMPD experiments, the working medium is thus essentially gaseous. The reaction cell was first evacuated to rotary vacuum and by appropriate opening of the valves, filled with MoF_6 at the required pressure from the feed cell. The entire assembly was found to have a leak rate better than 5×10^{-9} mbar-lit/sec.

In the first set of experiments at room temperature, the emission of the laser was tuned to the required transition and focussed by a 20 cm focal length lens right at the centre of the IRMPD cell filled with MoF_6 at ~1-2 mbar pressure (Figure 3). While the laser is capable of delivering energy in excess of 2 J, an aperture had to be used to keep the energy of the coupled beam within 800 mJ in order to prevent optical damage of the anti reflection coating of the ZnSe windows of the cell. Several experiments were carried out by varying the lasing transition. The absorption band centre of ($\nu_3+\nu_5$) combination band spreads over 1045cm[1] to 1055cm^{-1} (~P(22) to P(10) of the 9 micron band of CO2 laser emission spectrum)[4]. Thus the operation of the laser on 9P(10) causes selective excitation and dissociation of lighter isotopic molecular species leading to an enrichment of heavier ones in the un-dissociated product. At the end of each experiment, the un-dissociated MoF_6 was collected in a leak-tight test tube using a liq. N_2 cryo-trap, treated with 1N HCl solution and analysed with TIMS for any alteration in the isotopic ratio. A very slight change in the $^{100/98}$Mo concentration was observed in this case in our experiments as the coupled energy here was much lower, about 1/4th of what was used in reference 4.

In the next set of experiments, the MPD cell was immersed in dry ice-ethanol slurry and by varying the quantity of dry ice, the cell could be maintained at -58°C where the vapour pressure of MoF_6 was estimated to be ~1.4 torr[5]. At this temperature, the ground state population rises to ~18%. The experiments were

Laser line	Energy/ pulse	Temp of MPD cell	Total no of exposures	Isotopic % of ^{98}Mo			Isotopic % of ^{100}Mo		
				Natural	Post exposure	% change	Natural	Post exposure	% change
9P(10)	~800 mJ	-58°C	816000	24.198	25.017	3.4	9.669	10.331	6.8

Table 2: Experimental conditions and changes in the concentration of ^{100}Mo and ^{98}Mo on irradiation with 9P(10) line.

once again repeated under similar conditions with the laser being tuned, as before, to the 9P(10) transition. An increase of nearly 6.8% in the concentration of ^{100}Mo and ~ 3.4% in that of ^{98}Mo was observed amounting to a separation factor (defined as $\beta = (R_m/R_m^o)_{irrd} / (R_m/R_m^o)_{natural}$ where R_m = Isotope X/Isotope 92) of 1.12 and 1.09 respectively. The experimental conditions and the results are summarised in Table 2 and the variation in the concentration of all the isotopes in the product are as shown in Figure 4. We note here that although such cooling was also attempted in reference 3 where the excitation source was a CO_2 laser pumped para-H_2 Raman laser operating at 728 cm^{-1}, not much advantage with respect to enrichment factor is reported. Needless to say, employing a CO_2 laser is far more advantageous and

convenient. It is very well known that IRMPD is intensity driven process requiring a single isotopic species to absorb several tens of photons to reach the dissociation limit for separation. Effective coupling of laser energy in conjunction with an increased ground state population is the key to enhance the efficiency of enrichment. We were unable to couple higher energy into the MPD cell due to the damage of the anti reflection coated window at the entry port. Usage of uncoated optics (Brewster windows/salt windows) in place of coated optics is being tried to improve energy coupling and the results of the same shall be presented in the conference.

Acknowledgements

The authors gratefully acknowledge the colleagues of ChTG for providing the sample and the support with regard to handling of MoF_6, FCD for the analysis, and the able technical assistance of L. D. Kanthe throughout the work. The authors also thankfully acknowledge the constant support of Head, L&PTD and AD, BTDG.

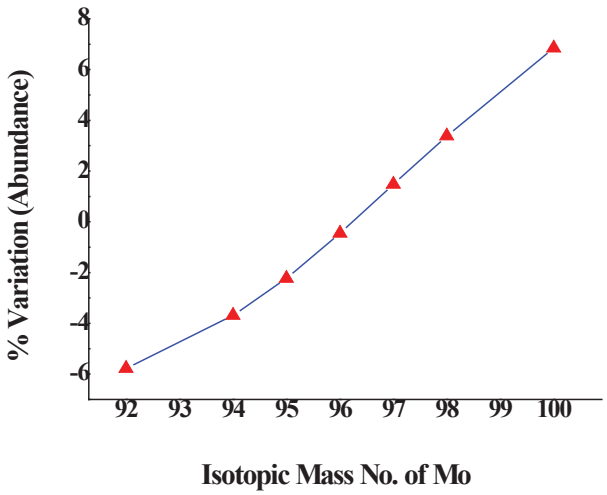

Figure 4. Percentage change in the concentration of the isotopes of Mo post irradiation.

References

1. C. F. Weaver and H. A. Freidman, Oakridge National Laboratory, US Atomic Energy Commission, October (1967).
2. T. Oyama et al, *Laser Chem*. **8**, 235 (1988).
3. T. Noda et al, *Journ. Nuclear Materials* **715,** 307-15 (2002).
4. S. M. Freund and J. L. Lyman, *Chem. Phys. Lett.* **55**, 435 (1978)
5. George H. Cady, Goerge B. Hargreaves, *Journ. Chem. Soc.* https://doi.org/10.1039/JR9610001563, 1563-68 (1961).

Simulation of transient photo plasma and ion collection dynamics using two-dimensional Particle-in-cell (PIC) methods for Laser Isotope Separation of Ytterbium

G.Sridhar, B.Jana, S.Baruah, S.Kundu, S.Sethi

ATLA-F, Beam Technology Development Group,
Bhabha Atomic Research Centre, Mumbai - 400 085
Email: gsridhar@barc.gov.in

Abstract: In this paper, the study of laser produced transient photo plasma behaviour to the static electric field and their effect on the ion collection dynamics for the novel collection geometry with four electrode configurations namely Plate -Grid- Grid - Plate (PGGP) using 2D Particle-in Cell (PIC) code is presented. Trajectory of electrons and ions in the presence of boundaries and the electrodes was simulated. Suitable animations were generated for visualisation from the phase space of ions and electrons. The effect of plasma densities, the geometry, applied electric field and the location of plasmas on the ion collection dynamics on both cathode and anode were estimated. The distribution function of the ions reaching electrodes with position, energy and their angular spectrum were evaluated. The ions collection efficiency on cathode and anode were estimated and compared with the experimental results of recently conducted laser-based separation experiments of Ytterbium-176 for medical applications.

Introduction

The plasma generated in Laser Isotope Separation (LIS) process is of special category as they are produced by nanosecond laser pulses generating plasma densities varying from 10^6 to 10^{10} per cc. Plasma decays to the boundaries and the electrodes with a life time varying from few microseconds to 100 microseconds depending on plasma densities and geometries [1]. In LIS process the ions are extracted from the photo plasma by electro static methods using parallel plate extraction configuration or their variants. The fields applied were varying from 150 V/cm to 750 V/cm between the plates. Plasma simulation is a very useful tool for understanding laser produced plasma experiments as it can generate data and insight of the process which is otherwise impossible or difficult to obtain experimentally and also save number of experiments if it properly addressed in the modelling. Generally, plasma simulations are based on fluid based and "superparticle" based models. Characteristic time and length scales for plasma are given by plasma frequency and Debye shielding length which depends on the plasma density and electron temperature. With present moderate computing facility, we can handle 10^4 to 10^8particles which has heavier mass and high value of charge but the charge to mass ratio remains same as individual plasma particles. Hence the force and acceleration experienced in an electromagnetic environment imitates closely to individual particle [2-4]. In this paper, we have studied plasma collection dynamics of Ytterbium photo plasma using particle-basedsimulation.

Description of the simulation

Recently laser-based separation of isotopes, having application in medical (Therapeutic and Diagnostic) and industrial application have attracted lot of interest such as Yb-176, Yb-168, Lu-177, Sm-153 and other isotopes. In this paper, laser produced Yb-176 is considered. Yb-176 is selectively excited and ionised by narrow band

three colour resonant photo ionisation mechanism through auto ionisation energy levels. The additional energy of three photons above ionisation energy is carried totally by electrons due to their low mass and constitutes the electron temperature for the generated plasma. The efficiency of LIS process is highly determined by the ion collection methods without self-sputtering.

Plasma dynamics was studied using well established XOOPIC (X-windows based object-oriented Particle-In-Cell) open source code developed by The Plasma Theory and Simulation Group, developed at University of California, Berkley [5]. XOOPIC is a 2 D code in both Cartesian and cylindrical geometrical options with three velocities and two spatial coordinates and widely used till now. This code has both electrostatic and electromagnetic models along with Monte Carlo collisional models. Extending this work to full three-dimensional BARC developed 3D PIC code of Pasupat [6] is being carried out. The incremental time step shall be of the value of 0.2 / plasma frequency so that convergence is guaranteed and the particle does not move out of the particular mesh in single time step.

In this paper, recently proposed ion collection geometry is considered for simulation[7]. Instead of simple plate plate ion collection, four electrodes were proposed to take advantage of minimum voltage required to extract ions using closely spaced grids to the plasma and also to reduce the energy of ions reaching cathode using retarding electric field to ensure minimal sputtering. Ion collection model in Plate-Grid-Grid-Plate (PGGP) configuration in XOOPIC 2D open source code was made. Parametric studies of ion collection model with two plasma densities of YB (8e9 & 4.4e9 per cc) and the effect of spatial meshing on the ion collection along the height of the cathode is carried out. Plasma density of 4.4e9 per cc was estimated from the depletion in the abundance of Yb-176 on the tail. Plasma is located symmetric to the cathode and anode grid and the cathode and anode plates. The separation between the grid is 50 mm and among the plates 130 mm respectively.

Fig 1 shows the 2D model of Yb experiment in PGGP ion collection configuration for computation of PIC code in XOOPIC. Grid of 0.25 mm conductor with 5 mm space was implemented. Spatial resolution of the computational spatial mesh should accommodate this grid size to avoid field distortion around grid.

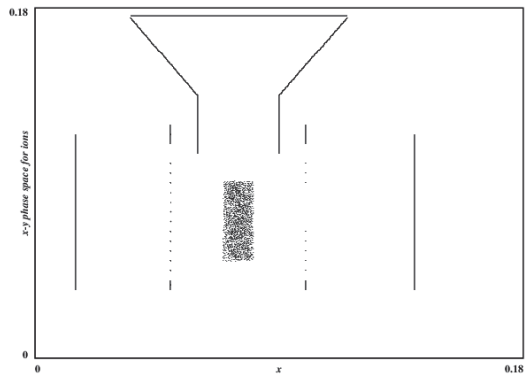

Fig 1: XOOPIC model for Yb experiment1

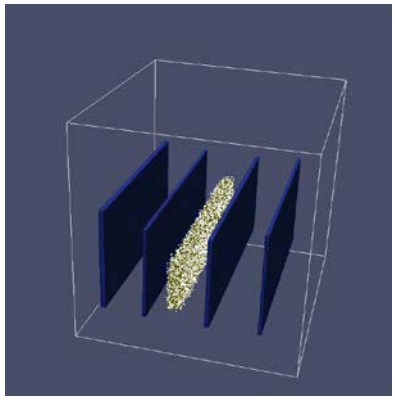

Fig 2: Pasupat 3D PIC model for Yb experiment

Fig 2 is 3D model for BARC-Pasupat3D. Here Grid is modelled as the foil with suitable transparency. Full 3D geometry Pasupat 3D run was tried. Even after 200 hours, only 0.5 microsecond evolution was achieved due to

computational intensity for assumed plasma density of 4.4e9 per cc. Parallel processing is in progress.Further results will be presented for PIC -2D simulation.

Fig3 is the electro static potential of PGGP for Yb experiment without central plasma. Left side cathode, cathode grid, right side anode grid, anode plates and top tail plateswerekept at potential of -500, -1500 V,0, 500 and 100 v respectively.The grid structures are evident on the fig 3. Fig4 is the potential 3D plot with the presence of plasma after 5 microseconds. The plasma potential is seen as the hump in the middle of the plot and deviations of potential near anode (kept at 500 V at extreme right) is also visible in this plot. Plasma acquires positive potential higher than that of anode grid will start diffuse slowly towards anode grid. Anode plate and tail were kept positive to repel the possible ions reaching and guide ions towards the cathode.This geometry may also lead to ion oscillation among the cathode and cathode grid perpetually, if the potentials of the electrode are not properly chosen, which was observed in our simulation.Energy and angular distribution of ions at cathode and anodes were plotted. The percentage of ion collection of cathode, anode and top plates were estimated for both plasma densities.

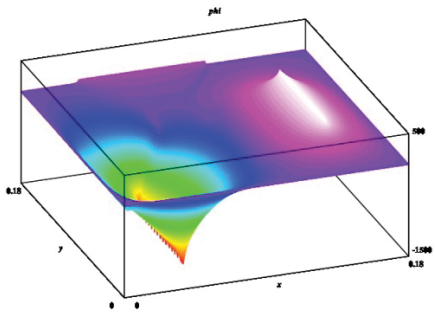

Fig 3: ES potential of Yb experiment without plasma

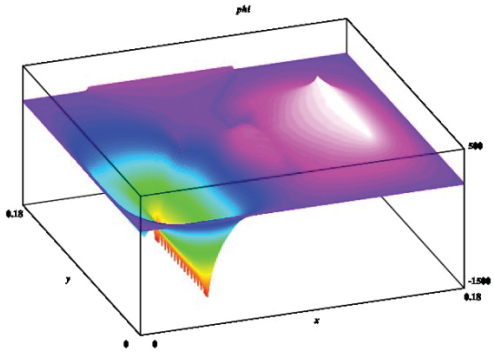

Fig 4: ES potential with plasma

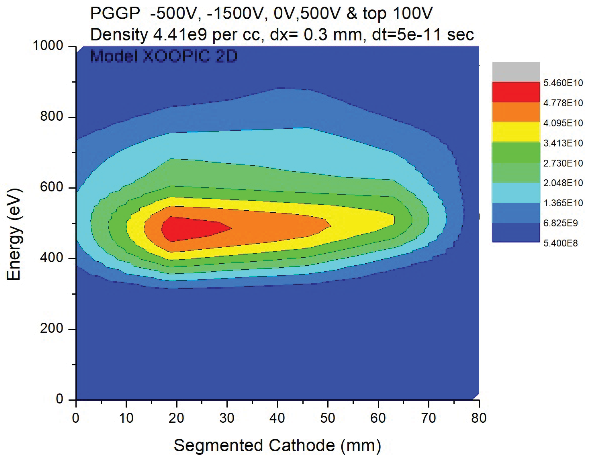

Fig 5 Energy spectrum of ions at cathode

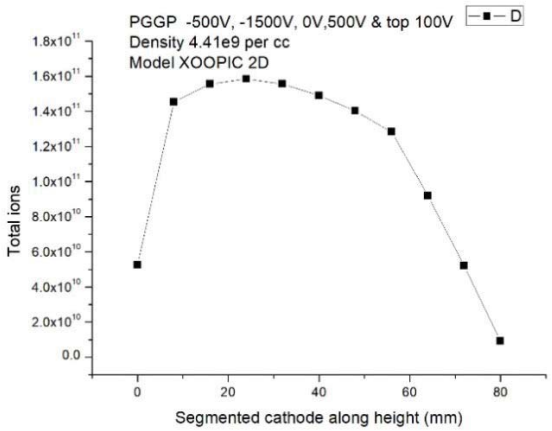

Fig 6 ion distribution along the cathode height

Fig 5 shows the energy spectrum of ions landing on the cathode along the height of the cathode (height of 80 mm) majority of ions reaching cathode with 500 eV energy as expected from the analytic calculations. Fig 6 shows the ion distribution along the height of the cathode. From this plot, we can estimate the percentage of ion collected in cathode from the known ions loaded in the computations. Cathode ion collection efficiency was estimated from Fig6 was 62% which is closer to the observed result of the Yb separation experiment carried in BARC facility.

Conclusion

Simulation work was carried out to understand the laser produced photo plasma placed among the new geometry of ion collection. Parametric studies of ion collection with plasma density, geometry and the potential were carried out. Energy and angular distribution of the ions reaching cathode was predicted which will be a useful input for further study of self-sputtering. The ion collection efficiency of laser produced transient plasma was estimated and compared with experimental observations.

Acknowledgment
Authors acknowledge the technical discussion with Dr Raghawendra Kumar for using Pasupat 3D plasma simulation and 2D PIC code. Authors acknowledge the support and encouragement of Dr Archana Sharma, AD, BTDG during the course of this work.

Reference

1)Kartik Patel, V.K.Mago, J.Appl. Phys., p4371, vol 78 (1995))
2) R.J.Procassini, C.K.Birdsall,E.C.Morse, Phys.Fluids B 2, 3191 (1990).
3) C.K. Birdsall and A.B.Langdon, Plasma Physics via Computer Simulation (McGraw-Hill, New York, 1985).
4) R.W.Hackney and J.W.Eastwood, Computer Simulation Using Particles (McGraw-Hill, New York, 1981).
5) J.P. Verboncoeur, A.B. Langdon and N.T. Gladd, Comp. Phys. Comm., 87, May11, 1995, pp. 199-211.
6) "IMPLEMENTATION OF UNIAXIAL PERFECTLY MATCHED LAYER (UPML) IN 3D PARTICLE-IN-CELL (PIC) CODE PASUPAT", R. Kumar, D. Biswas and G. Singh, *BARC/2015/E/020*, [2015]
7) B.Dikshit, A.Sharma, IEEE Trans. Nucl.Sci. [2021]

In-situ laser cutting for repair/replacement of injection valves of emergency core cooling system at KKNPP-2 reactor

B. K. Saini[1], M. K. Bairwa[1], R. K. Jain[1], A. A. Raju[2], Rajpal Singh[1], Benny John[3], Binu Gopal[4], Bhaskar Paul[1], Jata Beshra[1],Vijay Bhawsar[2], B. Ekka[1], Vijay Bhardawj[1], Vijay Shukla[1], R. Arya[2], B. N. Upadhyaya[1*], K. S. Bindra[1]

[1]*Laser Technology Division, Raja Ramanna Centre for Advanced Technology, Indore-452013, India*

[2]*Laser Electronics Division, Raja Ramanna Centre for Advanced Technology, Indore-452013, India*

[3]*Nuclear Power Corporation of India Limited, Mumbai-400085, India*

[4]*Kudankulam Atomic Power Project, NPCIL, Kudankulam, Tamilnadu-581400, India*

*E-mail: bnand@rrcat.gov.in

Abstract: In Kudankulam Nuclear Power Plant (KKNPP-2), there was specific and urgent requirement for repair/replacement of injection valves of emergency core cooling system by cutting of 17 mm thick SS321 pipe joints during its shutdown for maintenance. This report provides details of development of laser cutting technology for cutting of pipes connected with injection valves using in-house developed 500 W average power fiber coupled pulsed Nd:YAG laser. An orbital laser cutting manipulator and a small size compact laser cutting nozzle were specially developed and laser process parameters were optimized for cutting under challenging conditions of space restriction and high radiation dose. By using this laser cutting technology, four pipe joints and four bevels were cut successfully at KKNPS-2 reactor in minimum possible time and with minimum radiation dose consumption.

Introduction: Kudankulam Nuclear Power Station Unit-2 (KKNPS-2) is a water-cooled water moderated 1000 MWe energy reactor which was commissioned in Kudankulam with Russian collaboration and the reactor started commercial operation in 2017. Agrawal et al. have already published details of reactors at Kudankulam[1]. During recent shutdown, laser cutting of pipelines of emergency core cooling system was urgently required for repair of some of safety injection valves of the system. The cutting of pipes at some locations was required with presence of coolant in reactor since pressure vessel is at higher elevation with respect to injection valves. During operation of the reactor, fluid passing was observed through injection valves of emergency core cooling system. It was noted that the valves placed in vertical orientation never had fluid passing issue. The fluid passing was observed only in valves placed in horizontal position. Thus, it was decided to change the position of the valves from horizontal to vertical during shutdown. A section of pipeline at the required location was ice plugged by flowing liquid nitrogen using ice plugging freeze box. Due to ice plugging, a cutting technique with lower heat generation was desired, thus cutting by laser was preferred as compared to manual grinding to cut and chamfer the pipelines. The pipeline is made of SS321 material with 159 mm outer diameter and 17 mm thickness. Total of four cuts in horizontal and vertical pipeline positions at different elevations of reactor building along with chamfering/beveling of pipes for re-welding was required while holding the reactor coolant by ice plugging. For this laser cutting requirement, a motorized orbital laser cutting tool was designed and fabricated in short time. It was a difficult task to replace these valves by conventional mechanical methods due to space constraint, complexity of ice-plugging location near the pipe, high radiation dose involvement, requirement of cutting of 17 mm thick stainless steel, longer process time, and subsequent secondary waste generation. Thus, it was decided

to cut these pipe joints using laser cutting technology. Laser cutting technology includes development of motorized special compact and very light weight laser cutting fixture, laser cutting nozzle for large thickness and optimization of laser cutting process parameters. This remotely operated laser cutting technology was successfully deployed for cutting of four number of pipe joints and bevel cut of pipe ends with minimum radiation dose consumption and in minimum possible time.

Experimental details and results:

For deployment of laser cutting technology, a compact orbital laser cutting tool, which can rotate in a total circumferential outer diameter of 300 mm around the pipe of 159 mm outer diameter was developed in a very short time. The orbital laser cutting tool is able to grip on the pipe with spring loaded mechanism and rotates along the pipe circumference with the help of a very small geared assembled driver with rollers using a micro DC motor. The rotation speed of laser cutting tool around the pipe can be varied in the range of 5-100 mm/min. The orbital cutting tool can grip pipes of diameter in the range of 158 mm to 163 mm. The tool also holds the laser cutting nozzle, and is remotely operable using flexible fiber optic beam delivery and motion controller from a distance of ~150 m. When the tool rotates on the vertical pipe, it has a tendency to slip down, which is prevented by using a guiding- ring below the tool, which is engaged with the upper part of the tool and keeps the tool at its location using two roller guides. The tool has a very light weight of ~2 kg along with laser cutting nozzle and can be mounted in ~1 min. time. Figure 1 shows laser cutting tool mounted on pipeline in reactor for cutting operation.

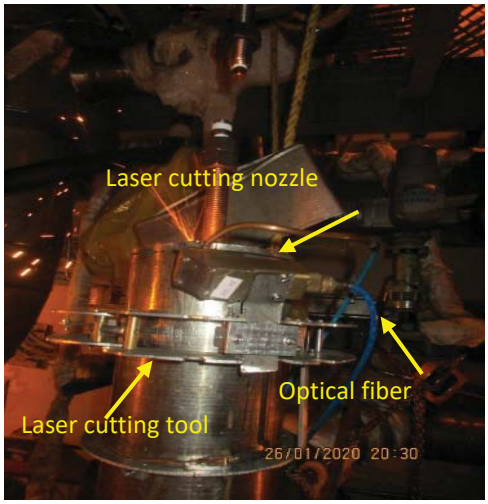

Fig. 1: Laser cutting tool with nozzle mounted on pipeline in reactor for laser cutting operation.

An indigenously developed 500 W average power and 10 kW peak power fiber coupled pulsed Nd:YAG laser system having three time shared fiber ports of 400 μm core diameter and 150 m long length was deployed for cutting operation. Laser pulse duration can be varied in the range of 2-20 ms and pulse frequency in the range of 1-100 Hz. A 90° bending nozzle was utilized at the fiber end for laser cutting at required locations. Laser beam was focused to a spot diameter of 1 mm using a 1:2.5 imaging ratio ½" diameter optics. Laser cutting parameters such as pulse energy, pulse duration, cutting speed were optimized using oxygen as assist gas. Initially, mock up trials were carried out outside reactor building to qualify laser cutting tool and cutting

process. After qualification, laser system was shifted in reactor building at required height for in-situ cutting. For cutting of pipeline, nozzle was kept at right angle with pipe surface, whereas for beveling nozzle was mounted at an angle with respect to normal of the pipe surface. In view of remote cutting operation, an online CCD camera viewing system was also utilized at actual cutting location for monitoring of laser cutting process. Total cutting time for each location was ~50 minutes. Figure 2 shows laser cut ring removed from pipeline end face after beveling and Fig. 3 shows surface of beveled pipe end for re-welding. Laser cutting and chamfering/beveling were performed successfully for replacement/repair of four injection valves in KKNPS-2 reactor with minimum ice plug holding time and radiation dose consumption. This laser cutting technology can be deployed in future requirements as and when required.

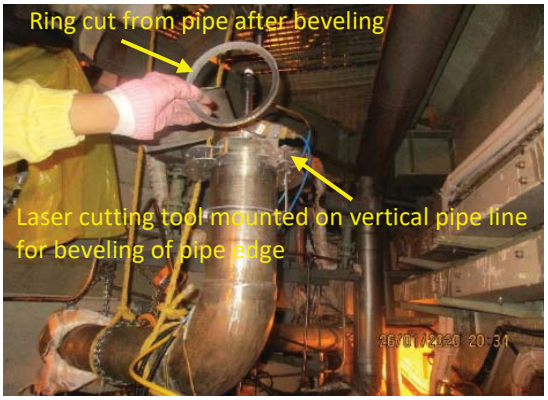

Fig. 2: Laser cut ring removed from pipeline end face after beveling.

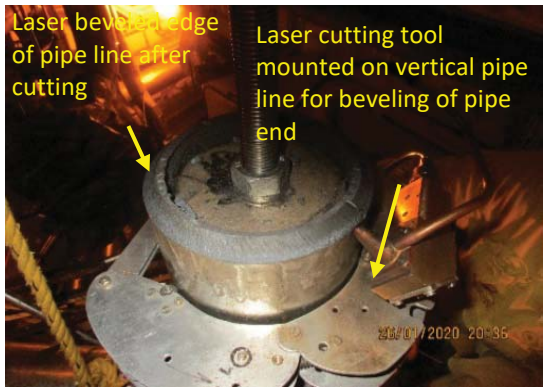

Fig. 3: Surface of bevelled pipe end for re-welding.

Laser cutting of the pipeline was carried out at four locations at a cutting speed of ~25 mm/min. and time for cutting at each location of the pipe was ~20 minutes. Kerf width was measured to be 1 mm. Due to pulsed operation, heat affected zone was confined to within 200 μm at the cut surface. Radiation dose consumption was minimized by means of remote operation. Total time for cutting operation and secondary waste generation was also minimized due to small size of the laser beam used for cutting as compared to larger cut width usually obtained in conventional mechanical methods. Table-1 shows pipeline and laser cutting parameters for 17 mm thick SS321 tubes of KKNPS-2 reactor.

Table-1: Pipeline and laser cutting parameters for 17 mm thick SS321 tube.

Pipe parameters			Laser cutting parameters	
I.	Tube material	Stainless Steel 321	Laser pulse energy	80 J
II.	Tube outer diameter	159 mm	Laser pulse duration	12 ms
III.	Wall thickness	17 mm	Laser pulse frequency	4 Hz
IV.	Thickness at cutting location	17 mm	Focused spot diameter	1 mm
			Oxygen gas pressure	14 bar

Conclusion:

In conclusion, remotely operable laser cutting technology was developed and deployed successfully for in-situ laser cutting of four number of pipe joints of 17 mm thick pipeline in KKNPS-2 reactor. It includes development of a special compact, light weight orbital cutting tool and a laser cutting nozzle for use in a space restricted region of 300 mm diameter. Using this laser cutting technology, four pipe joints and four bevels were cut successfully at KKNPS-2 reactor in minimum possible time and with minimum radiation dose consumption.

References:

1. S. K. Agrawal, et al., Nuclear Engineering and Design 236 (2006) 812–835.

Laser cutting of up to 30 mm thick SS316Lusing 500 W average power pulsed Nd:YAG laser for nuclear field applications

M. K. Bairwa[1], Vijay Bhardwaj[1], R. K. Jain[1], Vijay Shukla[1], S. K. Sharma[1], Rajpal Singh[1], B. K. Saini[1], Bhaskar Paul[1], Pawan Kumar[1], B. Ekka[1], Prabhat Kumar[1], Jata Beshra[1], A. A. Raju[2], S. K. Sah[2], Vijay Bhawsar[2], J. Khanwalkar[2], R. Arya[2], B. N. Upadhyaya[1*], K. S. Bindra[1]

[1]*Laser Technology Division, Raja Ramanna Centre for Advanced Technology, Indore-452013, India*
[2]*Laser Electronics Division, Raja Ramanna Centre for Advanced Technology, Indore-452013, India*
[*]E-mail: bnand@rrcat.gov.in

Abstract: There is a specific requirement for cutting of up to 30mm thick SS316L header pipes in Tarapur Atomic Power Station (TAPS-1&2) for replacement purpose. This report provides details of development of laser cutting technology for cutting of up to 30 mm thick SS316L using 500 W average power fiber coupled pulsed Nd:YAG laser. A compact laser cutting nozzle has been specially developed and laser cutting process parameters have been optimized for cutting of large thickness of SS316L. This remotely operable laser cutting technology will be used for cutting of 30 mm thick SS316Lheader pipes at TAPS-1&2nuclear reactor to minimize radiation dose consumption and time as compared to conventional mechanical methods and will also useful in laser cutting of thick steel sections in various industrial applications.

Introduction: Laser cutting of metals is required in various industries due to its advantage of non-contact nature, high processing speed, capability of automation, and remote processing. Stainless steel structures are extensively used in nuclear and shipping industries to have high strength and stiffness. It is required to cut these steel structures for maintenance, dismantling or decommissioning purposes. In view of remote operation with fiber optic beam delivery, low running cost and low amount of secondary waste generation, laser cutting is a preferred choice as compared to mechanical, plasma, arc and abrasive water jet cutting in nuclear installations. Since, most of the steel structures used in nuclear power plants have a thickness in the range of 4 to 100 mm, laser processing parameters needs to be established for this cutting range. Further, for dismantling work in a highly radioactive environment, cutting tool needs to be operated remotely from a large distance. Laser cutting of thick section of stainless steel requires high average power and high peak power Nd:YAG laser with good beam quality[1].Laser cutting of 10 mm thick SS in dry air environment using 5 kW CW fiber laser using nitrogen as assist gas has been reported by Wandera *et al.*[1]andlaser cutting of up to 300 mm thick steel sheets has also been reported using 30 kW fiber laser[2]. For cutting of thick stainless steel with CW lasers, high output power of a few kilowatts is required, whereas a long pulse (ms) laser of low average power of a few hundreds of watts having a peak power of the order of few kilowatts is sufficient for similar application. Although cutting with CW lasers provides a higher cutting speed, but results in a larger heat affected zone (HAZ), whereas cutting with ms pulse laser provides a lower cutting speed, but results in a very low heat affected zone of only a few hundreds of micron. Ghany *et al.*[3] have reported a comparison of CW and pulsed laser cutting and it has been shown that cutting with pulsed lasers is better due to small HAZ, kerf width and taper angle as compared to CW lasers. For pulsed Nd:YAG laser cutting of thick section of steel, millisecond duration pulses are preferable since the thermal time constant for thick sheet of stainless steel is of the order of tens of ms. In this paper, we have performed study on laser cutting of up to 30 mm thick SS316L plate using 500 W average power pulsed Nd:YAG laser and optimized laser cutting process parameters.

Experimental details: Laser cutting experiments were carried out using an in-house developed long pulse Nd:YAG laser of 500 W average power and 10 kW of peak power with maximum pulse energy of 280 J at 40 ms of pulse duration. Laser pulse duration can be varied in the range of 2-40 ms and pulse repetition rate in the range of 1-100 Hz. Laser beam was delivered through a 400 µm core diameter and 0.22 numerical aperture (NA) optical fiber and has been equipped with three time shared fiber ports. Figure. 1 shows a view of 500 W average power fiber coupled pulsed Nd:YAG laser used in cutting experiments. Laser beam was initially collimated using a collimating lens(Ø12.7mm) of 20 mm focal length and then beam path was bent by 90° using a 45º bending mirror of reflectivity 99.96%(Ø 25.4mm) and finally focused using a focusing lens(Ø12.7mm) of 60 mm focal length to have a 1:3 imaging ratio with a resulting focus spot diameter of 1.2 mm. This focusing objective (bending nozzle) was tested for a gas pressure in the range of 4-16 bars with 2 mm of orifice diameter. Using this bending nozzle, cutting of up to 25 mm thickness has been performed in a single pass due to sufficient depth of focus and energy per pulse. However, it was not possible to cut above 25 mm thickness in single pass due to insufficient depth of focus. So, the depth of focus was increased by using 1:4 imaging ratio of the optics, but with increased size of focus spot to 1.6 mm, energy was not sufficient to melt even up to 25 mm thickness. In view of this, a new technique for cutting was implemented. In this cutting technique, initially a section of 7-9 mm thickness from material is removed by grooving at an angle and then remaining thickness is cut in single pass. Initially, laser cutting was performed by keeping the nozzle at an angle of 60º from upper surface of SS316L plate for making 9 mm deep V-groove on the sample, which was required to reduce the thickness as shown in Fig.2. After cutting a V-groove, it was possible to lower the nozzle by 7 mm below the upper surface of the SS316L plate as shown in Fig.3 and now an effective thickness of 23 mm needs to be cut. Laser cutting of the remaining thickness was successfully carried out using single pass laser cutting method. It was not possible to lower down the nozzle up to the full depth of the V-groove of 9 mm from the upper surface of the SS316L plate, as it was required to maintain a stand-off distance of 2 mm between nozzle tip and work piece and also V-groove width is smaller than the nozzle tip width. Table-1 shows laser cutting process parameters for different thickness of SS316L.

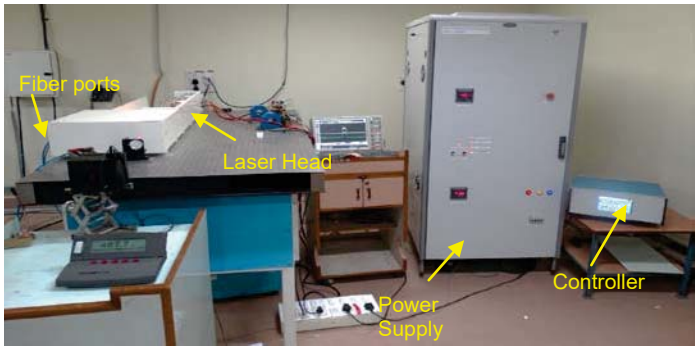

Fig. 1: A view of 500 W average power pulsed Nd:YAG laser used in cutting experiments.

Plates of SS316L having thickness of up to 30 mm were taken as samples for cutting experiments. During the laser cutting process, these plates were clamped in a fixture mounted on a motorized XY-table providing speed variation in a wide range between 5-500 mm/min. Figure 2 shows V-groove of 9 mm thickness generated on the surface of SS316L. Figure 3 shows the experimental set up for laser cutting experiments. Figure 4 shows the cut surface of 25 mm thick SS316L in single pass and Fig. 5 shows cut kerf of 30 mm thick SS316L.Laser cutting

fixture holds the plate in such a way that there is a gap between the bottom surface of sample and top of XY-table, so that it allows a free flow of molten material from the cut kerf during laser cutting process. Oxygen has been used as assist gas with outlet pressure varying in the range of 7-16 bar to enhance process speed and cutting depth in ferrous metals as extra energy is released from exothermic reaction of iron and oxygen. Since, the reaction has a very high yield above 1000^0C, the surface area on which the oxygen jet interacts must be above this temperature in order to produce complete combustion within the gas footprint, which is easily achieved with an industrial laser of high power.

Table-1: Laser cutting process parameters for different thickness SS316L plate samples.

Sl. No.	SS316L plate thickness	Cutting Passes /Nozzle angle from normal	Thickness (mm)	Laser cutting Speed (mm/min)	Laser process parameters			
					Pulse Energy (Joule)	Pulse Duration (ms)	Frequency (Hz)	Assist gas pressure
1.	22 mm	Single pass and 0^0	22	20	125 J	20	2	O_2, 13 bar
2.	25 mm	Single pass and 0^0	25	10	125 J	20	2	O_2, 16 bar
3.	30 mm	2 passes for V-groove at 30^0	12	50	110 J	12	4	O_2, 7 bar
4.	30 mm	Single pass and 0^0	23	20	125 J	20	2	O_2, 14 bar

Fig. 2:A cut piece of 9 mm thickness removed from 30 mm thick sample.

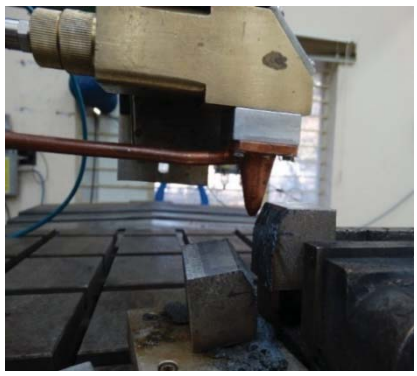

Fig. 3: A view of laser cutting nozzle with beam bending at 90°.

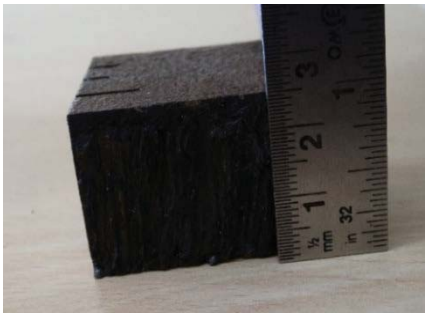

Fig. 4. Single pass cut surface of 25 mm thick SS316L.

Fig. 5. Cut kerf of 30 mm thick SS316L.

For cutting of 30 mm thickness, initially, a V-groove of 12 mm length (9 mm depth) was made on SS316L sample using 110 J of pulse energy with pulse duration of 12 ms at 4 Hz of repetition rate and low oxygen pressure of 7 bar. This low pressure was optimized to minimize oxygen gas consumption during cutting process. The cutting speed was 50 mm/min. For remaining effective thickness of 23 mm of SS316L sample, laser pulse energy was increased to 125 J with 20 ms pulse duration and 2 Hz of repetition rate and oxygen pressure was also increased to 14 bar. The cutting speed was kept at 20 mm/min. With this two-step process, laser cutting of 30 mm thickness was successfully achieved. Figure 6 shows cut kerf on top and bottom surface and Fig. 7 shows surface roughness of 30 mm thick SS316 measurement using ten point method. Top surface kerf of 1.386 mm and bottom surface kerf of 0.354 mm was measured. Further, surface roughness of 465 µm was measured on cut surface of 30 mm thick SS316L. Since heat affected zone is very small, re-welding can be performed after removing ~600-800 µm oxidized layer from the surface.

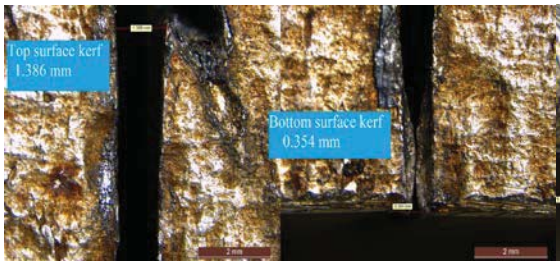

Fig. 6. Cut kerf on top and bottom surface of 30 mm thick SS316L.

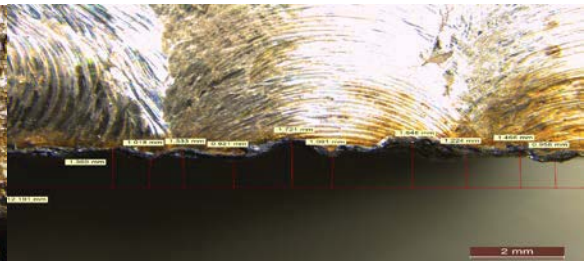

Fig. 7. Surface roughness measurement of 30 mm thick SS316L using ten point method.

Conclusion:

In conclusion, laser cutting of up to 30 mm thick section of SS316L in dry air environment has been demonstrated and investigated using 500 W average power and 10 kW peak power fiber coupled pulsed Nd:YAG laser. The cutting has been performed in two steps, initial cutting up to a depth of 7 mm at an angle followed by through and through cutting of 23 mm. With increase in thickness of cutting, it was required to increase pulse energy, assist gas pressure, and depth of focus for successful cutting of the material. This development will be used at TAPS-1&2reactor for refurbishment applications to reduce manrem consumption and time.

References:

1. Wandera et al., *Jounral of Laser Application***21(3),** 154 (2009).
2. Tamura et al., *Journal of Nuclear Science and Technology* **53(6)**, 916 (2016).
3. K.Abdel Ghany and M. Newishy, *Journal of Materials Processing Technology***168**, 438 (2005).

Growth of Bulk Size Organic Single Crystal by a Novel Immersing ampoule Sankaranarayanan–Ramasamy (ISR) Method for NLO Applications

P. Karuppasamy[1*], T. Kamalesh[1], Muthu Senthil Pandian[1], P. Ramasamy[1], Sunil Verma[2,3], A. K. Karnal[2,3]

[1]*SSN Research Centre, Sri Sivasubramaniya Nadar College of Engineering, Chennai-603110, Tamil Nadu*

[2]*Laser Materials Development and Devices Division, RRCAT, Indore-452013, Madhya Pradesh*

[3]*Homi Bhabha National Institute (HBNI), Anushakti Nagar, Mumbai-400094, Maharashtra*

*Email: karuppasamyp75@gmail.com; karuppasamyp@ssn.edu.in

Abstract

The organic nonlinear optical (NLO) single crystals of 2-aminopyridinium 4-nitrophenolate 4-nitrophenol (2AP4N) were successfully grown by a novel Immersing ampoule Sankaranarayanan–Ramasamy (ISR) method. The crystal structure was confirmed by single crystal X-ray diffraction (SXRD) analysis. The crystalline planes and phase purity were analyzed by powder x-ray diffraction (PXRD) measurement. The optical quality of the grown crystal was analyzed by UV-Vis NIR and Birefringence measurement. The third-order nonlinear optical susceptibility ($\chi^{(3)}$) has been studied using Z-scan technique at 632.8 nm.

Introduction

Nonlinear optical (NLO) materials have attracted considerable attention owing to their potential applications in the areas of laser science and optical technologies[1]. Organic materials are of more interest because of their low cost and fast response. The advantage of an organic crystal is that the structure can be easily fine-tuned and to get the required NLO properties. They also possess a high laser damage threshold, fast optical response and high nonlinear optical susceptibilities compared to inorganic crystals[1-2]. The ISR crystal growth method is a suitable way to grow a unidirectional bulk size single crystal and also having reduced optimizing parameters compared to the SR method. A special design has been made on the growth ampoule to reduce the difficulty of growing unidirectional single crystals. In the present work, the 2AP4N crystal was grown by ISR method. The grown crystals were subjected to SXRD, PXRD, UV-Vis NIR, Birefregence and Z-scan technique.

Synthesis and crystal growth

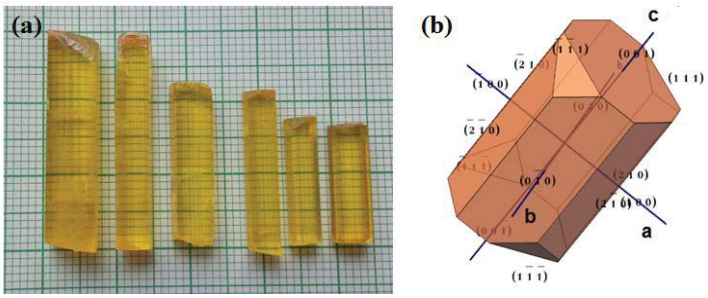

FIGURE 1. (a) As grown 2AP4N single crystals and (b) its morphology

The starting materials of 2-aminopyridine (2AP) and 4-nitrophenol (4NP) were taken in the stoichiometric ratio 1:2 for the synthesis of 2-aminopyridinium 4-nitrophenolate 4-nitrophenol (2AP4N)

compound. Initially, the solution was stirred well for one day until a homogenous solution was obtained. The prepared solution was filtered and then poured in a glass crystallizer and it was kept a dust-free atmosphere. The 2AP4N crystal was formed randomly in a crystallization dish after a few days. Further, the synthesized 2AP4N material was recrystallized several times for improving the crystal quality. The good quality and bulk size single crystals of 2AP4N have been obtained in a period of 30 days and the grown 2AP4N crystals and the morphology are shown in Fig.1 (a) and (b) respectively.

Novel Immersing ampoule Sankaranarayanan–Ramasamy (ISR) method

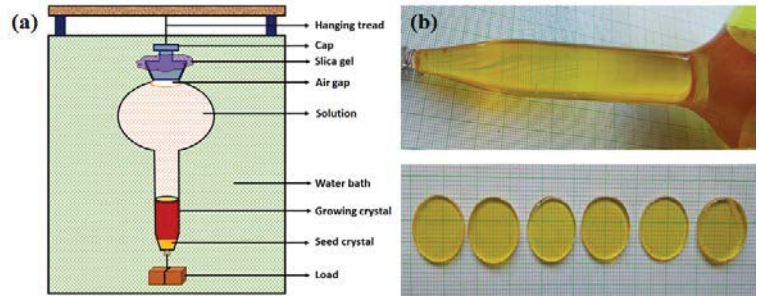

FIGURE 2. (a) schematic ISR system and (b) grown crystal & its wafers

The suitable size of the ampoule was selected and cleaned properly with double distilled water, acetone and methanol solvent. The seed crystal was selected along a <001> direction (c-axis) and it was mounted at bottom of the glass ampoule. The charge material was dissolved in a high purity methanol solvent and prepared saturated homogeneous solution at 45°c. The same solution (300ml) was poured into the growth ampoule without any disturbance of the seed crystal. Then the growth ampoule was sealed by a glass cap and fix the silica gel for avoiding any leakage of air or solution (keep small air gap in the ampoule). The air cap is the major role for avoiding the developing pressure in the solution due to the temperature gradient (cooling or heating). The ampoule was stretched at the top and bottom portion using a steel wire. It has to be immersed (360°) and suspended vertically in a center of the water bath and the heavy load (steel bar) has been held at bottom of the ampoule for avoiding oscillation. The suspended ampoule is looking vertically axis-symmetric with respect to the center of gravity, it is more advantageous for the growth of a unidirectional single crystal[4]. Now the concentration of the solution can be controlled by the suitable temperature provided to the system. The good quality with large size single crystal was obtained by optimizing only one growth parameter is cooling rate. The cooling rate 0.2°C per day was used. The schematic diagram of the ISR system and the grown 2AP4N single crytal & its wafers are shown in Fig. 2 (a) and (b) respectively.

RESULTS AND DISCUSSIONS

X-Ray Diffraction Analysis

The 2AP4N crystal was subjected to single-crystal XRD analysis using a Bruker AXS Kappa APEX II CCD diffractometer equipped with monochromatic MoK_{α} radiation (λ = 0.710 Å). The structure of 2AP4N crystal was confirmed. The grown crystal belongs to the orthorhombic crystal system with space group $Pna2_1$. The calculated lattice parameters are a = 13.15 Å, b = 10.95 Å, c = 12.24 Å, $\alpha=\beta=\gamma$ =90° and volume (V) =

1758 Å^3. These values are well-matched with the reported literature[5]. The PXRD study for the 2AP4N crystal was carried out using PANalytical X-ray diffractometer with the CuK_α radiation (λ = 1.5406 Å) at room temperature in order to determine the planes present in the 2AP4N crystal and its phase purity. The ISR method grown crystal was sliced and characterized by using PXRD. The obtained intensity peaks show (001) family plane and hence the unidirectional growth by ISR method grown 2AP4N crystal is confirmed[4]. The PXRD patterns of 2AP4N in a powder form and sliced wafer are shown in Fig. 3 (a) and (b) respectively.

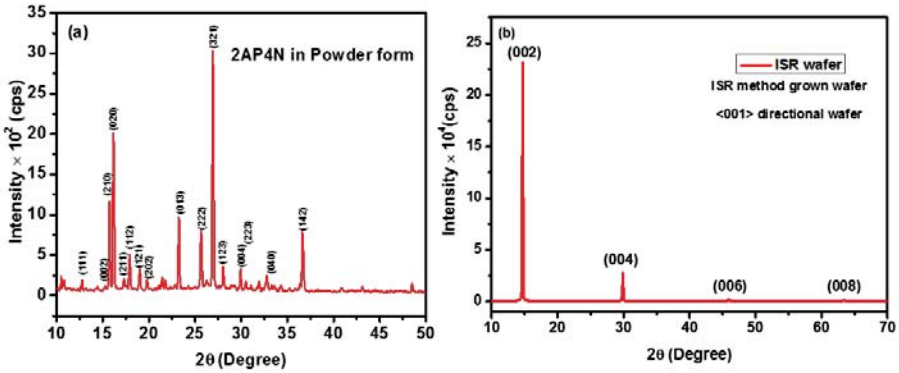

FIGURE 3. PXRD spectrum measured for 2AP4N (a) powder and (b) wafer

Optical Transmittance and Birefrergence measurement

The high optical transparency of single crystals are more favorable for optical device applications[3]. The optical quality of ISR method grown 2AP4N single crystal was recorded using Perkin-Elmer Lambda-35 spectrophotometer in the range of 200-1100 nm. It shows the 80% optical transmittance at the higher wavelength and the lower cut-off was found to be 470 nm. The grown crystal has good optical transmission in the entire visible and near IR regions. The higher transmittance of the grown crystals may be attributed to lesser defects. The same crystal has been subjected to the birefringence measurement using He-Ne laser (632.8 nm) with a power of 10 mW. The uniform interferogram is indicated that the grown crystal is optically higher homogeneities. The optical transmittance and birefringence patterns of 2AP4N crystal are shown in Fig. 4 (a) and (b) respectively.

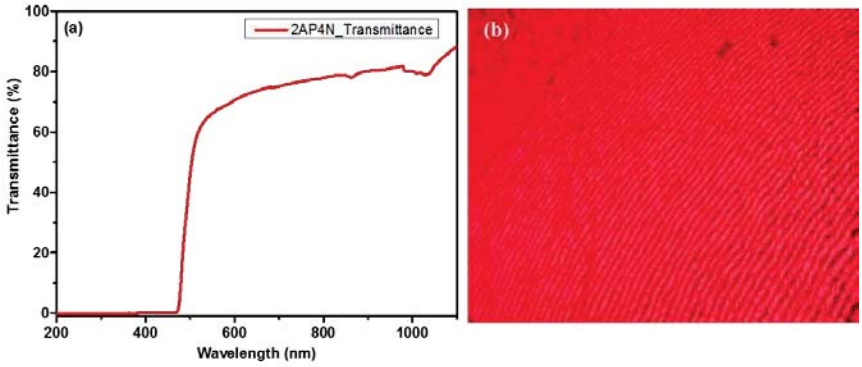

FIGURE 4. (a) Optical transmittance and (b) Birefringence pattern

Z-Scan Analysis

The third-order NLO properties of 2AP4N crystal were investigated using Z-scan technique using He-Ne laser (632.8 nm)[5-6]. In this experiment, the laser source with a power of 25 mW was used and its beam diameter is 5 mm. The polarized Gaussian beam of mode TEM00 was focused by a convex lens (focal length is

300 mm) to produce the beam waist ω_0 = 24.18 µm. The sample was fixed on a holder (90º) and it was moved along the Z-axial direction, which was parallel to the direction of propagation of the laser beam. The precise movement given to the translation system by the programmable driver is controlled by the computer. The corresponding transmitted intensity through the sample was collected by a photo-detector and it was measured by the digital power meter. The closed and open aperture Z-scan spectra are shown in Fig. 5 (a) and (b) respectively. The nonlinear refractive index (n_2) and absorption coefficient (β) were calculated using the following relations[5]. The calculated value of nonlinear refractive index (n_2), nonlinear absorption (β) and third-order nonlinear susceptibility ($\chi^{(3)}$) are 2.38 × 10^{-11} m^2/W, 2.58× 10^{-04} m/W and 8.68 × 10^{-07} esu respectively.

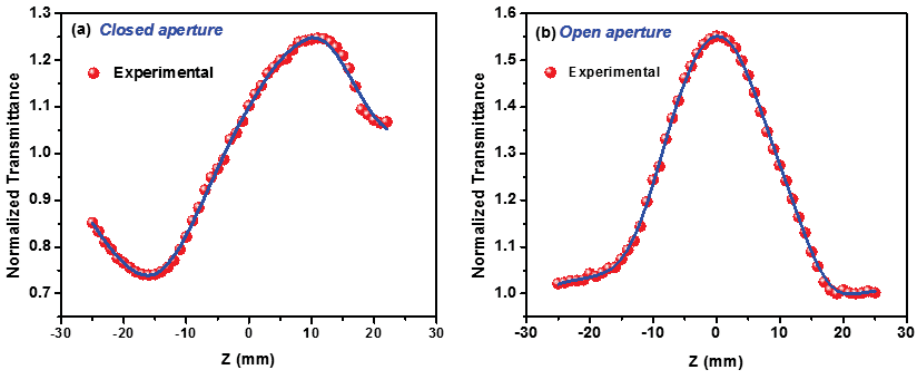

FIGURE 5. (a) Closed aperture and (b) Open aperture Z-scan spectrum of 2AP4N crystal

Conclusions

Good quality and large size nonlinear optical 2AP4N single crystals were grown by the novel Immersing ampoule Sankaranarayanan–Ramasamy (ISR) method. The grown crystal belongs to the Orthorhombic system with the space group $Pna2_1$. The good optical transmission clearly shows that the crystal has less defects. The crytal has higher optical homogeneities in nature. The Z-scan experimental results confirmed the large value of nonlinear optical absorption coefficient (β) and nonlinear optical refractive index (n_2). Thus, all the findings and various studies suggested that the 2AP4N crystal may be a suitable candidate for the fabrication of the second-harmonic generation (SHG), third-harmonic generation (THG), optical limiting, optical switches and photonic device applications.

Acknowledgment

The authors gratefully acknowledge DAE-BRNS, Government of India for the financial support (Ref. no. 34/14/06/2016-BRNS/34032).

References

1. P.N. Prasad, D.J. Williams, Introduction to Nonlinear Optical Effect in Molecules and Polymers, John Wiley & Sons, Inc., 1991.
2. D.J. Williams and Angew. *Chem., Int. Ed. Engl*. **690** (1984).
3. K. Sankaranarayanan, P. Ramasamy, *Cryst. Res. Technol*. **3**, 225 (2006).
4. M. Jaya Prakash, T. P. Radhakrishnan, *Cryst. Growth Des*. **5**, 721 (2005).
5. P. Karuppasamy, Muthu Senthil Pandian, P. Ramasamy and Sunil Verma, *Opt. Mater*. **79**, 152 (2018).
6. M. Sheik-Bahae, A. A Said and E. W. Van Stryland, *Opt. Lett.* **14**, 955 (1989).

Crystal Growth and Characterization of Semi-organic Piperazinium Tetrachlorozincate monohydrate (PTCZ) Single Crystal for Nonlinear Optical (NLO) Applications

Z. Nawas Sherif[1]*, B. Sahaya Infant Lasalle[1], T. Kamalesh[1], P. Karuppasamy[1], Sunil Verma[2,3], Muthu Senthil Pandian[1], P. Ramasamy[1]

[1]SSN Research Centre, Sri Sivasubramaniya Nadar College of Engineering, Chennai-603110, Tamil Nadu

[2]Laser Materials Development and Devices Division, RRCAT, Indore-452013, Madhya Pradesh

[3]Homi Bhabha National Institute (HBNI), Anushakthi Nagar, Mumbai-400094, Maharashtra

*Email: nawassherifz100@gmail.com ; nawassherifz@ssn.edu.in

Abstract:

Optically high quality semi-organic single crystal of piperazinium tetrachlorozincate monohydrate (PTCZ) was grown by conventional slow evaporation solution technique (SEST). The structure of the grown crystal was confirmed by the single-crystal X-ray diffraction (SXRD) analysis. The various (hkl) planes and phase purity of the material have been confirmed by the powder X-ray diffraction (PXRD) analysis at room temperature. The various functional groups were confirmed by the Fourier-transform infrared (FTIR) spectroscopy. The chemical etching process has been carried out on the grown crystal. The crystalline perfection of the PTCZ has been investigated by high-resolution X-ray diffraction (HRXRD) analysis.

1. Introduction:

The technological society of optoelectronics and photonics has created more attention on organic nonlinear optical (NLO) materials. Nonlinear optics is a frontier of science and technology that plays a major role in the emerging field of photonics, which involves several applications. However, in the form single crystals are most important for a wide range of optoelectronic applications such as laser harmonic generations (SHG, THG, 4HG), sum or difference frequency generation (SFG, DFG) and optical parametric generation, amplification or oscillation (OPG, OPA, OPO)[1]. However, organic materials may suffer from many problems such as volatility, low thermal stability, poor mechanical stability, etc. Whereas, inorganic materials possess excellent mechanical and optical properties but have a low effect of nonlinearity. However, these difficulties are overcome to introduce a new phase of semi-organic single crystal and it can be grown bulk form with higher quality. Because it reflecting effects from both the organic and inorganic aspects and remarkably excellent characteristics. Piperazine and its substituted materials are useful for pharmacophores that can be found in many drugs. The derivative of piperazine is found in biologically active components across various therapeutic areas such as antifungal, antibacterial, antimalarial, and etc[2]. In this view, research has more attracted and considerable attention in the development of good NLO materials. In the present investigation, the optically high quality semi-organic single crystals of PTCZ have been grown by the solution method. The grown PTCZ single crystals were subjected to various characterizations such as SXRD, PXRD, FTIR, chemical etching and HRXRD analysis.

2. Experimental

2.1 Material synthesis, crystal growth and morphology

The analytical grade of piperazine ($C_4H_{10}N_2$), zinc chloride ($ZnCl_2$) and hydrochloride acid (HCl) were taken in the ratio of 1:1:2 in water to syntheses of $[C_4H_{12}N_2]$ $ZnCl_4 \cdot H_2O$ (PTCZ) material. The same material has been taken in a glass container based on the solubility data. The transparent solution was obtained by continuously stirred for few hours at room temperature. The prepared homogenous solution was filtered into a glass crystallizer using Whatman filter paper. The filtered solution was poured into the glass petri-dish and covered by thick polythene sheet with few holes to make the solvent controlled evaporation at room temperature. The PTCZ single crystal was harvested after 20 days from the mother solution. The synthesized materials have been purified by the repeated crystallization process. The optically good quality PTCZ single crystals with the dimension of 3 × 2 × 2 mm^3 have been obtained after few weeks. The grown PTCZ single crystals are shown in Fig. 1(a). The morphology of the grown crystal was indexed by WinXMorph software and is shown in Fig. 1(b).

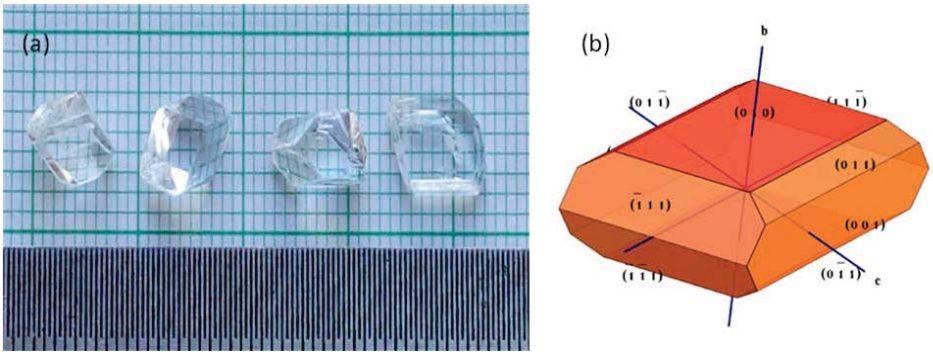

Figure 1 (a) As grown crystals of PTCZ and (b) Morphology of PTCZ

3. Results and discussion

3.1 X-ray diffraction (XRD) analysis

The grown PTCZ crystal was subjected to SXRD at room temperature using EnrafNonius CAD4-F diffractometer with MoK_α monochromatic (λ= 0.710 Å) radiation. From the observation, the PTCZ crystal belongs to monoclinic with unit cell parameters of a = 6.58 Å, b = 12.80 Å, c = 14.04 Å and β = 92.73°, which is well-matched with the reported value[3]. The PXRD spectrum is shown in Fig. 2(a). From the spectrum, the well-resolved intense peaks were observed with specific 2θ angles, which indicates that the grown crystal is good in structural/ crystalline perfections.

3.2 FTIR Spectral Studies

Fourier transform infrared (FTIR) spectroscopy is an important tool to analyze the various functional groups in the given structure. It gives broad information about chemical bonding and molecular related vibrations. The FTIR spectrum of the PTCZ crystal was recorded using ATR mode at room temperature in the wavenumber range between 500 cm^{-1} to 4000 cm^{-1} by using the Perkin-Elmer spectrometer and the recorded FTIR spectrum of PTCZ is shown in Fig. 2(b). From the spectrum, the peak at 3539 cm^{-1} is indicated that the strong N-H stretching vibration. The peaks at 3019 cm^{-1} and 2782 cm^{-1} indicate that the absorbance of C-H

stretching mode. The peaks at 1635 cm^{-1} and 1551 cm^{-1} are assigned to the NH_2^+ deformation in the piperazinium moiety[4]. The peak at 1441 cm^{-1} belongs to CH_2 stretching presence in the piperazinium ring wall. The peaks at 1305 cm^{-1} and 1187 cm^{-1} indicate the symmetric mode of stretching and in-plane bending vibration of C-H group. The N-H bending mode occurred at 911 cm^{-1}. The deformation of C-N is observed at 860 cm^{-1}. The peak at 557 cm^{-1} is indicated due to the presence of C-C-N deformation.

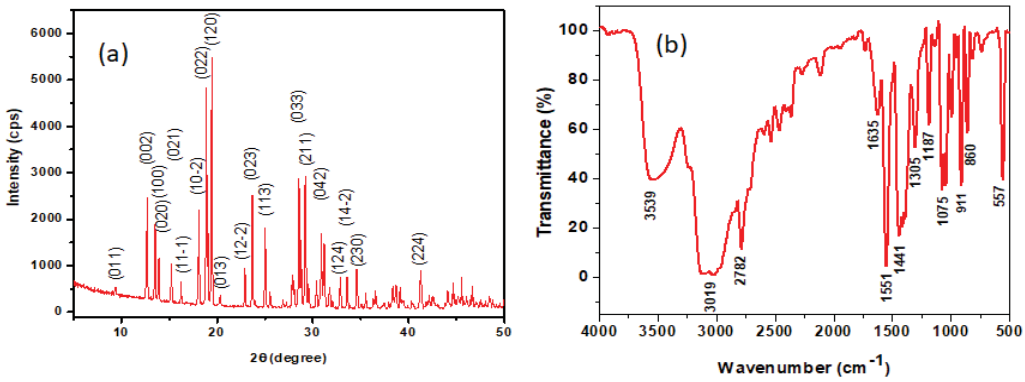

Figure 2 (a) PXRD spectrum and (b) FTIR spectrum of PTCZ

3.3 Chemical Etching analysis

The NLO efficiency mainly depends on the quality of the grown crystal, because the imperfection or impurities may accumulate to develop the dislocations in the crystal during the growth process (any growth methods). The etching process has been carried out on the grown PTCZ single crystal using water as an etchant at room temperature. First, the prepared PTCZ single crystal was dipped in the Millipore water for 2 seconds and it was cleaned properly with tissue paper. Second, the same surface was examined by an optical microscope with suitable magnification. Here, the etch pits are not formed and it could not be seen. The same process was repeated for 5 seconds, the elongated linear etch pits were observed on the surface. Randomly distributed but strictly oriented etch pits are seen. When the time increases the etch pits enlarge it's size retaining their geometrical shape and do not disappear suggesting that the pits are due to dislocations. The etched surface of the PTCZ single crystal is shown in Fig. 3(a). The etch pits density (EPD) of the PTCZ single crystal was analyzed manually using an optical microscope and it can be calculated by the number of etch pits followed by a given area. The calculated EPD of the PTCZ single crystal was found to be 3.2×10^3 cm^{-2}.

3.4 HRXRD

Crystalline perfection is a major role in their optical device performance, which depends on the growth techniques and environments. The crystalline atomic perfection of the grown single can be investigated by the high-resolution X-ray diffraction (HRXRD). The grown single crystal was mounted on the PXRD holder and gets the diffraction patterns for the PTCZ crystal. The HRXRD has been done on the selected (hkl) plane, at $2\theta = 17.5°(\omega = 8.75°)$. The monochromatic $CuK\alpha_1$(1.5406Å) X-ray beam has been obtained from four bound silicon (220) bouncer. Further, that beam has been collimated by controlling the slits (horizontal/vertical: 0.5 mm/ 0.25 mm). The obtained fine beam is used for this analysis. The preliminary scanning of fine calibration offset such as ω, 2θ, φ, χ and Z are analyzed with respect to the selected (hkl) plane and it is set to be zero position. The rocking curve (RC) was recorded by the ω-scan where the detector was kept at the Bragg angle position with horizontal slit opening at front of the point detector, without alignment of the sample or any other position. An HRXRD diffraction curve or RC-spectrum of the PTCZ crystal is shown in Fig. 3(b). The full

width at half maximum (FWHM) of the RC was found to be 17.06 arc sec, it indicating that the crystalline perfection of the grown PTCZ single crystal was good. This low FWHM is represents that there is no any structural distortion and low/very low angle grain boundaries present in the grown PTCZ single crystal. However, such types of single crystals are more useful for high-performance nonlinear optical (NLO) devices.

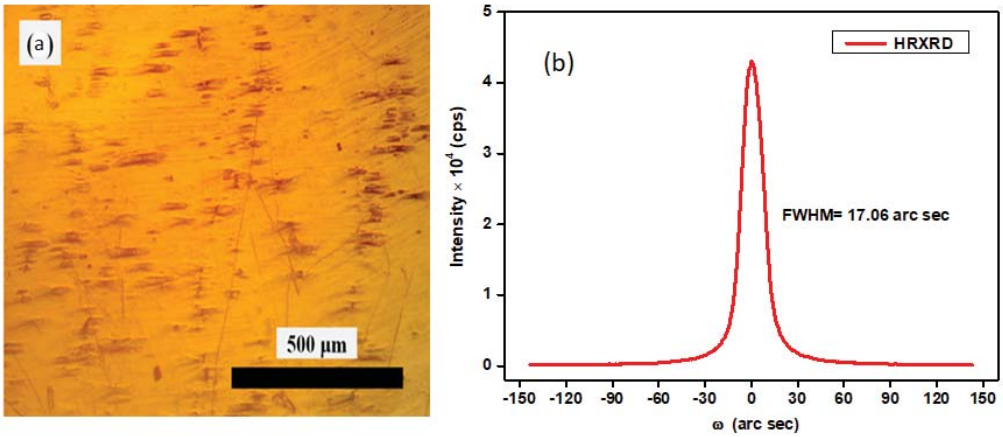

Figure 3 (a) Etched surface for 5 sec and (b) HRXRD spectrum of PTCZ single crystal

4. Conclusions

The optically good quality semi-organic NLO single crystals of piperazinium tetrachlorozincate monohydrate (PTCZ) were grown by slow evaporation solution technique (SEST). The lattice parameter and various (hkl) planes were confirmed by XRD analysis. The morphology of grown crystal has been indexed by WinXMorph software. The FTIR spectral analysis confirms the functional groups present in the grown crystal. The chemical etching reveals that the grown crystal has less dislocation. The grown crystal has good in crystalline perfection, which was 17.06 arc sec. From these observations, it has been concluded that the grown PTCZ single-crystal is more suitable for nonlinear optical applications.

References

[1] P. E. Britton, N. G. R. Broderick, D. J. Richardson, P. G. R. Smith, G. W. Ross, and D. C. Hanna, *Optics Letters*, **23**, 1588 (1998).

[2] N. Prabavathi, A. Nilufer, V. Krishnakumar, *Spectrochim. Acta A,* **121**, 483 (2014).

[3] R. Kefi and C. Ben Nasr, Z. Kristallogr. NCS 220 (2005) 241-242.

[4] P. Karuppasamy, M. Senthil Pandian, P. Ramasamy, Journal of Crystal Growth, 473 (2017) 39–54.

Bulk growth of Organic Non-linear optical Triphenylphosphine Oxide 4-Nitrophenol (TP4N) Single Crystals by Sankaranarayanan–Ramasamy (SR) method

T. Kamalesh[1]*, P. Karuppasamy[1], Muthu Senthil Pandian[1], P. Ramasamy[1], Sunil verma[2, 3], A.K. Karnal[2, 3]

[1]*Research Centre, Sri Sivasubramaniya Nadar College of Engineering, Chennai-603110, Tamil Nadu*

[2]*Laser Materials Development Devices and Division, RRCAT, Indore-452013, Madhya Pradesh*

[3]*Homi Bhabha National Institute, Anushakti Nagar, Mumbai-400094, Maharashtra*

Email: kamaleshkamal918@gmail.com

Abstract

The optically good quality, bulk size organic Triphenylphosphine Oxide 4-Nitrophenol (TP4N) single crystal was grown by Sankaranarayanan-Ramasamy (SR) method. Transparent, yellow color and <011> oriented unidirectional bulk single crystal with 171 mm length and 15 mm diameter was grown by SR method. The grown TP4N unidirectional crystal was subjected to various characterization studies such as powder X-ray diffraction (PXRD), high-resolution X-ray diffraction (HRXRD), UV-Vis NIR measurement and Birefringence interferometry technique.

1. Introduction

Good quality and bulk size organic single crystals are essential for optical applications such as nonlinear optics (NLO), piezoelectric devices and frequency mixing. The organic crystals are fascinating, because of high hyperpolarizability (β), high laser damage tolerance, inexpensive, fast response, ease of fabrication and high synthetic flexibility [1]. Compared to inorganic crystals, organic crystals possess less thermal and mechanical stability but more hyperpolarizability (β). Crystal growth researchers are much interested in the 4-nitrophenol based nonlinear optical crystals. The 4-nitrophenol is a phenolic material and it has the nitro group (NO_2) at one end and it has the hydroxyl group (OH) in a benzene ring at the other end. It has one-dimensional (1D) donor-acceptor π system, and the presence of proton transfer of the phenolic OH with various organic and inorganic bases results in an enhancement of the hyperpolarizability of both species. For practical application, large size crystals with good optical transparency and the ability to withstand a high laser power are much needed. However, growing large size and good quality organic crystals is still a challenge for the researchers. Solution and melt crystal growth techniques are widely used to grow a bulk size single crystal [2]. Among all the techniques, the slow evaporation solution technique (SEST) is the simplest due to easy operation. The SEST has the limitation that the crystal grows in its natural morphology with different facets. When the second harmonic generation (SHG) element is obtained from such a crystal, a substantial amount of the crystal goes as waste while cutting it along phase-matched directions. To overcome this drawback of the SEST, Sankaranarayanan-Ramasamy (SR) method is effectively used to grow these crystals in which we can grow large size single crystal along the preferred crystallographic direction. The advantages of the SR method are the whole solute can be converted into a crystal, less thermal stresses and prevention of microbial growth. In the present article, TP4N single crystals are grown by the SR method. The SR TP4N crystal were characterized using powder X-ray diffraction (PXRD), high-resolution X-ray diffraction (HRXRD), UV–Vis NIR and birefringence analysis.

2. Experimental procedure

2.1 Slow evaporation solution technique (SEST)

Triphenylphosphine oxide (TPPO) and 4-nitrophenol (4NP) were taken in the stoichiometric ratio of 1:1. The calculated amount of materials (4NP and TPPO) were dissolved in methanol solvent. The solution was prepared and filtered into a crystallizing dish. It was covered with a thick polythene sheet and then placed at room temperature. After a few weeks, the pale yellow color TP4N single crystals were harvested. This was further improved by recrystallization process to remove the impurities. The optically transparent TP4N single

crystals size of 12×11×9 mm^3 were harvested in 27 days (Fig. 1 (a)). The morphology of the TP4N single crystal is shown in Fig. 1 (b).

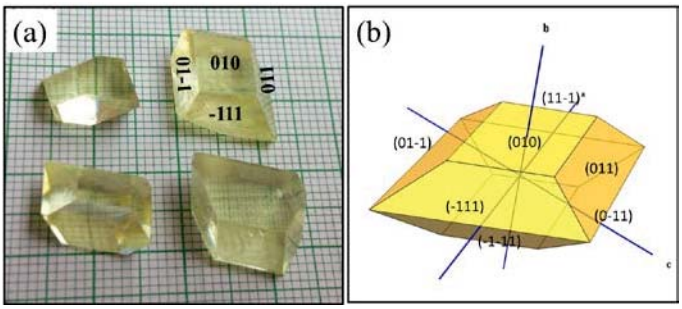

FIGURE.1 (a) As grown TP4N SEST crystals and (b) its morphology

2.2 Sankaranarayanan-Ramasamy (SR) Method

The TP4N single crystal is grown by the Sankaranarayanan-Ramasamy method. The SR method consists of a water bath, glass ampoule, ring heater, temperature controller and sensors. Initially, a seed crystal was grown by the solution method and good transparent TP4N single crystal was selected. The seed crystal was cut along the (011) direction (thickness-1.5mm and diameter-3.5mm). The ampoule was made up of glass material with three portions, the bottom is V-shaped to mount the seed, the middle was cylindrical and the top portion was pot-shaped. The seed (011) was slowly fixed with the bottom of the ampoule and four times recrystallized TP4N material was used to prepare the solution. Then the TP4N solution was filtered by Whatman filter paper and the filtered TP4N solution was slowly poured into the ampoule without disturbing the seed. The top portion of the ampoule was covered by a plastic cover with few holes to control the solvent evaporation. The whole ampoule was housed in a water bath, a two-ring heater placed at the top and bottom of the ampoule. The top and bottom of the ring heater connected to the temperature controller (with ± 0.1˚C accuracy), provides 37˚C (solvent evaporation) and 32˚C (growth region) respectively. The experimental setup of the Sankaranarayanan-Ramasamy(SR) method is shown in fig.2 (a). All the experimental conditions were observed and after the 3 days, the seed crystal started to grow. In the first 10 days, a V-shaped portion (bottom) of the ampoule was grown at the rate of 4mm/day. In another 38 days, TP4N crystal was grown (Middle portion) at the rate of 3 mm/day. Therefore the TP4N SR crystal (171 mm length and 15 mm diameter) was grown within 51 days (Fig. 2 (b)). In the SR method, the TP4N solution was put up in an ampoule with a small seed, the entire amount of the solute was converted into TP4N crystal thus achieving solute-crystal conversion efficiency of nearly 100% [3].

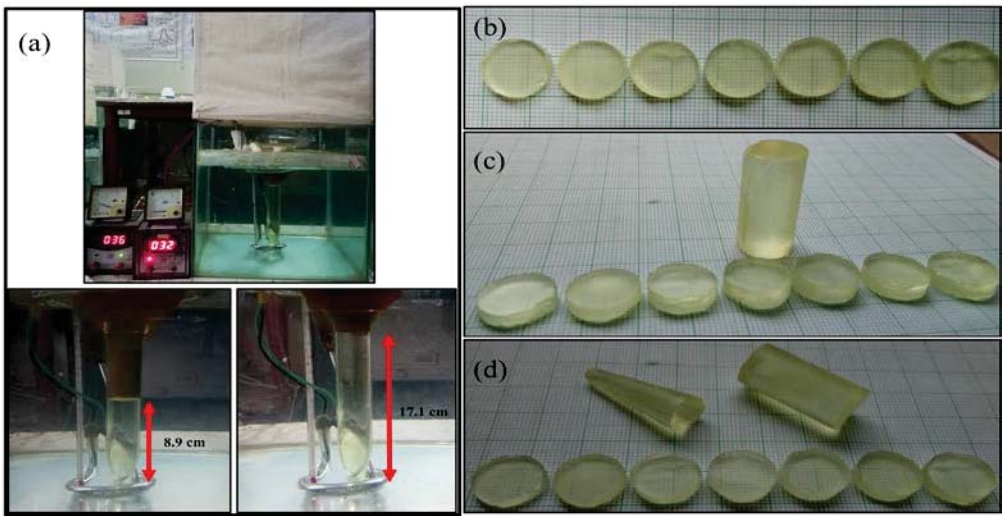

FIGURE.2 (a) Experimental setup of SR method and (b, c & d) Cut and polished SR TP4N crystals

3. Results and discussion

3.1. Powder X-ray diffraction (PXRD) studies

The TP4N powder sample was analyzed by PANalytical X'Pert Pro (λ = 1.5406 Å) PXRD measurement with the scanning ranges from 10˚ to 80˚ (step size of 0.02˚) at room temperature to find the crystallinity and phase purity. The PXRD spectrum of TP4N is shown in Fig. 3 (a). From the figure, sharp peaks and different hkl planes such as (01-1), (110), (02-1), (02-2), (1-1-3) (211) and (020) are observed. It indicates that the grown TP4N has good crystalline perfection.

3.2. High-Resolution XRD (HRXRD) analysis

The crystalline perfection of the TP4N single crystal was characterized by HRXRD measurement using a PANalytical multifunctional X-ray diffractometer. The well collimating monochromated CuKα1 X-ray beam was received from four bounce monochromator of Ge (200) crystals set in a dispersive (+,-,-,+) configuration. The TP4N wafer was subjected to the PXRD along the <011> direction and the spectrum is shown in Fig. 3 (b). The obtained peaks are (011), (022) (033) and (044) and hence it confirms that the grown crystal becomes a single grain. However, the (hkl) plane of (011) has been selected for HRXRD measurement. Fig. 3 (c) shows the HRXRD data, which was collected on a (011) plane with the Bragg geometry angle 2θ = 10.9˚ of TP4N crystal. From the figure, the appeared diffraction curve (DC) is a single peak without any satellite peaks at the corresponding 2θ position, which indicates that the TP4N single crystal is without structural grain boundaries. The full width at half maximum (FWHM) of the peak is 18.1″. The very sharp DC and absence of satellite peaks show that the TP4N has good crystalline perfection [4].

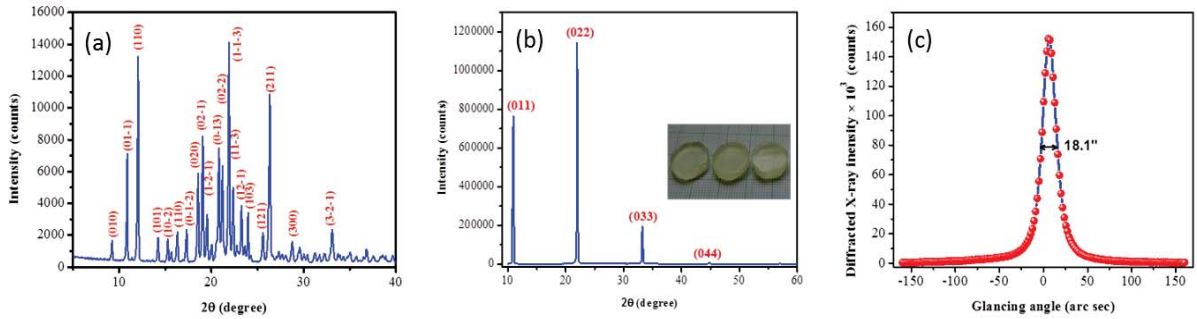

FIGURE.3 (a) Powder XRD pattern, (b) XRD spectrum of the <011> directed TP4N crystal and (c) Rocking method curve of SR grown TP4N single crystal

3.3. UV-Vis NIR spectral analysis

The high transmittance with high band gap value of the organic single crystals is important in the optoelectronic and laser-based device applications. The optical transmittance of SR-grown TP4N crystal with a thickness of 4 mm was characterized by a Perkin-Elmer Lambda-35 spectrophotometer in the range of 200 - 1100 nm. Fig. 4 (a). shows the optical transmittance spectrum (thickness-4 mm) of the TP4N single crystal. The SR grown TP4N crystal has higher optical transmittance (83%) in the near IR region, 60 to 80 % in the visible region and than suddenly decreased. The cut-off wavelength of the SR TP4N crystal was found to be 382 nm. The yellow color presented in the TP4N crystal is because of NO_2 chromophore [5]. The TP4N single-crystal has low absorption in the visible region and hence it is suitable for NLO applications.

3.4. Birefringence Studies

Birefringence interferometry gives a qualitative evaluation of the uniformity of dislocation density in the crystal. In this experiment, the optical homogeneity of the SR method grown TP4N crystal (1 mm thickness) was characterized by the polarized Gaussian beam (TEM00) of He-Ne laser (wavelength= 632.8 nm, Power=10 mW). A beam expander (10X) has been used at the front of the laser source for increasing the laser beam size

from 0.7 mm to 7 mm. The diameter of the output laser beam was controlled by an aperture placed at the front of the sample. The sample (011) was fixed in between the two polarizers. The polarized laser beam is passed into the sample to get ordinary (O-ray) and extra-ordinary (E-ray) rays. These two rays were analyzed by an analyzer (another polarizer) and the interference pattern was got. The obtained interferograms of TP4N single crystal is shown in Fig.4 (b). Normally, the fringes appear irregular on the screen is due to the poor optical homogeneity and quality of the material. The regular fringes with equal spacing reveal high optical homogeneity and quality of the material and also regular fringes suggest that the uniform dislocation density inside the crystal [6]. As seen in the birefringence images the TP4N SR crystal has a better interferogram.

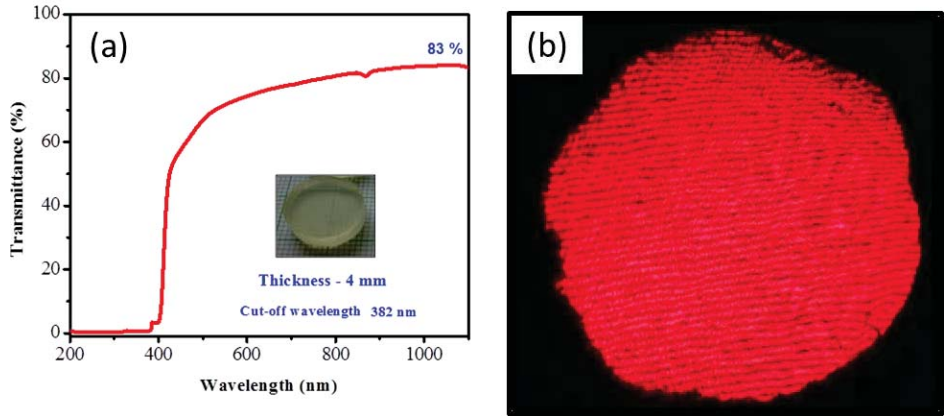

FIGURE.4 (a) UV-Vis NIR spectrum and (b) Birefringence interferogram of TP4N single crystal

4. Conclusion

The good quality single crystal of Triphenylphosphine Oxide 4-Nitrophenol (TP4N) of the dimension 171 mm length and 15 mm diameter was grown along (011) plane by Sankaranarayanan-Ramasamy (SR) method. The various (hkl) planes were analyzed by PXRD. The crystalline perfection was investigated by HRXRD measurement, it was found to be 18.1 arc sec. The UV-Vis NIR spectrum shows that the grown crystal (4 mm thickness) has higher optical transmittance (83%) in the near IR region. The birefringence interferogram reveals good optical homogeneity of the (011) oriented SR grown TP4N crystal.

Acknowledgment

This work was supported by the BRNS project (Ref. 34/14/06/2016-BRNS/34032), Government of India.

References

1. H.G. Gallagher, R. M. Vreelj and J. N. Sherwood, *J. Crystal Growth* **250** 486 (2003) .

2. Krishnakumar, M. Rajaboopathi and R. Nagalakshmi, Physica B Condens. Matter 407 1119-1123(2012).

3. K. Sankaranarayanan and P. Ramasamy *J. Exp. Indust Crystallogr* **41** 225-230 (2006).

4. S. K. Kushwaha, N. Vijayan, G. Bhagavannarayana, *Mater. Lett* **62** 3931-3933 (2008).

5. N. Sudharsana, V. Krishnakumar and R. Nagalakshmi, *J. Cryst. Growth*. **398** 45-57 (2014).

6. Indranil Bhaumik, R. Bhatt, S. Ganesamoorthy, A. Saxena, A. K. Karnal, P. K. Gupta, A. K. Sinha and S. K. Deb. *Appl. Opt* **31** 6006-6010 (2011).

Investigations on structural, optical, and electrical properties of Neodymium doped rubidium titanyl phosphate single crystal (Nd: $RbTiOPO_4$)

Rajesh Narayana Perumal [a, b*], Arulmani Marimuthu [a, b]

[a] *Centre for Radiation Environmental Science and Technology, Sri Sivasubramaniya Nadar College of Engineering, Kalavakkam, Chennai 603 110, India*
[b] *Department of Physics, Sri Sivasubramaniya Nadar College of Engineering, Kalavakkam, Chennai 603 110, India*
EMail: rajeshnp@ssn.edu.in, arulmaniphysics@gmail.com

Abstract

Rubidium titanyl phosphate (RTP) single crystals are very much attractive and important in electro-optics [1]. In the isostructural KTP series, Rubidium titanyl phosphate has recently attracted special interest because of its high thermal stability and good optical nature. The materials with efficient second-harmonic generation require non-linear materials with various desirable properties, and hence they are widely used in non-linear optics, electro-optics device applications [3-5]. The non-linear optical properties of RTP crystals are similar to potassium titanyl phosphate single crystals. However, RTP crystals are most effective as electro-optical modulators, waveguides, and high-intensity Q switch applications due to lower conductivity. RTP is one of the non-linear ferroelectric single crystal extensively used in periodically poled structure making, these devices are most beneficial for the quasi-phase-matching (QPM) application for obtaining high intense laser output [6].

At atmospheric pressure RTP crystallizes below Curie temperature and exhibits non-centrosymmetric orthorhombic crystal structure with the space of $Pna2_1$ [7]. At higher temperatures, RTP structure display a reversible ferroelectric-to-paraelectric phase shift, with the Curie temperature ranging from 785°C to 829°C depending upon the composition and growth temperature. After the second-order phase change, the crystal structure is owned by the centrosymmetric space group of Pnan [8]. The crystal structure of the material was constructed through the three-dimensionally joined TiO_6 and PO_4 groups where rubidium ions are positioned in the two sites [9]. The materials' high temperature phase transition properties are of great interest in high thermal stability and are excellent in electrical nature.

Neodymium doped Rubidium Titanyl Phosphate (RTP) single crystal was grown using a high-temperature flux solution method with rubidium polyphosphate flux. Though doping does not induce changes in growth temperature, variations in material properties were observed while characterizing the grown crystal. Figure 1 shows the as grown crystal and Figure 2 shows the cut and polished crystal. Powder x-ray diffraction of Nd: RTP suggested the orthorhombic structure with small structural distortion. The optical quality of the material was studied using optical transmittance and absorption studies. The variation in the optical band gap due to Nd doping was also analyzed. The dielectric polarization, ion hopping, activation processes, and the dielectric, conductivity, and resistivity nature of the material were studied using impedance analysis. The properties were studied from room temperature to 850°C and frequencies from 100 Hz to 8 MHz. and the results were compared with flux-grown pure

RTP single crystals. The result exhibited superior properties on Nd doping in RTP. The low and static dielectric constant exhibited by Nd: RTP made it suitable for NLO applications. The ferroelectric nature of the Nd: RTP was analyzed from room temperature to 180oC at an applied field of 4 kV and the PE loop was found with values of polarization and coercive field as 0.15 μC/cm2 and 1.79 kV/cm, respectively.

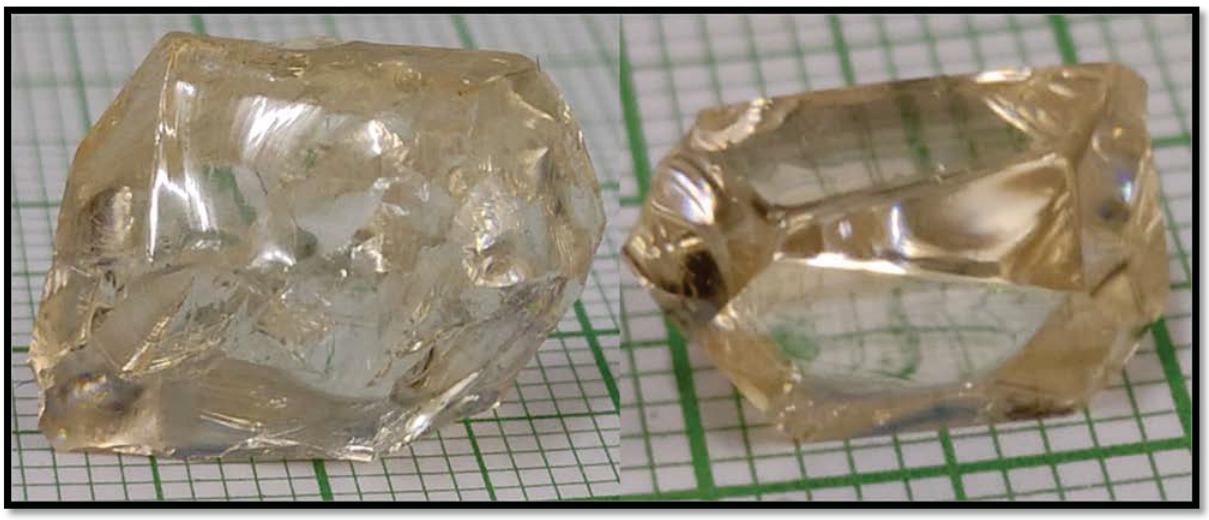

Fig 1: *As grown Nd: RTP single crystals*

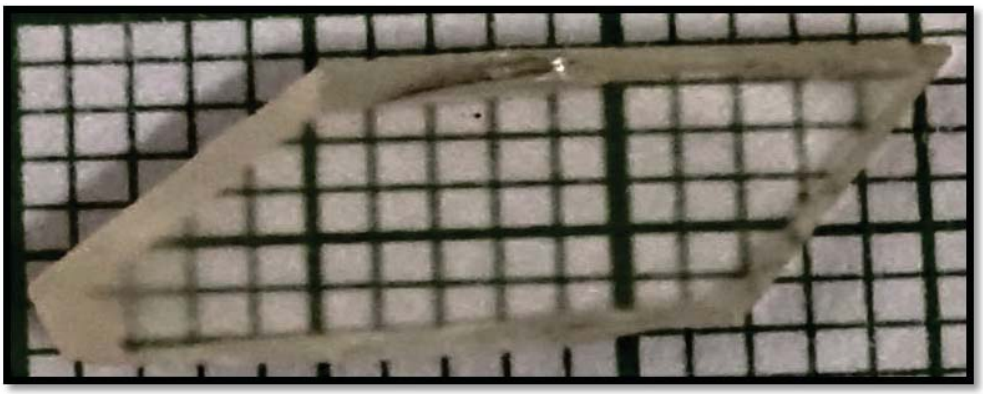

Fig 2: *Cut and polished portion of Nd: RTP*

References

[1] Y.J. Yu, X.Y. Chen, C. Wang, C.T. Wu, M. Yu, G.Y. Jin, High repetition rate 880 nm diode-directly-pumped electro-optic Q-switched Nd:GdVO4 laser with a double-crystal RTP electro-optic modulator, Opt. Commun. 304 (2013) 39–42.

[2] H. Albrecht, P. Villeval, C. Bonnin, Study of RTP crystal used as electro-Optic modulator, Opt. InfoBase Conf. Pap. (2006) 3–5.

[3] C. V. Kannan, S. Ganesa Moorthy, V. Kannan, C. Subramanian, P. Ramasamy, TSSG of RbTiOPO4 single crystals from phosphate flux and their characterization, J. Cryst. Growth. 245 (2002) 289–296

[4] Y.S. Oseledchik, S.P. Belokrys, V. V. Osadchuk, A.L. Prosvirnin, A.F. Selevich, V. V. Starshenko, K. V. Kuzemchenko, Growth of RbTiOPO4 single crystals from phosphate systems, J. Cryst. Growth. 125 (1992) 639–643..

[5] J. Guo, B. Raghothamachar, M. Dudley, J.J. Carvajal, A. Butt, M.C. Pujol, R.M. Sole, J. Massons, M. Aguilo, F. Diaz, Effect of doping on crystalline quality of rubidium titanyl phosphate (RTP) crystals grown by the TSSG method, Mater. Res. Soc. Symp. Proc. 1698 (2014).

[6] A. Fragemann, V. Pasiskevicius, J. Nordborg, J. Hellström, H. Karlsson, F. Laurell, Frequency converters from visible to mid-infrared with periodically poled RbTiOPO4, Appl. Phys. Lett. 83 (2003) 3090–3092.

[7] A. LYAKHOV, A. SELEVICH, A. VERENICH, Crystal structure of rubidium titanyl phosphate α-RbTiOPO, Russ. J. Inorg. Chem. 38 (1993) 1040–1042.

[8] C. V. Kannan, S. Ganesamoorthy, C. Subramanian, P. Ramasamy, Dielectric properties of self-flux-grown RbTiOPO4 single crystals, Phys. Status Solidi Appl. Res. 196 (2003) 465–470.

[9] E.I. Agapova, V.I. Voronkova, E.P. Kharitonova, I.N. Leont'eva, S.Y. Stefanovich, N.I. Sorokina, A.P. Dudka, O.A. Alekseeva, N.N. Kononkova, Synthesis and properties of zirconium-doped RbTiOPO4 single crystals, Crystallogr. Reports. 53 (2008) 285–290.

Design and analysis of silicon photonic switch matrix for reconfigurable electronic-photonic integrated circuits

Mubarak Ali M, Madhupriya G, Indhumathi R, Krishnamoorthy Pandiyan
Integrated Optics Lab, Centre for Nonlinear Science and Engineering (CeNSE),
School of Electrical & Electronics Engineering, SASTRA Deemed University, Thanjavur-613401, Tamil Nadu, India.
Email: krishpandiyan@ece.sastra.edu

Abstract In this article a silicon photonic switch matrix (PSM) is designed for reconfigurable electronic-photonic integrated circuits (RePIC), which includes the 1x1 ON-OFF silicon photonic switch and a tunable directional coupler (TDC). The proposed PSM routes the incoming four light signals in all the possible directions with the help of six 1x1 ON-OFF switches and a TDC. The control of the ON-OFF switch and the tunable directional couplers are performed using the forward-biased PIN junction configuration utilizing the plasma dispersion effect, where the change in refractive index is obtained by altering the carrier concentration with the external electric field. The individual components are designed using the beam propagation method (BPM) and the transmission characteristics are converted into a compact numerical model (CNM) and are utilized in a block-based circuit design approach for large-scale photonic integrated circuits. This provides flexibility in expressing large-scaled photonic circuits without performing the physically-based electromagnetic simulation.

Keywords: silicon photonics, reconfigurable electronic-photonic integrated circuit, photonic switch matrix, reconfigurable directional coupler.

I. Introduction

The research on photonic integrated circuits has emerged from the last decades, which integrates active and passive photonic components in a monolithic or heterogeneous way on a single chip. The photonic IC platforms such as SoI, SiN, InP, and LNoI are being developed to an industrial scale [1, 2]. Further, the heterogeneous integration of lithium niobate (LN) with SoI waveguides has attracted significant interest, which enabled electro-optical tunable resonators, Mach-Zehnder modulators, and Mid-IR modulators. The industry ready silicon platform such as SoI follows a zero-change CMOS fabrication process to fabricate the silicon photonic components.

II. Design of photonic switch matrix

The proposed photonic switch works based on the ON-OFF switching mechanism using a 1x1 directional coupler. This can be viewed with a traditional 2x2 directional coupler with a waveguide that is internally terminated. The architecture view of the 1x1 ON-OFF photonic switch is shown in Fig.1(a). During the absence of an external electric field, the incoming light takes the cross-state operation and the maximum light intensity is absorbed with the help of termination block [1,2], and a very minimum, negligible amount of intensity will be available at the access waveguide, this state of operation is considered as OFF-state. With an external electric

field, the incoming light traverses in the same waveguide without coupling to the adjacent waveguide, hence a maximum amount of intensity will be available at the end of the access waveguide. This state of operation is known as ON-state [3].

The input-output electric field relations in terms of field-coupling coefficient (κ) is derived as follows [4]. The electric field of the light at the output port (E_o) is expressed using equations (1) and (2), in which the equation (2) acts as the characteristic equation for the 1x1 ON-OFF photonic switch.

$$\begin{bmatrix} E_{o1} \\ E_{o2} \end{bmatrix} = \begin{bmatrix} \sqrt{1-\kappa(V)} & j\sqrt{\kappa(V)} \\ j\sqrt{\kappa(V)} & \sqrt{1-\kappa(V)} \end{bmatrix} \begin{bmatrix} E_{i1} \\ E_{i2} \end{bmatrix} \tag{1}$$

where, E_{o1}, E_{o2} represents the output electric fields of the input lights, E_{i1}, E_{i2} are the electric fields of the input lights, κ is the cross field-coupling factor, and $\kappa(V)$ represents the voltage-controlled field-coupling factor, which is obtained by forward biased PIN configuration [1,4].

$$E_o = \sqrt{1-\kappa(V)}E_i \tag{2}$$

The value of the field-coupling factor decides the ON-state, tunable-sate, and OFF-state operation. The maximum value field-coupling coefficient (κ ~1), leads to maximum coupling to the terminal block, and the minimum value (κ ~0) results in the transmission of the input light to the output port.

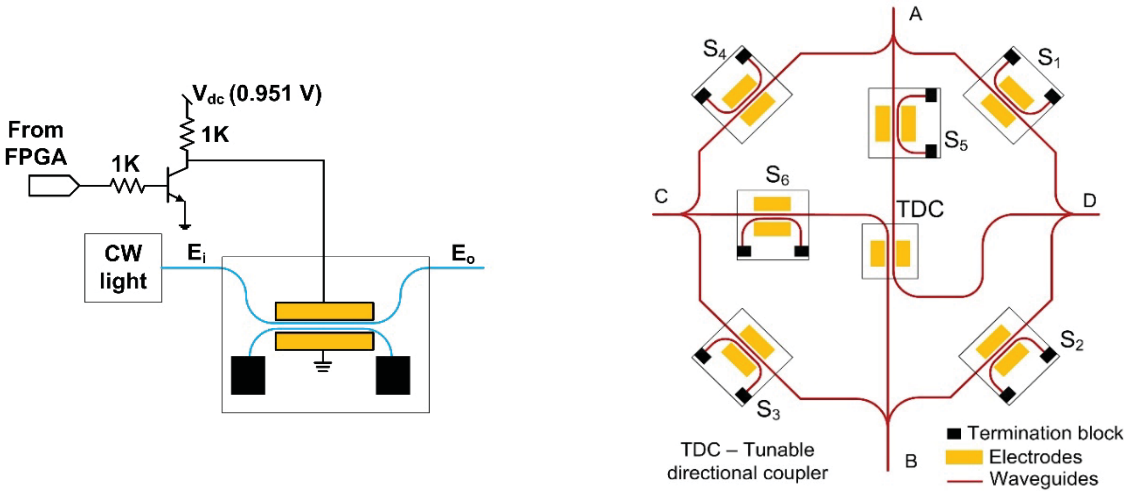

Fig.1 The schematic representation of (a). 1x1 silicon photonic switch [1] (b) the proposed reconfigurable photonic switch matrix.

The proposed reconfigurable switch matrix is shown in Fig.1 (b), where it includes 6-number of 1x1 switches (S_1 to S_6) and a tunable directional coupler. Based on the developed compact numerical model of 1x1 photonic switch, and the tunable directional coupler the photonic switch matrix is constructed [4,5].

III. Results and discussion

The light signal available at port-A and port-C can simultaneously be routed to port-B and port-D respectively, and its transmission characteristics are shown in Fig.2 (a). To establish path A to B, switches S_1, S_4 should be maintained in OFF-state, switch S_5 should be maintained in the ON-state, and the tunable directional coupler (TDC) should be maintained in the cross-state. At the same time, to establish the path from C to D, switch S_3 should be maintained in OFF-state, switch S_6 should be maintained in ON-state, and the TDC is already configured in cross-state. The input lights at port-A and port-C take cross-state propagation in TDC and propagate to the respective output ports port-B and port-D. The incoming light at port-A is routed to port-D via switch S_1, at the same time the switches S_4 and S_5 are maintained in OFF-state to avoid the interference due to light at the port-C is illustrated in Fig.2 (b). Similarly, the routing paths from A to C is established. In the same way, the routing paths from C to B is established by maintaining the switch S_3 in ON-sate the switch S_6 in OFF-state. Similarly, the path B to D is established.

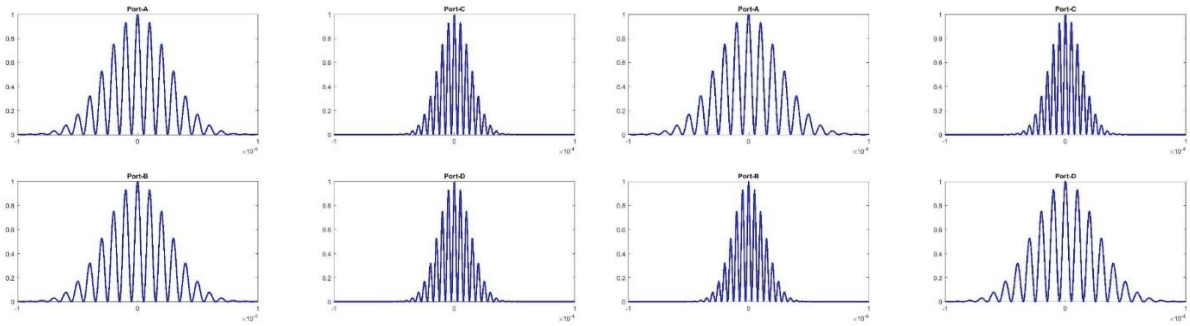

(a) (b)

Fig.2 Simulation results for the configuration of (a). bar-state (A to B, C to D) routing and (b). cross-state (A to D, B to C) routing.

IV. Conclusion

In this paper, we proposed a reconfigurable photonic switch matrix and numerically demonstrated using two 1x1 photonic switches and a tunable directional coupler. The designed 1x1 photonic switch shows an ON-state insertion loss of 0.02 dB at 0.951 V and an OFF-state loss of -11.04 dB at 0 V. The same geometrical dimensions were adopted for the tunable directional coupler, that exhibits only bar-and cross-state operation. Numerical simulations confirming the photonic switch matrix and various figures of merit are calculated from the simulation results. In conclusion, based on the optimum performance, the photonic switch matrix can be used for the reconfigurable photonic integrated circuits.

References

1. M.A.Meerasha, T.S. Meetei, G. Madhupriya et al. *J Comput Electron* 2020, **19**, 1651.
2. M. A. Meerasha, and K. Pandiyan Electronics Letters, 2020, **56**, 1130
3. Daniel Pérez-López, Ana M. Gutierrez, Erica Sánchez, et al. *Opt. Express* 2019, **27**, 38071.
4. Bogaerts, Wim, Daniel Pérez, José Capmany, et al. *Nature* 2020, **586**, 207.
5. Lu, Zeqin, Han Yun, Yun Wang, et al. *Optics express* 2015, **23**, 3795.

Synthesis, crystal growth and characterizations of 2-amino-5-nitropyridinium trichloroacetate (2A5NPTCA): an efficient single crystal for optoelectronic applications

V. Sivasubramani, Muthu Senthil Pandian*, P. Ramasamy

Research Centre, Sri Sivasubramaniya Nadar College of Engineering, Chennai-603110, Tamil Nadu

Email: sivasubramaniv1989@gmail.com

Abstract

2-amino-5-nitropyridinium trichloroacetate (2A5NPTCA), a potentially useful compound has been synthesized and grown as optically transparent single crystals by conventional method with a span of 90 days. The structure formation was confirmed by the SXRD analysis. The grown crystal belongs to the monoclinic crystal system with the centrosymmetric space group, $P2_1/n$. The grown crystal possesses 60% of optical transmittance in the visible and NIR region and thermally stable upto 158°C. The LDT property was evaluated by Nd: YAG laser of wavelength 1064 nm. The third-order nonlinearity and optical limiting properties were evaluated using a diode laser operated at 532 nm.

1. Introduction

In recent years, intensive research has been undertaken on organic nonlinear optical (NLO) materials because of their potential applications in frequency mixing, electro-optical modulation, optical switching, optical telecommunications, optical data storage, laser devices, terahertz wave generation and detection, etc [1-2]. The organic NLO materials have attracted a great deal of attention for material scientists owing to their immense features including synthetic flexibility for making novel materials, the existence of macroscopic nonlinearity, ultrafast optical response time and ease of device fabrication process. The rapid advancements in optical communication systems have led to a demand for organic NLO materials for the high performance of optical devices. In this context, 2-amino-5-nitropyridine (2A5NP) chromophore is a remarkable cation for NLO applications as they have π-conjugated push-pull charge transfer structure. In this chromophore, the amino group acts as an electron donor and the nitro group acts as an electron acceptor to induce the large nonlinearity. The pyridine ring plays a significant role in the cationic bonding site [3]. In addition, the presence of pyridinium nitrogen and amino group in this chromophore plays as proton acceptors to induce a large NLO response. Owing to the asymmetry of charge transfer π-conjugated structure of 2A5NP chromophore, it is recognized as a noteworthy candidate for the building blocks of NLO applications. Among the organic and inorganic materials, the trichloroacetic acid-based complexes possess excellent NLO and physico-chemical properties. From the above discussion, it is very interesting to investigate the 2A5NP chromophore associated with trichloroacetic acid for crystal engineering. The detailed literate report reveals that there are no significant studies on bulk crystal growth and physico-chemical investigations on 2A5NPTCA single crystals. Only, the structural properties have been investigated by Yvette et al [4]. Therefore, the present investigation has been taken up to grow optically transparent 2A5NPTCA single crystals by slow evaporation solution technique (SEST) and to study its structural, optical and thermal properties.

2. Synthesis and crystal growth of 2A5NPTCA

The title compound was synthesized using the raw material of 2A5NP and trichloroacetic acid in the equal molar ratio of 1:1 at 50°C. HPLC grade methanol was used as solvent for synthesis. The solubility of the title crystal was carried out by the gravimetric method in the temperature range from 35-55°C. The solubility of 2A5NPTCA material was found to be 5.01 g/100 mL in methanol at 35°C. Transparent single crystals with the dimension of 10×7×3 mm^3 were harvested after 90 days. The reaction scheme and photograph of as-grown crystals are shown in *Figure 1. (a) and (b)*, respectively.

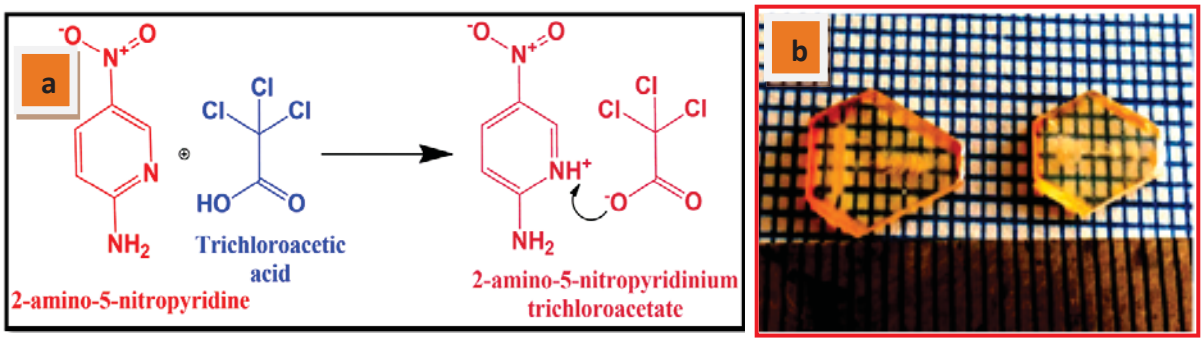

Figure. 1 (a) Reaction scheme and (b) photograph of as grown 2A5NPTCA single crystals

3. Characterizations

The formation of 2A5NPTCA single crystal was confirmed by the single-crystal X-ray diffraction (SXRD) analysis using Bruker AXS Kappa APEX-II single-crystal X-ray diffractometer, equipped with graphite-monochromated MoK_α radiation (λ=0.71073Å). The linear optical properties were evaluated using a UV-Vis-NIR spectrophotometer (Model: Perkin-Elmer Lambda 35) in the scanning range of 200 nm to 1100 nm. The thermal property was analyzed using the Perkin-Elmer Diamond thermogravimetric (TG) and differential thermal analysis (DTA) instrument in the temperature range of 30°C to 300°C with nitrogen atmosphere. The LDT measurement for the 2A5NPTCA single crystal was carried out using a Q-switched Nd: YAG laser (Make Litron Lasers, UK) having a fundamental wavelength of 1064 nm. To determine the third-order NLO properties of the grown crystal, the single-beam Z-scan technique has been conducted by employing a diode laser of wavelength 532 nm. The power of the laser was 100 mW. For this experiment, the Gaussian beam was focused onto the crystal and then the sample was smoothly translated along the -Z and +Z direction with the propagation direction of the laser beam. For each translation, the intensity of the transmitted light was measured by the open/closed aperture placed in a far-field as a function of sample position. For the case of closed aperture (CA) measurement, the intensity of the source light was recorded by the photodetector by fixing an aperture radius of 2 mm. The optical limiting (OL) property of the 2A5NPTCA single crystal was measured using CW laser operated at 532 nm.

4. Results and discussion

The SXRD result reveals that the grown crystal belongs to the monoclinic crystal system with a centrosymmetric space group, $P2_1/n$. It crystallizes with four molecules in the unit cell. The molecular weight and density are found to be 302.5 g/mol and 1.726 g/cm^3, respectively. The obtained unit cell parameter values are a = 14.33 (±0.02) Å, b = 6.932 (±0.011) Å, c = 12.479 (±0.020) Å, α = γ = 90°, β = 103.01° (±0.03), Volume (V) = 1208 (±6) $Å^3$. The obtained results are agreed well with the previously reported values [4]. The

well-polished 2A5NPTCA single crystal with a thickness of 2 mm was subjected to the UV-Vis NIR transmittance analysis and the recorded spectrum is shown in *Figure 2 (a)*. The result illustrates that the grown crystal has a lower cut-off wavelength at 405 nm which facilitates it to be a good candidate for frequency conversion applications. More than 60% of optical transmittance in the visible and NIR region of the grown crystal is attributed to the occurrence of less absorption and the less scattering centers. Hence, it is noticed that the optical transmittance of the grown crystal seems to be quite good and this property leads to the positive sign for its usefulness in the linear and nonlinear optical device applications [5]. The appearance of reddish-yellow color in the title crystal can be attributed to the presence of NO_2, NH_2, NH^+ and COO^- chromophores.

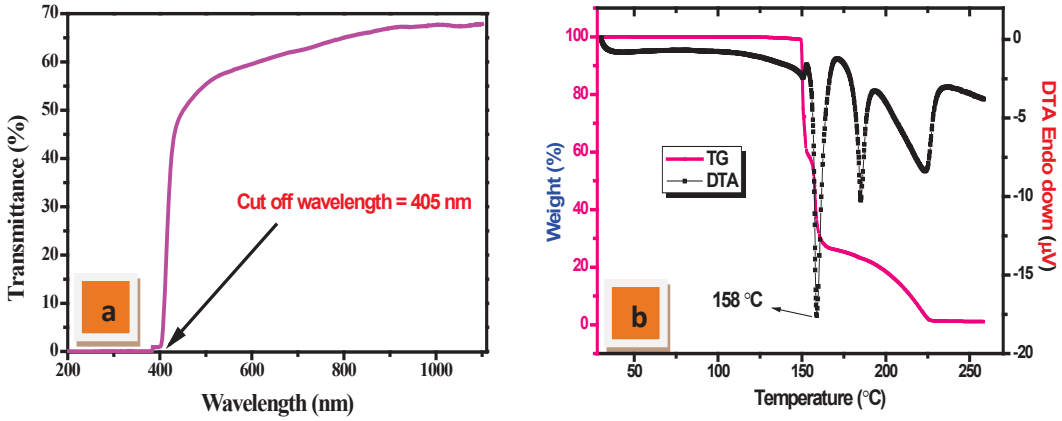

Figure 2. (a) UV-vis-NIR and (b) TG and DTA spectra

The recorded TG-DTA spectra are shown in *Figure.2 (b).* The TG spectrum shows that there is no peak in the temperature range between 30°C to 150°C which evidences the absence of moisture in the grown crystal. The dissociation in the temperature range between 150°C to 225°C is due to the elimination of volatile gaseous products. The sharp endothermic peak was observed in the DTA spectrum at 158°C which reveals the good crystalline quality and phase purity of the grown crystal. There is no endothermic or exothermic peak observed in DTA spectrum in the temperature range from 30°C to 150°C which reveals the absence of any structural changes upto 150°C. The good thermal stability of the 2A5NPTCA single crystal is attributed to the presence of multiple hydrogen bond interactions between 2A5NP and trichloroacetic acid moieties.

The polished 2A5NPTCA single crystal was placed at the focal point of the laser for the LDT analysis. The laser beam falls onto the crystal surface and then the occurrence of visible damage can be seen when exceeding the threshold with the exposure of high-power laser. The laser damage was determined by the visible microdot/fracture onto the crystal surface and the corresponding intensity of the laser was measured using the power meter. From the analysis, the LDT for the grown crystal was calculated to be 3.1 GW/cm^2. The normalized open aperture (OA) spectrum of the 2A5NPTCA single crystal is shown in *Figure 3 (a)*. Here, the transmittance is found to be maximum at the focus (Z=0) when increasing optical intensity, which indicates the nonlinear saturable absorption and positive absorption coefficient of the grown crystal. The CA spectrum is presented in the inset of *Figure 3 (a)*. It clearly shows that the grown crystal possesses the configuration of the pre-focal peak to post-focal valley in transmitted intensity which indicates the occurrence of negative nonlinear refractive index and it is facilitating the self-defocusing effect. The arising of the self-defocusing effect is due to the local change of refractive index with temperature. The calculated values of third-order nonlinear refractive index (n_2), third-order nonlinear absorption coefficient (β) and third-order nonlinear susceptibility ($\chi^{(3)}$) are

found to be 7.24×10^{-8} cm^2/W, 0.09×10^{-4} cm/W and 4.2×10^{-8} esu, respectively. Such type of materials is more desirable for the development of the protection of optical sensors like night vision devices [6]. The measured OL response of the title crystal is shown in *Figure.3 (b)*. It reveals that the intensity of the output transmittance linearly increases at low input intensity and then the output transmittance reaches flat beyond the 6.7 mW/cm^2. This indicates the obvious OL behavior of the grown single crystal. Hence, the obtained results are very interesting which satisfies the essential requirement for the OL device applications. All the above experimental results lead to conclude that the grown 2A5NPTCA crystal is a promising candidate for optoelectronic device applications.

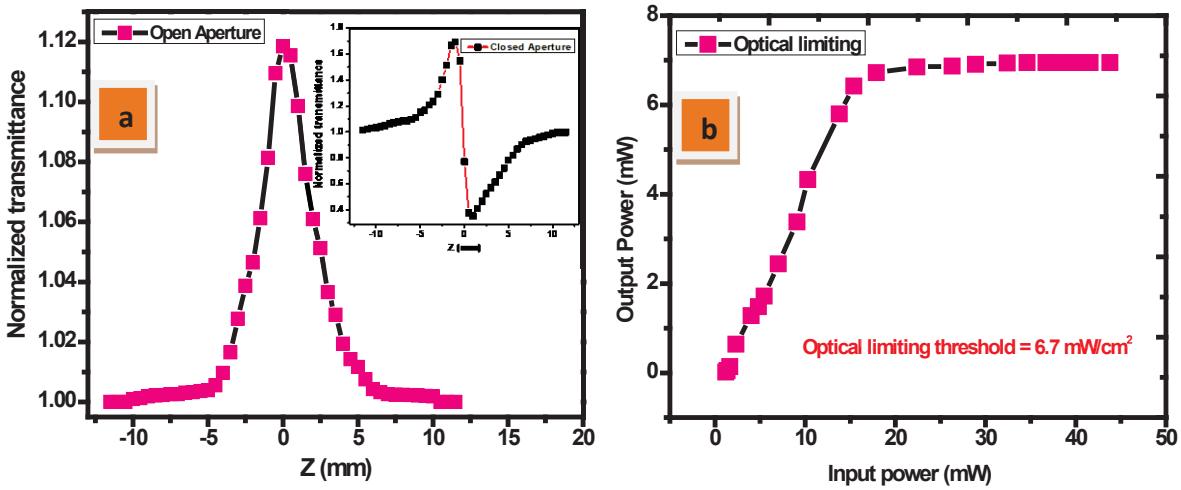

Figure 3. (a) OA spectrum (Inset CA-spectrum) and (b) OL spectrum of 2A5NPTCA single crystal

5. Conclusion

The high NLO active 2A5NPTCA single crystal was successfully grown by the SEST with a size of $10\times7\times3$ mm^3. The formation of crystal structure was confirmed by SXRD analysis. The grown crystal possesses more than 60% of optical transparency in the visible and NIR region. The LDT of the grown crystal was found to be 3.1 GW/cm^2. The Z-scan study reveals that the grown crystal exhibited a large nonlinear absorption behavior. The third-order susceptibility and optical limiting threshold of the grown crystal are found to be 4.2×10^{-8} esu and 6.7 mW/cm^2 at 532 nm, respectively.

References

1. T. Pal, T. Kar, G. Bocelli, and L. Rigi, Cryst. Growth Des, 3, 13-16 (2003).
2. M. Dadsetani, and A. R. Omidi, J. Phys. Chem. C, 119, 16263-16275 (2015).
3. V. Sivasubramani, V. Mohankumar, M. Senthil Pandian, and P. Ramasamy, CrystEngComm, 37, 5662-5678 (2017).
4. Y. Le Fur, M. Bagieu-Beucher, R. Masse, J.F. Nicoud, and J.P. Lévy, Chem. Mater, 8, 68-75(1996).
5. M. Senthil Pandian, N. Pattanaboonmee, P. Ramasamy, and P. Manyum, J. Cryst. Growth, 314, 207-212 (2011).
6. Zhou, Yun-shan, En-bo Wang, Jun Peng, Jie Liu, Chang-wen Hu, Ru-dan Huang, and Xiaozeng You, Polyhedron, 18, 1419-1423 (1999).

Acknowledgment

We acknowledge Dr. Vinitha Gandhiraj, School of Advanced Sciences, VIT University (Chennai Campus) for providing the Z-scan facility and Dr. Soma Venugopal Rao, Advanced Center of Research in High Energy Materials, University of Hyderabad for the LDT facility.

A technique for directly cutting type-I SHG plates from as-grown KDP crystal and assessment of its orientation

S. K. Sharma*[1], Yashpal Singh[1], Indranil Bhaumik[1,2] and A. K. Karnal[1,2]

[1] *Crystal Growth Laboratory, Crystal Growth and Instrumentation Section, Laser and Functional Materials Division, Raja Ramanna Centre for Advanced Technology, Indore, (M.P.) 452013*

[2] *Homi Bhabha National Institute, Training School Complex, Anushakti Nagar, Mumbai 400094, India*

*e-mail: sks@rrcat.gov.in

Abstract: In this article a technique is presented to cut type-I SHG elements conveniently from as-grown KDP crystal using a diamond coated wire saw. For this purpose, a mount was designed and fabricated which was fixed on the sample stage of the wire saw. The mount facilitates to maintain azimuthal angle (φ) at 45° for the direction normal to the cutting plane. This mount was used to successfully slice an as-grown KDP crystal to prepare type-I SHG plates. The orientation of the plate was confirmed by SHG test using an Nd:YAG laser confirming the acceptable angular accuracy of ± 0.5° from the normal to the plate.

1. INTRODUCTION

Potassium dihydrogen phosphate, KH_2PO_4 (KDP) is an important nonlinear optical crystal for frequency doubling, tripling, and Q switching of high power Nd doped glass or YAG laser.[1] KDP belongs to tetragonal point group ($a = b \neq c$) and hence is a uniaxial crystal having a single optic axis along its crystallographic c-axis. Preparation of a specific device from an as-grown KDP crystal requires to cut it normal to a specified direction usually defined by two angles namely, θ - the polar angle, and φ - the azimuthal angle. θ denotes the angle between the direction and the z-axis, while φ is the angle made with x-axis in the x-y plane as shown in Fig. 1(a). KDP crystal is usually grown by platform technique where the growth morphology acquires usually a shape like tetragonal-pyramidal as shown in Fig. 1(b).[2-3] It has well defined faces denoted by Miller indices {100} and {101} called as prismatic and pyramidal faces, respectively. The edges between adjacent prismatic faces denotes the direction of crystallographic c-axis. These direction and faces are normally used as reference for cutting the crystal for specific device application. KDP is predominantly employed for laser frequency doubling and Q-switching of high power Nd doped solid-state lasers. For SHG application, the crystal is required to cut perpendicular to the phase matching direction defined by two angles (θ_{PM} and φ_{PM}) with respect to crystallographic axes.

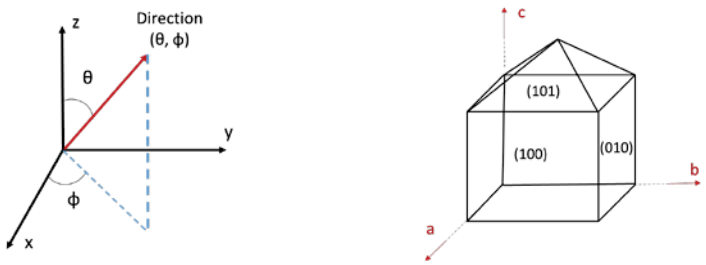

(a) (b)

Fig. 1 (a) Schematic showing a direction (θ,φ) with respect to Cartesian axes, and (b) Schematic of the morphology of KDP crystal grown by platform technique with directions marked along crystallographic axes.

There are two types of phase matching in case of KDP crystal called as type-I and type-II.[4] The azimuthal angle for type-I phase matching is 45° while that for type-II is 90°. This makes it difficult to orient the KDP crystal particularly for cutting type-I plate because the crystal cannot be mounted using any of its natural face as base. To solve this problem we designed a mount, which facilitates to maintain the required azimuthal angle 45°. This technique makes it easy to slice type-I SHG oriented plate just in single cut. To test this mount a KDP crystal of dimensions 59×57×89 mm^3 (a×b×c) was grown and cut slices using a diamond wire saw. The prepared plates were found to be oriented to type-I SHG direction within an accuracy of ±0.5°.

2. EXPERIMENTAL DETAILS

2.1 Methodology

To cut large size KDP crystals for SHG and electro-optic elements a diamond coated wire saw *model STX 1202* [Fig. 2(a)] is used. This machine is equipped with a square flat sample stage in the horizontal plane for placing crystal of size up to 300mm×300 mm cross-section. The sample stage has facilities of x-y translation in horizontal plane and rotation about vertical direction to this plane as shown in Fig. 2(b). The diamond coated wire runs along x-axis reversibly and has facility of precisely move down to cut the sample.

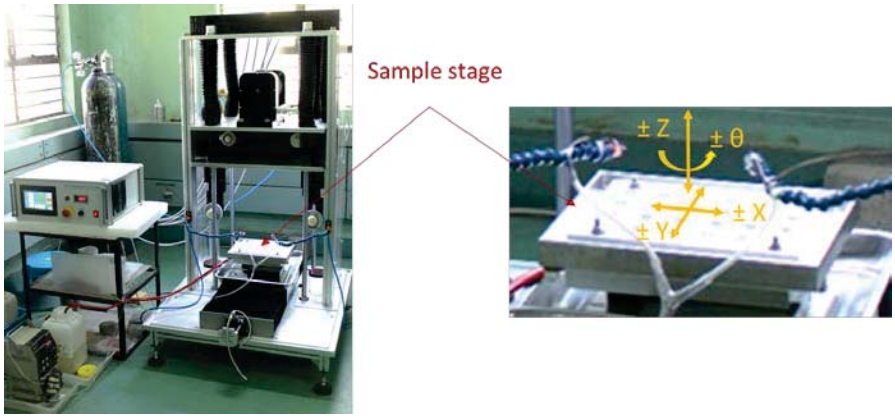

(a) (b)

Fig. 2 (a) Diamond coated wire saw, and (b) enlarged view of its sample stage with depiction of its motions.

The motions of the sample stage and the cutting wire make it suitable to cut a plate normal to any natural face of KDP crystal namely (100) or (101) because these faces are easily identifiable in the crystal morphology and can easily be placed on the sample stage. This makes it easy to cut type-II SHG oriented plate from as-grown KDP crystal as it requires only the motion available in the sample stage but cutting a type-I SHG plate is not possible as there is no such motion available to rotate the sample about another axis, which lies normal to z-axis. This problem is common for commercially available cutting machines. To solve this problem KDP crystal geometry, phase matching angles and the available motions of the sample stage were analysed and devised a mount as shown in Fig. 3(a). It is made of aluminum and having two flat faces at top with 45° inclination from the vertical plane to each side as shown schematically in Fig. 3(b). It makes it easy to achieve azimuthal angle (φ) to be 45°, if KDP crystal is placed with its two adjacent natural prismatic faces in contact with the two slanting faces of the mount, no matter crystal cross-section be square or rectangular. This mount was locked on the top of the sample stage of the diamond wire saw with its edge between two slanting faces lying along the y-axis. Table 1 lists the required orientation of sample stage with respect to a specific orientation of KDP crystal placed on the stage.

Further, as temperature and wavelength involved influence the value of θ_{PM} without affecting the value of φ_{PM}, the same mount can be used for any correction in the polar angle if required.

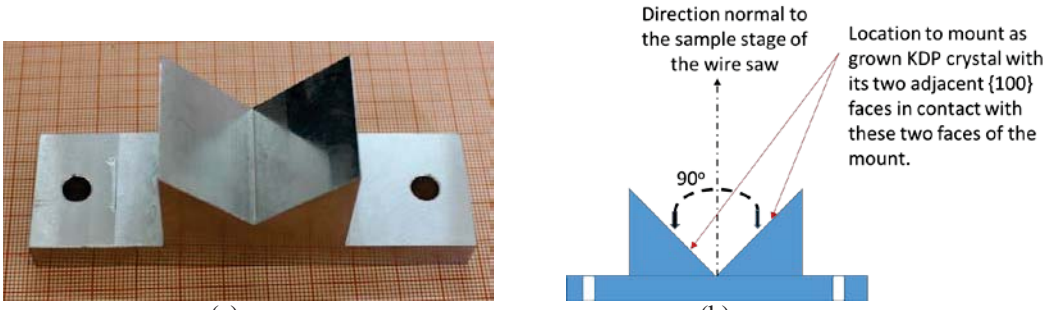

(a) (b)

Fig.3 (a) Actual photo of the mount fabricated, and (b)schematic view of the mount showing location of placing KDP crystal for directly cutting type-I SHG plate from as-grown KDP crystal.

Table 1: Details of the orientation of sample stage with respect to specific orientation of KDP crystal placed at the stage

SHG type	Phase matching angle for laser wavelength 1064 nm[5]		Sample stage rotation (θ)	
	Θ_{PM}	Φ_{PM}	For KDP placed with its c-axis along y-direction of stage	For KDP placed with its c-axis along x-direction of stage
Type-I	41.2°	45°	48.8°	41.2°

2.2 Crystal growth and processing

For testing the mount, a KDP crystal of dimension 59x57x89 mm^3 was grown as shown in Fig. 4(a) using slow cooling technique of solution crystal growth. The solution was prepared using once recrystallised AR grade KDP chemical in high purity demineralized water obtained from a *Millipore* make water purification system. A small size seed crystal was placed at the center of a perspex make platform. The growth parameters were controlled during the growth period resulted in to a visibly transparent crystal without any spurious nucleation.

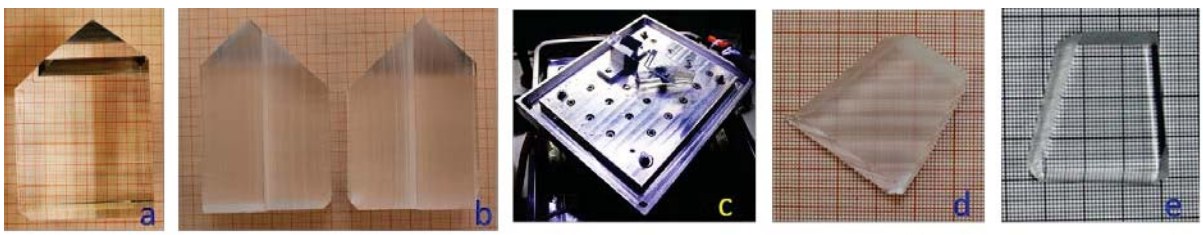

Fig.4 (a) As-grown KDP crystal, Size:59x57x89 mm^3 (a×b×c), (b) the crystal cut into four pieces along c-axis, (c) crystal fixed at the mount and the stage is rotated, (d) as-cut type-I SHG plate, and (e) polished type-I SHG plate.

The crystal was first cut using the wire saw along c-axis and prepared four crystals of cross-section about 28x28 mm^2. Fig. 4(b) shows the photographs of these four pieces. Each of the four pieces has two adjacent natural {100} faces with an intermittent natural edge along c-axis. One of the crystal piece was fixed on the mount to cut type-I SHG plate as shown in Fig. 4(c). Fig. 4(d) shows one of such plates and Fig. 4(e) shows the polished SHG type-I plate.

3. ASSESSMENT OF ORIENTATION OF THE PREPARED TYPE-I SHG PLATE

For geometrical assessment, we calculated the angle occurs at the natural prismatic face of KDP with respect to c-axis when we cut out a type-I SHG plate. This angle (let say α) comes out to be,

$$\alpha = \arctan(\sqrt{2}\tan\theta_{PM})$$

For θ_{PM} =41.2°, α comes out to be 51.1°, while that measured on the actual KDP crystal by a mechanical goniometer is ~ 51° (±1°) confirming the prepared plate is quite close to the intended application.

Further the prepared sample plate was tested for accuracy of its orientation using an Nd:YAG laser. The plate was mounted on an orienter and optimized for maximum SHG output (green color). In this situation, the reflected beam from the front face was located and the shift in the angle from the normal to the plate was geometrically calculated. The obtained value showed that the deviation from exact SHG orientation is within ± 0.5° which is acceptable for the device performance. This test confirms that the designed mount and technique working well.

4. CONCLUSION

In conclusion, a methodology has been developed to directly cut as-grown KDP crystal for the fabrication of type-I SHG elements using a diamond coated wire saw. For this purpose, a mount has been designed and developed. From an as- grown transparent KDP crystal of size 59×57×89 mm^3 SHG type-I oriented sample plates have been successfully cut and tested, exhibiting orientational accuracy to be within ± 0.5°. This technique makes it easier to cut type-I SHG plates, which is usually considered cumbersome.

ACKNOWLEDGEMENTS

The authors thank Shri Deepak Daiya, Scientific Officer, Laser Technology Division, RRCAT for testing the angular accuracy of the prepared SHG plates.

REFERENCES:

1. N. P. Zaitseva, J. J. De Yoreo, M. R. Dehaven, R. L. Vital, K. E. Montgomery, M. Richardson, L. J. Atherton, *J. Crystal Growth*, **180**, 255 (1997).
2. N. P. Zaitseva, L. N. Rashkovich, S.V. Bogatyreva, *J. Crystal Growth*, **148**, 276 (1995).
3. S. K. Sharma, Sunil Verma, Yeshpal Singh, K. S. Bartwal, *Cryst Eng Comm,* **15**, 9995 (2013).
4. R. L. Sutherland, D. G. McLean, S. Kirkpatrick, Handbook of Nonlinear Optics, Marcel Dekker, Inc., New York, 2003.
5. V. G. Dmitriev, G. G. Gurzadyan, D. N. Nikogosyan, Handbook of Nonlinear Optical Crystals, 2nd Edition, Springer Series in Optical Sciences, Berlin, 1997.

Synthesis of copper doped lithium tetraborate ($Cu:Li_2B_4O_7$) nanoparticles and their characterization for structural and thermoluminescence properties

S. Kar[1,*], C. Debnath[1, 2], Sunil Verma[1,2], V.S. Tiwari[1,2], A.K. Karnal[1,2]

[1] *Optical Composite Materials Lab, Ceramic & Composite Materials Section, Laser & Functional Materials Division, Raja Ramanna Centre for Advanced Technology, Indore - 452013, India*

[2] *HomiBhabha National Institute, BARC Training School Complex, Anushakti Nagar, Mumbai - 400094, India*

*Email: sujan@rrcat.gov.in

Abstract:

Cu doped lithium tetraborate powder was synthesized by solid state reaction, and there-afterhigh energy ball mill was used for preparing the nanoparticles. Milling parameters were optimized to get nanometer size particles.Synthesized nanoparticles were characterized for structure by XRD and TEM, and optical properties by thermoluminescence. Observed particle sizes were in the range of 200 nm, and the thermo-luminescence study shows 7-8 times lower TL intensity from nanocrystalline samples as compared to polycrystalline sample, indicating its usefulness for dosimetry applications in high radiation environment.

1. Introduction

Lithium tetraborate is an important optical material for higher order harmonics of Nd:YAG laser. It is also a very useful thermoluminscence dosimetry material having Z_{eff}= 7.25, which is very close to human tissue [1]. Thermoluminescence properties of this material arise due to the presence of point defects. Recently, we investigated the TL properties of Mn doped LTB single crystal and found that the TL intensity is a very sensitive function of mass of the pellet [2]. Tekenaga et al. [3] studied copper doped lithium tetra borate and confirmed that copper doped lithium tetraborate gives better TL intensity than Mn doped lithium tetraborate. Use of nanoparticles is being explored as it leads to newer properties due to dimensional confinement.Nanoparticles have a very large surface area to volume ratio, which results tremendous changes in properties of the material with respect to bulk. If the size of the nanoparticles become very close to the de Broglie wavelength or the Bohr exciton size, an effect known as quantum confinement comes into play. This changes the forbidden gap width and forms new energy levels [4].In this paper we report synthesis of copper doped lithium tetraborate nanoparticles by high energy ball milling,their structural characterizations and thermoluminescence study.

2. Material synthesis

Stoichiometric composition of Li_2CO_3 and B_2O_3 were used to prepare $Li_2B_4O_7$ powder. Two chemicals were mixed for 1hr. in agate mortar. 0.2 Mol % CuO was added to the mixture to get Cu doped lithium tetraborate. The mixture was then milled for 1hr. at the rate of 300 rpm in a high energy ball mill. Homogeneously mixed powder was filled in a platinum crucible and was kept in the furnace and heated up to 400 °C at the heating rate of 100 °C per hour and kept for 3hr. This powder was removed from the crucible and again mixed in an agate mortar for 1h. This mixture was kept in a platinum crucible again and annealed at 750 °C for 10hr. In this process the single phase LTB polycrystalline powder was obtained. The material, prepared by solid state reaction was weighed and divided into 2 parts to put it into ball mill containers. For wet grinding, ethyl alcohol is used as a grinding medium. Milling was done for different milling time with milling speed 500 r.p.m. As the

speed of machine is very high during rotation, temperature of the bowl may increase abruptly. To avoid this, pause time is required in between two rotation cycles. Pause time was set as 5 min for every cycle. Ball to powder mass ratio (BPMR) is also an important factor to reduce the particle size. In our experiment BPMR was kept 2:1. Milling is done for different time duration 5hr., 10hr. and 15hr. After milling, the powder was taken out for characterizations.

3. Characterizations

Powder XRD study: The synthesized nanoparticles were examined by powder X-ray diffractionusing Cu $K\alpha_1$ radiation (λ = 1.5418716Å, Rigaku Geiger Flex X-ray diffractometer) to identify the crystalline phases and to estimate the crystallite size. The XRD patterns were obtained with 2θ in the range of 20 to 70 degree by step scanning, using 2θ increment of 0.01 degree. All peaks of X-ray diffraction were matching with known data (JCPDSfile no. 84-2191). XRD pattern of 5h, 10h and 15 h milled LTB powder is shown in fig. 1.

Transmission electron microscopy study: The Cu:LTB powder samples obtained after 15 hour milling were dispersed in ethanol using ultrasonication for five minutes. The suspended particles are lifted on a carbon coated copper grid with the help of forceps. Then the grid is dried on filter paper under an infrared lamp. For TEM measurements 100 kV was applied, and the obtained TEM micrographs are shown in fig. 2.

Thermoluminescence study: Thermoluminescence study of prepared Cu:LTB nanoparticles was done. Pallets were prepared from Cu:LTB nanoparticles as well as from polycrystalline sample by hydraulic pallet press machine. These pallets were irradiated with X-rays at lithography beam line (BL-07) of Indus-2 SRS facility.In this experiment X-ray spectral energy band of 3-10 keV was used for irradiation. Thermoluminescence spectrum of X-ray–irradiated samples was taken by thermoluminescence dose reader analyzer (model- RA 04). In each case heating rate was kept as $2^oC/s$. TL glow curve of nano crystalline samples were compared with that of polycrystalline sample. TL glow curves of Cu doped LTB pallet made from polycrystal and nanoparticles are shown in figure 3 (a) and 3 (b) respectively.

4. Results and discussion

Nanoparticles of lithium tetraborate prepared through wet grinding process in a planetary ball mill were investigated for their phase, crystallinity, microstructure and particle sizes. The crystalline phase was determined by powder X-ray diffraction (XRD). It has been observed that as we increase the milling time XRD peaks become broader. From the powder XRD pattern effective crystallite size was calculated using full width half maxima (FWHM) approach on the line broadening of XRD peaks. The apparent crystallite size D was calculated from the relation $D=\lambda/B \cos \theta_B$, where λ is the wavelength used and B is the broadening. Calculated size was approximately 40 nm. It can be seen through the TEM micrograph that particle size is varying from 200 nm to 1 μm. It was observed that particle size calculated from TEM analysis is much bigger than the crystallite size. This is because in a single particle many crystalline particles are present. All crystallites are not separate. In our experiment it has been observed that the TL intensity decreases almost 7-8 times in case of nanocrystalline sample as compared to polycrystalline sample. This decrease in TL intensity is due to less energy storage capacity of nanoparticles. Drastic decrease of TL output (7-8 times lower) from pellets prepared

using LTB nanocrystals as compared to those prepared using polycrystals after irradiation with same dose levels suggest that TL materials in nanocrystalline form are suitable for measurement of dose in high radiation environments.

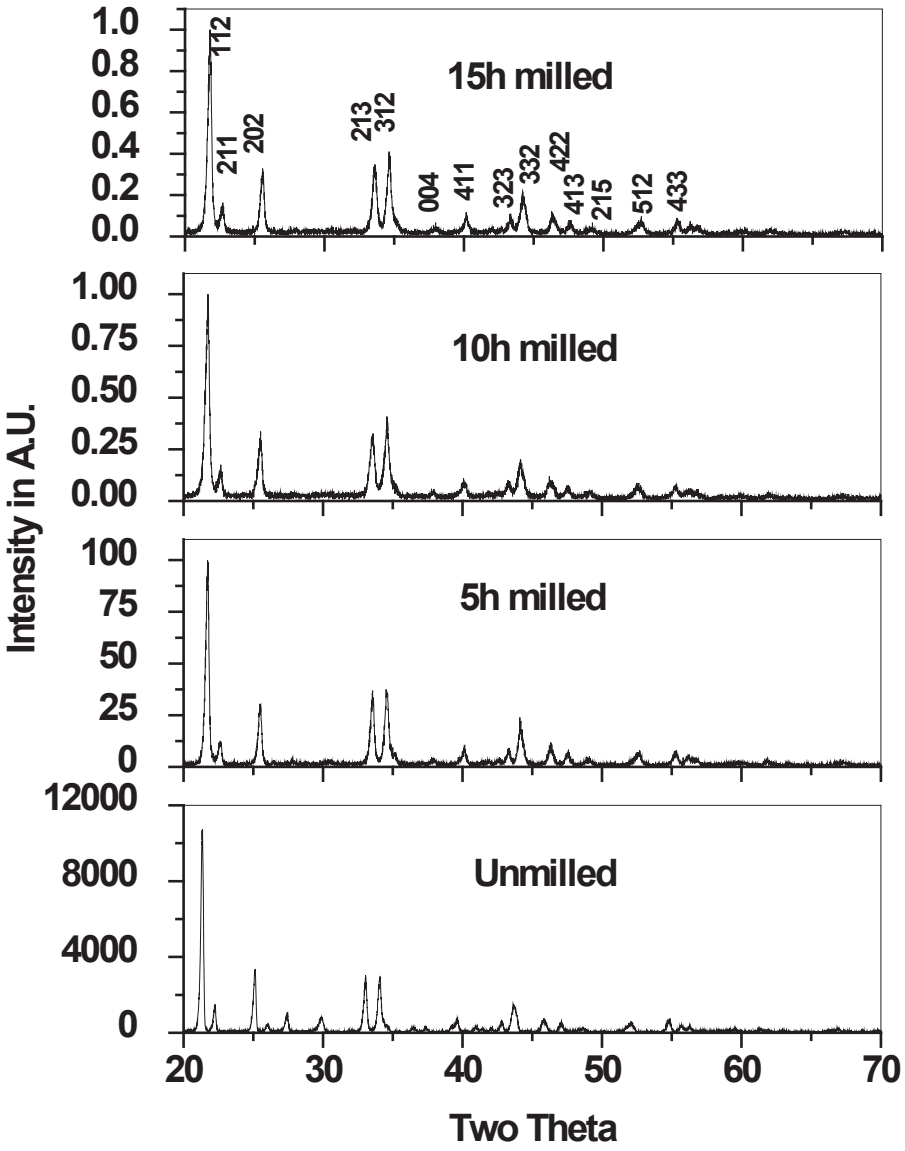

Fig. 1 XRD pattern of ball milled Cu: LTB powder

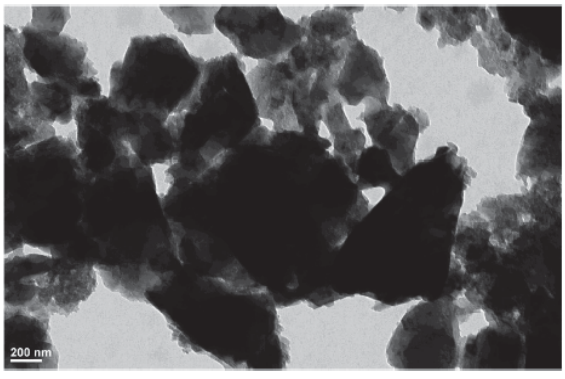

Fig. 2 TEM micrograph of LTB nanoparticles

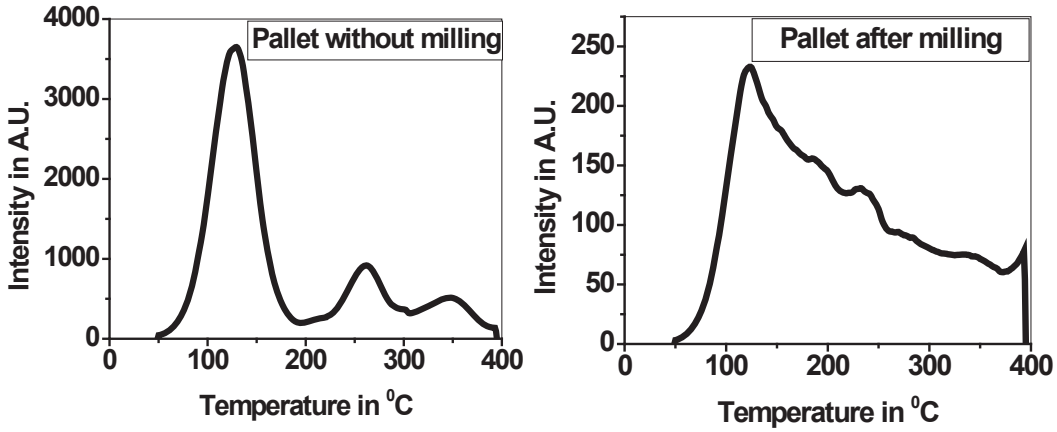

(a) (b)

Fig. 3TL glow curve of Cu: LTB (a) polycrystalline pallet and (b) palletof nanoparticles

5. Conclusions

Cu doped lithium tetraborate nanoparticles were prepared by high energy ball milling technique. Different parameters like ball to powder mass ratio, rpm, milling time etc. were optimized to get almost uniform particle size.It has been observed that wet grinding is preferred to get smaller particle size. XRD results show that the prepared particles retain the phase and the crystal structure of the lithium tetraborate powder. The thermoluminescence study shows 7-8 times lower TL intensity from nanocrystalline samples as compared to polycrystalline sample, indicating its usefulness for dosimetry applications in high radiation environment.

References:

[1] C. Furreta, M. Prokic, R. Salamon, V. Prokic, G. Kitis, Nucl. Instum. Methods Phys. Res. Sect. A**456** (2001)411

[2] S. Kar, S. Bairagi, C. Debnath, S. Verma, K. S. Bartwal, Appl. Phys. Letters **101** (2012) 071904

[3] M. Takenaga, O. Yamamato, T. Yamashita, Nucl. Instru. Methods **175** (1980) 77

[4] V. S. Kortov, Radiat. Meas. 45 (3-6) (2010) 512.

Linear and 3rd order nonlinear optical properties of $LiNbO_3$/PMMA nanocomposite

C. Debnath*[,1,2], Sunil Verma[1,2], Sujan Kar[1], V. S. Tiwari[1,2], A. K. Karnal[1,2]

[1] *Optical Composite Materials Lab, Ceramic & Composite Materials Section, Laser & Functional Materials Division, Raja Ramanna Centre for Advanced Technology, Indore - 452013, India*

[2] *Homi Bhabha National Institute, BARC Training School Complex, Anushakti Nagar, Mumbai - 400094, India*

*Email: cdebnath@rrcat.gov.in

Abstract

Lithium niobate ($LiNbO_3$; LN) is an important nonlinear optical (NLO) material. In this paper, linear and nonlinear optical properties of PMMA and 0.10 wt% LN/PMMA nanocomposites are reported. The linear refractive index (n) was obtained by prism coupling method, the transmittance was obtained using UV-vis-NIR spectrophotometer, and the nonlinear optical properties were measured using Z-scan technique. Using open aperture Z-scan technique, saturable absorption was found in the 0.10 wt% LN/PMMA nanocomposite whereas reverse saturable absorption was found in pure PMMA. Self-focusing nature of nonlinearity was found in LN/PMMA nanocomposite by closed aperture Z-scan. The nonlinear absorption coefficient (β) of PMMA, nonlinear refractive index (n_2) and saturable intensity (I_S) of 0.10 wt% LN/PMMA nanocomposite are computed.

1. Introduction

Lithium niobate ($LiNbO_3$; LN) is technologically important material having perovskite structure with interesting ferroelectric, piezoelectric, pyroelectric and optical properties. It is extensively used in photonics and telecommunication industry for frequency conversion and electro-optic modulation [1]. Currently there is a strong interest in organic-inorganic hybrid composite materials due to ease of fabrication and wide range of nonlinear optical applications [2, 3]. The second order nonlinear response of the LN/PMMA nanocomposite material has been recently reported [4]. Z-scan technique is used for measurement of real and imaginary part of third order susceptibility ($\chi^{(3)}$) of the material, which is responsible for nonlinear refraction (n_2) and nonlinear absorption (β) respectively. For saturable absorption, the saturable intensity is measured [5].

2. $LiNbO_3$/PMMA nanocomposites

The nearly stoichiometric LN nanoparticles with average diameter ~ 100 nm were synthesized by citrate gel method [6, 7]. To get LN/PMMA nanocomposite having LN nanoparticle concentration of 0.10 wt%, the synthesized LN nanoparticles were dispersed homogeneously into a polymer matrix, poly (methyl methacrylate) (PMMA) by following a chemical method [4]. Here, the LN nanoparticles were first dispersed into the monomer, methyl methacrylate (MMA) which remains in liquid form under normal condition, and after dispersing, the liquid MMA is then solidified by polymerizing in a controlled manner by adding very small amount of initiator, 2,2'-azobisisobutyronitrile (AIBN) followed by heating. An element of 0.5 mm thickness and 22 mm diameter was cut and polished from the synthesized 0.10 wt% LN/PMMA nanocomposite. The PMMA and 0.10 wt% LN/PMMA nanocomposite are shown in figure-1.

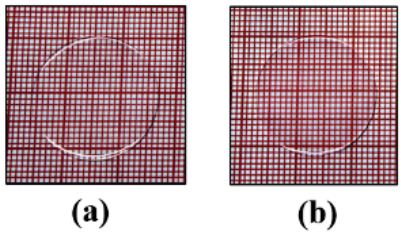

Fig. 1. *0.50 mm thick, PMMA (a) and 0.10 wt% LN/PMMA nanocomposite (b)*

3. Optical characterization

The transmittance of 0.5 mm thick PMMA and 0.10 wt% LN/PMMA nanocomposite obtained using UV-Vis-NIR spectrophotometer is shown in figure-2. The samples show high transparency (T_{PMMA}~90% & $T_{LN/PMMA}$~70%) in visible range. The linear refractive indices (n) of these materials at different wavelengths (λ= 0.407, 0.532, 0.828, 1.064 and 1.551 μm) were obtained by prism coupling method as shown in figure-3. Sellmeier equation (1) with the coefficients B_1 and C_1 were obtained by fitting the experimental data, and shown plotted in figure-3.

$$n^2 = 1 + \frac{B_1\lambda^2}{\lambda^2 - C_1} \;;\; \lambda \text{ in } \mu m \qquad (1)$$

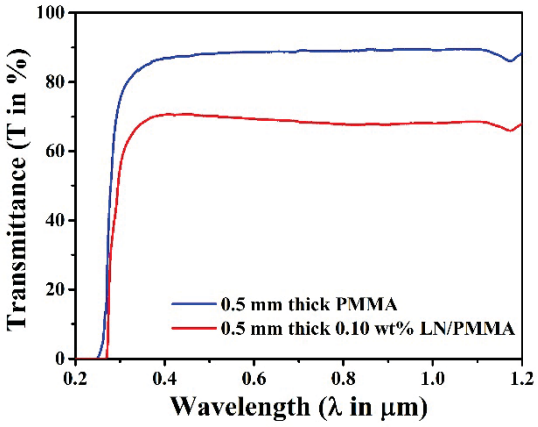

Fig. 2. *Transmittance spectra of 0.50 mm thick PMMA and 0.10 wt% LN/PMMA nanocomposite*

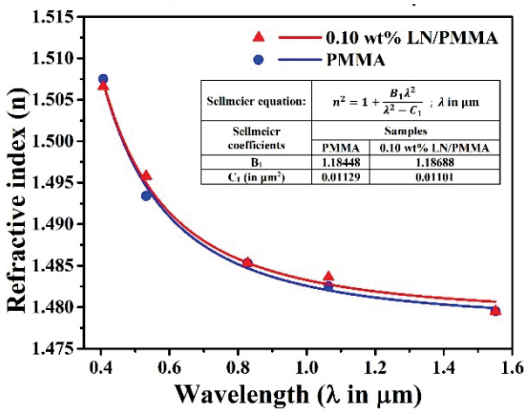

Fig. 3. *Refractive index as a function of wavelength for PMMA and 0.10 wt% LN/PMMA nanocomposite*

A Z-scan experiment was set-up using 21 mW He-Ne laser, convex lens of 11 cm focus length, sample stage with 30 mm scanning length for measuring the 3rd order NLO properties of the nanocomposites. The schematic of the set up is shown in figure 4. Here, the sample is scanned along the Z-axis through the focus (Z=0) of a Gaussian beam, and the power transmitted through the sample is measured as a function of the position of the sample. In close aperture configuration, the power transmitted through an aperture placed in the far field is measured as a function of sample position (Z). In open aperture configuration, the aperture is removed during measurement.

The open aperture Z-scan trace for normalized transmittance (transmittance normalized w.r.t the linear transmittance) of PMMA and 0.10 wt% LN/PMMA nanocomposite are shown in figure-5(a) and 5(b). In open aperture Z-scan trace, a peak was found at beam waist (Z=0) for 0.10 wt% LN/PMMA nanocomposite whereas a valley was observed in case of PMMA. The peak represents negative nonlinear absorption such as saturable

absorption (SA), and the valley represents positive nonlinear absorption such as reverse saturable absorption (RSA) and/or two-photon absorption.

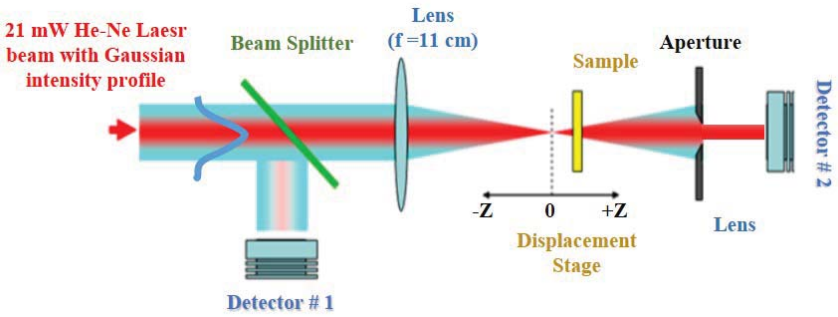

Fig. 4. *Schematic of optical set-up for Z-scan experiment*

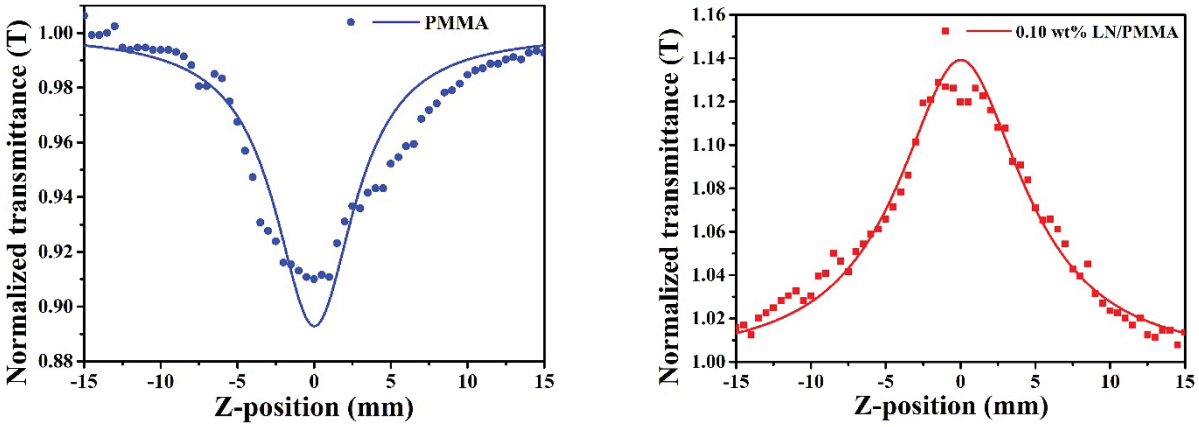

Fig. 5. *Open aperture Z-scan traces for normalized transmittance of (a) PMMA and (b) 0.10 wt% LN/PMMA nanocomposite*

The absorption coefficient (α) for RSA and SA as a function of incident intensity (I) is given by [5],

$$\alpha(I) = \beta I \quad ; \text{For RSA} \tag{2}$$

$$= \frac{\alpha_0}{1+I/I_S} \quad ; \text{For SA with saturable intensity, } I_S \tag{3}$$

The open aperture normalized transmittance is given by [5],

$$T = \frac{T_{nonlinear}}{T_{linear}} = \frac{ln[1+\beta I_0(z)L_{eff}]}{\beta I_0(z)L_{eff}} \quad ; \text{For RSA} \tag{4}$$

$$= e^{\alpha_0 L}\left[1 + \sum_{m=1}^{\infty} \frac{(-\alpha_0 L)^m}{m!} q_m(\rho)\right] ; For\ SA \tag{5}$$

Here $L_{eff} = \{1\text{-}exp(-\alpha_o L)\}/\alpha_o$ is the effective sample length for the actual sample length, L. $I_o(Z)$ is the axial intensity of the Gaussian beam. α_0 is the linear absorption coefficients. The terms $q_m(\rho)$ are obtained using Adomian decomposition method [5] where, $\rho = I_0(Z)/I_S$. The open aperture trace for PMMA was fitted with the expression (4) whereas for 0.10 wt% LN/PMMA the open aperture trace was fitted with the expression (5).

The closed aperture trace for 0.10 wt% LN/PMMA nanocomposite is shown in figure-6. Here self-focusing nature of nonlinearity in LN/PMMA nanocomposite is evident. In case of PMMA, no significant self-focusing or defocusing nonlinearity was observed in PMMA. The experimental data were fitted with the following expression of closed aperture normalized transmittance

$$T = 1 - \frac{4\Delta\Phi_0 x}{(1+x^2)(9+x^2)} - \frac{4\Delta\Phi_0^2(5-3x^2)}{(1+x^2)^2(9+x^2)(25+x^2)} + \frac{32\Delta\Phi_0^3 x(11-x^2)}{(1+x^2)^3(9+x^2)(25+x^2)(49+x^2)} \quad (6)$$

where, $x = -Z/Z_R$, $Z_R = 2.279\ mm$ => Rayleigh range and $\Delta\Phi_0 = 2\pi n_2 I_0(0) L_{eff}/\lambda$

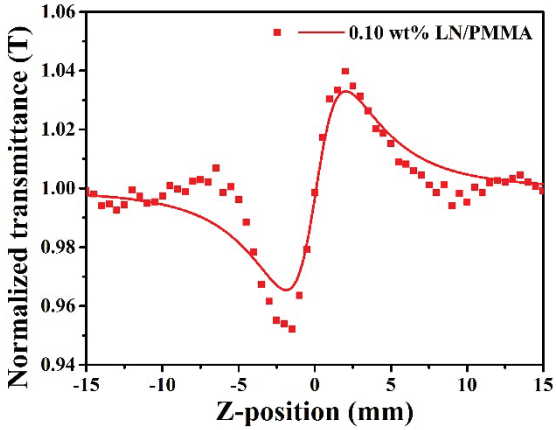

Fig. 6. *Closed aperture Z-scan traces for normalized transmittance of 0.10 wt% LN/PMMA nanocomposite*

The measured value of nonlinear absorption coefficient (β) of PMMA is $+2.51\times10^{-5}$ m/W whereas for 0.10 wt% LN/PMMA nanocomposite the values of nonlinear refractive index (n_2) and saturable intensity (I_S) were found to be $+1.66\times10^{-12}$ m^2/W and 1.90×10^6 W/m^2 respectively.

4. Conclusions

PMMA and 0.10 wt% LN/PMMA nanocomposite were prepared for linear and nonlinear optical characterizations. Both the materials were highly transparent (T_{PMMA}~90% & $T_{LN/PMMA}$~70%) in visible range. The linear refractive index (n) was obtained by prism coupling method and the nonlinear optical properties were measured using Z-scan technique. Negative nonlinear absorption (saturable absorption) was found in LN/PMMA nanocomposite by open aperture Z-scan technique whereas positive nonlinear absorption (reverse saturable absorption or two-photon absorption) was found in PMMA. Self-focusing nature of nonlinearity in LN/PMMA nanocomposite was found by closed aperture Z-scan experiment.

References

[1] J.E. Toney, Lithium Niobate Photonics, *Artech House Publishers*, (2015).

[2] E. Śliwińska, S. Mansurova, U. Hartwig, K. Buse and K. Meerholz, *Appl. Phys. B* **95**, 519 (2009).

[3] S. A. Sadeq, S. K. Al-Hayali, S. W. Harun and A. Al-Janabi, *Results Phys.* ***10****, 264 (2018).*

[4] C. Debnath, Sunil Verma, S. Kar, K.S. Bartwal, V.S. Tiwari and A.K. Karnal *Appl. Phys. A* **126**, 611 (2020).

[5] B. Gu, Y. X. Fan, J. Wang, J. Chen, J. Ding, H. T. Wang and B. Guo, *Phys. Rev. A* **73**, 065803, (2006).

[6] C. Debnath, S. Kar, Sunil Verma and K.S. Bartwal, *J. Nanosci. & Nanotech.* **15**, 3757 (2015).

[7] C. Debnath, S. Kar, Sunil Verma and K.S. Bartwal, *Opt. Mater.* **37**, 804 (2014).

Growth and investigation of thermo-optic coefficient of cesium triborate single crystals for nonlinear optical application

A. Saxena[1], Ratna Karn[1], P.A. Darshan[3], M. Soharab[1,2], R. Bhatt[1,2], Indranil Bhaumik[1,2], B. K. Sajith[1], A.K. Karnal[1,2]

[1]*Crystal Growth and Instrumentation Section, Laser Functional Materials Division, Raja Ramanna Centre for Advanced Technology, Indore-452 013, India*

[2]*Homi Bhabha National Institute, Training School Complex, Anushakti Nagar, Mumbai-400094, India*

[3]*Cochin University of Science and Technology, Cochin, Kerala, India.*

E.mail: amitsaxena@rrcat.gov.in

Abstract

Cesium triborate (CsB_3O_5) single crystals were grown by low gradient Czochralski technique. Powder XRD measurements of the grown crystals confirmed the formation of single phase. Samples were cut from these crystals and transmission spectra was recorded. Refractive indices in different crystallographic directions were obtained for different wavelengths using prism coupling method at four wavelengths. Sellmeier coefficients and birefringence were determined from this data. Thermo-optic coefficients were also determined from the ttemperature dependence of refractive index data in the temperature range between 30 and 150°C for the wavelengths of 532, 828, 1064 and 1551 nm and like most of the borates it possessed negative thermo-optic coefficient of refractive index

Introduction

Solid-state laser sources in the UV regions are scarce. There is high demand of efficient, compact solid-state laser sources in these regions for applications, such as deep UV lithography, mass-spectrometry, biology and medicine [1-3]. Borates have gain importance as nonlinear optical (NLO) materials due to their ability to produce compact UV laser through harmonic frequency generation using IR lasers by second, third and higher harmonic generations [3,4]. Borates are being considered as a potential NLO materials to fulfill this demand owing to their favourable optical and NLO properties like, high NLO coefficient, moderate birefringence, large laser damage threshold, transparency till deep UV range, etc. [5-7].

Cesium triborate (CsB_3O_5, CBO) is one of the important material of the borate family and attracting attention due to its excellent optical and NLO properties for harmonic generation in UV region like, deep UV transparency (170-3000 nm), NLO coefficient $d_{14} \approx 0.468 \times d_{11}$ ($\beta-BaB_2O_4$), high damage threshold ~ 26 GW/cm^2 at 1.053 μm, 1.0 ns along with high chemical stability [3]. The basic structural unit of CBO belongs to nonplanar $(B_3O_7)^{5-}$ anionic groups which is slightly different from the planar $(B_3O_6)^{3-}$ with one of the boron atom is changed in structural coordination from trigonal to tetrahedral and results in interesting optical properties like deep UV transparency [2]. The higher value of second order susceptibility is alone not sufficient to establish a crystal as a good NLO crystal. Along with nonlinear parameters, optical properties such as birefringence, absorption edge, walk off angle, laser damage threshold also equally matters. Moreover, in comparison with other borate crystals such as

BBO and LBO, CBO has advantages of congruent melting that can be utilized to grow crystals from congruent or near-congruent melts at fast growth rate by Czochralski or top-seeded solution growth (TSSG) technique [7].

Thought, the growth of CBO crystal from stoichiometric melt using Cz method is reported, but still the growth of high-quality crystal free from cracks, inclusions and striations is a challenge because of high viscosity due to B_2O_3 and volatility of Cs_2O [5]. The conditions for obtaining good quality crystals by Cz method is yet to be established. In order to address the issues, this work focuses on growth of CBO single crystals by low gradient Czochralski technique to establish conditions for the growth of good quality crystals. The grown crystals were investigated for structural, optical absorption, refractive index and birefringence characteristics. Further, as the knowledge of the thermo-optic coefficient (TOC) is of prime importance for the design and operation of nonlinear optical elements and devices [5], TOC were also determined.

Crystal Growth

For crystal growth, the starting material was synthesized from high purity (99.9%) chemicals Cs_2CO_3 and B_2O_3 in stoichiometric composition (Cs_2O:$3B_2O_3$ ~ 1:3) [6]. Cesium carbonate is highly hygroscopic chemical which needs extra precaution at the time of weighing to avoid inclusion of moisture. Handheld halogen lamp was used to keep surroundings warmer, while taking it out of bottle as well as during weighing. After being accurately weighed and mixed homogeneously, it was then transferred to a platinum crucible and melted at 900°C in several batches. Preliminary safety precautions were followed throughout the process as cesium carbonate is toxic and boron oxide is irritant for skin. The crucible was placed in a log gradient ~1°C/cm single-zone furnace controlled by a programmable Eurotherm temperature controller. Czochralski technique was adopted to grow crystal. Initial runs were tried with platinum wire cold finger as a seed. Fig. 1 (a) shows the CBO crystal grown using platinum wire as cold finger. Seeds crystals were prepared from the wire grown crystal and seeding was done as per the novel seeding discussed in ref. [8]. After seeding the growth was initiated by employing a slow pulling of 0.2 mm/h and rotation of 6-10 rpm. After the growth, crystal was detached carefully from the melt and allowed to cool slowly to room temperature at a rate of 20°C/hr to avoid cracks and residual strain resulting from rapid temperature change. Fig. 1(b&c) shows the photographs of the grown CBO crystals grown by seeded growth.

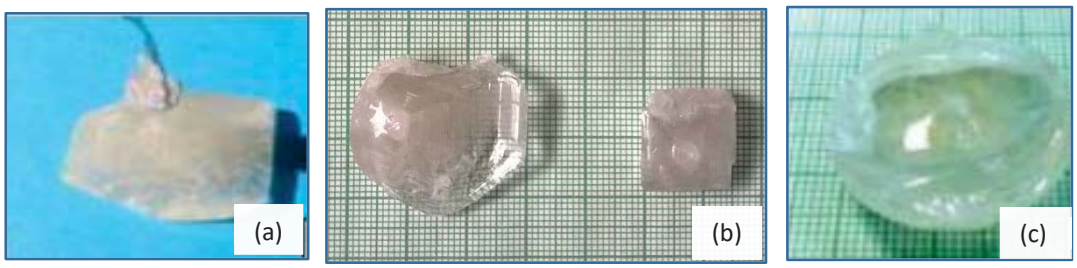

Fig. 1 CBO crystals grown by Cz-method on platinum wire (a) and using seed crystal (b & c).

Characterization

The phase formation and purity of the grown crystal was evaluated using x–ray diffraction (XRD) technique and comparing it with JCPDS (The International Centre for Diffraction Data Sample) database. Results were in accordance with JCPDS file number #740357 and lattice parameters calculated using Qbasic software were in accordance with actual parameters as a = 6.2135 Å, b = 8.5322 Å, c = 9.1841 Å and $\gamma = \beta = \gamma = 90°$. Fig. 2(a) shows the direction dependent refractive index of CBO crystal measured at room temperature using prism coupling technique [9]. Instrument used for refractive index measurement was a commercially available prism coupler manufactured by Metricon Corp., UK with model 2010/M with five different laser wavelengths 407, 532, 828, 1064 and 1551 nm. The different refractive index along principal direction x, y and z depicts CBO belongs to a biaxial system. The knowledge of refractive index is a preliminary requirement to establish the usefulness of the crystal as a nonlinear element in optical and optoelectronic processes. The observed variation in refractive index along different directions with wavelength shows that birefringent phase matching of the fundamental and harmonic waves in the transparency range is possible by angle tuning and CBO can be used as a NLO material. The corresponding Type-I & Type-II phase matching angles for the three-wave interaction can estimated from the measured refractive index values. The refractive index data were fitted to Sellmeier equation to determine coefficients A, B, C and D using the following equation where wavelength λ taken in μm.

$$n^2(\lambda, T) = A(T) + \frac{B(T)}{\lambda^2 - C(T)} - D(T)\lambda^2$$

The measured values are summarised in Table 1. Birefringence is evaluated by calculating the difference in refractive indices measured along different directions.

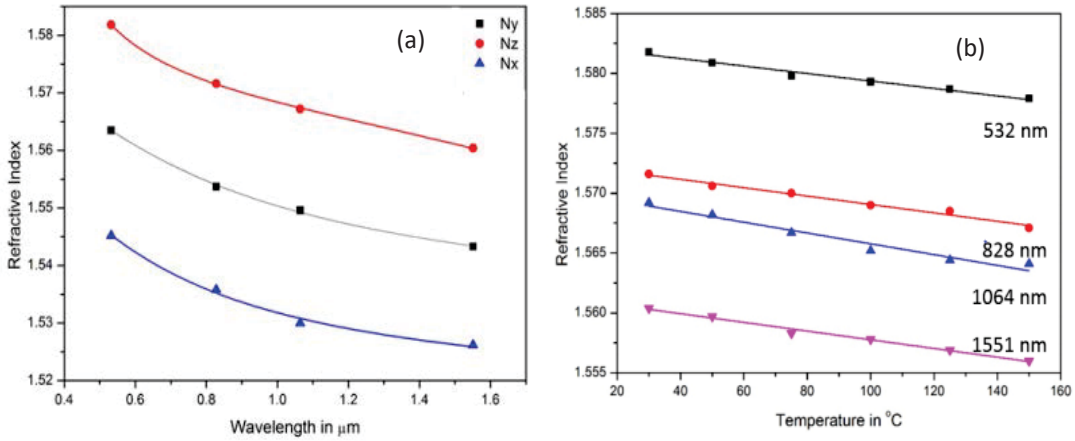

Fig. 2 (a) Direction dependent refractive index measured at room temperature and Sellmeier fit of the data of CBO crystal measured for different wavelength and (b) Temperature dependent refractive index of CBO crystal measured for different wavelength

Fig. 2(b) shows the temperature dependent refractive index of CBO crystal measured in the range of 30-150°C. The decrease in the value of refractive index with increasing temperature depicts a negative thermo-optic coefficient of CBO crystal.

The linear fit of the data yields the value of the thermo-optic coefficient (dn/dt) [10], which is found to be ~ -3.12x10^{-5} for 532 nm wavelength. The estimated values are summarised in Table 2. The negative value of dn/dt indicate crystal may behave as a negative thermal lens when operated at high power radiation.

Table 1 Sellmeier coefficients of CBO crystals

R.I.	A	B	C	D
n_x	2.3197	0.0353	-0.2314	0.0020
n_y	2.3700	0.0495	-0.3771	0.0023
n_z	2.4607	0.0117	-0.2132	0.0012

Table 2 Thermo-optic coefficient of CBO for different wavelengths

Wavelength (nm)	(dn/dT) x 10^{-5}/°C
532	-3.1177
828	-3.5016
1064	-4.5048
1551	-3.6306

Conclusion

Single crystals of Cesium triborate were grown by low gradient Czochralski technique. X-ray powder diffraction analysis confirmed the formation of the desired single phase of the grown crystals. Polished samples were prepared from the grown crystals and subjected transmission and refractive index measurements. Refractive indices along principal directions (x, y, and z) were measured for different wavelengths and temperature. Sellmeier and Thermo-optic coefficients were estimated from the measured refractive index data. Like other borates crystal, the thermo optic coefficient were found to be negative.

References

1. Xianchao Zhu, Heng Tu, Ying Zhao and Zhanggui Hu, Crystals 7 (2017) 83.
2. C. T. Chen , T. Sasaki , R. K. Li, Y. C. Wu , Z. S. Lin , Y. Mori , Z. G. Hu , J. Y. Wang , S. Uda, M. Yoshimura and Y. Kaneda, Nonlinear Optical Borate Crystals Principles and Applications, Wiley-VCH Verlag & Co. KGaA (2012).
3. Yicheng Wu, Takatomo Sasaki, Sadao Nakai, and Atsushi Yokotani, Honggao Tang, Chuangtian Chen, Appl. Phys. Lett. 62 (1993) 2614.
4. D. Rajesh, M. Yoshimura, H. Shimatani, Y. Mori, R. Jayavel, and T. Sasaki, Crystal Growth & Design, 8 (2008) 3713.
5. T. Saji, N. Hisaminato, M. Nishioka, M. Yoshimura, Y. Mori, T. Sasaki, J. Crystal Growth, 274 (2005) 183.
6. Shanshan Liu, Guochun Zhang, Xiaomao Li, Feng Yang, Yong Bo, Peizhen Fu and Yicheng Wu, CrystEngComm, 2012, 14, 4738.
7. R. Bhatt, S. Ganesamoorthy, Indranil Bhaumik, A.K. Karnal, and V.K. Wadhawan, Optical Materials, 29 (2007) 801.
8. Indranil Bhaumik, S. Ganesamoorthy, R. Bhatt, R. Sundar, A.K. Karnal and V.K. Wadhawan, J. Crystal Growth, 243 (2002) 522.
9. Indranil Bhaumik, R. Bhatt , S. Ganesamoorthy, A. Saxena, A.K. Karnal, P.K. Gupta, A.K. Sinha, S.K. Deb, Applied Optics, 50 (2011) 6006.
10. M. Soharab, Indranil Bhaumik, R. Bhatt, A. Saxena, A.K. Karnal, Appl. Phys. B 125 (2019) 84.

Design and development of monocrystalline AlGaAs/GaAs DBR mirrors with reflectivity exceeding 99% at 1064, 1100 and 1550 nm photonic band

Geetanjali Vashisht,[1,2*] Suparna Pal,[2,3] S. K. Khamari,[1] R. Kamparath,[3] A. Khakha[1], R. Kumar, [1]
C. Mukherjee,[2,3] V. K. Dixit[1,2] and T. K. Sharma[1,2]

[1]Semiconductor Materials Laboratory, Materials Science Section, RRCAT, Indore- 452013.

[2]Homi Bhabha National Institute, Training School Complex, Anushakti Nagar, Mumbai- 400094

[3]Optical Coatings Laboratory, Laser Technology Division, Raja Ramanna Centre for Advanced Technology, Indore-452013, M.P., India.

Email: *geetanjali@rrcat.gov.in

Abstract

$Al_{0.9}Ga_{0.1}As$/GaAs based monocrystalline distributed Bragg reflector structures are designed to have higher reflectivity (R) at technologically important wavelengths of 1064, 1100 and 1550 nm. The designed structures are epitaxially grown on (001) oriented GaAs substrate by metal organic vapour phase epitaxy technique. Subsequently, the structural and crystalline quality of the grown structures are evaluated using high resolution x-ray diffraction measurements. R ~ 99% is achieved in the desired wavelength range which confirm their suitability in many applications including laser interferometry based gravitational wave detection, laser frequency stabilization for optical atomic clocks, high Q oscillators, vertical cavity surface emitting lasers, distributed feedback lasers, resonant cavity enhanced photodetectors, terahertz radiation sources and detectors.

Introduction

Distributed Bragg-reflector (DBR) is the fundamental structure used in various high performance opto-electronic devices such as high Q oscillators, vertical cavity surface emitting lasers, distributed feedback lasers, resonant cavity enhanced photodetectors, terahertz radiation sources and detectors. In recent years, a significant interest has grown up in the DBR structures due to their novel applications in both fundamental and advanced phenomena that are characterized by the strong light matter coupling. It includes the formation of exciton-polariton quasi particles that are desired for the fundamental process in matter at high temperature including Bose-Einstein condensation[1], quantized vortices[2], long-range spatial coherence[3], superfluidity[4] and solitons[5]. High quality monocrystalline AlGaAs/GaAs based DBR structures are the ideal choice to observe these phenomena. Such DBR structures are also proposed for highly sensitive and precise measurements such as laser interferometry based gravitational wave detection and laser frequency stabilization for optical atomic clocks due to the low thermal noise[6]. Thus, in this work, DBR stacks consisting of the alternate layers of low (AlGaAs) and high (GaAs) refractive index material with quarter wavelength thickness ($\lambda/4n_{eff}$) are used to obtain higher reflectivity in the designed wavelength band. The reflectivity for the specific wavelength range mainly depends upon the number of layers in the given stack, refractive indices and individual layer thicknesses. In view of above, the specific DBR structures are designed to cover the technologically important wavelengths of 808, 880, 1064, 1150 and 1550 nm with higher reflectivity. Numerical simulations based on Fresnel equations are initially performed using filmetric software to design the DBR structure for optimized number of layers for higher reflectance at required wavelength[7]. The designed DBR structures are thereby grown by metal organic vapour phase epitaxy (MOVPE) and characterized by high resolution x-ray diffraction (HRXRD) measurements. Further, the reflectivity measurements are performed on these DBR structures, which shows R~ 99% in the desired wavelength range. The optimum DBR mirrors are used to design the

micro-cavity structure consisting of InGaAs quantum well emitter between the two AlGaAs/GaAs DBRs to investigate the exciton-polariton strength in the matter.

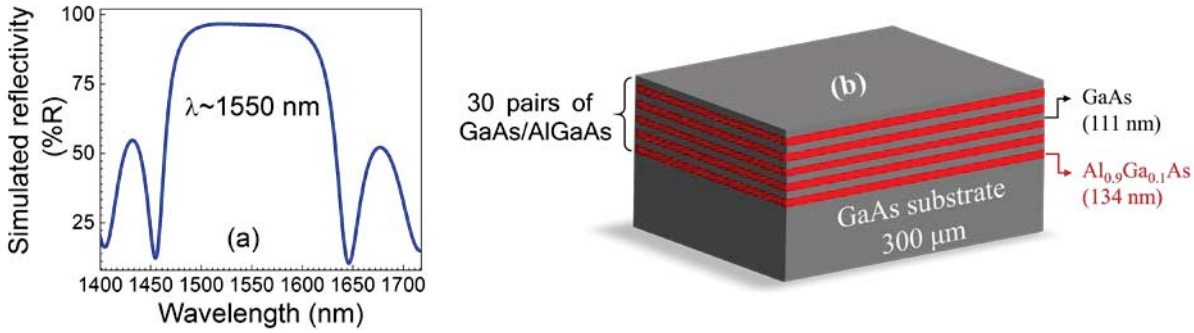

***Figure 1**: (a) Simulated reflectivity curve of a 23 period $Al_{0.9}Ga_{0.1}As$/GaAs DBR stack with the individual layer thickness of 134 and 111 nm respectively (b) Schematic layer diagram of a 30 period AlGaAs/GaAs DBR structure designed for the photonic stopband around 1550 nm.*

Experimental Details

High reflecting AlGaAs/GaAs DBR structures are designed with an aim of achieving the simulated reflectance spectra for the required wavelength spans by using Filmetric software. Fresnel reflection occurs at every AlGaAs/GaAs interface resulting into constructive interference leading to a very high reflectance at the designed wavelength. Reflectivity value changes with the angle of incidence. In AlGaAs/GaAs DBR structures, the reflectivity at the normal incident angle is in general given by[8]

$$R = \left[\frac{1 - \left(\frac{n_{GaAs}}{n_{AlGaAs}} \right)^{2N}}{1 + \left(\frac{n_{GaAs}}{n_{AlGaAs}} \right)^{2N}} \right]$$

where n_{GaAs}, n_{AlGaAs}, and N are the GaAs (high) refractive index, AlGaAs (low) refractive index and number of layer pairs in DBR stack respectively. Thus, higher the number of layers result in higher reflectivity, while the contrast of refractive indices in layers controls the band width of the reflectivity profile. Generally, a broad spectral reflector requires a large refractive index variations in layer pairs. Figure 1 (a) shows the simulated reflectivity profile of a 23 period DBR stack based on $Al_{0.9}Ga_{0.1}As$/GaAs alternate multilayers with the thickness of 134 and 111 nm respectively. Each layer thickness ($t \sim \lambda/4n_{eff}$) is decided by the refractive index of the material (n_{eff}) and the quarter wavelength for the central wavelength of photonic stopband. The simulated reflected profile is designed for the important wavelength of 1550 nm[9-10]. The simulated reflectivity profile shows the maximum reflectivity of 96 % at 1550 nm for the 23 period DBR stack. However, this reflectivity magnitude can be increased by including more periods in the stack. Therefore, 30 period $Al_{0.9}Ga_{0.1}As$/GaAs DBR structure (S1) with the similar thicknesses is grown on (001) oriented GaAs substrate by MOVPE as shown in figure 1 b. MOVPE growth is performed at 700 °C under 50 mbar reactor pressure using the precursors of trimethyl-aluminium, trimethyl-gallium, and arsine sources. A thick GaAs buffer layer of 350 nm is grown on 300 μm GaAs substrate followed by $Al_{0.9}Ga_{0.1}As$/GaAs DBR stacks. Similarly, 25 period $Al_{0.9}Ga_{0.1}As$/GaAs DBR structures with varying thicknesses (S2 and S3) are also grown by MOVPE. The structural parameters and crystalline quality of the grown structures are characterized by the HRXRD measurements. These measurements are performed for (004) reflections using PANalytical X'PERT

diffractometer having x-ray source of $CuK_{\alpha 1}$ (1.5405Å) and Ge (220) four-bounce crystal monochromator. Subsequently, the reflectivity measurements are performed in the infrared range on the grown structures using a Cary 5000 spectrophotometer using V-W absolute measurement accessory.

Sample No.	Period of $Al_{0.9}Ga_{0.1}As$/GaAs stack	Layer thickness (± 2 nm)		Central wavelength of photonic stopband (nm)
		$Al_{0.9}Ga_{0.1}As$ epilayer	GaAs epilayer	
S1	30	134	111	1550
S2	25	92	84	1100
S3	25	89	78	1064

Table-1: Detailed layer structure and their thicknesses for sample S1, S2 and S3.

Results and Discussion

Figure 2 represents the ω-2θ plot of MOVPE grown AlGaAs/GaAs DBR samples S1 and S2 for (004) reflections. The fringes observed in the HRXRD profile indicate the good crystalline quality of the grown structures. The structural parameters such as aluminium composition and layer thicknesses are estimated by simulating the HRXRD profiles using X'Pert Epitaxy software as summarized in Table 1. Aluminium composition is same in all the DBR structures, while individual layer thickness is varied depending on the required photonic stopband wavelengths ($t \propto \lambda$).

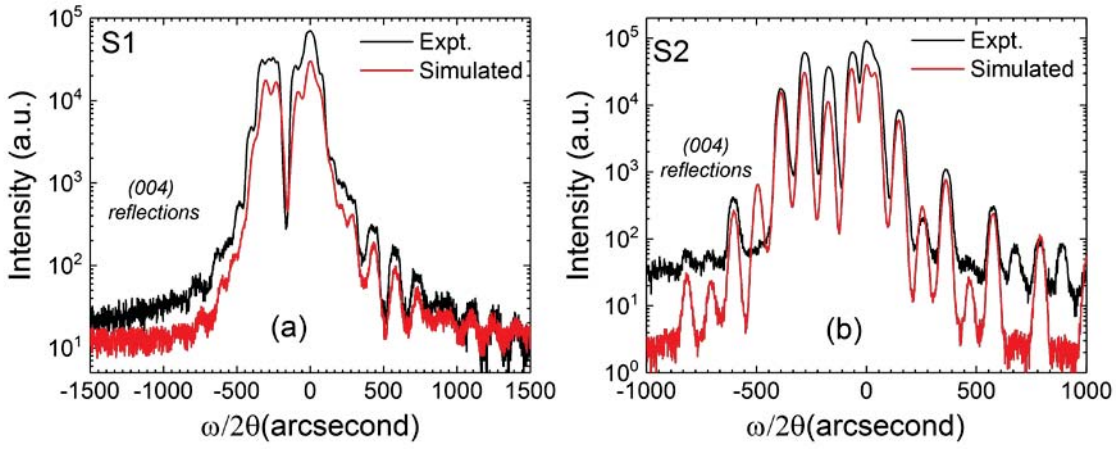

***Figure 2**: (a) Experimental and simulated HRXRD (004) patterns of AlGaAs/GaAs DBRs with different layer thicknesses (a) $Al_{0.9}Ga_{0.1}As$/GaAs (134/111 nm × 30 pairs) and (b) $Al_{0.9}Ga_{0.1}As$ /GaAs (92/84 nm× 25 pairs).*

Figure 3 shows the experimentally measured reflectivity profile of the AlGaAs/GaAs DBR samples S1, S2 and S3 respectively. High reflectivity wavelength range (commonly known as photonic stopband) results from the constructive interference of the light wave at each AlGaAs/GaAs interface. These DBR samples show high reflectivity (R~99%) at the required wavelength range. Such high reflectivity values with wide stopband range (~ 100 nm) and sharp reflectivity oscillations confirm that the grown DBR structures are of highly uniform and are of monocrystalline nature. Thus, MOVPE grown AlGaAs/GaAs DBR structures show a great potential to be used in opto-electronic devices for abovementioned applications. In view of this, a $3\lambda/2n_{eff}$ thick GaAs/InGaAs/GaAs

quantum well based microcavity structure surrounded by two AlGaAs/GaAs DBR are designed and subsequently grown by MOVPE. The detail investigations will be discussed during presentation.

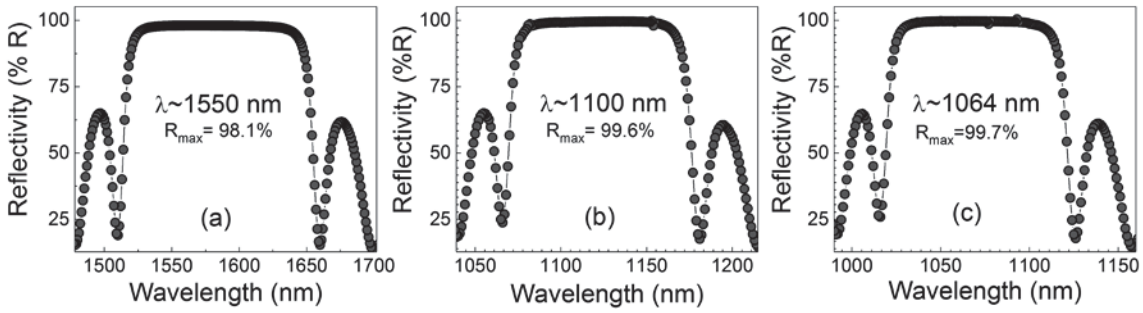

***Figure 3**: Measured reflectivity spectrum of $Al_{0.9}Ga_{0.1}As$/GaAs DBR structures designed for photonic stopband around wavelengths of (a) 1550 nm, (b) 1100 nm and (c) 1064 nm.*

Conclusions

In order to achieve reflectivity > 99% at 1064, 1100 and 1550 nm wavelength range, AlGaAs/GaAs DBR structures are designed and grown by MOVPE. The sharp fringes observed in HRXRD pattern confirm the good quality of mirrors. Reflectivity ~ 99% is achieved in these DBR structures at the desired wavelength range. A wide stopband of ~100 nm with sharp sideband oscillations on both sides of stopband along with its crystalline nature confirms that these high reflectivity monocrystalline mirrors are suitable for several advance applications.

Acknowledgement

Authors acknowledge Mr. U. K. Ghosh and Mr. A. K. Jaiswal for the technical support. Authors also acknowledge Sh. S. V. Nakhe, Director Materials Science Group and Sh. D. Das, Director RRCAT for the encouragement and constant support during the course of this work.

References

1. N. S. Voronova et al., *PRL* **115**, 186402 (2015).
2. L. Tinkler et al., *Appl. Phys. Lett.***106**, 021109 (2015).
3. J. Kasprzak et al., *Nature* **443**, 409 (2016).
4. A. Amo et al., *Nature Phys.* **457**, 291 (2009).
5. M. Sich et al., *Nat. Photonics* **6**, 50 (2012).
6. G. D. Cole et al., *Nat. Photonics* **7**, 644 (2013).
7. *https://www.filmetrics.com/reflectance-calculator*
8. P. J. Delfyett, Chapter Lasers, Semiconductor, Encyclopedia of Physical Science and Technology (Academic Press) Ed. by R. A. Meyers, 443 (2003).
9. W. Xie et al., *Micromachines* **10**, 549 (2019).
10. G.Vashisht et al, *J. Opt. Soc. Am. B* **35**, 2405 (2018).

Detection of refractive index inhomogeneity in large size Neodymium (Nd)-doped phosphate glass slabs using a small size laser beam

Sanjiv Kumar Tiwari*, Sarvendra Singh, Y. Pavan Kumar, Rishipal, G. Muralidharan, A. K. Biswas, M. P. Kamath, N. S. Benerji and K. S. Bindra

Optics Design and Development Laboratory, High Energy Optics Section, Laser Technology Division, Raja Ramanna Centre for Advanced Technology, Indore 452013

*sanjiv@rrcat.gov.in

Abstract

A simple experimental technique is presented to detect refractive index inhomogeneity in the order of 10^{-3} in large size Nd-doped phosphate glass slabs using a small size rectangular laser beam. The glass slab is scanned across the beam and the recorded images are stitched to get one single image and mapping of the local refractive index variation over the whole slab volume is performed. The stitched schlieren/shadowgraphic image provide a good qualitative estimate of the homogeneity of the glass sample. The technique is simple and useful for testing of the laser glass which is under development.

Introduction

Small coefficient of intensity dependent refractive index and suitable stimulated emission cross section make Nd-doped phosphate glass as the most suitable active medium for the kJ class lasers[1]. RRCAT has undertaken a project of indigenous development of high power Neodymium (Nd)-doped phosphate glass laser, for which the Nd-doped phosphate glass slabs with specified dimensions are being developed at CGCRI, Kolkata. Homogeneity is an important optical property of the laser glass which greatly affects the performance of the laser systems. It does not only affect the laser wave-front quality but ensures safe and damage-free high-peak-powered laser operation also. The laser glass must be homogeneous and free of stress, striae, bubbles and inclusions. The index inhomogeneity must be within the tolerance limit (of the order of 10^{-5}or better) to qualify the glass for its use as an active medium of the laser. Therefore, the accurate measurement of the optical homogeneity of the doped bulk glass is of critical importance for the development of laser glass.

In general, interferometric[2], schlieren[3] and shadowgraphic[3] techniques are used to detect optical inhomogeneity of the transparent glass materials. Interferometric technique provides high precision measurement of optical inhomogeneity (of the order of 10^{-5} or better). Such types of high precision measurements are not applicable when the glass sample is under development and the inhomogeneity is large enough (up to the order of 10^{-3}). Schlieren shadowgraphy is highly advantageous due to its high sensitivity in this regime of inhomogeneity. Also, the Schlieren setup is simple and does not require a reference beam unlike the interferometric technique. Generally, imperfections in a transparent medium like glass, generated during the melting and casting process results in inhomogeneities in the refractive index of the medium. When light rays pass through regions of imperfections, light rays deflect and scatter. This fractional deflection of the light rays

results in distortion of the wave-front of the light beam. The resultant deflection of the light rays produce intensity change in corresponding portions of the image of the light beam and therefore can be used to identify the inhomogeneity of the glass medium.

Experimental setup

In this paper, a simple schlieren shadowgraphy technique is presented to detect the refractive index inhomogeneity in large size Neodymium (Nd)-doped phosphate glass slabs of size ~ 300 mm (length) × 180 mm (width) × 50 mm (thickness) using a moderately small size laser beam. An expanded, collimated and spatially-filtered laser beam of rectangular cross-section 50 mm × 60 mm (derived from a He-Ne laser) was used in the experiments (as shown in the schematic of the Figure 1 and photograph of Figure 2). This beam was passed through the test glass slab (both entrance and exit faces optically polished with surface figure better than λ) and the transmitted beam from the glass slab was made incident on a spherical convex lens of focal length 500 mm to focus and image it on a screen (kept at far field of the lens). The image on the screen was recorded using a CCD camera (Make: Imaging Source, Germany, Model: DMK 23UX236, having 1920×1200 pixels with the size of a pixel 2.8 µm × 2.8 µm). A knife edge is kept at the focal position of the focusing convex lens to block the zero-order and negative frequency components of diffraction. This results in increased contrast of the recorded far-field images. Since, the test glass slab size was large enough in comparison to the size of the laser probe beam; therefore, the glass slab was kept on a motorized translation stage and scanned transversely across the laser beam in both horizontal and vertical directions to cover/expose the complete glass slab with the laser beam for its different positions. Overlap area of ~20 % between adjacent images was done to perform stitching. For each scanned position of the slab, the images of the transmitted light were recorded. Finally, all the recorded images (total 21 small images) corresponding to each scanned position of the glass slab were stitched to form one larger image corresponding to the complete slab.

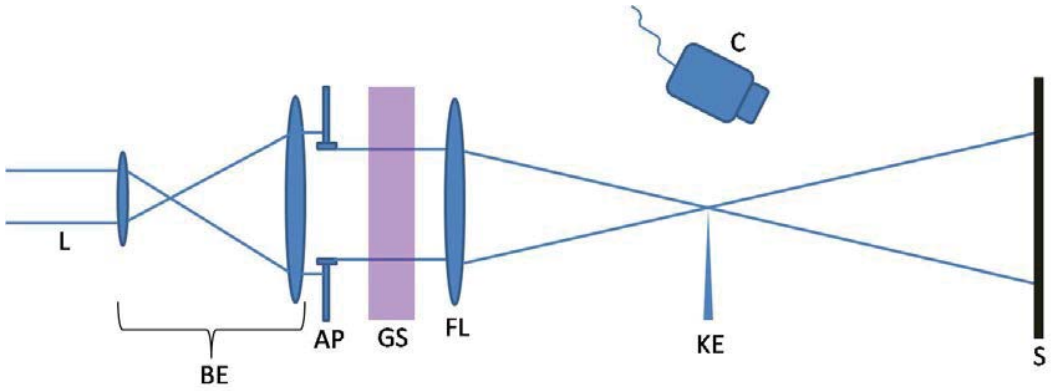

Figure 1. Schematic of the experimental setup. L: He-Ne laser, BE: beam expander, AP: rectangular aperture, GS: glass slab, FL: focusing lens, KE: knife edge, S: screen, C: CCD camera.

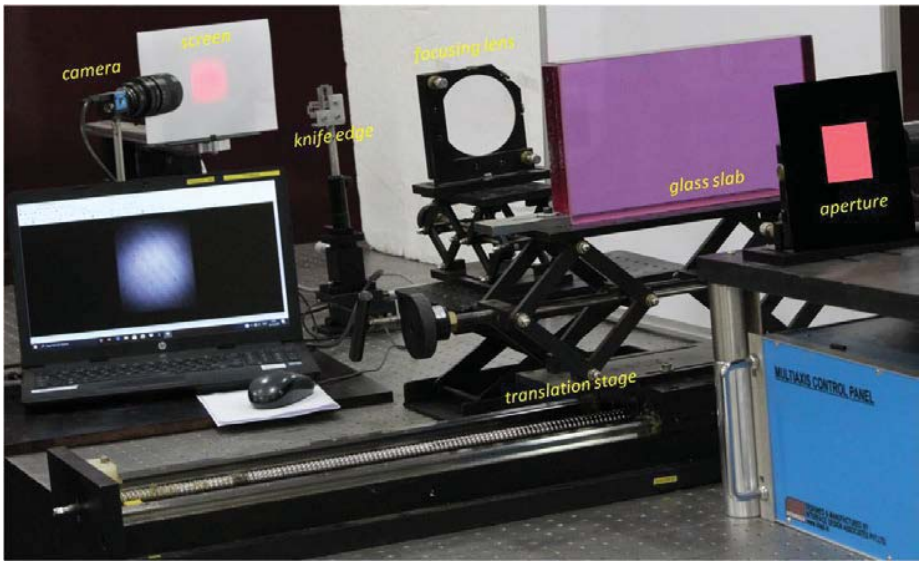

Figure 2. Photograph of the experimental setup

Results

Figure 3 and Figure 4 show the stitched images of the shadowgraphy (when knife edge is not blocking the main beam) and schlieren (when knife edge is blocking the main beam) respectively. It is evident from these figures that there is nearly one to one correspondence of the observed defects in both of the images. The schlieren image provides more contrast than the shadowgraphic image. The continuity of the observed index inhomogeneity defects in between the different image frames of small size is also evident from the both of the image shown in Figure 3 and Figure 4. This ensures that the stitching of the small schlieren images works well and none of the defect information is missed, therefore, actual position of the refractive index inhomogeneity in the large size glass slab can be detected precisely using a moderately small size laser probe. This technique is especially useful in the laboratories where small size optics is available in general and an experimental setup can be arranged quickly using standard optical components. Therefore, this scanning and stitching schlieren technique offers an easy and simple alternative to detect the optical inhomogeneity in large size glass slabs using a small laser beam.

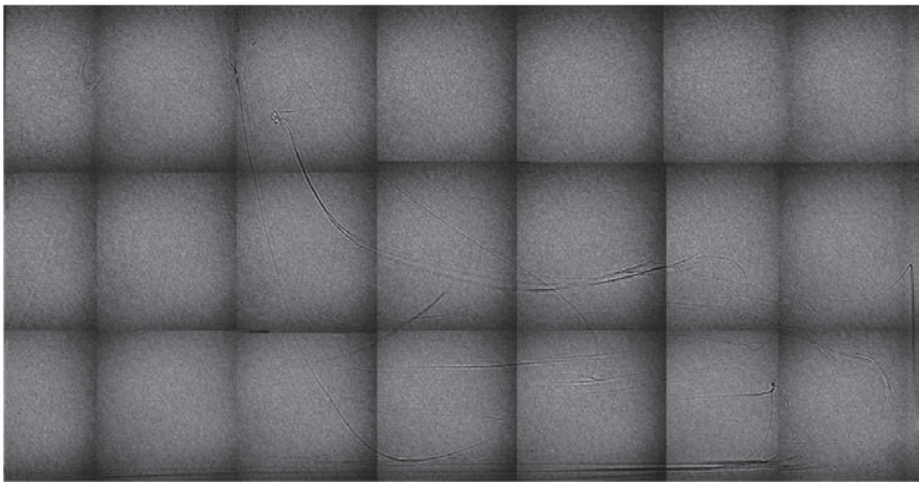

Figure 3. Stitched shadowgraphic image of the test glass slab.

Figure 4. Stitched schlieren image of the test glass slab.

Conclusion

In conclusion, a simple home-made laboratory technique is presented to detect refractive index inhomogeneity in the order of 10^{-3} in large size Nd-doped phosphate glass slabs using a small size rectangular laser beam. The large size glass slab is scanned across the beam and all the recorded images were stitched to get one single image and the mapping of the local refractive index variation over the whole slab volume is performed at millimeter scale. The stitched schlieren/shadowgraphic image provide a good qualitative estimate of the homogeneity of the glass sample. The technique is simple and useful for testing of the laser glass which is under development. The setup is being used regularly to test the Nd-doped phosphate glass slab samples melted in 5 liter facility at CGCRI, Kolkata for the indigenous development of kJ class Nd-doped phosphate glass laser at RRCAT.

Acknowledgements

We thank Dr. K. Annapurna, Glass Technology Division, Central Glass and Ceramic Research Institute, Kolkata for providing the test samples of Nd-doped phosphate glass slabs. We acknowledge Shri S. S. Thangavel, Shri G. Ragoubady and Shri Anil Kumar, Optics Design and Development Laboratory, RRCAT, Indore for polishing the test sample.

References

1. Lilli Hu, *et. al.*, *High Power Laser Science and Engineering* **2**, 1 (2014).
2. Daniil T. Puryayev, *Optics and Laser Technology* **30**, 235 (1998).
3. G. S. Settles and M. J. Hargather, *Meas. Sci. Technol.* **28** 042001 (2017)

Nonlinear optical study of differently coloured, free-flowing, dye-based fountain pen inks

Ajay A.R.[a], Aji Alexander[b] and Reji Philip[b]

[a]*Department of Physics, Amrita Vishwa Vidyapeetham, Amritapuri-690525, India*

[b]*Raman Research Institute, Sadashivanagar, Bangalore-560080, India*

Email:[a] AjayaR@am.students.amrita.edu, [b] reji@rri.res.in

Abstract

We report nonlinear optical transmission measurements of a set of thirteen dye-based fountain pen inks, carried out using the open aperture Z-scan experiment. 532 nm, 5 ns laser pulses obtained from a frequency-doubled Nd:YAG laser have been used for the measurements. The materials show reverse saturable absorption (RSA) at high laser fluences. The nonlinear absorption coefficients have been determined by numerically fitting the measured data to the nonlinear propagation equation. Because of the strong RSA, the materials exhibit an excellent optical limiting property, which has potential applications in protecting human eyes and sensitive optical detectors from harmful laser radiation.

Keywords: Ink, Open aperture Z-Scan, Excited State Absorption, Reverse Saturable Absorption, Nonlinear absorption coefficient.

1. Introduction

Nonlinear optics is the study of the interaction of intense optical radiation with matter [1]. From various reports in literature it is evident that organic dyes exhibit interesting nonlinear optical behaviour. Inks, which belong to the family of dyes, are colloidal systems of fine pigment particles dispersed in a solvent. The pigment may or may not be coloured, and the solvent may be aqueous or organic [2]. Literature reports show that inks have applications even in dye-sensitized solar cells [3]. While examining the nonlinear behaviour of a medium, a Z-scan measurement without aperture (open-aperture Z-scan) is usually used to measure the material's nonlinear absorption coefficient [4]. In the present work we investigate the absorptive optical nonlinearity of a few commercially available, chemically unbroken, free-flowing, dye-based fountain pen inks, using the technique of open aperture Z-scan.

2. Experimental

Thirteen colour variants of the *Daytone* brand ink (manufactured by *Daylight Industries*, India) were used for the investigations (Fig. 1, top panel). All samples were diluted in water to give a linear transmission of 70% at 532 nm when taken in a 1 mm path length cuvette. The Absorption Spectra of the prepared samples taken using a UV-Vis-NIR spectrometer (Perkin Elmer, Lambda 750) reveal strong absorption in the visible spectral region.

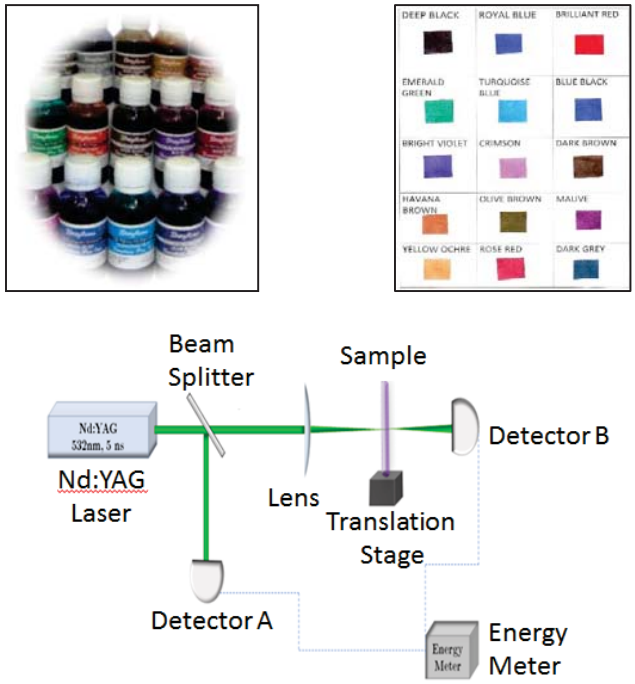

Figure 1: The ink samples and their colour codes (top). The open aperture Z-scan setup (bottom).

The open aperture Z-scan experimental setup is shown in Fig. 1 (bottom panel). The laser source used for our measurements is a frequency-doubled Q-switched Nd:YAG laser producing 5 ns laser pulses at 532 nm. The laser pulse energy used is 50 µJ. The beam is split into two using a beam splitter and the reflected beam is taken as a reference beam whose energy is detected by the pyroelectric detector A. The transmitted beam is focused using a plano-convex lens of focal length 10 cm. The transmitted beam is allowed to pass through the sample taken in the cuvette and the transmission is measured by the pyroelectric detector B. The cuvette is mounted on a motorized linear translation stage so that it can be positioned at different places with respect to the beam focus on the beam axis. The input energy per unit area, i.e. the optical fluence, keeps changing as the sample changes position. During the experiment the optical transmission of the sample at various positions is measured. The experiment is automated by means of a LabVIEW program. The graph plotted between the sample position and the normalized transmittance gives the open aperture Z-scan curve, from which the nonlinear absorption coefficient can be calculated.

3. Results and discussion

The open aperture Z-scans measured for some of the ink samples are shown in Fig. 2. In a Z-scan experiment using a Gaussian laser beam, each z position corresponds to an input laser energy density (fluence) of

$$F_0(z) = 4\sqrt{ln2E_{in}}/\pi^{3/2}\omega(z)^2, \qquad (1)$$

where E_{in} is the input laser pulse energy, and ω(z) is the beam radius. In general, for an effective third-order nonlinearity involving absorption saturation and excited state absorption, the sample transmission is given by

$$F(z)/F_0(z) = exp - [\frac{\propto}{1+I(z)/I_s} + \beta I(z)]l \qquad (2)$$

where F(z) = transmitted fluence, α = linear absorption coefficient, I = intensity at z (W/cm^2), I_s = saturation intensity (W/cm^2), and β = third order nonlinear absorption coefficient (cm/W). After calculating I(z) (which is given by (F(z)/τ, where τ is the laser pulse width) the non-linear absorption coefficient of the sample can be numerically estimated from the Z-scan curve by using equation 2. The β values obtained for the samples are given in Table 1.

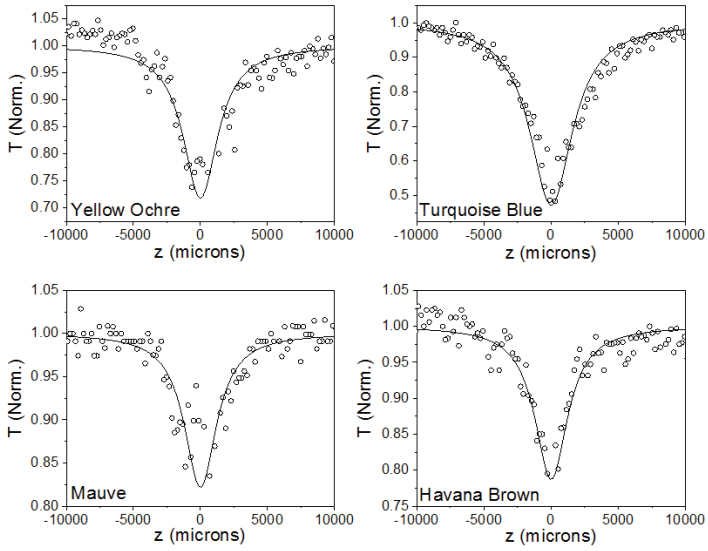

Figure 2: Open aperture Z-scan curves measured for some of the ink samples. Circles are data points while solid curves are numerical fits calculated using Eqn.2.

It is found that β is minimum for the ink *Crimson* (3 × 10^{-10} cm/W) and maximum for the ink *Turquoise Blue* (42.9 × 10^{-10} cm/W), with an order of magnitude difference between the values. Reverse saturable absorption (RSA) arising from excited state absorption (ESA) is the origin of the observed strong nonlinearity. These β values are in the order of those reported for good optical limiters in literature, showing that the ink samples studied are potential optical limiters which can be used for the protection of human eyes and sensitive detectors from powerful laser radiation. RSA is prominent for materials in which excited state absorption (ESA) is larger than ground-state

absorption. This is the case with all the ink samples we have investigated. The saturation intensities are found to be high for the samples so that absorption saturation effects are relatively weak compared to the optical limiting effect.

Ink	β ($\times 10^{-10}$ cm/W)
Crimson	3.0
Brilliant Red	4.5
Deep Black	6.0
Blue Black	7.0
Dark Grey	7.9
Rose Red	8.5
Mauve	10.0
Olive Brown	10.2
Dark Brown	12.0
Havana Brown	13.0
Yellow Ochre	17.0
Emerald Green	27.0
Turquoise Blue	42.9

Table 1: Third order nonlinear absorption coefficient values calculated for the ink samples from the open aperture Z-scan measurements.

4. Conclusions

The nonlinear optical transmission of 13 different free-flowing dye-based inks at 532 nm for 5 ns laser pulses has been studied by the open aperture Z-scan technique using a frequency-doubled Q-switched Nd:YAG laser. The samples show prominent reverse saturable absorption (RSA) behavior, because of which they show an excellent optical limiting behaviour. A comparative measurement of the nonlinear absorption coefficients has been carried out for the studied inks under identical experimental conditions. The comparison shows that the color *Turquoise Blue* has maximum nonlinearity compared to the other color variants, making it the most suitable sample among the studied media for optical limiting applications.

References

1. R. W. Boyd, *"Nonlinear Optics", Academic Press* (2008).

2. J. T. Kunjappu, *"Essays in ink chemistry: (for paints and coatings too)'', Nova Science Publishers*, 2001.

3. X. Cai, Z. Lv, H. Wu, S. Hou, D. Zou, *J. Mater. Chem.* **22** (2012) 9639.

4. M. Sheik Bahae, A.A. Said, T.M. Wei, D.J. Hagan, E.W. Van Stryland, *IEEE J. Quant. Electron*. **26** (1990) 760.

Synchronization and inverse-synchronization of self-pulsating non-symmetric coupled diode laser system

Prachi and S. Sivaprakasam*

[1]*Department of Physics, Pondicherry University, Pondicherry- 605014*

prakasam.phy@pondiuni.edu.in

Abstract:

Two semiconductor diode lasers are mutually coupled with one laser subjected to an optical feedback. The lasers are biased near threshold and are subjected to relatively weaker coupling resulting in self pulsating nature of the optical output intensity. Central optical frequencies of these two lasers are controlled so as to enable a detuning in their frequencies and intensity correlation between these two lasers are found to exhibit a smooth transition from positive to negative correlation. Numerical simulations of the suitably modified Lang - Kobayashi model[1] constitute this study.

Introduction

It is well known that diode lasers form the back-bone of the optical communications. In the recent decades, interest had grown several fold towards understanding of the dynamics of diode lasers due its potential is structuring secure optical communication. The basic requirement of such a system would involve a minimum of two diode lasers of which one of the lasers would be the source of chaos. All these studies involving mutually coupled diode lasers[2-7] had focused on chaotic oscillations of laser output intensities and their synchronization characteristics. Synchronization properties involved in studying the nature of its correlation, viz., positive or negative. A negatively correlated dynamical system is also termed as inverse-synchronization or anti-synchronization[8,9]. Two diode lasers, Driver laser (DL) and Driven laser (RL) are coupled face-to-face and the driver laser is subjected to an optical feedback obtained from an external cavity mirror. This external cavity mirror provides an optical feedback with a time delay of τ_{ext}. Figure 1 is the schematic of this system which is thus an asymmetrically coupled

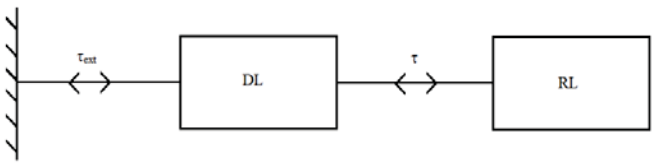

Fig.1, Schematic of the system under consideration. DL is the driver laser and RL is the driven laser

Model:

Dynamics of an external cavity diode laser is modeled by the well known Lang-Kobayashi[1] rate equation model and the suitably adapted rate equations for laser field (equations 1 and 2) and carrier densities (equations 3 and 4) are shown below.

$$\frac{dE_1(t)}{dt} = \frac{1}{2}\left(G_1 - \frac{1}{\tau_p}\right)E_1(t) + \kappa E_1(t-\tau_{ext})e^{-i\omega_1\tau_{ext}} + \eta E_2(t-\tau_1)e^{-i\omega_2\tau_1} \quad \ldots(1)$$

$$\frac{dE_2(t)}{dt} = \frac{1}{2}\left(G_2 - \frac{1}{\tau_p}\right)E_2(t) + \eta E_1(t-\tau_1)e^{-i\omega_1\tau_1} \quad (2)$$

$$\frac{dN_1(t)}{dt} = \frac{J_1}{e} - \frac{N_1}{\tau_n} - G_1|E_1(t)|^2 \quad (3)$$

$$\frac{dN_2(t)}{dt} = \frac{J_2}{e} - \frac{N_2}{\tau_n} - G_2|E_2(t)|^2 \quad (4)$$

Where, E and N represent the complex electric field and carrier density of diode lasers. Complex electric field is decomposed into field amplitude and phase to carry out simulations. The subscript 1 and 2 correspond to driver laser and driven laser respectively. Here the line width enhancement parameter α=3.8, carrier life time $\tau_{n=}$ 2 ns, photon life time τ_p=2ps, $J_{1,2}$ are the bias current densities and *e* is elementary charge. The rate of optical feedback for the driver laser is governed by feedback coefficient κ and η is the mutual coupling strength. The laser oscillation frequencies are ω_1 and ω_2 . Frequency detuning of the laser frequencies is $\Delta\omega=\omega_1-\omega_2$. The feedback delay time and the time delay between the lasers are kept at 10 ns.

Results

We solve the rate equations numerically using RK-4 algorithm for delay – differential equations. We consider non-zero detuning ($\Delta\omega=\omega_1-\omega_2$) for our simulations. We simulated the temporal evolution of laser field amplitude and phase for a set of detuning parameters ranging from 7.0GHz to 7.2GHz. The temporal evolutions exhibit self pulsating un-damped relaxation oscillations.

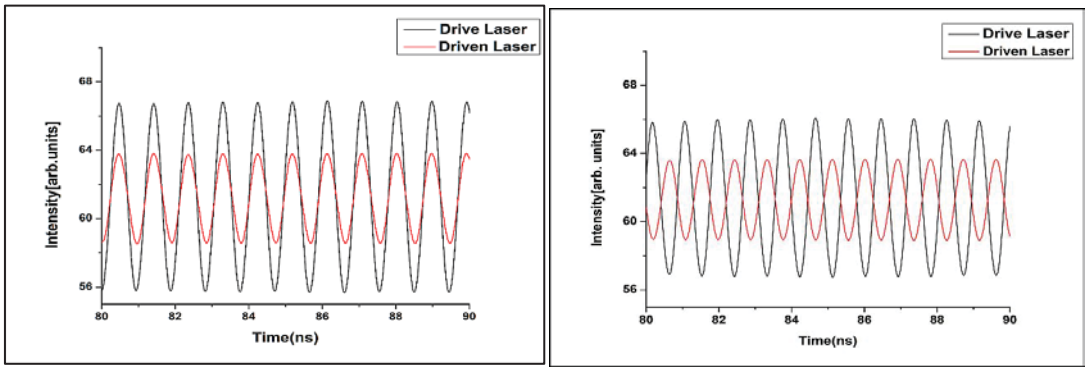

Fig. 2(a) Fig. 2(b)

Figure 2. temporal evolutions of the laser field amplitude at 7.0 GHz detuning (figure 2(a)) and at 7.2 GHz figure 2(b))

As shown in figure 2 (a) and (b), the laser are positively correlated for a detuning of 7.0 GHz and are inversely correlated for a detuning of 7.2 GHz. The nature of synchronization is realized by plotting the synchronization plots in which the driven laser output is plotted against the driver laser output. For an ideal synchronization the synchronization plot should be a straight line with a positive slope and for inverse-synchronization a straight line with a negative slope. Though there are studies on both the states of synchronization, the transitions characteristics are not well understood. In order to understand this transition character, we varied the detuning in smaller steps from 7.20 GHz to 7.0 GHz and observed a smooth transition of the sign of synchronization. This transition is shown in figure 3. The synchronization plot acquires relatively more variance at 7. 15 GHz and the variance further increases for 7.10 GHz. However, when the detuning in decreased further to 7.0 GHz the lasers

are positively synchronized. To understand their correlations, we carried cross – correlation calculations for the laser output amplitudes and the results are shown in figure 4.

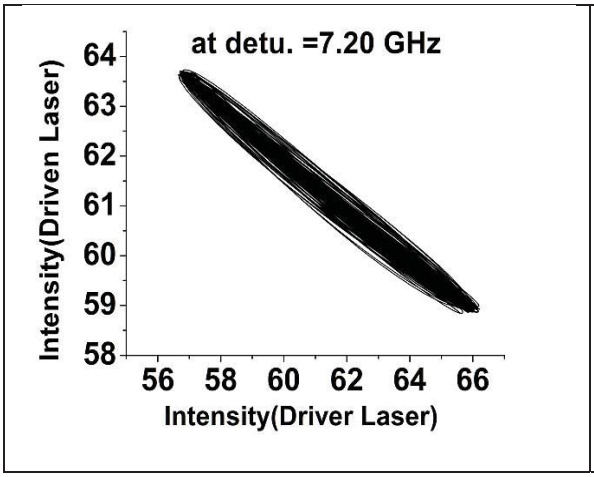

Figure 3(a)

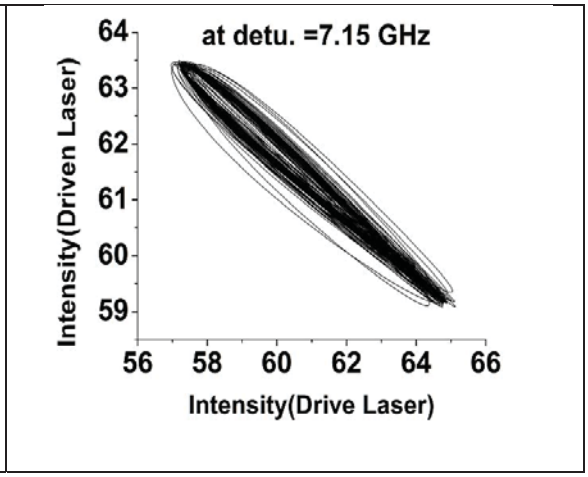

Figure 3(b)

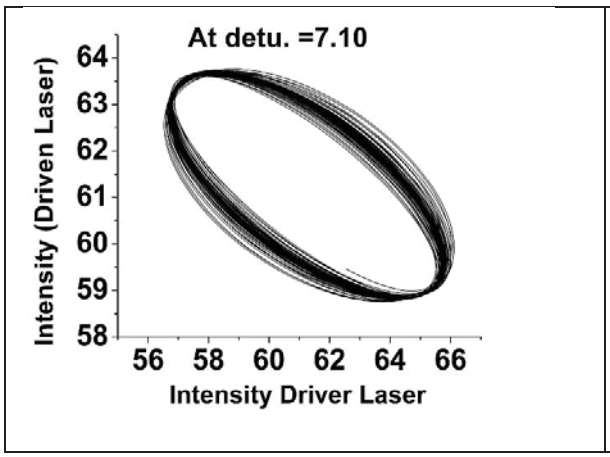

Figure 3(c)

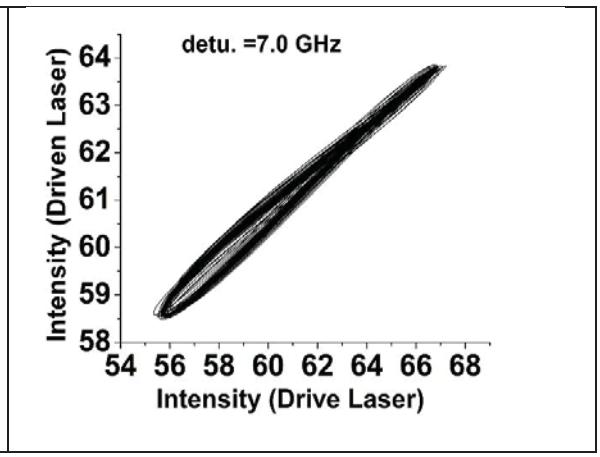

Figure 3(d)

Figure 3. The Synchronization plots for the field amplitudes of the two lasers are a detuning of (a) 7.2 GHz, (b) 7.15 GHz, (c) 7.10 GHz and (d) 7.0 GHz

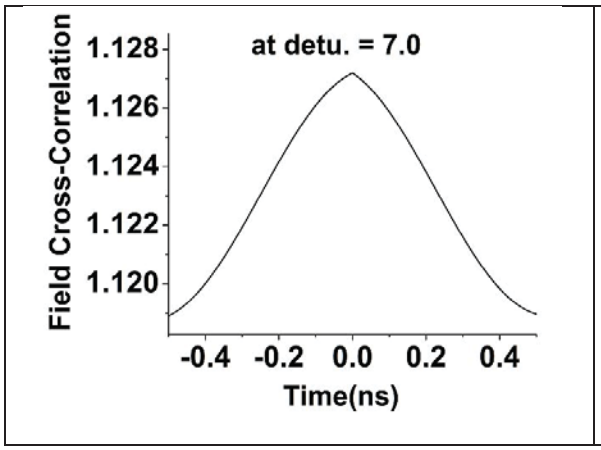

Figure 4(a)

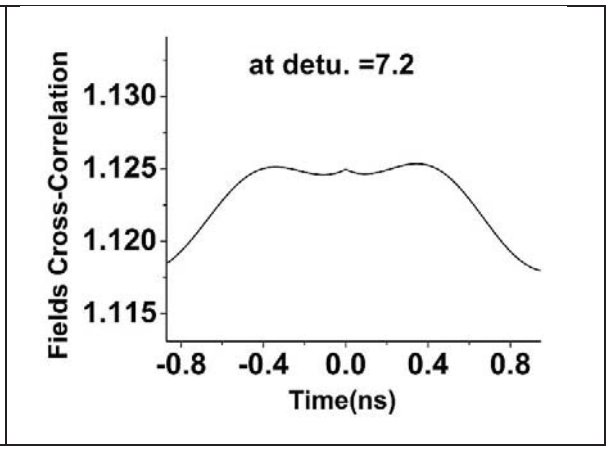

Figure 4(b)

Figure 4, The cross – correlation plots between the laser output corresponding (a) synchronization and (b) inverse synchronization

For a positively synchronized situation, the cross-correlation exhibits a distinct positive peak at zero-delay as shown in figure 4(a). Whereas, when the laser amplitudes are inversely synchronized, the cross – correlation loses its central peak which exhibits a relatively diminished peak at zero delay almost tending towards an inverse character.

We examined the power spectra of the both the lasers (the results are not included in this write up considering the space limitation) under the conditions of synchronization and inverse synchronization. We have found that there is no loss of spectral content even if the lasers are inversely synchronized. Preservation of spectral content is essential towards the applicability of this system for information exchange. The significance of inverse synchronization may be understood from the corresponding phase evolutions and their correlations and this investigation is ongoing.

Conclusions:

A non-symmetric system of coupled diode lasers is investigated for their synchronization properties. The lasers are operated at near – threshold conditions. Frequency detuning between the diode lasers are controlled and the corresponding synchronization of the laser field amplitudes are studied. The lasers exhibit a smooth transition from synchronization to inverse synchronization upon varying the frequency detuning between their emission frequencies. The inverse synchronization character is established from synchronization plots and cross-correlation plots. The significance of such smooth transition is being investigated for their potential applicability of information exchange.

References:

1. R. Lang and K. Kobayashi, *IEEE Journal of Quantum Electronics,* **16**, 0347 (1980).
2. S. Yanchuk, K. R. Schneider and L. Recke, *Phys. Rev. .E* **69**, 056221 (2004).
3. J. F. M. Avila, R. Vicente, J. R. R. Leite and C. R. Mirasso, *Phys. Rev. E* **75,** 066202 (2007).
4. P. Kumar, A. Prashad and R. Ghosh,*J. Phy. B. Mol. Opt. Phys.* **42,** 145401 (2009).
5. P. Rees, P. S. Spencer, I. Pierce, S. Sivaprakasam and K. A. Shore, Phys. Rev. A. **68**, 033818 (2003).
6. O. Vaudel, J. F. Hayau and P. Besnard, *Opt. Quant. Electron,* **40,** 109-118 (2008).
7. I. Wedekind and U. Parlitz*, Phys.Rev. A* **66,** 026218 (2002).
8. K. Srinivasan, D. V. Senthilkumar, K. Murali, M. Lakshmanan and J. Kurths, *Chaos* **21,** 023119 (2011).
9. D. V. Senthilkumar, J. Kurths and M. Lakshmanan, *Chaos***19**, 023107(2009).

Potential Energy Distribution study and Molecular Properties of 1,3-Diphenyl Propenone

Revathi Haldorai[a], M. Thirumalaikumar[b], S.Sampathkrishnan[c], C.Charanya[d] N.Balamurugan[e*],

[a]*Department of Chemistry, Karpagam Academy of Higher Education, Eachanari, Coimbatore 641021, Tamil Nadu, India.*

[b] *Department of Applied Chemistry, Sri Venkateswara College of Engineering, Sriperumbudur 602105, Tamil Nadu, India.*

[c] *Department of Applied Physics, Sri Venkateswara College of Engineering, Sriperumbudur 602105,Tamil Nadu, India.*

[d]*Research Scholar, Department of Applied Physics, Sri Venkateshwara College of Engineering, Sriperumbudur 602105, Tamilnadu, India.*

[e]*Department of Physics, Dhanalakshmi College of Engineering,Tambaram, Chennai, Tamilnadu, India*

[*] Corresponding author Email: n_rishibalaa@yahoo.co.in (N.Balamurugan).

Abstract

The Fourier Transform Infrared (FTIR) and Fourier transform Raman (FT-Raman) spectra of 1,3-Diphenyl Propenone were recorded in the regions 4000-400 cm^{-1} and 4000-100 cm^{-1}, respectively, in the solid phase. Molecular electronic energy, geometrical structure, harmonic vibrational spectra was computed at the DFT/ 6-31G(d,p) and three parameter hybrid functional Lee-Yang-Parr/6-31G(d,p) levels of theory. The vibrational studies were interpreted in terms of potential energy distribution (PED). The results were compared with experimental values with the help of scaling procedures. Most of the modes have wave numbers in the properties of Mulliken population analysis have been calculated. Besides, thermodynamic properties were performed.

1. Introduction

1,3-Diphenyl Propenone is the derivative of the chalcone moieties have evoked a great deal of interest due to their biological properties and characteristic conjugated molecular architecture. Chalcones have been considered derivatives of the 1,3-diaryl-2-propene-1-one parent compound composed of two phenolic rings, referred to as the A and B rings. Many of them possess important pharmacological properties, such as analgesic [1], arthritis [2], anti-inflammatory [3], anti-pyretic [4], anti-bacterial [5], anti-viral [6,7], and anti-cancer effects.They were also potentially useful for many industrial products and phytochemical applications, including food sciences. Nowadays, a number of comparative pharmacological investigations of the chalcones have showed good antioxidant activity with low side effects. In this present study, a complete vibrational analysis of the molecule was performed by combining the experimental (FTIR and FT-Raman) data and theoretical information using Pulay's DFT based scaled quantum mechanical (SQM) method. Moreover, the Mulliken population analysis of the 1,3-Diphenyl Propenone compound has been calculated and the calculated results have been reported. Finally, the thermodynamic properties of the optimized structures were obtained theoretically from the harmonic vibrations.

2. Experimental details

A pure sample of 1DPP was purchased from Sigma - Aldrich Chemical Company, St. Louis, MO, USA,

and used as such for spectral measurements. The Fourier transform infrared (FTIR) spectrum of this compound was recorded in the region 4000-400 cm^{-1} on a Brucke model IFS 66 V spectrophotometer using the KBr pellet technique. The spectrum was recorded

3. Results and discussion

3.1. Molecular geometry

The numbering system adopted in the molecular structure of 1DPP is shown in Fig. 1. The optimized geometrical parameter calculated by DFT/B3LYP with 6-31G(d,p) basis set is listed in Table 1. Table 1 compares the calculated bond length and bond angles for 1DPP with those of experimental data . From the theoretical values, it is found that some of the calculated parameters are slightly deviated from the experimental values, due to fact that the theoretical calculations belong to molecule in the gaseous phase and the experimental results belong to molecule in solid state.

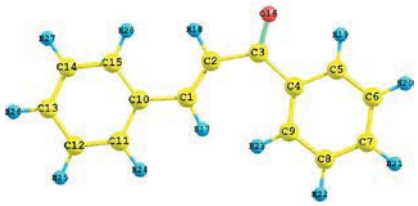

Fig. 1. *The optimized molecular structure of 1, 3-Diphenyl Propenone*

3.2. Vibrational band assignments

According to the theoretical calculations, 1,3-Diphenyl Propenone has a structure of C_1 point group symmetry. The molecule has 28 atoms and 78 modes of fundamental vibrations. We have taken recourse to the calculation and visualization of contribution of internal coordinates in each normal mode by Gaussian package [15] and chemcraft program. The harmonic vibrational frequencies calculated for the 1,3-Diphenyl Propenone compound at B3LYP level using 6-31G(d,p) along with the observed FT-IR and FTR frequencies for various modes of vibrations .Therefore, a linearity between the experimental and scaled calculated wave numbers for DFT method of 1,3-Diphenyl Propenone can be estimated by plotting the calculated versus experimental wave numbers as shown in Fig. 2. The correlation coefficients (R2) for experimental and observed wave numbers computed from the DFT method were found to be 0.9932. It can be noted from the R2 values that the theoretical prediction is in good agreement with the experimental wave numbers. Also Fig.2 reveals the overestimation of the calculated vibrational modes due to neglect of Lorentzian band shapes were used with a bandwidth of 40 cm^{-1}. Figs. 3 and 4 shows a comparative representation of theoretical and experimental FT-IR and FT-Raman spectra,respectively.

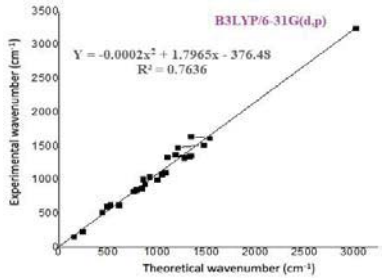

Fig. 2. *Correlation diagram for the theoretical and experimental wave number of 1, 3- Diphenyl Propenone*

Table 1
Optimized geometrical parameters for 1, 3-Diphenyl Propenone computed at DFT with 6-31G(d,p) basis set.

Parameters Bond length (Å)	Exp[a]	B3LYP/ 6-31G(d,p)	Parameters Bond angle (°)	Exp[a]
C(16)-H(29)	1.10	1.10	H(29)-C(16)-C(11)	120.00
C(15)-H(28)	1.10	1.10	H(29)-C(16)-C(15)	120.00
C(14)-H(27)	1.10	1.10	C(11)-C(16)-C(15)	120.00
C(13)-H(26)	1.10	1.10	H(28)-C(15)-C(16)	120.00
C(12)-H(25)	1.10	1.10	H(28)-C(15)-C(14)	120.00
C(10)-H(24)	1.10	1.10	C(16)-C(15)-C(14)	120.00
C(9)-H(23)	1.10	1.10	H(27)-C(14)-C(15)	120.00
C(8)-H(22)	1.10	1.10	H(27)-C(14)-C(13)	120.00
C(7)-H(21)	1.10	1.10	C(15)-C(14)-C(13)	120.00
C(6)-H(20)	1.10	1.10	H(26)-C(13)-C(14)	120.00
C(3)-H(19)	1.11	1.11	H(26)-C(13)-C(12)	120.00
C(3)-H(18)	1.11	1.11	C(14)-C(13)-C(12)	120.00
C(2)-H(17)	1.10	1.10	H(25)-C(12)-C(13)	120.00
C(1)-C(11)	1.35	1.52	H(25)-C(12)-C(11)	120.00
C(11)-C(16)	1.34	1.42	C(13)-C(12)-C(11)	120.00
C(15)-C(16)	1.34	1.42	C(1)-C(11)-C(16)	120.00
C(14)-C(15)	1.34	1.42	C(1)-C(11)-C(12)	120.00
C(13)-C(14)	1.34	1.42	C(16)-C(11)-C(12)	120.00
C(12)-C(13)	1.34	1.42	H(24)-C(10)-C(5)	120.00
C(11)-C(12)	1.34	1.42	H(24)-C(10)-C(9)	120.00
C(3)-C(5)	1.50	1.50	C(5)-C(10)-C(9)	120.00
C(5)-C(10)	1.34	1.42	H(23)-C(9)-C(10)	120.00
C(9)-C(10)	1.34	1.42	H(23)-C(9)-C(8)	120.00
C(8)-C(9)	1.34	1.42	C(10)-C(9)-C(8)	120.00
C(7)-C(8)	1.34	1.42	H(22)-C(8)-C(9)	120.00

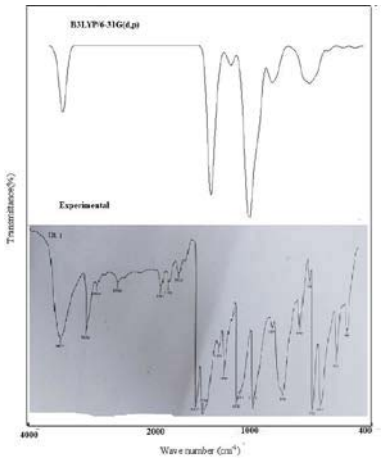

Fig.3 *Comparative representation of FT-IR . spectra for 1, 3-Diphenyl Propenone*

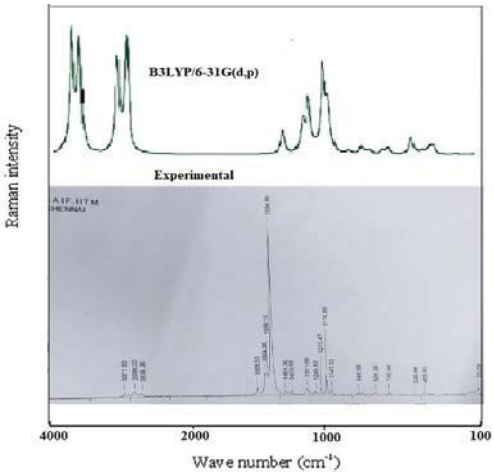

Fig.4 *Comparative representation of FT-Raman spectra for 1, 3-Diphenyl Propenone*

4. Other molecular properties

4.1 Mulliken atomic charges

Mulliken atomic charge calculation has an important role for the application of quantum chemical calculation of the molecular system. Atomic charge affects dipole moment, polarizability, electronic structure and other molecular properties as the system. The calculated Mulliken charge values of 1,3-Diphenyl Propenone are listed. It is clearly shown that the carbon atom attached with hydrogen atom is negative, whereas the remaining carbon atoms are positively charged in the 1,3-Diphenyl Propenone compound. The oxygen atoms have more negative charge whereas all the hydrogen atoms have the positive charges. The more positive charge of carbon is found for the compound for C1, C3 and C7; it is mainly due to the substitution of negative charge of an oxygen atoms. The lone pare of oxygen atom (O16) shows the charge transferred from O to H. Illustration of atomic charge plotted for B3LYP/6-31G (d,p) level have been shown in Fig. 5

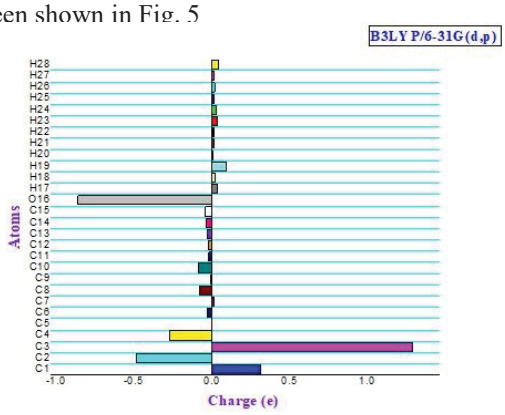

Fig. 5. *The Histogram of Calculated Mulliken charge for 1, 3-Diphenyl Propenone molecule.*

5. Conclusion

The FT-IR and FT-Raman measurements have been made for the 1,3-Diphenyl Propenone molecule. The complete vibrational assignment with PED was calculated using SQMF method.The equilibrium geometries and harmonic frequencies of 1,3-Diphenyl Propenone were determined and analyzed at DFT level of theories utilizing 6-31G (d, p) basis set. The difference between observed and calculated wavenumber values of the most of the fundamental modes is very small. The calculated normal-mode vibrational frequencies provide thermodynamic properties by way of statistical mechanics.

References

1. G.S.B. Viana, Bandeira, M.A.M. Matos, F.J.A., *Phytomedicine*, **10,** 189–195 (2003).

2. J.Rojas, M. Payá, J.N Domínguez, and M. L Ferrándiz, *Eur. J. Pharmcol* **465**, 183–189 (2003).

3. Z.Nowakowska,. *Eur. J.Med. Chem*., **42**, 125–137 (2007).

4. M.Al Rahim, A.Nakajima, N.Misawa, K.Shindo, K.Adachi, Y.Shizuri, Y.Ohizumi,,and T.Yamakuni, *Eur. J. Pharmacol.,* **600,** 10–17 (2008).

5. S.F Nielsen, M. Larsen, T. Boesen, K. Schonning, and H. Kromann,. *J. Med. Chem.,* **48,** 2667–2677 (2005).

6. M.A.Ali, M. Shaharyar, and E. De Clercq, . *J. Enzyme Inhib. Med. Chem.,* **22**, 702–708 (2007).

7. J.C Onyilagha, B. Malhotra, M.Elder, C.J .French and G.H.N Towers, *J.Plant Pathol.,* **19**, 133–137 (1997)

QPM grating structure for simultaneous RGB generation for projection display applications

Indhumathi Ravi Rajan[1] · Mubarak Ali Meerasha[1] · Madhupriya G[1] ·
Shanmugam Boomadevi[2] · Krishnamoorthy Pandiyan[1]

[1]*Integrated Optics Lab, Centre for Nonlinear Science and Engineering (CeNSE), School of Electrical & Electronics Engineering, SASTRA Deemed University, Thanjavur-613401, Tamil Nadu, India.*
[2]*Department of Physics, National Institute of Technology, Tiruchirappalli - 620015 Tamil Nadu, INDIA*
Email: krishpandiyan@ece.sastra.edu

Abstract:

Laser based projection displays (LBPD) require a compact device to generate high intense simultaneous RGB of pure colours with a single pump source. In this work, we investigated phase reversal (PR) and segmented grating structures for optimal generation of RGB at 450, 530 and 650 nm. Several different configurations of the segmented and the PRPPLN structures were optimized for 355, 491, 480, 473, 480, 505, and 430 nm pump sources. The RGB emissions varied from 632-656 nm for red, 504-532 nm for green and 449-484 nm for blue, respectively for different configurations of the pump and the structure.

Keywords:
Simultaneous RGB generation · phase shifter · quasi-phase-matching · periodically poled lithium niobate (PPLN) device

Introduction:

Simultaneous laser systems have already been demonstrated by building an additional setup to generate the desired pump wavelength [1]. But such a configuration could make the laser system bulkier. Thus, in order to bring down the size of the device, special attention was given to choose the most suitable pump wavelength with respect to the commercially available laser source. Further, proper domain engineering of the QPM device could help to phase match many wavelengths simultaneously in a single device. An alternative approach could be to cascade an array of wavelength converters, making the system expensive and bulky. Efficiency [5,6] of such a device depends on the domain shape, duty ratio, device length etc. Several techniques have been investigated for the purpose of identifying the optimal structure for a given pump wavelength to produce multiple harmonics. Techniques such as aperiodic, apodization/chirped grating structures and phase reversal structures are a few widely explored [3,4]. In this work we analyse the different structures that can be used to generate red (R), green (g) and blue (B) at 650, 530 and 450 nm, respectively with a single pump source. Development of such a system would reduce the overall size, cost and complexity, contributing to the current commercial scope in laser-based projection display (LBPD) technology.

Results and discussions:

We consider a simple PPLN structure of 1 cm length, containing 3 sections (0.3, 0.3, 0.4 cm) as shown in fig. 1(a). The calculated phase matching periods are 2.2 µm for blue, 1.8 µm for green, and 1.65 µm for red and the devise was pumped with 355 nm source to produce type 0 DFG outputs at 640, 532, 458 nm as illustrated in fig. 1 (b, c, d).

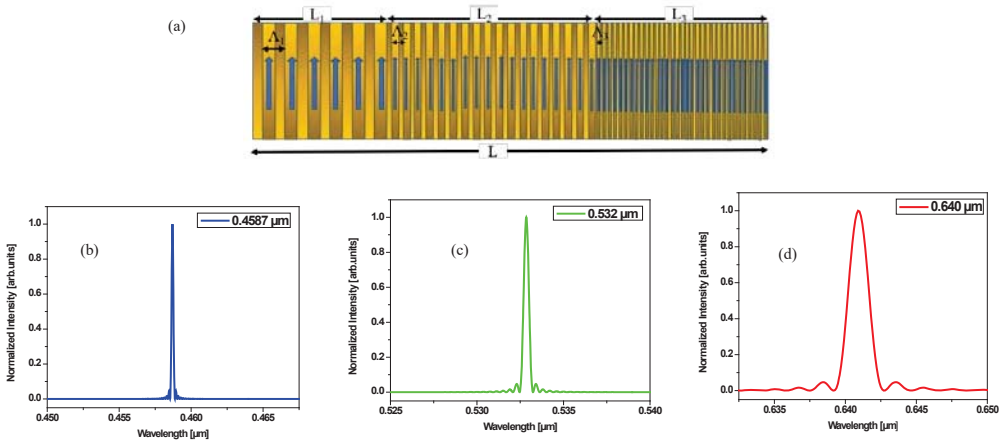

Fig. 1. (a) Schematic representation of a PPLN structure containing 3 different segments. DFG intensity (b) Blue (458.7 nm), (c) Green (532 nm), and (d) Red (640 nm) emission wavelengths.

Another PPLN structure with 7 randomly distributed phase reversal domains [2] as shown in fig. 2. (a), different configurations, were studied for 491, 480, 473 nm pump sources (fig. 2. (b,c,d)). The most significant results are tabulated in table. 1.

Si. no.	***Input (nm)***	***Period width (µm)***	***Phase shifter width (µm)***	***Number of phase shifters (µm)***	***Output (nm)***
1.	491	14	10	7	517 & 635
2.	480	12.4	8.4	7	504 & 639
3.	473	10.4	5	7	496 & 656

Table. 1. Tabulates the domain width, phase shifter width, number of phase shifters and the corresponding output wavelengths for 491, 480, 473 nm pump sources.

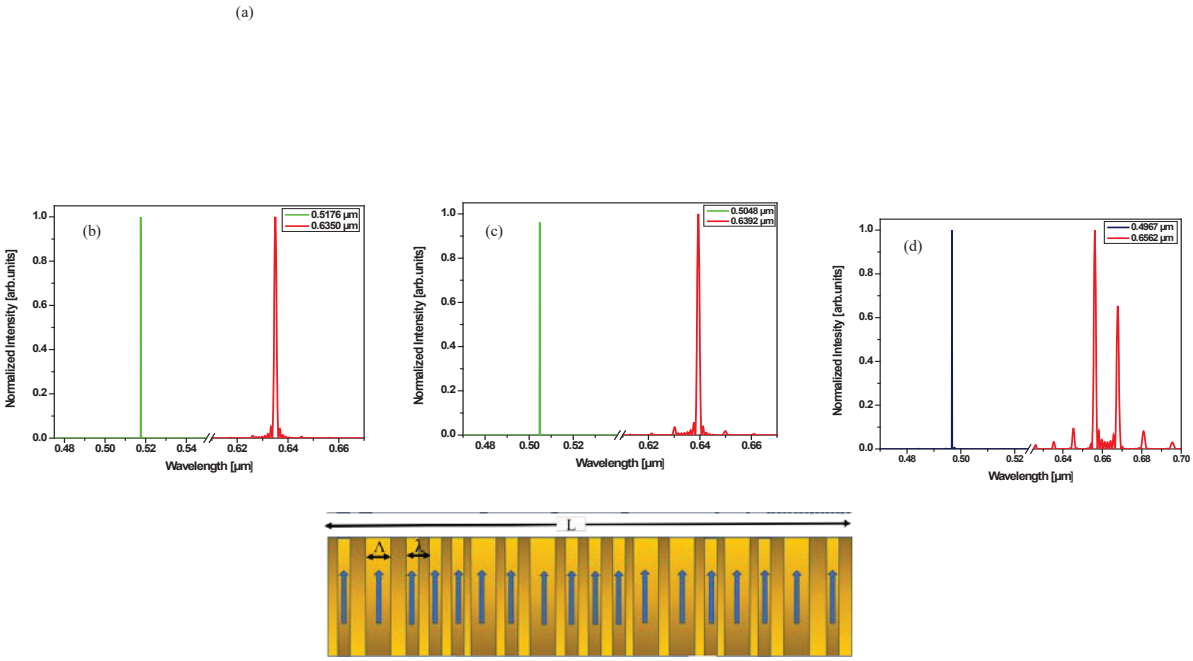

Fig. 2. (a). Schematic representation of PRPPLN structure containing 7 PS domains distributed randomly and DFG spectrum for (b) pump=491 nm, (c) pump=480 nm, (d) pump=473 nm.

Eight randomly distributed phase shifters at the location, 1670, 3340, 6600, 8330, 10000, 11670, 11700, 18350, and 20000 with phase shifter and the grating period widths fixed at 8.12 μm was pumped at 505 nm (fig. 3). This configuration produced emissions at 484, 534, and 632 nm corresponding to red, green and blue wavelengths.

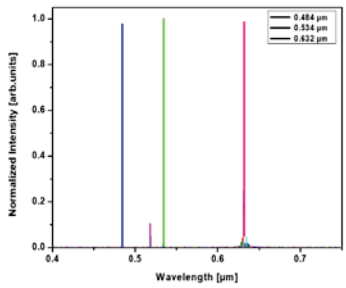

Fig. 3. Type 0 DFG spectrum for PRPPLN structure with pump=505 nm.

A pump of 465(B) nm was used to produce output emissions at 532(G) and 632(R) nm, as illustrated in fig. 4. (b). This is a simple design containing 20000 domains separated into two segments with 10000 domains each. The grating period was fixed at 8.2, and 5.4 μm for the first and the second segment respectively as shown in fig. 4(a).

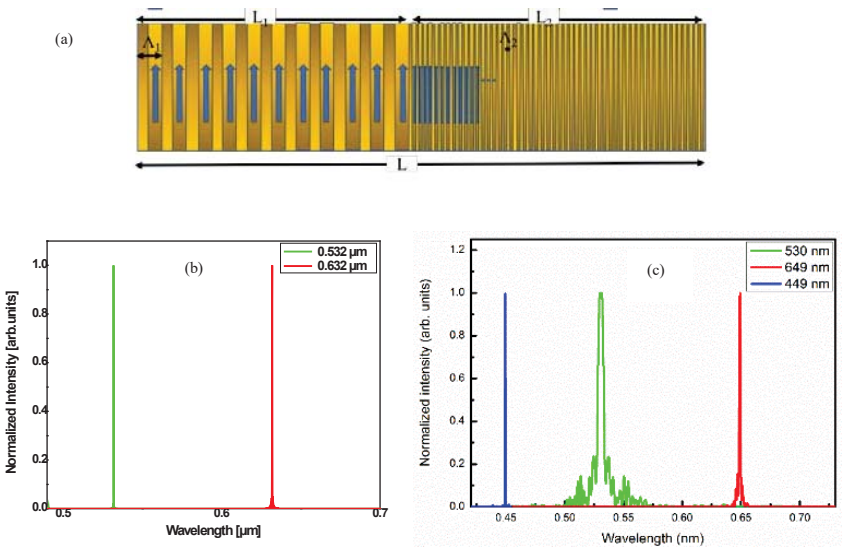

Fig. 4. (a) Schematic representation of segmented PPLN structure containing 2 segments and intensity spectrum for (b) pump=505 nm and (c) pump=430 nm.

A segmented PRPPLN structure with 2 segments pumped with a 430 nm laser source used to generate blue, green and red at 449, 530, 649 nm respectively is shown in fig. 4 (c). The domain width was fixed at 5.03 µm throughout the length of the device, whereas the PS domain width was fixed at 5.03 µm and 3.68 µm for the first and second segments respectively. The PS domains were distributed randomly throughout the length of the device.

Acknowledgment:

The authors would like to acknowledge the Core Research Grant Scheme, Science and Engineering Research Board (SERB), (Ref. No.: CRG/2018/001788) and the Indo-Uzbek bilateral scheme Department of Science and Technology (DST), (Ref. No.: INT/Uzbek/P-16), Govt. of India for the financial support

Conclusion:

We presented a theoretical investigation to design suitable phase reversal and segmented QPM grating structures for simultaneous RGB generation by type 0 difference frequency generation in periodically poled lithium niobate device. The output RGB emissions varied from 632-656 nm for red, 504-532 nm for green and 449-484 nm for blue, respectively for different configurations of 355, 491, 480, 473, 480, 505, and 430 nm pump sources and the structural parameters.

References:

1. H. H. Lim, O. Prakash, B. Kim, K. Pandiyan, M. Cha and B. K. Rhee, Opt. Express 15, 18294 (2007).
2. N. Balaji, T. S. Meetei, M. M. Ali, S. Boomadevi, M. Senthilkumar, and K. Pandiyan, J. Light. Technol. 37, 3, (2019).
3. D. K. Choge, H. X. Chen, Y. B. Xu, L. Guo, G. W. Li and W. G. Liang, Appl. Sci. 8, 629, (2018).

4. M. Robles-Agudo, R. S. Cudney, L. A. Ríos, opt. exp. 10663, 14, 22, (2006).
5. D.H. Jundt, Opt. Lett. 22, 1553–1555 (1997).
6. M.M. Fejer, G.A. Magel, D.H. Jundt, R.L. Byer, IEEE J. Quant. Electron. 28, 2631–2654 (1992).

Nonreciprocal light propagation in novel photonic crystal/metal hybrid structure

Nikhil P P and Chandrasekharan K

Laser and Nonlinear Optics Laboratory, National Institute of Technology Calicut, India

Email: csk@ nitc.ac.in

ABSTRACT

Herein, we report a passive nonlinear photonic diode by making use of the non-reciprocity in light transmission by cascading a reverse saturable absorber (RSA) and saturable absorber (SA) in tandem. A 1-D polymer photonic crystal with a cavity layer, containing phthalocyanine, is selected as RSA material while a 50 nm thin layer of gold is chosen for SA. The localized mode of the photonic cavity is designed at 532 nm, which is the excitation wavelength of the laser used in the study. Due to high optical density of states in photonic crystal cavity and resultant enhanced light-matter interaction leads to giant enhancement in the nonlinear absorption of the dye. The forward and reverse diode actions were studied using nanosecond pulsed laser by varying the input fluencies. Our structure offers high non-reciprocity factor with low input threshold, with good chemical and mechanical stability, making it a potential candidate towards realizing all-optical analogous of electronic devices.

INTRODUCTION

The past few decades witnessed remarkable technological advancement in replacing conventional electronic devices with integrated photonic systems with superior performances. The photonic integrated chips (PIC) require all-optical elements to control the light propagation. The optical diode is one of the fundamental elements in optical communication systems. Similar to its electronic counterpart, optical diode can block the propagation of light in one direction, while letting in the other direction.

All-optical diodes have been realized earlier by means of linear and nonlinear optical effects such like non-reciprocal optical resonators[1], 1-D photonic crystals[2-4] , electro-tunable liquid crystals[5-6], coupled cavity QED system[7], micrometer-scale ring-resonators[8], the opto-accustic effects[9], or the thermo-optic effect in silicon rings[10]. Although these systems are conceptually novel, practical realizations of these structures are still challenging. However, relatively simple structures have been made by making use of asymmetrical nonlinear absorption of light[11-13]. A Saturable Absorber (SA) and Reverse saturable absorber (RSA) is juxtaposed in the beam direction causes axially asymmetric transmission of light. Apart from the easiness in fabrication, these systems have scalable-low cost design, which makes them potential candidate in integrated devices.

MATERIALS AND METHODS

1-D Photonic crystal comprising of two polymers polyvinyl carbazole(PVK,Sigma Aldrich, Mw=1,100,000) and Cellulose acetate(CA, Mw=100,000,Acros Organics) with refractive index 1.69 and 1.47 respectively were spin coated on glass substrate with quarter wave optical thickness. A metal free phthalocyanine dye (29H, 31H-Phthalocyanine) is incorporated in CA film to form a defect layer. The optical limiting actions of the nonlinear photonic crystal (NL-PhC) were studied using a Q-Switched Nd:YAG laser, having 7ns pulse width, 532 nm wavelength. The structure of fabricated NL-PhC is given in Figure 1.

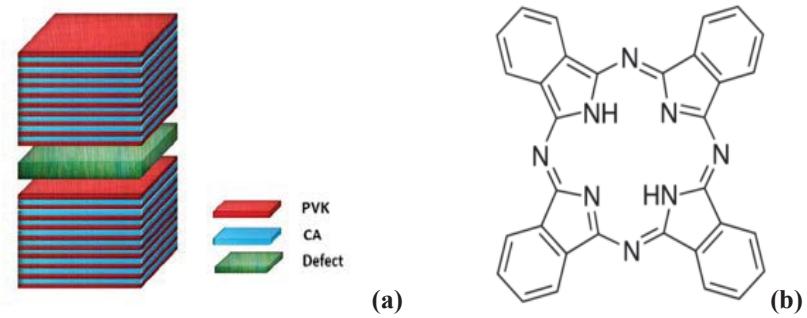

Figure 1 (a) The structure of 1-D PhC with cavity. Both DBR made up of 10 bilayers of PVK-CA, having quarter-wave optical thickness. The defect layer (CA doped with NLO dye) has half-wavelength thickness.(b) Structure of phthalocyanine dye

Results and Discussion

The nonlinear optical characterizations were done using z-scan technique with a Q-switched Nd:YAG laser(pulse width 7 ns, wavelength 532 nm). The input energy is fixed at 10 uJ and focal length of the lens is 15 cm. The nonlinear transmittance vs input fluence graph of the reference sample (phthalocynine doped CA film) and NL-PhC is shown in Figure 2. The nonlinear absorption in reference sample is insignificant while the NL-PhC shows better nonlinearity. This is atributed to the strong confinement of optical field in the resonant microcavity. Numerical simulations using transfer matrix formalism shows intense field distribution at the defect layer (Figure 3).

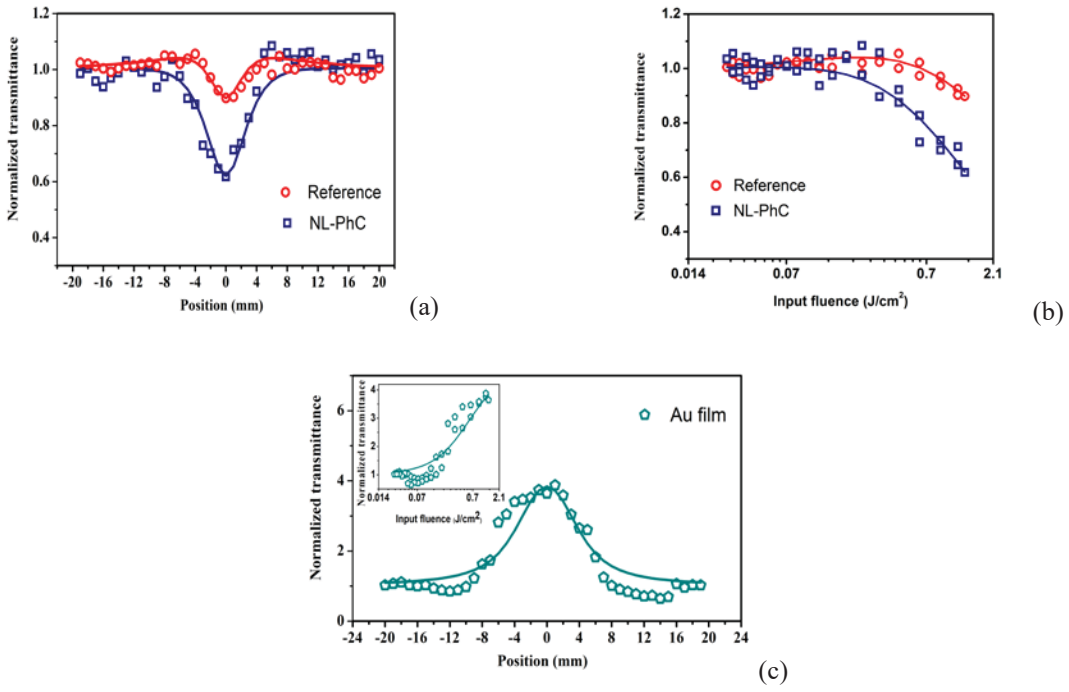

Figure 2. (a) The open aperture z-scan signature and (b) Optical limiting action of reference and NL-PhC (c) Z scan signature and optical limiting curve (inset)of Au film. Solid lines are theoretical fittings

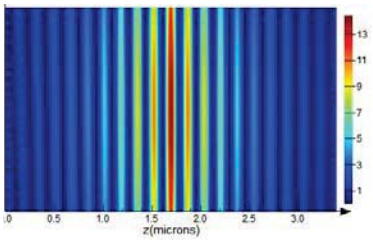

Figure 3 Spatial intensity distributions in defective photonic crystal when exciting with 532 nm wavelength. Colour bar represents intensity

The increase in the transmittance of Au film with increase in fluence is the characteristic feature of SA type nonlinearity. For the hybrid SA/RSA structure, the abrupt change in the nonlinear phenomena causes non-reciprocal transmission of laser beam. When light first excites the SA material, the net transmittance gradually increases from its linear transmittance due to the depletion of the ground state. This enhanced output intensity then passes through the RSA medium, eventually causes a reduction of transmittance. Since the SA is more dominant over RSA, in our case, the net output will be increase in transmittance on increasing input intensity. This is a typical behaviour of forward bias operation in an electronic diode. On other hand, when RSA is placed in front of SA, the output intensity gets attenuated due to RSA behaviour. In that case, the output intensity from RSA material is not sufficient to induce the nonlinear effects in SA material. Furthermore, the linear transmittance of the SA medium is only 20% in our case. Thus, on increasing the input pulse intensity, the resultant will be decrease in transmittance. The diode action is shown in figure 4.

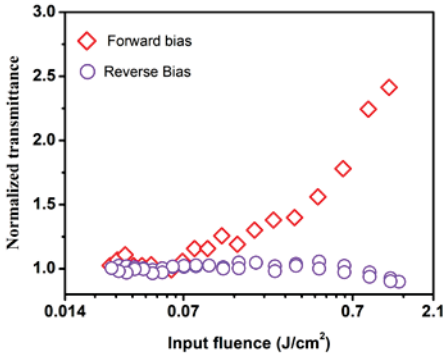

Figure 4 Optical diode actions (forward and reverse biases)

The non-reciprocity factor(NRF) is the contrasst ration of nonlinear transmittance in forward and reverse bias is given by

$$NRF|_{dB} = 10\log(T_{FB}/T_{RB})$$

Where T_{FB} and T_{RB} are the forward and reverse bias transmittances. The system exhibited good non-reciprocity and the measured value of (NRF) is 4.3 dB at an input intensity ~0.28 GW/cm^2.

CONCLUSION

In summary, the optical diode action is demonstrated in PhC/metal hybrid structure. The strong light localized mode in PhC leads to enhanced NLA coefficients. By utilizing the asymmetry in NLA coefficients of NL-PhC

and gold layer, we obtained high contrast nonreciprocal light transmission. We propose this structure for various applications in nanophotonics and for realizing all-optical devices with better on-chip integrability.

References

1 L. Bi, J. Hu, P. Jiang, D. H. Kim, G. F. Dionne, L. C. Kimerling and C. A. Ross, *Nat. Photonics*, 2011, **5**, 758–762.

2 S. R. Entezar and R. Vatannejad, *J. Nonlinear Opt. Phys. Mater.*, 2016, **25**, 1–7.

3 K. JAMSHIDI-GHALEH and Z. SAFARI, *Int. J. Mod. Phys. Conf. Ser.*, 2012, **15**, 48–53.

4 M. D. Tocci, M. J. Bloemer, M. Scalora, J. P. Dowling and C. M. Bowden, *Appl. Phys. Lett.*, 1995, **66**, 2324–2326.

5 C. Wang, C. Chen, H. Jau, C. Li, C. Cheng, C. Wang, S. Leng, I. Khoo and T. Lin, *Nat. Publ. Gr.*, 2016, 1–7.

6 J. Hwang, M. H. Song, B. Park, S. Nishimura, T. Toyooka, J. W. Wu, Y. Takanishi, K. Ishikawa and H. Takezoe, *Nat. Mater.*, 2005, **4**, 383–387.

7 P. Yang, X. Xia, H. He, S. Li, X. Han, P. Zhang, G. Li, P. Zhang, J. Xu, Y. Yang and T. Zhang, *Phys. Rev. Lett.*, , DOI:10.1103/PhysRevLett.123.233604.

8 Z. Yu and S. Fan, *Nat. Photonics*, 2009, **3**, 91–94.

9 M. S. Kang, A. Butsch and P. S. J. Russell, *Nat. Photonics*, 2011, **5**, 549–553.

10 L. Fan, J. Wang, L. T. Varghese, H. Shen, B. Niu, Y. Xuan, A. M. Weiner and M. Qi, *Science (80-.).*, 2012, **335**, 447–450.

11 R. Philip, M. Anija, C. S. Yelleswarapu and D. V. G. L. N. Rao, , DOI:10.1063/1.2794015.

12 B. Anand, R. Podila, K. Lingam, S. R. Krishnan, S. Siva Sankara Sai, R. Philip and A. M. Rao, *Nano Lett.*, 2013, **13**, 5771–5776.

13 E. Shiju, M. Bharat, N. K. Siji Narendran, D. Narayana Rao and K. Chandrasekharan, *Opt. Mater. (Amst).*, 2020, **99**, 109557.

Optical response of anatase TiO_2: The role of exact exchange on predicting exciton binding energy

Sruthil Lal S B[1, *)], D Murali[2)], Matthias Posselt[3)] and Alok Sharan[1, a)]
[1](Department of Physics, Pondicherry University, R. V. Nagar, Kalapet, Puducherry, India)
[2](Indian Institute of Information Technology Design and Manufacturing (IIITDM), Kurnool, Andhra Pradesh, India)
[3](Helmholtz-Zentrum Dresden-Rossendorf, Bautzner Landstraße 400, 01328 Dresden, Germany)

Corresponding author: [a)]aloksharan@gmail.com, [*)]getsruthil@gmail.com

Abstract. We computed the fundamental bandgap and excitonic optical response of anatase TiO_2 by employing state-of-the-art many-body perturbation theory (MBPT) formalism. Quasiparticle energies and fundamental gap are obtained as first-order correction to Kohn-Sham DFT eigenvalues with G_0W_0 scheme within MBPT. Kohn-Sham DFT eigenvalues with HSE06 hybrid exchange-correlation functional are used as zero-order wavefunctions on which G_0W_0 corrections are applied. Also, within MBPT, the dielectric function of anatase is calculated from the solutions of the Bethe-Salpeter equation (BSE). The Green's function (G) for MBPT calculations used in this work are built from Kohn-Sham orbitals computed with HSE06 hybrid exchange-correlation functional. Since the amount of exchange fraction(α) which defines the HSE06 hybrid functional is material dependent, the BSE optical spectra computed on top of respective KS-DFT eigenvalues also become sensitive to α . In this report, we analyze the role of fraction of exact exchange for the accurate prediction of electronic and optical properties of anatase TiO_2. The dependence of quasiparticle gap, dielectric function and exciton binding energy on the exact exchange fraction (α) is investigated systematically from well-converged many-body perturbation theory calculations.

INTRODUCTION

Anatase form of Titanium Dioxide (TiO_2) is the most photo-catalytically active TiO_2 polymorph among its other naturally occurring phases-rutile and brookite. High carrier mobility due to smaller effective mass of conduction band electrons, low recombination rate of photo-excited charge carriers coupled with wide optical gap (UV region) of anatase is responsible for its efficient use in different applications. Besides used in various forms in photo catalysis, it finds applications in reducing CO_2 into hydrocarbon fuels and also as absorber material in dye sensitized solar cells [1,2]. It has been understood that, after excitation, the conduction band electrons in anatase TiO_2 remains bound to holes in the valence band forming excitons. The character as well as binding energy of excitons, its life-time and spatial localization within the crystal governs the dynamics of charge carriers following the absorption of light. Excited states in solids are routinely probed by a combination of photoemission, inverse photoemission, angle resolved photoemission experiments and so on. Experiments are usually supported by theoretical calculations simulating the photo-response in order to supplement experiments and, more importantly, to make useful and reasonable predictions. On the theoretical side, Hedin's GW method and Bethe-Salpeter Equations (BSE) within the many-body perturbation theory (MBPT) form the state-of-the-art tools for simulations from first-principles of quasi-particle excited states and optical response [3,4].

Within the framework of MBPT, G_0W_0 method provides accurate quasi-particle bandgaps for wide variety of materials. In the G_0W_0approximation, where G is the Green's functions and W is the screened Coulomb interaction, the quasi-particle (QP) wavefunctions and eigen energies$\left(E_n^{QP}\right)$ are calculated as first-order perturbative correction $E_n^{QP} = \epsilon_n + \langle\psi_n|\Sigma\left(E_n^{QP}\right) - V_{xc}|\psi_n\rangle$ to appropriate independent particle wavefunctions and energies [4]. In the expression for E_n^{QP}, ψ_n is the zero-order independent particle wavefunction with energy ϵ_n on which the QP corrections are applied. In practical MBPT simulations, ψ_ns are density functional theory (DFT) eigenvalues of Kohn-Sham equations [5] with an appropriate flavor of exchange-correlation functional. This method has proven to be sufficiently accurate, provided the zeroth order wavefunctions are chosen correctly. For transition metals and other systems involving localized d and f electrons, as in TiO_2, Kohn-Sham Density functional theory wavefunctions with exchange correlations given by screened hybrid functional is deemed a much better zero order wavefunction [6].

Standard hybrid functionals, describing the exchange interactions, admixes a fraction of exact Fock exchange(α) to the DFT exchange; while the correlations are treated at the level of standard DFT. In contrast to standard DFT functionals, hybrid functionals formally describe two particle scattering processes with the introduction of nonlocal exchange. It remedies the "bandgap problem" exhibited by standard DFT functionals, yields correct ordering of bands, and more importantly, represents the localization of orbitals more accurately than standard DFT functionals [6]. Screened hybrid functionals are an improvement over the standard hybrids. Introducing an additional screening parameter(ω) essentially restrict the computation of exact Fock exchange only to the small inter-electronic distances where Coulomb potential is dominant. Consequently, screened hybrid functionals are rather computationally less challenging than standard hybrid functionals, but they provide the same accuracy as the latter.

In all practical simulations the choice of α cannot be fixed as it is highly material dependent [7]. This suggests that, for a given material, α can be adjusted to reproduce a known observable. The rationale of tuning α is the interpretation of dielectric constant as inverse screening. An increase in α implies lowering dielectric constant of the material and consequently electronic interactions are screened less.

In this work we investigated the electronic structure and optical properties of TiO_2 Anatase from first principles based on $G_0W_0$and Bethe-Salpeter-Equation (BSE) within the Many-Body Perturbation Theory (MBPT) framework. Quasiparticle energies are calculated as first-order perturbations to Kohn-Sham orbitals and energies obtained with screened hybrid functional approximation for the electronic exchange-correlation interactions. We use the recipe of HSE06 screened hybrid functionals as parametrized by Heyd-Scuseria-Ernzerhof. The standard HSE06 framework mixes 25% exact exchange with standard DFT functional. However, this choice of α does not lead to equally accurate and reliable prediction of physical quantities for all class of materials. Hence in this work, we choose 20, 25, 30 percentages of exact exchange to understand the role of exact exchange fraction, particularly, on the prediction of QP gap, optical response and exciton binding energy of anatase T_iO_2. Respective functionals with mixing fraction α is denoted as HSE06(α) in this report. All the results presented in this report are well tested for its convergence with respect to relevant computational parameters, though not shown explicitly in the body of the paper.

METHODS

Projector Augmented Wave (PAW) method, as implemented in Vienna Ab-initio Simulation Package (VASP) [8], is used in DFT and MBPT calculations to determine quasi-particle and optical properties of anatase TiO_2. For all sets of calculations, Kohn-Sham orbitals are expanded in the plane wave basis with an energy cut-off of 520 eV. Brillouin zone integrations are performed on a $6 \times 6 \times 3$ un-shifted Monkhorst-Pack grid. The anatase unit cell is fully structurally relaxed ab-initio until the force on all the atoms is less than 10^{-6} eV/atom and with pressure tolerance of 10^{-5} eV/A^0. For G_0W_0 quasi-particle calculations, KS-DFT eigenvalues with HSE06(α) hybrid functional has been used to construct the reference Hamiltonian. In contrast to the standard prescription of HSE06 functionals, we have used three different exact exchange fractions $\alpha = 20, 25, 30$ %, while keeping the screening parameter fixed as in the standard HSE06. The quasi-particle eigenvalues and QP gap are obtained as first order perturbation correction (G_0W_0) to KS-DFT eigenvalues calculated with HSE06(α) functionals. We obtained QP gaps converged to within 0.01 eV with 256 bands, $6 \times 6 \times 3$ kpoint grid and 100 points on the frequency grid. The outcomes of G_0W_0 calculations, together with the calculated screened Coulomb interaction in the previous G_0W_0 step has been utilized for solving BSE to calculate the dielectric function. BSE is solved in the Tamm-Dancoff approximation, as implemented in VASP. While constructing BSE Hamiltonian 8 valence bands and 16 conduction bands with a $6 \times 6 \times 3$ kpoint grid was used which yields first optical excitation energy and exciton binding energies, converging within 10 meV.

RESULTS AND DISCUSSION

Structure and Electronic Properties: The relaxed tetragonal lattice (space group: $I4_1/amd$) structure of anatase TiO_2 is characterized by lattice parameters a = 3.805 A^0 and c/a ratio of 2.57. Electronic structure and optical properties are further calculated on this energetically relaxed structure. The standard HSE06 functional (i.e., with 25% exact exchange) yields an indirect bandgap of 3.67 eV, which is overestimated with respect to the bandgap of anatase reported in the literature from experiments. The closest we arrive to the experimental band gap is with a modified HSE06(20) functional (3.34 eV, indirect). In general, band gap shows a linear increase with the

increase in exchange fraction, consistent with the literature. Analysis of electronic density of states of anatase reveals that, at band edges, valence bands are mainly composed of O 2p states while the Ti 3d states makes most of the conduction bands. However, the σ overlap between Ti 3d (eg) and O 2p orbitals results in the bonding σ band appearing below the fermi level (predominantly O 2p character) and σ*orbitals above fermi level (predominantly Ti 3d). The strong hybridization of O 2p and Ti 3d states is an indication of strong covalent interaction of the Ti-O bond. Moreover, $O-p_{\pi}$states (out of Ti_3-O cluster) at the top of the valence band and $Ti-3d_{xy}$ occupying the bottom of the conduction band primarily determine the character of optical excitation from around the band edge region [9, 10].

Quasiparticle gap and optical properties: Quasiparticle energies obtained with G_0W_0 calculation on HSE06(α) functional starting points is summarized in Table 1. The direct gaps of anatase thus obtained with $\alpha = 20, 25, 30$ % are all larger than the direct optical gaps measured from experiments. Such an overestimation is intrinsic to the G_0W_0 method partly due to the fact that self-consistency is not enforced in the perturbative correction. As α is increased the quasiparticle correction obtained from G_0W_0 calculation starting from corresponding HSE06(α) band structure tends to be vanishing. A non-vanishing QP correction would imply that increasing α makes the starting wavefunction more accurate at capturing quasiparticle interactions, but it is only at the expense of the bandgap being overestimated further. The best agreement with experiment is obtained with our well converged G_0W_0 calculation on HSE06(20) wavefunctions which yields a QP gap of 4.1 eV [11, 12].

α	HSE06 Band gap (eV)	QP gap (eV)	QP Correction (eV)	First Excitation (eV)	Exciton Binding Energy (meV)
0.20	3.34	4.10	0.76	3.911	189
0.25	3.67	4.17	0.50	3.949	225
0.30	4.01	4.25	0.24	3.992	260

Table 1: HSE06 bandgap, QP gap, QP correction, first optical transition and exciton binding energy obtained from BSE with HSE06 zero-order wavefunctions with different fraction of exact exchange.

The imaginary part of the dielectric function along the direction perpendicular to crystallographic c axis ($\epsilon_2^{\parallel}$) and parallel to it ($\epsilon_2^{\perp}$) calculated from the solution of BSE are shown in Figure 1. BSE is solved on top of G_0W_0 calculation with HSE06(α) starting points. Irrespective of the choice of α, the first optical transition is obtained for light polarized in the xy plane of the anatase crystal ($\epsilon_2^{\perp}$) [11-13]. This corresponds to excitation of bound excitons occurring well below the quasiparticle gap. In addition, the oscillator strengths of transitions in $\epsilon_2^{\perp}$ is larger than $\epsilon_2^{\parallel}$ owing to strong optical anisotropy of anatase crystals. The character of band edges, as described in the previous section, that favor transitions selectively for parallel polarizations result in a large anisotropy. Peaks in both $\epsilon_2^{\parallel}$ and $\epsilon_2^{\perp}$ are observed to be blue-shifted as the exchange fraction is increased from 20% through 30%.

The choice of α in the HSE06(α) reference Hamiltonian also affects the nature of excitons predicted from respective BSE calculations. As given in Table 1, the excitons become more strongly bound as more fraction of exact exchange is added to the HSE06 functional. When α is increased the bandgap predicted by HSE06(α) functional widens. The G_0W_0 quasiparticle gap also increases in the same way (though corrections becomes smaller). As the gap becomes larger, the screening becomes less and less efficient. Therefore, the electron-hole interactions are less screened making them more bound as revealed by the increase in exciton binding energy. Among $\alpha = 20, 25, 30$ %, the first optical transition (3.911 eV) and exciton binding energy (180 meV) predicted from our BSE calculation with HSE06(20) zero-order wavefunction agrees closely with a recent work by Baldini et.al [14]. They measured, with ARPES, the binding energy of excitons in anatase T_iO_2 to be 160 meV.

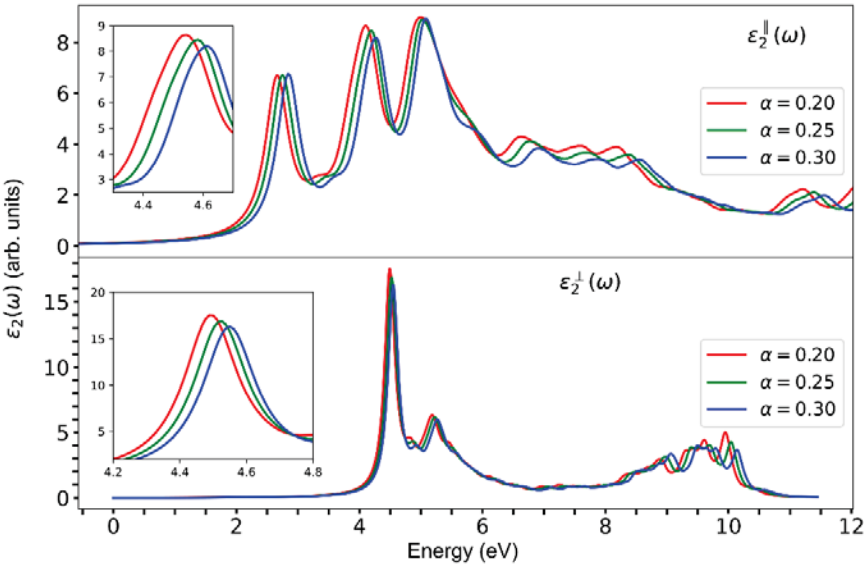

Figure 1: Imaginary part of dielectric function of anatase TiO_2 obtained from the BSE eigenvalues along the direction (a). perpendicular to crystallographic caxis $\left(\epsilon_2^{\parallel}(\omega)\right)$ and (b). parallel to it $(\epsilon_2^{\perp}(\omega)$. Each curve in the panels represent dielectric function for particular value of α. First optical transition in the $\epsilon_2^{\parallel}(\omega)$ direction leads to bound excitons with binding energies increasing linearly with α. All other transitions lead to resonant excitons over the continuum of excited states.

CONCLUSION AND OUTLOOK

Quasiparticle gaps and dielectric function of anatase TiO_2 has been obtained within the state of the art G_0W_0 method and the solution of Bethe-Salpeter Equations, respectively. Quasi-particle corrections to KS-DFT eigenvalues are obtained as first order perturbations. In the KS-DFT, HSE06 functional with exact exchange fractions is used to represent the exchange-correlation interactions. We have demonstrated that, due to the identification of exchange fraction as inverse dielectric screening, the screening of electronic interactions in anatase TiO_2 decreases as fraction of exchange in the hybrid functional is increased. Increase in α results in an increase in quasiparticle gap, and the redshift of first optical excitation and the binding energy of excitons. It has been shown that the first optical excitation leads to the formation of strongly bound exciton below the fundamental gap. The binding energy of exciton is estimated to be 160 meV in agreement with the literature, for $\alpha = 20\%$. It is overestimated when we use $\alpha = 25$ and 30%, due to underscreening.

REFERENCES

1. Fujishima and K. Honda, *Nature* **37,** 1238 (1972)
2. B. O'Regan and M. Grätzel, *Nature* **737,** 1353 (1991)
3. Hedin, L. *Physical Review*, **139**, 3A, A796 (1965)
4. Onida, G., Reining, L., Rubio, A. *Reviews of modern physics*, **74**, 2, 601 (2002)
5. Kohn, Walter, and Lu Jeu Sham, *Physical review* **140**, 4, A1133 (1965)
6. Bechstedt, F., F. Fuchs, and G. Kresse., *physica status solidi (b)* **246**, 8, 1877 (2009)
7. de PR Moreira, Ibério, Francesc Illas, and Richard L. Martin., *Physical Review B* **65**, 15, 155102 (2002)
8. Hafner, Jürgen., *Journal of computational chemistry* **29**,13, 2044 (2008)
9. Perdew, John P., Matthias Ernzerhof, and Kieron Burke. *The Journal of chemical physics* **105**, (22), 9982 (1996)
10. R. Asahi, Y. Taga, W. Mannstadt, and A. J. Freeman, *Physical Review B* **61**, 11, 7459 (2000)
11. Landmann, M., E. W. G. S. Rauls, and W. G. Schmidt., *J. of phys.: condensed matter* **24**, 19, 195503 (2012)
12. Chiodo, L., García-Lastra, J.M., Iacomino, A., Ossicini, S., Zhao, J., Petek, H. and Rubio, A., *Physical Review B*, **82**, 4, 045207 (2010).
13. A Thatribud, *Mater. Res. Express* **6**, 095021 (2019)
14. Baldini, E., Chiodo, L., Dominguez, A., Palummo, M., Moser, S., Yazdi-Rizi, M., Auböck, G., Mallett, B.P., Berger, H., Magrez, A. and Bernhard, C., *Nature communications*, **8**, 13 (2017).

Decoherence in lambda and ladder systems

K. Yadav[a,*] and A. Wasan[b]

[a]*Department of Physics, Ahir College, Rewari, 123401 India*

[b]*Department of Physics, Indian Institute of Technology, Roorkee, 247667 India*

[*]kavitayiitr@gmail.com

ABSTRACT

Decoherence effects in three-level lambda and ladder systems are studied theoretically using density matrix formalism. In particular hyperfine and optical decoherence are discussed causing variation in electromagnetically induced transparency (EIT) window. However, decoherence in quantum systems is inevitable.

1. INTRODUCTION

Atomic coherence plays an important role in the study of atom-photon interactions. The effects of atomic coherence are extensive e.g. coherent population trapping (CPT)[1], stimulated Raman adiabatic passage (STIRAP)[2], lasing without inversion (LWI)[3], electromagnetically induced transparency (EIT)[4]. EIT, a quantum interference phenomenon, is mainly observed in three-level atomic systems which causes transparency by quenching absorption of a medium. Three type of three-level systems, lambda (Λ) and cascade (Ξ) and V are mainly utilized to study the EIT phenomenon[5]. Depending on the nature of decay pathways, various interesting features are observed in these systems. The width of transparency window obtained in EIT is determined by the dephasing rate between the long lived states.

Atomic coherence is a result of multiple interfering absorption paths for the radiation interacting with the resonant transitions. When the decay rate of atomic coherence at the forbidden transition is slower than at the allowed transition, the interference leads to dramatic modifications of the optical response of the system[6]. Decoherence rates are integral to all coherence effects since coherence between energy levels cannot exist if the decoherence rates are too large. In an open quantum system uncontrollable interaction with the environment may lead to the loss of information initially stored in its states. This phenomenon is commonly known as loss of coherence or decoherence. To analyze the coherence term in an atomic system, one should also incorporate the decoherence effects. In this work, we explore the effect of decoherence in the three-level Λ and Ξ systems. Mainly two types of decoherence, i.e., hyperfine and optical decoherence exit in these systems[7].

This paper is inclusive of the theoretical model for the three-level Λ and Ξ systems in section 2. Section 3 consists of the results and discussion part, finally in section 4 we present the conclusion of this work.

2. THEORETICAL MODEL

We discuss the phenomenon of EIT in two types of three-level systems, lambda (Λ) and cascade (Ξ) with levels named as $|1\rangle$, $|2\rangle$ and $|3\rangle$. The probe field frequency Ω_p acts on the transition $|1\rangle$-$|2\rangle$ and the control field

frequency Ω_c couples the $|2\rangle$-$|3\rangle$ transition as shown in Fig.1. The corresponding detuning terms are defined as $\Delta_p = \omega_{12} - \omega_p$ and $\Delta_c = \omega_{23} - \omega_c$, here ω_{ij} is the $|i\rangle \rightarrow |j\rangle$ atomic transition frequency. In both the systems these transitions are electric dipole allowed but the transition $|1\rangle$-$|3\rangle$ is dipole forbidden. The spontaneous decay rates from the excited states $|2\rangle$ and $|3\rangle$ are Γ_2 and Γ_3, respectively. To analyze the optical properties of the three-level Λ and Ξ, systems in ^{87}Rb atom we take $5S_{1/2} \rightarrow 5P_{3/2}$ and $5S_{1/2} \rightarrow 5P_{3/2} \rightarrow 5D_{5/2}$ transitions, respectively as shown in Fig. 1.

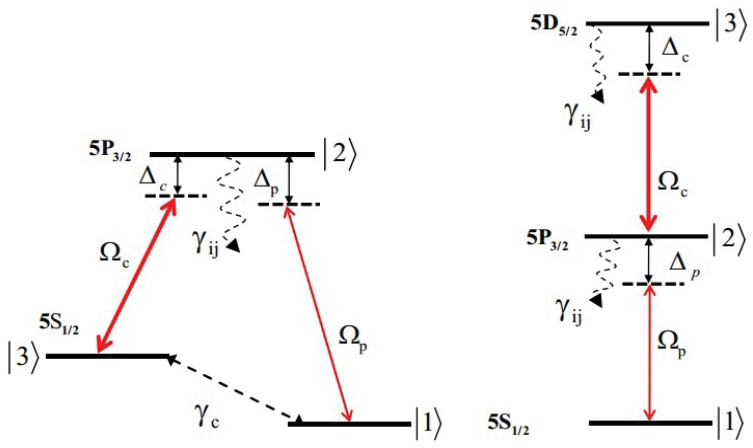

Fig. 1 The EIT scheme in the three-level Λ (left) and Ξ (right) systems. The dotted lines represent dephasing in the ground levels denoted by γ_c and zigzag lines represent decay rates from excited states denoted by γ_{ij}.

3. RESULTS AND DISCUSSION

Decoherence in Λ system: First, decoherence effects in a three-level Λ system are discussed. The time of flight through the laser field aids the hyperfine decoherence because the system loses coherence when the atoms leave the interaction region. Decoherence mainly appear due to the dephasing in the ground levels $|1\rangle$ and $|3\rangle$[7]. This decoherence (γ_c) can be described as:

$$\gamma_c = \frac{\sqrt{\pi}}{2d} v ,$$

where d is the diameter of the beam and v is the most probable velocity of the atoms. It is evident from the above relation that for a tightly focused beam, a high decoherence is observed. It decreases the interaction time of the atoms with the beam, consequently coherence exists for a lesser time in the system. In the three-level Λ system, the steady state solution for the coherence term ρ_{12} can be obtained by solving the density matrix equations under a weak probe approximation as follows[8]:

$$\rho_{12} = \frac{i\Omega_p/2}{(\frac{\gamma_{12}}{2} - i\Delta_p) - \frac{(\Omega_c/2)^2}{[\gamma_c - i(\Delta_P - \Delta_c)]}}.$$

The optical decoherence for the system is $\gamma_{ij} = (\Gamma_i + \Gamma_j)/2$, here $\Gamma_1 = \Gamma_3 = 0$. It is observed that the laser line width also plays an important role in the dephasing, a large laser line width will suppress the EIT transparency

window. The finite linewidth increases the dephasing rate of the off-diagonal coherence terms. If γ_1 and γ_2 are the probe and control lasers line widths, respectively, then decoherence terms γ_{12} and γ_{23} are defined as[9]:

$$\gamma_{12} = \frac{\Gamma_2}{2} + \gamma_1, \gamma_{23} = \frac{\Gamma_2}{2} + \gamma_2.$$

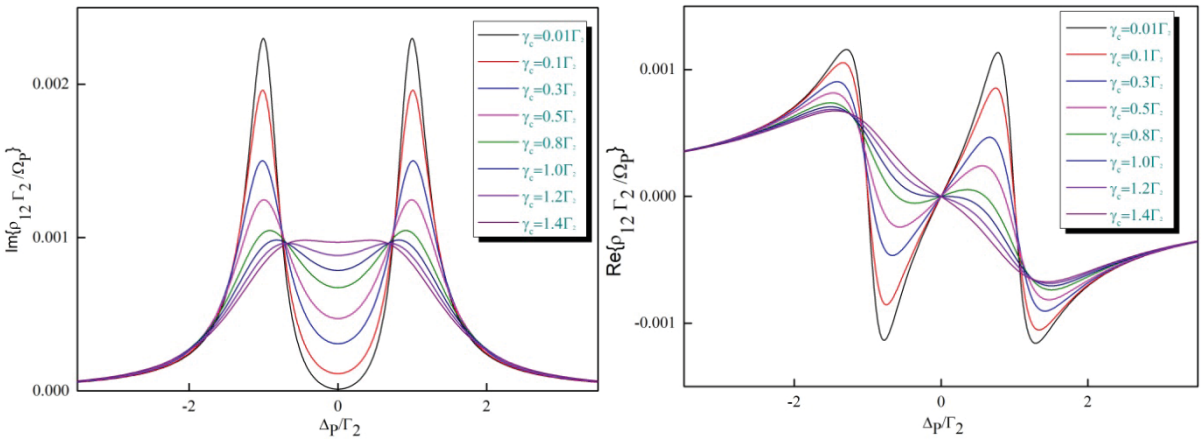

Fig. 2 Absorption and dispersion profile in Λ system with different γ_c. In the calculation, parameters are $\Omega_p = 0.001 \times \Gamma_2$ *and* $\Omega_c = 2 \times \Gamma_2$

Fig. 2 shows the absorption and dispersion behavior of the three-level Λ system with different values of dechorenec (γ_c) arising because of the dephasing between the ground states $|1\rangle$ and $|3\rangle$. It is observed that with increasing dephashing in the ground levels, transparency window deteriorates. For high values of γ_c, there is complete loss of transparency and the absorption peaks start flattening at the line center with a subsequent change in the dispersion profile. However, the linewidths of lasers show negligible effect on the transparency window of this system.

Decoherence in Ξ system: In a Ξ system, decoherence appear mainly because of the optical deoherence. Decays outside the three-level system cause optical decoherence, hence deteriorate the EIT phenomenon. The steady state solution of this system can be written as[8]:

$$\rho_{12} = \frac{i\Omega_p/2}{(\frac{\gamma_{12}}{2} - i\Delta_p) - \frac{(\Omega_c/2)^2}{[\frac{\gamma_{13}}{2} - i(\Delta_P + \Delta_c)]}}, \quad \gamma_{12} = \frac{\Gamma_2}{2} + \gamma_1, \gamma_{23} = \frac{\Gamma_3}{2} + \gamma_1 + \gamma_2 .$$

Fig. 3 shows the absorption and dispersion behavior of the three-level Ξ system with linewidths of the lasers varying from 50KHz to 3MHz. It is evident from the plots that lasers with small linewidths are required for achieve narrow EIT. In Ξ type EIT systems the decay rates from the excited state also change the transparency window significantly. The higher lying Rydberg states with lower decay rates lead to the enhancement of EIT effect[10].

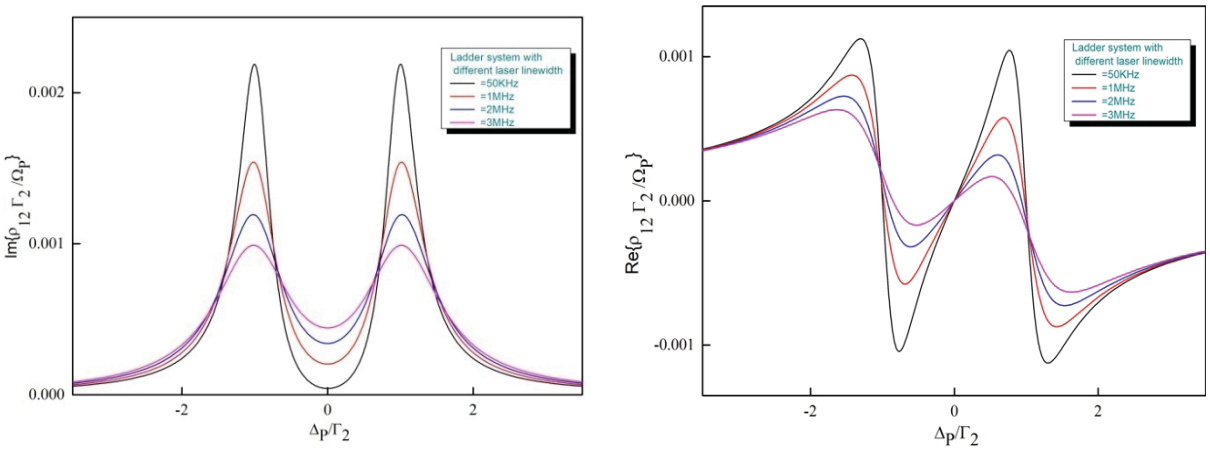

Fig. 3 Absorption and dispersion profile in Ξ system with different laser linewidths. In the calculation, parameters are $\Omega_p = 0.001 \times \Gamma_2$ *and* $\Omega_c = 2 \times \Gamma_2$

CONCLUSION

We have theoretically discussed deoherence effects in three-level Λ and Ξ systems. To obtain narrow EIT linewidths, it is highly desirable to control decoherence. Cold atoms are borne out to be an effective host to study the coherence related phenomena increasing the light-atom interaction time. Use of buffer gas can also decrease the time of flight.

ACKNOWLEDGEMENT

KY acknowledges QOP lab Physics department IITR. KY is thankful to Ahir College, Rewari.

REFERENCES

1. E. Arimondo, *Prog. in Optics* **35**, 257 (1996).
2. J. R. Kuklinski, U. Gaubatz, F. T. Hioe, and K. Bergmann, *Phys. Rev. A*. **40**, 6741 (1989).
3. S. E. Harris, *Phys. Rev. Lett.* **62**, 1033 (1989).
4. S. E. Harris, J. E. Field, and A. Imamoğlu *Phys. Rev. Lett.* **64**, 1107 (1990).
5. M. Fleischhauer, A. Imamoğlu, and J. P. Marangos. *Rev. Mod. Phys.***77**, 633 (2005).
6. A. Sargsyan, D. Sarkisyan, U. Krohn, J. Keasveney, and C. Adams, *Phys. Rev. A*. **82**, 45806 (2010).
7. E. Figueroa, F. Vewinger, J. Appel, and A. I. Lvovsky. *Opt. Lett.* **31**, 2625 (2006).
8. S. Khan, V. Bharti, and V. Natarajan. *Phys. Lett. A* **48**, 4100 (2016).
9. J. Gea-Banacloche, Y. Li, S. Jin, and M. Xiao. *Phys. Rev. A* **51**, 576 (1995).
10. K. Yadav and A. Wasan, *Phys. Lett. A* **381**, 3246 (2017).

The Third Order Nonlinear Optical Exploration in Novel Heterocyclic Schiff Base Dye: Z-Scan Measurements

Mohd Mehkoom[1], S. M. Afzal[1]*, Salman A. Khan[2]

[1]*Physics Department, Aligarh Muslim University, Aligarh -202002, (UP) India*

[2] *Physical Sciences Section, School of Sciences, Maulana Azad National Urdu University, Hyderabad-500032, Telangana, India*

*Corresponding Author; Email: drsmafzal62@gmail.com

Abstract

In the present paper, we have synthesized a Heterocyclic Schiff Base dye under microwave irradiation. The structure of the dye was confirmed doing FT-IR, NMR spectroscopy, and elemental analyses. The molecule was screened for third order NLO response. The nonlinear refraction (n_2) and nonlinear absorption (β) of this novel material were studied by the Z-scan technique using a continuous wave diode laser of 120 mW operating at 520nm. These third order nonlinear optical properties were investigated at several dye solution concentrations and several laser powers. The values of n_2 and β are found to vary linearly with concentration and power. Further, the optical limiting characteristic of the dye was also studied and the dye evinced a good limiting response at 520nm.

1. Introduction

Now a day there is a great search for optical materials such as organics, organometallics, nanomaterials, semiconductors etc. which are having large third order nonlinearity due to their various application in high optical density, optical data storage, photodynamic therapy, optical limiters etc[1,2]. Nonlinear refraction and nonlinear absorption have important technological applications, like fast optical switches, protective shields for eyes or equipment from intense laser beams. Organic dyes with large third order nonlinear optical properties are always have been in great demand for above applications. Their nonlinear optical properties depend upon various factors like π-electron delocalization length, donor-acceptor substituent, charge orientation, charge –transfer complex formation, dimensionality, etc[3,4]. The present report deals with the synthesis and NLO characterization of new dye 1,3-diethyl-2-thioxo-5-(2,3,4-trimethoxybenzylidene) dihydropyrimidine-4,6(1H, 5H)-dione (D1). The Z- scan technique [3] has been used to study the nonlinear refractive index(n_2) and absorption coefficient (β) of dye D1. These studies have been carried out at different dye solution concentrations using a continuous wave (CW) diode laser.

2. Experimental details

Synthesis

A mixture of the 3,4,5-trimethoxybenzaldehyde (0.025 mol) and 1,3- diethyl-2-thiobarbituric acid (0.025 mol) in absolute ethanol (35 mL) and few drops of pyridine was refluxed at 80 ^{0}C for 1 hour with continuous stirring. The reactions were monitored through TLC using solvent system ethyl acetate: benzene (2:8), when the reaction was found to be complete, then reaction mixture was cooled in an ice bath and the product thus formed was filtered washed with water and recrystallized by distilled ethanol and chloroform. The chemical structure of the dye molecule (D1) is shown in Fig.1.

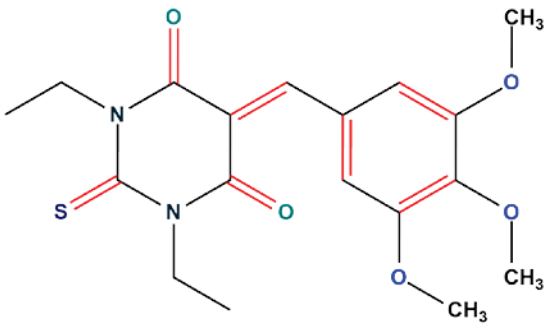

Fig.1. *Chemical structure of dye D1 with molecular formula (**$C_{18}H_{22}N_2O_5S$**).*

1,3-diethyl-2-thioxo-5-(3,4, 5-trimethoxybenzylidene) dihydropyrimidine-4,6(1H, 5H)-dione (D1):

Orange color solid (Chloroform); Yield: 75.25%; IR (KBr) ν_{max} cm^{-1}: 2948 (C–H aromatic), 2911 (C–H aliphatic), 1668 (C=O), 1648 (C=C), 1216 (C–O), 1149 (C=S), 1121 (C–N); ^{1}H – NMR ($CDCl_3$) δ: 8.26 (s, CH=C), 7.86 (s, 1H, CH aromatic), 7.68 (s, 3H, Chromatic), 4.56 (t, CH_3–CH_2–N), 1.28 (q, CH_3–CH_2–N); 3.85 (s, 3H, CH_3–O), 3.76 (s, 3H, CH_3–O), 3.66 (s, 3H, CH_3–O).

Z-scan details

We have used open aperture and closed aperture Z- scan technique[5] to measure nonlinear refractive index, n_2 and nonlinear absorption coefficients, β of dye D1. Herein the continuous wave (CW) diode laser of 120mW operating at 520 nm was employed. The dye solution sample poured in a 1 mm quartz cuvette is translated at the long travel stage for the z-scan measurements. A lens of focal length 5 cm is used to focus the laser beam at the sample and an iris aperture is placed far away from the focus for the closed aperture scans. Open aperture measurements are done by opening the iris fully. The other experimental details are given in our previous paper[4].

3. Result and discussion

The peak-valley normalized transmittance curve obtained from closed aperture z-scan data are shown in Fig. 2(a) and (b). These figures indicate that the sign of the nonlinear refractive index is negative ($n_2 < 0$), i.e., self-defocusing nature for present dye at all concentrations and laser powers. The nonlinear refractive index n_2 is related with the following relation

$$|\Delta\Phi_0| = kn_2 L_{eff} I_0$$

Where, $|\Delta\Phi_0|$ is the on- axis phase shift and it is expressed as

$$\Delta T_{P-V} = 0.406(1-S)^{0.25}|\Delta\Phi_0|$$

The quantity $\Delta T_{P\text{-}V}$ is measurable and is defined as the difference in the peak-valley normalized transmittance. We can obtain the nonlinear refractive index by fitting the normalized transmittance curve with the following equation

$$T(close) = 1 + \frac{2(-\rho x^2 + 2x - 3\rho)}{(x^2+9)(x^2+1)}\Delta\Phi_0$$

where, $\rho = \frac{\Delta\Psi}{\Delta\Phi_0}$; with $\Delta\Phi_0$ and $\Delta\Psi$ are the phase shift due to nonlinear refraction and nonlinear absorption respectively, $\Delta\Psi = \beta I_0 L_{eff}/2$, and $x = z/z_R$ is related to the diffraction length of the beam, Z_R. Z is the position of the sample.

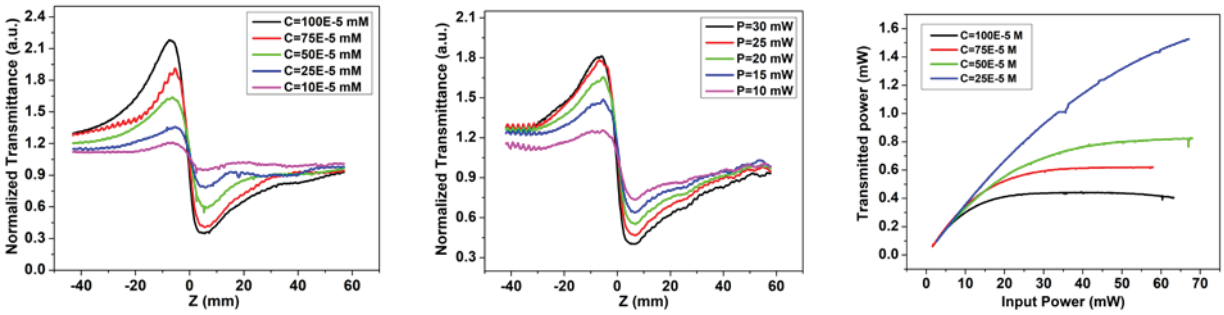

Fig. 2. *Closed aperture normalized transmittance at* ***(a)*** *25mW,* ***(b)*** *100x10^{-5} M,* ***(c)*** *optical limiting characteristics*

The values obtained for n_2 and β are represented in Table 1 and they are relatively high as compare to those of reported Schiff base organic dyes[3,6]. It is clear from Table 1 that the magnitude of nonlinear absorption coefficient (β), nonlinear refractive index (n_2) and nonlinear optical susceptibility, $\chi^{(3)}$ increases linearly with solution concentration and laser power. It is based on high thermal lensing effect at high concentration and laser power due to enlarge molecular interaction.

Table 1: Variation of n_2, β and $\chi^{(3)}$ with concentration and laser power.

C x10^{-5} [M]	n_2 x10^{-7} [cm^2/W]	β x10^{-4} [cm/W]	$\chi^{(3)}$ x10^{-6} [esu]	Power [mW]	n_2 x10^{-7} [cm^2/W]	β x10^{-4} [cm/W]	$\chi^{(3)}$ x10^{-6} [esu]
100	-2.10	-5.55	11.14	30	-2.23	-6.01	11.83
75	-1.52	-3.73	8.06	25	-2.10	-5.55	11.14
50	-1.23	-2.70	6.52	20	-2.05	-5.05	10.87
25	-0.68	-0.23	3.61	15	-1.97	-4.87	10.45
10	-0.15	-0.08	0.79	10	-1.89	-4.59	10.02

The optical limiting behavior of dye D1 at 520 nm wavelength for different concentrations is represented in Fig. 2(c). For low input power, the transmitted power increases linearly, but for high input power, the transmitted power gets saturated. The estimated optical limiting threshold values are tabulated in Table 2. This shows that the threshold value decreases as we increase the concentration. This is attributed to the fact that the number of absorbing molecules increases with increasing the dye concentration which in turn lowers the limiting threshold. From the above results, it is found that dye D1 possesses good optical limiting behavior at different concentrations. Hence the dye D1 evinces the potential for nonlinear optical and limiting applications.

Table 2: Optical limiting threshold of dye D1 at different concentrations.

Concentration x10^{-6} [M]	Optical limiting threshold [mW]
100	3.79
75	4.59
50	4.76
25	5.58

4. Conclusion

The present synthesized dye molecule D1 was screened for NLO characterizations. The values obtained of nonlinear optical parameters are high among these types of molecules and showing high nonlinear optical response. The obtained NLO results reveal the potential of D1 for photonics and NLO applications. The optical limiting behavior of D1 proves that such type of dyes has potential applications in the development of photonic devices like optical limiters for human eye and equipment safety.

References

1. Venugopal Rao, S., Naga Srinivas, N. K. M. & Narayana Rao, D. Nonlinear absorption and excited state dynamics in Rhodamine B studied using Z-scan and degenerate four wave mixing techniques. *Chem. Phys. Lett.* **361**, 439–445 (2002).
2. Khan, S. A. et al. Microwave assisted synthesis, spectroscopic studies and non linear optical properties of bis-chromophores. *Spectrochim. Acta - Part A Mol. Biomol. Spectrosc.* **137**, 1100–1105 (2015).
3. Afzal, S. M. et al. Physicochemical and nonlinear optical properties of novel environmentally benign heterocyclic azomethine dyes: Experimental and theoretical studies. *PLoS One* **11**, (2016).
4. El-Shishtawy, R. M. et al. Synthesis, linear and nonlinear optical properties of a new dimethine cyanine dye derived from phenothiazine. *RSC Adv.* **6**, 91546–91556 (2016).
5. Sheik-bahae, M., Said, A. A. & Van Stryland, E. W. High-sensitivity, single-beam n_2 measurements. *Opt. Lett*. **14**, 955 (1989).
6. Xu, W. et al. Two-photon absorption property and excellent optical limiting response of three Schiff base derivatives with large conjugated system. *Dyes and Pigments* vol. **160** 1–8 (2019).

Loading a magneto-optical trap in UHV using a Rb atomic beam source

Kavish Bhardwaj[a]*, S. P. Ram[a], S. Sarkar[a,b], V. B. Tiwari[a,b] and S. R. Mishra[a,b]

[a]*Laser Physics Applications Section, Raja Ramanna Centre for Advanced Technology, Indore-452013, India.*

[b]*Homi Bhabha National Institute, Training School Complex, Anushakti Nagar, Mumbai -400094, India,*

*E.mail: kavish@rrcat.gov.in

Abstract: We have developed a simple Rubidium (Rb) atomic beam source to load a magneto-optical trap (MOT) setup in ultra-high vacuum (UHV) environment. The atomic beam source is generated from a pair of Rb dispensers joined in parallel configuration and placed inside a glass jacket having a narrow tube structure opening in the UHV chamber. A MOT has been loaded using this source with 2.3×10^{7} atoms of ^{87}Rb at a background pressure of $\sim 3.5\times 10^{-9}$ Torr.

The magneto optical trap[1-3] (MOT) is nowadays used a basic tool to produce sample of cold atoms for variety of applications such as magnetic and optical trapping, studying quantum degenerate gases, precision measurements[4-5], quantum sensors[6], etc. The MOT is usually loaded from background vapour. However, the requirement of ultrahigh vacuum (UHV) environment for some applications of cold atoms makes it difficult to load MOT with background vapor. The MOT loading in UHV region can be achieved using various techniques such as using Zeeman slower devices, double-MOT setup, etc. However, the Zeeman slower cooled thermal atomic beam source generally involves ovens, shutters, differential pumping arrangement and complicated magnetic field design which results into a large setup. A double-MOT setup, in which UHV-MOT is loaded from vapor cell MOT, is also a widely used alternative to the Zeeman slower loaded UHV-MOT but it involves differential pumping arrangement and complications of pushing atoms from one chamber to another. Thus, simple and compact cold atom setups with UHV-MOT are still required for several applications.

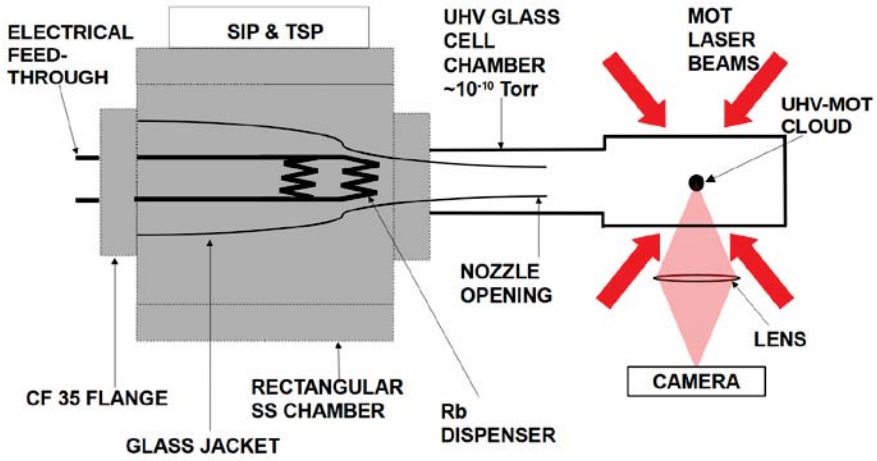

Fig. 1: Schematic of setup with Rb atomic beam source for loading of UHV-MOT. Two pairs of MOT laser beams are also shown in the figure and third pair of MOT beams is perpendicular to plane of paper.

Here, we present our work on the development of an UHV magneto-optical trap (MOT) loaded using a using a Rb atomic beam source. The atomic beam source is developed using a dispenser assembly containing a pair of

Rb-dispensers joined in parallel configuration and placed inside a glass jacket having a narrow tube structure opening in the UHV chamber. With this source, Rb vapor is directly injected into the MOT region without significantly changing the pressure in the UHV chamber.

The schematic of the MOT setup is shown in Fig. 1. A vacuum level of ~3.5×10^{-9} Torr is achieved in a glass cell using turbo-molecular pump (TMP), sputter ion pump (SIP) and titanium sublimation pump (TSP). The whole setup was baked at ~150 ^{o}C for 24 hours and degassing of dispensers and activation of TSP has been carried out for achieving UHV environment. The Rb-vapor is generated in the UHV chamber by flowing current through the dispensers. The photograph of the in-house developed Rb atomic beam source having glass jacket with nozzle opening is shown in Fig. 2. Here, two Rb dispensers (manufactured by M/s SAES dispensers) in parallel arrangement have been used. The temperature of dispenser reaches ~ 350^{0} C for passing 2.5 A current through each dispenser (estimated from the data sheet of the dispenser). After MOT loading, dispenser temperature is required to be brought down quickly to minimize the change in the UHV environment. Neglecting radiative cooling, the time required for the dispenser to cool down is inversely proportional to its conductance. The parallel arrangement not only lowers the current requirement in each dispenser, but also provides higher conductance for heat dissipation. In our setup, the atomic flux from the dispensers gets collimated to form an atomic beam. The hot atoms emitted by dispensers strike the glass jacket walls multiple times and eject in the form of a beam of atoms to reach the trap. The nozzle opening at the exit of the glass jacket acts as a collimator. The cooling and repumping beams in the MOT setup are generated from two extended cavity diode lasers operating at 780 nm. Three laser beams, with intensity ~ 20 mW/cm^2 in each beam and red-detuned by ~ 15 MHz to cooling transition (^{87}Rb $5S_{1/2}$ F = 2 $\rightarrow$ $5P_{3/2}$F' = 3), were retro-reflected to generate six MOT beams. A laser beam with power ~ 8 mW and nearly resonant to the repumping transition (^{87}Rb $5S_{1/2}$ F = 1$\rightarrow$ $5P_{3/2}$F' = 2) is mixed with one of the MOT beams. This repumping beam is used to avoid the collection of atoms in a dark state. A pair of magnetic field coils is used to generate an axial field gradient of 10 G/cm at the MOT centre position. The formation of MOT is observed by collecting the fluorescence of the trapped atoms on a CCD camera. In our setup, MOT cloud was formed by passing a total ~ 5 A current in the Rb dispenser assembly. The number and temperature of atoms trapped in MOT were estimated to be ~ 2.3×10^{7} and ~400 μK, respectively.

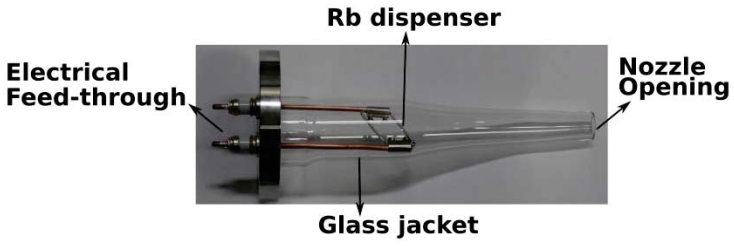

Fig. 2. The vacuum compatible feed-through inserted inside the UHV chamber with the Rb-dispenser assembly with two dispensers connected in a parallel geometry.

To study the loading behavior of MOT in the UHV environment we have measured the number of atoms with time. The temporal loading curve for the MOT can be generated by grabbing images of atom cloud in the MOT

in regular intervals. The number of atoms trapped in the MOT (N) is determined by balance between capture rate (R) and loss rate from the trap. The rate equation is given by[7]

$$\frac{dN}{dt} = R - \frac{N}{\tau} - \beta n N. \quad (1)$$

The third term represents loss rate due to two body collisions which is dependent on two body loss coefficient β and number density n. It becomes significant at high number densities trapped atoms[7]. The variation in the number of atoms with time has been shown in Fig. 3. From the variation in number of atoms with time, we have estimated a loading time (τ) ~4.5 s by fitting the experimental data to equation (1). We have also observed that when the dispenser current was switched off, the MOT decays slowly. This shows that the background vapour is less in the MOT region which is beneficial for performing experiments with the cold atom sample.

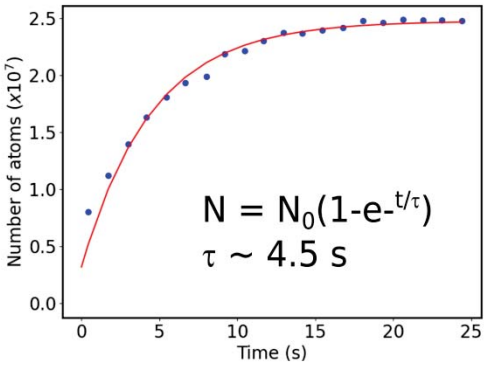

Fig. 3. Loading curve of MOT for current of ~ 5 A through the Rb dispenser assembly.

To conclude, we have developed a new Rb-source for loading of magneto-optical trap in an ultra-high vacuum environment (UHV) directly. Here, use of a glass jacket with nozzle opening to cover Rb-dispensers helps in loading the MOT but also maintains the UHV- environment. We have estimated loading time of MOT to be ~4.5 s which is much higher than the loading time of the MOTs loaded from background vapour (few hundreds of ms). This confirms that the MOT is formed in the UHV environment.

We are thankful to our colleagues S. Singh and V. Singh for useful technical discussions. We acknowledge the valuable support provided by the Glass & Ceramic Components Development Facility, RRCAT.

References:

1. E. L. Raab, M. Prentiss, A. Cable, S. Chu, and D. Pritchard, *Phys. Rev. Lett.* **59,** 2631 (1987).
2. M. Inguscio and L. Fallani, *Atomic physics:Precise measurements and ultracold matter* (Oxford University Press Inc, New York, 2013).
3. A. Steane and C. Foot, *Europhys. Lett.* **14**, 231 (1991).
4. B. Barrett, P.-A. Gominet, E. Cantin, L. Antoni-Micollier, A. Bertoldi, B. Battelier, P. Bouyer, J. Lautier, and A. Landragin, *Atom Interferometry, Proceedings of the International School of Physics "Enrico Fermi"* Vol. **188** pp. 493–555 (IOS Press, 2014).
5. T. Farah, C. Guerlin, A. Landragin, P. Bouyer, S. Gaffet, F. Pereira Dos Santos, and S. Merlet, *Gyrosc. Navig*. **5**, 266 (2014).
6. D. Budker and M. Romalis, *Nat. Phys*. **3**, 227 (2007).
7. D. Sesko, T. Walker, C. Monroe, A. Gallagher, and C.Wieman, *Phys. Rev. Lett*. **63**, 961 (1989).

Launching of laser cooled Rb atoms in atomic fountain geometry

S. Singh*[1], B. Jain[1], S. P. Ram[1], V. B. Tiwari[1,2] and S. R. Mishra[1,2]

[1]*Laser Physics Applications Section, Raja Ramanna Centre for Advanced Technology, Indore - 452013, India.*

[2]*Homi Bhabha National Institute, Training School Complex, Anushakti Nagar, Mumbai - 400094, India.*

*Email: surendra@rrcat.gov.in

Abstract: Here, we present our studies on launching of laser cooled Rb atoms in a fountain geometry. In our experiments, the laser cooled ^{87}Rb atoms in a magneto-optical trap (MOT) were launched in the vertical geometry using moving optical molasses technique to make atomic fountain. The atom launch velocity (υ_{atom}) was experimentally measured to be 0.48 m/s for the relative shift in the frequency of cooling laser beams of $\delta\nu_{launch}$ = 0.60 MHz. The atom launch velocity was also observed to increase with increase in the relative shift in the cooling laser beams detuning.

Atomic fountains are now a days one of the key techniques used in cold atom based precision sensors such as gravimeters, atom gyroscopes, atomic clocks, etc[1,2]. In an atomic fountain, the atoms from a cold atom source are launched in the vertical geometry using moving optical molasses technique. The source of the cold atoms to make an atomic fountain is usually a magneto-optical trap (MOT) and launching of atoms in fountain is usually accomplished either by a pushing beam or by moving molasses techniques.

Here, we present our studies on vertical launching of cold atoms in a Rb atomic fountain by using a moving optical molasses technique. The atoms trapped in the MOT were launched in the vertical geometry using moving optical molasses technique. The atom launch velocity (υ_{atom}) has been experimentally measured to be 0.48 m/s for the relative shift in the cooling laser beams detuning $\delta\nu_{launch}$ = 0.60 MHz. This fountain is a part of a setup being developed for measurement of acceleration due to gravity "g".

The laser system used here is an extended cavity diode laser (ECDL) which generates the cooling laser beam at wavelength of 780 nm along with an electro-optic phase modulator (EOM) working at 6.58 GHz to generate re-pumping laser beam. The schematic of the experimental setup, is shown in Fig. 1(a). The setup consists of a stainless steel octagonal chamber evacuated to a pressure of ~ $1x10^{-8}$ Torr using suitable vacuum pumps. The Rb-vapor is injected into the chamber by passing a DC current of ~ 3.2 A through a Rb-dispenser source. The dispenser source is inserted in the chamber through a vacuum compatible feed-through. The magnetic field gradient for MOT (~10 Gauss/cm) is produced by a pair of quadrupole coils. The intensity in each MOT beam is ~ 12 mW/cm^2 (power ~ 2 mW) in which cooling and re-pumping parts are mixed in ratio of 3:1. From the viewports in the upper part of the chamber, two MOT beams were directed downwards at + 45^0 and - 45^0 angle with respect to the vertical axis. Similarly through the viewports in the lower part of the chamber, another two MOT beams were directed upward in the counter-propagating arrangement of the previous two beams. Then, another horizontal counter-propagating pair of MOT beams was aligned through the chamber, to complete the requirement of six beams for a MOT. All six

MOT beams intersect each other at the center of the chamber. The cooling laser frequency was kept ~12 MHz red-detuned with respect to the cooling transition $5^2S_{1/2}$ (F = 2) → $5^2P_{3/2}$ (F'= 3) of ^{87}Rb.

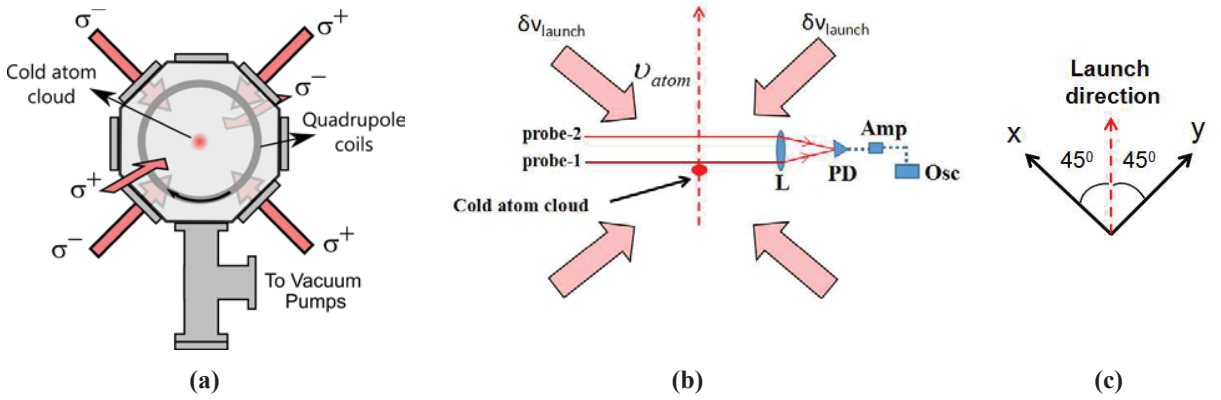

Fig. 1: (a) Schematic of the experimental setup; (b) Schematic of the atom launching and measurement of launch velocity. PD: Photodiode, Amp: Amplifier, Osc: Oscilloscope, probe-1 and probe-2: probe laser beams, $\delta\nu_{launch}$: relative red shift in the frequency of cooling laser beams, υ_{atom} : Launch velocity of atoms; (c) Schematic of the forces on MOT atoms due to imbalance of detuning of MOT beams.

The number of cold atoms in the MOT has been estimated by collecting the probe beam excited fluorescence from the MOT cloud on a calibrated CCD camera[3]. In our experiments, the measured cold atom number and the number density of the cloud were ~ 5.0×10^6 and 8.0×10^9 cm^{-3} respectively. The measured temperature of the cold atomic cloud in the MOT was ~ 200 μK. In order to launch atoms vertically, the frequency of two upper MOT beams directed downwards was red shifted ($\delta\nu_{launch}$), and the quadrupole magnetic field was switched-off. This results in imbalance of force on atoms in the molasses, with net force in the one (upward) direction (Fig. 1(b) and Fig. 1(c)). Molasses with net force on atoms in one direction are referred as moving molasses. The net force on atoms in molasses launches atoms in the vertically upward direction with launch velocity (υ_{atom}) to reach a certain height until the velocity of the atoms is reduced to zero. The schematic of detection of launching of cold atoms is shown in Fig. 1(b). Atoms are launched upwards by introducing a small red detuning $\delta\nu_{launch}$ in downward directed MOT beams as indicated in Fig. 1(b). The launch velocity of atoms along the vertical direction in the laboratory frame is given by [4,5],

$$\upsilon_{atom} = \frac{\lambda\,\delta\nu_{launch}}{\sqrt{2}} \qquad (1)$$

In order to measure the velocity of launched atoms experimentally, two vertically separated probe beams, each of size ~ 1 mm ($1/e^2$ radius) and power ~ 10 μW, were aligned above the cold atom cloud. The first probe beam was placed immediately above the atom cloud and the second probe was separated by a vertical distance of ~ 5 mm from the first probe beam. These two probe beams were focused on a sensitive photodiode for measurement of absorption signal during vertical flight of atoms. The size and power of the probe beams were optimized to get absorption signal with reasonable narrow width. The separation of the two probe beams was also optimized to get

well separated absorption signals. As the atoms are launched upward, interaction of these atoms with the probe beams is marked by absorption dip in the probe beam power observed by the photodiode. The time interval between the absorption dips in the probe beams power is used for the estimation of the launch velocity of atoms. Fig. 2 shows the experimentally observed probe beams absorption signals corresponding to $\delta\nu_{launch}$ = 0.6 MHz.

The atom launch velocity (υ_{atom}) is experimentally measured using relation,

$$\upsilon_{atom} = \frac{h}{(\Delta t_{d-d})} + \frac{1}{2} g\,(\Delta t_{d-d}) \qquad (2)$$

where h is the separation between the two vertically separated probe laser beams and Δt_{d-d} is the time interval between the two observed absorption dips in the probe signal and g is the acceleration due to gravity. The width of the experimentally observed signal depends on the velocity distribution of the cold atoms cloud, finite size of the probe beams etc.

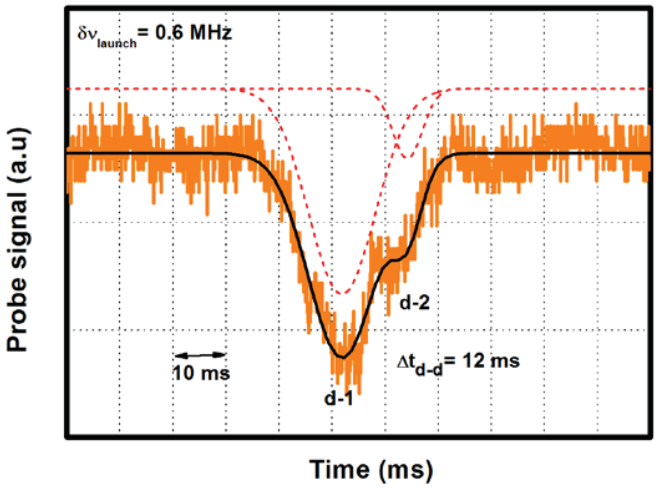

Fig. 2: Photodiode signals during the flight of atoms in the fountain for $\delta\nu_{launch}$ = 0.60 MHz. The black curve is the best fit to the observed signals corresponding two dips (d-1 & d-2) and the red curves are the individual curves used for generating the black curve.

As shown in the Fig. 2, the time interval between the absorption dips corresponding to $\delta\nu_{launch}$ = 0.60 MHz is 12 ms. The launch velocity (υ_{atom}) corresponding to $\delta\nu_{launch}$ = 0.60 MHz , as estimated using Eqn. (2), is 0.48 m/s. The estimated launch velocity (υ_{atom}) corresponding to $\delta\nu_{launch}$ = 0.84 MHz is ~ 0.60 m/s. The launch velocity can further be increased by increasing the launch detuning, $\delta\nu_{launch}$. Using Eqn. (1), the theoretically calculated values of launch velocity for $\delta\nu_{launch}$ = 0.60 MHz and 0.84 MHz are 0.33 m/s and 0.46 m/s, respectively. The deviation in experimentally measured launch velocity from its theoretically estimated value could be due to the misalignment and intensity imbalance in the MOT beams, and improper switching of magnetic field during the launch process.

In conclusion, we have presented our studies on launching of atoms in a Rb atomic fountain. In our experiments, the atoms produced in a magneto-optical trap (MOT) were launched in the vertical geometry using moving optical molasses technique. The atom launch velocity (υ_{atom}) was experimentally measured to be 0.48 m/s for the relative shift in the cooling laser beams of $\delta\nu_{launch}$ = 0.60 MHz. The atom launch velocity was also observed to increase with increase in relative frequency shift in the cooling laser beams.

Acknowledgements: Authors are thankful to K. Bhardwaj and S. Bhardwaj for their help during the experiments.

References:

[1] A. Peters, K. Y. Chung and S. Chu, *Meterologia* **38**, 25 (2001).

[2] Z. Lin, X. Zong-Yuan, Y. Wei, T. Biao, P. Wen-Cui, W. Yi-Bo, X. Peng, W. Jin, Z. Ming-Sheng, *Chin. Phys. Lett.*, **28**, 013701 (2011).

[3] S. Singh, V. B. Tiwari and S R Mishra, *Pramana - J. Phys*. **93(6)**, 91 (2019).

[4] M. Inguscio and L. Fallani, Atomic Physics: Precise Measurements and Ultracold Matter (New York: Oxford University Press Inc., 2013).

[5] V. Natarajan, Modern atomic Physics (CRC Press, Taylor & Francis Group, 2015).

Trapping of laser cooled atoms in time averaged adiabatic potentials

S. Sarkar[a,b]*, S. P. Ram[a], Kavish Bhardwaj[a], V. B. Tiwari[a,b] and S. R. Mishra[a,b]

[a]*Laser Physics Applications Section, Raja Ramanna Centre for Advanced Technology, Indore-452013, India.*

[b]*Homi Bhabha National Institute, Training School Complex, Anushakti Nagar, Mumbai -400094, India.*

*E.mail: sourabhs@rrcat.gov.in

Abstract : We have theoretically shown that time averaged adiabatic potential (TAAP) is a versatile scheme for trapping and manipulating laser cooled atoms. It allows a convenient conversion of one type of trapping geometry into another.

Trapping and manipulation of laser cooled atoms in different geometries is an important aspect for applications in various precision measurements[1] and fundamental understanding of physics[2,3]. Optical[4], magnetic[5,6] and hybrid[7] (using both optical and magnetic) fields can be used to trap atoms in potentials of different shapes such as double well[2,8], ring[6,7,9,10], arc[5,11] etc. The radio frequency (rf) dressed potentials or adiabatic potentials are the versatile tool to trap ultracold atoms in a variety of geometries[6,8,9]. Lifetime of the atoms in rf-dressed potentials is limited by Landau - Zener losses in the trap. This can be taken care to some extent by using a time averaging fields, called time orbiting potential (TOP) fields[12], along with the rf-dressed potentials. This combined trapping scheme, containing rf-fields for rf-dressed adiabatic potentials and TOP fields for time averaging, is known as time averaged adiabatic potential (TAAP)[10,13,14,15] scheme. Time averaged adiabatic potentials (TAAPs) offer a much larger scope to manipulate the trapping by changing the parameters of the TOP fields as well as the rf-fields. Such a large variation in atom trapping geometries can facilitate experimentalists to study some exotic quantum mechanical phenomena such as super-fluidity[3], Bose - Einstein condensation (BEC) in lower dimensions[3,7,10,11], vortex generation[14], tunnelling[2], atom-interferometry[1,16], etc. TAAP scheme also promises a quick conversion from one kind of trapping geometry to the other by changing the TOP field parameters.

In this work, we have theoretically proposed and investigated some interesting atom trapping geometries using TAAP scheme. It is also shown that conversion of one atom trapping geometry to another is easily possible by changing field parameters in TAAP scheme.

We consider the ^{87}Rb atoms in their $|F = 2, m_F = 2\rangle$ hyperfine dressed state corresponds to the $5S_{1/2}$ level. Our static in-homogeneous magnetic field is a quadrupole field of the form given as, $B_S(r) = B_q\ (x, y, -2z)$, where B_q is the gradient of the quadrupole field in radial (i.e. *x*-,*y*-) direction. Larmor frequency of the atoms in the quadrupole field is given as

$$\omega_0(r) = \frac{g_F \mu_B}{\hbar}\sqrt{x^2 + y^2 + 4z^2}. \qquad (1)$$

The radio frequency (rf) field is considered as

$$B_{rf}(t) = \{B_{rf}^x \cos(\omega_{rf} t), B_{rf}^y \cos(\omega_{rf} t - \alpha), B_{rf}^z \cos(\omega_{rf} t - \beta)\}, \qquad (2)$$

where B_{rf}^{x}, B_{rf}^{y} and B_{rf}^{z} are the rf-field amplitudes along *x*-, *y*- and *z*- directions respectively. ω_{rf} is the rf field frequency, α and β are the relative phases of the rf-field components. The expression for the rf-dressed adiabatic potential[3] for a general $|F, m_F\rangle$ dressed state is of the form

$$E_{AP}(r) = m_F \hbar \sqrt{(\Delta(r))^2 + (\Omega(r))^2} \ , \tag{3}$$

Above expression (Eq. (3)) of adiabatic potential has two terms. One of them is called detuning, which is given as

$$\Delta(r) = \omega_0(r) - \omega_{rf} \ . \tag{4}$$

The other term Ω(r) is called Rabi frequency[5], which can be written as

$$\Omega(r) = \left| \frac{g_F \mu_B}{\hbar} \frac{B_S(r)}{|B_S(r)|} \times B_{rf} \right| . \tag{5}$$

The most general TOP field has the following form

$$B_T(t) = \{B_T^x \cos(\omega_T t), B_T^y \cos(\omega_T t + \theta_1), B_T^z \cos(\omega_T t + \theta_2)\} , \tag{6}$$

where B_T^x, B_T^y and B_T^z are the magnitudes of the TOP fields along *x, y* and *z* directions respectively. θ_1, θ_2 are the relative phase angles of the TOP fields and TOP field frequency $\omega_T = 2\pi \times 7.5$ KHz.

By averaging over the period ($2\pi/\omega_T$) of a time averaging field, expression for TAAP can be written as

$$E_{TAAP}(r) = \frac{\omega_T}{2\pi} \int_0^{\frac{2\pi}{\omega_T}} E_{AP}\left(x + \frac{B_T^x}{B_q}\cos(\omega_T t), y + \frac{B_T^y}{B_q}\cos(\omega_T t + \theta_1), z + \frac{B_T^z}{2B_q}\cos(\omega_T t + \theta_2) \right) dt . \tag{7}$$

The expression for E_{TAAP} in Eq. (7) has been numerically evaluated by writing a code in Python. The trapping potentials E_{TAAP} for ^{87}Rb atom in $|F=2, m_F=2\rangle$ state have been evaluated corresponding to different values of rf-fields (B_{rf}^x, B_{rf}^y, B_{rf}^z, α, β) and TOP fields (B_T^x, B_T^y, B_T^z, θ_1, θ_2) parameters. Here *x*-*y* TOP field is used throughout the article with a phase difference of π/2 between *x* and *y* components of TOP fields**.**

Figure 1(A) shows conversion of a *x*-direction double well into a double along *y*-direction when *x*-TOP field is varied (keeping *y*-TOP field at a fixed value). Usually, in rf-dressed potential, a double well is formed along the direction of polarization of rf-field. In rf-dressed potential alone, it is not possible to alter the directionality of the well without changing the direction of the rf field. But here in figure 1(A), due to unequal values of the TOP fields, the directionality of the double well gets changed. Similarly, figure 1 (B) shows the results where a *y*-directional double well is getting converted into x-directional double well by changing *y*-TOP field (keep *x*-TOP field value fix) in TAAP scheme.

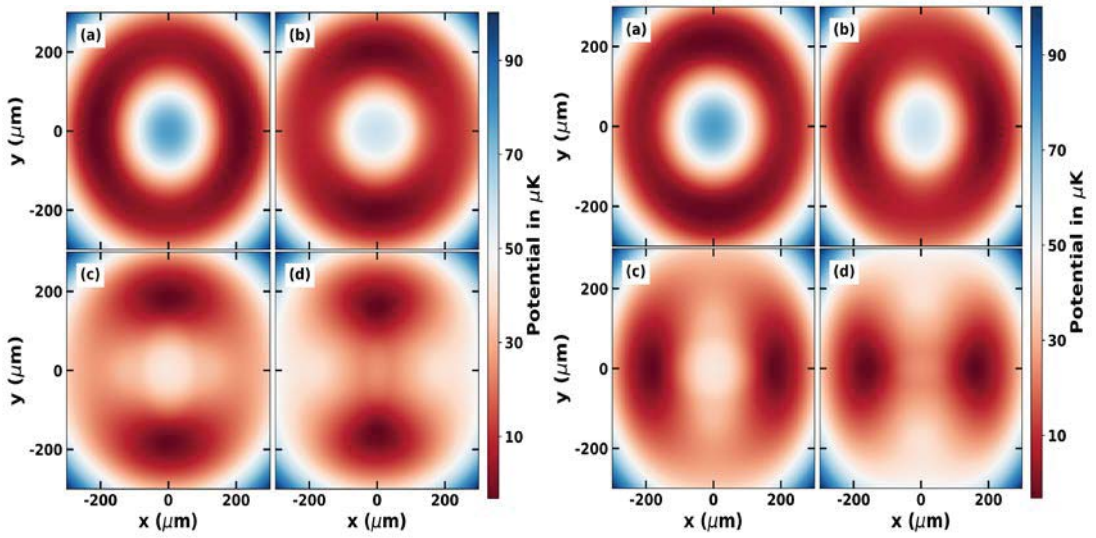

(A) **(B)**

Figure 1. Directional conversion between the double wells. ***(A)*** *x- directional double well is converted into the y-directional double well. RF field value* B_{rf}^{x} *= 500 mG. Value of* B_{T}^{y} *is fixed at 535 mG, and the* B_{T}^{x} *values are: (a)535 mG, (b)963 mG, (c) 1.39 G, (d)1.81 G respectively.* ***(B)*** *y- directional double well is converted into the x-directional double well. RF field value* B_{rf}^{y} *= 500 mG. Value of* B_{T}^{x} *is fixed at 535 mG, and the* B_{T}^{y} *values are : (a) 535 mG, (b) 963 mG, (c) 1.39 G, (d)1.81 G respectively. Quadrupole field gradient* B_q *= 90 G/cm, rf field frequency* $\omega_{rf} = 2\pi \times 1.4$ *MHz for both the two subfigures* ***(A)*** *and* ***(B)****.*

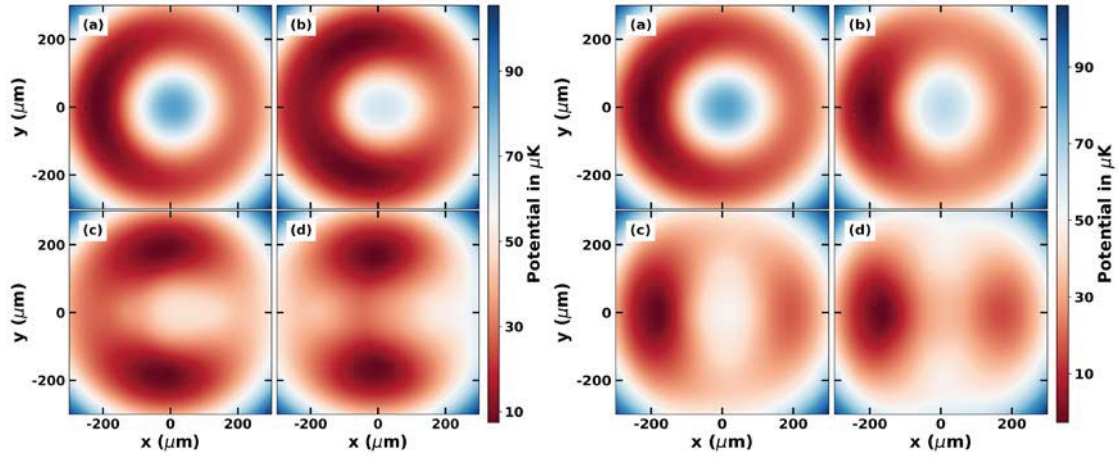

(A) **(B)**

Figure 2. Conversion of arc into double well. RF field values are $B_{rf}^{x} = B_{rf}^{y} = 500\,mG$, $B_{rf}^{z} = 700$ *mG and phase difference between x- and y-rf fields is π/2, rf field frequency* $\omega_{rf} = 2\pi \times 1.4$ *MHz and quadrupole field gradient* B_q *= 90 G/cm for both the two subfigures* ***(A)*** *and* ***(B)****.* ***(A)*** *Arc is getting converted into y-directional double well. Value of* B_{T}^{y} *is fixed at 535 mG, and the* B_{T}^{x} *values are: (a) 535 mG, (b) 963 mG, (c) 1.39 G, (d) 1.81 G respectively.* ***(B)*** *Arc is getting converted into x-directional double well.* B_{T}^{x} *value is fixed at 535 mG, and the* B_{T}^{y} *values are: (a) 535 mG, (b)963 mG, (c) 1.39 G, (d) 1.81 G respectively.*

Arc trapping geometry is needed when we want unequal population around the ring, rotation of an arc is a very good platform to study the dynamics[3,11] of atom cloud. Along with a circularly polarized rf field when we insert a *z*-rf field to a magnetically trapped atom cloud, then an arc type of trapping geometry is formed. Almost all the atom cloud can be brought into one side of a ring by the arc geometry. Figure (2) shows how does an arc trap is getting converted into a double well trap when we change the *x*-TOP (*y*-TOP) field values while keep fix the *y*-TOP (*x*-TOP) field value. The conversion of the arc shaped trap to double well shaped trap is not possible in rf dressing technique, unless the directionality of the rf field is changed. These kind of conversions show the versatility of the TAAP scheme. TAAP with multiple[13] rf frequency will lead to the formation of periodic potential geometry like lattices, multiple wells, etc.

In conclusion, we have theoretically shown that conversion between directions of trapping double well and conversion from arc trapping into double well trapping is achievable in TAAP scheme by modulation of TOP fields. The arc trapping or double well trapping geometries are very useful in studying Bose-Einstein condensation in lower dimensions, super-fluidity, atom- interferometry and tunnelling phenomena. We can study the dynamics of the atom cloud when one kind of geometry is converted into the other.

S. Sarkar is thankful for the financial support from RRCAT under the HBNI programme.

References:

1. A. Peters, K. Y. Chung, S. Chu, *Metrologia*, **38,** 25-61 (2001)

2. Michael Albiez, R. Gati, J. Folling, S. Hunsmann, M. Cristiani, M. K. Oberthaler, *Phys. Rev. Lett.* **95,** 010402 (2005)

3. A. Ramanathan, K. C. Wright, S. R. Muniz, M. Zelan, W. T. Hill, C. J. Lobb, L. Helmerson, W. D. Phillips, and G. K. Campbell, *Phys Rev Lett.* **106**, 130401 (2011).

4. K Henderson, C Ryu, C MacCormick and M G Boshier*, New J. Phys.* **11,** 043030 (2009)

5. A. Chakraborty and S. R. Mishra, *J. Kor. Phys. Soc.* **65**, 1324 (2014)

6. A. Chakraborty, S. R. Mishra, S P Ram, S. K. Tiwari, H. S. Rawat, *J. Phys. B: At. Mol. Opt. Phys.* **49,** 075304 (2016)

7. W. H. Heathcote et al. *New J. Phys*. **10**, 043012 (2008)

8. T. Schumm et al. *Nat. Phys.* **1**, 57 (2005)

9. O. Morizot, Y. Colombe, V. Lorent, and H. Perrin, *Phys. Rev. A*, **74**, 023617 (2006)

10. B. E. Sherlock, M. Gildemeister, E. Owen, E. Nugent, and C. J. Foot, *Phys. Rev. A,* **83**, 043408 (2011).

11. S. Gupta et al*. Phys. Rev. Lett*, **95,** 143201 (2005)

12. W. Petrichet al. *Phys.Rev. Lett.,* **74,** 0031 (1995)

13. I. Lesanovsky and W. von Klitzing, *Phys. Rev. Lett.,* **99**, 083001 (2007).

14. M. Gildemeister, B. E. Sherlock, C. J. Foot*, Phys. Rev. A*, **85,** 053401 (2012)

15. M. Gildemeister et al. *Phys. Rev. A*, **81**, 031402 (2010)

16. P. Navez et al. *New J. Phys.* **18**, 075014 (2016)

Studies on optimization of optical pumping of cold ^{87}Rb atoms using Stern-Gerlach (SG) technique

Vivek Singh[a,b,*], V. B. Tiwari[a, b] and S. R. Mishra[a, b]

[a]*Laser Physics Applications Section, Raja Ramanna Centre for Advanced Technology, Indore-452013, India.*

[b]*Homi Bhabha National Institute, Training School Complex, Anushakti Nagar, Mumbai - 400094, India.*

***E.mail:** viveksingh@rrcat.gov.in

Abstract: We report our studies on the optimization of optical pumping of cold ^{87}Rb atoms to a particular Zeeman hyperfine state (F=2, m_F = +2) using Stern-Gerlach (SG) technique. Nearly 55% of cold atoms number from Grey magneto-optical trap (G-MOT) have been optically pumped to m_F = + 2 state. These studies are expected to be useful in maximizing the number of atoms trapped in the magnetic trap on the atom-chip setup.

An atom-chip[1-2] with micron sized wire structure patterns on a reflecting surface provides platform for trapping and manipulation of atoms on a miniaturized scale. The manipulation of cold atoms have been demonstrated using atom traps, atom guides[3] and beam splitters[4]. Bose-Einstein condensation (BEC) on atom-chip has also been achieved[5]. Usually, cold atoms in an atom chip setup are produced in a magneto-optical trap (MOT) known as U-MOT using cooling laser beams reflecting from atom chip surface in presence of magnetic field produced by a U-shaped wire. The temperature of cold atoms is reduced and position of cold atoms is shifted closer to the atom chip surface in the subsequent stage of Grey-MOT (G-MOT). To trap these cold atoms on the atom-chip, these atoms need to be pumped efficiently into a trappable magnetic state.

Here, we report our studies on the optimization of optical pumping of cold ^{87}Rb atoms on atom-chip using Stern-Gerlach (SG) technique. We are able to transfer ~ 55 % of cold atoms from Gray magneto-optical trap (G-MOT) into m_F = + 2 state.

The details of the experimental setup can be found in our earlier published works[6-8]. The experimental setup consists of an octagonal vacuum chamber. A turbo molecular pump (TMP) (77 l/s), a sputter ion pump (SIP) (300 l/s) and a titanium sublimation pump (TSP) are the vacuum pumps used for creating the ultrahigh vacuum UHV with a base pressure of ~ 2.0 x 10^{-10} Torr in the chamber. The dispensers are located at a distance of ~ 17 cm from the center of the octagonal chamber. The Rb vapor is injected into the vacuum chamber after passing a current through this feed-through. This results in some increase in the pressure in the chamber, reaching the value ~ 3.5 x 10^{-10} Torr after the release of Rb-vapor from the dispensers. Four independent cooling laser beams (mixed with re-pumper laser beams) are used to form mirror MOT with quadupole field produced by U-shaped external wire as shown in Fig. 1. The various steps from MOT formation to G-MOT and imaging of cloud using CCD are controlled by an in-house developed FPGA based electronic controller system.

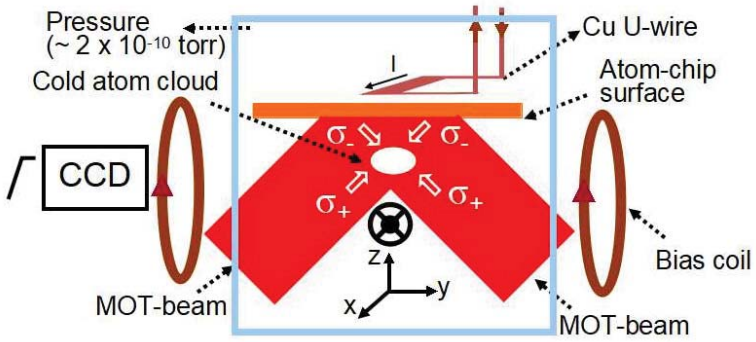

Fig. 1: Schematic of the atom-chip setup. Four MOT beams are marked by arrows and two counter propagating MOT beams are perpendicular to plane of paper, making required six beams for a MOT.

There are various consecutive stages involved in the process for optimization of optical pumping of ^{87}Rb cold atoms using SG technique in our atom-chip setup. The duration of first stage of laser cooling is around 20 s and can be divided into two phases. In the first phase, a U-MOT is formed from background Rb vapor generated by a dispenser source operating ~ 3.0 A. The current of ~60 A is passed in U-wire, and magnetic field of ~ 10 G in y-direction and ~ 1.5 G in z-direction is applied. The cooling laser frequency is detuned by ~ - 14 MHz from the resonance. The atom cloud in the U-MOT is formed ~ 6 mm below from the atom chip surface as shown in Fig. 2 (a). The number of cold atoms and the temperature of the atom cloud is ~ 5 x 10^7 and ~ 280 μK respectively.

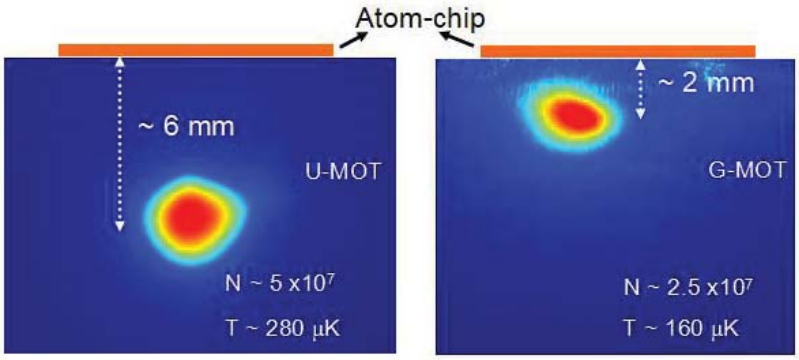

(a) *(b)*

Fig. 2: CCD images of ^{87}Rb atoms in atom cloud in (a) U-Magneto-optical trap (U-MOT) and (b) Gray magneto optical trap (G-MOT).

In the second phase, these cold atoms are moved vertically up (in z-direction) to a position ~ 2 mm from the chip surface. This is achieved by ramping the current in U-wire (60 A to 80 A) and Y-bias coil (15 A to 43 A) in 100 ms. During the compression, the laser cooling frequency was detuned to ~ -20 MHz to reduce the repulsive force resulting from multiple scattering processes within the dense cloud. The G-MOT stage is performed for ~ 10 ms as the cooling laser frequency is detuned to ~ - 40 MHz to lower the temperature of the cloud. The atom cloud in G-MOT is trapped ~ 2 mm from the chip surface as shown in fig. 2 (b). The total cold atom number and the average temperature of the atom cloud is found to be ~ 2.5 x 10^7 and~ 160 μK respectively.

After the G-MOT stage, all the magnetic fields and laser lights are switched off. A current value of 20 A is passed in copper Z-wire to generate magnetic field gradient force, called as Stern-Gerlach (SG) force, on cold atom cloud. This results in spatial separation of atoms populated in different magnetic hyperfine Zeeman states. The fluorescence image of cold atom cloud was then taken after evolution of atoms for a duration of ~ 3 ms (Fig.3(a)) in the force. The profile of cold atom cloud along z-direction was fit with three Gaussian distribution functions (red, green and blue) confirming the presence of cold atoms in m_F = {0, +1, +2} states respectively. The blue curve in all the figure shows m_F = +2 state atoms. The cold atoms present in m_F = +2 state experiences maximum SG force. As a result, this group of atoms are at the outermost position in the CCD images of the cloud.

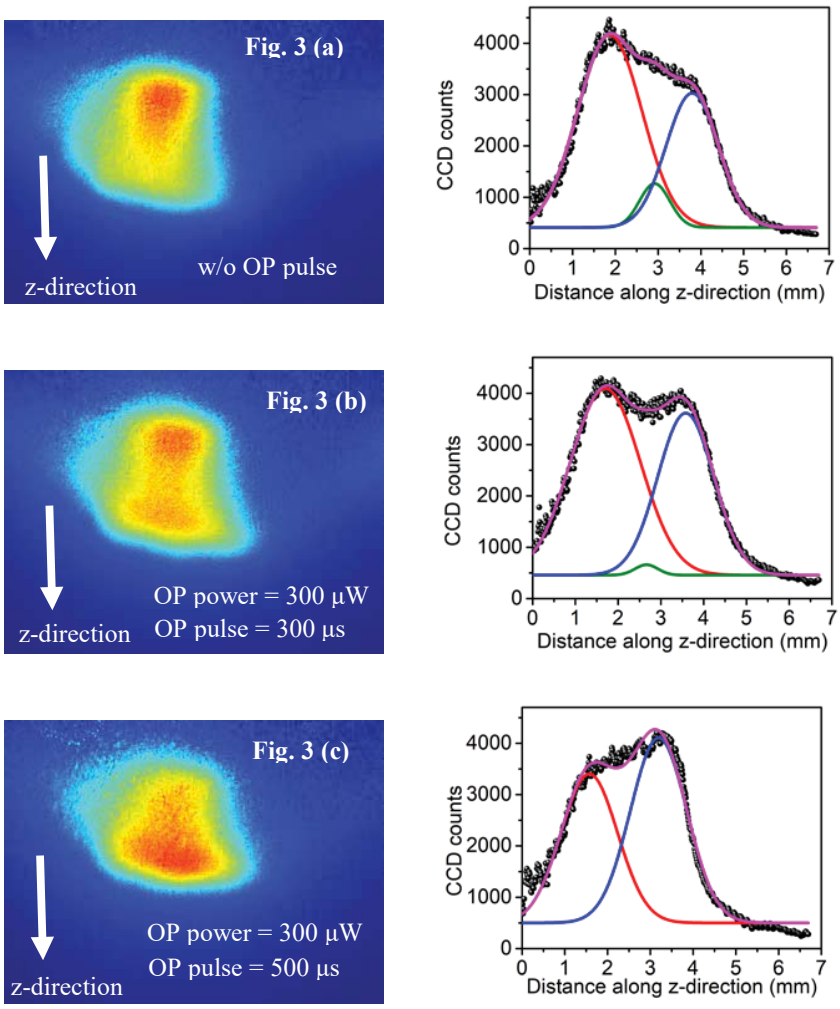

Fig. 3 : The cold atom cloud under Stern-Gerlach (SG) force for the characterization of the optical pumping process. (a) The effect of SG force on cold ^{87}Rb atoms, without any optical pumping, (b) By performing optical pumping for ~ 300 µs, ~ 32% atoms are in m_F = + 2 state w.r.t to atoms in G-MOT. (c) By performing optical pumping for ~ 500 µs, ~ 55 % atoms are in m_F = + 2 state w.r.t to atoms in G-MOT.

The m_F = {−2, −1} states are not seen in the image as they are accelerated upwards in the magnetic field gradient and lost to the chip surface. The power and pulse duration of optical pumping beam was varied to optimize the optical pumping. Fig. 3(a) shows the effect of SG force on cold ^{87}Rb atoms without any optical pumping beam. The corresponding line profile of cold atoms along z-direction is fit with three Gaussian distribution function confirming that cold atoms are in m_F = {0, +1 +2} states. We have found ~ 28 % of atoms in m_F = + 2 state with respect to number of atoms atoms in G-MOT. Fig. 3(b) shows the image of cold ^{87}Rb atoms after using 300 μs optical pumping (OP) pulse (σ^+ polarized light, power = 300 μW) in presence of ~ 3 G bias magnetic field. We have found that ~ 32 % atoms are transferred to m_F = + 2 state with respect to atoms in G-MOT. It is evident from Fig. 3(c) that, after using 500 μs optical pumping (OP) pulse (σ^+ polarized light, power = 300 μW, Intensity = 0.5 mW/cm^2) in presence of ~3 G bias magnetic field, ~ 55% atoms are transferred in m_F = + 2 state with respect to number of atoms atoms in G-MOT (the blue curve in Fig.3(c)).

In conclusion, we have studied optical pumping process using SG force. We are able to transfer ~ 55 % of cold ^{87}Rb atoms from Gray magneto-optical trap (G-MOT) to (F=2, m_F = + 2) state. This study is useful to maximize the number of atoms in the magnetic trap on the atom-chip.

We are thankful to A. Kak for fabrication of vacuum feed-throughs and R. Shukla and C. Mukherjee for fabrication of atom-chip, and Bhupinder Singh and M. S. Ansari for the development of switching circuit, and Ayukt Pathak for the development of FPGA based controller system. The assistance provided by Shri Amit Chaudhary during the experiments is also gratefully acknowledged.

References:

1. R. Folman, P. Kruger, J. Schmiedmayer, J. H. Denschlag, and C. Henkel, Microscopic atom optics:from wires to an atom chip, Adv. At. Mol. Opt. Phys. 48, 263 (2002).

2. J. Dendchlag, D. Cassettari, A. Chenet, S. Schneider, and J. Schmiedamayer, A neutral atom and a wire: towards mesoscopic atom optics, Appl. Phys. B **69**, 291 (1999).

3. D. Muller, D. Z. Anderson, R. J. Grow, P. D. D. Schwindt, and E. A. Cornell, Guiding Neutral Atoms Around Curves with Lithographically Patterned Current-Carrying Wires, Phys. Rev. Lett. **83**, 5194 (1999).

4. D. Cassettari, B. Hessmo, R. Folman, T. Maier, and J. Schmiedmayer, Beam Splitter for Guided Atoms, Phys. Rev. Lett. **85**, 5483 (2000).

5. D. M. Farkas, K. M. Hudek, S. Du and D. Z. Anderson, Efficient direct evaporative cooling in an atom-chip magnetic trap, Phys. Rev. A, **87**, 053417 (2013).

6. V. Singh, V. B. Tiwari, K. A. P. Singh and S. R. Mishra. On loading of a magneto-optical trap on an atom-chip with U-wire quadrupole field, J. Mod. Opt. **65**, 2332 (2018).

7. V. Singh, V. B. Tiwari, and S. R. Mishra, “On the continuous loading of a U-magneto-optical trap on an atom-chip in an ultra high vacuum,” Laser Phys. Lett. 17, 035501 (2020).

8. V. Singh, V. B. Tiwari, and S. R. Mishra, “Polarization enhanced tunable Doppler-free dichroic lock technique for laser frequency locking,” J. Opt. Soc. Am. B. 38, 249-255 (2021).

Quantum entanglement between atoms using quantized light

S. Kannan[1]

[1] *ISRO Inertial Systems Unit, Thiruvananthapuram, 695 013, India.*

Dr. Sudheesh Chethil[2]

[2] *Indian Institute of Space Science and Technology, Thiruvananthapuram, 695 547, India.*

Email: kns.phys@gmail.com[1]

Abstract: Since the famous 1935 paper by Einstein, Podolsky, and Rosen, the idea of entanglement has generated significant interest among physicists. It even inspired many works regarding the foundations of quantum mechanics. Recently the applications of entanglement span a wide spectrum such as quantum information theory, quantum computing, quantum cryptography etc. In this work our focus is on the quantum entanglement between atoms interacting *via* a quantized field. Considerable difference from the quasi-classical scenario in the photoelectron spectrum is seen when the quantum nature of the field is taken into consideration[1]. Thus for a complete understanding of the atom-field interaction, quantum description of the field is important. We use the model introduced by V. Peřinová et al.,[2] for our study. This model which comprises an atom with an auto-ionizing level and a two-level atom without any auto-ionizing level proved that the long-time behavior of atoms will show quantum correlation even when they are not interacting directly. Our aim in this work is to study the feature/features of the quantized field that will decide the degree of entanglement.

Optical excitation model

Let us consider two atoms, a and b, in an electromagnetic field. The atom a is a two-level atom and the atom b is an auto-ionizing system. We use n to denote the number of photons in a mode and $|0\rangle$ and $|1\rangle$ represents the ground states and excited states of the atoms ($|1\rangle_{\mathrm{b}}$ is the auto-ionizing state). $|E_d\rangle$ is the continuum state of the atom b and E_d is the energy difference between the ground state and the continuum state. For simplicity, we assume both the atoms interact with the same mode L of the electromagnetic field. We can write the levels of the atom by photon-number states:

$$|n\rangle_{\mathrm{L}} \otimes |0,0\rangle_{\mathrm{a,b}} , |n-1\rangle_{\mathrm{L}} \otimes |1,0\rangle_{\mathrm{a,b}} , |n-1\rangle_{\mathrm{L}} \otimes |0,1\rangle_{\mathrm{a,b}} ,$$

$$|n-2\rangle_{\mathrm{L}} \otimes |1,1\rangle_{\mathrm{a,b}} , |n-1\rangle_{\mathrm{L}} \otimes |0,E_d\rangle_{\mathrm{a,d}} , |n-2\rangle_{\mathrm{L}} \otimes |1,E_d\rangle_{\mathrm{a,d}} .$$

The Hamiltonian can be written as

$$H = H_{free} + H_{a-i} + H_{t-a} + H_{trans}, \tag{1}$$

where H_{free} is the Hamiltonian for the electromagnetic field and is equal to

$$H_{free} = \hbar\omega a_L^{\dagger} a_L, \tag{2}$$

with $a_L^{\dagger}$ and a_L being the creation and annihilation operators. The Hamiltonian H_{a-i} for the auto-ionizing system can be written as

$$H_{a-i} = E_b|1\rangle_{bb}\langle 1| + \int E_d\,|E_d\rangle\langle E_d|dE_d + \int (V\,|E_d\rangle_b\langle 1| + H.c.)dE_d + (\mu_b a_L|1\rangle_{bb}\langle 0| + H.c.) + \int (\mu\, a_L|E_d\rangle_b\langle 0| + H.c.)dE_d, \tag{3}$$

where E_b represents the energy difference between $|0\rangle_b$ and $|1\rangle_b$, μ_b and μ are the dipole moments or the strength of excitations from the ground state to the excited states, V is the Coulomb configuration interaction between the excited states of atom b. H_{t-a} is the Hamiltonian for the two level atom and can be written as

$$H_{t-a} = E_a|1\rangle_{aa}\langle 1| + (\mu_a a_L|1\rangle_{aa}\langle 0| + H.c.)\,, \tag{4}$$

E_a is the energy difference between the ground state and the excited state of the atom a and μ_a is the dipole moment. H_{trans} is the dipole-dipole interaction between the two atoms and is expressed as

$$H_{trans} = (J_{ab}|1\rangle_{bb}\langle 0||0\rangle_{aa}\langle 1| + H.c.) + \int (J|E_d\rangle_b\langle 0||0\rangle_{aa}\langle 1| + H.c.)dE_d, \tag{5}$$

J_{ab} and J denotes the energy transfer from $|0\rangle_b$ to $|1\rangle_b$ and to $|E_d\rangle$ respectively at the cost of decay from the state $|1\rangle_a$ to $|0\rangle_a$. Following the calculation in reference 1 and 2, it is easy to see that the long-time behavior of the system is characterized by complete ionization of the auto-ionizing atom and both the levels of the two-level atom being equally occupied.

Entanglement calculation

The entanglement between the bound-electron of two-level atom and the ionized electron in the auto-ionizing atom is created by the quantized field and the dipole-dipole interaction. Different types of quantized fields such as the coherent state ($|\alpha\rangle$), squeezed-vacuum state ($|\xi\rangle$), photon-added coherent state ($|\alpha, m\rangle$), etc., are studied. These states shows different photon-number distribution, different quadrature variances and photon-statistics. We have found that despite these differences when the mean photon number of these quantum states becomes same, the amount of entanglement created is also the same. We use negativity[3] to quantify the degree of entanglement.

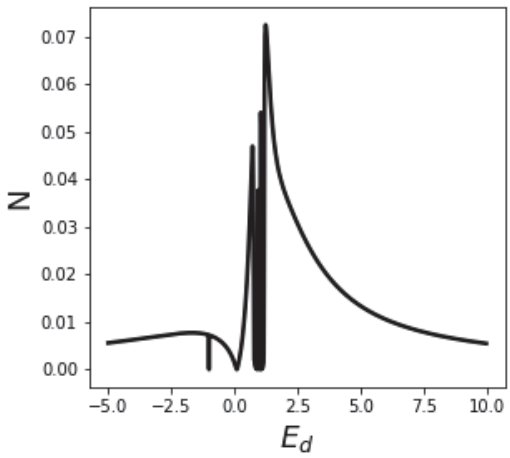

Fig. 1: Negativity between the electrons of the two atoms when the laser mode contains a mean number of photons of 4.5.

Conclusion

We have found that during atom-field interaction the degree of correlation only depends on the mean number of photons in the field and not on any other parameters. We have also extended the study to more than two-atom

scenario and the presence of multi-partite entanglement created due to the quantized field and dipole-dipole interaction is observed.

References

1. W. Leoński, and V. Bužek, *Journal of Modern Optics* **37**, 1923 (1990).
2. V. Peřinová, A. Lukš, J. Křepelka, and J. Peřina Jr, *Physical Review A* **90**, 033428 (2014).
3. G. Vidal and R. F. Werner, *Physical Review A* **65**, 032314 (2002).

Design and Development of mirror MOT Atom Chips for Cold Atom Interferometry

Hriday Dath, Dr. Radhika V. N., Harikrishnan A, , Rekha A. R.,

J Krishnakumar and Hemachandran S

ISRO Inertial Systems Unit (IISU), Vattiyoorkavu, Trivandrum.

E-mail: hridaysunildath@gmail.com

Abstract

Experiments involving laser cooled atoms to study the wave property of matter has garnered a lot of attention in the past decades. It shows real promise in inertial sensing, metrology, time keeping, studies on fundamental constants and quantum computing. In most such experiments the center of cold atom cloud generation and manipulation is integrated platforms known as atom chips. Chip provides the means for cold atom experiments to make the transition from laboratory demonstration to ruggedized, compact and more practical devices and to integrate complex infrastructure into miniaturized subsystems. In this paper we discuss the design and implementation of mirror MOT atom chip and atom cloud formation as well as atom cloud manipulation.

1. Introduction

In recent years, the wave nature of matter in the microscopic world has been an important topic of physics research and a driving force in developing modern scientific technologies. Apart from the possibility of understanding fundamental physics in multitude ways, interference of matter waves provides an unmatched tool for performing high precision measurements. Cold Atom interferometry is such a tool that exploits the wave property of matter to make measurement of inertial forces while promising very high accuracy. To have a miniaturized, stand alone measurement system for field applications in different environments, technology has to be realized in to a compact ruggedized model so that external disturbances will not affect the sensing. The atom chip technology is the most compelling method for integration and miniaturization of subsystems in cold atom technology.

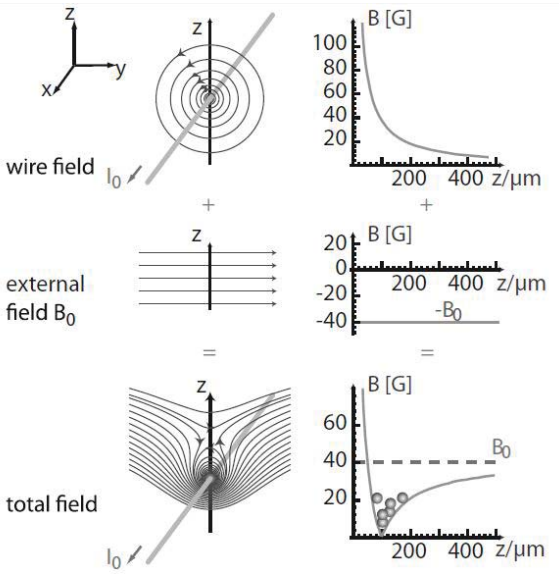

Figure 1: Principle of the magnetic microtrap. A homogeneous bias field B_0 is superposed on the field of a microscopic current carrying wire. The resulting field has a minimum along the wire axis. [4]

The atom chip is considered as a necessary tool in miniaturization and integration of cold atom experiments aimed with applications in the development of novel sensors required for precision measurements. It is a device intended to **miniaturize** setups and subsystems for quantum optics associated with **cold atom** experiments. Similar to role of the integrated circuits in electronics, atom-chip is expected to be a basic building block of atom optical devices for various applications in quantum information processing, communication, precision sensors, etc.. [1].

In recent years, there has been great progress towards integrating a wide range of optical, electric and magnetic elements into atom chips. The chip trapping promises low power consuming, heat efficient cooling and trapping method to achieve Cold Atom cloud and/or BEC in a portable and autonomous setup. Evidently, this was the reason behind atom chips being used in very recent, first demonstration of BEC in microgravity [2]. This establishes the fact that, atom chip is the ideal solution to achieve required compactness and ruggedness for atom interferometry in space.

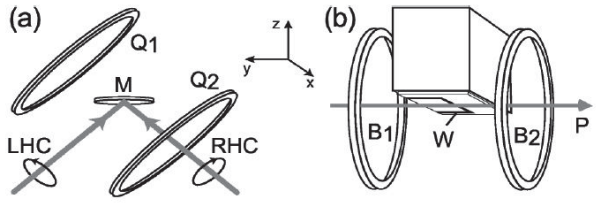

Figure 2: (a) Schematic of the mirror-MOT. M: mirror, Q1,Q2: quadrupole coils. (b) Setup of the experiment. W: microfabricated wire, B1,B2: bias coils, P: probe beam. (MOT beams and coils not shown.) [4]

In this document we will discuss a brief overview of the working and design of atom chips based on endeavors by different groups working in Cold atom technology development. We will also discuss initial design of mirror MOT atom chip intended to create cold atom cloud and compare the expected properties. The cloud manipulation and subsystem integration that can be achieved through the chip development will also be reviewed in detail.

2. Trapping Atoms using Chips

To achieve trapping fields in atom chips one does need to miniaturize the field generated with macroscopic Anti Helmholtz coils. Such trapping fields can be generated from superposing the magnetic field of a single wire with an external bias field B_0 (See Fig. 1). This configuration, which has previously been widely used to trap atoms, results in a line with zero field parallel to the wire at a distance

$$r_o = \frac{\mu_o}{2\pi}\frac{I}{B_o}$$

Where I is current through the wire and Bo is the external bias field. In the vicinity of zero field line, the field magnitude varies approximately linearly with a gradient that is equal to that of the wire alone. In this way, a two-dimensional quadrupole potential is obtained which has a steepness of

$$|\nabla B|(r_o) = \frac{2\pi}{\mu_o}\frac{{B_o}^2}{I}$$

close to the trap center [3,4]. To obtain a three-dimensional trap, a wire is bent at both ends so that it forms either a “U” or a “Z”. Compact chip magnetic traps used for trapping cold atoms reduce distance between the wire and the trap center by several orders of magnitude (from centimeter to microns). Microstructures required for trap formation require less current than macroscopic coils.

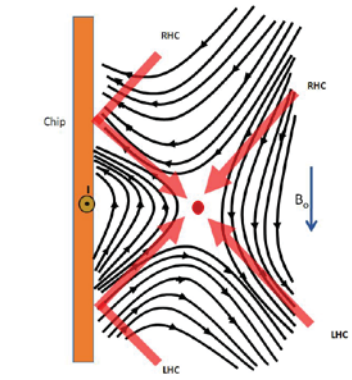

Figure 3: Magnetic field configuration and beam. B_o indicates the external magnetic field.

The prospects of integrating laser beams required for generating the MOT cooled atom cloud is rapidly evolving with different designs such as mirror MOT, pyramid MOT, grating MOT etc [1,5]. These chip trap configurations minimizes the number of laser beams to be directed into the vacuum chamber for cooling the atoms. The mirror-MOT [Fig. 2] is a one of the standard chip scale magneto-optical traps which cools and traps atoms close to a surface. It uses only four instead of the usual six laser beams, two of which are reflected off the mirror surface, with the polarizations and magnetic field orientation. The mirror MOT typically contains 10^6 atoms at distance from the surface typically larger than 1 mm.

3. Design of Atom Chips

Atom chips must incorporate the MOT trapping in the form of optical scattering forces and the coils required for generating quadrupole magnetic field gradient. Forces are made to be zero at the center of the trap by tuning the atom chip current, intensity and polarization of laser beams. The criticality in miniaturizing subsystems using atom chips comes in the form of less accessibility for cloud probing multiple directions. The chip design mentioned here has the symmetry in the chip surface that ensures zero unbalanced forces parallel to chip surface. The forces perpendicular to the chip surface are to be balanced with the laser beam alignment, intensity and polarization adjustment.

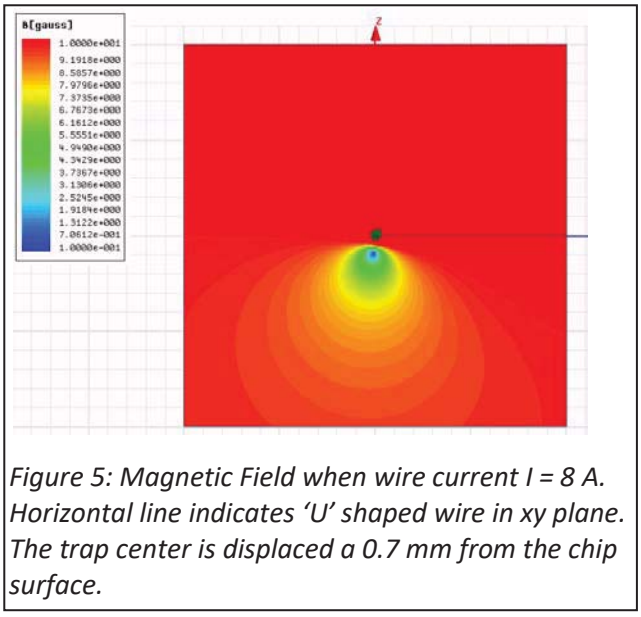

Figure 5: Magnetic Field when wire current I = 8 A. Horizontal line indicates 'U' shaped wire in xy plane. The trap center is displaced a 0.7 mm from the chip surface.

Unlike the conventional MOT, mirror MOT only uses 4 laser beams for cooling as shown in Fig 2. Two axial beams are taken along the chip surface as shown in Fig 2(b). Rest four cooling beams are generated from two beams incident on the chip mirror surface at an angle. The beams are kept having opposite circular polarization to enable MOT beam polarization criteria for Sub Doppler cooling. Thus the mirror-MOT uses four beams and a mirror as shown in Fig 3 to reproduce the exact laser-field configuration of the standard MOT in the half-space delimited by the mirror. It is derived from an earlier surface- MOT scheme, and has also been related to the 'pyramid MOT', which traps atoms inside a pyramid formed by four mirror surfaces. Although other planar mirror orientations exist that reflect beams in the right directions, the configuration on Fig 3 is the only one in which the reflected beams have the correct polarizations with respect to the magnetic quadrupole field.

To employ the mirror-MOT with a chip trap, the chip surface has to be reflective. The cloud will be formed close to the chip surface, where laser cooling is performed with aid of mirror surface on the chip. One method to achieve mirror MOT is to metal-coat the whole chip surface with the exception of narrow etchings separating the conductors [6]. This achieves a very good overall reflectivity, but some inevitable diffraction at the etchings. It has been reported that, the deformation of the light field due to these gaps does not seem to result in a significant degradation of MOT performance.

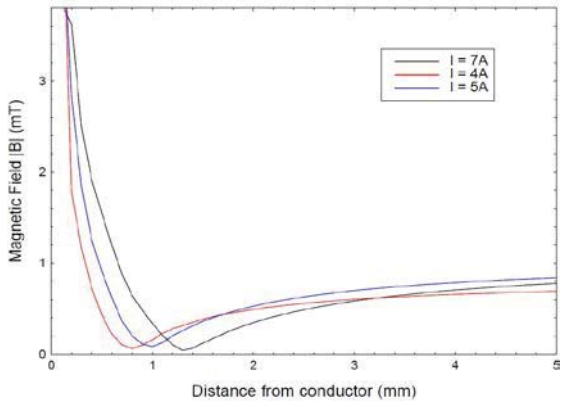

Figure 6: Variation of Magnetic Field with distance (wire current is varied for constant bias B_o = 10 G). The trap center shifts closer to chip surface with increase in wire current.

In the initial design idea atom chip will be having an area of 4 cm x 4 cm. The substrate on which chip fabrication has to be performed is chosen as p type Silicon substrate of 500 μm thickness. The Si substrate has to be insulated with a thermally grown 1 micron thick oxide layer on the surface. The wires and reflecting mirrors are photo lithographically patterned on the surface and Gold electroplating is used to micro fabricate gold wires and mirrors. On the bottom surface of the chip, another 'U' shaped wire of higher thickness made of copper will be pasted. This thicker wire will play a major role in cloud manipulation after MOT formation. The schematic for micro fabrication layers are shown in Fig 4. The wire geometry on chip surface is designed based on literature survey on mirror MOT atom chips established by many groups. Both 'U' shaped and 'Z' shaped wires are to be designed in geometry for sufficient cloud control.

4. Magnetic Field Analysis of Chip

Dimensions of chip wire were fixed based on different attempts of mirror MOT formation in literature [4, 6]. The magnetic field simulation of chip wire is carried out in Ansoft Maxwell. A 'U' shaped gold wire of length 60 mm, width 100 micron and thickness 10 micron was generated with dimensions as shown in the Fig 7. A constant Magnetic field of 10 G is applied perpendicular to the wire and wire is subjected to constant currents. The magnetic field gradient above the wire is monitored.

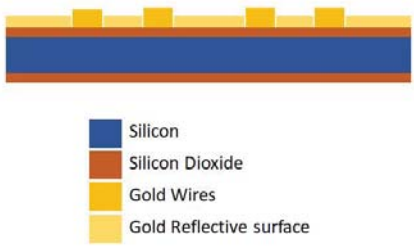

Figure 7: Schematic for design layers of atom chip (not in scale). Gold wire deposition is 10 µm and reflective laver thickness is 250 nm

Fig 6 shows the magnetic field gradient obtained in the plane perpendicular to the wire. The magnetic field minimum point is evidently seen in the figure. In this configuration, the 4 laser beams have to be aligned to this point to achieve mirror MOT. As the current through the wire is changed the magnetic field minimum point shifts its position. By varying the current for a constant bias magnetic field, trap point movement in z axis is shown in Fig 6. It can be seen that the trapped cloud position can be moved from/ to the chip surface by varying the current through the wire. It has to be noticed that by changing the current the magnetic trap gradient varies slightly.

5. Conclusion

Trapping of cold atoms using the atom chip magnetic traps is the most important step towards the miniaturization and integration of cold atom sensor technology. Development and fabrication of atom chips will most definitely be an asset to advancements in realizing the compact portable high precision inertial sensors based o Cold Atom Interferometry. In this paper we discuss the constraints that one has to navigate while designing an atom chip for cold atom experiments. We also briefly discuss the analysis of magnetic trap and the control of Cold atom cloud that can be achieved with the design of atom chips. The thermal simulation of the chip has to be performed to understand the constraints of Joule heating that will be introduced in the conductor. The fabrication process has to evolve with multiple trials to incorporate the wire geometry and mirror geometry and improve the efficiency of micro fabrication. The present design enables generation of the cold atom cloud from chip configuration for atomic interferometers and other applications.

6. References

1. Mark Keil, Omer Amit, Shuyu Zhou et al. *Journal Of Modern Optics*. **63**, 18, 1840–1885 (2016).
2. David C. Aveline, Jason R. Williams, Ethan R. Elliott et al.; *Nature*; **582**, 193-197 (2020).
3. R. M. Godun, M. B. Darcy, G. S. Summy and K. Burnett; *Contemporary Physics*, **42**, 77± 95(2001).
4. J. Reichel, W. Hänsel, and T. W. Hänsch; *Physical Review Letters*; **83**, Num 17(1999).
5. J. P. Cotter, J. P. McGilligan, et al.; *Appl. Phys. B;* **83** 122:172; (2016).
6. Vivek Singh, V. B. Tiwari, et al.; et al , J. Mod. Opt. **65**, 2332, (2018)

Generation of entangled Photon - Pair through difference frequency generation using Type 0 Quasi Phase Matched $LiNbO_3$

Adithya Ramesh*, Eswara Prasath* and Srikrishna V*
*Final year student, Department of Electronics and Communication Engineering, School of Electrical and Electronics Engineering, Sastra Deemed to be University

Abstract

Photons are elementary particles where entangled photon pair involve two photons which are linked together by a process called entanglement. Now these two entangled photons correlate their properties with each other where irrespective of the physical distance between them. Entangled Photon pair are at the heart of many quantum optics experiments such as quantum cryptography, quantum key distribution and useful for testing the fundamental laws of physics. We demonstrate generation of entangled photon pair with the help of type 0 quasi phase matched Lithium Niobate crystal. This is realized with the help of both Spontaneous Parametric Down Conversion (SPDC) and Difference Frequency Generation. SPDC is just the spontaneous splitting of a single photon of higher energy to two photons (signal and idler) lower energy. By introducing a single aperiodic domain in the $LiNbO_3$ structure generation of a broadband signal is made possible through similar modelling generation of entangled photon pair is suggested and possible.

Introduction

The use of Lithium Niobate as a nonlinear medium for the generation of a broadband signal is demonstrated. In a 1mm LiNbO3 polarization throughout the length of the ferroelectric crystal is found to be in randomly distributed manner. Through electro polling process on applying a electric field of 21KV/mm throughout the length of the sample to form domains with specific polarization and specific period. Lithium Niobate being a uniaxial crystal it possesses an ordinary axis and an extraordinary axis both with differing refractive indices for both the axis.

The setup consists of light source, a nonlinear crystal and a spectrum analyzer. The refractive index for each axis can be determined with the help of Sellmeier equation. Since refractive index of a nonlinear medium is a function of wavelength and temperature, the refractive index of each axis was determined for a range of wavelengths namely from 0.35µm to 2µm. Throughout the process the temperature was set as 24°C with which further calculations were made. The light source or pump was chosen as 0.933 µm with which the signal and idler wavelengths were calculated. It is assumed that the device length is 0.54 cm equal to 5400 µm where one aperiodic domain of width 27 µm is inserted at 4474 µm.

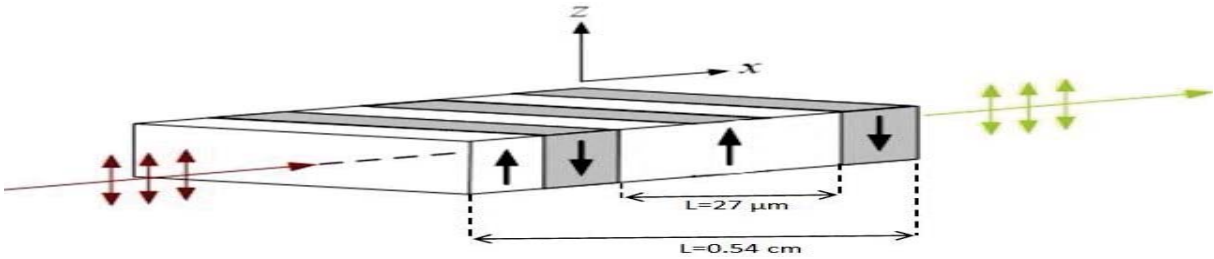

Figure 1.1 Gives a rough depiction on the device considered

Generation of the entangled photon pair

The length of the quasi phase matched $LiNbO_3$ device is 0.54 cm with the introduction of a single aperiodic domain at the middle of the device with a period of 27 μm. The wavelength of the pump is chosen as 0.933 μm. With the following assumptions made the output spectrum was analyzed through the simulation tools matlab and wolfram mathematica.

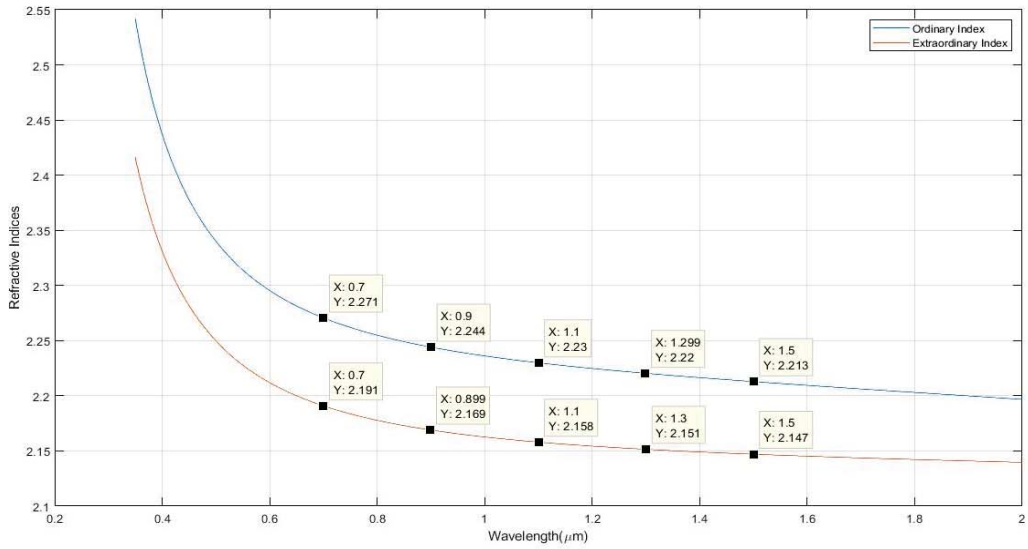

Figure 1.2 Gives the Sellmeier plot for Lithium Niobate obtained for a range of wavelengths (0.35 μm – 2.0 μm)

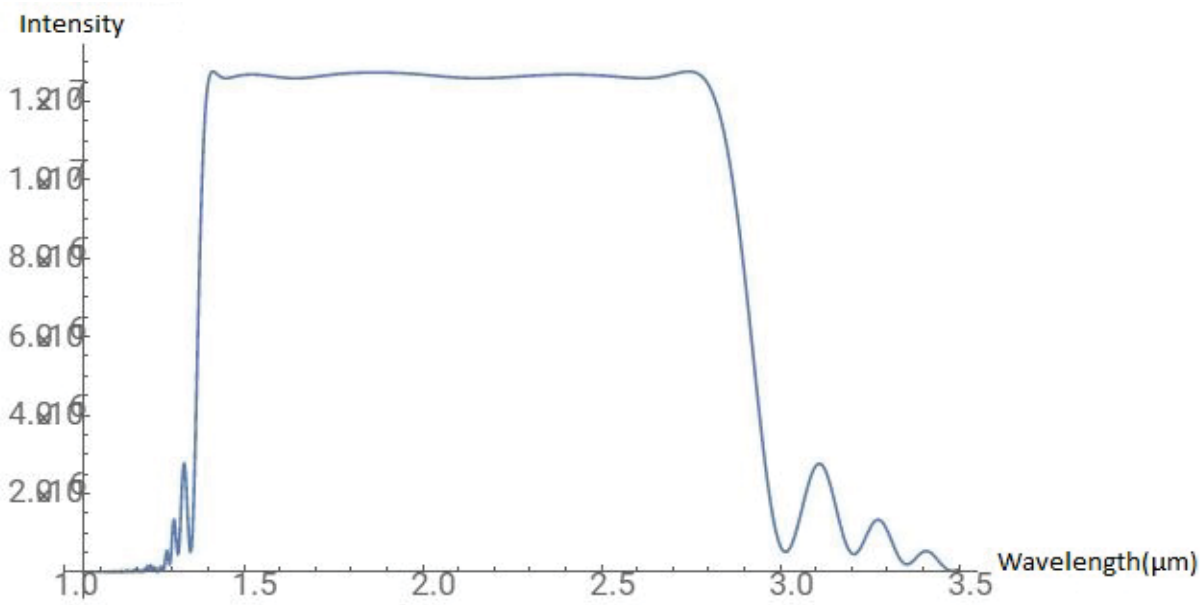

Figure 1.3 Represents the obtained broadband spectra as a result of placing the phase shifter at L= 4474 μm with width = 27 μm

The refractive index obtained for a range of wavelengths while keeping the temperature a constant will be used in calculating the signal and idler wavelengths. The obtained output spectrum is depicted through figure 1.3.

Further analysis was done by observing the fluctuations in the output spectra if any one of the input parameters were varied.

Initially the aperiodic domain was placed at L = 4474 μm, by varying the position of the domain to the middle of the device that is 2700 μm It is observed that there are multiple peaks with unequal intensity.

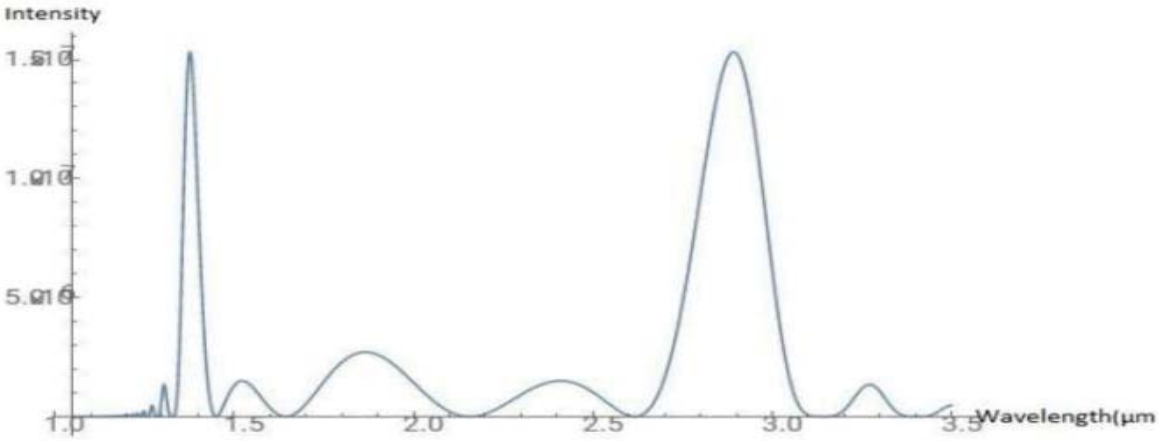

Figure 1.4 Output spectrum with location of the PS moved to L = 2700 μm

Similar fluctuation in the output was observed when the aperiodic domain was kept at L = 4474 μm but the width of the domain was varied to 21 μm from 27 μm.

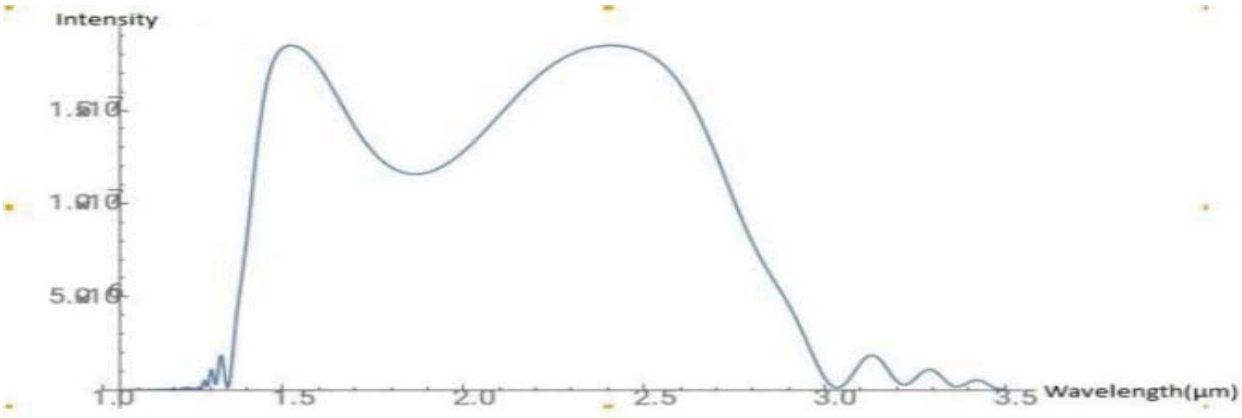

Figure 1.5 Output spectrum obtained when the width of the domain was only altered

Conclusion

We have demonstrated using simulation the generation of broadband response using difference frequency generation process and electro poled $LiNbO_3$ crystal as the nonlinear medium and adding a single aperiodic domain in the crystal structure. The temperature and grating period were 24 ˚C and 27 μm respectively were used to produce the near flattop broadband. The electro poled $LiNbO_3$ is normally known to produce a tolerance to temperature between plus or minus 3 ˚C to the set temperature. The location of the single aperiodic domain and width is important as when the phase shifter being placed in different positions within the device the broadband response produces a serious variation in the desired output either by not producing a band spectrum or producing a band spectrum with several points where a dip in intensity were found. Through similar mathematical and device modelling generation of entangled photon pair can be realized.

Phenomenal Optical Limiting Action from Gold and Silver through Au@Ag Core- Shell Nanostructures

E. Shiju[a], Abhijith T[b], D. Narayana Rao[c], K. Chandrasekharan[*a]

[a]Laser and Nonlinear Optics Laboratory, Department of Physics, National Institute of Technology Calicut, Kozhikode 673601, Kerala, India.

[b]Organic and Nanoelectronics Laboratory, Department of Physics, National Institute of Technology Calicut, Kozhikode 673601, Kerala, India.

[c]School of Physics, University of Hyderabad, Gachibowli, Hyderabad, 500046, India.

*csk@nitc.ac.in

Abstract

Here we report detailed nonlinear optical studies of Au @Ag core shell nanostructures under ns. The size and shell thickness of the core shells were obtained from TEM images. A significant blue shift from 519 nm to 411 nm in surface plasmon maxima is observed upon forming Ag shell over Au nanoparticles and a slight red shift (411 nm to 425 nm) is observed as the shell thickness increases. All the samples showed RSA behavior under ns excitation and extent of nonlinear absorption enhances on increasing the shell thickness. Nonlinear refraction properties of the samples are also analyzed and all the samples are found to be exhibited negative nonlinearity under ns excitation. Improved nonlinear optical activity is due to enhanced local field effect and nonlinear scattering effect

Introduction

Noble metal nanoparticle shows an inimitable absorption (surface plasmon resonance absorption) in the visible range of the electromagnetic spectrum, and it can be tuned over a wide range from UV to near infra-red by modifying the parameters like size, shape and surrounding dielectric medium [1]. Surface plasmon resonance (SPR) is the coherent oscillation of free conduction band electrons due to the interaction of electromagnetic field. The SPR of NSs causes a huge enhancement of the local field on the surface as well as near the nanoparticles surrounding, in addition to the enhancement of absorption and scattering [5-6].Formations of nanostructures with one or more elements are one of the easiest ways to modify optical properties of nanostructures, and it can be attained by forming an alloy, core-shell, and composite structures. Local field effect can significantly improve in metal-based core shells, which can be employed in surface-enhanced Raman spectroscopy. The SPR of the Au/Ag core shell structure can be potentially tailored by modifying the size and shape, width of the shell and the coupling of core and shell. Nano-sized materials with excellent NLO response have been getting special attention as optical limiters, [2]. Optical limiters attenuate strong laser beam by controlling output fluence/ intensity to a safe range and thereby protecting delicate optical instruments and human eyes.

Synthesis and characterizations of Au@Ag core-shell nanostructures

Chemical synthesis strategy was followed to synthesize Au@Ag core-shell metal nanostructures. In brief, citrate stabilized Au nanospheres were prepared and an Ag layer was coated over their surface. Turkervich method was used to synthesize the spherical Au nanoparticles. Core shell structure and morphology was analyzed using High resolution-transmission electron microscopy (HR-TEM) JEOL, JEM-2100. Z scan measurements of the samples were done under both ns and femto second region. A frequency doubled, Q switched Nd:YAG laser (wave length 532 nm, pulse width 7 ns and repetition rate 10 Hz) was used as ns excitation source.

Results and Discusions

High resolution-transmission electron microscopy (HR-TEM) technique was employed to investigate the size of synthesized nanostructures. TEM images reveal the presence of monodispersed Au nanospheres with an average diameter of 16 nm as shown in figure 1(a). TEM images of core-shell nanostructures synthesized using different amounts of $AgNO_3$ are shown in figure 1(b-e). The diameter of nanostructures is found to be systematically increased from 31 nm (t = 7.5 nm) to 61 nm (t = 22.5 nm) when the volume of $AgNO_3$ is increased from 0.1 to 0.8 ml. Inset of each TEM image shows the zoomed area TEM images of nanostructures.

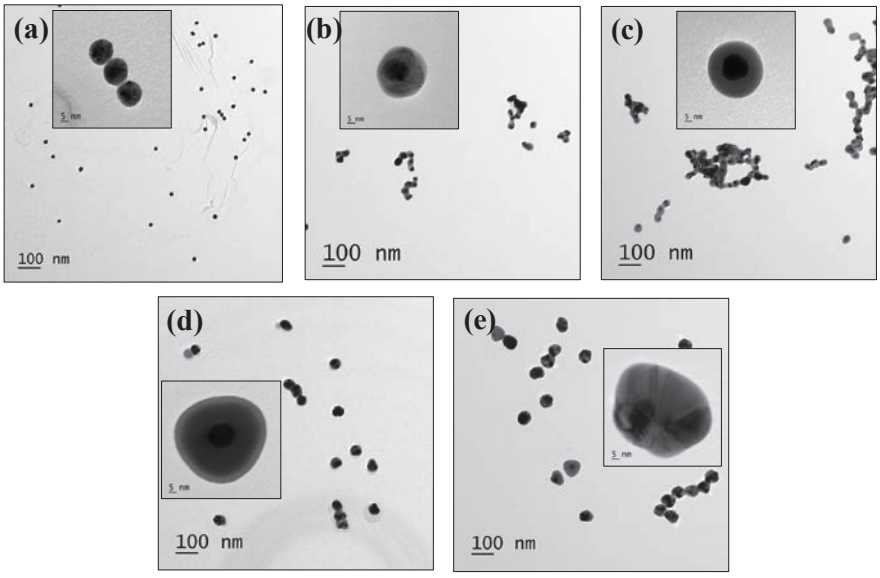

Figure1. *HR-TEM images and corresponding size distribution of (a) Au nanospheres, (b) 0.1 ml, (c) 0.2 ml, (d) 0.4 ml and (e) 0.8 ml $AgNO_3$ added Au@Ag core shell nanostructures. Inset of the images shows the zoomed area image of nanostructures.*

Au nanospheres exhibit a sharp extinction (or plasmon resonance) peak at a wavelength of 519 nm (figure 2). A significant shift in extinction peak is observed towards the blue wavelength region when they are coated with a layer of Ag. The peak position is slightly red shifted from 411 to 425 nm as the shell thickness of core-shell nanostructures increases from 7.5 to 22.5 nm

.

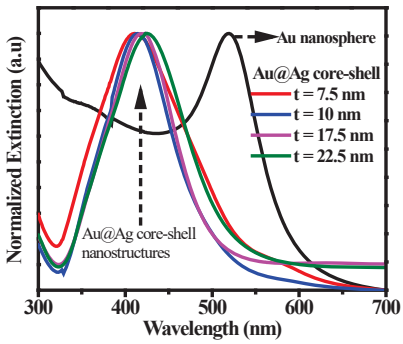

Figure 2.*Ultraviolet-visible extinction spectra of aqueous solutions of Au and Au@Ag core-shell nanostructures*

The transmitted data obtained from the Z scan experiment is given in figure 3. In a Z scan experiments, the valley (reduction in normalized transmittance) indicate the extent of nonlinear absorption. Au NSs as well as its core shell structures with varying thickness exhibited a central valley flanked by a two identical peaks on both sides of the valley. The peak flanking the valley is due to saturation of absorption at lower input fluences in addition to the NLA. On considering the weak saturation effect in addition with NLA, the NLA coefficient α (I) can expressed as [3]

$$\alpha(I) = \frac{\alpha_0}{1+\frac{I}{I_s}} + \beta_{eff} I \qquad (1)$$

Where α_0 is the intensity independent absorption coefficient at the laser wavelength used for excitation. I is input laser intensity and I_s saturation intensity. β_{eff} *is the* effective two photon absorption (TPA) coefficient which comprises both TPA and two step excitation of the system.

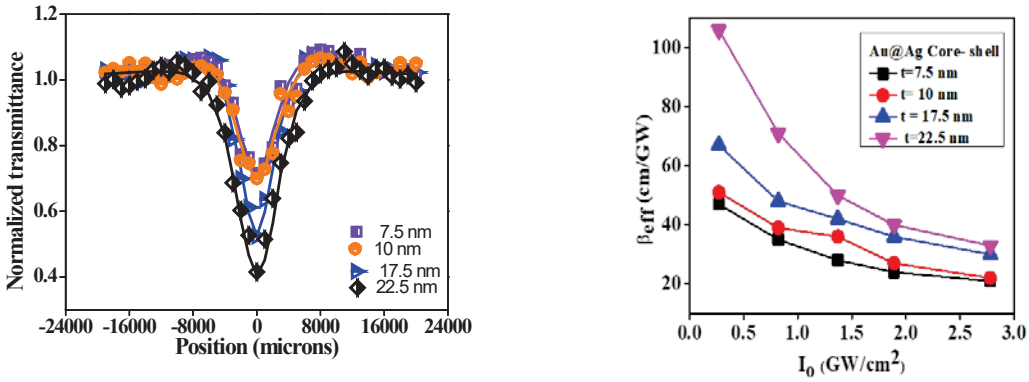

Figure 3. *Open aperture Z scan signatures and NLA coefficient plot as a function of axis intensity of Au@Ag core-shells with varying shell thickness under ns laser pulse excitation*

The NLA mechanism in Au Ns and Au@Ag core-shell can be discussed based on conjoint interaction of SPR, interband, intraband transitions [1,4]. The SA in association with free carrier absorption in the conduction band results in reverse saturable absorption (RSA) behavior. At high input intensity, even in the single photon absorption range, the effect of multi photon (especially TPA) is also having significant role. Hence the net NLA effect observed in Au@Ag core shell structure should be a combined effect of single photon assisted excited state absorption and simultaneous absorption of photons (genuine TPA). It is also evident from the NLA coefficient and on axis intensity plot, where a decrease in β value is observed upon increasing the intensity of both pure Au NSs and Au- Ag core shell structures. It is due to the bleaching of ground state electron up on increasing input intensity which consequently reduces the effective NLA [1,4].

Conclusion

Short pulse NLO optical nonlinearity of Au @ Ag core-shell NS were conducted at 532 nm wavelength. The core shell formation, particle size and shell thickness were obtained from the TEM analysis. The core shell structure found to display good NLA under ns and it is also observed that NLA is significantly enhancing on increasing shell thickness.

References

1. S. Edappadikkunnummal, S. N. Nherakkayyil, V. Kuttippurath, D. M. Chalil, N. R. Desai, and C. Keloth, *J. Phys. Chem. C*, 121, 48, 26976–26986, **2017**.

2.L. W. Tutt,T. F. Boggess, *Prog. Quantum Electron.,* 17, 299–338, **1993**.

3. Couris, S.; Koudoumas, E.; Ruth, A. A.; Leach, S. *J. Phys. B At. Mol. Opt. Phys.***1995**, *28* (20), 4537.

4. I. Papagiannouli, P. Aloukos, D. Rioux, M. Meunier, and S. Couris, *J. Phys. Chem. C*, 119, 12, 6861–6872, **2015**.

Broadband Nonlinear Optical Studies of a Novel Phthalocyanine Using MHz and kHz Femtosecond Pulses

Dipanjan Banerjee, K S Srivishnu, Jagannath Rathod, L. Giribabu, S. Venugopal Rao*

Advanced Centre of Research in High Energy Materials ***(ACRHEM),***

University of Hyderabad, Hyderabad 500046, Telangana, India.

*Corresponding author e-mail: soma_venu@uohyd.ac.in OR soma_venu@yahoo.ac.in

Abstract: We present extensive nonlinear optical (NLO) study of a novel Tri-methoxy-phenoxy-phthalocyanine (TMPC, Chemical Formula: $C_{68}H_{58}N_8O_{16}$) molecule with ultrafast laser pulses. We have utilized a ~150 fs oscillator pulses (Chameleon Ultra) at 80 MHz repetition rate as well as a 1 kHz, 50 fs amplifier pulses. We obtained the NLO coefficients by performing the Z-scan experiments using these pulses. The exotic molecule has exhibited a fine and significant nonlinearity, having a saturation absorption combined with reverse saturable absorption nature in open aperture configuration and a clear defocusing Kerr-lens effect in closed aperture mode.

1. Introduction:

Significantly rich distribution of delocalized π-electrons in the organic molecules such as porphyrins, phthalocyanines etc. has established them as potential candidates to be rigorously investigated for optical signal processing, optical switching, and optical power limiting [1-6]. Phthalocyanines, in particular and their derivatives whether in solution, thin films form, have been a prime subject for nonlinear optical investigations, photodynamic therapy, optical limiting and optical switching also. In this recent work, we have carried out our investigation to study the nonlinear optical domain of a novel Tri-methoxy-phenoxy-phthalocyanine (TMPC) molecule. We have implemented both MHz oscillator and kHz amplifier pulses as nonlinear probes.

2. Synthesis & Characterization section:

These Tri-methoxy-phenoxy-phthalocyanine were synthesized in the form of macromolecules utilizing the Matrix assisted laser desorption ionization (MALDI) technique and their structures are designed as follows.

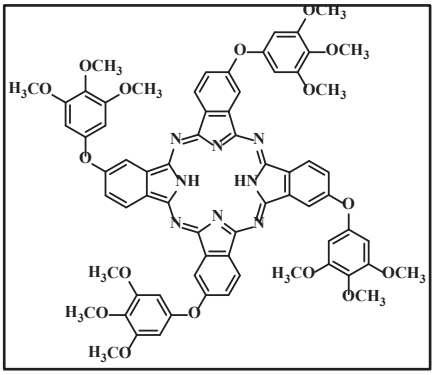

Figure 1. Molecular Structure of TMPC investigated in the present study.

2.1 UV-Visible Absorption spectra:

A Shimadzu UV–Visible–NIR (UV-3600) spectrophotometer was used to collect the absorption spectra of studied compound utilising various different solvents as DCM, Toluene, DMF, CAN, THF to make a keen

observation on the solvent effects on optical absorption. The molecule in solution form displayed clear absorption central peak, at 703 nm, in case of each different solvent as follows in Figure 1.

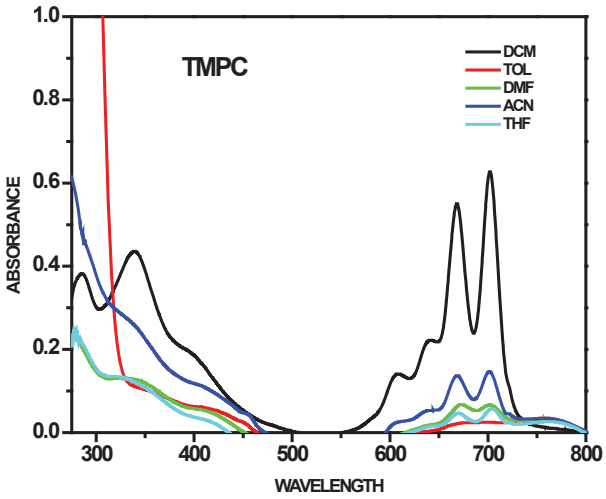

Figure 2. UV-Visible absorption spectra of TMPC with respect to different solvents.

3. Nonlinear Optical Measurements:

3.1 Experimental Details:

To explore the NLO coefficients of the afore mentioned phthalocyanine [2] TMPC compound in solution (solvent- DCM) form, first they were made interact with femtosecond oscillator pulses (Chameleon, 150 fs, 80 MHz, central wavelength at 800 nm) involving Z-scan measurements as a tool for NLO measurements. The input beam of 2 mm diameter was focused using a 10 cm plano-convex lens, that offered ~ (10-20) MW/cm^2 peak intensities into the system as a reason of the generation of high nonlinearity within. The estimated beam waist at the focus was nearly ~25 µm. In this presence of the high field intensity the TMPC compounds, dissolved into solution form, loaded in a quartz cuvette, were scanned throughout using a linear stage within -5Z_0 to 5Z_0 distance range, where Z_0 is the Rayleigh range (estimated approx. ~2.5 mm). The transmitted beam after the sample was collected through a thermal sensor connected to a power meter. Interconnecting all, the translational stage along with the power meter was correlated together and corresponding data was displayed by a LabVIEW program. The Z-scan details with amplified pulses can be found elsewhere [1]

3.2 Results & Discussion:

The generic multiphoton absorption influenced transmittance nature of z-scan process can be signified in a mathematical form as follows [7],

$$T_{OA(nPA)} = \frac{1}{[1+(n-1)\alpha_n L(I_0/(1+\left(\frac{z}{z_0}\right)^2))^{n-1}]^{\frac{1}{n-1}}} \quad \text{..... (1)}$$

The transmittance curve in case of closed aperture configuration will tend to follow this equation as,

$$T_{CA} = 1 \pm \frac{4\Delta\Phi\left(\frac{z}{z_0}\right)}{\left[\left(\frac{z}{z_0}\right)^2+9\right]\left[\left(\frac{z}{z_0}\right)^2+1\right]} \quad \text{..... (2)}$$

λ (nm)	$\beta \times 10^{-7}$ (cm.W^{-1})	σ_2 (GM) $\times 10^8$	Im ($\chi^{(3)}$) $\times 10^{-10}$ (e.s.u.)	$n_2 \times 10^{-11}$ (cm^2/W)	Re ($\chi^{(3)}$) $\times 10^{-10}$ (e.s.u.)	Total ($\chi^{(3)}$) $\times 10^{-10}$ (e.s.u.)
800	38	3.14	18.7	3.62	27.9	33.6
850	3.3	0.26	1.72	3.4	26.2	26.3
900	2.5	0.18	1.38	1.73	13.3	13.4

Table 1: Summary of the NLO coefficients obtained in the present study.

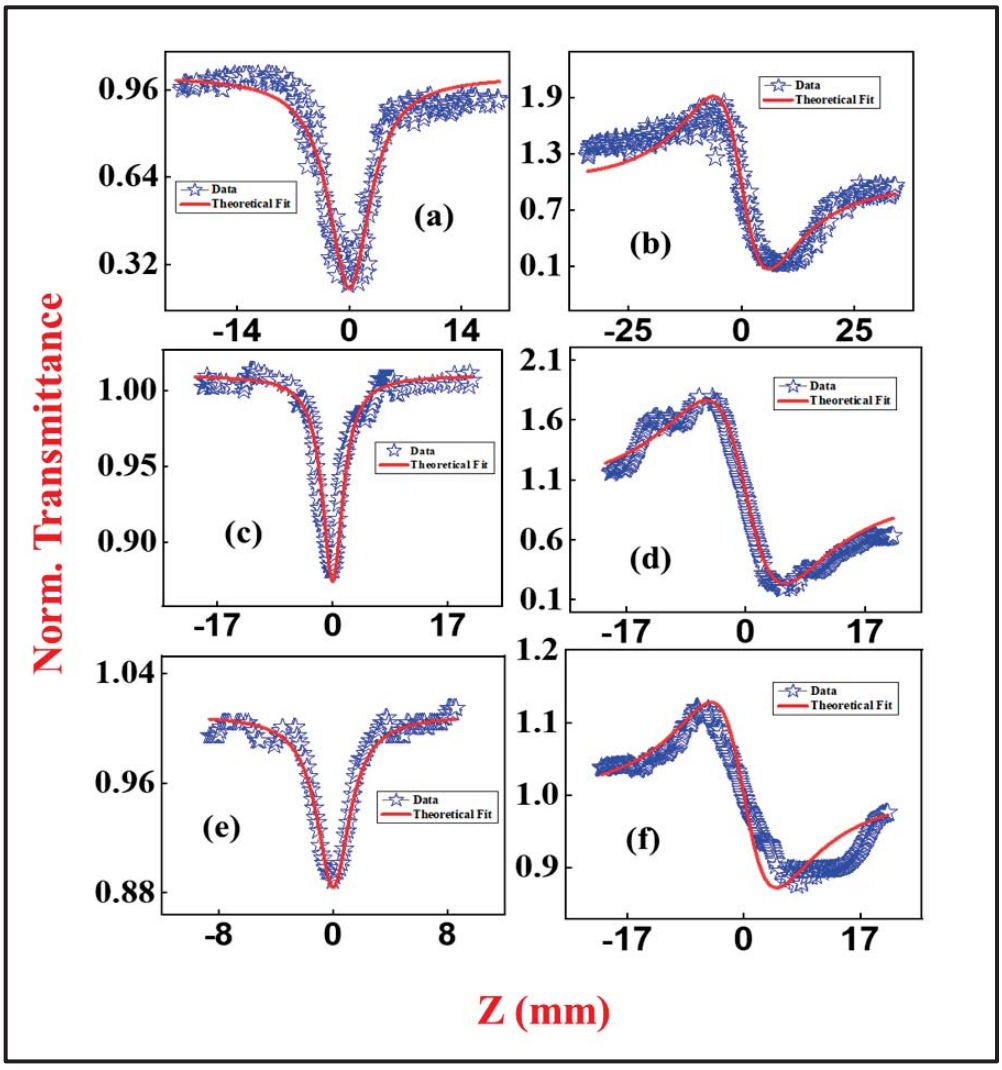

Figure 3. NLO OA and CA transmittance curves of TMPC for 800 nm oscillator pulses (a, b), 850 nm (c, d), 900 nm (e, f). Symbols represent the experimental data points and solid lines are the theoretical fits.

In this present investigation of the NLO domain of the aforementioned TMPC molecule, it has revealed fantastic nonlinear optical signatures to us, exhibiting pure reverse saturable absorption (RSA) curve in open aperture mode and a peak-valley nature in closed aperture configuration for oscillator pulses. It also has revealed exotic 'M' curved NLO nature in interaction with 800 nm fs amplifier pulses. We have extracted out the NLO coefficients by fitting the experimental data to the theoretical curves and calculated the significant NLO parameters [presented in table 1] in case of oscillator pulse nonlinear data and we are analyzing the fs amplifier

data. The TMPC phthalocyanine has exhibited significantly high two-photon absorption (TPA) [5,6] coefficients and cross-sections.

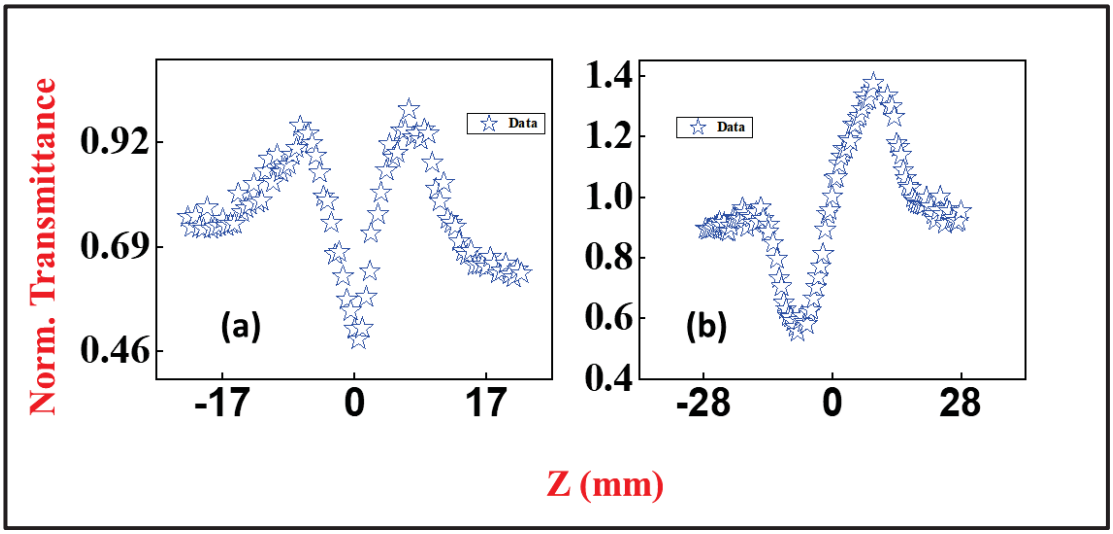

Figure 4. NLO OA (a) and CA (b) transmittance curves of TMPC using ~50 fs, 800 nm, amplifier pulses.

4. Conclusions:

The synthesised TMPC molecule has displayed significantly high TPA coefficients and cross-section values, making it an exotic candidate for NLO and photonic applications. We have studied its nonlinear nature first utilising MHz fs pulses, which essentially has dominant contribution from thermal nonlinearity and later we carried out the experiments with amplified 1 kHz pulses to assess its true (electronic) nonlinearity. All the results will be discussed in the conference presentation.

5. Acknowledgements:

Author S.V. Rao acknowledges DRDO for funding and facilities. Dipanjan acknowledges Dr. M.S.S. Bharati and Dr. Chandu Byram for their guidance.

6. References:

1. Somdatta Bhattacharya, Chinmoy Biswas, Sai Santosh Kumar Raavi, Jonnadula Venkata Suman Krishna, Narra Vamsi Krishna, Lingamallu Giribabu and Venugopal Rao Soma, *J. Phys. Chem. C,* **123**, 11118−11133 (2019).
2. Venugopal Rao, N. Venkatram, L. Giribabu, and D. Narayana Rao, *Journal of Applied Physics* **105**, 053109 (2009).
3. Sai Santosh Kumar, S. Venugopal Rao, L. Giribabu, D. Narayana Rao, *Chemical Physics Letters*, **447**, 274-278.
4. S.J. Mathews, S. Chaitanya Kumar, L. Giribabu, S. Venugopal Rao, *Materials Letters*, **61**, 4426 –4431 (2007).
5. S.J. Mathews, S. Chaitanya Kumar, L. Giribabu, S. Venugopal Rao, *Optics Commun*. **280**(1), 206-212 (2007).
6. N. Venkatram, D. Narayana Rao, L. Giribabu, S. Venugopal Rao, *Chemical Physics Letters*, **464**, Pages 211-215.
7. M. Sheik-Bahae, A. A. Said, T.-H. Wei, D. J. Hagan, and E. W. Van Stryland, *IEEE Journal of Quant. Electron.*, **26**, 760-769 (1990).

Photonic and electronic state nonlinear interactions in $BaTiO_3$ based Microcavity

Jitendra Nath Acharyya[1,] *, D. Narayana Rao[2], and G. Vijaya Prakash[1]

[1]Nanophotonics Lab, Department of Physics, Indian Institute of Technology Delhi, New Delhi 110016, India;

[2]School of Physics, University of Hyderabad, Hyderabad-500046, India;

*Email: jitendraphy12@gmail.com

Abstract: Ultrafast absorption dynamics and the interactions of photonic modes with the electronic states are investigated in $BaTiO_3$ (BTO) based optical microcavity. The cavity-enhanced transient dynamics reveal the excited state absorption at a picosecond time scale. Angle dependent photoluminescence behavior exhibits tunable emission from the defect energy states of BTO assisted by the photonic cavity modes. Third-order nonlinearity shows excited state absorption with seven-orders of magnitude enhancement in the two-photon absorption coefficient compared to bare BTO film. The optical properties are correlated with the transfer matrix method simulations. The novel optical structure can be envisaged in nonlinear optics and photonics.

1. Introduction

A photonic crystal is a novel class of optical media finding various applications in nanophotonics and nonlinear optics. [1-4] The optical microcavity is realized from a central defect layer sandwiched between two distributed Bragg reflectors. The optical field confinements and the control of spontaneous emission can be visualized through the interactions of the embedded material's electronic states and the photonic density of states of the photonic structures. Because of the intriguing properties of optical field modulations and controlled optical field propagation, this novel architecture finds applications in optical filer, optical switching, optical limiters, etc. [5,6]

Barium titanate is one of the layered perovskite structures which exhibits special electro-optical and magnetic properties because of the TiO_6 octahedra, which supports the Mott type exciton within the large electronic bandgap of the structures. [7-9] The enhanced features of excited state absorption and the photoluminescence of BTO are yet not explored in an optical microcavity. In this works, the linear and nonlinear optical properties of BTO based optical microcavity were investigated via optical pump-probe and single-beam Z-scan technique. The optical microcavity, realized from the central layer of BTO sandwiched between two distributed Bragg mirrors of (SiO_2/TiO_2) is fabricated using RF sputtering technique [Schematic Figure 1a]. The detailed fabrications procedures are given elsewhere. [10] The optical thicknesses of the constituent layers are found to be 55 nm, 73 nm, and 199 nm for SiO_2, TiO_2, and $BaTiO_3$, respectively.

2. Results and Discussions

2.1. Linear optical responses of $BaTiO_3$ microcavity

The linear transmission and reflections spectrum details provide the idea about the photonic band structure of a photonic crystal. Figure 1b shows the reflection spectrum of BTO based optical microcavity, where the dashed curve represents the TMM simulation. The photonic bandgap lies between 1.85 eV to 2.7 eV, with the photonic cavity mode at 2.23 eV. The angle-resolved reflection map is depicted in Figure 1c, where the white dots represent the experimental point. The blue shifting of photonic cavity mode can be attributed to the shortening of lattice constant encountered by the incident electromagnetic wave,[3] which can be expressed as follows

$E_{ph}(\theta) = E_c(1-(\sin^2\theta/n_{eff}^2))^{-1/2}$, where $E_{ph}(\theta)$ is the angle-dependent photonic cavity mode and E_c is the photonic cavity mode at normal incidence, and n_{eff} represents the effective refractive index of the optical microcavity.

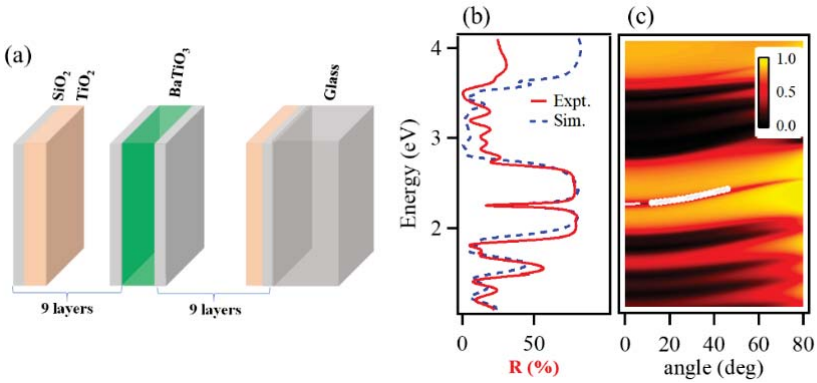

Figure 1. *(a) Schematic representation of the $BaTiO_3$ (BTO) based optical microcavity. (b) Refection spectrum of the microcavity. (dashed line represents the transfer matrix simulation). (c) Angle-resolved transverse optical field map (White dots represent the experimental data).*

The spontaneous emission of BTO is hugely modified inside the photonic crystal by the cavity photonic modes. The downward transitions for the radiative recombination [11] can be expressed by the Fermi's golden rule as $\Gamma_{i\to f} = (2\pi/\hbar)|V|^2\,\rho(E)$, where $|V|$ is the zero-point Rabi matrix element, and $\rho(E)$ is the final density of states. The radiative recombination is coming from the defect energy state of BTO, supported by the photonic cavity mode. The angle-dependent PL study, excited at 4.18 eV, reveals the prominent photonic cavity effect which is depicted in Figure 2b.

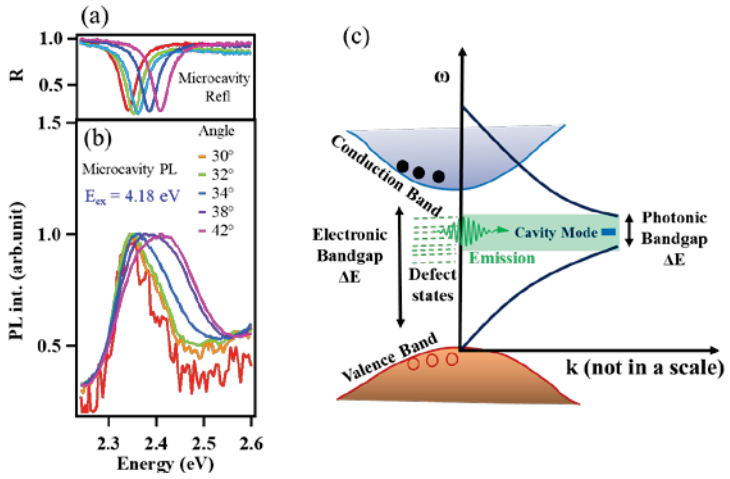

Figure 2. (a) *Angle angle-dependent reflection spectrum. (b) Angle dependent photoluminescence (PL) spectra of the microcavity (Excitation energy E_{ex} =4.18 eV) (c) Schematic representation of electronic and photonic energy band diagrams and the emission process in a photonic crystal.*

2.2. Nonlinear absorption dynamics of $BaTiO_3$ microcavity

The ultrafast absorption dynamics were investigated using optical pump-probe measurements using 3.54 eV (1 kHz, 120 fs) as pump obtained from an optical parametric amplifier (OPA) and broad-band white light as probe. Figure 3(b) represents the transient difference absorption (ΔA) spectrum pumping with 0.25 μJ pulse energy. A positive difference absorption (ΔA >0) spectrum is observed corresponding to the photonic cavity mode and other photonic *minibands* regions. The positive difference absorption spectrum can be attributed to the excited state absorption from the BTO defect energy states. As the pump pulse excites the optical microcavity, the defect energy states of BTO are populated, which exhibits excited absorption in the presence of the probe beam. The observed decay dynamics for three distinct regions of interest (Figure 3(c)) show two-time constants, with the larger one in the range of 15-50 ps and the shorter ones in the range of 5-8 ps.

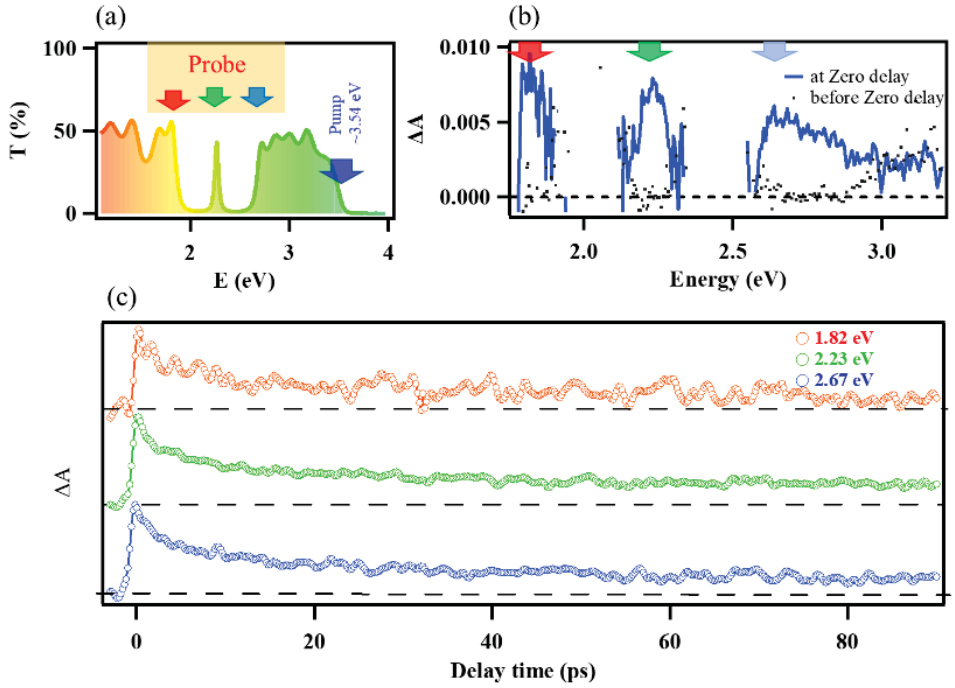

Figure 3. *Transient absorption measurements using 3.54 eV (120 fs, 1 kHz) as the pump of 0.25 μJ pulse energy and broad-band white light as the probe. (a) The transmission spectrum of the optical microcavity indicating the pump and probed regions. (a) Difference transient absorption (ΔA) spectra of $BaTiO_3$ based optical microcavity. (c) Temporal dynamics of transient absorption signals probed at 1.82 eV, 2.23 eV, 2.67 eV.*

The third-order nonlinear optical properties were investigated using a single-beam Z-scan technique [12] using a 1.55 eV Gaussian laser beam, focused with a convex lens of 15 cm focal length. The open aperture (OA) Z-scan trace (not shown here) shows reverse saturation absorption associated with saturation behavior which can be attributed to the two-photon absorption saturation. [4] The extracted two-photon absorption coefficient is found to be 3.85 x 10^{-5} m W^{-1}, which is seven orders of magnitude higher than the bare BTO film. The closed aperture (CA) trace shows the positive nonlinear refractive index in the order of 6.97x10^{-17} m^2 W^{-1}.

3. Conclusion

The interaction of photonic modes and ethe electronic states are visualized through the novel photonic architecture. The linear optical properties agree well with the transfer matrix simulations. The cavity mode assisted tunable photoluminescence behavior established the photonic cavity effect on the BTO spontaneous emission. The transient absorption dynamics reveal the enhanced features of the excited state absorption behavior of BTO_3. The single-beam Z-scan measurements showed seven orders of magnitude enhancement of the two-photon absorption coefficient of optical microcavity with respect to bare BTO film. The novel architecture is a promising candidate for optical limiters, ultrafast laser operations, and future photonic device applications.

Acknowledgments

The authors want to acknowledge DST-FIST funding for establishing the Ultrafast Optics facility (UFO). The authors acknowledge Professor Anurag Sharma, Coordinator UFO, IIT Delhi, for useful suggestions. JNA acknowledges DST-INSPIRE for research fellowship.

References

1. E. Yablonovitch, *Phys. Rev. Lett.* **58**, 2059 (1987).
2. S. John, *Phys. Rev. Lett.* **58**, 2486 (1987).
3. K. Pradeesh, J. J. Baumberg, and G. Vijaya Prakash, Opt. Express, **17**, 22171 (2009).
4. J. N. Acharyya, D. N. Rao, M. Adnan, C. Raghavendar, R. B. Gangineni, and G. Vijaya Prakash, *Adv. Mater. Interfaces* **7**, 2000035 (2020**)**.
5. M. Qiu, M. Mulot, M. Swillo, S. Anand, B. Jaskorzynska, A. Karlsson, and A. Forchel, *Appl. Phys. Lett.* **83**, 5121 (2003).
6. H. Nakamura, Y. Sugimoto, K. Kanamoto, N. Ikeda, Y. Tanaka, Y. Nakamura, and K. Asakawa, *Opt. Express* **12**, 6606 (2004).
7. S. G. Lu, Z. K. Xu, H. Chen, C. L. Mak, K. H. Wong, K. F. Li, and K. W. Cheah, *J. Appl. Phys.* **99**, 064103 (2006).
8. J. L. Clabel H, I. T. Awan, G. Lozano, M. A. Pereira-da-Silva, R. A. Romano, V. A. G. Rivera, S. O. Ferreira, and E. Marega Jr., *Phys. Chem. Chem. Phys.* **22**, 15022 (2020).
9. R. I. Eglitis, E. A. Kotomin, and G. Borstel, *J. Phys. Condens. Matter.* **14**, 3735 (2002).
10. N. K. Shihab, J. N. Acharyya, U. M. Rasi, R. B. Gangineni, G. Vijaya Prakash, and D. N. Rao, *Optik*, **207**, 163896 (2019).
11. E. Yablonovitch, *J. Phys. Condens. Matter* **5**, 2443 (1993).
12. M. Sheik-Bahae, A. A. Said, T. H. Wei, D. J. Hagan, and E. W. Van Stryland, *IEEE J. Quantum Elect.* **26**, 760 (1990).

Linear and Nonlinear Optical Excitons in Primary Cyclic Ammonium Based Inorganic-Organic Hybrid Semiconductor Series

Kshetra Mohan Dehury*, Prof. G. Vijaya Prakash

Nanophotonics Lab, Department of Physics, Indian institute of Technology Delhi, Hauz Khas, New Delhi 110016

*Phz188341@physics.iitd.ac.in

Abstract:

The low dimensional inorganic-organic (IO) hybrid semiconductors becomes a fascinating subject of interest due to their unique crystal structural packing and tunable optical exciton emission features. These naturally self-assembled 2D IO hybrid semiconductors form multiple quantum well (MQWs) like structure due to the quantum width limit of both organic moiety and inorganic network structure, enables stable room temperature excitons having large exciton binding energy. A systematic co-existence of two kinds of excitons observable from one-($\hbar\omega \geq Eg$) and two-photon ($2\hbar\omega \geq Eg$) excitations is carried out to probe into deeper details of sensitive structural changes in the IO-hybrids thin film and single crystals.

Introduction:

The low-dimensional 2D Inorganic-Organic (IO) hybrid semiconductors are represented by general formula $(R\text{-}NH_3)_2\text{-}MX_4$. They are derived from the fundamental AMX_3 type structure, where 'R' is the organic moiety, 'M' is the divalent metal (Pb^{2+}, Sn^{2+}, Cu^{2+} etc.) and 'X' is the halide-ion (Cl^-, Br^-, I^-) [1, 2]. The IO hybrid semiconductors forms multiple quantum well (MQWs) like structure where the inorganic network structure acts as a quantum well and organic moiety acts as a quantum barrier. The charge carriers are confined within the extended inorganic network structure due to the quantum confinement effect and large dielectric constant difference between the organic moiety and inorganic network structure[3]. These quantum and dielectric confinement effects are mainly responsible for the formation of Mott-type excitons which are stable at room temperature and showing strong excitons emission features of the IO hybrid semiconductors. The IO hybrid semiconductor formed different crystal packing structure (2D,1D,0D) depending upon the shape, size of the organic moiety, position of amino group and how these organic ammonium cation interlinked with the iodine of the extended inorganic network structure through hydrogen bridging[4]. In 2D IO hybrid semiconductors; the metal halide octahedra extend in both direction and organic moiety and inorganic network structure are formed a perfect layered structure arrangement with corner sharing PbI_6 octahedra. The optical exciton emission features of the low-dimensional IO hybrid semiconductors are strongly depends upon the choice of organic moiety and crystal structural packing (1D/2D/3D) within the extended PbI_6 network structure. A systematic coexistence of two types of excitons from thin film and single crystals bits are observed under one-photon (1PA-PL, 400 nm) and two-photon (2PA-PL, 800 nm, 120 fs, 84 MHz) excitation[5,6,7].

Experimental Techniques:

Thin film of all synthesized inorganic-organic (IO) hybrid semiconductors was obtained typically by using spin coating method on to a glass substrate. The obtained uniform thin films are used for glancing angle thin film

XRD (GAXRD) using Cu-K_α radiation (1.5418 Aº) with diffraction angle (2θ) 3º to 50º. The optical absorption spectra of all synthesized IO hybrid semiconductors are carried out using Shimadzu UV-VIS-NIR3600 spectrophotometer. The photoluminescence (1PA-PL, 2PA-PL) spectra, high resolution 1PA- and 2PA-PL spatial (PL/BF/DF) and line scan spectral mapping/imaging of single crystal bits of IO hybrid semiconductors were performed using advanced modified optical microscopes which is shown in Figure 1. This optical microscope is coupled with 400 nm, CW and high intensity femtosecond Ti: Sapphire laser with excitation wavelength 800 nm (120 fs, 84 MHz) through multimode optical fiber.

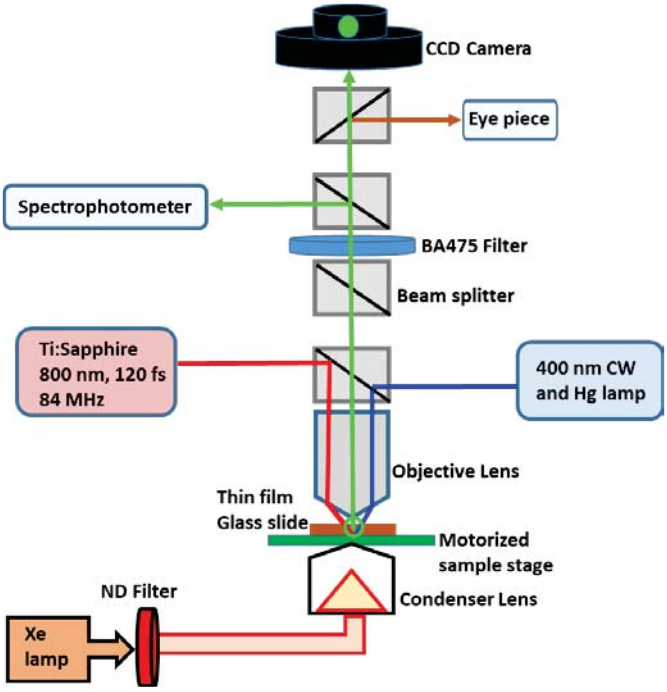

Figure 1. Schematic diagram of advanced modified optical microscope which is connected with 400 nm CW and high intensity Ti: Sapphire laser (800 nm, 120 fs, 84 MHz) through multimode optical fibers.

Results and Discussion

The optical features of organometal halide based IO-hybrids play a crucial role in attaining designed optical properties for various optoelectronic applications. The 2D inorganic organic hybrid semiconductors of the form $(R\text{-}NH_3)_2PbI_4$ shows strong Mott-type exciton features in the green spectral region. The quantum confinement effect along with large dielectric constant difference between the organic moiety and extended inorganic network structure will enhance the formation of stable exciton[3]. The Mott-type excitons are stable at room temperature and responsible for the strong exciton emission and absorption features of the IO hybrid semiconductors. The optical exciton and absorption spectra of one of the cyclic IO hybrid semiconductor CPPI (n=3) was shown in Figure 2 which shows strong exciton emission at 490 nm. The absorption spectra consists of strong exciton absorption peak around 484 nm which is due to the confinement of excitons in the lowest band gap of extended PbI_6 network structure. The charge transfer peak around at 350-400 nm arises due to the transfer of charge carrier from valance band of inorganic network structure to the HOMO (highest occupied molecular orbitals) of the organic moiety.

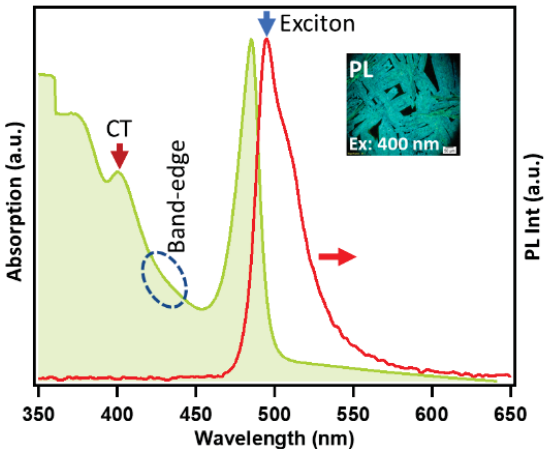

Figure 2. Exciton absorption (λ_{abs}~484 nm) and photoluminescence (λ_{PL}~490 nm) spectra of CPPI (n=3). The insert images showing the high resolution microscope PL images of CPPI (n=3). Ex: 400 nm, CW laser.

High resolution line scan PL spectral mapping/imaging of single crystal bits of IO hybrid semiconductors were performed using modified multifunctional optical microscope (Figure 1) which is connected with (i) 400 nm, for 1PA-PL and (ii) 800 nm (120 fs, 84 MHz) for 2PA-PL as an excitation source[5,6,7]. The one-photon (1PA-PL) induced photoluminescence provide information about the surface excitons (PL_{HE}) which are present in the nearly perfect and stress-free layers of the near-surface region. However two-photon induced photoluminescence (2PA-PL) gives an idea about the crumpled excitons (PL_{LE}) which are present in the low-lying excitation state due to the larger penetration depth (~1/α) and high intense photon energy (order of GW/cm^2)[5, 6]. High resolution line scan PL spectral mapping/imaging of CPPI (n=3) under one-photon (400 nm) and two-photon (800 nm, 120 fs, 84 MHz) excitation was shown in Figure 3. In 1PA-PL, the PL spectral is deconvoulated into surface excitons (PL_{HE}~490 nm) and crumpled exciton (PL_{LE}~510 nm). However two-photon (2PA-PL) excitation probes the overall crystals due to the larger penetration depth and provides information about low-lying crumpled exciton emission (PL_{LE}~510 nm).

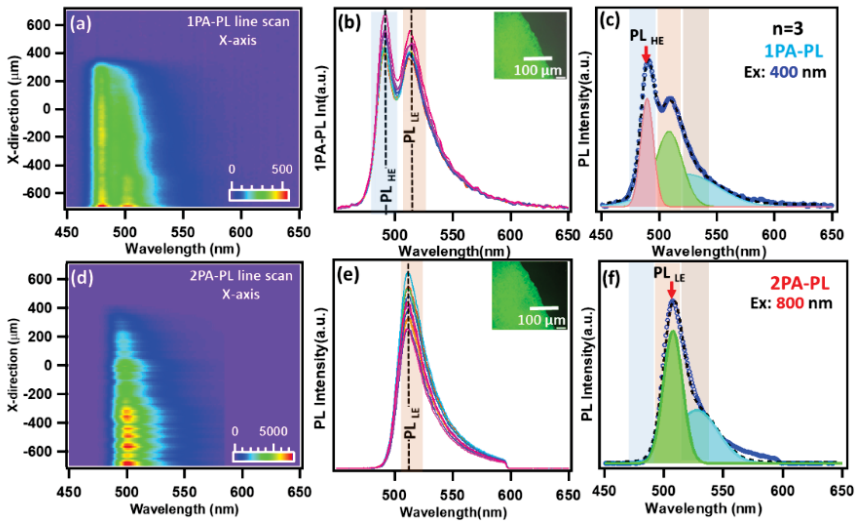

Figure 3 (a) Horizontal 1PA-PL line scan spectral mapping of CPPI (n=3) single crystal platelet monitored at PL_{max}=490 nm (b) 1PA-PL spectra extracted from various positions irrespective of depth/thickness (c) is

deconvoulated 1PA-PL spectra under one-photon excitation when excited with 400 nm, CW laser (d) 2PA-PL line scan spectral mapping of CPPI (n=3) single crystal platelet monitored at PL_{max} =510 nm (e) 2PA-PL spectra extracted from various positions (f) is the deconvoulated 2PA-PL spectra under two-photon excitation when excited with 800 nm (120 fs, 84 MHz). The Figure b & e inset images are respective confocal high-resolution microscope 1PA- and 2PA-PL images.

References:

1. D. B. Mitzi, *Chem. Rev.* **119**, 3033 (2019).

2. M. Shimizu, J.I. Fujisawa, and J. Ishi-Hayase, *Phys. Rev. B.* **71**, 205306 (2005).

3. T. Ishihara, X. Hong, J. Ding, and A. V. Nurmikko, *Surface science*, **267**, 323 (1992).

4. D. G. Billing, and A. Lemmerer, *CrystEngComm*. **9**, 236 (2007).

5. M. Adnan, J.J Baumberg, and G. V. Prakash, *Sci. Rep.* **10**, 2615 (2020).

6. M. Adnan, K. M. Dehury, P. K. Kanaujia, and G. V. Prakash, *J. Appl. Phys.* **128**, 023104 (2020).

7. M. Adnan, K. N. Rao, J. N. Acharyya, D. Kumar, K. M. Dehury, and G. V. Prakash, *ACS omega*, **4**, 19565 (2019).

Effects of High Repetition Rate Ultrafast Laser Pulses on Spatial Self-phase Modulation

Soumyodeep Dey and Prem Ballabh Bisht*

Department of physics, Indian Institute of Technology, Chennai 600036, India

*bisht@iitm.ac.in

Abstract: Femtosecond pulses from oscillators at high repetition rate (HRR) impart additional thermal effects to the materials under study. This results in temperature changes that leads to additional phase change to optical devices. Therefore, under HRR excitation, in the spatial self-phase modulation (SSPM) experiments the contribution of optical phase is generally masked by the thermally induced phase changes. In this work, the simulations by finite difference method have been used to distinguish the mismatch with the optical phase as a function of the pulse duration.

1. Introduction

Spatial self-phase modulation (SPM) experiments are a popular technique to estimate nonlinear refractive index of a materials[1]. The expected nonlinear refractive index supposed to be due to the optical Kerr effect (OKE) induced phase change in the material. However, under high repetition rate (HRR) ultrafast pulsed laser excitation, additional phase change is induced due to the thermal effect. Deng et. al.[2] have shown such an effect with the self-diffraction rings. The effect of pure thermally induced phase change in self-diffraction rings under continuous wave laser has been demonstrated by Harrison et. al.[3].

Study of thermally induced phase change can be useful to estimate the optimum pulse duration to look for pure OKE. In this work, we have simulated temperature rise inside a material due to HRR fs pulses by finite difference method (FDM). From this study, it can be seen that for a particular value of pulse duration it is possible to overcome the errors arising out of the thermal effects.

2. Theory

2.1. Temperature Rise Due to HRR Pulses

A simple model has been assumed to calculate the temperature rise inside the material studied under pulsed laser excitation. A square pulse replicating the same amplitude and duration has approximated the Gaussian laser pulse. The temperature rise has been assumed to be exponential during pulse duration (t_p) followed by the exponential relaxation till the next pulse arrives. The total temperature change ΔT due one pulse can be written to the form given by eq. 1. Here $t_{rise} = \omega_0/V_s$ and $t_{relax} = \omega_0^2 \rho C_p/4K$ are the rise time and relaxation time of the temperature, ω_0 is the spot radius, V_s is the velocity of sound in the sample and T_0 is the room temperature.

$$T_1(t) = T_0\left[1 - e^{-\frac{t}{\tau_{rise}}}\right], 0 < t < \tau_p,$$

$$T_2(t) = T_1(\tau_p)\left[e^{-\frac{t}{\tau_{relax}}}\right], \tau_p < t < \frac{1}{f_{rep}},$$

$$\Delta T = T_2\left(\tau_p + \frac{1}{f_{rep}}\right) - T_0 \quad (1)$$

2.2 Spatial Self-phase Modulation (SSPM)

When a high intense laser pulse travels through an optical medium, then some of the incident energy is absorbed by the medium depending on the absorption coefficient of the sample. For highly absorbing materials, the sample will heat up. As a result, changes in refractive index are observed as shown in Eq. 2. On the other hand, if the input electric field is high enough to induce OKE as given by Eq. 3. The refractive index of the sample will change along the transverse direction of the input beam.

$$\delta n_{TL} = \frac{dn}{dT}(T - T_o) \quad (2)$$

$$\delta n_{OL} = n_2 I \quad (3)$$

The phase $\Phi(r)$ of a Gaussian laser beam after passing through a material as a function of the transverse coordinate can be written as

$$\Phi(r) \approx \frac{k_0 n_0 r^2}{2R} + \Delta\phi \exp(-2r^2/\omega_0^2) \quad (4)$$

Where k_0, n_0 and R are the wave-vector, the refractive index and the beam radius of the Gaussian beam respectively. The amplitude of the phase change $\Delta\phi$ can be written as $\Delta\phi_{OL} + \Delta\phi_{TL} = k_0[\delta n_{OL} + \delta n_{TL}]L$. Where DF_{OL} and DF_{TL} are phase change due to OKE and thermal effects respectively. $\Delta T = T - T_0$ is the change in temperature, L is the length of sample and I is the input intensity. The far field diffraction pattern (as a function of diffraction angle q) can be written from the Fresnel-Kirchhoff diffraction formula[2] as

$$I(\theta) = I_0 \left| \int_{r=0}^{\infty} J_0(k_0 \theta r) \exp\left(-\frac{r^2}{\omega_0^2} - i\phi(r)\right) \right|^2 \quad (5)$$

Where I_0 is the incident intensity and $J_0(x)$ is the zeroth order Bessel function of first kind.

3. Results & Discussions

The parameters used in this work are given in table 1. For all the simulations, the average power (500 mW) as well as the repetition rate (82 MHz) of the input laser (λ = 780 nm) has been kept constant. The laser focus spot size (ω_0) has been taken as 10 mm. The pure optical nonlinear refractive index (n_2) has been assumed of the order of $10^{-16} m^2/W$. The solvent has been assumed ethylene glycol (parameters are given in table 1).

Table 1. Physical parameters of ethylene glycol solvent

Quantity	Values	Reference
Acoustic velocity (V_s)	1632.1 m/s	[4]
Density(ρ)	1110 kg/m^3	[5]
Refractive Index (n_0)	1.4163	[6]
Specific heat (C_P)	2690 J/kg.K	[4]
Thermal conductivity (K)	0.254 W/m.K	[5]
Thermo-optic coefficient (dn/dT)	$-4.8 \times 10^{-4} K^{-1}$	[4]

3.1. Temperature Rise

Equation 1 has been solved for $\sim 10^5$ number of pulses to achieve the steady state temperature as shown in fig. 1 (A). It can be seen that the steady state can be achieved after about 1 ms which is long enough for the case of long duration pulses. The calculated temperature changes as a function of pulse duration are shown in fig. 1 (B).

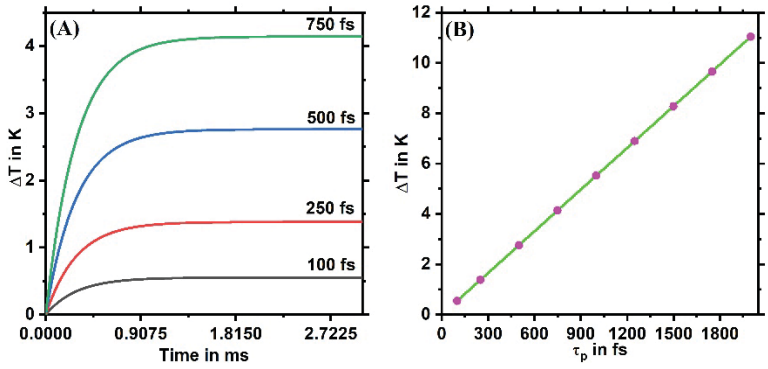

Fig. 1. (A) Temperature rises due to HRR pulses as a function of time. (B) Steady state temperature as a function of pulse duration.

3.2. Self-phase Modulation

The evaluated temperature changes from fig. 1 (A) has been used in eq. 2 to calculate the thermally induced phase change. At constant input average power, when the pulse duration increases the peak power decreases. As a result the OKE phase change decreases. On the other hand, the temperature increases at longer pulse durations. Equation 5 has been solved to obtain the self-diffraction pattern as shown in fig. 2 (B).

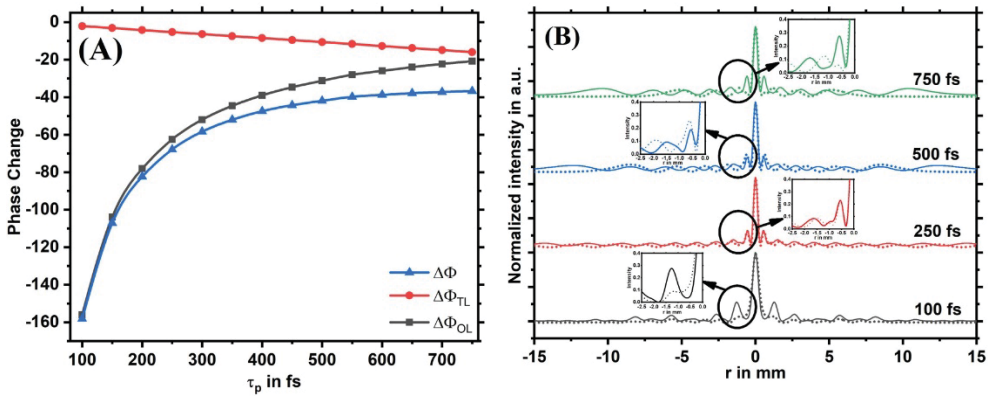

Fig. 2. (A) Thermal (DFTL), optical (DFOL) and total (DF) Phase change as a function of pulse duration. (B) Radial intensity profile due to self-diffraction. The dotted line represents when thermal effect is absent.

Figure 2 (A) is the plot of the total phase change ($\Delta\Phi$), optically induced ($\Delta\Phi_{OL}$) and thermally induced ($\Delta\phi_{TL}$) phase changes as a function of pulse duration. It can be seen that, for shorter duration of pulses the optically induced phase change is higher as compared to that due to the thermally induced. For longer pulse duration the $\Delta\Phi_{OL}$ as well as $\Delta\phi_{TL}$are approaching to the same value. In fig. 2 (B), for the case of 250 f s the lines of $\Delta\phi$ and $\Delta\phi_{OL}$almost coincide. But for other pulse durations, the two curves do not coincide specifically near r ≈ 0. From fig. 2 (A) it can be seen that, $\Delta\phi$ and $\Delta\phi_{OL}$ values are very near in case of 100 f s pulses. Even this small phase change (-2:12) can cause significant effect as shown in fig. 2 (B) (for 100 f s case).

4. Conclusions

FDM simulations have been done to study the thermally induced phase changes due to HRR pulses. Figure 1(A), shows that the longer duration pulses generate more heat into the material resulting in larger value

of phase change due to thermal effects. For a constant average power, both the optical and the thermal phase changes approach the common value as shown in fig. 2(A). From fig. 2(B) it can be seen that additional peaks appear for the case of longer (750 f s) as well as shorter (100 f s) pulse durations. On the other hand, for the case of 250 f s pulses the curve of DF and DFOL almost coincide. This indicates that the 250 f s is the optimum value of the pulse duration to avoid thermal effects in this system. The study of thermally induce phase change can be useful to choose optimum pulse duration in SSPM experiment to minimize the error in OKE measurements.

5. Acknowledgment

We thank the Defence Research and Development Organization (DRDO), New Delhi for financial support. One of us (SD) thanks DST, New Delhi for INSPIRE fellowship.

References

1. R. Wu, Y. Zhang, S. Yan, F. Bian, W. Wang, X. Bai, X. Lu, J. Zhao, and E. Wang, *Nano Lett.* **11**, 5159–5164 (2011).

2. L. G. Deng, K. He, T. Zhou, and C. Li, *J. Opt. A Pure Appl. Opt.* **7**, 409–415 (2005).

3. R. G. Harrison, L. Dambly, D. Yu, and W. Lu, *Opt. Commun.* **139**, 69–72 (1997).

4. P. Brochard, V. Grolier-Mazza, and R. Cabanel, *J. Opt. Soc. Am. B* **14**, 405 (1997).

5. C. Selvam, D.Mohan Lal, and S. Harisht, *J. Therm. Anal. Calorim*. **129**, 947—955 (2017).

6. H. El-Kashef, *Phys. B, Condens. Matter* **311**, 376—379 (2002).

All-normal dispersion Ytterbium doped fiber laser mode locked by nonlinear multimode interference based saturable absorber

Pradeep K. Gupta[1,2]*, C.P. Singh[1,2] P.K. Mukhopadhyay[1,2] and K.S. Bindra[1,2]

[1]*Laser Technology Division, Raja Ramanna Centre for Advanced Technology, Indore-452013.*

[2]*Homi Bhabha National Institute, Training School Complex, Anushakti Nagar, Mumbai-400094.*

*E-mail: pradeepg@rrcat.gov.in

Abstract: We report, mode locking operation using nonlinear multimode interference (MMI) based saturable absorber in Ytterbium doped fiber laser under all-normal dispersion configuration. The MMI is observed in step index single mode-multimode-single mode (SMS) fiber structure. Single pulse mode locking operation in the laser is realized at a very low pump power of ~56.3 mW at which laser generates 180 ps duration pulses at ~9 MHz repetition rate with measured signal to noise ratio of ~50 dB. This all-fiber integrated laser operates in multi pulse and noise-like rectangular pulse regimes at increased pump power.

Multimode interference (MMI) in optical fibers has been used for several applications viz. sensors, mode field adopters, wavelength tunable laser sources and high power fiber lasers with good beam quality. Current research on MMI in optical fibers has been extended beyond linear regime and use of MMI as saturable absorber (SA) based on Kerr induced nonlinear effect has been demonstrated. MMI was used as SA, for the first time, to passively Q-switch an Erbium (Er) doped fiber laser [1]. After that mode locking operation in fiber lasers using MMI based SA has been demonstrated in various operating regimes viz. anomalous dispersion, stretched pulse and all-normal dispersion (ANDi). For the construction of MMI based SA, different geometries of multimode fiber (MMF) were explored viz. step index [2], graded index [3], no-core fiber [4] or even their hybrid combinations [5] to design mode locked fiber lasers. Earlier studies show that due to very small self-imaging length of graded index MMF, it becomes very difficult to control the length of MMF with the fiber cleaver and combination of graded index and step-index MMF relaxes this requirement to some extent [4]. Considering these limitations, use of only step-index MMF for designing mode locked fiber lasers based on nonlinear MMI would be an easy and more viable solution. Although, Chen et al have demonstrated mode locking operation in Er doped fiber laser using step-index MMF in nonlinear MMI [2], mode locking in Ytterbium (Yb) doped fiber laser under ANDi configuration using MMI consisting of only step-index MMF has yet not been reported, to the best of our knowledge.

In this paper, we report mode locking operation in ANDi Yb doped fiber laser using step-index MMF in nonlinear MMI based SA. The MMI is observed in step index single mode-multimode-single mode (SMS) fiber structure. A fiber integrated acousto-optic tunable filter (AOTF) is incorporated in the laser resonator to provide pulse shaping mechanism of dissipative solitons as required in ANDi laser. Mode locking in single pulse operation was realized at a very low pump power of 56.3 mW where 180 ps duration pulses are generated at 9 MHz repetition rate. The signal to noise ratio (SNR) of the pulse train was measured to be ~50 dB. The laser also operates in multi-pulse and noise-like rectangular pulse regimes at higher pump powers.

The schematic of the all-fiber laser setup is shown in figure 1. The pigtailed fiber end of the laser diode (LD, 976 nm) was spliced to pump port of 976/1060 nm wavelength division multiplexer coupler (WDM). The

output port of WDM was fusion spliced to an 80 cm long Yb-doped fiber (YDF). The other end of YDF was fusion spliced to an 80:20 fiber optic coupler. The 80% port of the coupler was connected to the input port of a fiber integrated AOTF via a segment of ~11cm long step index MMF of 50 μm core diameter (cladding diameter 125 μm). The AOTF acts as a band pass filter (1.5 nm bandwidth) with central wavelength tunable from 950 to 1100 nm. The output fiber end of AOTF was joined to the signal port of WDM through a 14 m long SMF fiber spool followed by an in-fiber polarization insensitive isolator (ISO) to complete the unidirectional ring resonator. The MMF in combination with the SMFs on its both sides conform the SMS structure. The SMS has the maximum transmission for wavelengths for which the length of the MMF becomes an integral multiple of the self-imaging length corresponding to a particular wavelength. However, due to the optical Kerr effect the average refractive index of the core of the MMF is modified with intensity which in-turn leads to the self-imaging length to be a function of the intensity of the incident light. As a result transmission of the SMS structure varies dynamically with intensity and it acts as a saturable absorber. A polarization controller (PC) is used to apply stress in a section of MMF with the help of a knob for biasing and fine tuning of the transmission wavelength of the SMS structure. The output was taken through 20% port of the fiber coupler and pulses are detected with the help of a photodiode of 40 ps rise time and displayed on an oscilloscope of 2.5 GHz bandwidth. The output spectrum was characterized with the help of a wavelength meter.

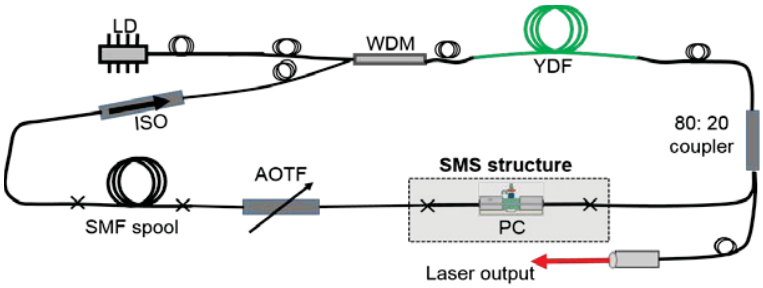

Fig. 1 Schematic of Yb doped mode locked fiber laser based on nonlinear MMI based saturable absorber.

The laser is first operated without AOTF in the cavity. The pump power is increased to 150 mW and the PC knob is continuously rotated to tune the transmission of SMS structure. The oscilloscope trace shows formation of pulses however stable mode locking could not be established as shown by modulation in the pulse train in figure 2(a). The optical spectrum of the laser is shown in figure 2(b) which is multi-peaked and ranges from 1040.7 to 1047.8 nm. The observed pulsing behavior of the laser suggests that nonlinear MMI is playing its role of SA and helping to create strong intensity fluctuation and chaotic train of pulses. However, as suggested by numerical simulation, a narrowband spectral filter is also needed for MMI based SA to be effective. Additionally, since the laser resonator is configured in ANDi configuration, a spectral filter with appropriate transmission bandwidth is required to stabilize the mode locking based on spectral filtering of chirped pulses. For this, an AOTF based band pass filter with tunable central wavelength is spliced in the resonator between SMS and ISO as shown in figure 1. After introducing AOTF in the resonator, pump power is increased and central wavelength of AOTF is continuously tuned by scanning its radio frequency. At 78 mW pump power and 134.13 MHz radio frequency of AOTF, a train of

relatively stable mode locked pulses is obtained as shown in figure 2(c). The optical spectrum of train of mode locked pulses is shown in figure 2(d) which is centered at 1045 nm with 0.6 nm spectral width. The pulse train still shows some amount of fluctuation in amplitude of the mode locked pulses. Passively mode locked lasers using

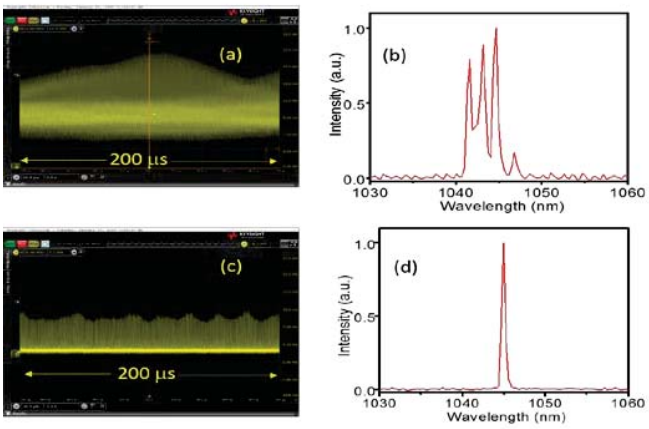

Fig. 2 Oscilloscope trace and corresponding optical spectrum of pulse train, (a, b) without AOTF in cavity and (c, d) with AOTF in the cavity.

saturable absorbers are known to exhibit such type of behavior due to relaxation oscillation initiated Q-switched mode locking instabilities. However, such type of instability can be avoided by pushing their threshold towards higher value by suitable choice of cavity parameters [6]. In our experiment, the stability of mode locked pulse train is improved by splicing a fiber spool (14m long SMF) between AOTF and ISO in the resonator. The oscilloscope trace of train of mode locked pulses is shown in figure 3(a) at 56.3 mW pump power after splicing the fiber spool in the resonator. The stability of mode locked pulse train is characterized by radio frequency (RF) measurements. RF

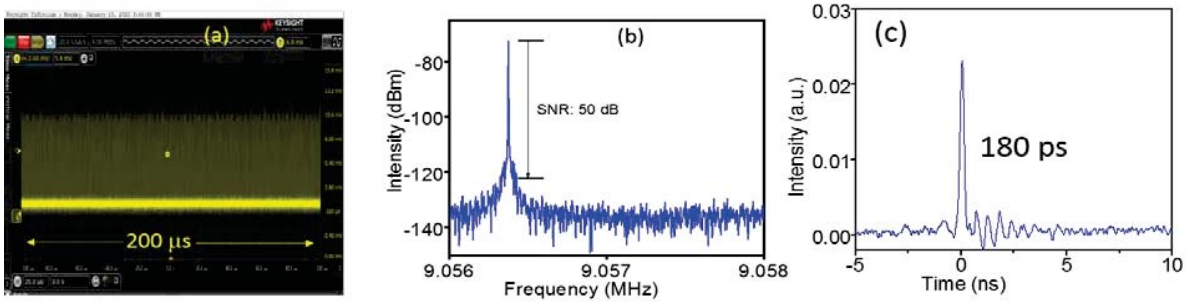

Fig. 3 (a) Stable mode locking operation with AOTF and fiber spool in the laser resonator, (b) RF trace of the train of mode locked pulses and (c) mode locked pulse at 56.3 mW pump power.

trace with 1 Hz resolution bandwidth is shown in figure 3(b). The RF trace is centered at ~9.05 MHz which is the fundamental repetition rate of mode locked pulses. The SNR was measured to be better than 50 dB which indicates reasonable stability of mode locked pulses. The average output power of the mode locked pulses at 56.3 mW pump power was measured to be 1.41 mW, which corresponds to 0.15 nJ single pulse energy. The individual pulse duration and the mode locking dynamics is studied by varying the pump power in the resonator. At 56.3 mW pump

power, the duration of mode locked pulse was measured to be 180 ps as shown in figure 3(c). With further increase in pump power the laser operates in multi-pulse burst regime and the number of pulses in the burst increases to ten at 88.7 mW pump power as plotted in figure 4 (a). The expanded view of group of pulses in a single burst is shown in figure 4(b). The multi-pulsing behavior in mode locked fiber lasers has been well reported [7] and is usually observed at increased pump powers due to energy quantization as a result of area theorems [8] for dissipative solitons. At 94 mW pump power, the individual pulses in the burst seem to be merged together to form a noise-like rectangular pulse of 2.03 ns duration as shown in figure 4(c). With further increase in the pump power, the mode locked pulses are deteriorated into random chaotic pulses.

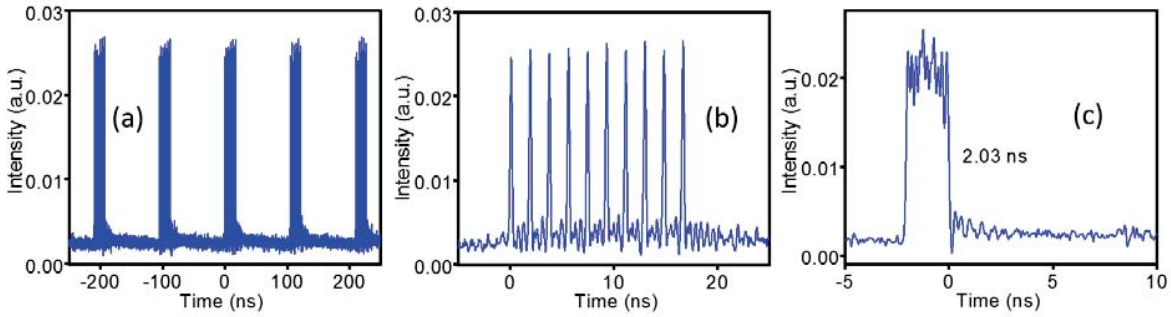

Fig. 4 (a) Burst of 10 pulses at 88.7 mW pump power, (b) expanded view of pulse burst and (c) noise-like rectangular pulses at 94 mW pump power.

In conclusion, we report the mode locking operation in ANDi Yb doped fiber laser using step-index MMF in nonlinear MMI based SA. The SMS structure consists of a step index multimode fiber spliced between standard single mode fibers. Single pulse mode locking operation in laser is realized at a very low pump power of ~56.3 mW at which laser generates 180 ps duration pulses at ~9 MHz repetition rate with measured signal to noise ratio ~50 dB. The laser operates in multi pulse and noise-like rectangular pulse regimes at increased pump power. The mode locked fiber laser we presented is in all-fiber format, very simple in design and may be used as seed source for ultrashort laser and amplifiers.

References:

[1]. S. Fu, Q. Sheng, X. Zhu, W. Shi, J. Yao, G. Shi, R. A. Norwood and N. Peyghambarian, Opt. Exp. 23, 17255-62 (2015).
[2]. T. Chen, Q. Zhang, Y. Zhang, X. Li, H . Zhang and W. Xia, Photonics Research 6, 1033-39 (2018).
[3]. Z Wang, J Chen, T Zhu, D. N. Wang and F Gao, Photonics Research 7, 1214-20 (2019).
[4]. S. Thulasi and S. Sivabalan, App. Opt. 59 7357-63 (2020).
[5]. Z. Wang, D. N. Wang, F. Yang, L. Li, C. Zhao, B. Xu, S. Jin, S. Cao and Z. Fang, J. Light. Technol. 35, 5280-85 (2017).
[6]. C. Honninger, R. Paschotta, F. Morier Genoud, M. Moser and U. Keller, J. Opt. Soc. Am. B 16, 46-56, 1999.
[7] X. Li, S. Zhang, Y. Hao, and Z. Yang, Opt. Exp. 22, 6699-6706 (2014).
[8]. W. H. Renninger, A. Chong and F. W. Wise, J. Opt. Soc. Am. B 27, 1978-82 (2010).

Volumetric propagation studies of ultrashort pulsed beams in nonlinear dispersive and aberrated optical systems

A.K.Sharma
Laser Technology Division, Raja Ramanna Centre for Advanced Technology, Indore 452013,MP, India
Email: aksharma@rrcat.gov.in

There has been never ending quest to generate spectrally ultra-broad bandwidth light sources to probe materials with unprecedented temporal resolution for various scientific applications and curiosity driven research. While such sources naturally occur (e.g. Stars), creating coherent broadband sources (e.g. Laser) is quite difficult in a practical situation. For instance, controlling phase slippage of different spectral components to generate high energy pulses with duration down to few optical cycles (*1 optical cycle at 1054 nm equals to 3.51 fs*) require special care not only in choosing laser materials and optical components but also need vibration-insensitive and thermally stable environment. Technique of chirped pulse amplification [1] is widely applied to built energetic ultra-short pulse laser systems, as it avoid problems of space-time distortions [2] of pulsed beams due to optical non-linearities and laser induced damage of optical components. Further, CPA based laser systems often use single or multiple dispersive optical elements that also change characteristic of pulsed beam due to spatio-temporal or spatio-spectral distortions (i.e. *electric fields E(x) or E(y) and E(t) or E(ω) are coupled*) [3-5]. The term space-time used earlier is to be differentiated with term spatio-temporal most often used for low order phase errors such as pulse front tilt. While spatio-temporal distortions occur in one plane (*mostly horizontal*) due to dispersive characteristic and positioning of the optical elements, misalignment and incorrect positioning of dispersive elements generate distortions in both x-t and y-t spaces of the pulsed beam. While such distortions are minimized in most of situations e.g. *generation of ultrashort laser pulses*, these are also used to optimize outcome of physical processes e.g. *efficient parametric generation, THz and x-ray generation* etc.

Next, chromatic aberration of a refractive optical system also severely distort characteristic of a pulsed beam owing to difference in group and phase velocities. For example, a lens system generate a radially dependent propagation delays causing a horse-shoe shaped space-time profiles [6-8]. Likewise, spatial aberration of optical systems (*e.g. spherical aberrations, astigmatism, coma, distortions etc*), orientation, refractive index mismatch and numerical aperture of a lens system also affect space-time profiles [7] especially for pulses with few cycle duration. The term distortion used for spatial aberration is to be differentiated with space-time or spatio-temporal distortion of pulse. Even in absence of spatial aberrations of wave-front of a beam or a optical system, non-linear phases in both space and time domain induced by optical non-linearities at higher pulse intensities, also affect characteristics of pulsed laser beams. Therefore, it is desirable to study volumetric propagation of ultrashort pulsed beams through a nonlinear dispersive and aberrated optical system that is often a case even in transporting intense beam from a CPA laser system for any application involving refractive (*e.g. lens, window*) or refractive components (*e.g. mirrors*). Propagation characteristic of femtosecond laser pulses have been extensively studied and shown both theoretically and experimentally, for example, role of angular dispersion, group delay and its dispersion, spatial chirp and aberrations of optical systems on space-time characteristic of ultrashort laser beams with duration even down to few cycles. While most of spatio-temporal model developed for ultrashort pulses describe complex evolution of pulses through linear and nonlinear dispersive medium, constant and linear phase terms are often ignored. Constant and linear phase terms and their various space-time coupling are also desirable respectively to account absolute phase and spatio-temporal distortions of the pulsed beams. Further, in most of reported literature, two-dimensional description of pulsed beam (*in x-t or y-t space*) has been used to carry out pulse propagation studies of radially symmetric beams.

While simultaneous use of two-dimensional description of pulsed beam can also be applied to study propagation characteristic of elliptic pulsed beam in x-t and y-t space considering respective dispersive and space-time coupling parameters for given practical situation, a three-dimensional description, in general, is desirable also to include induced (*optical non-linearities*) or fixed non-symmetric aberrations of the optical systems, constant and linear phase terms and their x-t or y-t coupling. For example, a three-dimensional model of ultrashort pulse propagation [9-12] through linear aberrated optical systems (*e.g. lens system*) have been reported that combine ray tracing and field estimation. In this paper, a two-dimensional model (in *1D space and 1D time for symmetric systems*) and three-dimensional model (in *2D space and 1D time for non-symmetric systems*) of ultrashort pulsed laser beams based on angular frequencies for pulse propagation studies through non-linear aberrated optical systems is presented to include constant/ linear phase terms and different space-time coupling (*x-t and y-t*) to account absolute phase and pulse-front distortions. While physical defects are modeled through amplitude mask, surface and bulk phase obscurrations are treated with phase masks, desirable to estimate quality of glass to build a laser system.

An ultrashort pulsed beam is considered to occupy a finite three-dimensional space (*transverse (x and y) and longitudinal time (t) dimensions*) and three-dimensional field of pulsed beams is expressed in terms of their spatial (k_x and k_y) and temporal (ω) angular frequencies as

$$E(x, y, t : z) = FT^{-1}E(k_x, k_y, \omega : z) \propto \int_{-\infty}^{\infty}\int_{-\infty}^{\infty}\int_{-\infty}^{\infty} E(k_x, k_y, \omega : z)e^{-j(xk_x + yk_y + t\omega)}dk_x dk_y d\omega \quad (1)$$

where $$E(k_x, k_y, \omega : z) = A(k_x, k_y, \omega)e^{j\ [\Phi_o + \Phi(k_x, k_y, \omega)]} \quad (2)$$

Operator FT^{-1} in Eq. (1) is three-dimensional inverse Fourier transformation. Functions $A(k_x, k_y,\omega)$ and $\Phi(k_x, k_y,\omega)$ in Eq. (2) is spectrally dependent amplitude and phase of the pulsed beam, while Φ_o is a spectrally independent phase offset i.e. phase constant. For symmetric systems, one space dimension in Eqs.(1) and (2) is ignored to evaluate electric field in x-t and y-t space either for elliptic beams or astigmatic systems.

To study propagation characteristic of such a pulsed beam (e.g. *initial Gaussian shaped distribution in space and time in the present case*) through an optical system, propagation distance is divided into finite steps such that diffraction, dispersion effects are decoupled from non-linear effects and estimated independently for each propagation step using well known Fourier transformation based angular spectrum propagation method. Likewise, optical elements are divided into segments. For example, a lens is treated as a single optical surface followed by a propagation through lens optical medium and another optical surface with suitable curvatures. While a single step for each optical surface bounded by two different optical medium is chosen such to consists of two steps with varying propagation distances through different mediums, varying refractive index is accounted by creating a three-dimensional index space to account dispersion and striae.

To account optical non-linearities, aberration and dispersion, diffraction step (*both inclusive*) followed by nonlinear step in contrast to symmetric split-step, has been taken in the present study and simulated using nonlinear operator in space-domain using function N(x,y,t) as $E(x, y, t : \Delta z) = E(x, y, t : 0)\ \ N(x, y, t : \Delta z)$ and diffraction operators in frequency-domain using three-dimensional transfer function $H(k_x, k_y,\omega)$ as $E(k_x, k_y, \omega : \Delta z) = E(k_x, k_y, \omega : 0)\ \ H(k_x, k_y, \omega)$. Three-dimensional operator $H(k_x, k_y, \omega)$ include constant, linear and higher order terms and their couplings, coefficients quantifiable for given optical system, to account for absolute phase, spatio-temporal distortion and aberrations. While static spatial phase (e.g. thermal) and intensity dependent spatial and temporal phases are included in function N(x,y,t) using beam-breakup or B-integral

defined as $B(r,t)=\frac{2\pi}{\lambda}\int n_2 I(r,t)dz$ (*n_2 is nonlinear refraction, z is length of nonlinear medium, and I(r,t) is the pulse intensity*), ionization dependent and non-instantaneous phases are not included in the present model. Present model works well to study propagation of chirped energetic pulses through aberrated optical systems (*inclusive of surface or bulk scatterers owing to physical or density dependent defects causing varying spatial frequency bands down-stream of non-linear slabs*) with moderate non-linearities. While numerical outcome of present model is cross-checked for spatial and temporal width for given estimated diffraction and dispersion as illustrated below, space-time evolution of pulsed beam is being validated with reported experimental observations under different practical situations involving surface aberrations and defects (*physical as well as phase obscurrations*) of optical system, differential arrival time of pulse-lets in presence of optical non-linearities.

For illustration purposes, an initial 20 fs duration chirp-free energetic Gaussian shaped pulse (E_p=2 mJ) at wavelength of 1054 nm is considered to propagate through 20 mm thick optical medium kept in vacuum and gaseous medium like air. While Figure 1 show composite images of beam profiles, pulse shapes and respective pulsed beam in space-time domain for pulse propagation through optical medium with pure quadratic and pure cubic dispersion in absence of non-linear phases, Figure 2 depict composite images of beam profiles and pulse shapes for a case of non-dispersive positive non-linear slab kept in vacuum and in negative nonlinear gaseous medium. It may be seen from Figure 1 that pulse is broadened to 78 fs while propagating through linear optical medium with quadratic dispersion and found to match well with estimated pulse width. Initial Gaussian pulse shape is transformed to asymmetric pulse with pedestals in case of pure cubic dispersion as expected, while beam profile remain unchanged in both the cases for given pulse propagation parameters (*Figure 1a*).

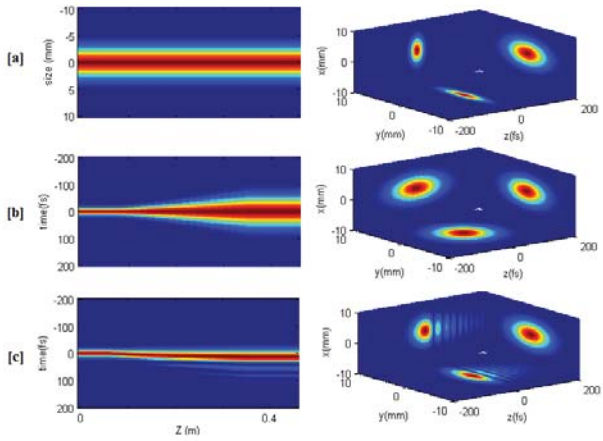

Figure 1: (a) Composite image of beam profiles with propagation along with initial Gaussian shaped pulsed beam in (3+1) space; Composite image of pulse shapes with propagation and propagated pulsed beam in (3+1) space at 0.5 m for pure quadratic dispersion of 27.5 fs^2/mm (b) and pure cubic dispersion of 47.7 fs^3/mm (c).

From Figure 2, it may also be seen that cumulative nonlinear phase generate rings in the beam profile and temporal pulse splitting for non-dispersive nonlinear slab (n_2=3.5.10^{-4} cm^2/TW) kept in vacuum (*on axis B-integral of ~4π*), while no temporal pulse splitting in the case of nonlinear slab kept in negative nonlinear gaseous medium (n_2 = -1.7.10^{-7} cm^2/TW) due to expected reduction of effective cumulative nonlinear phase. Observed focal length of nonlinear slab from simulated results also found to match well with estimated value of 2.8 m in case of non-dispersive nonlinear slab kept in vacuum. In contrast to self-focusing, Gaussian beam may get converted into a flat-top shaped beam profile at optimum propagation through negative non-linear optical medium and temporal pulse shape will also be flattened with asymmetric shape due to non-linear chromatic errors with blue-shifted radiation in the leading-front as shown in Figure 3.

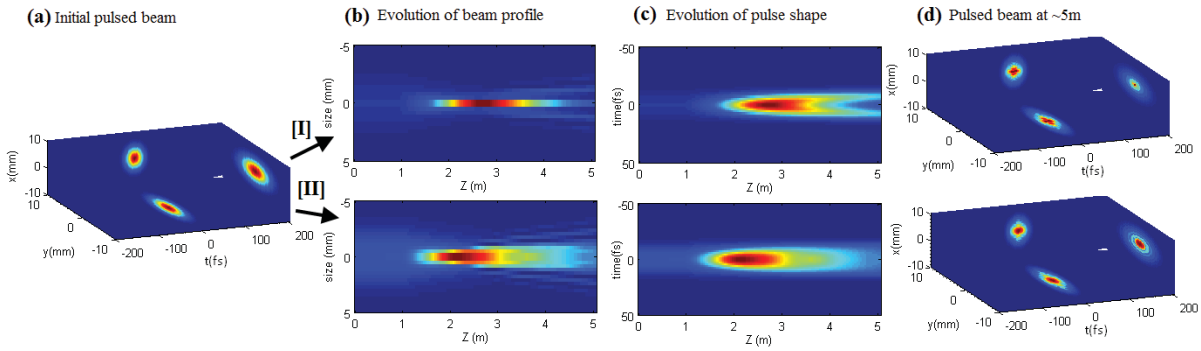

Figure 2: Initial and propagated pulsed beam in (3+1) space (a and d) and composite image of line-scanned beam profiles (b) and pulse shapes (c) with propagation distance for non-dispersive 20 mm thick positive nonlinear optical slab kept in vacuum (I) and in negative nonlinear gaseous medium (II).

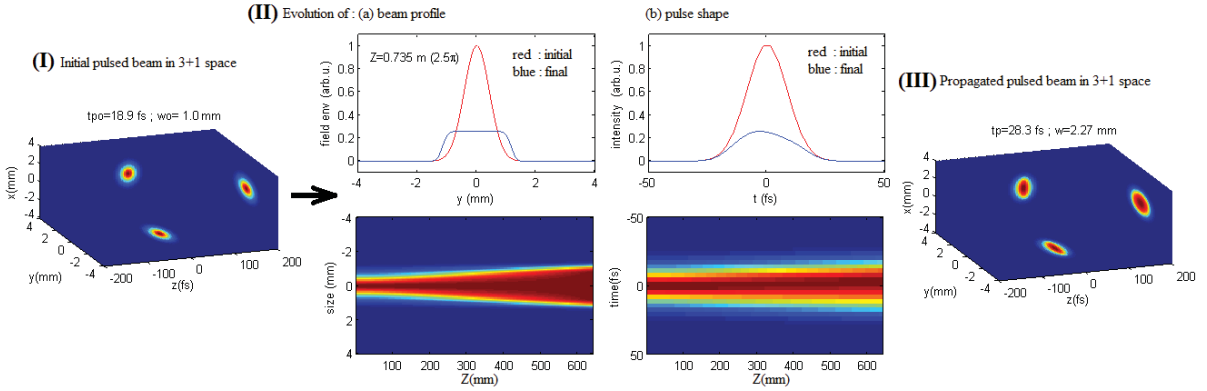

Figure 3 : *Initial and propagated pulsed beam in (3+1) space (I and III) and composite image of evolution (II) of beam profile (a) and pulse shape (b) with propagation distance for non-dispersive 73 cm thick negative nonlinear optical slab. Line scan of beam profile and pulse shape are also given in (II) for clearer illustration.*

In summary, a three-dimensional description of ultrashort pulsed laser beams based on angular frequencies is presented for volumetric pulse propagation studies through non-linear optical systems with non-symmetric aberrations. Constant/ linear phase terms and different space-time coupling (*x-t and y-t*) have been included in present model to account absolute phase and propagation delays due to difference in group and phase velocities. While three-dimensional description of ultrashort pulse propagation is quite good for low to mid band of angular frequencies, computational time for large sized ultrashort pulsed beams is reduced by optimizing upper-bound of angular frequency in space-time domain for desired accuracies in spatial and temporal domains. Higher band of spatial frequencies due to e.g. striae and bubbles acting as converging or diverging miniature lenses buried in glass shall be treated in future. Alternatively, a two-dimensional description in x-y or x-t space is applied for pulse propagation studies in such cases. Discussion is supported with few examples.

References:

1. D. Strickland, G. Mourou, Opt. Commun. **56**, 219 (1985).
2. R. E. Bridges, R. W. Boyd, G. P. Agrawal, J.Opt. Soc. Am B **13**, 3, 553 and 560 (1996).
3. S. Akturk, X. Gu, E. Zeek, R. Trebino, Opt. Exp. **12**, 4399 (2004).
4. S. Zhang, D. Asouber, R. Kammel, S. Nolte, F Wyowski, J. Opt. Soc. Am. A **31**, 11, 2437 (2014).
5. M. Rhodes, Z. Guang, J. Pease, R. Trebino, Appl. Opt. **56**, 11, 3024-3034 (2017).
6. M. Kempe, W. Rudolph, Phys. Rev. A **48**, 4721 (1993).
7. M. A. Gonzalez-Galicia, M. Rosete-Aguilar, J. Garduno-Mejia, N. C. Bruce, R. Ortega-Martinez, J. Opt. Soc. Am. A **28**, 10, 1979-1989 (2011).
8. B. Sun, P. S. Salter, M. J. Booth, J. Opt. Soc. Am. A **31**, 4, 765 (2014).
9. U. Fuchs, U. D. Zeitner, A. Tunnermann, Opt. Exp. **13**, 3852 (2005).
10. C. Bourassin-Bouchet, M. Stephens, S. deRossi, F. Delmotte, P. Chavel, Opt. Exp. **19**, 17357 (2011).
11. Z. Li, N. Miyanaga, Opt. Exp. **26**, 8453 (2018).
12. N. G. Worku, H. Gross, J. Opt. Soc. Am. A **37**, 2, 317 (2020).

Ultra-fast lattice dynamics in GaP/Ge(111) heterostructure measured with time-resolved x-ray diffraction

R. Rathore[1,2]*, H. Singhal[1,2], R. Roychowdhury[1,2], V. K. Dixit[1,2], T. K. Sharma[1,2] and J. A. Chakera[1,2]

[1] *Raja Ramanna Centre for Advanced Technology, Indore 452 013*

[2] *Homi Bhabha National Institute, Anushaktinagar, Mumbai - 400094*

*E.mail : ranjana@rrcat.gov.in

Abstract

In this paper, we present time resolved x-ray diffraction study of GaP/Ge(111) heterostructure sample using laser plasma Cu K_α (8.05 keV) x-ray source and 400 nm laser pump at pump fluence of ~6.5 mJ/cm^2. Diffraction peak from GaP-epilayer shifts towards lower angle indicating lattice expansion. It shows maximum strain of ~2.7×10^{-3} at ~80 ps after photoexcitation. At similar delays, the Ge (111) substrate shows lattice compression and corrosponding strain was ~7.5×10^{-4}. This study will enhance our physical understanding of thermal transport in GaP/Ge(111) heterostructure induced by ultra-fast impulses which is important to understand lattice dynamics and heat management at nanoscale.

1. Introduction

The investigation of ultra-fast dynamics of group III-V like GaP semiconductors on group IV substrates like Ge is necessary as they are important for the development of high efficiency multi-junction solar cells, wide range of detectors, advanced lasers, spintronics, and spin-photonic devices[1,2]. Ultra-fast lattice dynamics of materials after laser excitation is studied using time resolved x-ray diffraction (TXRD) technique which uses ultra-short optical pump and x-ray probe and gives the information of change in the angle of the diffracted x-rays as a function of delay between pump and probe[3-5]. An ultra-short x-ray pulse is generated by same ultra-fast laser which was used to pump the crystal resulting in virtually jitter free pump probe set-up. Ultra-fast structural dynamics of materials provide the information of length and time scales of lattice heating. This study will be helpful to increase the fundamental understanding of thermal transport in GaP/Ge(111) heterostructure induced by ultra-fast impulses which is important to understand lattice dynamics and heat management in nano-electronics[1].

In this paper, the time resolved x-ray diffraction study of strain oscillations in an impulsively heated GaP/Ge (111) heterostructure using wire target based laser plasma Cu K_α x-ray source is reported. The ultra-fast lattice dynamics of GaP(111) epilayer and Ge (111) substrate is studied by changing the delay between laser pump and x-ray probe pulses after the irradiation by 400 nm (second harmonic of 800 nm femtosecond laser) pump beam.

2. Experimental details

A 6.5 mJ, 50 fs, 1 kHz Ti:Sapphire laser operating at 800 nm, was used in this experiment. Figure 1 shows the schematic of experimental set-up. Energy band gap of GaP is ~ 2.26 eV which is considerably higher than the photon energy of the Ti:sapphire laser (~1.55 eV), hence single photon absorption of this pulse is not possible in GaP epilayer. To enable single photon excitation of the GaP epilayer, we have first converted a part

of the laser beam into second harmonic and then used it as pump pulse to irradiate the GaP (111) epilayer. The remaining fundamental part of laser beam was focused (using gold coated, f/8, 90° off axis parabolic mirror (OAPM)) on a moving Cu wire target (kept inside a vacuum chamber evacuated to 10^{-2} mbar) to generate laser plasma Cu K_α x-ray source (probe pulse). The emitted x-rays were focused using the polycapillary optics of 50 mm input and 100 mm output focal lengths. A moving transparent debris protection tape was placed in front of Cu wire target to protect the optics inside the chamber from Cu plasma debris. The focused x-ray beam was extracted from plasma chamber through 1 inch diameter, 25 μm thick kapton window. A Cd-Te detector was used to measure Cu K_α x-ray photon flux in single photon counting mode. The measured Cu K_α flux was ~ 2×10^9 photons/sr/s at laser intensity of ~3.2 × 10^{16} W/cm^2. The sample is consisted of 500 nm thick epitaxial layer of GaP grown on Ge (111) substrate and was placed outside the plasma chamber in symmetric Bragg geometry. The sample was grown using metal organic vapour phase epitaxy (MOVPE) technique. The characteristics of the sample such as crystalline and electronic band alignment properties and effect of germanium auto-diffusion on the bond lengths of Ga and P atoms etc., is reported in separate study[2,6]. The diffracted x-ray signals from GaP epilayer and Ge crystal were recorded simultaneously on x-ray CCD detector. The pump beam was focused with ~1.5mm×~5mm (FWHM) spot size on the sample. A delay line was set-up in air in the pump beam path that covers ~ 2 ns delay. The GaP (111) epilayer was pumped at laser fluence of ~6.5 mJ/cm^2, which is below its damage threshold (~ 13 mJ/cm^2). Pump and probe beams were matched spatially and temporally at the sample. The evolution of strain in the sample after laser excitation was recorded by varying the delay between laser pump and x-ray probe beam. In our setup, the lattice dynamics of both the epilayer and substrate can be probed simultaneously.

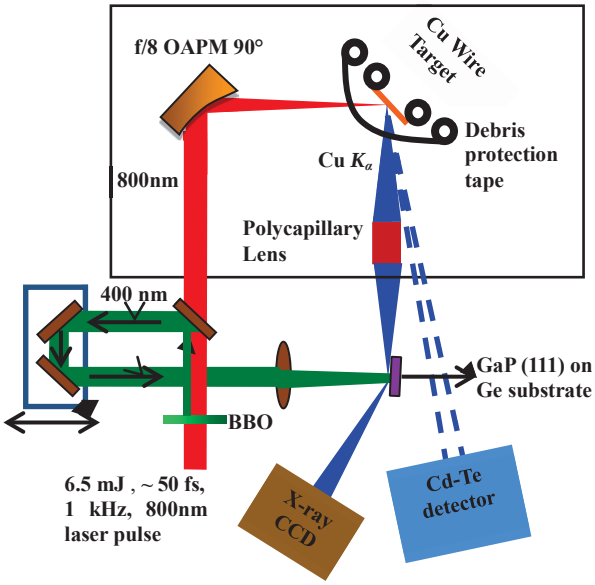

Figure 1: Experimental configuration of time resolved x-ray diffraction set-up

3. Results and discussion

The diffraction pattern from GaP epilayer and Ge (111) substrate after pumping of epilayer by laser pulse at ~80 ps delay was recorded on x-ray CCD, same is shown in figure 2(a). The diffracted x-rays from Ge

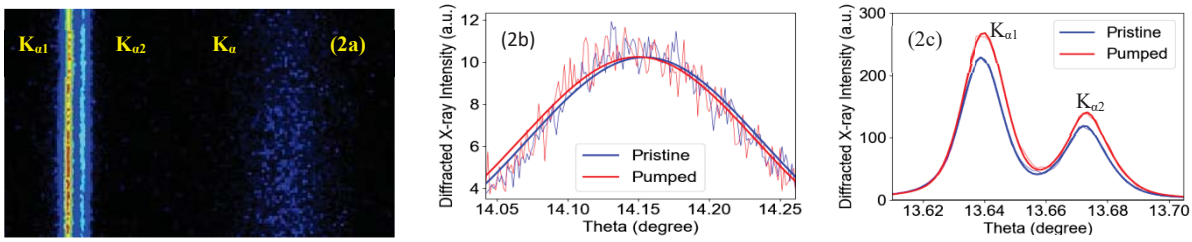

Figure.2: The diffraction pattern from GaP/Ge (111) heterostructure recorded on x-ray CCD at ~80 ps delay (a). (111) diffraction pattern of GaP epilayer (b) and Ge substrate (c).

substrate shows well resolved Cu $K_{\alpha 1}$ (8.047 keV) and $K_{\alpha 2}$ (8.027 keV) lines whereas diffraction pattern of GaP epilayer shows the broad Cu K_{α} line. Due to large lattice mismatch between GaP and Ge, its critical thickness is very small (7 nm). Therefore, it is expected that layer is completely relaxed via the formation of line defects, which results in the broadening of rocking curve. The diffraction profile for GaP and Ge for the pristine and irradiated conditions is shown in figure 2(b) & 2(c) respectively. Laser excitation of the epilayer launches a thermal strain in it, which results in its lattice expansion. As the thermal strain crosses the GaP epilayer, it first creates compression in Ge substrate. Afterwards, Ge substrate also shows thermal expansion. This strain (change in the lattice spacing) is manifested in terms of change in the angle of the diffracted x-rays. The strain propagation is probed by changing the delay between the pump and probe pulses. Approximately 80 ps after photoexcitation, expansion of the GaP lattice reaches its peak value. At this delay, it shows strain of ~2.7×10^{-3}. At similar delays, Ge substrate shows lattice compression and corresponding strain was ~7.5×10^{-4}. Detailed results will be presented.

4. Conclusion

Ultra-fast lattice dynamics of GaP/Ge(111) heterostructure using wire target based laser plasma Cu K_{α} x-ray source has been studied. After the laser irradiation of epilayer, lattice expansion was observed in it. When strain wave reaches Ge substrate, it results in compression of the substrate. Finally, substrate also shows thermal expansion. This study will enhance our physical understanding of thermal transport in GaP/Ge(111) heterostructure induced by ultra-fast impulses which is important to understand lattice dynamics and heat management at nanoscale.

5. References:

1. C. Nyby, A. Sood, P. Zalden, A. J. Gabourie, P. Muscher, D. Rhodes, E. Mannebach, J. Corbett, A. Mehta, E. Pop, T. F. Heinz, and A. M. Lindenberg, *Adv. Func. Mater.*, **30**, 2002282 (2020).

2. V. K. Dixit, S. Kumar, S. D. Singh, S. K. Khamari, R. Kumar, P. Tiwari, D. M. Phase, T. K. Sharma, and S. M. Oak, *Appl. Phys. Lett.,* **104**, 092101, (2014).

3. S. Höfer, T. Kämpfer, E. Förster, T. Stöhlker, and I. Uschmann, *Struct. Dyn,.* **3**, 051101 (2016).

4. F. Zamponi, Z. Ansari, M. Woerner, T. Elsaesser, *Opt. Exp,.* **18**, 847 (2010).

5. R. Rathore, H. Singhal, and J. A. Chakera, *J. of Appl. Phys.,* **126**, 105706 (2019).

6. R. Roychowdhury, P. Rajput, S. Kumar, R. Kumar, A. Bose, S. N. Jha, T. K. Sharma, and V. K. Dixit, *J. of Synch. Rad.*, **28**, 2 (2021).

Complete temporal reconstruction of attosecond pulse trains from high-harmonic generation in an argon filled cell

M. Kumar*[1], A. Ansari[1], H. Singhal[1,2] and J.A. Chakera[1,2]

[1]Raja Ramanna Centre for Advanced Technology, Indore 452 013, India

[2]Home Bhabha National Institute, Anushakti Nagar, Mumbai 400 094, India

*Email: mukund@rrcat.gov.in

Abstract:

We present an experimental study on complete temporal characterization of attosecond high-harmonic pulse trains, generated in an argon filled gas cell. The characterization has been carried out using FROG-CRAB cross-correlation technique. The cross-correlation is performed by simultaneous focusing of high order harmonics and the dressing IR pulse in low pressure gas sheath and the generated photoelectrons are detected using MBeTOF spectrograph. The spectrogram is generated by stacking the photoelectron spectrum generated at different delay between the two beams (high-harmonics and IR) and complete temporal profile of attosecond pulse trains is successfully retrieved using PCGPA algorithm. The duration of individual attosecond pulse in the pulse train is measured to be ~300as to ~400as, and width of complete pulse envelop is ~15 fs (FWHM).

Introduction:

High order harmonic generation (HHG) is a well established route to produce attosecond duration extreme-ultraviolet pulses. The high order harmonics are generated by focusing an ultrashort laser ($I \sim 10^{14\text{-}15}$ W/cm^2) pulses in gaseous medium and the odd harmonic orders of the fundamental laser frequency are produced[1]. The coherent generation process enables the high-harmonics to be phase locked, which leads to generation of attosecond pulses. For a multi-cycle laser pulse, a train of attosecond pulses are generated[2]. Complete characterization of such pulse trains may reveal information about interaction of a photo-electron with atomic/molecular coulomb field in presence of a strong laser field[3]. It is therefore essential to precisely characterize the attosecond pulses to probe ultrafast phenomena[4], molecular tomography[5] and also to control the attosecond electron wavepackets[6].

Temporal characterization of the attosecond pulses is extremely challenging. Conventional methods such as autocorrelation used for characterization of ultrashort pulses cannot be used this case, as the wavelength of attosecond pulses (high-harmonics) is in extreme-ultraviolet range, and no non-linear medium is available in this wavelength range. For such pulses, several techniques have been proposed, however only few studies have been experimentally reported, in which complete characterization of such pulses is successful[7-9]. All these techniques rely on the generation of photoelectron (PE) through photo-ionization of atom, which is a replica of the attosecond pulses. Cross-correlation of the attosecond pulse with an IR dressing laser field, generates photoelectron peak correspond to odd harmonic orders as well as sideband photoelectron peaks (correspond to even harmonic order). With change in the delay between the two pulses, the intensity of sideband peak oscillates and this is used to extract the temporal structure of the attosecond pulses. One of the well known techniques is "Reconstruction of attosecond beating by interference of two photon transition" (RABITT), which only gives an estimate of average duration of attosecond pulses in pulse train[8]. However, the complete characterization of such attosecond pulse trains cannot be achieved using this technique. The other technique which can be used for

complete temporal characterization is "Frequency resolved optical gating for complete reconstruction of attosecond bursts"[10] (FROG-CRAB). This technique is analogous to the blind "FROG" technique, used for characterization of fs IR laser pulses, where the pulse to be characterized is decomposed in different temporal slices, using the gate pulse and then the spectrum of each slice is measured[11]. This creates a 2D data set, known as spectrogram or FROG trace.

$$S(\omega,\tau)=\left|\int_{-\infty}^{\infty} dtG(t)E(t-\tau)e^{(i\omega t)}\right|^2 \qquad (1)$$

Here τ is variable delay between the pulse and gate, E(t) is the field which is to be characterized and ω is laser frequency. The gate pulse may be related / unrelated to signal or it may be an unknown pulse (blind FROG). Various efficient iterative algorithms, such as "Principal component generalized projections algorithm (PCGPA) is then be used to extract the signal pulse *E(t)* as well as gate pulse G(t)[12]. Both signal and gate pulse are not known prior to reconstruction (in Blind Frog), they are simultaneously reconstructed from the recorded spectrogram. To characterize the attosecond pulse trains, the photoelectron spectrum generated by simultaneous focusing of high order harmonics and IR dressing laser field is recorded as a function of the delay between the two pulses, till the two pulses are overlapped . When two pulses are overlapped in time, the photoelectron peak correspond to odd harmonic orders as well as sideband peak, correspond to even multiple of laser frequency are simultaneously observed. When these two pulses get separated temporally, the sideband peak disappears. The intensity of sideband peak oscillates with change in delay at $2\omega_L$, where ω_L is the frequency of dressing laser field. The FROG-CRAB technique (similar to FROG algorithm), with the gate pulse as phase gate[10] ($G(t) \sim e^{i\phi(t)}$) and "Principal Component Generalized Projection Algorithm" (PCGPA) is used to reconstruct the CRAB trace as well as to extract the temporal profile of the signal and gate pulse.

In this paper, we present complete temporal characterization of attosecond high order harmonic pulse train generated in argon filled gas cell using FROG-CRAB technique. The cross-correlation photoelectron signal is generated by simultaneous focusing of higher harmonics and the dressing IR pulse in low pressure gas sheath and detected them using magnetic bottle electron time of flight (MBETOF) spectrograph. After this, the FROG-CRAB technique is applied for the temporal reconstruction of attosecond pulse train of the high-harmonics. The reconstruction discloses the temporal structure of attosecond high-harmonic pulse trains and the temporal profiles of the individual attosecond pulses as well. The duration of individual attosecond pulses is measured to be in the range of ~300as to ~ 400as, with an overall attosecond pulse train envelope duration of ~15 fs (FWHM).

Experimental setup:

The experiment has been performed using Ti: sapphire (central wavelength λ_o = 800nm) laser system, which can deliver ~50fs (FWHM) duration pulses, at 1 kHz repetition rate. A schematic of the experimental setup is shown in Fig 1a. The laser pulse is splitted into two parts using beam splitter (BS). The energy of the transmitted laser beam is ~ 4mJ and the energy of reflected laser beam is ~1mJ. The transmitted beam is focused in an argon filled cell of ~ 5mm length using a plano-convex lens of focal length 550mm for generation of higher harmonic orders. The generated harmonics are focused in a low pressure helium/neon gas sheath ($p \sim 10^{-5}$mbar), using a grazing incidence toroidal mirror (R_s~25mm and R_m~10m), which leads to photo-ionization of

atoms present in the gas sheath. The generated photoelectrons are detected using an in-house developed magnetic bottle electron time of flight electrograph (MBETOF).

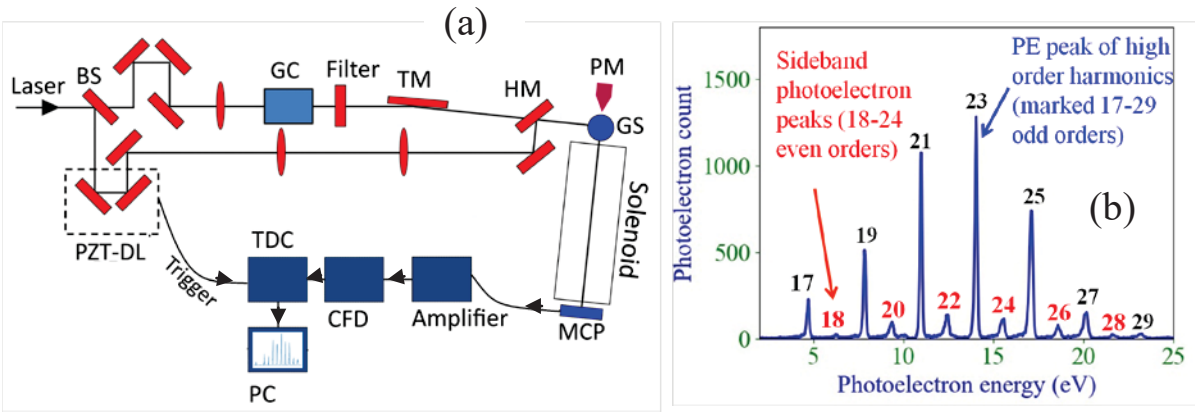

Figure 1: *(a) Schematic of experimental setup used for complete characterization of attosecond high-harmonic pulse train using FROG-CRAB technique, (b) The photoelectron spectrum generated be simultaneous focusing of higher harmonics and dressing IR laser beam in low pressure helium gas sheath at ~ 3×10^{-5} mbar pressure.*

The spectrograph consists of a permanent magnet separated by a solenoid to generate a magnetic bottle configuration, which guides the electrons generated in interaction region (gas sheath) to the micro-channel (MCP) detector. The MCP generates the timing signal of individual electrons falling on it. Every electron is amplified by MCP to 10^6 at the exit and it generate electrical signal upon striking the anode. The MCP signal is amplified by an RF amplifier and detected using time to digital convertor (TDC). The energy resolution *(E /ΔE)* of MBETOF varies from ~400 to ~200 in the photoelectron energy range from ~10eV to ~25eV, which is sufficient for the present experiment. For the cross-correlation measurement, a closed loop piezo electric transducer (PZT) based delay line is installed in the path of the dressing laser beam (reflected from BS). The two beams are then recombined using a holed mirror (HM), where harmonic beam pass through the central hole of HM and dressing beam reflects from the surface. The dressing beam is focused in the gas sheath using plano-convex lens. The spatio-temporal overlapping of higher harmonic beam and the IR laser beam is very crucial to observe the sideband photoelectron peak, as slight misalignment of any of the beams leads to disappearance of the side-band signal. The spatio-temporal overlapping was achieved by observing the interference fringe generated by the overlapping of dressing IR beam and the IR beam which generates harmonics. The alignment is highly sensitive to vibrations, the vibration isolation pads were placed beneath all the experimental tables containing optical elements. A typical photoelectron spectrum is shown in Fig 1b. The position of harmonic orders in the recorded PE spectrum is performed by adding the ionization potential (IP) of sheath gas atom (Neon: IP~21.56eV) to the PE energy and divided by the photon energy of harmonic generating IR laser pulse (~ 1.55eV). The spectral position of 17^{th} to 27^{th} odd harmonic orders and the generated sideband correspond to 18^{th} to 26^{th} even harmonic orders are marked in Fig 1b.

Result and Discussion:

For complete characterization, the photoelectron spectra are recorded by varying the delay between the harmonic and dressing IR laser beam. The scan is taken over a delay of ~ 300fs, till the sideband photoelectron peak is observed in the spectrum. The scan is taken in a delay step size of ~ 20nm (corresponds to ~ 132 as), over a length of ~ 40µm. This corresponds to recording of (40/0.02) ~2000 data files and their post processing thereafter. Thus a Labview automation subroutine is developed at RRCAT, which automatically move the PZT

stage, record data from TDC and save it in separate files. The details of this automation subroutine will be reported separately.

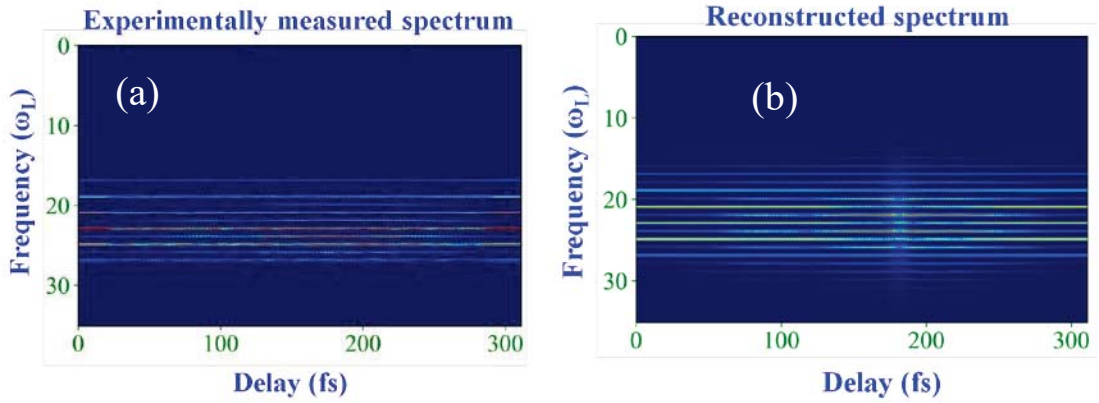

Figure 2: *(a) The experimentally measured spectrogram generated by column stacking of the harmonic spectra derived from the recorded photoelectron spectrum at different delay between the higher harmonics and the dressing IR laser pulse (b) the reconstructed spectrogram using FROG-CRAB algorithm. The frequency on y-axis is multiple of driving laser frequency (ω_L).*

The post processing of data is performed using python code, which generates spectrogram from experimentally recoded photoelectron spectra. The spectrogram is interpolated to generate 8192×8192 matrix. The background noise in the spectrogram is removed using moving average and Baseline-Removal functions of python subroutines. Figure 2a shows the spectrogram generated from the experimentally measured photoelectron spectra and column stacking of these data according to increasing delay between the two pulses. The FROG-CRAB reconstruction algorithm is written in python and it is used to reconstruct the signal (attosecond pulse train) and gate (IR dressing pulse) and the reconstructed spectrogram is shown in Fig 2b. It may be seen in Fig 2b that the reconstructed spectrogram matches closely with the experimentally measured spectrogram.

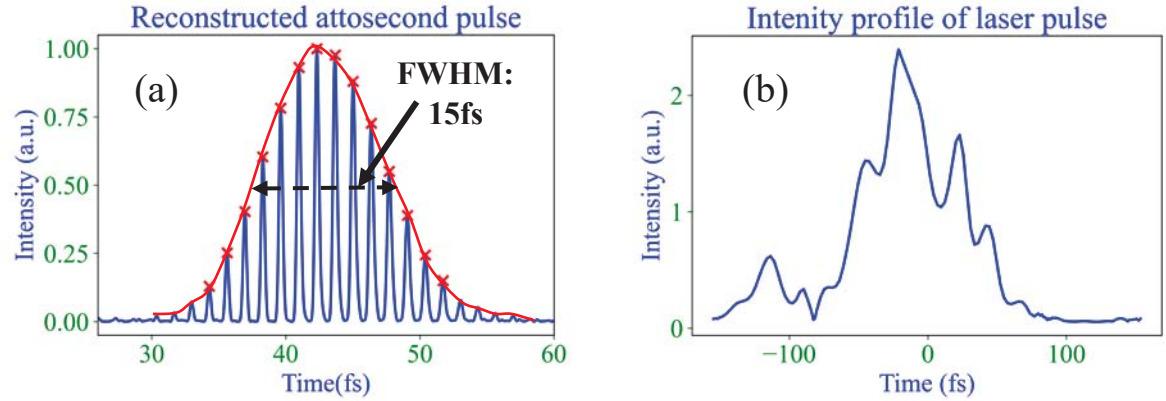

Figure 3: *The reconstructed temporal profile of attosecond pulse trains (signal) generated in argon filled cell, (b) the reconstructed IR dressing laser beam profile (gate). Both viz. the signal and gate pulse are reconstructed using FROG-CRAB algorithm.*

The reconstructed attosecond pulse train (signal) is shown in Fig 3a and the reconstructed IR dressing laser pulse (gate pulse) in Fig 3b. The FWHM width of the attosecond pulse train envelope is measured to be ~

15fs and the width of individual attosecond pulse varies from ~ 300as to ~ 400as. The width of the reconstructed dressing IR pulse is found to be ~ 70fs, which is close to the FWHM of the IR laser pulse measured using autocorrelation technique.

Conclusion

In conclusion, we have designed and developed a facility to fully characterized attosecond pulse train envelope generated through high order harmonic generation using FROG-CRAB technique. The cross-correlation photoelectron spectrum by simultaneous focusing of high-harmonics and IR laser pulse is recorded. The spectrogram is generated by column stacking of the photoelectron spectrum recorded at a different delay between the two pulses. This experimentally measured spectrogram is smoothened and background subtracted. The signal and gate pulse is reconstructed using FROG-CRAB algorithm and the reconstructed spectrogram matched well with the experimentally measured spectrogram. The duration of attosecond pulse is measured to be in the range of ~ 300as to ~ 400as. The overall attosecond pulse train envelope duration is calculated to be ~ 15fs (FWHM).

References

1. C. G. Wahlström *et at, Phys. Rev. A* **48***, 4709 (1993)*
2. P. Antoine *et al, Phys. Rev. Lett.,* 77**,** 1234 *(1996)*
3. K. P. Singh *et al*, *Phys. Rev. Lett.* **104**, 023001 (2010)
4. A. R. Beck *et al, Chem. Phys. Lett.,* **16,** 119 (2015)
5. P. Peng *et al, Nat. Rev. Phys.* **1***,* 144 (2019)
6. S. Haessler *et al*, *Nat. Phys.* **6**, 200 (2010)
7. P.M. Paul et al, *Science* **292**, 1689 (2001).
8. H.G. Muller, *Appl Phys B,* **74**, s17 (2002).
9. K. Varjú et al, *Laser Physics* **15**, 888 (2005).
10. Y. Mairesse *et al*, *Phys. Rev. A*, **71** 0011401(R) (2005).
11. D. J. Kane, IEEE J. Selec. Topics Quan. Elec., **4** 278 (1998)
12. D. J. Kane, IEEE J. Quan. Elec., **35** 421 (1999)

Measurement of Refractive index and Absorption coefficient of 3, 4, 5 -Trinitro 1-H Pyrazole using Terahertz Time-domain Spectroscopy

Rajesh Koalla, Chandan Ghouri, Shivanand Mangali, Naveen Periketi, and A.K. Chaudhary*

Advanced Centre of Research in High Energy Materials (ACRHEM), University of Hyderabad, Hyderabad 500046, Telangana, India

*Corresponding author e-mail: akcphys@gmail.com, akcsp@uohyd.ernet.in

Abstract: This paper reports the terahertz time-domain spectroscopy of 3, 4, 5 -Trinitro 1-H Pyrazole (explosive) between 0.1-1.8 THz range. We employed an indigenously designed terahertz system using LT-GaAs photoconductive antenna as a source and ZnTe crystal an electro-optic detector. In addition, we ascertained the value of refractive index and absorption coefficient of the 3, 4, 5-Trinitro 1 –H Pyrazole in solid powder form.

1. Introduction:

Terahertz Time-domain spectroscopy is an attractive and unique nonionizing and non-destructing spectroscopic technique in the far-IR range. During the past two decades, it has been used in wide range of research applications such as detection of explosives, drugs, biological molecules and identification of concealed objects [1]. Different from the conventional spectroscopic techniques, THz-TDS can provide both types of information in terms of absorption coefficient and the refraction index of a sample with a high signal-to-noise ratio (SNR). The conventional explosives or high energy molecules are sensitive to shocks and incident X-ray radiation and get ionization under the influence of incident radiation. Therefore, there is a need of new types of high explosive molecules with good thermal stability, insensitive to external shocks and high performance [2]. Pyrazole based compounds have attracted renewed attention due to their high heat of formation and density and good thermal stability. 3, 4, 5 -Trinitro 1-H Pyrazole consists of density 2.1 g/cm^3 with detonation velocity and detonation pressure of the order of 9.40 km/s and 41.60 GPa, respectively [3]. As compared to premium high energetic materials such as RDX, HMX, it possesses high detonation velocity and pressure which indicates it's stability and pressure insensitivity [3]. Therefore, it is very safe for long-distance transportation. The structure of 3, 4, 5 Trinitro 1-H Pyrazole is shown in Figure 1(a). To the best of our knowledge, it is the first report on terahertz based characterization in solid powder form.

Table1: *Comparative physical properties of premium explosives with Pyrazole.*

Explosive	Detonation Velocity (km/s)	Detonation Pressure (GPa)	Melting Point (^{o}C)	Density (g/cm^3)	Energy of Explosion (kcal/g)
RDX	8.86	34.23	205.5	1.82	1.25
HMX	9.10	39.40	276	1.91	1.25
3,4,5-Trinitro-1H Pyrazole	9.40	41.60	185	1.86	1.51

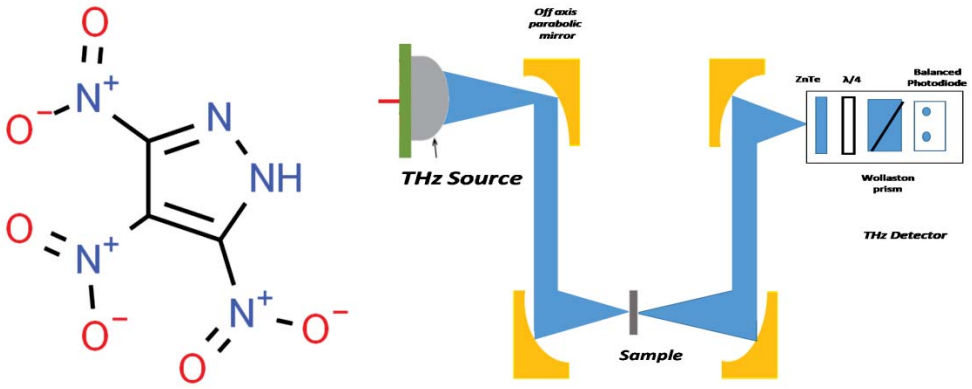

Figure 1: (a) structure of 3, 4, 5-Trinitro 1-H Pyrazole (b) experimental schematic set up for the THz time-domain spectroscopy.

2. Sample Preparation and Experimental Method:

The sample pellets of 12 mm diameter of weight 500 mg were prepared by mixing 100 mg of sample with 400 mg of Teflon [polytetrafluoroethylene (PTFE)] powder. Particle sizes are minimized by mixing the compound and PTFE powder to make a homogeneous mixture. The mixture was subjected to press mills for preparation of pellet. The whole mixture was loaded into a die and pressed with 2 tons of hydraulic pressure. The diameter and thickness of pellets are 12 and 2.16 mm, respectively. A pure teflon pellet of identical size was also prepared and used as a reference.

Figure. 1(b) shows the experimental layout of THz generation and detection. A Ti: sapphire laser-tunable oscillator with pulse duration of 140 fs at a repetition rate of 80 MHz (coherent chameleon ultra-II made) was used as a pumping source. A beam splitter (90:10) was used the laser beam was split into a pump and probe. A transmitted pump beam is used for pumping the Photoconductive antenna for terahertz generation. A half axis parabolic mirror is used to collimate and focus the generated THz radiation was detected by Electro-optical sampling technique using ZnTe Crystal. In the detection arm, the reflected beam is passed through a linear translation stage and loosely focused on detecting setup. The detecting system is connected to a low-noise current preamplifier, which is fed to the lock-in amplifier (Stanford Research Systems, model no. SR830). A mechanical chopper operating at 1.5 kHz is used as a reference to the lock-in amplifier (Stanford Research Systems, model no. SR830). The data acquisition and motion control of the delay stage are done by software using the Lab View program. All measurements were carried out at room temperature under ambient conditions.

3. Results and Discussion:

A typical response of THz time domain temporal and spectral profiles for air, teflon and pyrazole are shown in figure 2 (a), (b) and (c) respectively. The air, Teflon show highest transmission between 0.1 – 1.5 THz range whereas the pyrazole show a short drop at 1.2 THz after that it shows another peak between 1.2 – 1.8 THz range.

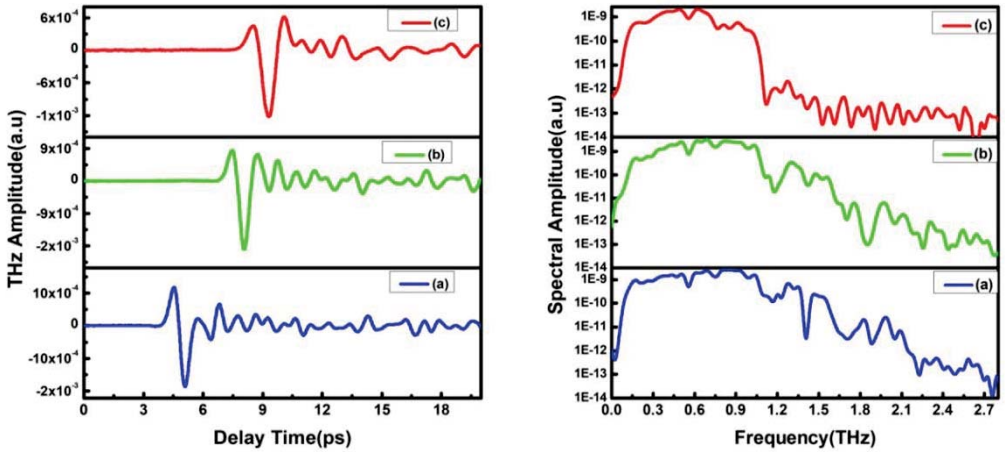

Figure 2: Terahertz temporal profiles and corresponding frequency domain spectrum of (a) Air (b) Teflon and (c) 3, 4, 5 –Trinitro 1-H Pyrazole

Refractive index (n(ω)) and absorption coefficient (α(ω)) were calculated from the FFT spectrum. The intensity ratio of the transmitted radiation from the sample and reference provides the actual transmittance of the sample pellets and is given by eq. (1):

$$T = \frac{|\ E_{sam}\ |}{|\ E_{ref}\ |} \qquad (1)$$

It is related to the complex refractive index N = n + ik, where the real part corresponds to the refractive index and the imaginary part is molar absorptivity. the absorption coefficient (α) is calculated using eq. (2).

$$\alpha(\omega) = -\frac{1}{d}\ln T \qquad (2)$$

Where "d" is thickness of the sample, and the refractive index is calculated using eq. (3)

$$n(\omega) = 1 + \frac{\Delta\Phi C}{2\pi\upsilon d} \qquad (3)$$

Where "ΔΦ" is phase difference between the reference and the sample, c is velocity of light, υ is frequency in THz region.

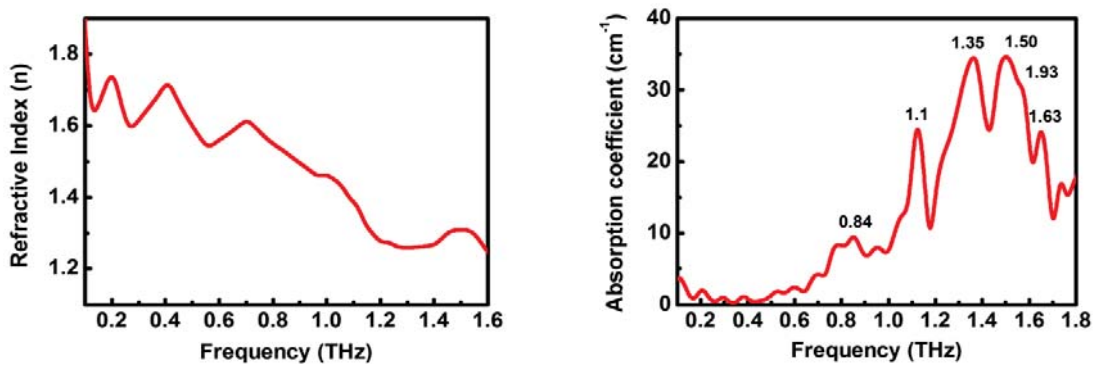

Figure 3: (a) Refractive index, (b) Absorption coefficient of the 3, 4, 5 –Trinitro 1-H Pyrazole

The refraction index and absorption coefficient of 3, 4, 5 Trinitro 1-H Pyrazole in the 0.1–2.5 THz region shown in Figures 3 (a) and 3(b). The refraction index varies between 1.8 and 1.3 in the range of 0.1–2.5 THz. Figure 3(b) shows the absorption coefficient peaks of 3, 4, 5 Trinitro 1-H Pyrazole located at 0.84, 1.10, 1.35, 1.50, 1.63,THz, respectively. The corresponding absorption coefficients are 9.43, 24.5, 34.45, 34.60, 24.19 cm^{-1}, respectively.

4. Conclusions:

We have successfully studied the Terahertz time-domain spectroscopy of 3, 4, 5-Trinitro 1-H Pyrazole between 0.1 – 2.5 THz range. The value of refractive index and Absorption coefficient are also calculated. The value of refractive index varies between 1.8 to 1.3 range.

5. Acknowledgment:

The Authors gratefully acknowledge the financial support provided by the DRDO, Ministry of Defence, and Govt. of India under ACRHEM Phase –III No. ERIP/ER/1501138/M/01/319/D (R&D). And Dr. Ganesh Damarla for many fruitful discussions and the Director, ACRHEM for encouragement.

6. References:

1. Liu Jia, Wen-Hui Fan, Xu. Chen, and Jun Xie. "Identification of high explosive RDX using terahertz imaging and spectral fingerprints." In *Journal of Physics: Conference Series*, 680 (1), 012030. IOP Publishing, (2016).
2. D.Ganesh, E. Narsimha Rao, M. Venkatesh, K. Nagarjuna, G. Vaitheeswaran, A. K. Sahoo, and A. K. Chaudhary. "Time-domain terahertz spectroscopy and density functional theory studies of nitro/nitrogen-rich aryl-tetrazole derivatives." *ACS Omega,* 5 (6), 2541-2551 (2020).
3. M. Venkatesh, K.S. Rao, T.S.Abhilash, S.P. Tewari, and A.K. Chaudhary, 2014. Optical characterization of GaAs photoconductive antennas for efficient generation and detection of Terahertz radiation. *Optical Materials*, *36*(3), 596-601 (2014).
4. P. Ravi, G. M. Gore, V. Venkatesan, Surya P. Tewari, and A. K. Sikder. "Theoretical studies on the structure and detonation properties of amino-, methyl-, and nitro-substituted 3, 4, 5-trinitro-1H-pyrazoles." *Journal of hazardous materials,*183 (1-3), 859-865 (2010):
5. Li, Bu-Tong, Lu-Lin Li, and Lin-Li Liu. "Thermal stability and detonation characters of nitro-substituted derivatives of pyrazole." *Molecular Physics,* 118 (15), e1708491 (2020).
6. Hervé, Grégoire, Christian Roussel, and HervéGraindorge. "Selective Preparation of 3, 4, 5-Trinitro-1H-Pyrazole: A Stable All-Carbon-Nitrated Arene." *AngewandteChemie International Edition,* 49 (18), 3177-3181 (2010).

Anisotropic non-wetting metallic surfaces engineered via femtosecond Laser micromachining

Md Abu Taher, Sri Ram G Naraharisetty, D Narayana Rao
School of Physics, University of Hyderabad, Gachibowli, Hyderabad, India 500046
Email: taherphys20@gmail.com

Abstract:

The stainless steel and copper surfaces were engineered to show anisotropic non-wetting property using controlled and precise micromachining with femtosecond pulses. These surfaces have potentially anisotropic due to the raster scan and - dimensional laser ablation capability of the focused femtosecond pulses. The water droplets on the irradiated surface took the form of an ellipsoidal shape with two different contact angles from two orthogonal azimuthal directions. The surfaces' wetting property evolves from hydrophilic to superhydrophobic nature as time passes till achieving a stable contact angle after three months or even more time. An experimental method to calibrate the ellipsoidal droplet volume and analytical calculations for hydrophilic and hydrophobic surfaces is presented over a broad range. The comparative study of the evolution of anisotropic contact angles and their droplet spreading dynamics are studied. Triple contact line (TCL) theory predicts the contact angle depends only on the droplet's pinning boundary and irrelevant to the surface roughness inside the droplet. We proved that the ellipsoidal droplets are indeed fitting to the TCL theory with high accuracy. This work experimentally validates the TCL theory over a broad range of contact angles with reasonable confidence.

Abbreviations fs: Femtosecond, FESEM: Field Effect Scanning Electron Microscope, LDW: Laser Direct Writing. TCL: Triple contact line, CA: Contact Angle, Cu: Copper, SS: Stainless Steel, 2-D: Two-dimensional, 3D: Three-Dimensional.

Introduction:

A water droplet kept on an fs patterned surfaces forms an ellipsoidal shape rather than a spherical one, with a contact angle depending on the surface's properties[1,2]. As the surface's roughness increases, the contact angle increases and can behave as a superhydrophobic surface if the contact angles (CAs) are greater than 150º and these surfaces behaved the same as the ''lotus leaf effect'' [3]. There were reports to which showed mimicking naturally occurring functional surfaces[4]. Mimicking these surfaces is demonstrated on several surfaces such as ZnO nano rods[5], metallic surfaces[6], polymers[7], semiconductors[8], etc. On 2D symmetric surfaces, liquid wetting behavior is extensively referred by Wenzel[9] and Cassie Baxter models[10]. As per the Wenzel model, a liquid droplet penetrates partially into the micro-cavities on the surface. As in the Cassie-Baxter model, an intermediate interface is filled with air between the water droplet and substrate; the air on the surface valleys suspends the liquid droplet. These models interpret that the CAs are dependent on the surface roughness. The contact angle formation is a one-dimensional problem, as shown by Gao et al. [11]. The CAs do not depend on the surface roughness inside the droplet. Liu and coworkers further investigate this TCL theory to explain the wetting behavior on symmetrical droplets[12]. This theoretical work related the droplet's effective volume derived from the physical parameters of the triple contact line of a spherical droplet with the contact angle and compared their theory with the literature experimental values. All these works are restricted to the symmetric surfaces with spherical droplets. This

paper formulated and experimentally validated the TCL model on asymmetric droplets over a broad range of contact angles.

Experimental Techniques and Materials used:

Two different kinds of substrates, SS and Cu, were fabricated with line spacing from 15 µm to 60 µm at a fixed laser beam parameter (average power 1.05-Watt, Energy per pulse 5.25 µJ, focused spot diameter ~22 µm and fluence 1.3 J/cm^2) and for each spacing both in single and dual scan modes using fs fiber laser (Amplitude, Satsuma). Its central wavelength is 1030 nm, pulse duration of 350 fs, and operated at 200 kHz fixed repetition rate. The Schematic representation of the LDW setup is shown in Fig.1(A). The combination of half-wave plate and polarizer is used to control the laser power and the polarization state of the input beam. Laser patterning is performed in a raster fashion over the entire surface, as shown schematically in **Fig. 1(B)**, in the case of single scan substrates. For detailed laser writing setup and CAs measurements, refer to [1]; only brief experimental details are discussed here. The substrate is mounted on a computer-controlled -axis stage (Newport) for precise machining with 1µm accuracy, as illustrated in Fig**. 1(A)**. Surface morphological characterizations of SS/Cu substrates were carried out FESEM (Zeiss Ultra). The anisotropic droplet images were taken from two orthogonal directions, keeping the laser grooves' reference [1].

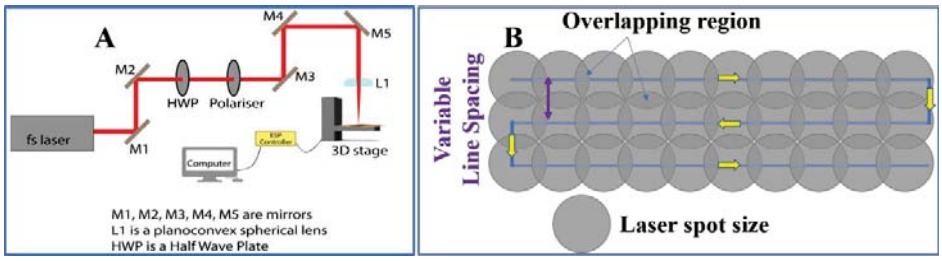

Fig. 1: *Schematic of (A) Experimental laser direct writing setup, (B) Periodic raster scanning processes.*

Results and Discussions:

Total 16 substrates of Cu and SS were fabricated with the fixed fluence of 1.3 J/cm^2, with line spacing of 15, 30, 45, and 60 µm. Each set of spacing is with both single and double laser scan methods, as presented in **Table 1**. Our laser fabricated surfaces yielded a very high contact angle of ~172° on Cu for the C5 substrate. The FESEM images are shown in **Fig. 2** of Cu and SS substrates, in 1st and 2nd column, respectively. Laser irradiated surfaces of four sets of line spacing between the two successive scans (as marked on the left side of **Fig. 2**). The single and double scan are represented in two sets of columns for each of the spacing. Each substrate's FESEM images are presented in two different magnifications to understand their macroscopic surface morphologies (scale bar is 20 µm) and microscopic nanostructures (scale bar 500 nm). The first scan of LDW increases the surface roughness and optical absorption compared to the un-patterned surface. Therefore, the second scan (orthogonal to the first scan) generates higher and smoother groove depth due to efficient materials' laser ablation. With the second scan groove being deeper over and on top of the first scan groove, the combination forms a very clear square grid microscopic structure formation. The microscopic surface morphologies of double scan substrates are different from single scan substrates, which can be observed from the higher magnified FESEM images.

Line spacing (µm)	Type of Scan	Cu substrates				SS steel substrates			
		No.	θ_x	θ_y	$\Delta\theta$	No.	θ_x	θ_y	$\Delta\theta$
15	Single	C1	167.7±1.2°	170.5±2.7°	2.8±1.5°	S1	164.1±0.8°	165.1±0.6°	1±0.2°
30	Single	C2	166.4±2.5°	168.6±1.8°	2.4±0.7°	S2	134.8±2.1°	141.6±1.5°	6.8±1.3°
45	Single	C3	165.1±2.4°	166.5±2.3°	1.4±0.1°	S3	163.2±0.1°	165.9±0.1°	2.7±0.0°
60	Single	C4	162.8±5.4°	166.1±3.5°	3.3±1.9°	S4	162.7±1.1°	164.6±1.4°	1.9±0.2°
15	Double	C5	169.3±1.4°	172.4±2.1°	3.1±0.7°	S5	164.8±0.9°	167.6±0.9°	2.8±0.0°
30	Double	C6	167.6±2.7°	169.2±2.7°	1.6±0.0°	S6	167.5±2.2°	168.4±2.1°	0.9±0.1°
45	Double	C7	167.1±1.2°	168.1±1.5°	1.0±0.3°	S7	168.3±1.9°	169.6±2.4°	1.3±0.5°
60	Double	C8	169.3±0.6°	171.0±0.7°	1.7±0.1°	S8	168.6±0.8°	171.1±1.0°	3.5±0.2°

Table. 1. *Laser irradiation parameters and anisotropic droplet parameters on laser patterned Cu and SS substrates.*

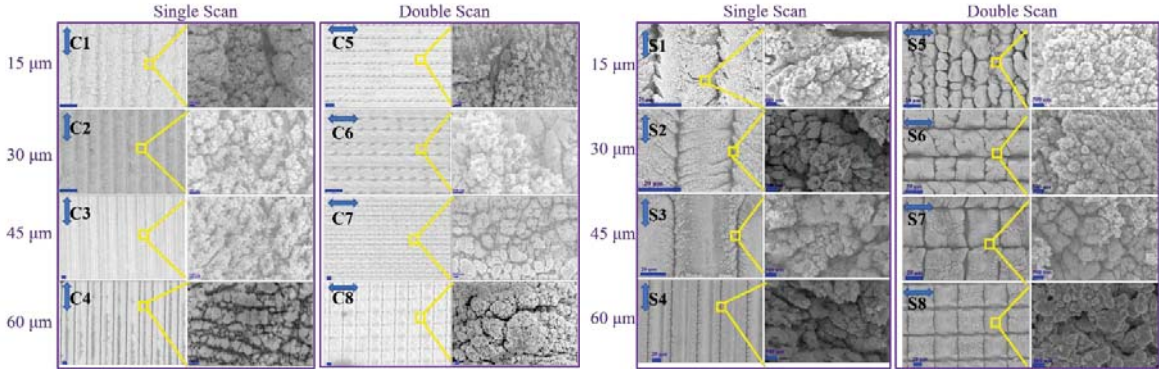

Fig. 2*. Optical micrographs of the fs laser irradiated Cu and SS substrates. The magnified images with a scale bar of 500nm are shown next to each substrates' main images (20 µm scale bar), and the arrows represent the scanning direction.*

Triple contact line theory and its approach to the hydrophilic surfaces:

After the evolution of more than three months, the anisotropic contact angles were presented for Cu and SS substrates in **Table 1**, derived from a large set of data collected for statistics. Also, during the evolution of the contact angles from the fabrication day, we collected the contact angle measurements. In each measurement, we got the CAs along the groove's direction and CAs orthogonal to the grooves. Apart from the CA's, we also measured the droplet dimensions in both the orthogonal directions. **Fig. 3(A) and (B)** gives the schematic illustration of the measured ellipsoidal dimensions or parameters. The length of the semi-major axis along the groove is '***a***' and the corresponding contact angle is '$\boldsymbol{\theta_X}$' is measured. Similarly, length of the semi-minor axis perpendicular to the groove is '***b,***' and the corresponding contact angle is '$\boldsymbol{\theta_y}$' is measured**.** Also, we measure the height of the droplet '***h***' and derive the value of '***c***' from droplet parameters. These parameters are shown in **Fig. 3(A) and (B)**; our length measurements are calibrated with a reference. The dimensionless effective volume function '$\boldsymbol{f(\theta_x, \theta_y)}$' is expressed by equation (1)[1].

$$f(\theta_x, \theta_y) = \frac{ab(h-c)^2}{c^2(2ch-h^2)} = \cot\theta_x \cot\theta_y \qquad (1)$$

The primary purpose of this dimensionless volume function, $f(\theta_x, \theta_y) = cot\theta_x\, cot\theta_y$, is to relate the ellipsoidal droplet's parameters with the contact angles in orthogonal directions for CAs greater than 90º. These droplet parameters must be unique for given contact angles determined by the droplet's pinning line boundary at the air, solid, and liquid interface. This function consists of the parameters of a, b, c, and h (where h is the height of the droplet). These parameters are experimentally measurable for a given sessile droplet. We calculated the functional values and compared it with $f(\theta_x, \theta_y) = cot\theta_x\, cot\theta_y$, orthogonal contact angles. We observed an excellent fit between the experimentally derived values of $f(\theta_x, \theta_y)$ for the observed CA's and the estimated $f(\theta_x, \theta_y) = cot\theta_x\, cot\theta_y$ [1]. This is a piece of direct evidence for supporting the TCL theory experimentally.

In contrast to the widely accepted Wenzel and Cassie models, TCL (triple contact line theory) predicts the contact angles depend only on the droplet's pinning line boundary and is irrelevant to the surface roughness inside the droplet. Surface roughness is essential for producing higher contact angles as it offers the barrier for the flow of the liquid. As we create anisotropic surfaces by LDW techniques, the surface offers two different barriers against the liquid flow in the orthogonal directions to form ellipsoidal droplets.

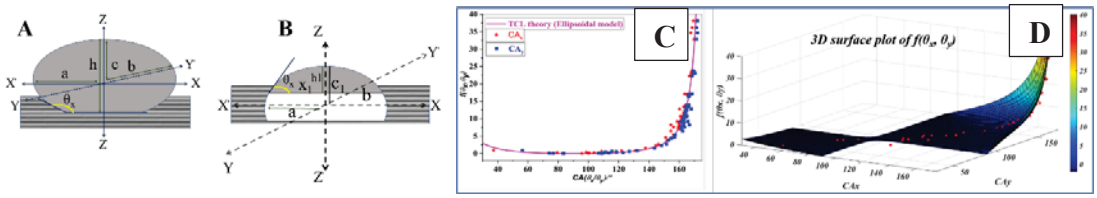

Fig. 3: *Schematic of anisotropic (A) Superhydrophobic and (B) hydrophilic water droplets laser irradiated substrates. C &D: Combined data points from Cu and SS together. These graphs show the variation of* $f(\theta_x, \theta_y) = \cot\theta_x \cot\theta_y$ *as a function of two anisotropic CAs. C: 2D plots of* $f(\theta_x, \theta_y)$ *vs CAs of water droplets on both Cu and SS substrates.*

TCL analysis for droplets on the Cu and SS surfaces:

The CAs given in **Table 1** is the statistical average of the several droplets formed on Cu patterned surfaces. Each droplet formed is taken as a data point for obtaining *a, b, c, h,* $_x$ and θ_y parameters of an ellipsoidal droplet. From there, we arrived at a dimensionless volume function value $f(\theta_x, \theta_y)$, which is obtained as per Equation (2). **Fig. 3A** shows a plot of the dimensionless function $f(\theta_x, \theta_y)$ on the y-axis and the contact angles of both along the groove and perpendicular to the groove is on the x-axis, for all the droplets formed on both Cu and SS. . The pink curve represents the theoretical value $(cot\,\theta_x\, cot\,\theta_y)$. The stars and blue colored squares represent the experimentally obtained data points corresponding to the CAs in the grooves' direction and orthogonal to the grooves, respectively, for a given functional value. The data points in this graph include the points obtained during the evolution of the Cu surface. Along the groove CAs value are represented as red stars, and across the groove are represented as blue squares. For a given set of the CAs (θ_x, θ_y) there is a unique value for the function $f(\theta_x, \theta_y)$. Hence, for a given droplet along the groove and across the groove will have same y-axis value on these plots. In other words, each droplet is a unique value in the y-axis with corresponding θ_x & θ_y values. The solid line is the predicted values from

TCL theory. One can see the correlation between the experiment and the theoretical values. The actual functional value always lies between the star and square point along the y-axis. There is a unique value of $f(\theta_x, \theta_y)$ for a given θ_x, θ_y value, hence this 2D figure is a projection of the actual 3D plot in the diagonal plane. The 3D plot of these values is shown in **Fig. 3D**. Each water droplet condenses to a single circular point in this graph having a unique function value $f(\theta_x, \theta_y)$ for a fixed θ_x & θ_y value. All the points correlate to the functional value, color grid surface, with a R^2-regression coefficient of 0.81 gives confidence in the model.

Conclusions:

We optimized the best conditions for Cu surface to behave as superhydrophobic with CA as much as 172º. We experimentally measured the dimensions of these ellipsoidal droplets from hydrophilic to superhydrophobic cases. Expressions for the ellipsoidal cap volume estimations were presented for the entire range of contact angles. A dimensionless volume function is presented and uniquely depends on the droplet's dimensions or the pinning boundary of the droplet. The experimentally measured data and theoretically predicted values of this function show very good correlation overall ranges of contact angles. We believe our work will help in developing new kinds of functional surfaces with intrinsic anisotropy and the droplet's non-contact volume calibration for many quantitative measurements.

References:

[1] M.A. TAHER, H. Prasad, navanithi Krishnan P K, N.R. Desai, S.R.G. Naraharisetty, Ellipsoidal droplet formation on anisotropic superhydrophobic copper surface, Surf. Topogr. Metrol. Prop. (2019). https://doi.org/10.1088/2051-672x/ab2d80.

[2] L. Tie, Z. Guo, W. Liu, Anisotropic wetting properties on various shape of parallel grooved microstructure, J. Colloid Interface Sci. 453 (2015) 142–150. https://doi.org/10.1016/j.jcis.2015.04.066.

[3] M.J. Nine, T.T. Tung, F. Alotaibi, D.N.H. Tran, D. Losic, Facile Adhesion-Tuning of Superhydrophobic Surfaces between “Lotus” and “Petal” Effect and Their Influence on Icing and Deicing Properties, ACS Appl. Mater. Interfaces. 9 (2017) 8393–8402. https://doi.org/10.1021/acsami.6b16444.

[4] Y. Si, F. Yang, Z. Guo, Bio-inspired one-pot route to prepare robust and repairable micro-nanoscale superhydrophobic coatings, J. Colloid Interface Sci. 498 (2017) 182–193. https://doi.org/10.1016/j.jcis.2017.03.063.

[5] M.T.Z. Myint, G.L. Hornyak, J. Dutta, One pot synthesis of opposing “rose petal” and “lotus leaf” superhydrophobic materials with zinc oxide nanorods, J. Colloid Interface Sci. 415 (2014) 32–38. https://doi.org/10.1016/j.jcis.2013.10.015.

[6] S. Milles, J. Dahms, M. Soldera, Stable Superhydrophobic Aluminum Surfaces Based on Laser-Fabricated Hierarchical Textures, (2021).

[7] D. Xia, X. He, Y.B. Jiang, G.P. Lopez, S.R.J. Brueck, Tailoring anisotropic wetting properties on submicrometer-scale periodic grooved surfaces, Langmuir. 26 (2010) 2700–2706. https://doi.org/10.1021/la904505n.

[8] M. Kumar, R. Bhardwaj, K.C. Sahu, Motion of a Droplet on an Anisotropic Microgrooved Surface, Langmuir. 35 (2019) 2957–2965. https://doi.org/10.1021/acs.langmuir.8b03604.

[9] R.N. Wenzel, Resistance of solid surfaces to wetting by water, Ind. Eng. Chem. 28 (1936) 988–994. https://doi.org/10.1021/ie50320a024.

[10] A.B.D. Cassie, Contact angles, Discuss. Faraday Soc. 3 (1948) 11–16. https://doi.org/10.1039/DF9480300011.

[11] L. Gao, T.J. McCarthy, How Wenzel and Cassie Were Wrong, Langmuir. 23 (2007) 3762–3765. https://doi.org/10.1021/la062634a.

[12] J. Liu, Y. Mei, R. Xia, A new wetting mechanism based upon triple contact line pinning, Langmuir. 27 (2011) 196–200. https://doi.org/10.1021/la103652s.

Estimation of Precise Concentration of N and NP Compound Fertilizers Sample with Laser Interaction Technique

P. Baikar, A. Rawankar, V. Kshirsagar, S. Jagtap
Department of Electronics and Telecommunication, Vidyalankar Institute of Technology
University of Mumbai, India
pujabaikar@gmail.com

Abstract
Fertilizer is an important factor in plant growth, which improves the productiveness of plants and enhance the natural fertility of soil. Detection of precise concentration of fertilizers sample is one of the key issues. In this paper, the laser interaction technique combined with Beer-Lambert's law were employed to design system setup able to record the absorption and concentration of fertilizers sample. When laser light interacts with fertilizers sample, the molecules present inside medium undergo vibrational state at appropriate frequency due to its chemical structure. The technique derives concentration of nitrogen and DAP compound fertilizers sample in terms of photodetector voltage with high precision.
Keywords: Beer-Lambert's law, LabVIEW, fertilizers, Transmittance, DAP.

1.Introduction

The primary nutrients like nitrogen (N), phosphorus (P), potassium (K) is naturally present in soil. Artificially these primary nutrients are provided through fertilizers to enhance the plant growth factor but excessive use of fertilizers is harmful for agricultural soil [5]. In order to control over-fertilization case, there is need to estimate the presence of fertilizer. It is very important to detect the presence of fertilizers sample inside agricultural soil for precision agriculture. However, the traditional soil testing methods has the disadvantages of taking large time for testing and expensive in cost [6].

The new proposed experimental technique gives the optical measurement of fertilizers samples by using visible and near infrared laser light with photodetector. In this work, laser absorption technique is totally based on the Beer-Lambert law which is applicable for detection of chemical samples. Beer's law states that the concentration of chemical solution (C) is directly proportional to the absorbance of sample (A). Lambert's law states that the length of absorbing medium is directly proportional to the absorbance of chemical sample (A) [1].

$$A = \log_{10} \frac{I_0}{I_1} \tag{1}$$

$$A = \varepsilon CL \tag{2}$$

From equation (1) and (2),

$$\log_{10} \frac{I_0}{I_1} = \varepsilon CL \tag{3}$$

The absorbance of chemical sample (A) is totally depending on the molar concentration (C) in [mol L^{-1}], molar absorptivity (Ɛ) in [$Lmol^{-1}cm^{-1}$], length of absorbing medium (L) in [cm]. In this work, when laser light of appropriate wavelength is passing through the fertilizers sample then the chemical species absorbs photon light. Depending on the chemical composition of fertilizers sample solution, it absorbs different wavelength of light [2]. From photon absorption of light in terms of photodetector voltage [mV] inside the absorbing medium, it is possible to detect presence of fertilizers sample [3].

2. System Setup

Figure. 1: Block Diagram of System Setup

In this experimental work, lasers with high power are used as a source with different wavelengths. When laser light is interacted with the fertilizers sample inside the container, the molecule in sample start vibrating at a particular wavelength of light and this vibration is totally depends on composition of fertilizers sample and chemical bonding between atoms [2]. From photon absorption in mV inside the absorbing medium, it is possible to determine and calculate the concentration of fertilizers sample [3]. LabVIEW programming is done in such a way that the absorption in terms of photodetector voltage and percentage concentration will be observed. Different fertilizers sample shows absorption at different wavelength of light [4]. In this technique Beer-Lambert's law derived in terms of photodetector voltage and concentration instead of intensity of light and concentration.

3. Experimental Section

Experimental platform consists of number of fertilizers sample and proposed system setup. In this, when laser light of selective wavelengths with high power are focused on fertilizers sample inside the absorbing medium then laser light is interacted with absorbing medium. Some amount of photon light is absorbed, some part is reflected within medium and remaining amount of light is transmitted [2]. The transmitted light is captured at the photodetector in terms of voltage (mV). The precise concentration of fertilizers sample is obtained by using laser absorption technique and the mathematical model for Beer-Lambert law is derived for fertilizers sample.

3.1. Concentration Analysis for Nitrogen Compound Fertilizer

Nitrogen compound fertilizers sample shows photon absorption of light at wavelength of 405 nm. The figure 2a shows the plot for varying concentration of nitrogen sample versus absorption loss. From figure 2a and 2b we get equation (4) and equation (5) respectively. The figure 2b shows plot for varying length of absorbing medium versus absorption loss. As length of absorbing medium start increasing then absorption loss goes on decreasing exponentially.

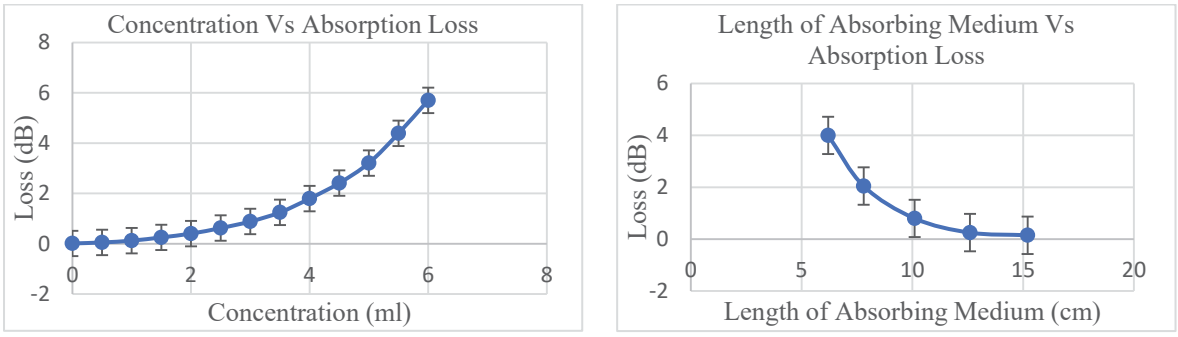

(a) (b)

Figure 2: Performance Plot of Nitrogen Compound Fertilizers Sample: (a)Concentration Vs Absorption Loss; (b)Length of Absorbing medium Vs Absorption Loss

$$20\log_{10}\frac{V_o}{V_i} = A_1C + B_1C^2 \quad \ldots\ldots (0\ ml \le C \le 6\ ml \text{ and } 0\ dB \le A \le 5.7\ dB) \tag{4}$$

$$20\log_{10}\frac{V_o}{V_i} = A_2\left[\frac{\mathrm{EXP[B_2.L]}}{L}\right] \quad \ldots\ldots (6.2\ cm \le L \le 15.2\ cm \text{ and } 0\ dB \le A \le 4\ dB) \tag{5}$$

From equation (4) and equation (5), the Beer-Lambert's law expressed as,

$$20\ \log_{10}\frac{V_o}{V_i} = \varepsilon\int(A_1C + B_1C^2)\,dC\,.\int\left(A_2.EXP\left[\frac{\mathrm{EXP[B_2.L]}}{L}\right]\right)dL \tag{6}$$

Transmittance is expressed as,

$$T = 10^{-\varepsilon\int(A_1C+B_1C^2)\,dC.\int\left(A_2.EXP\left[\frac{\mathrm{EXP[B_2.L]}}{L}\right]\right)dL} \tag{7}$$

Here V_o , V_i , C, L and T are expressed as output voltage, input voltage, concentration, length of absorbing medium and transmittance respectively. These A_1, B_1, A_2, B_2 are curve fitting constants. From above equations it clearly observed that the absorption loss is directly proportional to the concentration of sample and inversely proportional to the length of absorbing medium.

3.2. Concentration Analysis for NP Compound Fertilizers

NP compound fertilizer is a Di-Ammonium Phosphate (DAP) Compound fertilizer. This compound fertilizer is a combination of nitrogen and phosphate compound. DAP shows higher photon absorption of light at wavelength of 660 nm. The figure 3a shows the concentration of DAP versus absorption loss. As concentration of DAP increases then absorption loss start increases. From figure 3a and 3b we get equation (8) and equation (9) respectively. The Figure 3b shows length of absorbing medium versus absorption loss. As length of absorbing medium increases then absorption loss decreases.

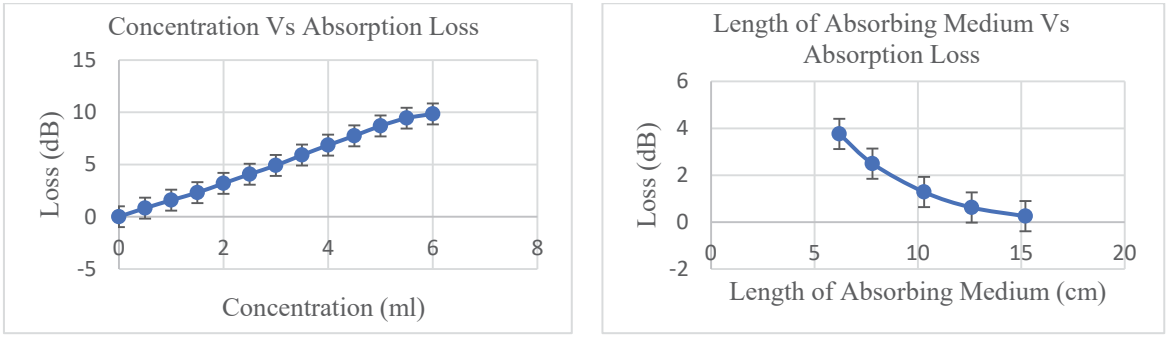

(a) (b)

Figure 3: Performance Plot of NP (DAP) Compound Fertilizers Sample: (a)Concentration Vs Absorption Loss; (b)Length of Absorbing medium Vs Absorption Loss

$$20\ \log_{10}\frac{V_o}{V_i} = A_1C + B_1C^2 \quad \ldots\ldots (0\ ml \le C \le 6\ ml\ and\ 0\ dB \le A \le 9.841\ dB) \tag{8}$$

$$20\log_{10}\frac{V_o}{V_i} = A_2.EXP[B_2.L] \ldots\ldots (6.2\ cm \le L \le 15.2\ cm\ and\ 0\ dB \le A \le 3.762\ dB) \tag{9}$$

Equation (8) and equation (9) expressed the Beer law and Lambert law for NP compound fertilizer in terms of photodetector voltage, concentration and length of absorbing medium. From equation (8) and equation (9), the Beer-Lambert's law expressed as,

$$20\ \log_{10}\frac{V_o}{V_i} = \varepsilon\int(A_1C + B_1C^2)\,dC\,.\int(A_2.EXP[B_2.L])\,dL \tag{10}$$

Transmittance is expressed as,

$$T = 10^{-\varepsilon \int (A_1 C + B_1 C^2)\, dC . \int (A_2 . EXP[B_2 . L])\, dL} \quad (11)$$

4. Results and Discussion

Different high-power lasers with different wavelengths are used in this experimental work. Fertilizers sample i.e. nitrogen and NP compound are detected at different laser light of wavelength. Detection is totally based on the absorption of light in terms of photodetector voltage. As the concentration increases in absorbing medium then corresponding output voltage is decreases because of absorption loss at a particular wavelength. Figure 4 represent that the different fertilizer absorbs different wavelength of light.

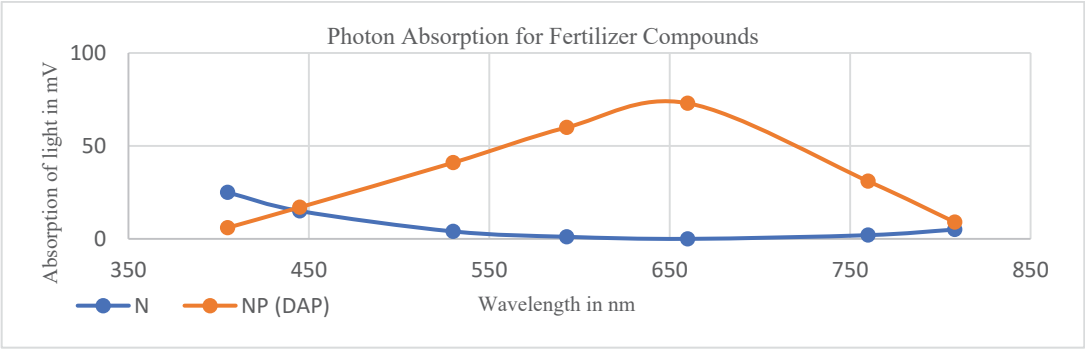

Figure 4: Absorption of Nitrogen and Di-Ammonium Phosphate in (mV) at different wavelength (nm)

Absorbance level of each nutrient is different at different wavelength. Nitrogen shows higher absorption at wavelength 405 nm. Di-Ammonium Phosphate shows the photon absorption of light at both wavelength 530 nm and 660 nm but absorption level is higher at wavelength of 660 nm in terms of photodetector voltage.

5. Conclusion

The experimental laser interaction technique is used to detect the precise concentration of fertilizers sample with different wavelengths of laser. Beer-Lambert law is derived in terms of photodetector voltage and concentration to preserve the natural fertility of agricultural soil. Absorption in terms of voltage for nitrogen and NP compound fertilizers sample are observed at wavelength 405 nm and 660 nm respectively. This experimental setup detects the presence of nitrogen and NP compound fertilizers sample in terms of photodetector voltage for approximately 69000 ppm concentration of aqueous solution. The same technique is applicable for detection of both single element and compound of chemical fertilizers sample. Furthermore, due to its cost effectiveness it can be easily adopted in many other application fields.

References

1. R. Liu, L. Tao, X. Tian, M. Mohammad, Y. Yang and T. Ren, *Sensors* **16**, 1234 (2016).
2. A. Rawankar, M. Nanda, H. Jadhav, P. Lotekar, R. Pawar, L. Sibichan, A. Pangare, *3rd Intern. Confer. on Micro. Photo.*, (2018).
3. P. Krishnan., J. Alexander, B. Butler and J. Hummel,". *Soil Science Sco. J.* **44**, 1282 (1980).
4. J. Piekarczyk, C. Kazmierowski, S. Krolewicz and J. Cierniewski, *Sel. Top. Appl. Earth Obs. Remote Sens.* **9**, 827 (2016).
5. K. Yusof, S. Isaak, N. Rashid, N.Mgajikin, *UTM Jurnal Teknologi*, **78**, 227 (2016).
6. P. Nie, T. Dong, Y. He and F. Qu, *Sensors* **17**, 1102 (2017).

Bioreduction Potentials of *Cynadon Dactylon* for EcoFriendly Silver Nanospheres

N. Venkateswara Reddy[a], L. Jyothi[c]*, T. Sreekanth[b], N. Sri Ram Gopal[c] and Narayana Rao Desai[c#]
[a]*Department of Physics and Chemistry, Mahatma Gandhi Institute of Technology, Gandipet, Hyderabad, Telangana, India: 500075*
[b]*Department of Physics, JNTUH College of Engineering, Nachupally, Jagitial, Telangana, India: 505 501*
[c*#]*School of Physics, University of Hyderabad, Telangana – 500046, India*
[*#]*E-mail address:* jyothik6@yahoo.co.in, dnrsp@uohyd.ac

Abstract: Silver nanoparticles (AgNPs) were biosynthesized using Cynadon dactylon extract by green synthesis at room temperature. The photoconstituents present in the extract act as reducing and stabilizing agents for AgNPs. Their size, shape, morphology and stability were investigated. The local field enhancement effect of AgNPs on the luminescence properties of $Eu(TTFA)_3$ and $Sm(TTFA)_3$ complexes were investigated. Luminescence intensities of the complexes were enhanced several times in the presence of silver and gets quenched with further increase of the concentration of AgNPs. The nonlinear optical properties (NLO) of NPs were studied using Z-scan technique in nanosecond time domain.

Introduction:

Synthesis of silver nanoparticles (Ag NPs) using plant extracts is an emerging field of nanotechnology due to extraordinary properties and their novel applications in fields of science and technology such as optoelectronics, pharmaceuticals, biomedicine and photonics. Various conventional methods such as chemical, microbes mediated synthesis etc., are being utilized for the preparation of silver particles. Microbial mediated synthesis is not feasible for large scale production of NPs due to heavy lab maintenance. Whereas, biological synthesis of Ag NPs using plants extracts is an easy, efficient and environment friendly way. Surface Plasmon absorption of metal nanoparticles arises from collective oscillations of free electrons. It can be tuned by changing the parameters like size and shape of nanoparticles. Localized surface plasmons modify the optical properties of rare earth ions. Luminescence enhancement depends on multiple parameters a) coupling distance between the metal nano particles b) distance between the metal naoparticles and rare earth ions c) concentration of rare earth ions and metal nano particles [1]**.** Here, Ag nano particles synthesized via biosynthesis method allows the fine control of coupling distances of metal nano particles and rare earth ions. Hence there is plasmon induced local field enhancement of rare earth ion emissions.

Materials and Methods: Synthesis of Nanoparticles

Fresh Cynadon dactylon leaves were thoroughly rinsed in deionized water several times. Ten grams of leaves were chopped into pieces, homogenized and boiled in 100 ml of distilled water for 5 min. The mixture was then cooled down to room temperature and filtered with Whatman no. 1 filter paper. The filtrate was again filtered with 1 mm filter paper to remove granules and later refrigerated at 4 ^{0}C for further use. Briefly, 1 mM silver nitrate ($AgNO_3$) aqueous solution was prepared and used for the synthesis of Ag NPs. 3 ml of leaf extract was mixed with 30 ml of 1 mM $AgNO_3$ solution. Initially the solution was transparent and after few minutes the solution turned into dark reddish colour indicating the formation of Ag NPs. All these processes have been carried out at room temperature. The experiment was repeated thrice to confirm the reproducibility. Active compounds present in Cynadon dactylon extract were responsible for the reduction of silver ions.

Results and Discussion

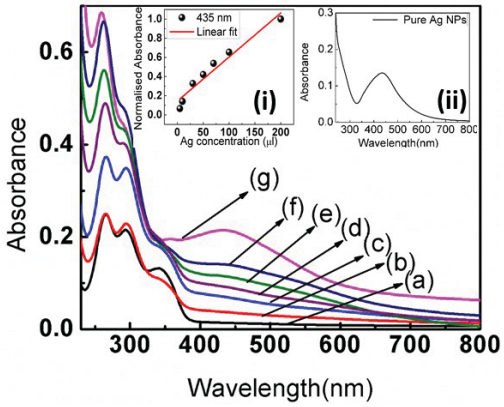

Fig.1. *UV-Vis absorption spectrum of different concentrations of Ag NPs with Eu 20 µM. Inset Fig. shows (i) Increase in absorption with Ag NPs concentration (ii) surface plasmon absorption peak of pure Ag Nps*

When the aqueous $AgNO_3$ was added to the Cynadon dactylon extract, the colour of the reaction mixture turned from transparent to dark reddish due to excitation of surface Plasmon of AgNPs. Formation of the AgNPs was confirmed by monitoring the surface Plasmon resonance (SPR) peak of the metallic nanoparticles, which is around 435 nm as shown in inset Fig. 1(ii). The spherical shape of AgNPs leads to single SPR band as predicted from the Mie theory. Fig. 1. shows the absorption spectra of different concentrations (5, 10, 20, 50, 70, 100 and 200 µl) of Ag NPs with 20 µl concentration of $Eu(TTFA)_3$ solution. Absorption of the combined solution of AgNPs and Eu complex with the bands at 262, 342 and 435 nm, and the absorption band at 300-400 nm are slightly red-shifted due to the interaction between AgNPs and complex molecules, i.e. Plasmon field around the Ag NPs affecting the Eu^{3+} ions. With increase in the concentration of AgNPs, surface Plasmon peak at 435 nm is same as that of the pure Ag colloidal solution as shown in inset Fig. 1(i). Inset Fig. 1(i) shows linear increase in the absorbance with increase of AgNPs concentration in 20 µl europium complex solutions indicating that the AgNPs did not agglomerate.

Fig. 2 represents the transmission electron microscopy (TEM) images of the synthesized Cynadon dactylon extract capped AgNPs. TEM analysis (Fig. 2a) clearly revealed the uniform and well dispersed formation of spherical nanoparticles. From Fig. 2 (b&c) crystalline nature of the AgNPs and its correspnding planes are observed, which are supported by XRD in Fig. 2. Spherical particles' mean diameter was 6.5 nm with ranging from 3-14 nm (Fig. 2d).

Figs. 3(a) and (b) shows the absorption spectra of pure $Eu(TTFA)_3$ and $Sm(TTFA)_3$ complexes with absorption bands at 262 and 342 nm. Figs. 3(c) and (d) correspond to the luminescence spectra of pure $Eu(TTFA)_3$ and $Sm(TTFA)_3$. Fig 4(a) and (b) show the luminescence emission spectra of $Eu(TTFA)_3$ and $Sm(TTFA)_3$ with Ag NPs respectively excited at 350 nm. In the case of Eu^{3+} ions, electric-dipole transition band at 614 nm ($^5D_0 \rightarrow {}^7F_2$) is sensitive to the local environmental fields and its enhancement factor (EF) is 8.7 while magnetic dipole transitions at 577 nm and 590 nm ($^5D_0 \rightarrow {}^7F_0$ and $^5D_0 \rightarrow {}^7F_1$) EFs are 3.8 and 5.4 in the presence of AgNPs. Inset fig shows the dependence of luminescence intensity on the concentration of Eu complex (20, 30, 40 μl) with varying Ag concentration from 5 to 200 µl. Enhancement of luminescence intensity is seen for 20µl Eu complex

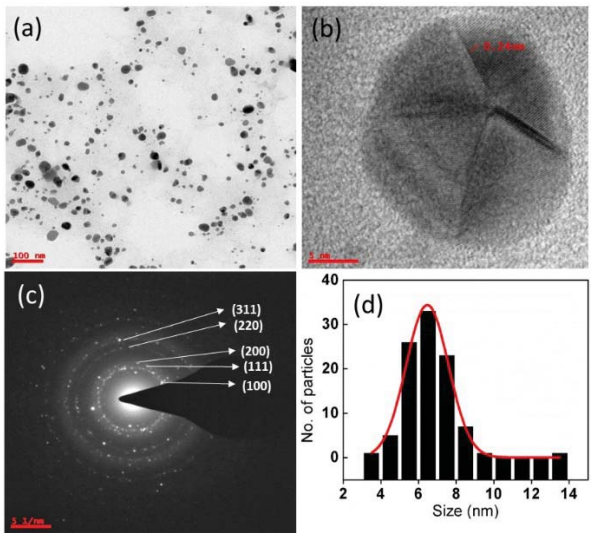

Fig. 2. *TEM images of bio reduced Ag NPs*

in different concentrations of AgNPs. Fig 4(b) shows the emission spectra of $Sm(TTFA)_3$ with different concentration of AgNPs. The magnetic dipole transition bands at 566 nm ($^4G_{5/2} \rightarrow {}^6H_{5/2}$) and 602 nm ($^4G_{5/2} \rightarrow {}^6H_{7/2}$) enhanced by 1.8 and 3 respectively and electric dipole transition band at 645 nm ($^4G_{5/2} \rightarrow {}^6H_{9/2}$) enhanced by 3.6. Enhancement of luminescence intensity is seen for 220µl Sm complex in different concentrations of AgNPs. It has been reported by many groups [2] that the scattering spectra of AgNPs lie at around 600nm for a particular distance between the AgNPs. As the scattering spectra of the NPs can be tuned depending on the distance between the NPs, the emission intensity enhances when the emission spectra of rare-earth ion overlaps with the scattering spectra of the NPs. When the distance between NPs decreases, the scattering at 612 nm initially increases, this makes the increase of the overlap between the scattering of AgNPs and the emission band of Eu^{3+} ions resulting in the enhancement of luminescence. Then it decreases as the distances between NPs further decrease, which result in the decrease of coupling efficiency between the AgNPs and Eu^{3+} ions, and the decrease of the enhancement factor of luminescence. This could be the reason why we did not observe increase in luminescence intensity for other concentrations of Eu^{+3} (40 µl and 60 µl) and Sm^{3+} (200 µl and 240 µl) ions as shown in the inset Fig. 4. Overall enhancement in luminescence of Eu^{3+} and Sm^{3+} ions in the presence of Ag NPs is found to be 20 and 5 times respectively, when compared to pure Eu^{3+} and Sm^{3+} ion solution.

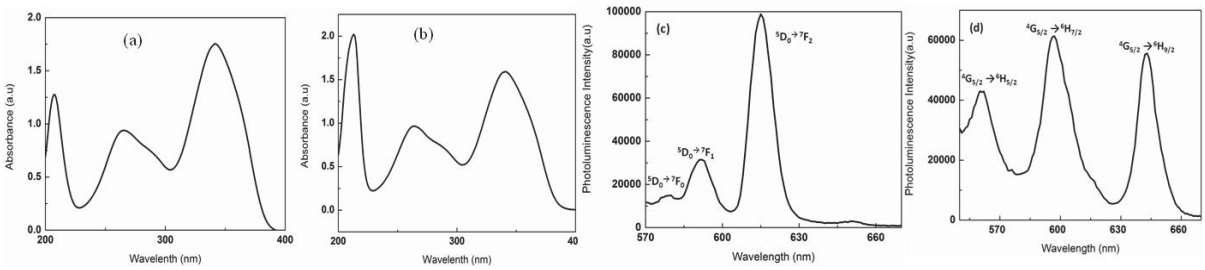

Fig. 3. *Absorption spectra of pure (a) $Eu(TTFA)_3$ and (b) $Sm(TTFA)_3$ and PL spectra of pure c) $Eu(TTFA)_3$ and (d) $Sm(TTFA)_3$*

Fig. 5(a) shows the open aperture Z-scan data with nanosecond laser at different input intensities. We observed reverse saturable absorption (RSA) behaviour in the green synthesized Ag NPs which are attributed to the

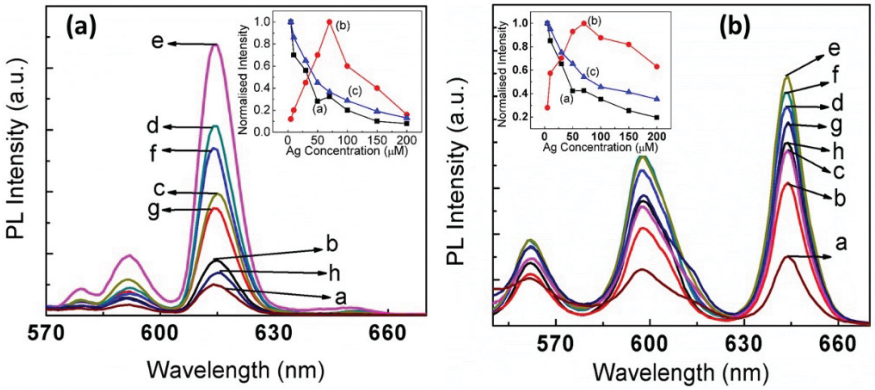

Fig. 4 (a). *Luminescence emission spectra (λ_{exc}= 350 nm) of 20μl Eu(TTFA)$_3$ with different concentrations of Ag NPs: a) 5, b) 10, c) 30, d) 50, e) 70, f) 100, g) 200 μl. Inset fig shows dependence of Ag concentration on the PL intensity. Eu complex concentration is (a) 10μl (b) 20 and (c) 30μl.* ***4 (b)*** *Luminescence emission spectra (λ_{exc}= 350 nm) of 240μl Sm(TTFA)$_3$ with different concentrations of Ag NPs: a) 5, b) 10, c) 30, d) 50, e) 70, f) 100, g) 200 μl. Inset figure shows dependence of Ag concentration on the PL intensity. Sm complex concentration is (a) 200μl (b) 220 and (c) 240μl.*

excitations from surface Plasmon resonance (SPR) band to the free carrier band of Ag NPs and two-photon absorption (TPA) from ground state. From the fit we estimated α_2 to be 10.2×10^{-9} cm^2/W for different input intensities in the range of 0.78 GW/cm^2 to 3.9 GW/cm^2. This value is almost same for different input intensities. Fig. 5(b) shows the optical limiting threshold and value which is found to be 0.05 J/cm^2.

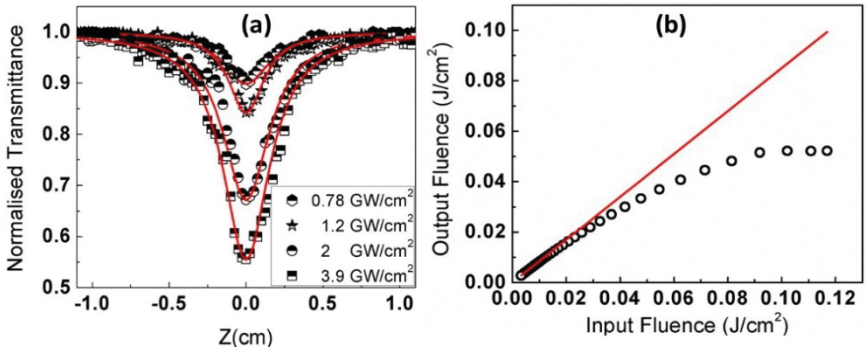

Fig. 5(a) Open aperture Z-scan curves, (b) Optical limiting curves of Ag NPs with 532 nm, 30ps pulse width and 10Hz reprate.

Conclusions: Biosynthesized Ag NPs have been successfully synthesized utilizing **Cynadon dactylon *extract*** as capping and reducing agent. Luminescence enhancement and quenching of RE ions have been observed in the presence of such nanostructures. Hence, these NPs show applications as luminophores with good optical limiting characteristics.

References

[1] S. Prathap Chandran, Minakshi Chaudhary, Renu Pasricha, Absar Ahmad, and Murali Sastry, Biotechnol. Prog. 22, 577−583 (2006).

[2] M. Ringler, A. Schwemer, M. Wunderlich, A. Nichtl, K. Kurzinger, T.A. Klar, and J.Feldmann, Phys. Rev. Lett. 100, 203002 (2008).

Perfect absorption in a pulsed laser deposited sub-wavelength thick indium tin oxide thin film via Kretschmann-Raether geometry

*Sumit Goswami, Ashwini Kumar Sharma

Department of Physics, Indian Institute of Technology Guwahati, Guwahati, Assam, India-781039

*Email: sumit.goswami@iitg.ac.in

In this report, we have experimentally demonstrated near-perfect absorption (~99.83%) of incident *p*-polarized light around the technologically important telecommunication wavelngth (1550 nm) in a pulsed laser deposited indium tin oxide thin film of thickness less than 100 nm excited through Kretschmann-Raether geometry. A theoretical model, based on the transfer matrix method, accurately reproduces the experimentally observed absorption spectra. This behavior is linked to the epsilon near zero mode, and rigorous calculation of the local field intensity enhancement factor establishes substantial enhancement of electric field inside the film as the main catalyst behind such a high degree of absorption.

From the beginning of the last decade, transparent conducting oxides (TCOs) like indium tin oxide (ITO), aluminum/germanium doped zinc oxide (AZO/GZO) have paved the way for the new exciting field of research based on epsilon near zero (ENZ) property of such materials. The vanishingly small permittivity of these ENZ materials at the juncture of dielectric-to-metal transition has led to many trendsetting phenomena like squeezing of the electromagnetic wave energy[1], perfect absorption (PA)[2, 3], extremely high optical nonlinearity[4], etc. Amongst these, PA in sub-wavelength thick films turns out to be fundamentally fascinating and technologically paramount from the device application point of view. In a pioneering work, Luk *et al.*[2] demonstrated PA in several sub-wavelength thick ITO thin films backed by silver superstrate and have discussed ENZ mode mediated PA. Soon after this work, Yoon *et al.*[3] presented broadband PA in unpatterned ENZ films, devoid of any backing superstrates. However, in both of these reports, PA was not achived at telecommunication wavelength, which is pivotal when it concerns actual real-life devices.

Here, we experimentally achieved about 99.83% absorption at and around the telecommunication wavelength in an ITO thin film of thickness less than 100 nm when probed via Kresthmann-Raether configuration. Experimental results and subsequent theoretical analysis are presented in the following sections.

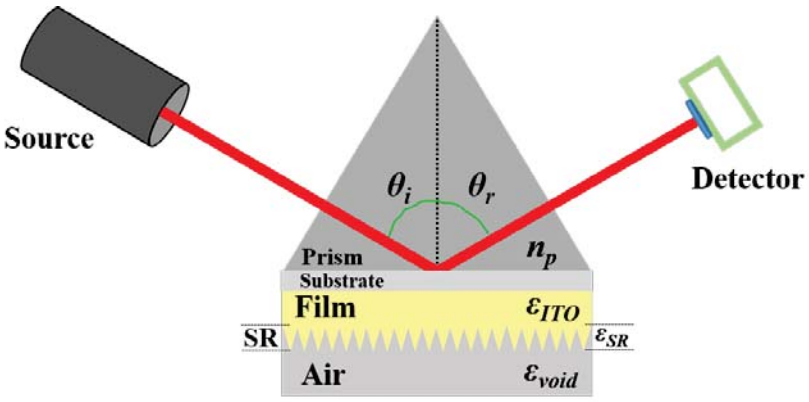

Figure 1: Schematic of the Kretschmann-Raether geometry based set up.

Experimental and Characterization techniques

ITO thin films were deposited onto the coring glass substrate using a Q-switched Nd:YAG laser (Spectra-Physics) operated at 532 nm wavelength. During the deposition, substrate temperature and chamber pressure were maintained at 400 °C and 0.05 mbar of helium gas, respectively. The film's thickness, surface roughness, and dielectric permittivity were analyzed using spectroscopic ellipsometry (SEMILAB GES5E) instrument. A virtual surface roughness layer defined by Bruggemann effective medium approximation (BEMA) on top of a thin film dispersion layer characterized by a combination of Drude and Gaussian oscillators was used to model ellipsometric data. Excitation of ENZ mode was realized in a Kretschmann-Raether configuration, as shown in figure 1. ITO films were placed upside down onto the right-angle BK7 glass prism by employing an index matching fluid. A purely *p*-polarized light generated in the ellipsometer was employed at several incident angles through the slanted face of the prism, and the reflected spectra were collected using an analyzer equipped with a NIR detector over the wavelength range 900 – 1700 nm.

Numerical simulation based on Transfer matrix method

Reflection and transmission spectra of a multilayer system can be accurately simulated by employing the transfer matrix method (TMM). TMM typically correlates the electric and magnetic field of the first layer to the last layer. A Matlab code based on TMM was modified to take into account the contribution of the surface roughness. Surface roughness described by BEMA was included in the simulation as a uniaxially anisotropic layer. For *p*-polarized light, the matrix component of any intermediate layer is defined as[5],

$$M_i = \frac{1}{2}\begin{pmatrix} \left(1+\frac{\varepsilon_i k_z^{i+1}}{\varepsilon_{i+1} k_z^{i}}\right) e^{-ik_z^i L_i} & \left(1-\frac{\varepsilon_i k_z^{i+1}}{\varepsilon_{i+1} k_z^{i}}\right) e^{-ik_z^i L_i} \\ \left(1-\frac{\varepsilon_i k_z^{i+1}}{\varepsilon_{i+1} k_z^{i}}\right) e^{+ik_z^i L_i} & \left(1+\frac{\varepsilon_i k_z^{i+1}}{\varepsilon_{i+1} k_z^{i}}\right) e^{+ik_z^i L_i} \end{pmatrix} \quad (1)$$

where ε_i and ε_{i+1} are the dielectric constant of two back to back layers and L_i is the effective thickness of the i^{th} layer. $k_z{}^i$ is the *z*-component of the wavevector is defined as,

$$k_z^i = \sqrt{\varepsilon_i k_0^2 - k_x^2} \quad (2)$$

where k_0 is the incident wavevector, and k_x is the *x*-component of the imparted to the incident wavevector due to the oblique incidence. So, the total transfer matrix of an *N*-layer system is given by,

$$M = \left(\prod_{i=1}^{N} M_i\right) = \begin{pmatrix} M_{11} & M_{12} \\ M_{21} & M_{22} \end{pmatrix} \quad (3)$$

Subsequently, the reflection coefficients and, thereby, the amplitude is given by,

$$\begin{aligned} r_{TM} &= \frac{M_{21}}{M_{11}} \\ R_{TM} &= \left|r_{TM}\right|^2 \end{aligned} \quad (4)$$

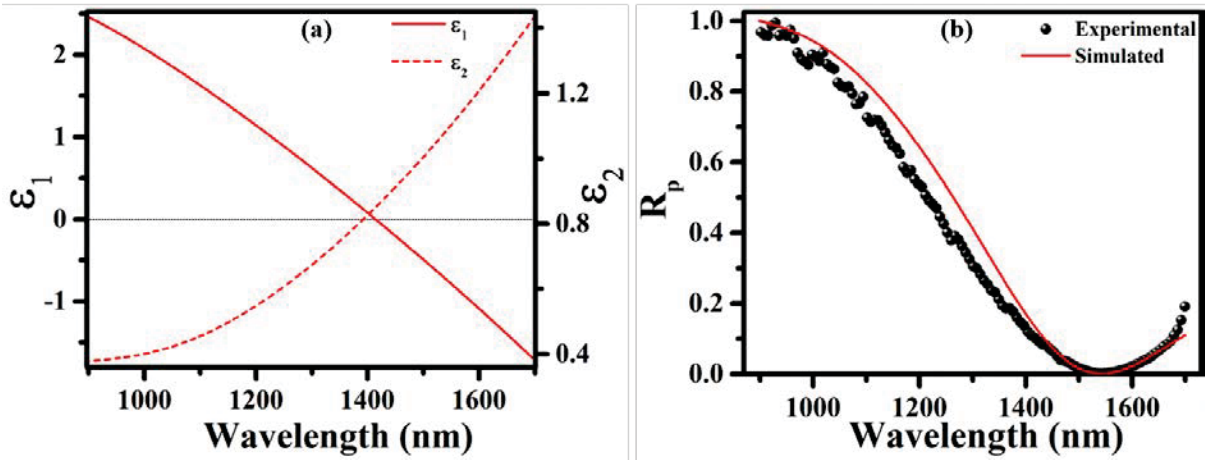

Figure 2: (a) Variation of real (ε_1) and imaginary (ε_2) part of permittivity. The black dotted line in the middle represents the 0 value of the real part of permittivity.; (b) experimental and simulated reflection spectra of *p*-polarized light over the wavelength range 900-1700 nm.

Results and discussions

Figure 2 (a) shows the variation of the real (ε_1) and imaginary (ε_2) part of permittivity of the pulsed laser deposited ITO thin film over the wavelength range 900-1700 nm. Real permittivity exhibited a clear cutoff at the wavelength 1415 nm; wherein the value of the imaginary part of permittivity is also relatively low (~ 0.85). Thus ENZ condition is fulfilled in this region. To further validate the results, reflection spectra were also taken over a range of incident angles from 50° to 70° at an interval of 1°. The frequency of the experimental data was increased to around 56° in order to accurately pinpoint the PA point. The highest value of absorption (~ 99.83%) was achieved at the angle of incidence of around 56.75° at the wavelength of 1541 nm. These values, along with measured film thickness (90 nm), perfectly satisfy the PA condition[2] :

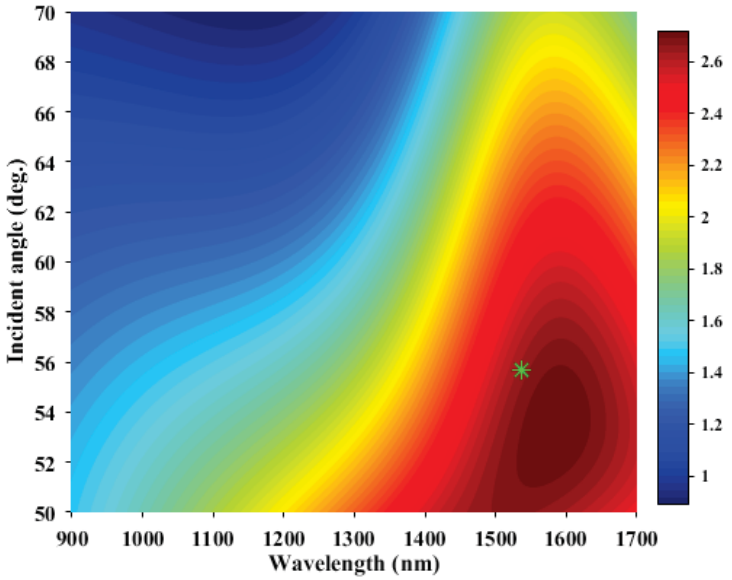

Figure 3: Angular distribution of the local field intensity enhancement factor (LFIEF) over the wavelength range 900 – 1700 nm. The colorbar beside the map indicates the exact value of LFIEF. The green star represents the simulated PA point.

$$\frac{2\pi d_{PA}}{\lambda_{PA}} = \left[\frac{\varepsilon_1^2 + \varepsilon_2^2}{n_p^3 \varepsilon_2}\right] \frac{1}{\tan\theta_{PA} \sin\theta_{PA}} \quad (5)$$

where n_p is the refractive index of the prism. Here we have neglected the film's surface roughness since it is significantly less than the film thickness. One thing to notice from the PA condition is that the value of the real and imaginary part of permittivity ultimately dictates the PA wavelength and angle. Thus, we can shift the PA point at our will for an absorber of given thickness just by playing with the disperison property of the material. Figure 2 (b) depicts the experimentally measured reflection spectra along with simulated one in the wavelength range of 900 – 1700 nm. We can see that the simulated spectra almost precisely matches with that of the experimental one. It provides concrete proof that our simulation method, as discussed in the earlier section, is quite handy when it comes to the films with small surface roughness values.

To further understand the physical origin of the ENZ assisted PA in sub-wavelength thick ITO thin film, we also calculated the local field intensity enhancement factor (LFIEF) inside the film. As depicted in figure 3, there is a strong enhancement of the electric field near the PA region. However, the strongest enhancement point is slightly redshifted as compared to the PA point. This is in line with several earlier reports[2, 6].

Conclusions

In conclusion, the experimental demonstration of perfect absorption using Kretschmann-Raether geometry is achieved in an unpatterned ITO thin film. The combination of real and imaginary parts of the film proved pivotal when it concerned the PA condition. The electric field is strongly enhanced locally when the incident wavelength is close to the ENZ wavelength and provides the necessary loss mechanism for PA. PA in the telecommunication wavelength could be very beneficial for absorption-based device applications.

References

1. Silveirinha, M. G.; Engheta, N. *Phys. Rev. B* **2007,** 76, (24), 245109.
2. Luk, T. S.; Campione, S.; Kim, I.; Feng, S.; Jun, Y. C.; Liu, S.; Wright, J. B.; Brener, I.; Catrysse, P. B.; Fan, S. *Phys. Rev. B* **2014,** 90, (8), 085411.
3. Yoon, J.; Zhou, M.; Badsha, M. A.; Kim, T. Y.; Jun, Y. C.; Hwangbo, C. K. *Sci. Rep.* **2015,** 5, 12788.
4. Alam, M. Z.; De Leon, I.; Boyd, R. W. *Science* **2016,** 352, (6287), 795-797.
5. Le Ru, E.; Etchegoin, P., *Principles of Surface-Enhanced Raman Spectroscopy: and related plasmonic effects*. Elsevier: 2008.
6. Badsha, M. A.; Jun, Y. C.; Hwangbo, C. K. *Opt. Commun.* **2014,** 332, 206-213.

Nanosecond laser texturing with in-situ glass particle deposition on steel mesh for oil water separation

S.Ahlawat[a*], A. Singh[a], P. K. Mukhopadhyay[a], R. Singh[b], K.S. Bindra[a]

[a]*Laser Technology Division, Raja Ramanna Centre Advanced Technology, Indore, M.P. 452013, India*

[b]*Laser and Functional Materials Division, Raja Ramanna Centre Advanced Technology, Indore, M.P. 452013, India*

Email: rsunita@rrcat.gov.in

Abstract:

We report that laser texturing with in-situ glass particle deposition on stainless steel meshes can produce superhydrophilic meshes for gravity driven oil water separation application. The glass particle deposition resolved the problem of the gradual loss of hydrophilicity of the laser textured bare stainless steel mesh during storage, which renders the mesh unusable for oil water separation. We showed that the glass particle coated stainless steel mesh could perform oil water separation with an efficiency of ~96% for various oils and could be stored up to the tested duration of ~8 months without any significant degradation.

Introduction:

The laser surface texturing as a method to induce superhydrophilicity in porous or mesh-like metals has received considerable attention recently [1,2] where the induced superhydrophilicity has been exploited for highly efficient oil water separation which can have applications in the areas where oil and water get inadvertently mixed such as oil spilling/leakage in water, industry waste water etc. However, no attention has been paid to the long term stability of the superhydrophilicity and the usability for oil water separation of the prepared metallic meshes. This is important as the well-known wettability transition phenomenon of the laser textured metallic surfaces [3,4] is expected to cause a gradual loss of superhydrophilicity upon storage in ambient air and hence affect the oil water separation efficiency. Therefore, we investigated the loss of superhydrophilicity and oil water separation efficiency of laser textured stainless steel mesh and observed a complete transition to superhydrophobicity and total failure of oil water separation within 75 days of storage in ambient atmosphere. In Further, as a solution to this problem, we have shown that using a glass cover plate over the steel mesh during laser processing results in deposition of micron/submicron sized glass particles over the mesh via a process known as laser induced plasma assisted ablation (LIPAA) [5]. The glass being inherently inert and hydrophilic, when deposited in the form of micron/submicron sized particles imparted stable superhydrophilicity to the prepared mesh. The glass particles coated mesh could be used for oil water separation for oils like mustard oil, kerosene and petrol with efficiency ~96% without any significant degradation upon storage up to the tested duration of ~8 months.

Experimental:

Figure 1A shows a schematic of the experimental setup. Briefly, a frequency doubled Nd:YAG laser at 532 nm with repetition rate of 18 kHz and pulse duration of ~ 200 ns was used for texturing. The laser average power was varied from 1 W to 2.5 W. The laser beam was focused with a 25 mm focal length lens resulting in a focal spot of ~68 μm. The stainless steel (SS 316) mesh (# 300 i.e. 300 meshes in an inch length) samples were placed on a motorized XY stage and were scanned in parallel lines relative to the stationary laser beam with a scanning line separation of 25 μm and scan velocity of 5 mm/s. During glass particle deposition, a ~1.2 mm thick soda

lime glass plate was placed over the mesh. To avoid sticking of the mesh with the glass plate during laser processing, a ~100 µm thick spacer was inserted between the mesh and the glass plate. The morphological examination of the textured meshes was carried out using a field effect scanning electron microscope (Carl Zeiss Sigma 02). The compositional analysis of the samples was carried out using an Energy-dispersive X-ray (EDX) analysis system (Element EDS system, EDAX Inc.). To characterize the wettability of the mesh surfaces, liquid contact angle was analysed using a home-built set-up. In this setup, light from an illumination lamp was passed through an aperture and illuminated a ~5 µl liquid droplet. The droplet was then imaged using an USB microscope (Research India MPC27). The contact angle of the droplet was calculated using ImageJ image analysis software.

Results and Discussion:

Figure 1B shows a stainless steel mesh which was laser processed without any glass cover plate i.e. bare mesh. The laser processing was carried out at average laser power of ~1 W. The laser processed area of the mesh appeared blackish, which may be due to the light trapping effect of micro/nano structures/particles formed during laser processing as well as due to chemical surface modification. However, when the laser processing was carried out with the glass cover plate on the mesh at a laser power of ~ 2.5 W, the processed mesh area appeared to be whitish. In this case also the mesh was covered with micron/submicron sized particles but the EDX analysis of these particles showed that they are mainly composed of Si, Na, Mg, Ca and O which are known to be the main constituents of soda lime glasses. These results suggested that the particles deposited over the mesh must have originated from the ablation of the soda lime glass plate during the laser processing. Such glass particle deposition may occur via a process known as laser induced plasma assisted ablation (LIPAA) [5] in which the intense plasma formed during laser ablation of mesh can interact with the top cover plate and ablate it. This is depicted in a schematic shown in Fig 2D.

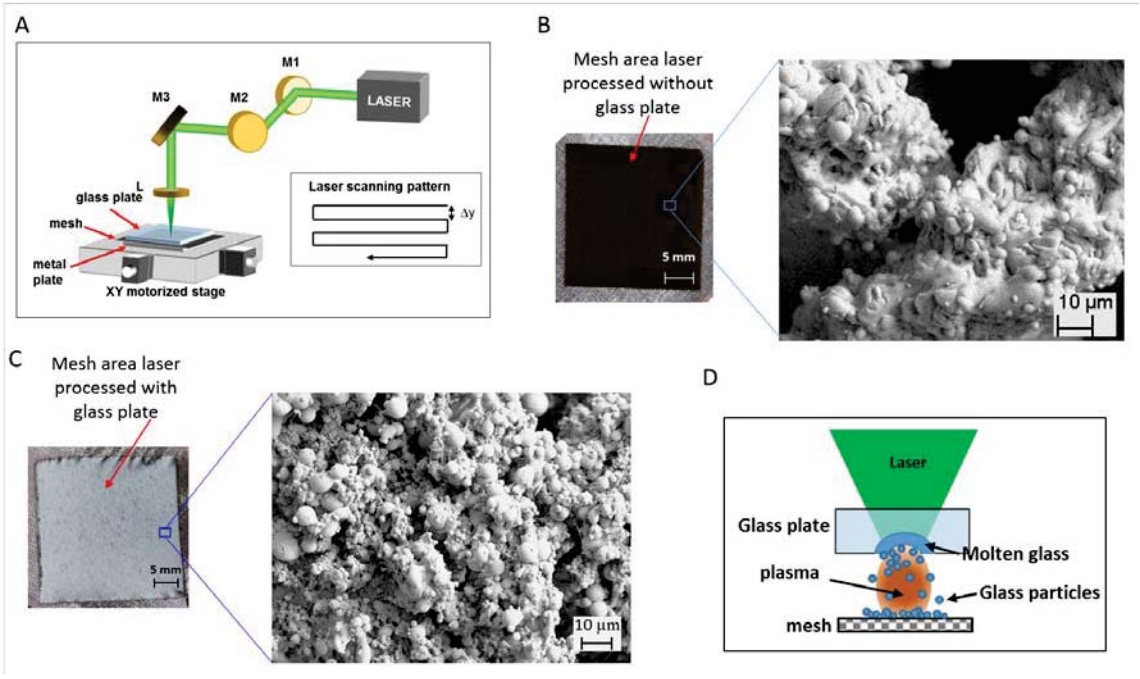

Figure 1(A) A schematic of the laser texturing set up. M1-M3: beam steering mirrors, L: beam focusing lens, Δy: inter-line separation (B) Photograph and SEM micrograph of the laser textured mesh without any glass plate. (C) Photograph and SEM micrograph of the laser textured mesh with the glass cover plate. (D) A schematic of the glass particle deposition phenomenon during laser processing.

The unprocessed stainless steel mesh was hydrophobic and exhibited a static contact angle of ~110° as shown in Fig. 2A. Immediately after laser processing, the meshes with glass particle deposition (GPcoatedM) or without glass particle deposition i.e. bare mesh (BareM) were found to exhibit superhydrophilicity as also shown in Fig. 2A. The superhydrophilicity observed in the case of the BareM may be due to the combined effect of laser ablation induced micron/submicron scale metal features as well as the formation of metal oxides which are known to be hydrophilic. Similarly, in the case of the GPcoatedM, the presence of micron/sub-micron sized glass particles and their intrinsic hydrophilic nature may have resulted in the observed superhydrophilicity. Figure 2B shows the time-evolution of water contact angle and it may be noted that while the BareM gradually lost superhydrophilicity and became superhydrophobic with a contact angle of 156°±1° within a duration of ~75 days. The reason for this transition has been known to be the reactive nature of the metallic oxides formed during laser processing which react with the gases and moisture present in the ambient air and. Such reaction results in adsorption of organic matter over the metal surface making it superhydrophobic. However, Fig. 2B also shows that the GPcoatedM maintained its superhydrophilicity even after a time duration of ~8 months. The reason for this stability of the GPcoatedM may be the inherently non-reactive nature of the glass particles.

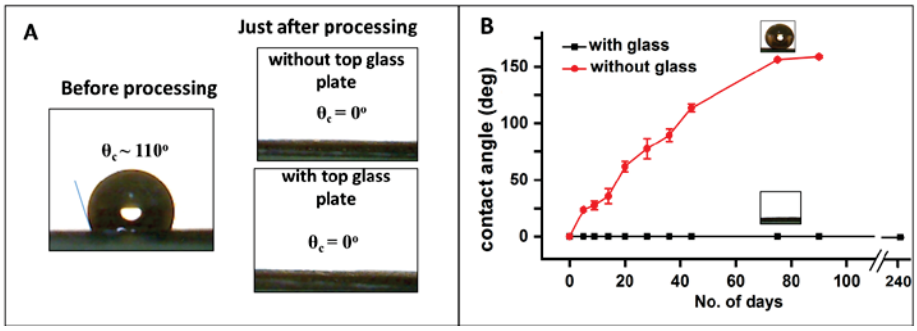

Figure 2. (A) Contact angle of a water droplet on the mesh before processing i.e. pristine mesh and immediately after laser processing without/with top glass cover plate. (B) Evolution of the contact angle of the laser processed meshes after being left in ambient air.

When water is poured over the laser textured superhydrophilic mesh, the rough surface features of the mesh get impregnated with water and a thin film of water is formed over the mesh. When an oil droplet approaches such a pre-wetted mesh, the pockets of water trapped in the rough surface do not allow the oil droplet to make a contact with the mesh. Similarly when a mixture of oil and water is poured over the mesh pre-wetted with water, the oil being lighter than water hits the mesh first, but not being able to make contact with the mesh rises upwards, and the water passes through. Even when all the water is passed through, the oil is still retained over the mesh as long as the water film is present over the mesh. Thus as long as the mesh is superhydrophilic which is the case with freshly prepared BareM, freshly prepared GPcoatedM as well as aged GPcoatedM, it can serve to separate oil/water mixture as shown in Fig 3A. The aged BareM became superhydrophobic after 75 days of storage in ambient atmosphere and did not allow formation of thin film when pre-wetted with water. When the oil/water mixture is poured over it, the oil being lighter first makes contact with the mesh and wets the mesh and some quantity of oil may also pass through before it is displaced by the heavier water phase. Since a layer of oil has got spread over the mesh, the water is not able to pass through and the oil being lighter than water moves upwards and sits over water layer. Thus, the mesh completely loses its separation action as shown in Fig. 3B. The separation efficiency of water from an oil/water mixture was calculated as $\eta = m_c/m_o \times 100\%$, where m_c and m_o are the original mass of water and the mass of water collected after separation, respectively. The separation

efficiency was found to be > 96% for all the freshly processed meshes i.e. BareM and GPcoatedM (Fig. 3C). The separation efficiency of the BareM dropped to 0% after 75 days of storage whereas the separation efficiency of the GPcoatedM did not change significantly over the investigated time duration of 240 days. Furthermore, different oils such as mustard oil, kerosene and petrol could be separated from oil water mixture with efficiency > 96% (Fig. 3D).

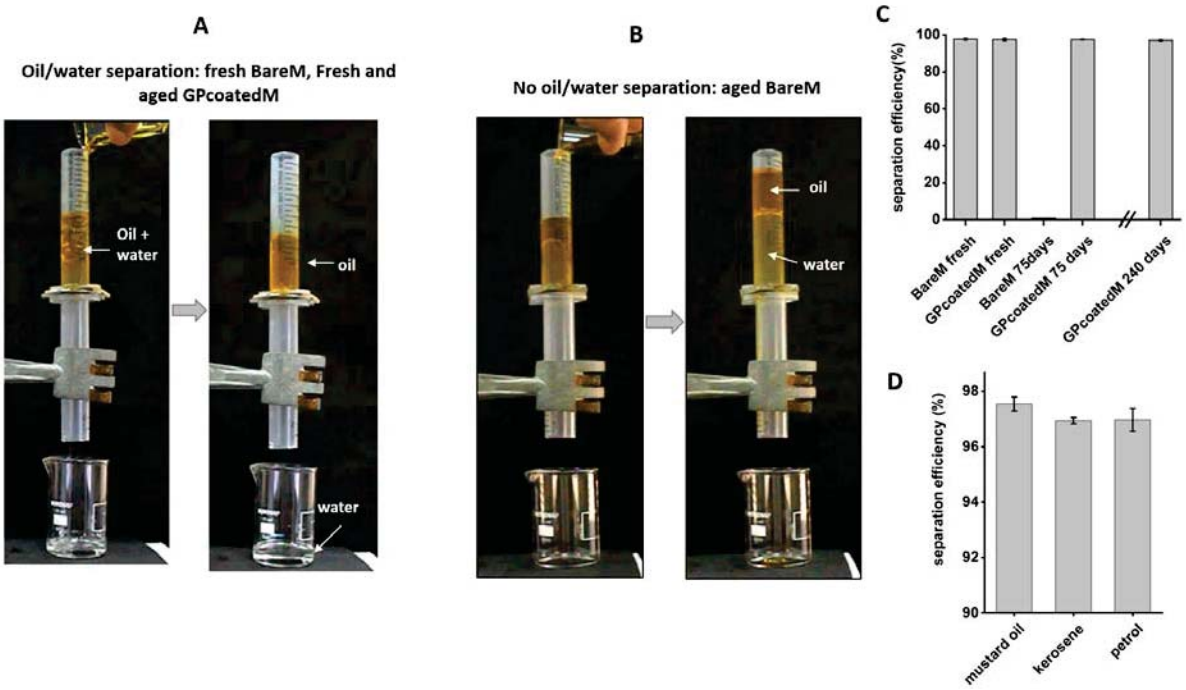

Figure 3. Schematic and photographs of (A) oil/water separation through superhydrophilic mesh, the case applicable on BareM fresh, GPcoatedM fresh and GPcoatedM aged meshes (i) during and (ii) after pouring of oil water mixture (B) no oil water separation, applicable on BareM old mesh (i) during and (ii) after pouring of oil water mixture

Conclusion:

We have shown that by using a glass plate over the stainless steel mesh during nanosecond laser processing, micron/submicron sized glass particles could be deposited over the mesh. These glass particles endowed long term superhydrophilicity to the mesh and allowed the use of the prepared mesh for efficient oil/water separation even after a long storage durations. Further, as the glass particle deposition occurs during the laser processing, the advantages associated with laser texturing, such as chemical-free and one-step process, are still retained.

References:

1. K. Yin, D. Chu, X. Dong, C. Wang, J.-A. Duan, J. He, *Nanoscale* **9,** 14229–14235 (2017).
2. Z. Lian, J. Xu, Z. Wang, Z. Yu, Z. Weng, H. Yu, *Langmuir* **34,** 2981–2988 (2018).
3. J.T. Cardoso, A. Garcia-Girón, J.M. Romano, D. Huerta-Murillo, R. Jagdheesh, M. Walker, S.S. Dimov, J.L. Ocaña, *RSC Adv.* **7** 39617–39627(2017).
4. Z. Yang, X. Liu, Y. Tian, *J. Colloid Interface Sci.* **533** 268–277(2019).
5. T.U. Rahman, Z.U. Rehman, S. Ullah, H. Qayyum, B. Shafique, R. Ali, U. Liaqat, A.H. Dogar, A. Qayyum, *Opt. Laser Technol.* 120 (2019) 105768.

Simulation Studies of Photonic Nanojets and Photonic Nanojet Assisted Nano-structuring on Metallic Substrates

B. Sugathan[1,2], J. P. Nilaya[1,3], V.P.M Pillai[2], D.J. Biswas[1]

[1]Laser and Plasma Technology Division, BARC, Mumbai-400085

[2]Department of Optoelectronics, University of Kerala, Kariavattom, Thiruvananthapuram, Kerala-6955881

[3]Homi Bhabha National Institute, Anushakti Nagar, Mumbai-400094

Email: bijoysugathan@gmail.com

Abstract:

Simulation studies of Photonic nanojets and fabrication of nanoholes on Stainless Steel (SS) substrate experimentally by the photonic nanojets using particle assisted laser exposure method is reported. The nanojet simulation study has been carried out for three different incident laser wavelengths for the case of spherical particles of three different diameters. Experiments performed with polysterene particles of 1 μm, 0.5 μm and 0.3 μm exposed to laser of wavelength 1064 nm yield results that agree with the simulation.

1. Introduction

Optical lithography is an important and powerful technique emerging in the recent years to create fine nano-structuring and modifications in a remote and controlled manner on a substrate and the limit in the focusing ability set by diffraction is overcame by special methods. The conventional far-field techniques are limited by the spatial resolution of a lens which, in turn, is limited by diffraction limit and is approximately one half of the wavelength. Some near-field techniques, such as NSOM (Near field Scanning Optical Microscopy), laser in combination with AFM (Atomic Force Microscope) probe etc. are made use of to overcome these limitations. One of the promising and powerful technique developed to overcome the diffraction limit is by using a dielectric sphere in combination with laser beam, where the confinement of the light in the form of photonic nanojet (PNJ) underneath the particle can be achieved to within less than half of the wavelength. PNJ was theoretically demonstrated by Chen et.al. for the first time by using finite-difference time-domain (FDTD) numerical modeling.[1] It is defined as a non-resonant phenomenon, in which a properly illuminated dielectric microparticle will focus the light in the vicinity of the microparticle at the shadow side.[2] It was found that PNJs thus produced have waists smaller than the diffraction limit and there is an enhancement in the intensity of the backscattered light by several orders of magnitude.[3] One of the important aspects of this photonics nanojet is that, it can propagate over a length of several wavelengths without any appreciable divergence making it most appropriate for applications in many areas such as laser surface nanostructuring/nanopatterning, Raman spectroscopy, optical data storage and tissue engineering.

2. Theory and Simulation

Simulation studies were carried by solving Maxwell's equations using Comsol mulltiphysics 3.4. which is based on finite elemental analysis method (FEM) similar to that of Patil et.al[4]. FEM is a numerical technique used for solving partial differential equations (PDE) and integral equations. In FEM based analysis, the structures are split into elementary sub-spaces, the value of electromagnetic field for each element is calculated and finally the value for the total field is arrived at by interpolation method. The simulation

experiment comprises of illumination of a dielectric sphere by using a Gaussian shaped uniform plane wave propagating along the x-axis, where the electric field oscillation takes place in the z- axis. The variations in the electric field as a function of propagating distance are defined by the Eq. 1.[4.]

$$E(x,y) = E_0\sqrt{\frac{w_0}{w(x)}}e^{-(y/w(x))^2}\cos\left(-kx + \eta(x) - \frac{ky^2}{2R(x)}\right) \text{ ---------- (1)}$$

$$w(x) = \sqrt{1+\left(\frac{x}{x_0}\right)^2} \text{ ---------- (2);} \qquad \eta(x) = \frac{1}{a}\,tan\left(\frac{x}{x_0}\right) \text{---------- (3)}$$

$$R(x) = x\left(1+\left(\frac{x_0}{x}\right)^2\right) \text{---------- (4);} \qquad \text{where,} x_0 = \frac{\pi w_0^2}{\lambda} \text{ ---------- (5)}$$

3. Results and Discussions

The first set of simulation experiments were carried out with spherical particles with a diameter of 1 µm. The refractive indices chosen for the particle (polystyrene (PS) particle) as a function of wavelength are 1.63 at 355 nm, 1.59 at 532 nm and 1.57 at 1064 nm[5]. Refractive index of the surrounding medium is chosen as 1.0 as it is assumed that particle in air for simplicity. Fig. 1 depict the electric field intensity distribution of photonic nanojet by a particle of 1 µm diameter when illuminated by a plane wave of wavelength 355 nm, 532 nm, and 1064 nm. Fig. 1.d shows the transverse intensity profile of photonic nanojet generated by a particle with 1 µm diameter when irradiated with plane waves with afore mentioned wavelengths. From the figures it is clear that intensity enhancement is highest when the particle is irradiated with shortest wavelength i.e., 355 nm, and intensity enhancement is lowest when the particle is irradiated with longest wavelength 1064 nm in this case. Intensity enhancement factors are 3.649, 3.459, 2.405 respectively for the wavelengths of irradiations 355 nm, 532 nm and 1064 nm. The full width at half maximum (FWHM) calculated from the intensity profile of the photonic nanojet for different irradiation wavelength 355 nm, 532 nm and 1064 nm are 140 nm, 200 nm and 438 nm respectively.

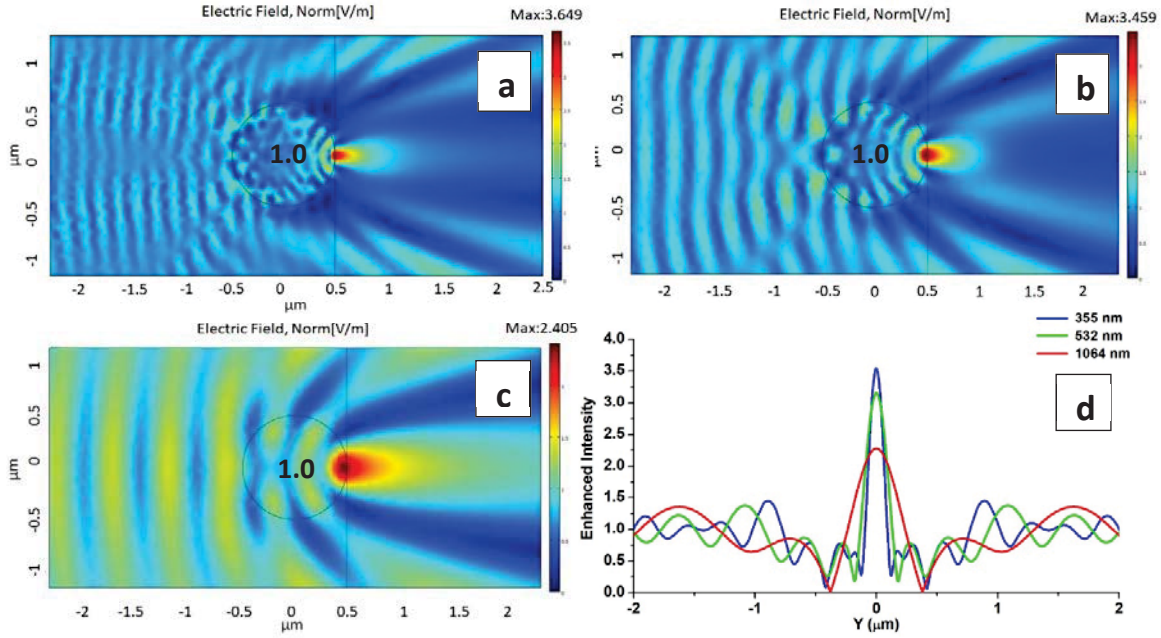

Fig. 1. Electric field Intensity distribution of photonic nanojet by a particle of 1.0 µm dia. illuminated by a plane wave of wavelength a. 355 nm b. 532 nm c. 1064 nm.d. Transverse intensity profile of photonic nanojet generated by particle with 1.0 µm diameter when irradiated with plane waves of different wavelengths.

The next set of simulations were then carried out for particles with diameter 0.5 µm and 0.3 µm also. It can be seen that the enhancement in the field intensities in these two cases is lesser compared to that of larger particle (1 µm). The measured enhanced field intensity values are 3.012, 2.396 and 1.776 for the irradiation wavelengths 355 nm, 532 nm and 1064 nm for particles with 0.5 µm diameter and 2.189, 1.805 and 1.387 respectively for particles with 0.3 µm diameter. The full width at half maximum (FWHM) calculated from the intensity profile of the photonic nanojet for different irradiation wavelength 355 nm, 532 nm and 1064 nm are 136 nm, 214 nm and 476 nm respectively for 0.5 µm particle and 140 nm, 200 nm and 438 nm respectively for 1 µm particle. A clear decrease in the enhanced intensity value and an increase in the FWHM of the spot size is evident with increase in the particle size. Fig. 2 depicts the transverse intensity profiles of photonic nanojet for three different particles with diameters 0.3 µm,0.5 µm and 1 µm when irradiated with wavelengths 355 nm.

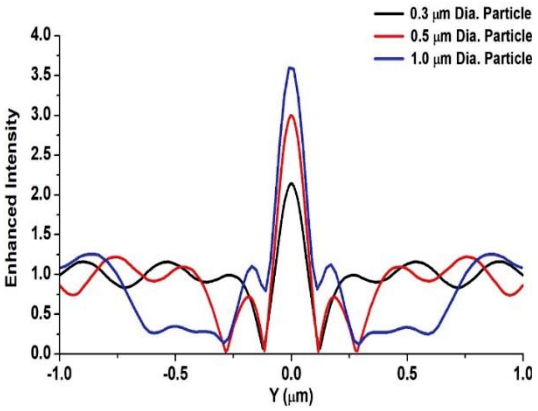

Fig. 2. Transverse intensity profile of photonic nanojet generated by particles of different diameters when irradiated with plane waves with a wavelength of 355 nm

We then experimentally fabricated nano holes on Stainless Steel (SS) substrates by using photonic nanojet. A monolayer of polystyrene (PS) particles (Sphereotech inc. USA) was made on the substrate as depicted in Fig. 3. Monolayer formation of the particles was ensured by proper cleaning of the substrate surface, proper dilution of the particles followed by ultrasonication as well as by keeping the substrate at an angle of 15 ^{0} at the time of deposition. The experimental setup used for nanostructuring consisted of a Perspex chamber vacuum sealed by the sample holder at one end and a BaF_2 Brewster window at the other end. A rotary pump was connected to the chamber in order to prevent any redeposition of the removed particles. An Nd: YAG laser (Model-SL 332-T, Ekspla) capable of delivering single mode pulses of pulse duration 300 ps at 1064 nm and 532 nm wavelengths was used as the source of irradiation. In the first set of experiments, SS substrate with a layer of 1 µm diameter was irradiated using laser pulse of 1064 nm wavelength beginning from a very low fluence. Substrate surfaces prior to and after laser irradiation were analyzed using AFM (XE 100, Park Systems). AFM in Fig. 4.a depicts the nano pits (nano holes) formed on the SS substrate after irradiating the surface containing 1 µm diameter particles with 1064 nm at a fluence of 36.6 mJ/cm^2. As seen in the pit profile in Fig. 4.b pits having a depth of ~ 2.5 nm were formed on the substrate. So, this fluence is considered as the threshold fluence for pitting in these conditions. In order to understand the effect of laser fluence on the size (both depth and width) of the pit the experiment was repeated for different laser fluence values. For a laser fluence of ~ 65 mJ/cm^2 depth of the nano holes were increased to ~40 nm and the width was increased to ~300 nm and is depicted in Fig. 5.

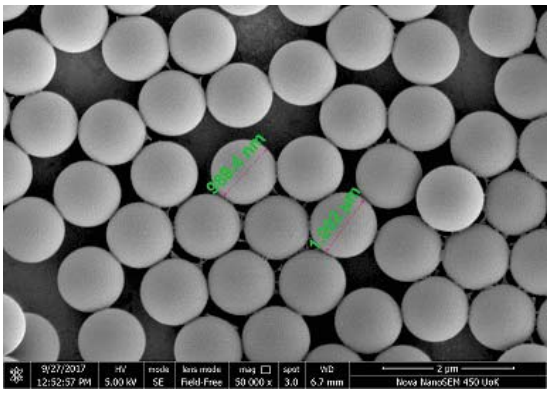

Fig. 3. SEM micrograph of SS substrate coated with monolayer of PS particles of 1 µm dia.

The experiments were repeated using smaller particles such as 0.3 µm and 0.5 µm and also for a different wavelength of 532 nm. Experimentally also It was observed that, as the particle size reduces, the threshold fluence for nano hole formation increases. Further it also reduces with reducing irradiation wavelength. It was also observed that as predicted by the simulation results, as the particle size increased, the depth of penetration too increased. More results will be presented during the conference.

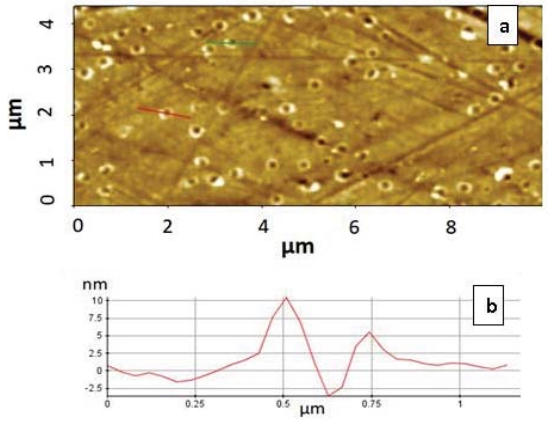

Fig. 4 AFM micrograph depicting the nano pits formed on SS substrate by using PS particles of 1 µm dia at 1064 nm irradiation and fluence of 36.6 mJ/ cm^2: b. Profile of a nanopit showing depth of ~ 2.5 nm.

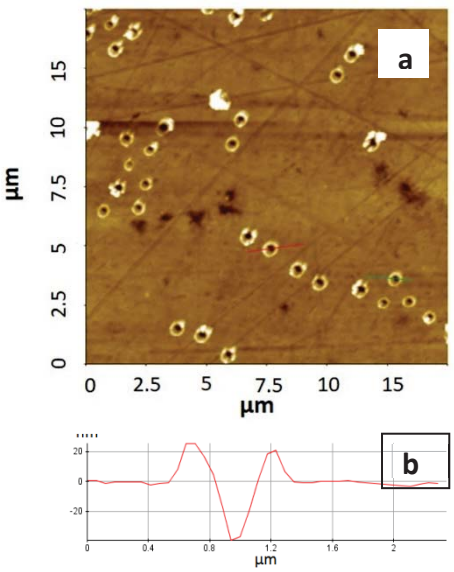

Fig. 5 AFM micrograph depicting the nano pits formed on SS substrate by using PS particles of 1 µm dia at 1064 nm irradiation and fluence of 65 mJ/ cm^2: b. Profile of a nanopit showing depth of ~ 40 nm

4. Conclusions:

In conclusion, simulation studies on photonic nanojets were carried out by using Comsol multiphysics 3.4 and nanoholes were fabricated on SS substrate using particle assisted dry laser exposure methods. Experimental results corroborates results obtained by simulation.

Acknowledgements:

The authors greatly acknowledge Pankaj Kushwaha, RRCAT, Indore, Aniruddha Kumar and M. B. Sai Prasad for many useful discussions during the course of the work. B. Sugathan also acknowledges UGC, Government of India, for granting him a research fellowship.

References:

1. Z. Chen, A. Taflove, and V. Backman, *Opt. Express*. **12**, 1214 (2004).

2. R. Chen, J. Lin, P. Jin, M. Cada, Y. Ma, *Optics Communications*. **456**, 124593 (2020).

3. P.K. Kushwaha, H.S. Patel, M.K. Swami, P.K. Gupta, *International Conference on Optics and Photonics*, 9654 (2015).

4. H. S. Patel., P. K. Kushwaha, M. K. Swami, *Optics communications* **415,** 140(2018).

5. B. Zhang, J. Hao, Z. Shen, H. Wu, K. Zhu, J. Xu, J. Ding, *Appl. Opt*. **57**, 8331(2018).

Suppression of stress corrosion cracking susceptibility of shear cut surface of 304L stainless steel through laser shock peening

R. K. Gupta*[1], A. K. Rai[2], D. C. Nagpure[1], R. Biswal[3], P. Ganesh[1], S.K. Rai[4], K. Ranganathan[2], K. S. Bindra[2], R. Kaul[1]

[1]Laser Materials Processing Division; [2]Laser Technology Division; [3]Fibre Sensors & Optical Spectroscopy Section; [4]Synchrotrons Utilization Section

Raja Ramanna Centre for Advanced Technology, Indore-452013

*E.mail: ramgupta@rrcat.gov.in

Abstract: Shear cutting of SS sheets introduces significant tensile residual stress on the cut surfaces, which makes them prone to Stress corrosion cracking (SCC). Laser shock peening (LSP) of shear cut surface has been carried out using in-house Nd:YAG laser. The study involved characterization of shear cut surface of laser peened and unpeened specimens w.r.t residual stress, SCC, microstructure, crack density, hardness and X-Ray diffraction. LSP modified the residual stresses on the shear cut surfaces from tensile to compressive. The study demonstrates the potential of LSP in preventing the SCC damage of shear cut SS sheets stored in stock yard.

1.0 Introduction: Austenitic stainless steels (ASS) are extensively used for the fabrication of components in nuclear and process industries due to high general corrosion resistance and high temperature strength. SCC is a serious type of material degradation involving service/storage of stressed components in susceptible corrosive environment. The phenomenon of SCC is known to occur in the event of simultaneous presence of (i) susceptible material, (ii) exposure to corrosive environment, and (iii) tensile stress above a threshold [1]. Many research studies have suggested that surface condition plays a very significant role in the initiation of stress corrosion cracks [2-3]. Surface modifications introduced by cutting, machining and grinding operations may introduce significant residual stresses. Shear cutting/machining of austenitic SS leaves a work hardened surface layer associated with high density of strain-induced martensite, and lattice defects like mechanical twins and dislocations [4]. Surface working operations result in enhanced electrochemical activity of the resultant surface, which is of serious concern with respect to SCC [5-7]. A study demonstrated that surfaces cut by cut-off wheels and shear cutting methods are susceptible for SCC due to high tensile residual stresses while surfaces cut by bandsaw are resistant to SCC in susceptible environment [8]. Process of LSP, because of its ability to introduce residual compressive surface stresses without introducing any thermal effects into the material, has attracted immense interest for enhancing the life of components operating under fatigue and SCC-prone conditions [9,10]. Peyre et al. have demonstrated that LSP can effectively prevent initiation of SCC in 316L SS in boiling $MgCl_2$ solution [11]. Authors own laboratory have also demonstrated the use of laser peening for pitting, SCC and fatigue life performance improvement [12]. The present study has been undertaken with objective to explore the use of laser peening to minimize the SCC susceptibility of the shear cut surfaces of SS with high tensile stresses.

2.0 Experimental procedure: The study was performed on a 10 mm thick sheet of 304L stainless steel (SS). The chemical composition of the SS sheet (in wt%) was: 0.02 C/18.03 Cr/10.55 Ni/1.22 Mn/0.28 Si/0.277

Mo/0.001 S/0.015 P/bal. Fe. The 304L SS sheet was shear cut into specimens of dimensions 60 x 25 x 10 mm for subsequent experiments. The specimens were ultrasonically cleaned in soap and acetone medium.

Laser shock peening of shear cut surfaces of 304L samples was carried out using indigenously developed high energy flash lamp pumped electro-optically Q-switched Nd: YAG laser system with maximum laser energy of 7J. During the laser peening, the specimen surface is covered with a black color adhesive PVC tape (thickness-100 μm) and around 1 mm thick layer of flowing water is maintained to confine the plasma formed as a results of laser beam interaction with the tape. The sacrificial layer of black PVC-tape also serves as a protecting material to the substrate from the unwanted thermal effects, which may otherwise introduce undesirable residual tensile stresses. The details of experimental set up are provided elsewhere [12-13]. Laser peening is carried out with a laser energy of 2.5 J with pulse width of 10 ns and pulse repetition rate 2 Hz. During peening process, the laser spot diameter on the sample surface is maintained to 3 mm with axial laser beam overlap of 70% and track to tack overlap of 58%. It should be noted that while conducting multiple i.e., double and triple laser peening treatment, new PVC tape was applied after each peening treatment. As sheared and sheared + laser peened specimens were characterized w.r.t optical microscopy, micro-hardness (force=100gf; dwell time: 10 Sec.), residual stress using X-ray diffraction and accelerated SCC test in boiling magnesium chloride as per ASTM G36 [14].

3.0 Results and Discussion: Shear cut surfaces carried signature of mechanical deformation. Laser-peened and unpeened shear cut surfaces had similar visual appearance. Micro-hardness (knoop) measurements performed on the polished cross-section of shear cut specimens showed increased micro-hardness near the sheared edge (Fig.1), which is attributed to extensive plastic deformation near shear the cut edge.

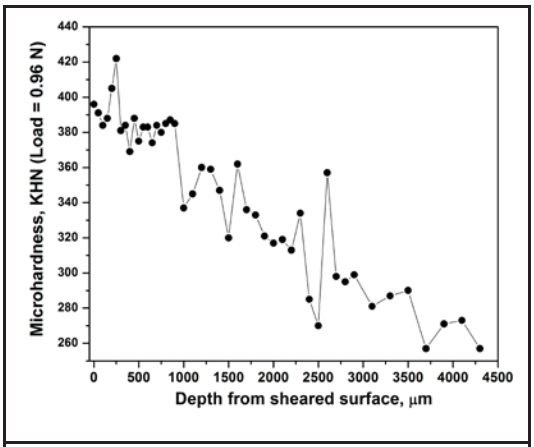

Fig.1. Micro-hardness profile along the depth of a un-peened shear cut surface of 304 L SS.

After double and triple LSP, surface tensile stress is modified to compressive stress. Fig.2 shows the comparison of residual stress profiles of double and triple peened shear cut surface as compared to unpenned surface. It is also clear that triple peening is more effective than double in suppressing the tensile stresses generated in shear cutting process. It may be noted that, in case of triple peened sample (Ref. Fig.2), in one of the laser peened location tensile stress was recorded due to tearing of tape and consequent melting. X ray diffraction pattern obtained from the shear cut and polished surfaces revealed strong signature of cold work and state of stress in case of shear cut surface in the form of significant peak broadening. Whereas the diffraction pattern of polished sample carried very sharp peaks of austenite indicative of stress free state.

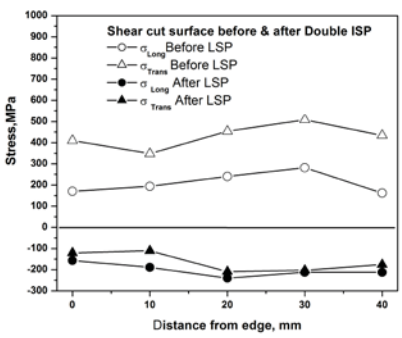

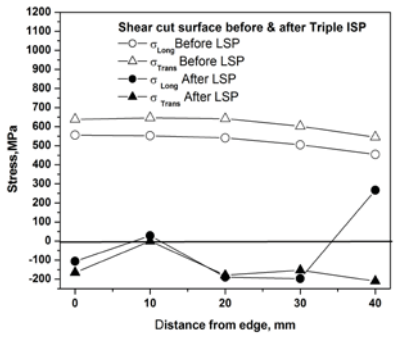

Fig.2. Residual stress profiles before & after double & triple laser peening of shear cut surface of 304L SS

These results supplement the residual stress data of as-shear cut surface. Details of XRD results could not be presented due to paucity of space. Exposure to 8 hrs long SCC testing of unpeened and laser peened samples

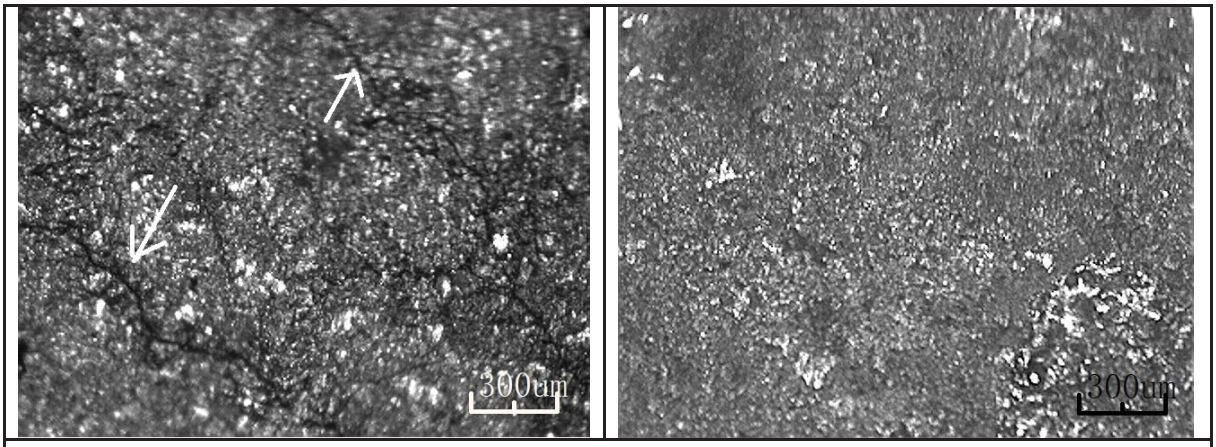

Fig.3: Micrographs of shear cut surfaces of (left) unpeened and (right) triple laser peened 304L SS specimens after undergoing 8h long accelerated SCC test as per ASTM G36. Cracks are marked with arrows.

(double and triple) showed extensive cracking on unpeened shear cut surface as shown in Fig.3 while almost no cracks were seen in laser peened shear cut surfaces (Fig.3). Crack density measurement (crack length mm/cm^2) was also calculated at 80X magnification using an optical microscope. The difference of crack density in unpeened and laser peened samples after exposure to SCC test are presented in the Fig.4. Crack density measurements confirmed that, LSP treatment has played vital role on controlling the SCC damage on shear cut surfaces carrying high magnitude of tensile stresses in as shear cut condition.

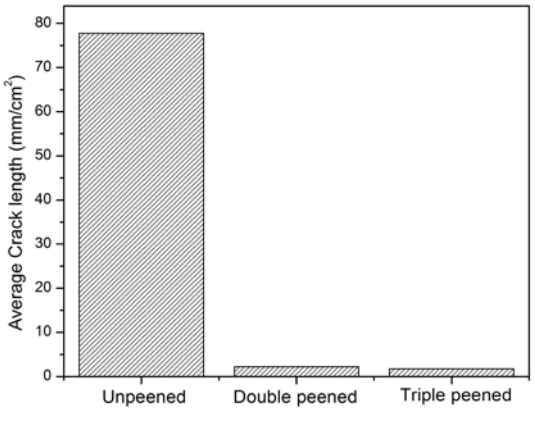

Fig.4. Comparison of average crack length in unpeened, double and triple peened shear cut surfaces after exposure to SCC test (ASTM G36).

From the above results, it is clear that as-shear cut surfaces of 304L SS carrying high tensile residual stress and high hardness are highly prone to SCC damage. Laser shock peeing is found to be very effective in suppressing the SCC damage in shear cut surfaces by modifying the surface stresses from tensile to compressive.

4.0 Conclusion: The results of the study demonstrates that laser shock peening is highly effective in suppressing stress corrosion cracking on shear cut surfaces of 304L SS. With respect to double peening triple laser peening is more effective. Laser peening brought about many fold reduction in SCC induced crack density as compared to unpeened shear cut surface. The technique holds promise towards treatment of shear cut edges of austentic stainless steel for preventing possible cracking during their storage in susceptible coastal environment.

Acknowledgement

Authors would like acknowledge Mr. Ram Nihal Ram for specimen preparation.

References

1. J.R. Davis, Ed., Stainless Steels, *ASM Specialty Handbook, ASM International*, Materials Park, OH, 169 (1999)
2. J. Isselin, A. Kai, K. Sakaguchi, and T. Shoji, *Metall. Mater., Trans*. **39A**, 1099 (2008)
3. P.L. Andresen and M.M. Morra, *J. Nucl. Mater*., **383**, 97(2008)
4. S. Suzuki, K. Takamori, K. Kumagai, A. Sakashita, N. Yamashita, C. Shitara, and Y. Okamura, *E-J. Adv. Maint.,* **1,** 1(2009)
5. S. Ghosh and V. Kain, *J. Nucl. Mater*., **402**,62(2010)
6. S. Ghosh and V. Kain, *Mater. Sci. Eng., A*. **527**, 679(2010)
7. S.G. Acharyya, A. Khandelwal, V. Kain, and I. Samajdar, *Mater. Charact*., **72**, 68(2012)
8. M J Suma, S. Mahadevan, Anita Toppo, Shaju K.Albert, S. Arun Kumar, *Mater. Corros.,* **71**(7), 1(2020)
9. R. Fabbro, P. Peyre, L. Berthe, and X. Scherpereel, *J. Laser. Appl*., **10**, 265(1998)
10. L. Berthe, P. Peyre, X. Scherpereel, R. Fabbro, and M. Jeandin, *Surf. Engg. Ser.*, **1**, N.B. Dahotre, Ed., *ASM International*, Materials Park, OH, 465(1998)
11. P. Peyre, X. Scherpereel, L. Berthe, C. Carboni, R. Fabbro, G. Be´ranger, and C. Lemaitre, *Mater. Sci. Eng., A.* **280**, 294(2000)
12. R. K. Gupta, N. Prasad, A. K. Rai, R. Biswal, R. Sundar, P. Ganesh, K. Ranganathan, K. S. Bindra and R. Kaul, *Lasers Manuf. Mater. Process*., **5** (2018.) 270.
13. A. K. Rai, R. Biswal, R. K. Gupta, R. Singh, S. K. Rai, K. Ranganathan, P. Ganesh, R. Kaul and K. S. Bindra, *Surf. Coat. Technol*., **358** (2019) 125.
14. ASTM G36 (94), *ASTM International,* Pennsylvania (2013)

Oxygen Vacancies Effect on Ferroelectric and Dielectric Properties in $Sr_{0.5}Ba_{0.5}Nb_2O_6$ Ceramic for Micro-positioner

S. Karmakar[1], Rachna Selvamani[2], S. M. Gupta[1] V. S. Tiwari[1] & A. K. Karnal[1]

[1]*Laser Functional Materials Division, Raja Ramanna Centre for Advanced Technology, Indore-452013*
[2]*Structure and Dynamics Section, Solid State Physics Division, Bhabha Atomic Research Centre, Mumbai-400085*
Email: sanjib@rrcat.gov.in

ABSTRACT

Effect of oxygen vacancies on ferroelectric and dielectric properties are investigated in $Sr_{0.5}Ba_{0.5}Nb_2O_6$ (SBN) ceramics synthesized by standard solid-state reaction method. The phase analysis has revealed formation of tetragonal tungsten bronze (TTB) P4bm crystal structure without any impurity phases. Relaxor-like dielectric behavior and a ferroelectric-like field induced polarization (P-E) loop are observed for air sintered SBN ceramic. High dielectric loss and a leaky P-E hysteresis loop are observed for SBN ceramic when sintered in vacuum. The leakage results are explained with the help of Raman spectroscopy considering transformation of NbO_6 octahedron to NbO_5 hexahedron.

INTRODUCTION

Among the class of materials known as relaxor ferroelectrics, strontium barium niobate (SBN) has received particular attention due to its excellent pyroelectric, photorefractive, and electro-optic characteristics [1-2]. The ferroelectric SBN crystal has a tungsten bronze type structure belonging to the tetragonal system, with a space group *P*4*bm* (*C*4v) [3-4]. As for other crystals having this structure, the general formula of a lattice cell of SBN can be written as $(A1)_4(A2)_2(B1)_2(B2)_8O_{30}$, so that different types of cationic sites are available in this host crystal. The A1 sites are partially occupied by Sr^{2+} ions, the A2 sites are randomly occupied by the Sr^{2+} and Ba^{2+} lattice ions, while the B1 and B2 sites are completely filled by Nb^{5+} ions. In spite of the wide band gap in SBN, this material shows high conductivity, which often depends upon the sintering conditions [5-6]. It is believed that the high conductivity is related to the presence of oxygen vacancies but conduction mechanism is not fully understood. In order to investigate the role of oxygen vacancies, the $Sr_{0.5}Ba_{0.5}Nb_2O_6$ ceramics is sintered in air and vacuum. Dielectric and ferroelectric properties revealed high conduction in vacuum sintered SBN ceramic. A mechanism based on transformation of NbO_6 to NbO_5 has been revealed with the help of Raman spectroscopy.

EXPERIMENTAL

$Sr_{0.5}Ba_{0.5}Nb_2O_6$ (SBN50/50) ceramic are synthesized by conventional solid-state reaction method using high-purity SrO, BaO and Nb_2O_5 as starting materials. The calcination is carried out at 1200°C for 6hrs. The green pallets are sintered at 1400°C in air and vacuum (10^{-6}mbar) for 2hrs. The density of the sintered pellets, ~95% of the theoretical values, are measured by liquid displacement method. The sintered pallets are crushed to fine powder for structural analysis (Rigaku X-ray diffractometer, Cu Kα). Dielectric measurements are carried out using an automated HP4194A impedance analyser over a frequency range of 100 Hz–1 MHz at various temperatures. All the data are collected during the cooling cycle. The electric field-induced polarization (P-E loop) measurements are conducted on a Radiant Workstation PE Materials Analyser using a standard waveform at 1 kHz. Raman spectra of

sintered samples are recorded in a micro-Raman Spectrometer (LABRAM HR-800), working in a backscattering configuration, equipped with an Ar^+ ion (λ = 488 nm) laser. The spectral resolution of the system is 1 cm^{-1}.

RESULTS & DISCUSSION

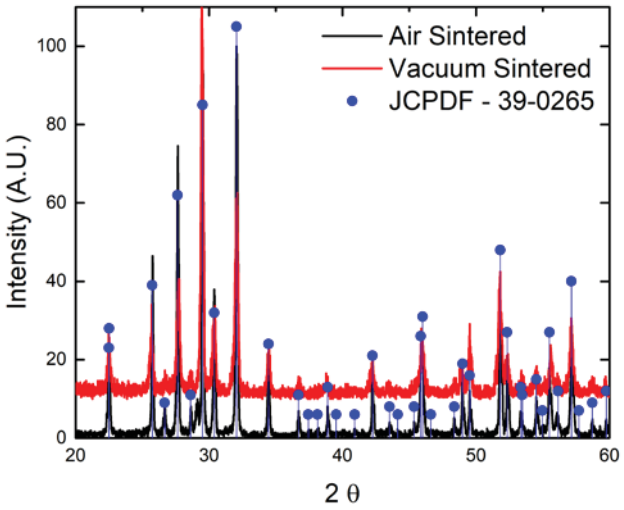

Fig1. XRD pattern of Air and vacuum sintered SBN 50/50

Figure 1 compares the powder XRD patterns of air and vacuum sintered SBN50/50 ceramic samples. No impurity phase, corresponding to Nb_2O_5 as reported by previous researchers [7] in oxygen deficient SBN50/50 ceramic samples, is observed. All the major peaks of XRD pattern are indexed with tetragonal tungsten bronze (TTB) P4bm crystal structure with JCPDF No.39-0265 No effect on crystal structure due to sintering environment is observed. The calculated lattice parameter for both the samples are a=b=12.466(3) Å; c=3.955(1) Å, which is consistent with the earlier reported parameters in the literature.

Temperature dependence of dielectric constant (ε) and dialectic loss tangent (tan δ) for air and vacuum sintered SBN50/50 ceramic is compared in figure 2. For the sake of clarity, data is shown for 100 Hz, 10 kHz and 1 MHz only. It is clear from the figure that air sintered SBN50/50 ceramic shows a diffuse phase transition peak and the temperature of peak maximum is found dependent on the measured frequency, which is similar to the typical relaxor-like dielectric behavior. Maximum dielectric constant (ε_m) decreases and temperature of the ε_m (T_m) shifts towards higher temperature with increase in frequency. No phase transition peak is observed for vacuum sintered SBN ceramic. Both the dielectric constant and tanδ are observed to increase continuously with increase in temperature. The vacuum sintered SBN50/50 ceramic show high dielectric constant and loss at all the frequencies and temperature. Absence of the phase transition peak is due to the high dissipation loss, which seems to mask the peak.

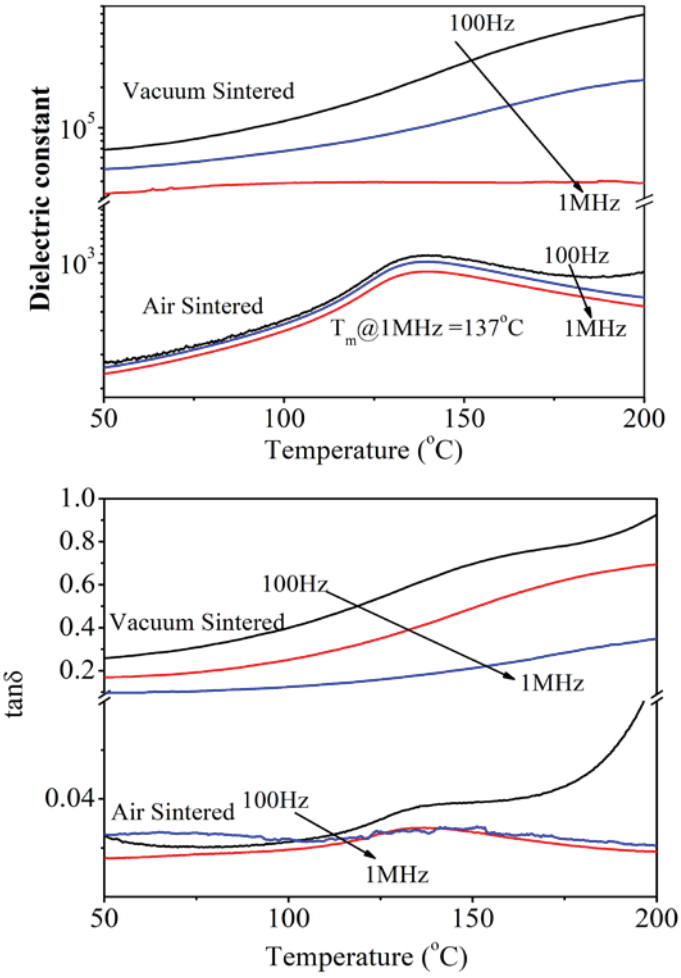

Fig2. Temperature and frequency dependent dielectric constant (upper) and loss (lower) of Air and vacuum sintered samples.

Similar behavior has been reported in many ferroelectric perovskites like other lead-free sodium bismuth titanate (NBT) [8] and bismuth titanate (BT) [9] in which high dielectric loss is associated to presence of the oxygen defects. Therefore, vacuum sintered SBN50/50 ceramic sample indicates high dielectric losses due to oxygen defects. Field induced polarization (P-E) loop (fig. 3) and strain (fig. 4) for vacuum sintered SBN50/50 ceramic is compared with that of air sintered SBN. A well-defined ferroelectric-like P-E curve is observed for air sintered SBN50/50 ceramic having with P_r= 3.2 μC/cm^2 and coercive field Ec= 15.5kV/cm along with ~ 4μm displacement is observed compared to leaky hysteresis P-E loop for vacuum sintered SBN ceramic.

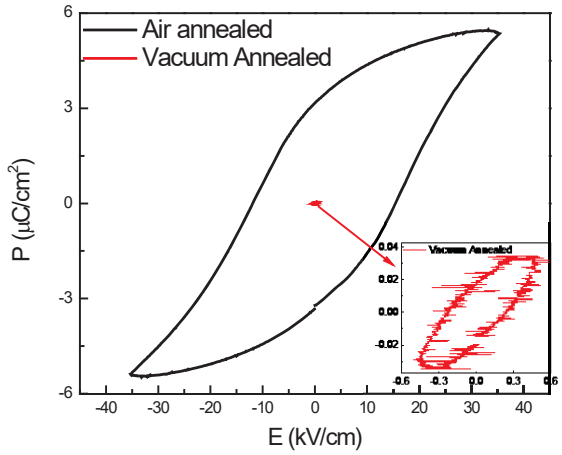

Fig 3. P-E loop of air and vacuum sintered SBN 50/50

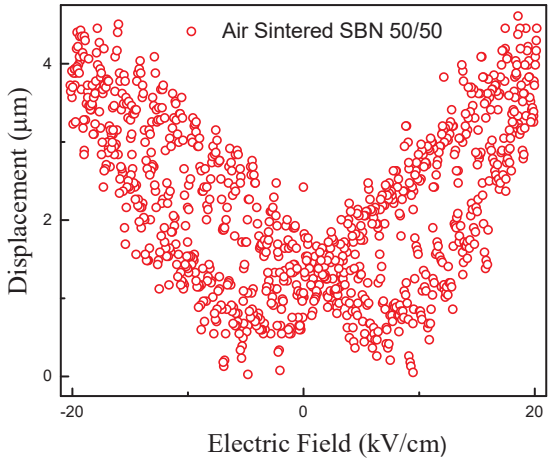

Fig 4. Field induced strain measurement of SBN 50:50

Figure 5 compares room temperature Normalized (with respect to intensity of 630cm^{-1}) Raman spectra of air and vacuum sintered SBN50/50 ceramics. Consistent with earlier reports, the Raman spectrum showed two strong and broad bands around 250 cm$^{-1,}$ 630 cm^{-1} along with another weak band at around 840 cm^{-1}. Out of possible 120 Raman active modes, significantly lower modes are generally observed because of the lattice disorder. The two strong modes around 250 and 630 cm^{-1} are assigned to transverse A1 symmetry modes (NbO_6), which are related to ionic displacements parallel to the ferroelectric axis. The peak at ~ 840 cm^{-1} is assigned to B1 and B2 modes. An important feature inferred from the normalized Raman spectra is that position of 630 cm^{-1} mode is red-shifted and intensity of 830 cm^{-1} mode is reduced when oxygen vacancies are created by sintering SBN ceramic in vacuum, which may be associated with change in NO_6 octahedra. Y. Li et al [10] have discussed the electronic structure of oxygen deficient $Sr_{0.6}Ba_{0.4}Nb_2O_{5.8}$ using first principal calculations and suggested that oxygen vacancies energetically prefer to appear in the B corners of NbO_6 octahedron. Hence NbO_6 octahedron transform to NbO_5 hexahedron via the change of the Nb-O bond angles in ab plane. Sintering SBN50/50 ceramic samples in vacuum involves evolution of oxygen (O_2) from SBN structure via the following reaction:

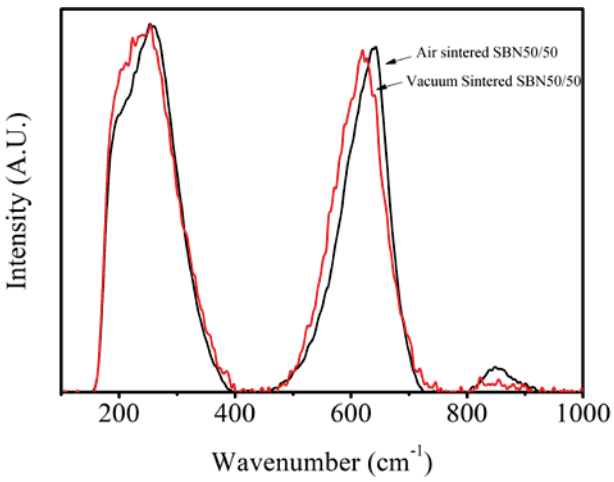

Fig 5. Raman spectra of air and vacuum sintered ceramic

$$O_o^x \rightarrow V_o^{\bullet\bullet} + 2e' + \frac{1}{2}O_2(g).$$

The electrons released during this process may either recombine (i) with positively charged oxygen vacancies ($V_O^{\bullet\bullet}$) to preserve electroneutrality or (ii) may be donated back to Nb^{5+} cations of NbO_6 octahedron, leading to a change in the average Nb valence and an increase in the electrical conductivity as observed in dielectric and polarizations studies. These results are in concurrence with our dielectric and polarization studies of SBN50/50 ceramic. However, the detail dynamics of these bands is matter of further investigation.

CONCLUSIONS:

Effect of oxygen vacancies on ferroelectric and dielectric properties has revealed that high dielectric loss and leaky P-E loop is due to the release of electron in vacuum sintered $Sr_{0.5}Ba_{0.5}Nb_2O_6$ (SBN) ceramic. Phase analysis has revealed formation of tetragonal tungsten bronze (TTB) P4bm crystal structure and no impurity phase is detected. Raman spectroscopy has revealed decrease in the intensity of the mode at 840 cm^{-1}, which may be related to transformation of NbO_6 octahedron to NbO_5 hexahedron.

ACKNOWLEDGMENT

The authors are thankful to Mr. Prem Kumar of LFMD, RRCAT for XRD measurements.

REFERENCES

1. M. Glass, *Appl. Phys. Lett.,* **13**, 147 (1968).
2. M. D. Ewbank, R. R. Neurgaonkar, W. K. Cory, and J. Feinberg, *J. Appl.Phys.,***62**, 374 (1987).
3. P. B. Jamieson, S. C. Abrahams, and J. L. Bernstein, *J. Chem. Phys.*,**48**, 5048 (1968).
4. H. Y. Lee and R. Freer*, J. Appl. Phys*. **81**, 376 (1997).
5. S. Dandeneau, Y. Yang, B.W. Krueger, M. A. Olmstead, R. K. Bordia, and F. S. Ohuchi, *Appl. Phys. Lett*., **104**, 101607 (2014).
6. S. Huang, C. Feng, L. Chen and X. Wen, *Solid State Comm.,* **133**, 375 (2005)
7. J.A. Bock, J. H. Chan, Y. Tsur, S. Trolier-McKinstry and C. A. Randal, *J. Am. Ceram. Soc.*, **99**, 3435 (2016).
8. R. Selvamani, G. Singh, Vasant Sathe, V S Tiwari and P K Gupta, *J. Phys.: Condens. Matter,* **23**, 055901 (2011).
9. S. Rachna, S. Bhattacharyya and Surya M. Gupta, *J. Phys. Chem. Solids.*, **69**, 822 (2008).
10. Y. Li, J. Liu, Y. Chen, X. Zhang, X. Wang, F. Wang, W. Su, J. Li and C. Wang, *Comp. Mater. Sci.,***155**, 393 (2018).

Pulsed Laser Deposition assisted fabrication and characterization of bio-inspired plasmonic nanostructures for efficient absorption of broadband optical radiation

U. Chakravarty[1,4], Jai Khare[1], M.P. Joshi[1,4], C. Mukherjee[2,4], Rashmi Singh[3]

[1]*Photonics Nanomaterial Lab, Laser Materials Processing Division,*

[2]*OpticalCoatings Lab, Laser Technology Division*

[3]*Nano-Functional Materials Lab, Laser and Functional Materials Division*

Raja Ramanna Centre for Advanced Technology, Indore 452 013

[4]*Homi Bhabha National Institute, Training School Complex, Anushaktinagar, Mumbai 400094*

Email: uday@rrcat.gov.in

Abstract

We report fabrication and characterization of bio-inspired metallic nanostructures as an efficient absorber of broadband solar light radiation. We used bottom (hydrophobic) and top (hydrophilic) surface of Palash leaf (scientific name "Butea Monsperma") as a template substrate to grow nanostructures of Cu using the method of pulsed laser deposition. Optical image and reflectivity data of two surfaces coated with Cu showed that the Cu coated top leaf surface is shiny metallic,while the bottom surface has black appearance with strong and broad band optical absorption. The naturally occurring hierarchal micro/nano structures on the bottom hydrophobic surface of these leaves are responsible for similar hierarchal micro/nano structures of Copper. These hierarchal Cu nanostructures enable the excitation of surface plasmons over a wide range optical spectrum and black color appearance of leaf surface. Thermal images of these surfaces under solar light also showed substantial rise of surface temperature (by 90%) for Cu coated hydrophobic leaf surface over deposited Cu film of same coat thickness. Temperature rise has been correlated with absorption strength and local field enhancement. Fabrication of such plasmonic structures on bio-inspired surfaces can be utilized as strong absorber of solar light in many applications including photovoltaic, thermo-plasmonic, solar heating applications etc.

Introduction

Development of strong and broadband visible light absorber materials for various device applications such as photovoltaics, thermo-plasmonics, photo detector/energy meter etc. is an active area of material research. In that respect 1several novel and exotic material systems have been investigated for broadband visible light absorption or as a perfect black material [1,2]. Most material systems for broad band absorption are based on surface plasmon resonance (SPR) induced absorption from metallic nano/micro structures of different shape, density and morphology [1-4]. Effort therefore is made to grow such dense microstructures using variety of deposition techniques [1-4]. Bio-inspired materials such as plant leaf, insect wing etc. are known to be composed of dense microstructures and which is responsible for their different wetting properties i.e. hydrophobic or hydrophilic surfaces and also wide range color appearances. Recent studies have shown successful utilization of these biomaterials, particularly the leaf, as a template substrate to grow metallic nanostructures. The scope of finding dense nanostructure in leaves can be identified by looking for hydrophobicity and small roll off angle of water droplet. The durability and strength of leaf template is also very desirable for practical uses. Palash plant (scientific name "Butea Monsperma") leaves have these features and also have potential for fabricating large surface area of nanostructures particularly for thermo-plasmonic applications. In this work we report efficient bio-inspired broadband absorber material fabricated using pulsed laser deposition of Cu on Palash leaf. Detailed SEM images of grown nanostructures of Cu

reveal dense nanospikes network and hierarchical nano/microstructure when coated on hydrophobic surface of leaf (the bottom surface of leaf). While the top surface of leaf, which is hydrophilic in nature, did not show such hierarchical nano/microstructures. The Cu coated Palash leaf bottom (hydrophobic side) has very low reflectivity and hence appears black whereas the Cu coated Palash leaf top (hydrophobic side) has higher reflectivity with metallic shiny appearance. Copper coated nano-micro particles on bottom leaf surface enables the excitation of surface plasmons which helps in efficient coupling of light and hence dark coloration. This higher absorption in Cu coated Palash leaf bottom results in ~90% increase in temperature over planar Cu film (from room temperature of 26^0Cto ~ 47^0C) as seen from thermal image. These plasmonic nanostructure coated surfaces can be utilized in many applications including thermo plasmonic, solar heating applications etc.

Experimental Details

We used pulsed laser deposition (PLD) method to grow metallic nanostructures of Cu on these leaf surfaces. PLD deposition set up is shown in Figure 1 (a) where leaf substrates are mounted inside a vacuum chamber (10^{-4} Torr pressure) and Cu target was ablated using 5 ns, 10 Hz repetition rate second harmonic (532 nm) pulses of Q-switched Nd:YAG laser. Laser fluence used was ~10 J/cm^2.The deposition was taken on both the top and bottom surface of Palash leaf and simultaneously on glass slide as shown in Fig. 1(a). The bare film of Cu on glass slide was used for comparing reflectivity data and also to measure Cu film thickness. Thickness of the deposited film was measured using mechanical stylus based surface profilometer. A 45 minute PLD process produced ~ 70 nm thick Copper film on Palash leaf. The quantitative reflectivity measurement was made using CARY 5000 spectrophotometer equipped with integrating sphere in Diffuse + Specular (D+S) mode. The nano/ micro structures of coated samples were analysed using SEM (Sigma 02, Carl Zeiss) images. The thermal images for temperature rise measurement was recorded using Fluke make thermal camera.

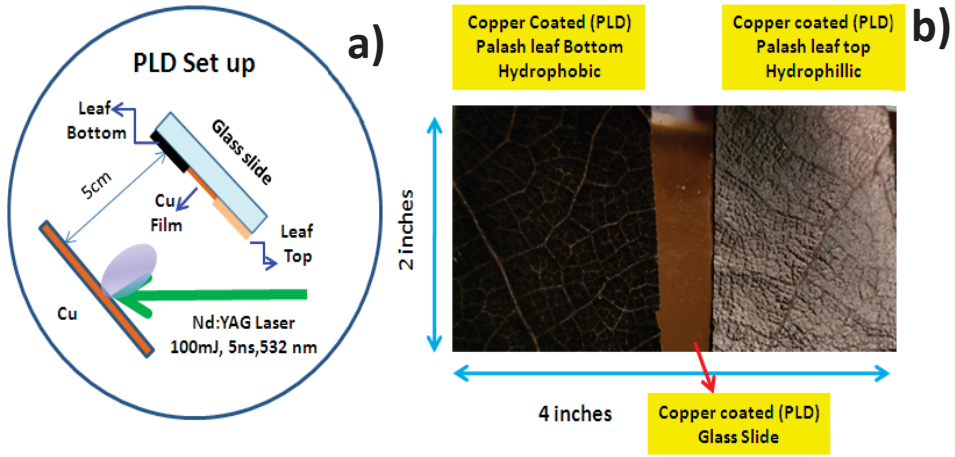

Fig. 1a) Schematic of PLD set up(Top view) b) 70 nm thick Copper coated Palsh Leaf. Fig. 2b) Copper coated substrates. The left side image is the Palsh leaf bottom (hydrophobic side). The right side image is Palsh leaf Top (hydrophilic side). The middle is highly reflecting pure Copper film (70 nm) thick grown on glass slide

Result and Discussion

As seen from Fig. 1b), the Cu coated palash leaf bottom (hydrophobic side) appears black with low optical reflectivity. The right side image is ofCu coated palash leaf top (hydrophillic side) having metallic shine appearance with higher optical reflectivity. The middle image is highly reflecting pure Copper film (70 nm) grown on glass slide. Fig. 2 a) shows the thermal image of these three sample exposed to sun light. The Palash leaf bottom (hydrophobic side) appears hottest (maximum

Temperature of 47^0 C)owing to high absorption of broadband solar light. The right side image of Palash leaf top (hydrophillic side) appears moderately heated (~35 C) due to less absorption of solar light. The middle image of Copper film (70 nm) grown on glass slide appears coolest at room temp ~ 25C due to lowest absorption of solar radiation. The higher absorption in black color appearing leaf can be attributed to the nano/micro structures of Cu on its surface. These structures are seen from SEM image of Copper coated Palash leaf in Fig.2 b).TheCu coated on hydrophobic sideshows a dense network of nanospikes of Cu and typical of hierarchical structures. The rightside SEM image of Cu coated on hydrophilic side shows absence of hierarchical structuresand appears as a coarse continuous film of Cu. The difference in microstructures of Cu on these leaf surfaces are primarily due to different wetting properties i.e. hydrophobic and hydrophilic surfaces.

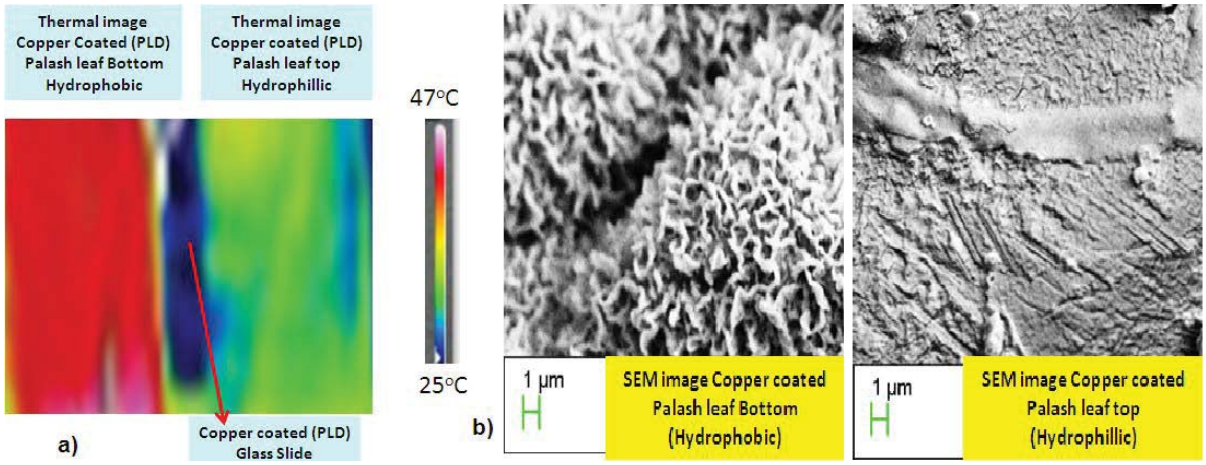

Fig. 2a) The thermal image of Copper coated on two sides of Palash leaf and also bare Cu film of glass slide. Fig.2 b) SEM image of Copper coated on bottom and top surface of Palash leaf.

To get further insight and correlate temperature rise with different microstructures of Cu, we measured optical reflectivity of Cu coated leaf samples. Fig. 3 a) shows the integrated (diffuse and specular) reflectivity data of bare Palash leaf and 70 nm thick Copper coated Palash leaf bottom (R_{sp}) and also of planar Cu film (R_p). Hydrophobic bottom side having dense nanospike network of Cu show broadband absorption as evident from low reflectivity as compared to bare leaf and planar Copper film. The Fig. 3 b) shows the reflectivity data of top of bare Palash leaf along with and 70 nm thick Copper coated on leaf top. Due to coarse deposition of Cu on this surface we observe less broadband absorption as evident from reflectivity data. Temperature rise was analytically formulated by considering total absorption of light by considering light coupling through excitation of surface plasmons in these nano/micro structures [5-7].Temperature enhancement was observed to be strongly dependent on both the absorption (1-R) and field enhancement [5-7]. The temperature enhancement in metal coated leaf due to surface plasmon over a planar solid metal (T_{sp}/T_p) can be obtained as

$$\frac{T_{sp}}{T_p} = \frac{\|E_{sp}\|^2}{\|E_p\|^2}\frac{(1-R_{sp})}{(1-R_p)} = \frac{I_{sp}}{I_p}\frac{A_{sp}}{A_p}$$

Where E_{sp} and E_p is the electric field associated with surface plasmon and the planar Cu target on optical field irradiation. A_{sp} and A_p are the respective optical absorption fraction of the Cu coated Palash and Planar Cu. The prerequisite for temperature enhancement i.e. large optical absorption is present in metal coated hydrophobic side of Palash leaf. The value of A_{sp}/A_p at 500 nm (solar spectrum peak) is 1.5. Further, by considering the Electric field enhancement factor the temperature

enhancement measured from the thermal image (47^0C/25^0C=1.9; 90% increase in temperature over planar Cu film) can be validated.

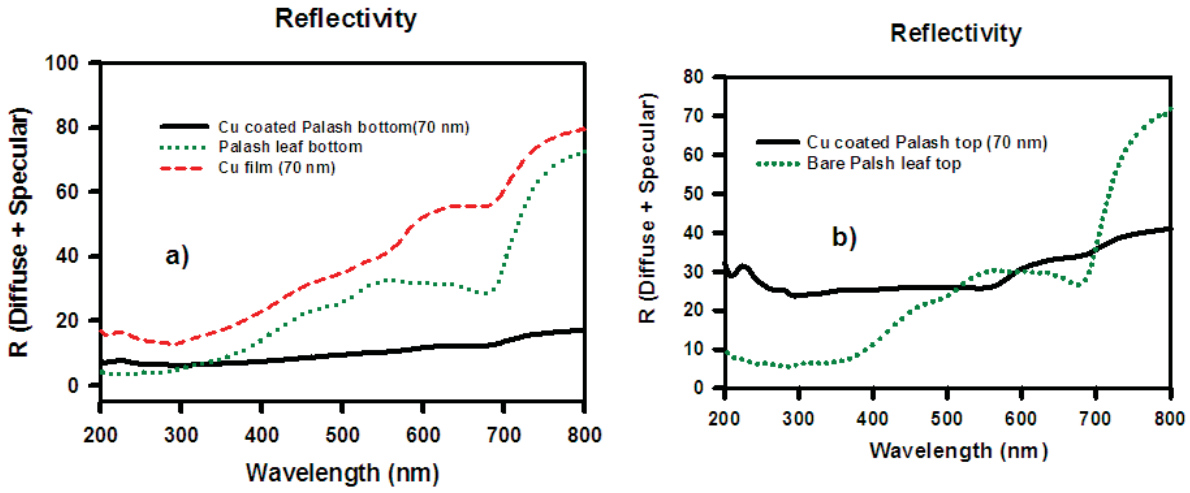

Fig. 3 a) Reflectivity of bottom of bare Palash leaf and 70 nm thick Copper coated Palash leaf bottom and planar Cu film. Fig. 3 b) Reflectivity of top of bare Palash leaf and 70 nm thick Copper coated Palash leaf top.

Conclusion

Cu metal nanostructure based broadband absorber material was fabricated on palash leaf surface using the PLD method. The study clearly brings out the role of hydrophobicity of the leaf surface for identifying potential template substrate for fabricating broadband absorbing material. The dense nanospike network and hierarchical nano/microstructure of Cu on Palash leaf was identified using SEM analysis of Cu coated leaves. Coating with Copper metal helps in efficiently exciting surface plasmons which lead to strong light coupling in such material. The broadband absorption clearly leads to the efficient temperature enhancement as evident from the thermal imaging. This simple and economically viable utilization of leaf surface as substrate material will be useful to fabricate compact and fast heating materials for solar heat/steam generation, thermo-plasmonics and photo thermal applications.

Acknowledgement

The authors would like to thank Dr. Raj Mohan and Shri Rajiv Kamparath RRCAT for their help and support

References

1) Wang, X., He, Y., Liu, X., Cheng, G., & Zhu, J. (2017). Solar steam generation through bio-inspired interface heating of broadband-absorbing plasmonic membranes. *Applied Energy*, *195*, 414-425.
2) Ebihara, Y., Ota, R., Noriki, T., Shimojo, M., & Kajikawa, K. (2015). Biometamaterials: Black ultrathin gold film fabricated on lotus leaf. *Scientific reports*, *5*, 15992.
3) Dao, T. D., Pham, D. D., Nguyen, T. A. H., Tran, T. V. H., Hoang, C. V., & Pham, T. T. (2020). Bio-inspired broadband absorbers induced by copper nanostructures on natural leaves. *Scientific reports*, *10*(1), 1-8.
4) Kobayashi, M., Furusawa, T., Chikuta, T., Shimojo, M., & Kajikawa, K. (2019). Broadband light absorber property of metal-coated pillars on cicada wings. *Optical Materials Express*, *9*(7), 2761-2768.
5) Johnson, P. B., & Christy, R. W. (1972). Optical constants of the noble metals. *Physical review B*, *6*(12), 4370.
6) Weber, W. H., & Ford, G. W. (1981). Optical electric-field enhancement at a metal surface arising from surface-plasmon excitation. *Optics letters*, *6*(3), 122-124.
7) Gamaly, E. G. (2011). *Femtosecond laser-matter interaction: theory, experiments and applications*. CRC Press.

Microwave-assisted preparation of green-emissive carbon dots for potential temperature sensing and pH sensing applications.

Shivanand H. Nannuri[1], Santhosh C[1,2], Sajan D. George[1]

[1]*Centre for Applied Nanosciences, Department of Atomic and Molecular Physics, Manipal Academy of Higher Education, Manipal, Karnataka, India-576104*

[2]*Centre of Excellence for Biophotonics, Department of Atomic and Molecular Physics, Manipal Academy of Higher Education, Manipal, Karnataka, India-576104*

Email id: shivanandhnannuri@gmail.com

Abstract

Carbon dots (CDs) is an emerging class of nanodots that are highly biocompatible and water dispersible. Besides, these particles are highly fluorescing and can be synthesized from naturally occurring materials via microwave or solvothermal techniques. In this work, we present the results of synthesis and characterization of the CDs using glucose as a starting material. A microwave synthesis route is adopted to prepare water-dispersible carbon dots at 160°C for 10 minutes. The as-prepared CDs are characterized by UV–Vis, photoluminescence, XRD, Fourier transform infrared spectroscopy, X-ray photoelectron spectroscopy, ζ-potential from which their structural information and property are interpreted. In addition, as-prepared C-dots demonstrate excellent pH sensing in the range of 3 to 8 and temperature sensing over wide-ranging temperature (30–65 °C) in water.

Introduction

Carbon dots (CDs) are an emerging class of carbon-based fluorescent nanoparticles with a size range of 2-10 nm. Most of the reported carbon dots comprise carbon atoms with considerable fractions of hydrogen, oxygen, and a trace amount of nitrogen and surface functional groups (e.g., carbonyl, carboxyl, hydroxyl, and amine groups). The low-cost synthesis, biocompatibility, tunable emission properties, chemical inertness, high photostability, and good intracellular solubility make CDs a favorable candidate for optical bio-imaging[1]. The accurate measurement of fundamental thermodynamic variables like temperature and pH is increasing importance due to their widespred applications in biology and medical diagnostics. As shown in Fig 1, laser-induced fluorescence setup-based nano-sensors offer potential applications because of their fast response, safety handling, and low cost.

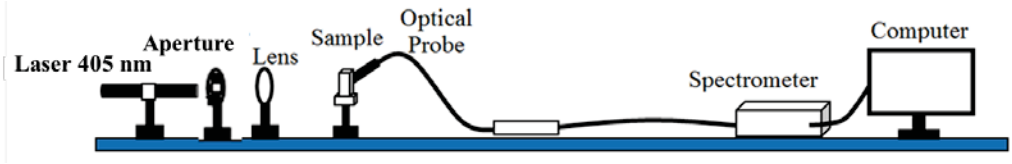

Figure:1. Laser-induced fluorescence setup

Synthesis of Carbon dots (CDs) by microwave method:

Carbon dots were synthesized by microwave method by using carbohydrates (glucose) in water. In a typical procedure, 1.5 g glucose and 0.2 g NaOH were added in 50 mL water under stirring. The solution was then transferred into a microwave vial and heated at a temperature of 160 °C for 10 min with 300 W power. The carbon dots solution was washed with dichloromethane to remove unreacted organic impurities. For further purification, carbon dots solution dialyzed with a dialysis bag (MWCO≈2000 Da) for 24 hours. Finally, black powder C-Dots were obtained by drying at 80°C.

Results and discussion:

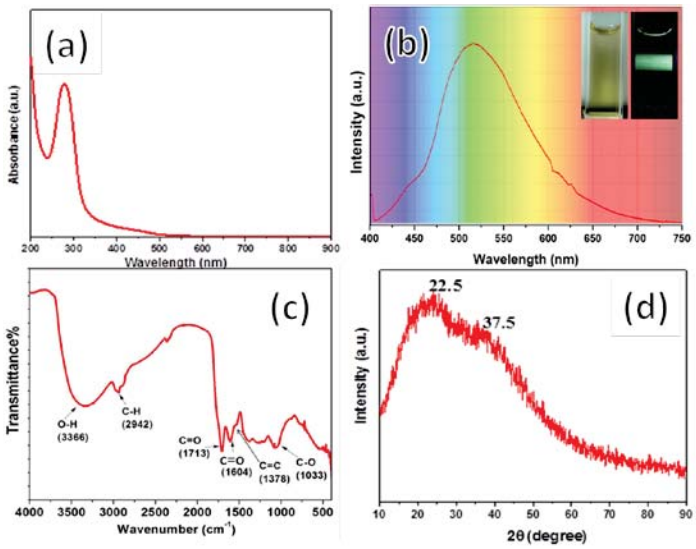

Figure:2. Absorption spectrum (a), emission spectrum (b), FTIR (c) , XRD (d) spectrum of CDs.

The UV-Vis absorption spectra and emission spectra of CDs were collected, as shown in Figure. 2 (a) and (b), respectively. Absorption spectra of C-dots show bands at 275 nm corresponds to the π-π* transitions of conjugated C=C bands and n–π* transition of the C=O bands[2]. Under 405 nm excitation, the carbon dots yield green emission at 520 nm fig 2(b). The photograph (Fig. 2b, inset) shows the CDs dispersed in water under visible light (left) and illumination at 405 nm (right). The XRD pattern of the CDs fig. 2(c) shows a broad diffraction peak centered at The XRD pattern of the CDs (Fig.2d) shows a broad diffraction peak centered at 2θ =22.5° and 37.5°, which is attributed to the amorphous carbon phase[2]. The surface functional groups of the CDs are detected by FTIR fig. 2(c) characteristic absorption bands of O–H (3366 cm^{-1}), the stretching vibration band of C=O (1713 cm^{-1}, 1604 cm^{-1}), and the stretching vibration bands of C–O (1033 cm^{-1}). Moreover, the peaks at 2942, 1378 cm^{-1} are associated with the stretching and bending vibrations of C–H, C=C, respectively[3].

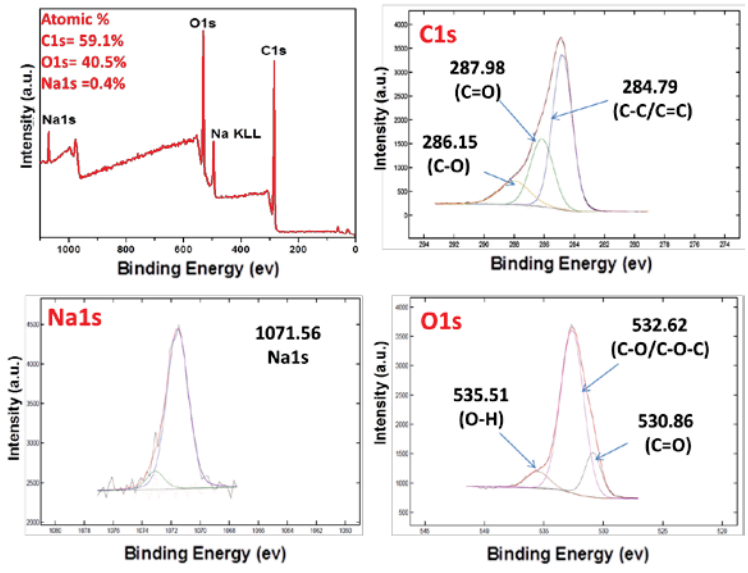

Figure:3 XPS spectra of survey scan of CDs and C1s,Na1s and O1s.

The XPS measurement showed the existence of two elements, C and O (Fig. 3). The deconvolution of the C1s spectrum of the CDs indicated the presence of three types of carbon bonds 284.79 eV (C-C/C=C), 286.15 eV (C-O) and 287.98 eV (C=O). The deconvolution of the O1s peaks could attribute to the 530.86 eV (C=O), 532.62 eV (C-O/C-O-C) and 535.51 eV (O-H) and accounting for 59.1%, 40.5% and 0.4% of C, O and Na elements in the CDs[4].

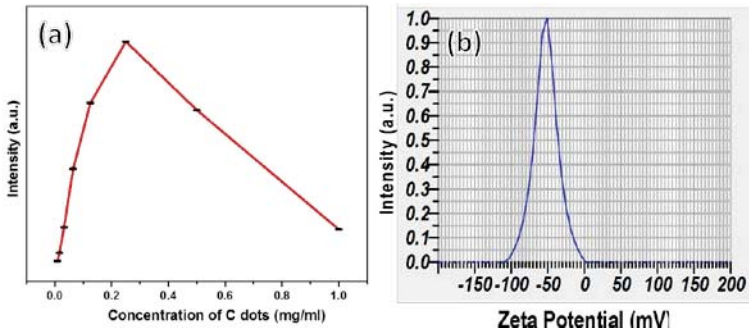

Figure :4 Concentration-dependent emission and zeta potential of CDs

The effect of CDs concentration in the range of 0.08 to 1 mg/mL was investigated. From the concentration-dependent emission shown in Fig. 4, the PL intensity decreased at lower and higher concentrations, at 0.25 mg/mL achieved maximum intensity. The emission increased because of the reduction in self-absorption quenching and collisional quenching at high-concentration[5]. The zeta potential of the CDs in the water was -52.5 mV, thus indicating the electrostatic stabilization of the CDs in an aqueous solution, as shown in Figure 4(b).

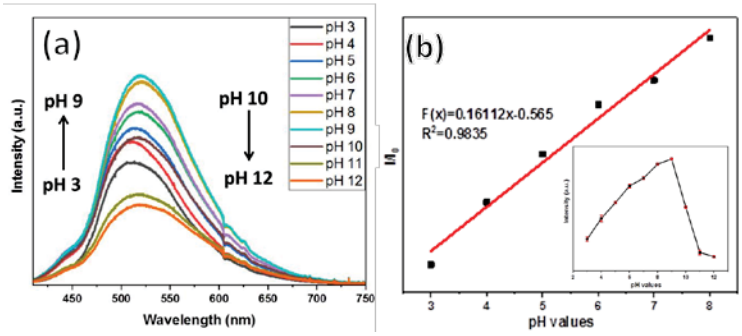

Figure 5. pH-dependent emission of CDs

The pH of the medium has a substantial influence on the emission intensity of fluorescent CDs. It is evident in Fig. 4 that the fluorescent intensity increased gradually by varying the pH values from 3 to 9, while the fluorescence intensity decreased rapidly in the range of 10 and 12. The CDs showed an excellent linear relationship between the enhancing efficiency (I/I_0) and the pH range of 3 to 8. fitted as a function of F(x)= 0.16112x-0.565 with a correlation coefficient R^2=0.9835. Here, I is the integrated intensity at various pH, Io is the integrated intensity at pH 3 and x, and F(x) represents the variation of fluorescence intensity with pH value under 405 nm excitation. This could be used as a potential pH sensor in acidic conditions. For higher pH values from 6 to 9, the emission peak slightly redshifted from 510 to 520 nm. Yang et al., reported similar studies where the fluorescence of CDs enhanced along with pH value increasing from 1.48 to 7.56, then slowed down when the pH reaches the values more than 8. Also, the redshift of fluorescence emission peak at high pH values.

This may be due to the deprotonation of surface groups of CDs at high pH values and might form a new surface state[6].

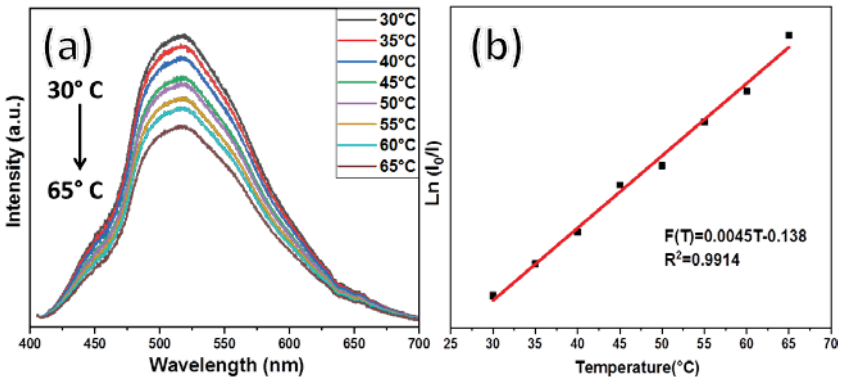

Figure 6. Temperature-dependent emission of CDs

More interestingly, the CDs very sensitive to temperature variation. Fig.6(a) shows the temperature dependence of emission spectra of the as-prepared CDs. The fluorescence intensity decreased by ~50% upon raising the temperature from 30°C to 65°C. Fig 6(b) shows the excellent linear relationship between the logarithm of intensity ratio (I_0/I) and the temperature. The linear curve can be fitted to the function of F(T)= 0.0045T-0138, with a correlation coefficient R^2=0.9914. Here, I is the integrated intensity at various temperatures, Io is the integrated intensity at 30°C, and T and F(T) represent temperature and fluorescence intensity at 405 nm laser excitation. The temperature-dependent fluorescence intensity decrease feature could be attributed to the temperature enhanced population of nonradiative channels of surface (trap/defect) states and excited electrons returned to the ground state through nonradiative relaxation[7]. Therefore, the CDs have the potential to be developed as a sensitive, robust temperature sensor.

Conclusion

CDs have been successfully synthesized by microwave treatment. FTIR, XPS characterizations confirm the formation of C-Dots. The as-prepared CDs possess excellent aqueous dispersibility. Based on the pH and temperature dependence of their steady-state fluorescence emission spectra, the as-prepared CDs can be used as potential pH sensors in acidic conditions and temperature sensors over the physiological temperature range (30–65 °C).

Refrences

1. Li H, Yan X, Kong D, Jin R, Sun C, Du D, et al. Nanoscale, Horiz 2020;5(2):218.

2. Wei J., Zhang X., Sheng Y., Shen J., Huang, P, Guo S, et. al. New Journal of Chemistry, 2014; 38(3):.906.

3.Kurdekar A., Chunduri .A., Bulagonda.P., et.al. Microfluidics and Nanofluidics, 2016;20(7), .99.

4. Jia, X., Li, J. and Wang, E., 2012. Nanoscale, 2012;4(18):5572.

5. Song, Y., Zhu, S., Xiang, S., Zhao, X., et.al. 2014.. Nanoscale, 2014;6(9): 4676.

6. Yang, M., Li, B., Zhong, K. and Lu, Y., 2018. Journal of Materials Science,2018; 53(4):2424.

7. Mohammed, L.J. and Omer, K.M., Nanoscale Research Letters, 2020; 15(1):1.

Optical Properties in CZF ferrofluids

Arkilang Challam, Mahendar Nandikonda, Md. Sharif C, Ashok Vudayagiri, R.Singh
School of Physics, University of Hyderabad, Hyderabad 500046, India
Email: arkilang22@gmail.com

Abstract: Copper Zinc Ferrite nanoparticles are dispersed in distilled water as their carrier liquid for preparing the different concentrations for magneto-optical characterization, and are subjected to uniform field where the Magneto-Optic rotation (MOR) is studied using green He-Ne laser of wavelength 543.5 nm to propagate through CZF. These ferrites are generally isotropic in nature, but under magnetization, the magnetic nanoparticles aligned themselves along the direction of an easy axis of the fluid, resulting to an increasing magnetic moment along an easy axis and decreasing magnetic moment along a hard axis of the ferrofluid, thus, making their isotropic behavior anisotropic.

Introduction: The interaction of light with matter is affected by the magnetic state of the medium and involves the electronic structure of the matter. Such interaction between electromagnetic radiation and magnetically polarized materials results in 'Magneto-Optic' effects [1]. Ferrofluids are the suspension of colloidal nanoparticles which have both the fluidity and magnetic behavior of the liquids and the magnetic materials respectively [2]. Ferrofluids are optically anisotropic which exhibit several optical properties such as Magneto-Optic and dielectric properties [3], dichroism, birefringence, etc [4]. Due to their stability, there are no phase separation or aggregation of particles even under strong magnetic field, they are excellent candidates to use for Magneto-Optic rotation (MOR) which is our main interest in this research. Ferrofluids can be synthesized by different methods such as co-precipitation, micro emulsion, ball milling, sol-gel method, etc [5]. In our experiment, co-precipitation method is used for synthesis of ferrofluids due to its less energy requirements and low cost. Brownian energy due to randomization of nanoparticles may not be able to overcome the dipole-dipole and van der Waal attractive forces, thus an extra repulsive force is needed to prevent agglomeration and sedimentation of magnetic nanoparticles. Coulomb repulsion is used when the particles are either positive or negative charges which is used for ionic ferrofluids where a polar carrier liquid (water) is needed, and Steric repulsion is used where the particles are coated with a suitable surfactant which is used for surfacted ferrofluid with any carrier liquid (water, oil, etc)]. However under breaking down of surfactants, there will be aggregations of nanoparticles. In our experiment, steric repulsion is used for synthesizing Cu-ZnFe2O4 ferrofluids with Dodecylbenzenesulfonic acid (DBSA) as a surfactant and water as a carrier liquid. In most experimental set-ups, the external field is applied parallel to the beam propagation, and are observing a MOR for higher fields of two orders of magnitude in Gauss with different concentrations. In our experimental set-up, the external field is applied perpendicular to the beam propagation, where magneto-optic effect is observed at low fields of single order of magnitude in Gauss with different concentrations of ferrofluids, where it reaches a maximum MOR after the threshold magnetic field occurs. MOR increases with an increasing in concentration till it reaches a critical concentration after where it drops. In our set-up, a laser beam is passed through the ferrofluids sample, in a direction perpendicular to a magnetic field, variation in the transmission will occur due to optical anisotropy of magnetic particles. The ferrofluids under the influence of an external magnetic field, the field will induce the magnetic and dielectric anisotropies, resulting to optical activity of the magnetized anisotropic, where it will

rotates the plane of polarization, the phenomena known as Magneto-Optic Rotation (MOR). The rotation of the rod-liked short chains of magnetic fluids is caused by the external magnetic field along the direction of the field. Applied magnetic field is used to revamp the optical properties of ferrofluids. Magneto-optic properties due to structural reorientation of the nanoparticles suspended in magnetic fluid, they can be used in developing photonic devices, like optical sensors, etc. In addition to optical-device applications, is is also used in detection system design for glucose concentration, measuring the speeds of artillery projectiles, estimating the properties of oscillating currents and in communication technologies. The DBSA coated Cu-ZnFe2O4 ferrofluids shows good response in magneto-optic effects at low fields of few gauss of magnetic fields, which can be applied to many physical measurements without the need of a high magnetic field. It is also very useful in sensing small magnetic field and adjustment of light intensity. It has a very good history of contribution in basic sciences, where in 1931, Allison using this method, detected a heavy isotope of hydrogen, and this motivated a Chemist Harold Clayton Urey to discover Deuterium which he won the Nobel prize in Chemistry in 1934.

Materials and Methods

1.1. Synthesis of Cu-ZnFe2O4 magnetic nanoparticles

For the synthesis of Cu0.8Zn0.2Fe2O4 magnetic nanoparticles by the co-precipitation technique, following steps are followed as shown in Figure 1.

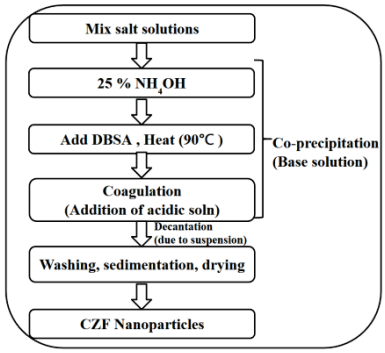

***Fig. 1**: Flowchart of the synthesis of Cu-ZnFe2O4 (CZF) nanoparticles.*

1.2. Physical properties of Cu-ZnFe2O4 NPs

In Figure 2(a), the crystalline structure of the Cu0.8Zn0.2Fe2O4 NPs is confirmed from an X-ray diffraction (XRD) analysis using Bruker powder diffractometer. The (111), (220), (311), (220), (400), (511), (440) and (533) diffraction peaks observed on the curves can be indexed to the spherical structure, and all the peaks were in good agreement with the Cu-ZnFe2O4 phase (JCPDS card 19-0629). The molecular structure of Cu-ZnFe2O4 molecule is represented in Figure 2(b) having molecular weight 304.62 g and density 5.5 g/mL at 300 K in nanopowder form. Cu-ZnFe2O4 is a dipolar compound having delocalized electrons together with DBSA as its surfactant which acts as a Bronsted acid-surfactant combined catalyst to avoid agglomeration and cluster formation of Cu-ZnFe2O4 NPs in a carrier liquid. The magnetic properties (Hysteresis loop) of NPs are shown in Figure 2(c) as measured at room temperature 300 K with a vibrating sample magnetometer (Lakeshore

VSM), where the saturation magnetization (MS) was determined as 76 emu/g. The particles showed no remanence or coercivity at 300 K, that is, super paramagnetic behaviour.

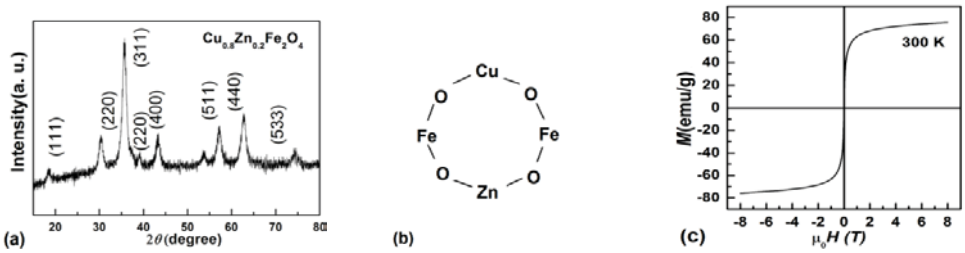

***Fig. 2**: At Room temperature (300K): (a) Powder XRD for DBSA coated Cu-ZnFe2O4 NPs. (b) Molecular structure of Cu-ZnFe2O4 molecule. (c) Hysteresis loop of super paramagnetic NPs.*

2. Experimental details

2.1. Preparation of Cu-ZnFe2O4 Ferrofluids

Water based Copper-Zinc ferrite ferrofluids are prepared by suspending the synthesized DBSA coated Cu-ZnFe2O4 nanoparticles in distilled water as a carrier liquid and sonicated for 20 minutes: 0.05 mg of synthesized Cu-ZnFe2O4 nanoparticles is mixed in 300 µL of distilled water, and the concentration of this ferrofluid is calculated as 0.17 mg/ml. This solution is again diluted into five different concentrations of 3.07×10-3 mg/ml, 3.67×10-3 mg/ml, 4.06×10-3 mg/ml, 5.05×10-3 mg/ml and 6.02×10-3 mg/ml as shown in Figure 3(a), and are tabulated in Table1. The response of Cu-ZnFe2O4 magnetic ferrofluids to a non-uniform strong magnetic field of two orders of magnitude in Gauss produced by permanent magnets (made up of a NdFeB material) is shown in Figure 3(b). Using Particle Size Analyzer (PSA, Model: Litesizer TM 500, from Anton Paar), the hydrodynamic diameters of different concentrations of ferrofluids are noted from the histogram plot. On increasing the concentrations of ferrofluids from 3.07×10-3 mg/ml to 6.02×10-3 mg/ml, the hydrodynamic diameter of particles decreases from 71.41 nm to 29.29 nm as shown in Figure 3(c) and is tabulated in Table 1.

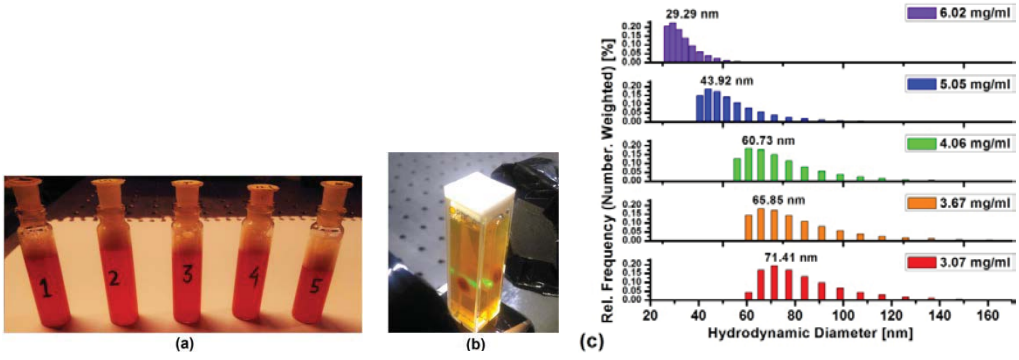

***Fig. 3**: At Room temperature (300K): (a) Synthesized Cu-ZnFe2O4 ferrofluids samples of different concentrations.(b) Nanoparticles (NPs) response between two permanent magnets. (c) Particle size distribution of different concentrations of Cu-ZnFe2O4 ferrofluids using PSA.*

Table 1: *Cu-$ZnFe_2O_4$ ferrofluid samples of different concentrations.*

Sample Name	Samples No	Volume of Ferrofluid solution having concentration of **0.17 mg/ ml** (μL)	Water volume (μL)	Concentration of Cu-$ZnFe_2O_4$ in distilled water (10^{-3}) (mg/ml)	Particle hydrodynamic diameter (nm)
	1	7.5	400	3.07	71.41
$CuZnFe_2O_4$	2	9	400	3.67	65.85
Ferrofluids	3	10	400	4.06	60.73
	4	12.5	400	5.05	43.92
	5	15	400	6.02	29.29

References:

1. Taskeya Haider, *International Journal of Electromagnetics and Applications.* **17-24** (2017).
2. Ibrahim Sharifi, H. Shokrollahi, and S. Amiri, *Journal of Magnetism and Magnetic Materials.* **903-915**, 324 (2012).
3. N.A. Yusuf and I.O. Abu-Aljarayesh, *Jordan Journal of Physics.* **1-46**, (2009).
4. J P Llewellyn, *J. Phys. D: Appl. Phys.* **95-104**, 16 (1983).
5.] J. Amighian, E. Karimzadeh, and M. Mozaffari, . *Journal of Magnetism and Magnetic Materials.* **157-162** 332 (2013).

Characterization of Aerosol Assisted CVD Grown Ni:ZnO Thin Films

Vipin K. Kaushik, Shweta Tiwari, Gourang Vani

Dept. of Appl. Phy. & Optoelectronics, Shri G. S. Institute of Technology and Science, Indore-452 003
E-mail: vip08007@gmail.com; vipink@sgsits.ac.in

Abstract:

Present work reports the successful growth and characterization of Ni:ZnO thin films with varying Ni-content in precursor solution (x_{Ni} = 0.0, 0.10, 1.00, 4.84, 9.25 and 13.27 *at.* %). An indigenously designed and developed aerosol assisted chemical vapour deposition system has been used for the growth of Ni:ZnO thin film at 500 °C. The average transmittance of pure and Ni-doped ZnO came out to be about ≥95 %. Raman spectroscopy, XRD and UV-VIS spectroscopy were utilized to investigate the optical and structural properties of Ni: ZnO thin films. Raman spectra of pure and Ni-doped ZnO thin films measured at room temperature in the wavenumber range 200-4000 cm^{-1}.

Introduction:

Due to its versatility, ZnO has drawn considerable attention, thin films of ZnO find a multitude of immensely impotant applications in electronic and optoelectronic devices such as photothermal conversion systems, transparent conductors, gas sensors for toxic and combustible gases and heat mirrors among many others [1]. Ni doped ZnO is considered as an important II-VI diluted magnetic semiconductor material due to its unique magneto-electrical and magnet-transport properties[2]. The microstructural and optical properties of ZnO are very much sensitive. NiO has face-centered rombohedral crystal structure with lattice constants: a = 4.17 Å, $\alpha = 90^{o}3.8'$ (at room temperature). NiO can also exhibit small deviations from strict stoichiometry, for example: [3] $Ni_{(1-\delta)}O$, where $0 < \delta < 5\ 10^{-3}$. At δ close to the upper boundary, the material is opaque with black/brownish colour, while with δ closer to zero the material becomes green and translucent (usually upon annealing). The resistivity can be lowered by inclusion of Ni^{+2} ions either through Ni vacancies and/or interstitial oxygen in NiO crystallites. The actual charge conduction mechanism in nickel oxide is still not clear [4].

TCOs are one of such type of semiconducting materials. TCOs are highly conducting with low absorbance in visible and near infrared (IR) region, but have high UV absorption properties since these materials have high transparency in the visible region of the electromagnetic spectrum. TCOs are wide band gap semiconductor that have relatively high concentration of free electrons in the conduction band. The conductivity and mobility of TCOs can be modulated according to the doping concentration that in turn improve transparency and band-gap for TCOs. TCOs represent a compromise between electrical conductivity and optical transmittance science for the device application careful balance between these properties are required.

Results and Discussion:

The films were grown by an indigenously developed aerosol assisted chemical vapour deposition system. The different mass proportion of zinc acetyl acetonate (w_1) and nickel acetyl acetonate (w_2) dissolved in a certain volume of isopropyl alcohol have been used to have the various concentration of precursor. Table 1 shows the experimentally chosen values of faction of nickel content in precursor solution (x_{Ni}), precursor concentration (PC), deposition time (D_t), thickness (t), deposition rate (D_R) and the optical band gap (E_g) of AACVD grown Ni:ZnO thin films.

The value of x_{Ni} have been calculated in atomic percent (*at.*%) and weight percent (*wt.*%). For these calculations the following expressions have been used.

$$x_{Ni} = (w_1 \times 100)/(w_1 + w_2) \quad (wt.\%)$$
$$= (w_1 \times 100)/(w_1 + w_2 \times C) \quad (at.\%) \quad (1)$$

Here, C is the ratio of molecular weight of nickel acetyl acetonate (258.93 amu) to the molecular weight of zinc acetyl acetonate (263.61 amu) i.e., 258.93/263.61 = 0.98. The formula used for the calculation of precursor concentration was (w_1 + w_2)/volume of IPA. To calculate the thickness of the present thin films the density method has been adopted. According to this method the thickness of the film can be calculated by using the following expression.

$$t = m_f / (d_f \times A_f) \quad (2)$$

Table 1: Experimental parameters of AACVD grown Ni:ZnO thin films

S. No.	w_2 (g)	w_2/w_1 Ratio	x_{Ni} (at. %)	x_{Ni} (wt. %)	PC (g/l)	D_t (min.)	t (nm)	D_R (pm/s)	E_g (eV)
1.	0.00	—	0.00	0.00	10.00	40	154	64	3.26
2.	0.002	1:1000	0.10	0.09	10.01	30	134	74	3.25
3.	0.02	1:100	1.00	0.99	10.10	40	185	77	3.24
4.	0.1	1:20	4.84	4.76	10.50	32	109	57	3.16
5.	0.2	1:10	9.25	9.09	11.00	35	216	103	3.13
6.	0.3	3:20	13.27	13.04	11.50	35	209	100	3.10

Here, m_f is the mass, d_f is the density and A_f is the surface area of Ni:ZnO thin films. In the present calculations the density and surface area of AACVD grown Ni:ZnO thin films were found to be 5.61 g/cm^3 and 1 cm^2, respectively. The mass of the deposited thin films have been calculated by the difference of pre and post deposition masses of substrate. The calculated values of thickness of the films have been shown in table 1. These values have further been used to calculate the rate of deposition D_R of thin films which is the ration of the film thickness and the time of deposition D_t as given in the table 1.

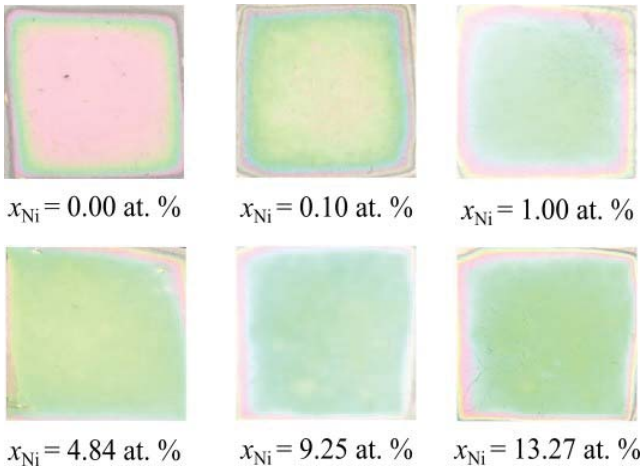

Figure-1: *Pictorial view of AACVD grown Ni:ZnO thin films with varying x_{Ni}.*

molecules at the heated substrate. The calculated value of average rate of deposition of the films was (0.335 ± 0.030) nm/s. The effect of Ni doping in the lattice of ZnO can be seen by the color of present films. As the x_{Ni} increases the reflation shifts form red wavelength to the green wavelength i.e. blue shifting of reflation and hence the red shift of absorption edge or band gap. The same has been confirmed by the optical spectroscopy of the films. The present film have been characterized for their structural and optical properties.

1. X-ray Diffraction Spectroscopy of AACVD Grown Ni:ZnO Thin Films

To focus on the structural properties of the grown films x-ray diffraction have been carried out. In this figure 2 the angle of diffraction (2θ) for a polycrystalline specimen has been plotted as a function of diffracted beam intensities where every single peak in the diffraction pattern corresponds to a set of crystallographic planes. The presence of number of diffraction peaks indicates that the films possess a polycrystalline structure. For all the samples three well-defined diffraction peaks (100), (002) and (101), have been used to calculate the lattice constant, lattice volume, crystalline size and the lattice strain of Ni:ZnO thin films are corresponding to the wurtzite (hexagonal) ZnO crystalline structure.

2. Raman Spectroscopy

Figure 3 shows the raman spectra of pure and Ni doped ZnO thin films measured at room temperature in the wavenumber range 200-4000 cm^{-1}. In case of undoped ZnO thin film, the strong and intense peak appearing at 1180 cm^{-1} has been designated as high frequency branch for the E2 mode of ZnO thin films. The blue shift in Raman spectra is observed and the corresponding peak value is centered around 1104 cm^{-1}. Raman spectra of Ni-doped ZnO shows the presence of large vibration mode centered around 560-565 cm^{-1} which can be assigned

as local vibrational mode bounded with the various donar defects. Moreover, the different peaks appearing at various energy values can be considered as second-order vibration mode, optical mode and the optical phonon mode.

3. Ultraviolet-Visible Spectroscopy of AACVD grown Ni:ZnO Thin Films

Ultraviolet-visible transmittance spectra of AACVD grown Ni:ZnO thin films having Ni-content x_{Ni} varying from 0.0 to 13.27 at.%. A STDFSM digital fiber spectrophotometer has been used to measure the transmittance spectra from 300 to 800 nm, of Ni:ZnO thin films deposited on soda lime glass substrates. The presence of clearly visible interference fringes in the visible region of transmission spectra justify that the present AAVCD grown Ni:ZnO thin films have optical uniformity with appreciable transmittance. As depicted by figure 4, within the high visible region of 550 to 800 nm the average optical transmittance (T_{avg}) of Ni:ZnO thin films is ≈ 90%. For all the films a sharp band edge absorption at ≥ 380nm wavelength has been observed which corresponds to the optical band gap of pure and doped ZnO. The variation of $(\alpha h\nu)^2$ as a function of indicant optical energy hν that can be used to determine Eg

The x-axis intersects of asymptote of $(\alpha h\nu)^2$ Vs. hν curve at $(\alpha h\nu)^2 = 0$ directly gives the bandgap of thin film. It is interesting to note that with the increase of x_{Ni} a monotonically decreasing trend in the bandgap of Ni:Zno have been observed. This is because with the doping of Ni^{+2} ions in the lattice of ZnO the presence of excess Ni^{+2} ions increases that dominate the band gap renormalization effect and hence reduce the band gap of Ni:ZnO as compare to that of ZnO thin film.

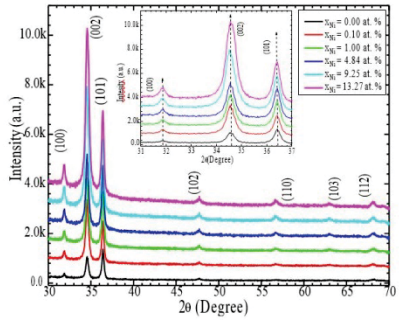

Figure-2: *θ-2θ scan of x-ray diffraction pattern of AACVD grown Ni:ZnO thin films. The effect of x_{Ni} over the shift in the position of three prominent peaks (100), (002) and (101) of Ni:ZnO has been highlighted by the inset of the figure*

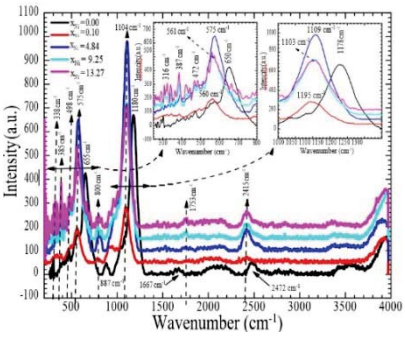

Figure-3:- *Raman spectra of AACVD grown Ni:ZnO thin films having different Ni-content.*

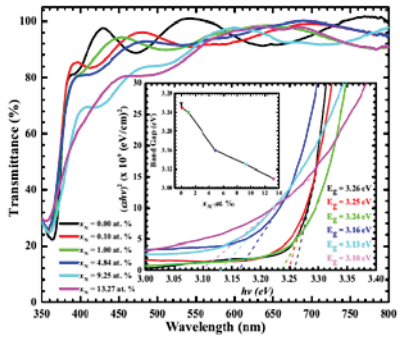

Figure:4:*Ultraviolet-Visible transmittance spectra of AACVD grown Ni:ZnO thin films having different Ni-content. Inset shows the variation of $(\alpha h\nu)^2$ and a function of incident photon energy hν. The plots are used to calculate the variation of optical band gap Eg as a function of x_{Ni} that has also been shown in the inset of figure.*

Conclusion

In summary, the deposition parameters like deposition temprature and precursor flow rate of indigenously designed and developed aerosol assisted chemical vapor deposition system have been successfully optimized for the fabrication of Ni:ZnO thin films. The present work can be concluded with the following scintillating findings.

Ni:ZnO thin films having various Ni contents x Ni , have been deposited on soda lime glass substrate kept at constant growth temperature of 500 ^{o}C.

Raman spectroscopy, XRD and UV visible spectroscopy measurements were utilized to investigate the effect of varying x Ni over the optical and structural properties of Ni:ZnO thin films.

The XRD of Ni:ZnO thin films reveals that the required phase is present with a little amount of impurities that matches well with the with JCPDS data indicating the hexagonal structure. The particle sizes measured by by the XRD Scherer's formula, values lattice constants and the volume of unit cell of Ni:ZnO were found to be in a good agreement with literature.

UV-VIS spectroscopy of gown films shows that the films were highly transparent in the visible spectra. The optical band gap of the films shows considerable decrease with increasing the dopant concentration suggest that, Ni doping successfully narrows the band gap of ZnO. The AACVD grown Ni:ZnO thin films were found to have low average absorbance ≈ 1% and high average reflectance ≈ 40%.

Raman spectroscopy of the films shows the presence of various vibrational modes like first and second-order vibration mode, optical mode (transverse) and the optical phonon mode (longitudinal). The doping of Ni $^{+2}$ ions in the lattice of ZnO were confirmed by the clearly observed shifts in the optical modes of ZnO thin films.

References

1. S. Ghosh, P. Srivastava, B. Pandey, M. Saurav, P. Bharadwaj, D. K. Avasthi, D. Kabiraj and S. M. Shivaprasad, "Study of ZnO and Ni-doped ZnO synthesized by atom beam sputtering technique", Applied Physics Materials Science and Processing, 90, 765-769 (2008).
2. K. karan, M. Chandramohan, R. Balamurali, S. D. Karan, V. and Mahalingam, "The Influence of Ni doping on the structural, optical and morfological properties of ZnO thin films grown by silar method", International Journal of Current Research, 4, 023-025 (2012).
3. M. R. A. Bhuiyan and M. K. Rahman,"Synthesis and Characterization of Ni Doped ZnO Nanoparticles", I. J. Engineering and Manufacturing, 1, 10-17 (2014).
4. T. Minami, "New n-Type Transparent Conducting Oxides", Cambridge University Press, 25, 38-44 (2000).
5. H. R Khan, B. Akramd , M. Aamira , M. A. Malikb, A. A. Tahirc , M. A. Choudharya , J. Akhtara, "Fabrication of Ni^{2+} incorporated ZnO photoanode for efficient overall water splitting" Applied Surface Science 490 (2019) 302–308 (2019).
6. N. Guermat , W. Daranfed , I. Bouchama , N. Bouarissa, "Investigation of structural, morphological, optical and electrical properties of Co/Ni co-doped ZnO thin films" Journal of Molecular Structure 51 (2021) 129134 (2020).
7. S. Prasad, S. Bansal, S.P. Pandey, "Structural, raman, photo-luminescent and optical investigation of sol-gel derived Co, Al and Ni doped ZnO thin films", Materials Today ,2214-7853, (2020).

Effect of melt pool geometry on laser polishing of Laser Additive Manufactured SS 304

Ambar Choubey[*1], A.N. Jinoop[2], Sabir Ali[1], S.K. Mishra[1], C.P. Paul[1, 2], K.S. Bindra[1, 2]

[1] Laser Technology Division, Raja Ramanna Centre for Advanced Technology, Indore-452013
[2] Homi Bhabha National Institute, Anushakti Nagar, Mumbai-400 078
[*]E-mail: ambarchoubey@rrcat.gov.in

Abstract: Laser Additive Manufacturing (LAM) is one of advanced manufacturing processes used for the fabrication of complex shaped components directly from 3D model data using shapeless raw material. Generally, waviness pattern is observed on the surface of LAM built structures. Post-processing techniques, like – polishing are necessary to be applied on LAM built components to reduce the waviness on the surface. In the present work, laser melting using CW fiber laser is used for the surface polishing of LAM built SS 304 sample. Different settings of laser process parameters are used for the optimization of the melt pool width and depth to achieve reduction in the surface waviness after solidification. The measured optimum melt pool depth and width is ~50 μm and 450 μm respectively at 200 W laser power, 70% line overlapping and 300 mm/s speed to achieve desire smooth surface.

Introduction: Laser Additive Manufacturing (LAM) is a disruptive technology used primarily for building for the fabrication of complex shaped components directly from digital model data. Stainless steel SS 304 is one of the popular alloys used for industrial applications due to its excellent mechanical properties and corrosion resistance. Literature shows that SS 304 components of various geometry and shapes can be built using LAM processes. However, the major problem associated with LAM components is its surface waviness and roughness, which reduces its use for many commercial applications. Laser Directed Energy Deposition (LDED) is one of the LAM processes that uses a laser beam to create a melt pool on the surface of a substrate/ previously deposited layer on to which raw material is added. The surface is not smooth after solidification and waviness is generated because of surface tension gradient of the liquid melt pool, surface waviness elimination is required for smooth surface finish. In general, the focused laser beam diameter in the range of 600 μm -100 μm similar to diameter of melt pool during laser treatment. Therefore, the roughness with spatial wavelength λ larger than melt pool diameter will not remove. Spatial waves greater than this limit can be considered as the surface waviness. Thus, using traditional laser polishing, it is possible to decrease the surface roughness significantly but not the waviness. Hence, there is a need for the investigation of the effect of melt pool geometry and its optimization for surface waviness removal. For melt pool analysis various thermal model were presented in the literature [1-2]. For explaining the effect of laser melt pool geometry on surface finishing improvement, both experimental and analytical work is performed in the present work. Waviness reduction is obtained at the optimum melt pool depth and width, which mainly depends on laser power, line overlapping and scanning speed. The knowledge generated in this study can help to understand the fast and non-contact CW laser polishing process of LAM built components having larger waviness.

Experimental Details: The SS 304 sample is fabricated by LDED based LAM method. A 2 kW continuous wave (CW) fiber laser-based LDED system is deployed for melting and layer by layer deposition of SS 304 using a coaxial nozzle for laser beam and powder delivery. The SS304 powder particles diameters was in the range of 45-

104 μm. The percent material composition of SS 304 powder is Si(0.8), C(0.08), Mo(2.5), Ni(12.2), S(0.03), Mn(1.4), Cr(17.3) and balance Fe. After LAM sample preparation, laser surface melting experiment is performed for polishing using CW fiber laser with a variable laser power in a range of 100–400 W, laser line overlapping in the range of 50%-90% and laser beam diameter in a range of 800 μm -200 μm at the focal position. The laser beam is delivered to the sample surface using a Galvano scanner which directs the laser beam in the x and y-axis. Single laser scans only x axis and double pass scanning in x and y-axis can be applied to the surface with maximum N number of laser passes. The thermo-physical property of SS 304 is taken from the literature [3].

Results and Discussion: It was observed that during LDED process, melted material is relocated on the surface in its molten state. The surface waviness is generated on as-built LDED sample because of temperature and surface tension gradient of the liquid melt pool. Marangoni forces generated along the melt pool lead to circulation of the liquid melt pool. The effect of gravity g in melt pool is accounted for pressure gradient and slight increase in surface height is seen. The pressure gradient is $dP/dx=\rho g\Delta h$, where Δh is the waviness height (Fig.1). The maximum height of surface waviness is given by $\Delta h_{max}=(3/2)(\Delta T/\rho g d)(d\sigma/dT)$, where ΔT is temperature gradient and $(d\sigma/dT)$ is the surface tension gradient. Δh also varies inversely with the depth of melt pool d and the gravity term. During laser polishing of LDED sample, large value of melt pool depth d is favorable for the reduction in surface waviness height. When laser falls on surface, the local melting takes place on the peak of the surface and fill in the valley as shown schematically in Fig. 1, where λ is the wavelength of the periodic structure of surface waviness and should also be eliminate after laser melting and polishing. Waviness is the measurement of the more widely spaced component of surface texture. Here the value of λ is ~0.5 mm measured using confocal microscope.

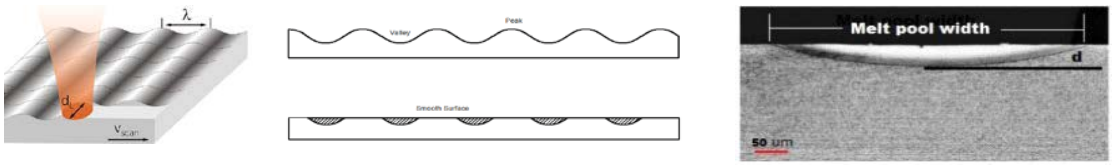

***Fig. 1(a)**: Schematic of waviness on the surface and effect of laser melting (b) after laser melting material melts from the peak and relocated in the valley(c) Optical microscope image of the cross section of the single-track Laser melted layer.*

For reduction of the waviness magnitude, a CW fiber laser beam of diameter w(z) and power P is applied on the surface for melting at the scan speed of V. Here, the equation $\lambda_a P=m[C_P(T_m-T_0)+L_f]+4k\ (T_m-T_0)\ (w(z)/2V\alpha)^{0.3}$ establish a relation between the required powers P to melt the surface of a material for a given speed V. Further, W. M. Steen [3] relates laser energy density (ED) in J/cm^2 with laser scanning speed using a simple relation $ED=(6000P/d_L V)$. A higher waviness reduction rate is observed for most of the metals and alloys during laser polishing in the range of ED value of 1800 to 3000 J/cm^2. The shape of the melt pool was a spherical shape as shown in Fig. 1 (c). Here $w(z) = d_L/2$.

(a) Melt pool depth analysis: Rosenthal Equation provides the analytical method to predict the thermal analysis during the fusion of metals. The Rosenthal equation, is given as follows

$$T = T_0 + \frac{\lambda_a P}{2\pi k r}\exp\left[-\frac{V(r+\xi)}{2\alpha}\right] \qquad (1)$$

Where, T_0 is the surface temperature, k is the thermal conductivity, λ_a is the surface absorption, V is the laser scanning speed, and α is the thermal diffusivity of the sample. The melt pool width is at its maximum when $dy/d\xi = 0$; The melt pool width L for low thermal diffusivities materials like SS 304 will be simplified as

$$L = 2d = \sqrt{\frac{8}{\pi e}\frac{\lambda_a P}{\rho C_p V (T_m - T_0)}} \qquad (2)$$

Where, ρ is the density. It was observed that the Rosenthal equation considered a semi-circular melt pool (perpendicular to the beam travel direction) as shown in Fig.1 (c). Hence, the calculated melt pool depth d is equivalent to a half of the melt pool width as d=L/2. For the SS 304, the melt pool depth d variation with laser power and speed ratio P/V is shown in Table 1. It shows clearly that for a given speed V the value of melt pool depth is higher for the higher power level and beneficial for the polishing.

Table 1: Variation of melt pool depth d with different power and speed levels for LAM SS 304.

S.No.	Power (W)	Speed (V) mm/s	(P/V) J/mm	Melt pool depth d in µm (Calculated value)	Melt pool depth d in µm (Experimental value)	Difference in calculated and experimental value
1	100	300	0.33	31.2	28.9	7.37%
2	100	500	0.20	18.9	17.5	7.41%
3	100	700	0.14	12.8	11.9	7.03%
4	150	300	0.50	44.8	43.7	2.45%
5	150	500	0.30	29.8	28.4	4.69%
6	150	700	0.21	20.2	18.7	7.42%
7	200	300	0.66	52.2	49.7	4.78%
8	200	500	0.40	38.1	36.4	4.46%
9	200	700	0.28	26.4	25.2	4.54%

At different values of P and V, there are multiple solutions, which give different melt pool depths as given in Table 1. A significant reduction of the waviness (elimination of λ according to Fig. 1) was observed with increase in the melt pool depth up to a certain level. In present experiment the optimum melt pool depth d is ~50 µm at 200 W CW laser power and 300 mm/s speed where waviness eliminates after solidification. If we increase the melt pool depth further, either by increase the laser power or lower the scanning speed beyond the optimum value, small surface waviness is again observed after melting and solidification because of hydrodynamic instabilities in the melt pool. Hence, it is necessary to control and optimized the melt pool depth with selection of optimized scanning speed (V) and laser power (P) during polishing.

(b) Melt pool width analysis: If molten zone width is optimum and sufficient for the liquid material during laser melting material, it fills in the valleys from the peak and improve surface smoothness. The width of the melted zone is measured using optical microscope. Fig. 2 shows the dependence of molten pool width with laser power P for a fixed value of processing speed V=500 mm/s. It increases almost linearly with the laser power in the range of 50 W to 400 W laser power in the present experiment. Higher value of laser power is beneficial but beyond an optimum value of laser power i.e. 200 W, a temperature gradient is established and this creates a surface tension gradient and again a surface waviness is observed in place of smooth surface. The experimental data shows that the speed V is

almost inversely proportional with the melt pool width and confirm the equation HAZ=$2\sqrt{\alpha t_d}$=$2\sqrt{\alpha}$ w(z)/V. Fig. 3 shows that in the range of V from 100 mm/s to 800 mm/s, the optimum value of melt pool width (~450 µm) is obtained at V=300 mm/s after that at higher V the melt pool width is small and unable to redistribute the material within the molten pool to fill valleys. Further, line overlapping also plays important role on the removal of surface waviness during laser melting. It was observed that the overlapping operation has significant effect on the removal of surface waviness, ripples, undercuts and bulges. Percentage line overlapping can be calculated using the hatch spacing of the drawing transferred to Galvano scanner according to relation Hatch Spacing = (1-overlapping) × laser spot diameter. There is an optimum value of line overlapping (~70%) where a smooth surface is achieved, free from waviness. Finally, waviness of LDED sample is completely eliminated at the optimum value of fiber laser power P=200 W, speed 300 mm/s and 70% laser line overlapping as shown in Fig. 4 (a) and 4 (b). Finally, wide (~ 450 µm) and large depth (~50 µm) melt pool is favorable for the waviness removal of as-built LDED SS 304 sample.

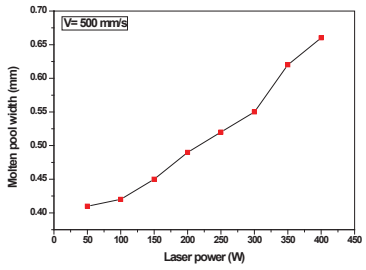

Fig. 2: *Variation of melt pool width with P.*

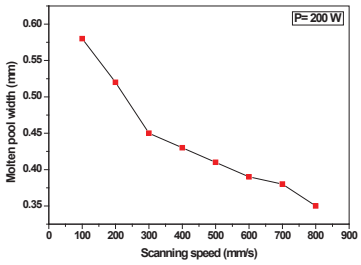

Fig. 3: *Variation of melt pool width with V.*

(a)

(b)

Fig. 4(a): *Surface of LDED built SS 304 sample before surface melting and polishing shows waviness* ***(b)*** *Sample surface after laser melting and polishing without waviness.*

Conclusion: Fiber laser based melting and solidification is a fast, dry and non-contact method for improving surface finish of LAM built components. From the analytical and experimental studies, it is found that, melt pool geometry plays an important role for the waviness removal and it depends on laser scanning speed, line overlapping and laser power. A relation is established between the melt pool geometry to the surface finish. In the present work, the calculated value of melt pool geometry is in good agreement with experimental values for laser polishing.

Reference:

1. Lan Chena et al. Additive Manufacturing **32** (2020) 101013.
2. J. Xie and A. Kar, J. Appl. Phys., **81(7)** (1997) 3015-3022.
3. W. M. Steen, “Laser Material Processing”, 2nd Ed., Springer-Verlag, London, 1998.

DSMC study on reduction of atomic vapour Doppler width for LIS

Tarang Garg, Sudarshan Baruah, G. K. Sahu

Advanced Tunable Laser Applications Facility, BTDG, BARC, Trombay – 400085

Email: tarang@barc.gov.in

Abstract

In Laser Isotope Separation (LIS) of ^{176}Yb, the Doppler width of the vapour plays an important role due to close isotope shift. One of the strategies of reducing Doppler with is to put array of multiple slits in evaporator along the source length. In this paper, we report the results of Direct Simulation Monte Carlo (DSMC) simulations performed with multiple slit configurations of varying slit lengths keeping overall vapour width and length constant. Our results show that Doppler width reduces as a function of the length-to-width ratio of the slit configuration.

Introduction

In Laser Isotope Separation of ^{176}Yb, the closest isotope affecting its selectivity is ^{173}Yb. The isotope shift between the two is 1.4 GHz in the first step and 0.3 GHz in the second step of the three step selective laser ionisation process [1]. Therefore, it is necessary to have sufficiently narrow line-width laser and reduced Doppler width of the vapour in the laser propagation direction. The theoretical basis of reducing Doppler width has been studied and reported earlier [2]. To produce a wedge shaped vapour column, use of collimated array of small diameter channels normal to laser direction was described. The experimental results were compared with theoretical estimates in the free molecular flow regime.

Direct Simulation Monte Carlo (DSMC) simulation is carried out to study the effect of varying slit length for an array of multiple slits on Doppler width of vapour in the laser-vapour interaction area. For parametric study, the total length and width of the vapour source are kept constant. To compensate for the change in the slit length, number of slits is changed so that total evaporating length remains same. A DSMC solver, “dsmcFoamPlus” [3], written in OpenFOAM framework has been used to study the evolution of the vapour flow. Division of the computational domain into cells were done using snappyhexmesh, mesh generation utility of the OpenFOAM package. Distribution of atomic velocity and number densities at different height from source have been computed and relevant results are presented

DSMC Method

Direct Simulation Monte Carlo is a numerical method to solve Boltzmann equation proposed by Bird[4]. It is a particle based method for solving rarefied gas flows. Herein each particle represents a large number of real molecules. This factor is generally called as weighting factor. In DSMC method, the domain is divided into cells smaller than mean free path and time marching is done with time step less than the mean collision time. This is a statistical method in which collisions within cells are

performed using probabilistic sampling method. Hence, typical particle count per cell should be more than 20 to get statistically relevant results [5].

Benchmarking of the DSMC solver

The code is benchmarked with the published results of Rosengard [6] for a freely expanding vapour at Knudsen number (Kn) of 0.38. The length averaged normalised number density obtained from this code and from Rosengard's empirical estimates, have been plotted in Figure 1 as a function of height from the evaporating source. In Figure 2, length averaged normalised number density along vapour width is plotted. In both the cases normalisation of number density has been done with respect to source number density. In both the two cases, the estimates from the code are found to be in good agreement with those of Rosengard's.

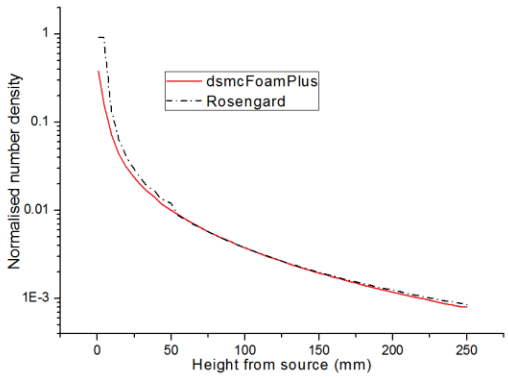

***Figure 1**: Length averaged normalised number density along height from source*

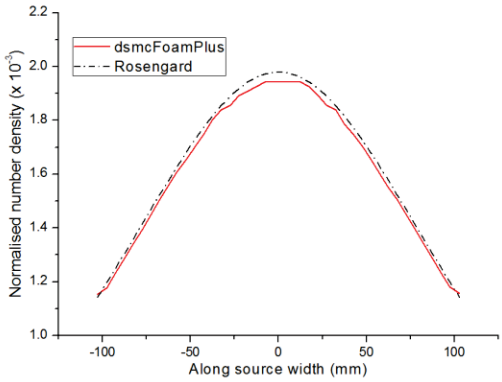

***Figure 2**: Length averaged Normalised number density along source width direction at 150mm from source. Normalisation has been done with respect to source number density*

Simulation Study

The geometries considered for simulation are shown in Figure 3. The computational domain is divided in two parts. The lower part consists of slit arrangement of with different configurations while the upper part is kept constant for all configurations. The evaporating surface width and its total length are kept constant at 5mm and 125mm respectively for all simulations. The length-to-width ratio (aspect ratio) of the slit arrangement is taken as 1, 2, 4, 12 and 25 for five different configurations having 21, 11, 6, 2 and 1 number of slits respectively. The ratio between slit height and its width is kept constant at 10. The upper part is a cube of side 200mm symmetric with respect to the bottom part. There is no computational boundary between the two parts. Following assumptions have been made:

1. The evaporator surface is at constant temperature of 800 K (Kn = 0.38).
2. The slit walls are at same temperature as of the evaporator surface and are reflecting atoms diffusively
3. The hard sphere collision model is valid.
4. There is no clustering of atoms to behave as a molecule.
5. The background air density is so low that it doesn't interfere with the vapour.

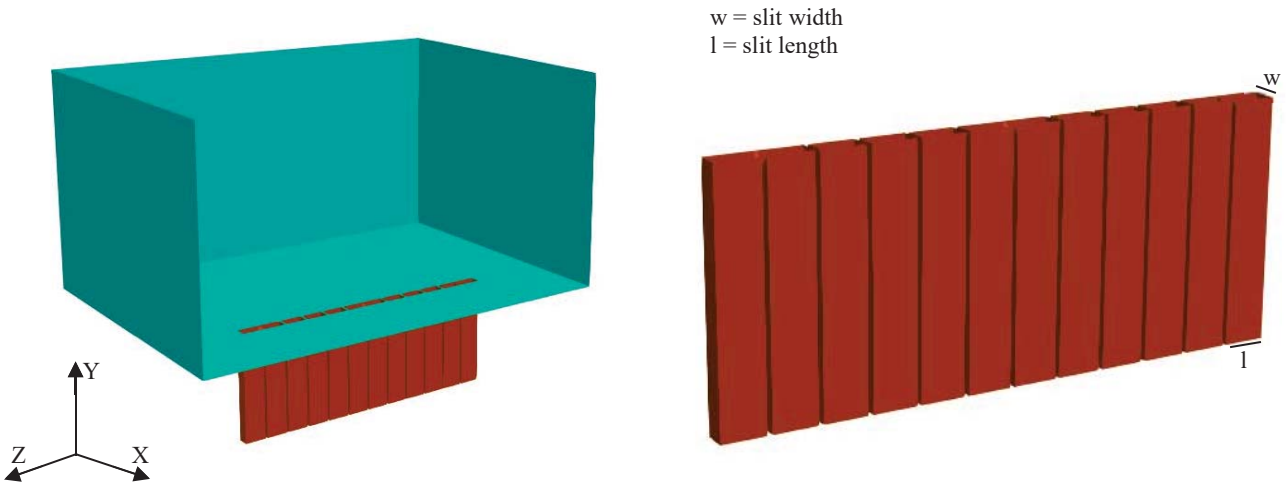

***Figure 3**: (a) Schematic of computational domain, (b)array of slits*

Results and discussion

Figure 4 shows variation of number density as a function of height from the source for various aspect ratios. Beyond the exit of the slit the number density is found to be slightly less for lower aspect ratios. This can be explained following Clausing [7]. With smaller aspect ratios, more atom-wall collisions take place which are diffusive, leading to more number of atoms going back towards source. This leads to lower atom densities for slit configurations with lower aspect ratios at the same height from the source.

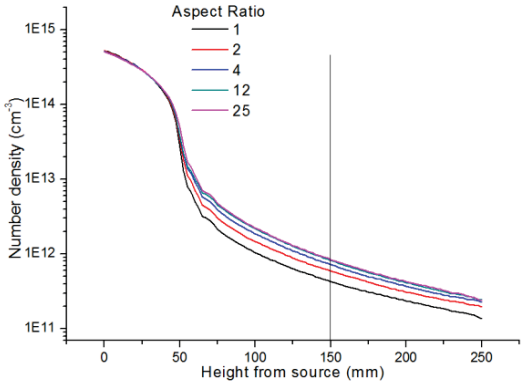

***Figure 4**: Number density along height from source for different aspect ratios*

The typical number densities required for laser atom interaction is in the order of 10^{11}-10^{12} atoms/cm^3 region [8]. Hence, the number density distribution and Doppler width of the vapour is investigated at height (150 mm) where number density is approximately 5x10^{11} atoms/cm^3. Figure 5 shows number density along slit length for different aspect ratios. At the centre, the number density for the lowest aspect ratio is found to be half of the highest case. However, it is observed to be slightly more uniform along the slit length.

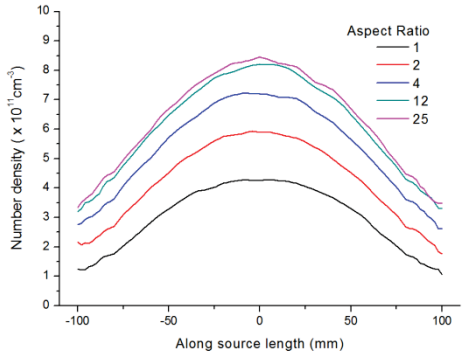

***Figure 5:** Number density along source length at laser-atom interaction height*

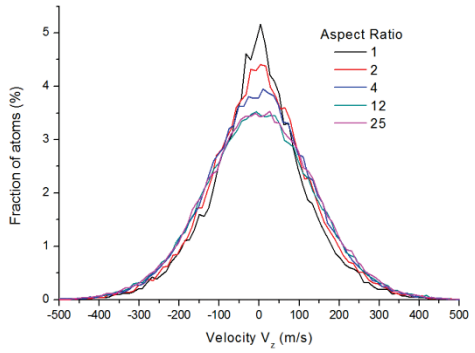

***Figure 6:** Distribution of atoms as a function of v_z at laser-atom interaction height*

Figure 6 shows the distribution of the atoms as a function of velocity along slit length at laser-atom interaction height (150 mm). Here, the Y-axis represents the fraction of atoms having velocity v_z and X-axis represent the velocity v_z along laser propagation direction. The figure shows that the peak of the distribution curve is highest for the lowest aspect ratio. This implies that the spread of v_z decreases with decreasing aspect ratio.

Since, distribution curves in Figure 6 are not strictly Gaussian; FWHM cannot be taken directly. The FWHM corresponds to 76% area under the standard Gaussian distribution. Hence, the equivalent velocity spread has been calculated by considering the width for which area under the curve is 76%.

The calculated Doppler width is shown in Figure 7 for different aspect ratios at laser wavelength of 555 nm [1]. It is found that Doppler width reduces strongly as the aspect ratio reduces to 1. This implies that using multiple slits of smaller length-to-width ratio results in lower Doppler spread. This can be beneficial for LIS process of elements having smaller isotopic shifts.

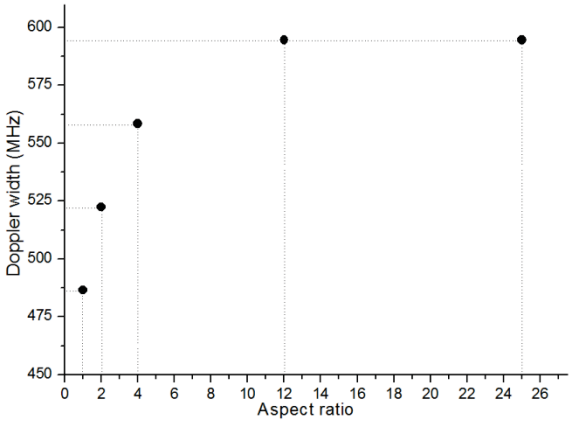

Figure 7: *Doppler width of the vapour calculated from the distribution functions for different aspect ratios*

Acknowledgements

We are thankful to our colleagues Dr B. Dikshit, Dr. B. Jana and Dr. A. K. Singh for insightful discussion in improving simulations. We are grateful to Dr. Archana Sharma, AD, BTDG for continuous inspiration and support. Use of ANUPAM super-computing facility is gratefully acknowledged.

References

[1] H. Park *et al.*, *J. Nucl. Sci. Technol.*, **45**, 111, (2008),

[2] B. Jana, A. Majumder, K. B. Thakur, and A. K. Das, *Rev. Sci. Instrum.*, **84**(10), 106113 (2013).

[3] C. White *et al.*, *Comput. Phys. Commun.,* **224**, 22, (2018)

[4] G. A. Bird, *Molecular Gas Dynamics and the Direct Simulation of Gas Flows*, 2nd ed. Oxford Science Publications, (1994).

[5] A. Venkattraman, A. A. Alexeenko, M. A. Gallis, and M. S. Ivanov, *AIP Conference Proceedings*,**1501,** 489(2012).

[6] A. Rosengard, *Rarefied Gas Dynamics: Space-Related Studies*, 312, (1989).

[7] P. Clausing, *J. Vac. Sci. Technol.*,**8**(5), 636–646, (1971).

[8] S. I. Yakovlenko, *Quantum Electron.*, **28**(11), 945, (1998),

.

Study of laser polarization dependant JxB acceleration in relativistic ultrashort laser foil interaction

T. Mandal*[1,2], V. Arora[2], A. Moorti[1,2] A. Uphadhyay[2], and J. A Chakera[1,2]

[1] *Homi Bhabha National Institute, Training School Complex, Anushaktinagar, Mumbai 400 094*

[2]*Raja Ramanna Centre for Advanced Technology, Indore 452 013*

*E.mail: tirtham@rrcat.gov.in

Abstract

We present the experimental study on generation and characterization of fast electrons in p-polarised, ultrashort, relativistic laser interaction (I_L ~ $4x10^{19}$ W/cm^2) with thin foil target. Direct evidence of JxB acceleration mechanism is inferred from fast electrons beam measurement along laser propagation direction apart from the low flux electron beam along the laser transverse/polarization direction. Strong polarization (*p* vs *s*) dependence of fast electrons is observed which is understood through role of pre-heating of the target. 2D PIC simulation also supports the experimental observations.

Introduction

In intense laser interaction with thin foil targets, energetic fast electrons (sub-MeV to tens of MeV) are generated through different mechanisms[1] including resonance absorption, vacuum heating, and JxB heating. Angular distribution measurement can be used to find out the applicable acceleration mechanisms. Study of fast electron generation and its transport through solid density matter is also of significant importance for the success of fast ignition concept in inertial confinement fusion, and other processes such as x-ray generation and proton/ion acceleration[1]. The JxB acceleration is the most dominant mechanism of laser energy absorption in the relativistic regime leading to fast electrons generation along the laser propagation direction. Most of the investigations on JxB acceleration have been performed using relatively longer pulse duration > 500 fs, and there are limited reports[2] using laser pulse of few tens of fs duration with ultrahigh relativistic laser intensity of >10^{19} W/cm^2.

In this paper, we present experimental study on fast electron generation in ultrashort laser interaction with thin metal foil targets at laser intensity of ~$4x10^{19}$ W/cm^2. Applicability of JxB acceleration mechanism was demonstrated through observation of a directed electron beam along laser propagation direction. Further, fast electron beams along transverse to the laser propagation were also observed. P-polarisation was found to be favourable for generation of fast electrons compared to s-polarisation. Generation of three electron beams and its polarization dependence observed in experiment was also replicated in 2D PIC simulation performed using EPOCH code[3].

Experimental setup:

The experiment was carried out using 150 TW Ti:Sapphire laser facility at RRCAT. The peak laser intensity on the target was ~ 4x 10^{19} W/cm^2 achieved by focussing laser pulse energy of ~1.5 J with duration ~25fs to an elliptical spot of ~5 μm x10 μm (FWHM) using off axis parabolic mirror (f/3.6). The ASE intensity contrast at 1 ns prior to fs pulse was measured to be < $2x10^{-10.}$ Thin foil target of Cu was irracdiated at an laser

incidence angle of ~30°. The fast electrons were detected using combination of phosphor screen and CCD cameras as shown in fig. 1(a). Al filter of 500µm thickness was used to shield the phosphor screen from ions, plasma light and low energy x-rays. The cut-off electron energy reaching the phosphor screen was ~350 keV. Energy spectrum of the electrons were measured using magnetic spectrograph consisting a rectangular dipole magnet with magnetic field (~700G) and a phosphor screen-CCD combination as a detector. To capture the electrons from target front, the target was rotated (indicated by dashed line target in fig 1.a) in such a way that the interaction incidence angle remains 30°, but electrons from target front can now be detected by the transverse DRZ phosphor screen setup.

Results and discussion:

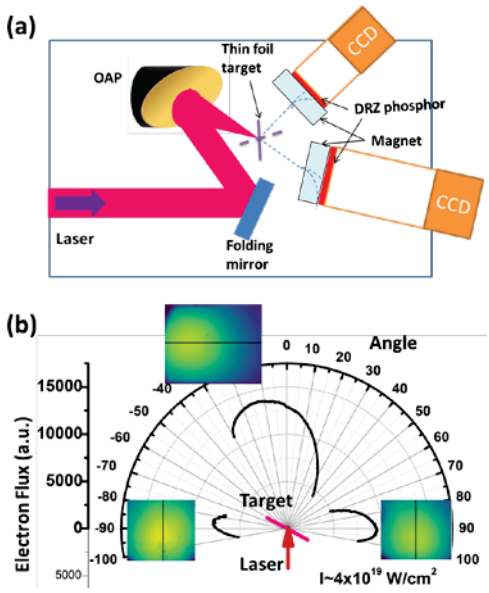

Fig 1.(a) Experimental setup geometry. (b) Polar plot of fast electrons in the plane of incidence with typecal spatial profile of fast electron beams in three direction.

Measurement of the angular distribution of electron emission showed generation of forward fast electrons with peak along laser propagation direction. In addition to forward electron beam, two electron beams in the transverse directions along laser polarisation were also observed. Typical electron beam profiles recorded on the phosphor screens along with their polar plot are shown in fig.1 (b) for Cu 7 µm target at *p* polarization and intensity of ~4x10^{19}W/cm^2. The electron beam charge (energy >300 keV) for the forward and transverse beam were estimated to be ~1150 ± 90 pC and ~115 ± 20 pC respectively. Generation of such fast electron beams were found for wide parametric variation of laser intensity (1 – 4 x10^{19} W/cm^2), angle of incidence (10^0 – 60^0), polarisation (p and s), laser pulse duration (30 – 400fs), and target thickness (2 – 100 µm), although variations in the electron beam parameters were observed. Next, the energy spectra measurements showed that the maximum energy (with fitted temperature) for the electron beam was ~3 MeV (0.43 MeV) at intensity of ~4 x 10^{19} W/cm^2.

Experimental observation of fast electrons along the laser propagation direction is consistent with the heating of electron by JxB mechnsism. Peak of the forward emitted electrons were found to be slightly deviated towards the target surface (e.g. ~10° for Cu 7µm target) and can be attributed to deviation by self-generated surface magnetic field at the front surface of the target. Further, it can be noted that, the measured fast electron temperature of ~0.43 MeV is smaller than the expected temperature of ~1.75 MeV from Wilks scaling[4] for JXB heating at laser intensity of ~4x10^{19} W/cm^2. This can be understood from the intense laser matter interaction occurring at a very sharp density gradient plasma created by ultrashort ultra high contrast laser pulses. Further, the escaping electrons can also lose a significant part of their energy in combating with the surface sheath field in order to come out of the foil target resulting into a much cooler spectrum.

For the transverse beam, maximum energy and temperature was found to be similar to that of forward beam. With change in polarisation from p to s, maximum electron energy and temperature reduced to ~1 MeV and 0.1 MeV respectively. Generation of such beams in laser polarization direction have been previously observed in laser gas and laser cluster interactions. However, in high intensity laser solid interaction, till now there are no reports on observation of transverse electron beam with p polarized laser beam. In the present experiment, the observed reduction of electron flux as well as electron energy in transverse direction on changing the laser polarization from *p* to *s* (shown in fig.2a) suggests that the origin of transverse beams is laser electric field in the polarization direction.

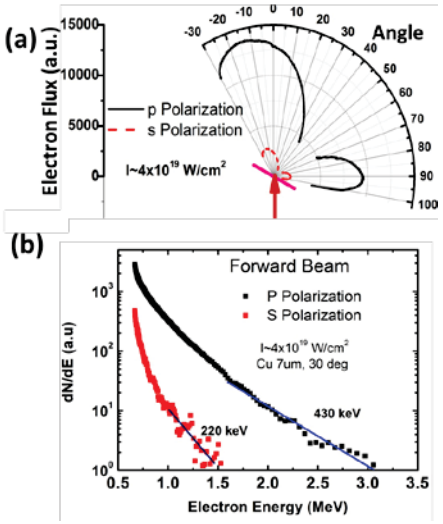

Fig.2 : (a) Fast electron angular distribution and (b)energy distribution for p and s polarized laser

In order to verify the role of polarisation dependent mechanisms on forward JxB heated fast electrons, study was also performed with s polarisation as shown in fig.2. The forward electron beam charge reduced by ~ 6 times from ~1150 ± 100 pC to 174± 30 pC with change in polarisation from p to s. Fast electron maximum energy (temperature) also reduced to ~1.5 MeV (~0.22 MeV) when s polarisation was used as shown in fig 2.b.

JxB mechanism responsible for acceleration of forward fast electron is expected to be independent of polarization (*p* or *s*). However, there are few reports where polarisation dependence was observed even in case of JxB mechanism[5], although no detailed physical reasoning was provided. Based on our experimental observation, we conjecture that some pre-generation and pre-heating of low energy electron happens in preformed preplasma in case of p-polarization which becomes favourable for JxB heating leading to higher flux and energy.

To understand the generation of fast electrons, 2D PIC simulation using code EPOCH was performed. Laser pulse of 30 fs duration, intensity of 2×10^{19} W/ and incidence angle of 30^0 was used. The target was 2 μm thick pre-ionized Cu with uniform density of 10 n_c. A pre-plasma precedes the target with the scale-length of ~ 0.5 μm. From the electron density map, it was found that energetic electrons were generated along the laser propagation direction as well as along the transverse direction. The polar plot of the electron angular distribution for both p and s polarization is shown in fig 3. The flux of electrons reduced significantly (~ 7X)in case of s polarization compared to p polarization. The energy analysis of forward beam showed that max energy reduced from ~3.5 MeV to ~1.5 MeV when the polarization was changed from p to s corroborating with the experimental results.

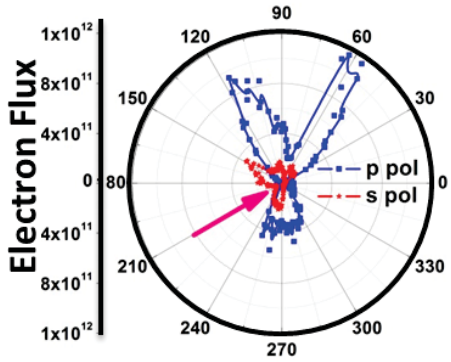

Fig.3. Polar plot p and s polarization interaction from 2D PIC simulation

In conclusion, we demonstrate the applicability of ponderomotive JxB acceleration through observation of directed forward beam in the interaction of ultra-short duration laser pulses with thin foil targets at laser intensity of ~$4x10^{19}$ W/cm^2. In addition, transverse beams along were also observed. Strong polarization dependence of forward fast electrons is explained from probable pre-heating. 2D PIC simulation supports our results.

Acknowledgements: The authors acknowledge the laser operation mechanical support provided by Shri R.A. Khan, Shri Ankit, Shri S. Meena and Shri K. Meena.

References

1. P. Gibbon, *Short Pulse Laser Interactions with Matter* (2005).
2. Y. Ping *et al, Phys. Rev. Lett.* **100**, 085004 (2008). P. K. Singh *et al, Sci. Rep.* **5**, 17870 (2015). B. I. Cho *et al, Phys. Rev. E* **80**, 055402 (2009). T. Mandal *et al, Phys. Plasmas* 26, 013103 (2019).
3. T. D. Arber *et al, Plasma Phys. Control. Fusion* **57**, 113001 (2015).
4. S. C. Wilks *et al, Phys. Rev. Lett.* **69**, 1383 (1992).
5. C. I. Moore *et al, Phys. Rev. Lett.* 82, 1688 (1999). L. Zhang *et al, Appl. Phys. Lett.* 100, 014104 (2012).

Study of fast electron transport in ultrahigh intensity laser matter interaction by 2D imaging of Cu K_α x-rays

T. Mandal*[1,2], V. Arora[2], A. Moorti[1,2] and J. A Chakera[1,2]

[1] *HBNI, Training School Complex, Anushaktinagar, Mumbai 400 094*

[2]*Laser Plasma Division, RRCAT, Indore 452013*

* *tirtham@rrcat.gov.in*

Abstract

Study of fast electron transport has been carried out through 2D Cu K_α imaging using a spherically bent quartz crystal spectrograph in ultra-short laser matter interaction at a laser intensity of ~$7x10^{19}W/cm^2$. Front and rear side x-ray source size was measured to be ~38±2 µm and ~47±2 µm for Cu 7 µm foil. A fast electron half divergence angle of ~17° inside solid density was estimated from the measured rear side source sizes with different thickness target foil. Such small divergence indicates towards collimation of the beam by magnetic fields at high laser intensity.

Introduction

In ultra-short, intense laser interaction with thin foil targets, energetic fast/hot electrons (sub-MeV to tens of MeV) are generated via various mechanisms[1]. These fast electrons propagate and deposit their energy in the overdense plasma and can eventually escape from the target. Study of fast electron transport inside solid material is a decade long research problem due to its immense importance for the success of fast ignition concept[1] of inertial confinement fusion (ICF). The transport of fast electrons in dense solid is a very complex and interesting subject due to presence of very high hot electron current (MA), drawing of return current for neutralization, electric field inhibition, generation of mega gauss magnetic fields etc. In particular, the magnetic fields can further act on the diverging fast electrons and collimate them. Studying the fast electron source sizes at the front and rear surfaces and finding divergence angle is therefore an important topic of research. The fast electrons generate characteristic x-ray line radiation during its propagation in the material. The measurement of x-ray source sizes at the front as well as rear surface will indirectly provide insight about electron transport processes. Monochromatic imaging of x-ray source using a spherically bent quartz crystal[2] provides 2D image of the x-ray source.

In this paper, we report the investigation of fast electron generation and transport in intense laser matter interaction through 2D imaging of Cu K_α source at target front and rear surfaces. Front x-ray source size was measured to be ~38±2 µm. The rear x-ray source size was estimated to be ~47±2 µm and 58±4 µm for Cu 7 µm and Cu 25 µm foil respectively. A fast electron half divergence angle of ~17° inside target material was calculated from the fitting of rear side source sizes.

Experimental Setup

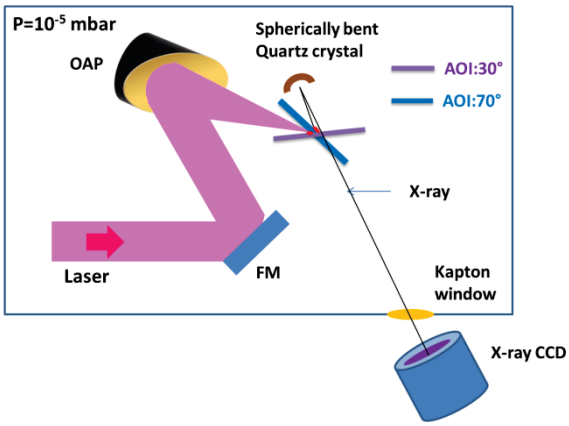

Figure 1: Schematic of the experiment setup for x-ray imaging from both front and rear surface

The experiment was performed with a maximum laser energy of ~2.2J and pulse duration of 25fs using 150TW Ti:sapphire laser system at RRCAT, Indore. The schematic of the experimental setup for the Cu K_α x-ray source imaging is shown in Fig. 1. The laser beam was focussed using an off axis parabolic mirror (F/2.4) to a focal spot of 7µm x 5µm (FWHM) containing ~24% of laser energy. The peak laser intensity was calculated to be ~7 x 10^{19} W/cm^2. The contrast of the ASE prepulse at 1ns was measured to be better than 2x10^{-10} while for replica fs prepulse arriving 11ns prior to main pulse, the contrast is measured to be >10^{-7}. The laser beam was focused on Cu foil targets (of thickness 7µm and 25µm) at two incidence angles viz. 30° and 70°.

High resolution spherically bent quartz crystal spectrograph was designed and setup to image Cu K_α (8.048 KeV) source at the target front and rear surfaces. A spherically bent quartz crystal (size:15x50mm) of lattice spacing $2d_{002}$=1.542A° and radius of curvature of 250mm was used for the monochromatic x-ray imaging. The Bragg angle for the Cu K_α for this crystal is ~88.7°. An indirect detection x-ray CCD camera (Spectral Instrument) was used as detector which was kept outside the experimental chamber. X-ray (~ 8 keV) from interaction region (inside chamber at vacuum level of ~10^{-5} mbar) was transmitted through Kapton window to the x-ray CCD camera kept outside at atmospheric pressure. In order to image the Cu K_α source, the crystal was kept at a distance of ~140mm from the source (interaction point) for a fixed source to detector distance of ~1000mm. The magnification was ~8.1. For front side imaging, incidence angle was kept at ~30°, such that the crystal faces the target front surface and interaction region in the normal direction and therefore will provide near circular x-ray images. For rear side imaging, the target was rotated in clockwise direction keeping the crystal position fixed such that the crystal faces the rear surface of the target. However, the incidence angle was limited to ~70° in this case.

Results and discussion

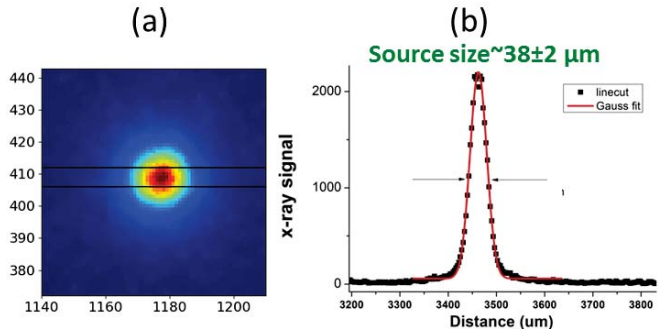

Figure 2: (a) Cu K_α source image recorded from the front surface. (b) Line cut of the image for size measurement. The region of interest is marked by horizontal lines in figure (a) for taking lineout for source size measurement.

Figure 2 (a) shows the front side Cu K_α source image as recorded on the x-ray CCD camera. Nearly circular images with high signal to noise ration of >30 was obtained. Fig. 2(b) is the line cut of the image which was fitted to a Gaussian distribution to estimate of x-ray source size. The average front side souce size was calculated to be ~38±2 µm.

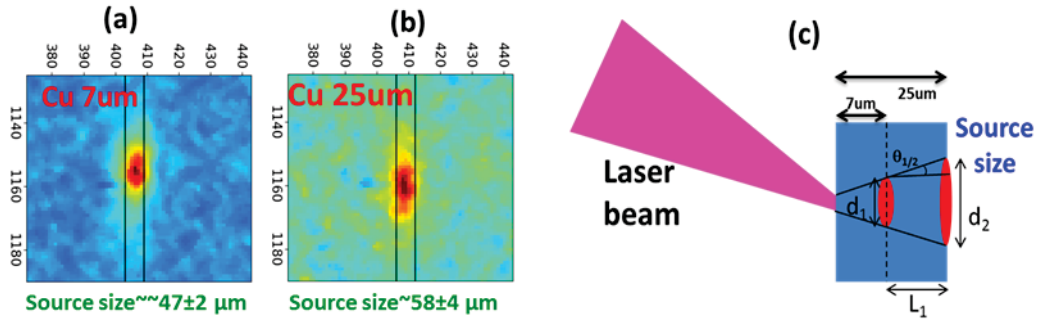

Figure 3: (a) and (b) Cu K_α source image recorded from the rear surface for Cu 7um and 25um foil thickness. (c) Schematic of fast electron divergence measurement from source size. The region of interest is marked by verticle lines in figures (a) and (b) for taking lineout for source size measurement.

Figure 3 (a) and (b) shows the Cu K_α source image at the rear surface for Cu 7µm and 25µm foil thickness. As the incidence angle was ~70° in this case, the crystal looks the rear side image from an angle (Fig. 1) and therefore the images are compressed horizontally. However, the line cut along verticle direction (binned between the marked verticle lines) will give the estimate of source size. The rear side source size was estimated to be ~47±2 µm and 58±4 µm for Cu 7 µm and Cu 25 µm foil respectively. Figure 3(c) shows the schematic of fast electron divergence measurement from source size. The fast electron half divergence angle can be calculated as $\theta_{1/2} = \tan^{-1}[(d_2-d_1)/2L_1]$ where, d_1 are d_2 are source sizes for Cu 7 and 25µm foil and L_1 is the difference in thickness of the two foils. A fast electron half divergence angle of ~17° inside target material was calculated from rear source sizes using the above relation. Such small divergence indicates the role of self-generated magnetic fields on collimating fast electrons. The divergence data matches well with the other reported results[2,4-6] at similar intensity.

In conclusion, we have performed 2D imaging of Cu Kα source from target front and rear surface using a quartz crystal spectrograph. Front side source size as well as rear side source size was estimated for Cu 7 µm and Cu 25 µm foil. A fast electron half divergence angle of ~17° inside target material was calculated from the fitting of rear side source sizes.

Acknowledgements: The authors acknowledge the laser operation mechanical support provided by Shri R.A. Khan, Shri Ankit, Shri S. Meena and Shri K. Meena.

References

1. M. Tabak *et al*, *Phys. Plasmas* **1**, 1626 (1994).
2. K. L. Lancaster *et al*, *Phys. Rev. Lett.* **98**, 125002 (2007).
3. B. Borm *et al*, *Phys. Plasmas* **26**, 023109 (2019).
4. J. J. Santos *et al*, *Phys. Rev. Lett.* **89**, 025001 (2002).
5. R. B. Stephens *et al*, *Phys. Rev. E* **69**, 066414 (2004).
6. J. S. Green *et al*, *Phys. Rev. Lett.* **100**, 015003 (2008).

Tunable electron beams from laser wakefield acceleration by controlled injection

S. Mishra*[1], B. S. Rao[1,2], A. Moorti[1, 2] and J. A. Chakera[1, 2]

[1]*Laser Plasma Division, Raja Ramanna Centre for Advanced Technology, Indore-452013*

[2] *Homi Bhabha National Institute, Training School Complex, Anushakti Nagar, Mumbai-400094*

*Email: shikham@rrcat.gov.in

Abstract: We present controlled electron injection using sharp density transition scheme which enhances the stability and repeatability of the laser wakefield electron accelerator. Generation of electron beams with tunable energy between 100-250 MeV was observed using Ti: Sapphire laser pulses of intensity ~3.5×10^{19} W/cm^2 (a_0 ~ 4) interacting with 4 mm long helium gas-jet target plasma at an electron density of ~ 6.8×10^{18} cm^{-3}. With the use of a knife edge in the gas flow, a density transition is created. Next, by varying knife edge position inside the gas-jet, accelerator length was varied and its effects on electron beam energy and divergence was also studied.

Introduction: Laser wakefield acceleration (LWFA)[1] is being intensely investigated due to its capability to offer large electric field of the order of hundreds of GV/m for acceleration of electron bunches with energy several 10s of MeV to GeV[2-5] in a compact set-up. LWFA experiments usually rely on self-injection of background plasma electrons into the laser driven plasma wave by non-linear process of wave-breaking[6]. In this regime, the intensity of the drive laser pulse is high enough to excite large amplitude non-linear plasma wave and induce self-injection of electrons. The injected electrons are trapped in the plasma wave and the huge longitudinal electric field of the plasma wave rapidly boosts these electrons to extremely high energies (typically ~ 100MeV/mm). While the self-injection precludes the need for external electron source for injection, it suffers from inherent limitations e.g., absence of control over exact locations of injection, the amount the injected electrons and the accelerated electron beam parameters. To overcome these limitations, different controlled methods were suggested and investigated in which electron injection is achieved by various mechanisms viz., density down ramp[7], ionization induced[8], colliding laser pulses[9], and sharp density transition[10].

Here, we present tunable energy electron beams from LWFA using controlled injection via sharp density transition scheme. In this scheme a knife edge (blade) is introduced in the supersonic flow of the gas jet to produce a sharp density transition[10]. The focus of the drive laser pulse and the gas jet entrance were adjusted in such a way that the laser pulse experiences a density spike (which has sharp trailing edge) at the beginning of the laser interaction with the gas jet. As the laser pulse goes through the plasma with sharp downward density transition, the plasma wavelength λ_p increases abruptly from its value in the high-density region to the low-density one. Here, the plasma wavelength is given by $\lambda_p = 2\pi c/\omega_p$ where c is the speed of light and $\omega_p = (n_e e^2/\varepsilon_0 m_e)^{1/2}$ is the plasma frequency, with e, m_e, n_e being electron charge, mass, and density, respectively. Such an abrupt increase in the plasma wavelength results in injection of a fraction of the plasma electrons into the accelerating phase of the plasma wave. The characteristic length of the density transition should be of the order of λ_p for this scheme to be operational.[10] The scheme allowed us to generate tunable electron beams between 100-250 MeV, at a background plasma density of ~6.8×10^{18} cm^{-3} in a 4mm long helium gas jet, by controlling the location of injection and consequently accelerator length with the help of the knife edge. A 25fs, 150TW Ti: sapphire laser with a focused intensity of ~3.5×10^{19} W/cm^2 was used to drive the LWFA.

Experimental Set-up: Fig.1a shows the schematic of the experimental set-up. The 25fs, 150TW Ti: Sapphire laser operating at central wavelength of 800nm was focused to a spot size $w_0 \approx 6$ μm (radius at $1/e^2$) using f/5 off-axis parabolic mirror, and resulting intensity of $I_L \approx 3.5\times10^{19}$ W/cm^2 (for a slightly stretched pulse duration of ~50fs) ($a_0 \approx 4$) was used. A knife edge (blade) was inserted (Fig.1b), from the direction of laser incidence, in a 4mm long helium gas-jet to create a sharp density transition at the entrance of the gas jet. A typical expected density profile is shown in Fig.1c. The knife-edge could be scanned in the longitudinal direction to change the effective gas-jet length (after the density transition) and hence to tune the electron beam energy. The laser pulse channeling inside the plasma was monitored on a CCD camera by side-view imaging. A narrow 2ω band-pass filter was kept before the CCD Camera to preferentially collect nonlinear Thomson scattered laser light from the plasma. A C-shaped permanent dipole magnet with effective magnetic field strength of 0.75 T, within a pole gap 10 mm over 75mm length, was kept at 13cm from the gas-jet to disperse the electron beam produced from LWFA. A phosphor screen (DRZ-high) was placed after the magnet, at 115cm from the gas-jet, to record electron beam profile and its spectrum. The electron spectrometer provides resolution of 5% at 100 MeV and 10% at 200 MeV, considering electron beams of 10mrad divergence.

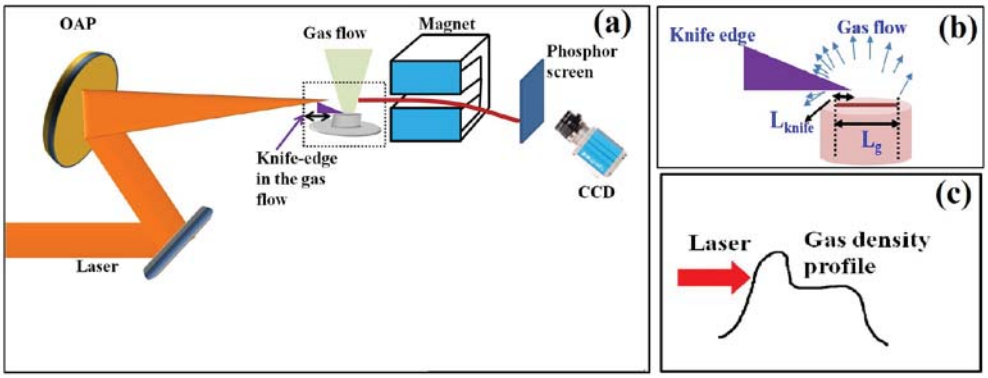

Figure 1(a) Schematic of the laser wakefield acceleration set up with a knife-edge (blade) inserted in the helium gas jet flow (b) Inserted knife edge in the gas-flow, L_g is the gas length of 4mm, L_{knife} is length of gas jet covered by knife, Acceleration length is $L_{acc} = L_g - L_{knife}$ (c) A typical expected gas density profile

Results and Discussion: To clearly demonstrate the controlled injection due to the density-transition, the plasma density is chosen such that the LWFA is operated below the self-injection threshold. In this condition, we could observe the laser channeling due to self-focusing in the side-imaging of the plasma accelerated electron beam recorded on the phosphor screen. Thereafter, we inserted the knife edge (blade) in the gas flow to introduce sharp density transition (in the downstream gas flow) and scanned its location axially along the gas jet length ($L_g \approx$ 4mm) to change the location of the density transition. After the insertion of the knife-edge, electron beams started to appear on the phosphor screen after careful adjustment of laser focus and plasma density (below self-injection threshold only). This confirmed that the knife-edge indeed facilitates external control on electron injection and variability of its axial location allows changing the accelerator length (L_{acc}). We varied the accelerator length ($L_{acc} = L_g - L_{knife}$) from 1mm to 3.5 mm by changing the axial location of knife-edge, L_{knife} from 3mm to 0.5mm in the gas jet. Here, we show the electron beams observed at plasma density of 6.8×10^{18} cm^{-3} for stable laser interaction conditions. Transverse profiles of typical electrons beams produced for different lengths of the accelerator are shown in Fig 2(i). The variation of electron beam divergence with the accelerator length, L_{acc} is also shown in Fig. 2(ii). Electron beam divergence decreases from

about 36mrad at L_{acc} = 1mm to a minimum value of ~8mrad for L_{acc} ≈ 1.6 - 2mm and then increases again with increasing the L_{acc}. Next, we show typical electron beam spectra recorded for three different accelerator lengths in Fig.3 (i). For the accelerator length of 3mm, quasi-monoenergetic electron beam with peak energy of ~150MeV was observed. Further at 2mm and 1.6m, we observed higher energies of 180MeV and 250 MeV respectively. Further reduction in length led to decrement in electron beam energy.

The variations in electron beam divergence and energy with accelerator length can be understood by Fig. 2(ii) and Fig.3 (ii) together. As we increase the accelerator length from 1mm to 1.6mm, we observe energy enhancement as well as decrement in electron beam divergence. This indicates that electrons experience only accelerating field over the distance of 1mm to 1.6mm which resulted in gain in energy (E) and hence longitudinal momentum ($p_z \approx E/c$). Further, divergence of an electron beam depends on the ratios of the transverse and longitudinal momenta (divergence, $\Delta\theta \approx p_{r,max}/p_z$). Here, the transverse field remains same over all accelerator distances. Therefore, the increased longitudinal momentum from 1mm to 1.6mm is likely to be responsible for decreased electron beam divergence. Further increase in accelerator length from 1.6mm to 3.5mm shows a contrast in behavior. From accelerator length beyond 1.6mm, apparently the electrons experience decelerating field (dephasing) resulting in loss of energy and therefore longitudinal momentum. Hence, both the divergence and the energy degrade for accelerator length >1.6mm. The observed variation of the divergence and the energy on either side of 1.6mm indicates that the dephasing length is approximately equal to the acceleration length at that injection location.

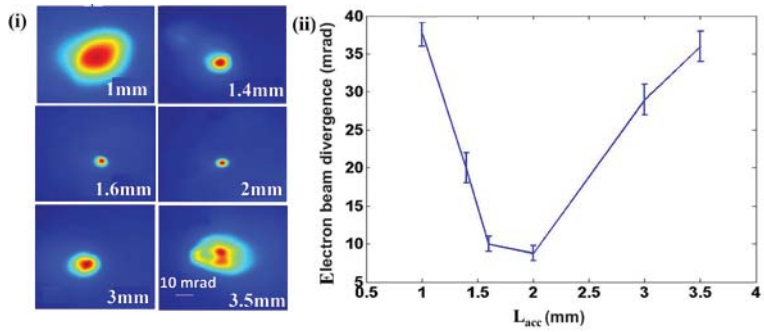

Figure 2 (i) Transverse profiles of typical electron beams observed at a plasma density of 6.8×10^{18} for different accelerator length (L_{acc}) of 1, 1.4, 1.6, 2, 3, and 3.5mm, corresponding to different knife-edge locations(ii) Electron beam divergence variation with accelerator length (L_{acc}).

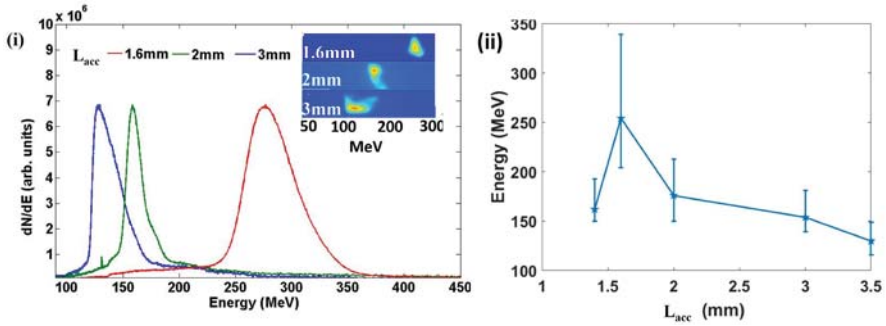

Figure 3 (i) Typical spectra of the electron beam produced at a plasma density of 6.8×10^{18} cm^{-3} for different accelerator length (L_{acc}) corresponding to different knife-edge locations (ii) Variation of the electron beam energy with accelerator length (L_{acc}).

Conclusion: We presented controlled electron injection using sharp density transition mechanism and acceleration of electrons in laser wakefield accelerator. Study showed generation of a tunable energy electron beam in the of 100-250 MeV by varying accelerator length or injection location with the help of density transition injection. The full potential of the scheme shall be investigated in future to produce high quality tunable electron/x-ray beams for various applications.

References:

1. T. Tajima and J. M. Dawson, *Phys. Rev. Lett.* **43**, 268 (1979).
2. E. Esarey, C. B. Schroeder, and W. P. Leemans*, Rev. Mod. Phys.* **81**, 1229 (2009) and references therein.
3. B. S. Rao, A. Moorti, R. Rathore, J. A. Chakera, P. A. Naik et al., *Phys. Rev. ST Accel. Beam* **17**,011301 (2014).
4. D. Hazra, Shikha Mishra, A. Moorti, and J. A. Chakera, *Phys. Rev. Accelerator and Beams* **22,** 074701 (2019).
5. A. J. Gonsalves, K. Nakamura, J.Daniels, C. Benedetti, C. Pieronek et al., *Phys. Rev. Lett*. **122**, 084801 (2019).
6. S.V. Bulanov, F. Pegoraro, A. M. Pukhov, and A. S. Sakharov*., Phys. Rev. Lett*. **78**, 4205 (1997).
7. C. G. R. Geddes, K. Nakamura, G. R. Plateau, Cs. Toth, E. Cormier-Michel et al., *Phys. Rev. Lett*. **100**, 215004 (2008).
8. A. Pak, K. A. Marsh, S. F. Martins, W. Lu, W. B. Mori, and C. Joshi, *Phys. Rev. Lett*. **104,** 025003 (2010).
9. J. Faure, C. Rechatin, A. Norlin, A. Lifschitz, Y. Glinec and V. Malka, *Nature (London)* **444**, 737 (2006).
10. K. Schmid, A. Buck, C. M. S. Sears, J. M. Mikhailova, R. Tautz, *Phys. Rev. ST Accel. Beams* **13**, 091301 (2010).
11. W. Lu, M. Tzoufras, C. Joshi, F. S. Tsung, W. B. Mori, J. Vieira, R. A. Fonseca and L. O. Silva, *Phys. Rev. Spec. Top.Accel. Beams* **10**, 061301 (2007).

X-ray spectral measurements from laser plasmas using a gated Micro-channel plate detector

A. Kumar[1], S. Barnwal[1], M.L.Sharma[1], A. Singh[1], S. Jain[1], A.P. Kulkarni[1], S. Nigam[1],
Y.B.S.R. Prasad[1], N.S.Benerji[1], K.S.Bindra[1,2]
[1]*Laser Technology Division, RRCAT, Indore 452013, M.P., India*
[2]*Homi Bhabha National Institute, Training School Complex, Anushakti Nagar, Mumbai, 400094*
*Email: katul@rrcat.gov.in

ABSTRACT

X-ray spectral studies have been carried out from laser-irradiated copper target using transmission grating coupled with gated MCP detector. With a gating time-window of ~ 11 ns (FWHM), the X-ray spectra of copper plasma was recorded in multiple shots by delaying the window across the laser pulse in time steps of ~ 1 ns. Temporal evolution of spectrum at time steps of ~ 1 or 2 ns were retrieved from various difference spectra obtained by subtracting spectra of successive delays. This provided useful information on the spectral content of plasma as well as their temporal evolution on fast time scale.

INTRODUCTION

The development of high energy high power (HEHP) laser systems delivering short duration intense laser pulses led to research in the area of high density high temperature plasmas. The study of laser plasmas is very important due to their applications in the areas of inertial confinement fusion (ICF)[1, 2], generation of extremely high shock pressures[3, 4], intense x-ray backlighting sources[5], table top charged particle acceleration[6] and, higher order harmonic generation[7, 8] etc. The laser produced plasmas are much different from other types of plasmas in terms of their dimensions (few hundreds of microns) and duration (few ns). Because of these characteristics, the study of laser produced plasmas requires diagnostics with good temporal (ns) and spatial (microns) resolutions, different from that of other types of plasmas. As the temperatures of laser plasmas are typically in the range of few eV - hundreds of eV (millions of degrees), these plasmas are strong sources of x-rays and thus, studies on the x-ray emission gives information about the laser produced plasmas, their evolution and the laser-plasma interaction.

The time-resolved x-ray measurements[9] can be classified into three categories: a) detectors like x-ray photodiodes covered with different thin foils providing continuous temporal information in several spectral ranges b) detectors like MCP based pinhole cameras providing space resolved information in different time-windows[9] and c) detectors like x-ray streak cameras providing both time and space/spectrally resolved information by coupling to pinhole camera/spectrometers[9]. The high speed gated micro channel plates (MCP) are useful for time-resolved x-ray measurements in a variety of research studies such as laser plasma interaction, capillary discharge plasmas, plasma focus, tokomaks etc. The transmission grating spectrometer (TGS) with gated MCP is a simple diagnostics in such experiments. It can be used to carry out time-resolved spectral study of X-rays emitted from the plasma.

In this paper, a transmission grating spectrometer coupled with a gated MCP was used to investigate the temporal variation of the soft x-ray emission from laser-irradiated copper target. The details of experimental set-up, obtained results and their analysis form the basis of this paper and given in subsequent sections.

EXPERIMENTAL SETUP

The experiments were performed using a high-energy high-power Nd:glass laser system at RRCAT[10]. A schematic diagram of the experimental setup is shown in Fig 1(a). The Nd:glass laser output (~ 1 ns) was focused by using a plano-convex lens (f =50 cm) on to the copper target resulting in laser intensities of ~10^{14} W/cm^2. The targets were mounted on target movement system placed inside plasma chamber at vacuum ~5x10^{-5} mbar. Using this movement system, fresh target surface can be used for experiments in each laser shot.

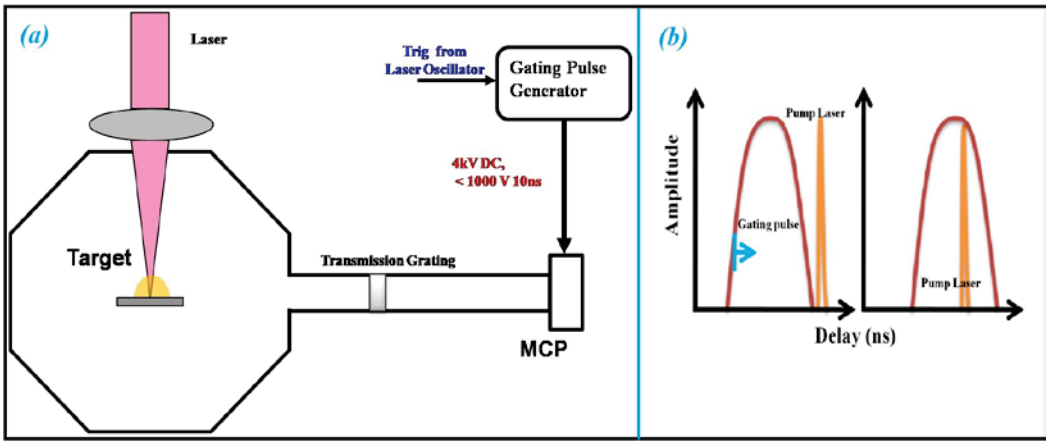

Figure 1: (a) Experimental set-up, (b) The schematic of gating delay w.r.t. pump laser

The copper plasma emits X-ray radiation consisting both line as well as continuum with a spectral profile that strongly depends on the plasma temperature. The x-ray emission from copper plasma was spectrally dispersed using a free-standing transmission grating (700 l/mm) and recorded on a micro channel plate (MCP) detector. The phosphor screen of the MCP converted this into the visible wavelength range (P43-Green) which was then imaged using a canon digital camera (DSLR). In order to confine the 'image capture time' to few nano-seconds instead of recording the time-integrated spectra, the micro channel plate of the MCP was biased with a pulsed voltage instead of DC as described below.

A gating pulse generator unit was developed to apply a voltage pulse on the single stage MCP detector for these experiments. The HV stack was made using number of MOSFETs (IRF840) in series and it was triggered by a gate driver circuit as shown in Fig. 2(a). This unit also includes a HV DC-DC converter based supply of ~ 4 kV for biasing of phosphor section of the MCP detector. The complete unit was configured for its fast MCP gate output of ~ 11 ns FWHM with 1 kV under 100X probe as load. The delay between the laser pulse and the applied gate pulse on MCP was varied using a delay box as shown schematically in Fig 1(b) The response time of the pulse generator with respect to its trigger input was also measured to be less than 70 ns. The pulse output with the transport line connected to the MCP is shown in Fig. 2(b). A vacuum diode detector

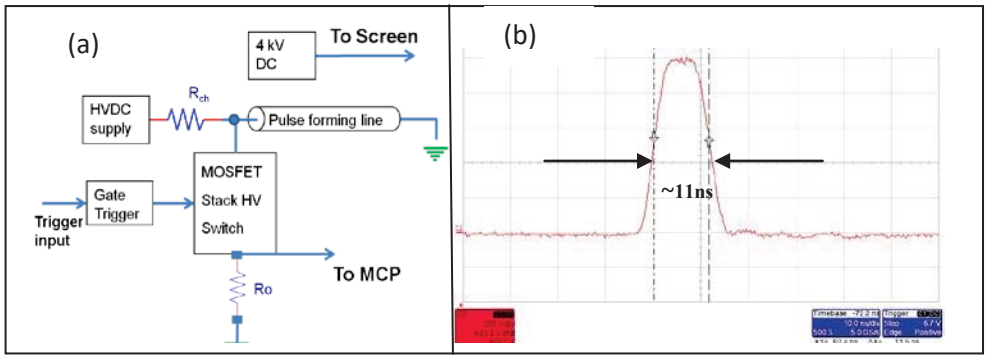

Figure 2: (a) Block diagram of MCP gating circuit and (b) MCP gating pulse of ~ 11 ns FWHM

with 2.4 µm Al foil (transmission < 3nm and 17-25 nm) was also placed to get a rough idea about x-ray emission temporal profile of the plasma.

RESULTS AND DISCUSSION

Initially, the delay of the applied voltage pulse on MCP was adjusted such that there is no overlap between the MCP ON time-window (~ 11 ns) and laser plasma. In this case, no spectral emission was observed in the images recorded by MCP detector. This is being called as zero delay. Then, the gate window was shifted in steps of ~1ns towards the laser pulse by introducing suitable delays and the spectra were recorded. In this way, the X-ray emission spectra from copper plasma were recorded in multiple shots at different delay times under identical experimental conditions as shown in Fig.3 (a). All these curves are obtained by normalizing them with their zeroeth order maxima. In these spectra, various distinct line emissions superimposed over the continuum in soft X-ray region were observed. For example, emissions at 1.0 nm, 2.1 nm, 4.1 nm, 5 nm and 7.6 nm were observed along with broad continuous spectra as shown in Fig 3 (a). Emissions at 1.0 nm and 2.1 nm might be due to L-shell transitions in the copper plasma.

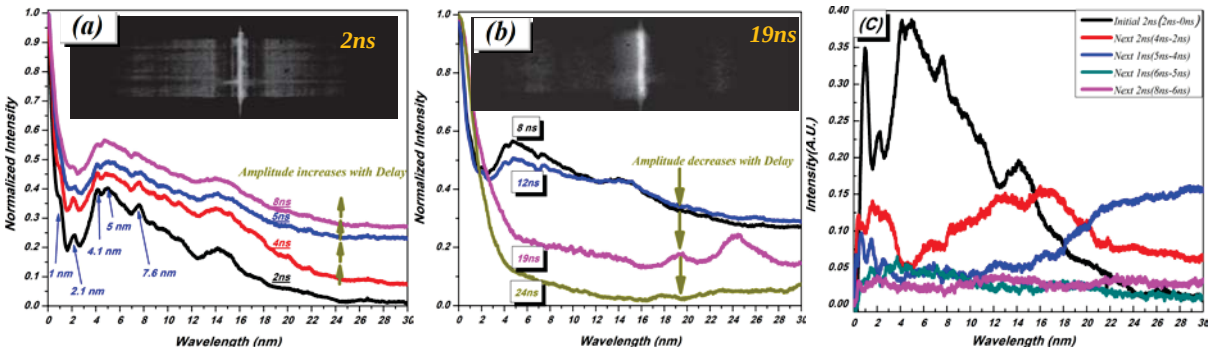

Figure 3: The X-ray emission Spectra from copper target at (a) increasing & (b) decreasing delays and (c) Difference spectra with respect to time

These spectral features (x-ray emission lines) could only be distinctly observed for initial delays of few ns as the overlapping between the MCP gate pulse (~ 11 ns) and the initial x-ray emissions from plasma was for few ns (2-3 ns) only. It is to be noted here that the duration of the x-ray emission from plasma at the wavelengths below 25 nm is only ~few ns which was also seen from the signals recorded using the x-ray diode with 2.4 µm Al filter (transmission < 3 nm and 17 - 25 nm). This gives an approximate idea of the duration of X-ray emission which is longer than the duration of pump laser and much shorter than the lifetime of plasma. The spectral features mentioned above slowly merged in the background of continuum for longer delays where emissions are integrated on the MCP detector for longer time periods. Hence, the initial delay of ~ 2 ns seems to be best suited for getting the spectrum with better contrast. If we look at the continuum spectra in Fig. 3(a), its amplitude increases with initial delays from 2 ns to 8 ns where the gate-window of detector is shifting in time to capture more and more emissions from plasma. For later delays i.e. 10 ns onwards as shown in Fig 3(b), it starts falling due to initial part of emissions are out of the ON 'time window' of the MCP detector. For delays 19 ns onwards, gate-window has almost passed out of the x-ray emissions and therefore negligible emissions are recorded.

Ideally, gate-window of detector should be smaller than the duration of x-ray emissions in order to record its temporal evolution. But due to limitations on the switching electronics, it was not possible to obtain below certain value. The gate-window here is large enough to make it practically difficult to record x-ray

spectra in smaller time-window. Thus, a different approach was adopted here to obtain temporal information from these time-integrated spectra already recorded for initial delays. Spectra recorded at two such consecutive delays were subtracted to get a *difference* spectra e.g. spectrum recorded at initial 2 ns delay was subtracted from that of 4 ns delay to get spectrum which is actually time-integrated over the next 2 ns (between 2 and 4ns). In this way, various *difference spectra* were obtained for initial delays as shown in Fig. 3(c). These act as snapshots of spectra for a smaller time-window of either 1 ns or 2 ns. Such a temporal evolution of plasma has been obtained up to ~ 8 ns time. A closer look at these spectra reveals some interesting facts. In the first 2 ns time, the continuum plasma emission peaks around wavelength region of 4 - 8 nm. In next 2 ns time, the overall emission falls and the peak shifts towards 14 - 16 nm spectral regions. The emission further shifts beyond 20 nm in next 1 ns time. The various spectral features could be seen with good contrast for the first 2 ns time. Such, a shift in the spectral emission with time may provide much useful information about the plasma dynamics which is presently under investigation.

SUMMARY

In this paper, time resolved x-ray emission studies from laser produced copper-plasma have been conducted. The x-ray emission from copper plasma was recorded using TGS with gated MCP, in multiple shots by varying the gate-window across the laser pulse in steps of ~ 1 ns. Apart from the continuum, distinct line emissions were observed which were seen with good contrast for initial delay of ~ 2ns. The amplitude of the spectrum increases with time up to 8ns and after that decreases with increase in delay. A different approach was used to get time-resolved information of the recorded spectrum with a time-resolution less than the duration of gate-window. For that, difference spectra were obtained from subtraction of spectra at two consecutive delays. These spectra clearly showed how the x-ray spectrum of copper plasma is shifting from shorter to longer wavelength region in a time scale of ~ 1 - 2 ns. Further analysis of these spectra is in progress.

Acknowledgments

Authors would like to gratefully acknowledge help received from Dr. M. S. Ansari and other HPL Electronics Section team members. Authors also would like to acknowledge the contributions of Shri S. R. Patwa, Shri K.K. Mani and Shri Manish Mehar for all the support provided during these experiments.

References

1. Dong et al., *Nucl. Fusion* **58,** 016038 (2018).
2. Betti R. et al., *Nat. Phys.* **12***,* 435 (2016).
3. Siegfried H. et al., *Mod. Phys.,* **81***,* 1625 (2009).
4. M. D. Salas et al., *17th Shock Interaction Symposium, Rome, Italy, 4-8 September 2006.*
5. C. A. Back et al. *Phys Rev Lett.* **87***,* 5003 (2001)
6. R Bingham et al., *Plasma Phys. Control. Fusion* **46**, R1 (2004)
7. J. J. Macklin et al., *Phys Rev Lett.* **70***,* 766 (1993).
8. G. Vampa, et al. *Phys Rev Lett.* **113**, 073901 (2014).
9. N. M. Ceglio et al., *Applied Optics,* **22***,* 318 (1983).
10. A.S. Joshi, et al, *EPJ Web of Conferences* **59***,* 08001 (2013).

Study of spatio-temporal reshaping of ultrashort laser pulse due to plasma defocusing

A. Ansari[a], M. Kumar[a], H. Singhal[a,b] and J.A. Chakera[a,b]

[a]*Raja Ramanna Centre for Advanced Technology, Indore, M.P.- 452013*

[b]*Homi Bhabha National Institute, BARC Training School Complex, Anushakti Nagar, Mumbai- 400094*

E-mail: ajmal@rrcat.gov.in

We have numerically investigated the propagation of ultrashort laser pulse in Neon gas at hundreds of mbar pressure by solving the three-dimensional (3D) wave equation. Laser intensity spatio-temporal profile at different location in the gas target at different gas pressures are studied. Reshaping and self-compression of the laser pulse in time without any subsequent dispersion compensation are observed. We have calculated a compressed output laser pulse ~17 fs from a Fourier transform limited 45 fs Gaussian input pulse by passing through 5 mm gas cell at 400 mbar pressure.

Higher order Harmonics (HOH) are generated by interaction of intense ultrashort laser pulses with a gas target through a non-linear process[1]. To obtain the maximum harmonic intensity, it is necessary that generated harmonics at each points in the gas medium should add constructively (i.e. minimize the phase mismatch). The phase matching condition is optimized by varying the laser intensity[2], gas pressure and gas target position with respect to the laser focus position[3]. Intensity of the driving laser beam is very crucial in phase matching condition. It should be sufficiently high to generate ionization (called critical ionization) such that phase mismatch due to plasma dispersion is balanced by the phase mismatch due to atomic dispersion. But if the laser intensity is increased to above saturation intensity (i.e., intensity at which given atom is fully ionize), then intensity of HOH start decreasing due to large phase mismatch. In order to understand this, it is required to study the evolution of ultrashort laser beam and its intensity as it propagate through the gas medium. In this work, we have carried out the numerical investigation of the propagation of the driving ultrashort laser pulse by solving the three-dimensional (3D) wave equation. Laser intensity spatio-temporal profile at different location in the gas target at different gas pressures are studied. It shows the reshaping and *self-compression* in time without any subsequent dispersion compensation[4]. The mechanism behind the self-compression can be understand by two simultaneous processes. First, increase in spectral bandwidth by phase modulation due to rapidly changing plasma refractive index, and second, spatio-temporal reshaping of pulse due to interplay between plasma induced defocusing and laser beam diffraction.

The propagation of the driving laser beam is calculated by numerically solving the 3D wave equation[5] which contains the diffraction term and plasma defocusing term. In our case, the laser intensity is above saturation intensity and gas pressure is about hundreds of mbar so that plasma dispersion is very high in comparison of other dispersion. Hence, plasma defocusing and diffraction terms are considered and other terms such as dispersion, self-focusing and ionization loss terms are neglected. The wave equation in moving cylindrical coordinate frame ($z' = z$ and $t' = t–z/c$) and taking slowly varying envelope approximation (i.e., neglecting $\partial^2 E/\partial z'^2$) can be written as follows:

$$\nabla_{\perp}^2 E(r,z',t') - \frac{2}{c}\frac{\partial^2 E(r,z',t')}{\partial z' \partial t'} = \frac{\omega_p^2(r,z',t')}{c^2} E(r,z',t') \qquad (1)$$

where $\omega_p(r,z',t')=\left[\frac{e^2 n_e(r,z',t')}{\varepsilon_0 m_e}\right]^{1/2}$ is the plasma frequency, z' is the propagation coordinate, and r is the transverse coordinate and t' is the retarded time.

As the ionization in our case is tunneling ionization, free-electron density, $n_e(r,z',t')$ can be calculated using the ADK ionization rates[6] and higher degree of ionization is considered. By taking Fourier transform, equation (1) becomes

$$\nabla_\perp^2 \tilde{E}(r,z',\omega)-\frac{2i\omega}{c}\frac{\partial \tilde{E}(r,z',\omega)}{\partial z'}=\tilde{G}(r,z',\omega) \tag{2}$$

where $\tilde{E}(r,z',\omega)=\hat{F}[E(r,z',t')]$, $\tilde{G}(r,z',\omega)=\hat{F}\left[\frac{\omega_p^2(r,z',t')}{c^2}E(r,z',t')\right]$ and $\hat{F}$ is the Fourier transform operator acting on temporal coordinate. These equations are solved, for each value of ω, using a Crank-Nicholson routine. Typical grid points used in calculation are 2^{13} points in time, 250 points along the radial direction, and 600 points along the propagation direction.

In our numerical study, we consider Neon gas interact with 3.7 mJ, 45 fs IR Gaussian transform limited pulse centered at 800 nm wavelength. The geometry of the gas target is a gas cell of 5 mm in length. The pressure profile along the gas cell is assumed to be constant inside the cell and has a Lorentzian shape at both ends. The laser pulse have a beam size ~7 mm (a half-width at $1/e^2$ of intensity) and focused by a one inch lens of 750 mm focal length at the center of the gas cell. Numerically estimated spot size is ~28.14 μm (a half-width at $1/e^2$ of intensity) and peak intensity ~6.2×10^{15} W/cm^2 (Note: these values are estimated for vacuum condition). At this intensity, gas medium should be ionized to 200% but due to defocusing effect, this is not the case.

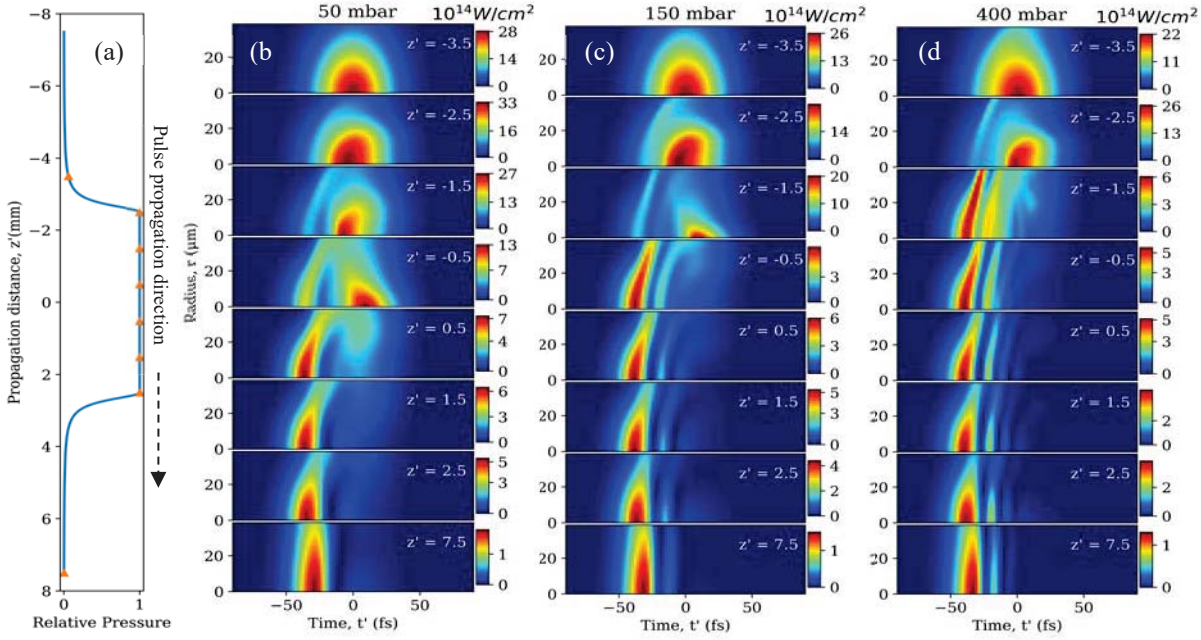

Fig.1 Spatio-temporal intensity profile of laser pulse as laser pulse propagate towards +z' direction in gas cell at propagation coordinate from z'=-3.5 to 7.5mm at three gas pressures (b) 50 mbar, (c) 150 mbar and (d) 400 mbar. The relative pressure profile is shown in (a).

Spatio-temporal profile of the laser pulse at different locations as the beam propagate through the gas cell is shown in fig.1. It shows the plasma defocusing effect in both space and time due to rapidly ionization of the gas medium leads to rapid decrease in plasma refractive index. This plasma defocusing effect increases with increase in gas pressure and the length over which the overall spatio-temporal reshaping occurs, start decreasing with increase in pressure. The overall spatio-temporal reshaping of pulse due to plasma defocusing effect[7], diffraction of the laser beam and self phase modulation (SPM), results in *self-compression* of pulse at the exit of the gas medium. This phenomena can be understand with the fig.2 which shows the temporal profile and corresponding spectrum of the pulse at different propagation coordinate as beam propagate in the gas cell at 400 mbar pressure. As the laser pulse start entering in the gas medium (at z'= -3.5), the leading edge of the pulse interact with the gas medium. Since the gas pressure is sufficient (~50 mbar) to decrease the plasma refractive index, and hence pulse start defocusing in time and asymmetric spectrum broadening due to SPM. When pulse entered into the gas medium (at z'=-1.5), the leading edge of the pulse suffer more rapid change in plasma refraction index causing more plasma defocusing in time. There is splitting of the pulse with each pulse having duration smaller than the input pulse. The pulse is defocused much earlier the vacuum peak of the pulse (i.e., t'=0), the peak of the pulse envelope formed earlier in time (t'<0). There is generation of additional blue shifted frequencies due to SPM which broadens the frequency spectrum[8]. When the pulse propagate more inside the gas cell, since the laser pulse intensity already drop down due to defocusing, no more change occur in pulse temporal shape. At the output, we get self-compressed pulse with peak envelope earlier in time and overall blue shifted frequency broadened spectrum laser pulse.

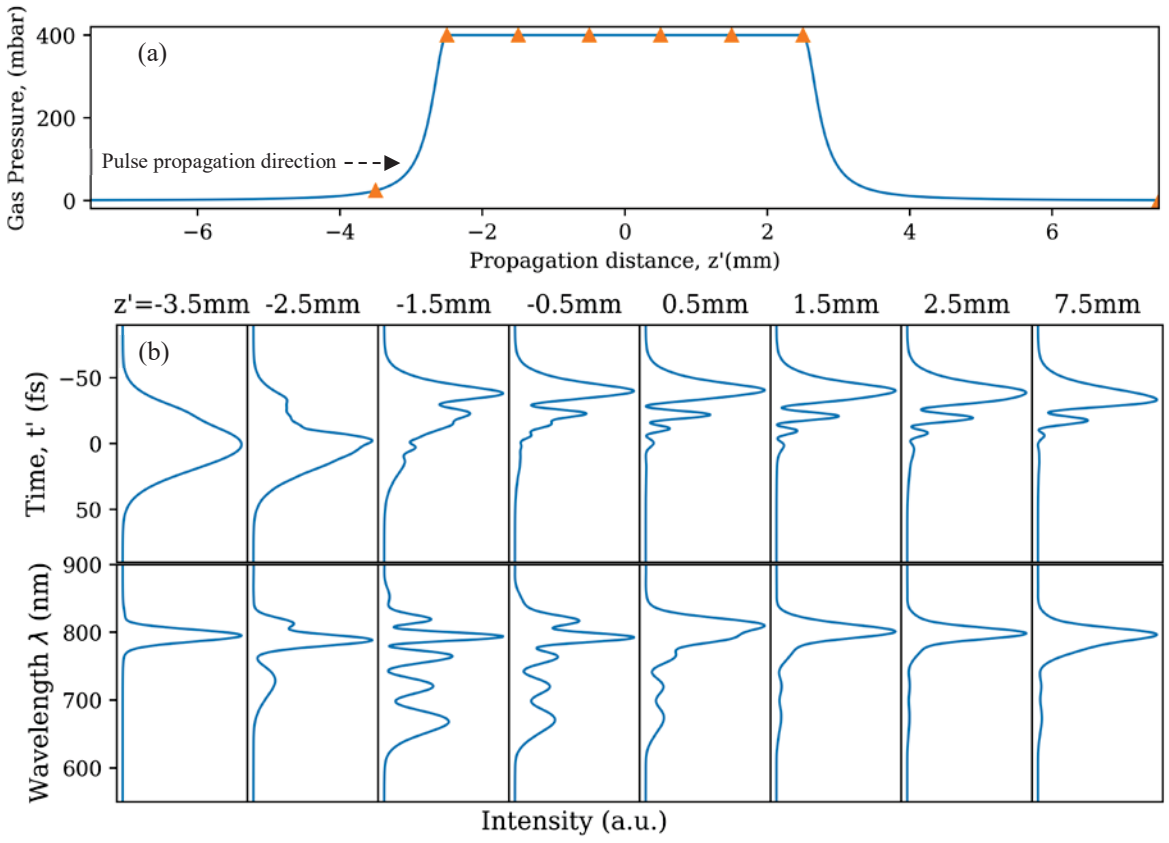

Fig.2. Temporal profile, (a) and corresponding frequency spectrum, (b) of the laser pulse as beam propagate in +z direction in the gas medium at 400 mbar pressure.

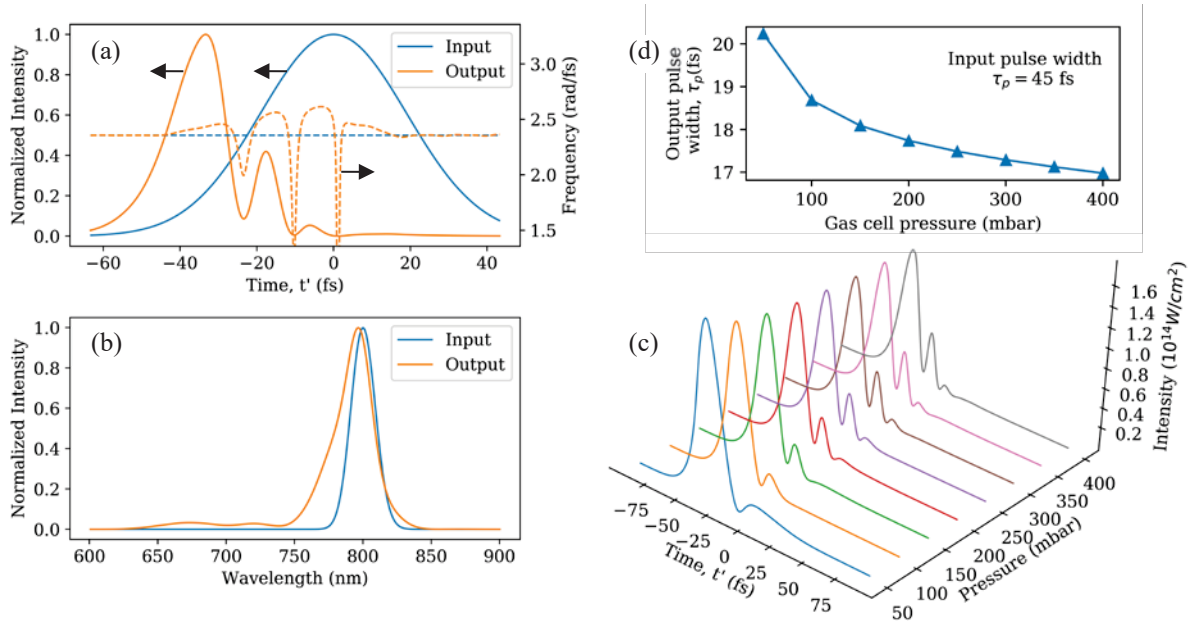

Fig.3 (a) Comparison of Temporal profile and instantaneous frequency of the output laser pulse with input laser pulse when it passed through the gas cell filled at 400 mbar of Ne. (b) Corresponding frequency spectrum of the input and output pulse. (c) Variation of the temporal profile of the output pulse with the gas cell pressure showing that temporal width of the pulse continue to decrease to ~17 fs at 400 mbar. (d) Variation of the output pulse width with the gas pressure.

The laser pulse after passing through the gas cell filled at 400 mbar pressure is *self-compressed* to ~17 fs due to spatio-temporal reshaping of the pulse as shown in fig. 3(a) and peak of the envelope appeared at ~ -35 fs with almost linear positive chirp is observed. [Input pulse is transform limited Gaussian pulse with pulse width ~ 45 fs (FWHM)]. Corresponding frequency spectrum of the output pulse is shown in fig. 3(b). It is clearly show that the output pulse is blue shifted with a broadened spectrum with respect to the input pulse. The temporal profile of the output pulse is calculated at various different pressures in fig. 3(c). It shows that as the pressure is increased, pulse width decreases and the peak envelope of the pulse is shifted to more earlier in time. Fig 3(d) shows that temporal width of the output pulse is continue to decrease with increase in pressure and attain a value ~17 fs at higher pressure.

In conclusion, spatio-temporal profile of the laser pulse inside the gas medium during propagation is numerically studied. Temporal splitting of the pulse and formation of peak earlier in time due to plasma defocusing is observed. At output of the gas medium, self compressed pulse is observed.

1. A. L'Huillier and P. Balcou, *Phys. Rev. Lett.* **70**, 774 (1993).
2. P. Rudawski et al, *Rev. Sci. Instrum.* **84**, 073103 (2013).
3. P. Balcou, P. Salieres et al, *Phys. Rev. A.* **55**, 3204–3210 (1997).
4. N. L. Wagner et al, *Phys. Rev. Lett.* **93**, 173902 (2004).
5. M. Geissler et al, *Phys. Rev. Lett.* **83**, 2930–2933 (1999).
6. M. V. Ammosov, N. B. Delone, and V. P. Krainov, *Sov. Phys. JETP* **64**, 1191–1194 (1986).
7. S.C. Rae, *Optics Communications*, **104**, 330-335 (1994).
8. W. M. Wood, G. Focht, and M. C. Downer, *Opt. Lett.* **13**, 984 (1988).

Stimulated Raman and Brillouin scattering processes in magnetized doped semiconductors: A comparative study

Jaivir Singh[1], Arun Kumar[1], Sunita Dahiya[1], Navneet Singh[2], Manjeet Singh[3,*]

[1]*Department of Physics, Baba Mastnath University, Asthal Bohar – 124021 (Rohtak) India*
[2]*Department of Physics, Rajiv Gandhi Government College for Women, Bhiwani-127021, India*
[3]*Department of Physics, Government College, Matanhail – 124106 (Jhajjar) India*

*Email: msgur_18@yahoo.com

Abstract: An analytical investigation of the stimulated Raman (SRS) and Brillouin (SBS) scatterings of the coherent Stokes mode is undertaken in magnetized diffusive semiconductors. SRS and SBS gain constants have been obtained. The magnetic field is found to subsequently augment the gain constant of the scattered mode. SRS and SBS gain constants are effectively influenced by magnetic field such that the cyclotron frequency becomes comparable to the optical (for SRS) or acoustical (for SBS) wave frequency.

1. Introduction

The study of stimulated Raman scattering (SRS) and stimulated Brillouin scattering (SBS) processes has been the subject of intense investigations as these have manifold technological applications in optoelectronic devices as well as provide understanding of the light-matter interactions in quantum electronics. One of the most important applications of these processes in optoelectronics is to remove the phase aberration of the electromagnetic fields as well as their amplification, i.e. optical signal processing[1]. In a crystalline medium, SRS and SBS are very closely related phenomena as the former occurs via optical-phonon (OP) mode while the latter originates from acoustic phonon (AP) mode vibrations. In spite of such closeness, these phenomena are usually studied independently assuming that the second-order forces responsible for them are different, viz., the finite differential polarizability gives rise to SRS, while the electrostrictive strain produces SBS in a material medium[2,3]. Stimulated scattering of an intense beam of electromagnetic waves in plasma has been studied by a number of authors[4-6]. If the plasma is un-magnetized, the scattering results from parametric decay of the pump wave into another electromagnetic wave and either a Langmuir wave (SRS) or an ion-acoustic wave (SBS). In magnetized plasma additional electrostatic scattered modes exist and in general, the pump and scattered waves may be modified by the magnetic field[7-9]. Literature survey reveals that no attempt has so far been made on on simultaneous study of SRS and SBS in magnetized semiconductors.

Motivated by the above discussion, in this paper we have presented a comparative study of SRS and SBS processes in a magnetized diffusive semiconductor. The nonlinearities taken into account are the electronic nonlinearity due to the nonlinear current density and the nonlinear polarization due to nonlinear coupling between the resulting acoustical-optical mode and the scattered electromagnetic wave.

2. Theoretical Formulations

We consider the homogeneous medium with electrons as carriers being subjected to an external magnetic field B_0, parallel to the propagation vector $\vec{k}$ and the spatially uniform pump wave $E_0 \exp(-i\omega_0 t)$. The intense laser excitation is responsible for the generation of material excitation within the crystal, which then leads to the

stimulated scattering processes; the molecular vibrations are responsible for SRS and the acoustic mode for SBS. Due to electromagnetic field, the ions within the lattice move into nonsymmetrical position, usually producing a contraction in the direction of the field and an expansion across it. The electrostatic force thus produced is the origin of the differential polarizability and electrostriction in the medium. The polarizations due to molecular vibrations and the electrostriction are given by

$$\vec{P}_{mv} = \varepsilon_0 N(\partial\alpha/\partial u)_0 u(r,t)^* \vec{E}_0 \tag{1}$$

$$\vec{P}_{es} = -\gamma \vec{E}_0 \frac{\partial u(r,t)^*}{\partial r}, \tag{2}$$

where $u(r,t)$ is the relative displacement of oscillators from the mean position of the lattice. Eq. (1) shows that due to the non-vanishing differential polarizability $(\partial\alpha/\partial u)_0$ in the Raman active medium, the optical field derives the molecular vibrations, which in turn modulates the dielectric constant, resulting in a nonlinear induced polarization $\vec{P}_{mv}$. Similarly, in a Brillouin active medium, an acoustic mode is generated due to electrostrictive strain, leading to the energy exchange between electromagnetic and acoustic fields, and give rise to $\vec{P}_{es}$. Now, applying the procedure adopted in our earlier work [7] to the present field configuration, the Stokes mode of this scattered component at $\omega_s = \omega_0 - \omega$ can be obtained as

$$n_s^* = \frac{-\omega_M^2 P_{nl}}{e|\bar{E}|}\left[1 - \frac{(\omega_s^2 - \omega_M^2 - i\omega_s\nu)(\omega^2 - \omega_M^2 + i\omega_s\nu)}{k^2|\bar{E}|^2}\right]^{-1}, \tag{3}$$

where $\bar{\omega} = \omega - kv_0$, $\bar{E} = (eE_0/m)$, $\omega_M^2 = \frac{\omega_p^2\bar{\omega}\omega_c\varepsilon_L}{\varepsilon_1\omega(\bar{\omega}+i\nu-\omega_c)}\left[1 - \frac{\omega_p^2\bar{\omega}\varepsilon_L}{\varepsilon_1\omega_c(k^2c_L^2D-\omega^2)}\right]$, $\omega_c = \frac{eB_0}{m}$, $\omega_p = \left[\frac{n_0e^2}{m\varepsilon_0\varepsilon_L}\right]^{1/2}$,

D is diffusion coefficient.

The resonant Stokes component of the induced current density due to the finite nonlinear polarization of the medium has been deduced neglecting the transition dipole moment, which can be represented as

$$J(\omega_s) = \frac{i\varepsilon\omega_p^2\bar{\omega}}{\omega(\bar{\omega}+i\nu-\omega_c)} - \frac{\omega_M^2 P_{nl}}{(\nu - i\omega_0)}\left[1 + \frac{(\omega_s^2 - \omega_M^2 - i\omega_s\nu)(\omega^2 - \omega_M^2 + i\omega_s\nu)}{k^2|\bar{E}|^2}\right]^{-1}. \tag{4}$$

The Raman active medium is taken as consisting of N harmonic oscillators per unit volume, characterized by its position x and normal vibrational coordinates u (x, t). In a Raman active medium the scattering of the pump wave is enhanced due to the excitation of a molecular vibrational mode. As $(C/\rho)^{1/2}$ is the acoustic velocity in the crystal, we have the equation of motion of an independent oscillator as

$$\frac{\partial^2 u}{\partial t^2} + \omega_T^2 u + 2\Gamma_v \frac{\partial u}{\partial t} = \frac{1}{2M}\varepsilon_\infty(\partial\alpha/\partial u)_0 E_0 E_1^*. \tag{5}$$

Treating the induced nonlinear polarization P_{cd} as the time integral of the nonlinear current density J_{nl}, we obtain the nonlinear Raman polarization due to the finite perturbed current density from Eqs. (4) and (5) as

$$[P_r]_{cd} = \frac{\omega_{Mr}^2\varepsilon_0\varepsilon_\infty N(\partial\alpha/\partial u)_0^2 E_0^2 E_1}{2\omega_0\omega_s M(\omega_T^2 - \omega^2 + i\omega\Gamma_u)} \times \left[1 + \frac{(\omega_s^2 - \omega_{Mr}^2 - i\omega_s\nu)(\omega_T^2 - \omega_{Mr}^2 + i\omega_T\nu)}{k^2|\bar{E}|^2}\right]. \tag{6}$$

Following Singh et.al.[7], the third-order Raman susceptibility is obtained from Eqs. (6) and (7) as

$$\left[\chi_R^{(3)}\right]_{eff} = \frac{\varepsilon_\infty N(\partial\alpha/\partial u)_0^2}{2M(\omega_T^2 - \omega^2 + i\omega\Gamma_u)}\left[1 + \frac{\omega_{Mr}^2}{\omega_0\omega_s}\right]. \quad (7)$$

Following Singh et.al.[7], we obtained the Raman gain constant from imaginary part of Eq. (7) as

$$g_R(\omega_s) = \frac{k\varepsilon_\infty N(\partial\alpha/\partial u)_0^2\Gamma_u|E_0|^2}{16\varepsilon_L M\omega_T[\{\omega_T - (\omega-\omega_s)\}^2 + \Gamma_u^2/4]}\left[1 + \frac{\omega_{Mr}^2}{\omega_0\omega_s}\right]. \quad (8)$$

The threshold pump field to incite SRS can be obtained by setting $\left[P_r\right]_{cd} = 0$. This yields

$$|E_{0th}|_r = \frac{m}{ek}\left[(\omega_s^2 - \omega_{Mr}^2 - i\omega_s\nu)^{1/2}(\omega_{Mr}^2 - \omega_T^2 + i\omega_T\nu)^{1/2}\right]. \quad (9)$$

The phenomenon of SBS is analogous to SRS with the acoustic waves due to electrostriction playing the role of the molecular vibrations. The equation of motion for u (x, t) in the acoustical branch is given by

$$\frac{\partial^2 u}{\partial t^2} - \frac{C_\alpha}{\rho}\frac{\partial^2 u}{\partial x^2} + 2\Gamma_\alpha\frac{\partial u}{\partial t} = \frac{\gamma}{2\rho}\frac{\partial}{\partial x}(E_0E_1^*), \quad (10)$$

with γ being the electrostrictive coefficient.

We proceed in similar way as followed in above to study SBS and the Brillouin gain constant of the Stokes mode. The Brillouin gain constant and threshold condition required for inciting SBS has been obtained as

$$g_B(\omega_s) = \frac{\Gamma_a\gamma^2k^3|E_0|^2}{8\rho\varepsilon\omega_a[(\omega_a - kv_s)^2 + \Gamma_a^2]}\left[1 + \frac{\omega_p^2\bar{\omega}_a\omega_c}{\omega_0\omega_s\omega_a(\bar{\omega}_a + i\nu - \omega_c)}\left(1 - \frac{\omega_p^2\bar{\omega}_a}{\omega_c(k^2c_L^2D - \omega_a^2)}\right)\right]. \quad (11)$$

$$|E_{0th}|_b = \frac{m}{ek}\left[(\omega_s^2 - \omega_{Mb}^2 - i\omega_s\nu)^{1/2}(\omega_a^2 - \omega_{Mb}^2 - i\omega_a\nu)^{1/2}\right]. \quad (12)$$

3. Results and Discussion

For numerical appreciation, this analysis is applied to a semiconductor crystal, viz. n-type InSb crystal as an active medium and irradiated by a 10.6 μm CO_2 laser. The material constants have been taken from Ref.[9]. From Eqs. (9) and (12), it is found the external magnetic field reduces the threshold fields for both processes to an appreciable extent in the highly doped medium. The threshold fields for both stimulated scattering processes increase linearly with the increase in carrier concentration of the medium. With the above-mentioned parameters, $|E_{0th}|_r$ is found to be ~ 8×10^5 Vm^{-1} for SRS when $\omega_c \sim \omega_v$ and $|E_{0th}|_b$ is found to be ~10^5 Vm^{-1} for SBS when $\omega_c \sim \omega_a$, which agrees well with the literature[3].

Eqs. (8) and (11) can be used to estimate the ratio (g_R/g_B) between the gain constants for SRS and SBS in terms of material parameters. This enables one to estimate qualitatively the gain constant of one of the stimulated scatterings in terms of the gain constant of the other. Fig. 1 depicts the dependence of $g_{R,B}$ on the externally induced magnetic field via the cyclotron frequency ω_c. $g_{R,B}$ is fairly independent of ω_c, at a lower magnitude of B_0. But as ω_c approaches the molecular vibrational-acoustic wave frequency, $g_{R,B}$ increase rapidly and then saturates at a higher magnitude of B_0. Thus a higher magnitude of $g_{R,B}$ is obtained at cyclotron frequencies comparable to the pump frequency (i.e., $\omega_c < 0.1\omega_0$), which is independent of the external magnetic field. The magnetic field B_0 is effective only when the cyclotron frequency ω_c is comparable to the molecular vibrational or the acoustical wave frequency as is evident from the enhancement parameter ω_M (via ω_R). And for $\omega_c >> \omega_v$, ω_a), it is found that ω_M (via ω_R) becomes independent of ω_c. Hence the coherent laser may be tuned by

operating the magnetic field (cyclotron frequency) around the vibrating phonon frequency. In the case of a transversely applied magnetic field, it has been found that the magnetic field is effective only when the cyclotron frequency ω_c exceeds the vibrational phonon frequency of the scattering medium. Thus the circular polarization induced by the longitudinal magnetic field saturates the Stokes gain at higher magnetic fields.

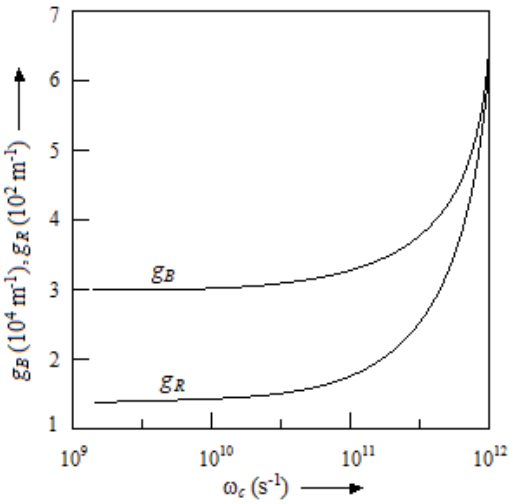

Fig. 1: Dependence of $g_{R,B}$ on the externally induced magnetic field (via cyclotron frequency ω_c)

It can be further inferred from Eqs. (8) and (11) and subsequently from Fig. 1 that SBS has a larger gain constant as compared to SRS process. This outcome is in agreement with the investigations carried out by Maier, Wendl, and Kaiser[10] where they had compared both steady-state gain and the corresponding transient response of the competing processes. It has been observed from the preceding analysis that the ratio of the SRS and SBS gain constants under the same pump intensity indicates that SBS exhibits higher gain than SRS by a magnitude ω_v/ω_a. This result is in conformity with those obtained with the semi classical theory by Sen and Sen[3]. From the above discussion, we may conclude that a substantial enhancement of SRS and SBS gain constants can be achieved in magnetized diffusive semiconductors by nanosecond pulsed moderate power infrared laser irradiation.

References

[1] M. Grower, D. Proch, *Optical Phase Conjugation* (Springer, Berlin, 1994).

[2] P.K. Sen and P. Sen, *Phys. Rev. B* **33**, 5038 (1986).

[3] P. Sen and P.K. Sen, *Phys. Rev B* **31**, 1034 (1985).

[4] H. A. Baldis, D. M. Villeneuve, C. Labaune, et al. *Phys. Fluids B* **3**, 2341 (1991).

[5] D.M. Villeneuve, H.A. Baldis, *Phys. Fluids* **31**, 1970 (1988).

[6] H. Liang, L. ZhanJu, Z.C. Yang, X. Jiang, F. Wu, H.X. Yan, L. Bin, *Chin. Sci. Bull*. **57**, 2747 (2012).

[7] M. Singh, P. Aghamkar, N. Kishore, P.K. Sen, M.R. Perrone, *Phys. Rev. B* **76**, 012302 (2007).

[8] S. Sharma, G. Sharma, M.P. Rishi, *Phys. B: Cond. Mat*. **328**, 255 (2003).

[9] J. Gahlawat, S. Dahiya, M. Singh, *Arab. J. Sci. Eng.* **46**, 721 (2021).

[10] M. Maier, G. Wendl, W. Kaiser, *Phys. Rev. Lett*. **24**, 352 (1970).

Energy Dependent Study of Confined Laser Generated Air Plasma

D. P. S. L. Kameswari[1], Nagaraju Guthikonda[1], S. Sai Shiva[1], P. Prem Kiran*[1,2]

[1] *Advanced Center for Research in High Energy Materials, University of Hyderabad, Gachibowli, Hyderabad,*

[2] *School of Physics, University of Hyderabad, Gachibowli, Hyderabad*

Correspondence E-mail: premkiranuoh@gmail.com

Abstract: A numerical study of effect of laser energy on geometric confinement of laser generated air plasma is performed using FLASH 2D radiation hydrodynamic code. The 10 ns laser generated air plasma is confined laterally using a glass tube of length 12 mm and diameter 8 mm. The study is performed for three laser energies of 50, 200 and 400 mJ to understand the effect of the input laser energy on the enhancement in plasma parameters. The results show that the interaction of reflected shock wave along radial direction with the plasma core has led to a pronounced increment in the plasma parameters. This work discusses the dynamics of confined air plasma in detail.

Introduction: A laser beam when focused into a gas creates an intense spark leading to formation of plasma. The plasma emits radiation across the em region of the spectrum, popularly known as laser–induced breakdown (LIB) of a gas. The plasma and the shock wave associated with it expand freely into surrounding ambient air [1-3]. Confining the freely expanding shock wave (SW) with solid walls of a medium results in reflection of the SW due to impedance mismatch. The reflected SW interacts with the plasma core resulting in complex plasma dynamics. Interaction of reflected SW with plasma shows an effective increment in the plasma parameters such as number density (N_e) and electron temperature (T_e) leading to an increment in the plasma lifetime. Confined laser plasmas find a wide range of applications in aerodynamics and aero acoustics [4, 5], aerospace, military, and transportation applications to mitigate blast or shock impact in the lateral direction by placing foam materials [6], and surface cleaning based on the laser-induced shock wave generation [7]. Different aspects of the confinement such as the spectroscopic diagnostics of confined plasma [5, 8-10], effect of shape of confining geometry [11, 12], confinement of plasma ablated from different metal targets were studied using LIBS [11, 13-19]. However, a quantitative analysis of air or gaseous samples using LIBS is limited due to its relatively low signal when compared to solids. Tao et.al, [20] has studied the pressure evolution in the air plasma confined in a microhole, upto few tens of nanoseconds due to the smaller dimensions of the confining geometry. Popov et. al., [21] has studied the LIBS in air confined by a brass chamber. However, a detailed study on the SW dynamics inside the tube, quantitative study of enhancement in the plasma parameters due to interaction between plasma core (PC) and the reflected SW, effect of laser energy on confined plasma parameters was sparsely studied. Hence a numerical study of the effect of laser energy (intensity) on SW evolution inside the confining tube, SW interaction with plasma were presented in this paper.

Simulation Details: The simulations were performed in a glass tube over a computational domain of 6×6 cm with a minimum mesh size of 30×30 μm along laser (Z - axis) and radial (R - axis) directions. Fig.1 shows the cross-section of the computational domain where two glass plates are placed opposite to each other

perpendicular to the laser propagation direction. The ambient air conditions are considered at normal temperature and pressure (NTP) with a mass density of 1.3×10^{-3} gm/cm^3.

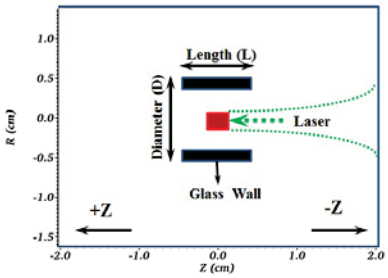

Fig. 1 Simulation domain showing the laser beam focussed at the centre of the confining tube

A 10 ns laser pulse at second harmonic of Nd-YAG (532 nm) of different energies 50, 200 and 400 mJ is focused to a spot size of 500 µm, at the center of the glass tube. The length of the confining glass tube is considered to be 12 mm and the separation between them is taken as 8 mm, respectively. The hydrodynamic phenomena of the laser generated plasma and shock wave, interaction of shock wave with the solid walls, and the interaction of reflected shock with the plasma core (PC) generated at the focal volume, is studied using the conservative equations of mass, momentum and energy (eq. 1 – eq. 5). The simulations were performed using FLASH 2D radiation hydrodynamic code [22].

$$\frac{\partial \rho}{\partial t} + \vec{\nabla}.(\rho\vec{v}) = 0\,, \tag{1}$$

$$\frac{\partial(\rho\vec{v})}{\partial t} + \vec{\nabla}.(\rho\vec{v}\vec{v}) + \nabla P_{tot} = 0, \tag{2}$$

$$\frac{\partial E_{tot}}{\partial t} + \vec{\nabla}.[(\rho E_{tot} + P_{tot})\vec{v}] = Q_{las} - \nabla q, \tag{3}$$

$$P_{tot} = P_{ele} + P_{ion} \tag{4}$$

$$E_{tot} = E_{ele} + E_{ion} + \frac{1}{2}\vec{v}.\vec{v} \tag{5}$$

Here, ρ is the total mass density, $\boldsymbol{v}$ is the average fluid velocity, P_{tot} and E_{tot} are the total pressure and total specific energy which are the sum of electron, ion pressures, respectively given in equations (4) – (5). Q_{las} is the energy due to laser heating. The Harten-Lax-van Leer-Contact (HLLC) scheme [23] is used to determine the inter cell fluxes. To close the above equations (1) – (3), the multi-temperature gamma equation-of-state (EOS) for air is considered [24]. The EOS of glass is generated using IONMIX code [25]**.** An adaptive mesh refinement method is used to discretize the domain. Solving the above equations, the temporal evolution of plasma parameters and SW dynamics were studied.

Results and Discussions: The plasma generated at the center of the glass tube expands freely into the surrounding medium, until the SW encounters the boundaries of the confining tube. When the SW interacts the glass boundaries, it is reflected back after few hundreds of nanoseconds and travel towards the plasma core (PC). The SW interacting with the PC compresses the PC along radial direction leading to expansion of plasma along axial (laser propagation axis). The compression of the PC along radial direction leads to a raise in temperature and number density at the PC. Depending on the energy of the incident laser beam, a quick or delayed reflection the SW [1, 2] is observed. A SW generated from 50 mJ reaches the glass wall at 4.5 µs and that in the case of 400 mJ reaches at 1.8 µs. Figure. 2 (a & b) compare the laser induced air plasma expanding freely in ambient air with that of the confined air plasma generated in a tube for 50 mJ laser energy**.** The effect

of the interaction of SW with PC is clearly seen in Fig.2 (a & b). The temporal evolution of plasma temperature is shown in Fig. 2(a) and number density in Fig. 2(b).

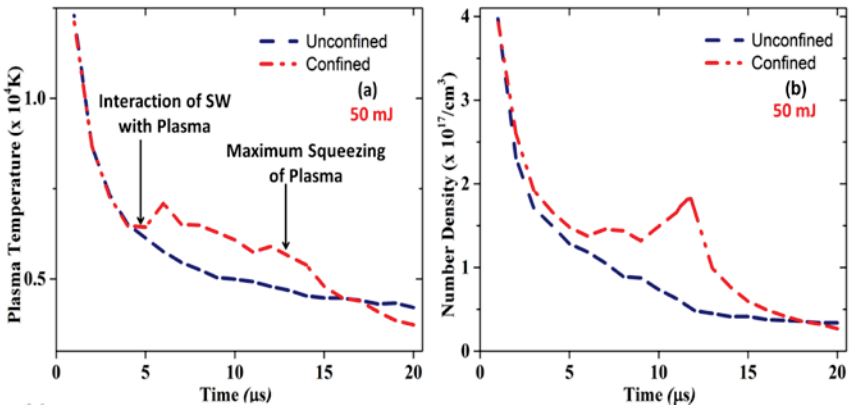

Fig. 2 A comparison of temporal evolution of (a) electron temperature and (b) number density in confined and unconfined geometry along radial direction for an input laser energy of 50 mJ

It is clearly observed from fig.2 (a) that until 5 μs the evolution of temperature is similar in both the confined and unconfined geometries. However, after 5 μs due to the interaction of the reflected SW with the PC a sudden raise in plasma temperature is observed. A similar increment is also observed at 13 μs where the reflected SW is reaching the center of the PC resulting in maximum squeezing of the PC. Later, the temperature of the PC has decreased below the value of the free expansion because of the rapid expansion of the PC (rarefaction). The number density of the plasma is maximum at the time of maximum squeezing of the plasma core. Hence it is observed that the plasma temperature has increased by a factor of 1.16 and number density by a factor of 3.60. The enhancement in the plasma temperature is observed to be increasing with increasing input laser energy. Table. 1 shows the enhancement factor in plasma temeprature and number density with varying input laser energies.

Input Laser Energy (mJ)	Time of maximum enhancement (μs)	Enhancement Factor in T_e	Time of maximum enhancement (μs)	Enhancement Factor in N_e
50	13	1.16	14	3.60
200	10	1.66	10	1.77
400	10	1.91	9	1.92

Table.1 Enhancement in the plasma parameters showing the time where a maximum enhancement and enhancement factor is achieved when compared to their corresponding free expansion

From Table. 1 it can be understood that the enehancement in plasma temeparture has increased with the increase in the input laser energy. The maximum enhancement factor of T_e is observed to be 1.16, 1.66 and 1.91 for the laser energies of 50, 200 and 400 mJ, respectively at 13, 10 and 10 μs from t=0. The time of maximum squeezing is delayed for lower energy because of the less initial velocity of SW when compared to higher energy SW evolution. However, the enhancement in number density is observed to decrease with the increasing laser energy from 50 mJ to 200 mJ and slightly increased from 200 mJ to 400 mJ. A similar trend in electron temperature and number density is proposed by Hayat et. al [19] where lateral confinement of laser ablative plasma from a Magnesium target is presented for different fluences and by Atiqa et.al.[26] where magnetic confinement of the laser ablative plasma from a graphite target is discussed.

A raise in laser energy leads to an increment in the pressure of the SW. However, the increment in shock pressure along radial direction is not much significant when compared to that of along the axial direction. This is because of more energy deposition taking place along the laser propagation direction, leading to an asymmetric expansion of plasma and SW. By the time of the SW interaction with the PC, the pressure at the PC almost reaches the ambient atmosperic pressure. Hence, a slight compression by SW is leading to a maximum enhancement in number density. The pressure gradient between the reflected SW and PC in case of 200 mJ is not much prominent and hence enhancement in the number density due to SW compression is less when compared to 50 mJ. However, in case of 400 mJ the SW is interacting with the PC at 4 μs, the density at the SF is more due to the interaction at the early timescales, the density gradient between SF and PC were little high leading to an effective raise.

Conclusion: The effect of geometric confinement of laser generated air plasma under different input laser eneergies is presented. The reflected SW interacting with PC is observed to enhance the plasma number density, temperature and the life time. It is observed that an increase in input laser energy is enhancing the increment of plasma parametes due to compression of PC along radial direction.

Acknowledgement: Authors thank DRDO for financial support.

References:

1. S. Sai Shiva, et al., *Physics of Plasmas,* **24**, 083110 (2017).
2. S. Sai Shiva, et al., *Physics of Plasmas,* **26**, 072108 (2019).
3. C. Leela, et al., *Laser and Particle Beams,* **31**, 263-272 (2013).
4. W.A. Hollingsworth, *British Aeronaut. Research Council Rept. 17,985,* (1955).
5. S. Zhang, Y.-T. Zhang, and C.-W. Shu, *Physics of Fluids,* **17**, 116101 (2005).
6. B.W. Skews, M.D. Atkins, and M.W. Seitz, *Journal of Fluid Mechanics,* **253**, 245 (1993).
7. D. Jang, et al., *Journal of Applied Physics,* **106**, 014913 (2009).
8. P. Yeates and E.T. Kennedy, *Journal of Applied Physics,* **110**, 063303 (2011).
9. K. Choudhury, et al., *Physics of Plasmas,* **23**, 042108 (2016).
10. F. Huang, et al., *Physics of Plasmas,* **22**, 063509 (2015).
11. X.K. Shen, et al., *Journal of Applied Physics,* **102**, 093301 (2007).
12. Q. Wang, et al., *Physics of Plasmas,* **25**, 073301 (2018).
13. L.B. Guo, et al., *Optics Express,* **19**, 14067-14075 (2011).
14. Z. Hou, et al., *Optics Express,* **21**, 15974-15979 (2013).
15. L. Xiongwei, et al., *Journal of Analytical Atomic Spectrometry,* **29**, 2127-2135 (2014).
16. X. Gao, et al., *Journal of Physics D: Applied Physics,* **48**, 175205 (2015).
17. X. Li, et al., *Journal of Physics D: Applied Physics,* **50**, 015203 (2017).
18. Y. Fu, Z. Hou, and Z. Wang, *Optics Express,* **24**, 3055-3066 (2016).
19. A. Hayat, et al., *Applied Physics A,* **123**, 505 (2017).
20. S. Tao and B. Wu, *Applied Physics B,* **113**, 251-258 (2013).
21. A. Popov, F. Colao, and R. Fantoni, *Journal of Analytical Atomic Spectrometry - J ANAL ATOM SPECTROM,* **24** (2009).
22. B. Fryxell, et al., *The Astrophysical Journal Supplement Series,* **131**, 273-334 (2000).
23. E.F. Toro, *Riemann Solvers and Numerical Methods for Fluid Dynamics: A Practical Introduction*. 2009: Springer Berlin Heidelberg.
24. C. DeMichelis, *IEEE Journal of Quantum Electronics,* **5**, 188-202 (1969).
25. J.J. Macfarlane, *Computer Physics Communications,* **56**, 259-278 (1989).
26. A. Arshad, et al., *Applied Physics B,* **122**, 63 (2016).

Laser-Plasma Accelerated Proton Beam Focussing Optics using High Voltage Pulsed Power Solenoid

M. Tayyab[1], S. Bagchi[1], A. Moorti[1,2] and J. A. Chakera[1,2]
[1]*Advanced Plasma Acceleration Section, Laser Plasma Division, Raja Ramanna Centre for Advanced Technology, Indore – 452 013*
[2]*Homi Bhabha National Institute, Anushakti Nagar, Mumbai – 400 094*

M. L. Sharma[3], K. Aneesh[3] and S. Nigam[3]
[3]*Capillary Discharge XRL Laboratory, High Energy Laser Physics Section, Laser Technology Division, Raja Ramanna Centre for Advanced Technology, Indore – 452 013*
Email: tayyab@rrcat.gov.in

Abstract: The energetic yet diverging proton beam (~ 4 MeV) generated by the interaction of 25 fs, 800 nm Ti: Sapphire laser pulse with thin metallic foil targets has been re-focussed in ambient air at a distance of 1.2 m from its origin. An in-house developed high voltage pulsed power solenoid producing magnetic field of 5.3 T at a current of 7.5 kA over a duration of 50 μs has been used for this purpose. The overall transmission factor of the solenoid has been estimated to be ~30%. The refocussed proton beam could be used for performing experiment on static and time-resolved radiography e.g., of microstructures and dense plasma, and also cell irradiation for biological applications in near future.

In recent times, the interaction of intense, ultra-short femtosecond laser pulses with matter has gained considerable attention owing to its underlying physics as well as potential applications[1]. Such interaction results in formation of high energy charged particles and photons which has opened possibilities in various fields of research and development[2]. In particular, the present report focusses on the potential utilization of laser plasma accelerated proton beams generated from the interaction of such laser pulses with thin metallic foil targets.

When an intense, femtosecond laser pulse interacts with a thin metallic foil target, the high electric field associated with the laser pulse ionizes the foil and releases electrons which further interacts with the laser pulse using various collisional and collective absorption mechanisms resulting in formation of dense plasma. Mechanisms like $J \times$ B acceleration, applicable in case of intense, ultrashort interaction of laser with dense plasma, leads to generation of highly energetic "hot' electrons which leave the foil target due to their inherent high kinetic energy. While these electrons leave, they induce a positive charge on the initially neutral foil target forming a distinct layer of positively and negatively charged surface, conventionally called as "sheath" layer[3], on the target surface. The magnitude of the electric field present in such a sheath layer can momentarily reach up to ~TV/m. With the presence of such high magnitude electric field, the hydro-carbon contaminants normally present on the foil surfaces are field ionized and accelerated to high energies and thereby reducing the potential difference. The accelerating electric field can simply be expressed[4] in the form $E_{accl} = k_B T_e^{hot}/e \,.\max\{\lambda_D,\ L_n\}$ where ($k_B T_e^{hot}$) represents the "hot" electron temperature (in eV) and λ_D is the Debye length of the plasma; L_n is the local plasma scale length and 'e' is the electronic charge. The presence of a local plasma scale length (L_n) can be detrimental for the formation of the accelerating electric field and is therefore avoided. Notably, such an electric field formation occurs both on the front (facing the laser) as well as the rear surface of the foil. However, because of the presence of unwanted pre-pulse in the laser system, the pre-plasma forms on the front surface yielding a considerable local plasma scale-length and thereby, reducing the accelerating electric field magnitude in the front surface[5]. Therefore, most energetic ion emission is observed in

the rear surface of the foil target. This mechanism of accelerating lighter ions is known as "Target Normal sheath acceleration (TNSA)".

Though with the increase of the laser pulse intensity, other mechanisms of ion acceleration also have been identified, but the TNSA mechanism still remains most well studied and consistent acceleration mechanism. However, the lighter ion beams generated by this mechanism still suffers from the following two major drawbacks[6] (i) divergence and (ii) broad, continuous ion energy distribution. Both these drawbacks, considerably hinders application of such beam in practical situations. Evidently, there are two ways to tackle this problem, namely, (a) controlling the laser plasma interaction in such a way that it yields (nearly-) collimated (quasi-) mono-energetic ions beam, else (b) using suitable beam transport system for TNSA accelerated ion beam leading to beam collimation and controllable energy range selection. Although, the first option seems more alluring and has been attempted worldwide with various approaches, but so far has been not very successful. In this manuscript, we have followed the second approach by placing a beam controlling active element[7] in the path of the laser-plasma accelerated ion beam. We demonstrate that the proton beam generated from such an interaction can effectively be refocussed by placing a high pulsed power solenoid[8, 9] placed in the beam path.

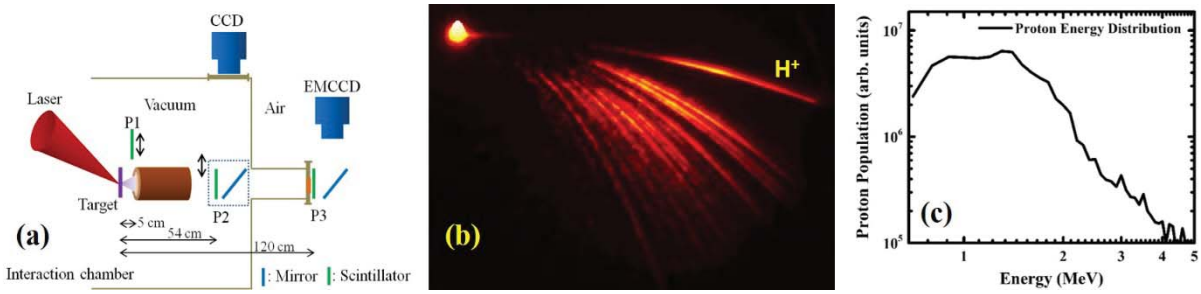

Fig. 1: (a) Schematic diagram of the experimental set up. (b) TNSA accelerated ion emission characteristics as recorded by the Thomson Parabola Ion spectrograph (TPIS), proton (H^+) tracked is marked (c) Proton energy spectra retrieved from (b).

The experiments were performed with 25 fs, 800 nm, 150 TW laser at Laser Plasma Division, RRCAT. The schematic diagram of experimental set up is shown in figure 1(a). The laser beam after the compressor has been guided by dielectric coated turning mirrors to an off axis parabolic mirror (OAPM) having an effective focal length of 300 mm. The OAPM focuses the beam to a focal spot size of 5 µm in diameter resulting in net on target intensity of ~ 1×10^{20} W/cm^2. Aluminium foil of 0.75 µm thickness has been used as the target. The entire experimental assembly including the laser pulse compressor has been evacuated to a base pressure of 5×10^{-5} mbar to avoid any non-linear phenomena during propagation of the laser beam. The final optimization of the laser focusing conditions as well as characterization of ion emission characteristics from the plasma has been performed with a Thomson Parabola Ion spectrograph (TPIS). The TPIS consists of parallel electric and magnetic fields which deviates the incoming ions through a 100 µm diameter pinhole at its entrance to parabolic trajectories based on their charge-to-mass (q / m) ratio. The deflected ions are then detected using a 75 mm diameter Micro-Channel Plate (MCP) detector attached to the TPIS. The ion trajectories formed on the MCP is then imaged by an EMCCD camera to record them in single shot basis. The raw images are then processed with inhouse developed analysis routine to retrieve the ion energy distribution of different charged species. Figure

1(b) shows the typical parabolic trajectories of ions recorded through TPIS. For easy identification, the proton track is marked in the figure. Figure 1(c) displays the proton energy distribution derived from figure 1(b). Proton energies up to 4 MeV can be unambiguously observed in the figure.

Once the interaction of the laser pulse with the foil target is optimized, the TPIS is then replaced by a scintillator screen to monitor the beam profile on a single shot basis. An inhouse developed pulse power solenoid is then placed in the proton / ion beam path at a distance of 50 mm from the foil. The solenoid consists of 88 single turns of SWG-16 grade enamelled copper wire wound over 35 mm diameter, 150 mm long bobbin offering net inductance of 65 μH. A pulse power supply based on capacitive discharge scheme has been made to drive the solenoid with currents up to 8 kA. The capacitor bank of the power supply offering net capacitance of 200 μF / 10 kV is charged using a doubler-circuit connected to a 4.5 kV, 50 Hz transformer. An externally controllable triggered spark-gap initiates current through the coil. A Rogowski coil is also incorporated to get current pulse signal which is calibrated using PEM make CWT-60 standard coil. Online monitoring of resultant magnetic field was performed using DTM-141 Digital Teslameter. The solenoid characteristics were studied offline before using it in the experiments. Typical profile of the current passing through the solenoid and the resultant magnetic field is shown in figure 2(a). The solenoid was operated in sync with the laser operation to ensure that the ion beam passes through it during the time duration marked by the vertical dashed lines in figure 2(a). The linearity of the solenoid functioning with increasing current values are depicted in figure 2(b).

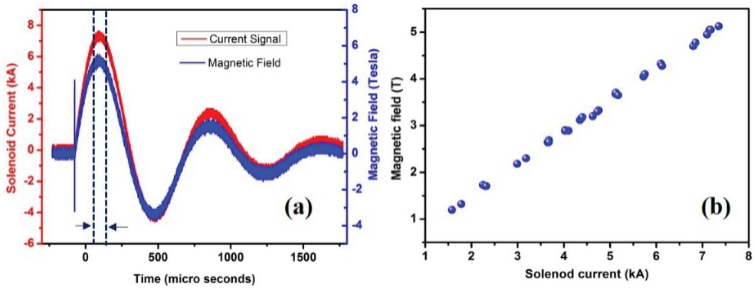

Fig. 2: (a) Typical waveforms of current passing through the solenoid and corresponding magnetic field recorded during the experiment. The 'time' region marked by two vertical dotted lines near the first peak refers to the passage time of protons through the solenoid. (b) Linearity of the resultant magnetic field of the solenoid with increasing driver current.

To verify the effect of the solenoid on the proton / ion beam, it is important to monitor the beam profile. This has been performed with scintillator screen placed at different positions (P1, P2, P3) as shown in the figure 1(a). The screen was imaged by a 14-bit CCD camera to monitor the beam profile for every single laser exposure. Figure 3(a) shows the proton beam profile at the input the solenoid (using P1) i.e., at a distance 50 mm from the target foil plasma. The diverging nature of the proton beam is evident in the beginning. While figure, 3(b) displays the re-focussed proton beam profile recorded at a distance 1.2 m away from the plasma (using P3). The difference in size is evident and clearly identifies the role of pulsed solenoid on the proton beam. Suitable metallic filters were used to ensure that only the protons having energies > 4 MeV will reach the scintillator screen. Notably, when the solenoid was not powered, no scintillation was recorded as the net flux on the scintillator would have too small due to its inherent divergence. Though the scintillator provided information

about the proton beam profile, however, for the quantification of the number of protons reaching the scintillator, CR-39 sheets were placed at its place. After suitable post-processing of the exposed CR-39 sheets, around 10^{7-8} protons for every laser shot were estimated to enter the solenoid with an overall transmission factor of ~30%.

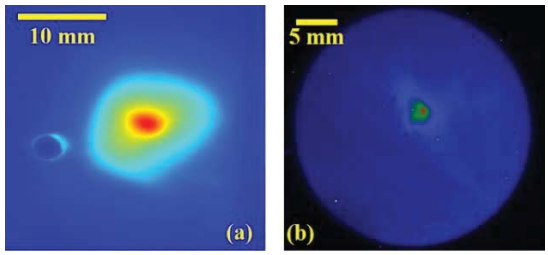

Fig. 3: Proton beam profile (a) before the solenoid and (b) in ambient air at a distance 1.2 m from the target foil.

In summary, we have demonstrated control and refocussing of laser-plasma accelerated proton beam by an inhouse developed high pulsed power solenoid. The use of solenoid shows that the by judicious choice of its operating parameters, protons having relatively small energy variation can be focussed at different distances which open us possibilities of sing such short pulse proton beam in reality. In near future, we plan to use such beam to radiography of dense plasma as well as applications related to irradiation of biological cells[10] and tissues.

Acknowledgement: The authors (MT and SB) acknowledge help from Shri R. A. Khan, Shri Ankit and Shri S. Meena for their help in laser operations, Shri K. Meena, Shri S. Sebastian, Shri K. C. Parmar and Shri R. P. Kushwaha for their help in providing mechanical jobs related support during the experiment. The authors (MT and SB) also acknowledge help from Shri A. Kumar and Shri S. Das for their help in online calibration of Solenoid Magnetic field.

References:

[1] H. Daido, M. Nishiuchi, and A.S. Pirozhkov, Reports Prog. Phys. **75**, 056401 (2012).
[2] A. Macchi, Rev. Mod. PHYSICS, **85**, 751 (2013).
[3] E. Brambrink, M. Roth, A. Blazevic, and T. Schlegel, Laser Part. Beams **24**, 163 (2006).
[4] S.C. Wilks, A.B. Langdon, T.E. Cowan, M. Roth, M. Singh, S. Hatchett, M.H. Key, D. Pennington, A. MacKinnon, and R.A. Snavely, Phys. Plasmas **8**, 542 (2001).
[5] J. Fuchs, Y. Sentoku, E. Humières, T.E. Cowan, J. Cobble, P. Audebert, A. Kemp, A. Nikroo, P. Antici, E. Brambrink, A. Blazevic, E.M. Campbell, J.C. Fernández, J. Gauthier, M. Geissel, M. Hegelich, S. Karsch, H. Popescu, M. Roth, J. Schreiber, R. Stephens, and H. Pépin, Phys. Plasmas **14**, 053105 (2007).
[6] M. Schollmeier, K. Harres, F. Nürnberg, A. Blaževi, P. Audebert, E. Brambrink, J.C. Fernández, K.A. Flippo, C. Gautier, M. Geißel, B.M. Hegelich, J. Schreiber, M. Roth, M. Schollmeier, K. Harres, F. Nürnberg, A. Blaževi, P. Audebert, and E. Brambrink, Phys. PLASMAS 15, 053101 (2008).
[7] T. Bartal, M.E. Foord, C. Bellei, M.H. Key, K. a. Flippo, S. a. Gaillard, D.T. Offermann, P.K. Patel, L.C. Jarrott, D.P. Higginson, M. Roth, A. Otten, D. Kraus, R.B. Stephens, H.S. McLean, E.M. Giraldez, M.S. Wei, D.C. Gautier, and F.N. Beg, Nat. Phys. **8**, 139 (2012).
[8] V. Kumar, Am. J. Phys. **77**, 737 (2009).
[9] D. Shuman, E. Henestroza, G. Ritchie, W. Waldron, D. Vanacek, and S.S. Yu, Proc. IEEE Part. Accel. Conf. **2005**, 3798 (2005).
[10] J. Bin, K. Allinger, W. Assmann, G. Dollinger, G.A. Drexler, A.A. Friedl, D. Habs, P. Hilz, R. Hoerlein, N. Humble, S. Karsch, K. Khrennikov, D. Kiefer, F. Krausz, W. Ma, D. Michalski, M. Molls, S. Raith, S. Reinhardt, B. Röper, T.E. Schmid, T. Tajima, J. Wenz, O. Zlobinskaya, J. Schreiber, and J.J. Wilkens, Appl. Phys. Lett. **101**, 243701 (2012).

Development of UHV compatible SS 316L-Kovar welding joint using fiber coupled pulsed Nd:YAG laser for accelerator applications

Vijay Bhardwaj*, Pawan Kumar, Prabhat Kumar, Mahendra Kumar Bairwa, Rajpal Singh, B. K. Sindal, D. P. Yadav, B. N. Upadhyaya, K. S. Bindra

Laser Technology Division, Raja Ramanna Centre for Advanced Technology, Indore-452013

*E-mail: vbhardwaj@rrcat.gov.in

Abstract: Dissimilar material joining is a challenging task due to large differences in physical and chemical properties of the materials, which are responsible for high distortion, excessive residual stresses and formation of intermetallic phases leading to deterioration of the weld quality. Laser welding provides accurate solution for joining of dissimilar materials as compared to conventional welding methods due to high power density source and low energy input process. Pulsed Nd:YAG laser system with optimized process parameters has been used to make dissimilar material joint of SS 316L flange to Kovar sleeve of alumina ceramic chamber for fast pulsed magnet in Indus-2. Laser welded joint has successfully achieved the permissible helium leak rate of $<1x10^{-10}$ mbar.l/s for ultra high vacuum applications (UHV).

Introduction:

Dissimilar metal joints are particularly common in components used in power generation[1], chemical, petrochemical, photonics[2], accelerator[3] and nuclear industries[4]. It increases the flexibility in design and production and often results in economic advantageous over the components manufactured from the single material[5]. Expensive materials with specific properties can be used in critical locations with less expensive alloy being used in supporting roles[5]. Despite of all positive impacts of dissimilar joints, there are certain shortcomings of the same i.e., challenges in considering the joining technology arises due to different thermophysical properties of the two dissimilar materials, which have considerable effect on joining process as well as on weld properties[6]. As far as thermal joining process is concerned for dissimilar joints, there are several challenges related to the material properties[5,6], namely: 1) different coefficient of thermal expansion resulting in large distortion and residual stresses, 2) widely different thermal conductivity resulting in uneven heat dissipation responsible for asymmetric weld bead formation or incomplete fusion, 3) large difference in melting temperature i.e., melting point of one material in close proximity to the boiling temperature of the second material may cause unwanted weld quality, and 4) limited solubility of the two joining materials in each other resulting in formation of intermetallic phases in the weld zone, which are generally brittle in nature causing inadequate weld properties. Above mentioned effects resulting from different material properties are strongly related to the weld heat input and tend to be more detrimental in case of high heat input. Thus, weld quality of dissimilar joint may be assured by controlling heat input or by limiting it[6]. As compared to conventional welding technologies, laser welding technology is the best solution for dissimilar weld joint due to accurate control of heat input. High power density of focused laser beam can melt all the engineering materials and provides better solution for welding of dissimilar materials having large difference in thermal conductivity[5]. The low energy input in laser welding process reduces the size of heat affected zone (HAZ) resulting in reduction of residual stresses[6]. Precise control over the location and energy of the laser beam on weld interface can be used to control the fusion ratio in the case of welding of dissimilar materials of large melting temperature difference[5]. The problem of intermetallic phase formation may be avoided by using low input laser energy resulting in rapid

solidification with high heating and cooling rate giving limited time to phase formation responsible for weld failure in service[1]. Finally, we can summarize that laser welding technology is a better option for dissimilar material joining as compared to conventional welding methods. Further, in laser welding technology for dissimilar joints, pulsed laser welding is a better choice as compared to CW laser welding due to low heat input requirement to achieve the same penetration depth[7]. Dissimilar metal joint of SS316L to Kovar is widely used in accelerator applications[8]. Kovar is an iron-nickel- cobalt base alloy having thermal expansion coefficient close to glass & ceramic, thus finds application in metal to glass/ceramic joint and acts as an intermediate between the same[1]. In this paper, we report on the successful development of pulsed laser welding process of SS316L flange to Kovar sleeve joint of alumina ceramic UHV chamber for fast pulsed magnet called pinger magnet to be used in Indus-2 synchrotron radiation source (SRS).

Experimental setup details:

An in-house developed fiber coupled pulsed Nd:YAG laser system with 250 W average power, 5 kW maximum peak power, 2-20 ms pulse duration, and 1-100 Hz repetition rate has been used for laser welding of SS316L and kovar . Laser beam has been delivered through a 600 μm core diameter and 0.22 numerical aperture (NA) silica-silica fiber. At the exit fiber end, laser beam has been focused to a diameter of 1.2 mm using 1:2 lens imaging configuration. Figure 1(a) shows the experimental setup for laser welding of SS316L flange with Kovar sleeve of alumina ceramic chamber. It comprises of CNC gantry stage used to trace the desired weld path, a compact laser welding nozzle having provision to purge argon inert gas at the weld interface coaxially with the laser beam. Figure 1(b) shows the weld joint configuration comprises of location of SS 316L flange joint with Kovar end sleeve and location of braze joint of alumina ceramic chamber with kovar sleeve. Alumina ceramic chamber of height 330 mm is kept stationary at the gantry stage and nozzle is forced to move in a circular path of diameter 128 mm i.e., weld center of SS 316L and Kovar joint of thickness 0.5 mm as shown in figure 1(b). Before proceeding to actual welding, a guiding red beam of He-Ne laser is used to trace the circular weld profile with the help of CNC gantry stage and it is ensured that red poining beam maintains its position throughout the track i.e., laser beam center must align with the weld center. Table 1 shows the chemical composition of SS316L and Kovar.

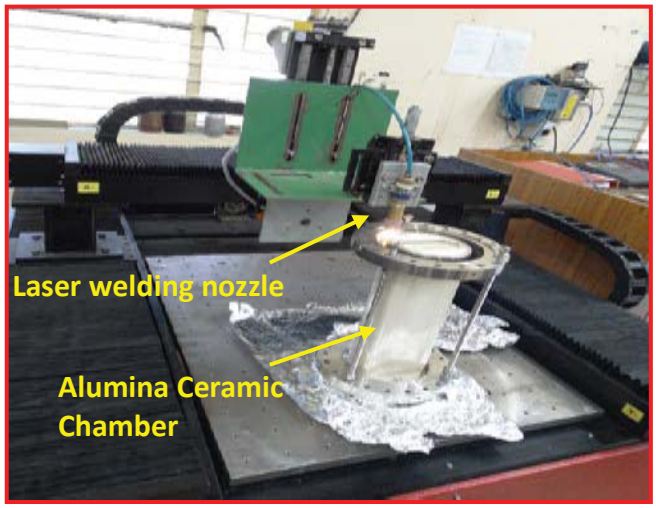

Figure 1(a): Experimental setup for laser welding of SS 316L flange with Kovar sleeve of alumina ceramic chamber.

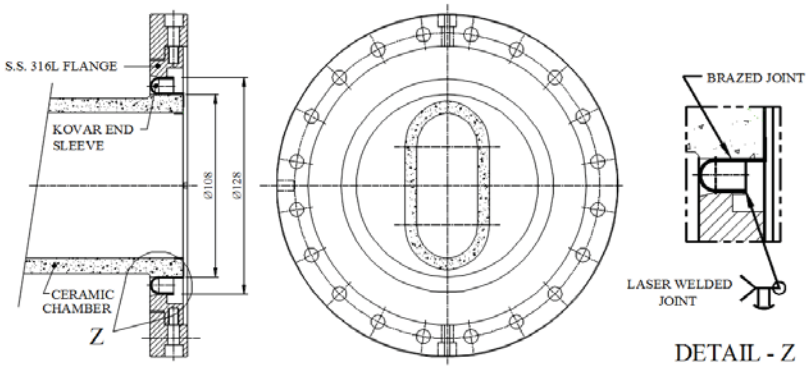

Figure1 (b): Detail drawing of weld joint configuration

Table-1: Chemical composition of SS316L and kovar

Alloy	Fe	Cr	Ni	Co	Mn	Si	Mo	P	S	Ti	Cu
SS 316L	Balance	16.33	10.01	-	1.65	0.70	2.07	0.03	0.02	0.02	0.12
Kovar	Balance	-	29.71	17.01	0.35	0.54	0.01	-	-	0.04	0.07

Results and Discussion:

Ultra-high vacuum compatible alumina ceramic chamber is required to be used for fast pulsed magnet called pinger magnet in Indus-2 SRS to mitigate the eddy current issues. This chamber contains helium leak tight SS316L flange to Kovar sleeve welded joint. Helium leak rate $<1x10^{-10}$ mbar.l/s is desired for its UHV compatibility. It is required to carry out autogenous weld with minimum heat input to avoid any damage to nearby alumina to Kovar brazed joint. The pulsed Nd:YAG laser welding process is suitable for this dissimilar joint application as discussed earlier. Two pass welding mode has been opted to ensure helium leak tightness of the order of $<1x10^{-10}$ mbar.l/s. In the first pass, high pulse energy is used to get weld penetration up to 0.5 mm (thickness of weld joint) and in the second pass low pulse energy laser beam is used to smoothen the weld bead. Smoothening pass is mandatory to ensure helium leak tightness as in this pass weld bead roughness is minimized and undulations in the first pass get re-melted to fill any cracks/porosities. The Laser welding process has been developed successfully and laser welding of one such chamber was performed successfully with helium leak rate of $<1x10^{-10}$ mbar.l/s. Table-2 shows the optimized process parameters used for successful development of the weld joint. Figure 2 shows a close view of the weld bead of SS 316L flange weld joint with Kovar sleeve of alumina ceramic chamber. Figure 3(a) shows the microscopic cross-section of SS 316L weld joint with Kovar. Figure 3(b) show the magnified view of the same, it can be observed that no cracks/porosities occur in the weld joint and a reinforcement of Δy=0.35 mm was achieved, which will helps to make this joint ultra-high vacuum compatible.

Table-2: Laser process parameters.

Optimized process parameters	Laser pulse energy (J)	Pulse width (ms)	Pulse frequency (Hz)	Argon gas pressure (kg/cm^2)	Weld speed (mm/min)
1st Pass	40	20	4	2	60
2nd Pass	20	20	6	2	90

Figure 2: Close view of weld bead of SS 316L flange joint with Kovar sleeve

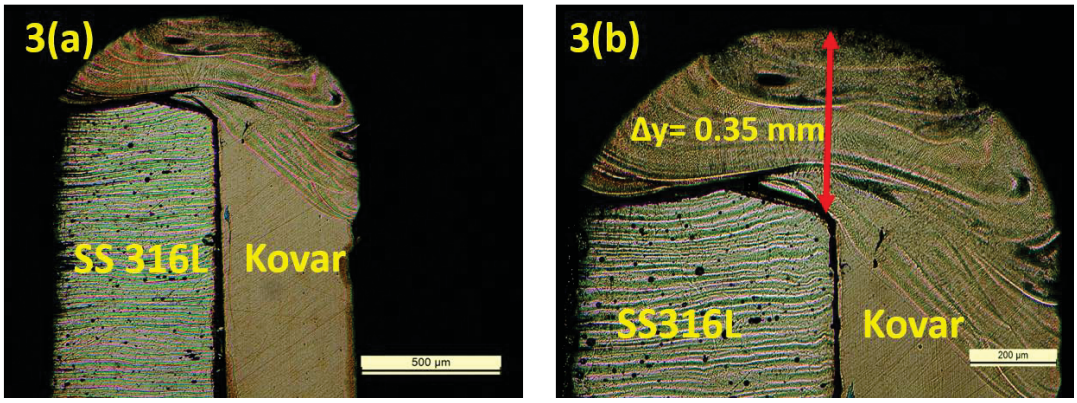

Figure 3: a) Weld joint cross-section under optical microscope, and b) magnified view of weld joint under optical microscope.

Conclusion: In conclusion, pulsed Nd:YAG laser welding of SS316L flange with Kovar sleeve of alumina ceramic chamber has been carried out successfully without damaging the brazed joint of alumina and Kovar on the other side of the chamber. Laser process parameters were optimized for good quality welding of dissimilar materials SS316L and Kovar and helium leak rate of $<1x10^{-10}$ mbar.l/s was achieved, which is good enough for ultra-high vacuum applications.

References

1. H. A. Ardakani and H. N. Moosavy, *Optics and Laser Technology*, **115**, 62 (2019).
2. M. M. A. Fadhali, Saktioto, J. Zainal, Y. Munajat, A. Jalil, and R. Rahman, *AIP Conference Proceedings*, **1217**, 147 (2010).
3. Y. Saito, M. Kinsho and Z. Kabeya, *Journal of physics: conference series*, **100**, 1(2008).
4. A. Murgan, R. S. Santosh, R. Raju, A. K. Lakshminarayanan and S. K. Albert, *Advance Engineering Forum,* **24,** 40(2017).
5. Z. Sun and J. C. Ion, *Journal of Material Science*, **30**, 4205(1995).
6. S. Katayama, *Handbook of Laser Welding Technologies*, 2013.
7. E. Assuncao and S. Williams, *Optics and Laser in Engineering Technology*, **51**, 674 (2013).
8. D. P. Yadav, K. C. Ratankala and S. K. Shukla, *InPAC,* 2011.

Development of 0.9 J pulse energy microsecond pulse Nd:YAG laser and its application to cutting of MEMS devices from ceramic substrate

Vijay Shukla[1*], Bhaskar Paul[1], M. K. Bairwa[1], V. Bhardwaj[1], Rajpal Singh[1], Dipen Vachhani[3], Rahul Shukla[2,4], K. K. Pant[3], C. B. Panwar[3], D. Narwat[3], R. Arya[3], B. N. Upadhyaya[1,4] and K. S. Bindra[1,4]

[1]*Laser Technology Division, Raja Ramanna Centre for Advanced Technology, Indore-452013, INDIA*
[2]*Synchrotrons Utilization Section, Raja Ramanna Centre for Advanced Technology, Indore-452013, INDIA*
[3]*Laser Electronics Division, Raja Ramanna Centre for Advanced Technology, Indore-452013, INDIA*
[4]*Homi Bhabha National Institute, Training School Complex, Anushaktinagar, Mumbai-400094, INDIA*
*E-mail: shuklavs@rrcat.gov.in

Abstract: In this paper, we report on the development and characterization of a flash lamp pumped, optical fiber coupled microsecond pulse Nd:YAG laser. The laser provides a maximum pulse energy of 0.9 J at 62 μs pulse duration and pulse frequency can be varied in the range of 1-20 Hz. Laser beam has been delivered through an optical fiber of 200 μm core diameter and 0.22 numerical aperture with 90% transmission efficiency. This laser has been used for evaporative cutting of 600 μm thick alumina wafer (100 mm x 100 mm) on which MEMS device was fabricated by UV-SLIGA technique. Evaporative cutting technique has been used to avoid damage to MEMS structure as the sample can't sustain high pressure gas for removal of material as used in normal melt cutting process. The cutting parameters were optimized and MEMS device having minimum features of 20 μm (both moving and stationary) was removed successfully without any damage.

Introduction: Miniaturization is an important trend in many modern technologies. Micromachining of materials with micron resolution at high speed is a widespread technology used in several industries. Micromachining is utilized in manufacturing of high-tech microproducts for biotechnological, microelectronics, telecommunication, MEMS, and medical applications. A variety of ceramic materials such as zirconium and aluminum carbide are widely used in the field of microelectronics and in other MEMS-type devices. The test devices for integrated circuits, substrates for sensors and detectors, microcavity structures inside biomedical or chemical diagnostics, and transducers are possible applications. Alumina ceramic is widely used in the fields of integrated circuit chip substrate and packaging materials because of its good thermal conductivity, dielectric properties, and mechanical strength. However, high hardness and brittleness of alumina ceramic materials due to chemical bonding, including the ionic bond and covalent bond, make the traditional processing usually difficult. In this case, laser cutting is obviously advantageous due to its noncontact nature, flexibility, high efficiency, minimum heat affected zone, and easy control on laser output[1]. Laser power density, pulse energy and pulse duration are important parameters for laser material processing. Lasers widely used for material processing are CO_2 laser, eximer laser, Nd:YAG laser, and fiber laser. Nd:YAG lasers operating at 1.064 μm offer the advantage of compactness and beam delivery through an optical fiber. Absorption of most of the materials at Nd:YAG laser wavelength is much larger than that at CO_2 laser wavelength. The Nd:YAG lasers can be pumped by flash lamp, arc lamp or laser diode. The flash lamp or arc lamp is much more rugged and cost effective than diode pumped lasers in industrial environments.

Pulsed lasers are preferred for machining of ceramics due to better and more effective control of heat input as compared to continuous wave mode. Laser cutting of ceramics depend on laser wavelength, laser pulse duration

and the absorptivity characteristics of ceramic being machined. Thermal conductivity of structural ceramics is generally poor as compared to metals. Laser machining of ceramics is difficult due to large scattering that appears for many common laser wavelengths, which restricts localized energy absorption. For various ceramic materials, the physical processes governing material removal are varied depending on their thermal properties. Pulsed mode (PM) lasers are therefore more suitable for ceramic cutting due to the significant reduction in heat accumulation[2,3]. Studies have been carried out to demonstrate cutting of ceramics with millisecond[4], nanosecond[5], picosecond, and femtosecond lasers[6]. Nedialkov et al., 2003, studied laser ablation of alumina, aluminum nitride, and silicon nitride using nanosecond pulse Nd:YAG laser with different wavelengths[8]. Liu et al. have studied ultrafast structuring of ceramics using femtosecond laser, whereas Karnakis et al. have used nanosecond copper vapor laser (511 nm) and picosecond Nd:YVO_4 laser to drill holes in ceramic materials[9,10]. Depth of cutting is very low in case of cutting with ns, ps or fs pulse lasers due to lower pulse energy. Although milisecond pulse Nd:YAG lasers provide better material removal rate, but it also requires flow of assist gas at higher pressure to remove molten material. As high assist gas pressure results in shock to the sample, it may damage moving and stationary parts of MEMS structure. Thus, instead of melting and removing the material, evaporative cutting technique has been adopted using high energy microsecond pulse Nd:YAG laser to achieve larger depth of cutting.

Experimental details: Figure 1 shows schematic of microsecond pulse Nd:YAG laser. The laser pump chamber consists of a 6 mm diameter and 100 mm long 1.1% atomic Nd^{3+}-doped Nd:YAG rod. It also contains two 6 mm bore diameter flash lamps placed in a double elliptical gold coated reflector. Both the ends of the Nd:YAG rod are plane-parallel to each other and are anti reflection (AR) coated at 1064 nm wavelength. The laser pump chamber made of SS316L has been placed in a hemispherical resonator as shown in Fig. 1. A closed-loop deionized water chiller at 20°C has been used to remove heat load from pump chamber. Hemispherical stable resonator was designed to provide better misalignment sensitivity and pulse to pulse stability for whole range of pump operation as compared to other resonator configurations. Laser resonator consists of an 8 m ROC concave high reflectivity mirror M1 (R~99.5%) and a plane output coupler mirror M2 of reflectivity 40%. Mirror M1 is placed at a distance of d_1=53 cm from principal plane of the rod and mirror M2 is placed at a distance of d_2=15.7 cm from principal plane of the rod for full range of pump power stability of the resonator.

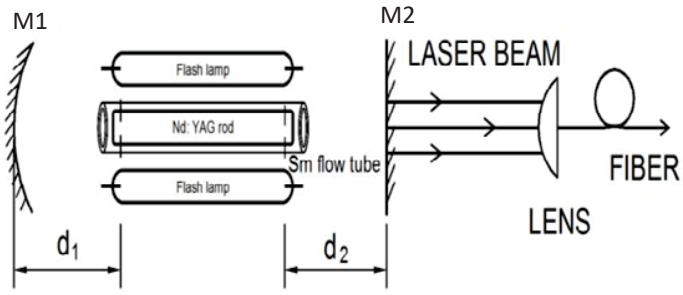

Fig. 1: A schematic of hemispherical resonator with dual flashlamp pumped Nd:YAG rod.

The optical pulse from flashlamp, output laser pulse temporal profile and output average power have been recorded with variation in input pump voltage. Output laser pulse was monitored using fast photodiode make Thorlabs (DET100A). For laser material processing experiments, output laser beam was coupled through an optical fiber of 200 µm core diameter using a plano-convex lens of 30 mm focal length. The output from the optical fiber was focused on the job using a focusing objective. The focusing geometry consists of a plano-convex fused silica collimating lens having a focal length of 40 mm and a plano-convex focusing lens of 40 mm focal length, which are mounted in a focusing objective. A 1:1 imaging ratio results in a focal spot of size 200 µm. Focus position was kept ~2 mm away from the tip of focusing nozzle.

Results: Figure 2 shows the temporal profile of the flash lamp pulse (red colour) and laser pulse (blue colour) at 1200 V. There is a delay in start of laser pulse and flash lamp pump pulse due to required threshold for pulse build-up. Figure 3 shows variation in average output power as a function of pump input voltage at different repetition rates of 1, 5, 10 and 20 Hz. It is observed that the output power varies linearly with input voltage. At the maximum input voltage of 1200 V and 20 Hz of repetition rate, the maximum average output power of 18.2 W was achieved. With increase in input voltage from 500 V to 1200 V, variation in pulse duration from 72 to 62 µs was observed. This may be due to the fact that as the photon number density in the upper level is more, pulse build up time is shorter. It is to be noted that in our case the flash lamp pump pulse duration is around 70 µs, which is much shorter than the spontaneous emission lifetime of Nd:YAG (230 µs).

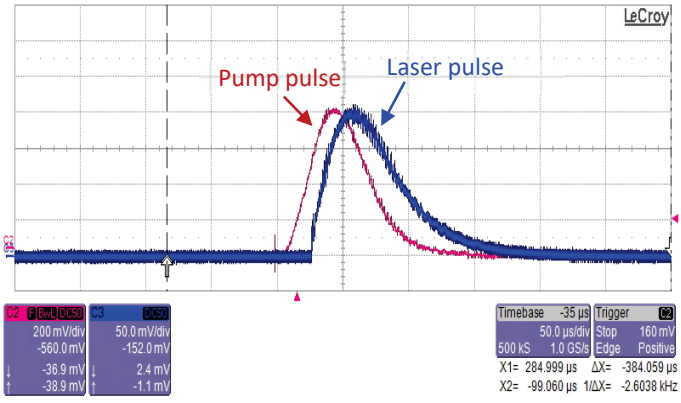

Fig. 2: Temporal profile of flash lamp pulse (red colour) and laser output pulse (blue colour).

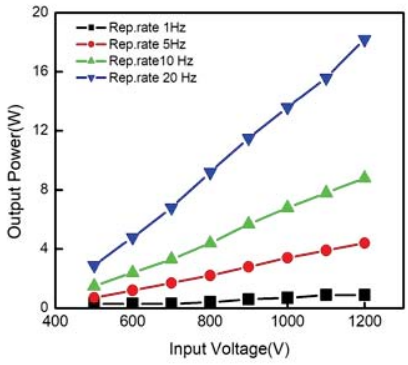

Fig. 3: Variation of average output power as a function of input voltage at different repetition rates.

Laser parameters such as laser pulse energy, cutting speed and repetition rate were optimized for ablation cutting of ceramic substrate having MEMS devices. Six numbers of MEMS devices of size (15 mm x10 mm) and two numbers of (20 mm x15 mm) were cut out from ceramic substrate of size 60 mm x 60 mm. Table-1 shows optimized laser cutting parameters. MEMS were characterized after cutting to confirm that there is no damage to the structure during cutting process. In a single pass 200 µm of material was evaporated and it

required three laser passes to cut full depth of 600 µm. Figure 4 shows laser cutting nozzle used for cutting of alumina substrate. Figure 5 shows alumina substrate with MEMS devices cut out from the substrate and Fig. 6 shows cut kerf on alumina substrate. A cut kerf of 440 µm was measured with ejection of material on the edges of the cut surface.

Table- 1: Laser cutting process parameters for 600 µm thick Alumina ceramic substrate.

Description	Cutting passes	Thickness	Laser cutting speed	Laser process parameters		
				Pulse energy	Pulse duration	Frequency
Alumina substrate	Three	600 µm	15 mm/min	450 mJ	62 µs	20 Hz

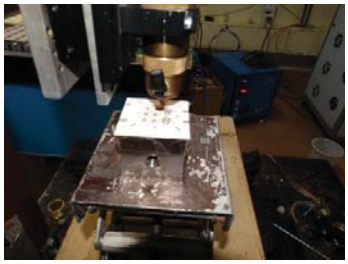

Fig. 4: Laser cutting nozzle.

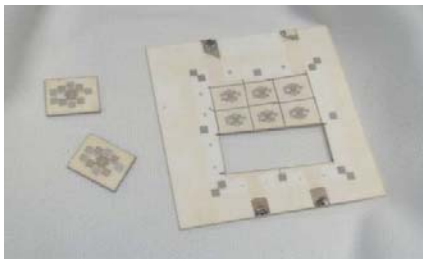

Fig. 5: MEMS devices cut from alumina substrate.

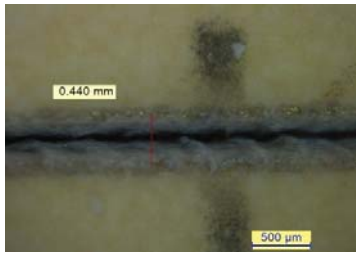

Fig. 6: Cut kerf on alumina substrate.

Conclusion: In conclusion, we have developed a microsecond pulse Nd:YAG laser for evaporative cutting of ceramic substrates. A maximum pulse energy of 0.9 J, pulse duration of 62 µs, maximum average power of 18.2 W and maximum peak power of 14.5 kW has been achieved. This laser has been successfully utilized for laser micromachining of 600 µm thick alumina ceramic substrate to cut out MEMS devices fabricated using UV-SLIGA technique. A total of eight MEMS devices were cut out from ceramic substrate without any damage to MEMS.

References:

1. A. N. Samant and N. B. Dahotre, J. Eur. Ceram. Soc. 29, 969–993 (2009).
2. C. Durand et al., International Journal of Product Res. 34(5) (1996) 1417-1428
3. X. Chen, X. Liu, Journal of Laser Applications 11(6) (1999) 268-272
4. F. Quintero et al., Proceedings of SPIE 4419 (2001) 756-760
5. M.R.H. Knowles et al., International Journal of Advanced Manufacturing Technology 33 (2007) 95-102 References 229
6. D. M. Karnakis et al., Proceedings of the Fourth International WLT – Conference on Lasers in Manufacturing, Munich (2007)
7. X.C. Wang et al., Optics and Lasers in Engineering 48 (2010) 657-663
8. N. N. Nedialkov, et al., XIV International Symposium on Gas Flow, Chemical Lasers, and High-Power Lasers, vol. 5120 of Proceedings of SPIE, pp. 703–708, November 2003.
9. D. Karnakis et al., 5th Photon Processing in Microelectronics and Photonics, vol. 6106 of Proceedings of SPIE, San Jose, Calif, USA, March 2006.
10. D. Liu et al., Proceedings of the 26th International Congress on Applications of Lasers and Electro-Optics (ICALEO ’07), pp. 12–18, November 2007.

Theoretical Estimation of Isotopic Concentration of Yb-176 Produced through Three-Step Resonant Photoionization Method

Biswajit Jana and Biswaranjan Dikshit

ATLA Facility, BTD Group, Bhabha Atomic Research Centre, Mumbai-85, India.

Email: biswajit@barc.gov.in

Abstract

Highly enriched Ytterbium 176 (Yb^{176}) isotope is used to produce Lutetium 177 (Lu^{177}) radioisotope which has a potential application in cancer treatments. The Yb^{176} isotopic enrichment is achieved by Atomic Vapor Laser Isotope Separation (AVLIS) method. The targeted Yb^{176} isotope is selectively excited and ionized through three-step resonant photoionization method. In this paper, the ionization yield of the process is estimated using rate equation approach. From the spectral overlap of between laser profile and absorption profile of the transition in both first step and second step, the isotopic composition of Yb photoions is calculated in the laser-atom interaction volume. The variations of Yb^{176} photoion concentration with laser line-width and absorption line-width are studied to get the good selectivity of the scheme.

1.0 Introduction

Today the Lu^{177} radionuclide attracts a considerable attention for its use as Lu^{177} labeled radiopharmaceuticals in targeted radionuclide therapy for cancer treatments. It is produced by neutron irradiation [1] of either Lu^{176} in direct route through reaction of Lu^{176} (n, γ) Lu^{177} or Yb^{176} in indirect route via Yb^{176} (n, γ) Yb^{177}reaction and the product Yb^{177} ($t_{1/2}$ ~1.9 hrs) spontaneously decays to Lu^{177}. In order to get the required specific activity of Lu^{177} in indirect route, the isotopic concentration of Yb^{176} targeted material needs to be enriched more than 97% . The enrichment of Yb^{176} isotope from its natural abundance (i.e 12.88 %) is achieved through Atomic Vapor Laser Isotope Separation (AVLIS) method [2]. The Yb metal evaporates and forms a collimated atomic beam. The particular Yb^{176} isotope is selectively excited and photoionized. The produced photoions are extracted to a desired location with a minimum contamination of the product because of the scattering of undesired isotopes on the product collector plates. Thus the enriched Yb^{176} material is produced. The selective excitation and ionization of targeted isotope is the heart of the above processes. The efficient three step resonant photoionization scheme for Yb was given by Borisov et.al. [3]. Here the selective photoionization of Yb^{176} isotope and the composition of different isotopes in laser-atom interaction volume are studied. The variations of Yb^{176} isotopic concentration with laser line-width and absorption width are carried out.

2.0 Formulation of problem

Figure 1 shows the three-step resonant photoionization scheme of Yb^{176} along with its relevant energy levels and the various processes involved in the photoionization process. Three tunable dye lasers of wavelength λ_1, λ_2 and λ_3 are used in subsequent steps. The Yb^{176} atoms at ground level are resonantly excited to first excited level by λ_1 laser. The excited atoms are again excited by λ_2 laser to a second intermediate excited level and further excited to an autoionization level using λ_3 laser. The atom at autoionization level gets immediately ionized by decaying to the continuum and produces a pair of electron and photoion.

The population of atoms at any level is governed by these three processes like laser induced stimulated emission (ω_i), laser induced absorption (ω_i) and spontaneous emission (A_{ij}). The laser induced excitation (ω_i) rate is decided by the product of transition cross-section (σ_i) and available photon flux (J_i) of the incident laser beam.

At a particular point in the interaction volume, the time dependent populations of different energy levels are governed by the following rate equations 1(a-d).

$$\frac{\partial n_1}{\partial t} = \sigma_1 J_1 \left(-n_1 + n_2 \frac{g_1}{g_2}\right) + A_{21} n_2 \quad (1a)$$

$$\frac{\partial n_2}{\partial t} = \sigma_1 J_1 \left(n_1 - n_2 \frac{g_1}{g_2}\right) - \frac{n_2}{T_2} + A_{32} n_3 + \sigma_2 J_2 \left(-n_2 + n_3 \frac{g_2}{g_3}\right) \quad (1b)$$

$$\frac{\partial n_3}{\partial t} = \sigma_2 J_2 \left(n_2 - n_3 \frac{g_2}{g_3}\right) - \frac{n_3}{T_3} - \sigma_3 J_3 n_3 \quad (1c)$$

$$\frac{\partial n_4}{\partial t} = \sigma_3 J_3 n_3 \quad (1d)$$

The variables n_k and g_k are the normalized population and degeneracy of k^{th} energy level respectively. The A_{mn} is the rate of spontaneous emission from the level 'm' to level 'n', T_2 and T_3 are the radiation life time of atoms at excited level '2' and level '3'. These are coupled equations and solved numerically. The time integrated population of autoionization level '4' gives the yield of photoionization process.

For a given neutral atom density at the interaction volume, the Yb^{176} atoms density is estimated from its natural abundance of 12.88 % in the target materials. The initial normalized density of Yb^{176}atoms at various energy levels are given as $n_1 = 1$, $n_2 = 0$, $n_3 = 0$ and $n_4 = 0$. The incident photon flux (J_i) is estimated with a given laser power P_{avg_i} as

$$J_i(t) = \frac{P_{avg\_i}}{Repf \times h\nu_i \times A_i} \times \frac{f_i(t)}{\int f_i(t) dt} \quad (2)$$

where $h\nu_i$ is the individual photon energy, A_i (~1 cm^2) is the cross-sectional area of laser beam, Repf (~12.5 kHz) is pulse repetition rate of the laser and the function $f_i(t)$ is the temporal profile of copper vapor pumped dye laser pulse for i^{th} laser beam.

In order to estimate the isotopic composition of various Yb isotopes, the spectral overlap between laser profile and absorption profile of the transition is considered. The spectral overlap is taken into account by defining the effective process cross section of each isotope (σ_{ij}) [4] as

$$\sigma_{ij} = \frac{\lambda_i^2}{4} A_{ji} \int_{-\infty}^{\infty} S_{abs}(w) S_{las}(w)\, dw \quad (3)$$

where $S_{abs}(w)$ is the absorption line shape for the particular isotope and $S_{las}(w)$ is profile of laser, λ_i is the wavelength of the transition. It is basically the product of peak transition cross-section (σ_0) and the overlapping fraction of spectral profiles. Thus the effective cross-section of each isotope are calculated and used to estimate their ion concentration respectively.

3. Results and Discussions

Fig. 2 shows the absorption profile of the first step transition along with the isotope shifts and the relative intensities of various transition lines of Yb isotopes. The spectral profile of even isotope is taken as Voigt profile which is the convolution of Gaussian profile with in-homogeneous Doppler broadening and Lorentzian profile with homogeneous broadening. In case of odd isotopes, the hyperfine components of Yb^{171} and Yb^{173} atomic transition are calculated and each hyper fine component is fitted with Gaussian profile with Doppler broadening. Here the Doppler width is taken as 500 MHz. The single mode laser is used for the excitation process. The

laser's spectral profile is considered as Lorentzian type. Sankari et. al. [5] also studied the effect of line shape on selective ionization. When the λ_1 laser is resonantly tuned to the line of Yb^{176} isotope, a good spectral overlap between Yb^{176} spectra and laser profile gives a good excitation of Yb^{176}. In the same time, a very poor spectral overlap of the tail part of laser profile and nearby lines of Yb^{174}, Yb^{171} and Yb^{173} isotopes separated by ~ 0.95 GHz, 1.2 GHz and 1.5 GHz gives the unwanted excitation of these isotopes. The relative composition of different Yb isotopes after 1st step resonant excitation of Yb^{176} is shown in fig. 3. A large fraction ~ 0.73 of Yb^{176} is excited as its transition is resonant. The other isotopic compositions are 0.20, 0.03, 0.02 and 0.02 for Yb^{174}, Yb^{172}, Yb^{171} and Yb^{173} respectively.

Fig. 4 shows the absorption profile of second-step transition along with the isotope shifts and relative intensities of different Yb isotopes. It is seen that two nearby hyperfine components of Yb^{173} tare placed closely on both side of the targeted Yb^{176} component in second step. They are separated from the Yb^{176} line by 316 MHz and 406 MHz respectively. It seems that the Yb^{173} is the most influential isotope in second step but its transition component in the first step is far way separated by ~1.5GHz. Thus a very high selectivity of Yb^{176} excitation is obtained by suppressing the other isotopes as the selectivity in multi-step photoionization process is defined as the product of the selectivity in each step. Fig. 5 shows the relative intensity of different isotopes after two-step resonant excitation of Yb^{176}.

The isotopic concentrations of different Yb isotopes in the interaction volume are decided by the ionization yield of different isotopes in selective photoionization process. To avoid the effect of laser power broadening, the laser powers are taken as 0.5W, 1.5W and 25 W in consecutive steps. With these above powers a reasonable ionization yield of Yb^{176} ~ 0.3 is easily achieved. The isotopic concentration of Yb^{176} photoions is calculated from the model and its parametric studies are carried out. As the laser line-width increases, the spectral overlapping fraction of adjacent undesired isotope increases. It decreases the relative isotopic concentration of desired Yb^{176}. Fig. 6 shows the variation of Yb^{176} concentration with laser line-width for different value of Doppler width. It is examined the spectral line-width of both λ_1 and λ_2 laser are to be less than 200 MHz to get the Yb^{176} abundance more than 99% in the interaction volume.

4. **Conclusions**

Three-step three color resonant photoionization scheme has been used to selectively excite and ionize the targeted Yb^{176} isotope. The variations of Yb^{176} isotopic concentration with different laser line-widths and atomic absorption line-width have been carried out. It has been found that the high value of Yb^{176} enrichment could be achieved when the line widths of both lasers used in first step and second step are less than 200 MHz, the Doppler width is also less than 300 MHz.

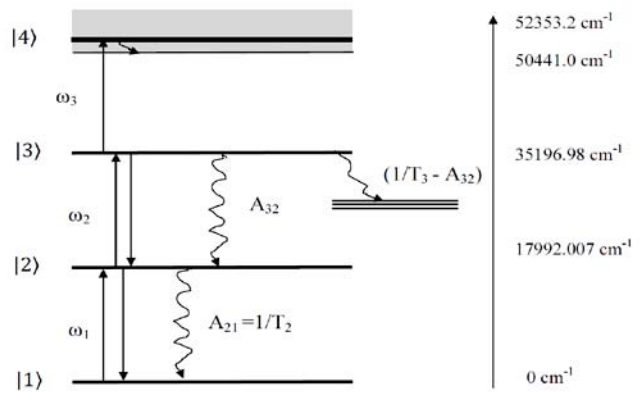

Fig.1: Three-step three-color resonant photoionization scheme of Yb^{176} atoms along with relevant energy levels and various atomic transition processes.

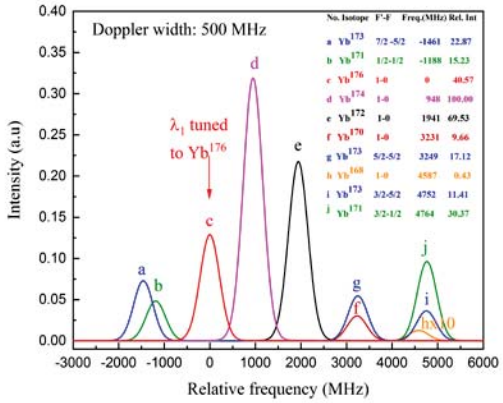

Fig.2. Absorption profile of first step transition for Yb isotopes width Doppler width 500 MHz.

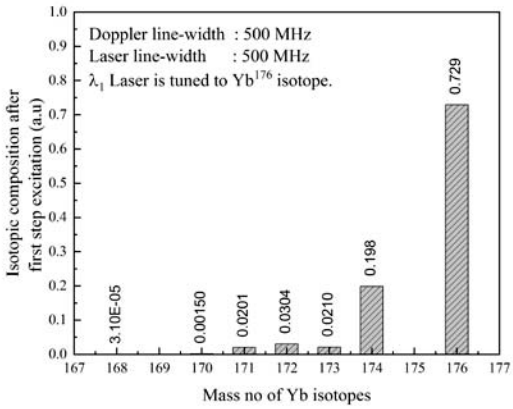

Fig.3.Isotopic composition of various Yb isotopes after first step resonant excitation with λ_1 laser tuned to Yb^{176}.

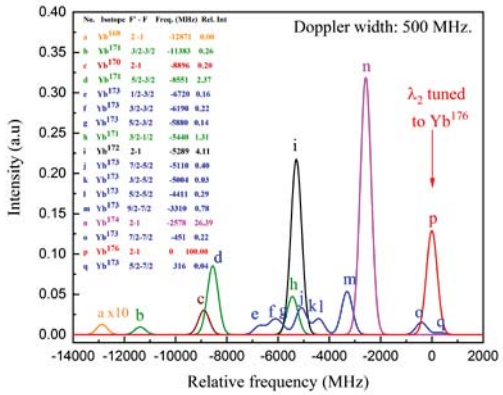

Fig.4. Absorption profile of second-step transition for Yb isotopes width Doppler width 500 MHz.

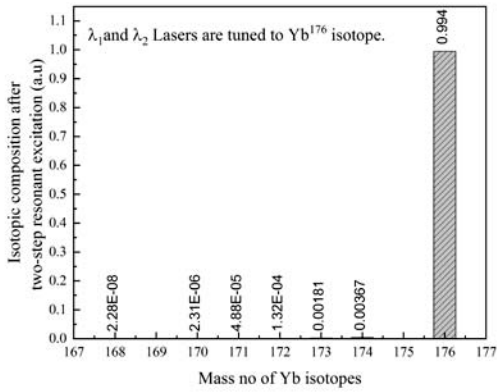

Fig.5. Isotopic composition of different Yb isotopes after two step resonant excitation with λ_1 and λ_2 laser tuned to Yb^{176} transition line.

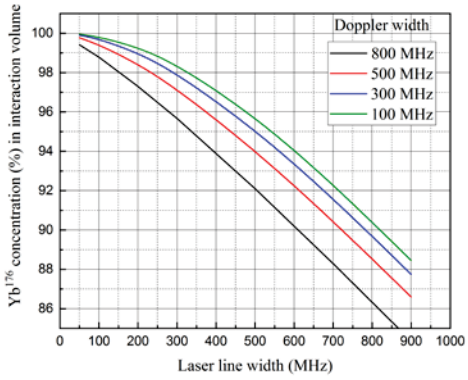

Fig.6. Variation of Yb^{176} concentration with laser line-width for different value of Doppler widths.

Acknowledgement: Authors are thankful to Dr. Archana Sharma, AD, BTDG for her encouragement and support.

References

1. A. Dash, M.R.A. Pillai and F. F. Knap,Nucl Med Mol Imaging ., **49**, 85 (2015).

2. S. I. Yakovlenko, Quantum Electronics, **28**, 945 (1998)

3. S. K. Borisov, M.A. Kuzmina and V. A. Mishin , Journal of Russian Laser Research, **17**, 332 (1996).

4. Letokhov V. S., Mishin V. I. and Puretzky A. A. (1977), Prog.Quant. Electr, 5, 139 (1977).

5. M. Sankari, P.V. Kiran and M.V. Suryanarayana, J. Opt. Soc. Am. B, **25**, 1820 (2008).

Simulation of optical emission spectra of Hastelloy plasma for Laser-induced breakdown spectroscopy applications

M.S. Suryan Sivadas[1], Lekha Mary John[1], K. K. Anoop[1,*]

[1] *Department of Physics, Cochin University of Science and Technology, Kochi-682 022, India*

*Email: anoopkk@cusat.ac.in

Abstract

We simulated the optical emission spectra of Hastelloy plasma at typical physical conditions of laser-induced plasmas. For a particular combination of electron temperature and electron number density (e.g., T_e=1 eV and N_e=10^{17} cm^{-3}), the populations of lowest three ions of a particular element are calculated using Saha-LTE formulas and the intensities of all known transitions are calculated using Boltzmann distribution accounting for fractional ion populations, abundance of the elements, and spectral broadening. The characteristic emission lines and corresponding emission intensities of the spectra represent each element's abundance in the sample. This simulation is a convenient and straightforward method for performing laser-induced breakdown spectroscopy (LIBS) applications of multi-element samples.

1. Introduction

Atomic emission spectroscopy (AES) is a widely used diagnostic tool for the compositional analysis of multi-element samples (alloys, compounds, soil, rock etc.). In AES, the samples are generally excited through electrical discharge or laser ablation process. The vaporized sample goes to high-temperature plasma state and emits characteristic emission lines of each constituent element in the sample. The emission spectrum from the plasma then utilizes for qualitative and quantitative analysis of multi-element samples. In this work, we simulated the optical emission spectrum of Hastelloy (a commonly used Alloy sample in the industry with nickel: 56 wt%, molybdenum:17 wt%, chromium: 16.5 wt%, iron: 6 wt%, Tungsten:4.5 wt%) plasma at typical physical conditions of laser-produced plasmas.

2. Simulations Details

This section describes the steps we followed to simulate the optical emission spectrum of high-temperature Hastelloy plasma in the spectral range of 200-600 nm. To start the simulation, we only need three pieces of information: the plasma temperature T_e, electron number density N_e, and the number fraction of atoms of elements in the plasma $\{N_X\}$, where X denotes the component elements. For the alloy in question, the composition is given in Table 1. To simulate the Hastelloy plasma spectrum at LTE, we use a model shown in reference 1, with some simplifications[1]. Even though a simplified model, the generated spectrum is useful for identifying prominent lines in the experimental spectra (e.g., LIBS applications). We could split the simulation into three steps, which are described below;

Element	Ni	Mo	Fe	Cr	W	Sum
W_X	0.560	0.170	0.060	0.165	0.045	1.000
N_X (rounded)	0.604	0.112	0.068	0.201	0.016	1.000

Table 1: Composition of Hastelloy

Step 1: Calculating Species Contributions

In the plasma, an element X is present in its neutral state, as well as in first few ionized states. Each of them will have

their own contribution depending on their population, which depends on T_e. For the simulation, we only need the fractional population $N_{X,s}$ (proportional to their actual number) of a species *X*-*s* such that $\sum_s N_{X,s} = N_X$. Since the plasma is assumed to be in LTE (local thermodynamic equilibrium), we could use the Saha ionization equation[1,2], which gives these populations' ratios. Putting the values of known fundamental constants, this can be written as

$$f_{X;s,s+1}(T_e, N_e) \stackrel{\text{def}}{=} \frac{N_{X,s+1}}{N_{X,s}} = 6.009 \times 10^{21} \left[\frac{T_e^{3/2}}{N_e} . \frac{U_{X,s+1}(T_e)}{U_{X,s}(T_e)}\right] e^{-V_{X,s}/T_e} \quad (1)$$

Where $U_{X,s}$ is the partition function for species *X*-*s*, defined as $\sum_k g_k e^{-E_k/T}$, g_k and E_k are the statistical weight and energy of the state *k* of the species in the plasma. $V_{X,s}$ is the ionization potential for this species.

Now we have $N_{X,s+1} = f_{X;s,s+1} N_{X,s}$, which can be found as we know the contribution of neutral atoms, $N_{X,I}$. We considered only the first three ions, other than the neutral one (i.e., *s* is I, II, III and IV). Then, after doing a little algebra, this could be found as

$$N_{X,I} = \frac{N_X}{1 + f_{X;I,II}(1 + f_{X;II,III}(1 + f_{X;III,IV}))} \quad (2)$$

Step 2: Estimation of Peak Line Intensity

To compute the intensity of available lines of a species *X*-*s*, we made some assumptions, which will simplify the model: We assume little absorption effects, and there are no contributions in the emitted radiation other than line emissions. Resulting peak intensity of the transition $k \rightarrow i$ could be written as[1]

$$I_{ki}(\lambda_{ki}) = \frac{1}{4\pi} N_k A_{ki} \epsilon_{ki} \quad in\ some\ a.u. \quad (3)$$

where we have omitted the species-index to make the equation more readable. Here, $\epsilon_{ki} = hc/\lambda_{ki}$ is the energy of emitted photon and A_{ki} is the transition probability (Einstein coefficient). Assuming a Boltzmann distribution, we can find the population of state *k* as $N_k = N g_k e^{-E_k/T_e}/U(T_e)$, where *N* is the total poluation of the species. The values of these spectroscopic quantities can be found at NIST's atomic spectra database[3].

Step 3: Generating the Spectrum

Finally, we should give each line a broadened profile, like what we see in the real-world spectrum. Many mechanisms are causing broadening including the Doppler and Stark, with the latter being dominant. But, calculating Stark broadening involves the difficult task - calculation of collisional cross-sections[2]. We consider the plasma as an optically thin medium, limiting the collisional and self-absorption effects in the plasma. So, we consider only a broadening attributed to the resolving power *R* of our *virtual* spectrometer. This is given by a width of $w_{ki} = \lambda_{ki}/R$ at the half maximum, and gives a Gaussian shape to the line:

$$I_{ki}(\lambda) = I_{ki}(\lambda_{ki}) e^{-4log2[x_{ki}(\lambda)]^2}, \ where\ x_{ki}(\lambda) = \frac{\lambda - \lambda_{ki}}{w_{ki}} \quad (4)$$

To get the intensity collected at sample point $\lambda_{(m)}$, we sum the contributions from all lines. This generates a sequence $(\lambda_{(m)}, I_{(m)})$, which mocks the characteristic emission lines of the real-world plasma spectrum.

3. Results and Discussion

We have simulated the spectrum of Hastelloy plasma at two typical physical conditions of laser-produced plasmas (i) at T_e = 1.0 eV, N_e = 10^{17} cm^{-3} and (ii) at T_e = 0.5 eV, N_e = 10^{16} cm^{-3}. The obtained results are shown in Fig.1. Both use equidistant sampling in 200-600 nm spectral region, with a resolution R = 1000 (We could also use non-uniform sampling, with more samples in regions having more density of lines). We took necessary spectroscopic data from NIST database[3]. Only lines having related data like A_{ki} available are used in the simulation. The simulated spectrum shows all possible transitions and corresponding intensities of all species in the plasma. The persistent and strong lines of each element observed in the simulated spectrum are distinctive tool for qualitative and quantitative elemental analysis in LIBS applications. Some of the intense emission lines of Hastelloy plasma observed at T_e = 1 eV are 232.22 nm (Ni I), 352.45 nm (Ni I), 221.65 nm (Ni II), 231.60 nm (Ni II), 248.33 nm (Fe I), 358.12 nm (Fe I), 238.20 nm (Fe II), 259. 94 nm (Fe II), 357. 87 nm (Cr I), 520. 84 nm (Cr I), 283.56 nm (Cr II), 205.559 (Cr II), 400.88 nm (W I), and 207.91 (W II). Fig. 1 also shows a strong dependence of electron temperature and number density on emission spectra. As expected, more energetic and intense UV transitions are observed at T_e = 1 eV compared to T_e = 0.5 eV. The results imply that one has to choose a wide spectral window (starting from 200 nm) to get enough emission lines for LIBS analysis. We need to consider additional parameters like collisional broadening, the role of ambient pressure, self-absorption etc. to get the exact emission spectrum of laser-produced plasmas. Since LPP generation is a complex phenomenon, more theoretical and experimental investigations are needed in this research field.

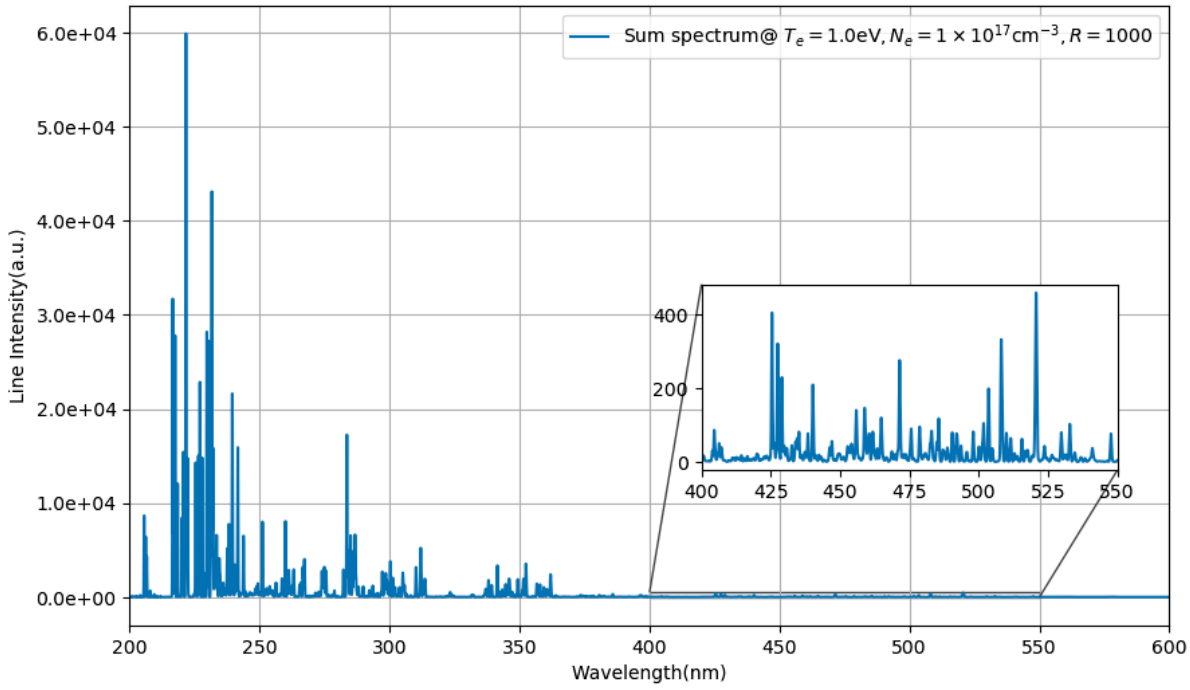

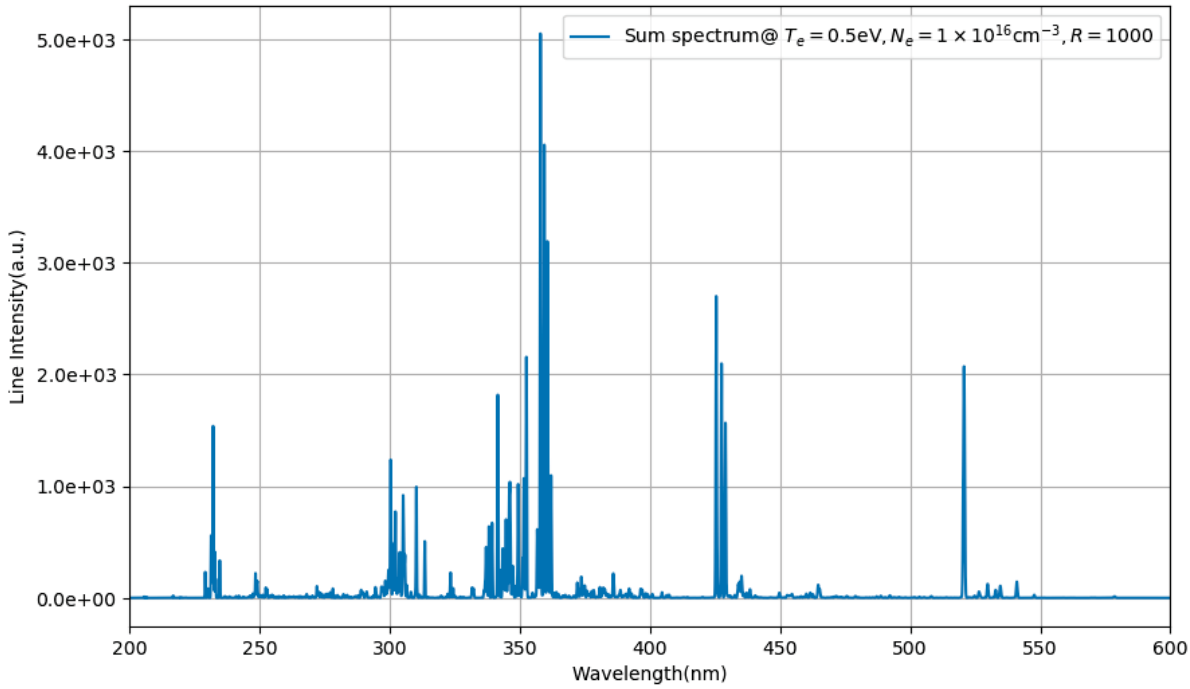

Figure 1: Simulated optical emission spectrum of Hastelloy plasma at 1.0 eV electron temperature (T_e) and an electron density (N_e) of 10^{17} cm^{-3}. The inset represents the zoomed view of 400-550 nm spectral region. Bottom figure represents the same for T_e = 0.5 eV, N_e = 10^{16} cm^{-3}.

Our study provides a convenient method to simulate the optical emission spectrum of high temperature and number density plasma of Hastelloy sample. We used Saha-LTE and Boltzmann distribution and the NIST atomic spectra database to simulate the emission spectrum of the multi-element sample. Even though the studied plasma doesn't precisely mimic the laser-produced plasma (LPP), the spectra simulated at typical physical conditions of LPP can be used for laser-induced breakdown spectroscopy (LIBS) applications. The persistent, strong lines and the corresponding intensities provide the qualitative and quantitative information of each element present in the sample. Our study also provides the information on suitable spectral window one has to choose for LIBS investigations and data analysis. The simulated optical emission spectra of high temperature and number density plasmas have numerous industry, material science, geology, agriculture, and space exploration applications. Comparing the simulated spectrum with the experimental spectrum is a direct route to identify the elements present in multi-element samples.

References

[1] Reinhard Noll. Laser-Induced Breakdown Spectroscopy, Fundamentals and Applications. *Springer-Verlag Berlin Heidelberg* (2012).

[2] Hans R. Griem. Principles of Plasma Spectroscopy. *Cambridge University Press*, Cambridge, United Kingdom (1997).

[3] A. Kramida, Yu. Ralchenko, J. Reader, and and NIST ASD Team. NIST Atomic Spectra Database (ver. 5.8), [Online]. Available: https://physics.nist.gov/asd [2021, January 10]. *National Institute of Standards and Technology*, Gaithersburg, MD. (2020).

Quantitative Elemental Analysis of Copper Alloy using Laser-Induced Breakdown Spectroscopy

Lekha Mary John[1], K. K. Anoop[1,*]

[1] *Department of Physics, Cochin University of Science and Technology, Kochi-682 022*

*Corresponding Author: anoopkk@cusat.ac.in

Abstract

We investigated the reliability of Calibration Free Laser-Induced Breakdown Spectroscopy (CF-LIBS) in the quantitative elemental analysis of a Copper alloy. A frequency-doubled Q-switched Nd:YAG laser was employed to generate the plasma plume from the Brass target. The experiments were carried out at rough vacuum condition, and the characteristic emission lines of laser-produced plasma were used to determine the plasma parameters. The plasma temperature and electron density were estimated by the Boltzmann plot method and the Stark broadening method, respectively. The concentrations of elements in the brass alloy were evaluated by the Calibration free LIBS (CF-LIBS) analysis. To prove the trustworthiness of the method, a comparison between the CF-LIBS results with the nominal concentrations was carried out. It was found that the CF-LIBS results agree well with the nominal concentrations, with relative uncertainties of constituent elements less than 3%.

1. Introduction

Laser-induced breakdown spectroscopy (LIBS) is an analytical technique based on atomic emission spectroscopy. It has shown great potential over other parallel analytical methods due to its unique features, such as its fast in situ analysis of multi-elemental samples without any sample preparation. Analysis can be done on any sample irrespective of its physical state and consuming only some micrograms of the samples. Its portability and remote analyzing capability make it a useful analytical tool for industry, agriculture, and space exploration. This method is based on the spectral analysis of atomic emission lines from the laser-produced plasma. A powerful laser beam is focused onto a target material, creating a minor ablation of material from the surface sample. The ablated cluster is called transient microplasma of the sample consisting of free electrons, neutral atoms, ions, etc. When the laser-produced plasma de-excites, light emission occurs, and that is collected and dispersed in a spectrometer. It contains characteristic emission lines that provide the elemental composition of the sample[1].

Brass is generally used in applications that are decorative for its bright gold-like appearance. In industry, brass is used primarily in applications that require low friction due to its corrosion resistance. Exact quantification of brass is needed in most cases since the price and quality of brass is mainly depend on the amount of Copper. Due to the fast in situ analysis, LIBS is an appropriate method for the quantification of alloys. We used the CF-LIBS method for laser-induced plasma characterization and abundance estimation of a brass alloy in the present work. Our investigations reveal that LIBS is a versatile tool for elemental identification and alloy classification in industry and material science.

2. Experimental Details

The standard experimental setup of LIBS, given in reference (1), was used to record optical emission spectrum from laser-produced plasma (LPP) of brass alloy[1]. A frequency-doubled Q-switched Nd: YAG laser (λ=532 nm, τ=10 ns, E=40 mJ) was used to ablate the target at rough vacuum (1 Torr) condition. The applied fluence $F \approx 75$

J/cm^2 was sufficient to produce intense light emission from plasma plume. The characteristic emission lines from LPP were then collected using a lens system, and directed to a portable fiber optics spectrometer (Ocean HDX-XR). We used the background-corrected optical emission spectrum for further compositional analysis.

3. Methodology for Quantitative Analysis

For the meaningful application of thermodynamic expressions related to fundamental plasma parameters and the concentration of analyte species, the plasma should satisfy Local Thermodynamic Equilibrium (LTE). Hence LTE is an essential requisite for getting reliable quantitative results, and it is crucial to assess whether a plasma region has achieved LTE during the observation window. The most popular method for evaluating the LTE of plasma is the McWhirter criterion, and it states the existence of critical electron number density. The lower limit of the electron density for which the plasma will be in LTE is[2].

$$n_e(cm^{-3}) \geq 1.6 \times 10^{12} T^{1/2} (\Delta E_{nm})^3 \quad (1)$$

ΔE_{nm}(eV) is the energy difference between upper and lower states, and T(eV) is the plasma temperature. Plasma temperature is calculated using the Boltzmann plot method, and electron number density is computed using the Stark broadening method. The quantitative analysis is carried out by an approach proposed by Ciucci et al.[3]. Under LTE conditions, the integral intensity of an optically thin emission line is,

$$\overline{I_\lambda^{ki}} = F C_s A_{ki} \frac{g_k e^{-(E_k/k_B T)}}{U_S(T)} \quad (2)$$

where I_{ki} represents the measured integral line intensity and F is an experimental parameter that considers the optical efficiency of the detection system and the plasma density and volume. C_s is the relative concentration of emitting species in the plasma, A_{ki} is the transition probability (Einstein A coefficient), g and E(eV) represents the degeneracy and energy of the particular state respectively, T (K) the plasma temperature, k the Boltzmann constant and $U_s(T)$ the partition function. When we take logarithms of both sides, and on rearranging, a linear equation is obtained the familiar form of Boltzmann plot equation is,

$$y = ln \frac{\overline{I_\lambda^{ki}}}{g_k A_{ki}},\ x = E_k,\ a = -\frac{1}{k_B T},\ b^s = ln \frac{F n_p C_s}{U_S(T)} \quad (3)$$

The slope of the plots is related to the plasma temperature, while the intercept b^s is proportional to the logarithm of the species concentration. By this, one can calculate the concentration of the species,

$$C_s = \frac{1}{F} U_s(T) e^{b^s} \quad (4)$$

The F factor can then be determined using normalization relation since the sum of the relative concentrations of all the elements must be unity. The concentration of the corresponding element in the sample is the sum of the concentrations of the neutral and single ionized species, the total concentration for a given element M is given by,

$$C_M^{TOT} = C_{M^{(I)}} + C_{M^{(II)}} \quad (5)$$

When only the concentration of one species of a given element is known, it is possible to calculate the concentration of the other ionization stages by making use of the Saha-Boltzmann equation while the electron number density n_e and plasma temperature T is known[4],

$$\frac{n_e N_S(z+1)}{N_S(z)} = 6.04 \times 10^{21} T_{eV}^{3/2} \frac{\mathrm{U_S(z+1)}}{\mathrm{U_S(z)}} \exp(-\frac{\chi_z^S}{T_{eV}}) \quad (6)$$

Where $N_s(z)$ and $N_s(z+1)$ are, respectively, the population of the ground state of the neutral atomic species and that of the single ionized species and χ_Z is the ionization energy of the species in the ionization state Z.

Result and Discussion

Fig. 1 represents the optical emission spectrum of a Brass alloy recorded at 1 Torr background pressure. The persistent and strong lines of Copper and Zinc are marked in the spectrum. The reduced background pressure limited the intense light emission from Oxygen, Nitrogen and Hydrogen etc. The Lorentzian fitted emission lines are used for finding plasma parameters and the elemental composition of brass. The Boltzmann plot, generated using spectral line intensities of neutral species of Copper (Cu I: 465.112 nm, 510.554 nm, 515.391 nm, 521.82 nm, 793.313 nm and 809.263 nm) and Zinc (Zn I: 468.013 nm, 472.215 nm, 481.053 nm and 636.234 nm), is shown in Fig. 2. The plasma temperature calculated from the slope is 11600 ± 400 K. The electron number density is determined from the Stark broadening of the emission line at 515.554 nm (Cu I). The value of n_e in the brass plasma is obtained to be 2.89 x 10^{18} cm^{-3}. Plasma satisfies the McWhirter criterion; therefore, the plasma is in local thermodynamic equilibrium (LTE). For quantifying elemental contents in the sample, we have computed the relative concentration of Cu I and Zn I from the y-intercept of the Boltzmann lines. The ratio of the number density of neutral and ionized Copper and zinc species was calculated using the Saha-Boltzmann equation. Using these number density values; we have determined the weight percentage of Zn and Cu in the brass sample. The ratio of Zn and Cu concentrations in the brass sample obtained from the CF-LIBS analysis is 35±3 % : 65±1.5 %, and that of the certified ratio is 34 : 66. The obtained results indicate that the accuracy error of the LIBS method is less than 3%. Even though CF-LIBS provides good accuracy, more investigations are needed to improve the accuracy of LIBS method so that it can be used as a more reliable quantitative analytical technique, especially for remote and in situ applications in industry, agriculture, and geochemical analysis.

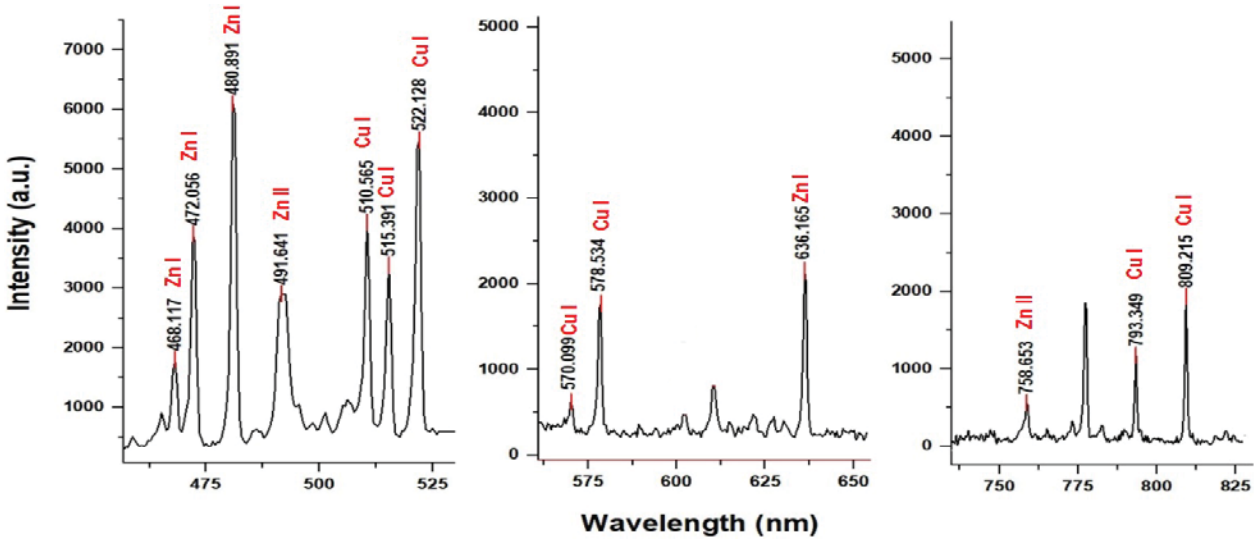

Figure 1: Portions of the LIBS spectrum of a brass sample. Persistent and strong lines of Cu and Zn are marked. The spectrum was recorded at laser fluence F = 75 J/cm^2 under 1 Torr of air atmosphere.

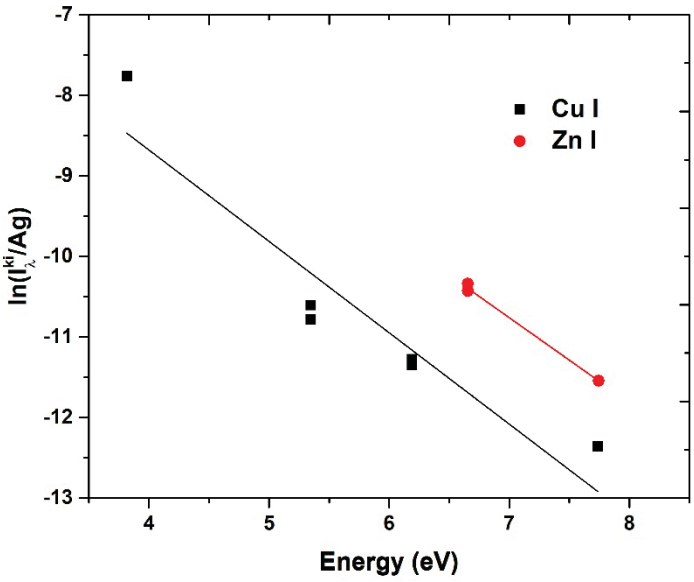

Figure 2: Boltzmann plot of the species in the Brass alloy

Conclusions

In conclusion, we investigated the reliability of CF-LIBS technique for quantitative elemental analysis of a multi-element copper alloy. A frequency-doubled nanosecond laser pulse from the Nd:YAG laser was used to ablate the brass target at 1 Torr background air pressure. The plasma temperature (11600±400 K) and electron density (2.89 x 10^{18} cm^{-3}) were estimated by the Boltzmann plot method and the Stark broadening method, respectively. We have also quantified brass sample using the CF-LIBS technique, and the obtained abundance (weight percentage) is 65±1.5% of Copper and 35±3% of Zinc. The elemental concentrations obtained from the CF-LIBS technique are in excellent agreement (accuracy error < 3%) with the nominal concentration. Our results conclude that CF-LIBS is a reliable analytical technique for multi-elemental compositional analysis.

References

1. D. A. Cremers, and L. J. Radziemski, Handbook of laser-induced breakdown spectroscopy, *John Wiley & Sons*, (2013).
2. R. Gaudiuso, M. Dell'Aglio, O. D. Pascale, G. S. Senesi, and A. D. Giacomo, *Sensors*, **10**, 7434 (2010).
3. A. Ciucci, M. Corsi, V. Palleschi, S. Rastelli, A. Salvetti, and E. Tognoni, *Applied spectroscopy*, **53**, 960 (1999).
4. V. K. Unnikrishnan, K. Mridul, R. Nayak, K. Alti, V. B. Kartha, C. Santhosh, G. P. Gupta, and B. M. Suri, *Pramana,* **79**, 299 (2012).

Concentration dependent optical studies of Nd^{3+}-doped P-Ba-La glasses for future photonic applications

P.Ramprasad and C.K. Jayasankar

Department of Physics, Sri Venkateswara University, Tirupati-517 502.

Email: ckjaya@yahoo.com

Abstract

The investigation of the concentration dependent spectroscopic characteristics of Nd^{3+} ion in $Ba(PO_3)_2$+La_2O_3 glasses have been carried out. Based on well known Judd-Ofelt (JO) formalism, the three JO phenomenological intensity quantitative parameters and radiative characteristics were determined from the absorption spectra. From these intensity parameters various radiative properties such as spontaneous de-excitation probability, radiative lifetime, luminescence branching ratios which are useful to assess the potentiality of the glasses have been evaluated. The de-excitation spectra observed for these glasses yield three prominent levels of $^4F_{3/2}\rightarrow$ $^4I_{9/2}$, $^4I_{11/2}$ and $^4I_{13/2}$ for which effective bandwidths and stimulated de-excitation cross-sections are quantified.

1. Introduction

Now-a-days the development of needy materials for photonics applications has been carried out that includes synthesis of many trivalent rare earths (RE^{3+}) embedded matrices, consisting of glasses, crystals and glass-ceramics. Mainly, glass based materials have been focused by many scientists as they found to be very good host materials for rare earth ions because the hosts possess wide transmission range covering from mid-infrared (IR) to ultraviolet (UV), good thermal and mechanical stabilities, chemical, high nonlinear refractive index, reduced multiphonon non-radiative probabilities due to relatively low phonon energy and in turn enhances the quantum yields. In this connection, phosphate glasses are very good preferred host materials for RE ions owing to their chemical durability, manufacturability, optical properties, mechanical stability, and advantage in economy. However, relatively poor chemical durability restricts phosphate glasses for a wider application. On the other hand, presence of the alkaline earth metal and alkali oxides in the P_2O_5 matrix enhances the glass transition temperature and chemical durability [1,2]. So that, in the present work BaO and La_2O_3 are chosen as a modifiers and also the addition of BaO and La_2O_3 improves the glass stability and the glasses can be tuned for many more different optical devices. By making use of the inhomogeneous broad optical lines that is manifested as larger broadening of the absorption and de-excitation levels of Nd^{3+} ions have been exploited for variable and ultra-fast laser gain medium. By considering all these motives, the present work aims to study the concentration dependent spectral properties of Nd^{3+} ions in $Ba(PO_3)_2$+La_2O_3 glasses to develop future photonics devices.

2. Experimental details

Barium metaphosphate glasses (PBaLa) with composition of 47.5 $Ba(PO_3)_2$ +(5-x) La_2O_3+x Nd_2O_3, where (x = 2.0, 1.0, 0.5 and 0.1 mol %), referred as $PBaLaNd_{2.0}$, $PBaLaNd_{1.0}$, $PBaLaNd_{0.5}$ and $PBaLaNd_{0.1}$, correspondingly, have been developed. The stoichiometric components of the batches were melted in a silica crucible at 1200^0C for 1h. These glasses were annealed at 400^0C for 14 h and cooled slowly to room temperature to eliminate the thermal stress induced with these glasses during forced sudden quenching method.

The refractive index have been determined using Abbe refractometer at 589.3 nm (sodium vapour lamp). The density has been determined by following Archimede's method where water has been used as immersion liquid. The luminescence (excitation and de-excitation) and experimental lifetimes were measured using spectrofluorimeter (Edinburgh FLS 980) with intense xenon source for optical de-excitation and 808 nm laser diode for NIR de-excitation has been used as the source of excitation.

3. Results and Discussion

Fig. 1 depicts the characteristic absorption levels of $PBaLaNd_{1.0}$ glass measured in the 400-940 nm region. The measured absorption levels are attributed to the $4f^3 \rightarrow 4f^3$ levels from the $^4I_{9/2}$ ground state to different excited energy states of Nd^{3+} ion. The located and assigned absorption levels, accurate peak locations (λ_p) and their oscillator strengths (experimental (f_{exp}) and calculated (f_{cal})) are tabulated in Table 1. The characteristic Judd-Ofelt (JO) parameters, Ω_λ (λ = 2, 4 and 6), are determined by the method of least square fit between the experimental (f_{exp}) and calculated (f_{cal}) oscillator strengths following the method outlined earlier by our group [3,4].

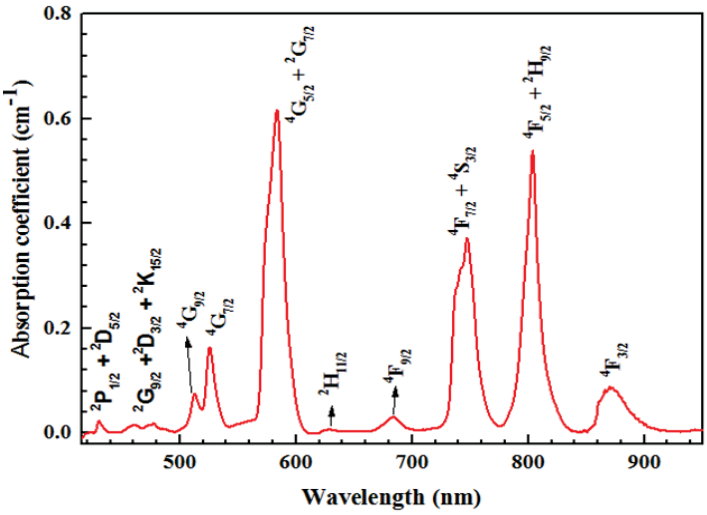

Fig.1. *Optical absorption spectrum of $PBaLaNd_{1.0}$ glass.*

Table 1. Assignment of absorption transitions, peak positions (λ, nm) experimental (f_{exp} , x 10^{-6}) and calculated (f_{cal}, x10^{-6}) oscillator strengths for $PBaLaNd_{1.0}$ glass.

Transition $^4I_{9/2}\rightarrow$	λ (nm)	Oscillator strengths	
		f_{exp}	f_{cal}
$^4F_{3/2}$	877	3.24	2.89
$^4F_{5/2} + {}^2H_{9/2}$	804	10.35	9.95
$^4F_{7/2} + {}^4S_{3/2}$	747	10.47	10.81
$^4F_{9/2}$	684	1.47	0.83
$^2H_{11/2}$	629	0.43	0.23
$^4G_{5/2} + {}^2G_{7/2}$	584	23.22	23.16
$^4G_{7/2}$	527	4.51	6.24
$^4G_{9/2}$	513	2.84	3.87
$^2G_{9/2} + {}^2D_{3/2} + {}^2K_{15/2}$	477	0.66	0.94
$^2P_{1/2} + {}^2D_{5/2}$	430	0.37	0.69
		δ_{rms} = ±0.86	

The level at 804 nm is very commonly followed for the excitation (optical pumping) of neodymium-diluted laser glasses, either by semiconductor GaAs laser diodes or flash lamps [5]. The evaluated JO intensity parameters ($\Omega_{\lambda=2,4,6}$) of the $PBaLaNd_{1.0}$ glass are estimated to be Ω_2=7.08× 10^{-20} cm^2, Ω_4=5.34× 10^{-20} cm^2, and Ω_6=7.60× 10^{-20} cm^2 and in turn spectroscopic quality factors (χ) is 0.70. The quantities of the JO intensity parameters determined in this work enhances in the order of $\Omega_6 > \Omega_2 > \Omega_4$. Normally, the values of Ω_2 depends on the covalence nature and asymmetry between ligand anions and rare-earth ions, but the values of Ω_4 and Ω_6 are attributed to the bulk properties that includes rigidity and viscosity of the surrounding host medium [6]. **Fig. 2** represents the near infrared (NIR) de-excitation spectra for variety of concentrations of Nd^{3+} ions in PBaLaNd glasses. The de-excitation levels belonging to the $^4F_{3/2} \rightarrow {}^4I_J$ (J = 13/2, 11/2 and 9/2) levels are assigned at 874, 1055 and 1325 nm, correspondingly. The electronic level scheme showing the de-excitation and excitation levels of Nd^{3+} doped PBaLaNd glass medium is presented in **Fig. 2(b).**

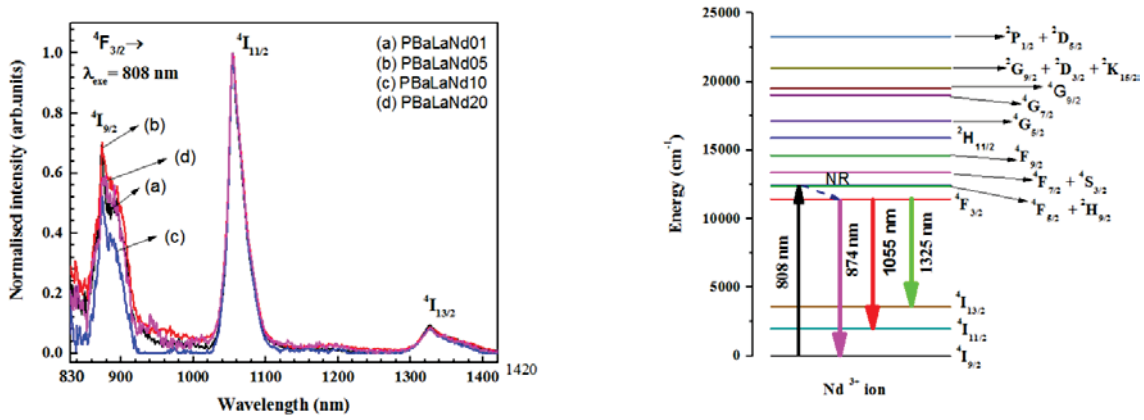

(a) (b)

Fig. 2. (a) *Concentration dependent NIR emission spectra of PBaLaNd glasses. (b) Partial electronic level scheme of PBaLaNd glass.*

The intensity of $^4F_{3/2} \rightarrow {}^4I_{11/2}$ luminescence transition depends only on 'χ' which is nearly unity for many commonly studied phosphate laser gain media glasses. To be more precise, in meta-phosphate laser gain glasses the luminescence intensities are nearly 0.5% , 5-10%, 50-60% and 30-40% for the radiative luminescence that starts from the excited energy level $^4F_{3/2}$ to the $^4I_{15/2}$, $^4I_{13/2}$, $^4I_{11/2}$ and $^4I_{9/2}$ terminal states, respectively.

4. Conclusions

Spectroscopic study of Nd^{3+}:barium phosphate based laser glasses have been prepared and characterized through absorption and emission analysis. The Judd-Ofelt intensity quantities have been utilised to predict the radiative characteristics of the fluorescent states of PBaLaNd glasses. The de-excitation spectra of the titled glasses exhibited strong near infrared de-excitation at 1055 nm belonging to $^4F_{3/2} \rightarrow {}^4I_{112}$ transition. The evaluated results showed that the present PBaLaNd glasses could be considered for the development of efficient NIR emission and optical amplification at 1055 nm.

Acknowledgments:

Prof.C.K. Jayasankar is highly thankful to DAE-BRNS, Mumbai (No.2009/34/36/BRNS/3174, dt.12-02-2010) and UGC-BSR Faculty Fellowship, New Delhi (No.F.18-1/2011 (BSR) dated 24-11-2017) for financial support.

References:

1. .O. Omarani, S. Krimi, J. J. Videan, I. Khattech, A. El. Jazoulli and M. Jemal, J. Non-Cryst. Solids 390, 5-12 (2014).
2. R.K. Brow, J. Am. Ceram. Soc. 76, 913-980 (1993).
3. A. Renuka Devi and C.K. Jayasankar, Mater. Chem. Phys. 42 106-119 (1995).
4. S. Surendra Babu, P. Babu, C. K. Jayasankar, A. S. Joshi, A. Speghini and M. Bettinelli, J. Phys.: Condens. Matter 18, 3975–3991 (2006).
5. S.S. Wang, Y. Zhou, Y.L. Lam, C.H. Kam, Y.C. Chan and X. Yao, Mater. Res. Innov. 1, 92-96 (1997).
6. C.K. Jorgensen, R. Reisfeld, J. Less- Common Met. 93,107-112 (1983).

Three-Step Lithium Photoionization by Optogalvanic Spectroscopy

V. K. Saini*, G. N. Tiwari, and S. K. Dixit

Fibre Sensors and Optical Spectroscopy Section, Raja Ramanna Centre for Advanced Technology, Indore 452013, India.

*Email: vksaini@rrcat.gov.in

Abstract

This paper describes three-step photoionization of lithium (Li) in hollow cathode (HC) discharge lamp by optogalvanic (OG) technique. The atomic vapour of Li is produced in HC lamp by sputtering method. The HC lamp used is in-house developed. The Li photoionization is carried out by copper vapour laser pumped dye lasers through its intermediate energy states with transitions ($0 \rightarrow 14904$ cm^{-1}) at 670.8 nm, ($14904 \rightarrow 31283$ cm^{-1}) at 610.4 nm and ($31283 \rightarrow > 43487.11$ cm^{-1}) for < 819 nm. This study demonstrates that HC lamp can be used efficiently to realize the photoionization pathways for any element in an easier and cost-effective way.

1. Introduction

In recent years, demand of lithium (Li) has been increased tremendously due to its heavy use in large power battery banks required for solar based electricity generation and to drive new generation electrical auto-vehicles. The use of Li is not only limited to these activities, however its isotopes are also important for nuclear industry. Natural Li consists of two stable isotopes ^{6}Li (7.52%) and ^{7}Li (92.48%). The isotope ^{6}Li has a very high neutron absorption cross-section that's why it is a rich source of tritium (T) needed for development of both the thermonuclear weapon and future controlled nuclear fusion. The separation of Li isotopes by lasers is an attractive and cost-effective method that needs the knowledge of its suitable energy levels and the absorption frequencies. Lithium has an ionization potential (I.P) of 5.39 eV [1] appropriate to two-step and three-step selective photoionization. Photoionization by two-step is although a simple method but needs tunable UV radiation at least in one of the two-steps [2]. The process of generation of UV radiation is more complexed and difficult as compare to visible radiation generation. Therefore, in present study, Li is photo-ionized by two-step resonant excitation followed by a non-resonant third-step ionization using laser radiation in the visible range by optogalvanic (OG) method. The energy levels of Li are well reported [3]; however, their use for multi-step excitation/photoionization is reported rarely and many crucial details are also still lacking. Therefore to investigate an efficient root of Li photoionization, it is essential to perform some concrete experimental research using a simple atomic reservoir such as hollow cathode (HC) lamp. In recent past, resonant laser photoionization of Ge has been reported in HC lamp [4]. In present experiment, we used home built HC lamp [5] to investigate the Li photoionization scheme through its intermediate energy states with transitions ($0 \rightarrow 14904$ cm^{-1}) at 670.8 nm, ($14904 \rightarrow 31283$ cm^{-1}) at 610.4 nm and ($31283 \rightarrow > 43487.11$ cm^{-1}) for < 819 nm by OG method.

2. Pathway for Li three-step photoionization

Figure 1 shows the pathway for resonance ionization of Li atoms through its intermediate energy states. The Li atoms available in 2s ($^2S_{1//2}$) ground state is resonantly excited to first 2p ($^2P_{1/2,3/2}$) energy state using pulse laser tunable across 671 nm. Subsequently, in second step, the population from 2p state is further excited into higher energy 3d ($^2D_{3/2,\ 5/2}$) state by another laser pulse of photons with wavelength ~ 610.35 nm. As I.P of Li is 5.39 eV and excitation energy corresponding to first and second-step transitions are ~ 1.84 and 2.03 eV respectively

[6], therefore excited Li atoms from 3d state can be ionized by the photons with wavelength shorter than 819 nm. In the present experiment, either of the first or second step laser pulse can serve the purpose to photo ionize Li atoms, as the pulse energy is sufficient to bridge the gap between the Li ionization and 3d excited state.

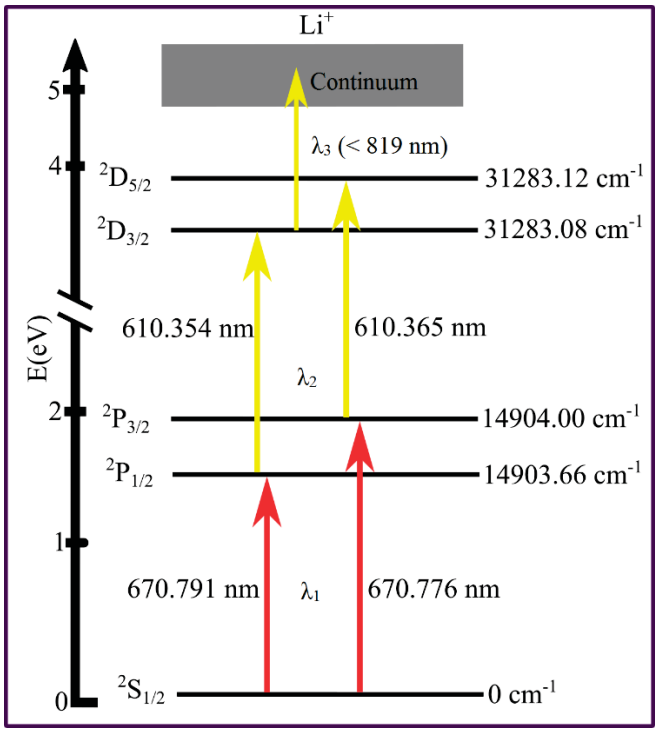

Fig. 1 *Three-step selective photoionization pathway for Lithium*

3. Experimental details

The schematic of experimental setup used to realize above described photoionization scheme using OG spectroscopy by laser multi-step excitation technique is shown in Fig. 2. In-house developed HC lamp [5] with neon as buffer gas and Li as cathode is used to generate the Li atomic vapour. An electrical discharge is applied to HC lamp by a high voltage power supply through a 10 kΩ ballast resistor. The resulting signal due to three-step ionization is coupled to boxcar integrator (SRS-250) through 47 nF capacitor. The signal is recorded by a data acquisition system developed in-house, using computer controlled dye laser wavelength scanner and data acquisition card (Advantech, USB-4716). The CVL pumped two independent dye laser system in synchronization with each other, is used to excite the step-wise Li transitions. The layout of experimental setup is arranged keeping in mind the optical delay between green (510.6 nm) and yellow (578.2 nm) components of CVL pump laser and the delay (~ ns) required in between first and second resonant step of lithium excitation. In present CVL laser system, the yellow component appears after ~ 20 ns time interval of green laser pulse. The used system delivers the laser output powers of around 100 mW from dye laser-1 (~ 2.5 GHz, 635-680 nm, DCM dye, 2.6 mM) and 150 mW from dye laser-2 (~ 2 GHz, 600-625 nm, Rh-640 dye, 0.16 mM) at 6.5 kHz repetition rate, those are sufficient to saturate the respective first and second step of Li transitions as shown in Fig. 1. Two spherical lenses L1 and L2 each of focal length 30 cm are used to focus the laser beams in to HC discharge from opposite sides. For accurate and precise tuning of the dye laser wavelengths corresponding to respective Li transitions, a computerized motor control is provided to each of the dye laser. A precise

wavelength meter (WS-7, HighFinesse) with high accuracy is used to monitor dye laser wavelengths. A PIN-photodiode (PD) is used as a trigger to generate the gate window to retrieve the OG signals form HC lamp through boxcar-integrator (SRS-250) on a computer.

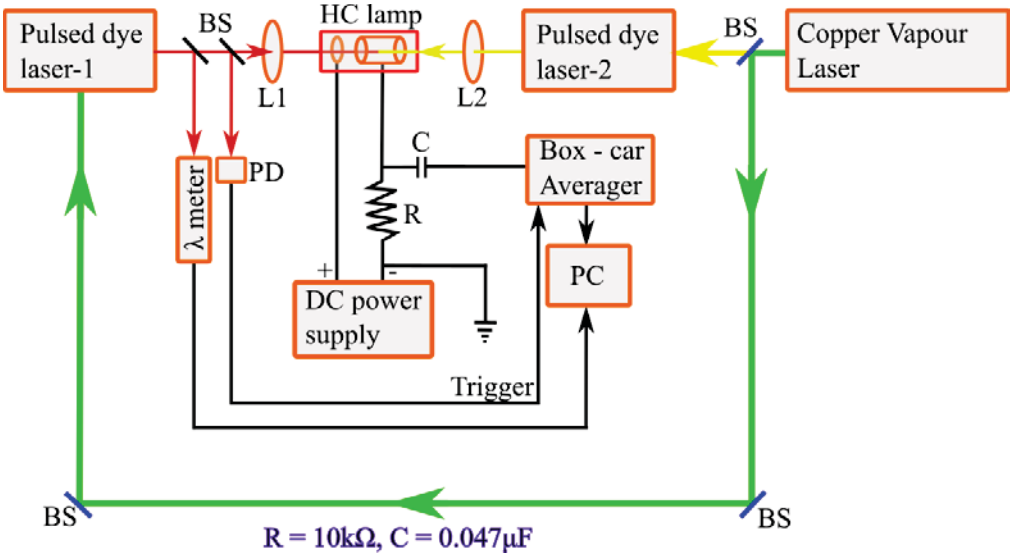

Fig. 2 *Three-step OG spectroscopy setup for lithium selective-photoionization*

4. Results

In HC discharge, the origin of optogalvanic (OG) effect can be understood by two different mechanisms. First one, the laser excitation of atoms from lower to higher electronic sates leads to an increased cross-section for electron impact ionization and the excited atoms thus ionized. The ionization of excited atoms results in the decrease of HC discharge impedance and results an OG signal. In present setup, when HC discharge current decreased up to threshold current (~ 25 mA) and dye laser-1 is scanned from 670.70 to 670.95 nm, an OG spectrum as shown in Fig. 3(a) is observed with slightly reduced strength of Li signal however with clear D_1 and D_2 components. This spectrum is noisy because of instant background disturbance present in the lab, although OG signal is still clearly retrieved. Similarly, the dye laser-2 is scanned from 610.30 to 610.52 nm across 610.365 nm wavelength that corresponds to second-step for Li ($^2P_{1/2,3/2} \rightarrow {}^2D_{3/2,5/2}$) excitaion from its excited state, in absence of laser light from dye laser-1. An OG spectrum with weak signal strength at 610. 365 nm is observed as shown in Fig. 3(b). The fine structure components and isoptopic signature are not clear, however a cumulative signal is explicit. This signal occurs from Li excited state transistion possible in HC discharge because few higher enegy states close to ground state are possibly populated by the elctronic impact excitaion in HC dischrge lamp. Now, the experiment is repeated with laser radiation from both the dye lasers allowed to pass through the negative glow region of HC lamp, keeping the dye laser-2 wavelength fixed at 610.36 nm and scanning only the wavelength of dye laser-1 in the range of 670.70 to 67.90 nm. An intersting result with remarkable enhancement (~ 10 fold) in Li signal with moderately resolved D_1 & D_2 lines is observed as shown in Fig. 3(c). The enhanced OG signal is observed when both the first and second step transitions are excited simultaneously with a few nano-second inter-delay between them followed by non-resonant third-step ionization at 610.36 nm wavelenth. Similar, results were obtained by scanning the wavelength of dye laser-2 in the range of 609 to 613 nm while keeping the wavelength of dye laser-1 fixed at 670.78 nm which corrsponds to

Li first-step resonant transtion ($^2S_{1/2} \rightarrow {}^2P_{1/2,3/2}$). The effect of dye laser-2 power is also observed on Li OG signal. The enhancement is observed only at higher power levels that ensure about the cascaded three-step photoionization of Li in HC lamp by OG effect.

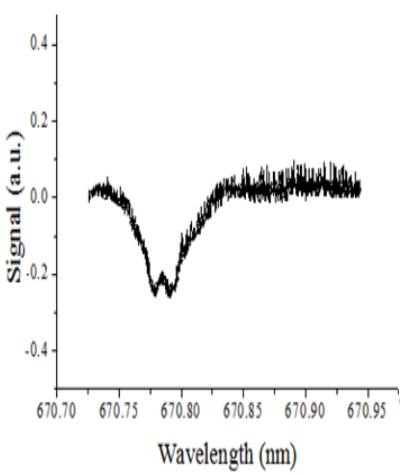

Fig. 3(a)

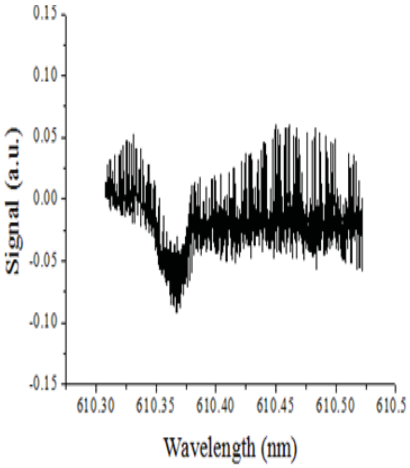

Fig. 3(b)

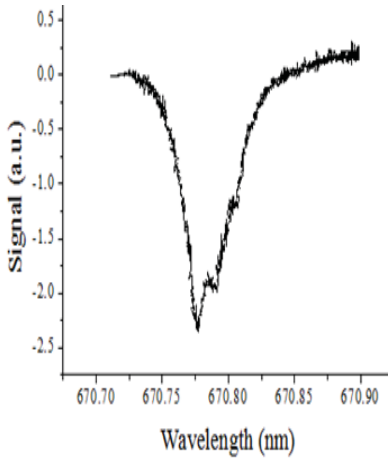

Fig. 3(c)

5. Conclusion

In summary, three-step Li photoionization scheme is realized by OG spectroscopy using in-house developed HC lamp. Pulsed OG effect has been detected across 671 nm Li transition from its ground state to excited state. Li OG signals are observed with good S/N ratio at moderate incident laser power (~50 mW) obtained from CVL pumped dye laser (~2.5 GHz, 20 ns, 635-680 nm). Doppler limited OG spectrum resolved the two Li (D_1 & D_2) lines fairly. This study demonstrates that HC lamp based photoionization setup would be suitable to realize the photoionization pathways for any element in an easier way with cost-effectiveness, especially for refractive elements that require very high temperature to be atomized.

References

[1] J. E. Sansonetti, W. C. Martin, Handbook of Basic Atomic Spectroscopic Data, J. Phys. Chem. Ref. Data **34**, 1559 (2005).

[2] I. E. Olivares and A. E. Duarte, J. Opt. Soc. Am. B, 15, 1932 (1998).

[3] NIST Atomic Spectra Database (ver. 5.3), Online available: http://physics.nist.gov/asd for atomic transitions and emission line intensity.

[4] D. Scarpa, A. Barzakh, D. Fedorov, A. Andrighetto, E. Mariotti, P. Nicolosi and A. Tomaselli, Rev. Sci. Instr. 87, 02B708 (2016).

[5] V. K. Saini, P. Kumar, K. K. Sarangpani, S. K. Dixit and S. V. Nakhe, Rev. Sci. Instr. 88, 093101 (2017).

[6] G. Herzberg: Atomic Spectra and Atomic Structure, (Dover Publications, Inc., New York, 1994).

Automation of Delay Scan Photoelectron Spectroscopy Experiments

H. R. Bundel, Shradha Tiwari, Himanshu Singhal*, Mukund Kumar*, J A Chakera* and Viraj Bhanage

Laser Controls & Instrumentation Division,

** Laser Plasma Division, RRCAT, Indore*

Email:bundel@rrcat.gov.in

Abstract:

Reconstruction of attosecond pulse generated by higher order harmonics of femtosecond laser pulse is carried out by delay scan photoelectron spectroscopy technique. Large no. of spectrogram data sets are required as input to computational frog-crab algorithm applied for reconstruction of attosecond pulse. These huge data sets are acquired by conducting the delay scan photoelectron spectroscopy experiments. A typical experiment runs for ~12 hours and generates thousand of data files.This paper describes the development of automation software to generate 2-d spectrogram data from electron time of flight spectrograph in synchronization with a PZT delay stage, both interfaced to PC.

Introduction:

Reconstruction of attosecond pulse generated by higher harmonics of femtosecond laser pulse[1,2] is carried out by delay scan photoelectron spectroscopy technique. For reconstruction of attosecond pulse, huge set of data is required to be input to frog-crab algorithm of pulse reconstruction, which runs on computing server. Data acquisition in experimental studies of delay scan photoelectron spectroscopy experiments becomes tedious when one needs to acquire data by synchronizing two or more equipments for very long duration. This introduces an added difficulty, since multiple data points are acquired in a short time. In such scenario, human error can render all data useless. Hence, automation of experimental setup becomes essential. This paper describes the development of automation software to generate 2-d spectrogram data from electron time of flight spectrograph in synchronization with a piezoelectric translation stage (PZT).

Experimental Setup Description:

The experimental setup is shown in figure 1. The setup is used to generate the attosecond XUV pulses and characterize their temporal profile. A 1 kHz, 6 mJ, 50 fs Ti:Sapphire laser is used in as a source of XUV pulses. The laser pulse is first splitted into two parts using a beam splitter in the ratio: reflected(R)-20% and transmitted(T)-80%. Transmitted beam is focussed on a gas cell (GC) filled with argon gas due to which higher order harmonics of laser are generated at odd multiple of laser photon energy ($h\nu_L$). These harmonics are then allowed to pass through a 750 nm thick Al filter to remove the co-propagating laser pulse. After filtering, the harmonics are then focussed using a toroidal mirror (TM) onto a low density gas sheath (GS). The reflected part of laser is used to generate cross correlation between harmonics and laser beam. This laser is passed through a piezoelectric transducer controlled delay line and then recombined with harmonic beam on a holed mirror (HM). Harmonics are passed through HM and laser reflected from HM. These two pulses are focused and matched spatially and temporally on GS. Harmonics generated photo-electrons from GS at an energy $(2n+1)h\nu_L - IP$, where IP is ionization potential of gas and 2n+1 is order of harmonic.

The harmonics are generated at odd multiple of laser photon energy, when IR laser pulse also interact with the harmonics it generates with photo-electron at energy $(2n+1)h\nu_L$ - IP ± $h\nu_L$. Energy of these photo-electrons lies in between photo-electrons of harmonics and hence they are known as side bands. It may be noted that each side band is generated from two paths i.e. $(2n-1)h\nu_L$ - IP + $h\nu_L$ and $(2n+1)h\nu_L$ - IP - $h\nu_L$. With the changing delay these two paths interfere with one another and generate a beating pattern at frequency double of laser frequency. This signal is detected by a magnetic bottle time of flight spectrograph (MBTOF) which is composed of a permanent magnet (PM), a solenoid and a micro channel plate (MCP). The time of electron strike on MCP depends on the energy of electron. The electrons detected by the MCP generate a low voltage spike which is amplified by amplifier (~300 MHz bandwidth). Then, this signal is converted into a timing signal using a constant fraction discriminator (CFD). Finally the signal is measured by a time to digital converter (TDC). Trigger to TDC is generated by a photodiode sensing the scattering of laser pulse. TDC generates the spectrum of harmonics and their sidebands by making a histogram of ~10000 events. This histogram shows number of events versus time of event and gives the time at which electron strike MCP. This time is then converted into energy of harmonic orders and spectrum is generated.

Data is gathered by acquiring MBTOF spectrum after changing the position of PZT stage. The control software we have developed controls this aspect of experiment.

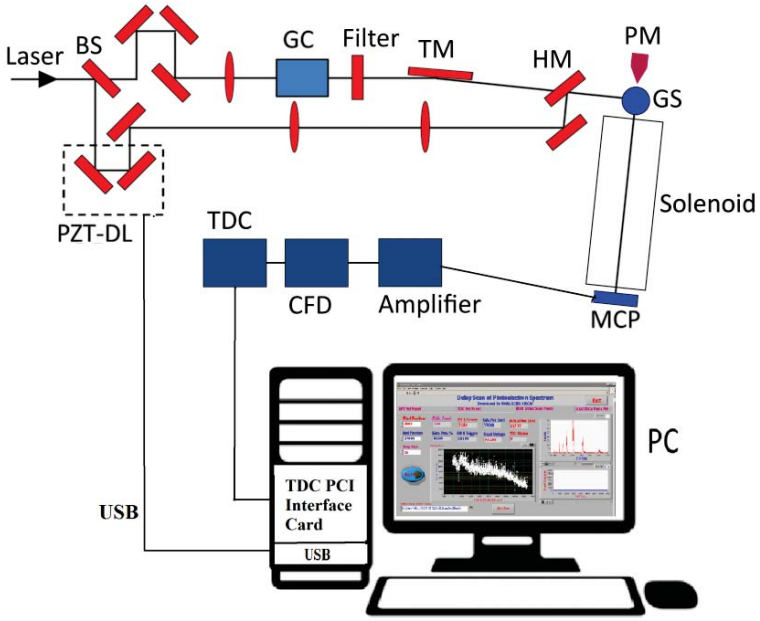

Figure 1: Experimental setup

DAQ System Description:

DAQ system is PC based and runs automation software developed to carry out delay scan photoelectron spectroscopy experiments. The TDC is Roentdek GmbH Model: TDC8HP with resolution of 25 picosecond and range ~1 nanosecond to 1 microsecond. The PZT delay stage is Thorlabs Model: PAZ 009 having resolution: 10 nm and range ~40 micron. The PC connects to PZT delay stage through USB bus. We have installed TDC PCI interface card in PC to acquire data from time to digital convertor (TDC). The communication to PCI TDC interface card is through dynamic-link library and PZT stage is controlled through ActiveX control.

Automation software[3,4] is developed using labview platform which provides GUI to user for acquiring 2-d spectrogram data of events occurring during the experiment. The event driven, dataflow and GUI capabilities of labview are utilized to develop the software.

The software provides various facilities to user to setup the experiment. Automated initialization and configuration of instruments is carried out at application software startup. This ensures reliable data collection during experiments. We have provided user interface (*figure 2a*) for configuring settings of PZT delay stage according to experiment. The user can set calibration constant and position of PZT stage from the dedicated panel. A panel to verify PZT movement is also provided (*figure 2b*).

Similarly, we have provided a separate panel (*figure 2c*) to configure settings of TDC controller for ease of operation. The software allows user to set time of flight (TOF) range, TOF bin size, TOF offset, time of exposure, acquisition channel, trigger channel, pre-delay and post-delay for stabilization of TDC data. It also provides user to save or reload configuration data file. We have also provided a panel to carry out the initial settings for a particular experiment (*figure 2d*).

The software provides a separate panel named 'Delay Scan Panel'(*figure 2e*) for data acquisition. This panel allows user to set delay scan start position, end position, scan step and data folder for saving. The acquired TDC data with the changing position of delay stage is plotted online. The TDC histogram is also plotted online. All data capturing is synchronized with trigger received by TDC.

During experiment TDC data is acquired at user defined delay step (minimum 10nm) from start position to end position (max. 40 micron) as per preset scan range. Data files with name of current delay position and time stamp is generated. After each experiment a new data directory is generated by software for easy handling large number of data files. Acquired data of total TDC counts versus delay position is plotted in a graphical window on PC screen for monitoring purpose. The multiple data sets thus collected for several runs of experiment is then saved in the PC in spreadsheet format for further analysis. The saved data can be also viewed offline by importing save data in 'Load Data from File' panel (*figure 2f*).

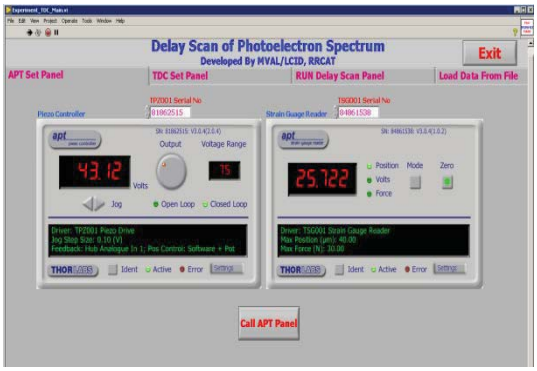

Figure 2a: Delay Stage Configuration Panel

Figure 2b: Delay Stage Control Sub Panel

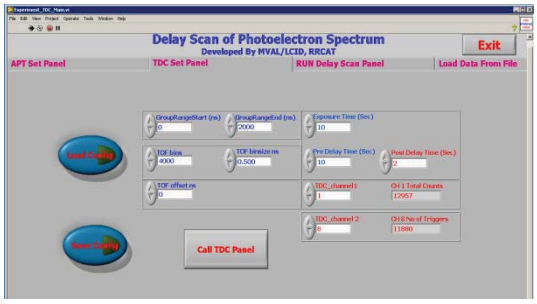

Figure 2c: TDC Configuration Panel

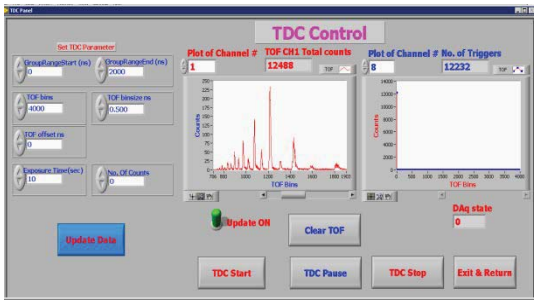

Figure 2d: TDC Control Sub Panel

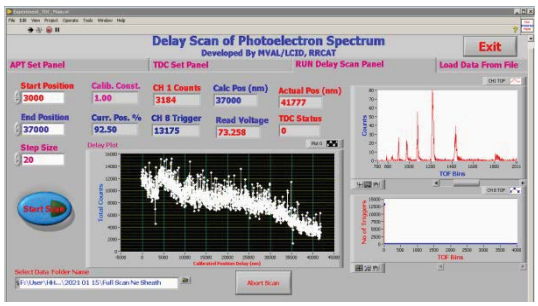

Figure 2e: Delay Scan Panel

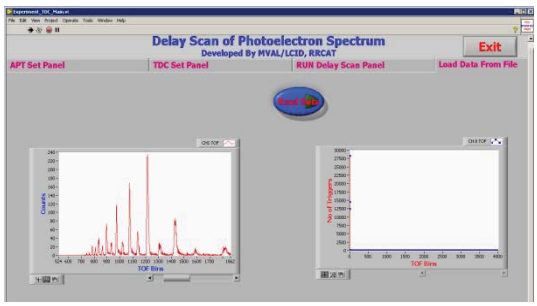

Figure 2f: Load Data File Panel

Figure 2(a to f): Automation Software screenshots

Results and Discussion:

A typical experiment runs for around 12 hours and the developed DAQ software generates ~2000 no. of 2-d spectrogram files for each run. The large no. of data files thus generated by the software, are fed to server running computational frog-crab algorithm. The algorithm then generates attosecond pulse temporal profile. The software is being used in the laboratory for continuous data acquisition. This automation has resulted in automated data acquisition and storage in a compatible format for computing server. This automation saves a lot in terms of time & efforts and provides user with an easy platform to conduct their experiments.

References:

1. "Complete temporal reconstruction of attosecond high-harmonic pulse trains" Kyung Taec Kim, Dong Hyuk Ko, Juyun Park, Valer Tosa and Chang Hee Nam, *New Journal of Physics* **12,** 083019 (13pp) (2010)

2. "Frequency-resolved optical gating for complete reconstruction of attosecond bursts" Y. Mairesse and F. Quéré, *PHYSICAL REVIEW* **A 71**, 011401(R) (2005)

3. "Automation of Resonant Ultrasound Spectroscopy Experiments" Bundel H.R., Tiwari Shradha, Chandra Sharath L. S., Deshpande P. P. and Bhanage Viraj, *National Laser Symposium (NLS-26)*, BARC, Mumbai, Dec., 20-23, 2017

4. "Software framework for automation of Laser Physics Experiments" Pathak A.K., Deshpande P.P., Bhanage V.P., Tiwari S., Joshi M.J., Bundel H.R., Navathe C.P., *National Laser Symposium (NLS-24)*, RRCAT, Indore, Dec., 2-5, 2015

Improving the Signal-to-Noise Ratio of Atomic Transitions in LIBS Using Two-dimensional Correlation Analysis.

Linga Murthy Narlagiri, S. Venugopal Rao*

Advanced Center of Research in High Energy Materials (ACRHEM),
University of Hyderabad, Hyderabad 500046, Telangana, India
Corresponding author e-mail: soma_venu@uohyd.ac.in OR soma_venu@yahoo.ac.in

Abstract: We demonstrate the improvement in the signal-to-noise ratio of the LIBS spectra using the 2D correlation spectroscopy analysis, the time resolved LIBS spectra from the gated spectrometer is used for this analysis. The correlations between LIBS peaks were also visualized. Correlation strengths of the atomic transitions were visualized in case of Aluminium (Al), Copper (Cu), and Brass targets. The improvement is demonstrated in case of aluminium transitions and the diagonal of the 2d analysis is used for the demonstration of the improvement in the spectra in case of LIBS peaks of aluminium.

Introduction: The plasma formed when the intense pulsed laser interacts with the target material emits ionic and atomic emissions during the recombination. This analytical spectroscopy technique is called laser induced breakdown spectroscopy (LIBS)[1]. LIBS was applied on diverse samples like samples from mining, archaeology, explosives, metals, alloys, etc. Femtosecond LIBS also contains molecular transitions which can be used in further understanding the material[2-4] used as target.

Experimental Procedure: Figure 1 depicts the experimental schematic of the nanosecond LIBS setup. A nanosecond Nd: YAG laser of 7 ns pulse duration at 532 nm with an average pulse energy of 42 mJ was used for the breakdown of the samples.

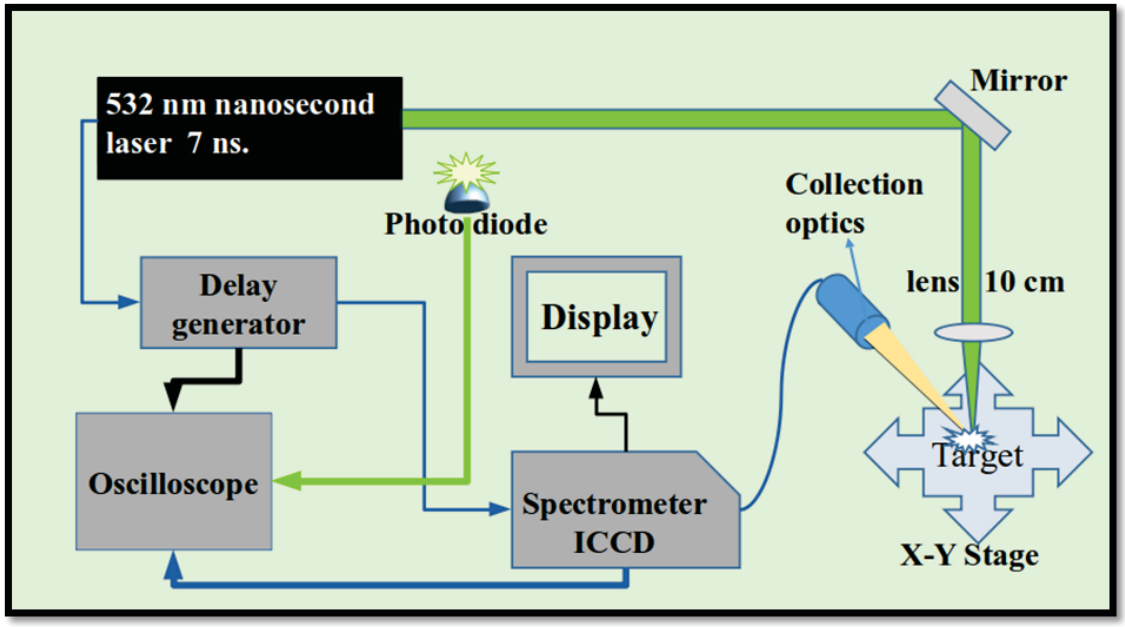

Fig. 1 *The schematic of the LIBS experiment where the plasma emissions are collected using the gated spectrometer which is triggered using the reference signal from the laser via delay generator.*

The collected LIBS signal was fed to the ICCD and spectrometer combination and as the plasma emissions from metals are high the initial delays are kept at 1 µs and also the gate width of 1 µs was set. Each spectrum is the accumulation of 10 acquisitions. The exposure time was set to 2 milliseconds, with a gate delay of 1 µs including all the insertion delays. A 600 µm optical fiber was used to couple the collected light to the spectrometer and ICCD, which was triggered by the delay generator output. The nonlinear variations in the intensity of the peaks with increasing the compositions are the primary motivation for this work to study the correlation between the transitions in the LIBS spectra.

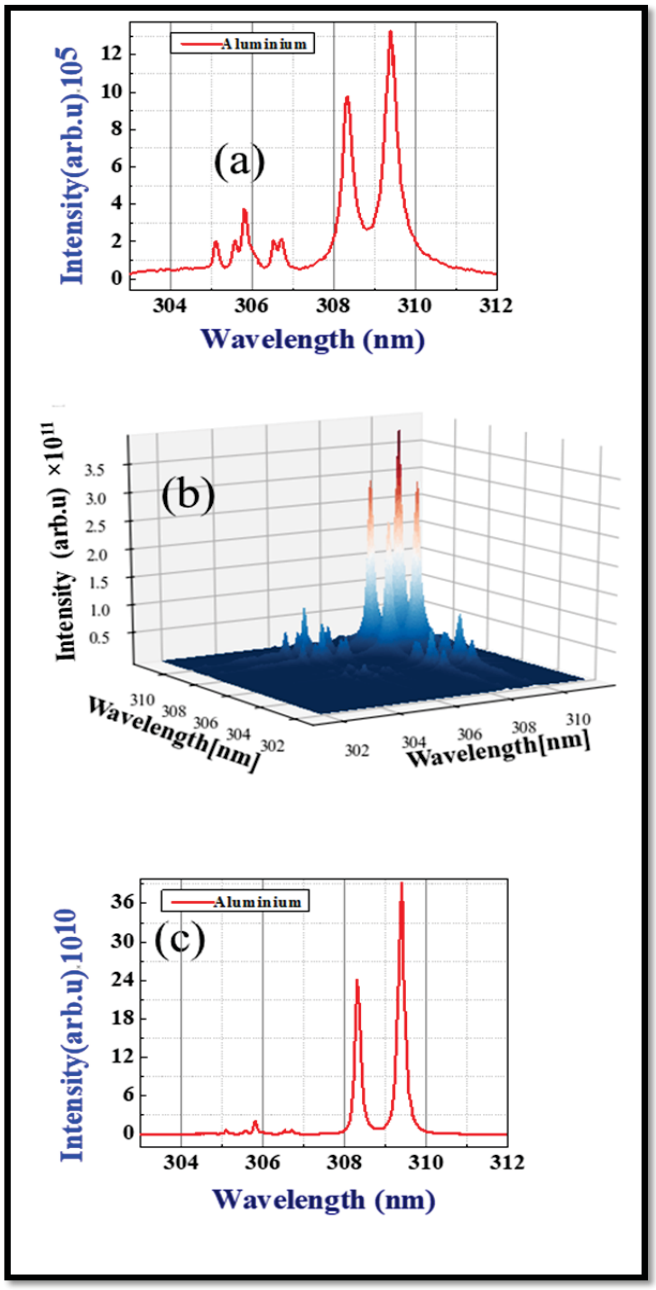

2D correlation spectroscopy was first introduced by Isao Noda[5]. The spectra with systematic perturbations like electric field, magnetic field, chemical composition, and also the time resolved spectra are used for studying the correlations between transitions in the spectrum. It is used for various spectroscopy methods like infrared and Raman spectroscopy.[6,7] Here in this study the time-resolved LIBS spectra is used for the correlation and signal-to-noise ratio improvement studies. The cross-peaks gives the information on the correlation strength of the peaks.[8] The figure.2 contains the original spectra and the surface plot of the 2D correlation analysis and the diagonal extracted from the analysis. The contour plots of the 2D correlation analysis the three different targets in used for the analysis are shown in the figure 3 below.

of

Fig. 2 *The regular LIBS spectra of (a) Aluminium target in the spectral range of 303-312 nm and the corresponding (b) 2D correlation spectra and (c) diagonal of the 2D correlation analysis of the LIBS spectra is plotted.*

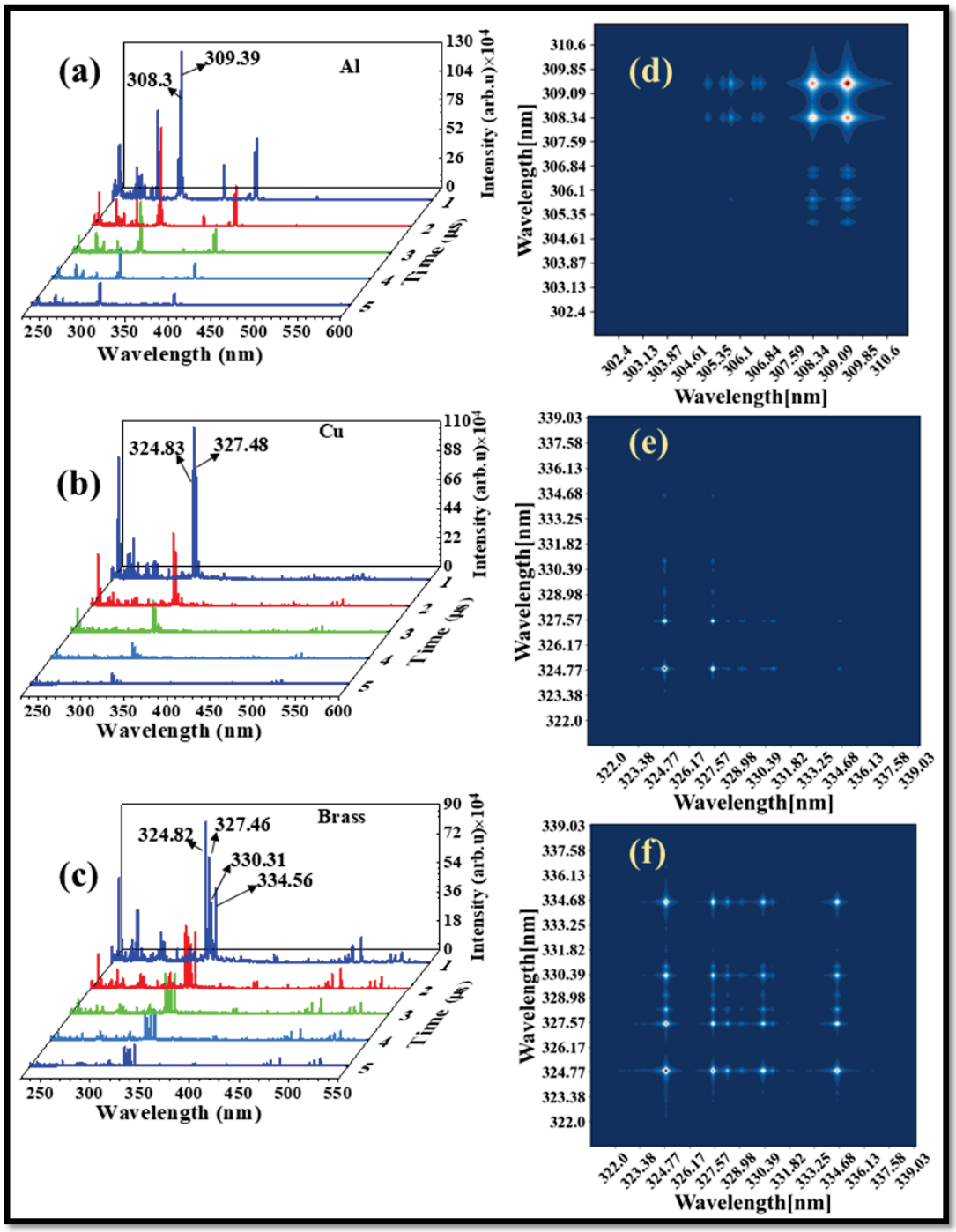

Fig. 3 *The time-resolved LIBS spectra of (a) Aluminium (b) Copper (c) Brass at five different gate delays with regular interval of 1 μs and are used for the 2D correlation studies of (e) Aluminium (f) Copper (g) Brass targets, respectively.*

Results and Discussion:

The S/N ratio was improved and the correlations between the transitions were visualised in the above two figures. Here the off-diagonal peaks, called cross-peaks, in the 2D plots show the correlation strength between the peaks. The diagonal peaks are called auto-peaks. The intensity of the diagonal peaks depends both on the intensity and the correlation between the transitions in the regular LIBS spectra. It is observed that the cross-peaks are more intense than the actual peak at 308.3 nm. In copper the 324.83 nm and 327.48 nm peaks are

correlated which was anticipated. It was observed that the zinc peaks in the brass are correlated to the copper peaks in the figure 3(f) zinc first ionised peak at 334.5 nm is correlated with the copper first ionised peaks. Further studies need to be done for better understanding the correlations from the 2D analysis which might turn into a potential tool for data analysis in LIBS.

Conclusions:

Femtosecond LIBS spectra usually contain molecular emissions.[9,10] Those studies can be extended using the presented analysis aiding in improvement of the signal-to-noise ratio in cases where the S/N ratio is poor. For example, in the case of stand-off LIBS the S/N ratio diminishes as the distance is increased[11]. The images can also be used for deep learning models like convolution neural networks (CNN) and also the diagonal of the 2D analysis for classification, prediction studies.

References:

1. S. N. Thakur and J. P. Singh, Fundamentals of laser induced breakdown spectroscopy. In *Laser-induced breakdown spectroscopy*, Elsevier, 2007, 3-21.
2. S. S. Harilal, J. Yeak, B. E. Brumfield, J. D. Suter and M. C. Phillips, Dynamics of molecular emission features from nanosecond, femtosecond laser and filament ablation plasmas, *Journal of Analytical Atomic Spectrometry*, 2016, **31**, 1192-1197.
3. S. A. Kalam, N. L. Murthy, P. Mathi, N. Kommu, A. K. Singh and S. V. Rao, Correlation of molecular, atomic emissions with detonation parameters in femtosecond and nanosecond LIBS plasma of high energy materials,*Journal of Analytical Atomic Spectrometry*, 2017, **32**, 1535-1546.
4. E. N. Rao, P. Mathi, S. A. Kalam, S. Sreedhar, A. K. Singh, B. Jagatap and S. V. Rao, Femtosecond and nanosecond LIBS studies of nitroimidazoles: correlation between molecular structure and LIBS data, *Journal of Analytical Atomic Spectrometry*, 2016, **31**, 737-750.
5. I. Noda, A. E. Dowrey and C. Marcott Noda, Isao, et al. "Generalized two-dimensional correlation spectroscopy." *Applied Spectroscopy,* **54(7)**, 2000, 236A-248A.
6. I. Noda, Generalized two-dimensional correlation method applicable to infrared, Raman, and other types of spectroscopy, Applied *Spectroscopy*, 1993, **47**, 1329-1336.
7. I. Noda, A. E. Dowrey and C. Marcott, Two-Dimensional Infrared (2D IR) Spectroscopy, *Modern polymer spectroscopy* ,1999, 1-32.
8. M. A. Czarnecki, Interpretation of two-dimensional correlation spectra: science or art?, *Applied Spectroscopy*, 1998, **52**, 1583-1590
9. C. G. Parigger, Atomic and molecular emissions in laser-induced breakdown spectroscopy, *Spectrochimica Acta Part B: Atomic Spectroscopy*, 2013, **79-80**, 4-16.
10. C. G. Parigger and J. O. Hornkohl, Computation of AlO $B^2\Sigma^+ \rightarrow X^2\Sigma^+$ emission spectra *Spectrochimica Acta Part A: Molecular and Biomolecular Spectroscopy*, 2011, **81**, 404-411.
11. Murthy, N. L., Kalam, S. A., & Rao, S. V. Stand-off Femtosecond Laser Induced Breakdown Spectroscopy of Metals, Soil, Plastics and Classification Studies. In *2019 Workshop on Recent Advances in Photonics (WRAP),* 2019, **1-3**, IEEE.

Assessment of hand sanitizers using vibrational spectroscopy methods

Soumyabrata Banik[1], Sindhoora Kaniyala Melanthota[1], Krishna Kishore Mahato[1], Anjana Anandan Vannathan[2], Sib Sankar Mal[2], Nirmal Mazumder[1,*]

[1]*Department of Biophysics, Manipal School of Life Sciences, Manipal Academy of Higher Education, Manipal, Karnataka, India-576104*

[2] *Materials and Catalysis Lab, Department of Chemistry, National Institute of Technology Karnataka, Surathkal, Karnataka, India-575025*

*Corresponding author Email**:** nirmaluva@gmail.com

Abstract:

With the advent of public health emergencies, maintaining proper hygiene can lower the risk of contamination and diseases. Recently, the use of hand sanitizer (HS) has seen increasing use with the outbreak of COVID-19. Even though very basic in composition, the alcohol concentration in the HS plays a predominant role in the process of disinfection. Thus, assessing the quality of HS is important. In this study, different vibrational spectroscopic techniques were used for the assessment of various commercially available HS along with in-house prepared HS using the WHO protocol. Fourier-transform infrared spectroscopy (FTIR) and Raman spectroscopy were used to quantify the alcohol and water concentration in the HS. The presence of ethanol and isopropanol in HS were confirmed using FTIR based on absorption peaks at 1050 cm^{-1} and 1221 cm^{-1} respectively, whereas the peak at 1650 cm^{-1} helped to quantify the amount of water in HS. Further, Raman peaks at 881 cm^{-1} and 816 cm^{-1} also confirmed the presence of ethanol and isopropanol added to the samples under study.

Keywords: Disinfectant**,** Hand sanitizers, Fourier-transform infrared spectroscopy, Raman spectroscopy

Introduction:

Vibrational spectroscopic methods are used to study and understand the matters' composition, electronic, and physical structure based on the interaction of matter with radiative energy thereby causing vibration of the chemical bonds. Its application has been found in almost all the experimental disciplines of science. Vibrational spectroscopies have been used to detect the minerals constituents in soil or rocks, determine the various compounds in fruits, vegetables, and oils, study the progression of chemical reactions, perform elemental analysis in various biological and non-biological samples, detect toxic compounds and pathogens in water, food or blood are among a few to be mentioned [2-6]. Apart from these, spectroscope has also been used to study and analyse various components to perform a qualitative and quantitative assessment of multiple solutions. With the advent of public health adversaries, the need of maintaining proper hygiene can reduce disease transmission to a great extent. In the recent outbreak of COVID-19, studies have shown that using HS can be an effective way to avoid falling sick and prevent the spread of the disease [7]. HS is either commercially available or can be prepared using the WHO-approved protocol [8]. Increasing demand of HS have seen a lot of variation in the alcohol level in the same which plays the most important part in disinfection. Also, many manufacturers were also found to add harsh chemicals, which can cause allergic reactions in the user. Thus, it is important to assess HS for their quality control. Various methods such as gas chromatography or alcoholmeter are used for assessment of HS but they are often don't give all the necessary information or being expensive to use. In this work electromagnetic radiation-based vibrational spectroscopic techniques have been used as an alternative approach for quantitative and qualitative analysis of alcohol-based HS. These methods are rapid, fast, less-expensive and are much easy to use. With the rapid development of modern spectrometer in illumination sources and detectors, the compact instruments are manufactured and can be easily carried to a remote location for sample analysis.

Methodology:

Commercial HS from eight different brands were purchased from the local market for use in experiments and have been labelled as A-H for ease in representation. Further, HS were freshly prepared in-house using the WHO-approved protocol with varying concentration of alcohols (ethanol & isopropanol- from 50-100 %) along with water, glycerol and 3% hydrogen peroxide and used for the spectroscopic analysis at room temperature. The vibrational spectroscopic techniques such as FTIR spectroscopy and Raman spectroscopy were used in this

study for the evaluation of different HS. ATR-FTIR spectra were recorded using a Bruker 4000 (USA) spectrometer in the spectral range of 4000–600 cm^{-1} to analyse the chemical composition of HS. A portable Near-IR Raman spectrometer (AvaRaman-785 TEC, Avantes BV, The Netherlands) was used to record and analyse various HS sample's Raman spectra. The system is equipped with a diode laser (wavelength and bandwidth are 785 nm and < 0.2 nm), spectrometer (AvaSpec-ULS2048LTEC) with grating (785-1080 nm), slit-25, DCL-UV/VIS, TE cooled, Raman probe, and sample holder. The samples were loaded (200 µL in each well) in a 96-well plate (Eppendorf, Germany), and the laser is focused using Raman probe which was placed perpendicular to the plate at a focal length of ~ 1 cm for spectrum acquisition. A Raman spectrum was recorded from the blank well for background vibrational spectrum. The integration time is 10 secs for a single spectrum. The average spectrum was plotted after acquiring three spectra from the same field of view. Recorded spectra were analysed over the wavenumber range 0–3600 cm^{-1}.

Results:

FTIR spectroscopy:

FTIR was used to study the commercially available HS as well as the different grades of HS prepared in-house according to the WHO protocol. Fig.1A and B shows the FTIR spectra of various brands of HS. Upon spectral analysis of commercial HS, they were matched with the spectra of undiluted ethanol and isopropanol. Based on this, the type of alcohol present in an HS was identified and the HS was divided into two groups: HS with ethanol (A, B, C, D, E) and isopropanol (F, G, H), respectively. The FTIR spectra of ethanol and isopropanol as shown in Fig. 1 inferred that ethanol has a characteristic peak at 881 cm^{-1} and isopropanol at 817 cm^{-1} due to symmetric C-O stretching in the molecule. Moreover, ethanol-based HS shows a peak at 1050 $cm^{-1,}$ whereas isopropanol-based HS shows at 1126 cm^{-1} due to characteristic asymmetric C-O stretch. The peak at 1650 cm^{-1} indicates the characteristic -OH bending mode of water.

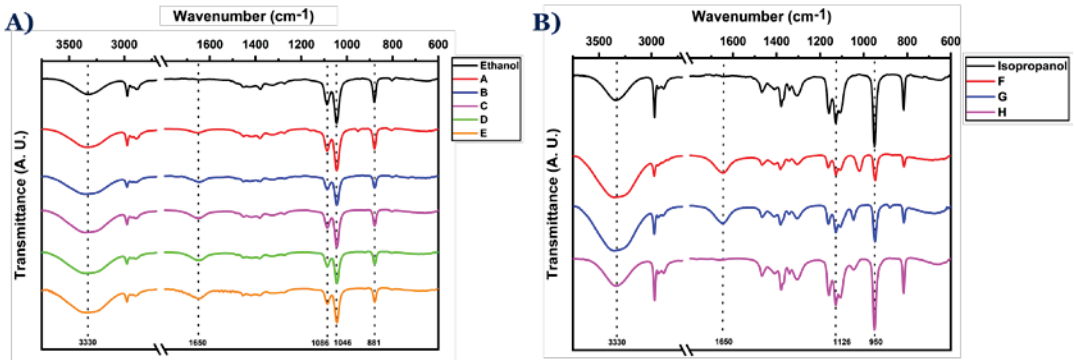

Fig. 1: *FTIR spectra of various brands of HS; A) ethanol based, and B) isopropanol based. The major spectral features associated with alcohols and water are indicated in the graphs.*

Quantifying the amount of alcohol content is essential to meet the quality control and assurance process of HS. FTIR measurements were undertaken for different grades of HS with various alcohol (ethanol and isopropanol) concentrations from 50-100%. Fig. 2A and E shows the combined FTIR spectra of the HS with varied ethanol and isopropanol concentrations respectively. There are three prominent peaks observed at 881 cm^{-1}, 1046 cm^{-1}, and 1650 cm^{-1}, which correspond to symmetric C-O stretch, asymmetric C-O stretch, and O-H bending water mode, respectively [9-10]. It was also observed that the percentage of transmittance changes with an increase in ethanol concentration. The transmitted intensity at the peaks 1046 cm^{-1} and 1650 cm^{-1} were observed to gradually decreases and increases with an increase in ethanol concentration, respectively (Fig. 2B and C). The calibration curve was plotted considering the variation of intensities in 1046 cm^{-1} and 1650 cm^{-1} with the change in concentrations, as shown in Fig. 2D, suggests a reasonable coefficient correlation (R^2 = 0.96 & 0.98 respectively) values. Similarly, HS with varied isopropanol concentrations were also examined and three prominent peaks were observed at 817 cm^{-1}, 1127 cm^{-1}, and 1650 cm^{-1}, which correspond to symmetric C-O stretch, asymmetric C-O stretch, and O-H bending mode of water, respectively. Similarly, the transmitted

intensity at 1127 cm^{-1} and 1650 cm^{-1}, were observed to change with the variation in isopropanol concentration and the calibration curve was plotted considering the same suggested a good coefficient correlation (R^2) values as shown in Fig. 2H.

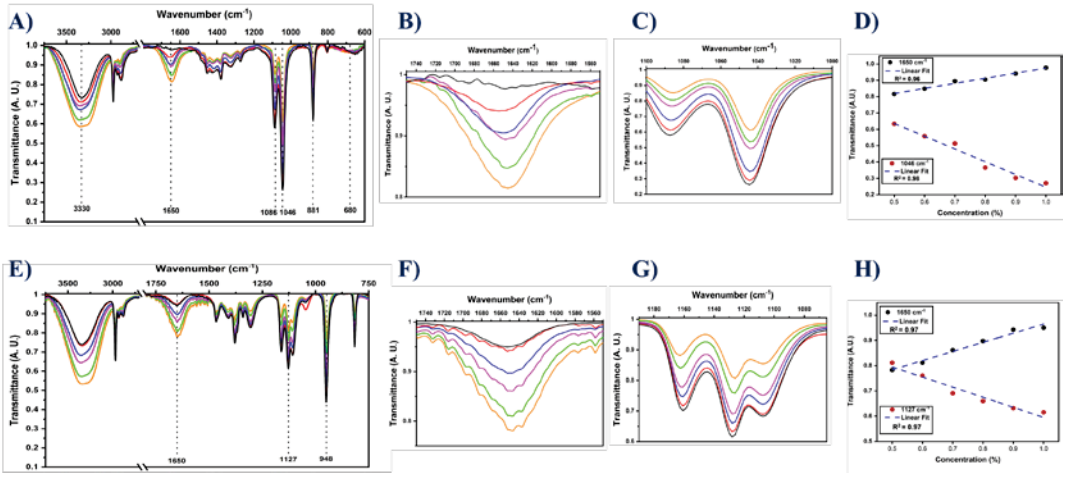

Fig. 2: *FTIR analysis of in-house prepared HS. (A)and (E)shows the spectra of in-house prepared HS with various concentrations of ethanol and isopropanol respectively. (B) and (F) shows the variation of the FTIR transmittance as a function of alcohol concentration whereas (C) and (G) shows transmittance as a function of water. (D) and (H) are the integrated linear plots with varying alcohol and water concentration. The data is plotted as a function of transmittance intensity. The statistical values estimated for each recombination path are reported.*

The plotted wavenumber of the HS with different concentrations of alcohol shows a shift in peak wavenumber with the change in alcohol concentration. Even though FTIR provides a simple, fast, and accurate process for analysis of HS, often overlapping of different functional groups are observed. Thus, a more accurate spectroscopic method based on Raman scattering which provides fingerprints for different chemical compounds should be further employed.

Raman spectroscopy:

The different ingredients added to formulate HS as well as the variation in alcohol concentration among the HS was determined using Raman spectroscopy. Raman spectra of the different grades of HS were acquired and analysed. Fig. 3A and B show the Raman spectra of ethanol and isopropanol based commercial HS. Raman spectrum can distinguish them due to specific Raman fingerprints at 883 cm^{-1} (ethanol) and 816 cm^{-1} (isopropanol) based HS [11].

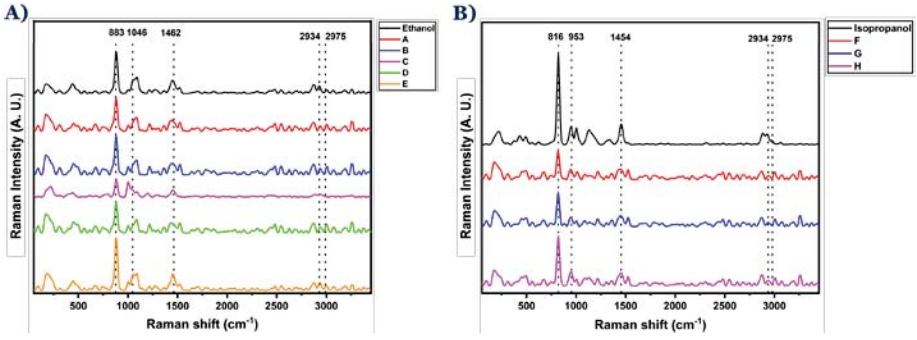

Fig. 3: *Raman spectra of various brands of HS; A) ethanol based, and B) isopropanol based. The major spectral features associated with alcohols and water are indicated in the graphs.*

Ethanol and isopropanol-based HS were prepared in-house according to the WHO protocol. Raman spectra of these HS were acquired with varying concentrations of ethanol and isopropanol. Fig. 4A and D shows the acquisition and analysis of Raman spectra of ethanol and isopropanol-based HS with concentration ranges from 50% to 100% respectively. The fingerprint Raman intensity of 883 cm^{-1} corresponding to C-C-O symmetric

stretching vibration modes in ethanol, increases with an increase in concentration as shown in Fig. 4B. The same has been confirmed with the linear plot indicating that Raman spectroscopy can identify the ethanol-based HS with varying concentrations of alcohol. The Raman spectra for isopropanol-based HS with varying alcohol concentrations were acquired, and analysed is shown in Fig. 3D. The peak at 816 cm^{-1} was observed to be the fingerprint peak related to isopropanol, which rises due to the C-C-O stretching in the isopropanol molecule and was found to vary in intensity with change in concentration.

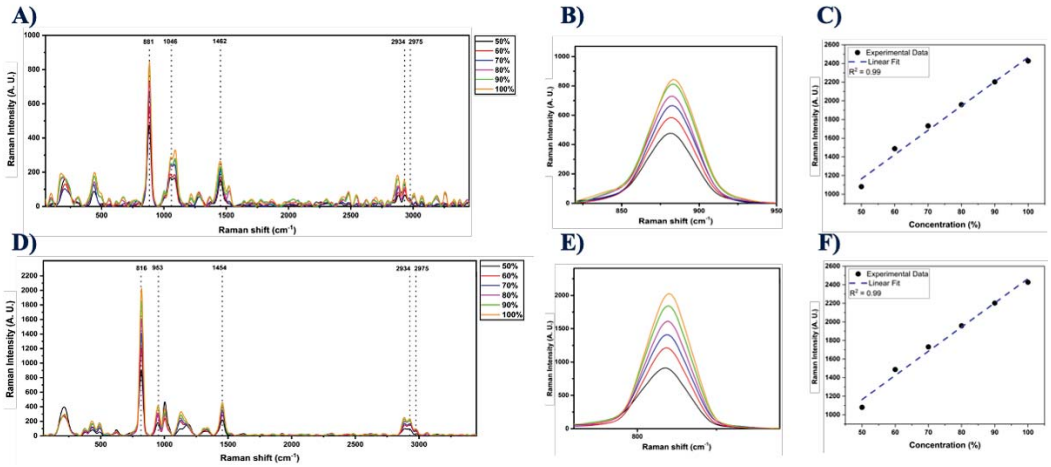

Fig. 4: *Raman analysis of in-house prepared HS. (A)and (D) shows the spectra of in-house prepared HS with various concentrations of ethanol and isopropanol respectively. (B) and (E) shows the variation of the Raman intensity as a function of alcohol concentration. (C) and (F) are the integrated linear plots with varying alcohol. The data is plotted as a function of transmittance intensity. The statistical values estimated for each recombination path are reported.*

The variable intensities, as shown in Fig. 3E were also plotted, showcasing to increase linearly. Apart from these prominent peaks, various other peaks can also be inferred from the spectrum and it can be observed that ethanol shows C–O stretching at 1046 cm^{-1} and CH_3 rocking at 1079 cm^{-1} indicated by two small bands in the same region as observed in the spectra. Anti-symmetric vibration of CH_3 in ethanol is also observed at 1462 cm^{-1}. Further, CH_2 asymmetric stretching vibration modes at 2934 cm^{-1} and CH_3 asymmetric stretching vibration modes at 2975 cm^{-1} were also observed [12-13].

Conclusion:

In this work, various vibrational spectroscopic techniques were applied to characterize commercial HS and are compared with in-house prepared HS to determine the efficiency of the technique. FTIR and Raman spectroscopy being vibrational spectroscopic methods, efficiently demonstrated their ability for the quantification of alcohol and water content in the HS. They also elucidated its role in quantitative and qualitative identification of the chemical compositions of the HS. FTIR confirmed the presence of ethanol or isopropanol in HS based on the presence of absorption peak at 1050 cm^{-1} and 1221 cm^{-1} respectively. Further, the amount of water content in the sanitizer could be quantified based on the intensity of the -OH bending peak at 1650 cm^{-1}. Apart from this, other basic components of the HS such as oxidising agent (H_2O_2) or glycerol can also be identified for their presence in the HS with FTIR spectroscopy. On the other hand, Raman spectroscopy detected the presence of different constituents based on the characteristic's vibration of the bonds specific to the chemicals. It could distinguish between the presence of ethanol or isopropanol based on the peaks at 881 cm^{-1} and 816 cm^{-1} respectively. This method was used in complement to FTIR as Raman peaks are more specific for the distinction of chemical bonds. Therefore, these two spectroscopic techniques provided alternatives in probing and characterizing the different constituents of the HS.

Acknowledgement:

The authors thank the Department of Science and Technology (DST), Government of India, for the financial support (DST/INT/THAI/P-10/2019 and DST/INT/BLG/P-03/2019). NM thank Dr. K. Satyamoorthy, Director, Manipal School of Life Sciences (MSLS), MAHE, for his encouragement and Manipal Academy of Higher

Education, Manipal, for providing the infrastructure and facilities. SKM thanks MAHE for Dr. T.M.A. Pai Ph.D. fellowship. SSM thank the Vision Group on Science and Technology (VGST, No. KSTePS/VGST-RGS - F/2-18-19/GRD No.805|315) for the financial help.

References:

1. D. N. Sathyanarayana, *New Age International* (2015).
2. C. Hecker, J. H. Dilles, M. Meijde and F. D. Meer, *Geochem Geophys Geosyst*. **13**, 3 (2012).
3. K. I. Poulli, G. A. Mousdis and C. A. Georgiou, *Anal Bioanal Chem*. **386**, 5 (2006).
4. J. Ullrich, R. Moshammer, A. Dorn, R. Dörner, L. P. H. Schmidt and H. Schmidt-Böcking, *Rep Prog Phys*. **66**, 9 (2003)
5. R. Sahu and S. Mordechai, *Future Oncol*. **1**, 5 (2005).
6. D. K. Sarfo, A. Sivanesan, E. L. Izake and G. A. Ayoko, *RSC Adv*. **7**, 35 (2017).
7. Centers for Disease Control and Prevention. Prevention of Coronavirus Disease 2019 (COVID-19). https://www.cdc.gov/coronavirus/2019-ncov/prepare/prevention.html. Accessed January 2021.
8. Guide to local production: WHO-recommended handrub formulations. https://www.who.int/publications/i/item/WHO-IER-PSP-2010.5. Accessed December 2020.
9. P. R. Griffiths, *John Wiley & Sons* (2006).
10. B. C. Smith, *Spectrosc*. **32**, 4 (2017).
11. Z. Jin, Q. Chu, W. Xu, H. Cai, W. Ji, G. Wang, B. Lin and X. Zhang, *IEEE Photonics Technol Lett*. **30**, 4 (2018).
12. A. Emin, A. Hushur and T. Mamtimin, *AIP Adv*. **10**, 6 (2020).
13. I. H. Boyaci, H. E. Genis, B. Guven, U. Tamer and N. Alper, *J Raman Spectrosc*. **43**, 8 (2012).

Development of a time-of-flight mass spectrometer for isotope selective photoionization of medical isotopes

A.U. Seema [1*], D. Biswal [1], R.C. Das [1,2] and Asawari. D. Rath [1,2]

[1] *Beam Technology Development Group, Bhabha Atomic Research Centre, Trombay, Mumbai – 400085,* India.

[2]*Homi Bhabha National Institute, Training School Complex, Anushaktinagar, Mumbai 400094, India*

[*]Email: auseema@barc.gov.in

Abstract

We have indigenously developed a high temperature effusive atomic beam based linear time-of-flight mass spectrometer for experimental demonstration of isotope selective photoionisation of medical isotopes. The atomic vapour source developed can be operated at high temperatures and is efficient to generate effusive atomic beam of most of the elements of interest. The performance of the mass spectrometer was tested by carrying out single colour multi-photon photoionisaton of atomic samarium. We have achieved a mass resolution better than 500 for this instrument which is desirable for isotope selective photoionisation studies of isotopes of medical importance like Sm, Yb and Lu.

1. Introduction

Time-of-flight mass spectrometer (TOFMS) has been an attractive choice of instrumentation for spectroscopic diagnosis due to its accurate mass determination, rapid data acquisition and high sensitivity. The basic working principle involves acceleration of ions through an electric field of known strength, which confers the same kinetic energy to all ions of equal charge. After gaining the kinetic energy, the ions are allowed to travel through a field-free drift tube. The time taken by the particle to reach the detector placed at the end of the flight tube is directly proportional to square root of mass-to-charge ratio $(m/q)^{1/2}$. Hence by measuring this flight time accurately, the m/q of the particles can be calculated.

The simplest TOFMS consists of an ion source in a high vacuum chamber, ion extraction and acceleration stages and a detector situated at the end of an evacuated drift tube. The ions formed in the laser-atom interaction zone are accelerated out of the source towards the collector by either one or a series of constant electric fields. Pulsed or continuous fields can be used for acceleration. In either case, the velocity of the ions in the field-free region is a function of their m/q values. Hence the arrival of ions of different m/q values can be registered in time by a high temporal resolution detector placed at the end of the drift tube. If only singly charged ions were present, then the group of ions having the lightest mass will reach the detector first, followed by the groups with successively heavier masses. Thus, it is possible to get the entire mass spectrum for each ionising pulse in every few micro seconds. Hence the use of a TOFMS as a spectroscopic diagnostic tool in isotope selective photoionization experiments will have the advantage that, it is possible to determine the relative isotopic ratios more accurately, even in the presence of random variations in the source conditions, provided the variations affect different masses in an analogous manner. The TOFMS developed for the photoionization experiments is a Wiley-McLaren type[1] mass spectrometer. The schematic of the time-of-flight mass spectrometer and the experimental set-up used for the photoionization experiments are shown in the Figs.1 & 2 respectively.

2. TOFMS components

The TOFMS consists of a high temperature oven kept in a high vacuum chamber for producing the atomic vapours of the element under consideration, a series of electrodes for extracting and accelerating the photoions and a drift tube. At the end of the drift tube, a micro channel plate (MCP) detector is used for detecting the arrival time of different ions with high accuracy. We have used a Baspik make chevron type MCP (Model: DV2510A) with a gain of 10^7 at an operating voltage of 2400 V and a rise time less than 1ns.

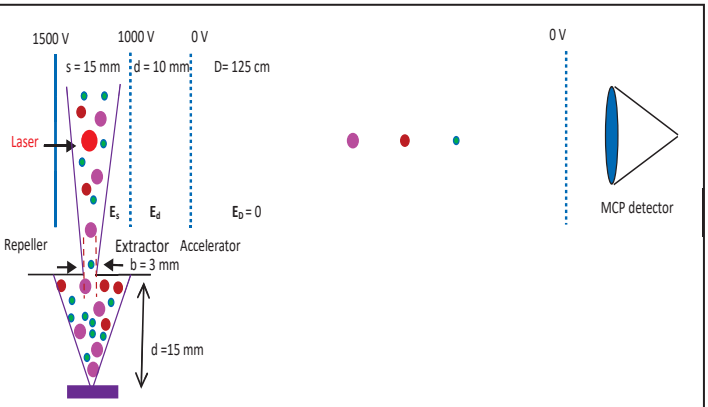

***Fig. 1**: Schematic of TOFMS*

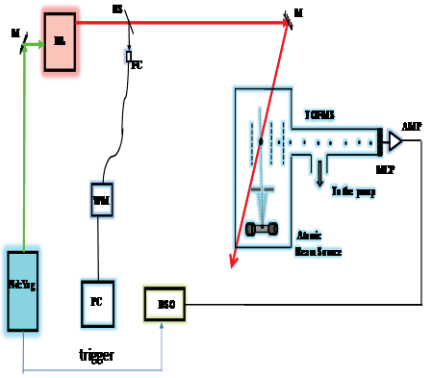

***Fig. 2**: Schematic of the experimental set-up*

A Pfeiffer, make turbo molecular pump HiPace 400 with a pumping speed of 355 l/s for N_2 backed by of magnetically coupled rotary vane pump model, Duo 10M with a pumping speed of 10 m^3/h is used to evacuate the chamber to a pressure better than $2x10^{-6}$ mbar which is required for carrying out the photoionisation experiments. Two full range gauges are used in the chamber at two different locations, one connected in the ionisation chamber and the other connected nearer to the detector for the online monitoring of the vacuum conditions inside the TOFMS. The detailed design aspects are given in the following section.

2.1 Atomic Vapour Source

A resistively heated, water cooled atomic vapour source was developed for producing atomic vapours of Sm. The oven was made of tantalum foil of thickness 25 μm rolled into a cylinder of radius 7mm and length 7 cm. The two ends of the rolled tantalum sheet are closed with caps made of molybdenum. Two water cooled copper feedthroughs are used to hold the oven assembly. The electrical connections to the oven are made through copper feed throughs. The molybdenum caps provide electrical contact between the tantalum oven and the copper feed throughs. Atomic vapours of Sm are generated by resistively heating few hundred mg of Sm metal sample placed inside the tantalum oven. The vapours effuse out of a hole of diameter 1mm drilled at the centre of the tantalum oven. To reduce the Doppler width of the atomic beam source, the Sm vapour effusing out of the oven orifice of 1mm diameter is further apertured by using a fixed circular aperture of diameter, b = 3mm kept at a distance of, d = 15mm from the oven orifice as shown in Fig. 1.

The reduced Doppler width[2] is given by,

$$\Delta\nu_{red} = \sin\theta\, \Delta\nu_D$$

,where $\Delta\nu_D(\mathrm{Hz}) = 7.16X10^{-7}\nu_0(\mathrm{Hz})\sqrt{\frac{T(K)}{M(amu)}}$

is the Doppler width at equilibrium temperature T, M atomic mass in amu and ν_0 is the line centre of absorption line profile. The reduced Doppler width of the samarium atomic absorption line in the interaction zone at 800K is calculated to be ~ 100 MHz.

2.2 Time-of-Flight Analyzer with Ion optics assembly

In present system, the TOF assembly, a linear flight tube with double stage extraction is used. The extraction stages are separated by three ion optics plates namely, repeller, extractor and accelerator. Repeller and extractor are15mm apart whereas the separation between extractor and accelerator is kept at 10 mm using insulator (macor) beads. These three ion optics plates are circular plates of 70 mm diameter and are made from 2 mm SS sheet. The extraction and the accelerator plates have circular aperture of diameter 20 mm at the center, which are covered by 50 lines/inch SS mesh/grid, having 90% transmission. After the accelerator, follows the field-free drift tube. The length of the flight tube is 125cm. One end of the flight tube holds the ion optics and the other end one gate valve is connected to separate the detector region from the flight tube assembly. The photograph of the time-of-flight mass spectrometer developed is shown in Fig. 3.

3. Performance testing of the TOFMS

The TOFMS was performance tested for mass resolution. For this purpose, natural samarium sample was loaded in its atomic beam generator and evaporated by resistive heating in the temperature range 800 K. A single-colour resonance of Sm at 683.9 nm was used for multi-photon ionization. An Nd:YAG pumped dye laser, with a combination of LDS and DCM dyes with ethanol solvent is used for getting the lasing at the required wavelength. The dye laser output with a pulse repetition rate 20 Hz, pulse duration 6 ns and pulse energy 10 mJ was used for single-colour muti-photoionization. The laser beam was focused in the interaction zone of TOFMS using a lens of focal length 25 cm to ~ 100 μm. At these high intensities, we observed both Sm^+ and Sm^{++} ions in the TOFMS at flight times 34μs and 24μs respectively as shown in Fig.4(a). Sm has seven natural isotopes (^{144}Sm,^{147}Sm, ^{148}Sm, ^{149}Sm, ^{150}Sm, ^{152}Sm, ^{154}Sm) with natural abundances of 3.1, 15, 11.3, 13.8, 7.4, 26.6 and 22.6 percentages respectively. The mass spectrum exhibiting the seven natural samarium isotopes of doubly ionized Sm is shown in Fig. 4(b). The mass spectrum does not reflect the natural abundance of different isotopes because it depends on where exactly the laser wavelength is fixed in between the resonances of ^{144}Sm and ^{154}Sm isotopes with respect to the isotope shifts. Another reason for the disagreement with the natural abundance could be the polarisation effects, since we have used a linearly polarised laser for the photoionisation process.

3.1 Mass Resolution of TOFMS

If ion formation is limited to a plane parallel to the source electrode and if all the ions are formed with zero initial velocity, then flight time will be same for all the ions with same m/q value and the overall resolution of the TOFMS would be limited by the resolution of the ion detector. But in experimental conditions, due to the ubiquitous initial space and kinetic energy distributions, the resolution of the TOFMS depends on its capability to reduce the time spread caused due to these two factors. The spread in the flight time due to the initial space

distribution can be compensated either by making the longitudinal length over the region where ions are formed smaller or by space focussing, where the flight time of the different ions are made independent of its position, by adjusting the electric field ratio E_d/E_s. Since we are using a double field system for ion extraction and acceleration, the space focussing condition is achieved by adjusting the fields E_d and E_s. The typical values of the electric fields used in this set up is 33 V/mm in the extraction region and 100 V/mm in the acceleration region. The energy resolution is achieved by using the collimated atomic vapour source whereby limiting the transverse distribution of the initial velocity components. With the electric fields mentioned above, the typical flight time (t), obtained for doubly ionised samarium isotopes is around 24 μs with fwhm (Δt) of the mass peaks ~ 22 ns. Hence, we have achieved a mass resolution, (t/2Δt) better than 500 by using this TOFMS.

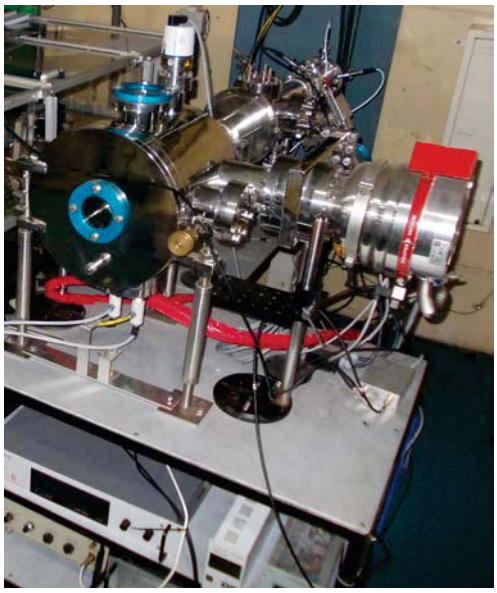

Fig. 3: *Photograph of the indigenously developed TOFMS*

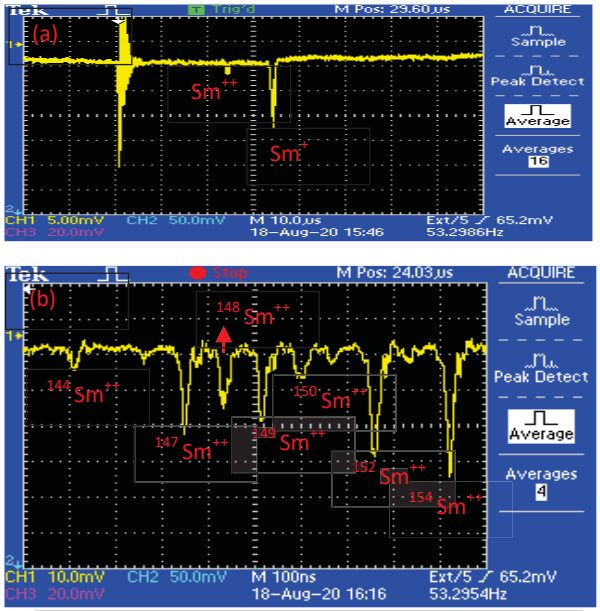

Fig: 4: *(a) TOFMS spectrum of Sm^+ and Sm^{++} (b) Mass spectrum of Sm^{++}*

Conclusions: We have indigenously developed a high temperature effusive atomic beam based linear time-of-flight mass spectrometer with mass resolution better than 500 for isotope selective photoionisation of medical isotopes. The time-of-flight mass spectrometer developed was further utilised for the process qualification of isotope selective photoionisation of medical isotope of ytterbium. The details of the process qualification using the TOFMS will be presented in another manuscript.

Acknowledgement

The authors are thankful to Dr.(Smt.) Archana Sharma, AD, BTDG for the encouragement and support to carry out this work.

References:

1. W.C.Wiley and L.H. Mclaren, *Time-of-flight mass spectrometer with improved resolution* .The review of scientific instruments, **26**, No.12, 1149 (1955).

2. W. Demtroder, *Laser spectroscopy: basic concepts and instrumentation*. (Springer Science & Business Media (2013).

Elemental Identification and Alloy Classification by Laser-Induced Breakdown Spectroscopy

Supriya K.[1], Megha Mohan[1], Balakrishna Prabhu B. N.[2], K. K. Anoop[1,*]

[1]*Department of Physics, Cochin University of Science and Technology, Kochi-22, India*

[2]*Centre for Integrated Studies, Cochin University of Science and Technology, Kochi-22, India*

[*]Email: anoopkk@cusat.ac.in

Abstract

We investigated the feasibility of Laser-Induced Breakdown Spectroscopy (LIBS) technique for elemental identification and alloy classification in industrial applications. A frequency-doubled nanosecond Nd:YAG laser was used to generate the plasma from the alloy samples (copper alloys: industrial grade Brass and Bronze) kept at atmospheric conditions. The characteristic emission lines in the optical emission spectra were then used for elemental identification and alloy classification. We developed a computer program to analyze the spectrum, which compares the peaks from the spectrum with the persistent and strong lines of elements from the National Institute of Standards and Technology (NIST) database and identifies the elements present in the sample. It thus classifies the copper alloys based on their chemical composition. Our study confirms that LIBS is a viable method for compositional analysis of multi-element samples.

1. Introduction

Laser-Induced Breakdown Spectroscopy (LIBS) is a promising analytical technique that has gained considerable attention due to its fast and reliable detection method. LIBS has demonstrated its unique features as an analytic technique, allowing fast, contact-less, multi-elemental analysis of almost any sample type with practically no sample preparation[1]. In LIBS, a high-energy pulsed laser is focused on a sample's surface to generate a plasma that vaporizes a small amount of the sample. This transient plasma emits electromagnetic radiations, consisting of discrete lines and bands corresponding to the neutrals, atomic, ionic species of the plume, and a broad underlying continuum. These discrete lines, which provide the "spectral signatures" of the material, are used to develop the qualitative and quantitative analytical information of the sample. In principle, LIBS can directly address and simultaneously detect atomic and molecular species of all types of samples in its surrounding environment using a single laser shot. Like any other analytical technique, LIBS is not without its limitations. LIBS has higher limit of detection (LOD), shot-to-shot variations, and sample matrix effect compared to other spectroscopic techniques[2].

During the last two decades, there has been considerable progress in exploring LIBS's different applications, including remote material assessment in nuclear power stations, geological elemental analysis in space exploration, and other industrial applications[3]. Because of its intrinsic versatility, LIBS has been widely used for metallic alloy identification and classification. The mechanical, structural, and electrical properties of an alloy strongly depend on its composition. The copper alloys are widely used for industrial applications because of its wear-resistance, electrical and thermal conductivity, and corrosion resistance properties. In the present work, we investigated the feasibility of the LIBS method for elemental identification, and alloy classification of two most commonly used copper alloys (industrial grade Brass and Bronze).

2. Experimental Details

A standard LIBS experimental setup has been used for recording the optical emission spectra of alloy samples. A frequency-doubled nanosecond Nd:YAG laser beam (λ=532 nm, τ=10 ns pulses) with 40 mJ pulse energy was focused using a bi-convex lens (f = 25 cm) onto the target material at atmospheric pressure. The laser fluence at the focal spot was approximately $F \approx 100$ J/cm^2, which is higher than the threshold fluence needed to ablate the Cu alloy targets. Optical emission from the laser-produced plasma (LPP) was collimated and focused using two bi-convex lenses of focal lengths 15 cm and 10 cm, respectively. The focused light was collected using an optical fiber, connected to a portable spectrometer (Ocean HDX-XR). The recorded LIBS spectra were then used for qualitative elemental analysis and alloy classification.

3. Qualitative Elemental Analysis

The basis of any LIBS measurement is the plasma's emission spectrum, which contains information about the elements present in the target material. Figure 1 represents the portions of the LIBS spectra recorded from Brass (a & b) and Bronze (c & d) alloys at F = 100 J/cm^2 under ambient conditions. The characteristic emission lines and corresponding intensity information are essential for analyzing the sample, either qualitative or quantitative. The qualitative analysis seeks to establish the presence of a particular element in the sample. The critical step is identifying each emission line of a specific element in its neutral or ionized state. The emission peaks in the LIBS spectrum are the characteristic of different elements present in the sample. We developed a computer program to identify the intense peaks in the LIBS spectra. Comparing these emission lines with the NIST atomic spectra database and the Kurucz database identifies the elements present in the multi-element samples[4, 5].

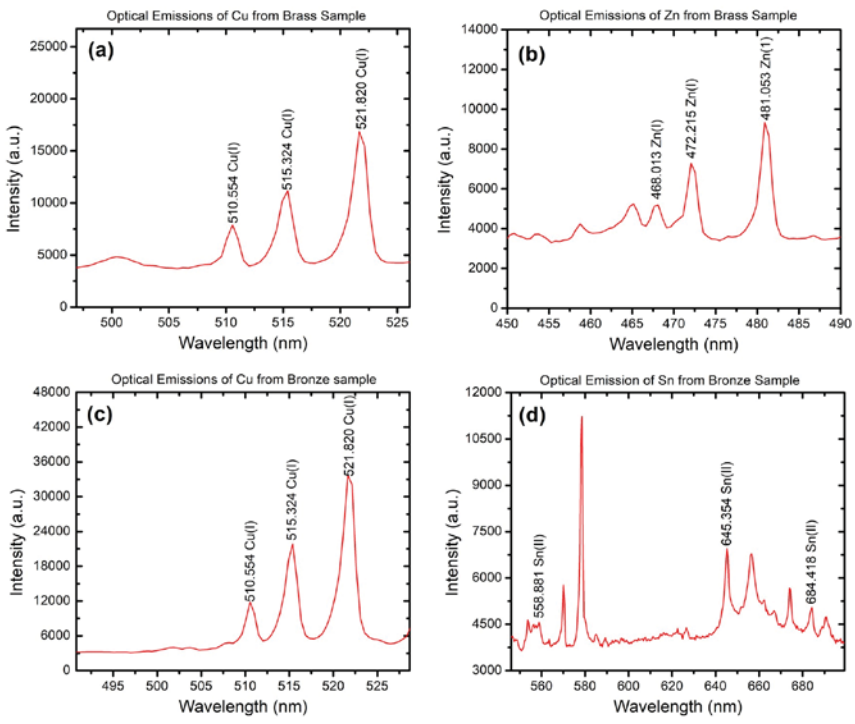

Figure 1: LIBS spectra of Brass and Bronze alloy recorded at F=100 J/cm^2 under ambient conditions. The persistent lines of Cu, Zn and Sn are marked in the spectra.

Fig. 1(a) and 1(b) represents the characteristic emission lines of copper and zinc in the Brass alloy, whereas Fig. 1(c) and (d) shows the same for copper and tin in the Bronze sample. The essential spectroscopic data of the

persistent lines (of Cu, Zn, Sn) used for the qualitative elemental analysis and sorting of alloys are shown in table 1. Spectroscopic data, along with intensity information, can be used for abundance estimation of any multi-element samples. We have also observed persistent and strong lines of Nitrogen and Oxygen at wavelengths 567.75 nm, 593.908 nm, 744.509 nm, 868.546 nm and 777.349 nm, 844.633 nm 927.194 nm respectively, which is due to the breakdown of the ambient atmosphere at the laser focal spot[6]. Since the characteristic emission lines of constituent elements are in the 460-690 nm region, our study indicates that LIBS in the visible region is sufficient to sort copper alloys based on their composition.

Wavelength (nm)	Energy Lower – Upper (eV)	Transition Lower - Upper	Term Symbol Lower - Upper	Degeneracy Lower - Upper
510.554 (Cu I)	1.388 – 3.816	$3d^9 4s^2$ - $3d^{10} 4p$	$^2D_{5/2}$ - $^2P_{3/2}$	6 - 4
515.323 (Cu I)	3.785 – 6.191	$3d^{10} 4p$ - $3d^{10} 4d$	$^2P_{1/2}$ - $^2D_{3/2}$	2 - 4
521.820 (Cu I)	3.186 – 6.192	$3d^{10} 4p$ - $3d^{10} 4d$	$^2P_{3/2}$ - $^2D_{5/2}$	4 - 6
468.013 (Zn I)	4.006 – 6.654	$3d^{10} 4s\ 4p$ - $3d^{10} 4s\ 5s$	$^3P_0$ - $^3S_1$	1 - 3
472.215 (Zn I)	4.029 – 6.654	$3d^{10} 4s\ 4p$ - $3d^{10} 4s\ 5s$	$^3P_1$ - $^3S_1$	3 - 3
481.053 (Zn I)	4.077 – 6.654	$3d^{10} 4s\ 4p$ - $3d^{10} 4s\ 5s$	$^3P_2$ - $^3S_1$	5 - 3
558.881 (Sn II)	8.853 – 11.071	$5s^2 5d$ - $5s^2 4f$	$^2D_{3/2}$ - $^2F_{5/2}$	4 - 6
645.354 (Sn II)	7.053 – 8.973	$5s^2 6s$ - $5s^2 6p$	$^2S_{1/2}$ - $^2P_{3/2}$	2 - 4
684.418 (Sn II)	7.053 – 8.864	$5s^2 6s$ - $5s^2 6p$	$^2S_{1/2}$ - $^2P_{1/2}$	2 - 2

Table 1: Spectroscopic data of persistent lines (of Cu, Zn, Sn) used for the qualitative elemental analysis of alloy samples

4. Computational Method for Data Analysis.

Qualitative analysis of a LIBS spectrum is a repetitive and tedious process. For complex substances such as alloys with more than one element present in them, manually looking for each element would take up much time. The repetitive process can be automated using computational methods. The current algorithm takes up a LIBS spectrum and processes it to find the peaks above a certain intensity baseline. The intensity baseline is placed to eliminate noise that is captured by the spectrometer. If not eliminated, the noisy peaks might interfere with the algorithm and be detected as other elements and might cause a false-positive result. The algorithm then uses a standard database imported from the available NIST Atomic Spectra Database and compares the peaks with lines of all the database elements. The database provides the wavelength, relative intensity, species designation, transition probabilities, energies and quantum numbers of the upper and lower levels. We used a Hit interval (probable wavelength shift in experimental data) of 0.2 nm and appropriate intensity cut off for analyzing different portions of LIBS spectra. The element would be considered to be present if at least three peaks match with persistent or strong lines in the database. All these parameters in the program are variables and can be modified according to the need. The algorithm has provisions to check custom lists of elements, and hence the choice of whether to use strong or persistent lines is available. Based on set criteria such as Hit interval and intensity cut off, the algorithm then assigns an element as present or absent. This process is repeated for each element in the checklist which can be custom-defined. The program gives back a list of elements that satisfy the given criteria and classifies the material into different alloys. Fig. 2 shows the screenshot of the output of the spectrum analysis software. The vertical lines in each spectrum show the persistent lines of constituent elements in the alloy targets. The computational method provides a fast, convenient, and effective platform for elemental detection and sorting of alloys based on their elemental composition.

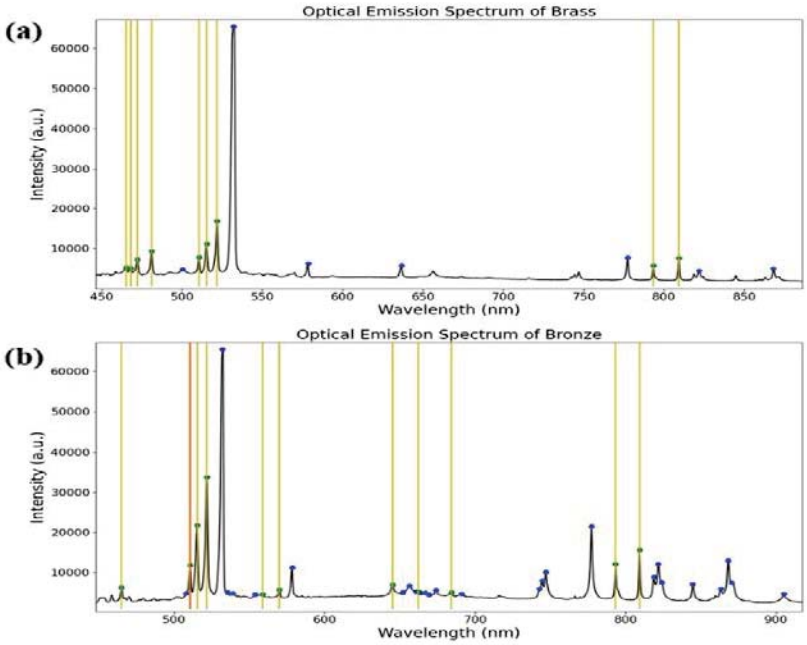

Figure 2: Screenshot of the output of the spectrum analysis software. The vertical lines represent the persistent lines of constituent elements present in Brass and Bronze alloys.

Conclusion

We investigated the feasibility of laser-induced breakdown spectroscopy method for elemental detection and alloy classification. A nanosecond Nd:YAG laser was used to ablate the Brass and Bronze alloys at atmospheric pressure condition, and a portable fiber optic spectrometer was used to record the optical emission spectra. The persistent and strong lines of Cu, Zn, and Sn were used to confirm the elemental composition, and differentiate the alloy samples. An indigenously developed spectral analysis software provides a fast, convenient and efficient way of elemental detection and sorting of alloys based on their composition.

References

[1] D. A. Cremers and L. J. Radziemski, *Handbook of Laser-induced Breakdown Spectroscopy*, Wiley (2006).

[2] ReinhardNoll, VolkerSturm, ÜmitAydin, DanielEilers, ChristophGehlen, ManuelaHöhne, AndréLamott , JoachimMakowe, JensVrenegor, *Spectrochimica Acta - Part B Atomic Spectroscopy*, **63**, 1159 (2008).

[3] F. Anabitarte, A. Cobo, and J. M. Lopez-Higuera, *ISRN Spectrosc*, **2012**, 1 (2012).

[4] Kramida, A., Ralchenko, Y., Reader, J., & The NIST ASD Team, *NIST Atomic Spectra Database (ver. 5.6.1)*, (2019).

[5] Peter L Smith, Claas Heise, Jim R Esmond, and Robert L Kurucz. *Atomic spectral line database* (2016).

[6] R. D. Harris, D. A. Cremers, M. H. Ebinger, and B. K. Bluhm*, Appl. Spectrosc*, **64**, 366 (2004).

Studies on Raman spectroscopy of pure ghee and vanaspati

A. Dalal[1], A. Srivastava[1], Alka[1], N. Kumar[1], H. Krishna[1] and S. K. Majumder[1,2]

[1]Laser Biomedical Applications Section, Raja Ramanna Centre for Advanced Technology, Indore-452013

[2]Homi Bhabha National Institute (HBNI), Training School Complex, Anushakti Nagar, Mumbai-400 094

Email: shkm@rrcat.gov.in

Abstract

The results of a Raman spectroscopic study on pure ghee (made from cow and buffalo milk) and vanaspati are presented. A home-built Raman set up with 532 nm excitation was used to measure Raman spectra from the pure ghee and vanaspati samples. Though the spectra of all the samples were seen to be primarily characterized by the Raman peaks characteristic of hydrocarbon molecules and carbonyl group of esters, significant spectral differences across various Raman bands were observed between vanaspati and both the types of pure ghee. While the pure ghee made from buffalo milk showed enhanced contribution of the Raman signatures of saturated fatty acids as compared to vanaspati, a number of significantly different Raman bands characteristic of beta carotenoids were observed for the pure ghee made from cow milk with respect to the vanaspati indicating inherent compositional differences.

Introduction

Pure ghee, made from either cow or buffalo milk, is a form of clarified butter which is widely used in the Indian subcontinent as a cooking medium. In addition to its culinary uses, ghee also plays a major role in the traditional Indian system of medicine. It is an effective delivery medium for hydrophobic drugs used in Ayurveda. The major components of pure ghee are the fats (99% or above). Most of this fat is saturated and is primarily made up of triglycerides, with much smaller quantities of diglycerides, minute amounts of free fatty acids, phospholipids and sterols, and traces of vitamins A, D, E, and K[1–2]. A less-expensive variant of ghee, known as vanaspati, is prepared by hydrogenation of vegetable cooking oil such as palm oil and is widely popular in India as a cheaper substitute of pure ghee. However, vanaspati contains trans fats, which increases the risk of coronary heart disease upon consumption[3]. Moreover, traces of nickel and lead often found to be present in vanaspati are known to be toxic to human health.

Since the physical properties of both pure ghee and vanaspati are alike, unscrupulous vendors often adulterate pure ghee with vanaspati for commercial benefits. At present, there does not exist any method which can provide, in a rapid and non-destructive way, insight into the chemical composition of pure ghee and vanaspati that can form the basis of quantitative discrimination between the two.

Raman spectroscopy, essentially a vibrational spectroscopic technique, has garnered a great deal of interest in recent years for monitoring foodstuff. Its attractiveness comes from its ability to provide quantitative information about the chemical composition of any material in a non-destructive manner. Basically, it probes the vibrational energy levels of molecules, and specific peaks in the Raman spectrum correspond to particular chemical bonds or bond groups. Because of its chemical specificity, it is expected to discern the subtle changes in the chemical composition between pure ghee and vanaspati.

We report here the results of an exploratory study carried out to evaluate the applicability of Raman spectroscopy for characterizing pure ghee (made from cow and buffalo milk) and vanaspati. The objective is to assess whether pure ghee can be differentiated from vanaspati based on the measured Raman spectral signatures of the two.

Materials and method

Figure 1 shows the schematic of the experimental set-up for the Raman spectroscopic measurements. The set up uses a 532 nm diode-pumped solid-state laser (EXLSR-532-300-CDRH, Newport corporation) for Raman excitation. Combination of a half-wave plate and a polarizer controls the power of the laser on the sample plane. The dichroic mirror reflects the excitation light which is passed through an objective lens for focusing it onto the surface of the cuvette containing the sample. The Raman signal backscattered from the sample following removal of the elastically scattered excitation component is focused onto the tip of a detection fiber connected to a Raman spectrograph equipped with a thermoelectrically cooled, back-illuminated, deep depletion CCD camera for spectral measurements.

Pure ghee made from cow as well as buffalo milk and vanaspati purchased from the local market were used in the present study. Prior to the Raman measurements, the samples of ghee or vanaspati were taken in a glass beaker, which was then put in a hot water bath until the samples were transformed into their liquid form. Subsequently, 3.5ml of the liquid sample was put in a quartz cuvette and thawed to the room temperature for measuring Raman spectra. For each of the samples of ghee or vanaspati, the Raman spectra were recorded from five different spatial locations across the surface of the cuvette containing the sample. The optical power delivered onto the sample was ~50 mW and spectral acquisition time was 5 seconds.

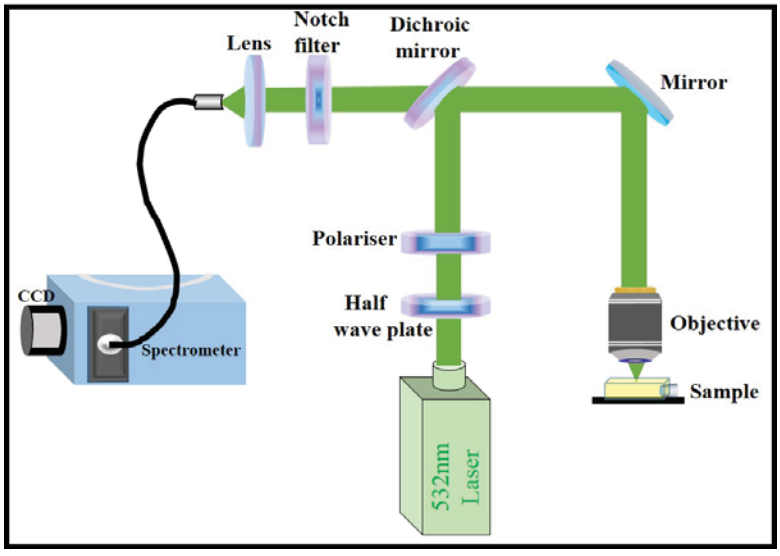

***Figure 1**: Schematic of experimental arrangement of Raman system*

Results and Discussion

Figure 2(a) shows the mean-normalized Raman spectra measured from vanaspati (shown by red colored line) and pure ghee made from cow milk (shown by black colored line). Each spectrum is the average over the

spectra acquired in five different measurements. The grey colored background represents ±1 standard deviation. It is apparent from the figure that the spectra of both vanaspati and pure ghee are characterized by a few common Raman bands occurring at 968, 1063, 1083, 1265, 1300, 1440, 1650, 1747 cm^{-1}. These bands are known to correspond to different modes of vibration of fatty acids[4-5]. However, one can see that the spectrum of pure ghee made from the cow milk has some additional Raman bands appearing at 1008, 1150 and 1525 cm^{-1}. These Raman bands, believed to be characteristic of beta carotenoids[4-5], are absent in the spectrum of vanaspati. For a better understanding of the spectral differences between vanaspati and pure ghee made from cow milk, a difference spectrum was derived from the measured Raman spectra of the two. Figure 2(b) plots the difference spectrum. The grey band in the difference spectrum shows the confidence interval, calculated by multiplying the standard error with a t-value corresponding to 95% confidence and the degrees of freedom equal to sum of total spectra minus one. The Raman bands, which lie outside this confidence interval, represent the bands of statistically significant spectral differences. One can see that significant spectral differences exist at 1008, 1150 and 1525 cm^{-1}, where intensity values are considerably higher in the Raman spectra of pure ghee made from cow milk indicating contribution of beta carotenoids. Statistically significant spectral differences are also present at 968, 1265, 1440, 1570 and 1650 cm^{-1} where intensity values are higher in the Raman spectra of vanaspati indicating higher contribution of fatty acids in vanaspati.

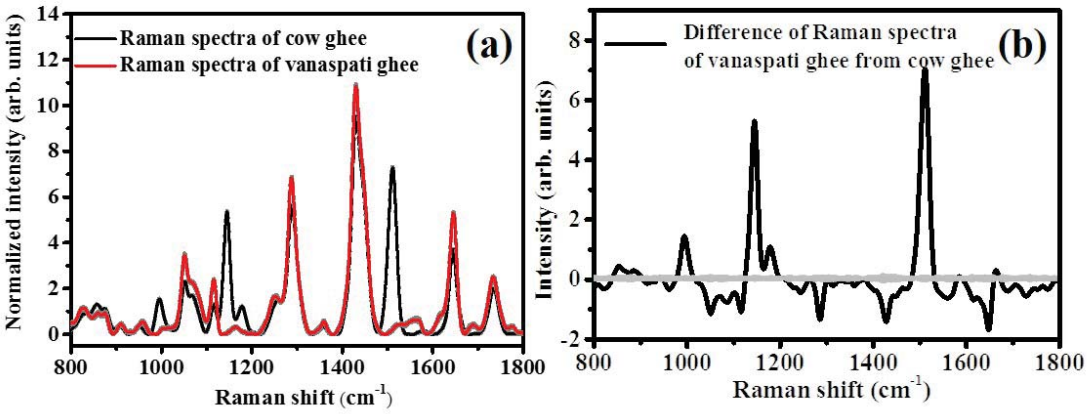

Figure 2: (a) *Measured Raman spectra of pure ghee made from cow milk (black line) and vanaspati (red line).* ***(b)*** *Difference Raman spectrum of vanaspati subtracted from pure ghee made from cow milk.*

Figure 3(a) shows the mean-normalized Raman spectra measured from vanaspati (shown by red colored line) and from a pure ghee sample made from buffalo milk (shown by black colored line). Each spectrum is the average over the spectra acquired in five different measurements. The grey colored background represents ±1 standard deviation. It is apparent from the figure that the spectra from both vanaspati and pure ghee made from buffalo milk are characterized by Raman bands characteristic of fatty acids only and unlike pure ghee from cow milk, Raman signatures characteristic of beta carotenoids are absent in the spectrum of pure ghee from the buffalo milk. However, significant differences in the intensities across all the Raman bands are clearly visible in the spectra which are evident from figure 3(b) that plots the difference spectrum between the two. It can be seen that the intensities of all the Raman bands (at 840-890, 1063, 1083, 1300, 1440 cm^{-1}) characteristic of saturated fats are significantly higher in the spectra of buffalo ghee as compared to vanaspati indicating higher relative

contribution of saturated fats[4-5] in the pure ghee made from buffalo milk. In contrast, the intensities of Raman bands at ~ 968, 1265, 1570 and 1650 cm^{-1} characteristic of the vibration modes of unsaturated fats are found to be considerably higher in vanaspati as compared with pure ghee made from buffalo milk indicating higher relative contribution of unsaturated fats in vanaspati.

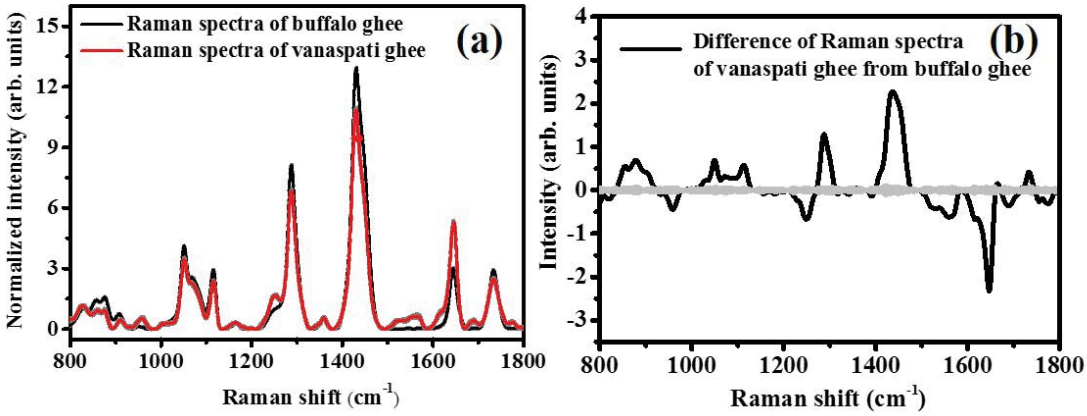

Figure 3: ***(a)*** *Measured Raman spectra of pure ghee made from buffalo milk (black line) and vanaspati (red line).* ***(b)*** *Difference Raman spectrum of vanaspati subtracted from pure ghee made from buffalo milk.*

The results of the study suggest that Raman spectroscopy has potential for rapid characterization and differentiation of the pure cow and buffalo ghee from vanaspati.

References:

1. M. L. Sserunjogi, R. K. Abrahamsen and J. Narvhus, *Int. Dairy Journal*, **8**, 677, (1998).
2. K. Chinnadurai, H. K. Kanwal, A. K. Tyagi, C. Stanton and P. Ross, *Lipids in Health and Disease*, **12**, 121, (2013).
3. M. P. Iqbal, *Pak. J. Med. Sci*, **30**, 194, (2014).
4. R.M. El-Abassy, P.J. Eravuchira, P. Donfack, B. von der Kammer, A. Materny, *Vibrational Spectroscopy*, **56**, 3-8, (2011).
5. A. Nedeljkovic, P. Rosch, J. Popp, J. Miocinovic, M. Radovanovic, P. Pudja, *Food Anal. Methods, **9**, 1315–1320 (2016)*

Raman spectroscopy for monitoring temperature-induced changes in mustard oil

A. Srivastava[1], A. Dalal[1], H. Krishna[1] and S. K. Majumder[1,2]
[1]*Raja Ramanna Centre for Advanced Technology, Indore 452013, India*
[2]*Homi Bhabha National Institute, Mumbai 400094, India*
Email:shkm@rrcat.gov.in

Abstract: The results of an exploratory study to evaluate the potential of Raman spectroscopy for monitoring the temperature-induced changes in mustard oil are presented. A home-built Raman set up with 785 nm excitation was used to measure Raman spectra from mustard oil heated at various temperatures up to 200°C for varying time durations. While the spectra were observed to show changes across various Raman bands for the oil heated at and beyond 125°C, these spectral changes were the most significant at higher temperatures near 200°C indicating deterioration of natural ingredients of oil along with formation of oxidation products due to heating. The results suggest that heating of oil at temperatures between 75°C-125°C is safe for the purpose of cooking.

Introduction

Mustard oil, primarily used as cooking oil, is essentially a vegetable oil which is an important source of nutrition. It mainly consists of oleic acid, erucic acid and linoleic acid[1]. In addition, it also contains good amount of vitamin E, vitamin A and pigments like chlorophyll that add to its nutritional value. Though mustard oil is widely used for cooking in northern and north-eastern belts of India thereby making it the country's second most important edible oil after groundnut, the temperature at which the oil can be heated during cooking so as to keep its nutritional value intact is not known to date.

In order to find the temperature that can be considered safe for cooking with mustard oil, it is important to know how heating of the oil at various temperatures may lead to alterations in its chemical composition. Since Raman spectroscopy, a vibrational spectroscopic technique, has the intrinsic ability to detect molecular information in a material, it is expected that the technique will be able to discern subtle chemical changes associated with heating thereby making it particularly suited for determining the safe cooking temperature(s) for the mustard oil. We report here an exploratory study to evaluate the potential of near-infrared (NIR) Raman spectroscopy for monitoring the temperature-induced changes in mustard oil.

Materials and Methods

Figure 1 shows the schematic of the experimental set-up for the NIR Raman measurements. The set up uses a 785nm diode laser (CL-2000, CrystaLaser) for Raman excitation. The output of the laser is collimated by the achromatic doublet lens and is passed through the laser clean up filter. The beam then falls on the dichroic filter which reflects the laser light onto the sample through the microscope objective lens. The backscattered Raman signal is collected by the same objective lens and is passed through the dichroic filter which transmits the beam to the notch filter to separate the Rayleigh scattered light from the collected output signal. The beam is then passed through the lens which couples it to the Raman spectrograph (SR-303iA, Andor Shamrock)

equipped with a thermoelectrically cooled, back-illuminated, deep depletion CCD camera (DU416A-LDC-DD, Andor).

Mustard oil purchased from the local market was used in the present study. For the Raman measurements, 120µL of the oil was put in shallow round dip created on a metal substrate made of aluminium and the Raman excitation beam was made to fall on the oil from the top. Raman spectra were measured from the oil at room temperature as well as from the heated oil. For heating, 30ml of the oil was taken in a bottle made of borosilicate glass and heated at 75℃, 125℃ and 200℃ using a microwave oven. These temperatures were chosen as they are close to home cooking and frying temperatures (pan frying temperature is around 125℃, normal frying temperature is around 160℃-190℃ and deep frying temperatures is higher than 175℃). Raman spectra were recorded from the samples of oil heated at each of these temperatures for varying durations of time (30 minutes, 1 hr, 2hrs and 3hrs). In order for recording Raman spectra of oil heated at a particular temperature for a chosen time duration, 120µL of the oil was taken out from the glass bottle kept in the microwave oven where it was heated at that particular temperature for that chosen time duration leaving the bottle containing the remaining oil in the oven for getting heated for longer time durations at that temperature. This process was repeated for completing measurements from oil heated for various time durations at a particular temperature as well as for different temperatures.

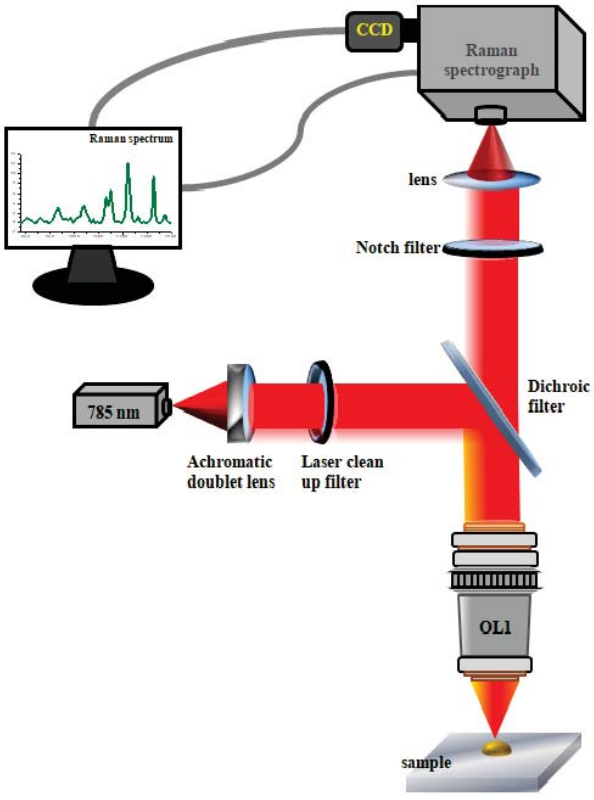

Figure 1. Schematic of the Raman experimental setup.

Results and Discussions

Fig. 2(a) shows the Raman spectrum of mustard oil at room temperature (before heating). The spectrum is the average of the Raman spectra measured from five different spatial points of the samples. The integration time used for the spectral measurements was 1 s, five accumulations and the laser power measured at the sample surface was ~60 mW. One can see that the spectrum is characterized by a number of Raman bands located between 800 cm^{-1} to 1800 cm^{-1} which correspond to particular chemical bonds or bond groups. For example, the Raman band at 865 cm^{-1} is assigned to phospholipids[2,3], the band at 970cm^{-1}, corresponding to out of phase HC=CH wag vibration of *cis* double bonds, is assigned to fatty acids methyl esters[2,4], the bands between 1063-1083cm^{-1} are assigned to saturated fatty acids[2] and the relatively smaller bands at 1156cm^{-1} and 1526cm^{-1} are assigned to beta carotenoids[2]. Similarly, the bands at 1264cm^{-1} corresponds to =CH bending, scissoring and 1300cm^{-1} corresponding to C-H bending, twisting, the Raman band at 1440cm^{-1} is assigned to the saturated fatty acids[2], the 1656cm^{-1} band corresponds to *cis* double bond stretching for unsaturation and the 1748cm^{-1} band has been assigned to ester stretching triacylglycerol[5,6].

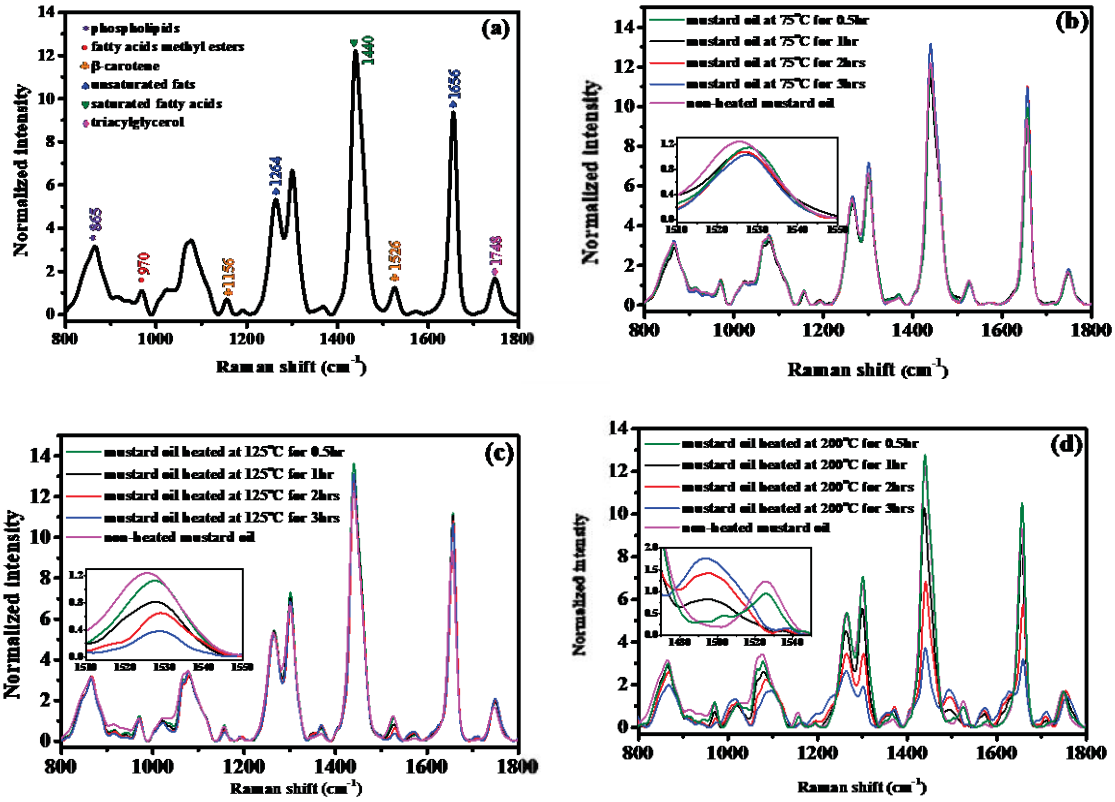

Figure 2. Raman spectrum of (a) non-heated mustard oil used in the study, (b) mustard oil heated at 75°C, (c) mustard oil heated at 125°C and (d) mustard oil heated at 200°C.

Figs. 2(b)- 2(d) display the mean normalized Raman spectra corresponding to mustard oils heated at 75°C, 125°C and 200°C for varying durations of time (30 mins, 1hr, 2hrs and 3hrs). A close look at the figures shows the following points which are worth noting. It can be seen that while the Raman spectra of the mustard oil heated at 75°C do not show any appreciable changes as compared to that of the mustard oil at room temperature (non-heated) irrespective of the durations of heating, when the temperature was raised to 125°C, spectral changes start becoming appreciable and gradually get more prominent with the increase in the duration of

heating. For example, one can see that the intensities of the Raman bands at 1156 and 1526 cm^{-1} get reduced in the heated oil and the amount of reduction increases with the increase in the duration of heating. The plausible reason for this reduction in the Raman intensity appears to be the deterioration of beta carotene present in the oil[2,7]. When the oil is further heated to 200℃, considerable changes were observed at Raman bands from 1220cm^{-1} to 1329cm^{-1}. This indicates change in lipid structure due to the oxidation and formation of toxic aldehydes[8]. The ratio of intensities of Raman bands at 1264cm^{-1} and 1300cm^{-1}bands can be used to determine the loss of unsaturation in the heated samples[2,8]. It is also evident from the figure that characteristic Raman peak of beta carotene at 1526cm^{-1} is completely destroyed after half an hour of heating and a shifted band appears at 1493cm^{-1} which may be due to the isomerization of beta carotene[9]. The intensity of 1493cm^{-1} band also increases with the duration of heating. The decrease in intensity of 1440cm^{-1} Raman band indicates the oxidation of saturated fatty acids with heating[2].

The results of this preliminary study appear to suggest that the temperature range between 75℃-125℃ can be considered safe for cooking with mustard oil. This is because Raman spectra of the oil heated at temperatures in this range did not show any visible changes in any of the Raman bands clearly suggesting that heating through this temperature range does not cause any appreciable changes in the chemical composition of the mustard oil (from its non-heated state).

References:

1. G.A. Antova, M. I. Angelova-Romova, Zh. Y. Petkova, O. T. Teneva and M. P. Marcheva, *Bulgarian Chemical Communications*, **49**, 55-60, (2017).
2. N. Ahmad, M. Saleem, H. Ali, M. Bilal, S. Khan, R. Ullah, M. Ahmed and S. Mahmood, *Laser Phys. Lett.*, **14**, 095603, (2017).
3. H. Ali, H. Nawaz, M. Saleem, F. Nurfis and M. Ahmed, *J. Raman Spectroscopy*, **47**, 706-11, (2016).
4. B. Muik, B. Lendl, A. Molina-Diaz and M. J. Ayora-Canada, *Chem. Phys. Lipids*, **134**, 173-82, (2005).
5. M. A. Carmona, F. Lafont, C. Jimenez-Sanchidrian and J. R. Ruiz, *Eur. J. Lipid Sci. Technol.*, **116**, 1451-6, (2014).
6. S. Gallier, K. C. Gordan, R. Jimenez-Flores and D. W. Everett, *Int. Dairy J.*, **21**, 402-12, (2011).
7. C. Medina-Gutierrez, C. Frausto-Reyes, J. Medina-Valtierra, R. Jaimes-Reategui, H. Garcia-Lopez and J. R. Molina-Contrearas, *Proc. of SPIE*, **6046**, (2006).
8. M. Saleem, N. Ahmad, R. Ullah, Z. Ali, S. Mahmood and H. Ali, *Food Analytical Methods*, **13**, 1292, (2020).
9. D. Qiu, S. Shao, B. Zhao, Y. Wu, L. Shi, J. Zhao and Z. Chen,J*ournal of Food Biochemistry*, **36**, 1745, (2011).

Precise determination of laser wavelengths pertaining to three-step selective photoionization for enrichment of ^{176}Yb and qualification of process selectivity

D. Biswal[1], A. U. Seema[1], R. C. Das[2,3], D. R. Rathod[1], A. K. Singh[1], A. Khattar[1], J. S. B. Singh[1], A. Wahid[1], P. R. Mohite[1], S. K. Maurya[1], J. S. Dhumal[1], J. Thomas[1], Asawari. D. Rath[1,3*], S. Kundu[1*]

[1] *Tunable Laser Section, Advanced Tunable Laser Applications Facility, BTDG, BARC, Mumbai-400085.*

[2] *Laser & Plasma Technology Division, BTDG, BARC, Mumbai-400085.*

[3]*Homi Bhabha National Institute, Mumbai-400094.*

*Email: asawarim@barc.gov.in, skundu@barc.gov.in

Abstract: Isotopically pure ^{176}Yb is a pre-requisite for production of the medical isotope ^{177}Lu in nuclear reactor using no carrier added route, demanding highly enriched (> 97%) isotope separation of this isotope from its natural abundance of 12.73%. Resonance ionization mass spectroscopy is performed to precisely determine laser wavelengths pertaining to the three-step photoionization scheme available in literature for selective ionization of ^{176}Yb. Further, a protocol is developed to mimic the separation process in a time of flight mass spectrometer and qualify laser parameters like wavelength, intensities, etc. to achieve desired enrichment.

Introduction

Lutetium-177 is one of the most important medical isotopes, currently high in demand for its two-fold applications in radiopharmaceutical industry of diagnostic as well as therapeutic. Albeit it is not existed in nature, it can be produced by two routes namely neutron irradiation of ^{176}Yb or ^{176}Lu[1]. The isotope ^{176}Yb has very low neutron absorption cross-section as compared to ^{176}Lu, nevertheless the Yb route is gaining popularity owing to its potential of no carrier added production of ^{177}Lu. For high specific activity production of the medical isotope, highly pure Yb-176 is a pre-requisite. Recently we demonstrated enrichment of ^{176}Yb from its natural compositon to > 97% by selective three-step photoionization employing single mode process dye lasers developed in-house. This paper presents our work on precise determination of the laser wavelengths pertaining to selective photoionization of ^{176}Yb using a time of flight mass spectrometer (TOFMS). Further, the selective ionization process was mimicked in the TOFMS and laser parameters like their intensities were optimized to achieve spectroscopic selectivity of > 99% for ^{176}Yb and qualify the process.

The seven naturally occuring isotopes of ytterbium are ^{168}Yb (0.13%),^{170}Yb (3.03%), ^{171}Yb (14.31%), ^{172}Yb (21.82%), ^{173}Yb(16.13%), ^{174}Yb (31.84%), and ^{176}Yb (12.73%). Owing to its fully filled 4*f* subshell and two valence electrons, it has simpler atomic structure with ground level configuration $4f^{14}6s^2\ 1S^0$. The first ionisation potential of Yb I is 6.25 eV (50441cm^{-1})[2]. The most efficient three-step photoionization (PI) scheme for Yb available in literarure is $6s^2\ ^1S_0$(0 cm^{-1}) $\rightarrow 6s6p\ ^3P_1$ (17992 cm^{-1})$\rightarrow$ $4f^{13}6s^26p$ $(7/2, 3/2)_2$ (35197 cm^{-1}) $\rightarrow$ $4f^{13}6p^26s$ (52353cm^{-1}) as shown in Figure-1[3]. The constituent energy levels and transitions of this scheme are well characterized in literature for their spectroscopic parameters like isotope shifts, hyperfines structures, level life times, excitation cross-sections, etc [3,4,5, 6]. The odd isotopes of Yb exhibit hyperfine structure and its spread encompasses the spectral lines corresponding to even isotopes. Reported separation of ^{176}Yb transition lines in first and second step from the closest neighbouring spectral features of other isotopes is 954 MHz and 316 MHz

respectively as shown in Figure-2. Consequently efficient isotope separation of ^{176}Yb using this scheme necessitates use of single mode(SM) lasers with linewidths ≤250 MHz for desired isotipoc enrichment of > 97% in first and second steps of the photoionization ladder. The ionizing transition at 582.7 nm shows a broad line shape (~13cm^{-1}) and thus a multi-mode laser can be used as third step laser.

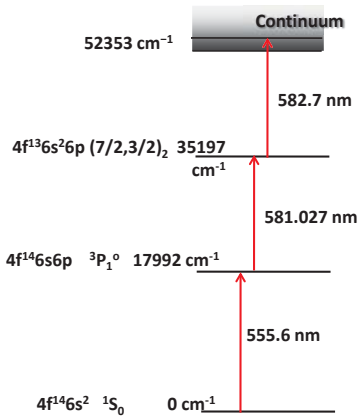

***Figure-1**: Three-step selective photoionization scheme for Yb*

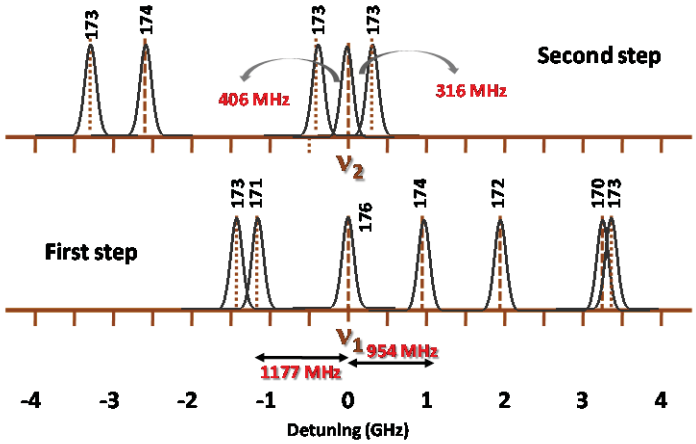

***Figure-2**: Spectral features of Yb isotopes in the vicinity of the ^{176}Yb spectral lines pertaining to first and second step excitations*

Experimental

The experimental set up consists of two main modules: three pulsed dye laser systems (two stabilised single mode lasers for excitation and one broadband laser for ionization) pumped by CVL/DPSSL lasers and a linear TOFMS integrated with a water-cooled resistively heated effusive atomic vapour source. Both the modules are indigenously designed and developed. Details of design and development of both single mode process lasers and TOFMS are presented as separate papers. Well-collimated atomic beam of Yb was generated by resistively heating few hundred mg of Yb in metal form placed inside a tantalum oven made from rolling tantalum foil into a cylinder of 60-70mm length and 5-6mm diameter. The reduced Doppler width of the atomic lines in the interaction zone is calculated theoretically to be ~ 100MHz. The average output power of the dye lasers of pulse repetition rate of 6.25 kHz was approximately 30mW at 555nm, 100mW at 581nm and 1.9W at 582nm. The laser wavelengths were monitored by M/s. Angstrom, Russia make wave meter Model No- WS UL. Combined beam of all the three lasers was sent through the interaction zone of TOFMS to overlap with Yb atomic beam. The resulting mass spectra from TOFMS were monitored on a digital storage oscilloscope and recorded for further analysis.

Results and Discussion

TOFMS is a fast and powerful diagnostic tool for understanding kinematics and dynamics involved in selective resonant photoionization processes and becomes a natural choice to cater to the objective of this work. The qualification of lasers and their wavelength determination was performed stepwise.

Step-I: All the lasers were operated in multi-mode configuration (typical line widths ~ 9 GHz for λ_1 and λ_2, ~ 3 GHz for λ_3) and set in resonance with respective transitions of ^{176}Yb PI scheme as shown in Figure-1. The reported transition wavelengths served as starting point for this. Using the isotope shifts data from literature, λ_1 and λ_2 were tuned to maximize ^{176}Yb ion yield. In the later stages of the experiment, these values served as

starting point for precise wavelength tuning. The mass spectra recorded after optimization of λ_1 and $\lambda_2$are shown in Figure-3. They clearly indicate ionization of all Yb isotopes.

Step-II: λ_1 was set in SM configuration followed by its fine tuning to maximize ^{176}Yb ion yield. It improved the enrichment of ^{176}Yb drastically as illustrated in Figure-4.

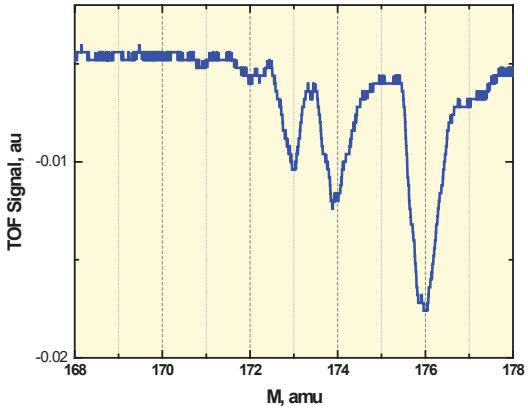

***Figure-3**: Mass spectra of Yb isotopes with all lasers in multimode configuration after setting λ_1 and λ_2 to obtain maximum ion yield of ^{176}Yb (line widths of first and second laser ~9 GHz; of third laser ~ 3 GHz)..*

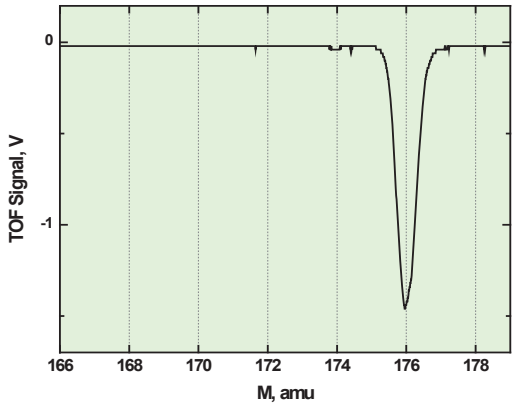

***Figure-4**: Resonant photoionization spectra in TOFMS showing Yb isotopes with λ_1 in single mode and λ_2, λ_3 in multimode configuration. There is remarkable improvement in selectivity of ^{176}Yb as evident from spectra.*

Step-III: Subsequently, the second step laser was set in SM configuration followed by its fine tuning to maximize ^{176}Yb ion yield. With both first and second steps excited by SM lasers of line widths ~ 100 MHz, the selectivity of ionization process enhanced further as can be seen in Figure-5. Narrow line widths of ~ 100 MHz of the first and second step lasers had two-fold effect on the ionization process. Firstly, it improved isotopic selectivity of ^{176}Yb . Secondly, the ionization efficiency of the targeted isotope significantly enhanced compared to multimode lasers owing to better spectral density of photons causing first step and second step excitations. The transition wavelengths for ^{176}Yb determined in the above process are given in Table-1.

***Table-1**: Transition wavelengths for selective three-step photoionization of ^{176}Yb*

λ_1(cm^{-1})	λ_2(cm^{-1})	λ_3(cm^{-1})
17991.969	**17205.088**	**17156.49**

Further, the dependence of selectivity on laser intensities was evaluated. At higher intensities, even with SM lasers, other isotopes were seen owing to saturation broadening. When λ_1 and λ_2 pulse energies were reduced to ~< 5 and 16 μJ/pulse respectively, which were focussed to an area of ~ 3 mm^2 in the laser-atom interaction region of TOFMS, isotopic enrichment S_{176} of > 99% was achieved for ^{176}Yb with an enrichment factor α_{176} of 1047 as shown in Figure-5. Here, isotopic enrichment S_{176} is defined as the fractional abundance of ^{176}Yb ions in the Yb photo-ions generated during selective photoionization while enrichment factor α_{176} is defined as the ratio of fractional abundance of ^{176}Yb in Yb photo-ions (product) to its natural fractional abundance (feed). Before the enrichment experiment, laser intensities intended for actual experiments were applied and tested for selectivity in TOFMS to ensure enrichment of > 99% for ^{176}Yb. Thus, the selective ionization process was

replicated in TOFMS and qualified. It may be noted that TOFMS spectra illustrate spectroscopic enrichment while in actual enrichment experiment; overall enrichment is expected to be lower than this value owing to factors like non-selective pick up, neutral vapour deposition on product collectors, etc. By employing the single mode lasers and the transition wavelengths with intensities qualified by above procedure an enrichment of ≥ 97% was realized for ^{176}Yb with production rate of ~ 3 mg/hr in experimental demonstration of ^{176}Yb isotope separation.

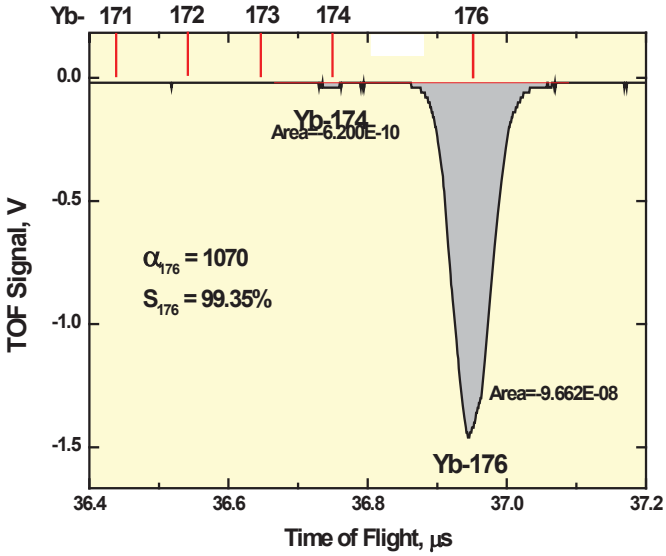

Figure-5: *Mass spectrum of Yb isotopes showing selective photoionization of Yb-176 with enrichment factor of ~ 1047 and selectivity of 99.35%. The laser energies for first and second step excitation are ~ 5μJ/pulse and 16 μJ/pulse respectively focused to ~ 3 mm^2. Here, isotopic enrichment S176 is defined as the fractional abundance of 176Yb ions in the Yb photo-ions generated during selective photoionization while enrichment factor α176 is defined as the ratio of fractional abundance of 176Yb in Yb photo-ions (product) to its natural fractional abundance (feed).*

Conclusion

We have successfully demonstrated three-step selective photoionization of ^{176}Yb from natural Yb sample. The transition wavelengths for three step resonant photoionisation of ^{176}Yb were precisely determined to the accuracy of ± 30MHz. Protocol/methodology was established for qualification of selective photoionization process in terms of laser wavelengths, intensities and spectroscopic selectivity by using TOFMS as diagnostic tool. The protocol was successfully used for laser qualification during laser isotope separation experiment to realize production of ~ 97% enriched ^{176}Yb at ~ 3 mg/hr.

Acknowledgement

Authors thank Dr. Archana Sharma, AD, BTDG, for her deep interest and constant support during this work.

References

1 A. Dash, M. R. A. Pillai, and F. F. Knapp Jr., *Nucl Med Mol Imaging* **49,** 85 (2015).

2 W.C. Martin, Romuald Zalubas, and Lucy Hagan, *NSRDS-NBS* **60,** 373(1978).

3 B. B. Krynetskii, V. A. Mishin, and A. M. Prokhorov, *Zhurnal Prikladnoi Spektroskopii* **54**, 558(1991)

4 W. A. van Wijngaarden, J. Li, *J. Opt. Soc. Am. B*, **11**, 2163(1994).

5 W. Jin, T. Horiguchi, M. Wakasugi, T.Hasegawa, and W. Yang, *J. Phy. Soc. Jap.* **60***,* 2896(1991).

6 S. K. Borisov, M. A. Kuz'mina, and V. A. Mishin, *Journal of Russian Laser Research* **17**, 332(1996).

Trace elemental detection in liquid sample using Laser Induced breakdown spectroscopy and its application in environmental field

Keerthi K[1]., Anish Kumar Warrier[2], Sajan D. George[1], Suresh D. Kulkarni[1], Santhosh C[1]. and Unnikrishnan V. K.[1]

[1]Department of Atomic and Molecular Physics, Manipal Institute of Technology, Manipal Academy of Higher Education, Manipal 576104, India

[2]Department of Civil Engineering, Manipal Institute of Technology, Manipal Academy of Higher Education, Manipal 576104, India

* E-mail: keerthiedattummal@gmail.com, unnikrishnan.vk@manipal.edu

Abstract

Though Laser Induced Breakdown Spectroscopy (LIBS) is a promising analytical method to monitor heavy metals in aqueous solutions on-site, its sensitivity for such studies is still a problem. Most of the LIBS investigations were performed on solid and gas samples that provide a uniform surface, greater reproducibility, and sensitivity. In this work, we focus on investigating the performance of the liquid LIBS technique using drop coating deposition on different substrates. Our results reveal that this system may be useful in designing a robust method for trace elemental detection in environmental samples. An attempt has been made to investigate the presence and bioaccumulation of metallic elements in Swarna river water at Udupi using a developed laser induced breakdown spectroscopy technique.

Introduction

Laser Induced Breakdown Spectroscopy (LIBS) is the most promising technique for the rapid quantification of trace metals in common fluids. Research in liquid sample studies using Laser Induced Breakdown Spectroscopy (LIBS) is a rapidly growing research field [1,2]. The studies range from different experimental configuration to the development of new plasmonic nanoparticle assisted enhancing substrates for real-world applications[3]. Thus, even for specialists, it is a very challenging task to handle liquid samples as compared to solid specimens. It is a fast method that requires little or no sample preparation. Unfortunately, laser-generated plasmas in liquids present several experimental challenges[4]. When the plasma is induced by nanosecond laser pulse inside the liquid bulk, fast quenching of laser-induced plasma occurs,[5] and atomic emission becomes weak in its intensity having a short lifetime. This work communicates the feasibility of LIBS to analyze the liquid samples using three different substrates viz. glass, Polymethyl methacrylate (PMMA), Teflon using dried droplet analysis. The experimental method consists of sample deposition, drying and analyzing steps. Micro volumes of droplets are manually loaded onto different substrates using calibrated micropipette and dried using microwave oven. The developed SELIBS substrate can currently be fabricated on a large scale at relatively low-cost, toward real-world applications in biomedical and environmental fields.

2. Experimental

2.1 Drop coating deposition

For overcoming the well-known drawback and difficulties arises from the physical properties of the liquid sample substrate coating method can be used. Liquid to solid conversion can be done by drying liquid solution on a suitable solid substrate. The sample deposition can be performed either by dipping the substrate on to the solution or drying the microliters of the solution onto the substrate. This approach will help to reduce expense and system complexity. One of the main advantages of this approach is the lack of experimental modification, thereby reducing the cost and system complexity. Figure.1 shows a schematic diagram of drop coating deposition, which includes loading, drying, and LIBS analysis.

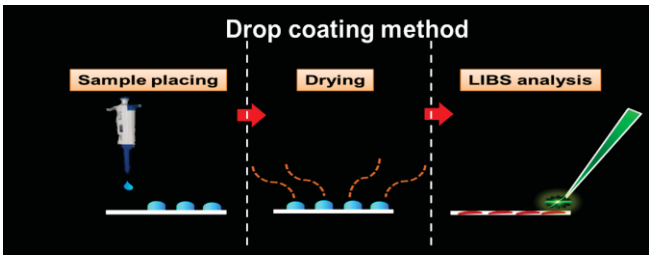

Figure.1 Schematic diagram of drop coating deposition

3. Result and discussion

3.1 Liquid studies using the drop coating method

In order to explore this observation, we started our work on drop coating with glass as a substrate. 1000ppm copper sulfate solution was prepared by dissolving copper sulfate on de-ionized water. 10ul of 1000ppm copper sulfate solution was deposited on the glass slide surface using a micropipette. To measure how many shots were necessary to completely remove the deposited analyte particle from the substrate itself. The variation of CuI-521.8 line intensity as a function of the number of laser shots, of 6mJ, fired at an area of Cu deposited substrate is plotted in Fig. 2. This investigation was carried out by monitoring the intensity decrease of the Cu emission intensity at 500-525 nm wavelength regions as a function of the number of laser shots. The signal intensity rapidly decreases with an increase in the number of laser shots. The decrease of signal intensity indicates the removal of Cu from the irradiated sample area. It can be seen that about five shots are required to nullify the spectral intensity, which most probably indicates the complete removal of Cu from the irradiated sample area.

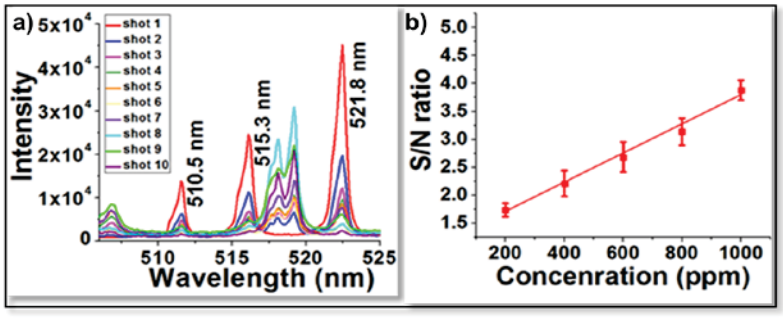

Figure.2 *a) Decrease of 1000ppm Cu emission intensity as a function of the number of laser shots focused on a glass slide to remove deposited analyte b) Calibration curve of Cu built by using a glass slide*

Different concentrations of Cu solutions were monitored by the drop coating deposition method on glass slide substrate. The analyte sample with different concentrations (Cu 200mg/L – 1000mg/L) was analyzed.10ul of the solution was used for each measurement and recorded by single pulses having energy 6mJ. Five LIBS spectra were recorded from different spots to evaluate the standard deviation. Figure.7 depicts the calibration curves of the Cu (324.8 nm) emission line. Data points represent the average signal to background(S/B) ratio of five spectra and error bars represent the standard deviations.

3.2 Detection of trace elements in Swarna river water

Nowadays, owing to haphazard urbanization and industrialization, the quality and quantity of water are turning out to be a major threat to mankind. The river water is becoming polluted day by day due to industrialization, urbanization, sewage waste, increase in population, dead bodies burning ash, and agricultural practices. The optimized drop coating deposition method was used for detecting trace elements in Swarna river water from malpe in the Udupi district.

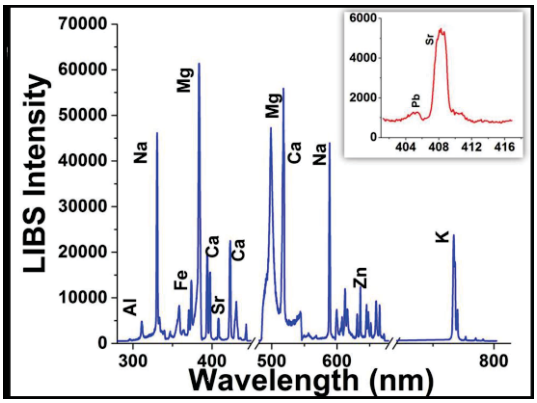

Fig.3. LIBS spectra of Swarna river water using drop coating deposition

The LIBS spectrum of Swarna river water has been recorded using the drop coating deposition method in the spectral region 300–800 nm and is shown in Fig. 3. The recorded spectrum consists of the number of atomic emission lines of varying intensities. These LIBS emission lines have been recognized using NIST spectral data. The recorded LIBS spectrum shows the presence of atomic lines of the macronutrients, (Na, K, Ca, Mg) micronutrients (Fe, Zn, Cr, Sr), and toxic metals (Pb). Insets are also used in Fig. 3 to get the details in the spectral ranges from 405 nm to 407 nm with enlarged intensity scales. The detected elements are presented in Table .1 with their emission wavelength. ICP-OES studies on the same samples need to be conducted to confirm these observations.

Element	Al	Ca	Pb	Sr	Fe	Mg	Na
Species	Al(I)	Ca(I)	Pb(I)	Sr(II)	Fe(I)	Mg(I)	Na(I)
Line(nm)	310.2	422.69	405.8	407.78	373.6	518.36	589.14
Element	Zn						
Species	Zn(I)						
Line(nm)	636						

Table.1 Elemental species detected from the Swarna river.

4. Conclusion

The present study demonstrates the capability of the LIBS technique for the elemental analysis of water samples without sample treatment in a short duration. It is found that the limit of detection for all elements of interest in drop coating deposition methods is better than direct bulk and liquid jet methods. The obtained result shows that the developed drop coating deposition on the substrate is efficient for detecting trace elements in contaminated environmental samples. Results demonstrate the analytical capability of the drop coating deposition method; as a potential target material for liquid sample analysis by the LIBS technique. The main advantages of using drop coating deposition in the liquid application are as follows: (1) It can avoid the problem of the sample inhomogeneities and splashing (2) it provides a more stable signal than the bulk liquid and jet method; (3) it is easier to perform calibrations since the sample can be coated and dried without affecting the optical alignment, and (4) It can be applied in biomedical field where the sample quantity is limited. The drop coating deposition has proven to be cable of detecting a very lower concentration using 10uL of analyte quantity with high specificity, but achieving a single molecule in any highly diluted solutions (parts per trillion) remains a challenge. The drop coating deposition study could be further extended by applying more robust sampling enrichment and applying nanoparticles for enhancing the LIBS intensity.

References

[1] A. De Giacomo, C. Koral, G. Valenza, R. Gaudiuso, and M. Dell'Aglio, *Nanoparticle enhanced laser-induced breakdown spectroscopy for microdrop analysis at subppm level*, Analytical chemistry **88**, 5251 (2016).
[2] Q. Lin, X. Han, J. Wang, Z. Wei, K. Liu, and Y. Duan, *Ultra-trace metallic element detection in liquid samples using laser induced breakdown spectroscopy based on matrix conversion and crosslinked PVA polymer membrane*, Journal of Analytical Atomic Spectrometry **31**, 1622 (2016).
[3] Z. Abdel-Salam, S. M. Alexeree, and M. Harith, *Utilizing biosynthesized nano-enhanced laser-induced breakdown spectroscopy for proteins estimation in canned tuna*, Spectrochimica Acta Part B: Atomic Spectroscopy **149**, 112 (2018).
[4] A. De Giacomo, M. Dell'Aglio, F. Colao, R. Fantoni, and V. Lazic, *Double-pulse LIBS in bulk water and on submerged bronze samples*, Applied surface science **247**, 157 (2005).
[5] D. A. Cremers, L. J. Radziemski, and T. R. Loree, *Spectrochemical analysis of liquids using the laser spark*, Applied spectroscopy **38**, 721 (1984).

Speckle Interferometry to determine thickness of PVA doped Graphene Oxide of film

Athira.A[*], Alok Sharan[*a]

[*]*Department of Physics, Pondicherry University, R V Nagar, Kalapet, Puducherry, India*

E-mail: athira7rythm@gmail.com, [a] aloksharan@gmail.com

Speckle interferometry technique is recently used in different studies such as measuring large object deformations by using temporal evolution of speckles [1]. It has also been used to measure micron size particle based on the temporal evolution of the speckle pattern [2], as well as film thickness are determined based on the electronic speckle interferometry [3]. In this study, we obtained a surface topography of films using Speckle Interferometry Technique. Simple experimental arrangement, non-destructive and non-contact measurement mode are the salient features of this technique. When laser beam is incident on any rough or diffusive surface, with the roughness to be order of the wavelength of incident light or more and smaller than coherence length of incident laser beam, more likely we see a randomly distributed pattern containing spots of light formed with varying sizes, which is a speckle pattern. In a speckle interferometry, we intentionally superpose it with a coherent reference beam. As a result, we have an interference between a speckle field and the reference light waves.

Experimental setup: We choose to implement on a Michelson interferometer geometry with one arm containing the reference light wave and the other arm has specimen under study as shown in fig(1). We initially setup the arrangement for zero path difference on the image plane. We record the interference pattern digitally using CCD Camera at the screen position. Then, subsequently insert the reference sample as well as the desired sample in the arms of the setup and acquire images at each instant. These images are subtracted by using code written in MATLAB and the film thickness is obtained. In this work, we obtain the thickness of poly vinyl alcohol – graphene oxide (PVA –GO) film by using speckle interferometry. Here the film was coated on a cleaned and treated glass plate. First, we mount two identical glass plate without any film deposition in both the arms of the interferometer set up and adjust to zero path difference to obtain the fringes due to glass plate alone. For studying the thickness of film, the blank glass plate from the 2nd arm is replaced by film coated glass plate. If the film surface is rough, then we got a speckle pattern on the image plane and the speckle pattern gives the film information's.

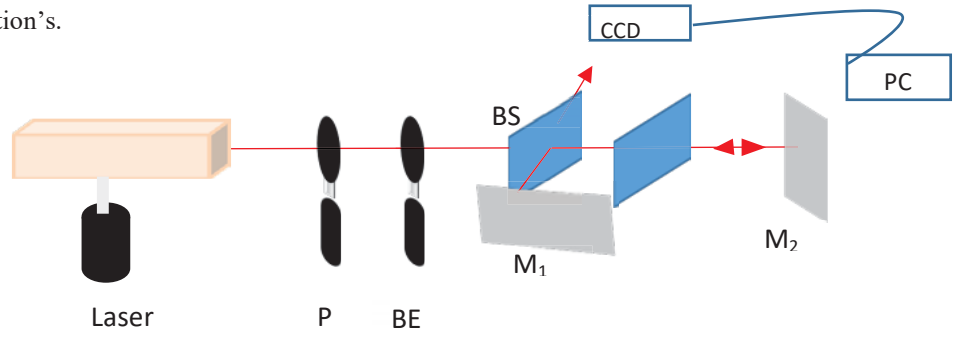

Fig (1) Schematic of Michelson Interferometer. P: Polarizer, BE: Beam Expander, M: Mirror, BS : Beam Splitter

Principle: If a plane wave is incident normally on a film of thickness d, then the waves reflected from the upper surface interfere with the waves reflected from the lower surface. It is clear that, the wave reflected from the lower surface of the film traverses an additional optical path of $2nd$, where n represents the refractive index of the material of the film. If the film is placed in air, then the wave reflected from the upper surface of the film will undergo a sudden change in phase of π. Then the condition for destructive or constructive interference will be given by,

$$2nd = \begin{cases} n\lambda & Destructive\ Interference \\ \left(n + \frac{1}{2}\right)\lambda & Constructive\ Interference \end{cases}$$

where $n = 0, 1, 2, \ldots$ and λ represent the wavelength.

For the non-normal incidence, wave reflected from the upper surface of the film interfere with the wave reflected from the lower surface of the film. The later travels an additional optical path Δ, which is given by,

$$\Delta = 2\, n_2 \cos\theta \qquad (1)$$

Where θ is the angle of refraction and n_2 is refractive index of the medium [4]

In the present study, we have two different set of images one with glass plate – glass plate and the other being film coated glass plate– glass plate reflecting surfaces. The image obtained by glass plate – glass plate surfaces is subtracted from the image obtained by film coated glass plate – glass plate surfaces to give the thickness of the film. The intensity distributions are recorded using a digital camera, which produces electrical signals stored in the computer memory in the form of digital JPEG image files. After capturing each file the intensity distribution due to glass plate – glass plate is subtracted from that of film – glass plate in the computer and the subtracted image is displayed on the monitor. This subtraction is performed by pixel by pixel (one pixel is equivalent to 6.45 μm).

Preparation of PVA Solution: 5 wt% PVA solution is prepared using stirring with heating process. For this 1.25 g PVA is heated and mixed with 25 ml distilled water for 1 hr at 100^0 C for getting transparent PVA solution.

Preparation of 0.3 wt % PVA-GO solution: Graphene oxide is prepared through modified hummers' method. For 0.3 wt% PVA-GO solution, 5.1 mg of graphene oxide is dissolved in 1.6 mL distilled water using ultra-sonication for 10 minutes to get GO solution first, Each 1.6 ml GO solution is slowly added to 2ml of PVA solution under constant stirring for 40 minutes for obtaining PVA-GO solution.

Film Preparation: Doctor Blade method is used to make PVA-GO films. For this purpose 5 drops of composite solution is dropped on a clean glass plate, and then casted on the entire surface by using another glass slide. Resultant film is allowed to dry for 24 hrs for getting PVA-GO films

Result and Discussion: The resultant fringe patterns obtained from the interferometry arrangement is shown in below. Fig.(**a**) represents the fringe pattern of reference beam due to the glass plate-glass plate combination. It is a net like structure, represents the intersection of the interference pattern due to each glass plates placed on the two mirror positions. Fig (**b**) represents the speckle pattern from the film surface alone. PVA – GO film is

transparent in nature. I.e. a portion of the beam is transmitted through the film and the transmitted light intensity is less. Therefore, the speckle pattern from the film surface may be arise due to the intensity distributions of the scattered light from the upper and lower surfaces of PVA – GO film. Fig (**c**) gives the fringe pattern due to glass plate-film combination. Compared to the reference beam, when film is inserted a change in the fringe pattern is clearly visible. This change in the pattern contains film information. Fig (**d**) is the subtracted image of glass plate- glass plate from glass plate – film image. This fringe represents the optical thickness of film alone. From this, we can find out the thickness of film.

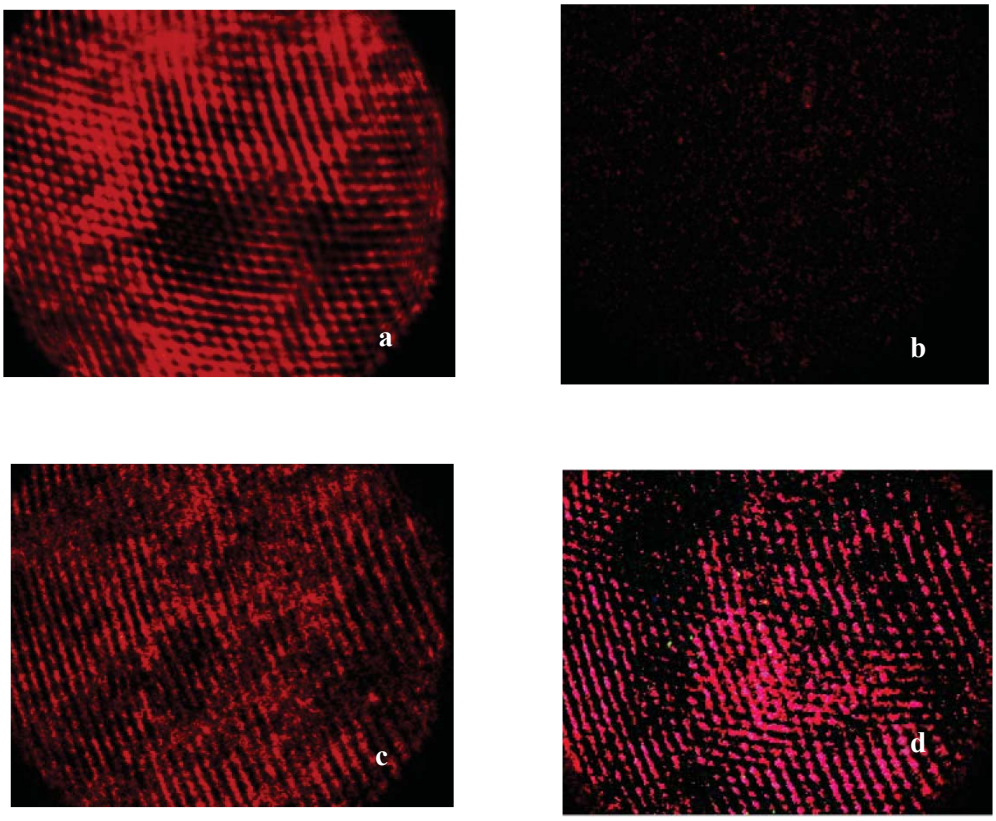

From the resultant specklegram, the difference between two points on consecutive bright or dark fringes along X –axis or Y – axis and this difference multiplied by the pixel size of 6.45 μm gives the optical thickness. Using equation (1) thickness of film is obtained as around 56μm. Here refractive index of PVA-GO film is calculated using Brewster angle method and is obtained as 1.51. Thickness of PVA-GO film is also compared using optical microscopy having least count 10μm. The result shows good agreement with the result from Speckle Interferometry. For this, the measurements were carried out from the glass plate in which the film is coated. Then the readings were taken out from the film surface. In addition, the subtracted Vernier scale positions give the film thickness. The readings were carried out at least of five different positions on the film surface. Moreover, it is fall in the range of 50 -60 μm.

Conclusion: In our study, we presented a simplest experimental arrangement to find out the thickness of films. The main advantages of this work are, thickness was obtained in a non-contact mode only, which do not cause any additional deformation on film surface and this arrangement is easy to set up and understand. Thickness of

film measured using speckle interferometry is almost matched with the film thickness obtained from optical microscopy.

References:

1. C Joenathan, *Applied Optics*, Vol. 37, May 1998
2. Luis J Mendoza- Herrea, *Optics and Lasers in engineering*, Vol. 140, May 2021
3. Canan Karaalioglu, *Optics Communications,* 234(269-276), 2004
4. Ghatak, Ajoy, *Optics* (2nd ed.), New Delhi, Tata McGraw-Hill (1992)

Vortex Beam based Micro-Raman Spectroscopy of optically Trapped Functional Erythrocytes

Ghanashyam C, Santhosh Chidangil and Aseefhali Bankapur*

Department of Atomic and Molecular Physics, Manipal Academy of Higher Education, Manipal-576104

Email: asif.bankapur@manipal.edu

Abstract

Altering the laser beam profile from Gaussian to vortex beam using a spiral phase plate and subsequently using it for optical trapping in an unconventional face-on orientation and for simultaneous micro-Raman spectroscopy presents a prospect of studying conformational state of hemoglobin (Hb) molecules near the erythrocytes membrane. In this study the Raman spectra recorded using the vortex as well as the Gaussian beam has been compared to identify the oxygenation status of Hb molecules near the membrane and inside the bulk of the cell respectively. We also discuss the possible reason for the observed difference in distribution of oxy/deoxy Hb molecules inside the cell.

Introduction

The pursuit of methods for analysing the biomolecules with a view to get deeper insights into the biological processes and early diagnosis of diseases is an ever-growing field of research. Among the methods, Raman spectroscopy has been successfully employed to determine the molecular structure, its constituents, and interaction between them [1]. Raman spectroscopy relies on the inelastic scattering of light by the molecule and carries the fingerprint rotational and vibrational information of the sample.

Erythrocytes are primarily responsible for carrying oxygen throughout the body. The erythrocytes concentration in blood is approximated to be 4-6 $\times$ 10^9 cells/mL and are the most copious cells in humans. They are 6-8 μm in diameter and 2 μm thick with a shape of biconcave disks [2]. The Raman spectra of erythrocytes are dominated by the vibrational modes from hemoglobin (Hb) as 33 % of erythrocytes is Hb by volume. There has been a long-standing interest in the Raman spectroscopic investigation of erythrocytes; primarily due to oxy-deoxy transition in erythrocytes that leads to significant structural modifications in Hb. This following research mainly concentrates on obtaining Raman signals from erythrocytes trapped in face-on orientation using vortex beam with a focus on obtaining Raman signals exclusively from the boundary of the cell.

Experimental

The experimental setup used for our experiment is shown in figure 1. The usage of 785 nm can be attributed to the following considerations. The efficiency of Raman scattering has a λ^{-4} dependency, indicating the desirability of shorter wavelengths. However, the shorter wavelengths present the problem of laser-induced photodamage. Moreover, the choice of 785 nm reduces the fluorescence effect that can mask the weak Raman signals. Thus 785 nm appears to be the right choice [3]. The Galilean type beam expander is used to overfill the back aperture of the microscope objective so as to focus the light efficiently. The 1:1 telescopic arrangement is

for quick correction on any possible misalignments and also for the sub-micron displacement of the focal spot. The dichroic mirror is used for reflecting the laser beam while transmitting the Raman signals and visual light from halogen lamp. The laser is focused on the sample by the objective lens and the backscattered light is collected by the same objective and focused onto the spectrometer slit by an f/4 lens. The high pass edge filter is used to remove the Rayleigh scattered signal and pass only the Raman signal to the spectrometer. The Raman signal is dispersed using the Horiba Jobin Yvon iHR320 using 1200 grooves/mm grating blazed at 750 nm. Signal detection is performed by liquid nitrogen cooled charge-coupled detector operating at 140 K.

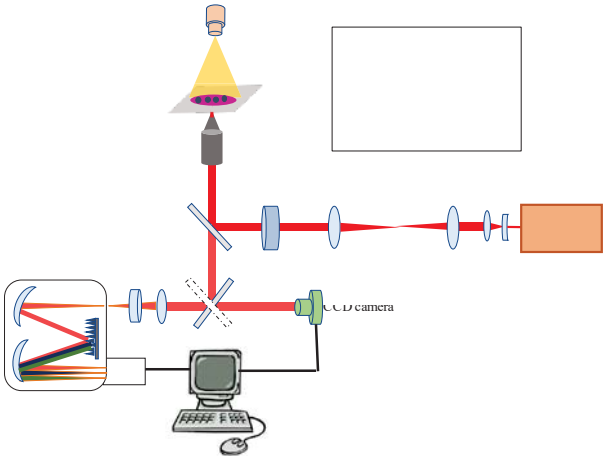

Figure 1. *Schematic representation of the micro-Raman setup*

Spiral phase plate with topological charge m=12 was introduced into the aligned micro-Raman setup and we could observe the laser beam with vortex or donut shaped profile. The inner diameter of the vortex beam was set to about 7.8 μm. This size for the donut focal spot of the vortex beam ensures optical trapping of erythrocytes (6-8 μm) by its outer rim and excites simultaneous Raman scattering.

Results and Discussions

The introduction of spiral phase plate changed the laser profile from Gaussian to vortex having a central null region with intensity distributed in a doughnut shape. The conversion was confirmed by taking the image of the laser beam focussed using microscope objectives and are shown in figure 2A. Single, live erythrocytes were trapped using a vortex beam both in face-on and edge-on orientation. Figure 2B shows the images and schematic representation of optical trapping using Gaussian and vortex beams. The usage of the Gaussian beam for trapping results in the flipping of erythrocytes to acquire edge-on orientation as shown in figure 2(B(a)). This flipping of erythrocytes is to align its symmetry axis perpendicular to the beam axis to maximize the overlap between cell and trapping beam We made a successful effort in trapping erythrocytes as a flat disc (face-on orientation) using the vortex beam as shown in figure 2(B(b)). This required precise alignment of the optical set up so that the intensity distribution throughout the rim of the vortex beam is uniform. The optical force acting on the cell was perfectly balanced by fine adjustment of SPP using an XY translational stage.

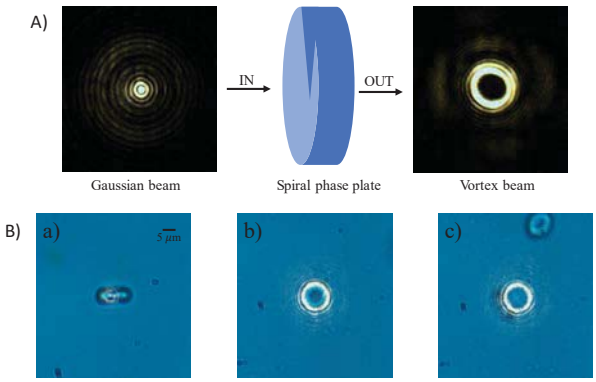

Figure 2. *Image of the Gaussian and doughnut (vortex) beams focussed using 40x microscope objective(A). Optical trapping of single, live RBC(B) using (a) Gaussian beam, (b) vortex beam (face-on orientation), (c) vortex beam (edge-on orientation),*

Micro-Raman spectroscopy measurements were performed on single, optically trapped erythrocytes using Gaussian as well as vortex beams. During Raman measurement, the cell was trapped in an edge-on orientation with the Gaussian beam and was trapped in face-on orientation while using the vortex beam. The single-cell spectrum in both cases (Figure 3 and 4) has all prominent spectral features from hemoglobin, proteins, lipids and carbohydrates. On comparing the spectral features of heme, it has been observed that the vortex beam excited spectrum is dominated by the contribution from hemoglobin molecules in an oxygenated state whereas that recorded using the Gaussian beam showed contributions from hemoglobin molecules in both oxygenated state (oxy-state) and deoxygenated state (deoxy-state). The Raman frequencies at 672, 1222, 1373, 1397, 1559, 1616, and 1637 cm^{-1} are relatively intense in vortex beam excited Raman spectra, whereas the peaks at 1116, 1522, 1548, and 1602 cm^{-1} are intense in the Gaussian beam exited spectra. Additionally, the peaks at 562 and 1564 cm^{-1} are present in former spectra, and peaks at 749, 1211, and 1607 cm^{-1} are present in the latter spectra. The Raman peaks listed above and their relative intensity variations are well understood and reported as markers for the oxy/deoxy state of hemoglobin [4].

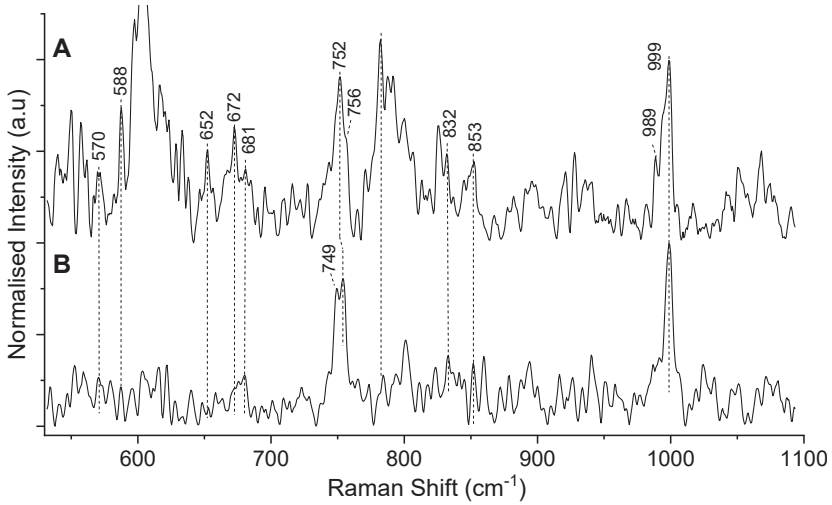

Figure 3: Raman spectra of trapped single ERYTHROCYTES (low frequency region) recorded using the vortex beam (A) and Gaussian beam (B). Power density: ~ 3.6 ×10^4 W/cm^2, Integration time: 40 s, average of 2 accumulations.

Considering the fact that oxygen influx in erythrocytes is through the cell membrane, the oxygen concentration/tension near the cell membrane should be more compared to that inside the bulk of a cell. The cytoplasmic diffusion has been reported to be a dominant barrier for efficient oxygen transport in erythrocytes[5]. This diffusion should create an oxygen gradient in erythrocytes with its concentration being more near the cell membrane. At ambient conditions, the erythrocytes will have hemoglobin molecules in both the oxy and deoxy state, but with the above-mentioned gradient in oxygen tension and its influence on hemoglobin's oxygen affinity, one can expect that most of the hemoglobin molecules close to the erythrocytes membrane should be in oxy state. On contrary the Raman spectra recorded using the Gaussian beam show a mixture of R- and T- state of hemoglobin; more specifically, no oxygen saturated hemoglobin.

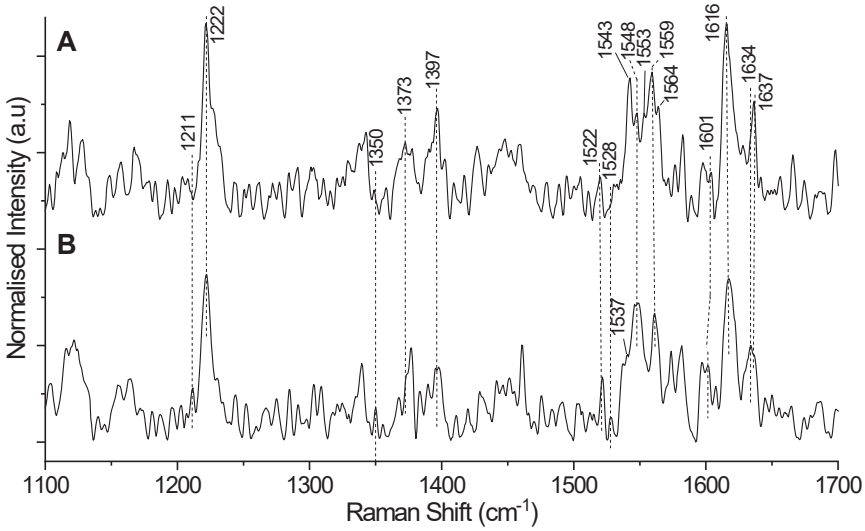

Figure 4: Raman spectra of trapped single ERYTHROCYTES (high-frequency region) recorded using the vortex beam (A) and Gaussian beam (B). Power density: ~ 3.6 ×10^4 W/cm^2, Integration time: 40 s, average of 2 accumulations.

Conclusion

It has been found that most of the hemoglobin molecules in the vicinity of the cell membrane are in the oxy-state, and molecules inside the bulk of the cell are a mixture of oxy and deoxy states. This observation suggested that a concentration gradient in oxy-Hb is present inside the erythrocytes with its maxima being close to the cell membrane. This is possible because oxygen is readily available near the cell membrane and its concentration decreases away from it owing to diffusion induced retardation.

References

1. C. Zong, M. Xu, L.-J. Xu, T. Wei, X. Ma, X.-S. Zheng, R. Hu and B. Ren, Chemical reviews **118** (10), 4946-4980 (2018).
2. W. R. Premasiri, J. C. Lee and L. D. Ziegler, The Journal of Physical Chemistry B **116** (31), 9376-9386 (2012).
3. A. Bankapur, E. Zachariah, S. Chidangil, M. Valiathan and D. Mathur, PLoS one **5** (4), e10427 (2010).
4. B. R. Wood, P. Caspers, G. J. Puppels, S. Pandiancherri and D. McNaughton, Analytical and Bioanalytical Chemistry **387** (5), 1691-1703 (2007).
5. S. L. Richardson, A. Hulikova, M. Proven, R. Hipkiss, M. Akanni, N. B. Roy and P. Swietach, Proceedings of the National Academy of Sciences **117** (18), 10067-10078 (2020).

DEVELOPMENT OF A COMBINED LIBS-RAMAN SPECTROSCOPIC SYSTEM FOR RAPID CHARACTERIZATION OF PLASTICS

Adarsh U.K[a]., Bhoje Gowd E [b], Aseefhali Bankapur[a], Santhosh Chidangil[a], and Unnikrishnan V.K[a]*

a. *Department of Atomic and Molecular Physics, Manipal Academy of Higher Education, Manipal, Karnataka, India*

b. *CSIR-National Institute for Interdisciplinary Science and Technology (NIIST) Trivandrum, Kerala, India*

*email: unnikrishnan.vk@manipal.edu

ABSTRACT

The invention of plastic materials has evoked an insurrection in manufacturing industries, but along with the ever-intensifying hazard of plastic solid waste. The recycling industries which are important in plastic waste management are challenged by the absence of a proper plastic sorting system. The current article discusses about the progress in development of an integrated LIBS and Raman spectroscopic system for the rapid characterization of plastics. We have successfully developed the system using single source and single detector optical scheme that makes it cost-effective. Four industrially important plastic classes were successfully characterized using the system with the help of multi-variate data analysis technique.

INTRODUCTION

The invention and development of plastic materials, especially thermo-plastics, had an impact in making our day-to-day life easy. Because of their characteristic properties like heat-induced molding, weightlessness, toughness, and cost-effectiveness, plastics are widely used in different industries like food, electronics, toy, and construction. But this increase in plastic usage is eventually causing an increase in plastic solid-waste from post-consumer products that is triggering serous impacts on environment[1]. The plastics discarded in water bodies and landfill causes severe health hazards because of the pollution as well as the presence of potentially hazardous additives in them[2]. Since there exists no proper plastic-waste disposal method without interrupting environment, an established plastic waste management method is the plastic recycling. The quality of recycling and thus ecological and economic impact is defined by the accuracy in sorting the collected plastic wastes in to the native plastic classes like PET, PC, PE, PMMA, PP, PVC, PS, etc.[3].

The application of spectroscopic techniques for the plastic identification and characterization is gaining attention and are been under investigation for the said purpose. The major spectroscopic techniques including near-infrared (NIR), x-ray fluorescence (XRF), laser induced breakdown spectroscopy (LIBS), and Raman spectroscopy are being examined for the specific application of plastic identification and sorting. Some inherent drawbacks of these methods are preventing them from being the best method for sorting plastics. Recent studies suggests that a single method of analysis alone cannot provide an accurate assessment of all commonly used plastic classes[4].

A possible solution for tackling the drawbacks of spectroscopic methods is to combine them together in a system so that the weakness of one method can be compromised with the advantage of the other. The benefit of combining LIBS and Raman spectroscopic techniques together is that the combined elemental and structural information of the sample can be obtained using a single system that will be complementary and can act like inter-confirmatory to ensure the maximum possible accuracy for the sorting system. Our group has reported the combined LIBS-Raman system with multiple detectors for plastic identification[5] by combining it with the chemometric tools. Use of multiple detectors make the system costlier and bulkier. Also, the optimized analysis time required for a single sample, especially for Raman analysis is 40 seconds that reduces the total number of samples analyzed per hour considerably, preventing it from being an ideal system for industry-oriented plastic sorting. Thus the objective of this work is to develop a compact and portable LIBS-Raman device dedicated for plastic analysis with considerably less analysis time. Also, the over-all cost of the system is to be reduced for a wide practical application.

METHODOLOGY

Experimental Set-up

The system was designed and developed using a single source and single detector for both LIBS and Raman analysis of samples without any disturbance or rearrangements to the optical alignment. The laser source used is a pulsed nano-second Nd:YAG laser operating at 532 nm wavelength. Laser repetition rate was fixed at 10 Hz for the output having a pulse width of 6 ns. A Czerny-Turner spectrograph (Andor-Kymera 328i)-CCD (Andor iDus) combination was used for resolving and detecting collected signal. The optical alignment of the system is represented in figure 1. The signal collection geometry was realized in back-collection mode where a single lens is used for both focusing the beam and collecting the signal. A 60mm focal length 2" diameter lens was used for signal collection for ensuring maximum signal collection efficiency. A 200mm focal length 2" diameter lens was used for coupling the signal to spectrograph. A laser energy regulator device that was developed in the laboratory was used to tune the laser energy in accordance to whether LIBS is to be carried out or Raman analysis of the sample.

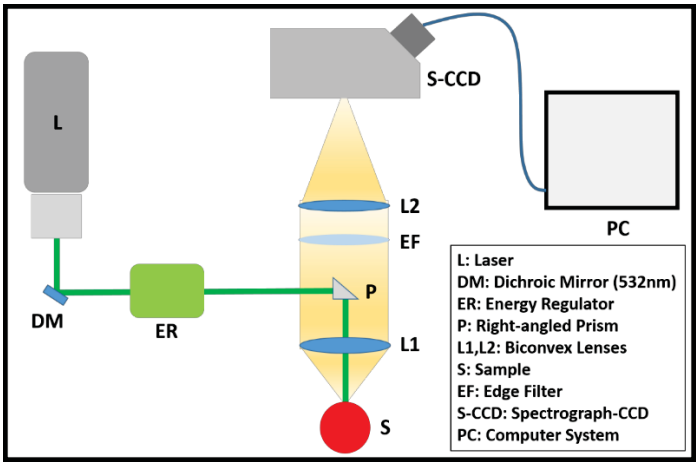

***Figure 1**: Experimental setup for LIBS-Raman study of plastics*

Samples Used

All preliminary studies in the proposed system was carried out using virgin plastic samples procured from CSIR-National Institute for Interdisciplinary Science and Technology (NIIST) Trivandrum. Laboratory-made samples including polypropylene (PP), polycarbonate (PC), Polymethylmethacrylate (PMMA), and polylactic acid (PLA), which are industrially important plastic classes were subjected for analysis.

Experimental Procedure

All samples where in the form of granules having a dimension of about 4mm. Samples were stuck on the sample holder using double sided tape. Different acquisition settings were applied for LIBS and Raman as follows: LIBS experiments were carried out by applying a laser energy of 5mJ, which is significantly less compared to the previous reports. The LIBS acquisition was performed in the single-shot mode where only a single pulse from the laser is used for ablation and excitation of the sample. The edge filter (532nm) in the setup shown in figure 1 was mounted in a rotatable filter wheel thus allowing it only during the Raman analysis. Exposure time of 0.05second was applied and a total of ten spectra in a wavelength region dominated by CN molecular emission bands were collected from each plastic class. All LIBS spectra were background subtracted and normalized with respect to CN molecular emission band at 388.31nm. Since LIBS was performed in ambient air, the air breakdown spectra were also recorded and compared with the sample spectra to check for air contribution in the sample spectra.

Raman spectra of the samples were collected by keeping the edge filter in position and applying a laser energy of 2mJ for excitation and an exposure time of 4 seconds. This reduced acquisition time helps to analyze the samples rapidly using the proposed system. As in the case of LIBS, a total of ten spectra were collected from each sample class for analysis. All Raman spectra were background subtracted and normalized with respect to the highest peak (since no emission bands are common for all samples).

RESULTS AND DISCUSSION

The LIBS spectra of PP, PC, PMMA, and PLA samples with that of ambient air prior normalization are shown in figure 2a.

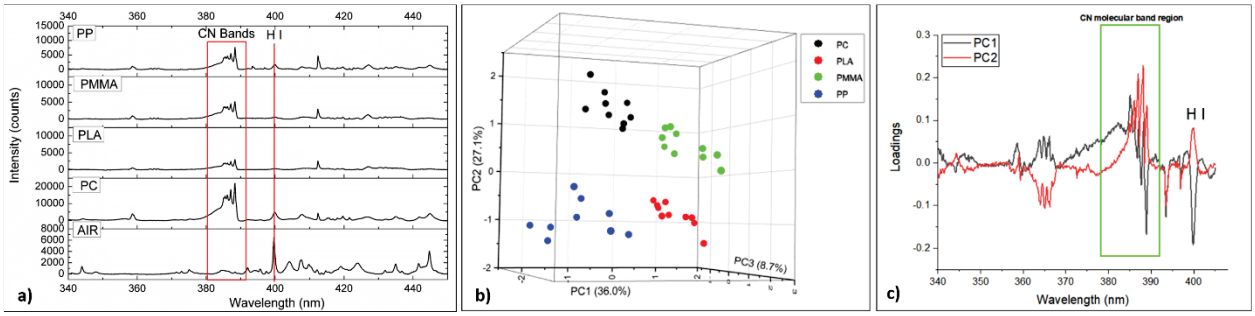

***Figure 2**: a) LIBS spectra of PP, PMMA, PLA, and PC samples with LIBS spectra of ambient air b) PCA score plot on LIBS data, and c) Loadings plot based on PCA results*

Figure 2a suggests that the CN molecular emission rises purely from samples since it is absent in air spectra. A common emission line in samples and air is the hydrogen emission line at 399.8nm. A variation in spectra is expected in the region containing these lines and thus the principal component analysis was performed in the range from 340 to 410nm after normalization. Corresponding PCA score plot, and loadings plot for first two components are shown in figure 2a and 2b, respectively.

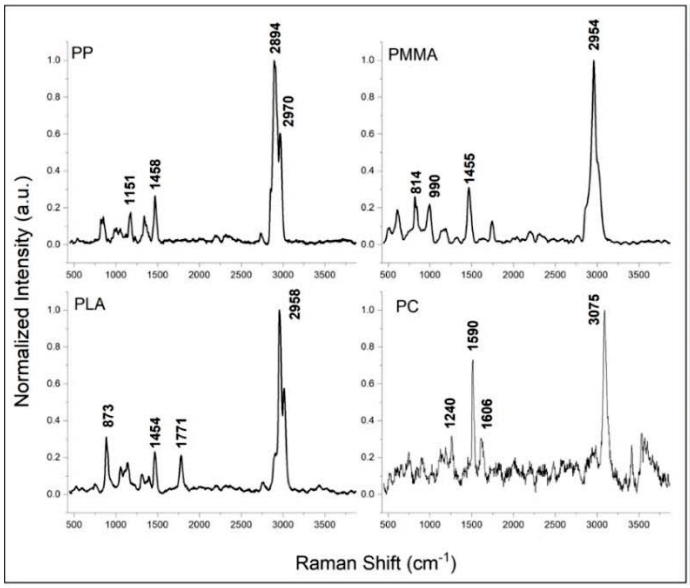

Raman Shift (cm^{-1})	Band Assignment
PP	
1151	C-C stretching
1458	CH_2 bending
2894, 2970	CH_3 stretching
PMMA	
814	C-O-C stretching
990	O-C stretching
1455	O-CH_3 bending
2955	α- CH_3 stretching
PLA	
873	C-COO stretching
1454	CH_3 bending
1771	C=O stretching
2958	CH_3 stretching
PC	
1590,1606	Ring stretch
1240	C-O deformation
3075	C-H stretching

***Figure 3**: Raman spectra of PP, PMMA, PLA, and PC samples*

The PCA score plot proposes a good classification of the samples based on the LIBS spectra. All four samples are separately classified without any ambiguity. The loadings plot suggests that the major variance in the spectra is caused due to the variations in CN molecular emission bands at 388.31nm, 387.12nm, and 386.17nm and hydrogen emission line at 399.8nm. Thus for the four plastic classes considered for the study, LIBS analysis in the wavelength region from 340nm to 410nm offers a good classification and can be used for building a classification model.

Since the samples considered does not have close-comparable elemental composition, any ambiguous results were not expected. To ensure the ability of the system to perform LIBS and Raman, and as a confirmatory study for the results obtained from LIBS analysis of virgin plastics, Raman analysis was also performed. This inter-validation will be crucial when the system is applied for analyzing post-consumer plastics in real-world conditions. The corresponding Raman spectra of samples are shown in figure 3 along with assignments for four major Raman bands from each class. From figure 3, it can be identified that the Raman spectra of different

plastic classes are visually itself different based on the characteristic emission bands. Yet a PCA analysis was carried out on the data collected during Raman analysis and the corresponding score plot and loadings plot for first two components are shown in figure 4.

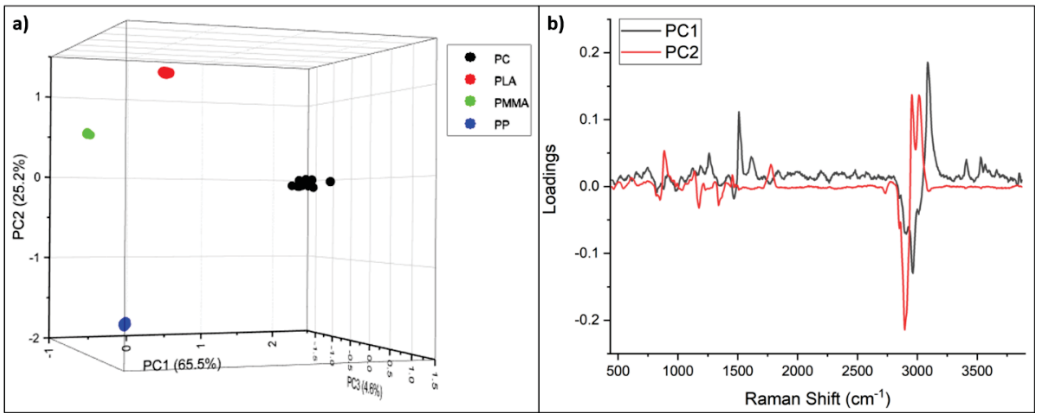

***Figure 4**: Results of PCA analysis on Raman data a) Score plot, b) Loadings plot*

As anticipated from the spectra, a good clustering of data can be seen in the score plot in figure 4. The loadings plot (fig.4.b) also suggests that emission lines from a sample is characteristic to that sample and that provides a good variance among the data. Thus by combining these two techniques, a more accurate and rapid device can be developed with inter-confirmatory capabilities.

Since this results are of a preliminary study using virgin plastics, it can be considered as a motive for carrying forward the proposed research using real-life samples like post-consumer plastics with different additives and fillers in their matrix.

CONCLUSIONS

A combined LIBS-Raman plastic characterization and sorting system using single source – single detector optical alignment has been realized in a compact and portable manner. The total analysis time required for one sample using both technique has been reduced considerably compared to the previous reports. The preliminary evaluation of the system using four different virgin plastic types including PP, PMMA, PC, and PLA shows the capability of the developed instrument to carryout both LIBS and Raman analysis without altering the optical alignment and in a short interval of time. A good classification of the samples based on the data collected is also obtained that promises the application of the system for the analysis of real-life plastic samples in future studies.

REFERENCES

1. Lazarevic D, Aoustin E, and Buclet N, Brandt N. Plastic waste management in the context of a European recycling society: Comparing results and uncertainties in a life cycle perspective. Resources, Conservation and Recycling. **2010**;55(2):246-259
2. Lithner D, Larsson Å, Dave G. Environmental and health hazard ranking and assessment of plastic polymers based on chemical composition. Science of the Total Environment. **2011**;409(18):3309-3324
3. Hopewell J, Dvorak R, Kosior E. Plastics recycling: challenges and opportunities. Philosophical Transactions of the Royal Society B: Biological Sciences. **2009**; 364(1526):2115-2126.
4. Michel A. P., Morrison A. E., Preston V. L., Marx C. T., Colson B. C., and White H. K., Rapid Identification of Marine Plastic Debris via Spectroscopic Techniques and Machine Learning Classifiers. Environmental Science & Technology. 2020 54(17), 10630-10637.
5. Shameem K. M., Choudhari K. S., Bankapur A., Kulkarni S. D., Unnikrishnan V. K., George S. D., and Santhosh C,. A hybrid LIBS–Raman system combined with chemometrics: an efficient tool for plastic identification and sorting. Analytical and bioanalytical chemistry, 2017, 409(13), 3299-3308.

Optical and spectroscopic properties of Sm^{3+} ions doped fluoroborosilicate glasses for photonic device applications

Megala Rajesh, B. Deva Prasad Raju*

[1]*Department of Physics, Sri Venkateswara University, Tirupati-517502, India*

[2]*Department of Instrumentation, Sri Venkateswara University, Tirupati-517 502, India*

Email: drdevaprasadraju@gmail.com

Abstract :

The Sm^{3+} ions doped fluoroborosilicate (SBNCSm) glasses were prepared using melt quenching technique. For the synthesized glasses absorption and photoluminescence emission spectra were recorded. From absorption spectra J-O parameters were evaluated. The glass doped with 0.5 mol % Sm^{3+} ions (SBNCSm05) has the highest emission intensity for $^4G_{5/2} \rightarrow {}^6H_{7/2}$ transition (600 nm). The fluorescence emission parameters were calculated form emission spectra. The SBNCSm05 glass attain highest σ_{emi} (11.23 x 10^{-20} cm^2), gain bandwidth (16.22 x $10^{-25}cm^3$) and optical gain parameter (19.85x 10^{-25} cm^2s). The obtained values suggested that SBNCSm05 glasses can be used as a potential candidate in photonic device applications.

1. Introduction:

In recent years, scientist were very fascinated in the field of luminescence exhibited by the materials activated with rare earths (RE) and transitions metal (TM) ions due to their wide applications in up-converters, hole burning high-density memories, light-emitting diode (LEDs), modern telecommunication (optical fiber amplifiers, waveguide lasers, optical luminescence solar energy concentrators. The low phonon energy host materials will give higher radiative emission efficiencies due to decrease in non-radiative losses. The glasses activated using RE^{3+} ions mainly used in various applications like solid-state lasers, medicine, military, day-to-day lightening, and modern communications systems [1-4]. Among the glass host materials, the borosilicate glasses are excellent host materials for RE ions doping. The incorporation of alkali/alkaline fluoride to borosilicate glass host will modify the structural groups of the host glass and the coordination of the boron, reducing the phonon energy dispersion and scattering losses of the borosilicate glass host and increases its mechanical strength. Calcium fluoride (CaF_2) and sodium fluoride (NaF) were included in the present investigated glass composition.

The Sm^{3+} ions doped materials are potentially used in the visible lasers, high-density optical devices, bio-friendly lighting sources, and under see communication and high power lasers. Furthermore, The Sm^{3+} ions activated glass hosts are used in micro beam radiation therapy (MRT) (i.e., preclinical radiation treatment for cancer and also used traffic signals and headlights in vehicles. Based on these, the trivalent samarium ions doped glass is superior to the other RE ion-doped host matrices. Owing to these interesting properties and their extensive applications in modern technology, in this present work, trivalent samarium (Sm^{3+}) ions were selected as doping ions in the aforementioned fluoroborosilicate glasses. In this present work, upon considering the above mentions points, the authors prepared fluoroborosilicate (SBNC) glasses activated with different concentrations of Sm^{3+} ions. Various physical, optical and spectroscopic properties were analysed to optimize Sm^{3+} ions concentration in synthesized SBNC glasses. The obtained results suggested that the SBNCSm glasses could be used as potential candidates for photonic display device application.

2. Experimental :

The fluoroborosilicate glasses activated with different concentrations of Sm^{3+} ions were synthesized by adopting the melt quenching method. For the present work, glass composition is as follows (35-x) SiO_2 + 25 B_2O_3 + 10 Na_2CO_3 + 15 NaF + 15 CaF_2 + x Sm_2O_3 (where x = 0.1, 0.5, 1.0, 1.5 and 2.0 mol %). The glass preparation procedure was explained in **[5].** The synthesized samples were named as SBNCSm01, SBNCSm05, SBNCSm10, SBNCSm15 and SBNCSm20 for Sm^{3+} = 0.1, 0.5, 1.0, 1.5and 2.0 mol% respectively. Synthesized sample's refractive index and density were determined with an Abbe refractometer (using $C_{10}H_7Br$ as contact liquid) and Archimedes principle (using distilled water as immersion liquid) respectively. The absorption spectra were measured with JASCO model V-570 UV-vis –NIR spectrometer with 1 nm resolution within 300 to 2000 nm wavelength range. The emission profile was recorded using FLS -980 fluorolog-3 spectrophotometer. All the experiments were performed at room temperature (RT) only.

3. Results and Discussions:

The various physical properties such as refractive index (n = 1.664), thickness (t = 0.303 cm), density (δ = 2.5375 g/cm^3), dielectric constant (ε = 2.709) were calculated for SBNCSm05 glass.

3.1. Optical absorption spectra and JO Intensity parameters

Fig. 2 shows the optical absorption spectrum of SBNC glass doped with 0.5 mol% Sm^{3+} ions within 300 to 1800 nm spectral ranges. It was noticed that the spectrum consists of 04 peaks in visible (359, 373, 400, 436, and 475 nm corresponding to the transitions $^4I_{9/2}$ → $^4D_{3/2}$, $^4L_{17/2}$, ($^4D_{5/2}$, $^6P_{5/2}$), $^6P_{3/2}$, ($^6P_{5/2}$, $^4P_{5/2}$) respectively) and 06 peaks in the NIR region (937, 1071, 1218, 1364, 1466 and 1517 nm corresponding to the transitions $^4I_{9/2}$ → $^6F_{11/2}$, $^6F_{9/2}$, $^6F_{7/2}$, $^6F_{5/2}$, $^6F_{3/2}$, $^6H_{15/2}$ respectively).

Table 1. *The values of oscillatory strength (experimental (f_{exp}) and calculated (f_{cal})) for various absorption bands in SBNCSm05 glass.*

Absorption transition	Wavelength (λ) nm	*Oscillatory strength (X 10^{-6})*	
		f_{exp}	f_{cal}
$^4I_{9/2}$ → $^4D_{3/2}$	359	1.251	0.984
$^4I_{9/2}$ → $^4L_{17/2}$	373	1.454	2.512
$^4I_{9/2}$ → ($^2D_{5/2}$, $^6P_{5/2}$)	400	8.942	8.743
$^4I_{9/2}$ → $^6P_{3/2}$	436	0.315	0.005
$^4I_{9/2}$ → ($^4P_{5/2}$, $^4P_{5/2}$)	475	2.656	0.245
$^4I_{9/2}$ → $^6F_{11/2}$	937	0.848	0.601
$^4I_{9/2}$ → $^6F_{9/2}$	1071	3.970	3.826
$^4I_{9/2}$ → $^6F_{7/2}$	1218	6.127	6.261
$^4I_{9/2}$ → $^6F_{5/2}$	1364	4.814	4.799
$^4I_{9/2}$ → $^6F_{3/2}$	1466	3.848	3.849
$^4I_{9/2}$ → $^6H_{15/2}$	1517	2.404	0.031
		δ_{rms} = 1.06 x 10^{-6}	

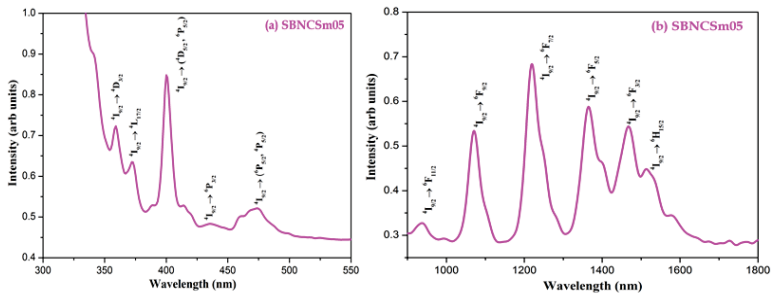

Fig.1 Optical absorption spectra of SBNCSm05 glass

The optical absorption spectra of all the SBNCSm glasses under investigation have similar band positions as SBNCSm05 glass except their intensity. For Sm^{3+} ion in SBNC glasses, the transitions that follow $|\Delta J| \leq 6$ selection rule and are induced electric dipole and transitions which follows $|\Delta J| = 0, \pm 1$ are magnetic dipole [18,35]. It is observed that $^6H_{5/2}$ → $^6P_{3/2}$ and $^6H_{5/2}$ → $^6F_{7/2}$ were treated as hypersensitive transitions for SBNCSm glasses. In general, the intensity of the absorption bands was measured in oscillatory strength. The calculated (theoretically determined) oscillatory strength (f_{cal}) were evaluated by employing the Judd-Ofelt theory. The obtained f_{exp} and f_{cal} values of SBNCSm glasses are presented in Table 1.

Table 2. *J-O spectral intensity parameters of SBNCSm glasses*

Glass sample	JO parameters (x 10^{-20} cm^2)		
	Ω_2	Ω_4	Ω_6
SBNCSm05	3.51	8.10	4.36
SLfSfASm10 **[3]**	2.73	7.49	3.01
SNbKZfSm10 **[4]**	1.19	6.71	2.48
BPbBaLiSm10 **[1]**	2.649	4.247	4.183
LCZSFBSm10 **[2]**	2.44	8.54	6.40

Table 3. *The radiative parameters values for SBNCSm05 glass*

Transition	SBNCSm05		
	S_{ed}	A	β_R
$^4G_{5/2} \rightarrow {}^6H_{5/2}$	15.49	32.90	0.05
$^4G_{5/2} \rightarrow {}^6H_{7/2}$	245.22	259.65	0.43
$^4G_{5/2} \rightarrow {}^6H_{9/2}$	183.60	183.60	0.30
$^4G_{5/2} \rightarrow {}^6H_{11/2}$	70.23	70.23	0.12
	A_T = 604.30 τ_R = 1654 µs		

Judd-Ofelt theory is a well-established method to evaluate spectral intensity parameters (Ω_2, Ω_4, and Ω_6) of lanthanide ions activated glass hosts materials. The phenomenological spectral intensity parameters are useful in describing selective information related to the fluorescent material's performance and efficiency. The JO parameters are evaluated for the present investigated SBNCSm glasses, and the resulted values are shown in Table 2, along with previously reported values. The values of JO intensity parameters for all concentrations of Sm^{3+} ions doped SBNC glasses followed the $\Omega_4 > \Omega_6 > \Omega_2$ trend. The magnitude of these intensity parameters increased with concentration of Sm^{3+} ions, attains maximum to SBNCSm05 glass (Ω_2 = 3.514 x 10^{-20} cm^2, Ω_4 = 8.103 x 10^{-20} cm^2 and Ω_6 = 4.365 x 10^{-20} cm^2) and decreased with further increase in the Sm^{3+} ions concentration.

3.2. Emission spectral analysis

Fig. 2 depicts the emission spectra of investigated SBNCSm glasses within 500 to 850 nm spectral range. The emission profile was recorded under 405 nm wavelength excitation. Four emission peak positions were noticed in the Fig.4 at 563, 600, 647 and 718 nm and the corresponding transitions are $^4G_{5/2} \rightarrow {}^6H_{5/2}$, $^4G_{5/2} \rightarrow {}^6H_{7/2}$, $^4G_{5/2} \rightarrow {}^6H_{9/2}$ and $^4G_{5/2} \rightarrow {}^6H_{11/2}$ respectively. It is observed that, transition $^4G_{5/2} \rightarrow {}^6H_{7/2}$ (600 nm) has the highest peak spectral intensity than the rest of the transitions.

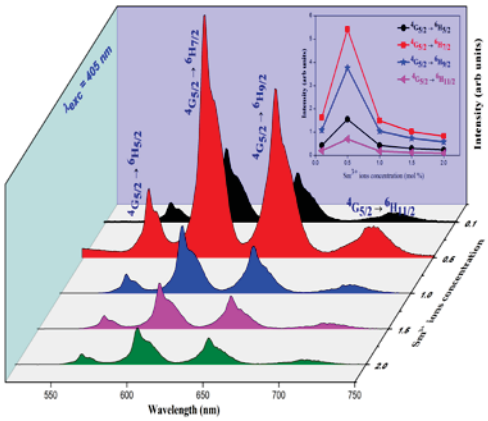

Fig 2. *The fluorescence emission profile of SBNCSm glasses.*

Table 4. *Comparison of characteristic laser parameters for $^4G_{5/2} \rightarrow {}^6H_{7/2}$ (600 nm) of SBNCSm05 glass with reported literature*

Glass sample	λ_p	$\Delta\lambda_{eff}$	σ_{emi} (x 10^{-20} cm^2)	σ_{emi} x $\Delta\lambda_{eff}$ (x 10^{-25} cm^3)	σ_{emi} x τ_{mes} (x 10^{-25} cm^2s)
SBNCSm05	600	14.44	11.23	16.22	19.81
SLfSfASm10 **[4]**	599	14.52	9.23	13.40	35.45
BLPbASm10 **[5]**	600	10.59	7.23	7.59	11.7
PMZSSm10 **[6]**	600	18.43	9.57	17.63	6.41
PKANbSm10 **[7]**	599	15.07	11.52	17.35	13.54

It was also noticed that the intensity of the emission peaks was increase with the increase in the concentration of Sm^{3+} ions up to 0.5 mol% Sm^{3+} ions doped glass (SBNCSm05) and further enhance in the concentration of Sm^{3+} ions the emission intensity was decreased. This decrease in emission intensity at higher Sm^{3+} concentration may be due to the concentration quenching effect. This was due to the cross-relaxation

energy transfer at a higher concentration of Sm^{3+} ions because while an increase in the Sm^{3+} ions concentration, For SBNCSm05 glass, the fluorescence emission peak corresponding to transition $^4G_{5/2} \rightarrow {}^6H_{7/2}$ (600 nm) has attains maximum spectral intensity than the remaining. Using these radiative parameter values (table 3) and emission data the fluorescent emission parameters were calculated and tabulated in the table 4. From the Table 4, among the four transitions of the optimized SBNCSm05 glass, transition $^4G_{5/2} \rightarrow {}^6H_{7/2}$ emitted visible radiation at 600 nm has attains high values of stimulated emission cross-section (σ_{emi}), gain bandwidth (σ_{emi} x $\Delta\lambda_{eff}$), optical gain parameter (σ_{emi} x τ_R) and experimental branching ratio (β_{exp}). The comparison of emission parameters of $^4G_{5/2} \rightarrow {}^6H_{7/2}$ transition of optimized glass (SBNCSm05) with reported literature was shown in Table 7. From the table 7 the $\boldsymbol{\sigma_{emi}}$ value of SBNCSm05 glass (11.23 x 10^{-20} cm^2) was higher than SLfSfASm10 glass (9.23 x 10^{-20} cm^2) [1] , BLPbASm10 (7.23 x 10^{-20} cm^2) [5], PMZSSm10 (9.57 x 10^{-20} cm^2) [6] and TWGSm10 (6.99 x 10^{-20} cm^2) [7].

4. Conclusions :

The oxyfluoroborosilicate glasses doped Sm^{3+} ions were prepared. The high values of the JO parameters were suggested that, the environment around the Sm^{3+} ions in the SBNC glass was covalent, regid, and highly asymmetric in nature. The values spectroscopic parameters (stimulated emission cross-section (σ_{emi} = 11.23 x 10^{-20} cm^2), gain bandwidth (σ_{emi} x $\Delta\lambda_{eff}$ = 16.22 x 10^{-25} cm^3) and optical gain parameter ((σ_{emi} x τ_R = 19.81 x 10^{-25} cm^2) suggested that the investigated SBNCSm glasses could be used in the development of photonic device applications.

5. Acknowledgments:

Prof. B. Deva Prasad Raju is highly thankful to DST-SERB, Govt. of India for sanctioning major project (File. No. EEQ/2016/000041) dt: 17-01-2017. Megala Rajesh is very much thankful to the Department of Science and Technology, Govt. of India for the award of DST-INSPIRE fellowship (IF150753) to pursue Ph.D.

References:

1. N. Srinivasa Rao, Megala Rajesh, G. Rajasekhara Reddy, B. Deva Prasad Raju, S. Dhanapandian, *Opt. Mater* **97** 109360 (2019).
2. Sd Zulfiqur Ali Ahmed, C. Madhukar Reddy, B. Deva Prasad Raju, *Spectrochim. Acta* **103** 246–254 (2013).
3. C.S. Dwaraka Viswanath, C.K. Jayasankar, *Ceram. Intern.* **44** 6104-6114 (2018).
4. K. Linganna, Ch. Basavapoornima, C. K. Jayasankar, *Opt. Commun*. **344** 100-105 (2015).
5. N. Deopa, A.S. Rao, *Opt. Mater.* **72** 31–39 (2017).
6. F. Ahmadi, R. Hussin, S. K. Ghoshal, *J. Non-Cryst. Solids* **448** 43-51 (2016).
7. T. Srihari, C.K. Jayasankar, *Opt. Mater.* **66** 35–42 (2017).

Laser spectroscopy of TaC in jet-cooled beam

Sheo Mukund[1,*], Soumen Bhattacharyya[1,2], and S.G. Nakhate[1,2]

[1]*Infrared Laser Spectroscopy Section, Physics Group, Bhabha Atomic Research Centre, Mumbai-400085, India*

[2]*Homi Bhabha National Institute, Bhabha Atomic Research Centre, Mumbai-400085, India*

[*]Email: sheo@barc.gov.in

Abstract

We report the first observation of the harmonic and anaharmonic vibrational frequencies of the $X^2\Sigma^+$ ground electronic state and a low-lying $A^2\Delta$ state in TaC molecule. The investigation was carried out by laser-induced dispersed fluorescence spectroscopy in a pulsed supersonic molecular beam setup. The TaC molecules were produced by the reaction of laser ablated Ta metal plasma with 1% CH_4 gas seeded in helium. Dispersed fluorescence spectra were recorded by exciting the isolated rotational lines of the $^2\Pi_\Omega$–$X^2\Sigma^+$ (v,0) bands.

Introduction

Transition-metal carbides, in particular TaC has the highest melting temperature among other physical and chemical properties. The information on the molecular properties of such transition-metal carbides are vital to determine various physical and chemical properties, as these materials plays important role in material science, thin films and nanotechnology[1,2]. As pointed out by Krechkivska and Morse[3], group 3–5 monocarbide are more difficult to produce than those of groups 8–10 because of atypical conditions needed for their formation. This is the reason why their spectroscopic investigation has been impeded and the only experimental study on TaC has been reported by Krechkivska and Morse[4]. However, to the best of our knowledge, experimental determination of the ground state vibrational frequency and observation of the low-lying states in TaC molecule has not been reported. There are a few *ab initio* studies on this molecule[5].

In this paper, we investigated vibrational structure of the ground electronic state and observation of the low-lying electronic states of TaC. Usually isovalent molecules exhibit the same ground state electronic configuration and term symmetry. However, while the $^2\Delta$ ($1\sigma^2 2\sigma^2 1\pi^4 1\delta^1$) state is the ground state for VC and NbC, the $^2\Sigma^+$ ($1\sigma^2 2\sigma^2 1\pi^4 3\sigma^1$) state is the ground state for TaC. The different ground state in TaC molecule, as compared to VC and NbC, is due to the net relativistic stabilization of the 6*s* orbital in Ta atom. Due to this effect, the contraction of 3σ orbital in TaC resulting in the $^2\Sigma^+$ ($1\sigma^2 2\sigma^2 1\pi^4 3\sigma^1$) state falls below the $^2\Delta$ ($1\sigma^2 2\sigma^2 1\pi^4 1\delta^1$) state. Moreover, since the 3σ orbital in TaC has 6*s* in atomic character, this unpaired electron couples with the ^{181}Ta, nuclear spin, I =7/2 to give the unusual hyperfine coupling case $b_{\beta S}$ with the total spin momentum, $\boldsymbol{G} = \boldsymbol{I} + \boldsymbol{S}$, which can take the values 3 and 4. The interaction energy is given by $b_F \mathbf{I}\cdot\mathbf{S}$, where b_F is the Fermi Contact parameter. Thus, each rotational level of the ground state is split into two hyperfine components belonging to the G = 3 and 4 and is separated by $4b_F$ = 0.52 cm^{-1}. The dispersed fluorescence (DF) spectra were recorded from the excited electronic states reported by Krechkivska and Morse and vibrational frequencies for the ground $X^2\Sigma^+$ state and observation of $A^2\Delta$ state are reported.

Experimental

The TaC molecules were produced in a pulsed supersonic molecular beam (SMB) setup[6]. A rotating and translating tantalum metal rod was ablated with the third harmonic beam of a Nd:YAG laser having pulse energy

~10 mJ, focused to a spot of ~1 mm^2 area. The resulting tantalum metal plasma reacted with 1% methane seeded in helium gas, generating TaC molecules at low temperature by supersonic expansion. The molecules in the beam were probed at right angle to the supersonic expansion axis by a tunable pulsed dye laser. The resulting laser-induced fluorescence (LIF) was gathered by a collection optics in orthogonal direction to the laser beam and SMB axes. The LIF was dispersed by a monochromator and detected by a Peltier cooled photomultiplier tube (PMT). The PMT signal was further amplified and integrated by a gated Box-car integrator and stored on a computer. The DF spectra were obtained from the excited electronic states reported by Krechkivska and Morse by exciting the isolated rotational lines. Typical DF spectral line widths (FWHM) were ~50 cm^{-1} at the best obtained resolution.

Results and Discussion

Dispersed fluorescence spectra were recorded from the observed TaC transitions over the range 17850-20000 cm^{-1} from the ground $X^2\Sigma^+$ state, reported by Krechkivska and Morse. In their work, they reported transitions having the upper state symmetry $^2\Pi_{1/2}$. Apart from this, other spectral features were found as complex overlapping bands which remained unanalyzed, without establishing the upper state symmetries. The DF spectra were recorded in the wavelength region 400-900 nm by exciting a single rotational level within the various excitation bands. We observed vibrational progression v = 0–5 for the $X^2\Sigma^+$ ground state. A DF spectrum recorded by exciting an isolated rotational line at 18618.30 cm^{-1} from one of the unanalyzed band [18.61] $^2\Pi_\Omega$–$X^2\Sigma^+$ (v,0) is shown in the Figure 1.

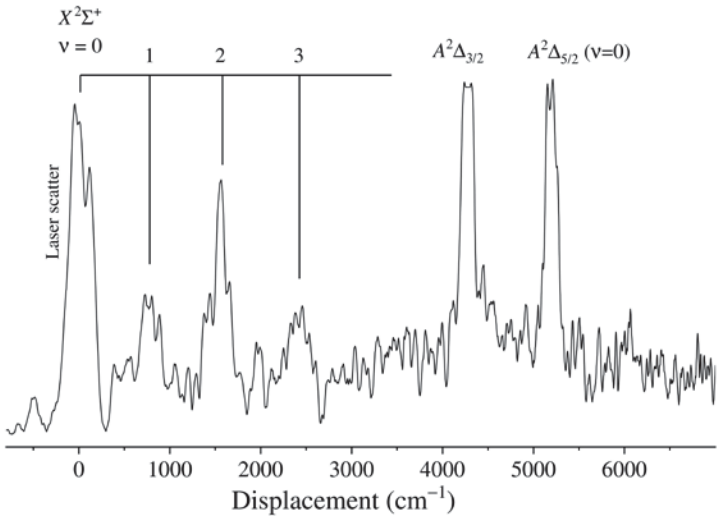

Figure 1. *Laser-induced dispersed fluorescence spectrum of TaC molecule observed by exciting an isolated rotational line at 18618.30 cm^{-1} form the [18.61] $^2\Pi_\Omega$–$X^2\Sigma^+$ (v,0) band. The x-axis shows the displacement in cm^{-1} from the excitation line.*

The equilibrium vibrational constants for the ground $X^2\Sigma^+$ state were obtained by fitting term values to an anharmonic oscillator formula,

$$\Delta G = G(v) - G(v) = \omega_e v + \omega_e x_e v(v+1) \quad (1)$$

where v is a vibrational quantum number, $G(v)$ is term value of v^{th} vibrational level and, ω_e and $\omega_e x_e$ are harmonic and anharmonic vibrational constants. We determined ω_e = 778(4) cm^{-1} and $\omega_e x_e$ = 1.9(7) cm^{-1} for the

ground state. In addition, the $A^2\Delta$ state, which was identified as the ground state in isoelectronic VC and NbC molecules, was also observed at $T_0 = 4775$ cm^{-1} (see Figure 1). The observed vibrational frequency of the $X^2\Sigma^+$ ground state and term energy of the $A^2\Delta$ state in this work are in good agreement with the *ab initio* calculations reported by Majumdar and Balasubramanian, respectively at 748 cm^{-1} and 4847 cm^{-1}.

References

1. R. Teghil, A. De Bonis, A. Galasso, P. Villani, and A. Santagata, *Appl. Surf. Sci.* **254**, 1220 (2007).
2. A. Fukunaga, S. Chu, and M. E. McHenry, *J. Mater. Sci. Lett.* **18**, 431 (1999).
3. O. Krechkivska, and M.D. Morse, *J. Phys. Chem. A* **117**, 13284 (2013).
4. O. Krechkivska, and M.D. Morse, *J. Chem. Phys.* **133**, 054309 (2010).
5. D. Majumdar, and K. Balasubramanian, *Chem. Phys. Lett.* **284**, 273 (1998).
6. S.G. Nakhate, S. Mukund, and S. Bhattacharyya, *J. Quant. Spectrsc. Rad. Trans.* **111**, 394 (2010).

Detection of antioxidant compounds using Surface enhanced Raman scattering spectroscopy

Sweta Sharma[1], Aarti Jaiswal[2] and K. N. Uttam[1]
[1]*Shah's Spectroscopy Laboratory, Department of physics, University of Allahabad*
[2]*Centre for Material Sciences, University of Allahabad*
Email: swetasharma3989@gmail.com

Abstract

Plasmonic nanoparticles are highly potential candidates for the fabrication of the simple, rapid, selective and specific SERS detection systems for analytes of plant origin offering very low detection limits. The study describes a simple approach for the synthesis of silver nanoparticle colloidal solution using chemical reduction method that can be used for enhancing the Raman spectral signatures of the plant phenolic compounds like ferulic acid and sulphosalicylic acid. The Raman spectral signatures of the phenolic compounds excited by 785 nm laser shows vibrational spectral features that are peculiar for each phenolic compound having the capability to detect these compounds even at 1 μM concentration. The vibrational spectral signatures obtained in this study are very helpful in conceptualizing, designing and fabricating simple, rapid and cost effective onsite detection of the detection of plant derived products with very low detection limits.

Introduction

Antioxidant compounds like ferulic acid and sulphosalicylic acid are important natural 'plant phenolic compounds' having substantial lipid and water solubility possessing immense beneficial effects on human health. They are reported to have UV-protection, cardiovascular protection, anti-carcinogenic, free radicals scavenging capability, DNA damage repair and andanti-inflammatory properties. Furthermore these compounds have also much industrial applicability like natural food preservative, production of paints, paper, and cosmetics. Particularly, the food industry has increasingly considered the use of natural phenolic antioxidants as an efficient strategy to retard oxidative deterioration in food-based systems and thereby maintain their sensory characteristics [1]. Therefore, there is an increasing demand of methods for extraction of natural antioxidants from plant materials and the protocols and techniques for their characterization, detection and quantification. Characterization and quantification of phenolic compounds is conventionally performed by mass spectrometry (MS) and various combinations of chromatographic procedures such as ion exchange chromatography, gel filtration chromatography and high pressure liquid chromatography. Some of these techniques are although sensitive and accurate but they require specialized facilities, equipments/instrumentations and are high cost and non-portable. These techniques also require expensive materials, qualified operators, multi-step sample preparation and complex analytical procedures [2].

Thus there is a need to develop detection systems that have ease of operation and provide high selectivity and sensitivity towards a range of metal ions *in situ* in real-time. Vibrational spectroscopic probe like Raman spectroscopy produces characteristic fingerprint spectra of the sample by the interaction of the incident monochromatic light with the vibrations of the chemical bonds of the sample. Although Raman spectroscopy is a widely recognized and powerful technique in many fields of science, conventional Raman spectroscopy is limited by low cross section (10^{12}-10^{14} times smaller in comparison to fluorescence) resulting in low signal and poor efficiency. In order to enhance the Raman scattering signal, the advancements in the resonance Raman technique can be utilized. Surface-enhanced Raman scattering (SERS) spectroscopy significantly augments the scattering and provides large enhancement of several orders of magnitude (~10^6) in the Raman cross-section on

prepared metal surfaces especially prepared silver (Ag), gold (Au) and copper (Cu) nanoparticles by the means of localized surface Plasmons without the need of new components or instrumentation [3].

In this study, we report the synthesis of silver nanoparticles synthesized by chemical reduction method using sodium borohydride. The synthesized nanoparticles have been used for the surface-enhanced Raman scattering detection of the antioxidant compound: ferulic acid, and sulphosalicylic acid. The optimized synthesis process and surface enhanced Raman scattering signals deduced in this study are useful in conceptualizing and designing devices for the specific and sensitive detection of antioxidant compounds at very low concentrations.

Materials and Methods

Silver nitrate ($AgNO_3$), sodium borohydride ($NaBH_4$), NaOH, ferulic acid and sulphosalicylic acid were procured of analytical grade from the Sisco Research Laboratories, Mumbai, India and were used without further purification. All the solutions were prepared in distilled water. The silver nanoparticles were synthesised with the help of sodium borohydride ($NaBH_4$) as a reducing agent. 10 ml of 10 mM $AgNO_3$ and 30 ml of 10 mM $NaBH_4$ solution was prepared in distilled water. The solution of $AgNO_3$ was added drop-by-drop in the $NaBH_4$ solution kept in ice bath in an opensystem under continuous stirring. After colloidal solution synthesis, the solution was kept in dark. In order to investigate the LSPR properties of the synthesized colloidal solution, the solution was characterized using ultraviolet-visible spectroscopy. The ultraviolet-visible measurements were acquired by using fibre optic spectrometer (AvaSoft-3648, Avantee, Netherland) in the spectral region 200-800 nm at 2.3 nm resolution. The synthesized silver nanoparticles colloidal solution was used for recording the SERS spectra of the ferulic acid and sulphosalicylic acid.

Surface enhanced Raman scattering (SERS) measurements of the metal ions

The ferulic acid and sulphosalicylic acid were dissolved at a concentration of 1 mM concentration in distilled water and the resultant solutions were mixed with synthesized silver colloidal solution in order to obtain their SERS spectra. The surface-enhanced Raman scattering measurements were performed on confocal micro Raman mapping system (UniRAM). The SERS signals were excited by 350 mW, 785 nm near infrared diode laser. The metal-nanoparticles solutions were kept in sample container and placed on the sample platform. The laser beam was focused on the sample surface with the help of 10x objective lens. The scattered signals were detected by thermoelectrically cooled charge coupled device detector together with 600 groove/mm grating with the help of Andor Solis software. The spectra were collected in the spectral range 0-2000 cm^{-1} at an integration time of 10 sec. The obtained spectra were denoised by Savitzky-Goley algorithm using 3 data point polynomial window and 21 points window size. Further the baseline of the spectra has been corrected by piece-wise correction method using Origin 9.0 Pro software. The reproducibility of the results were ascertained by analysing three different and independent experiments and the obtained resultant average intensity has been reported in the form of mean ± standard error.

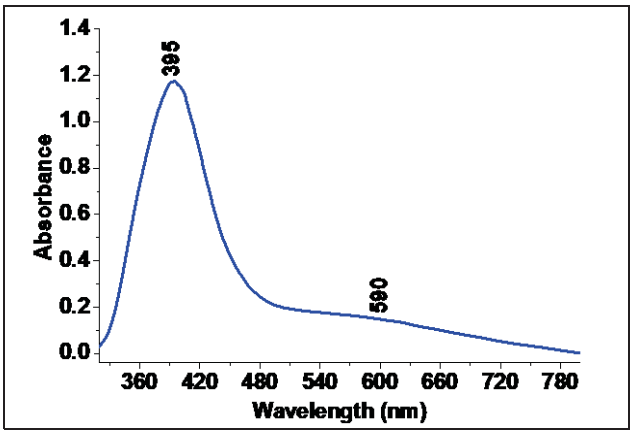

Figure 1: Ultraviolet visible spectra of the synthesized silver nanoparticles colloidal solution

Results and discussion

Figure 1 shows the recorded ultraviolet-visible spectrum of silver nanoparticles colloidal solution synthesized by chemical reduction method using sodium borohydride as reducing agent. The analysis of the silver nanoparticles colloidal solution shows a strong band at 395 nm and a weak band at 590 nm. The band 395 nm arises due to LSPR band of silver nanoparticles. The LSPR band is observed due to the oscillations of the electromagnetic field of the incident electromagnetic wave are in resonance with those of the local electromagnetic field of the nanoparticles and is characterized by the resonance oscillation frequencies. The LSPR arises due to the confinement of the electric field in a small metallic sphere whose radius is much smaller than the wavelength of the electromagnetic radiation. This property can be tuned by controlling parameters like shape, size, uniformity and surface coating and can be used for the biosensing applications in the field of biology, pharmaceutical and chemistry [4].

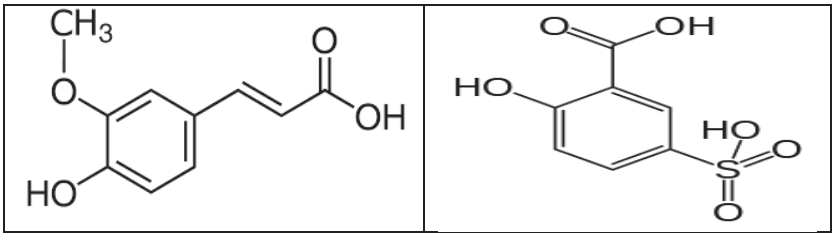

Figure 2: Molecular structure of (a) Ferulic acid and (b) Sulphosalicylic acid

The synthesized silver nanoparticles have been used for recording the SERS spectra of the antioxidant compounds like ferulic acid and sulphosalicylic acid at 1.0 μM concentration. Figure 3 shows the recorded SERS spectra of the like ferulic acid and sulphosalicylic acid on silver colloidal solution. The analysis of the SERS spectra of the ferulic acid on silver nanoparticles colloidal solution shows several peaks at wavenumbers 247, 320, 389, 433, 511, 610, 740, 816, 933, 965, 1118, 1191, 1245, 1367, 1483, 1579 and 1613 cm^{-1}. The peak at 247 cm^{-1} arises due to β (C-OOH) and β (O-CH_3). Three small peaks originating at 320, 389 and 511 cm^{-1} develops due to C-O-CH_3 bending mode, β (O-H) and γ (C-C-C) respectively. Small band is also located at 610 cm^{-1} which corresponds to β (C-O) and β(O-H) in COOH vibrations. Moreover, bands are also observed at 740, 816 and 965 cm^{-1} is assisgned to β (C-C-C), ring breathing and γ (C-H) vibrations respectively. Furthermore, 1483 cm^{-1} is also observed which develops due to OCH_3 bending and O-H bending. The spectrum also shows very intense peaks at 1118, 1245 and 1367 cm^{-1} developing de to in plane C-H bending, C-O stretching and COO stretching respectively. In addition, to these peaks, vibrational frequencies are also observed at 1597 and 1613 cm^{-1} correspomding to C=C stretching and phenyl ring deformation respectively [5].

Similarly the analysis of the SERS spectra of the sulphosalicylic acid shows prominent peaks at 363, 434, 599, 667, 731, 808, 891, 943, 1023, 1081, 1151, 1243, 1289, 1372, 1553, 1575 and 1605 cm^{-1}. The bands at wavenumbers 363, 434, 599 and 667 cm^{-1} arise due to torsional O-H and out of plane bending phenyl ring vibrations respectively. The vibration arising at 731 cm^{-1} corresponds to stretching phenyl ring vibrations. The Raman signatures seen at 808, 891 and 943 cm^{-1} develop due to C-H out of plane bending vibrations. Furthermore, bands arising at 1023 and 1081 cm^{-1} are assigned to S-OH and C-COOH stretching vibrations respectively. In addition, the bands observed at 1151, 1243, 1289 and 1372 cm^{-1} correspond to in plane C-H bending, stretching SO_2 vibrations, in plane CH_3 bending and stretching (C-O)-C vibrations respectively. A weak band developing at 1575 cm^{-1} corresponds to stretching vibrations of phenyl rings [6]. The limit of detection and limit of quantification have been estimated and it lies in the micro-molar range.

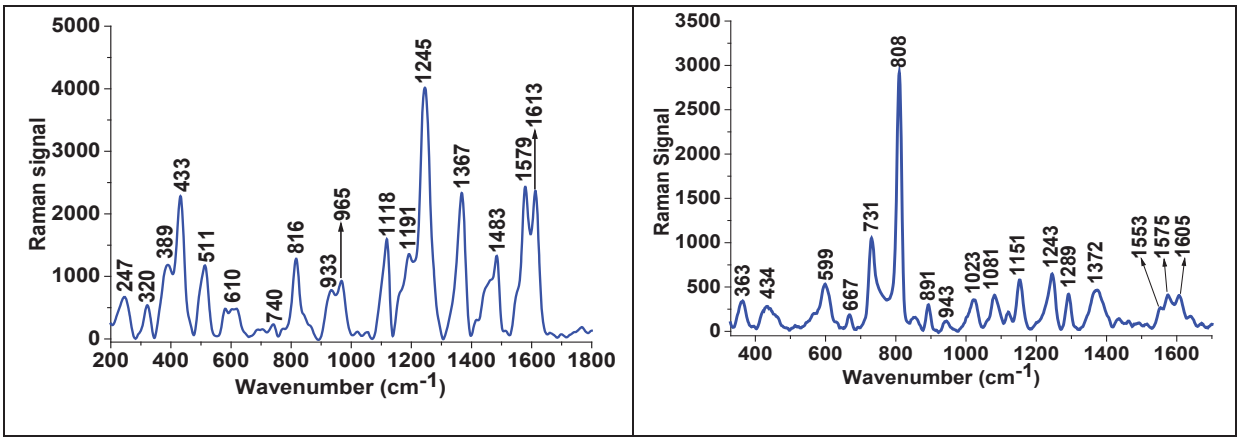

Figure 3: SERS spectra of (a) Ferulic acid and (b) Sulphosalicylic acid on silver nanoparticle colloidal solution.

The vibrational spectral signatures obtained in this study are very helpful in conceptualizing, designing and fabricating simple, rapid and cost effective onsite detection of the detection of plant derived products with very low detection limits

References

1. E. A. Abourashed, *Antioxidants*, 2, 4 (2013).

2. S. Sharma, A. Jaiswal, K. N. Uttam, *Analytical Letters*, 53, 2355 (2020).

3. S. Sharma, A. Jaiswal, K. N. Uttam, *Analytical Letter, Accepted 2020.*

4. I. Aguilar-Hernández, N. K. Afseth, T.López-Luke, F. F. Contreras-Torres, J. P. Wold, N. Ornelas-Soto, *Vibrational Spectrosc*., 89, 113 (2017)

5. E. Clavijo, J. R. Menendez and R. Aroca, J Raman Spectrosc. 39, 1178 (2008).

6. H. T. Varghese , C. Y. Panicker and d. Philip, J. Raman Spectrosc. 38, 309 (2007).

Confocal Raman Micro-spectroscopic Investigation of Phytochromes Present in the Petals of Different Cultivars of Bougainvillea Flowers

Aradhana Tripathi[1], Aishwary Awasthi[1], Sweta Sharma[1, 2] and K N Uttam[1]
[1]Saha's Spectroscopy Laboratory, Department of Physics, University of Allahabad, Allahabad
[2]Department of Applied Science and Humanities, Faculty of Engineering and Techniques, Khwaja Moinuddin Chishti Language University, Lucknow
Email: aardhanagate@gmail.com

Abstract

Bougainvillea is an ornamental flower which has an immense value in landscaping, pharmaceutical and cosmetic industries. The colour of the flowers is a function of plant pigments and therefore it is very essential to identify the pigments present in the flowers using automated cost effective and rapid techniques. Keeping this fact in mind, the study highlight the applicability of the confocal Raman microspectroscopy for the non-destructive, label free, rapid identification and characterization of the biochemicals present in the delicate biological samples having complex matrix like flowers. The Raman spectra of the different cultivars of bougainvillea have been recorded using 785 nm laser in the spectral region <2000 cm^{-1}. The analysis of the spectral signatures reveals that different cultivars of bougainvillea have different biochemical composition and are rich in carotenoids, flavonoids, phenolic and cuticle compounds and they can be readily evaluated with the help of the detected Raman spectral features. The spectral signatures obtained in this study can be used by the planners and industrial personals for the effective use of bougainvillea flowers for allied purposes.

Introduction

Flowers are the wonderful gift of nature and are available in different attractive colours, shapes, forms and odours. Bougainvillea also known as paper flower belongs to family *Nyctaginaceae* and is a widely grown flower [1]. This bougainvillea plant is a thorny, woody, climbing vine that grows well in warm climate and requires well-drained soil. It is widely used for landscaping and beautification. Bougainvillea is also used in pharmaceutical industries. Different parts of bougainvillea have immense medicinal values as they are used for the treatment of cough, sore throat, diarrhoea, stomach acidity and diabetes. Besides having ornamental and medicinal values, it is recently being recognized as pollution tolerant plant that can help in the mitigation of air pollution especially greenhouse gases. The leaf of bougainvillea is also referred to as dust mitigator and therefore bougainvillea is highly recommended for plantation in urban and industrial areas having high particulate loading in the atmosphere. On account of its wider adaptability to different agro climatic regions of the world and bright inflorescence, it can be planted in traffic island, central verge, and polluted soil for beautification, landscaping and use by different industries [1].

Microscopy coupled non-invasive and label free vibrational spectroscopic probes like confocal micro Raman spectroscopy have recently shown their applicability for the simultaneous characterization of multi-components of the samples of biological origin. It provides chemical signatures of the compounds present in the samples by using the phenomena of the inelastic scattering of light due to rotational and vibrational modes of the bonds of the molecules. It can also identify the relative quantity of the molecules, crystallinity or type of polymorphic structures and stress and strain states. Raman spectroscopy can be exploited for the economical and rapid identification and classification of biochemicals present in flowers according to taxonomy and phylogenetic relationship [2].

Despite the immense potential of non-destructive spectroscopic techniques, there are very few reports that describe the application of state of art technique confocal micro Raman spectroscopy for the characterization of biochemical present in the flowers. The aim of the present study is to explore the potential of confocal Raman spectroscopy for the identification and characterization of biochemicals present in the petals of different cultivars of bougainvillea flowers. The obtained spectral features have been pre-processed and correlated with biochemicals present in the petals of bougainvillea. The spectral signatures obtained in this study are useful in monitoring the different phenotypes of the flowers which is highly desirable in the floriculture, pharmaceutical and pigment industry. Moreover, the biochemical information obtained from this study can act as source of new innovative materials having the potential to be used in the future industrial applications.

Materials and methods

Sample collection

Different cultivars of healthy bougainvillea flowers having red, pink and pinkish-white colour were collected from the Roxburg Botanical Garden of University of Allahabad, Allahabad. The healthy flower samples were sorted and washed with double distilled water and dried at room temperature to remove surface contamination. Then the petals of the flowers samples were used for the biochemical investigation using confocal micro Raman spectroscopy.

Confocal micro Raman measurements

Raman measurements were also performed on the petals of the cultivars of bougainvillea by using confocal micro Raman mapping system (UniRAM) equipped with 785 nm laser as an excitation source and a high resolution SR 303i-A imaging spectrograph, thermoelectrically cooled charged couple device detector and BX43 microscope. The Raman signals were acquired on the adaxial surface of the bougainvillea flowers by focussing the 785 nm laser with the help of 10x objective lens and exciting the Raman signal in the spectral region <1700 cm^{-1}. Good signal-to-noise ratios were obtained in 5 second integration time on using exciting power of 60 mW. All spectra were obtained thrice for each sampling positions and average intensity was observed. The obtained spectral features were exported to Origin 8.0 software package and analyzed. The spectra were pre-treated by smoothing in order to remove unwanted signals and denoised the observed signals. Smoothing was performed by Savitzky Goley algorithm using third order polynomial and window of twenty one data points. The broad and undulating background in the spectral features were removed by baseline correction using rectangle method. In order to obtain statistically significant results, 9 floral samples were analysed for each cultivar. After pre-treatment, the average intensity pattern obtained for each spectral signal which was presented in the form of mean ± standard error. From each sample, single spectrum was acquired making a total of 9 spectra per floral sample.

Results and discussion

Figure 1 represents the optical images, confocal images and its corresponding Raman spectra in the spectral region <1700 cm^{-1}. Table 1 gives the value of the observed Raman bands in different variety of bougainvillea, detected phytochemicals and evaluated area by the curve fitting of the spectral signature of thephytochemicals present in the flower samples. The shape analyses of the spectral signature such as peak position, area of the profile, breadth yield identification and amount of the phytochemical present in the flower sample. The position of the peak of the spectral signature provides the identification of the phytochemical while

the areal intensity depicts the level of concentration of the detected phytochemical in the flower. In addition, breadth of the spectral profile yields impact of the surrounding phytochemicals.

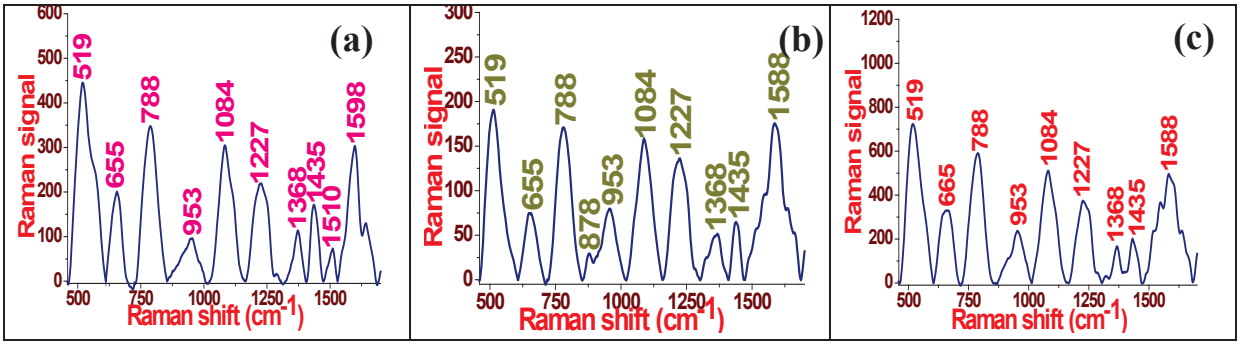

Figure 1: Recorded Raman spectra of the (a) pink, (b) pinkish-white, and (c) red bougainvillea.

In order to reduce dimensions of the complex data sets of the Raman measurements, the data have been subjected to multivariate analysis using principal component analysis. The score plot and loading plot generated from principal component analysis have been analysed for observing the possible class clustering and identification of the important wavenumbers that display major variation. The eigen value plot of the principal component analysis reveals that it is able to capture 81.39% of the total variation in the data. The analysis of the scatter plot reveals that scores of the principal component 1 are able to capture 70.92% of the total variation while principal component 2 is able to capture 10.47% of the total variation in the data sets. The scattering plot also reveals that score of the pink, pinkish-white and red cultivars lies at different coordinates indicating that the Raman scattering signatures of the different cultivars are different. In order to identify important points of variation, the loading plots have also been analyzed. The analysis of the loading plot reveals the loadings of principal component 1 shows positive loadings at 788, 1084, 1227 and 1384 cm^{-1}. The loadings of principal component 2 are also positive at 1384, 1510 and 1598 cm^{-1}. In addition, the loadings of principal component 2 are negative at 742 and 797 cm^{-1}. These results show that principal component analysis in combination with Raman scattering is highly efficient artificial intelligence tool for the characterization of the biosamples.

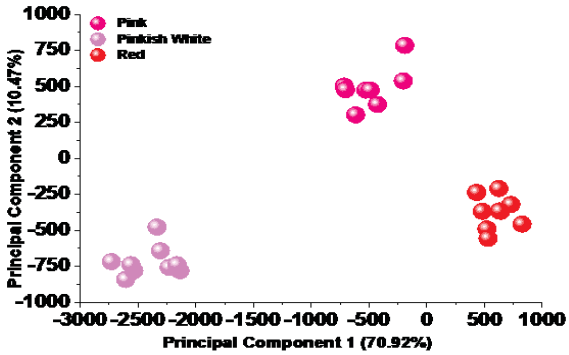

Figure 2: Scatter plot of principle component analysis of the Raman spectral data of the petals of the different cultivar of bougainvillea flowers.

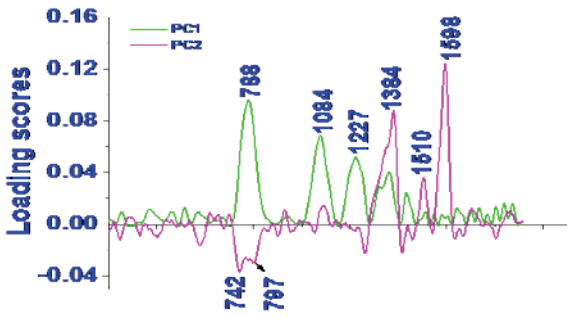

Figure 3: Loading plot of principal component analysis of the Raman spectral data of the petals of the different cultivar of bougainvillea flowers.

The analysis of the Raman spectra reveals that the spectrum shows the presence of peaks at different wavenumbers caused by the vibrations of the molecules that correspond to the presence of different phytochemicals present in the flowers. Strong peaks appearing at the wavenumber 519 and 1084 cm^{-1} have been identified to arise as due to the cellulose [3] while the peak observed at 788 cm^{-1} denotes the presence of lignin in the petals of bougainvillea

flower. The comparison of the area of the curve fitting analysis reveals that area of the cellulose band at 519 cm^{-1} is highest in the red flowers in comparison to pink and whitish pink flowers. The band of lignin at 788 cm^{-1} does not show much variation in the different cultivars of the bougainvillea flowers. In addition, the peak appearing at 1435 cm^{-1} arises due to δ ($O\text{-}CH_3$), δ (CH_2) guia acyl ring vibrations of lignin [4]. A weak peak located at 953 cm^{-1} is attributed to the carotenoid while the peak appearing at 1368 cm^{-1} corresponds to the esterified pectins. The comparison of the area of the carotenoid band at 953 cm^{-1} shows that the area of this band is greatest in the pink and red flowers than in the whitish pink flowers. The Raman band detected at 1227 cm^{-1} has been identified as Keracyanin like anthocyanin compounds. The comparison of the area of the anthocyanin band shows that its area is maximum in pink and red flowers than in pinkish-white flowers. In the pink flowers, a small band is seen at 1510 cm^{-1}. This band is observed due to stretching mode of C=C in the central polyene chain of the carotenoid [5]. This band appears only in the pink bougainvillea flowers. In the bougainvillea flowers, band centred in the spectral region 1580-1600 cm^{-1} belongs to the aromatic ring vibrations of the phenolic compounds. In the pink flowers the phenolic band appears at 1598 cm^{-1} while in the whitish-pink and red flowers, the band of phenolic compounds appear at 1588 cm^{-1} [6]. The comparison of the area of the phenolic band reveals that its area is maximum in the pink flowers while its area is compatibly less in whitish pink and red flowers. In addition, the peak observed at 655 cm^{-1} is identified due to the methionine (amino acid) [7, 8]. Thus the Raman measurements reveal presence of different phytochemicals in varying amount in the petals of different colour flowers. The spectral signatures obtained in this study can be used by the planners and industrial personals for the effective use of bougainvillea flowers for allied purposes.

Table 1: Observed Raman bands, detected phytochemicals and their areal intensity

Observed Raman band (cm^{-1})	Detected phytochemical	Areal intensity of the different peaks of the bougainvillea cultivars		
		Pink	Pinkish-white	Red
519	Cellulose	55.16 ± 7.82	47.84 ± 9.99	70.81 ± 8.77
655	Methionine (Amino acid)	38.64 ± 4.62	34.73 ± 13.17	21.45 ± 4.95
788	Lignin	457.03 ± 40.66	406.36 ± 83.86	476.09 ± 54.18
953	Pectin	26.84 ± 4.02	7.13 ± 2.87	13.33 ± 2.68
1084	Cellulose	350.00 ± 50.63	167.14 ± 7.29	325.51 ± 34.27
1227	Keracyanin like anthocyanin	247.03 ± 41.91	122.04 ± 0.89	250.18 ± 21.89
1368	Esterified pectin	191.26 ± 10.67	50.11 ± 12.24	161.97 ± 20.31
1435	Lignin	168.13 ± 16.15	129.23 ± 10.14	153.09 ± 24.85
1510	Carotenoid	97.16 ± 2.71		
1588	Phenolic compounds		58.43 ± 13.98	36.99 ± 9.50
1598	Phenolic compounds	200.05 ± 9.94		

Data are the means ± standard error of three independent experiments.

References

1. R. Balasaraswathi, S. Sadasivam, M. Ward, J. M. Walker , *Phytochemistr*y 47, 1561 (1998).
2. M. S. Ali, S. A. Ibrahin, F. Ahmed, M. K. Pervez, *Nat. Prod. Res.* 19, 1 (2005).
3. H. Schulz, M. Baranska, R. Baranski, *Biopolymers* 77, 212 (2005).
4. G. Sonja, B. Malgorzata, S. Hartwig, H. Paul, M. Maurizio, *J. Raman Spectrosc.* 42,1240 (2011).
5. S. Sharma, S. Srivastava, R. Singh, K. N. Uttam, *Spectroscopy Letters,* 50, 115, (2017).
6. J. Trebolazabala, M. Maguregui, H. Morillas, A. Diego, J. M. *Spectrochim. Acta Part A* 105, 391 (2013).
7. M. N. Merzlyak, M. T. Bernt, N. K. Razi *Journal of Experimental Botany.* 59, 349 (2008).
8. S. Sharma, R. Uttam, A. S. Bharti, N. Shukla, K. N. Uttam, *Natl. Acad. Sci. Lett.* 42, 365 (2019).

Laser Interferometry for distance measurement: Demonstration in laboratory

Sreelekshmi C. A.[2], Hriday Dath[1], B. V. S. Shravan[1], Dr. Radhika V. N.[1], Dr. Umesh Kadhane[2], J. Krishnakumar, S. Hemachandran

[1] *ISRO Inertial Systems Unit, Vattiyoorkavu,* [2]*Indian Institute of Space science and Technology, Valiamala*

E-mail: radhikavn@gmail.com

Abstract

Laser Interferometry is a widely used and reliable technique for measurement or estimation of various parameters including distance, velocity, gravity, refractive index of a material, etc. A modified Mach Zender interferometer is realized in laboratory on an optical breadboard with optical components and a translation stage. The translational stage has been used to give movement to two of the mirrors, thereby introducing a known path length difference. The fringe movements are captured in a photodetector to estimate the distance moved using an algorithm. The paper gives details on the interferometry setup, laser locking, fringe capture and algorithm to estimate the distance. This work is further planned to be extended for estimating local gravity in laboratory.

1. Introduction

The interferometry technique allows us to extract information and measurements from data collected by superimposing waves to cause the phenomenon of interference. In most of the light interferometers, light waves from a single source are split into two beams those travel in different optical paths and then recombined to produce interference pattern. The desired information can be extracted from this interference fringe pattern. Michelson, Mach-Zender, Sagnac, Fabry-Perot etc. are some of the interferometric configurations which are in use nowadays, depending up on the studies aimed at. These configurations are based on the difference in the relative optical paths of waves taking part in the phenomenon of interference.

Interferometry is considered to be an important technique for the measurement of small displacements, refractive index changes, surface irregularities, plasma density, density of neutral particles, etc. in various fields of science and technology due to its high precision and ease of experimental set up. Its application extends into various fields including spectroscopy, quantum mechanics, nuclear and particle physics, fiber optics, oceanography, remote sensing, plasma physics and astronomy [1].

A laser interferometry experiment has been carried out in the laboratory for deducing the screw gauge induced path difference to one of the interfering beams. The present study focuses on estimating the rate of rotation from the interferogram captured using the photodiode. The theory and experiment in detail are described in the further sections of this paper.

2. The Interferometry Experiment

2.1 Saturation Absorption Spectroscopy module for laser locking

The desired frequency of the input laser beam with narrow line-width is chosen by the frequency selective feedback and the laser frequency locking mechanism, based on saturation absorption spectroscopy. This eliminates the effects

of slow drifts like small temperature fluctuations for frequencies within the locking window and also eliminates unwanted noises, for the entire duration of the interferometry experiment. The optical module for laser locking is given in fig. 2.1. In saturation absorption spectroscopy, the laser beam is divided into two counter-propagating beams of different intensities called pump beam and probe beam. Pump intensity has higher intensity while probe beam has lower intensity. Both the beams are allowed to pass through the Rb vapour cell and probe beam is detected using a photo-detector. The intensity ratio of the pump and probe beams is controlled to get well defined saturated absorption peaks.

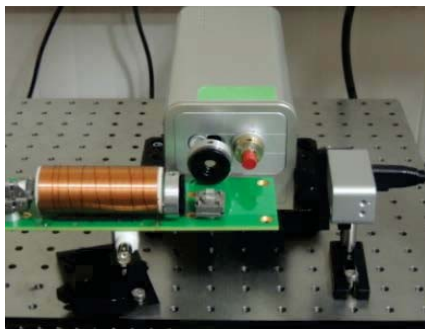

Figure 2.1: *SAS set up for laser frequency locking*

2.2 The interferometry experiment

The schematic diagram of the optical set up used for the interferometry experiment is given as Fig. 2.2. The light intensity in one of the combined directions is measured with a photo detector. The intensity seen at the photodiode is sensitive to both the amplitudes and the relative phases of the two beams as they interfere at the second beam splitter. Both the mirrors M1 and M2 are mounted on a translation stage with capability of 1 div rotation = 0.25 mm horizontal movement. The stage is provided with X and Y adjustments independently so as to change the optical path length between the two interferometric arms.

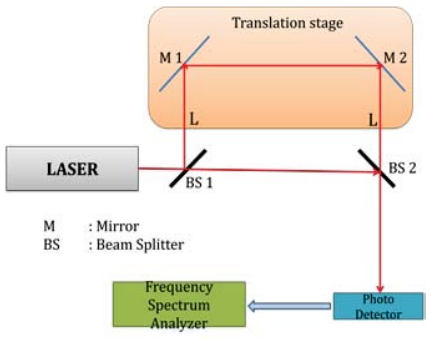

Figure 2.2: *Interferometry set up*

The interference data recorded with the laser, first unlocked and then properly locked to a definite transition of ^{85}Rb evidently shows the difference in the stability of the interferogram (fig. 2.3), thus confirming the importance of laser frequency locking in our experiment.

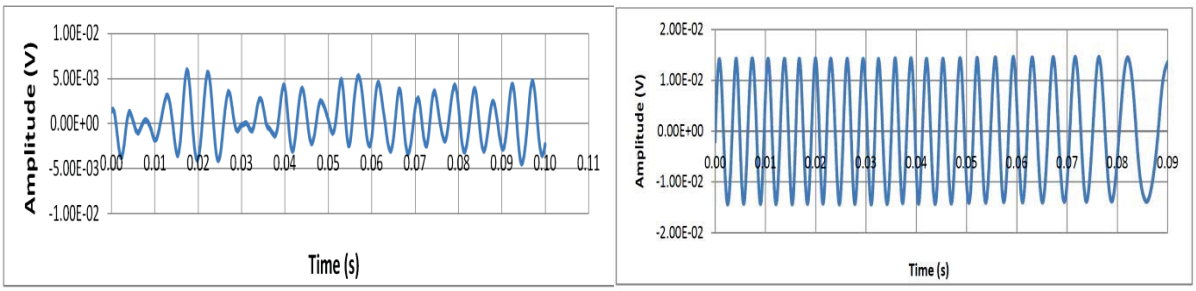

(a) **(b)**

Figure 2.3: *The interference data recorded with the laser (a) unlocked and (b) properly locked*

The path length L is varied by introducing a horizontal displacement to the translation stage on which mirrors M1 and M2 are mounted. Displacement of interference fringe during this operation is captured in photodiode. The fringe patterns are then analyzed to derive at the rate of rotation of the screw gauge which induced changes in path length.

The rotations to the screw gauge are done manually with hand in a slow, moderate and fast rate. The photodiode data recorded at various rate of rotations are given in fig. 2.4. The entire experimental set up is mounted on an optical table over a seismic platform in order to isolate it from external vibrations and thereby eliminating unwanted noises.

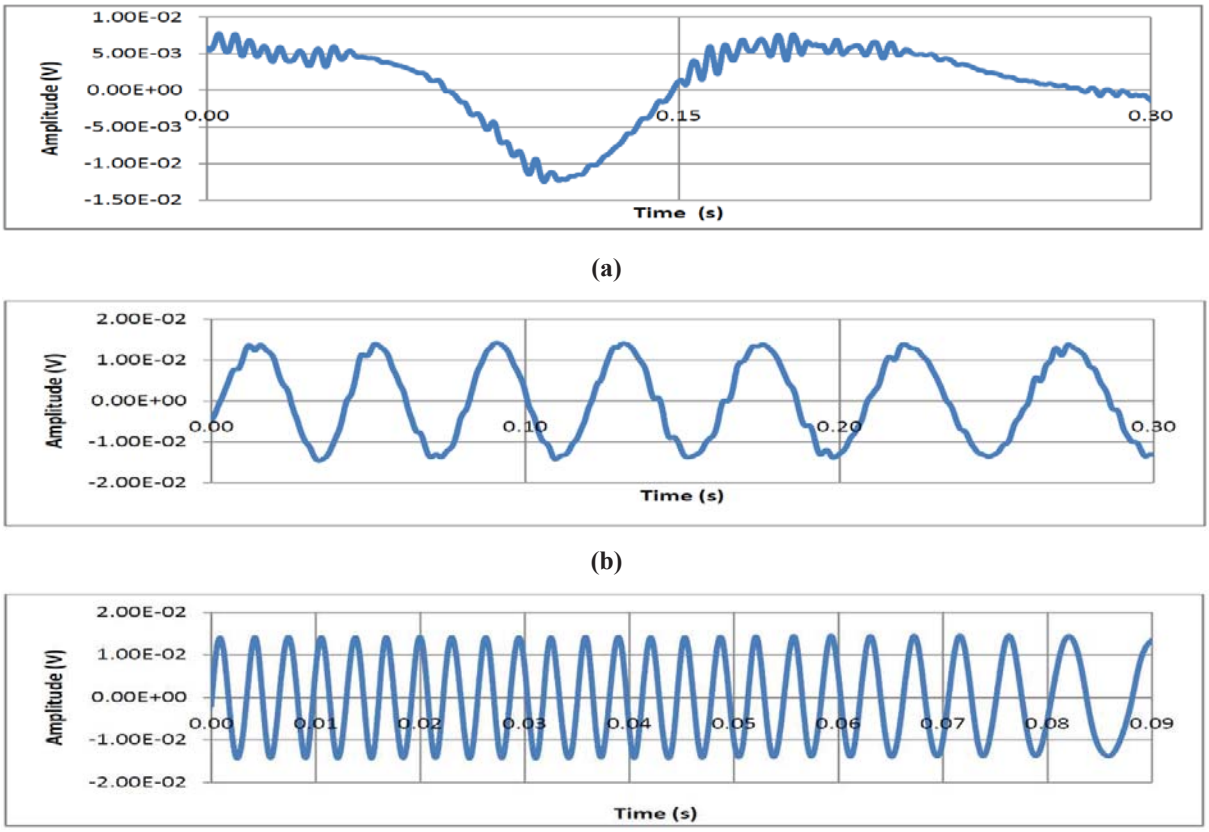

Figure 2.4: *Interference data recorded during (a) Slow (b) Moderate and (c) Fast rotations*

3. Results and discussions

In the interferogram, a change of one dark fringe (intensity = 0) to the next bright fringe (intensity = max.) corresponds to an extra path difference of λ/2, in addition to the existing path difference which can be counted as one zero crossing in the photodiode data as the intensity goes from minimum to maximum[2]. This extra path difference of λ/2 is induced by the rotation of screw gauge to the translational stage on which the two mirrors are mounted. Here, due to our interferometry arrangement and screw gauge orientation, one fringe change corresponds to a path difference of λ/4. To get the path difference induced at different times due to the rotations given to the system, the number of dark-bright fringe changes

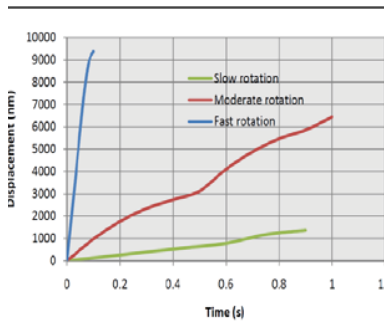

Figure 3.1: *Path difference induced via the translation stage*

(zero crossings) is counted from the real time data captured and the path difference is calculated as multiples of λ/4 to a fixed period. This has been plotted with path difference on y-axis and time on x-axis (fig. 3.1).

The number of rotations has been calculated by considering the screw gauge measurement. One complete rotation of the screw corresponds to d = 0.25 mm displacement. The relation between the number of zero crossings n and number of rotations R is given by,

$$R = \frac{n\,\lambda}{4\,d}$$

where λ is the wavelength of the source laser (780 nm).

The rate of rotation is also calculated and plotted with number of rotations per second on y-axis and time on x-axis (fig. 3.2). The average numbers of rotations per second in the case of slow, moderate and fast rotations are found to be 0.0059 s^{-1}, 0.0257 s^{-1} and 0.4368 s^{-1}, respectively.

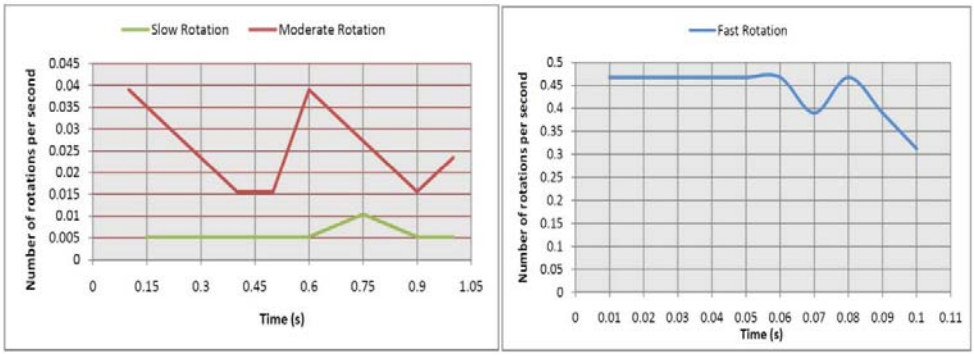

(a) **(b)**

Figure 3.2: *Rate of rotation of the micrometer screw*

Another study has been attempted to compare the theoretical and experimental values of number of interference fringes obtained by giving a known rotation to the screw gauge manually. By one complete rotation of the screw, a total path difference of 0.5 mm is introduced to the interferometry path and the corresponding number of fringes is calculated to be 1282. Experimentally, the value was found to be 1307, verifying the displacement estimation algorithm. The small deviation in the experimentally obtained value is attributed to the errors due to manual rotation of the screw.

5. Conclusion

The laser interferometry module for the calculation of an extra path difference induced to one of the interferometry paths by means of a screw gauge is realized. Rate of rotation is calculated from the interferogram obtained out of the experiment. The studies were carried out with both unlocked and locked laser conditions and the interference pattern obtained out of the properly locked laser was observed to be very stable compared to the unlocked system.

6. References

[1] K. G. Libbrecht and M. W. Libbrecht, *Am. J. Phys.* **74,** 12 (2006).

[2] Z. Zabek, T. Knap and W. Kielek, *Metrologia* **41,** 414–420 (2004).

Influence of solvents on the kinetics of ground-state bleaching and vibrational levels of the first excited state, and excited-state absorption of IR800 dye.

Sajin Ponnan, Desai Narayana Rao and Sri Ram G Naraharisetty
University of Hyderabad, Hyderabad

Abstract:

Using transient absorption spectroscopy at 800nm pump and white-light continuum probe we observed the ground state bleaching, stimulated emission, vibrational levels of first excited state and excited-state absorption, and their relaxation kinetic of IR800 dye. And we observed the influence of different solvents in those properties, we used Acetone, Dichloromethane (DCM), Dichlorobenzene (DCB), Ethanol, Methanol as solvents. We observed that the absorption peak varies from 780nm to 830nm with different solvents. Nondegenerate pump-probe studies have performed using home-built transient absorption spectrometer and 2D colour contour plot with time delay in X-axis, the wavelength in Y-axis and the difference absorption (ΔA) as colour were plotted using Origin pro software. Ground state bleaching is observed around 800nm wavelength, stimulated emission is observed around 840nm wavelength, vibrational levels of first excited state-observed between 700nm to 800nm range and excited-state absorption is observed around 570nm wavelength. Relaxation kinetics are plotted and fitted with double exponential curve fitting using origin pro and we obtained the decay constants τ_1 and τ_2.

Introduction:

Solvents play a very important role in the absorption and relaxation dynamics of dyes. This is due to the different channels and methods that energy transfer happens. Because of these energy transfer happens in a few picoseconds to nanosecond time span we use ultrafast pump-probe spectroscopy to study these ultrafast dynamics. Here we have studied behaviour of IR-800 dye in five different solvents.

Experimental Setup

The commercially available IR-800 dye dissolved in five different solvents, Ethanol, Methanol, Acetone, DCB and DCM are taken in a 1mm quartz cuvette as a sample cell. The steady-state absorption spectrum is taken using a commercial spectrometer (JASCO V-670 UV-Vis Spectrometer). It has a very sharp absorption peak around 770nm to 830nm for different solvents. Laser irradiation may degrade the dye, hence we have recorded and confirmed the absence of photodegradation by taking steady-state absorption spectra before

and after the pump-probe experiment. Since the dye has very strong absorption around 770nm to 830nm, we choose 770nm to 830nm for each solvent in OPA as the pump beam. We performed pump probe spectroscopy using home-made transient absorption spectrometer.

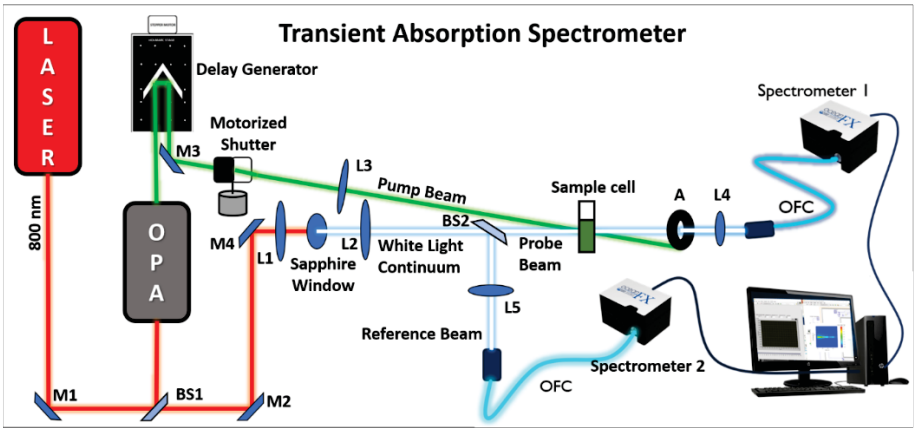

Figure 1: Schematic diagram of Transient absorption spectrometer

Results

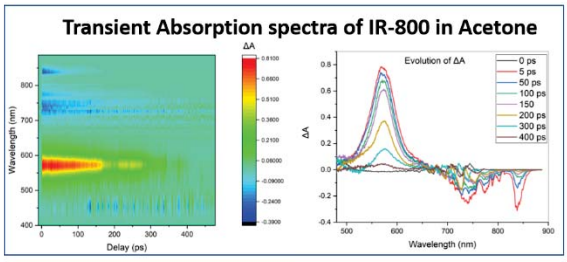

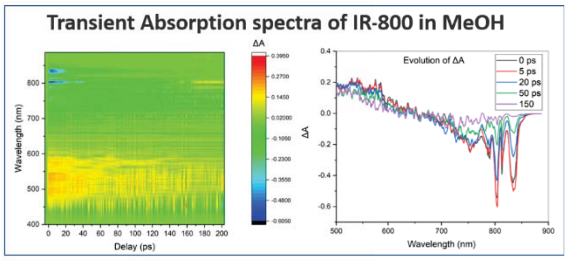

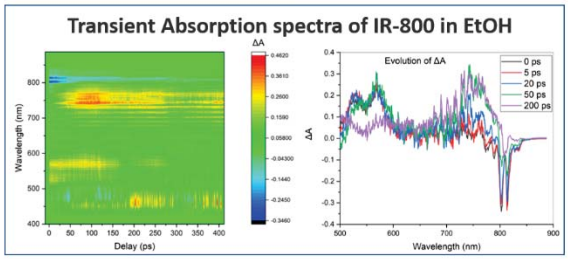

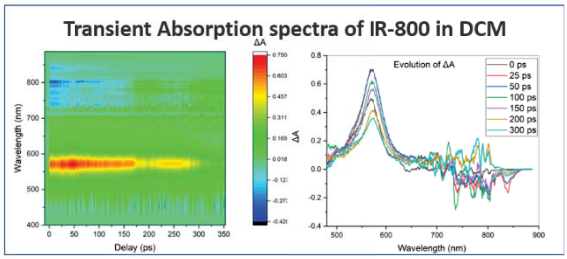

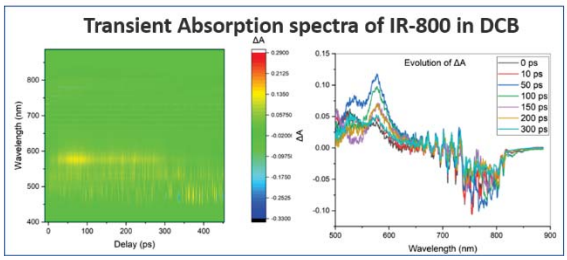

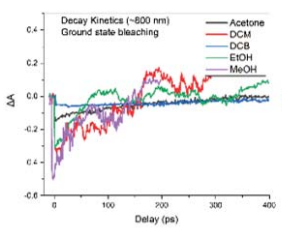

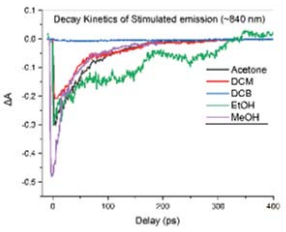

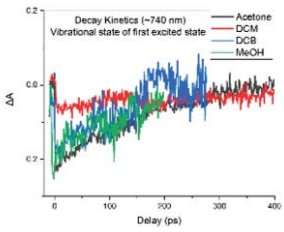

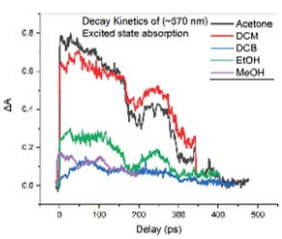

Conclusion

We have studied the excited state absorption and relaxation kinetics of IR-800 dye in five different solvents, by excited using a pump of 770nm to 830nm and probed with a white light supercontinuum. Then a 2D colour filled contour plot was made using origin software. The transient absorption spectra at various time delays inferred that ΔA decreases with increasing time delay. Curve fitting done using the exponential decay equation $y = A_1 * \exp(-x/\tau_1) + A_2 * \exp(-x/\tau_2)$, where t_1 and t_2 values give the period of decay. We compared the relaxation time of excited state of IR-800 in different solvents.

References

[1] C Sahoo, M Sethupathy, Nabil A Saad, D. Narayana Rao and Sri Ram G. Naraharisetty "Ultrafast pump-probe signal detection using a data acquisition card" Journal of Instrumentation, 2018 JINST 13 P10027. DOI 10.1088/1748-0221/13/10/P10027

[2] Dipak Kumar Das, Krishnandu Makhal and Debabrata Goswami, Observing ground state vibrational coherence and excited state relaxation dynamics of a cyanine dye in pure solvents, DOI: 10.1039/C7CP08605A (Paper) Phys. Chem. Chem. Phys., 2018, 20, 13400-13411

[3] Peter K.WalhoutJoseph C.Alfano1YoshifumiKimura2CarlosSilvaPhilip J.ReidPaul F.Barbara, Direct pump/probe spectroscopy of the near-IR band of the solvated electron in alcohols, Chemical Physics Letters, January 1995, Pages 135-140

THz- TDS As a Diagnostic Tool for Monitoring the Water Content in Different Coloured Indian Almond (Catappa) Leaves.

Nagaraju Menchu, Chandan Ghorui, Ganesh Damarla and Anil Kumar Chaudhary*

Advanced Centre of Research in High Energy Materials (ACRHEM), University of Hyderabad, Hyderabad 500046, Telangana, India.

*Corresponding author e-mail: akcphys@gmail.com, akcsp@uohyd.ernet.in

Abstract: This paper reports the terahertz-time domain spectroscopy (THz-TDS) as an efficient diagnostic tool for monitoring the water and chlorophyll contents in the green and coloured leaves. The study was carried out between 0.1-3.5 THz frequency range on different colored leaves such as green, light green, light red, dark red, and dry plucked from an Indian almond tree. The study reveals the significant changes in the absorption coefficient and the refractive index of different colored leaves attributed to the leaf's water and chlorophyll content. The green-healthy leaf shows higher absorption coefficients than other colored leaves and dry leaf at 0.24, 0.54, 0.74, and 1.14 THz frequencies. We also observed the chlorophyll signature peak at 0.34 THz [1], and the green leaf showed higher chlorophyll content than all other leaves.

1. Introduction:

The plant's green-colored leaf contains water molecules and several secondary metabolites that participate in the photosynthesis process and responsible for the fruit's growth and crop yield [2]. In plants, leaves water is a constituent of protoplasm and acts as a solvent in absorbing nutrients when they dissolve in water. It is also used for the transpiration carrier of nutrients from the soil to green plant tissues. The end products of photosynthesis are also conveyed through the water to various plant parts. The leaf's water content is also reflected in its color in terms of chlorophyll content in the leaves. The color change usually happens before the leaves fall off of the tree.

THz radiation has lower energy and deeper penetration depth; it can be used for non-destructive and noninvasive tool to analyze explosives, drugs, and bio-molecules. Also, the plant's health can be monitored by measuring the water content in the leaf. This can provide valuable information in irrigation and for better understanding the plant physiological condition [3]. The early detection of drought stress can help to take proactive action related to plants' health monitoring to improve the overall productivity [4]. This technology could be a potential tool in measuring and observing water content in plant leaves. There are many groups including our group has reported the THz based estimation of water content in different types of plant leaves and rose petals [5]. The water concentration in the leaf can be ascertain using THz radiation in transmission mode.

2. Experimental details:

A Ti:sapphire femtosecond oscillator (Coherent, Chameleon Ultra II) was used as a source. It delivers *p*-polarized femtosecond pulses of 140 fs at 80 MHz repetition rate, tuned between 780- 850 nm. The variable attenuator VA was used to attenuate the average output power, and the pulses were allowed to incident on the ZnTe crystal (110 cut) of 2.0 mm thickness for THz generation. The fs-laser pulses were loosely focused on the crystal using plano-convex lens L1 with a focal length of 30 cm. The generated THz pulses were collected using two off-axis parabolic mirrors (PM1, PM2). The residual transmitted laser pulses from the source were separated from the THz radiation using a high-resistivity float zone silicon plate and black polythene filter. After the filter, the off-axis parabolic mirrors were used for collimating the THz radiation, and the sample is placed in between them. PM2 focused the generated THz radiation, after the sample, on to the photoconductive antenna, which was coupled with the preamplifier, and the output of the preamplifier was fed to the lock-in amplifier. The output of the lock-in amplifier was sent to the computer for the recording of time and frequency domain signal using LabVIEW [6].

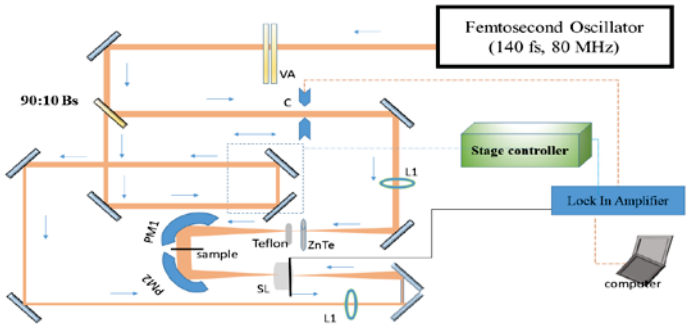

Figure. 1 *Experimental schematic of the Terahertz time domain spectroscopy.*

The experiment was conducted in two steps. In the first part, different colored leaf samples, viz. green leaf, light green leaf, light red leaf, dark red leaf, and dry leaf were plucked from the Indian almond tree, located in our campus. These leaves were cleaned to remove dust particles using dry tissue paper, after cleaning the thickness and weights of leaves were measured. The sample name, thickness, and weight measurements are shown in table 1. In the second part, the collected sample leaves were subjected to the THz radiation for recording of the time domain spectroscopic data.

Figure.2 *Photographic images of the leaves from Indian almond tree taken for tera-hertz time-domain transmission studies. (a) Green leaf, (b) light green leaf, (c) Light red leaf, (d) dark red leaf, (e) naturally dried* leaf.

Figure 2 shows the five different coloured leaves taken for the preliminary study of the variation in the water content using THz-TDS.

3. Results and discussions:

In the transmission mode, the time-domain terahertz spectra of different coloured leaves of the Indian almond tree are showed in fig.3(a), and the corresponding frequency domain spectra are showed in fig.3(b). The dry leaf has shown higher spectral amplitude from the frequency domain spectra, the green leaf has the lowest, and light green, light red, and dark red have approximately the same spectral amplitudes observed. The variation in the spectral amplitude of prominent signature peaks of water (i.e., 0.24, 0.54, 0.74, and 1.14 THz) in the samples are visualized in the bar graph in figure 4 (b). This graph clearly shows that the dry and green leaf have weak and robust absorption bands, respectively, and the other three colored leaves show reasonably strong absorption bands but lower than the green leaf. These results suggest that light green, light red, and dark red leaves have less water content than a green leaf but higher than the dry leaf. The calculated absorption coefficients of the sample are shown in figure 3(c). These results indicate that green leaf has the highest absorption coefficients, the dry leaf has the lowest values, and the other 3 colored leaves have approximately the same values. This variation in absorption coefficients are shown in the bar graph in fig.4(a). The green, dry, and other three cloured leaves have strong, weak, and reasonably strong absorption coefficients at prominent water peaks, respectively. We observed a strong dispersion in the refractive index, which could be attributed to the leaf's significant water content shown in figure 3(d). The study also confirms that the green leaf has higher absorption coefficients as compared to dry and other colored leaves. This is a clear indication of the reduction of water concentration in colored leaves[7]. The refractive index of dried leaf is highest, i.e., 4, and it is approximately 3 for other leaves at 0.1 THz frequency.

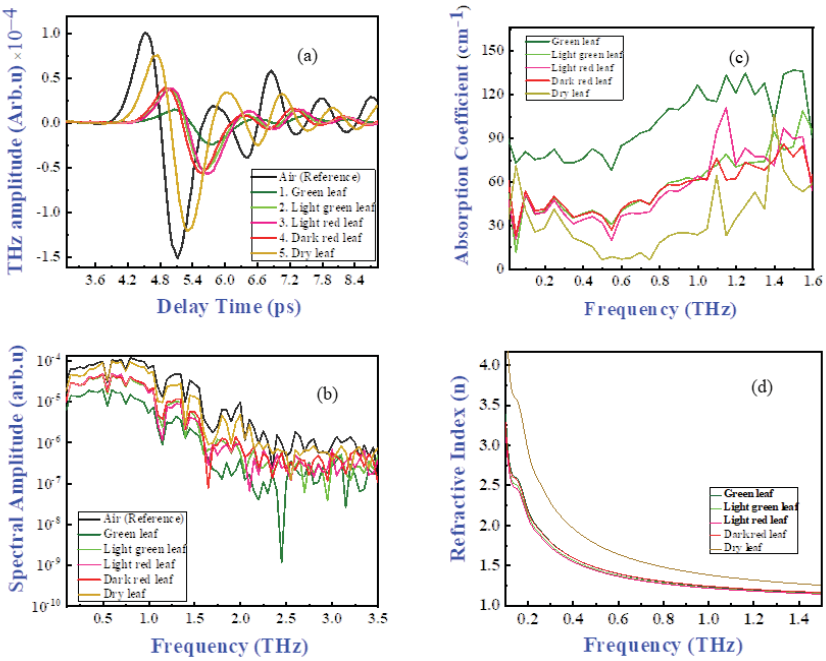

Figure.3 *(a) The time-domain terahertz signal of five different coloreds and naturally dried leaves of the same tree (b) FFT of the time domain signal (c) absorption coefficient (d) refractive indices of five different leaves. The corresponding spectra of other colored leaves are labels, respectively.*

We also observed the chlorophyll signature band at 0.34 THz [1] and the green leaf shown higher chlorophyll content compared to other leaves. And for the dry leaf the chlorophyll band is flattened due to lowest chlorophyll level in the leaf.

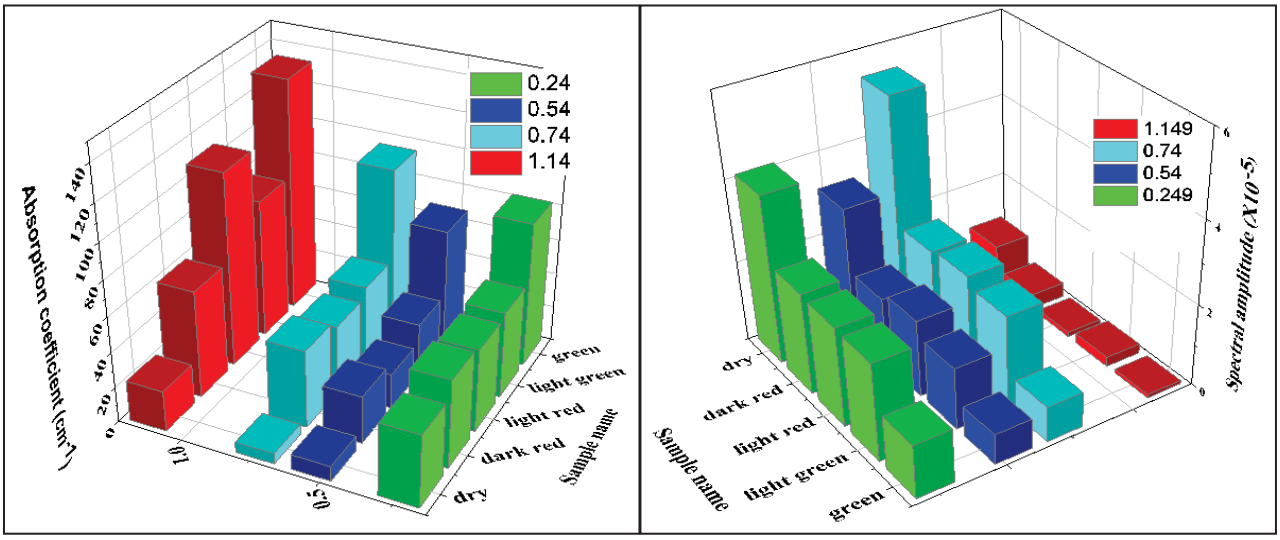

***Figure 4*:** *The prominent signature peaks of water content in leaves visualized in bar charts in terms of (a) absorption coefficient and (b) spectral amplitude.*

4. Conclusions:

We have successfully demonstrated the use of THz-TDS spectroscopy as a diagnostic tool for monitoring the water content in leaves on different colored Indian almond leaves. We also ascertained the refractive index and absorption coefficients of these leaves betweeen 0.1-1.4 Thz range. The signature peak of chlorophyll in leaf was observerd at 0.34 THz frequency. It is the first feasibility study for Indian almond leaves of different colored . The value of absorption coefficient is highest for the green leaf which confirms the presence higher water concentartion.

Acknowledgment: The author thanks the DRDO, Ministry of Defence, and Govt. of India (ERIP/ER/1501138/M/01/319/D(RD)) for funding, and also thank The Director ACRHEM for constant support and encouragement during the experiment.

5. References:

1. C. Wagner et al, ICIMTW, *IEEE,* 1 (2011)
2. López-López, Manuel, et al. *Remote Sensing,* 8.4 **276** (2016).
3. Li, Bin, and Xuting Zhao. *IRMMW-THz*. *IEEE*, (2018).
4. Li, Bin, Yuan Long, and Hao Yang. *Int. J. Agri. and Biological Engg.***11.3**, 178 (2018)
5. D.Ganesh and A.K. Chaudhary, WRAP-*IEEE*, (2017)
6. D.Ganesh, M. Venkatesh and A.K. Chaudhary, Applied Optics, **57**, 8743(2018)
7. Browne, Marvin, et al. *Plant direct* 4.4 (2020): e00197.

Synthesis and Spectroscopic Characterization of Orange-Red Emitting $Sr_2Sb_2O_7:Eu^{3+}$ Phosphor for White Light Emitting Diodes

Anns George[1,2], P R Biju[1]*
[1]School of Pure & Applied Physics, Mahatma Gandhi University, Kottayam, Kerala- 686560, India
[2]Assumption College Autonomous, Changanacherry, Kottayam, Kerala -686103, India

Abstract

Europium doped Strontium Antimonate phosphor was synthesized by high-temperature solid-state reaction method. XRD analysis confirmed its orthorhombic structure with the space group Imma. Under near-UV excitation, the emission spectra of the samples consist of characteristic emission peaks of Eu^{3+} ions corresponding to $^5D_0$ -^7F_J (J = 0,1,2,3,4,) transitions. The CIE chromaticity coordinates and CCT values confirm orange -red emission in the warm CCT region with high color purity. The results suggest that the prepared phosphor has potential application as an orange-red phosphor in phosphor converted white light emitting diodes and optoelectronic devices

INTRODUCTION

During the past few decades rare earth (RE) ion doped materials have attracted extensive attention due to their rich luminescent properties and potential applications. Inorganic phosphors doped with rare earth ions is one of the most promising materials for a variety of applications in solid state lighting, optical communication fields, solid state lasers and field emission displays [1]. However, low color rendering index and high correlated color temperature due to deficiency of the red light component have seriously limited the quality of white light in commercial phosphors converted WLED [2]. Therefore, numerous efforts have been made to develop new phosphors that can emit suitable red light. Luminescence properties of various phosphor materials depend highly on the crystallographic structure of the host lattice and nature of the activator ion. Thus choosing the host lattice and the activator ion as well as understanding the chemistry and structure plays a crucial role in phosphor synthesis. Europium ions are widely used as activator for red luminescence in phosphor due to their unique intra-configurational f-f transitions, which can occur as sharp and intense emission lines [3]. $Sr_2Sb_2O_7$, one of the ternary antimonate has an orthorhombic weberite structure with Sr and Sb cations forming a distorted face centered cubic array [4]. This structure is relatively compact and the compound is optically transparent and chemically stable. Owing to its good physical and chemical stability $Sr_2Sb_2O_7$ could be a favorable host for phosphor materials [5,6]. In the present work Eu^{3+} ions doped $Sr_2Sb_2O_7$ phosphors were synthesized by conventional solid state reaction method and optical properties of the samples were studied.

MATERIALS AND METHODS

$Sr_{(2-x)}Sb_2O_7$: x Eu^{3+} (x = 0, 0.08 mol %) phosphors were synthesized by the conventional high temperature solid state reaction method. The stoichiometric amount of raw materials were mixed thoroughly and ground in an agate mortar for 1 hour to get a homogenous mixture. The mixture was transferred into a platinum crucible and initially heated at a temperature of about 600^{o}C for 5 hours and was allowed to cool. The mixture was again ground in an agate mortar and

the homogeneous mixture was heated at a high temperature of 1000°C for 4 hours. After calcinations, the samples of the prepared phosphor sample was determined by powder X-ray diffraction analysis (XRD) using PANalytical X'Pert Pro Diffractometer with Cu- Kα radiation at λ=1.5403 Å with an applied voltage of 45 kV and 30 mA anode current. The surface morphology of the phosphor samples were determined by scanning electron microscope (JEOL JSM-6390). The room temperature photoluminescence excitation (PLE) and photoluminescence emission (PL) spectra of phosphor was recorded on a Horiba Jobin-Yvon Fluromax-4 with 150 W excitation of Xe-arc lamp.

RESULTS AND DISCUSSION

X- Ray Diffraction Analysis and Scanning Electron Micrographs

Figure 1 shows the X-ray diffraction pattern of pure $Sr_2Sb_2O_7$ and Europium doped $Sr_2Sb_2O_7$ samples. XRD pattern of both the samples are similar which indicates that doping of Eu^{3+} ions does not change the crystal structure or induce any new phase. From the XRD spectrum the average crystallite size of the phosphor was calculated using the Debye- Scherrer formula [7] and the average crystallite size was found to be 51 nm.

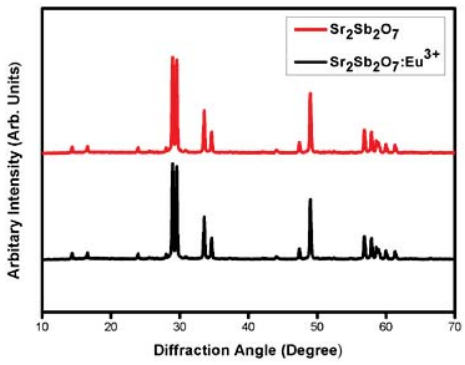

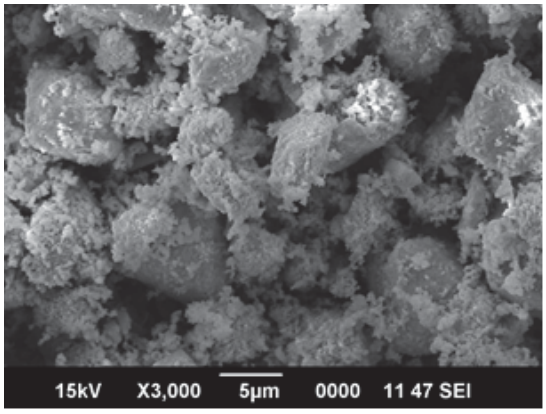

Figure 1 *XRD spectra of $Sr_2Sb_2O_7:Eu^{3+}$ phosphor.* **Figure 2.** *SEM image of Eu^{3+} doped of $Sr_2Sb_2O_7$*

The Scanning electron micrographs (SEM) of $Sr_2Sb_2O_7$ host and Eu^{3+} samples are given in Fig. 2(a) and Fig. 2(b). SEM images shows that particles are slightly agglomerated and fluffy mass made up of irregularly shaped aggregates could be seen in both images. The particle sizes were found to be in the micrometer range which is a suitable size for fabrication SSL devices. Also, the morphologies of pure and doped samples are almost same indicating that doping of Eu^{3+} ions did not alter the particle size and agglomeration.

Photoluminescence Excitation and Emission Spectra

Figure 3 shows the excitation spectra of the prepared phosphor at an emission wavelength of 612nm. Narrow excitation peaks are observed in the longer wavelength region which can be assigned to the intra-configurational f-f transition of Eu^{3+} ions. The peaks at 393 nm due to $^7F_0 \rightarrow ^5L_6$ transition and 464 nm due to $^7F_0 \rightarrow ^5D_2$ are more intense compared to other peaks. The intense excitation peaks suggests that the prepared phosphor can be effectively excited by NUV

(393 nm) or blue light (464 nm), which matched well with the emission wavelength of NUV or blue LED [8].

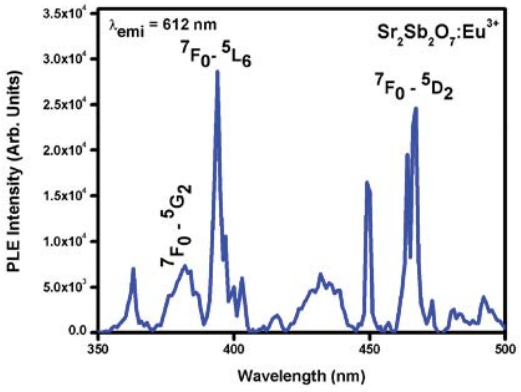

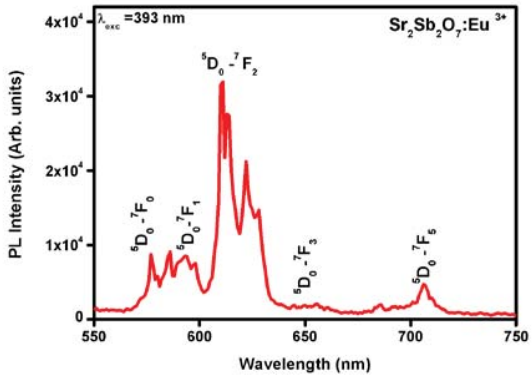

Figure 3 *Excitation spectra of $Sr_2Sb_2O_7:Eu^{3+}$ phosphor at λ_{em}=612 nm.* **Figure 4** *Emission spectra of $Sr_2Sb_2O_7:Eu^{3+}$ phosphors at λ_{exc} = 393 nm.*

Figure 4 shows the emission spectra of Eu^{3+} doped $Sr_2Sb_2O_7$ phosphor excited at 393 nm in the range 550 to 750 nm. The emission spectrum consists of a series of sharp peaks at 577 nm ,592 nm ,612 nm ,650 nm and 705 nm which can be assigned to $^5D_0$ -^7F_J (J=0,1,2,3,4) transitions of Eu^{3+} ions. According to Judd-Ofelt theory, the emission lines are a cumulative effect of the magnetic dipole (MD) transition and the electric dipole (ED) transition depending on the specific environment of Eu^{3+} ions [4]. It can be seen that the peak at 612 nm corresponding to $^5D_0$ -$^7F_2$ transition has the highest intensity.

The Figure 5 shows the overall mechanism of energy transfer at 393 nm excitation. Under 393 nm excitation the electrons in the ground state of Eu^{3+} ions get excited to the upper $^5L_6$ level. These electrons then relax to the lowest excited level $^5D_0$ by nonradiative (NR) energy transfer and finally get de-excited to the ground state ^7F_j (j = 0,1,2,3,4) by radiative transitions. This give rise to the characteristic emission of Eu^{3+} ions in the 550 to 750 nm range producing yellow, orange red and red emissions. The important measurement for specifying the property of a phosphor is the color. To evaluate the material performance on color luminescent emission, the CIE chromaticity coordinates *x, y* of the sample was calculated under 393 nm excitation. According to NTSC standard CIE for red color is (0.67, 0.33). In the present work, the CIE chromaticity coordinates of the sample was found to be (0.637, 0.363) under 393nm excitation and is shown in Figure 6. This corresponds to orange-red emission. The color temperature of lamps makes them visually "warm", "neutral" or "cool" light sources. The correlated color temperature of the phosphor was calculated from the chromaticity co-ordinates using McCamy's approximate formula. The CCT values was calculated and is found to be in the warmer region i.e., CCT<3200 K which makes it suitable for indoor application [6]. The color purities of the prepared phosphor are found to be 88% which indicates that the prepared phosphor has high color purity.

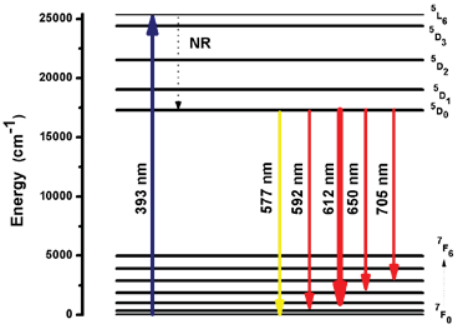

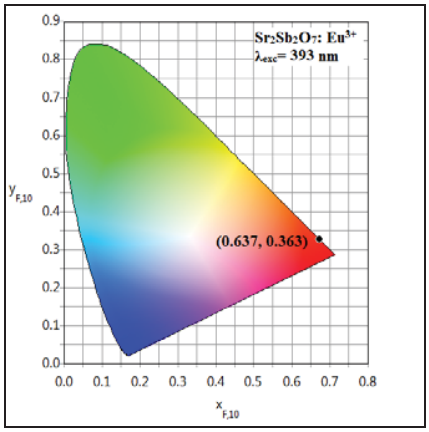

Figure 5 *Energy level diagram of Eu^{3+} ion in $Sr_2Sb_2O_7$:Eu^{3+} phosphor.* **Figure 6** *CIE chromaticity co- ordinates*

CONCLUSION

Europium doped Strontium Antimonate phosphor was synthesized via solid state reaction method. XRD analysis indicates that doping of Eu^{3+} ions does not change the crystal structure or induce any new phase. SEM analysis indicates that particle sizes are in the micrometer range. Under 393 nm excitation, the emission spectra of the sample shows five emission peaks at 577 nm ,592 nm ,612 nm ,650 nm and 705 nm corresponding to $^5D_0$ -^7F_J (J = 0,1,2,3,4,) transitions of Eu^{3+} ions. The CIE coordinates of the sample was found to be (0.637, 0.363) under 393 nm with high color purity and CCT in the warm region. The results suggest that the prepared phosphor has potential applications as orange-red phosphor in pc-WLEDs and optoelectronic devices.

REFERENCE

1. Zhiguo Xia, Quanlin Liu, 2016, Progress in Materials Science. 84, 59-117.
2. S. Ye, F. Xiao, Y.X Pan, Y.Y Ma, Y Zhang, 2010, Materials science and Engineering R. 71 (2010) 1-34.
3. W. B. Dai, M. Zhou, Z.Y Xian and L.K Zeng, 2014, RSC Adv. 4, 25470
4. Liurong Shi, Jiachi Zhang, Huihui Li, Pengfei Feng, Xue Liu, Zhonguie Fu, Yuhua Wang, 2013, Journal of Alloys and Compounds. 579, 82-85.
5. ShiyueYao, Xuan Zhou, Yanling Huang, Zuoshan Wang, Yumei Long, Weifeng Li, 2015, Journal of alloys and compounds. 653, 345-350
6. Lu cai and Juan C. Nino, 2007, Acta Crystallographica Section B. ISSN 0108-7681.
7. Jing Wang, Yu Cheng, Yalin Huang, Peiqing Cai, Sun ll Kim and Hyo Jin Seo, 2014, J. Mater. Chem. C. 2, 5559.
8. Koen binnemans, 2015, Coordination Chemistry Reviews. 295, 1-45

Influence of Nanosecond Laser Induced Micro-grooved Stainless Steel on Cellular Behaviour

S. Kedia[1,*], A. G. Majumdar[2], M. Subramanian[2], A. K. Sahu[3], J. P. Nilaya[1,4]

[1]*Laser & Plasma Technology Division, Bhabha Atomic Research Centre, Mumbai 400085*
[2]*Bio-Organic Division, Bhabha Atomic Research Centre, Mumbai 400085*
[3]*Glass & Advance Ceramics Division, Bhabha Atomic Research Centre, Mumbai 400085*
[4]*Homi Bhabha National Institute, Training School Complex, Anushaktinagar, Mumbai 400094*

[*]Email: skedia@barc.gov.in

Abstract: We present a robust method for improving biological performance of 316L stainless steel (SS) through nanosecond laser surface texturing. Two types of micro-groove patterns were generated on 316L SS at different laser powers and investigation pertaining to adhesion, orientation, and spreading of U2OS osteosarcoma bone cells was carried out. Qualitative and quantitative analysis revealed contact guidance and larger cell density on laser textured samples in comparison to pristine 316L SS sample. This can be attributed to the laser induced change in the topographical microstructure in the micro-grooves which provided appropriate anchoring to the cells for attachment and contact guidance.

Introduction:

Laser surface texturing (LST) process has gained great interest in medical, and industrial applications because of its potential to alter the surface properties such as, surface roughness, surface energy, wettability, porosity, and oxidation of bio-materials. Additionally, LST is a chemical free, fast, reproducible, versatile, one step, and an econimic technique which does not require pre or post processing of the samples [1]. The 316L stainless steel (SS) bio-implants have been extensively used in orthopaedic, dentistry and craniofacial surgeries because of its multiple advantages viz., fracture toughness, tensile strength, fatigue, wear resistance and cost effectiveness [2]. However, this biomaterial has deficiency in bio-functionality and that can be improved by altering its topographical nano/micro structure and/or surface chemical compositions [3]. In bio-functionality, osseointegration, a measure of cell attachment, cell expansion and cell proliferation, is the foremost requirement of an artificial implant in human body and depends largely on their sub-scale surface properties [4].

Materials and Methods:

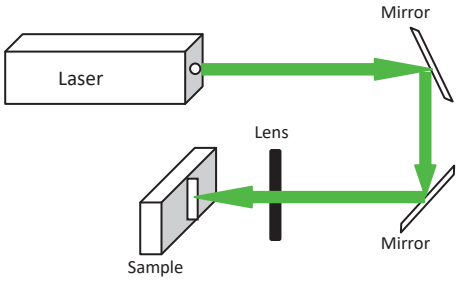

Fig. 1- *Experimental set-up used for LST*

Table-1: *Laser power, groove width, average surface roughness and water contact angle of SS, SS-1 & SS-2*

Sample	Laser Power	Groove width	Average surface roughness	Water contact angle
SS	-	-	0.08µm	$78^o \pm 2^o$
SS-1	10 mW	4µm	0.26 µm	$105^o \pm 2^o$
SS-2	100 mW	20 µm	0.23 µm	$> 150^o$

In this paper, we present the results of our investigations on adhesion and contact guidance of U2OS osteosarcoma bone cells on laser induced micro-grooved 316L SS sample surface. For LST, a 10 Hz Q-switched nanosecond Nd:YAG laser operating at a wavelength of 532 nm and delivering pulses of duration 6 ns

was employed. The laser beam was focused onto the sample using a cylindrical lens of focal length 10 cm and it focused the beam in line shape of dimension (9000 μm × 20 μm) on the sample surface. This lead to large area surface processing of the sample that in turn leads to reduction in the processing time. The sample, mounted on a computer controlled XY-translational stage, was scanned at a linear speed of 5μm/sec along x-direction. Schematic diagram of the experimental set-up used for LST is as shown in Fig. 1. Two types of micro-grooves were generated at different laser powers such as, 10mW and 100mW, and samples are referred as SS-1 and SS-2, respectively. The results of LST samples were compared with results obtained for pristine sample named as SS. Surface topography, average surface roughness and water contact angle of all samples were characterized using Field Emission - Scanning Electron Microscope (FE-SEM), profilometer and water contact angle measurements, respectively. The U2OS osteosarcoma bone cells were procured from National Cell Repository, National Centre for Cell Science, Pune, India. Cells were cultured in Dulbecco's Modified Eagle Medium supplemented with 10 % fetal bovine serum and maintained at 37 ℃ and 95 % relative humidity under an atmosphere of 5 % CO_2. Primary antibody against α-tubulin was procured from Sigma Aldrich. AlexaFluor-488 tagged secondary antibody was procured from Jackson Immunoresearch. Immuno-fluorescence staining was used to investigate adhesion, density, orientation, spreading and contact guidance of the cells on SS, SS-1 and SS-2 sample surfaces. For this, about 0.4 x 10^6 cells were seeded in 60 mm dishes containing the sample to be evaluated. Before seeding, sample surfaces were sterilized with 70 % ethanol. Post seeding, cells were allowed to attach on the sample for 48 hours, followed by immunofluorescence staining that involved cells to be fixed with 3.5 % paraformaldehyde, followed by permeabiliziation in PBS containing 0.2 % Triton-X-100 for 10 minutes. Cells were then blocked using 5 % bovine serum albumin in PBS containing 0.1 % Tween-20 and then treated with primary antibody against α-tubulin overnight at 4℃, followed by treatment with AlexaFluor-488 tagged secondary antibody for 3 hours at room temperature. Nuclei were stained using 10 μM Hoechst 33258. Sample surfaces were then visualized under a Zeiss LSM 780 microscope. Attached cells were scored by capturing about 10 random fields at 20X magnification, followed by counting number of nuclei per field. Each experiment was repeated for three times.

Results and discussion:

The FE-SEM images and the water contact angle of SS sample shown in Fig. 2a revealed that, the pristine sample surface has rough topography with hydrophilic nature. The confocal image of the bone cells in Fig. 2a showed a random arrangement of the cells on SS sample surface. Large numbers of filopodia were extended in all directions from the central part of each cell. Figs. 2b and 2c show, the laser induced micro-grooves and the microstructures within the grooves of samples SS-1 and SS-2, respectively. It can be noticed in the magnified FE-SEM images of the samples that, with increased laser power from 10 mW to 100mW, the micro-groove width increased along with a significant variation in the microstructure. The sample SS-1 textured at lowest laser power contains porous surface. The porosity, however, reduced and surface became denser as laser power was increased for sample SS-2. The water contact angle measurement revealed that the wettability of the sample reduced after laser treatment and the samples SS-2 and SS-3 became hydrophobic (Fig. 2b) and superhydrophobic (Fig. 2c), respectively. The chosen laser power, corresponding groove width, average surface roughness, and water contact angle of all samples are listed in table-1. There was a significant increment in the surface roughness and a corresponding increase in the surface area of the samples following laser texturing. However, not much variation in surface roughnesses between sample SS-1 and SS-2 was observed. Well aligned

bone cells along the major axis of grooves with reduction in their aspect ratio were observed on the surface of LST samples. Squeezing of cytoplasm in the vertical direction and spreading along the grooves with extensively long dominated micro-spikes in filopodia indicated contact guidance of the cells along the grooves. Additionally, asymmetry in the intensity of actin fibers indicated, the cells were migrating along the grooves following a stretch, bind and retract process [5]. Such directional expansion of cytoplasm was not observed on the SS sample. Chen *et al.* reported that, the edges of the grooves differ in reactivity due to the existence of more valencies, and this controls the extracellular matrix protein of the cells which, in turn, is responsible for adhesion mechanism and contact guidance [6]. Also unlike in case of pristine SS sample, the anchoring locations of the cells were aggregated at the bottom and ridges of the grooves in case of samples SS-1 and SS-2. The filopodia of the cell appear to have sensed the surroundings and guided the locomotion of cells along the grooves in LST sample surface. The mechanism of contact guidance of cells has a great potential in inducing specific cell response leading to tissue engineering [6-7]. This can limit the scar tissue formation in the wound area and can promote osseointegration.

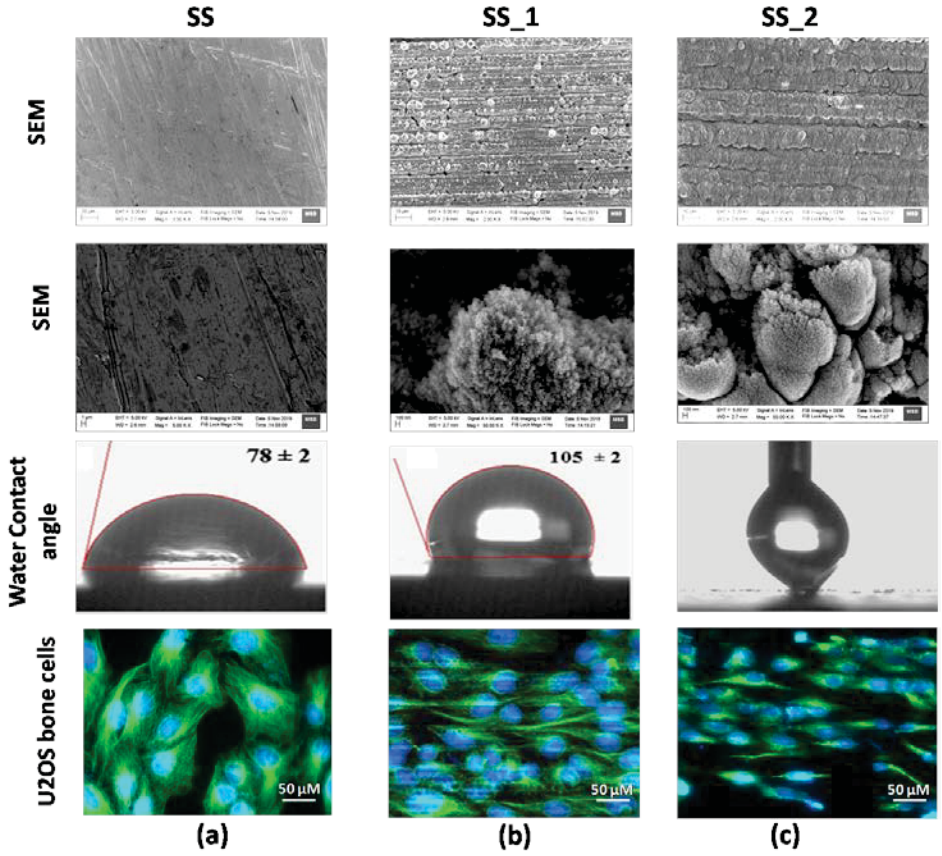

Fig 2: SEM image, magnified SEM image, water contact angle and confocal microscope image of U2OS bone cells on (a) SS, (b) SS-1 and (c) SS-2.

Fig.3 shows the quantitative evaluation of cellular attachment on the SS, SS-1 and SS-2 samples based on microscopic image analysis. More numbers of cells were found to be attached on SS-1 and SS-2 samples in

comparison to that of SS surface. This confirmed better adhesion and viability of cells on the LST samples, which can be attributed to the increase in the surface roughness due to which the probability of anchoring and adhesion of the cells increased.

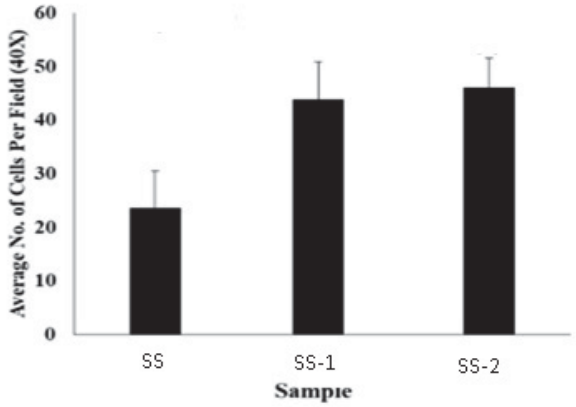

Fig 3: *Quantitative evaluation of cellular attachment on control and LST samples based on microscopic image analysis.*

In conclusion, large area surface texturing to generate micro-groove patterns on 316L SS were performed by focusing a nanosecond pulse laser through a cylindrical lens on the sample surface. Laser power dependent variation in the surface morphology of 316L SS sample leads to superior osseointegration. The micro-groove patterns with nanostructures therein supported adhesion, alignment and contact guidance of the U2OS bone cells on LST samples. Asymmetry in the intensity of the actin fibers of bone cells revealed their migration along the grooves.

Acknowledgment: The authors gratefully acknowledge the constant guidance and support of Head, L&PTD and AD, BTDG.

References:

1. S. Shaikh, D. Singh, M. Subramanian, S. Kedia, A. K. Singh, K. Singh, N. Gupta and S. Sinha, *J. of Non-crystalline Solid* **482**, 63 (2018).
2. J.R. Davis, Introduction to stainless steels, Alloy Digest Sourcebook: Stainless steels, ASM International, 2000.
3. A. Bekmurzayeva, W. J. Duncanson, H. S. Azevedo, and D. Kanayeva, *Materials Science and Engineering: C*, **93,** 1073 (2018).
4. L. Gaviria, J. P. Salcido, T. Guda, and J. L. Ong, *J. Korean Assoc. Oral. Maxillofac. Surg.* **40,** 50 (2014).
5. M. Martinez-Calderon, M. Manso-Silvan, A. Rodriguez, M. Gomez-Aranzadi, J P. Garcia-Ruiz, S. M. Olaizola, and R. J. Martin-Palma, *Sci. Rep.* **6,** 36296 (2016).
6. J. Chen, S. Mwenifumbo, C. Langhammer, J. -P. McGovern, M. Li, A. Beye, and W. O. Soboyejo, *J. Biomed Mater Res B Apl Biomater* **82,** 360 (2007).
7. J. Zhang, Y. Guan, W. Lin, and X. Gu, *Surface and Coating Technology*, **362,** 176 (2019).

Pulsed Laser Deposition of Zirconia Thin Film on Ti6Al4V Bio-alloy to Improve Tribological Properties

*S. Kedia[1], J. P. Nilaya[1,2]
[1]*Laser & Plasma Technology Division, Bhabha Atomic Research Centre, Mumbai 400085*
[2]*Homi Bhabha National Institute, Training School Complex, Anushaktinagar, Mumbai 400094*
[*]Email: skedia@barc.gov.in

Abstract: Pulsed laser deposition of zirconia (ZrO_2) thin film was carried out on grade-5 titanium metal by employing a nanosecond Nd:YAG laser. The measured average surface roughness and wettability of the titanium sample were found to decrease after coating. Micro-Raman analysis revealed monoclinic phase of ZrO_2 thin film. The lower wear trace depth, investigated by ball-on-disc test in dry condition, suggests reduced coefficient of friction for coated surfaces. These results indicate that ZrO_2 coating can be used as promising candidate for improving the tribological properties of Ti6Al4V bio-alloy.

Titanium based bio-alloys such as, titanium-6Aluminum-4vanadium (Ti6Al4V) have been extensively studied for their use as artificial dental and orthopaedic implants since decades. This bio-alloy has good biocompatibility, mechanical strength, and excellent corrosion resistance. However, it shows poor tribological properties which need to be improved for its use in load-bearing applications [1]. Also, the extent of wear and friction of such artificial implant decides its durability in human body. Different techniques have been developed such as, surface coating, surface texturing, laser treatment and sand blasting to improve the surface properties of Ti6Al4V samples [2]. Reports show, thin film coating of zirconia (ZrO_2), a material with good tribological properties, fracture toughness and biocompatibility, on Ti6Al4V surface can improve its wear resistance [1, 3-4]. Various methods such as, plasma spray, sputtering, chemical vapour deposition and pulsed laser deposition (PLD) can be used for thin film coating on bio-implants [5]. However, PLD has advantages of precise control over the thickness of the film deposited in addition to maintaining the stoichiometry of the film as that of target material. The PLD is a physical phenomenon wherein, when irradiated by a laser pulse of appropriate energy, duration and wavelength, the vapourised target material forms a plume of atoms, molecules, ions, and molten globules that expands in the chamber maintained at ultra high vacuum and gets deposited on the substrate surface kept at an appropriate distance facing the target.

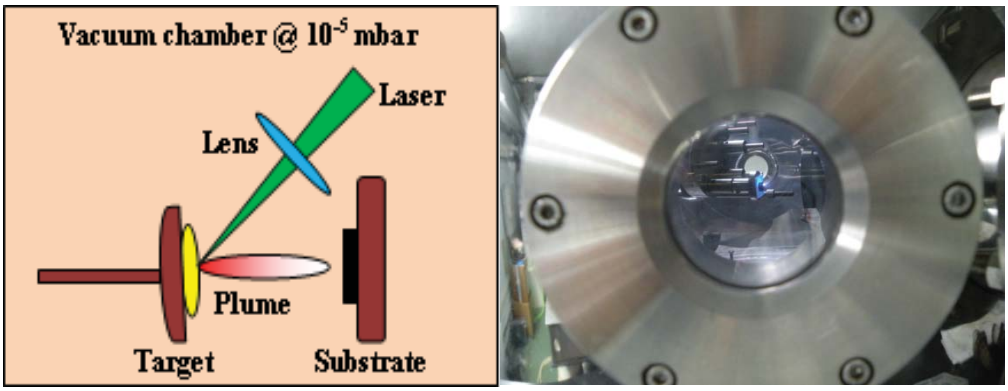

(a) (b)

Fig. 1: *(a) Typical set-up for Pulsed Laser Deposition, and (b) Photograph of PLD chamber in which ZrO_2 target and ablated plume are visible*

In this paper, we present, our studies on tribological performance of the ZrO_2 coated Ti6Al4V using a ball-on-disc tribometer in dry ambient condition. For this, PLD of ZrO_2 thin film was performed on Ti6Al4V samples measuring 20mm × 10 mm × 1mm. The third harmonic of a nanosecond Nd:YAG laser (355 nm) at 10 Hz repetition rate and of 6 ns pulse duration was employed to ablate the ZrO_2 circular pellet of diameter about 10 mm. The laser beam at 200 mW power was focused on the target through a 500 mm focal length lens. The temperature of the substrate (Ti6Al4V) on which coating is to be done was maintained at 200 °C and the deposition was carried out for an hour (36000 number of laser exposures). The distance between target and substrate was kept fixed at 30 mm and the background pressure in the chamber was about at 2 x 10^{-5} mbar. Fig. 1a shows the typical PLD set-up and a photograph of PLD chamber showing ZrO_2 pellet/target and laser ablated plume is depicted in Fig 1.b. respectively. Average surface roughness and wettability of the samples prior to and after coating were measured using profilometer and water contact angle measurement, respectively. Micro-Raman analysis of thin film was done at excitation wavelength of 532 nm, over a spectral range of 100–2000 cm^{-1} with spectral resolution of 1cm^{-1}. The dry sliding wear tests were performed using ball-on-disc machine (M/s. Anton Paar) at a constant sliding speed of 5.2 cm/sec under a load of 2N. A standard Stainless Steel ball of diameter of 5 mm was used as counterpart of Ti6Al4V. The ball moves repeatedly along a circular path on the substrate surface, increasing the wear with each cycle as entailed by the laod and the sliding speed. The worn surfaces of both coated and uncoated samples were compared using profilometer data.

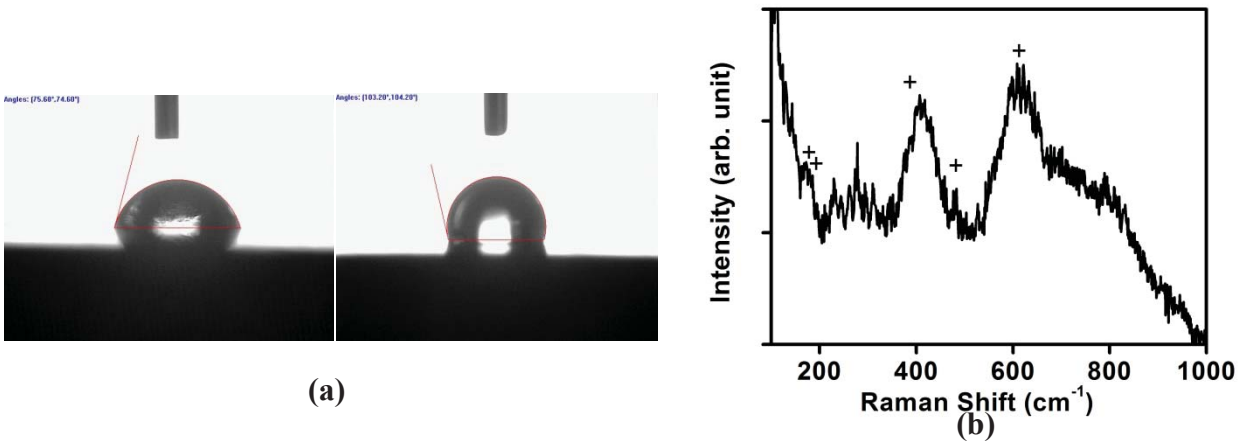

Fig. 2: *(a) Water contact angle of uncoated and coated Ti6Al4V sample, and (b) Raman spectrum of ZrO_2 coated Ti6Al4V sample*

The average surface roughness (R_a) of Ti6Al4V sample reduced from 1.8 µm to 1.4 µm post ZrO_2 coating. Fig. 2 shows, the wettability of Ti6Al4V surface also reduced and water conatct angle increased from 75^o to 103^o post the ceramic coating of the surface. Fig. 2b is the Raman spectrum of ZrO_2 thin film on Ti6Al4V sample with the peaks at 181 cm^{-1}, 192 $cm^{-1,}$ 385 cm^{-1}, 480 cm^{-1} and 610 cm^{-1} suggestive of moniclinic phase of ZrO_2.

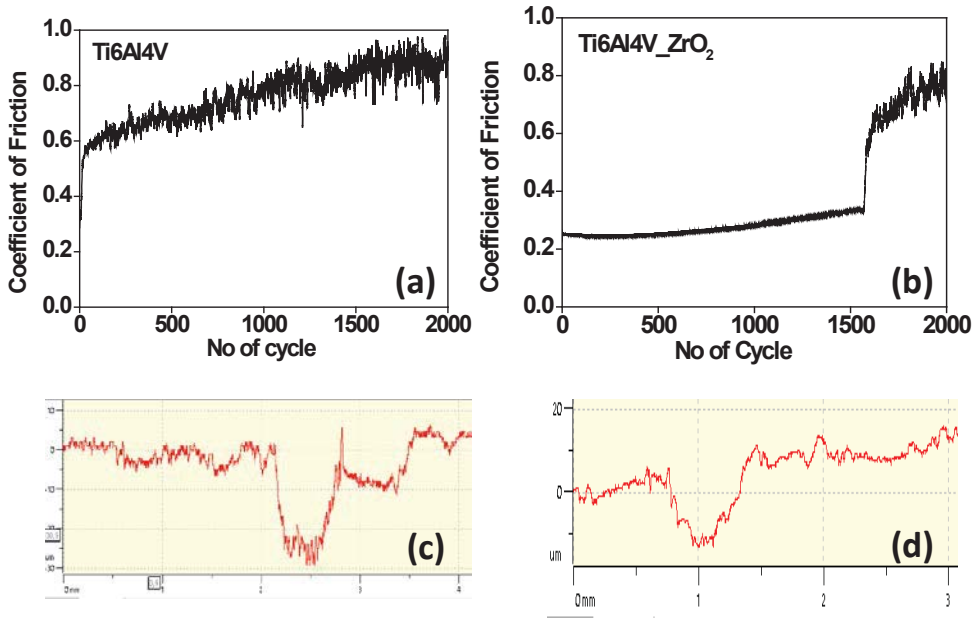

Fig. 3: *Coefficiaent of friction as a function of number of cycles (a) uncoated Ti6Al4V, (b) ZrO_2 coated Ti6Al4V, and depth profile of wear track (c) uncoated Ti6Al4V, and (d) ZrO_2 coated Ti6Al4V*

Figs. 3a-3b show, the coefficient of friction (COF) for uncoated and coated Ti6Al4V samples, respectively, as a function of number of sliding cycles. The initial COF for uncoated sample was around 0.55 at a load of 2N and it reaches to a maximum value of about 0.97, whereas the minimum and maximum values of ZrO_2 coated sample were 0.29 and 0.85, respectively. Figs. 3c-3d show, the uncoated sample exhibited a deeper wear, whereas the coated sample displays a relatively compact groove. This significant reduction in COF and depth of the wear track indicate improved tribological properties of Ti6Al4V post ZrO_2 coating.

In conclusion, the present work addressed the study of tribological behaviour of PLD coated Ti6Al4V sample. The average surface roughness and wettability of the surface reduced after thin film coating. Monoclinic phase of ZrO_2 was found on the Ti6Al4V surface from Raman analysis. A notable reduction in COF and depth of the wear trace indicated superior tribological properties of ZrO_2 coated Ti6Al4V.

Acknowledgements: The authors gratefully acknowledge the constant guidance and support of Head, L&PTD and AD, BTDG.

References:

[1] M. Berni, N. Lopomo, G. Marchiori, A. Gambardella, M. Boi, M. Bianchi, A. Visani, P. Pavan, A. Russo and M. Marcacci, *Materials Science and Engineering C* **62,** 643 (2016).

[2] S. Shaikh, S. Kedia, D. Singh, M. Subramanian, and S. Sinha, *Journal of Laser Application*, **31**, 022011 (2019).

[3] G. S. Kaliaraj, V. Vishwakarma, K. Alagarsamy and A. M. K. Kirubaharan, *Ceramics International* **44** 14940 (2018).

[4] S. Saleem, R. Ahmad, R. Ayub, U. Ikhlaq, W. Jin, and P. K. Chu, *Applied Surface Sciences* **394,** 586 (2017).

[5] Z.Teuberova, M. Seydlova, T. Dostalova, B. Dvorankova, K. Smetana, M. Jelinek, P. Masinova, T. Kocourek, K. Kolarova and J. Wilson, *Laser Physics* **17**, 45 (2007).

Picosecond Laser Nano-pitting on Stainless Steel by Micro-particle Lens Array to Improve Hydroxyapatite Growth

S. Kedia[1, *], A. K. Sahu[2], J. P. Nilaya[1,3]

[1]Laser & Plasma Technology Division, Bhabha Atomic Research Centre, Mumbai 400085
[2]Glass & Advance Ceramics Division, Bhabha Atomic Research Centre, Mumbai 400085
[3]Homi Bhabha National Institute, Training School Complex, Anushaktinagar, Mumbai 400094

[*]Email: skedia@barc.gov.in

Abstract: Self-assembled transparent particle mask for laser assisted nano-pitting array on stainless steel substrate surface was investigated for bio-application. Monolayers of polystyrene micro-particles were deposited on 316L stainless steel and optical near-field lithography was performed using single shot picosecond laser irradiation at 532 nm. A variety of nano-pit patterns were generated on the substrate surface depending on the exposure conditions. Scanning electron microscope images confirmed denser growth of hydroxyapatite in the nano-pit region in comparison to plain surface when immersed in simulated body fluid for 24 hours indicating a superior biocompatibility and a probable faster method of improving the effectiveness of a biomaterial over large surfaces.

The possibility of enhancement of material properties by surface modification/texturing has resulted in an increased research activity in the field of surface modification that can be achieved by the interaction of the surface with various beams, e.g., electron beams, ion beams, plasma, and lasers. Of these, laser surface processing has advantages of being a chemcial free contactless process capable of generating complicated structures, maskless processing, and ability to work in air/vacuum/liquid environments. In addition, the possibility of a wide range of modifications, e.g, structuring, oxidation, nitridation, etching and deposition of biomaterials that can improve the bio-functionality, mechanical properties and tribological properties of biomaterial [1] make this method more attractive. In general, resolution of laser induced features are limited by diffration limit. However, optical near field techniques overcome this limitation and can be used to generate smaller features [2, 3]. Microparticle lens array is one such method of nano patterning in which spherical transparent micro-particles are deposited over the target substrate in the form of monolayer and subsequently irradiated by an appropriate laser beam [4]. The spherical particles acting as transparent micro lenses focus the incoming radiation, leading to a high intensity region of evanescent waves underneath the microparticles that can raise the substrate surface temperature leading to its melting and even vapourisation. This, in turn, causes pitting on the surface in the nanometer scale [4, 5-6].

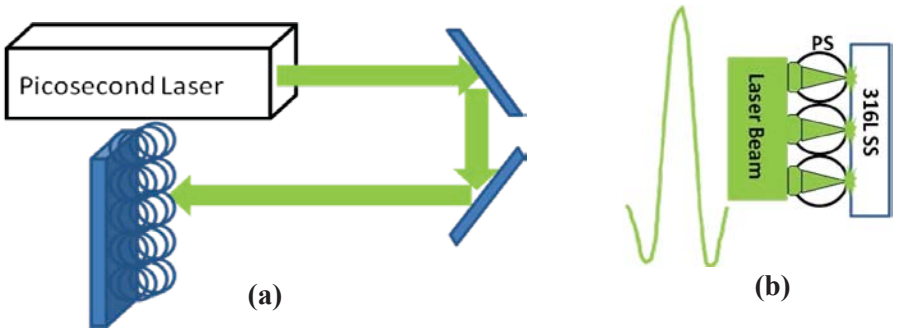

Fig 1: ***(a)*** *Experimental set up for nano-patting of 316L SS bio-material using a picosecond laser, and (b) Illustration of laser beam focusing through PS particle micro lens on 316L SS surface.*

In this work, we present the experimental results of laser assisted nano pitting on a biomaterial, 316L stainless steel (SS), and the improvement in the growth of Hydroxyapatite (HAP), the bone cement and an essential intermediary for the integration of the implant with the body, for the case of laser treated samples as against the untreated plain biomaterial. For these experiments, commercially available colloidal solution of monodispersed polystyrene micro-spheres (PS) of diameter ~1 µm was used. Monolayers of PS were deposited on mirror polished circular 316L SS substrates. The as received colloidal solution of PS (2.5 wt%) was suitably diluted using methanol and ultrasonicated for 30 minutes to remove particle clustures in the solution. An optimized volume of diluted PS solution was drop casted on SS substrates and allowed to dry under ambient conditions. The second harmonic of a picoseocnd Nd:YAG laser (M/s. Ekspla) operating at at 532 nm and capable of delivering a maximum of ~ mJ/pulse at a repetition rate at 10 Hz and pulse width of 30 ps was used as the coherent irradiation source. The schematic diagram of the experimental set-up used in this work is shown in Fig. 1a. Number of laser irradiated samples were prepared by exposing the substrate surface to a single laser pulse (beam diameter ~ 6 mm) of different laser powers, such as 50 mW, 80 mW and 100 mW and examined using Sacnning Electron Microscope (SEM) and Atomic force microscope (AFM). The exposed samples were cleaned off the remnant PS particles shot by chemcial method. The patterned samples where dipped in Simulated Body Fluid (SBF) prepared in house for 24 hours to observe the growth of hydroxyapatite on patterened sample surface. The list of salts and their weight used to prepared 1L of SBF is given in Table-1 [7].

Table-I: *Salts and their weights used for the preparation of 1 litre of SBF.*

Salts	NaCl	$NaHCO_3$	KCl	$Na_2HPO_4.2H_2O$	$MgCl_2.6H_2O$	$CaCl_2.2H_2O$	Na_2SO_4	$(CH_2OH)_3CNH_3$
Weight (gm/litre)	6.54	2.26	0.37	0.17	0.30	0.36	0.07	6.05

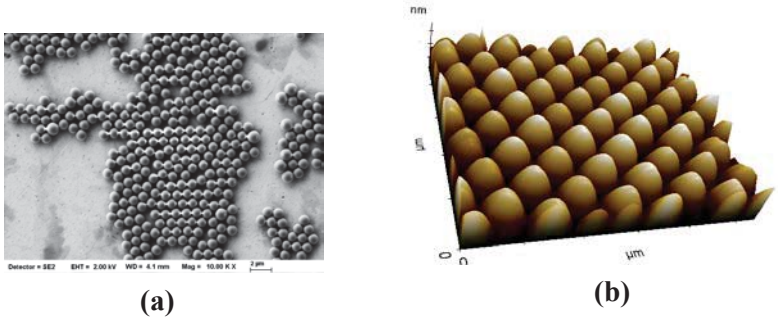

Fig 2: (a) SEM image and **(b)** AFM image of PS micro-particle monolayer on 316L SS substrate

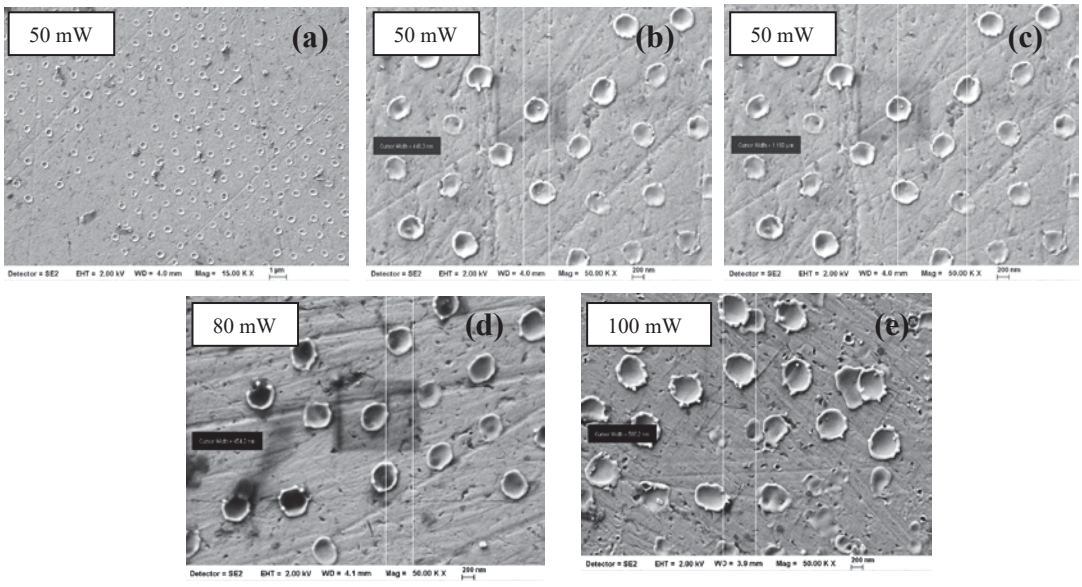

Fig 3: *SEM images of nano-pits generated on 316L SS samples using picoseconds laser at (a-c; for different magnification) 50mW, (d) 80 mW, and (e) 100 mW*

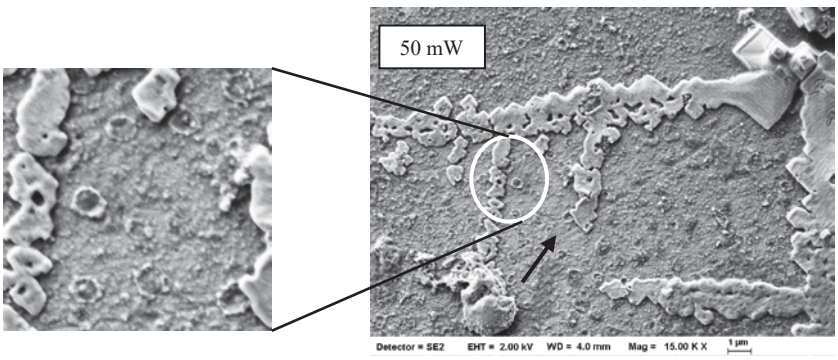

Fig 4: *SEM images show the growth of HAP ~~grown~~ on pitted and un-pitted regions on 316L SS sample*

Fig. 2a-2b are the SEM and AFM images of PS particles deposited on SS substrate, respectively. The close packed monolayer of PS is clearly visible in the images. Figs. 3a-3c shown the SEM images (at different

magnification) of nano-pits generated on SS substrate at 50mW laser power. The diameter of the pit was measured as ~ 448 nm (Fig. 3b) and separation between the two pits was measured as 1180 nm, as expected for a close packed monolayer, in Fig. 3c. The pit diameter increased with increase in laser power. Figs. 3d and 3e show SEM images of the substares irradiated at 80 mW and 100mW where diameters of the pit were measured as 454 nm and 566 nm, respectively. As stated before transparent/semi-transparent particulates act as focusing media and enhance the intensity of the incident radiation underneath the particulates. The increased intensity leads to enhanced absorption by the substrate causing surface pitting as a result of ablation even when the incident laser intensity is well below the ablation threshold [8]. The distribution of light between micro-particle and substrate controls the feature of the pits, Fig. 1b. Light enhancement under the particle also depends upon the particle size and the laser wavelength. It is shown that the light enhancement increases as particle diameter increases and light wavelength decreases [9]. In the present work however, the particle size and laser wavelength were maintained constant, and hence the increase in pit diameter is directly attributable to the increase in incident laser power. Fig. 4, show the SEM image of 50 mW laser power patterned SS sample dipped in SBF for 24 hrs. Denser growth of HAP was observed at and near the pitting area (magnified SEM image). However, discrete nucleation of HAP was observed on plain region, maked with arrow in the figure. Faster growth of HAP on nano-pits as compared to the untreated surface may be attributed to the depth of the feature that can increase the residance time and hence the interaction of SBF solution with material surface. This is a positive indication of the probability of better acceptance of the laser treated biomaterial by the body. More systematic studies on the sub-nano level topographical and chemical changes in pitted area followed with time dependent growth of HAP on the sample, other parameters e.g., corrosion resistance, anti bacterial behaviour etc are in progress.

In conclusion, nano-pits with various diameters were generated on 316L SS substrates by irradiating the monolayer PS sample using single shot picosecond laser pulse. The generation of nano-features are attributed to enhancement of light energy at near field through the micro-particles. Immersion of laser treated samples in SBF revealed that the surface pitting supported denser growth of HAP that is attributable to higher residance time of SBF and, in turn, longer interaction time between SBF and the substrates.

Acknowledgment: Authors thank useful discussions with Mr. Bijoy Sugathan. The authors also gratefully acknowledge the constant guidance and support of Head, L&PTD and AD, BTDG.

Reference:

[1] M. J. K. Lodhi, K. M. Deen, M. C Geenlee-Wacker, W. Haider, *Additive Manufacturing* **27,** 8 (2019).
[2] A. Khan, Z. Wang, M. A. Sheikh, D. J. Whitehead, and Lin Li, *Applied Physics Letter,* **258**, 774 (2011).
[3] T. C. Chong, M. H. Hing, L. P. Shi, *Laser Photon Rev.* **4**, 123 (2010).
[4] B. Sugathan, J. P. Nilaya, M. Pillai and D. J. Biswas, *AIP Advances* **8**, 115110 (2018).
[5] W. Guo, Z. B. Wang, L. Li, D. J. Whitehead, B. S. Lukyanchuk and Z. Liu, *Applied Physics Letter,* **90**, 243101 (2007).
[6] S. M. Huang, Z. Sun, B. S. Lukyanchuk, M. H. Hing, and L. P. Shi, *Applied Physics Letter* **86**, 161911 (2005).
[7] S. Shaikh, S. Kedia, A. K. Singh, K. Sharma, S. Sinha, *J. Laser Appl.* **29,** 022004 (2017).
[8] J. P. Nilaya, D. J. Biswas, *Appl. Surf. Science* **256,** 1867 (2010).
[9] M. H. Hong, Y. Lin, G. X. Chen, L. S. Tan, Q. Xie, B. Lukyanchuk, L. P. Shi and T. C. Chong, *Journal of Physics* **59**, 64 (2007).

Infrared Laser Assisted Deactivation of Bacteria and Virus Samples

Tatsat Dwivedi, M. B. Sai Prasad, J. Padma Nilaya*[a], Laser & Plasma Technology Division, BTDG, BARC.
Vandan Nagar[1,3], A.V.S.S.N. Rao[2,3], R. Shashidhar[1,3], S. K. Ghosh[3],
Food Technology Division[1], Molecular Biology Division[2], Bio Science Group[3], BARC
[a]*Homi Bhabha National Institute, Anushaktinagar, Mumbai-94*
*Email: jpnilaya@barc.gov.in

Abstract

It is well-known that the exposure of bacteria and germs to electromagnetic radiation can lead to their annihilation. In the present study, we have attempted to characterize the effect of laser radiation on test samples comprising of bacteria and viruses. A pulsed TEA (transverse excitation atmosphere) CO_2 laser that operates in the mid-IR region of the electromagnetic spectrum has been employed for the studies. The *Aeromonas* enteric bacterium and its specific virus, P2 bacteriophage, cultured on a typical matrix of Tryptic Soya Agar (TSA), served as the test samples. Agar overlay technique was used to examine the test results. Detailed analysis of the laser exposed samples showed complete neutralisation of bacteria and viruses for appropriate laser parameters.

Introduction

It is widely acknowledged that electromagnetic radiation effectively neutralises bacteria and germs[1-3] under controlled conditions. While gamma and UV radiation[4] have the effect of degrading the genetic material of the organisms, exposure to infrared wavelength causes a rise in temperature which in turn results in their annihilation[5]. Excimer lasers and Infrared lasers have also been tried for decimating viruses and bacteria[6-8]. We in the present work, have studied the effect of a pulsed TEA CO_2 laser that operates in the 10 μm region, on the enteric bacterium, *Aeromonas*, and its specific virus, P2 bacteriophage, grown on TSA matrix[9]. The efficacy of such a laser towards decimating the bacteria/virus and thereby decontaminating the surfaces has been studied as a function of the laser power density, the pulsing frequency and its exposure time.

Experimental Work

Two types of samples, those of bacteria and virus, viz., the enteric bacterium *Aeromonas* (10^7cfu/ml) grown on Tryptic Soya Agar (TSA) matrix and P2 phage (lab isolate), a bacteriophage (a virus that feeds on bacteria) of Aeromonas hydrophila CECT 839T have been prepared and employed for laser irradiation studies. The details of the sample preparation and the methodologies adopted for the analysis post irradiation is elaborated in our recent work[10].

The pulsed CO_2 laser (Light Machinery, Canada) capable of delivering ~2 J/pulse and pulse repetition frequency ranging from 1-100 Hz was used as the source of irradiation. The schematic of the experimental set-up is shown in figure 1. A focusing lens (75 cm f) was used to gradually increase the laser fluence on the sample plane,

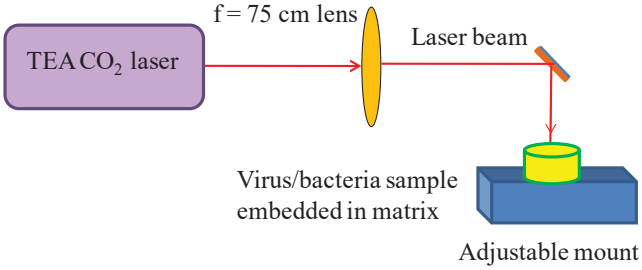

Figure 1. Schematic diagram of the experimental set-up

and the same was estimated by measuring the laser energy and the beam size at the target location.

In the first set of experiments, four different sets of bacterial samples were irradiated at different laser fluence and analysed (Table 1). No bacterial growth is expected to be observed in the laser-exposed zone in the event of its annihilation while normal bacterial growth is expected in the other regions. As can be seen from Table 1, except for case of sample 3 for which case, the fluence was not sufficient to cause annihilation, general cleaning of the bacteria could be otherwise observed for all the samples.

Sample	Distance from lens	Laser Fluence (J/cm^2)	Irradiation conditions	Inference
Sample 1	60 cm	4.3	5 pulses, 1Hz	Bacterial growth is inhibited
Sample 2	30 cm	1.2	5, 10 pulses, 1Hz	Bacterial growth is inhibited
Sample 3	10 cm	0.5	20 pulses, 1Hz	Bacterial growth not inhibited
Sample 4	0	0.4	Control (standard) (top half) Bottom (30Hz, 1 sec)	Growth present Growth inhibited

Table 1. Irradiation of bacterial samples with CO_2 laser (10.6 μm) at different fluences.

Figure 2 shows the case of sample 4 where the broad-based annihilation of the bacteria upon exposure to laser under unfocussed conditions i.e., ~0.4 J/cm^2 (1.824 J over an area of 25 mm x 18 mm), at a repetition rate of 30 Hz can be seen. The top half indicates the control standard (no laser exposure) while the bottom half indicates the irradiated region. In this case, though the fluence was less, but owing to the higher repetition rate (30 Hz), the growth of bacteria could be inhibited. Also, the underlying matrix remained intact during the process. It may be noted that the increased temperature effect at higher laser fluence may be achieved at a lower value as well, but for higher pulse repetition rates, due to inefficient/limited heat conduction between pulses.

Figure 2. CO_2 laser irradiation of Aeromonas (10^7cfu/ml) grown on Tryptic Soya Agar matrix.

Sample	Virus density (pfu/ml)	Focal distance	Laser Fluence (J/cm^2)	Region of irradiation	Inference
Sample 1	10^6	10 cm	0.535	Top (1 pulse, 1 Hz) middle (5 pulses, 1 Hz) Bottom (10 pulses, 1 Hz)	No observable killing of virus
Sample 2	10^6	20 cm	0.764	ditto	Partial killing of virus
Sample 3	10^6	30 cm	1.2	ditto	-* ++* +++* Ablation of matrix too observed
* + indicates effectiveness of virus decimation. Qualitative comparison of virus killing as shown in Figure 3.					

Table 2. Irradiation of virus samples with CO_2 laser (10.6 μm) at different fluences.

In the second set of experiments, virus samples, viz., P2 bacteriophage, at a concentration of 10^6 pfu/ml, were exposed to laser pulses of different fluence viz., 0.535 J/cm^2, 0.764 J/cm^2 and 1.2 J/cm^2 (as enumerated in Table 2). The irradiation was carried out at three different regions of the prepared samples, i.e., the top, middle and the bottom regions. A sample case is shown in figure 3. In order to test the effect of the laser radiation on the virus samples, the same have been exposed to *Aeromonas* bacteria post irradiation. To be noted that this virus, if present, feeds on the bacteria and doesn't allow its growth. It can be observed from Table 2 that, only for case of irradiation at 1.2 J/cm^2 (sample 3), the virus could be most effectively killed as is indicated by the presence of bacterial growth (in the bottom region as indicated in figure 3) and no such growth in the other regions (top and middle) where the virus was not affected by laser radiation. Partial killing of virus resulted in partial growth of bacteria (figure 3, middle region).

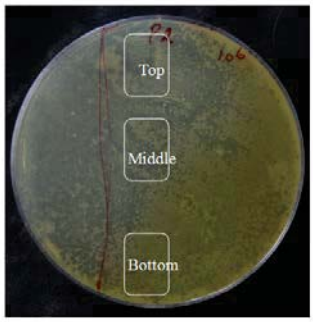

Figure 3. Effect on virus grown on TSA matrix for 1 (top), 5 (middle) and 10 (bottom) exposures (table 2). Growth of bacteria in the bottom trace indicates more effective killing of virus.

Sample	Virus density (pfu/ml)	Focal distance	Exposure time	Killing of virus
Sample 1	10^5	20 cm	1 sec	+/-
Sample 2	10^5	20 cm	5 sec	+/-
Sample 3	10^5	20 cm	10 sec	+
Sample 4	10^5	20 cm	15 sec	++
+/- denotes the very marginal killing of virus; + denotes more killing of the virus as compared to +/-; ++ denotes more killing of the virus as compared to +.				

Table 3. Irradiation of virus samples with CO_2 laser (10.6 μm) for different exposure times; Laser fluence = 0.764 J/cm^2, 1 Hz repetition rate, Peak power=9.1 MW, Average power=1.82 Watt, Power density=0.764 W/cm^2, Area of exposure=14x17 mm^2.

More studies were carried out with samples exposed to higher number of laser pulses and at higher repetition rates. In this regard, four samples, viz., sample 1, 2, 3, 4, as shown in figure 4, were irradiated at a constant fluence of 0.764 J/cm^2 (Table 3). The photographs shown in figure 4 are of the samples one day following the laser exposure. The clear gradation of the growth of bacteria and hence improved efficiency of virus decimation with increased number of laser pulses is evident for irradiation conditions as tabulated in Table 3. To be noted, the medium remained intact in the entire process.

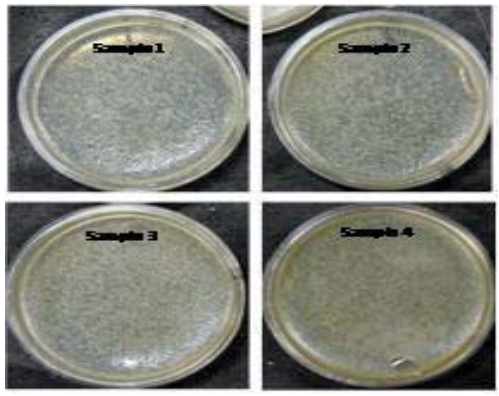

Figure 4. Gradual increase in decimation of virus visible in samples 1 to 4 as number of exposures increased (table 3).

Following this, two more samples, numbered 7 & 8 (figure 5) have been irradiated at a fixed fluence of 0.535 J/cm^2 but at 1 Hz and 10 Hz repetition rate respectively. A zone of matrix damage could be

seen for the case of irradiation at 10 Hz (as can be seen in figure 5) owing to rise in surface temperature.

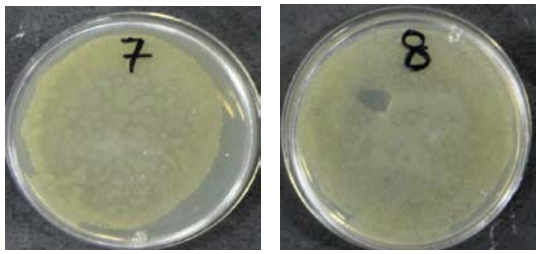

Figure 5. Increased repetition rate at the same fluence resulted in matrix damage in sample 8.

Conclusions

The effect of mid IR laser radiation on the bacterial and virus samples has been investigated and the results summarized. We observed that the extent of bacterial killing increased either with increased laser fluence (0.4 to 1.2 J/cm^2) or with increased number of pulses (1 to 30) and increased repetition rate. Even though the extent of P2 bacteriophage killing also showed similar trend, the effect is much less distinct. Importantly, the matrix in which the viruses are suspended seems to play a significant role. The results obtained from the present study provide a qualitative evidence for killing of viruses by CO_2 laser.

Acknowledgements

The authors sincerely acknowledge Dr. Archana Sharma, Associate Director, Beam Technology Development Group (BTDG) for initiating this work and for her continued guidance and support. They also acknowledge gratefully the encouragement of Head, L&PTD.

References

1. Y. S. Tapia Guerrero, *Materials (Basel)* **13(5)**, 1090 (2020).
2. T. W. Huber, *Applied Microbiology* **19(2)**, 383 (1970).
3. A. Anellis, D. Berkowitz, and D. Kemper, *Journal of Food Protection*, **40**, 313 (1977).
4. T. Kato et al., *Lasers in Surgery and Medicine* **23**, 299 (1998).
5. Michael F. Holick, *International journal of cancer research and treatment* **36(3)**, 1345 (2016).
6. Vicente M. Gomez-Lopez, *Trends in Food Science & Technology* **18**, 464 (2007).
7. Dieter Schuocker, High power lasers in production engineering, World Scientific Publications Co. Inc. (1999).
8. Gokce Meral, *Lasers in Surgery and Medicine* **32**, 197 (2003).
9. https://en.wikipedia.org/wiki/Trypticase Soy Agar.
10. Tatsat Dwivedi, M.B. Sai Prasad, J. Padma Nilaya, Vandan Nagar, R. Shashidhar, A.V.S.S.N. Rao, S.K. Ghosh, *BARC Newsletter*, July-August (2020).

Study of the effects of short term hyperglycemic exposures on human red blood cells

Yashveer Singh,[1,2] Aniket Chowdhury,[1,2] Raktim Dasgupta,[1,2] Shovan Kumar Majumder[1, 2]

[1]*Homi Bhabha National Institute, Training School Complex, Anushaktinagar, Mumbai 400094, India.*

[2] *Laser Biomedical Applications Division, Raja Ramanna Centre for Advanced Technology, Indore 452013, India.*

Email: yashveer@rrcat.gov.in

Abstract

Short term hyperglycemic stress on red blood cells (RBCs) have been studied using Raman optical tweezers having 532 nm excitation light. Use of 532 nm light for exciting Raman spectra also results in simultaneous photoreduction of intracellular hemoglobin (Hb). Since increasing glucose concentration was observed to limit the photoreduction effect in treated RBCs, prior formation of permanently oxidized Hb by hyperglycemia effects, offers a possible explanation. Any subsequent damage to RBC membrane due to hyperglycemia induced oxidative stress were also investigated using optical stretching experiments with the laser trap.

Introduction

About 422 million people worldwide are suffering from diabetes, and 1.6 million deaths are directly attributed to diabetes each year.[1] Both the number of cases and the prevalence of diabetes have been steadily increasing over the past few decades. The measurement of glycated hemoglobin A1c (HbA1c) level is the widely accepted indicator for glycemic control,[2] but it does not addresses short term fluctuation in the blood glucose level. However, it would be interesting to understand if two individuals, having similar HbA1c level but largely different glucose variability, would have the same or different level of risk for developing complications. Particularly in diabetes patients, the postprandial phase is known to be associated with a rapid and large increase in the blood glucose level.[3]

To investigate the short term hyperglycemia effects on RBCs , that may occur during the postprandial phase, we performed studies using single cell Raman spectroscopy. We made use of the fact that exposure to visible lasers is known to cause reduction of oxygenated hemoglobin (oxy-Hb) inside the cells.[4] Therefore, if short term hyperglycemia causes damage and denaturation of oxy-Hb via developing oxidative stress to cells it will aid in the formation of permanently oxygenated Hb that cannot be photoreduced [5] and such effects may be probed by recording Raman spectra from the cells. Since the increased oxidative stress may also alter the mechanical properties of cellular membrane, hyperglycemia exposed RBCs were studied using optical stretcher for comparing the elongation lengths with that for unexposed cells, and a reduced elongation for hyperglycemia exposed cells suggesting a loss of elastic nature could be observed.

Materials and methods

Fig. 1 shows a schematic of the experimental set-up. The 532 nm cw beam from a frequency doubled Nd: YVO_4 laser (Verdi -5, Coherent Inc) was used for both photoreducing single RBCs as well as exciting their Raman spectra. The laser beam was introduced through the illumination condenser into the cell sample placed on an inverted microscope (Axiovert 135 TV, Carl Zeiss). The elastically scattered laser light and Raman scattered light were collected by a microscope objective lens. The light was then passed through a notch filter to suppress the Rayleigh scattered light while the Raman signal passing through the filter was coupled to an imaging spectrograph (Shamrock SR-303i, Andor Corp). The spectrograph consists of a 1200 lines/mm grating blazed at a wavelength of 600 nm and a back-illuminated, thermoelectrically cooled CCD (iDus 401-BRDD, Andor Corp.) camera.

Raman spectra were recorded from single RBCs by manipulating the cells into the 532 nm laser beam with the help of a laser trap[6] formed using the 1064 nm beam from a Nd:YAG laser (Compass, Coherent Inc.). At the time of recording the spectra the cells were placed in the path of the 532 nm laser beam and the trap laser was turned off after positioning of the cells.

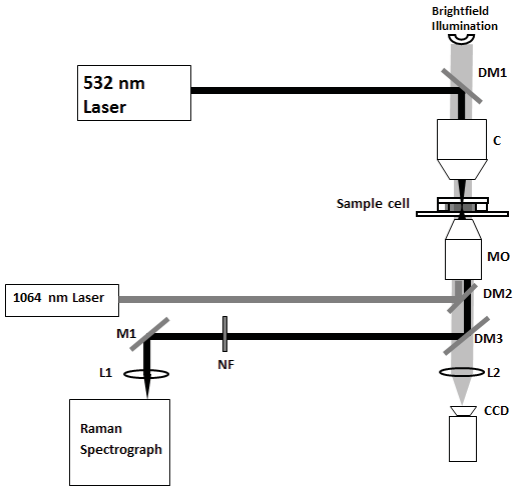

Fig.1. *A schematic of the experimental set-up. The beams from a 532 nm laser (for photoreduction and Raman excitation) and a 1064 nm laser (for optical trapping) were coupled to the sample via dichroic mirrors (DM1-DM3) though the condenser (C) and the objective lens (MO) respectively. The Raman signal was observed via a spectrograph-CCD system after rejecting the Rayleigh scattered light by using a notch filter (NF).*

Human blood samples obtained from blood bank of Choithram Hospital and Research Centre, Indore were used for the experiment. RBCs were separated from whole blood by centrifugation at 600g for 3 minutes. The separated RBCs were then washed with phosphate buffer saline (PBS) twice by centrifugation at 600g for 3 min and then resuspended in the same buffer. Appropriate dilutions of the cells in buffer solution containing 2% bovine serum albumin (BSA) were then used for the experiments.

For studying the short term hyperglycemic effects on RBCs, D-glucose was added to the cellular suspensions in varying concentrations from 5 mM (90 mg/dl) to 40 mM (720 mg/dl) and incubated for 3 hours before recording spectra.

For studying the effects of medium glucose on RBC membrane, optical tweezers based cell stretcher[7] was used. In this technique first a single RBC is trapped with optical tweezers using NIR laser and thereafter a fluid drag is applied on the trapped cell by applying medium flow around it. Any loss of elasticity for the cell leads to smaller increase in stretched length. In our experiments, single RBC were trapped under NIR laser tweezers using ~ 5 mW power and a constant velocity of 120 μm/s was used to uniformly move the sample chamber, resulting in the stretching of the trapped RBC along the flow. The percentage elongation for the RBCs were estimated as,

$$Percentage\ elongation = \frac{x - x_0}{x_0} \times 100$$

Where x_0 and x are the natural length and stretched length of RBC respectively .

Results and discussions

The Raman spectra from glucose incubated cells were recorded in a photo reduced condition by using 300 µW of power from the 532 nm laser. With increasing glucose concentration noticeable changes in the Raman spectra with respect to control were observed and the magnitude of the changes found to increase with glucose concentration (Fig. 2). The most significant spectral changes were seen as the increase in intensity of the Raman peaks at 1637,1582 and 1373 cm^{-1} with increasing glucose concentrations The observed spectral changes indicate the formation of permanently oxygenated Hb within the glucose incubated RBCs.[8]

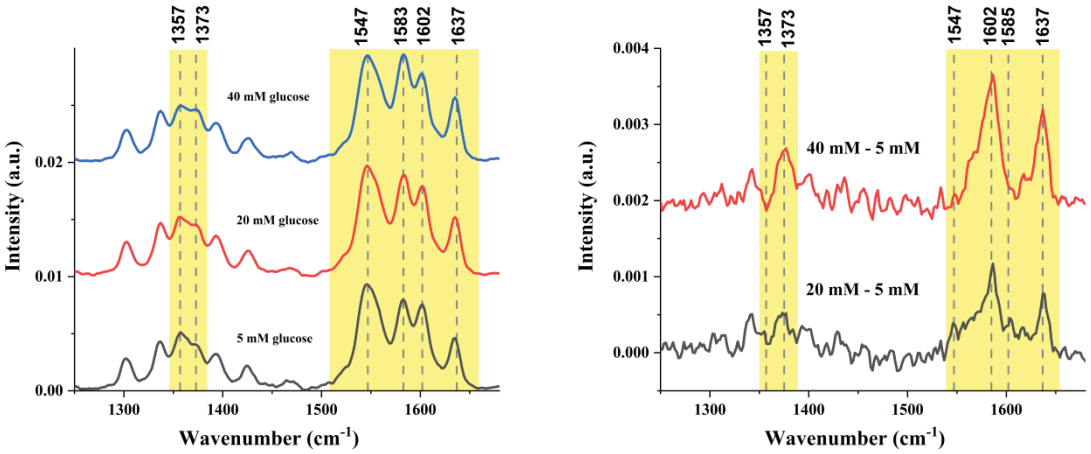

Fig.2. (A) *Mean Raman spectra of RBCs exposed to varying concentrations of glucose. The Raman bands with significant changes are marked and shown under shaded regions. (B) The difference spectra of RBCs exposed to 20 mM and 40 mM concentrations of glucose with respect to the mean spectrum from 5 mM concentration of glucose*

This permanently oxygenated form of Hb is known as hemichrome. The generated hemichrome is known to have a much higher affinity for RBC membrane.[9] This attachment is caused by an irreversible crosslinking involving both band 3 and spectrin in membrane.[10] This binding may weaken or disrupt the band 3-cytoskeleton linkage, triggering the clustering of band 3 and consequent membrane damage. To identify the possible membrane damage, optical tweezers based cell stretcher was used. A RBC when held in an optical tweezers was subjected to fluid drag by applying a medium flow around the cell leading to its elongation along the flow. Around 30 cells at each glucose concentration levels were studied under the optical stretcher and the mean percentage elongations at each concentration are plotted in the fig. 3. The reduction in elongated length under identical trap power suggests a detectable loss of elasticity for the cells under higher glucose concentration.

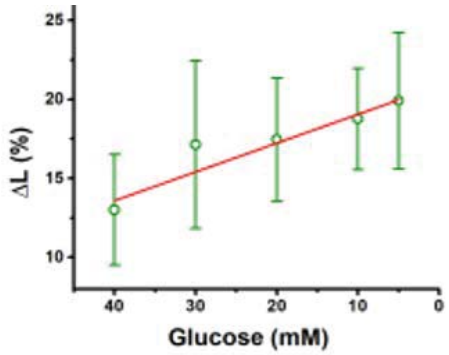

Fig.3. *Mean elongations against concentrations are plotted the linear fits are shown. The results obtained from samples indicate a possible reduction in elasticity of RBCs at high glucose concentrations. Although the scattering in data is large, similar trend could be observed from all the samples studied under optical stretcher.*

Conclusion

Using simultaneous laser induced photoreduction and Raman spectroscopy, changes suffered by RBCs under short term hyperglycemic scenario could be studied. The analysis of recorded Raman spectra suggests alteration in redox balance of cell that leads to oxidative damage to intracellular hemoglobin**.** Optical stretcher experiment enabled us to examine oxidative damage to cellular membrane showing reduced cell elasticity for hyperglycemic RBCs.

References:

[1] https://www.who.int/health-topics/diabetes#tab=tab_1

[2] IM Stratton, AI Adler, HA Neil, DR Matthews, SE Manley, CA Cull, D Hadden, RC Turner, RR Holman, *BMJ* **321**, 405 (2000).

[3] J Zhu, G Xing, T Shen, G Xu, Y Peng, J Rao, R. Shi, *Evid Based Complement Alternat Med*., 7923732 (2019)

[4] Y. Gu, P. Li, J. T. Sage, and P. M. Champion, *J. Am. Chem. Soc.* **115**, 4993 (1993).

[5] K. Ramser, E. J. Bjerneld, C. Fant, and M. Kall, *J. Biomed. Opt.* **8**, 173 (2003).

[6] R. Dasgupta and P. K. Gupta, *Opt. Lett.* **30**, 394 (2005).

[7] SK Mohanty, A Uppal, PK Gupta „*J Biophotonics* **1**, 522 (2008).

[8] B. R. Wood, B. Tait, and D. McNaughton, *Biochim. Biophys. Acta - Mol. Cell Res.* **1539**, 58 (2001).

[9] S. M. Waugh, B. M. Willardson, R. Kannan, R. J. Labotka, P. S. Low, *J. Clin. Invest.* **78**, 1155 (1986).

[10] J. M. Rifkind and E. Nagababu, *Antioxid. Redox Signal.* **18**, 2274 (2013).

Raman spectroscopy based detection of microalbuminuria: A feasibility study

Rashmi Shrivastava, Jyoti Kumawat, Amrita Srivastava, Nitin Kumar, Hemant Krishna and Shovan K. Majumder*

Laser Biomedical Applications Division, Raja Ramanna Centre for Advanced Technology, Indore-452013, India

E.mail : shkm@rrcat.gov.in

Abstract

Excretion of albumin in urine (microalbuminuria) is an important indicator for the onset of renal disease associated with conditions like diabetes and pre-eclampsia. Current methods of microalbuminuria detection are chemical intensive and time consuming. Here, a Raman spectrosocpy based method called drop-coating Raman spectroscopy (DCDRS) is explored for detection of microalbuminuria which does not require prior sample processing. Solution of Human serum albumin (HSA) at various concentrations was prepared in artificial urine and DCDRS spectra were recorded using visible laser. Results show identifiable differences in the region of 1400 to 1500 cm^{-1} even at low concentration of HSA (0.06mg/ml). DCDRS thus is a potential technique for microalbuminuria detection.

Introduction

Urinary albumin excretion (UAE) is a key indicator to detect renal complications in conditions like type 2 diabetes or pre-eclampsia[1,2]. Microalbuminuria, as it is called (UAE excretion of 0.025 to 0.5 mg/ml), has also been established as a risk marker for cardiovascular and kidney disease and is associated with related mortality risk. The conventional microalbumin measurement methods are chemical intensive and require sophisticated instruments and trained manpower. Alternative low-cost methods such as urinary dipsticks have exhibited poor sensitivity[3]. Thus, there is need for a reliable, accurate and rapid method of microalbuminuria detection.

Raman spectroscopy is a molecular sensitive technique and a promising alternative for microalbumin detection in urine. However, since Raman signals are inherently weak and the concentration of albumin to be detected is very low, various signal enhancement techniques are required to achieve the desired outcome. Several reports have recently demonstrated the application of surface –enhanced Raman spectroscopy (SERS) based approaches for enhancing the Raman signal from albumin[4,5]. Though these approaches have shown detection down to ng/ml of albumin, but the clinical translation of these techniques shall be rather complicated and associated with fabrication of a reproducible SERS substrate. To address this issue Flores-Guerrero *et al*. very recently reported a pilot study on urinary albumin detection by conventional Raman spectroscopy. However, it required high signal acquisition time of ~ 5 min[1].

In the current study we explore another variant of Raman spectroscopy called Drop Coating Deposition Raman Spectroscopy (DCDRS) for detection of microalbuminuria. It is a technique with no requirement of either specialized substrate or higher exposure times for signal enhancement. The technique relies on ‘coffee ring’

effect which results in analyte concentration at the edges of a drying drop[6]. The Raman signal from the concentrated analyte at the periphery of such a dried drop is significantly enhanced.

Materials and method

Instrumentation

The experimental arrangement used for DCDRS measurement consisted of a single mode laser (Spectra physics) with central wavelength of 532 nm as the excitation source. A half wave plate and polarizer are placed in the path of laser beam to adjust the power at the sample. The laser beam is then reflected by a dichroic mirror (DM) that is placed at an angle of 45°. Another mirror (M) is placed at an angle of 45° to steer the beam towards the sample, where the beam is focused onto the sample surface using an objective lens (20 X, 0.45 NA). The back scattered Raman signal from the sample is collected through the same objective lens, reflected by M and transmitted through DM and then finally passed through a notch filter which removes the elastically scattered Rayleigh component. The output of the notch filter is then focused using a lens on to the end of an optical fiber of 200 µm diameter. The fiber then leads to an imaging spectrograph (Acton Spectra Pro, SP-2300, and Princeton) equipped with a thermoelectrically cooled, back-illuminated, deep-depletion CCD camera (Figure 1).

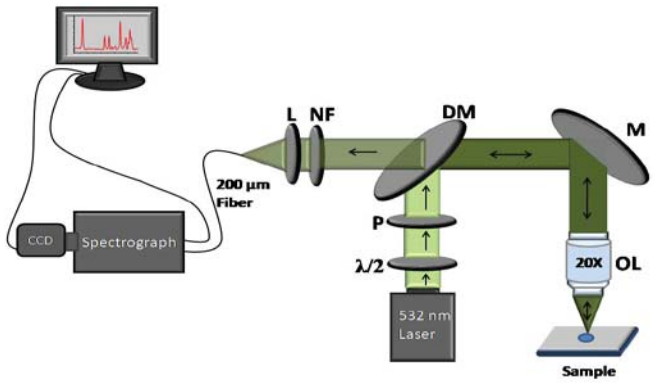

Figure 1: A schematic representation of the Raman spectroscopy set up for the DCDRS measurements. The abbreviations and their corresponding expansions are as follows: λ/2—Half wave plate, P—Polariser, DM—Dichroic mirror, M—Mirror, OL—Objective lens, NF—Notch filter and L—focusing lens.

Human serum albumin samples

Solutions of varying concentrations (0.02 mg/ml to 1 mg/ml) of Human serum albumin (HSA) (Sigma-Aldrich, USA) were prepared in deionized water as well as in artificial urine. Artificial urine was composed of urea, creatinine and uric acid at concentrations of 16.0 mg/ml, 1.04 mg/ml and 0.34 mg/ml, respectively.

Data acquisition and processing

To acquire the DCDRS spectra, a triplicate of 5 μl drops of each concentration of HSA in water or artificial urine was air dried on aluminium foil at room temperature and the laser was then focused at the periphery of each dried drop. DCDRS spectra were thus measured from five different points on the circumference of each dried drop. The incident laser power was 100 mW and 10 data were acquired from each point with acquisition time of 0.5 s each. The recorded Raman spectra were smoothened using a second order Savitzky-Golay

algorithm. The Raw measured spectra were processed to remove background signal followed by baseline correction using range independent background subtraction algorithm (RIA) to obtain zero baseline spectra[7].

Results and Discussion

To explore the feasibility of identification of low concentrations of HSA using DCDRS, the Raman signal were initially acquired from dried drops of aqueous solution of HSA. Characteristic Raman peaks of HSA at 1000, 1330, 1442 1545, 1600 and 1646 cm^{-1} were identified in DCDRS spectra of aqueous HSA to a concentration upto 0.08 mg/ml. Below this concentrations, only peaks at 1442, 1545 cm^{-1} and 1600 were identified upto a concentration of 0.02 mg/ml of HSA (Figure 2).

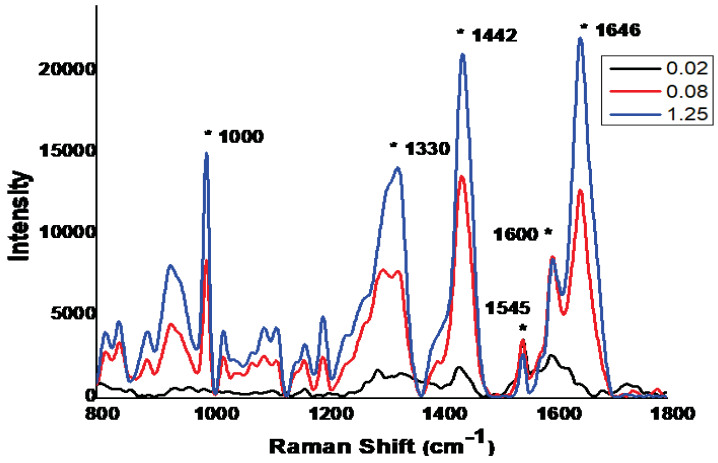

Figure 2: Drop-coated deposition Raman spectra of aqueous human serum albumin (HSA) at different concentrations(0.02 mg/ml, 0.08mg/ml and 1.25 mg/ml) .

Since HSA could be identified at low concentrations from its aqueous solution using DCDRS, further study was done to mimic real situation where DCDRS was explored for detect HSA in artificial urine. It was observed that the DCDRS spectrum of samples in artificial urine is primarily dominated by that of urea and creatinine which are seen to mask the HSA peaks. However, significant differences were noted in average DCDRS spectra in range from 1400 to 1500 cm^{-1} in HSA containing samples as compared to the control artificial urine (Figure 3). HSA specific peak at 1442 cm^{-1} was visible in all HSA containing samples but not in control artificial urine (Figure 3, inset). The band at 1442 cm^{-1} is assigned to CH_2 deformation of HSA. Other distinguishing features were an increase in peak ratio of 1418/1407 cm^{-1} and appearance of peaks at 1458 cm^{-1} in HSA containing samples.

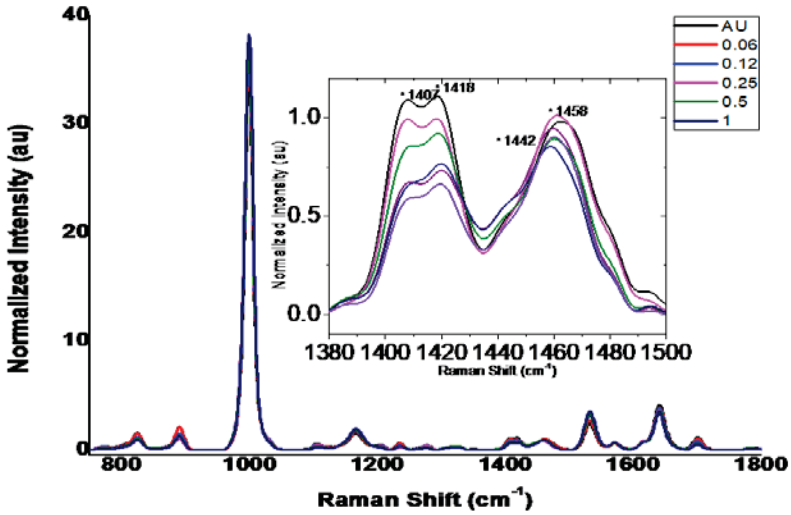

Figure3: Averaged Drop-coating deposition Raman spectra (Mean normalized) of different concentrations of human serum albumin (HSA) (0.06 mg/ml to 1.0 mg/ml) in artificial urine (AU). Inset: Magnified DCDRS spectra in region from 1380 to 1500 cm^{-1}.

The results obtained in this study suggest that DCDRS is a suitable tool for a rapid, reagent free qualitative diagnosis of microalbumiuria at initial stages of condition progression without the need of sample preparation. Details of this study will be presented in the poster.

References

1. J. L. Flores-Guerrero, A. Munoz-Morales, F. Nama-Jimenez, R. Perez-Fuentes, E. Torres-Rasgado, G. Ruiz-Vivanco, N. Gonzalez-Viveros and J. Castro-Ramos, *Diagnostics* **10**, 141 (2020).
2. M. Jayaballa, S. Sood, I. Alahakoon, S. Padmanabhan, N. W. Cheung and V. Lee, *Pregnancy Hypertens*. **5**, 303 (2015).
3. D.E. Busby and G.L. Bakris, *J. Clin.Hypertens.* **6,** 8 (2004).
4. A. Stefancu, V. Moisoiu, C. Bocsa, Z. Balint, D.T. Cosma, I. A. veresiu, V. Chis, N. Leopold and F. Elec, *Analyst,* **143,** 5372 (2018).
5. N. Chamuah, A. Saikia, A. M. Joseph and P. Nath, *Sens. Actuators B Chem.* **285**, 108 (2019)
6. S. B. Dutta, H. Krishna, K. M. Khan, R. Shrivastava, K. Sahu, S. Gupta and S. K Majumder , *Laser Phys.* **30**, 085602(2020)
7. H. Krishna, S. K. Majumder and P.K. Gupta, *J. Raman Spectrosc*. **43**, 1884 (2012)

Studies on photo stability of laser dye Rhodamine 110 (Rh 110) in aqueous binary solvents

Ayentika Sen, A. Wahid, A. Singh, Asawari D. Rath, S. Kundu*
[1]*TLS, ATLA Facility, BTDG, BARC, Mumbai-400085*
Email: ayentika_aug@yahoo.in

Abstract : Aqueous solvent based dye lasers offer significant enhancement in laser output stability as well as improved safety considerations involved in handling large volumes of dye solutions owing to the non-toxic, non-flammable and eco-friendly nature of water compared to conventional organic solvents. However, formation of non-emissive aggregates limits the utilisation of water as solvent for many Rhodamine class dyes including Rh 110. In this paper, studies on photo physical properties of Rh 110 along with the narrowband laser performance & photo-chemical stability in water-based binary solvent with high repitition rate Copper vapour laser (CVL) as pumping laser are presented.

Introduction:

Dye lasers are widely used as unique source of tunable laser radiation. Due to high conversion efficiency, continuous wavelength tunability & possibility to generate narrow-band laser (down to few tens of MHz), it is an indispensable tool for many applications in the field of physics, astronomy, spectroscopy, laser-based isotope separation techniques[1], medicine[2] etc. In laser-based isotope separation techniques, selective excitation & ionization of desired isotope has been targeted by using pulsed DL's with high peak powers at high pulse repetition rate (PRR~ multi-kHz). The choice of the dye as well as the solvent becomes very crucial for sustainable, efficient and long-term operation of such high-repetition-rate dye laser systems.

Laser based enrichment of ^{176}Yb has been demonstrated in BARC to produce the starting material for ^{177}Lu production in nuclear reactor. The radioisotope ^{177}Lu is known for its varied applications in cancer therapy. In order to use the reported ionization scheme[3] for selective photoionization of ^{176}Yb, Rh 110 is chosen as a potential candidate. Our results show that Rh 110 has a) good absorption cross-section (GSA) at the available pump wavelength of 511 nm and b) good photochemical stability so as to avoid the need for frequent replacement/replenishment of dye solution.

The need for a water-based dye laser system has arisen due to certain advantages of water over conventional organic solvents. Water is non-flammable, eco-friendly and does not require any special methods for disposal unlike organic solvents. Besides, its use as solvent offers better laser output stability owing to its superior thermo-optic properties compared to organic solvents[4]. Despite these advantages the use of water as a medium for dye lasers is limited by the low solubility of the organic dye molecules in aqueous media which increases their tendency to form aggregates which are usually known to be non-emissive in nature and thus reduce the lasing efficiency of the dye laser drastically. To circumvent this problem, we used water based binary solvents

e.g. n-propanol and ethanol in water and studied the performance of Rh 110 in terms of its lasing efficiency and photostability. To the best of our knowledge, this is the first report on the use of a binary solvent for development of Rh 110 based dye laser system.

Materials and methods:

Ethanol, n-propanol (HPLC grade) and Rh 110 as its chloride salt were procured from Sigma-Aldrich and used as received. Absorption and emission spectra of the samples were recorded by Thermo Fischer Scientific spectrophotometer and Fluoromax4 spectrofluorimeter (Make: Horiba) respectively. Lifetimes of the dye in different solvents were measured using a time-correlated single photon counting (TCSPC) based instrument from IBH, UK. To obtain the quantum yield of photo-degradation, experiments were performed using the green component (511nm) of CVL (PRR 6.25 kHz). The pump laser was focused by a lens onto the dye solution of appropriate concentration to ensure complete absorption of incident laser energy by the dye solution in the entire period of exposure (~1 hour). The number of photo-degraded dye molecules in the exposed volume of the dye solutions was quantitatively estimated from the measured absorbance, before and after exposure of pump beam using an absorption spectrophotometer.

Results and Discussions:

Absorption and Fluorescence measurements:

The absorption spectra of the dye in different solvent combinations are shown in Figure 1. As can be observed the absorption maxima undergoes a slight blue shift in wavelength with increase in polarity of the solvent. This may be due to the presence of a zwitterion in the ground state. Zwitterionic[5] dyes are reported to exhibit negative solvatochromism due to decrease in dipole moment in the excited state. The fluorescence spectra of Rh 110 are also presented in different solvents as depicted in Figure 2. The inset shows that fluorescence intensity increases with percentage of n-propanol and becomes saturated at ~20% n-propanol-water combination. The quantum yield of fluorescence as well as Stokes' shifts in different solvents are tabulated in Table 1. The average lifetime values of the dye in different solvents were determined by exponential fitting of the decay traces (Figure 3) and are mentioned in Table 1.

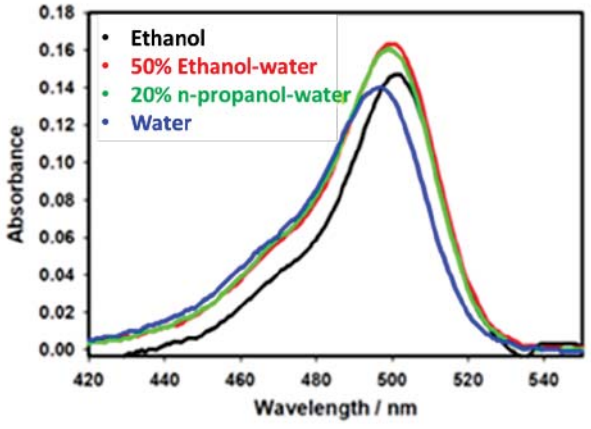

Figure 1. *Absorption spectra of Rh 110 in different solvents*

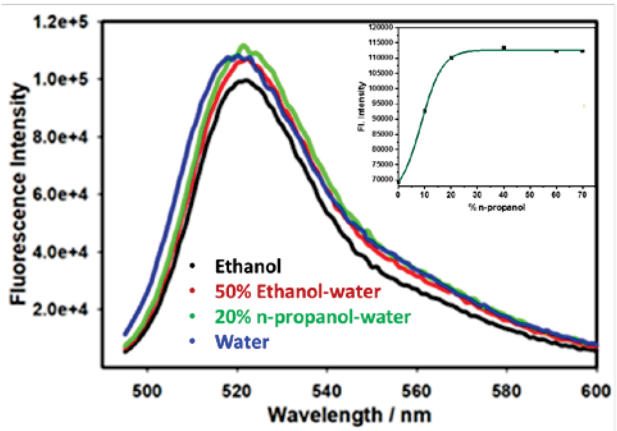

Figure 2. *Fluorescence spectra of Rh 110 in different solvents*

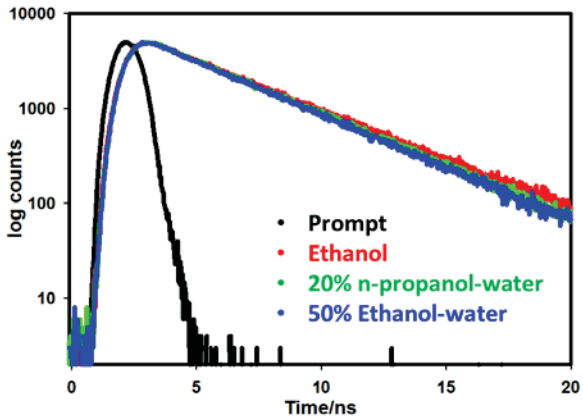

Figure 3. *Fluorescence decay curves of Rh 110 in different solvents*

Dye laser performance:

1. Efficiency of narrow band dye laser oscillator:

A narrow band dye laser oscillator, pumped by a copper vapour laser, was set up in a grazing-incidence-grating (GIG) configuration. The green (at 511 nm) and yellow (at 578 nm) components of CVL were separated by a dichroic mirror and the green component was used for pumping Rh 110 dye laser oscillator. The tuning curve of the dye was obtained by scanning of the wavelength of the dye laser through the gain profile of the dye and subsequently measuring the average pump and dye laser powers with power meter. The tuning curve is presented in Figure 4. Rh 110 is reported to exhibit lasing peak efficiency of 9% in methanol[6]. Our result indicates marginal increase in peak efficiency (~ 11%).

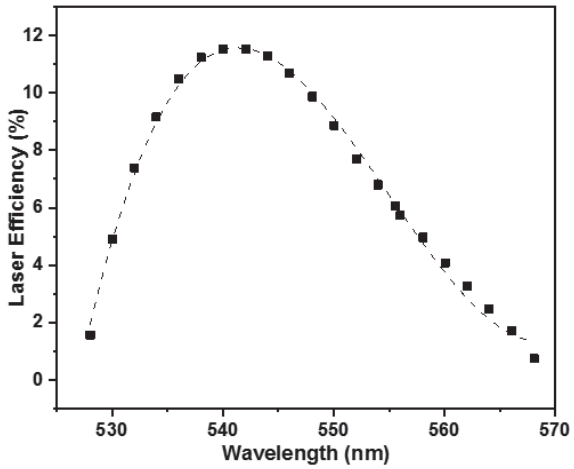

Figure 4. *Tuning curve of Rh 110 in 20% n-propanol-water (Pump Power: 6.2 W)*

2. Photo-stability studies:

Our studies on photostability of Rh 110 revealed its photo degradation quantum yield in 50% ethanol-water solution and 20% n-propanol-water solution to be $2.515 * 10^{-5}$ and $7.8 * 10^{-6}$ respectively. These results clearly indicated better photostability of Rh 110 in water-20% n-propanol solution. Rh 6G, a well-known laser dye belonging to the same class of compounds as Rh 110, is reported to exhibit the value of quantum yield of photo-

degradation as 8.5 * 10^{-6} in ethanol solution[7]. Our results show that a comparable photo-stability of Rh 110 could be achieved in 20% n-propanol solution. A more efficient solute-solvent interaction due to suitable polarity of the medium could probably be the reason for higher photo-stability of the dye in a binary mixture of water-n-propanol compared to that in ethanol-water solution.

Table 1. *Table showing different parameters of photo physical properties of Rh 110 in different solvents*

Dye	Solvent	Abs max (nm)	Fluorescence max (nm)	Ω_{abs}($cm^{2)}$ at 510.6 nm	Fluorescence quantum yield	Lifetime (ns)	Stokes shift (nm)
Rh 110	Ethanol	501	522	1.6 *10^{-16}	0.87	4.2	21
	50% EtOH-water	500	522	1.5 *10^{-16}	0.81	3.9	22
	20% n-prop-water	499	521	1.4 *10^{-16}	0.84	3.9	22
	Water	496	516	1.2 *10-16	0.83	4.1	20

Conclusion:

In conclusion, the results of this study clearly indicate higher photo-stability of the dye in n-propanol-water solvent compared to ethanol-water. The photo physical properties of the dye were investigated and are reported herein. Hence, a water-based binary solvent was used and an efficient and stable narrow band laser operation could be achieved.

References:

1. C. E. Webb, *High-Power Dye Lasers Pumped by Copper Vapor Lasers* **65,** 177 (1991)
2. A. Armenakas and Macrene*, Clinics in dermatology* **24**, 16 (2006)
3. H. Park, D. Kwon, Y. Cha, S. Nam, T. Kim, J. Han, Y. Rhee, D. Jeong and C. Kim, *J. Kor. Phys. Soc*. **49**, 382 (2006)
4. A. K. Ray, S. Sinha, S. Kundu, S. Kumar and K. Dasgupta, *Appl. Phys. B* **87**, 489 (2007)
5. F. L. Arbeloa,T.L. Arbeloa, I. L. Arbeloa,I. Garcı´aMoreno, A. Costela, R Sastre and F. Amat-Guerri, *Chem. Phys*. **236**, 331 (1998)
6. U. Brackmann, *Lamdachrome Laser grade dyes* **1,** III-113 (1986)
7. A. K. Ray, S. Kundu, S. Kumar, C. S. Rao, S. Mula, S. Sinha and K. Dasgupta, *Appl. Phys. B* **87**, 483 (2007)

Evaluation of an indigenously developed Ultraviolet-C light based wide area disinfection device for inactivation of SARS-CoV-2 virus and pathogenic bacteria

Khageswar Sahu[1], Vijay Kumar[1], M Aswin Kumar[2], Madhuri Taranikanti[2], Srinivas M[2], Shankar V. Nakhe[1] and Shovan Kumar Majumder[1,3]

[1] *Laser Group, Raja Ramanna Centre for Advanced Technology, Indore*

[2] *Employee State Insurance Corporation Medical College, Hyderabad*

[3] *Homi Bhaba National Institute, Training School Complex, Anushakti Nagar, Mumbai*

Email:khageswar@rrcat.gov.in,khageswar80@gmail.com

Abstract

We report the results of a study carried out to evaluate the efficacy of an indigenously developed wide area pathogen disinfection system emitting ultraviolet C (UV-C) for inactivation of severe acute respiratory syndrome corona virus-2 (SARS-CoV-2) virus and two pathogenic strains of bacteria, spread on inorganic surfaces. Real time polymerase chain reaction analyses of the swabs obtained from the virus-contaminated inorganic substrates exposed to UV-C emitted by the device, show increased cycle threshold value > 38 for the virus marker genes. Further, colony forming units assay of bacteria spread on plastic surface and exposed to UV-C show ~2.8 log survival loss. These results suggest inactivation of the SARS CoV-2 and bacteria spread on inorganic surfaces by the UV-C based wide area disinfection device.

Introduction

The pandemic corona virus disease -2019 (COVID-19) caused by severe acute respiratory syndrome corona virus-2 (SARS-CoV-2) has now spread to more than 190 countries. It is now clear that apart from the direct route of transmission resulting from inhalation of nasal and oral droplets produced during sneezing and coughing, contact routes through the fomites play important role in the transmission of COVID-19, as the causative virus. SARS-CoV-2 can persist on inanimate surfaces for long duration[1,2]. Hence, much importance has been attributed to prevention of COVID-19 transmission through environmental surface decontamination. Ultraviolet-C (UV-C) is an easily deployable and safer approach for inactivation of a wide range of microorganisms including corona viruses such as SARS-CoV-1[2-6].Hence, use of UV-C has attracted much interest for inactivation of SARS-CoV-2. In fact, recently the susceptibility of SARS-CoV-2 suspended in liquid medium to UV-C has been demonstrated[2]. However,efficacy of UV-C for inactivation of SARS-CoV-2 persistent on environmental surface has not been determined. Recently, we have developed a tower based wide area disinfection device which emits UV-C. In this paper, we report the efficacy of this wide area pathogen disinfection system for inactivation of SARS-CoV-2 spread on inorganic surfaces. In addition, the efficacy of the device for inactivation of two bacteria responsible for wide spread nosocomial infections worldwide, namely; *Pseudomonas aeruginosa* and Methicilin resistant *Staphylococcus aureus* (MRSA) has been evaluated to establish the utility of the device as a general disinfection device.

Materials and Methods

This study was conducted in a BSL-3 level facility associated with Employees State Insurance Corporation of India Medical College, Hyderabad,India. Swab samples of COVID-19 subjects suspended in viral transport

medium (VTM) with a known cycle threshold value (Ct) of 22-24 were used for validating efficacy of the indigenously developed wide area disinfection device; Neel Bhasmi. The device consists of a central tower fitted with 4 arms and a knob for height adjustment (figure 1 A). Each arm hosts 2 UV-C tubes (TUV 30, Philips) emitting 254 nm light. The device has inbuilt motion sensor which avoids unwanted exposure and a timer to ensure the time of exposure without manual intervention. To demarcate the effective area of illumination, the tower was set at 6 ft and all the four arms were spread out in horizontal direction with all the four UV tubes held in side-by-side orientation. The measured power density at 4 , 8 and 10 ft radial distance from the source were ~ 82.6, 13 and 6 $\mu W/cm^2$, respectively (figure 1 B). Also, for the tower height set at 6/7 ft and at a radial distance upto 8 ft, the power density on the floor and at different heights (1-5 ft) does not vary appreciably. For the virus inactivation study, a fixed volume of the VTM were smeared on a 10 mm circular spot on glass slides, sterile clothes, papers and plastics (figure 2). These samples were placed at different distances (4/8/10 ft) from the UV-C irradiation tower either on the floor or at a height of 3.5-6 ft above ground. After an exposure time of 90 min, the irradiated samples were swabbed, processed for RNA extraction, and RTPCR analysis. Following RTPCR analysis, the Ct values for the target sequences for two markers; ORF 1ab protein, and the E protein genes of the SARS-CoV-2 genome were enumerated. To ascertain the effect of UV-C, a negative result was confirmed only if Ct values were >38 in case of both the marker genes.

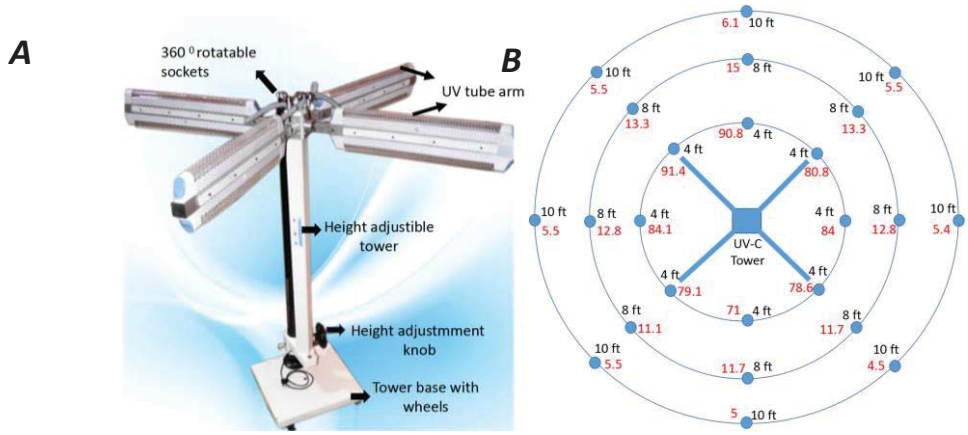

Figure 1: *(A) The tower based wide area sanitization device.(B): Radial distance dependent power density variation for Neel Bhasmi.The tower (blue square;centre) was set at 6 ft and all the four arms (solid blue lines) were spread horizontally with the UV tubes held in side-by-side orientation. The power density at each position (blue circle) is represented in red numerics.*

For bacteria inactivation studies, MRSA (ATCC 43300) and *P.aeruginosa* PA01 (MTCC 3541, IMTECH, Chandigarh, India) were cultured in tryptone soya broth (TSB). The bacterial suspensions in exponential phase were diluted to obtain ~10^7 or 10^6 colony forming units / ml. The bacteria suspended in sterile phosphate buffered saline were spread on sterile, polystyrene petridish (diameter:35 mm) and the petridishes without lids were placed at a distance of 8.5 ft from the central tower of the Neel Bhasmi, with tower height set at 6ft . The exposure time was set for 30 min to achieve a fluence of ~20 mJ/cm^2. Following UV-C irradiation, the bacteria suspensions were suitably diluted, plated on TSB plates and incubated for 24 h at 37^0C. The colony forming

units (CFU) for untreated control (C) and UV-C irradiated (U) groups were counted and the CFU per unit volume (CFU/ml) was enumerated. Reduction in CFU was calculated as follows:

Percent reduction = [C-U] / [C] x 100

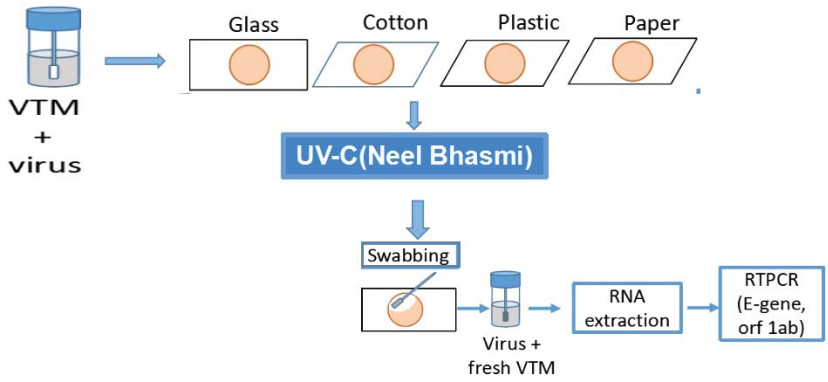

Figure 2: *Schematic of the experimental protocols used for UV-C mediated inactivation of SARS-CoV-2 spread on inorganic substrates.VTM : Virus transport medium. E-gene : Nucleocapsid gene. ORF 1ab: Open reading frame 1ab.*

Sample groups	Rate of negatives (Ct > 38 for E-gene & ORF 1ab)
Unirradiated control (n= 6)	6/6 (~100 %)
UV-C ~29 mJ/cm^2 (n = 6)	5/6 (~83 %)
UV-C ~68 mJ/cm^2(n = 4)	4/4(~100 %)
UV-C ~ 440 mJ/cm^2(n = 5)	5/5 (~100 %)

Table 1: *Efficacy of the wide area disinfection device for inactivation of SARS-CoV-2. Effect of UV-C emitted by the device on E-gene and ORF 1ab expression of oral swabs of COVID-19 subjects suspended in VTMs and spread on inorganic surfaces. Samples with Ct>38 for both the genes were termed as negative. Number of samples (n) and percentage (%) of double negatives are denoted in parentheses.*

Results and discussion

In this study, the VTMs containing SARS-CoV-2 were smeared on four different types of materials (glass, plastic,paper and cloth). These virus contaminated samples were placed at different distance from the central tower of the device and exposed to the three different UV-C fluence. Results show that, in all but one of the samples subjected to UV-C, Ct values are > 38 for both the marker genes analyzed (table 1). Hence, the percentage double negatives in all the UV-C treated samples are nearly > 95 %.These results suggest that damage to the virus spread on inorganic surface seems to have occurred with ≥ 29 mJ/cm^2.Further, the results of our microbiological assay (table 2) show ~2.8-3 log magnitude of inactivation for *P.aerugniosa* and MRSA. Since 3-log$_{10}$ (99.9%) inactivation of bacteria can be reasoned to be sufficiently therapeutic fraction, the results presented in this study also indicate the antibacterial effectiveness of this UV-C based wide area disinfection device.

Sample group	Survival loss (log_{10}) with respect to unirradiated control	
	MRSA	*P.aeruginosa*
UV-C ~20 mJ/cm^2 (n = 9)	~2.8 (p<0.05)	~3 (p<0.05)

Table 2: *Efficacy of the wide area disinfection device emitting UV-C for inactivation of MRSA and P. aeruginosa spread on plastic petridish. The bacteria samples were exposed to a fixed UV-C fluence of ~20 mJ/cm^2 by placing the petridish without lids on floor at 8.5 ft distance from the Neel Bhasmi tower . Number of samples (n) and p-value of student's t-test are in parentheses.*

In summary, in this study, the efficacy of the larger area disinfection device emitting UV-C for inactivation of SARS-CoV-2 spread on inorganic surface has been demonstrated. The inactivation of virus kept at distance of ~10 ft from the tower suggest its utility for the wide area disinfection. In addition, the inactivation of MRSA and *P. aeruginosa* smeared on plastic petriplate, caused by the UV-C, suggest the potential of the device to contain spread of infection whereever these two strains represent major threat of infectious disease spread through surface contact .

References :

1. N. Zhu ,D. Zhang , W. Wang , et al, *N Engl J Med*. **382**, 727 (2020)

2. Heilingloh et al. *Am J Infect Control,* **48,**1273(2020).

3. J.H.Yang ,U.I. Wu ,H.M. Tai ,W.H. Sheng. *J Microbiol Immunol Infect*. **52,** 487(2019)

4. A.H.Malayeri et al. *IUVA News,* **18,**4 (2020).

5. B.V. Sarada, R.Vijay, R.Johnson,T. Narasinga Rao,G. Padmanabham.*Trans Indian Natl Acad Eng.* **14**,1*(*2020)

6. C.P.Sabino et al. *J Photochem Photobiol B.* **212**,11999 (2020).

Investigation of Phytochromes Present in the Petals of Different Cultivars of Bougainvillea Flowers by Laser Induced Fluorescence Spectroscopy

Chhavi Baran[1], Rahul Uttam[2], Sweta Sharma[3, 4] and K N Uttam[4]
[1]*Centre for Environmental Science, IIDS, University of Allahabad, Allahabad,*
[2]*Centre for Material Science, IIDS, University of Allahabad, Allahabad,*
[3]*Department of Applied Science and Humanities, Faculty of Engineering and Techniques, Khwaja Moinuddin Chishti Language University, Lucknow*
[4]*Saha's Spectroscopy Laboratory, Department of Physics, University of Allahabad, Allahabad*
Email: chhavi.charvi@gmail.com

Abstract

Bougainvillea is an ornamental flower which has an immense value in landscaping, pharmaceutical and cosmetic industries. The colour of the flowers is a function of plant pigments and therefore it is very essential to identify the pigments present in the flowers using automated cost effective and rapid techniques. The laser induced fluorescence spectroscopy is highly efficient tool for the non-destructive, extraction free, label free, rapid and simultaneous multi compound detection that can be applied for the on-site detection of chemicals and pigments present in the biosamples. The current study aims at investigating the biochemicals present in different cultivars of bougainvillea flowers using laser induced fluorescence. The analysis of the acquired fluorescence reveals that the petals have rich presence of fluorochromes like chlorophyll, carotenoids, flavonoids and anthocyanins. The spectral signatures obtained in this study can be used by the planners and industries for the effective use of bougainvillea flowers for allied purposes.

Introduction

Flowers of bougainvillea serve as the reservoir of naturally occurring chemical compounds and structurally diverse bioactive molecules. The chemicals present in the flowers are important in pharmaceutical industry, cosmetic, food and as raw material for the extraction of dyes [1-3]. The function of biomolecules present in the flowers is characterized by their molecular structures that help in determining the quality of flowers. The extraction of bioactive compounds from the flowers and their quantitative and qualitative estimation is significantly important for exploration of new biomolecules that can be used by pharmaceutical and agrochemical industry directly or can be used as a lead molecule for synthesizing more potent molecules [4, 5]. For revealing information about the structure of phytochemicals, analytical techniques are required that are able to spectrally and spatially resolve bimolecular features at the cellular level with high sensitivity. High performance liquid chromatography (HPLC), thin layer chromatography (TLC), high performance thin layer chromatography (HPTLC), mass spectrometry (MS) are some of the prevalent analytical techniques for the analysis of bioactive compounds present in flowers [3]. Although some of them provide high end information about the constituents of the sample but most of these are limited by the time involving sample extraction procedure that disturbs the structure and configuration of the chemicals from their natural form and hence are generally regarded as destructive, labour consuming and least environment friendly [3].

This situation necessitates the need of exploring such technique that is sensitive, rapid, non-destructive, label-free and eco-friendly. These superior analytical features are readily found in optical spectroscopic technique like laser induced fluorescence [6]. The laser induced fluorescence spectroscopy relies on the detection of the radiation of the emitted photons by the fluorophore upon the absorption of the radiation. This

technique is non-invasive, noncontact, label free and relatively fast and provide information about the chemical composition of sample without the involvement of sample preparation stage. Also it shows high chemical specificity and provides information about a range of molecules simultaneously [8, 9].

Realizing the importance of non-destructive probe in the realm of compound identification, the present study exploits the utility of laser induced fluorescence spectroscopy for the *in situ* analysis of phytochemicals present in different cultivars of bougainvillea flower. For this, three widely grown bougainvillea cultivars (red, pink and pinkish-white) have been collected and their fluorescence spectral signatures have been investigated. The obtained spectral features have been pre-processed and analyzed with multivariate approach. The spectral features obtained are very useful in monitoring the biochemical composition of the samples of plant origin.

Materials and methods

Different cultivars of healthy bougainvillea flowers having red, pink and pinkish-white colour were collected from the Roxburg Botanical Garden of University of Allahabad, Allahabad. The healthy flower samples were sorted and washed with double distilled water and dried at room temperature to remove surface contamination. Then the petals of the flowers samples were used for the biochemical investigation using laser induced fluorescence spectroscopy.

Laser induced fluorescence measurements were performed on the adaxial surface of the petals of the flowers. Fluorescence emission signals from the fluorophore of the flowers were excited with 405 nm, 50 mW violet diode laser (Oxxius CE, model PS-007). For this, petals of the different colour flowers were clamped in sample holder and laser beam was focused on it in right angle geometry. The distance between the laser and the sample was kept 50 cm to avoid any kind of photo-damage. The emitted fluorescence was recorded with the help of 600 μm optical fibre coupled spectrometer (Ava-Soft 3648, Avantee, Netherland) in the spectral region of 400-800 nm at a resolution of 2.3 nm. The obtained data were analyzed with the help of Origin 8.0 software package.

Signal Processing

The obtained spectral features were exported to Origin 8.0 software package and analyzed. The spectra were pre-treated by smoothing in order to remove unwanted signals and denoised the observed signals. Smoothing was performed by Savitzky Goley algorithm using third order polynomial and window of twenty one data points. The broad and undulating background in the spectral features were removed by baseline correction using rectangle method. In order to obtain statistically significant results, 9 floral samples were analysed for each cultivar. From each sample, single spectrum was acquired making a total of 9 spectra per floral sample.

Figure 1: *Acquired optical images of the collected different variety of the bougainvillea flowers.*

Results and discussion

The recorded fluorescence spectrum of the different flower petals of bougainvillea is shown in Figure 1. The fluorescence spectra of pink and red bougainvillea show a strong band at wavelength 677 nm having a shoulder at 730 nm. These bands arises due to the chlorophyll molecules [6, 7]. In the pinkish-white bougainvillea flowers, the chlorophyll band is observed at 684 nm. In pinkish-white, pink and red bougainvillea, the florescence signals at 630, 620 and 614 nm are also observed that denotes the presence of anthocyanins in the floral petals [7]. Anthocyanins are responsible for the beautiful purple, blue and red colour of different fruits, flowers and vegetables and are water soluble compounds belonging to class of flavonoids [3, 8]. They possess antidiabetic, anticancer, anti-inflammatory and anti-microbial effects. They also help in the prevention of cardiovascular diseases [9]. In addition to these bands, emission bands are also observed at 467 and 516 nm in the pinkish-white and red bougainvillea flowers. These bands develop due to carotenoids [6, 7].

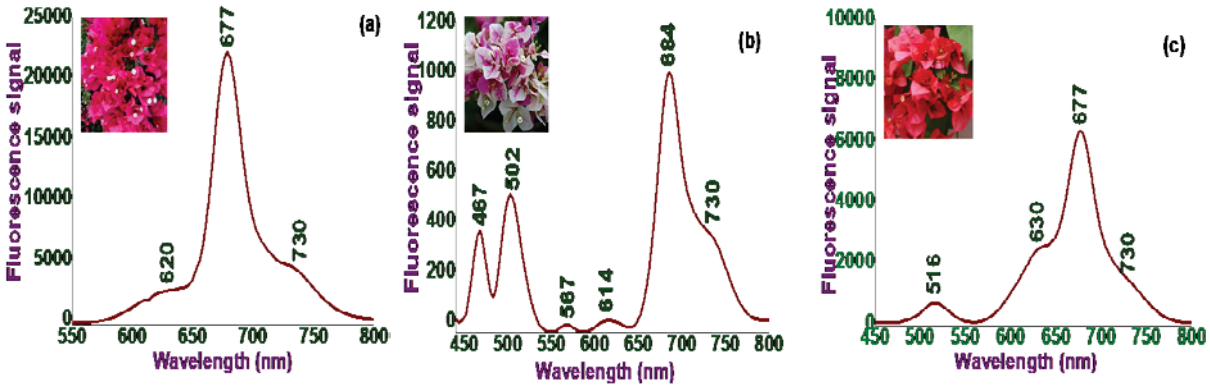

Figure 2: *Recorded laser induced fluorescence spectra of the (a) pink, (b) pinkish-white, and (c) red bougainvillea in the spectral region 400-800 nm.*

The presence of carotenoids in the petals of flower is responsible for beautiful bright yellow, orange and red colour. Carotenoids serve two key roles in plants; they absorb light energy for use in photosynthesis and they protect chlorophyll from photodamage. They have health-promoting effects: immune enhancement and reduction of the risk of developing degenerative diseases such as cancer, cardiovascular diseases, cataract and macular degeneration and plays a dual role in metabolism. Also, carotenoids facilitate plants in photosynthesis by absorbing light energy. Also carotenoids act as antioxidants in the human body and have strong cancer fighting properties. In the pinkish-white bougainvillea, the fluorescence bands at 502 and 567 nm are observed due to the presence of flavonoids [3]. Flavonoids are another class of plant pigments that are found along with the phenolic compounds, and are known to possess antioxidative, anti-inflammatory, anticancerous and anti-mutagenic properties. They also have the capacity to modulate key cellular enzyme functions [8, 9]

References

1. Schulz H, M. Baranska, R. Baranski R. *Biopolymers* 77, 212 (2005).
2. K. H. Eng, A. Azrina, T. S. Teng, L. S. Meng, *Food Nutr Res*. 61, 1361779 (2017).
3. G. Sonja, B. Malgorzata, S. Hartwig, H. Paul, M. Maurizio, *J. Raman Spectrosc.* 42, 1240 (2011).
4. D. K. Sharma, K. R. Shah, R. S. Dave, *Biotech. Res. Comm.* 1, 734, (2018).
5. K. P. Ingle, A. G. Deshmukh, D. A. Padole M.S. Dudhare, M. P. Moharil, V. C. Khelurkar, *Journal of Pharmacognosy and Phytochemistry* 6,32 (2017).
6. S. Sharma, S. Srivastava, R. Singh, K. N. Uttam *Spectroscopy Letters,* 50, 115 (2017).
7. M. N. Merzlyak, T. B. Melo, K. R. Naquvi, *Journal of Experimental Botany.* 59, 349 (2008).
8. T. Yoshikazu, S. Nobuhiro, O. Akemi , *The Plant Journal,* 54,733 (2008).
9. J. F. Reis, V. V. S. Monteiro, R. S. Gomes, M. M. Do-Carmo, G. V. Costa, P. C. Ribera, M. C. Monteiro, *J Transl Med* 14, 315, (2016).

Raman Spectroscopy for Dissolution Testing of Paracetamol Tablets: An Exploratory Study

V. Kumar[1], R. Shrivastava[1], J. Kumawat[1], N. Kumar[1], S. Maru[2] and S. K. Majumder[1, 3]

[1]*Laser Biomedical Applications Division, Raja Ramanna Centre For Advanced Technology, Indore-452013*

[2]*School of Pharmacy and Technology Management, SVKM'S NMIMS, Shirpur-400056*

[3]*Homi Bhabha National Institute (HBNI), Training School Complex, Anushakti Nagar, Mumbai-400094*

E.mail: shkm@rrcat.gov.in

Abstract:

Dissolution testing of a pharmaceutical drug is important to assess the bio-availability and therapeutic effectiveness of the drug. The techniques currently used for measuring dissolution are tedious and time consuming. We report here the results of an exploratory study to evaluate the applicability of Raman spectroscopy for measuring dissolution kinetics of paracetamol, a common pharamceutical drug to treat fever and pain. Paracetamol tablets were made to dissolve in water and Raman spectra were acquired from this aqueous solution at different points in time. The Raman peaks characteristics of paracetamol were observed to show successive increment in their intensities with increasing dissolution of the tablets in water. The results thus demonstrate the potential of Raman spectroscopy for testing dissolution of paracetamol tablets.

Introduction:

Dissolution is defined as the dynamic process by which active pharmaceutical ingredient (API) is transferred from solid dose state (tablet) to solution per unit time [1]. Testing of dissolution of a drug is therefore important to assess the *in-vivo* bio availability of the drug [2, 3]. In pharmaceutical industry the dissolution of drugs is regularly monitored for quality control and maintaining batch to batch consistency of the drugs. The conventional analytical techniques used for dissolution testing are *UV-Vis* spectrophotometry and High Performance Liquid Chromatography (HPLC). While UV measurements are quite sensitive, it lacks selectivity since presence of chromophores other than the API in a multi-component matrix may result in erroneous interpretation. Similarly, HPLC despite being a sensitive technique has several shortcomings. For example, it is time consuming, tedious and also requires pre-processing like filtration of samples prior to analysis.

Raman spectroscopy, essentially a vibrational spectroscopic technique, has garnered a great deal of interest in recent years for rapid pharmaceutical analysis. Basically, it probes the vibrational energy levels of molecules, and specific peaks in the Raman spectrum correspond to particular chemical bonds or bond groups. Since several APIs are known to have sharp and intense Raman bands in comparison with excipients [3], the technique is expected to have potential for measuring dissolution of an API present in a pharmaceutical drug.

We report here the results of an exploratory study carried out to evaluate the applicability of near-infrared (NIR) Raman spectroscopy for measuring dissolution kinetics of paracetamol, a common pharamceutical drug to treat fever and pain.

Materials and Methods

Figure 1 shows the schematic of the experimental set-up for the NIR Raman measurements. The set up uses a 785nm diode laser (Tech 510, Sacher Lasertechnik) for Raman excitation. The output of the laser is collimated by the collimating lens and is passed through the laser clean up filter. The beam then falls on the dichroic mirror which reflects the laser light onto the sample through the microscope objective lens. The backscattered Raman signal is collected by the same objective lens and is passed through the dichroic mirror which transmits the beam to the notch filter to separate the Rayleigh scattered light from the collected output signal. The beam is then passed through another lens which couples it to the Raman spectrograph (Acton SP2300, Princeton Instruments) equipped with a thermoelectrically cooled, back-illuminated, deep depletion CCD camera (PIXES 100,Princeton Instruments).

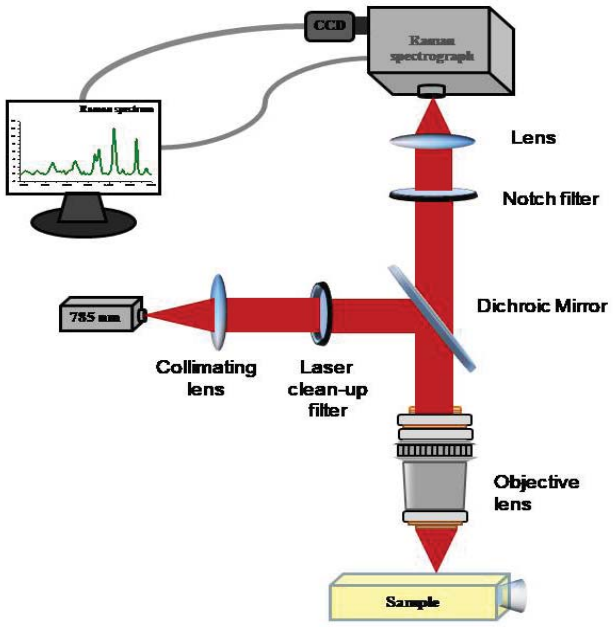

Fig.1: Schematic of the Raman spectroscopy setup

Pure paracetamol (acetaminophen) powder was obtained from Sigma-Aldrich and paracetamol tablets (Calpol 500mg) were obtained from a local pharmacy shop. All solutions were prepared in deionized water. The dissolution of paracetamol tablet was carried out by placing the tablet in 90 ml water in a glass bottle (250 ml) and stirring it at 60 rpm on a heated magnetic stirrer. The temperature of water was maintained at 37 °C throughout the experiment by the heated magnetic stirrer plate with temperature set at 37 °C. Three millilitre water sample was drawn into a quartz cuvette every 10 mins upto 90 mins for Raman spectroscopy measurements. The samples were replaced in the apparatus soon after individual measurements. All Raman measurements were made through lateral side of the sample filled cuvette, placed horizontally under the Raman excitation beam. The optical power delivered on to the sample was 100 mW and the spectra were acquired for an integration time of 30 s.

Results and Discussion

Figure 2, shows the Raman spectra of pure paracetamol powder and its aqueous solution. Paracetamol is a highly Raman active molecule and its Raman spectra shows several dominant peaks[4,5] at 686, 833, 892, 1202, 1267, 1355, 1398, 1587, 1639 and 1672 cm^{-1}. The peak assignment is shown in Table 1. All major peaks of paracetamol can be distinctly observed in the spectra of its aqueous solution except peaks at 1587, 1639 and 1672 cm^{-1}, which are merged with the water Raman peak in the region.

Table: 1

Raman Peaks (cm^{-1})	**Peak assignment**
686	out of plane C-NH deformation
833	C-N-C ring stretching
892	C-N-C ring breathing
1202, 1267	C-C ring stretching
1355	in plane C-NH deformation
1398	C-H deformation
1587	amide II (C-N stretching , N-H bending)
1639	N-H deformation
1672	amide I (C=O stretching)

During the dissolution process, the Raman spectra of dissolution media clearly show dominant characteristic peaks of paracetamol, the intensities of which increase with increasing time (Figure 3a). This suggests progressively increasing dissolution of paracetamol from the tablet. An area under curve plot against the time (Figure 3b) shows complete dissolution of the tablet being achieved at around 70 mins.

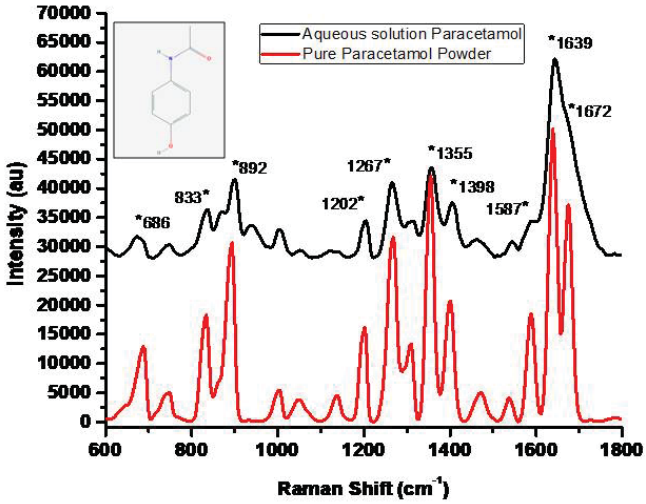

Figure 2: Raman spectra of pure paracetamol powder (red) and aqueous solution (black). Inset: Molecular structure of paracetamol.The spectra are offset for clarity.

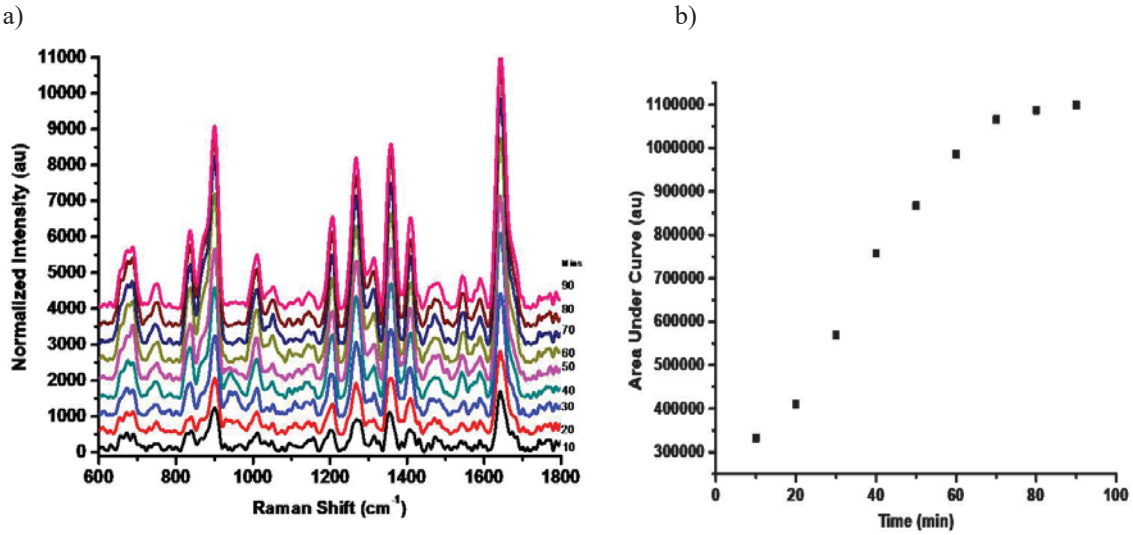

Figure 3:a) Raman spectra of dissolution media (water) at different time points (mins) during dissolution of paracetamol tablet (500mg) in water at 37 °C stirred at 60 rpm. The spectra are offset for clarity. b) Plot of Area under curve of Raman spectra (depicted in 3a) against time of dissolution.

The results thus demonstrate the potential of Raman spectroscopy for testing dissolution of paracetamol tablets. The technique can provide a rapid and sensitive alternative to the current dissolution testing methods with additional advantage of no prior sample preparation. The study shall be extended to study other APIs to elaborate on the scope of this technique in dissolution testing of other important pharmaceuticals.

References:

1) M. N. AlAmeri, N.Nayuni, K.G. AnilKumar, D. Perrett, A. Tucker, A. Johnston, *Results. Pharma Sci.* **2,** 1–8 (2012)

2) S. Alley, *Particle sciences, Drug Development Services, Technical Brief*, **5** (2010)

3) A. Paudel, D. Raijada, J. Rantanen, *Adv. Drug Deli. Rev.* **89**, 3–20 (2015)

4) C. Shende, W. Smith, C. Brouillette, and S. Farquharson, *Pharmaceutics* **6(4)**, 651-662 (2014).

5) A. Luisa, A. Coroian, A. Odagiu, A. Bebu, *ProEnviron.* **11**, 180-186 (2018)

Investigation on rectangular dark pulse in mode-locked fiber laser

Nitish Paul[1,2], C.P. Singh[1,2], P.K. Gupta[1,2], P.K. Mukhopadhyay[1,2] and K.S. Bindra[1,2]

[1]*Laser Technology Division, Raja Ramanna Centre for Advanced Technology, Indore-452013.*

[2]*Homi Bhabha National Institute, Training School Complex, Anushakti Nagar, Mumbai-400094.*

Email: nitishp@ rrcat.gov.in

Abstract: In this work we have analytically shown the existence of rectangular dark pulse using an ansatz in cubic quntic Ginzburg-Landau equation. The study shows the relationship between the pulse parameters and cavity parameters in case of rectangular dark pulse via a free parameter B contained in the ansatz. The variation of the pulse width, depth and output energy with B parameter are studied. Theoretically predicted results are supported by experimental observation in a uniquely designed all fiber linear cavity in all normal dispersion regime.

Research in the field of passively mode locked fiber laser has increased in last three decades because of its potential application in various fields such as tele-communication, micro-machining, sensors, bio-medical etc. Mode-locked laser generates short high intensity optical pulses in the output at a repetition rate governed by the cavity length. Optical pulses contain energy in much shorter time compared to cavity round trip time and there is no energy in between optical pulses, known as bright pulses. In case of dark pulses, an intensity dip in the continuous wave (CW) background is observed. The existence of dark pulse was first predicted theoretically by Hasegawa and Tappert [1] in 1975. After that in 1987 the existence was experimentally demonstrated by Emplit et al. [2]. Since then, a great amount of work had been done on dark pulse because of its captivating properties and advantages over the bright pulses. In optical communication and signal processing the use of the dark pulses has increased as they are less sensitive to the background noise, suffer less broadening during propagation and are less influenced by stimulated Raman scattering in comparison to the conventional bright pulses [3]. Experimentally, dark pulses of inverted bell shaped as well as rectangular profiles have been reported. Inverted bell-shaped pulses were analyzed using tangent hyperbolic function as a solution of non-linear Schrödinger equation (NLSE) or cubic quantic Ginzburg-Landau equation (CQGLE) which are used to model mode-locked fiber lasers. However for analysis of rectangular dark pulses (RDPs) in mode-locked fiber lasers, no function has been proposed so far.

In this paper we present an ansatz to model rectangular dark pulse. The ansatz is based on the ansatz proposed by Renninger et al [4] as a solution of CQGLE which predicts diverse bight pulse profiles including rectangular bright pulse. We have modified the ansatz to investigate rectangular dark pulse and derived relations between pulse and cavity parameters. Passively mode-locked fiber laser in the presence of fiber dispersion, nonlinearity and dissipative process due to the interplay between gain medium and loss in the cavity is modeled by:

$$iA_z - \frac{D}{2}A_{tt} + \gamma|A|^2A = i\sigma A + \frac{i}{\Omega}A_{tt} + i\alpha|A|^2A + i\delta|A|^4A \qquad (1)$$

where A is slowly varying envelope of the electric field, z is propagation coordinate along length of the fiber, t is time measured in the pulse frame, D is net dispersion of the cavity, γ is cumulated cubic nonlinearity in the medium, σ is related to gain or loss in the cavity, Ω represents total filtering effect due to gain medium and band-pass filter used in the cavity, α and δ are the coefficients of cubic and quintic term associated with saturable absorber respectively. The following ansatz has been used to realize RDP:

$$A(z,t) = \sqrt{\left(\Gamma - \frac{P_0}{M}\right) M^{-i\beta}}\; e^{i\theta z} \qquad (2)$$

where $M=\cosh\left(\frac{t}{\tau}\right)+B$ is real for all values of t. τ, P_0 ,β, θ, Γ all are real pulse parameters. Here all the pulse parameters are connected to system parameters $(D, \gamma, \Omega, \alpha, \delta)$ via free parameter B used in the ansatz. Since the number of pulse parameters and system parameters are same therefore the ansatz has a zero co-dimension. Among these five pulse parameters β and θ are dimensionless quantity, τ has the dimension of time, both P_0 and Γ have the dimension of power. To investigate how the pulse profile, evolves with free parameter B for a set of system parameters and to understand the effect of various system parameters on the pulse parameters for a fixed value of B, we have solved for all five pulse parameters in terms of system parameters. Inserting the ansatz in equation (1) and separating real and imaginary parts from the equation we got eight equations where two trivial equations are physically unacceptable. Other six equations are solved to find out pulse parameters. One of these six equations directly gives us the two possible solutions for chirp parameter β, one set of solution with positive chirp and other set with negative chirp. We have discarded the negatively chirped solution to focus on all-normal dispersion (ANDi) set up and the solution is given by $\beta=\frac{\Delta+4}{D\Omega}$, where $\Delta=\sqrt{3D^2\Omega^2+16}$ is a dimensionless parameter derived from the system parameters. After solving other equations we got four coupled algebraic equations involving four pulse parameters namely $\Gamma, P_0, \tau, \theta$

$$P_0=\frac{(B^2-1)}{B}\left[\frac{2\gamma(\Delta+2)}{\delta D\Omega}-\Gamma\right] \qquad (3.a)$$

$$\tau^2=-\frac{1}{\gamma P_0}\frac{(\Delta-4)(\Delta-2)}{12D\Omega^2}\left[B+\frac{\Gamma}{P_0}(B^2-1)\right] \qquad (3.b)$$

$$\Gamma=\frac{\frac{4\Omega\alpha\tau^2}{\Delta-2}+\left(\frac{B}{P_0}\right)\left(\frac{3\Delta+4}{\Delta+4}\right)}{\left[\frac{B^2-1}{P_0^2}-\frac{8\delta\Omega\tau^2}{\Delta-2}\right]} \qquad (3.c)$$

$$\theta=\frac{1}{\tau^2}\left\{\frac{D}{4}\left[\frac{\Delta-2}{\Delta-4}\right]+\Gamma\frac{B}{P_0}\left[\frac{(\Delta-4)(\Delta-3)}{3D\Omega^2}\right]\right\} \qquad (3.d)$$

It may be noted that expressions of P_0, τ, θ shown in equations (3.a), (3.b), (3.d) respectively are void of α whereas expression of Γ shown in equation (3.c) directly depends on α. This suggests that the depth of the dark pulse (depends on the value of Γ) is solely determined by the cubic term of the saturable absorber (α) if other system parameters are kept fixed. On the other hand, for a particular set of system parameters (a, experimental cavity design using NOLM as a saturable absorber and generating dark rectangular pulses) by changing the free parameter B it is possible to get various kind of pulse profiles both in dark and bright domain. Since we had six equations initially, therefore it is possible to solve for another quantity assuming that the energy of the pulse is controllable externally to account for gain in the experiment. Once we determine the values of the pulse parameters for a particular set of system parameters then it is possible to figure out the value of σ:

$$\sigma=-\frac{\Delta(\Delta-2)}{4\Omega\tau^2(\Delta+4)}+\Gamma\frac{B}{P_0}\left(\frac{2\Delta-6}{4\Omega\tau^2}\right) \qquad (4).$$

For dark pulses, $\sigma > 0$ because CW background is always present in the cavity which implies that the saturated gain lies above the

loss line. And to for bright pulse $\sigma < 0$ which is the condition for stability against the CW background in mode-locking process. Therefore, for dark pulse we must choose only those values of pulse parameters for which $\sigma > 0$. Since in this work our main goal is to provide an insight to RDP, we have chosen the value of free parameter B accordingly. In Fig 1. (a) the several RDPs are shown with increasing value of the free parameter B where the depth of the RDP (the difference between CW background and minimum of the pulse) remains constant with increase in the value of B. Width of RDP is 9.5 ps for B=200 which increases to 22.4 ps for B=10^6, where the values of pulse parameter are $P_0 = -7.24 \times 10^7, \Gamma = -73.06, \tau = 0.287, \beta = 0.34$ as shown in figure. In Fig. 1 (b) three quantities namely pulse width, pulse depth and output energy are plotted with -Log(B). The output energy is calculated by integrating the area under CW background curve. Here, output energy is analogous to the output power in an experimental set up. To get spectral information we did Fourier transformation of the pulse profile for B = 10^6 and the spectrum is shown in the Fig. 1 (c). It's a multipeak spectrum with three clearly distinguishable peaks. Experimental cavity which generates RDPs is developed to verify theoretical findings. It is a linear high finesse standing wave type cavity having 80 cm long Yb-doped fiber placed in between two high reflectivity loop mirrors. One loop mirror is based on by joining the output ports of a nearly 50/50 coupler (49.4:50.6) through ~ 1m long fiber segment whereas the other mirror is based on nearly 50/50 coupler (49.1:50.9) with a loop length ~1km. Due to the slight imbalance in splitting ratio of the couplers, the transmission of the loop mirrors become power dependent, however, due to the long loop length of the second loop mirror it predominantly acts as a saturable absorber and assists in mode-locking. To initiate the mode locking process a pair of polarization controller is attached on the fiber of second loop mirror.

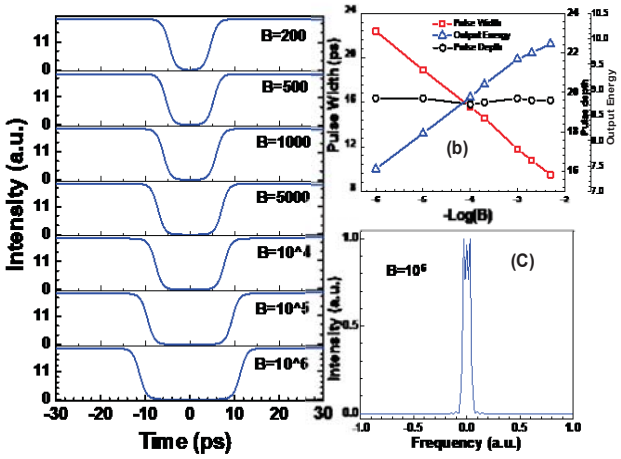

Figure 1. *(a) Variation of the width of RDP with free parameter B (b) Theoretically calculated variation of pulse width, depth and output energy of RDP with -Log(B), (c) Representative spectrum with B value.*

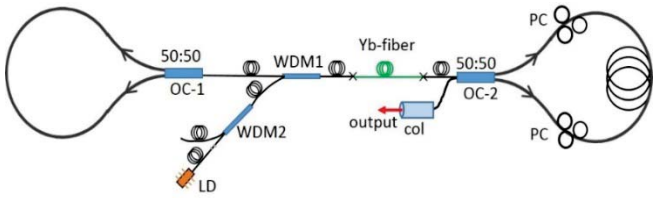

Figure 2. *Schematic of the laser setup.*

At about 58 mW of pump power the laser cavity with loosened PCs starts lasing in CW regime. As the pump power was increased to ~230 mW fluctuations in the output power was observed in the temporal profile on oscilloscope. In this condition, by slightly adjusting the PCs in the cavity stable train of mode-locked pulses with features of dark pulse at ~200 kHz repetition rate is observed. The mode-locked pulse train remains stable up to the pump power of 362 mW. With further increase of pump power, the train of dark pulses vanishes. Pulse train exhibiting dark pulse operation in the cavity at 362 mw pump power is shown in Fig. 3(a) and zoom in view of a single dark pulse is shown in the inset of the figure. Measured radio-frequency spectrum shown in Fig 3 (b) exhibits signal to noise ratio of ~44 dB which is low for a mode-locked lasser indicating that this state of operation is not robust. However we havee seen the cavity remains in this operating regime even for couple of hours.

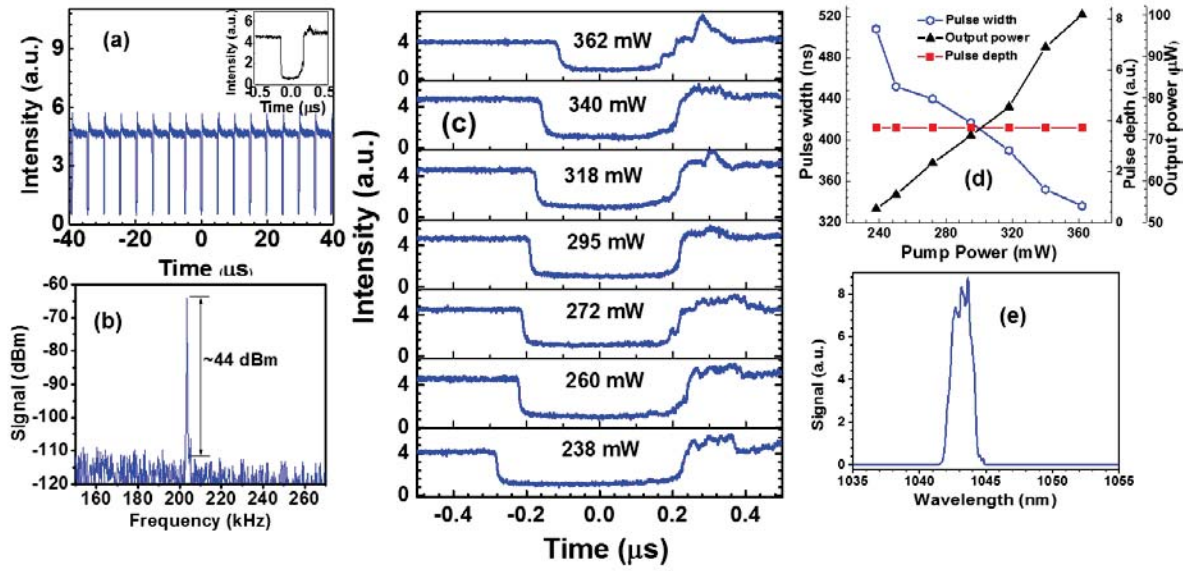

Figure 3. *(a) Oscilloscope traces of RDP train at ~362 mW pump power , inset: expanded view of a single RDP (b) RF spectrum at fundamental repetition rate, (c) oscilloscope traces of RDPs at various pump powers, (d) variation of pulse width, pulse depth and output power with pump power and (e) Spectrum of RDP at a pump power ~362 mW pump power*

Width of the dark rectangular pulse decreases with increase in the pump power as shown in Fig 3 (c). At ~238 mW pump power, the pulse width is ~507 ns with noisy background level. With increase in the pump power to 362 mW width reduces to ~336 ns corresponding to ~ 34% reduction in the pulse width is observed with increase in the pump power. The variation of pulse width, output power and depth of modulation with variation in the pump power is shown in Fig. 3(d). It can be seen that the pulse width (blue open circles) decreases monotonically whereas the pulse-depth (red solid square) remains nearly constant with increase of pump power. Overall the output power (black solid triangle) increases linearly with the pump power. Figure 3(e) shows a representative optical spectrum of the dark pulse. It can be seen that the spectrum is centered at ~1043.2 nm with estimated root mean square (RMS) width of ~2.06 nm.

Theoretically increase in the width of RDP with B value is observed, where increase in B value is analogous to decrease in small signal gain (g_0) achieved by decreasing the pump power experimentally. Further linear relationship between Log B value and g_0 was shown earlier for bright rectangular pulses [5].

In conclusion, investigation of RDP was carried out theoretically by taking an ansatz. Relationship between pulse parameters and cavity parameters is derived by substituting the ansatz in CQGLE. Theoretically predicted results of RDP are supported by experimentally observed results.

References

1. A.Hasegawa and F.Tappert, *Appl. Phys. Lett.,* **23**, 171 (1973).
2. P. Emplit, J. P. Hamaide, F. Reynaud, C. Froehly and A.Barthelemy, *Opt.Commun.* **62**, 374 (1987).
3. W. Zhao and E. Bourkoff, *J. Opt. Soc. Am. B.* **9**, 1134–1144 (1992).
4. W. H. Renninger, A.Chong and F.W. Wise, *Phys. Rev. A* **77,** 023814 (2008).
5. N. Paul, P.K. Gupta, C.P. Singh, P.K. Mukhopadhayay, K.S.Bindra, Rev. Sci. Instrum. **84**, 076107 (2013).

Numerical studies on propagation characteristics of dark pulses in optical fiber

Meghna Mukhopadhyay, Afreen Khursheed and Bhupendra Singh Kirar

Electronics and Communications Engineering Dept., Indian Institute of Information Technology, Bhopal 462003

Email: ec1735.iiitbhopal@gmail.com

Abstract: In this paper we report our studies on propagation characteristics of dark pulses through single mode fiber by numerically solving the nonlinear Schrödinger equation and compared the same with bright pulses with identical pulse parameters. Our studies show that a pair of dark solitons allow more proximity of the pulses and can tolerate higher losses in fiber than the bright counterpart and hence dark solitons are more favourable for high speed long-haul fiber-optic communications systems with high bit rate.

Optical fiber technology provides the fastest and most secure method of transmitting large amounts of data very cheaply. Conventionally, bright optical solitons are preferred in fiber-optic high speed long-haul optical communications systems due to the remarkable stability of soliton pulses during propagation in optical fiber. The bright solitons are formed due to the exact balance of third order nonlinearity known as self phase modulation (SPM) with the anomalous dispersion in silica optical fiber. Bright solitons are the solution of nonlinear Schrödinger equation (NLSE) under anomalous dispersion [1]. However, to maintain the soliton profile the peak power of the pulse needs to be maintained at a certain level depending on the dispersion and nonlinearity of fiber and hence the pulse power must be amplified periodically at certain distances to compensate the losses in fiber. However, the optical amplifier noise affects the timing jitter of optical pulses at the receiving end and eventually deteriorates the transmission characteristic kwon as Gordon-Haus effect [2]. Furthermore, in case of transmission of a plurality of optical soliton pulses carrying digital information, the soliton-soliton interaction also causes the timing jitter at the receiving end limiting the bit rate transmission in the communication system. In contrast to the bright pulses, dark pulses refer to an intensity dip over a continuous wave back ground and solitary dark pulses are formed as the natural solution of NLSE in normal dispersion as a result of balance of SPM with the normal dispersion in fiber[1]. The dark soliton has an advantage over the bright soliton in that it permits reduction of the Gordon-Haus jitter to about 70% and suppression of the soliton interaction without the requirement of any complex instrumentation [3]. Due to this advantage and with the recent progress in generation of dark pulses from fiber oscillators dark solitons are looking attractive for high-capacity long-distance transmission through optical fiber. However, though several reports on propagation characteristics of dark pulse in optical fiber are available in literature [4], the influences of loss and proximity of pair of dark solitons in comparison to bright counterparts are not readily available.

In this paper we report our studies on propagation characteristics of dark pulses through single mode fiber (SMF) by numerically solving the NLSE and compared the same with bright pulses with identical pulse parameters. Our studies show that a pair of dark solitons allow more proximity of the pulses and can tolerate higher losses in fiber than the bright counterpart.

The framework for numerical simulation of pulse propagation through optical fiber is shown in Fig.1(a). It consists of a source of optical pulse and a segment of SMF of length L. At the end of SMF we observe the temporal profile of the input pulse after propagating the fiber. The propagation of an optical pulse through SMF is governed by the Nonlinear Schrödinger Equation (NLSE) given by

$$\frac{\partial A(z,t)}{\partial z} + i\frac{\beta_2}{2}\frac{\partial^2 A(z,t)}{\partial t^2} = -\alpha A(z,t) + i\gamma \mid A(z,t)\mid^2 A(z,t) \qquad (1)$$

where A(z,t) is the slowly varying pulse envelope, z is the propagation coordinate, β_2 is the group velocity dispersion (GVD) parameter, α is the loss coefficient in fiber, γ is the cubic nonlinear coefficient of the fiber: $\gamma = n_2\omega_0 / cA_{eff}$ where n_2 is the coefficient of intensity dependent refractive index of the fiber, ω_0 is the central angular frequency, c is the velocity of light in vacuum and A_{eff} is the effective area of the core of the fiber. In the numerical simulation the input pulse is propagated through SMF by solving Eq. (1) using split-step Fourier method with relevant values of parameters of SMF e.g. β_2 = 23 ps^2/km (for normal dispersion) or -23 ps^2/km (for anomalous dispersion), $n_2 = 2.3\times10^{-20} m^2 W^{-1}$, $A_{eff} = 30\mu m^2$, $\omega_0 = 1.88\times10^{15} s^{-1}$ and $c = 3\times10^8 ms^{-1}$.

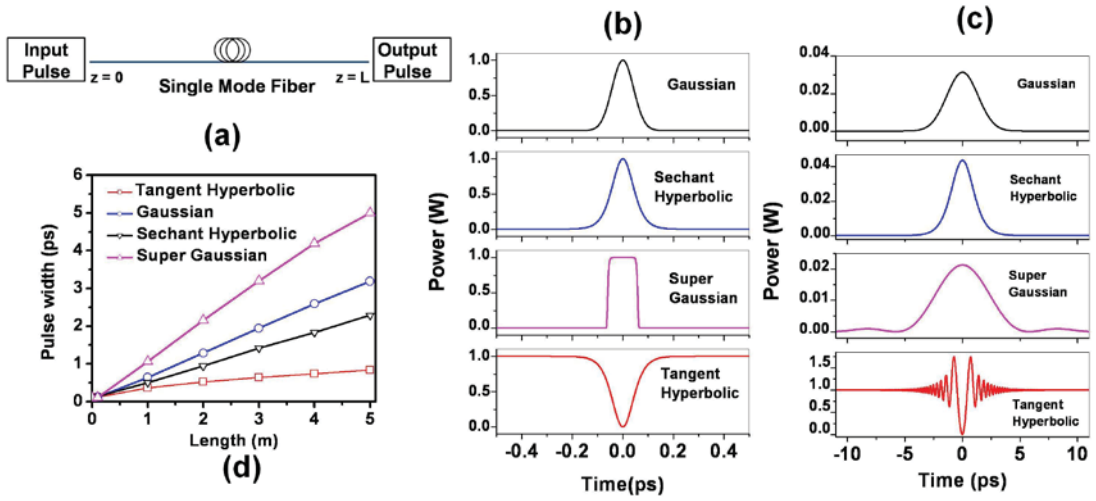

Figure 1: (a) Scheme for numerical simulation (b) input pulse profiles (c) output pulse profiles and (d) Variation of pulse duration (FWHM) with the length L of SMF for different pulse profiles.

The simulation is run for different input pulse profiles as listed in Fig.1(b) like Gaussian pulse with amplitude profile : $A(0,t) = \sqrt{P_0}\,\exp\left[-(t-\tau)^2/2T_0^2\right]$, Secant hyperbolic : $A(0,t) = \sqrt{P_0}\,\mathrm{sech}\left[(t-\tau)/T_0\right]$, Super Gaussian : $A(0,t) = \sqrt{P_0}\,\exp\left[-0.5((t-\tau)/T_0)^{2m}\right]$ and dark pulse: $A(0,t) = \sqrt{P_0}\,\tanh\left[(t-\tau)/T_0\right]$. Here P_0 is the peak power, T_0 is the 1/e width of the intensity profile (true only for Gaussian pulse), τ is a shift in time and m is the order of Super Gaussian pulse (m =10 is used in our simulation). The full width at half maximum (T_{FWHM}) of the pulse can be obtained as $1.665\times T_0$ (Gaussian type pulse) or $1.7627\times T_0$ (Hyperbolic type pulse). The respective pulse profiles after propagating a distance of 5m through the case of lossless SMF with T_{FWHM} = 0.1ps and P_0=1W are shown in Fig.1(c) for normal dispersion only by setting α = 0 and γ = 0. It can be seen the all pulse profiles are broadened due to the GVD in fiber. The computed variation of pulse duration (FWHM) with the propagation distance for different pulse profiles are shown in Fig. 1(d). It can be seen that the pulse broadening is maximum (by a factor of 50) for super Gaussian pulse and least (by a factor of 8) for dark pulses. Further there is no reduction of CW background power for dark pulses showing the advantage of dark pulses for high bit rate data transmission. However, the dark pulse develops oscillations in CW background power with decaying magnitude near the rising and falling edge of the pulse as can be seen

from Fig.1(c) which could be detrimental for high bit rate data transmission. Hence dark pulses only in normal dispersion are not favourable for data transmission.

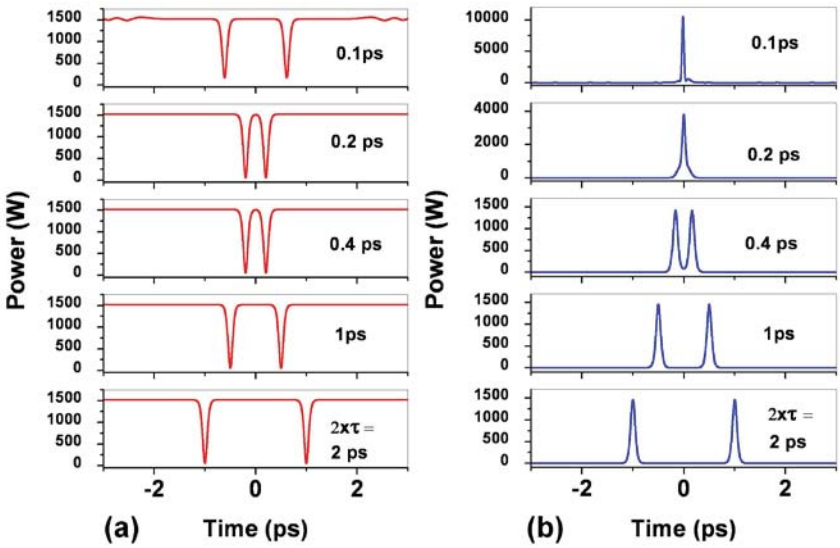

Figure2: Simulated profiles of pair of pulses for different values of initial pulse separation (2τ) through 5 m long lossless SMF (a) dark soliton pair in normal dispersion (b) bright soliton pair in anomalous dispersion.

Next we run the simulation to observe the influence SPM on the dark pulse profile after propagating through 5m long lossless ($\alpha = 0$) SMF under normal GVD ($\beta_2 = 23$ ps^2/km) by incorporating the value of γ in Eq.(1). The strength of nonlinear phase shift due to SPM was increased by increasing the CW background power of the dark pulse. As the CW back ground power (P_0) is increased the pulse is compressed in time and the fluctuation of power near the rise and falling edge of the dark pulse reduces. At a input power level of $P_0 = \beta_2/(\gamma T_0^2) \sim 1520$W the ripples in the CW background vanishes and dark pulse is transformed into fundamental dark soliton with the pulse profile at the exit of the fiber identical to that of the input pulse profile. It may be noted that the secant hyperbolic pulse also transformed into the fundamental bright soliton pulse with the peak power of 1520W under anomalous dispersion ($\beta_2 = -23$ ps^2/km) in the SMF. However, in the context of optical communication one needs to study the propagation characteristics of a train of dark solitons. For that purpose we investigated the propagation of a pair of dark soliton with varying time separation between the pulses. We define a pair of dark soliton by the following equation:

$$A(0,t) = \sqrt{P_0}\,(\tanh[(t-\tau)/T_0] \times \tanh[(t+\tau)/T_0], \text{ for } \tau \neq 0. \qquad (2)$$

Where P_0=1520W, $T_0 = 1.7627 \times T_{FWHM}$ and τ is the shift in time with respect to t=0. The dark soliton pair was propagated through a 5 m long loss less SMF. The simulated output pulse profiles with varying value of τ are shown in Fig. 2(a). It can be seen that the pulse separation is maintained for dark soliton pair during propagation till $2\tau = 0.2$ps and the individual pulses can be easily seen. However, as the pulse separation is reduced further the dark soliton pulses repel each other. It can be seen from the top panel of Fig.2(a) that for an initial pulse separation of 0.1ps, the pulses are repelled to a value of 1.24ps. Simulation shows that a maximum data bit rate of $\sim(2T_0)^{-1}$ can be reliably sent in the form of dark soliton pulses in fiber-optic communication. For comparison we also show the pulse pair profiles for bright solitons of 0.1 ps duration (FWHM) in 5m long SMF under

anomalous dispersion in Fig.2(b). It can be seen that the bright soliton pair are well separated up to an initial pulse separation of 0.4 ps and then as the initial pulse separation is reduced further, bright solitons attract each other and coalesce. Finally we have incorporated the term α in Eq.(1) to observe the influence of fiber loss on the transmitted profiles through the SMF. The simulation results for dark and bright pair of solitons are shown in Fig.3 which shows that the pulse profiles are distorted with increase in fiber loss as the pulses are deviated from the soliton condition due to the reduction of peak power. However, dark solitons are more immune to distortion due to loss than the bright solitons. It can be seen from Fig. 3 that even at high loss ($\alpha = 0.02$ cm^{-1}), the dark soliton pair can be distinctly identified whereas the bright soliton pair is completely merged. Further the attenuation of dark pulses are lesser than the bright pulses which reduces the number of repeaters for long haul transmission which in turn reduces the timing jitter in the pulses.

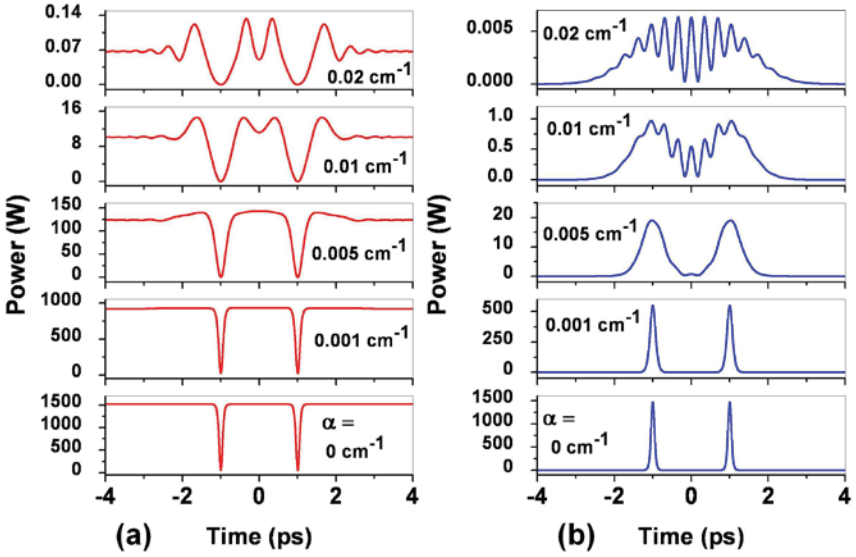

Figure 3: Influence of fiber loss on propagation of pair of pulses (a) dark soliton (b) bright soliton

In conclusion, we have studied the propagation characteristics of dark pulses through single mode fiber by numerically solving the nonlinear Schrödinger equation. The simulation results show that the dark soliton has favourable characteristics for high bit rate transmission through optical fiber as compared to the bright solitons.

References:

1. G.P. Agarwal, Nonlinear Fiber Optics, 3rd ed. Academic Press, San Diego, (2001).

2. J. P. Gordon and H. A. Haus, *Opt. Lett.* **11** (10), 665 (1986)

3. Y. S. Kivshar, *IEEE J. Quantum Electron.* **29**, 250 (1993)

4. W Zhao and E. Bourkoff, *J. Opt. Soc. Am. B* **9**, 1134 (1992)

Intensity referencing in fibre optics based temperature Sensing

V.K. Dubey, P. Saxena, Vivek G., Inderjeet Singh, Jitendra Kumar[1], Om Prakash[1], S.K. Dixit[1], R. Arya, S.V. Nakhe[2], *Laser Electronics Division, RRCAT, Indore*

[1] *Fibre Sensors & Optical Spectroscopy Section, RRCAT;* [2]*Laser Group, RRCAT*

Email: psaxena@rrcat.gov.in

Abstract

Fibre Bragg Grating (FBG) based sensing utilises edge filtering for wavelength to intensity conversion. For a FBG with known Bragg's wavelength (λ_B), a fixed optical band pass filter is employed along with sensitive photo-detection system to achieve a measurable electrical signal output. The linear portion of the characteristics curve of optical filter is used for intensity conversion corresponding to shift in λ_B in response to the varying temperature. The intensity referencing of the single point sensing FBG are validated and relative error due to optical power attenuation of the sensor head because of optical source power fluctuations, variation in remote sensing point distances etc. are compensated. The ratio- metric technique and polynomial curve fitting are used to compute the temperature and minimise errors in measurement due to optical power variation any-where in the system. Developed unit provides the measurement accuracy of ± 1^0C in the range of 25 -500^0C. The same unit with calibration can be used to interface FBGs with different Braggs wavelength.

Introduction

FBG based interrogator system [1] for measurement of temperature uses the shift in λ_B due to temperature variation. The shift in Bragg's wavelength due to variation in temperature is translated into intensity modulated signal using edge filter which is monitored using photodiode. Intensity referencing is used to incorporate ratio metric detection with an aim to minimize the error in measurement due to variation in optical power because of optical source power fluctuations and variation in remote sensing point distances etc. Calculating the ratio of the intensity modulated signal and reference for the temperature range between 25°C to 500°C, a characteristic polynomial is derived. Curve fitting of the acquired data is carried out to compensate the non-liner response of the edge filter. The developed system is successfully tested with C-band FBG at 1552.7 nm and is working as standalone monitor with overall full scale accuracy of ±1°C.

Experimental Setup

The block schematic comprising various optical and electronic components, is shown in figure 1. The optical components are C-Band ASE Source, FBG Sensor with λ_B 1552.7 nm, Optical circulator, Optical Coupler, Edge Filter with central wavelength 1550 nm, and FC/APC patch cords. The electronic components used are Photodetectors, Analog Front End (AFE) and a Data Acquisition System (DAQ) with high resolution ADC. The precision analog front end is developed indigenously using multi-layer PCBs for photo detectors. The printed circuit board is built on FR4 and ceramic base materials along with proper guarding and shielding to ensure ultra-low leakage operation, which is a key requirement in the intensity based FBGs interrogation. Photodiode signal conditioning is implemented using op-amp based trans-resistance amplifier having ultra-low bias current in the fA range. The detectors are used in pair for detecting modulated and reference optical signal for ratio-metric technique.

The C Band source is interfaced to the input port of the optical circulator and at the other port an FBG sensor is connected. Based on the temperature of the FBG, a particular wavelength gets reflected back and is available at the third port of the optical circulator. The reflected wavelength changes with temperature. There is a wavelength shift of approximately 10 pm/^{0}C with temperature.

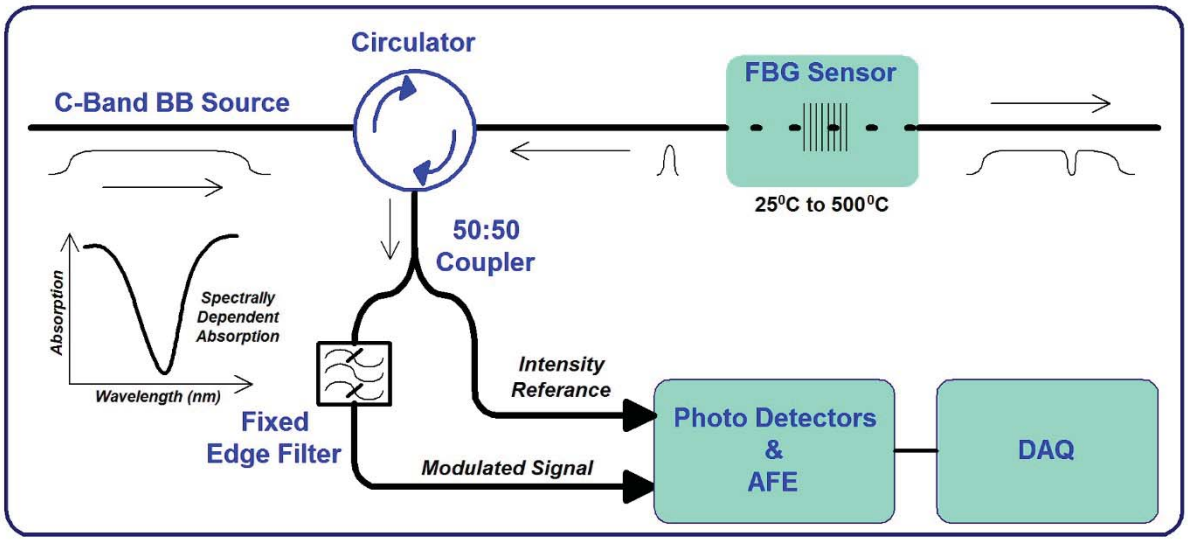

Figure 1. *Block schematic of the ratio-metric temperature measurement system.*

The reflected signal reaching at the third port of the circulator is divided in two parts using 50:50 dividers. One part of the coupler output is passed through an edge filter which provides intensity modulation on the reflected wavelength and then given to the detector. Other output is given directly to the detector. The detector outputs are digitized using 16-bit ADC interfaced with microcontroller board [2].

The FBG sensor is placed in a temperature controlled oven and temperature is varied between 25°C to 500°C in steps and corresponding detector's output signals are digitized. The ratio of the voltages before and after the edge filter is computed using microcontroller throughout the range. Then curve fitting is carried out for the available data points and is implemented and the controller displays the actual temperature. Figure 2 displays the photograph of the system.

Figure 2. *FBG Interrogator system using intensity referencing.*

Results and conclusion

The signals received are tabulated and ratio is calculated. Transfer characteristic of the interrogator system is as depicted in figure 3. The edge filter used has the peak wavelength of 1550 nm and hence falling edge of the edge filter is utilized with FBG at λ_B 1552.7 nm. The curve derived here is analyzed as a 5th order polynomial. The microcontroller receives input as ratio of optical power levels and using this 5th order polynomial, computes and displays the temperature over the range from 25°C to 500°C.

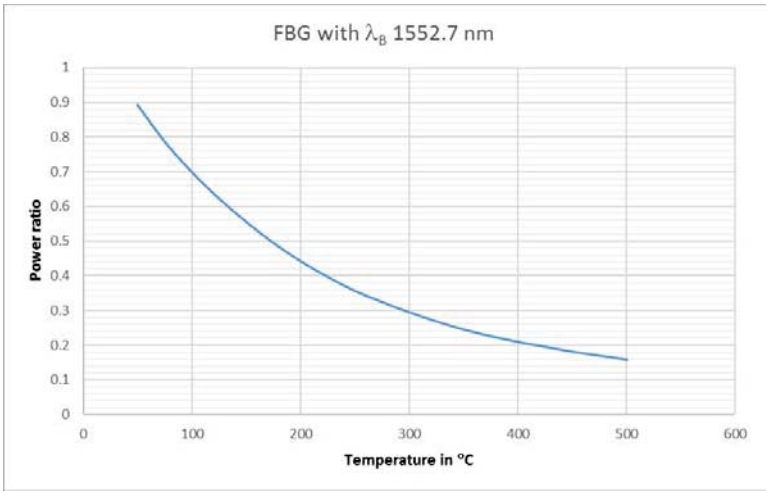

Figure 3. *Transfer characteristic of the Interrogator.*

In this work a low cost and accurate FBGs interrogation system has been designed and demonstrated using edge filtering along with intensity referencing. Temperature quantisation was done using ratio-matric measurement technique to make system immune to optical power fluctuations because of optical source power fluctuations and variation in remote sensing point distances etc. The developed unit is calibrated over the range from 25°C to 500°C with accuracy of ± 1°C.

Authors acknowledge sincere efforts of Shri Dheeraj Shukla in assembly of the unit.

References:

1. Alan D. Kersey, Michael A. Davis, Heather J. Patrick, Michel LeBlanc, K. P. Koo, C. G. Askins, M. A. Putnam, and E. Joseph Friebele, “Fiber Grating Sensors”, Journal of light wave technology, Vol. 15, No. 8, August 1997

2. Sang-Jin Choi, Young-Chon Kim, Minho Song and Jae-Kyung Pan, “A Self-Referencing Intensity-Based Fiber Optic Sensor with Multipoint Sensing Characteristics”, Sensors 2014, 14, 12803-12815; doi:10.3390/s140712803

TRIGGERING AND SYNCHRONISATION OF SPARK GAP SWITCHES USING OPTICAL BEAM DELIVERY SYSTEM

Ritu Agarwal, Amitava Roy, Archana Sharma

Accelerator and Pulse Power Division, Bhabha Atomic Research Centre, Mumbai-400085

Email: ritu@barc.gov.in;aroy@barc.gov.in;arsharma@barc.gov.in

Abstract : Triggered spark gap (SG) switches are one of the most essential components of Pulsed Power Systems. A laser triggered sparkgap (LTSG) system has been developed using Nd:YAG laser of 6-7 ns pulse duration with 19 fiber optic beam delivery system having less than 1 mJ of energy from each fiber. This paper describes the Laser triggering of SG having Laser (532 nm) focused on-axis of electrodes using optical fibers. The experiment was carried out using 0.15 μF/ 50 kV energy storage capacitors, discharged through stainless steel electrode of diameter 68 mm across 10 ohm non inductive load. The initial experiments demonstrated that for electrode gap of 5 mm and self breakdown voltage (SBV) of 16.5 kV, switching range of 16 % was obtained for Laser Pulse energy of 900 μJ. While for SBV of 20 kV, switching range of 12% was obtained at Laser energy of 800 μJ. It was observed that for lower Laser energy switching range reduces drastically. The SG has been tested upto of SBV of 32 kV under pressurized condition. Further studies have been carried out to improve switching range by varying various system parameters.

Key words: Nd:YAG laser, Laser triggered sparkgap (LTSG), Self breakdown voltage (SBV)

Introduction: Pulsed power is a technology that accumulates energy over a relatively long period and releases it into a load within a short time interval, thus generating high instantaneous power. Pulsed power systems are used for Flash X-ray production, high-power microwave generation, charged particle sources, radars, thermo-nuclear fusion reactions, radiation generation etc. The systems for these applications are typically large machines and are operated in a single-shot mode or at a low repetition rate. The synchronized triggering of two or more high voltage switches which should be capable of switching large currents and handling high voltages ranging from few kV's to 100's of kV, is one of the requirement for high performance of system. In this paper, triggering of spark gap switch with Laser[1,2] (532 nm, 7 ns pulse) focussed on-axis of electrodes using optical fibers with less than 1mJ of energy has been described. The triggering is achieved using single Laser pulse of 6-7ns FWHM. Switching time jitter is an important property to consider when selecting a closing switch for a pulsed-power system, and time-precise triggering may be achieved through the use of lasers. For a mid-gap laser-triggered spark gap using an Nd:YAG laser at 532 nm, where the laser pulse is guided via an optical fiber to the spark gap; the laser pulse energy and the applied voltage may be varied with nitrogen as the working gas. One drawback of the current laser triggering technology compared with other triggering techniques is that laser systems are more complex and prone to electromagnetic interference. However, the laser offers an alternative triggering device which is basically safer and simpler to use as it is isolated electrically from the SG.

High voltage switches: Depending on the type of energy storage element used in a pulse generator, closing or opening switches are used for capacitive and inductive energy storage, respectively. Power semiconductor switches like IGBTs, MOSFETs, SCRs can be used but their usage is limited up to a few kilovolts. The spark gap switches are most commonly used due to its advantages of high hold-off voltage, large conducting current, high energy efficiency and low cost. Spark gaps switches can broadly be classified as self-triggered and

triggered SG. Triggering is generally achieved by an external agency in the form of an electron-beam, a LASER beam or by raising the electric field in some part of the gap etc. Electrically triggering is having three electrodes geometry which requires trigger generator to initiate breakdown of SG. But the triggering time and jitter time in trigatron method of triggering is high. Also, parallel triggering of spark gaps through the trigatron method is difficult to achieve due to requirement of trigger voltage at third electrode which causes insulation problem.

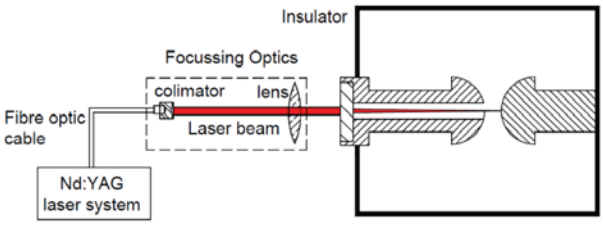

Fig.1: Schematic of Laser Triggered Sparkgap Switch.

In Laser Triggered spark gap switch, Laser can be focused using lens, on-axis[3] or mid-plane point between the electrodes. Fig.1, shows the schematic of laser triggered SG switch having Laser focussed on-axis. When the laser beam is directed at the surface of cathode of SG where the energy from laser causes thermo emission of electrons, and even an explosion of the cathode metal at the surface. In the presence of an electric field, the process develops in the same manner as in the presence of initiating plasma. It is interesting that the delay time of the discharge in the switch practically does not depend on which anode or cathode surface plasma is generated. Triggering of SG using Laser is the fastest way of triggering as compared to other triggering methods.

Design and simulation of LASER triggered spark gap switch: The Fig.2 displays CST EM STUDIO simulation of a laser triggered SG to obtain electric field distribution along cross section of the SG switch. For electrode separation of 4 mm at a potential of 15 kV with air medium, maximum field obtained is 38.87 kV/cm and field at the centre of bottom electrode is 22.79 kV/cm.

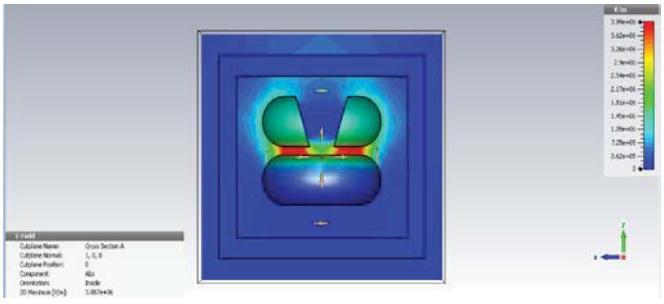

Fig.2 : CST simulation of Laser triggered Spark gap Assembly

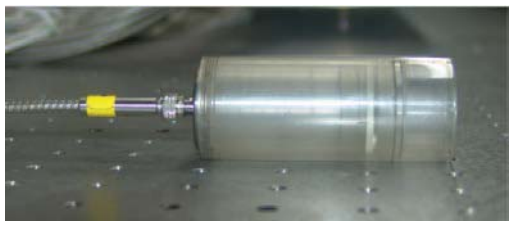

Fig.3: Focussing Optics for LASER beam

The laser beam is transmitted through a multimode 200 µm fiber with N.A=0.26, therefore gets diverged by an angle of 30 deg. Therefore, a collimator setup has been designed containing a convex lens of f_1 = 50 mm such that it made the diverging beam into a parallel beam. Further, the parallel LASER beam was focused at the surface of cathode by a converging lens of f_2 = 50 mm. Fig.3 depicts a typical collimator setup where a laser beam coming out from optical fibre and gets diverged in the air medium by around 30 deg. The collimator

converges the beam into a parallel beam. As the parallel beam passes through convex lens with focal length f_2, it gets converged at the surface of the cathode of the spark gap. This results in excitation of ions at cathode surface along with the ionisation of gas medium. The fibre optic core diameter is 200 µm and focal length of collimator (f_1) and converging lens (f_2) is same, so spot size of the focussed beam is 200 µm.

Experimental setup: A laser triggered SG system has been developed using Nd:YAG laser of 6-7 ns pulse duration with 19 fiber optic beam delivery system having less than 1 mJ of energy from each fiber. Innolas Spitlight 400 LASER setup is capable of producing 400 mJ maximum energy at 1064 nm and 200 mJ maximum energy at 532 nm with 6-7 ns pulse duration. As optical fibres of 532 nm are available, so present Laser system is used at 532 nm for laser triggering. It is having nineteen optical fibres and each fibre provides a maximum of 1 mJ of energy at 532 nm. The optical fibre[4] reduces the complex system of mirrors used to transport the laser beam to the spark gap switches. In order to pressurize the SG, a feed through window was required between focussing arrangement and SG assembly. For that study of percentage absorption of laser energy when passing through different materials (fused silica, glass and perspex) was carried out. It was observed that perspex scatters the laser light, glass absorbs more energy as compared to fused silica for the same thickness. Due to the absorption, the Laser energy further reduces. Hence, focussing lens itself is used as a feedthrough in the above experiments. The power density of laser beam when it hits the electrode is 0.40 GW/cm^2.

Fig.4(a) displays the Laser system and 4(b) shows spark gap switch with focussing optics being pressurized by N_2 gas. For the experimental setup, energy storage capacitors of 0.15 µF/ 50 kV has been discharged through laser triggered SG across non inductive load of 10 Ω. In order to increase the SBV of spark gaps, they were filled with N_2 gas at a pressure of 0.2 kg/cm^2. The pressurized gases follow Streamer theory and Paschen's law where the breakdown occurs at range of nano seconds.

Fig.4(a): Innolas SpitLight 400 LASER setup

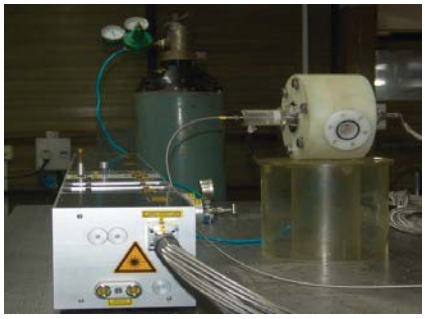

Fig.4(b): SG switch being pressurized by N_2 gas.

Synchronisation of two spark gap switches: Two spark gaps were triggered simultaneously and their synchronisation was measured. Fig. 5(a) shows the schematic for synchronisation of two Laser triggered spark gaps and 5(d) shows the circuit diagram. Fig. 5(c) shows the assembly of sparkgaps along with focussing optics. The gap spacing between the two electrodes was adjusted to 4 mm in each of the sparkgaps, having SBV obtained was 18.4kV and 18.6kV respectively. The collimator and lens assembly was same for both the sparkgaps with lenses having focal length of 5 cm. For jitter measurements, two current shunts of 50 mΩ each are connected across each load. The output discharge waveform of each spark gap was recorded using a 200 MHz Tektronix oscilloscope, capable of measuring jitter up to 1ns.The applied voltage was varied from minimum voltage to self breakdown voltage in step of 0.5 kV and the laser energy per pulse was kept constant at

<1 mJ. Fig.5(b) shows the output waveform for the synchronization of two SG with jitter < 5 ns at a charging voltage of 17.5kV. Further experiments demonstrate that for electrode gap of 5mm and SBV of 16.5 kV, switching range of 16 % was obtained for Laser Pulse energy of 900 µJ. While for SBV of 20 kV, switching range of 12% was obtained at Laser energy of 800 µJ. It was observed that for lower Laser energy switching range reduces drastically. The SG has been tested upto of SBV of 32 kV under pressurized condition.

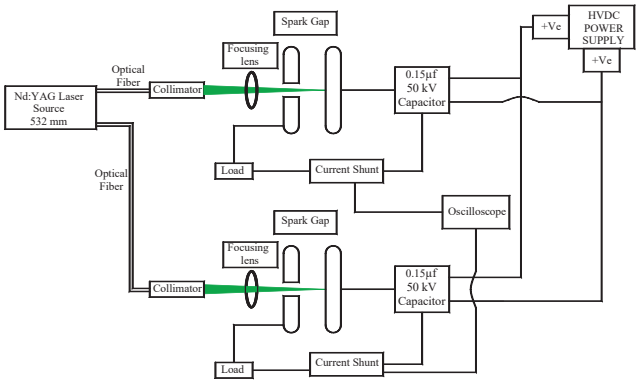

Fig.5(a): Schematic diagram for synchronisation of two Spark Gap switches

Fig.5(b): The output waveform of two switches showing jitter < 5 ns.

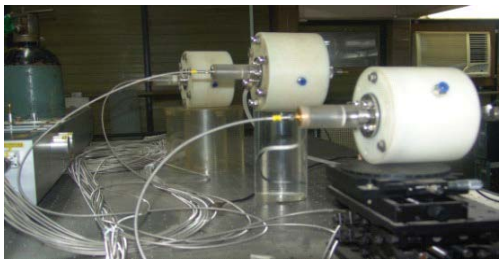

Fig.5(c): Photograph of sparkgaps assembly along with focussing optics

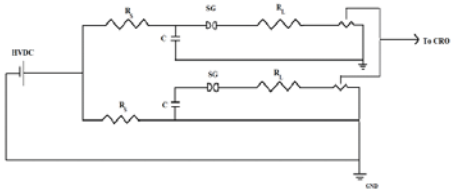

Fig.5(d): Circuit diagram for synchronisation of two spark gap switches

Conclusion: A fiber-delivered LTSG was developed comprising of a Nd:YAG laser connected to 19 optical fibers each carrying a maximum of 1 mJ energy at 532 nm. The synchronization of two SGs at lower voltages with jitter < 5ns has been achieved at laser energy < 1 mJ. The laser optics consists of collimator, optical fibre and convex lens has been used for laser beam focussing. The experiments are under way to improve the switching range and jitter of the SG with an ultimate aim to achieve laser trigger upto 100kV voltage.

References:

[1] S.F. Glover et. al. "Laser triggering of spark gap switches with less than 100µJ's of energy", *16th IEEE International Pulsed Power Conference*, 2007 .

[2] Anders Larsson et. al. "Laser trigerring of spark gap switches", *IEEE transactions on plasma Science*, VOL. 42, October 2014.

[3] O. Frolov et. al. "Gas filled laser triggered spark gap", *Czechoslovak Journal of Physics*, March 2004.

[4] H C Harjes et. al. " Laser triggering through fibre optics of low jitter spark gap". *IEEE transactions on plasma Science*, Volume:8, Sept.1980

Design of optical interface module for fiber delivered DPSSGL beam to pump dye laser amplifier

[1]A. Khattar, [2]A.K. Singh, [2]S. Kundu,

Tunable laser Section, ATLA- Facility, BTDG, BARC, Mumbai – 400085

Email: akhattar@barc.gov.in

Abstract:

The design of optical interface module (pump beam optics) for transversely pumped dyer laser amplifier (DLA) module is presented. The input beam for interface module, 532 nm Nd:YAG @ 6.25 kHz, is delivered by optical fiber . The first scheme employs independent collimation optics module for each optical fiber arranged in angular multiplexed fashion to aim at the dye cell. Its application is however limited to few fibers owing to space constraints. Another design of interface module is considered which enables easier handling of multiple fibers, reduce active alignment burden and reshape the pump laser beam for improved spatial overlap with signal.

Introduction:

Narrowband pulsed dye lasers are widely used tunable lasers for separation of isotopes of industrial, medical and strategic importance. These lasers are deployed in MOPA configuration to generate the process beam. Number of stages for amplification in MOPA is governed by the total power required for the process, seed signal strength from the oscillator, total available pump power and extraction efficiency of an amplifier in each stage. Diode pumped solid state green laser (DPSSGL, Nd:YAG second harmonic) delivered by optical fiber (600 μm, 0.22) [1] at 6.25 kHz is used for pumping of the master amplifier in transverse configuration. Optical interface module (pump beam optics) delivers the output of the optical fiber to the DLA in required dimensions. The exact match of the pump beam shape and size with the signal is essential for maximum efficiency and low amplified spontaneous emission (ASE) generation. Power scaling at this stage can be achieved by pumping with plurality of fibers, arranged in angular multiplexing configuration, from both sides. However, the extent of power scaling with multiple fibers is limited by capability of chosen pumping scheme to effectively concentrate this power into lasing zone of desired dimensions. Therefore, it is desirable to have pumping scheme capable of handling multiple fibers and reshapes the pump beam to create illumination bar which optimally fills the lasing zone.

In this paper two designs of optical interface module are considered. First scheme is simple in approach and utilize independent optics for generation of illumination bar dimension equal to flow channel length (in horizontal direction) for each fiber. The height of the illumination bar is controlled by common cylindrical lens. This scheme has limitation in addressing plurality of fibers due to space constraint in closely placing the independent optics of all the fibers at the operating distance. This limits the maximum no. of fibers to be used from each side. Second scheme takes care of above limitation and utilizes common optics for all the fibers, allowing adjacent placement of the fibers in compact manner. Therefore, this scheme permits use of more fibers in comparison to first one. In addition; this scheme enables homogenization of illumination bar in vertical direction by very nature of its design which helps in imparting better spatial profile to the output signal beam of the amplifier.

Designs for optical interface modules:

Design 1: In this design, DLA is pumped from both sides by DPSSGL beam at 532 nm and 6.25 kHz repetition rate, delivered by step index fibers (core size 600 µm, NA = 0.22) [1] using optical interface modules arranged in angular multiplexed fashion to form a line focus at the dye cell. The combination of collimation optics and focusing lens is designated as optical interface module. The interface module takes light from the fiber and acts in a way to create elongated image of the optical fiber output at the dye cell. As circular fiber face is to be imaged as elongated illumination bar, this scheme utilizes combination of spherical and cylindrical optics to achieve the desired spot size of 10 mm x 1 mm at the dye cell. Each fiber is placed in a V groove holder, as depicted in Fig. 2 which is placed in opto-mechanical mount with necessary tilt and translation control to precisely place the image at the dye cell. This scheme incorporates independent collimation optics module for each fiber and common focusing optics i.e. cylindrical lens as shown in Fig 1(a). The limitation of this scheme comes in handling multiple fibers for pumping DLA module. If multiple fibers are to be used for pumping from one side it can be achieved by increasing the launch angle of the each fiber (and its collimation optics) relative to the normal of the dye cell. However, the use of large angles for multiplexing is limited by the clear aperture of the focusing optics and dye cell holder eventually. Also various angles of fibers results in slightly different spot size at the target plane. Hence maximum launching angle is limited by acceptable tolerance in focused spot size. To avoid larger angles and accommodate more fibers these modules along with the fiber can be placed at longer distances in order to reduce the launching angle. However, this is limited by the available space and spherical aberrations of the focusing optics (as it will receive larger sized beam) placed near the dye cell. Another drawback of this scheme is the requirement of individual collimation optics for each fiber leading to large optics and mounts inventory requirement. As image of each fiber is aligned at the dye cell using individual tilt and translation controls leading to more degree of freedoms to maintain active alignment which could be detrimental in longer durations.

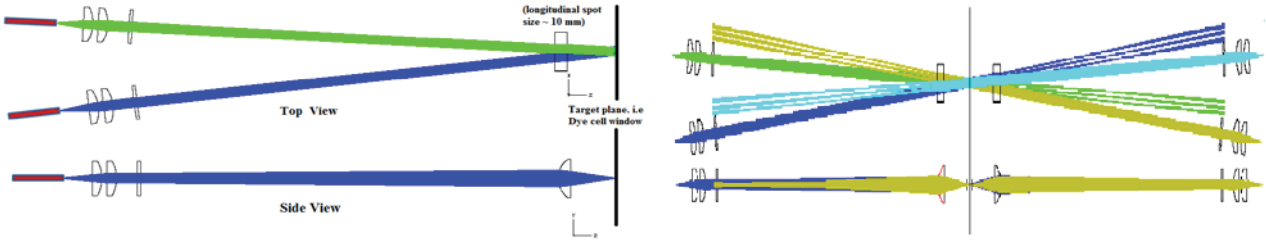

Fig. 1(a) Schematic of the DLA pumping scheme *(b) Schematic of double sided pumping*

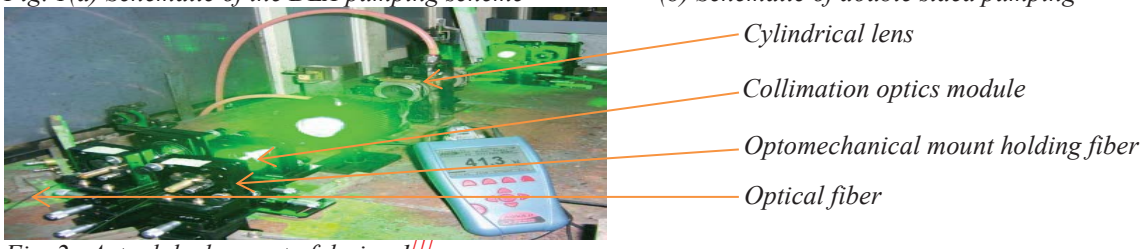

Fig. 2. Actual deployment of design 1[1]

Design 2: This design is modified version of interface module for enhanced transverse energy input in the form of rectangular illumination bar[2]. It makes use of an all spherical optics to create de-magnified image, of the

rectangular pupil created by two closely spaced parallel mirrors called folding bars [3] at the dye cell. The folding bars derives its name from the way it acts on the input beam to homogenize it in the vertical direction (where input beam suffer multiple reflections). The diverging beam from optical fiber is launched into these parallel mirrors which acts as a waveguide and causes beam to remain within the gap which otherwise was diverging. This results in beam homogenization which can be understood by considering diverging beam at the exit gap of the parallel mirrors to be sequentially folded like a piece of paper to fit into the gap. As the beam propagates through these mirrors it suffers reflection only in vertical direction and horizontal direction is allowed to expand which creates rectangular pupil at the exit gap of these mirrors. The beam intensity at this gap is imaged on to dye cell using all spherical relay optics with suitable demagnification to achieve desired spot size (10 mm x 1 mm) at the dye cell. In order to use multiple fibers in this scheme these are again placed in coplanar and angular multiplexed fashion (in X-Z plane) to aim at the common point which in this case is optics immediately following the mirrors. The design of the optics is such it brings rays emerging from all the fibers to a common plane. The number of fibers launched is limited by the geometry of the design but still can accept large numbers as compared to scheme 1 with minimal aberrations.

This scheme is different from one described above in the sense that it doesn't have individual alignment control of the fibers. Fibers must be placed in a coplanar way within a metal plate with their optical axis orientation angle fixed by the hard grooving in the structure. The angle is determined by the optical software simulation so as to direct beam from all the fibers at the dye cell and overlapping. The structural angles eliminate the requirement of individual tilt and translation control of the fiber and they can be placed in very close proximity. Overall five to six fibers can be easily placed in the design (X-Z plane) within a space of 10 mm in the plate with fixed angles with maximum angle being 8 degree relative to central fiber. However to further increase the number of fibers optics following the mirrors can be suitably designed for acceptance and spot size generation within required range. As can be seen that overall optical loss each beam suffers is more in this scheme. However the scheme is capable of delivering higher pump power into DLA module using multiple fibers owing completely to the advanced design and the way it operates on the rays in both directions.

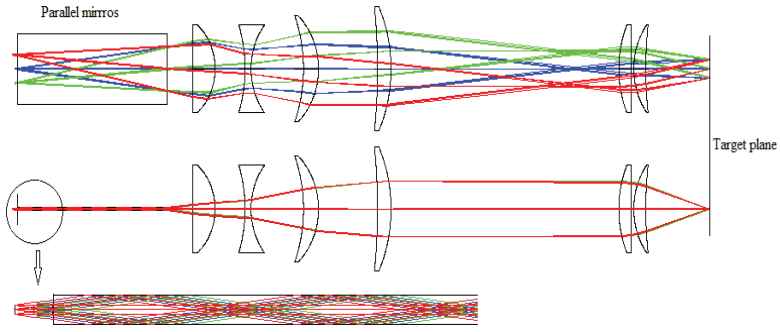

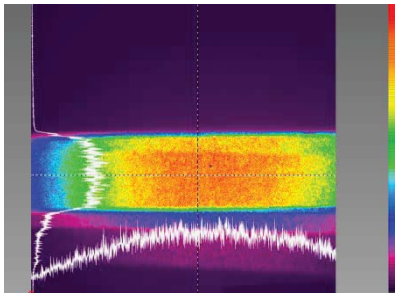

Fig 3. (a) Schematic of the design 2 with Top and side view in vertical direction with parallel mirrors i.e. folding bars. (b) Beam homogenization achieved

Simulation & Results: The optical fiber used for the schemes is large core multimode fiber, with fused silica core, of size 600 µm and Numerical aperture (NA) 0.22. The spot size obtained in two pumping schemes is evaluated using ray propagation calculations available in optical simulation software. Optical fiber is simulated by considering different points on periphery of the core as the individual point sources of NA 0.12 as it is the

exit beam NA from the fiber. It is also assumed all point sources emit light in cones which are parallel to each other. This is incorporated by using telecentric object space.

Design 1 beam size results:

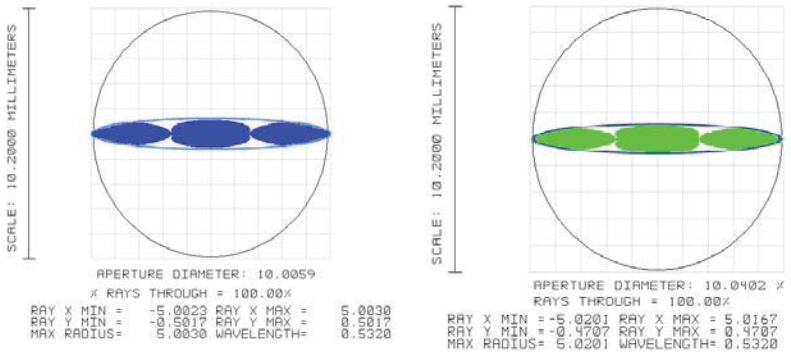

All dimensions in footprint diagram are in mm and wavelength in microns. Here smaller ellipse corresponds to different points on the fiber used for simulation. Total beam size is arrived at by considering the maximum and minimum value of the ray position in each direction.

Fig. 4. Beam footprint shown in different colours are for different launch angle of the fiber as shown in Fig. 1(a).

Design 2 beam size results:

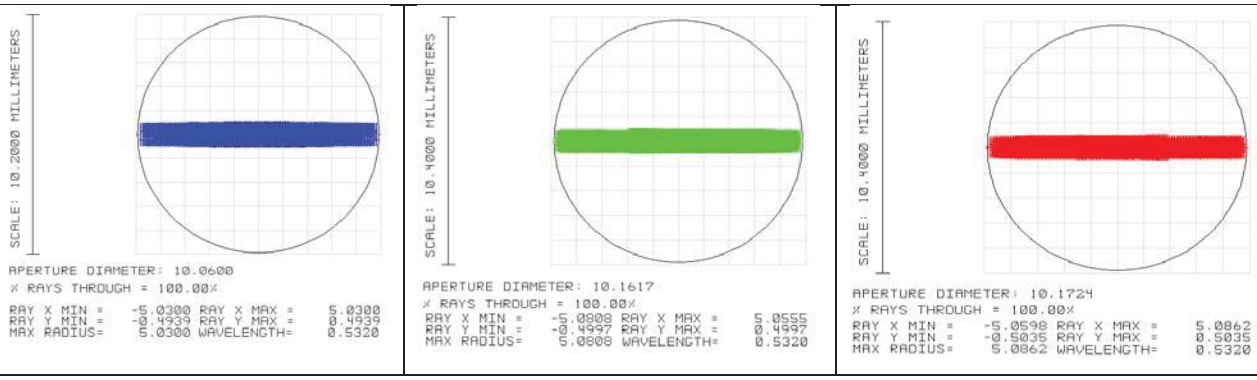

Fig. 5. Beam footprints shown in different colours are for different launch angle of the fiber as shown in Fig. 3(a).

It can be seen that spot size in design 1 is elliptical with major and minor axis as length and height of lasing zone in an amplifier. In design 2 the illuminating zone is rectangular and homogenized in vertical direction as shown in Fig 3(b). The homogenization in vertical direction is expected to yield better spatial overlap with signal

Acknowledgements:

Authors would like to express their sincere gratitude towards Dr. (Smt.) Archana Sharma, AD, BTDG for her constant encouragement and support for this research work.

References:

1. A. Khattar. *et. al*., *National Laser Symposium- **26**,*

2. Leon Scott Jr. *et al*., *United states patents,* **5, 355, 387***, Oct 11 (1994)*

3. Issac L. Bass*. Proc. SPIE* **1869***, pg 128-135, Aug. 7 (1993).*

Inscription of long period fiber grating near phase matching turning point by frequency doubled copper vapour laser

R. Mahakud, J.Kumar,V.K. Srivastava, S. Chaube, S. Kumar, U. Kumbhakar, O. Prakash, S.K. Dixit
FSOSS, Raja Ramanna Centre for Advanced Technology, Indore,
E-mail: rkmahakud@rrcat.gov.in

Abstract

The sensitivity of long-period fiber grating (LPG) operating near phase matching turning point (PMTP) has very high sensitivity to external perturbations such as temperature, refractive index and strain. In this work, LPGs operating near PMTP has been inscribed and further optimised with respect to fluence, focussing and period successfully in-house, using frequency converted copper vapour laser.

1. Introduction

Long period fiber gratings (LPGs) are passive optical components, inscribed in single mode fibers. A long period grating (LPG) is a refractive index periodic structure of period of few hundred microns in the core of a single mode optical fiber [1-4].Long period fiber gratings are useful for many optical devices and coupling systems and as physical, chemical and bio sensors. Some of techniques used for LPG inscription includes local exposure of the fibre to a UV laser, CO2 laser, femtosecond laser or by electrical arc discharge [1-2]. UV beam irradiation induce periodic refractive index structure is more conventional. Long-period gratings (LPGs) operating at and around the phase matching turning point (PMTP) possess some of the highest sensitivities to external perturbations in the family of LPG-based sensor devices [5]. By the choosing the grating period carefully, it is feasible to write LPGs operating near phase matching turning point suitable to develop high sensitive sensor for monitoring external parameters such as temperature, strain and refractive index (RI).

This paper presents the fabrication of the LPFGs in Ge-B doped fiber by UV writing, using in-house developed fabrication setup, with periods to couple to high order cladding modes is described. The UV beam (255 nm) generated from frequency doubled copper vapour laser inscribed LPGs operating near phase matching turn around point by point-by-point method.

2. Principle

The periodic modulation of RI in the fiber core of the long period fiber gratings causes the core mode to couple with a number of co-propagating cladding modes. Fig.1 shows the schematic of working of LPG in a optical fiber.The transmission (T) at wavelength (λ) is described by [1]

$$T(\lambda) = 1 - \left(\frac{\kappa^2}{\frac{\Gamma^2}{4}+\kappa^2}\right) sin^2\left(\sqrt{\frac{\Gamma^2}{4}+\kappa^2}\ L\right) \quad (1)$$

where L is LPG length and Λ is period. The detuning factor (Γ) and coupling coefficient (κ) are given as,

$$\Gamma = \frac{2\pi}{\lambda}\left(n_{co} - n_{cl,m}\right) - \frac{2\pi}{\Lambda}; \quad \kappa = \frac{\pi}{\lambda}\Delta n I \quad (2)$$

where n_{co} and $n_{cl,m}$ are effective RI of co-propagating core mode and m^{th} cladding mode and Δn is refractive index modulation in the fiber core. I is the overlap integral between the fundamental guided mode and the cladding modes in the core region. At phase matching, the resonant wavelength and transmission at that wavelength is given as,

$$\lambda = (n_{co} - n_{cl,m})\Lambda; \qquad T = cos^2(\kappa L) \tag{3}$$

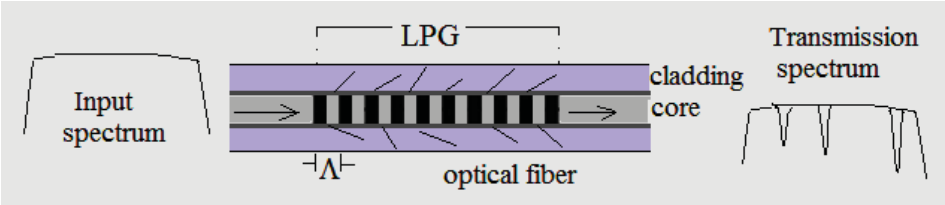

Fig.1 *Schematic of the LPG in a optical fiber, input and out put spectrum*

In order to predict coupling from the core to the different cladding modes, phase matching curves (λ vs Λ) are generated by calculating the dispersion of core and the cladding modes [5]. A single mode is coupled at two different wavelengths simultaneously for an LPG operating near turning point [5]. This is because the cladding mode's effective refractive index will decrease more than the effective refractive index of the core mode with increase in wavelength. This corresponds to the dual bands that become apparent in the LPG transmission spectrum. Figure 2 shows phase-matching curve for a typical cladding mode which has a PMTP in the observation band of 1200-1700 nm. At the turning point, the gradient of the curve tends to zero [|dΛ / dλ|→0]. The LPGs operating at/near turning point have very high sensitivity to external perturbations. The appearance of turning points moves towards shorter wavelengths with increase in cladding mode order.

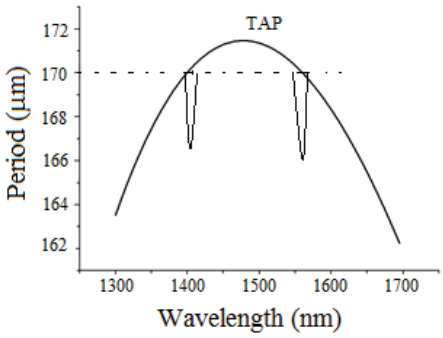

Fig.2 *Simulated curve for variation of wavelength with grating period for a typical cladding mode*

2. Fabrication process

Figure 3 represents the schematic of LPG fabrication by point-by-point method. The long period gratings (LPGs) were inscribed, in house, by frequency doubled copper vapour laser UV beam (255.3 nm, 25 ns, 6.5 KHz). LPGs were inscribed in single mode photosensitive Ge-B codoped fiber (PS 1250/1500, Fiber core). The fiber fixed on two V-grooves mounted on a three axis computer-controlled precision translation stage of resolution of 2 μm. The UV beam of diameter 4 mm was focused on to the fiber by a 10 × microscopic objective, affixed to a three axis mount for beam alignment and beam focussing on the fiber. The protective poly acrylate coating of the fiber was removed, cleaned and then fixed on the two V-grooves by two magnetic clamps for LPG writing. The focussing lens fixed and fiber movement programmed for LPG inscription. LPGs of different periods in between 150 μm to 210 μm inscribed to find out the period for which the resonant wavelength at PMTP obtained. The LPG transmission spectra were monitored by an optical spectrum analyser (OSA, Agilent 86142B) and a broad band light source of OSA (600-1700 nm).

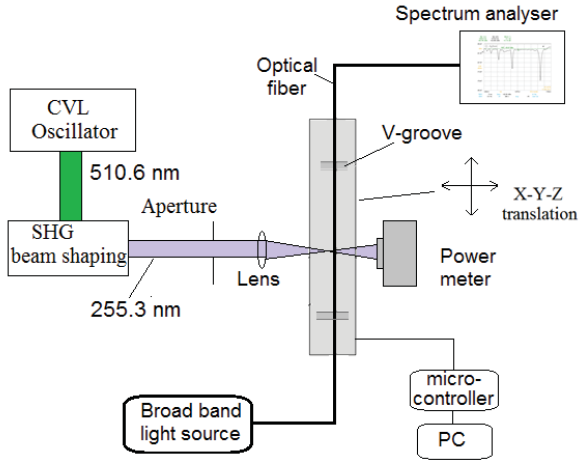

Fig.3 *Schematic of the LPG writing by 255.3 nm UV beam*

3. Results and Discussion

LPGs were fabricated following the procedures as described. The spectrum of gratings inscribed, for period varied in between 160 μm to 200 μm, observed to find out the typical period for which the LPG spectrum is near phase matching turn around point for the fiber used in the study. The resonant wavelength of the highest mode in the observation band (1000-1700 nm) increased with increase period. As PMTP approached, two resonant bands of the highest mode appeared. AT PMTP, only a single band observed. In this study for the fiber used, the PMTP observed for periods of 196 μm (11^{th} cladding mode) and 170 μm (12^{th} cladding mode). Figure 4a shows the transmission spectrum observed, near PMTP, for the period LPG of 196 μm and grating length of 12 mm. The resonant wavelength at PMTP is 1600 nm with bandwidth ~ 240 nm and transmission dip of 10 dB. The wavelength of the attenuation band for the penultimate cladding mode coupling is 1190 nm (~10 dB). Figure 4b shows transmission spectra for the LPG of period, Λ = 170 μm. The resonant wavelength (1590 nm, 13.2 dB) is near PMTP. Figure 5a shows the LPG spectra for two periods, 166 nm and 168 nm which are less than 170 μm. The separation between two resonant peaks of a typical mode increased with increase in the difference in grating period from that of PMTP. The grating period vs resonant wavelength for the periods near PMTP is shown in figure 5b. The period and wavelength for phase matching turn around point depends on effective refractive index of core and cladding and also RI changes in the core of fiber during fabrication. Different periods with the same fabrication conditions lead to resonances at specific wavelengths. The position of the attenuation band shifted toward longer wavelengths as the grating period increased for the PMTP. It was also observed that the position of resonant wavelength changed and period for PMTP changed with change in UV bean fluence used in LPG fabrication. The simulated phase-matching curve for a typical period may not fit precisely. This is due to change in effective index of photosensitive fiber core by UV excitation. For the periods above the period for PMTP, the transmission dip vanished as the resonant condition is not satisfied. The transmission follows the equation 1.

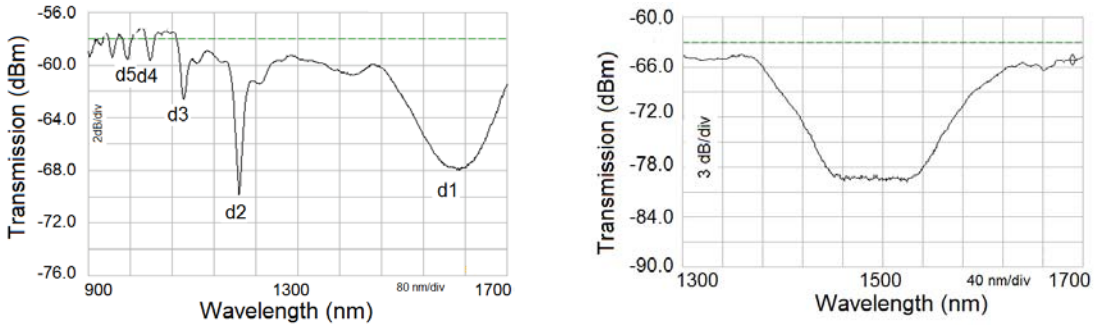

Fig.4 *Transmission spectra of LPG of period (a) 196 μm and (b) 170 μm*

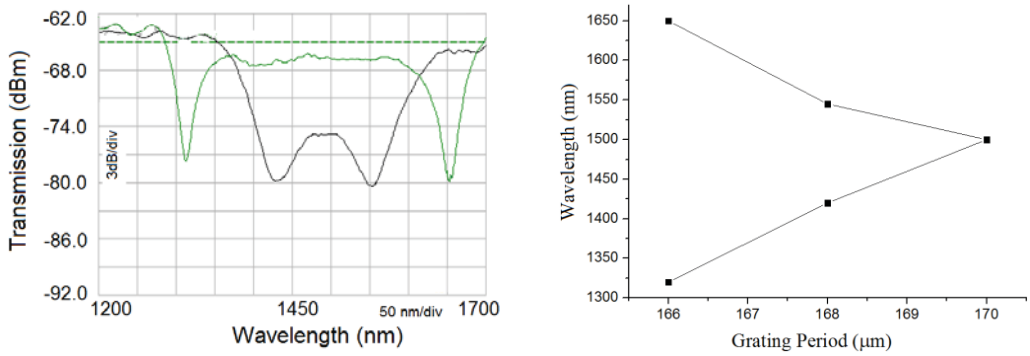

(a) (b)

Fig. 5 *(a) Transmission spectrum of LPG at two different periods and (b) grating period vs wavelength*

4. Conclusion

The fabrication of long period fiber grating near PMTP by frequency doubled CVL has been demonstrated. It was observed that the fabrication of LPG near PMTP requires a precise control of the grating period, grating length fiber alignment and UV fluence. The resonant coupling a typical cladding mode near PMTP splits into two attenuation bands, the wavelength laying on both sides of the resonant wavelength for PMTP. The fabrication of LPG near PMTP will be very useful for the development of high sensitivity sensors for temperature, chemical and bio-chemical sensing.

References:

1. R. Kashyap, *Fiber Bragg Gratings* (Academic, 1999).

2. A. Vengsarkar: J. Lightwave Technol. 14(1), 58 (1996)

3. T. Erdogan, J. *Optical Society of America A* **14**, 1760 (1997)

3. V. Bhatia, A. Vengsarkkar, *Opt. Lett*. **21**, 692 (1996)

5. Xuewen Shu, Lin Zhang, Ian Bennion, *J. Lightwave Technology,* **20**, 255 (2002).

6. B.Malo, J.Albert, K.O Hill, F.Bilodeau, D.C. Johnson, *Electronic Letters*, **30**, 442, (1994)

Studies on the thermal behaviour of different resonant modes of a long period grating

V. K. Srivastav, R. Mahakud, J. Kumar, S. Kumar, U. Kumbhkar, O. Prakash, S. K. Dixit
FSOSS, Raja Ramanna Centre for Advanced Technology, Indore,
Email: vkshrivastava @rrcat.gov.in

Abstract

This paper presents an experimental study on the blue shift of wavelength of different resonant modes of a long period fiber grating due to thermal relaxation of photo- induced refractive index in the fiber core. This irreversible change in resonant mode is significant as the initial design wavelength and is different for different modes. The LPGs used in the sudy was fabricated, in-house, using 255 nm UV beam obtained from frequency conversion of copper vapour laser (CVL).

1. Introduction

A long period fiber grating is a periodic refractive index modulation in the fiber core of period of the order of few hundred microns. Long period fiber gratings (LPGs) are useful elements in many optical devices and physical, chemical and bio sensors [1-4].The spectral characteristics of LPGs are much more sensitive to temperature, bending and surrounding refractive index (RI) in compared to a short period fiber grating. The most conventional technique for writing LPG, is the UV beam irradiation on photosensitive fiber to induce periodic refractive index modulation. The long period fiber grating couples the core mode to co-propagating cladding modes. A typical LPG is suitable for simultaneous measurement of multi-parameters [4-6]. This is because the resonant wavelengths corresponding to different cladding mode orders have different sensitivity to physical parameters such as temperature and density of a liquid. The difference in sensitivity allows decoupling of temperature effect from the other parameters affecting the resonant of different orders coupled. Hence precise knowledge of evolution of wavelength with temperature is very important.

In this paper, it is shown that the UV induced RI loss in the fiber core at elevated temperature leads to change in resonant wavelength significantly from the initial designed wavelength. This change is different for different modes due to difference in cladding mode dispersion. The difference in evolution of resonant wavelength of a thermally stable LPG in different modes investigated. The results explained in terms of change of thermo-optic coefficient and dispersion. The study will help in design and development of LPG based devices for multi parameter sensing.

2. Principle

The periodic modulation of RI in the fiber core of the long period fiber gratings causes the core mode to couple with a number of co-propagating cladding modes. The resonant wavelength and transmission at phase matching for the m^{th} cladding mode are described by [1]

$$\lambda_m = \left(n_{co} - n_{cl,m}\right)\Lambda = N_m \Lambda \quad (1a)$$

$$T_m = cos^2(\kappa_m L) \quad (1b)$$

where L is LPG length and Λ is period and κ_m is coupling coefficient. n_{co} and $n_{cl,m}$ are effective RI of co-propagating core mode and m^{th} cladding mode respectively. N_m $(=\left(n_{co} - n_{cl,m}\right))$ is termed as differential

effective RI. The coupling cofficient ($\kappa_m = \pi\Delta n\ I_m/\lambda$) depends on is refractive index modulation (Δn) in the fiber core and overlap integral (I_m) between the fundamental guided core mode and m^{th} cladding mode.

3. Experimental

Figure 1a shows the schematic of in-house LPG fabrication by point-by-point method using frequency doubled copper vapour laser (CVL- UV) beam (255.3 nm, 25 ns, 6.5 KHz) as writing source. The LPGs are inscribed in single mode photosensitive Ge-B codoped fiber (PS 1250/1500, Fiber core) for the present study. The UV beam of diameter 4 mm was focused on to the fiber by a 10 × microscopic objective, affixed to a three axis mount for focussing and alignment.

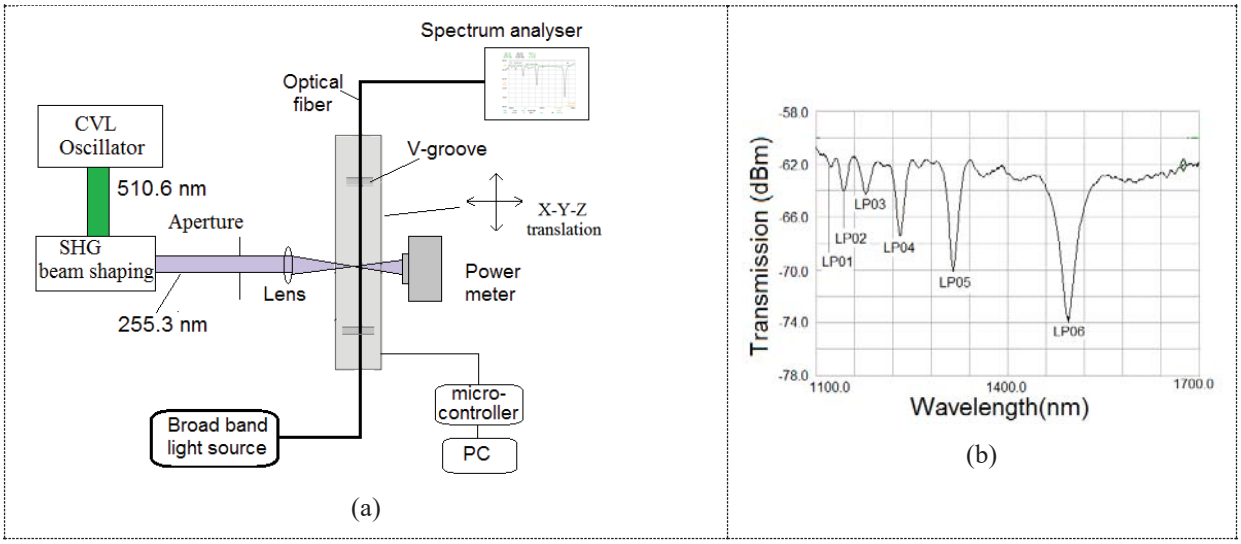

Fig.1 *Schematic of LPG writing set up by CVL-UV beam (b) Transmission spectrum of an inscribed LPG*

The LPG transmission spectrum was monitored by an optical spectrum analyser (OSA, Agilent 86142B) and a broad band light source of OSA (600-1700 nm). Fig 1b shows the transmission spectrum of a typical LPG (Λ = 320 μm) and length 10 mm, inscribed by the set up. The thermal behavior of the LPG was studied by heating it in a programmable PID controlled tubular oven. The oven temperature was measured by a thermocouple transducer. The wavelength and transmission of few modes recorded during annealing. The temperature of the oven brought down to room temperature to complete the annealing process. The resonant wavelength and transmission dip noted before annealing and after annealing. The spectral evolution of wavelength of few modes of the annealed thermally stable LPG recorded with change in temperature in the interval of 30 ^oC to 250 ^oC.

3. Results and Discussion

The LPG was annealed to study the effect of thermal relaxation on spectral evolution of a pristine grating with time and temperature. Figure 2a shows variation of resonant wavelength and figure 2b shows the transmission in different modes following the annealing process. The temperature elevated and annealed at 200 ^oC for 200 minutes and then rose to 250 ^oC and annealed further for 200 minutes. With increase in temperature, the resonant wavelength and transmission dip decreased. At a fixed temperature, the wavelength and transmission dip of all the modes (marked as LP06, LP05 and LP03) decreased with time.

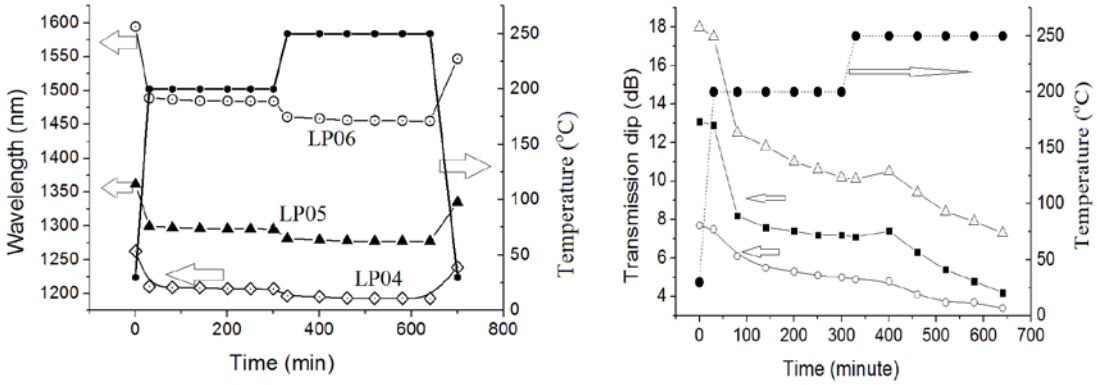

(a) (b)

Fig.2 (a) *Variation of resonant wavelength and temperature (b) transmission dip and temperature in different modes with time*

Following annealing process in time from 30 ^{o}C to 250 ^{o}C, the transmission dip decreased from 18 dB to 7.3 dB in LP 06 mode, 13.1 dB to 4.2 dB for LP05 mode and 7.7 dB to 3.4 dB in LP03 mode. The resonant wavelength blue shifted (from 1594 nm to 1455 nm, 1361 nm to 1277 nm and 1262 nm to 1193 nm for LP06, LP05 and LP03 modes respectively. After annealing, the temperature of grating brought down to room temperature of 30 ^{o}C. The decreases in resonant wavelength from the design wavelength due to thermal relaxation are 37 nm, 26 nm and 23 nm respectively for LP06, LP05 and LP03 modes respectively. During increase in temperature, the blue shift of resonant wavelength is combined effect of both the irreversible and reversible changes of core and cladding mode effective refractive index and the overlap integral of core and cladding modes in the fiber core. The reversible changes associated with thermo-optic coefficient and dispersion of core and cladding modes. At constant temperature, the resonant wavelength blue shifted and transmission dip decreased further irreversibly. The irreversible loss of RI due to thermal relaxation is associated increase in demarcation energy which is a function of time and temperature. The irreversible thermal decay of photo-induced refractive index leads to decrease in RI modulation and period averaged RI [1]. The decreases in photo-induced average RI in the fiber core lead to decrease in resonant wavelength. The decrease in RI modulation in the fiber core leads to decay in the grating strength. The reduction of resonant wavelength of LP06 mode is higher than LP05 and that of LP05 is higher than LP03. This is attributed to difference in modal dispersion ($\partial N_m / \partial \lambda$) of differential RI. Lower order cladding modes have lower dispersion of differential RI [5-6]. The difference in transmission dip and associated different loss during annealing is attributed to difference in overlap integral (I_m) between the fundamental guided core mode and m^{th} cladding mode. The higher order cladding modes have higher values of I_m as more power is confined in the core [6]. The spectral change with temperature for annealed gratings was found to be reversible in different temperature cycles in the interval of 30 ^{o}C to 250 ^{o}C. Thus the refractive index loss of the core and cladding modes is reversible for the operating temperature less than equal to 250 ^{o}C.

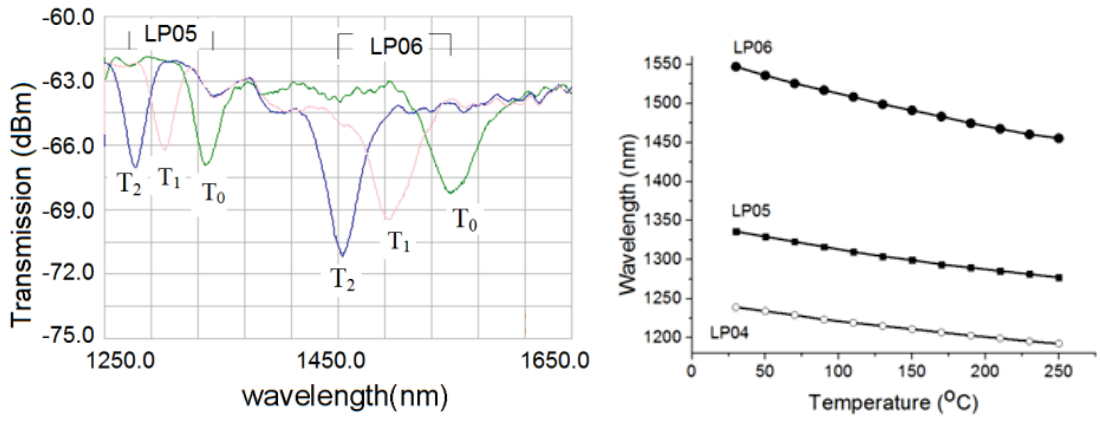

(a) (b)

Fig.3 *(a) Variation or resonant wavelength of post annealed FBG with increase in temperature (b) Transmission spectrum at different temperature*

Fig. 3a shows the transmission spectrum of LPG at 30 ^{o}C (T_0), 140 ^{o}C (T_1) and 250 ^{o}C (T_2) for LP06 and LP05 modes. Fig 3b shows the variation of resonant wavelength with temperature. Transmissions dip of LP 06 mode is increased from 4.5 dB to 7.5 dB. The increase is attributed to increase in overlap integral with temperature. The wavelength decreased due to decrease in differential RI (N_m) with increase in temperature. The average temperature sensitivities in the interval of 30 ^{o}C to 250 ^{o}C for LP06, LP05 and LP03 cladding modes are 416 pm/^{o}C, 267pm/^{o}C and 47 pm/^{o}C respectively. The difference in temperature sensitivities of various modes are attributed to difference in material dispersion and waveguide dispersion modes [ ].

4. Conclusion

In conclusion, the studies on the thermal behaviour of different resonant modes of an in-house fabricated long period grating are presented. The LPGs was fabricated using 255 nm UV beam obtained from frequency conversion of copper vapour laser (CVL). The UV induced RI loss in the fiber core at elevated temperature leads to change in resonant wavelength significantly from the initial designed wavelength. This change is different for different modes due to difference in cladding mode dispersion. The blue shift of resonant wavelength of a thermally stable LPG in different modes is higher for higher order modes. The results explained in terms of change of thermo-optic coefficient and dispersion. The study will help in design and development of LPG based devices for multi parameter sensing.

References:

1. R. Kashyap, *Fiber Bragg Gratings* (Academic, 1999).

2. A. Vengsarkar: J. Lightwave Technol. 14(1), 58 (1996)

3. T. Erdogan, J. *Optical Society of America A* **14**, 1760 (1997)

3. V. Bhatia, A. Vengsarkkar, *Opt. Lett*. **21**, 692 (1996)

5. Xuewen Shu, Lin Zhang, Ian Bennion, *J. Lightwave Technology,* **20**, 255 (2002).

6. B.Malo, J.Albert, K.O Hill, F.Bilodeau, D.C. Johnson, *Electronic Letters*, **30**, 442, (1994)

High temperature chirped FBG fabrication by thermal stretching of regenerated FBG

J. Kumar*[1], R. Mahakud[1], S. Kumar[1], U. Kumbhkar[1], O. Prakash[1,3], S. K. Dixit[1,3], S. V. Nakhe[2]

[1]*Fibre Grating Lab, Fibre Sensors and Optical Spectroscopy Section,* [2]*Laser Group*

Raja Ramanna Centre for Advanced Technology, Indore,

[3]*Homi Bhabha National Institute, Mumbai*, *E-mail: jkmadaan@rrcat.gov.in

Abstract

In this paper the fabrication of high temperature chirped fiber Bragg grating (CFBG) by thermal stretching of regenerated FBG is presented. Thermal regeneration of uniform FBG was carried out at 850 ^{o}C by applying step annealing schedule. The FBG was stretched by applying strain ~1200 με along the length of the grating. Chirped grating with reflection intensity 4500 (a.u.) and FWHM bandwidth ~ 7.1 nm was fabricated by applying thermal gradient from 860 ^{o}C to 900 ^{o}C across the length of strained thermally regenerated FBG. The fabricated grating can sustain temperature upto 900 ^{o}C.

Key words: Fiber Bragg grating, Chirped FBG, thermal regeneration, temperature sensor, gradient stretching

1. Introduction

Fiber Bragg gratings (FBGs) have been widely used in the applications of fiber lasers and sensors due to their inherent advantages such as high spatial resolution, single point as well as distributed sensing capabilities, high sensitivity, faster response time, accessing the difficult and remote locations and capability to work in harsh environment [1]. Chirped fiber Bragg gratings are usually fabricated by chirped phase mask, concatenated phase masks, tapered fibers, tilted fibers, interferometric techniques and by applying strain during fabrication of uniform FBG [2-5]. The chirped FBGs fabricated with these methods are type-I gratings so cannot sustain temperature more than 400 ^{o}C [6]. Thermally regenerated gratings from chirped gratings inscribed in hydrogenated fibers can sustain temperature can sustain temperature upto 900 ^{o}C [7]. But chirped phase masks required for FBG fabrication are costly and they are wavelength specific. High temperature chirped FBGs are useful in high-temperature communication components, dispersion compensators, optical fiber band-pass filter, high power fiber lasers and high temperature profile measurement [8-9]. In the present paper, we experimentally demonstrate the fabrication of chirped FBG from the gradient stretching of regenerated FBG at high temperature.

2. Fabrication of FBG using frequency converted copper vapour laser

The FBG writing source was high repetition rate (5.5 kHz) and high beam quality 255 nm UV radiation. UV beam was obtained from the second harmonic frequency conversion of copper vapor laser radiation (510 nm) [10]. About 10 mm beam with parameters λ ~ 255 nm, average power ~ 350 mW, pulse repetition rate ~ 5.5 kHz, pulse width ~ 30 ns and pulse energy ~ 54 μJ was used to write the FBG in hydrogen loaded telecommunication grade SMF-28 silica fiber. Hydrogen loading of the optical fiber was done at pressure of 100 bar at 100 ^{o}C temperature for around 144 hours (6 days). The FBGs were written just after removing the fibers from hydrogen loading set-up. The UV beam of dimension about 10 mm x 250 μm was focused on the fiber by a cylindrical lens of focal length 7.5 cm. The fiber was mounted ~ 0.5 mm behind the phase mask (Ibsen, Grating period = 1060 nm). The interference pattern formed between the +1 and -1 diffraction order of

phase mask produced the fringes of about 530 nm spacing on the fiber. Growth of FBGs was monitored online using a broadband ASE source (1525 nm-1560 nm), 3 dB coupler and optical spectrum analyzer (OSA). FBG of reflectivity 99.96% (transmission dip ~ 34 dB), FWHM bandwidth 1.67 nm and Bragg wavelength 1534.504 nm was inscribed with 3 minute of UV fringe exposure. Refractive index (RI) modulation was calculated from the reflectivity of the FBG. Fig. 1 shows the variation in RI modulation and FWHM bandwidth of FBG with cumulative UV fluence. RI modulation increases with increase in UV fluence and reaches to 3.25 x 10^{-4} at the cumulative fluence of 2.7 kJ/cm^2.

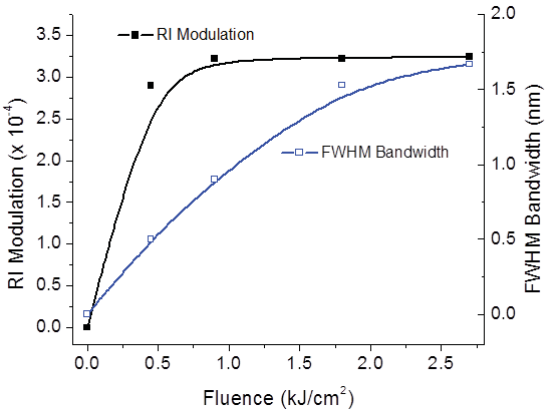

Fig. 1 *RI modulation and FWHM bandwidth of FBG with UV fluence*

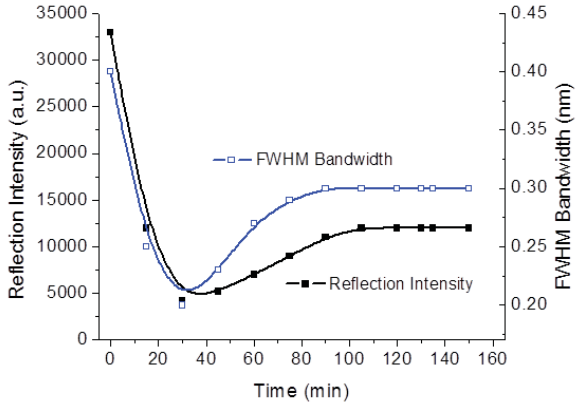

Fig. 2 *FBG reflection intensity and FWHM bandwidth during thermal regeneration*

3. Thermal regeneration characteristics of chirped FBG

Thermal regeneration of FBG is a process, in which the conventional type-I FBG (seed grating) is annealed at high temperature to form reborn and stable FBG. This regenerated FBG can sustain temperature from 900 °C to 1295 °C depending upon fiber doping and annealing schedule [11-13]. For the thermal treatment, the FBG was placed inside a mini heater (length~70 mm and inner diameter ~ 5 mm) by fixing it's both ends on micro-meter stages. The reflection spectrum of the FBG was recorded using FBG interrogator and displayed on computer screen. For the present experiment ramp annealing schedule was applied for the thermal regeneration of the grating. In this schedule the temperature of the FBG was raised to 850 °C from room temperature within 60 minutes and dwelled for 150 minutes. FBG reflection intensity decreased from 45,000 (a.u.) to 33,000 (a.u.) as the temperature was raised to 850 °C. The reflection intensity further decreased and reaches to 4250 (a.u.) as the FBG was kept at 850 °C for ~ 30 minutes. After this the FBG again started to re-grow and became stable at 12,000 (a.u.) within next 120 minutes. Fig. 2 shows the variation in reflection intensity and FWHM bandwidth during thermal regeneration. So the thermal regenerated FBG with reflection intensity ~12,000 (a.u.), bandwidth ~ 0.3 nm and Bragg wavelength ~ 1533.585 nm (at room temperature) was fabricated with this method.

4. Fabrication of chirped FBGs by gradient stretching

For the fabrication of chirped FBG with non-uniform periods a gradient needs to be applied along the grating length of the uniform FBG. This non-uniformity was achieved by applying strain to the thermally regenerated FBG and then placing the grating at graded temperature. For this purpose a mini heater of length 70 mm and high thermal gradient was used for the experiment. Fig. 3 shows the thermal profile of the mini heater used in present

experiment at different applied temperature at the central region. As shown in the figure, region-1 was used for the thermal regeneration and region-2 was used for the fabrication of chirped FBG. The Bragg wavelength of the FBG shifted to 1534.811 nm with applied strain ~1200 με. The position of the FBG was shifted to region-2 to for the thermal stretching at high temperature. Fig. 3 shows the gradient in heater temperature at region-2 with average central temperature at region-1. For a particular temperature of ~900 °C (region-1), the temperature gradient from 858 °C to 886 °C was observed for region-2. For the fabrication of chirped grating from normal grating the temperature of the FBG under strain was increased from room temperature to 900 °C. The thermal gradient at region-2 increases with increase in temperature and leads to change in FWHM bandwidth of the FBG. Fig. 4 shows the FBG interrogator traces upto 900 °C (region-1).

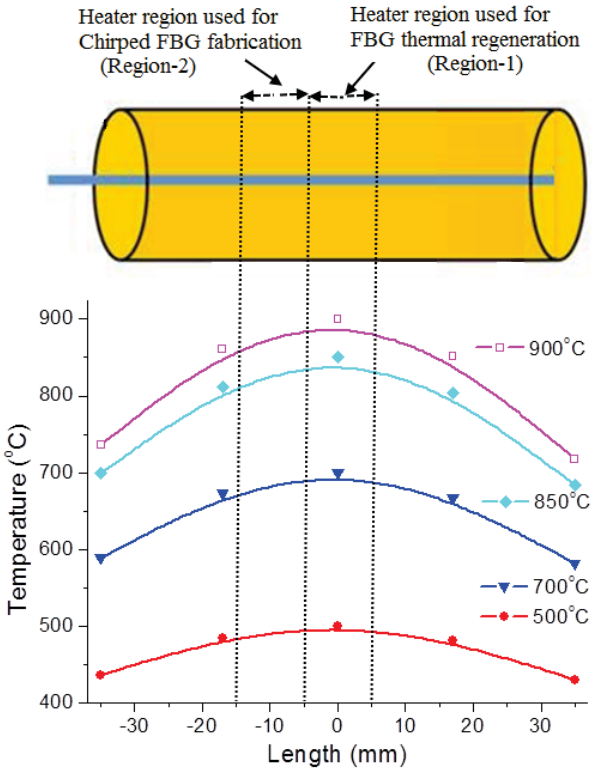

Fig. 3 *Thermal profile of the mini heater*

The FWHM bandwidth of the FBG increases from 0.3 nm to 1.9 nm and the reflection intensity decreases from 10,220 to 5,200 (a.u.). The heater temperature was dwell at 900 °C for 35 minutes. The FWHM bandwidth increases from 1.9 nm and reaches up to 7.1 nm within 35 minutes of heating. The reflection intensity decreased from 5,200 to 4,500 (a.u.) during this time. FWHM bandwidth of FBG with time at different central temperature of the oven is also shown in figure 5. It is clear from the figure that the bandwidth of the FBG increases rapidly as the fiber material is softened further. So the chirping of the FBG depends on the thermal gradient and the time of stay at that gradient. The fabricated high temperature chirped gratings will be useful for applications such as high temperature profile measurement, high power fiber laser and gain flattening filters.

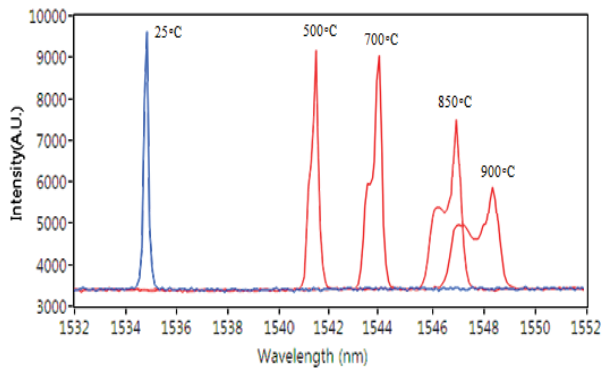

Fig. 4 *FBG interrogator traces during thermal stretching*

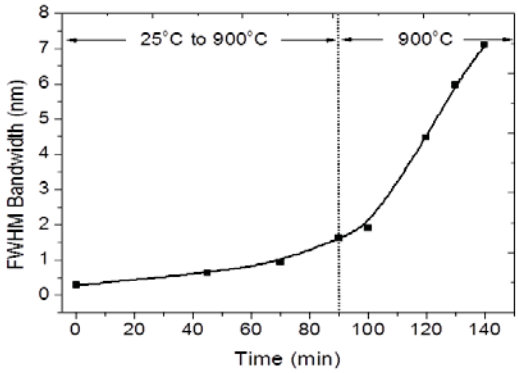

Fig. 5 *FWHM bandwidth of FBG with time at different central temperature of the oven*

5. Conclusion

In summary, the fabrication of high temperature chirped gratings of FWHM bandwidth ~7.1 nm is demonstrated. Thermal gradient profile of a mini-heater (70 mm length) was used for chirping of thermal regenerated gratings under strain. Fabricated gratings have advantages of both high temperature sensing and chirp profile.

References

1. J. Canning, “Fibre gratings and devices for sensors and lasers” Laser and Photonics Rev. vol. 2(4), pp. 275-89, May 2008.
2. M. Becker, T. Elsmann, I. Latka, M. Rothhardt, H. Bartelt, “Chirped Phase Mask Interferometer for Fiber BraggGrating Array Inscription” vol. 33(10), pp. 2093-2098, May 2015.
3. Y. Painchaud, A. Chandonnet, J. Lauzon, “Chirped fibre gratings producedby tilting the fibre” Electron. Lett. vol. 31, pp. 171-172, February1995.
4. K.C. Byron, K. Sugden, T. Bricheno, I. Bennion, “Fabrication of chirped Bragg gratings in photosensitive fibre” Electronics Letters vol. 29 (18), pp. 1659 – 1660, Sept. 1993.
5. P.Pérez-Millán, S.Torres-Peiró, J.L.Cruz, M.V.Andrés,” Fabrication of chirped fiber Bragg gratings by simple combination of stretching movements” Optical Fiber Technology vol. 14 (1),pp.49-53, January 2008.
6. J. Canning, K. Sommer and M. Englund, “Fibre gratings for high temperature sensor applications,” Meas. Sci. Technol. vol. 12(7), pp. 824-828, July 2001.
7. X. Qiao, Y. Wang, H. Yang, T. Guo,Q. Rong, L. Li, D. Su, K. Lim, H. Ahmad, “Ultrahigh-temperature chirped fiber Bragg grating through thermal activation” IEEE Photonics Technology Letters vol. 27 (12), pp.1305-1308, June 2015.
8. F. Ouellette, “Dispersion cancellation using linearly chirped Bragg grating filters in optical waveguides”, Opt. Lett. 12, pp. 847–849, 1987.
9. M.C. Farries, C.M. Ragdale, D.C.J. Reid, “Broadband chirped fibre Braggfilters for pump rejection and recycling in erbium doped fibre amplifiers” Electron. Lett. 28, pp. 487–489, 1992.
10. O. Prakash, R. Mahakud, S.K. Dixit, U. Nandy, “Effect of the spatial coherence of ultraviolet radiation (255 nm) on the fabrication efficiency of phase mask based fiber Bragg gratings” Optics Communications vol. 263 (1), pp. 65–70, 2006.
11. J. Canning, K. Sommer and M. Englund, “Fibre gratings for high temperature sensor applications,” Meas. Sci. Technol. vol. 12(7), pp. 824-828, July 2001.
12. G. Brambilla and H. Rutt, “Fiber Bragg gratings with enhanced thermal stability,” Appl. Phys. Lett. vol. 80 (18), pp. 3259-3261, May 2002.
13. N. Groothoff, and J. Canning, “Enhanced type IIA gratings for high-temperature operation,” Opt. Lett. vol. 29 (20), pp. 2360-62, Oct. 2004.

Development of automated polarization phase shifting laser Fizeau Interferometer for flatness measurement of polished optical surfaces

Y. Pavan Kumar*, Sarthak Gupta, Siddesh Pai, Deepak Daiya, Inderjeet Singh, Rishipal,
A. K. Biswas, Sarvendra Singh, M. P. Kamath, Rajiv Jain, P. Saxena, N. S. Benerji, K.S. Bindra
Raja Ramanna Centre for Advanced Technology, Indore, India.
*Email:ypk@rrcat.gov.in

Abstract

With ever increasing demand for high quality optics, Fizeau interferometers are extensively required in optical development facilities and laboratories for non-contact testing of surface flatness of polished optical components. An automated Polarization phase-shifting Fizeau interferometer has been developed for quantitative evaluation of flatness and 3-D surface form of optical surfaces. Motion control system and analysis software have been developed. The developed interferometer measures Peak-Valley deviation, aberrations and displays 3-D surface form of the polished optical surfaces.

1. Introduction

Fizeau interferometer (FI) is one of the most important optical metrology instruments at optics development facilities and laboratories for non-contact surface measurements of polished optical surfaces. FI is a two-beam interferometer where the interference is formed between the beams reflected from master flat surface and test surface (together they form an interference cavity). The shape of the interference fringes qualitatively represents the shape of the test surface. For precise quantitative measurement of the surface aberrations and 3-D surface form, phase shifting technique is to be applied. In phase shifting technique, the phase difference or the optical path difference between the interfering beams is modulated in steps by a defined amount using either (1) piezoelectric transducers, that displace the reference flat by a fraction of source wavelength or (2) by using polarization phase shifting in which phase shift is introduced between the orthogonally polarized interfering beams by rotating a polarizer. The advantage of the polarization phase shifting is that, the phase shifting element, i.e., the polarizer, is placed outside the interference cavity and hence the cavity is not disturbed during the measurement.

We have developed an automated Polarization phase-shifting Fizeau interferometer for evaluation of surface aberrations and 3-D surface form of polished optical surfaces using polarization phase-shifting. This device is named as “Fizeau interferometer for Optical Surface form Measurement Analysis and Routine Testing” in short “FIZOSMART”. The device consists of a beam expander with beam splitter, reference flat, polarization optical components for phase shifting, imaging lens, camera, motor controller and software for analysis.

2. Working Principle

Fig.1 shows schematic of a polarization phase shifting interferometer[1]. The input He-Ne laser beam is expanded using Microscope Objective (MO) and Collimating lens (TO). The interfering beams reflected from the reference flat surface (R) and the test surface (O) are made orthogonally polarized with respect to each other using a quarter wave plate (Q), placed between the interference cavity optics, with its fast axis at 45-degrees with respect to the polarization direction of the input laser beam. Quarter wave plate (Q) converts the polarization of the test

surface beam orthogonal (due to double passing of the test beam through Q) w.r.t the reference flat beam. These beams on passing through the second quarter wave plate, Q1, with its fast axis at 45-degrees, gets converted to right and left circularly polarized beams. The polarizer, A, selects a component of the orthogonally polarized circular beams along its pass direction and hence the beams interfere producing interference fringes which can be captured by camera (CCD). Rotating polarizer A in its plane introduces phase shift between the interference beams. Rotating the polarizer by 45- degrees, a phase shift

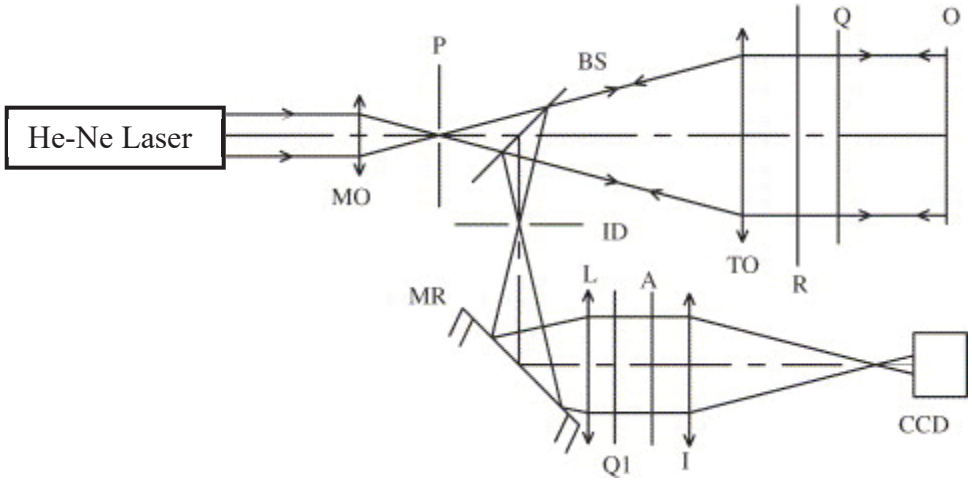

Fig 1. Schematic of the polarization phase shifting Fizeau interferometer. MO: Microscope Objective, P: Pinhole spatial filter, BS: Thin Beam splitter, TO: Collimating lens, R: Reference flat, Q: Quarter wave plate, O: Test object surface, ID: Iris diaphragm, L: Re-collimating lens, Q1: Quarter wave plate, A: Polariser, I: Imaging lens, CCD: camera.

of π/2 will be introduced and the fringes would shift by quarter of their fringe spacing. For deriving the phase map of the test surface, a total of five phase shifted interferograms are to be recorded by rotating the polarizer, in its plane, in steps by 0, 45, 90, 135 and 180 degrees, respectively, from its initial position using motorized polarizer rotator. Using the software, wrapped phase is obtained using the captured interferograms and unwrapped as per standard phase unwrapping procedure and finally the Zernike coefficients are evaluated. A short description of the theory of phase unwrapping is described below:

The general two beam interference equation to represent the intensity at a point *(x,y)* in the interference field is given by

$$I(x,y)=I_o(x,y)\{1+V(x,y)\ cos[\Phi(x,y)+\alpha_i]\} \quad (1)$$

Where, $I_0(x,y)$, $V(x,y)$ and $\Phi(x,y)$ are the mean intensity, fringe visibility and original phase difference between the two interfering beams, respectively. α_i is the modulating phase introduced by rotating polarizer by 0, 45, 90, 135 and 180 degrees that produces a phase of 0, π/2, π, 3π/2, 2π, respectively. Substituting the values α_i and taking the intensities at (x,y) as I_1, I_2, I_3, I_4, I_5 corresponding to each α_i, five equations are obtained. Solving the trigonometric equations, the original phase Φ at a point in the interference field is given by [2],

$$\Phi = \tan^{-1}\left[\frac{2(I_2 - I_4)}{2I_3 - I_1 - I_5}\right] \quad (2)$$

The calculated phase values are wrapped and by comparing the phase difference between adjacent pixels, the unwrapping/ phase integration is performed [3]. The phase variations are converted to Optical Path Difference (OPD) variations by using,

$$OPD = \left(\frac{\lambda}{4\pi} \right) \Phi \qquad (3)$$

The obtained OPD map is fitted to the Zernike polynomial to remove the X and Y tilt and to evaluate the Peak to Valley (P-V) deviation, RMS error, defocus, Astigmatism etc. of the test surface. These values along with the 3-D surface form of the test surface is displayed using software.

3. Results

Required motion control unit for rotating the polarizer along with software for interferogram acquisition and processing has been developed using open-source toolchains. The reference and test optics are aligned to produce interference fringes. The software automatically acquires five phase-shifted interferograms on pressing the START button and performs phase wrapping, unwrapping and calculates the Zernike coefficients. The surface aberrations are displayed in Seidel terms. The main screen displays the 3D surface form, 2D surface map, line profile of the test optics. Also, the individual Zernike coefficients such as X-tilt, Y-tilt, defocus and astigmatism as well as Peak to Valley and RMS of the test surface are displayed. Software is compatible with both Windows and Linux based operating systems.

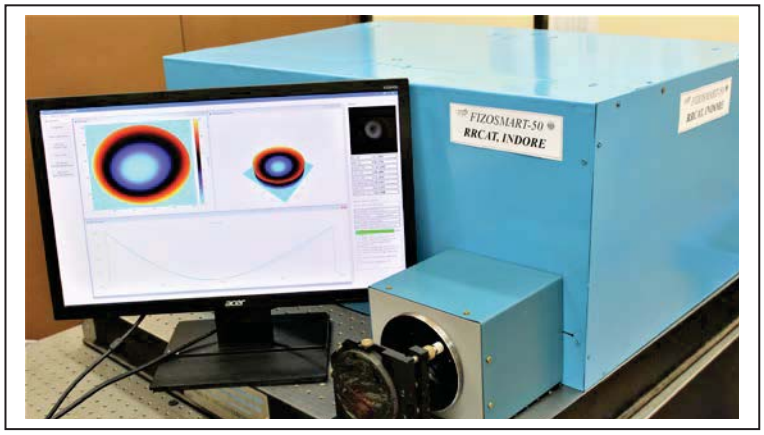

Fig.2 Photograph of FIZOSMART in operation

Developed laser interferometer is shown in Fig.2. Entire system is assembled on a 1m x 1m x 100 mm bread board. For testing the performance of the developed instrument, a test optics (mounted on a mirror mount, as shown in Fig.2) of long radius of curvature (slightly spherical) is used and is interfered with the instruments reference flat (flatness of the order of λ/15). Few interference power rings formed are phase shifted and the results displayed by the instrument are recorded. If N power rings appear in the field of view of the instrument, then the flatness of the test optics (Peak-Valley, P-V) will be Nλ/2. As shown in Fig.3, nearly three power rings appeared in the field of view of the instrument and hence the flatness (P-V) of the test optics should be of the order of 1.5λ. The P-V result shown by the instrument, as shown in Fig.3, is 1.5056λ and hence is matching with the theoretic estimation. Also, the same test object was tested for flatness using ZYGO interferometer. The results were found to be in good agreement.

The developed interferometer can measure surface form of the test optics up to a maximum diameter of 50.0 mm and with an accuracy of λ/10. Measurement of test optics up to diameter 100.0 mm is under progress.

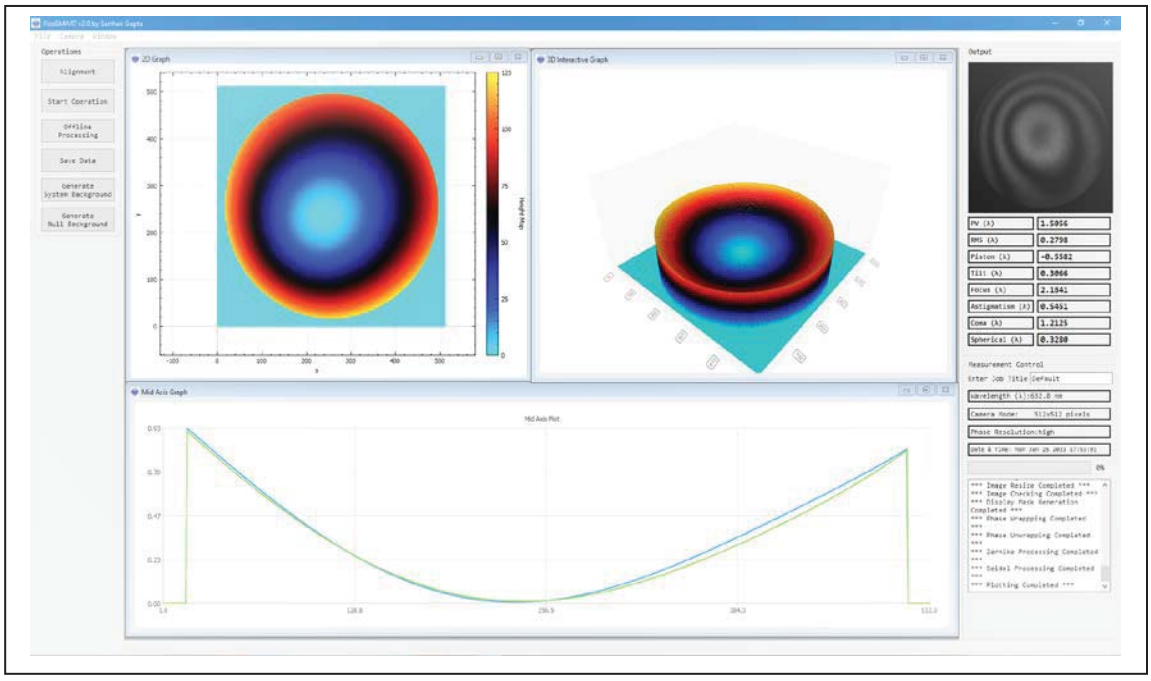

Fig.3 Measurement results of the test object as displayed by the software

4. Conclusions

We have developed a prototype automated laser Fizeau interferometer which can measure flatness and display the 3-D surface form, aberrations of the polished test optics surfaces. The measurement is fully non-contact in nature. The phase shifting element used is not a part of the interference cavity and hence does not disturb the interference cavity during measurement. The measurement accuracy of the instrument is better than λ/10 and also the results are highly repeatable to an order of λ/50. All the optical components used in the system are commercially available. All the mechanical components can be fabricated at normal mechanical workshops and no proprietary element is involved. The developed system is highly useful and workhorse in optical industry for surface flatness measurement of polished optical components such as laser glass windows, prisms etc.

Acknowledgements

We thank Shri. S. V. Nakhe, Director, Laser Group, RRCAT, for the whole-hearted encouragement, support and suggestions. We thank Shri. V.P Bhanage, Head, Laser Controls & Instrumentation Division, Shri. Rajesh Arya, Head, Laser Electronics Division & Solid State Laser Electronics Section, Dr. Sendhil Raja, Head, Advanced Electro-Optics Section for their constant support. We also thank Shri. Sanjiv Tiwari, Shri. G. Muralidharan, Shri. D. Raghunathan, Shri. S.S. Thangavel and all our other colleagues at ODDL, RRCAT for their support and contributions.

References

1. S. Chatterjee, Y. P. Kumar, B. Bhaduri, *Opt. & Las. Tech.* **39**, 268 (2007).
2. P. Hariharan, B.F. Oreb, T. Eiju, *Appl. Opt*. **26**, 2504 (1987).
3. K. Creath, *Progress in Optics*, **26**, E.Wolf, ed., 349 (1998).

Design and Simulation of MOEMS Mach-Zehnder Interferometer

Ashish Singh Bais and Joseph Thomas Andrews

Applied Photonics Laboratory, Department of Applied Physics & Optoelectronics,
Shri G. S. Institute of Technology and Science, 23 Park Road, Indore 452 003 MP, India
*Email: jtandrews@gmail.com

Abstract: Optical waveguide-based Mach-Zehnder Interferometer is designed, simulated using COMSOL Multiphysics and fabricated using UV-photolithography. The design and simulation results are discussed. The optimization values for use with 1.55μm is provided. The fabricated device finds various applications such as a Lab-on a chip and a point-of-contact device.

Introduction:

Micro-opto-electro-mechanical systems (MOEMS) are known for their high sensitivity to measurements, mechanical stability under various conditions, ease of fabrication process and capability of mass production [1]. Hence, MOEMS devices finds numerous applications in the field of bio sensing, bio imaging, medicine, material and food quality control etc. However, Mach-Zehnder and Michelson Interferometers are heart of many of these optical communication devices and components. These interferometers also find to be the key idea behind optical coherence tomography (OCT), a popular biomedical imaging and diagnosis setup. On the other hand, miniaturization of these devices requires suitable waveguide design and other electro-optic or magneto-optic components for optical modulation [2].

The waveguide fabrication technology has already proven that the low loss waveguide structures are possible with silicon on insulator (SOI) or polymer material (PMMA, SU8 etc.) based waveguide [3]. In order to ensure expected outcome, we simulate the device using COMSOL Multiphysics. Various parameter like dimension of waveguides, optical properties of material and various losses. The design is optimized for an input wavelength of 1.55μm. The fabrication tolerance are also estimated with simulation.

Theory

The basic rectangular waveguide structure consists of waveguide region of higher refractive index say n_1 and surrounded on all sides by lesser refractive index say n_2. It is not necessary that all surroundings have same refractive index. In our simulation we consider ridge waveguide structure. In ridge waveguide structure the strip of waveguide material is fabricated on a glass substrate.

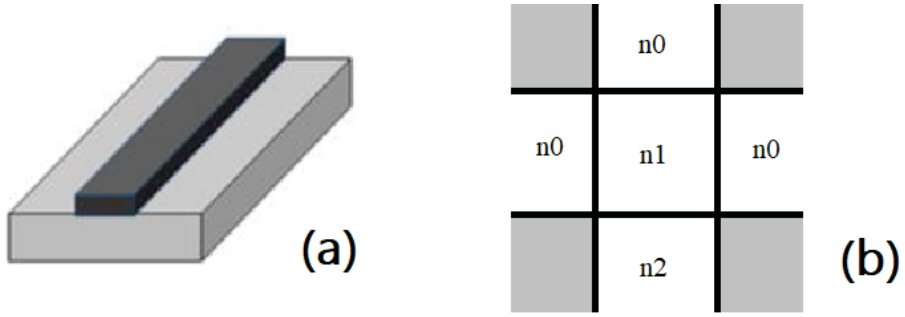

***Fig 1**: (a) ridge waveguide structure; (b) cross sectional view of rectangular waveguide equivalent to the ridge waveguide of fig (a).*

In fig 1(a) substrate (shown as pale grey color), has lower refractive index than that of the waveguide (dark color). The guided region is loaded with material of higher refractive index while the surrounding region is a rarer medium. Fig 1(b) shows cross sectional view of rectangular waveguide as shown in fig 1 (a). In this figure n_1 shows the refractive index of waveguide, n_2 shows refractive index of substrate and n0 shows refractive index of air so n_0=1. So $n_1 > n_2 \geq n_0$.

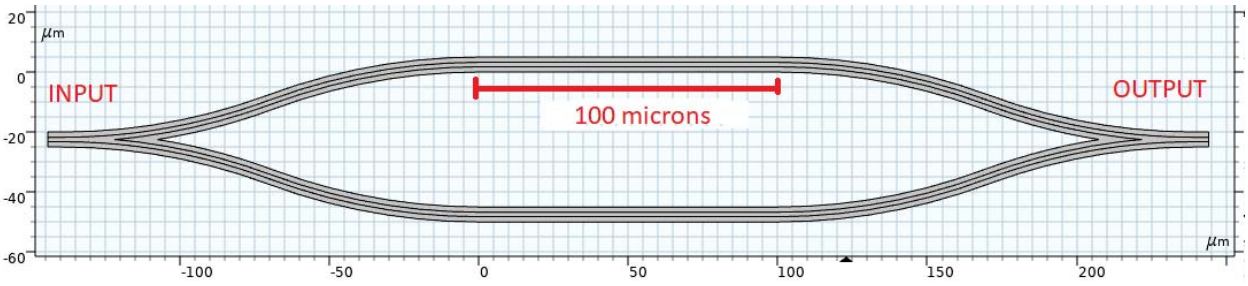

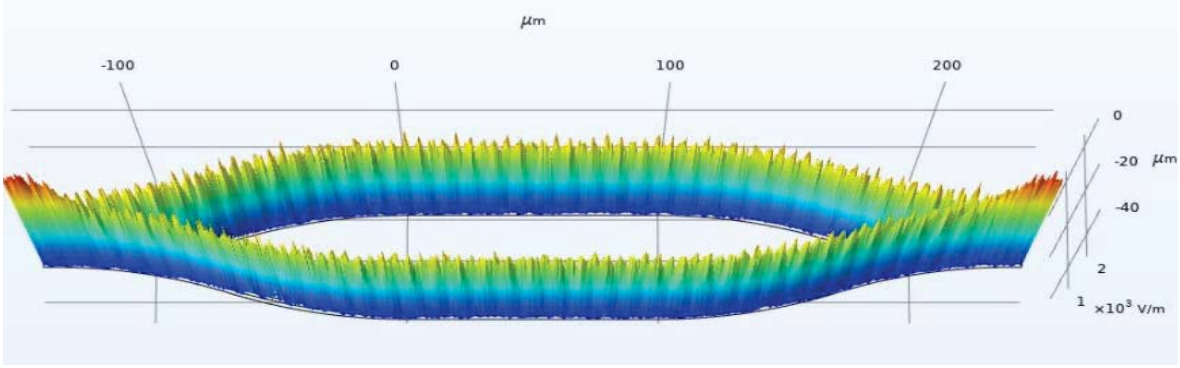

***Fig. 2**: (Top) Geometry of the Mach-Zehnder Interferometer. (Bottom) Simulated results at 1.55μm showing the transmitted electromagnetic waves. Red color represents maximum while blue color corresponds to minimum.*

Mode calculation:

According to theory of guided wave optics the number of modes M in a rectangular waveguide referring to input wavelength of light in free space λ, square cross section of width d and numerical aperture NA can be defined as [4]:

$$M \approx \frac{\pi}{d}\left(\frac{2d}{\lambda}\right)^2 NA^2 \#(1)$$

where $NA = (n_{core} - n_{clad})^{1/2}$.

Design and Simulation

We simulated a rectangular channel waveguide structure for single mode wave propagation with following parameters: waveguide material PMMA, refractive index of core for wavelength 1.55µm = 1.48, refractive index of cladding n_0 = 1(air), channel width = 1.5µm, channel height = 2µm. The schematic diagram of the Mach-Zehnder interferometer is shown in Fig. 2 (top).

The design used for simulation and the optimized simulated results at 1.55µm is shown in Fig. 2. The parameters are adjusted for various values of channel width, cladding index and for various source wavelengths of incident electromagnetic wave. The material parameters and waveguide dimensions are optimized for design wavelength of 1.55mm and shown in Fig. 2 (bottom). Perfect waveguiding along both arms of the Mach-Zehnder interferometer are clearly seen.

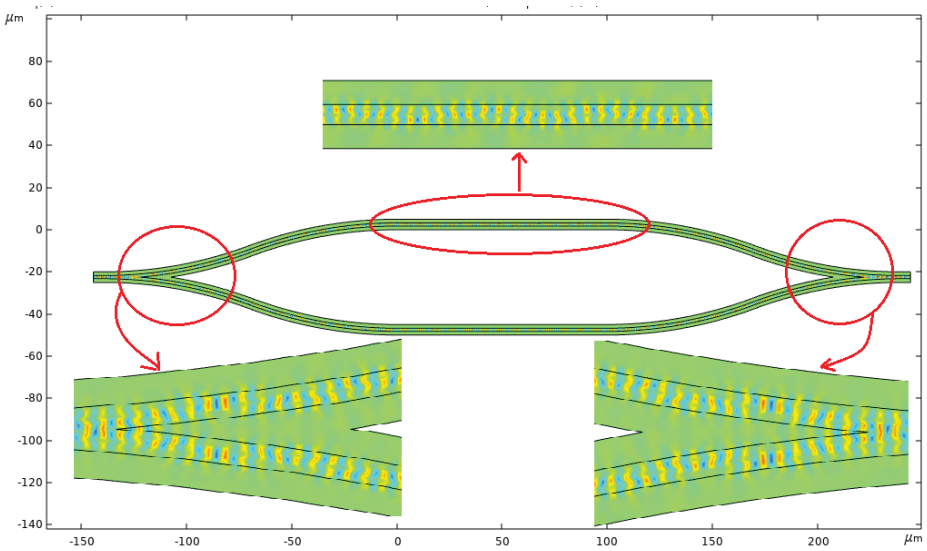

***Fig. 3**: 2D picture of the simulated waveguide structure.*

Figure 3, provides better insight into the waveguiding features and wave splitting and combining at the waveguide joints. The electromagnetic wave at the design wavelength of 1.55mm, exhibits perfect waveguiding, while all other wavelength leaks through the cladding channels and are not supported.

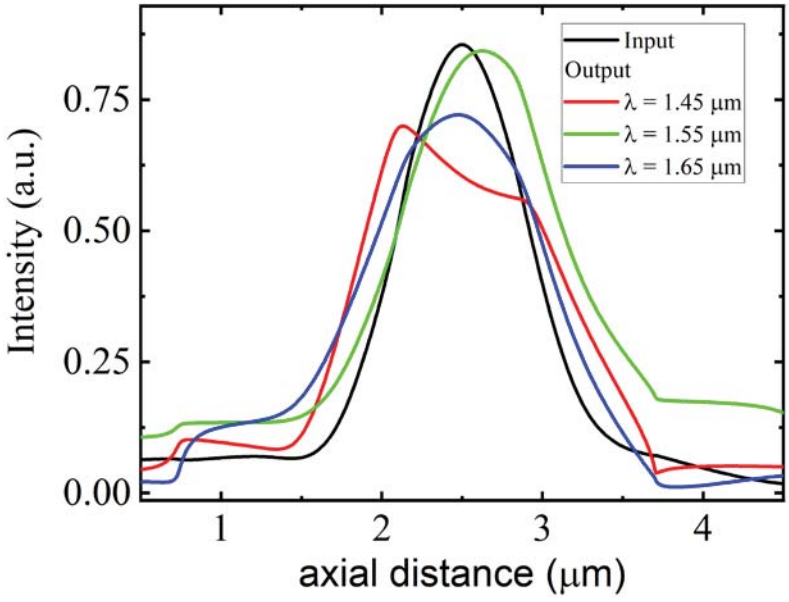

***Fig. 4**. Comparison of input and output signal intensity at different input wavelengths.*

For such small dimensions of the waveguides, the total optical loss is found to be very small. Accordingly, these waveguides readily satisfy the requirement for all optical waveguide interferometers. This leads to the estimation of tolerance limit of the proposed device. Simulation is repeated for incremental change in dimensions and loss measurement. The design is further optimized for lowest loss at design wavelength. The tolerance is measured for acceptable loss range of ±10% from the value measured for deign wavelength.

Conclusions

Mach-Zehnder interferometer in a area less than 1mm^2 is designed, simulated and fabricated. The fabrication of waveguide is performed using UV-photolithography. The fabricated optical waveguides behave like a Mach-Zehnder interferometer. Light coupled and decoupled through embedded optical fibers are measured at various modulation frequencies. The results are promising as a low-cost, home fabricated MOEMS interferometer for use in various application in bio-imaging, material testing as well as point of contact devices.

Reference:

[1] L. M. Lechuga, K. Zinoview, L. Fernandez, J. Elizalde, O. E. Hidalgo, and C. Dominguez. “Biosensing microsystem platform based on the integration of Si Mach Zehnder interferometer, microfluidics and grating couplers,” *in Proceeding of SPIE*, (2009).

[2] Y. Li, J. Jing, Y. Qu, Y. Miao, B. Zhang, T. Ma, M. Yu, Q. Zhou, and Z. Chen, Biomed. "Fully integrated optical coherence tomography, ultrasound, and indocyanine green-based fluorescence tri-modality system for intravascular imaging," Opt. Express 8, 1036-1044 (2017).

[3] J. Chen, P. W. Tse, and H. Zhang, “Integrated optical Mach–Zehnder interferometer-based defect detection using a laser-generated ultrasonic guided wave” Opt. Lett. 42, 4255-4258 (2017).

[4] Robert G. Hunsperger, “Integrated Optics Theory and Technology” 2009 sixth edition pp.45-47

Initial lab test results of Magneto-Optic Current Sensor diagnostic developed for plasma current measurement in tokamaks

Santosh P. Pandya[1,2], Kumudni Assudani[1,3], Praveenlal E. V.[1], Lavkesh T. Lachwani[1], Sameer Kumar Jha[1], M .V. Gopalakrishna[1] and Surya Kumar Pathak[1,4]

[1]*Institute for Plasma Research, Near Indira Bridge, Bhat, Gandhinagar – 382428, India.*
[4]*Homi Bhabha National Institute (HBNI), Anushaktinagar, Mumbai-400094, India.*
Email: [2]psantosh@ipr.res.in, [3]kumud@ipr.res.in

Abstract: Measurement of the plasma current is a fundamental parameter for plasma characterization in devices such as tokamaks. Conventionally, the plasma current measurement is performed by a Rogowski coil. However, there are a few drawbacks associated with this technique such as drift of integrator for long operation, electromagnetic interference and radiation-induced noise in case of nuclear environment. To resolve these issues, the Magneto-Optic Current Sensor (MOCS) based on the principle of Faraday effect can be utilized to measure the plasma current directly. The MOCS measures the rotation-angle of the linearly-polarized laser light passing through an optical fiber loop enclosing the current channel. The MOCS diagnostic is being designed and developed for the Aditya-Upgrade tokamak. In this paper, we report the development of a prototype MOCS diagnostic system, its initial testing results and comparison with a theoretical model.

1. Introduction

Measurement of the plasma current is the most direct evidence to determine the merit of a plasma discharge in tokamaks and fundamental parameter for plasma diagnostic. Reliable measurement of plasma current is an important parameter for the safe operation of Tokamak and real-time control as well. Conventionally, the plasma-current is measured by inductive sensors such as Rogowski coil or array of pick-up coils. The Hall-effect sensor is also utilized for the steady-state magnetic field / current measurements. However, in view of the future steady-state fusion devices such as ITER, DEMO and the present-day steady-state tokamaks, conventional plasma current measurement diagnostic techniques need to be replaced by measurement techniques that do not require integrators. Besides, the radiation-induced environment introduces noise in the conventional plasma-current measurement system. For steady-state plasma, accurate measurement of plasma current would be of concern due to the drift problem in the integrator. The magneto-optic effect in the optical fiber can be one such technique to utilize for this purpose [1]. Magneto-optic Current Sensor (MOCS) based on the principle of Faraday effect can be utilized to measure the plasma current directly by measuring the rotation angle of a linearly-polarized light passing through the optical fiber loop enclosing plasma current channel.

For the ADITYA-Upgrade tokamak [2] at IPR to measure plasma current in the range from few kA to hundreds of kA (typically flattop current ranges between 150- 250 kA), a prototype MOCS diagnostic system is designed, developed and tested for its functionality. Here we are reporting the design and development of a prototype MOCS to test the functional characteristics for a few tens of kA. Section-2 describes the basic principle. In section-3 calibration and initial results are described. Conclusions and future work are summarized in section-4.

2. Basic detection principle of MOCS

When a linearly polarized light is launched through a single-mode (SM) optical fiber-loop around a current-carrying conductor so that there is a magnetic field ($\vec{H}$) component parallel to the direction of propagation of

light (Fig.1a), then it is observed that the direction of polarization of the emergent light rotates through an angle (θ) according to eq.(1). This phenomenon is known as *Magneto-optic Faraday effect*.

$$\theta = V_\lambda \int_L \vec{H} \cdot dl = V_\lambda I \quad (1)$$

Here, V_λ is a Verdet's constant and L is the length of the optical fiber. The constant, V_λ, depends on the medium as well as the wavelength (proportional to $1/\lambda^2$). For a fused-silica fiber, $V_\lambda \sim 4.68 \times 10^{-6}$ rad/A at λ= 633 nm.

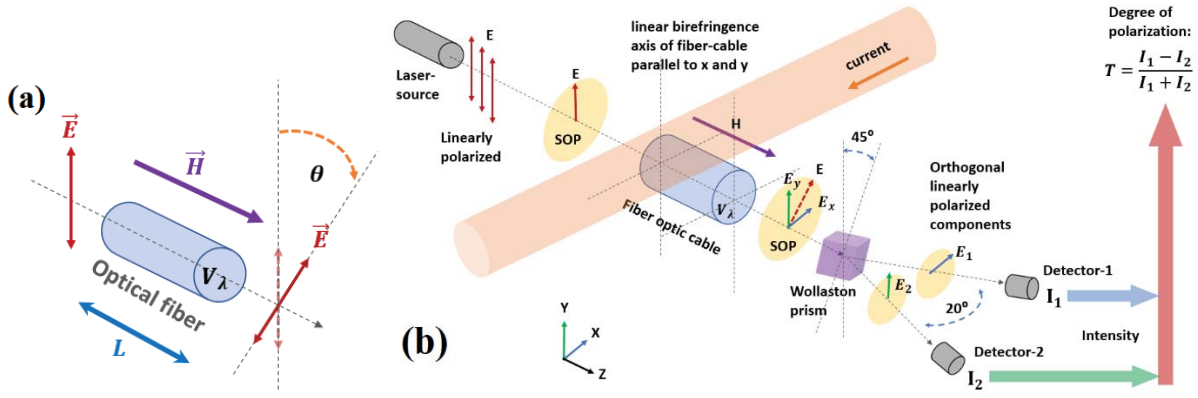

Figure-1*: (a) Magneto-optic Faraday effect and (b) Basic layout of the MOCS current detection setup in the lab*

Fig.1b shows an experimental setup of the MOCS system in the lab. The angle of rotation (θ) is measured using a Wollaston prism which produces two orthogonal linearly polarized beams of incident laser light with a small divergence of 20^0. The intensities of these two beams (I_1 and I_2) are detected separately by two photodiodes. If the optical axis of Wollaston prism is oriented at 45^0 w.r.t. the linear birefringence axis of fiber-cable (Y-axis in Fig.1b) then the amplitudes of the electric field ($\vec{E}$) of the light falling on the two photo-diodes, E_1 and E_2 and the degreee of polarization are described by eq.(2).

$$E_1 = \frac{E_x + E_y}{\sqrt{2}}, \qquad E_2 = \frac{E_x - E_y}{\sqrt{2}}, \qquad T = \frac{I_1 - I_2}{I_1 + I_2} = \frac{|E_1|^2 - |E_2|^2}{|E_1|^2 + |E_2|^2} \quad (2)$$

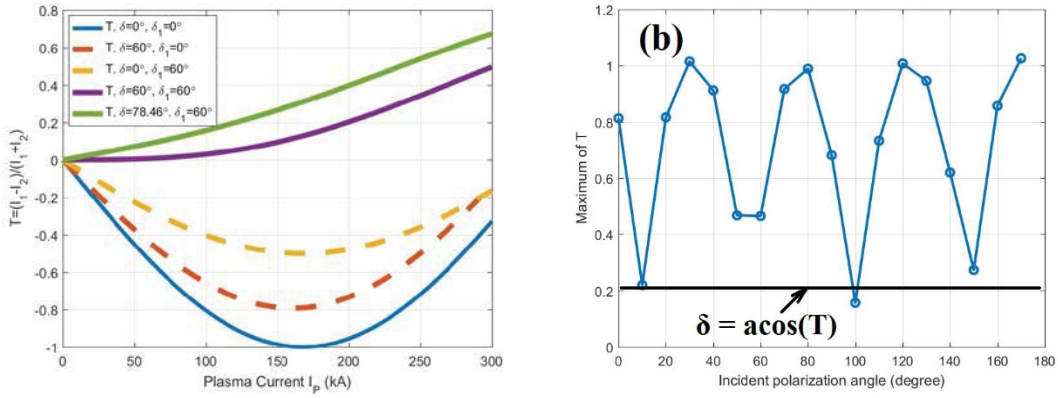

Figure-2: *(a) Degree of polarization as a function of plasma current using $T = -\sin 2\theta$, and Eq.(1) & (4) with a few values of* δ *and* δ_1*,(b)Measurement of linear birefringence of fiber-loop in the lab by taking* δ=acos(T_{min})

The measurement of plasma current can be carried out by the following method. The particular adjustment of the Wollaston prism as mentioned earlier is called the Sine-detector configuration and in the limit of linear birefringence δ≈0 or θ>>δ/2, the relation between the degree of polarization, T, and θ is given by $T = -\sin 2\theta$.

Since the direct measurement of T provides information about θ, it gives a measurement of plasma current (I_P) enclosed by the fiber loop (eq.(3)). Fig.2a shows such dependency in absence of linear birefringence, δ, for current up to 300 kA corresponding to the range of θ from 0 to 1.404 rad.

$$I_P = \theta/V_\lambda \equiv |-(sin^{-1}(T))/2V_\lambda| \quad (3)$$

This is valid only if the fiber preserves the State of Polarization in the absence of magnetic field/current and also has negligible linear birefringence. However, in reality birefringence is introduced in experimental setup due to bending of optical fiber, the pressure applied by fiber holding structures, temperature variation and intrinsic birefringence introduced during manufacturing processes. Fig.2b shows an example of measurement of linear birefringence of SM Aluminum coated fiber-loop having a total length of ~1.55 m and loop radius of ~0.30 m. Hence, considering the effect of the linear birefringence, δ, of the fiber-loop and linear birefringence, δ_1, of exit section (between fiber-loop and Wollaston-prism) on the degree of polarization, T can be estimated by [2]. Fig.2a depicts such effect of the linear birefringence with a few combinations of δ and δ_1 inferred from experiments.

$$T = \frac{I_1 - I_2}{I_1 + I_2} = \frac{|E_1|^2 - |E_2|^2}{|E_1|^2 + |E_2|^2} = -2cos(\delta_1 + \eta) \times sin(\chi)sin(\phi/2) \times [cos^2(\phi/2) + cos^2(\chi)sin^2(\phi/2)]^{\frac{1}{2}} \quad (4)$$

Where, $(\phi/2)^2 = (\delta/2)^2 + \gamma^2$, $\tan(\chi) = 2\gamma/\delta$, and $\eta = \tan^{-1}\left(cos\chi tan(\phi/2)\right)$

3. Initial test results of the prototype MOCS system in the laboratory

To test the MOCS concept in the lab, a prototype system has been developed and installed on a coil having an operation current range of 2 kA-30 kA. The Al coated SM fiber loops around the current-carrying channel having a diameter 0.22m. A calibrated CT-probe has been utilized to measure the current passing through the coil and response of the MOCS signal registered. He-Ne laser (λ=633 nm, 5 mW) having linearly polarized light has been utilized as a light source. A λ/2 wave-plate is used to align the polarization angle of incident light with the optical fiber axis. The setup is synchronized with DAQ and to set desired current-pulse duration & amplitude.

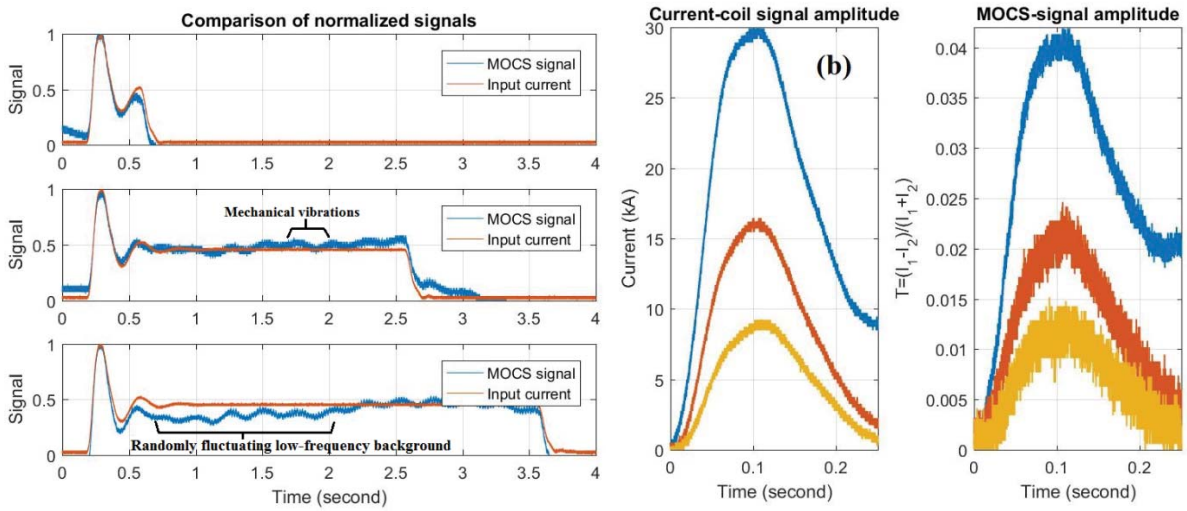

Figure-3: *(a) Comparison of different pulse duration between the normalized MOCS-signal and CT-probe signal and (b) Comparison of different current-pulse and MOCS-signal amplitudes after background correction.*

As shown in Fig.3a, the MOCS setup is responding to current pulses passed through the coil and a convincing signature of the faraday rotation is registered. The shape of the current pulse and time duration of the current pulse is detected by the MOCS and it is consistent (Fig.3a) for the different time duration. It has been observed that the amplitude of the MOCS-signal is proportional to the current amplitude passing through the coil (Fig.3b), where background correction is done by subtracting the background-level just before passing the current-pulse through the coil. By passing different known current amplitude through the coil, a calibration curve has been generated (Fig.4a). Fig.4b shows a reasonably good agreement of experimental data with the modelling results using eq.(4) where measured linear birefringence $\delta \approx 78.46^0$ and $\delta_1 \approx 60^0$ taken as input in the model. It is confirmed that the MOCS signal is purely optical and it is not electric-pickup. However, the baseline of the I_1-I_2 signal is randomly fluctuating around zero voltage-value with low-frequency amplitude which varies on the time scale of a few seconds (Fig.3a). It should be noted that the electronic noise level is within ~30mV. Care has been taken to isolate mechanical vibrations that can affect the background. The random fluctuating background appears only when light is passed through the optical fiber cable. This background could be resolved by using spun fiber and/or reflection method and is the future scope of the study as described in [3] and course of improvement.

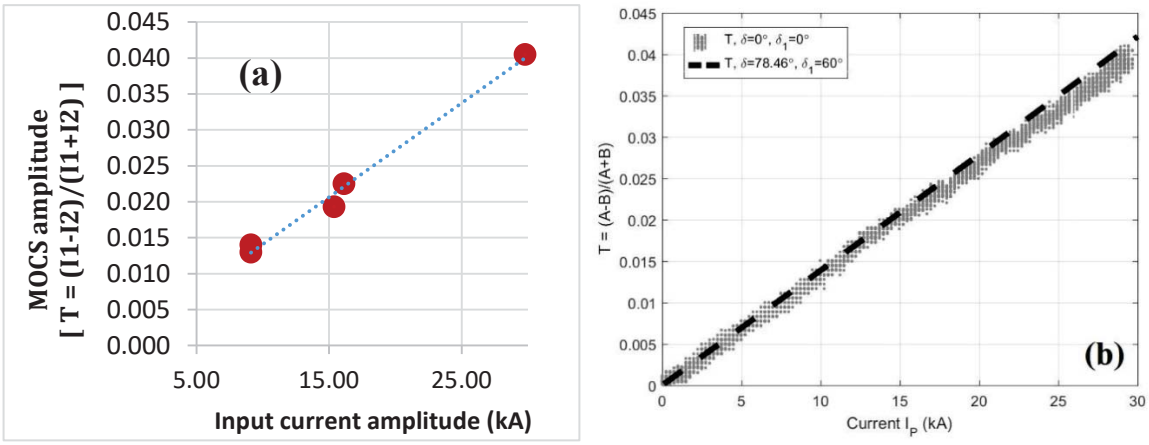

Figure-4: *(a) calibration curve (right), (b) comparison of experimental data (grey shaded area) with the modelling results (black dashed line) using eq.(4) where linear birefringence* $\delta \approx 78.46^0$ *and* $\delta_1 \approx 60^0$.

Conclusions and future work

A prototype MOCS is developed and tested for its functionality. The MOCS system gives a clear signature of the Faraday-rotation when a current is passed through the coil. The shape of the current pulse and time duration of the current pulse is detected by the MOCS and it is consistent with standard CT-measurement. It has been observed that the amplitude of the MOCS-signal is proportional to the current amplitude passing through the coil and the background signal level subtraction holds calibration. It is confirmed that the MOCS signal is purely optical and there is no electric-pickup. The experimental data agrees with the theoretical model by taking into account measured linear birefringence. As a next step, installation and operation of the MOCS-setup is envisaged for the ADITYA-U tokamak.

Acknowledgement: Mr. Manu Bajpai, SMARTX-C group members in the Beta-lab, IPR for providing us with the test facility and Dr. Raju Deniel for useful discussion and feedback.

References:

1. H. S. Lassing, *et.al.*, *Applied Optics*, **26**, No.12, pp2456-2460 (1987).

2. R. L. Tanna, *et.al.*, *Nuclear Fusion*, **59**, No. 11, 112006 (2019).

3. Ph. Moreau, *et.al.*, *Fusion Engineering and Design*, **86**, No. 6–8, 1222-1226, (2011).

Investigation of gamma radiation response of multimode graded index fiber in visible region for distributed dosimetry applications

S. Chaubey[1*], M. K. Saxena[1], J. Kishore[1], T. K. Sahu[2], G. Haridas[2], O. Prakash[1], S. K. Dixit[1]

[1]*Fiber Sensors Lab. (FSL), FSOSS, RRCAT, Indore, India -452013*

[2]*Health Physics Division, Bhabha Atomic Research Centre, Mumbai, India-400085*

[*]Email: smita@rrcat.gov.in

Abstract

This paper presents the studies on the effect of gamma radiation on multimode (MM) graded index fiber for intended application in gamma radiation dose distributed optical fiber sensor (DOFS). This study has been performed in real time using a visible light source and a spectrophotometer. Gamma radiation exposure of optical fiber induces increase in fiber attenuation which can be calibrated for the measurement of total absorbed dose. This study confirmed the feasibility of using a pulsed 532 nm laser as probe wavelength for the development of gamma radiation dose DOFS which can sense low level gamma radiation dose (< 1 Gy).

Introduction

Several applications likespace research, high energy particle accelerators and physics research experiments require detection of ionizing radiation. Ionizing radiations cause generation of defect centers in optical fibers (OFs), which result in creation of absorption bands in UV, VIS or near IR region. Due to this feature, when an OF is exposed to ionizing radiation, an increase in light attenuation occurs. This feature of OFs makes them extremely suitable for the development of fiber dosimeters[1].

In addition to the advantages of immunity to electromagnetic field radiation, small size, lightweight and capability of remote real time measurements, OF based dosimeters can be tailored by properly selecting the length of the sensor fiber, choice of fiber doping elements and choice of proper probe wavelength. This facilitates the development of fiber dosimeters in accordance with the required dose range.

DOFSs for gamma radiation dose further have the advantage of detecting the location of the gamma radiation dose as it involves the time of flight measurement in conjunction with Rayleigh scattering and formation of radiation induced color centers in OFs[2]. Such systems have been successfully implemented in the high energy accelerator facilities of CERN[3] to monitor radiation levels and predict equipment and material life times.

Authors have earlier demonstrated that multimode graded index fiber can be used as sensor fiber in gamma radiation DOFS in real time environments[2]. Since the standard commercially availabe optical time domain reflectrometers (OTDRs) are available with 850 nm and 1300 nm input probe wavelengths for MM fibers, it was observed that the minimum gamma radiation that could be detected with 5 m length of sensor fiber was 10 Gy. However, radiation levels present at particle accelarators, where distributed radiation sensing is particularly required, are generally quite low (< 10Gy). It was observed earlier that 10 m length of sensor fiber became almost dark at 532 nm after a gamma radiation exposure of 42.5 Gy. This indicated that the use of 532 nm as the probe wavelength for gamma radiation DOFS can further lower down the detection limilt well below 10Gy. Hence, to check the feasibilty of 532 nm as probe wavelength for gamma radiation DOFS, gamma radiation response of 4 m lenghth of MM graded index fiber was studied in visible region of light spectrum.

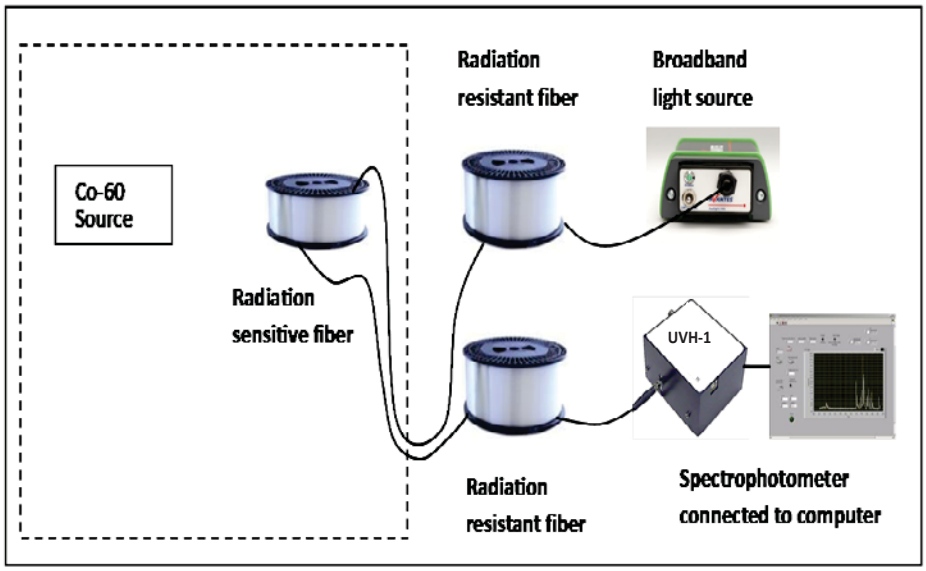

Fig. 1: Schematic diagram for the online study of gamma radiation response of MM graded index fiber arranged in the configuration of gamma radiation DOFS.

Experiment and results

Fig. 1 shows the schematic diagram for online study of gamma radiation response of radiation sensitive (RS) fiber (MM graded index, 62.5µm/125µm) in visible region of light spectrum. As this RS fiber was to be used in a DOFS, it was arranged in the configuration of gamma radiation DOFS. For this, 4 m length of RS fiber was wound on a fiber spool and connected between two fiber spools of non-radiation sensitive (NRS) fiber (communication grade MM, step index, 50µm/125 µm).

One end of RS fiber was spliced to one end of 195 m length of NRS fiber. Other end of this NRS fiber was then connected to the UV-visible broadband light source (model: Avantes, make: Avalight-HAL-S-Mini, 360 nm to 2500 nm) using a spliced MM patch cord. About 5 m length of similar NRS fiber was connected to the other end of RS fiber. The output end of this NRS fiber was finally connected to a UV-visible spectrophotometer (model: LR1, make: ASEQ Instruments, Ireland) through a spliced MM patch cord.

A gamma irradiation facility (Spec-300 Co-60) in RRCAT, Indore was used for gamma radiation exposure. The RS fiber was exposed to gamma radiation and online changes in transmission spectrum of sensor fiber were recorded at different gamma radiation doses in the dose range of 0.66 Gy to 17.32 Gy. The dose rate of gamma radiation source was 4 Gy/hr. Data processing and analysis of observed results showed considerable decrease of 60% in the transmitted output at 532 nm, after total gamma radiation dose exposure of 17.32 Gy.

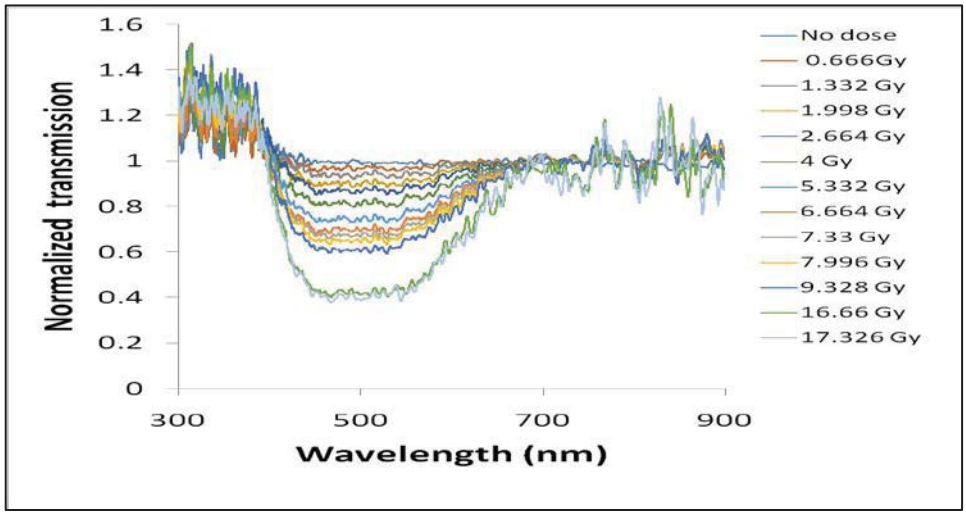

Fig. 2: Normalized changes in the transmission spectrum of sensor fiber at different gamma radiation exposures, observed in real time.

Fig. 2 shows the normalized changes in the transmission spectra of sensor fiber at different gamma radiation exposures, observed in real time. A significant decrease of 20% transmitted signal was observed at 532 nm even at a small gamma radiation dose of 0.66 Gy. The total decrease in transmitted signal at 532 nm was about 60% after a gamma radiation exposure of 17.3 Gy.

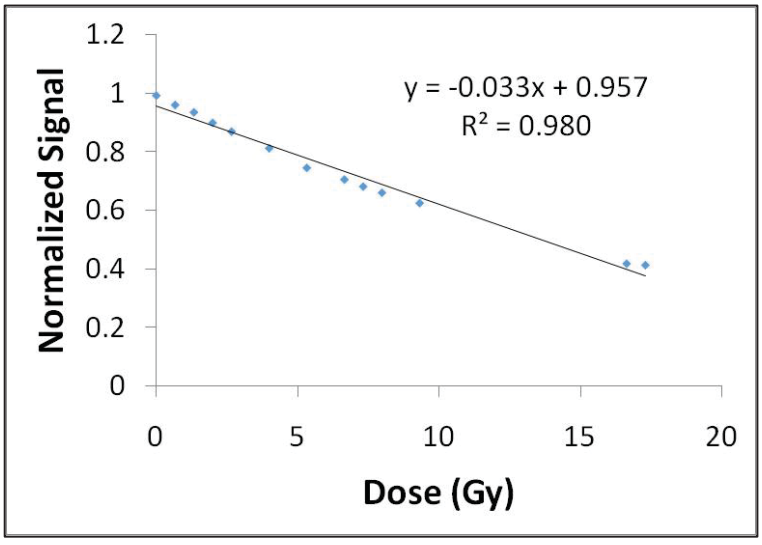

Fig. 3: Decrease in the normalized transmitted output at 532 nm, with increase in gamma radiation dose up to 17.3 Gy.

As shown in Fig. 3, the decrease in the transmitted output, with increase in gamma radiation dose was almost linear with a sensitivity of 0.825 %/m/Gy. It is also interesting to note that the room temperature relaxation of the exposed fiber for 49 days showed a 10-12% recovery of the signal.

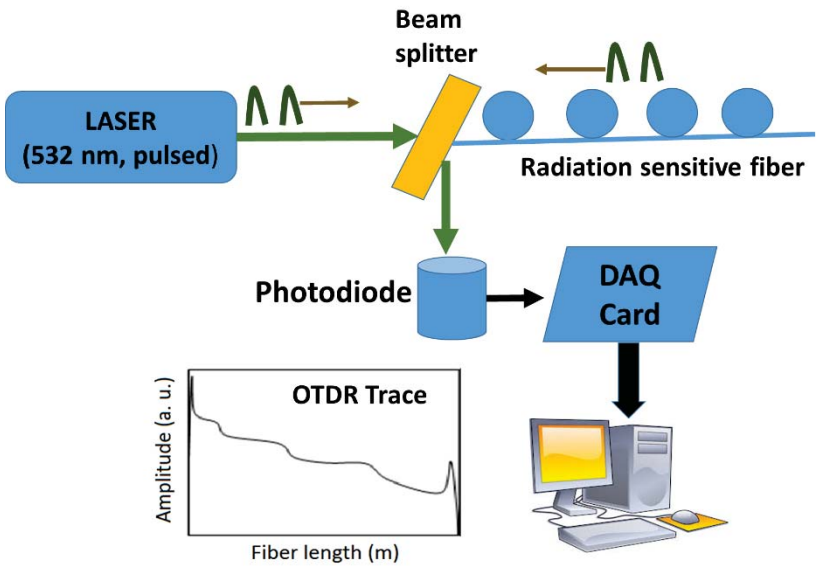

Fig.4: Schematic diagram for gamma radiation DOFS using a pulsed 532 nm laser.

It is, in near future, planned to develop and incorporate a 532 nm pulsed laser based OTDR system to detect the location of the radiation zone for the development of complete gamma radiation distributed optical fiber sensor (DOFS). A typical schematic diagram of the complete setup is depicted in Fig. 4. It also shows the expected OTDR signal from which radiation dose could be estimated.

Conclusion

In conclusion, the gamma radiation response of a MM graded index fiber in visible region of light spectrum, in real time is investigated for the intended development of a gamma radiation DOFS. Radiation induced attenuation is found to increase linearly with increase in absorbed gamma radiation dose. This study will help in the development of DOFS at 532nm wavelength to detect gamma radiation dose even for the dose well below 1 Gy level.

Acknowledgements

The authors are thankful to Dr. S. Kher, Ex-Head, FSL, FSOSS, RRCAT for his help and support.

References

1. S. Girard, J. Kuhnhenn, A. Gusarov, B. Brichard, M. V. Uffelen, Y. Ouerdane, and A. Boukenter, *IEEE Trans. Nucl. Sci.*, Vol. **60**, No. 3. (2013)
2. S. Chaubey, M.K. Saxena, S. Kher, T. K Sahu, G. Haridas, S.K. Dixit, *Proceedings of National Laser Symposium-28,* VIT, Chennai, Jan. 8-11, 2020.
3. D. Di Francesca , I. Toccafondo , G. Li Vecchi , S. Calderini, S. Girard, A. Alessi , R. Ferraro , S. Danzeca, Y. Kadi , and M. Brugger, *IEEE Trans. Nucl. Sci.*, Vol. **65**, No. 8. (2018)

Implementation of position measuring system for Hall probe alignment in undulator magnetic field measurement

Saif Mohd Khan*, Mona Gehlot[1], G. Mishra
School of Physics, Devi Ahilya VishwaVidyalaya, Indore, 452001, Madhya Pradesh, India.
[1]MaxIV Laboratory, Lund University, Sweden
*Email: saiffukhan@gmail.com

Abstract-

Position sensing detectors are silicon photodiodes that provide analog output signal directly proportional to the position of the light spot on the detector active area. In this paper we study the Hall probe alignment with the aid of a position measuring system based on tetra lateral pin cushion type position sensing detectors on magnetic field measurement of 20 mm period hybrid undulator. It is shown that by implementing the position measuring system in the Hall probe measurement bench, the straightness of the electron trajectory is improved.

1. Introduction

Undulator science is the key technology area for synchrotron radiation sources and free electron lasers. In a synchrotron radiation source, the relativistic electron beam travels through the undulator field and emit radiation, the radiation interfere constructively at each successive poles. The intensity adds at certain wavelengths resulting in a quasi monochromatic spectrum. In the free electron laser, the transverse motion of the electron in the undulator exchange energy with the electric field of the co-propagating laser to emit coherent radiation. The undulator magnet is a periodic magnetic field made up of dipole magnets to extract a sinusoidal magnetic field profile. The magnetic field of a real fabricated device deviates from the sinusoidal field thus introduces several quality reduction factors. Together with the magnetic field quality along the length of the undulator, a tight tolerance is set on the precise evaluation of the field integrals. Ideally both the field integrals should be zero along the beam axis so that there is minimum distortion on the propagating electron beam and the undulator remains transparent to the propagating electron beam throughout the length. A high accurate and precision magnetic measurement system is required to design and optimize the undulator to achieve this purpose. A standard procedure and method of measuring and characterizing the undulator is the Hall probe method. In this method a point to point field mapping is done along the length of the undulator and the field integrals are numerically calculated. The Hall probe has its limitations. In the Hall probe method, a carriage on the bench carries the probe through the undulator at a certain speed and delay while the measurements are being performed. The alignment errors of the probe motion from vertical, horizontal and axial carriage motion, carriage yaw error, and probe angle deviation are often put into the field of the undulator.

In this paper we discuss development and implementation of a position measuring system to control the vertical probe motion error during the probe motion on the linear stage. The scheme employs two position sensing detectors in combination with retroreflectors. It is shown that the system effective to obtain straightness in the electron trajectory and improves the field integral.

2. **Theory and Position measuring system**

The magnetic field of the undulator is given by

$$B_y = B_0 \cosh(k_u y)\sin(k_u z) \tag{1}$$

y, z are the vertical and longitudinal coordinates. The first and second field integrals of an undulator magnet are defined as [1],

$$I_1 = \int B_y dz \quad , \; I_2 = \iint B_y dz dz' \tag{2}$$

B_y is the vertical magnetic flux density and z is the longitudinal coordinate. Eq. (1) when multiplied by $q / \gamma mc$ indicates the angular and position of the electron beam. In practical units, Eq. (1) is read by

$$x'(mrad) = 0.3 I_1 (Tmm) / \text{E(Gev)}$$

$$x(\mu m) = 0.3 I_2 (Tmm^2) / \text{E(Gev)} \tag{3}$$

It is required that the probe moves along the undulator axis or with some pre-defined tolerable misalignment. Given some misalignment error in the vertical and horizontal direction while moving along the longitudinal motion, the probe incurs error, given from Eq.1 as

$$\frac{\Delta B}{B} = (2\pi / \lambda_u)^2 \cosh(k_u y) \frac{\Delta y^2}{2} \tag{4}$$

The schematic of the Hall probe bench is illustrated in Fig.1. The Hall probe bench uses a F.W. Bell make, Model No 8010 Tesla meter and F.W. Bell make probe [STF81-0402-10]. The probe stem is 50mm in length and held in a round support of 4mm diameter. The probe holder is mounted on a xy stage; 25 mm travel distance each and moves on a motorized z-linear stage of 1500mm length. A stepper motor with a single axis motion controller drives the xy stage unit on the z-linear stage. The motion controller is programmed to control the speed of the travel, delay time and step length of measurement by the user.

We have implemented 2D position sensing detector based position measuring system to align the Hall probe in both vertical and horizontal directions. For alignment there are two possibilities. The laser can be fixed on a position and 2D PSD can be mounted on the Hall probe sledge. Alternately the laser can be get reflected from the Hall probe sledge to the 2D PSD located and fixed. We implemented the second option. We use Thorlabs make PDP90A 2D lateral effect position sensing detectors which is tetra lateral PSD. It works in the range 320-1100nm. The tetra lateral PSD is a pin cushion type sensing device. The active area is 9 x 9 mm at the waist of the pin cushion. The area extends to 10 x 10 mm at the outermost regions. The calculations for the position measurement are done from the wider part of the sensor i.e. 10 x 10 mm. A 5mW Laser diode Ultra Low Noise (ULN) Coherent make, Part No 31-0144-000 with 635nm, 5mW power is used as the light source. The light from the laser goes to the retro reflector Newport make, Model No 05BR08AR.14 through a beam splitter. The retro reflector mount is in house designed and fabricated such that it can be rotated vertically and horizontally as per the user. It is shown in Fig.2. The Newport make Model No 10FC16PB.3 beam splitter (50:50) (BS) works in wavelength range 420-680nm. The light reflected from the retro reflector is then reflected towards the PSDs with the help of combination of protected silver coated mirrors (M1, M2, and M3) Thorlabs make, Model No. PFSQ10-03-P01 and this light passes through the combination of Neutral Density (ND1) filters which provides the transmittance of 1.5% of light towards the PSD. The ND filter mount is shown in Fig3. The power level of 40μW (1.5 % of 2.5mW) falls on the PSD such that the output voltage is ≤ 4V to

ensure the best signal-to-noise ratio and avoids signal saturation. The physical size of the components is summarized in Table 1. Light from the ND filters detected by the position sensing detectors mounted on small xyz stages for alignment. The actual light spot position is read as,

$$x = \frac{L_x(V_{BC} - V_{AC})}{2\sum V} \ , \ y = \frac{L_y(V_{AB} - V_{CD})}{2\sum V} \tag{5}$$

Where L_x length of the detector along x-axis is, L_y is length of the detector along y-axis. The offsets in the horizontal and vertical direction reads,

$$\Delta x = (x_A + x_B)/2, \Delta y = (y_A + y_B)/2 \tag{6}$$

Where x_A, x_B, y_A, y_B are the readings of the two PSDs employed in the set up. The resolution of position sensing detector is given by,

$$\Delta R = L_x \left(\frac{e_n}{V_o} \right) \tag{7}$$

Where ΔR is the resolution, L_x is the detector length which is 10mm, e_n is the output noise voltage which is $300 \mu V_{rms}$ for PDP90A and V_o is the SUM output voltage level. The position resolution of the position sensing detector is 1.7 micron. The position resolution is the minimum detectable displacement of the light spot incident on the position sensing detector. The position sensing detector is interfaced with Thorlabs make KPA101K cube Auto aligner. Embedded software allows the unit to communicate with the position sensing detector. USB connectivity provides PC controlled operation in Kinesis software provided by Thorlabs. Two different PCs are being used for the sake of convenience regarding our current setup but it can also be done with single PC.

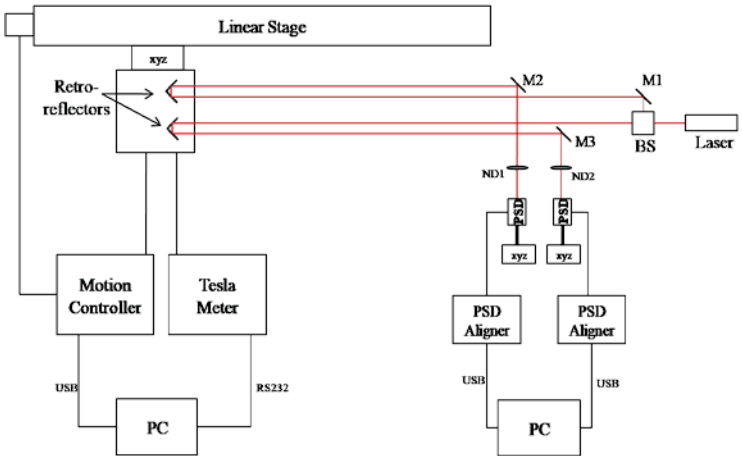

Fig.1 Hall probe bench

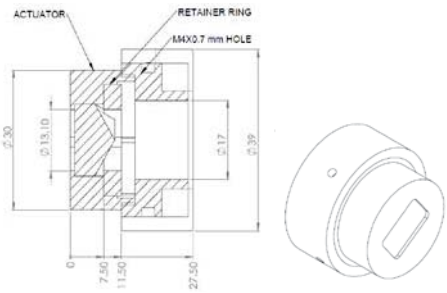

Fig 2 design of retro reflector mount

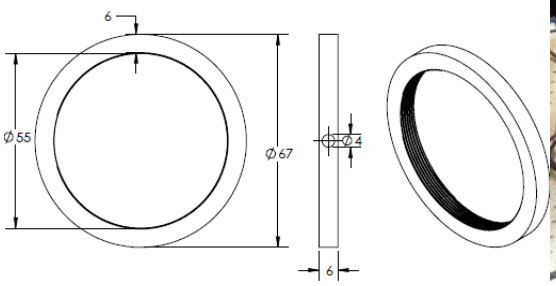

Fig 3 Design of ND Filter mount

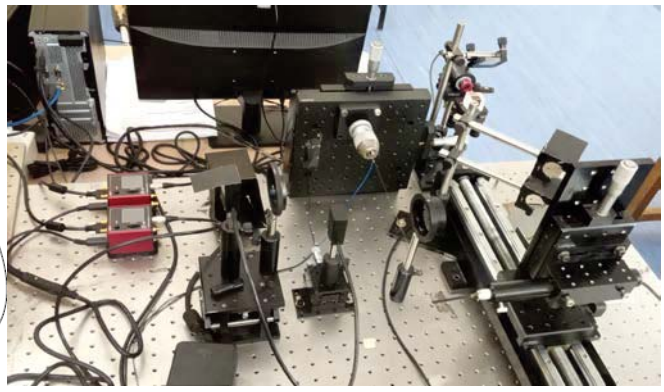

Fig.4 Complete position measuring system with PSDs

3. **Results and Discussion**

A complete photograph of the position measuring system is shown in Fig.4. After alignment of the Hall probe with PSD, the offset of the Hall probe is 225 micrometer in the undulator length. The result is shown in Fig.5. The field is mapped and the result is shown in Fig.6 for the second field integral. In Fig.6, the data is taken at a gap of 10 mm; the curve 1 represents the measurement without the implementation of the PSD in the Hall probe bench. The curve 2 is obtained after implementing the PSD in the Hall probe bench. The curve is still displaced from the axis and there is a field integral value at the end of 115 Gcm^2. From Eq. (3), this calculates to 43 micrometer offset from the undulator axis for an electron beam of 8MeV. For the curve 1, a similar calculation yields a trajectory offset of 1500 micrometer. The improvement in the trajectory offset is around 97%. [2-4].The horizontal displacement calculation from the PSD is shown in Fig.7.

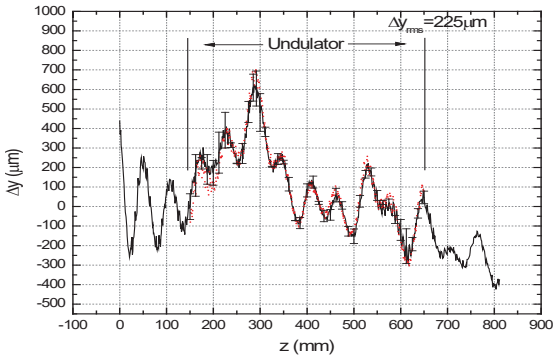

Fig.5 Hall probe sledge alignment by PSD.

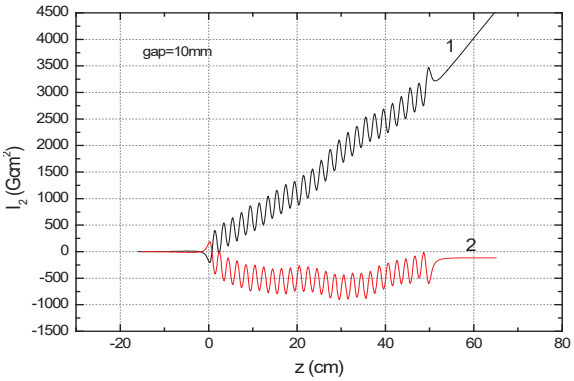

Fig.6 comparison of second field integral from Hall probe data

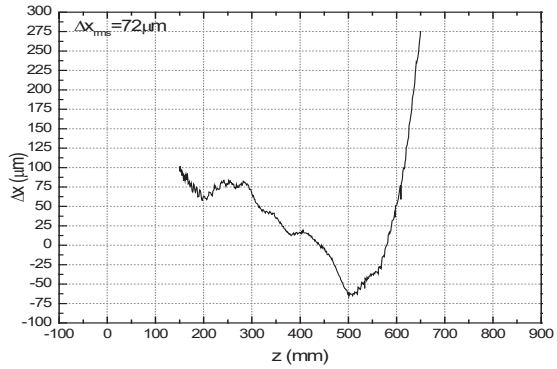

Fig7 x-Alignment by PSD

Table 1

Laser Spot size	01 mm
PSD wavelength range	320 nm – 1100 nm
PSD sensor size	09 mm × 09 mm
Retroreflector dimension	12.7 mm
Beam Splitter dimensions	25.4 mm× 25.4 mm× 25.4mm
Mirror dimensions	25.4 mm × 25.4 mm
ND filter diameter	55 mm

References

[1] J. Pflueger, Undulator technology*, Proceedings of the CAS- CERN Accelerator school: Free electron laser and energy recovery linacs*, Hamburg, Germany, 31 May-10 June, 2016.

[2] G. Mishra, Mona Gehlot, Roma Khullar, and Geetanjali Sharma, "Magnetic field integral requirements and measurement of 20-mm period hybrid undulator*", IEEE Transactions on Plasma science*, **Vol. 47**, No.7 (2019).

[3] Mona Gehlot, Saif Md. Khan, Frederic Trillaud, G.Mishra, Magnetic field integral measurements with stretchewire and Hall probe methods, *IEEE Transaction on Magnetics*, **Vol.56**, No.5 (2020)

[4] Mona Gehlot, G.Mishra, Magnetic measurement and analysis of trajectory straightness of 20 mm period hybrid Undulator, *Optik*, **203**, 164002 (2020).

Design and analysis of 2x1 photonic temporal multiplexer using SOI ring resonator for switching and logical applications

Madhupriya Ganesh, Mubarak Ali Meerahsa, Indhumati Ravirajan and Krishnamoorthy Pandiyan

Integrated Optics Lab, Centre for Nonlinear Science and Engineering (CeNSE), School of Electrical & Electronics Engineering, SASTRA Deemed-to-be University, Thanjavur-613401, Tamil Nadu, India.

E-mail: krishpandiyan@ece.sastra.edu

Abstract

In this work, we have designed 2x1 photonic multiplexer using ring resonators of 6 μm radius having an free spectral range (FSR) of 18~19 nm using silicon on insulator (SOI) platform. The transmission characteristics and coupling factors of both the all-pass and add-drop configuration are analysed especially for switching and configuring logical circuits.The numerical simulations of the ring configurations are done using the finite-difference beam propagation method (FD-BPM). The voltage tuning across the p-i-n juction has been demonstrated.Various design parameters are optimized to offer a switching voltage of 0.67 V. The design of 2x1 temporal multiplexer is implemented using ring resonator which has a minimum switching voltage and offers minimal losses.

Keywords: Silicon on insulator (SOI), all-pass ring, add-drop ring, photonic logic circuits

I. Introduction

The large scale integration of the photonic circuit have been emerging for the past few decades and still under research. This involves active integration of both the passive and the active components within a miniaturized chip.The photonic platforms that are compatible for micro ring resonator devices are silicon on insulator (SOI) [1] , GaAs-AlGaAs[2] and Lithium Niobate on Insulator (LNOI) [3]. Also hybrid integration of the LN on the silicon platform have been a wide area of research. Also these resonators are experimentally verified [4] which is inline with the theoretical models[5]. Micro ring resonators (MRR) have a wider variety of applications which includes filters and switches[6], sensors[7] and modulators[8].

II. Design of SOI micro-ring resonator

The proposed model of MRR, having a ring radius of 6 μm can be configured to work as a switch. By default the ring is in the off-state, since it has resonance at a wavelength of 1555 nm. So by applying voltage across the ring , the on-state can be tuned. Both the types, all-pass ring and add-drop ring have been analysed in this work.

The all- pass configuration is tuned initially to be in off-state. The SOI waveguide has a dimension of 450x200 nm with a bottom slab of 2.45 μmx50 nm dimensions, which has a top and bottom SiO_2 cladding of 3 μm and 2 μm in silicon substrate respectively. It consist of the bus and the ring waveguide, placed 0.3 μm apart and are tuned for a resonance drop in voltage.The voltage applied across the ring produces a considerable change in the refractive index.

The change in refractive index corresponds to the number of free charge carriers in the intrinsic silicon core *(i.e),*a change in carrier concentrations(ΔN, ΔP) given by the equation,[9]

$$\Delta N = \frac{In\tau}{qSL} \tag{1}$$

Where I is the injected current, S is the area of the intrinsic region and the non radiative recombination life time of τ= 4 ns and the saturation current relation is given by,

$$I = Is\left(e^{\frac{qV_d}{nKT}} - 1\right) \tag{2}$$

Where V_d is the driving voltage across the p-i-n junction diode having 'q' charges with reverse saturation current Is, K represents Boltzmann constant, T is the absolute temperature and n is the ideality factor. The relation between the applied voltage corresponding to Δn can be well explained by Soref relation [10].

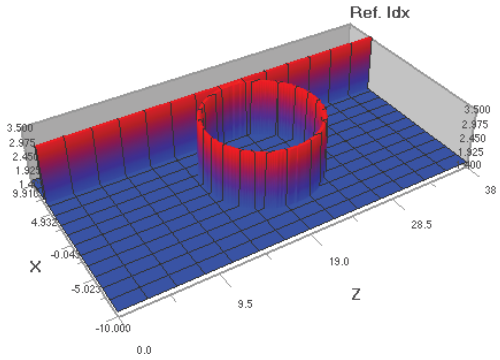

Figure 2: 3D refractive index profile of the ring resonator without applying external voltage

For the transmission characteristics at 0 V the device is in the off-state and a similar set of readings are taken at 0.67 V, which corresponds to change in index of Δn = 0.020.Comparing the resonance wavelengths in both the sets,the off-state of the device at 0 V has a maximum value when the voltage applied is 0.67 V *(i.e),* on-state.

III. Design of 2x1 photonic multiplexer using MRR

The FD-BPM numerical simulation of the 2x1 photonic multiplexer using ring resonators are based on the above theoretical modelling.

The working of the 2x1 photonic multiplexer is based on the logical truth table.The light input can be controlled by control inputs V_A and V_B at 1550 nm.

Case a) When both V_A =0 and V_B =0, both the MRR are at resonance and the light inputs are not allowed to propagate through the circuit.This case generally is generally considered as off-state.

Case b) When V_A =0 and V_B=0.67 V, then the MRR1 is at resonance and light does not propagate, whereas in MRR2 the light propagates.This yields I_B at the output port Y.

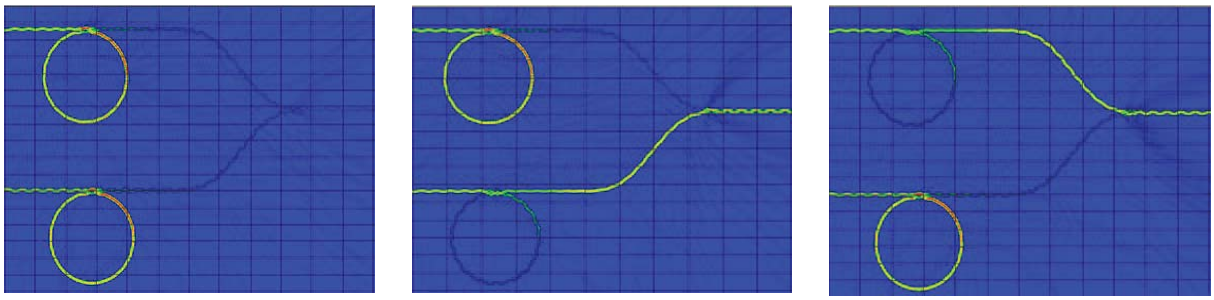

(a) (b) (c)

Figure 3: The photonic multiplexer operation a)V_A =0 &V_B =0 , b) V_A =0 &V_B =0.67 V and c) V_A =0.67 V & V_B =0

Case c) When V_A =0.67 V and V_B=0, then the MRR1 propagates the light input and the MRR2 is at resonance.The light from the MRR1 passes through the output port Y with intensity I_A.

Case d) When V_A =0.67 V and V_B=0.67 V, both the inputs propagate and interfere with each other when gives an intensity other than I_A and I_B which is not required. So this state is not allowed incase of multiplexer.

IV. Conclusion

We have demonstrated the modelling of 2x1 photonic multiplexer using micro-ring resonators. The principle of operation of the multiplexer is based on the voltage tuning mechanism at the p-i-n junction of the silicon waveguide structure, which enables active switching at 0.67 V at the resonant wavelength of 1555 nm.The designed MRR has FSR of 19 nm. The results obtained from numerical simulations of FD-BPM are verified by the theoretical calculation.Various figure of merit such as the transmission characteristics and FSR for both the all-pass and add-drop configuration have been analysed. These ring resonators can be configured further to implement any complex logical circuit applications.

ACKNOWLEDGMENT

This work was supported by the Science and Engineering Research Board (SERB), Department of Science and Technology (DST), Govt. of India (Ref. No.: CRG/2018/001788).

References

[1] L. Lu, L. Shen, L. Zhou, and J. Chen, “Silicon optical switch elements based on coupled-ring resonators,” *Opt. InfoBase Conf. Pap.*, vol. Part F83-A, pp. 4–6, 2017, doi: 10.1364/ACPC.2017.S4J.2.

[2] J. K. Rakshit, T. Chattopadhyay, and J. N. Roy, “Design of ring resonator based all optical switch for logicand

arithmetic operations - A theoretical study," *Optik (Stuttg).*, vol. 124, no. 23, pp. 6048–6057, 2013, doi: 10.1016/j.ijleo.2013.04.075.

[3] T. J. Wang and C. H. Chu, "Wavelength-tunable microring resonator on lithium niobate," *IEEE Photonics Technol. Lett.*, vol. 19, no. 23, pp. 1904–1906, 2007, doi: 10.1109/LPT.2007.907567.

[4] C. Wang, M. Zhang, M. Yu, R. Zhu, H. Hu, and M. Loncar, "Monolithic lithium niobate photonic circuits for Kerr frequency comb generation and modulation," *Nat. Commun.*, vol. 10, no. 1, pp. 1–6, 2019, doi: 10.1038/s41467-019-08969-6.

[5] W. Bogaerts, P. De Heyn, T. Van Vaerenbergh, K. De Vos, and S. Kumar, "Silicon microring resonators," vol. 73, no. 1, pp. 47–73, 2012, doi: 10.1002/lpor.201100017.

[6] Y. Tian, L. Zhang, Q. Xu, and L. Yang, "XOR/XNOR directed logic circuit based on coupled-resonator-induced transparency," *Laser Photonics Rev.*, vol. 7, no. 1, pp. 109–113, 2013, doi: 10.1002/lpor.201200036.

[7] L. Sun *et al.*, "Design and optimization of silicon concentric dual-microring resonators for refractive index sensing," *Opt. Commun.*, vol. 395, pp. 212–216, 2017, doi: 10.1016/j.optcom.2016.05.052.

[8] Q. Xu, B. Schmidt, S. Pradhan, and M. Lipson, "Micrometre-scale silicon electro-optic modulator," *Nature*, vol. 435, no. 7040, pp. 325–327, 2005, doi: 10.1038/nature03569.

[9] M. A. Meerasha, T. S. Meetei, G. Madhupriya, I. R. Rajan, M. Varadharajaperumal, and K. Pandiyan, "The design and analysis of a CMOS-compatible silicon photonic ON–OFF switch based on a mode-coupling mechanism," *J. Comput. Electron.*, no. 0123456789, 2020, doi: 10.1007/s10825-020-01550-1.

[10] R. Nandi, S. Kurudi, and B. K. Das, "Diffusion doped p-i-n/p-n diodes for scalable silicon photonics devices," *Integr. Photonics Mater. Devices, Appl. IV*, vol. 10249, p. 102490Q, 2017, doi: 10.1117/12.2265267.

Non Contact Method for Respiration Rate Measurement with Optical Interferometry

Anu Singh, Saurabh Mehta, Arpit Rawankar
Department of Electronics and Telecommunication, Vidyalankar Institute of Technology
University of Mumbai, India
asinghnu1996@gmail.com

Abstract

Respiration rate (RR) is vital indicator of individual's clinical condition. Commercial available devices for respiration measurement require straight contact of sensor to target surface which restrain the use of such devices in restrained environment. Hence there is a need to develop a non invasive or non contact method using optical interferometer. The proposed technique for RR measurement is compared with ECG derived RR. Subjects of different age group were monitored using ECG and proposed technique and deviation is calculated. The average deviation of proposed technique as compared to ECG is ± 0.15 breaths per min.

Keywords: Respiration rate, Homodyne detection, Michelson interferometer, ECG, baseline wandering.

1. Introduction

Crucial signs of subject which are generally monitored by clinical experts are temperature , pulse and respiration rate. The number of breathes taken by subject during time interval of sixty seconds in known as respiration rate. There are three main phases of respiration - inhalation, exhalation and control pause. The time duration of these phases decide the rate of respiration and abnormalities associated with subject. The traditional methods for measurement of respiration frequency include spirometers, sensors (inductive ,capacitive ,piezoelectric, magnetic)pulse oximeters and ecg derived respiration rate. The sensors methods have limitations of small measuring range, sensitivity and vulnerability to electric and magnetic fields[1]. These sensors require contact with the subject's body whose respiration frequency is to be measured. Sometimes the contact to the body's surface leads to damage or deformation of the body in stringent situations. Hence to satisfy the need a non invasive method which overcomes the limitations is developed using interferometry technique[2-4].Homodyne detection of Michelson interferometer is used to measure the vibration pattern on wrist wall .Later the baseline wandering of ECG and VCG signal is preserved to extract respiration rate[5]. The experiment was performed on subjects of different age group and gender. Breathing rate are compared to calculate the efficiency and deviation of interferometry method from ecg method

2. ECG derived Respiration Rate

A three lead module is used to monitor the electrical activity of heart with minimum distortion fig 1. This electrical signal gives the information regarding baseline wandering(respiration graph),abnormalities in breathing pattern, artifacts etc. various signal processing techniques are used to eliminate powerline interferences, electromyogram noise and motion artifacts .Heart rate variability and baseline wandering are important factor responsible for

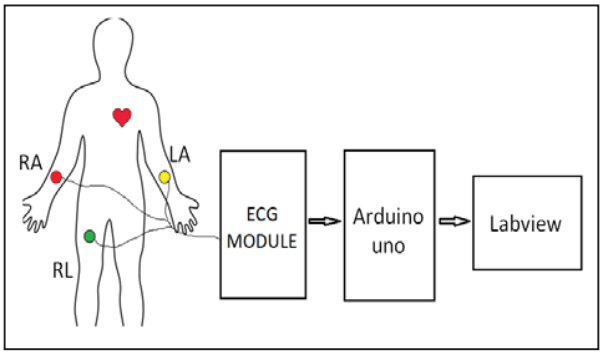

1. Measurement of ECG derived Respiration Rate

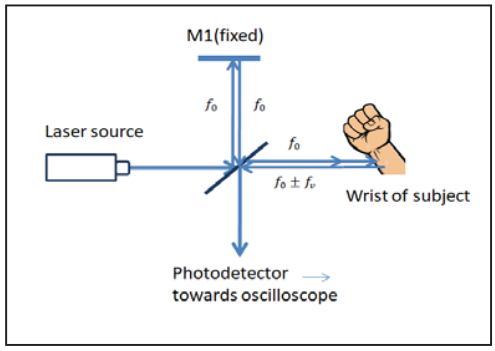

2. Michelson Interferometer with human subject

morphology of respiration graph. The rising edge of pattern is representation of inhalation while the falling ones as exhalation. The constant duration where there is no inhalation or exhalation is known as control pause.

3. Homodyne Detection of Respiration Rate using Michelson Interferometer

Interferometry consist of two main detection techniques-homodyne and heterodyne interferometry. Fig 2 shows the Michelson Interferometer with human subject using homodyne detection. The experimental setup is fixed with one movable mirror on the wrist of subject. A reflector mirror is placed on the wrist wall of subject such that the distance travelled by both the laser beams ie one from fixed mirror and other from target are equal before merging at beam splitter. The nano reflector on the subject's wrist vibrates with frequency of heart beat. A laser source of 650 nm as used as a light source. The laser beam is divided orthogonally into two equal beams of same frequency f_o by the beam splitter.These beams are incident on the mirrors where one is fixed and another is on reflector. As the vibration frequency f_m gets added to one of the frequency resulting $f_o \pm f_m$ .These frequencies get cancelled when combined by beam splitter and hence vibration frequency is recovered which is incident at the photodetector circuit.This obtained signal from subjects wrist is known as vibrocardiogram(VCG).

4. Results and Analysis

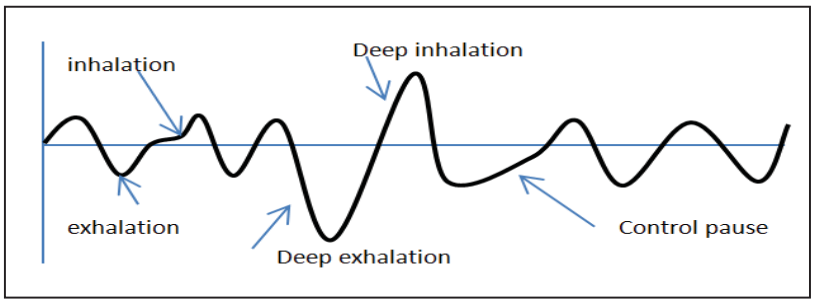

3. Phases of Respiration Rate

Above graph is a representation of respiration graph under normal condition with three main phases-inhalation , exhalation and control pause .the sharp concave up curve is known as deep inhalation while concave down as deep exhalation.. Respiration rate varies according to clinical condition and age group of subject. Age group of 12-25 yrs

have respiration rate of 12-20 breathes per minute while of toddler and children of 0.5-2 yrs have 24-30 breathes per minute. Below are the results of respiration rate graph derived from ECG and VCG techniques.

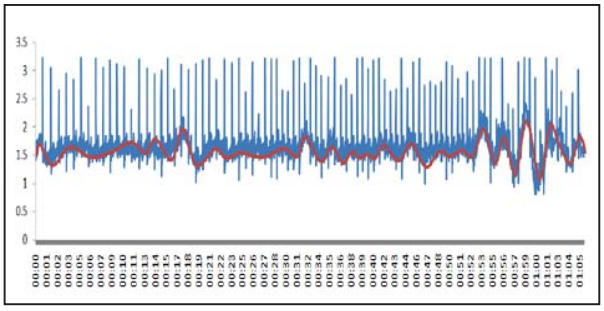

4. ECG signal graph 1

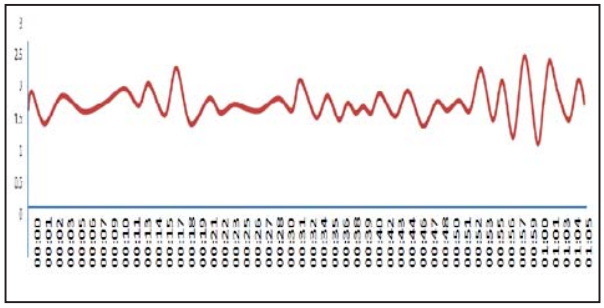

5. Respiration rate derived from graph 1

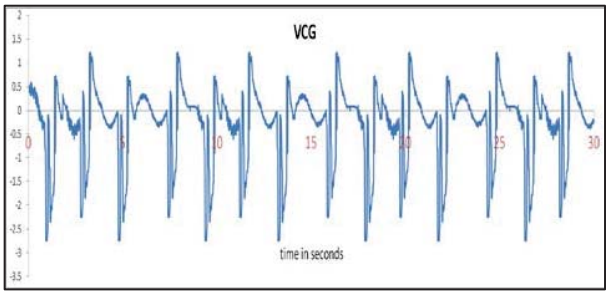

6. VCG signal graph 2

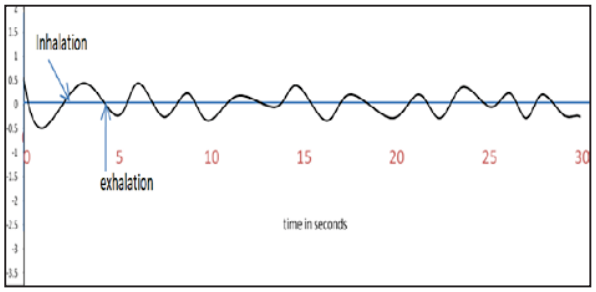

7. Respiration rate derived from graph 2

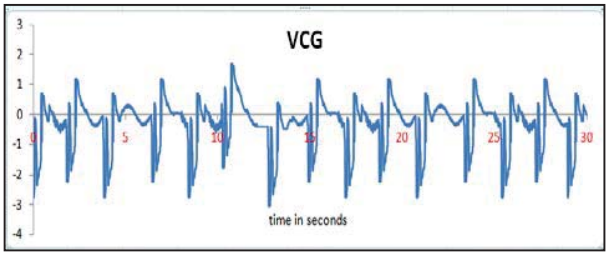

8. VCG signal graph 3

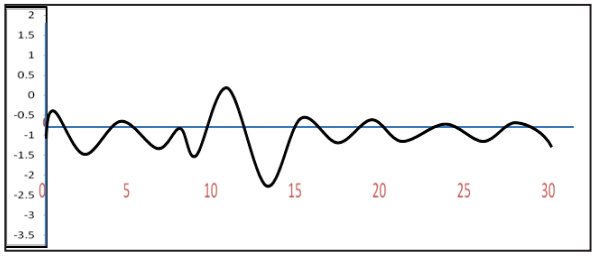

9. Respiration rate derived from graph 3

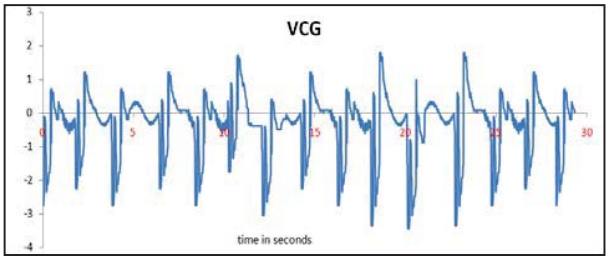

10. VCG signal graph 4

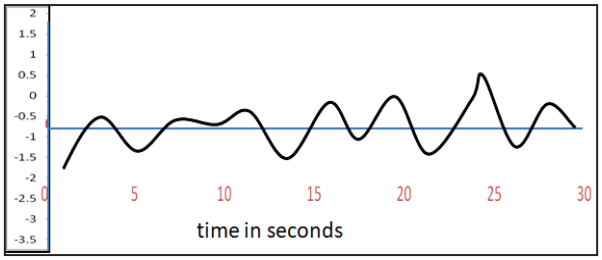

11. Respiration rate derived from graph 4

The respiration rates of several subject of similar age group are then combined to calculate group respiration rate.

The mean RR(respiration rate) is calculated for age group from both the methods and their deviation from each other is obtained. The mean deviation gives the error rate of VCG driven method for RR from ECG driven RR method.

Sr No.	Age group (in yrs)	Mean ECG derived RR (Breathes per min)	Mean VCG derived RR (Breathes per min)	Mean Deviation of VCG RR from ECG RR (Breathes per min)
1	10-12	26.4	26.5	+0.1
2	15-20	25.3	25.2	-0.1
3	21-25	17.2	17.4	+0.2
4	26-29	14.6	14.7	+0.1
5	30-32	16.5	16.6	+0.1
6	8-10	28.1	27.9	-0.1

Table 1.Comparison of respiration rate of ECG and VCG technique

5. Conclusion

The Michelson interferometer working on homodyne detection technique uses the vascular movements of wrist wall to move the nano reflector-mirror on wrist with the frequency of heart movements. This frequency is recovered from output to obtain respiration rate. Hence a non invasive or non-contact technique of frequency measurement of respiration rate is developed with deviation of ± 0.1 breathes per minute with comparison of respiration rate obtained from ECG.

REFERENCES

1 Giorgio Capelli, Cecilia Bollati, Cuido Giuliani Vol **47** No.6 pp 40-45 january 2005.

2 Umberto Morbiducci, Lorenzo Scalise, Mirko Demelis and Mauro Grigioni *Annals of biomedical Engineering*, Vol **35**, No.1 , pp 45-48 January 2007.

3 Puttnam, Ruben S. Louis, Jose Manuel , Delgado Mendinueta, Jun sakaguchi, Wener Klaus, Yukiyoshi kamino, Moriya Nakamura, Naoya Wada, Yoshinari Aawji, Atushi Kanno, *Benjamin J Journal of photonics*,**1**, doi:10.3390/photonics 1020110, 2014.

4 H Takashi, C Masuda, Y. Gotoh and J Komaya *IEEE transaction on instrumentation and measurement*, Vol **38**, No 2 ,April 1989.

5 M. De Melis, U. Morbiducci and L *29th international conference on IEEE EMBS*, France, august 23-26 ,2007.

Development of EPICS based control system for Nd:Glass laser amplifier

Hitendra Singh Chouhan*, O.P. Joshi, Bhupinder Singh, M.S. Ansari
Laser Power Supplies Division, Raja Ramanna Centre for Advanced Technology, Indore, India
Email: hitendra@rrcat.gov.in

Abstract: This paper reports development and testing of an EPICS based control and monitoring unit for Nd:Glass laser amplifier. EPICS platform is chosen because of the availability of open source software tools and applications. A general overview of the control system architecture as well as the software stack, implementation details, experiment result and future plans for the system are presented.

Introduction: High energy Nd:Glass lasers are widely employed for high energy density physics studies. RRCAT has a 400 J two-beam Nd:phosphate glass laser system based on MOPA architecture[1] and an ongoing project for development of 2-beam laser with target to achieve 1 kJ laser energy output. High energy laser pulses are obtained by amplification of seed laser pulses, generated by a laser oscillator, through cascade of several laser diode or flashlamp pumped laser amplifier stages. Except the diode pumped stages, which are standard commercial product, all flashlamp pumped amplifier stages have been developed in-house. While diode-pumped stages are driven by commercially available high current DC power supplies, flashlamp-pumped are powered by in-house developed HV and high peak current Pulsed Power Supplies (PPS). A typical PPS consists of capacitor banks along with a constant current charging supply and discharge circuit for delivering stored energy to flashlamp loads in the amplifier stage[2]. A control system with dedicated control modules for laser oscillator and each amplifier stage provides all control, supervisory and data acquisition features needed for proper operation of the entire laser system. Such control systems can be microprocessor/microcontroller based custom-built data acquisition and digital control system[3] or it can be based on industry standard systems e.g. CAMAC, NIM, VME, PXI, etc. While the former offers advantage of ease of maintenance and upgradability at much lower cost but lacks ruggedness, EMC performance and immunity to hostile industrial environment provided by the later. When reliability and EMI immunity are the priority, industry standard systems become a preferred choice. In this work, PXI based scheme has been adopted for development of the control system for the ongoing project for development of Nd: phosphate glass 2-beam, 1 kJ laser system. Software application development has been done using EPICS software tool which is the main focus of the paper.

System Architecture: The architecture of the Nd:Glass laser amplifier control system is shown in Figure 1. It is based on a three-layer design – Supervisory, Control and Field layers. User workstation is placed in the supervisory layer; controller machine is placed in the control layer while power supplies and other equipment belong to the field layer. Two numbers of input output controllers (IOCs), each of which interact through different PXIe interface cards, have been developed and installed on Linux based controller machine. IOC-1 is responsible for charging power supplies and monitoring feedback voltage while IOC-2 takes care of acquisition of current pulse from flash lamps. These operations are separated through different interface cards to avoid any resource conflicts between IOCs. User workstation provides operator interface (OPI) for monitoring and controlling the system through IOCs. OPI and IOC communicate over local area network (LAN) with the help of Channel Access (CA) protocol of the EPICS framework[4,5]. OPI acts as channel access client to access IOC

databases while IOCs act as channel access servers. IOC-2 logs acquired data to output file which can be accessed from OPI to view trends and perform analysis. Controller machine also takes care of network level access control through firewall to restrict any unauthorized access of IOC database.

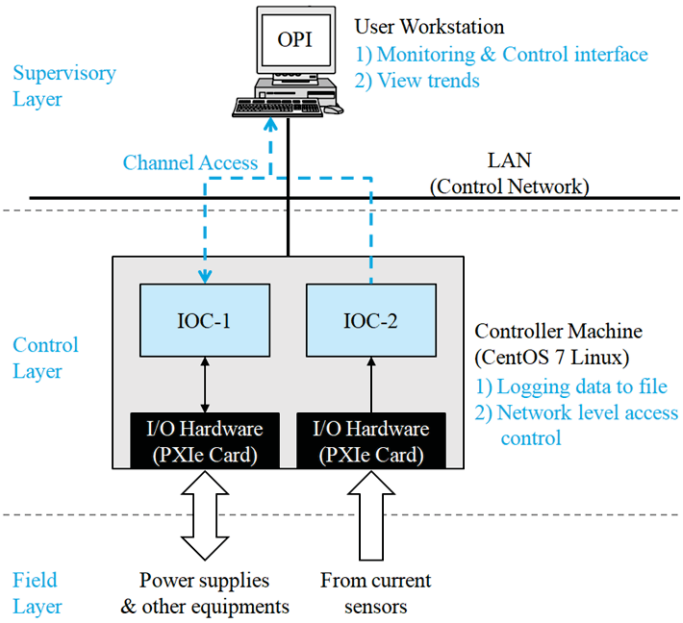

Figure 1: Architecture of the implemented control system

Software Stack: Figure 2 shows client and server open-source software stack used for the development of control system. The client user interfaces are developed in Qt and C++ over EPICS Qt framework[6]. To the Qt application, EPICS Qt layer facilitate access to EPICS data using Channel Access protocol. EPICS Qt framework supports code rich GUI development using Qt's IDE thus allowing incorporation of additional features to the application which would rather not feasible in case of other frameworks that supports only code free development. Asynchronous Channel Access Interface (ACAI) is responsible for handling low level Channel Access at the client side.

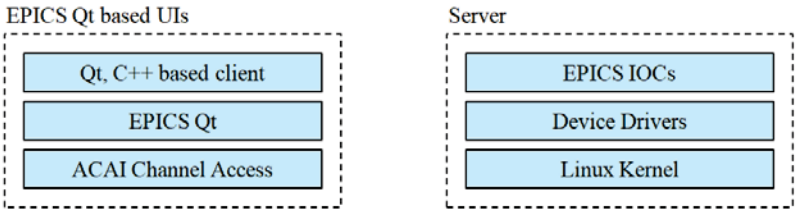

Figure 2: Software stack used for the development of control system

The server application runs on CentOS Linux based machine installed with NI-DAQmx[7] device driver which is freely available from National Instruments for controlling PXIe based data acquisition devices. EPICS IOCs are built on top of the server software stack. They actually provide control functionality utilizing device drivers.

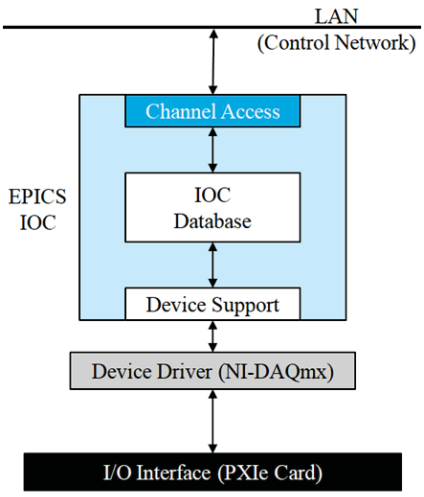

Figure 3: EPICS IOC components used/built

IOC Software Components: EPICS Base[5] is used as backbone for implementation of IOCs. Software components that have been used/built are shown in Figure 3. IOC database, which is a collection of named records of different types, is built to host process variables. Channel Access acts as an interface between IOC and the EPICS clients over LAN. It facilitates IOC database access to the OPIs over

Ethernet. Device support acts as an interface between database record and the device driver. Device support routines were developed to enable IOCs to access PXIe interface cards using NI-DAQmx device driver. These routines are developed in C utilizing API's of the device driver.

Network and Access Security: It is desirable to ensure IOC database security from any unauthorized access. Network level access security is provided to the controller machine by configuring the CentOS Linux built-in firewall. The firewall is configured to permit Channel Access traffic only from authorized OPI nodes on the control network while restricting others. It also enables to implement more than one independent control system on same network without interaction. Moreover, EPICS also has a mechanism to define different levels of access privilege to CA clients for accessing IOC database and it may further be utilized as per the requirement.

User Interface: Client side user interfaces for operation, control, data acquisition and analysis have been developed which provides ease of operation and display of post operation results through user friendly GUI. Qt, C++ and EPICS Qt framework are used for the development of these user interfaces. Screen-shot of the main control window for Nd:Glass laser amplifier control system is show in Figure 4. At present it supports control for up to two power supplies and can be upgraded to serve required number of power supplies. Preferences window allows user to pre-configure the control system according to particular experiment. Plot viewer window which displays the acquired current pulses from the flashlamps is shown in Figure 5. Software interlocks have been implemented for safe operation and to protect the power supplies in case abnormal condition is detected.

Figure 4: Control system user interface

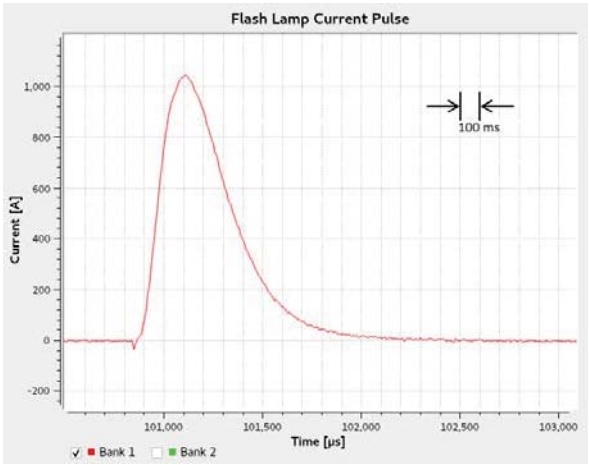

Figure 5: Acquired current pulse from the flashlamp

Results and Discussion: The developed control system software has been tested with two Pulsed Power Supplies. Schematic of the PPS with control system is shown in Figure 6. Operation of a typical PPS mainly involves two processes – 'energy storage' in HV capacitor banks followed by 'energy delivery' to flashlamp loads. Energy storage involves initiation of charging of all capacitor banks on receiving the 'Charge' signal and maintaining at set value by monitoring the capacitor bank voltage through 'feedback' and 'Charge Control' signals. Energy delivery is accomplished by two control signals 'Trigger' and 'Fire' which readies the flashlamp trigger circuit and initiates the flashlamp discharge respectively. Among the control signals, four are digital – Charge, Charge Control, Trigger and Fire and one is analog – Feedback. A multifunction PXIe module consisting of 32 analog inputs and 48 digital input/output lines have been used for generation and monitoring of these signals. The developed application software configures these lines for the required control signals and

allows their generation through user interface. In addition, some analog input lines have been configured to receive pulsed signals from current sensors which sense the pulsed current through flashlamps. Pulsed signals are acquired through a separate PXIe module to avoid any resource conflict. These pulses are recorded and displayed on user interface to indicate results of energy delivery process for further evaluation. Figure 5 shows the acquired current pulse from the flashlamp during discharge operation of one of the power supply.

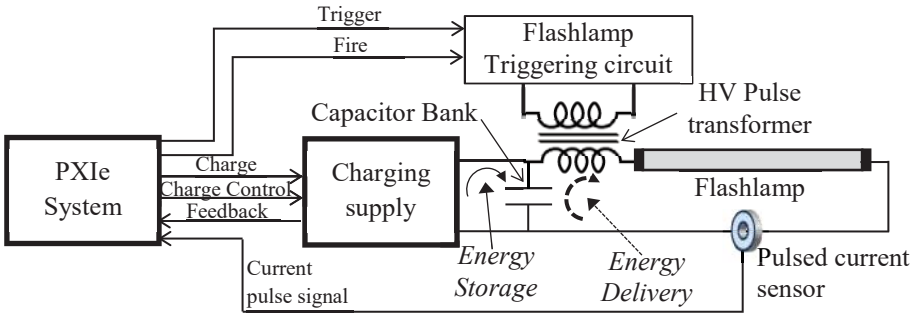

Figure 6: Block diagram of flashlamp pulsed power supply with PXIe control

Conclusion: Fully open source and EPICS based control system software has been developed and tested for Nd:Glass laser amplifier power supplies. Both, client side OPI and server side IOCs are developed for Linux platform. EPICS device support has been built to enable IOCs to interact through PXIe interface cards. OPI for the control system is developed using Qt, C++, EPICS Qt and associated libraries.

Modular and distributed approach allows integration of Relational Database (RDB) archiver to the system. Report generation and user management modules with authentication and authorization can also be incorporated. Further, modular approach leads to hardware independence, by re-writing device support module alone while keeping other software modules unchanged.

References:

1. A.S. Joshi *et al.*, *EPJ Web of Conferences* **59**, 08001-p.1 (2013) (http://www.epj-conferences.org/articles/epjconf/pdf/2013/20/epjconf_ifsa2011_08001.pdf).
2. Bhupinder Singh, M. S. Ansari and C. P. Navathe, *Proceedings of National Laser Symposium (NLS-21), BARC, Mumbai* (6-9 Feb. 2013).
3. C.P. Navathe, M.S. Ansari, Sameer Nigam, Sreedhar Nyapathi, Bhupinder Singh and Ramesh Chandra, *IEEE Transaction on Plasma Science*, Vol. **40**, No. 7, pp. 1898-1906 (2012).
4. Leo R.Dalesio *et al., Nuclear Instruments and Methods in Physics Research Section A: Accelerators, Spectrometers, Detectors and Associated Equipment*, Volume **352**, Issues 1–2, Pages 179-184, (1994).
5. Martin R. Kraimer, *EPICS Application Developer's Guide*, EPICS Base Release 3.15.6 (October 2018)
6. A. Rhyder et al., *Qt EPICS Development Framework*, PCaPAC 2010, Saskatoon (October 2010).
7. Ni.com, *NI-DAQmx*. Available from https://www.ni.com/en-in/support/downloads/drivers/download.ni-daqmx.htm. (Accessed: 12- Jan- 2021).

Development of a wavemeter based cavity stabilization system for the high repetition rate SLM OPO

C. S. Rao[a*] , P. Chakrabarthy[b], and N. Kawade[b]

Advanced Tunable Laser Facility[a], Laser & Plasma Technology Division[b],
Bhabha Atomic Research Centre, Trombay, Mumbai-400085
somu@barc.gov.in*

Abstract:

The paper describes the development of a wavemeter based cavity stabilization system to study the effect of cavity stability on the spectral stability of Fabry Perot etalon based SLM OPO. This helps in understanding and designing the wavelength stabilization system for the tunable SLM OPO for achieving long-term sustained frequency stabilized output. A user-friendly software has been developed to lock the OPO at a desired wavelength of interest. The spectral characteristics and long term frequency stability of the cavity stabilized SLM OPO has been studied. The mode hopping behaviour observed during long-term operation envisaged the implementation of synchronous etalon tuning with the cavity for achieving long-term frequency stabilization.

Introduction:

Optical Parametric oscillators (OPOs) are highly efficient solid state sources of coherent tunable radiation. Among various prominent tunable OPOs, the BBO crystal based OPO pumped with the third harmonic (355 nm) of a Q-switched Nd:YAG laser offers wide tuning range, both in the visible as well as in near-IR spectral range [1-2]. The narrowband OPOs operating at high repetition rate, continuously tunable at visible radiation, are pivotal to many basic and applied scientific applications such as sensitive and selective detection/analysis of trace gases and metrology by laser absorption spectroscopy, selective separation of isotopes/elements for radio-pharmaceutical using laser resonance photo-ionization spectroscopy etc. The medical isotopes of interest, especially ^{176}Yb and ^{176}Lu, to extract them from their natural isotopes using AVLIS process and for the spectroscopic studies to determine the process wavelengths for the efficient extraction of these isotopes, desires the development of a tunable lasers in the visible spectral range operating on a single longitudinal mode (SLM) with a narrow spectral linewidth (100–300 MHz) [3,4]. These applications not only require narrowband single longitudinal mode operation but also demand reliable and sustainable long term operation. Thus, these devices must be equipped with compatible wavelength locking systems to deliver the frequency stabilized output for longer duration operation at the desired wavelengths.

Recently, our group was involved in the development the high repetition rate (1 kHz) single longitudinal mode OPO by utilizing the Type-II phase-matched BBO crystal in double pass pump beam configuration using a single intra-cavity Fabry Perot etalon. The SLM OPO is tunable in the spectral region of 500-600 nm [5]. To design mode control and wavelength stabilization system for such tunable SLM laser to achieve long-term frequency stability and single mode operation, it is important to understand the dynamic behaviour of system along with disturbances ranges and study the controllability of the system. Therefore, in the first step, developed a high resolution wavemeter based locking system for the SLM OPO and studied the long-term frequency stability .

During the long-term testing of the SLM OPO, mod hoping has been observed after around 20 minutes of operation which is mainly due to stabilizing the cavity without synchronously changing the tilt angle of the etalon. Hence, it is proposed to implement the synchronous tuning of the etalon with the cavity length change. The methodology of the wavemeter based wavelength locking system and the observed spectral behaviour of the SLM OPO under active cavity stabilization has been discussed in the paper

Description of the SLM OPO and wavelength locking system:

The Fig. 1 shows the schematic of the Fabry Perot etalon based SLM BBO OPO cavity configuration and the wavelength locking system employed for the cavity stabilization of the SLM OPO. The etalon E is placed at an angle θ to the resonator axis, after the pump beam reflector in the Type-II BBO OPO cavity with double pass pump configuration. The tilting angle θ has to be adjusted so that the transmission peak of the etalon has to coincide with the mode nearest the peak of the OPO gain profile.

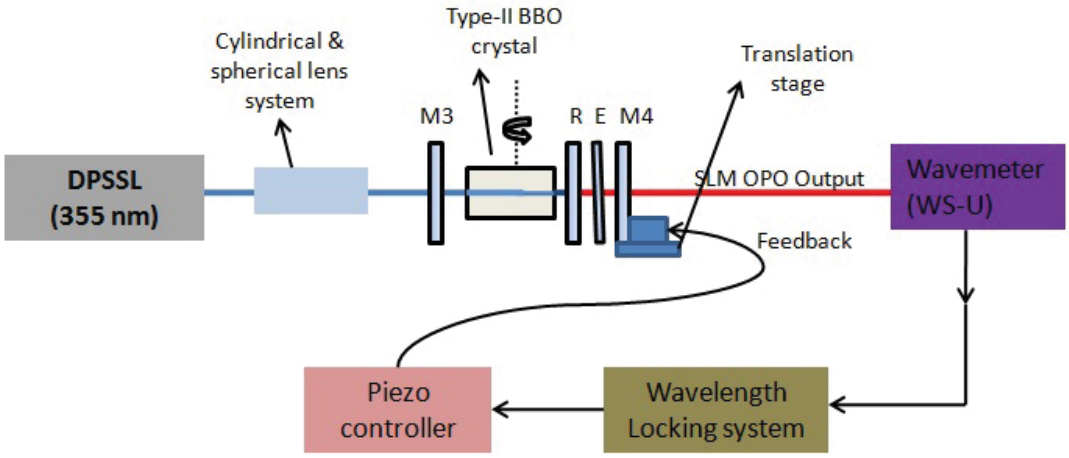

Fig.1: *Schematic of the experimental setup of SLM OPO. M1, M2: Pump beam routing mirror, M3, M4: OPO cavity mirrors, R: Pump beam reflector, E: FP solid etalon, M5: Pump beam reflector, M6, M7: Signal beam reflectors.*

The thickness of the FP solid etalon (E) was chosen to be 1.3 mm which corresponds to the Free Spectral Range ($\Delta\upsilon_{fsr}$) of 79 GHz and the finesse of the etalon is 22 @ 500-600 nm. The corresponding linewidth of an etalon transmission peak ($\Delta\upsilon_c$) is 3.59 GHz. The choice of this FP etalon was determined by the spectral linewidth of the Type-II BBO OPO in double pass pump beam configuration. The length of the SLM OPO cavity was kept within 5 cm, corresponding to an optical length of 7.5 cm, to increase the longitudinal mode discrimination. Therefore, the separation between the longitudinal modes $\Delta\upsilon$ is 2 GHz. The coarse wavelength tuning of the SLM OPO is accomplished through the stepper motorized rotation of the crystal with an angular resolution of 1 µrad. The etalon is mounted on optical holder which provides precise adjustments of yaw over a range of ±5 deg. and pitch over a range of ± 2 deg. The angular rotation of the etalon provides the fine adjustment of etalon transmission peak to coincide with the peak of the OPO cavity gain bandwidth which is achieved through the computer-controlled stepper motorized rotation with an angular resolution of 1 µrad. The fine wavelength tuning and the frequency stability of the SLM OPO are achieved by the OPO end mirror which is mounted on a PZT driven translation stage. The

maximum change in frequency achieved with a full 8 μm change in the cavity length due to PZT translation is ~ 58 GHz. The PZT is controlled through a PZT controller with a resolution of 1 nm that corresponds to a minimum controllable change in the frequency of 7.8 MHz.

As shown in the Fig.1, a high resolution wavemeter (WS-U, absolute wavelength accuracy 30 MHz) was used to measure the wavelength of the SLM OPO. Wavelength locking software which we have indigenously developed was used to acquire wavelength data continuously from the wavemeter. The software then compares the acquired wavelength data with the set locked wavelength value and generates an error signal corresponding to the change in the wavelength. The error signal is then applied to the feedback control loop of the end mirror PZT to change the cavity length of the OPO to set the desired wavelength value. The small incremental change in the frequency due to the change in the OPO cavity length is given by,

$$\Delta\upsilon = -\upsilon \frac{\Delta L}{L} \qquad (1)$$

where L is the cavity length of the OPO and is the central frequency of the SLM OPO.

The Fig.2 shows the GUI of the software developed for locking the wavelength of the SLM OPO.

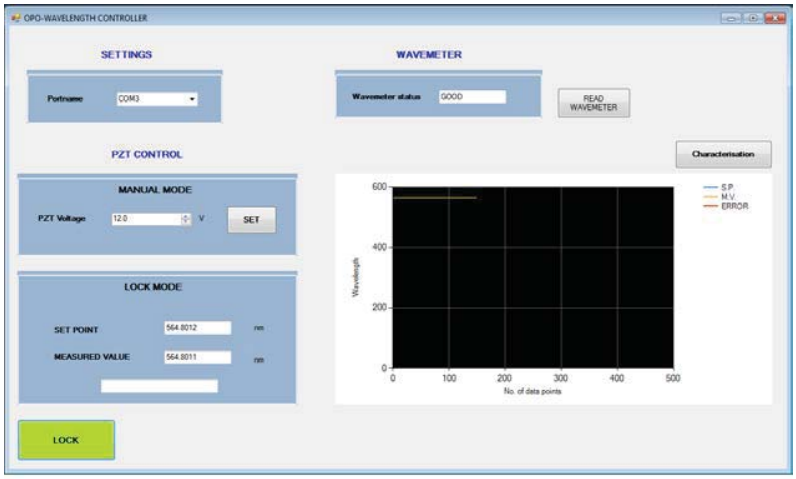

Fig. 2: *GUI of the wavemeter based wavelength locking software.*

Results &discussions:

The Fig.3 shows the long term stability of frequency stabilized OPO operating at a wavelength of 564.801 nm. The variation of the spectral linewidth of the OPO under locking condition is shown in the Fig. 3b. During the continuous 25 minutes of operation, the SLM OPO was operated mainly at the desired wavelength. The wavelength was observed with mean value of 564.80109 nm and a standard deviation of ± 76.74 fm without mode hop. However, the spectral linewidth of the SLM OPO under wavelength locking increases with time from 0.2 to 0.6 pm during the operation. As the etalon angle was not synchronously tuned corresponding to the change in the wavelength, it could not hold single mode condition. Hence, the linewidth of the SLM signal output increases slowly with the time leading to mode hopping after 25 minutes of operation which is shown in the Fig. 3b.

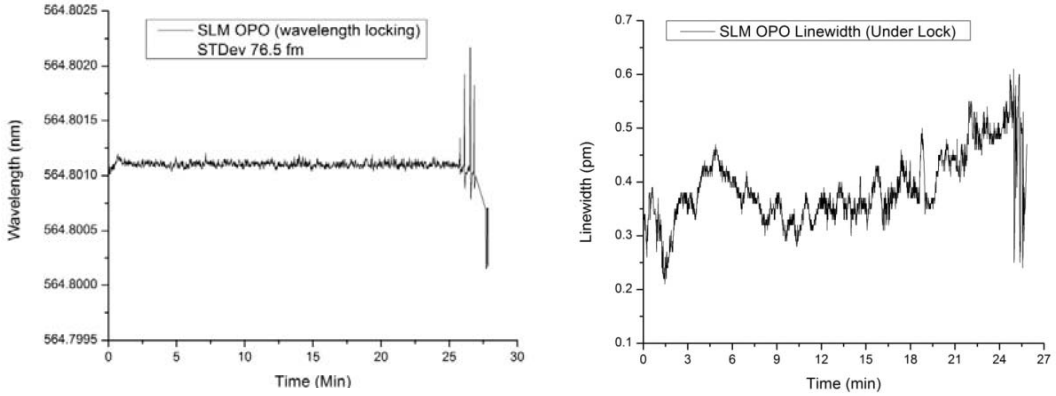

Fig. 3: A) Frequency stability B) linewidth @ 564.8012 nm under wavelength locking.

As discussed in the above section, the mode hopping was observed during the frequency stabilization process of the SLM OPO which can be circumvented by synchronously changing the cavity of the SLM OPO and the angle of the etalon to match the central frequency of the single mode with transmission peak of the etalon. The change in the etalon angle required to match the transmission peak of the etalon with the frequency change (Δυ) due to cavity length (ΔL) change can be obtained from the dispersion relation of the etalon given by,

$$\Delta\upsilon = \upsilon \frac{\tan(\theta/n)}{n}\Delta\theta \quad (2)$$

where, n is the refractive index of the etalon,θ is the angle of incidence, Δθ is the change in the tilt angle of the etalon. We are now working on the development of wavelength locking system by incorporating the synchronous angle tuning for the sustained long term SLM operation of the OPO without mode hopping.

Conclusion:

In conclusion, we have designed and developed a wavemeter based cavity stabilization system to lock the SLM OPO at a fixed wavelength. The spectral characteristics of the long-term stabilized SLM OPO have been studied. The mode hopping behaviour was observed after the 20-25 mins of operation that can be circumvented by implementing the synchronous angle tuning of the etalon along with the cavity length.

References:

1. L. K. Cheng, W. R. Bosenberg, and C. L. Tang, Appl. Phys. Lett. 53, 175 (1988).
2. R.C. Bapna, C.S. Rao, K. Dasgupta, Optics & Laser Technology, 40, 832 (2008).
3. H.M. Park, D.H. Kwon, Y.H. Cha, T.S. Kim, J.M. Han, K.H. Ko, D.Y. Jeong, C.J. Kim, J. Nucl. Sci. Technol. 45 (6) (2008) 111–116,
4. A.B. Dyachkov, et.al, Appl. Phys. B 121 (2015) 425–431
5. C.S. Rao, S. Kundu, Alok K. Ray, Optics & Laser Technology 138 (2021) 106878.

Microcontroller based Control for driving Multiple Direct Digital synthesizers.

Sasikumar.K.K, BVS. Shravan, Radhika.V.N, Rekha.A.R, Krishnakumar.J

ISRO Inertial Systems Unit, Trivandrum

sasikumarkk2000@gmail.com

1. Abstract:

In Cold Atom Interferometry experiments, intensity and frequency of laser beam need to be modified as required by the different processes (viz. Cooling Process, Atomic fountain, Detection) involved. For meeting such requirements, Acousto Optic Modulators (AOMs) are normally used which are suitably driven by Variable Frequency Oscillators. We used AOMs with Direct Digital synthesizers (DDS) as RF generators to control frequency and amplitude digitally. A Microcontroller based system was implemented to drive multiple Direct Digital synthesizers which are controllable via personal computer and able to generate corresponding bit pattern to drive the DDS independently for any input time profile. The design details, package designing and results of testing are discussed in the paper.

2. Design and implementation:

Fig 1 shows the block diagram of Microcontroller based Multiple DDS Control unit to generate RF frequency and amplitude to drive three AOMs.

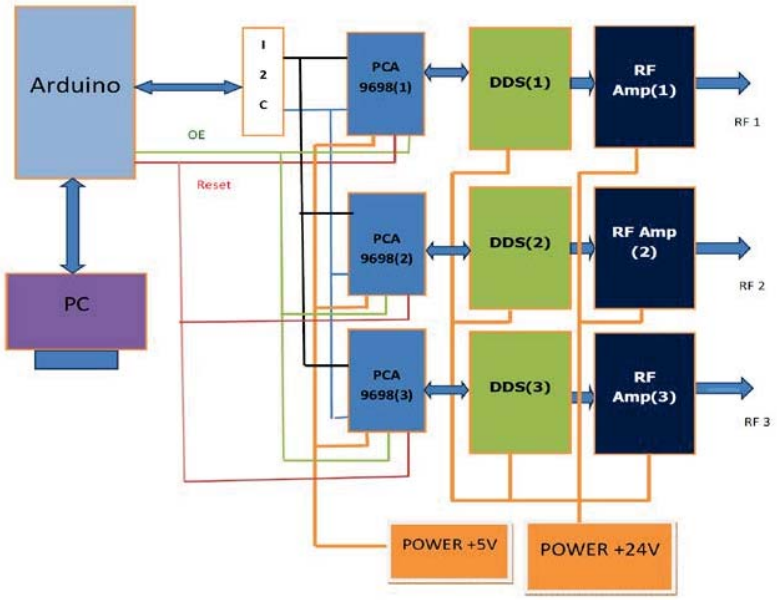

Fig 1: Block diagram of Multiple DDS control

Here three DDS modules are driven independently with different time profiles. The DDS are controlled using a Arduino Microcontroller which is connected by a PC. I^2C protocol was used to connect multiple DDS with Microcontroller. 40 bit IO extenders (PCA 9698 IC) capable of I^2C communication are used to interface the Microcontroller and DDS module. Data is initially sent to the IO port extenders where the serial data is converted into parallel form. DDS modules are connected with IO port extenders and each IO extender port is identified with specific 7 bit address. Microcontroller sends the data to the I^2C bus. Data consists of address of the IO extender port along with frequency and amplitude information. Data is received by the corresponding IO extender based on the address sent by the Microcontroller. Algorithms developed to separately address each device connected to the microcontroller as well as to command the required frequency and intensity requirement of the

AOM. DDS output power is further amplified to a significant level as required by the experiment by using RF Amplifiers.

A compact module (16 cm x 11.5cm x 15cm size) has been designed to integrate Microcontroller unit, three numbers of IO interfacing cards ,three numbers of DDS and corresponding RF Amplifiers .

3. Testing

Fig 2 shows the test setup to verify the performance of MDDS module. MDDS module was energized using a +24 V DC power supply and Microcontroller power was interfaced through Personal computer .The RF output is monitored using a spectrum analyzer. Arduino serial monitor facility was used to feed the data to the Microcontroller. The frequency and intensity of RF output recorded in Spectrum Analyzer is found matching with the digital input fed to Arduino. and verified with the input. Third harmonics frequency was present in the output spectrum, but with very low power. Fig 3 shows the Power Vs frequency plot of the MDDS system

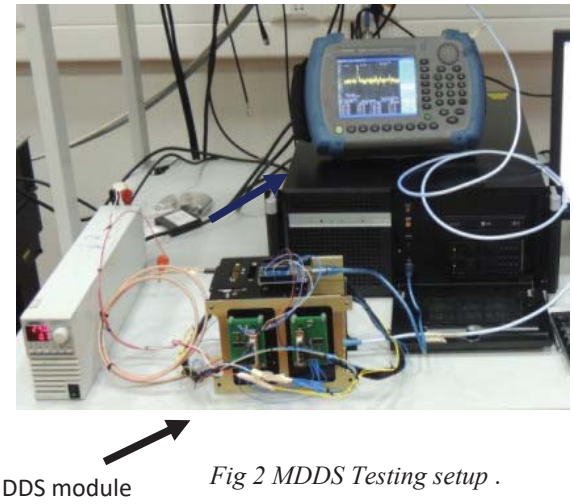

Fig 2 MDDS Testing setup .

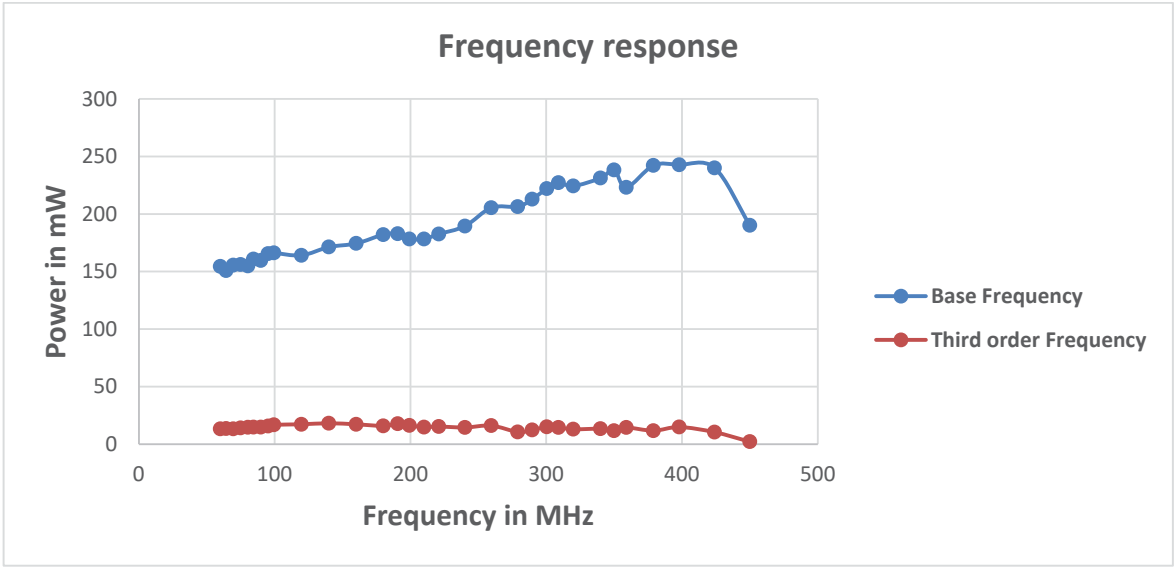

Fig 3: Gain vs Frequency response of the DDS

4. Results and Conclusion

- Developed algorithms to convert the frequency and intensity information into corresponding bit patterns to drive the DDS.
- Designed and realized an interfacing card to interconnect Microcontroller and DDS unit based on I2C protocol .
- Prepared I^2C based code to transfer the Frequency and Amplitude information to the corresponding DDS modules independently.
- Verified the performance of each DDS module based on the input time profile.
- A compact module (16 cm x 11.5cm x 15cm size) has been designed and realised to integrate the Microcontroller unit, IO interfacing cards, DDS and corresponding RF Amplifiers.
- Three number of DDSs (13 cm x 6 cm x 3cm size), three numbers of RF amplifiers (7.5 cm x 4.2 cm x 4 cm size),Micro controller (7 cm x 5.5 cm size) and three numbers of IO interface cards (7 cm x 5 cm size) integrated on the compact module and tested the output with respect to input time profile successfully.

References

1. Arduino, Store Arduino. "Arduino." *Arduino LLC* (2015).
2. McRoberts, Michael. *Beginning Arduino*. Apress, 2011.
3. Banzi, Massimo, and Michael Shiloh. *Getting started with Arduino: the open source electronics prototyping platform*. Maker Media, Inc., 2014.
4. Fukuhara, Ryan, et al. "I2C bus protocol controller with fault tolerance." U.S. Patent No. 6,728,908. 27 Apr. 2004.
5. Instruments, Texas. "TSC2003/I2C Touch Screen Controller." *Data Sheet SBAS* 162 (2001).
6. Andersson, Anders, and Daniel Van Berkom. "Multi-chip addressing for the I2C bus." U.S. Patent No. 6,629,172. 30 Sep. 2003.
7. Vankka, Jouko, et al. "A direct digital synthesizer with an on-chip D/A-converter." *IEEE Journal of Solid-State Circuits* 33.2 (1998): 218-227.
8. O'leary, Paul, and Franco Maloberti. "A direct-digital synthesizer with improved spectral performance." *IEEE transactions on communications* 39.7 (1991): 1046-1048.
9. Gould, Scott Whitney, et al. "Programmable array interconnect latch." U.S. Patent No. 5,732,246. 24 Mar. 1998.

Programmable Power Supply for Laser based Welding System

Vijay Bhawsar[a], Sudheer Kushwaha[a], Shryner Penumala[a], Jagriti Khanwalkar[a], B.N. Upadhyaya[b], R. Arya[a]
[a]*Laser Electronics Division, RRCAT, Indore,*
[b]*Laser Technology Division, RRCAT, Indore*
Email: vijay@rrcat.gov.in

I. ABSTRACT

Laser welding has gained great popularity as a promising joining technology and weld quality is strongly affected by the temporal pulse profile adopted in laser welding. This paper presents work on a C8051F120-microcontroller-based programmable power supply with average electrical power output of 10 kW for dual flash lamp pumped 500 W Quasi-CW Nd:YAG laser. The power supply incorporates a buck convertor based pulsed current source, HV trigger pulse source, simmer current source and a user friendly GUI with touch screen. The GUI allows the user to program various pulse parameters, temporal pulse profiles and a structured burst profile to achieve the required weld quality and finish. The power supply has been installed at Advanced Fuel Fabrication Facility (AFFF), BARC, Tarapur and is being used for welding of fuel pins.

II. INTRODUCTION

Laser welding has gained great popularity as a promising joining technology with high quality, high precision, high performance, high speed, good flexibility, and low deformation or distortion[1]. With the advancement of technology, lasers are progressing from experimental laboratory models to advanced engineered instruments and becoming sophisticated tools for various industrial and medical applications[2]. Different lasers being utilized for material processing applications are continuous wave (CW) or pulsed lasers with adjustable parameters and power levels as per requirements of the application[3]. Solid state lasers mainly Nd:YAG lasers are widely used for industrial applications. Selection of CW-mode or Quasi-CW-mode or pulsed mode of Nd:YAG laser is governed by properties such as reflectivity, conductivity of material to be welded, penetration depth of weld joint and spot size of laser beam. High power pulsed lasers are most effective for cutting and welding of thicker sections in thermally conductive and reflective alloys such as aluminum, titanium and zirconium with a trade-off of slower processing speeds[4]. Further weld quality is strongly affected by the temporal pulse profile adopted in laser welding. In comparison with the use of a normal rectangular pulse profile, stronger welds with a better homogeneity and a complex fracture mode are achieved by using a ramp-down pulse profile. This quality enhancement was contributed from the less degree of intermixing between two welding materials in melting pools[5].In this work development of a microcontroller-based programmable power supply for dual flash lamp pumped 500 W Quasi-CW Nd:YAG laser is presented that can be programmed for various pulse parameters, temporal pulse profiles and a structured burst profile to achieve the required weld quality and finish.

III. SYSTEM REQUIREMENTS

Two pulsed current power supplies each with average electrical output power of maximum 5000 W, that can be programmed to deliver different types of required current pulses to dual flash lamp pumped Nd:YAG laser based welding system, are required. Each power supply is required to perform these functions: (a) provide rectangular current pulses to pump the flash lamp with adjustable pulse parameters, (b) provide current pulses with profile that can be programed to have two or more rectangular segments with adjustable parameters, (c)

provide a high voltage flash lamp trigger pulse, (d) provide a continuous dc simmer current for flash lamp, (e) monitor status of power supply, laser system and lamp cooling chiller system, (f) provide a set of on/off control signals for various control actions and activation of safety interlocks and (g) provide a user friendly interface to generate programmable current pulses of different required profiles as well as accept user inputs and display system information.

The user friendly graphical user interface (GUI) should allow user to program various pulse parameters, pulse profiles, laser operating modes and should provide various notifications and fault indications visually and with audible alert. A high voltage flash lamp trigger pulse of the order of 15 to 20 kV is required to initiate an electric discharge between two electrodes of each flash lamp and create a conductive path between them. To establish a continuous dc simmer current of the order of 400 to 600 mA a simmer current source is required. When simmer current is established, the main pulsed current source can now pump current pulses in both flash lamps with adjustable pulse parameters and profile. The GUI should allow the user to program the laser operation in either (a) rectangular pulse mode with adjustable pulse amplitude from 110 to 300 A, pulse duration from 3 to 40 ms and pulse repetition rate from 1 to 100 Hz, or (b) pulse profile mode that can be programmed to have a minimum of 2 and maximum of 8 rectangular segments of adjustable amplitude from 110 to 300 A and duration from 5 to 35 ms. These current pulses are required to be delivered to flash lamps either in (a) Single shot mode, or (b) Continuous pulse train mode or (c) structured burst profile mode. In burst profile mode, controller should allow the user to program a structured sequence of four type of bursts of pulses with adjustable rectangular pulse or pulse profile and number of pulses from 2 to 999 in the burst.

An interlock system is required to read digital input signals from the power supplies representing status of various sub-sections of power supply as well as signals from lamp cooling chiller system, to update and initiate required control actions. Different digital input signals required to be monitored are Line over-voltage, line under-voltage, phase fail, phase imbalance, chiller water flow-fail, chiller water over-temperature and simmer fail. Optical isolation method is implemented to isolate digital input-output signals.

IV. DESCRIPTION OF THE SCHEME

The programmable power supply designed and developed for welding laser system consists of (a) power supply controller and (b) A power supply system consisting of a pulsed current source, a high voltage trigger and simmer current source for two flash lamp loads. The power supply controller is developed as a standalone unit, separate from the power supply system cabinets to facilitate the remote operation. The power supply controller receives user inputs for required laser operation mode and pulse parameters through GUI and generates an analog reference voltage waveform for two control channels for pulsed current source for two flash lamp loads, as per requirements. Each control channel consists of a pulse width modulation (PWM) controller that continuously monitors the flash lamp current, compares it with the required reference waveform and generates the PWM pulses for the switching device of the buck convertor based pulsed current source.

Power supply controller: The power supply controller has been designed using microcontroller C8051F120 of silicon laboratories operating at 44.2368 MHz system clock, installed on a development board. The analog reference voltage waveform is generated by using a 12-bit, serial digital to analog converter (DAC) TLV5618 of Texas Instruments, operating at 500 kbps serial clock interfaced on Serial Peripheral Interface (SPI) port of the

microcontroller. An external band gap reference TL431, with 2.5 V output and temperature coefficient of 30 ppm/^{o}C is used for better temperature stability of DAC output. Flash lamp load current is sensed using a hall effect based DC current sensor LT1005S of LEM and is amplified using an instrumentation amplifier AD620. A dedicated PWM controller SG3525 has been used for error amplification, proportional-integral (PI) control loop implementation and PWM signal generation for switching device of buck convertor. The GUI has been designed using a WVGA color TFT display having resolution of 800X480 pixels, with resistive touch screen panel, interfaced on Universal Asynchronous Receiver Transmitter (UART) port of the microcontroller using RS232 standard. The power supply controller allows the user to adjust the laser pulse parameters such that the average output electrical power of each flash lamp and pulse current source does not exceed the maximum limit of 5kW and 10kW for overall laser system.

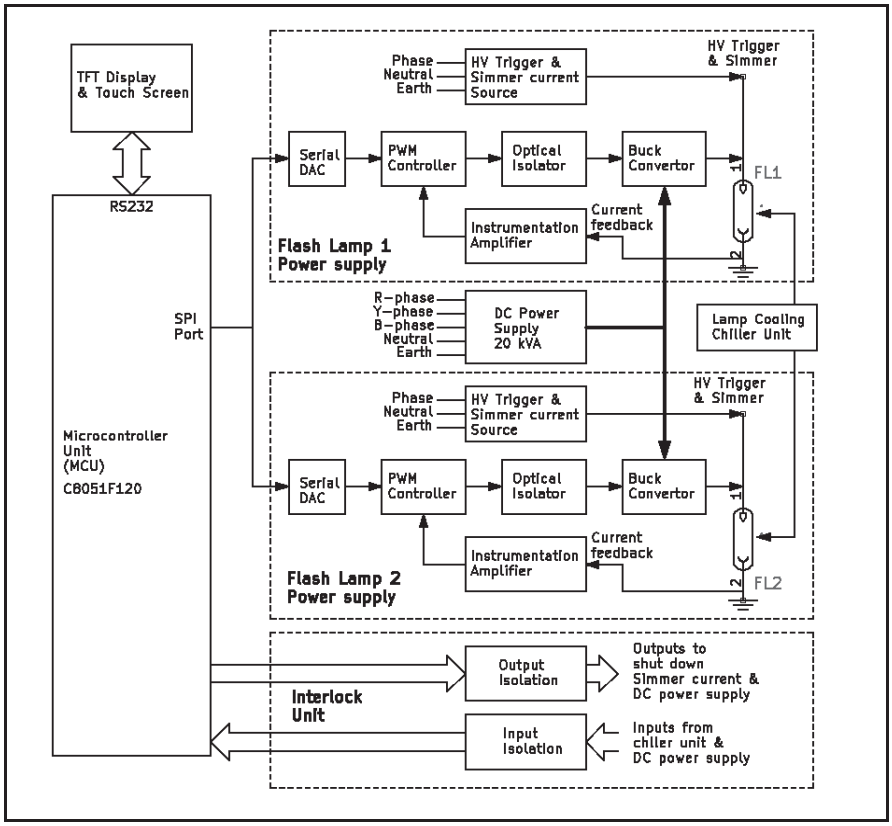

Figure – 1: Block schematic of welding laser power supply

Power supply: Each pulsed power source delivering power to one flash lamp consists of a buck convertor based pulsed current source driven by a three phase fed 20 kVA DC power supply. The buck convertor uses a switching device FZ600R12KE of Infineon Technologies, protected from higher dv/dt spikes by using an RCD snubber with capacitor voltage clamp. Each pulsed power source also has a high voltage flash lamp trigger pulse source and a resonant convertor based Simmer current source with voltage doubler output stage. Open circuit output voltage of simmer current source is 1500 V that drops down to 200 V when flash lamp load starts sinking 500 mA of simmer current. Flash lamp trigger pulse source uses a MOSFET to generate a 650 V pulse for driving the primary winding of a step up trigger pulse transformer with 1:30 turns ratio that generates a high voltage pulse of 20 kV of 100 mJ output energy to initiate an electric discharge between two electrodes of each flash lamp and generate a spark streamer of sufficient intensity to be taken over by 500 mA simmer source.

Pulsed current source, simmer and trigger source Interface: Output stage of simmer current source is protected from high voltage flash lamp trigger pulse by using high voltage diode stack. A coupling capacitor with a capacitance of 2 nf/40 kV has been used in the output stage of high voltage flash lamp trigger pulse source to block open circuit DC output voltage of simmer current source and save it from sourcing short circuit current through secondary winding of the trigger pulse transformer. A high voltage, high current contactor is used in the output stage of the pulsed current source to protect the switching device and free wheel diode of the buck convertor from high voltage trigger pulse.

Interlock: During the operation of the laser, a hardwired interlock circuit implemented by using discrete logic gates, continuously monitors three phase power line status and flash lamp cooling water chiller unit for different fault signals. Once any of the fault signal is detected, the safety interlock is activated to turn off the current pulse from pulsed power source and simmer current source by disconnecting power line input and also the output to the flash lamps by using contactors.

V. RESULTS AND CONCLUSION

The programmable power supply has been developed and tested to deliver rated average electrical power of 5 kW to the each of the two flash lamps to achieve average laser power of 500 W & test waveforms are shown in figure - 2. Safety interlocks have been successfully implemented and tested. The power supply has been installed at Advanced Fuel Fabrication Facility (AFFF), BARC, Tarapur and is being used for welding of fuel pins. Laser pulses with multi segmented temporal profile and structured burst sequence are highly useful in laser welding applications for various materials used in nuclear applications. The power supply controller provides convenience of programming the required laser waveshapes and fine adjustments in laser pulse parameters as well as laser output.

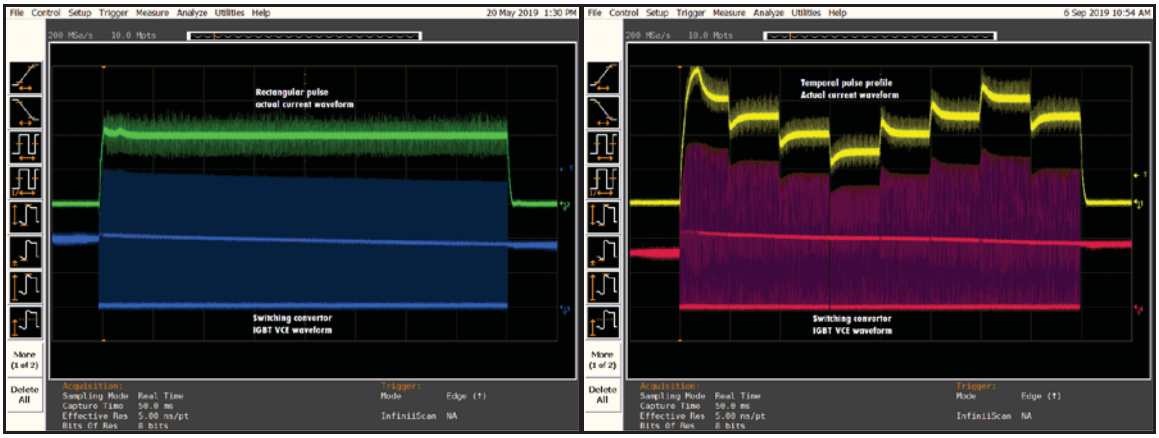

Figure – 2: Test waveforms

REFERENCES

1. G L Goswami and Dilip Kumar, *"laser materials processing"* Proceeding, Bull. Mater. Sci., **Vol 11**, Nos 2&3 November 1988, pp 213-224

2. Mohammed Naeem, Richard Jessett, John Chinn "*Welding performance of a 2 kW continuous wave supermodulated Nd:YAG laser – increased weld speed, weld penetration and reduced porosity with*

supermodulated output power", Proceedings of the **3rd** Pacific International Conference on Application of Lasers and Optics 2008, paper 303

3. Mohammed Naeem, Steve Keen "*Modulation techniques for enhanced materials processing using a SM fiber laser*", ICALEO® 2008: **27th** International Congress on Laser Materials Processing, Laser Microprocessing and Nanomanufacturing

4. Harald N. Bransh,"*Cutting and Welding Performance of High-power CW and Pulsed Nd:YAG Lasers*", https://doi.org/10.2351/1.5058542

5. Hui-Chi Chen, Guijun Bi, Bing Yang Lee, Chek Kweng Cheng, "*Laser welding of CP Ti to stainless steel with different temporal pulse shapes*", Journal of Materials Processing Technology, Volume 231, May 2016, Pages 58-65

Static Mode Performance Testing of a Streak Tube

Jankee Upadhyay *, Sudhir Kumar, Piyush Saxena, and R. Arya

Laser Electronics Division,

Raja Ramanna Centre for Advanced Technology, Indore,

*Corresponding Author: *Email:* janky@rrcat.gov.in

Abstract:

Different single shot S-20 streak cameras have been indigenously developed at RRCAT for various applications. With earlier developed streak cameras one could only achieve temporal and spatial resolutions up to 5 ps and 175 μm respectively. Moreover,they could not be operated selectively in synchroscan mode or single shot mode.With the objective of incorporating synchroscan mode or single shot mode with improved performance it is planned to develop streak camera using Photochron-5 S-20 Streak tube and MCP-125, S-20 Image Intensifier Tube from Photek . In this paper, static mode performance testing for a magnification of 2 of the tube is presented. In this regard, a high voltage divider network with adjustable voltages has been developed and used.

Introduction:

Streak tubes are used for the study of ultra fast optical phenomena and specifically measure the variation in light intensity as a function of time. Streak cameras are among the fastest detectors of light pulses. They are especially used in studies of laser plasma interaction, Equation of States studies and in measurement of electron bunch length in synchrotron radiation sources due to very fast response of ns and sub ns time resolution. Normally, the streak camera is used for measurement of single shot events where the accelerating grid is biased with DC voltage. However, for repetitive events, activating the accelerating grid with pulsed voltage can be provided for the selection of a single pulse to acquire proper streak images without integrating. However in order to use the streak camera in a synchroscan mode or single shot mode a suitable streak tube must be selected. The Photek Photochron-5[1] streak tubes have been installed in some of the world's best streak cameras with proven performance and reliability. The Photochron-5 was developed in collaboration with St Andrews University for use in Synchroscan cameras, and can achieve better than 2 ps time resolution in both single shot and synchroscan modes. Various application of the Photochron-5 streak tube includes development of Streak cameras for Equation of States studies[2,3] , Fusion Research ,Optical oscilloscope, LIDAR systems, Fluorescence Lifetime Imaging Microscopy (FLIM) ,Measurement of longitudinal electron beam parameters at indus-1 synchrotron radiation source using streak camera[4,5] and many more.

Key features of the Photochron - 5 Streak tube:

The Photochron-5 is having an S-20 Photocathode with Size of 8 mm slit,Synchroscan > 200 MHz. It provides a typical time resolution of 2 ps and can even provide up to 400 fs when using the streak tube with increased operating voltages however with decreased spatial resolution which is typically 50 lp/mm. Its spatial and temporal magnification can be altered by applying various combinations of voltages to its various electrodes as explained in the following section. It has Deflection Sensitivity of 75 V/cm and 250 V/cm in time Axis and spatial axis respectively. It can be used for UV, solar blind, visible & NIR responses. In addition to this it can be used with a mu-metal shield for high magnetic field environments.

There is a choice of input window available for the Photek streak tubes that include MgF2, fused silica and fibre optic. The Photochron-5 with MgF2 Input Window and Fibre optic Output Window has been optimised.The input window material of the photocathode would affect the overall sensitivity of the streak tube. The phosphor screen coated with P20 has its characteristic wavelength of 540 nm and anode efficiency of 12% which is measured as Optical Watts per Electrical Watts with 320 Photons/Electron at 5 kV .

Optimization and Operating Voltages

These tubes have an accelerator mesh and three focus electrodes.The tube can be operated over a range of voltages to

change electron optical magnification while maintaining minimum beam size within the deflector region to suit the requirements, which may be influenced by choice of solid state camera chosen. Table I shows the percentages of overall total voltage which is typically 7000V when applied to the cathode with screen and deflector region at ground and the corresponding magnification in temporal and spatial axes.

Voltages (V) %						Magnification	
Mode	**Cathode**	**Grid**	**Focus 1**	**Focus 2**	**Focus 3**	**Time**	**Spatial**
Mode 1	**-100**	**-75**	**-82**	**-78**	**-74.6**	**1.8 x**	**1.8 x**
Mode 2	**-100**	**-50**	**-65**	**-66**	**-76.6**	**1.8 x**	**2.1 x**
Mode 3	**-100**	**0**	**-29**	**-40**	**-76**	**2.6 x**	**2.6 x**
Mode 4	**-100**	**0**	**-44**	**-90**	**-71**	**3.9 x**	**3.9 x**

Table I: *Percentages of overall voltage applied to the cathode to* adjust *magnification*

Circuit Description:

Figure 1 shows a schematic diagram of the high voltage divider unit for testing the Photochron-5 in static mode. The divider network is powered with a 10 kV DC generated using a HV DC to DC converter (Pico make: Model:F121). High voltage thick film metal oxide resistors with 20 kV rating, 4 Watt power, with 2% tolerance are used for the divider network. In order to provide sufficient insulation ,the high voltage divider network has been housed in a box fabricated using 3 mm thick perspex sheet. Figure 2 shows a picture of the HV divider network.

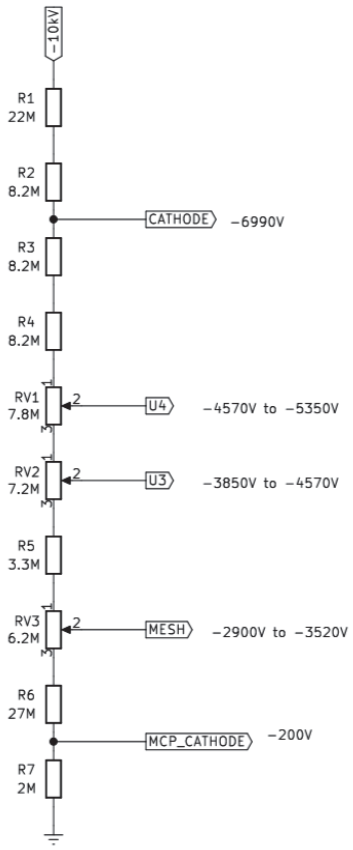

Figure 1. *Schematic diagram* of the high voltage divider network

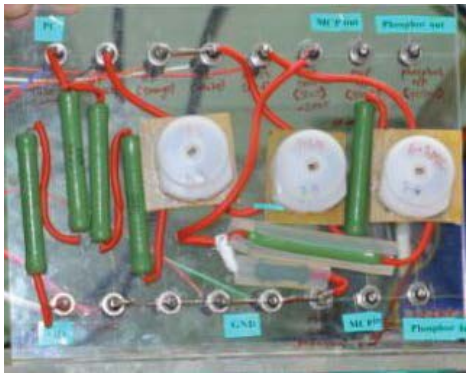

Figure 2: P*icture of the* High Voltage Divider Network

.

In addition to these high voltage resistors, special high voltage adjustable resistors have been used to adjust the required voltages at different electrodes. An experimental setup has been shown in Figure 3 for testing the Photochron-5 in the static mode. The magnification of the tube in time and space axes can be adjusted by varying the voltage across various electrodes as shown in the table I.

The static image after biasing various electrodes is shown in Figure 4.

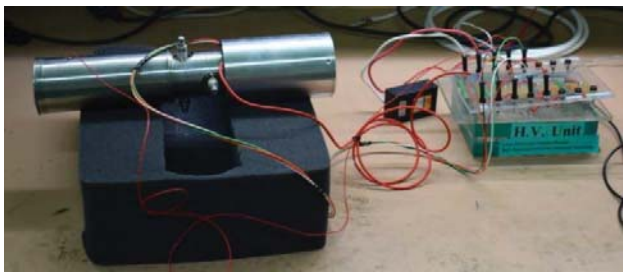

Figure 3: E*xperimental setup for static testing of the Photochron - 5 streak tube*

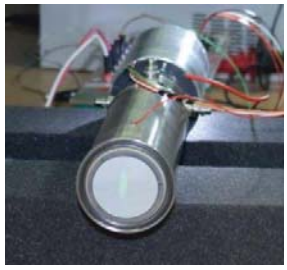

Figure 4: *An Static image* of the streak tube

Typical test voltage levels for various electrodes have been adjusted and set up to achieve magnification of 2X. Experimentally adjusted and set voltage parameters of the streak tube to achieve magnification of 2 are Cathode : -7000V, Mesh: -3540V ,U2: -4580V,U3: -4580V,U4:-5320V,Case: 0V/Earth, and Anode (Body): 0V/Earth

Conclusion:

In the present work, a high voltage (HV) divider network has been successfully developed and tested the performance of the Photochron-5, S-20 optical streak tube from Photek ,UK in the static mode with a magnification of 2. The HV divider network has been designed to provide adjustable voltages to work in different modes and for getting different magnifications in the temporal and spatial axes.

References:

1. Photek Limited, UK Streak Tube Photochron 5 ,Catalog Guide.
2. J.Upadhyay, M.L.Sharma, C.P.Navathe, R. Patidar, D.Dahiya, and A.Kumar, DAE-BRNS National Laser Symposium (NLS-22), Manipal University, Manipal, Karnatka, (2014).
3. M.J.Joshi, J. Upadhyay et al.“Design of microcontroller based system for automation of streak camera,” Rev. Sci. Instrum., 085106 (2010) 81.
4. J. Upadhyay et al. “Development of PCI controlled Gated Grid Optical Streak Camera”, RRCAT Report RRCAT/2012-12.
5. J. Upadhyay, Akash Deep Garg, Monika Jain, Avanish Ojha, Y. Tyagi, M.L. Sharma, T.A. Puntambekar, C.P. Navathe, and H.S.Vora“Measurement of longitudinal electron beam parameters using indigenously developed streak camera system at indus-1 synchrotron radiation source”, InPAC(2015), TIFR, Mumbai

Development of control software for cold atom interferometry experiments

Ayukt Kumar Pathak, Shradha Tiwari, P P Deshpande, Viraj Bhanage

MVAL, LCID, RRCAT, Indore-452013

ayukt@rrcat.gov.in

Abstract: Cold atom interferometry experiments are carried out in order to derive cold atom gravimeter measurements. It consists of processes such as laser cooling of Rb atoms, stabilization and compression of cold atom cloud, cooling in optical molasses etc. These events are controlled from devices such as Acousto-Optic Modulators (AOM), Power Supplies, and Mechanical Shutter which needs synchronised control with timing resolution of 1 microsecond for the events ranging up to 10s of seconds. This paper explains development of PC and FPGA based control software which consists of 32 Analog control channels and 24 Digital control channels.

Introduction: Cold atom interferometry experiments are carried out in order to derive cold atom gravimeter measurements[1, 2] . A setup for conducting cold atom interferometry experiments is being developed by Laser Physics Applications Section, RRCAT. The experiments involve processes such as laser cooling of Rb atoms, stabilization and compression of cold atom cloud, further cooling in optical molasses, launching of cold atoms in vertical upward direction, 1-D cooling using state selective Raman pulses and finally the Mach-Zehnder interferometer which is realized with a sequence of Raman pulses ($\pi/2$-π-$\pi/2$) in vertical geometry. The requirement of the control system can be explained by one of the operation, namely, optical molasses stage. In this step, temperature of the atom cloud is lowered to ~ 50 μK before launching them in upward direction. It requires reduction of frequency and power of the Magneto Optical Trap (MOT) laser beams in a precise and orderly manner which is achieved by controlling a pair of AOMs from 4 simultaneous analog control signals. Optical molasses continuous up to time scale of 10 ms which is divided in 5 segments of time with configurable amplitude in optional step or ramp manner.

In order to realize the above processes, an orderly operation of various devices such as 6 acousto-optic modulator (AOMs) (make: AA Opto-Electronic), 2 power supplies (make: Delta Elektronika) of magnetic coils, 6 mechanical shutters, 1 CCD camera (make: Pixelfly), etc. is automated and integrated in a single control software. Cold atom interferometry software requires definition of time duration and shape of amplitude for all control signals of constituent steps[3].

The design of control software for conducting these experiments becomes crucial as cold atom interferometry experiments require generation of above mentioned precisely timed control signals ranging from microseconds to seconds. In order to achieve the desired timing resolution of 1 microsecond and channel to channel synchronisation for over 32 channels; Field Programmable Gate Arrays (FPGA) based control system is designed. The paper discusses development of control software and software design features implemented in FPGA software and PC software to realize the experiment requirements.

Control Software Architecture: At the core of Control system are PC and Programmable Automation controller (PAC). NI make Programmable Automation controller c-RIO 9035 is used which consists of real time OS and

kintex-7 FPGA. PC is programmed to provide Graphical User Interface (GUI) and storage of experiment data and FPGA is programmed to generate analog and digital signal pattern with micro-seconds resolution and synchronisation.

NI LabVIEW is used to program PC and NI LabVIEW FPGA is used to program FPGA.

All of the devices are controlled through either analog control signal or digital control signal. These control signals are generated through a dedicated control channel from FPGA.

The required number of control channels is:

1.	Analog Channel with programmable ramp sequence generation	24
2.	Analog Channel with programmable step sequence generation	08
3.	Digital Channel	24

Table 1: List of Channels

If FPGA is programmed for complete configurable control sequences it runs out of logic gates and very less number of channels around 15 can be produced. So control sequence generation is divided between PC and FPGA. PC is used to format the data and FPGA is to generate the waveform with minimum logic gates. One of the methods for formatting at PC will be to generate set of all possible amplitude data for all channels with time step of 10 microseconds and transfer it to FPGA for generation. Since experiment duration is of the order of 10s of seconds so there will be millions of data produced and need to be transferred to FPGA. But in this case FPGA will run out of the memory element to hold data. So formatting of data at PC is optimised in such a way that minimum logic gates and memory element are used at FPGA.

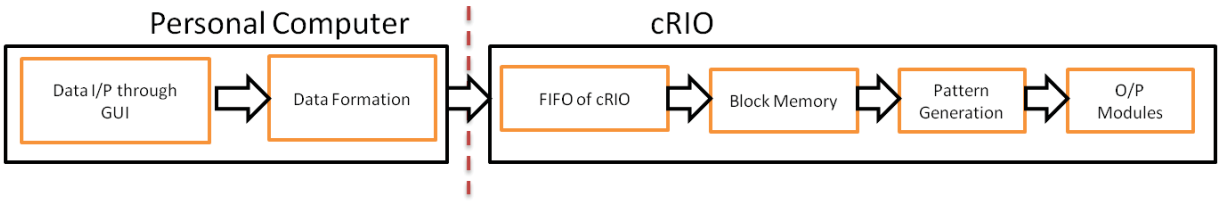

Figure 1: *Software Structure*

Figure 1 explains the software architecture. PC is providing GUI to take I/P for all channels. This data is formatted and transferred to FIFO of cRIO (Figure 1: Software Structure). It is then copied into block memory of cRIO to allow parallel access of data. This data is then used to generate pattern for each channel.

Control software Data Structure: There are two types of analog channels with 24 and 8 channel counts respectively. Type one analog channels has 10 segments in GUI and each segment has information of segment duration, final analog value and pattern of shape (Figure 2: Analog Channel input). This segment information is then formatted in 4 parts namely step time, Fractional change, Final analog value and no of steps (Figure 3:

Segment fragmentation). All the four parts are grouped in 4 separate arrays consisting information of all the channels. Step time array is explained in figure 4. First, step time of channels is grouped and then step time of all channels is grouped. Type two analog channels information is formated in 2 arrays of 80 elements for segment duration and final analog value respectively. Digital channel information is formatted in one array of 240 elements. In all it has 7 arrays which are transferred through FIFO to FPGA.

Figure 2: *Analog Channel input*

Figure 3: *Segment fragmentation*

Figure 4: *Generation of Array for step time values*

This Data is then transferred from FIFO to BLOCK memory of FPGA to allow parallel access.

For the analog channels, FPGA is programmed to generate final analog values from fractional input and transfer these analog values to output module. This process continues until complete segment is generated (**Figure 6.**). After generation of one segment next segment values are read from memory and process is repeated until final segment is generated. One set of control signal pattern is displayed in figure 5.

Figure 5: *One set of control signals*

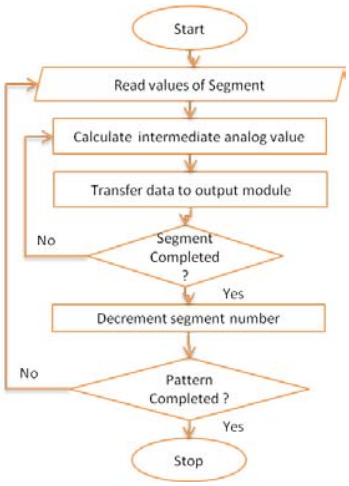

Figure 6: *Data Generation at FPGA*

Control Software Graphical User Interface:

Graphical User Interface is developed in LabVIEW. It has three types of control inputs viz. Analog channels (Ramp/Step), Digital channels and Analog channels (Pulse) (Figure 7: Graphical User Interface). Left panel of GUI consist of list of channels. Channel can be selected from list and one channel's control parameters are displayed in right side. By selecting control channel GUI allows entry of segment parameters. Each segment has two float data input for time and analog value and one drop down menu for type of change. All the experiment data can be saved and recalled by using graphical button available in GUI. There is one status bar displaying the status of software and necessary notification for experiment.

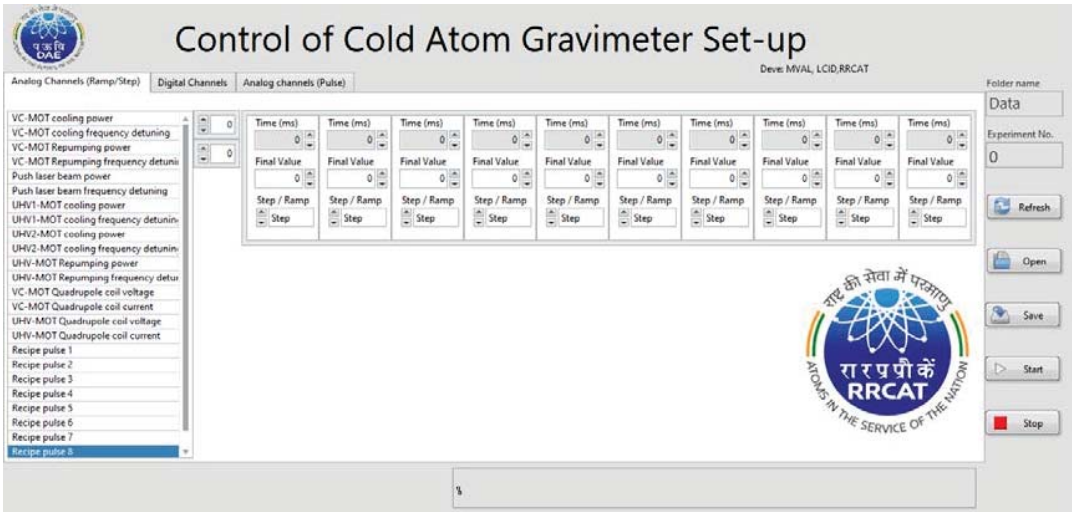

Figure 5: *Graphical User Interface*

Results: Software developed for PC and FPGA are tested for their timing requirements. It is able to generate synchronised control signals from 32 analog channels and 24 digital channels with timing resolution of 1 microsecond in time span of 10s of seconds. The resolution of output analog channel is 8 bit. In next stage of development, signal conditioning blocks will be integrated with FPGA output modules. Complete system will be integrated in control rack.

Acknowledgment: Authors wish to thank Shri S Singh, Smt B Jain, Shri S P Ram, Shri V B Tiwari and Shri S R Mishra from LPAS for their valuable technical discussion during development and support during the testing of software.

References:

1. A. Peters, K. Y. Chung and S. Chu, Meterologia 38, 25 (2001).
2. Z. Lin, X. Zong-Yuan, Y. Wei, T. Biao, P. Wen-Cui, W. Yi-Bo, X. Peng, W. Jin, Z. Ming-Sheng, Chin. Phys. Lett., 28, 013701 (2011).
3. Ayukt k Pathak, Shradha Tiwari, P P Deshpande, Viraj Bhanage, NLS 26, 2017.

Theses Abstract

Laser Drilling and Welding of Advanced Engineering Materials: An Experimental Investigation

Suman Chatterjee

Department of Mechanical Engineering, National Institute of Technology, Rourkela 769008

Abstract

Conventional drilling of advanced engineering materials is extremely difficult because of occurrence of rapid tool wear and frequent tool breakage. Likewise, conventional welding processes poses difficulty in fabrication works made of advanced engineering materials such as stainless steel, titanium alloy and shape memory alloy due to excessive heat generation causing high risk of contamination and distortion of weldment. Therefore, laser (Light Amplification by Stimulated Emission of Radiation) is gaining popularity for micro-drilling as well as welding because a high intensity heat source is applied at the precise location to achieve the desired output. The present study focusses on application of laser during micro-drilling, welding of similar/dissimilar materials. In order to gain insight into effect of process parameters on output measures during micro-drilling and welding on thin foils of 0.45 mm thickness, extensive experimental investigation is performed using millisecond pulsed Nd:YAG laser. During micro-drilling, it is observed that spatter area and heat affected zone (HAZ) increase with increase in laser current and pulse width due to increase in heat input causing more material to melt but sufficient time is not available for completely flushing away the molten material. As a result, heat is not properly dissipated resulting in increase in spatter formation and heat affected zone. It is also observed that increase in pulse frequency and gas pressure leads to decrease in spatter area because of formation of laser supported absorption (LSA) wave which blocks the input energy to penetrate adequately. During laser welding of similar materials, it is found that micro-hardness value in the fusion zone of the weldment is much higher than the base material for stainless steel in comparison with welding of titanium alloy. This phenomenon may be due to higher cooling rate observed in case of stainless steel as compared to titanium alloy. This drilling of titanium alloy and stainless steel have potential application in manufacturing of medical implant, compressor blading in gas turbine, turbochargers and steam turbine valve seat. Similarly, welding of thin sheets have potential applications in automobile, razor blades, jet planes, electrical circuits and micro-electromechanical systems.

Artificial intelligence (AI) techniques such as adaptive neuro-fuzzy inference system (ANFIS) and multi-gene genetic programming (MGGP) are used to predict the performance measures such as circularity (at entry and exit), heat affected zone, spatter area and taper for laser drilling process. Similar artificial intelligence techniques are used for the prediction of performance measures like bead width, heat affected zone, surface roughness and welding strength during laser welding. Comparative study of AI models suggests that MGGP predicts the performance measures in an effective manner as root mean square error (RMSE) for testing is minimum as compared to ANSIS in both laser drilling and welding operations and can be potentially used for accurate prediction of desired output.

Joining of dissimilar materials like shape memory alloy with titanium alloy and stainless steel is one of the challenging process due to the formation of brittle intermetallic compounds (IMCs). Therefore, the study is further extended to find the feasibility of dissimilar metal joining of nitinol, a shape memory alloy, with stainless steel and titanium alloy separately using copper as interlayer (100 μm foil) during fiber laser welding. Physical and mechanical analysis of the weldments reveals crack-free surface of weldpool and minimum percentage of porosity. The study indicates that minimum tensile strength of the welded joint is more than the ultimate tensile strength of the weakest intermediate material i.e. copper. The study examines the possibility of using high melting point intermediate layer material during welding of nitinol with other materials to avoid formation of unwanted phases.

Dissimilar metal joining of titanium alloy with stainless steel sheets having five millimeter thickness using CO_2 laser providing copper as interlayer using electroplating process. Presence of copper provides compatibility between titanium alloy and stainless steel during laser welding process and reduce brittle interfaces. The study suggests that the presence of interlayer during joining of dissimilar materials provides stable, crack-free and less brittle joints as compared to joining of dissimilar materials without interlayer. The study also examines the possibility of providing interlayer using coating technology during dissimilar metal joining. The dissimilar joining of advanced engineering materials helps to provide hybrid system performance finding potential application in the field of various industrial applications like seismic damping device, petrochemical devices, aerospace equipment and medical equipment.

Keywords: Titanium alloy; Stainless steel; Shape memory alloy; Laser drilling; Laser welding; Dissimilar laser welding; Electroplating; Interlayer; Radiographic; Surface integrity; Weld geometry; Pores analysis; Intermetallics; Fracture analysis; Adaptive neuro fuzzy inference system (ANFIS); Multi-gene genetic programming (MGGP).

1. Research Gap and Objectives

Extensive literature review reveals that the past works on laser drilling and welding on advanced engineering materials are limited to identify significant process parameters and their effect on performance measures. It is also noted that past research works are limited to drill thick sheets but hardly explored the possibility of laser drilling on thin sheets (foils). Likewise, few works focus on laser welding of dissimilar materials.

To address the above issues, followings are the primary research objectives of the present dissertation work:

- To study influence of process parameters on performance measures during laser drilling operation based on exhaustive experimental analysis.
- To study influence process variables on performance measures during laser welding of similar materials of thin sheets.
- To propose an artificial intelligence models for predicting the performance measures during laser drilling and welding operations.
- To explore the feasibility of laser welding of dissimilar materials like Nitinol, a shape memory alloy, with different advanced engineering materials using thin intermediate layer.
- To explore the feasibility of dissimilar laser welding of titanium alloy with stainless steel plates using electroplating technique for providing interlayer.

2. Organization of Thesis

To meet the objectives of the study, the present dissertation is presented in a following manner:

CHAPTER 1: INTRODUCTION

Chapter 1 introduces the motivation for the research with brief discussion on applications of laser material processing techniques such as laser drilling and laser welding processes on advanced engineering materials. The present chapter states the objectives of the research addressing the research gap. The chapter also presents the layout of the dissertation. The research plan is shown with the help of Figure 1.

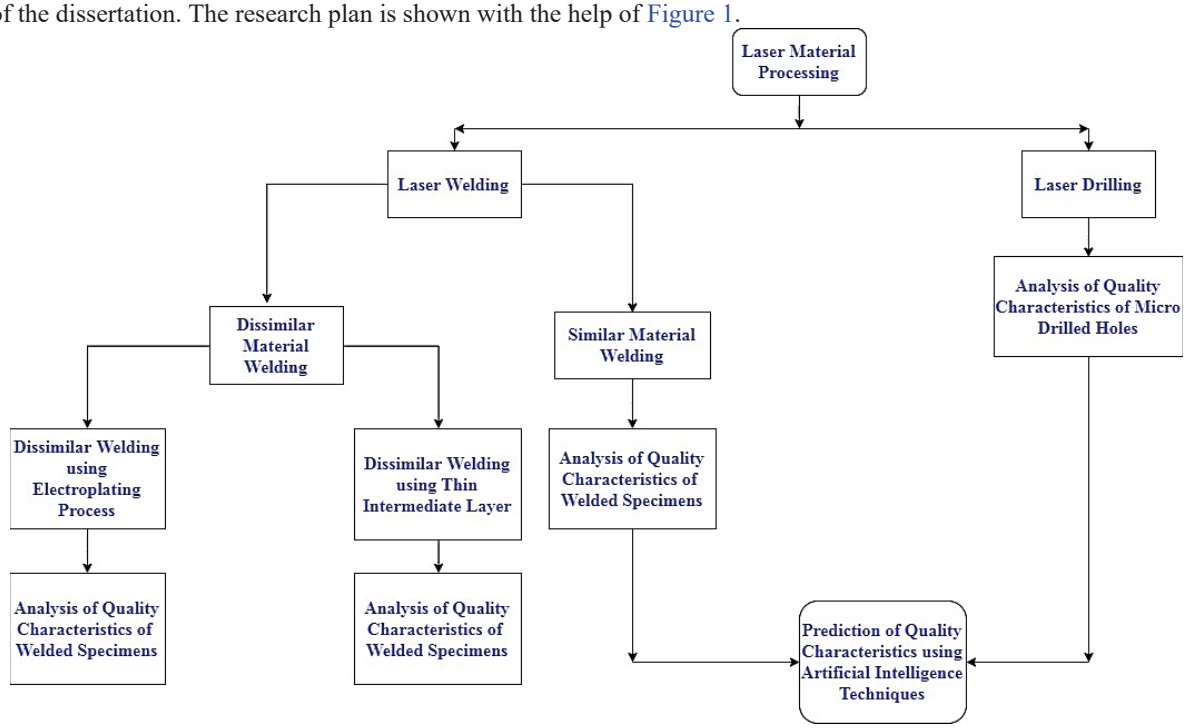

Figure 1: Research plan

CHAPTER 2: LITERATURE REVIEW

This chapter presents critical review on literature presents for the recent study. The study is restricted to the literature that are available with full text. The present chapter also highlights past research works relevant to the present study and provides background for the dissertation. Figure 2 indicates the percentage of articles in different study areas out of total articles cited in this work. It is evident from Figure 2 that less attempts have been made on laser drilling of thin sheets, laser welding of thin sheets, dissimilar laser welding using interlayer, dissimilar laser welding on shape memory alloy with other advanced engineering materials and application of artificial intelligence (AI) in laser material processing.

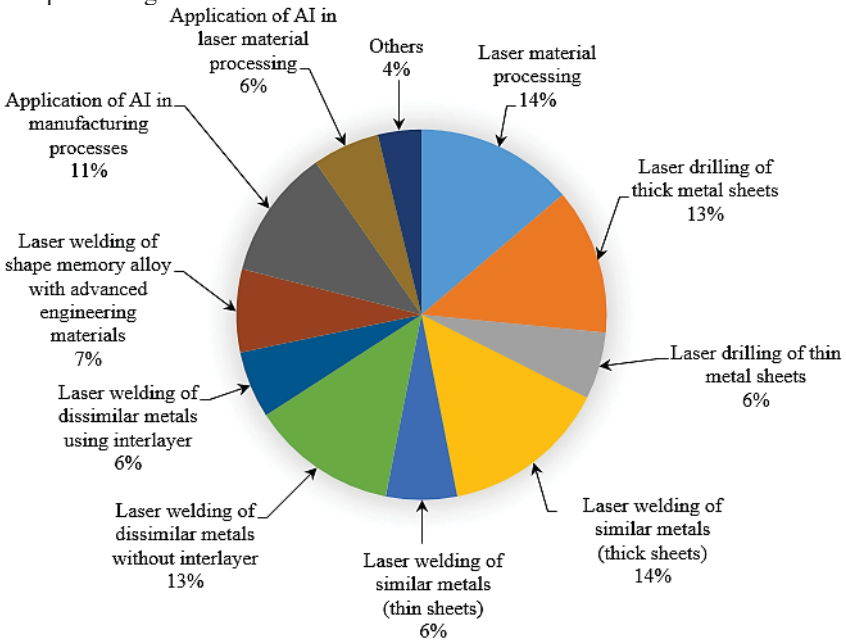

Figure 2: Pie-chart showing classification of articles referred in dissertation

CHAPTER 3: LASER DRILLING OF THIN SHEETS

In this chapter, laser drilling on stainless steel and titanium alloy of 0.45 mm (thin sheets) have been performed using millisecond pulsed Nd:YAG laser under identical parametric (experimental) conditions. A comparative study on parametric analysis has been made to identify influence of machining parameters such as laser current, pulse repetition rate, pulse width and gas pressure on quality characteristics of laser drilled samples. The quality of the laser drilled holes is measured on basis of circularity (at entry and exit), spatter area, taper and HAZ. It is observed that HAZ is higher for Ti6Al4V sheets as compared to AISI 316. Scanning electron microscope (SEM) images of the hole periphery reveals micro-cracks, burr formation and surface erosion. HAZ, micro-crack, surface erosion and burr near the micro-drilled holes on Ti6Al4V and AISI 316 can be visualized in Figure 3.

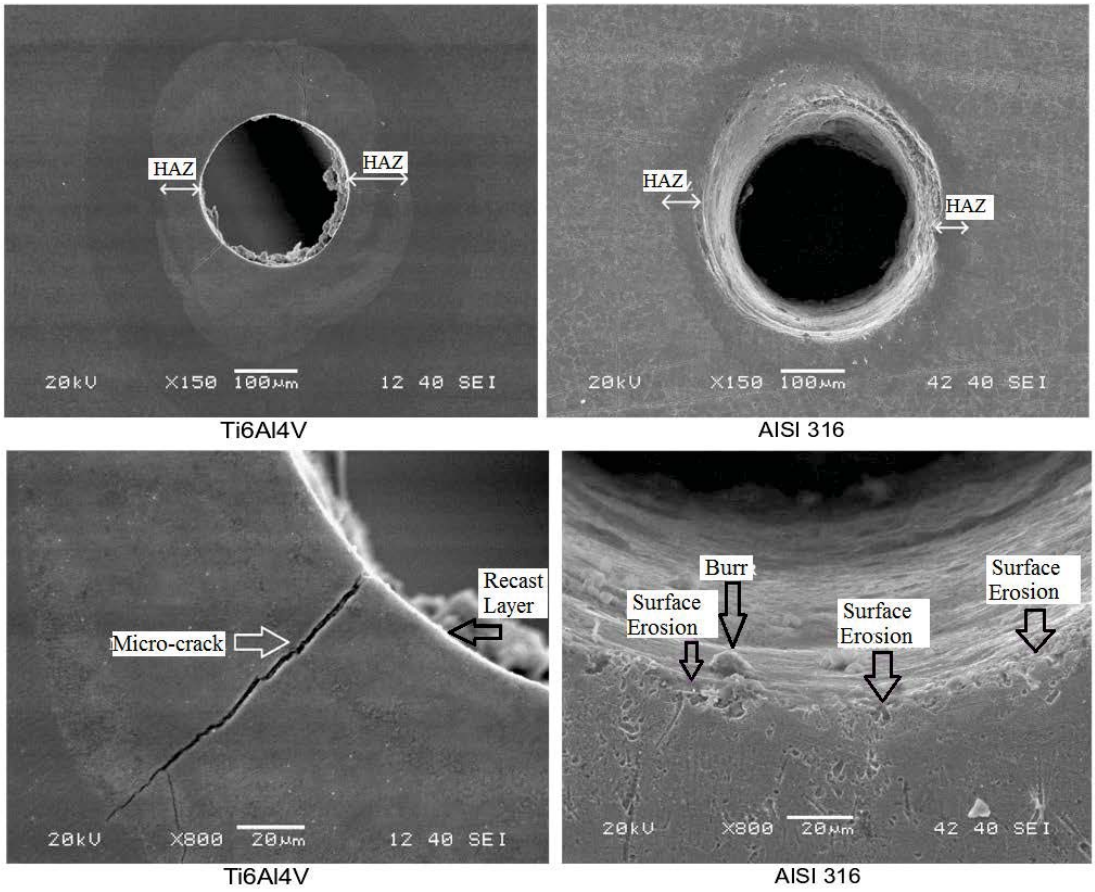

Figure 3: Laser micro-drilled holes

CHAPTER 4: LASER WELDING OF THIN SHEETS (SIMILAR MATERIALS)

In this chapter, an experimental study has been conducted to identify the influence of control parameters on quality characteristics such as surface integrity, heat affected zone and bead width during welding of similar materials of thin sheets (stainless steel with stainless steel and titanium alloy with titanium alloy) using pulsed Nd:YAG laser. The study examines the Vicker's micro-hardness of the welded samples near base material (BM), heat affected zone and fusion zone (FZ) (Figure 4(a)). It is observed that micro-hardness value is higher at FZ as compared to HAZ and BM for both the materials. The study also examines the influence of overlapping factor (Figure 4(b)) on weld strength and surface integrity of the weldments. The study is extended to examine the fractographic analysis of the fracture surface of the tensile test specimens (Figure 4(c)). The study reveals the presence of dimples and quasi-cleavage planes on the fracture surface.

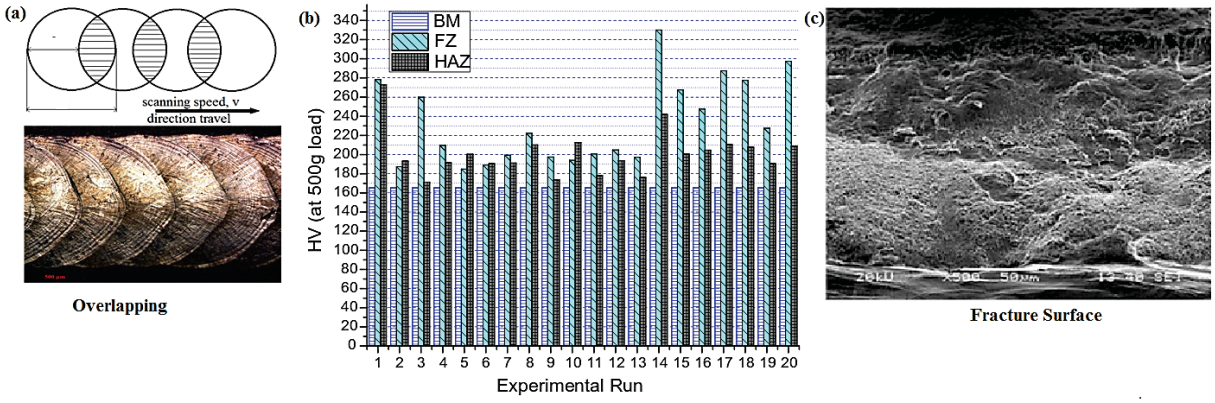

Figure 4: (a) Overlapping factor (b) Micro-hardness of weldment (c) Fracture surface of weldment

CHAPTER 5: PREDICTION OF QUALITY MEASURES USING ARTIFICIAL INTELLIGENCE TECHNIQUES

In this chapter, artificial intelligence (AI) techniques such as adaptive neuro fuzzy inference system (ANFIS) and multi gene genetic programming (MGGP) are used to predict the performance measures such as circularity at entry and exit, heat affected zone, spatter area and taper for laser drilling process. Similarly, ANFIS and MGGP have been used to predict the performance measures such as bead width, heat affected zone, surface roughness and welding strength of weldments during laser welding process. The study indicates that both the AI techniques adequately predict the performance measures for laser drilling and laser welding of AISI 316 and Ti6Al4V. However, MGGP model exhibits comparatively less root mean square error (RMSE) during testing phase. Therefore, it is corroborated that MGGP has superior prediction capability.

CHAPTER 6: WELDING OF DISSIMILAR MATERIALS USING INTERLAYER (NITINOL WITH STAINLESS STEEL)

Joining of dissimilar materials like nitinol with stainless steel is one of the challenging fabrication processes due to formation of brittle intermetallic compounds (IMCs) within the weldpool due to incompatible physical and metallurgical properties. In addition, transverse cracks appear in the weldpool because of different thermal expansion coefficients of the materials during dissimilar metal welding process without interlayer. In the present chapter, a thin film of copper (100 μm) is used as an interlayer during joining of stainless steel to nitinol plates in a butt joint configuration using continuous wave fiber laser system. The aim of the study is to investigate the effect of interlayer on the physical and mechanical properties of the welded joints. The micrograph shown in Figure 5(a) indicates three different zone such as base material (AISI 316), heat-affected zone nearer to AISI 316 side and fusion zone (FZ). Presence of planar, cellular and dendritic structure near the HAZ can be observed. However, as one moves from HAZ to FZ, presence of columnar dendritic and equiaxed grain structures can be seen. Likewise, three zones can also be observed in nitinol side. Figure 5(b) shows the fracture surface of the joint welded at 600 W and 8.5 mm/s during tensile test. The fracture surface shows cup and cone shape and dimples indicating ductile failure of the weldment.

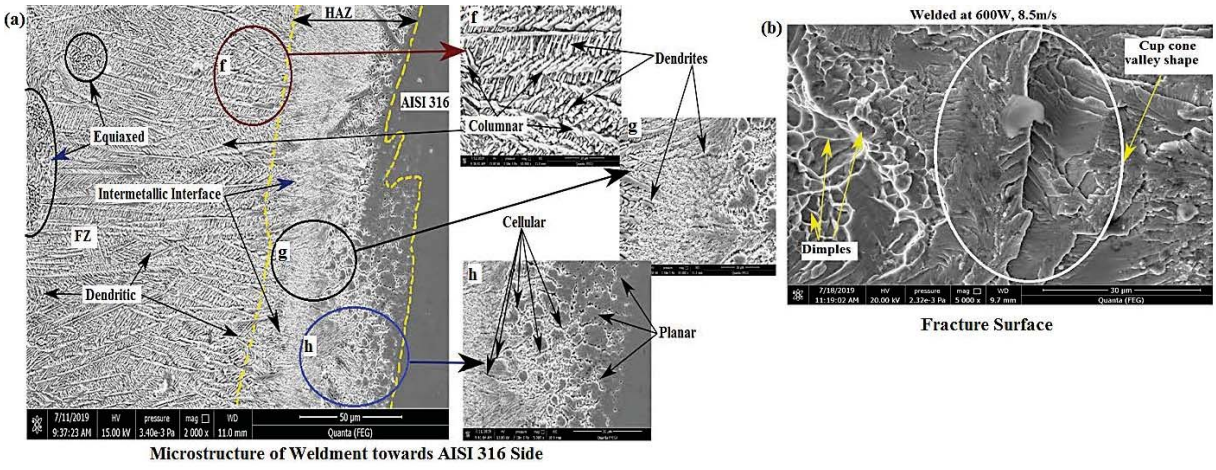

Figure 5: Micrograph of weldment of dissimilar materials (NiTi and AISI 316)

CHAPTER 7: WELDING OF DISSIMILAR MATERIALS USING INTERLAYER (NITINOL WITH TITANIUM ALLOY)

Cai et al. [16] have pointed out that joining of nitinol with titanium alloy without interlayer is difficult because severe mechanical and metallographic problems arise due to chemical and physical incompatibilities of both the materials. In the present study, copper is used as an intermediate layer to restrict the formation of brittle intermetallic and obtain good weldability during joining of nitinol with titanium alloy using fibre laser. The present chapter aims at analyzing the possibility of welding of 1.8 mm thick titanium alloy with 1.7 mm thick nitinol using copper as an intermediate layer by shifting the laser offset towards titanium side by 60% and focused at an angle of 15^0 with the

vertical axis. The experimental investigation is conducted using a high power continuous wave (CW) 6 kW fiber laser in a butt joint configuration. Figure 6(a) shows the weld geometry which is distinguished by five different regions such as base material (NiTi), heat affected zone near NiTi (HAZ_1), fusion zone (FZ), heat affected zone near Ti6Al4V (HAZ_2) and base material (Ti6Al4V). Presence of crater and root effect is clearly visible in the figure. Magnified image HAZ_1 region shown in Figure 6(b) clearly indicates presence of planar grain structure near the base material and HAZ interface, cellular grain structure in the HAZ region and dendritic grain structure in the fusion zone of the bead geometry. The microstructural analysis indicates the presence of two different regions within the HAZ such as H_1 (inter-critical heat affected zone) and H_2 (fine grain heat affected zone). Figure 6(c) shows the presence of nano-cracks, droplets, quasi-cleavage and dimples on the fracture surface during tensile test of joint. Figure 6(d) shows the welding strength of weldments at different parametric settings. It is observed that highest welding strength is obtained at parametric setting of 800 W laser power and 17 mm/s welding speed.

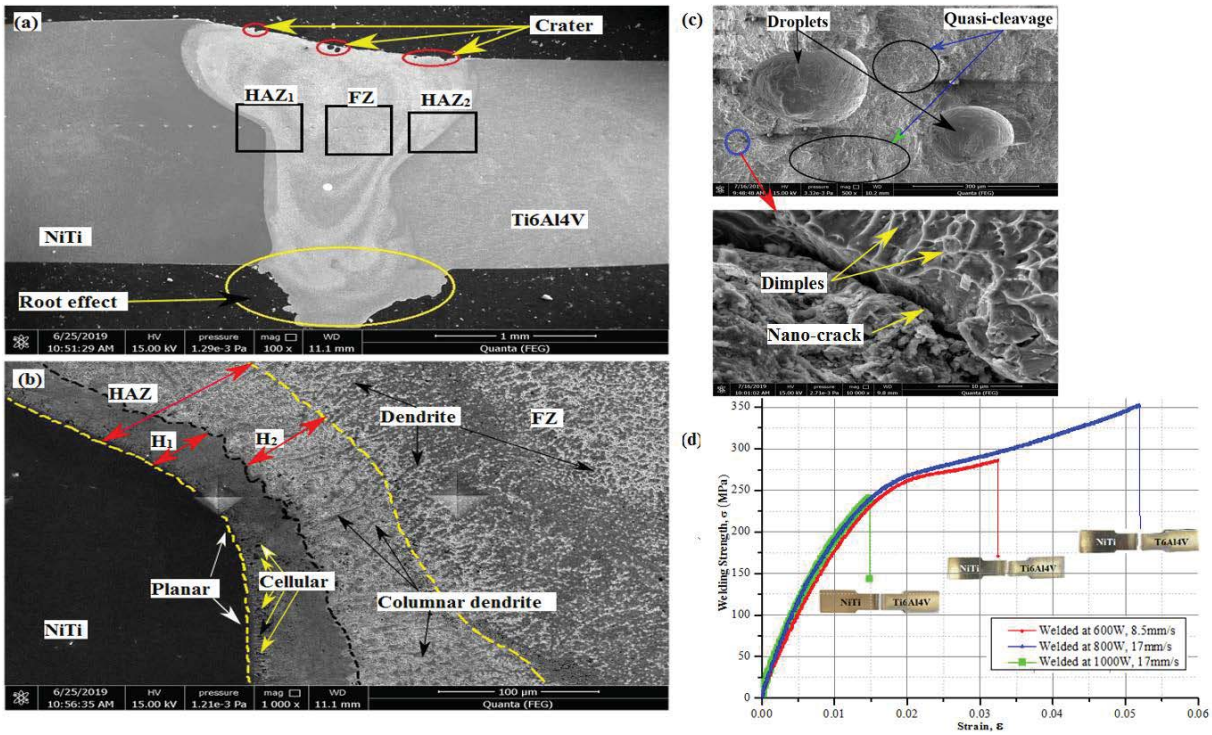

Figure 6: Micrographs of weldment of dissimilar materials (NiTi and Ti6Al4V) (a) weld geometry, (b) microstructure of HAZ_1 region, (c) fracture surface analysis and (d) stress strain graph of the weldments

CHAPTER 8: LASER WELDING OF DISSIMILAR MATERIALS PROVIDING INTERMEDIATE LAYER THROUGH ELECTROPLATING

This chapter deals with possibility of using electroplating technique (copper plating) for providing intermediate layer for during butt welding of titanium alloy with stainless steel using 3.5 kW laser power continuous wave (CW) CO_2 laser. The present study explores the influence of intermediate layer on weld morphology. Analysis of weldment reveals that crack free surface can be obtained (Figure 7(a)) and welding strength of 34 MPa can be attained using the proposed methodology (Figure 7(b)). Success of the welding opens the possibility of using high melting point intermediate layer material during welding of titanium alloy to stainless steel to avoid the formation of unwanted phases and improve weldability.

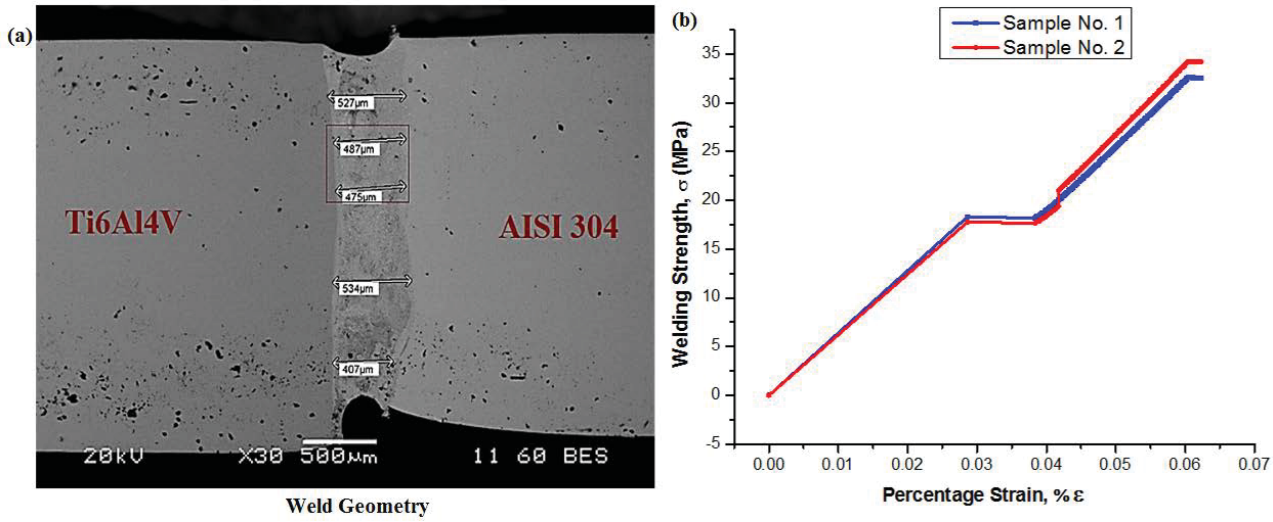

Figure 7: (a) Weld geometry of the weldment (b) Stress strain graph of the weldment

CHAPTER 9: EXECUTIVE SUMMARY, CONTRIBUTIONS AND FUTURE SCOPE OF WORK

This chapter presents the major findings and contribution towards the research in the field of study. The chapter also discusses future scope of the present research work. Finally, the dissertation is ended with references and list of publications from the present research work.

3. Summary of Findings and Contribution to Research Field

Important research findings from the present work and contribution to the field are summarized as follows:

- During laser drilling operation, it is observed that spatter area increases initially with increase in laser energy but decreases after a certain value of laser energy. This phenomenon may be attributed to formation of laser supported absorption (LSA) wave after a certain value of laser energy leading to blockage of laser energy. Therefore, material ejection gets reduced resulting in decrease of spatter formation.
- Examination of quality of micro drilled holes through micrography reveals that burr formation in the hole periphery increases with increase in pulse repetition rate. It is also observed that increase in laser energy leads to increase in heat affected zone (HAZ) and circularity but reduction in burr formation. Reduction in HAZ and circularity of hole is observed when gas pressure is increased.
- It is observed that resistance to micro cracking is more with stainless steel work piece as compared to titanium alloy work piece when both stainless steel and titanium alloy work pieces are laser micro-drilled under identical machining conditions.
- Crack intensity on drilled surface increases with increase in pulse repetition rate and gas pressure. However, severity of surface cracking largely depends on thermal conductivity, ultimate tensile strength and the fracture toughness of the work material during laser micro-drilling.
- During laser welding of foils of similar materials, it is observed that overlapping factor has significant effect on mechanical properties of the weldments. Spot overlapping factor (O_f) adversely influence the surface integrity (surface finish). However, welding strength increases with increase in overlapping factor. Overlapping factor decreases with increase in scanning speed (welding speed).
- From the present work, it is noted that MGGP model shows minimum root mean square error (RMSE) as compared to ANFIS model for selected performance measures during laser drilling and welding. MGGP can be treated as an adequate artificial intelligence model in predicting the performance measures for laser micro-drilling and welding.
- Providing copper foil as an interlayer during welding of sheets of dissimilar materials such as nitinol with stainless steel and nitinol with titanium alloy, crack free welded joints can be obtained. Thickness of interlayer plays a significant role to achieve welding strength. However, increase in thickness of interlayer beyond 100 µm softens the weldpool resulting in difficulty to attain good welding strength. Use of copper as an interlayer helps in attaining maximum welding strength of 219.74 MPa for weldments of nitinol with stainless steel and 353 MPa for weldments of nitinol with titanium alloy. The obtained ultimate tensile strength of the weldment is higher than ultimate tensile strength of copper.

- Laser welding of dissimilar materials such as stainless steel with titanium alloy both of 5 mm thickness has been attempted in a novel way providing copper as an intermetallic layer through electroplating process. Maximum welding strength of 34 MPa has been obtained and it is quite acceptable.

Studies on Electron Beam and Laser Surface Melting and Welding of INCONEL 718

Sumit Kumar Sharma

Indian Institute of Technology Kharagpur, Kharagpur - 721302

Abstract

The present study aims to investigating the effect of electron beam processing (surface melting and welding) and laser processing (surface melting and welding) of Inconel 718 on its microstructure, mechanical properties and electro chemical properties. The study has been divided in to four parts: (1) electron beam surface melting, (2) laser surface melting, (3) electron beam welding, and (4) laser welding of Inconel 718. Electron beam surface melting has been carried out at using an indigenously developed conventional electron beam processing unit (with a capacity of 80 kV acceleration voltage & a power of 12 kW) at a constant voltage of 40 kV with varying scan speed from 500 mm/min to 1000 mm/min. Electron beam welding of Inconel 718 alloy was carried out using a constant acceleration voltage of 70 kV, welding speed of 2000 mm/min under varied currents of 45 mA, 58 mA and 67 mA, respectively. Laser surface melting and welding of Inconel 718 was carried out using 2 kW continuous wave Yb-fibre laser. Surface melting has been conducted with a power of 400 watts, scan speed of 500, 750, and 1000 mm/min and with a spot diameter of 3 mm. Laser welding was carried out at constant power 1800 watt with a varying scan speed of 1400, 1200 and 1000 mm/min, respectively. The detailed study involves understanding of the effect of process parameters on surface morphology, bead geometry, microstructure, residual stress, microhardness, wear resistance, and electrochemical properties.

Electron beam surface melting forms a defect-free microstructure with the depth of melting varying from 240 μm to 720 μm and the depth of melting decreases with increase in scan speed. The microstructure of the melt zone is having dendritic morphology and consists of gamma (γ), gamma prime (γ′) and small fraction of gamma double prime (γ′′) along with few precipitates. Electron beam surface melting introduces residual compressive stress (-180 MPa to -1000.21 MPa) which varied with process parameters. Due to electron beam surface melting, there is increase in surface hardness from 278 VHN for as received Inconel 718 to 950 VHN for electron beam melted Inconel 718. Maximum microhardness is observed at a depth below 100 to 200 μm from the surface. Microhardness was also found to vary with heat input parameters. The optimum process parameters of electron beam surface melting corresponding to development of defect free microstructure with presence of compressive residual stress below yield strength. Due to electron beam surface melting, there is a significant decrease in corrosion rate with a maximum decrease observed for the samples melted with a scan speed of 1000 mm/min. The pitting corrosion resistance remained unaffected because of electron beam surface melting. Electron beam surface melting caused a marginal decrease in wear kinetics and wear coefficient.

Laser Surface melting offers a defect free melt zone with depth varying from 388 μm to 453 μm. In the microstructure, there is presence of gamma double prime (γ′′) phase in addition to gamma (γ) and gamma prime (γ′) phases. The microhardness of the melted zone was found to vary from 425 VHN to 475 VHN. A detailed electron back scattered diffraction (EBSD) analysis was conducted to understand the grain size and its distribution, grain boundary rotation angle, and texture. Laser surface melting with the parameters (750 mm/min) shows a minimum

wear kinetics under steady state wear. Wear coefficient was also found to vary with laser parameters and a minimum wear coefficient was observed when laser melted using scan speed 500 mm/min and power of 400 watts. Wear rate was found to be reduced due to laser surface melting and decreased with increase in scan speed.

Electron beam welding was successfully applied to weld Inconel 718 of thickness 3 mm. the microstructure was dendritic with the presence of gamma (γ) and gamma prime (γ') and gamma double prime (γ'') phases. There is improvement in microhardness due to electron beam welding (471.6 VHN to 520.5 VHN) as compared to as received Inconel 718. A detailed study of the mechanical properties shows that there is reduction in strength and percentage elongation due to electron beam welding as compared to base metal. Though the corrosion rate in 3.56 wt.% NaCl solution was reduced due to laser surface melting, however, pitting corrosion resistance was improved due to laser surface melting. Laser beam welding leads to marginally decrease in hardness for all the parameters except a few. There is a significant decrease in nano hardness and young modulus but increase in toughness due to laser welding. A detailed crystallographic texture was studied by electron back scattered diffraction (EBSD) analysis to know the crystallographic orientation.

Based on the detailed correlation between microstructure, process parameters and microhardness, the processing region for electron beam surface melting of Inconel 718 were as follows: at constant current of 10 mA, and acceleration voltage 40 kV with varied scan speed between 500 to 1000 mm/min. The most important outcome of electron beam surface melting of Inconel 718 is the increased corrosion resistance of electron beam surface melted specimens in comparison to as received Inconel 718. When processed using a scan speed of 750 mm/min and 1000 mm/min, an improvement in corrosion resistance property is observed for sample melted using a scan speed of 750 mm/min. (0.04 mm/year) as compared to 0.39 mm/year for as received Inconel 718. Laser surface melting of Inconel 718 was performed at constant power of 400 watts and with varying scan speed between 500 mm/min to 1000 mm/min. In laser surface melting the main outcomes are corrosion resistance, due to laser surface melting, there is improvement on corrosion resistance when processed using a scan speed of 500 mm/min (0.17 mm/year) and 1000 mm/min. (0.18 mm/year) as compared to 0.39 mm/year for as received Inconel 718. Electron beam welding of Inconel 718 has been carried out at constant scan speed of 2000 mm/min and acceleration voltage 70 kV with varied current of 45 mA, 58 mA, and 67 mA. Detailed study of the corrosion behavior in a 3.56 wt.% NaCl solution shows that there is no significant variation in corrosion rate due to electron beam welding. However, an improvement in corrosion rate could be achieved by proper selection of process parameters in electron beam welding. Laser welding has been carried out at constant power 1800 watt with varied scan speed 1000 mm/min to 1400 mm/min. However, there was improvement in hardness because of laser welding (278 to 319 VHN)

Inconel 718 possesses good fatigue strength, cryogenic properties, a high temp oxidation resistant and creep resistant properties. As a result, it is commonly used as structural materials over a wide temperature range starting from cryogenic temperature to as high as up to ~700°C. The possible application of the surface melted Inconel 718 will be components in aircraft engine like, spool, combustion casing, turbine disc, gear components etc. and the possible application of welded Inconel 718 will be components of jet engines, jet turbine like forging parts, pump components like stator and rotor, cryogenic storage tank, pressure vessels for rocket, etc.

Keywords: Electron Beam, Laser, Surface Melting, Welding, Inconel 718, Wear, Corrosion, EBSD

Efficient Terahertz (THz) generation from some indigenously grown organic nonlinear crystals and designing of band pass filters for spectroscopy of high energy materials.

Ganesh Damarla

University of Hyderabad, Hyderabad.

Thesis abstract

In this thesis, we focussed our study on addressing the generation of intense, broadband Terahertz(THz) radiation with nonlinear crystals of different kinds. Spectroscopic study has been done to extract the absorption coefficient and dielectric properties. Terahertz radiation has number of applications in the field of spectroscopy, biomedical, pharmaceutical industry, defence science and technology, telecommunications etc. The advancement in the electronics, data acquisition helped to fill the THz gap in the electromagnetic spectrum. One of the major challenges in THz technology is to overcome the atmospheric absorption which limits the use of THz spectroscopy and imagining from long to short distances. This problem can be solved by means of developing a high intensity THz radian sources and sensitive detector, post processing of obtained time domain spectrum with suitable algorithm to remove the interfering absorption lines cause by the atmosphere. We have also made an attempt to design and fabricate bandpass filters in THz region for sensing applications.

1. **Building of THz spectrometer:** A multipurpose THz generation and detection experimental setup has been designed where one can carry out different types of experiments such as optical pump terahertz probe, generation and detection of THz radiation using different types of materials. Since in current setup position of generator and detector components can be interchanged. Therefore, all four types of combinations like photoconductive antenna- antenna, antenna- nonlinear crystals, nonlinear crystal- antenna and nonlinear crystal- crystal as source and detector can be made. Moreover, this set-up can work in both transmission and reflection modes.

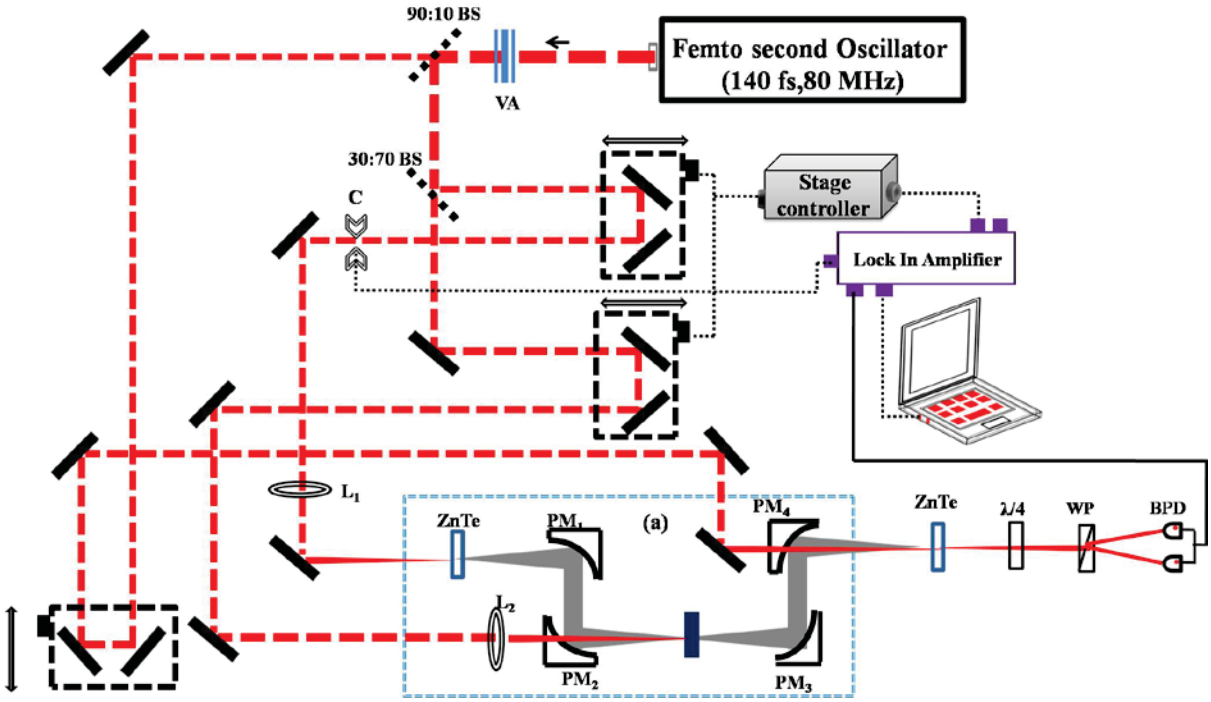

Figure1: Multipurpose THz generation and detection experimental

2.Genaration of THz from different organic crystals:

we have evaluated different types of indigenously grown organic crystals such as BNA OH1, LAP. These crystals were characterized in terms of growth solvent, optical transmission range, absorption coefficients. Since the transmission of all these crystals varying in optical domain therefore it also reflected their potential use as an efficient THz source. The solvent effect on THz generation ability of BNA crystals has been discussed. L-arginine phosphate monohydrate (LAP) has been studied as a THz source and its absorption and refractive index are reported in THz domain for the first time

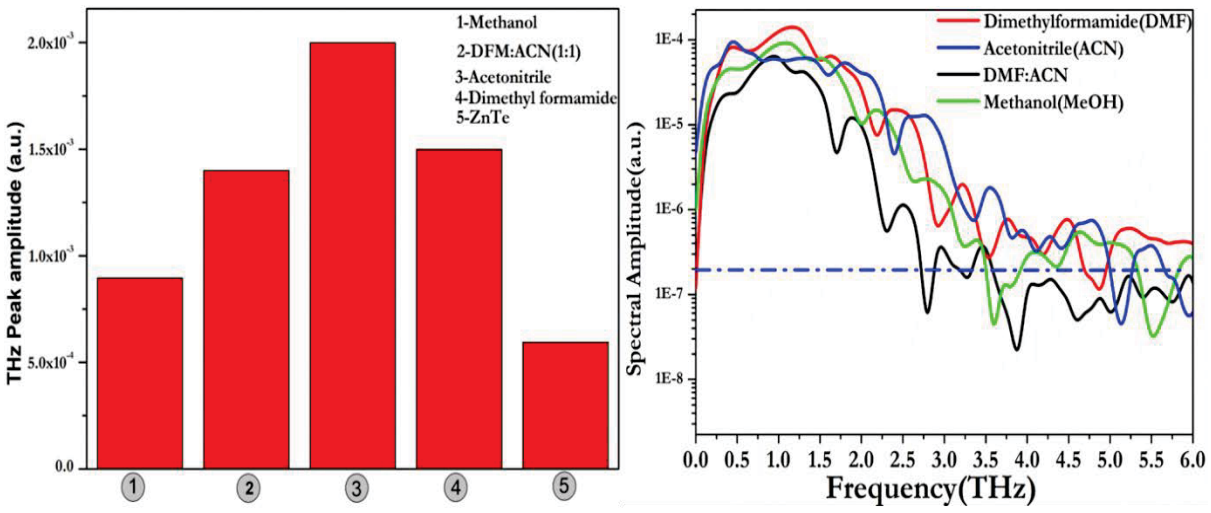

Figure 2a) Terahertz peak amplitude values of different solvents. b) Frequency domain spectrum of Terahertz radiation

3. THz spectroscopy:

The efficiently generated THz radiation was used to identify the signature absorption peaks of high-energy materials. we have studied the linear and nonlinear optical properties of newly synthesized tetrazole molecules using time- domain terahertz spectroscopy, UV−visible−NIR spectroscopy. We have also ascertained the absorption coefficients and refractive index between 0.1 and 2.2 THz range. In addition, we have performed single-molecule and single-crystal level Density functional theory (DFT) calculations. The theoretically calculated zone center vibrational frequencies at the solid level were compared with experimentally obtained found data, they are found to be good in agreement. We have also explained the optical sensitivity correlations using vibrational frequencies. The electronic absorption, refractive index, and birefringence studies reveal the feasibility of phase-matched nonlinear optical frequency mixing devices in the single-crystal form.

4. Temperature Dependent THz spectroscopy:

It is also very important to understand how these high-energy materials behave at high temperature. We have successfully recorded the temperature dependent variation in the refractive indices and absorption coefficients of NH_4NO_3, TNT and RDX explosives below their melting points. To the best of our knowledge this is the first demonstration of red shift effect and process of slow thermal decomposition mechanisms of these explosives in THz domain. It also helps to characterize the explosive molecules. In addition, the effect of change on the strength of THz signal of RDX in PTFE (Teflon) matrix is with respect to the concentration. Also a successful attempt was made to record the signature spectrum of RDX explosive sample under concealed condition.

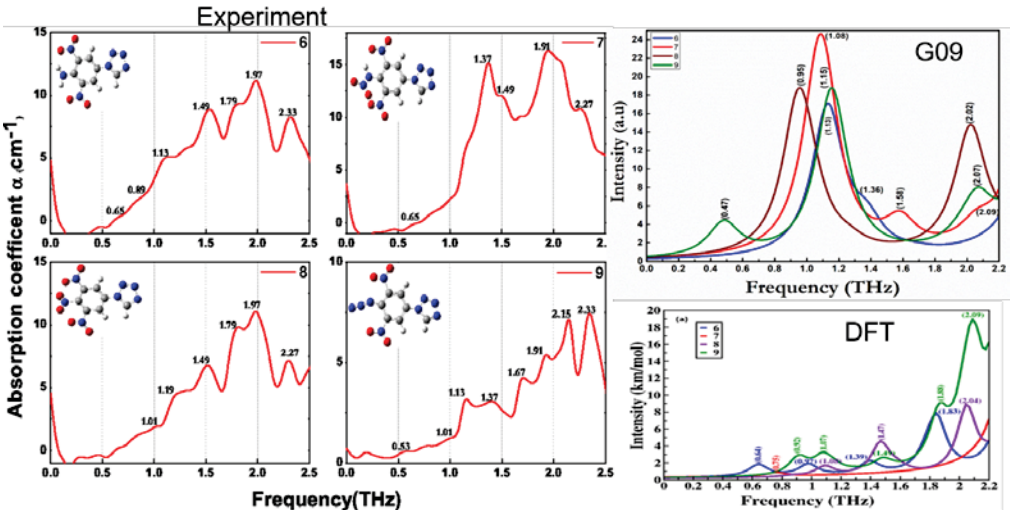

Figure.3 Terahertz absorption spectrum of Tetrazoles Molecules a) Experimental b) Gaussian 3) Density functional theory

5. Concealed Explosive detection:

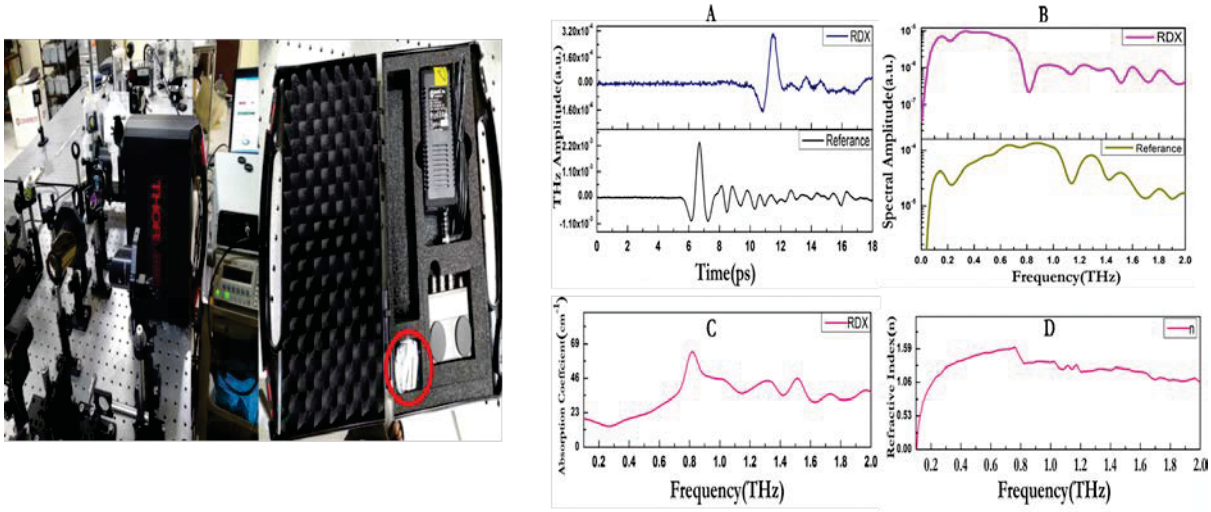

Figure 4 Concealed explosive detection.

6. Designing and fabrication of bandpass filters:

we have successfully simulated and fabricated metal mesh hole array type of band-pass filters by fabricating gold hole array on silicon substrate. Two bandpass pass filters having resonance with hole array periodicity of the order of 125, 150 µm having tunable resonance frequencies at 0.55, 0.66 THz, respectively. We have also theoretically designed low cost, flexible bandpass filters on polyamide substrate. The fabricated band-pass filters were used for trace level sensing of high-energy molecules by measuring the plasmonics shift. This study helps in developing the technology for metal mesh filter for trace level detection of explosives.

A Study of Nonlinear Optical Properties of Metamaterials

Dheeraj Dulhani

Devi Ahilya Vishwavidyalaya, Indore

Introduction

Metamaterials are known to have negative values of both dielectric constant (ε) and magnetic permeability (μ). When electromagnetic radiation is applied, the metamaterials shows the large response to the magnetic field while smaller response is noticed for electric field. Naturally occurring materials does not show negative values of ε and μ. However, *conventional metamaterials* are fabricated from composite structures of metallic wires and split-ring resonators (SRR). In such composite structures, metallic wires provide negative permittivity while the SRR provides negative permeability at certain frequency range [1]. The wide variety of such composite structures are available for microwave frequency regions. At higher operating frequencies such as optical region, losses are pronounced more. Detailed understanding is needed to design suitable composite structures for optical frequency regions which is about 400 – 700 THz [2].

SRR and metallic wire composite structure are made up of a regular pattern of the unit cell.Each unit cell has its own distinct property.Circular motion of current is analogous of the orbital motion of the electron in the atom, and as similar to atom it creates magnetic dipole moment, that's why a single SRR unit is known as Meta atom or Meta molecule, this structure consists inhomogeneities at a micro-scale when the size of the Meta-atom is comparable or greater than the wavelength of interest, it was defined by $\left(a/\lambda\right)$ Ratio[3], where a is the size of the unit cell and λ is the wavelength of interest, the smaller the ratio of $\left(a/\lambda\right)$ Is, the larger will be the quality factor of SRR. Since wave does not seem inhomogeneities of individual meta-atoms, while wave seems macroscopic homogeneous effective parameter of an SRR structure as a whole, like one, can find out homogeneous effective permittivity and effective permeability of the overall system as a response to applied electromagnetic radiation. Conversely, this ratio reaches 1, the performance of SRR degrades, and SRR becomes dysfunctional. The wavelength of interest seems individual inhomogeneities of the structure due to which effective medium theory (EMT) is failing to

define the individual microscopic parameters of the system.On the other hand, when $\left({}^{a}/_{\lambda}\right) \ll 1$, at higher frequencies the kinetic inductance becomes more dominating over geometric inductance, which weakens the magnetic response of the system. Accordingly, we call this factor as scaling down limit of the SRR structure, beyond that scaling down limit kinetic inductance becomes strong enough to saturate the blue-shifted resonance frequencies concerning for to the reducing dimensions.

The nonlinear optical properties of Metamaterial are considered in terms of its response to the magnetic field. The refractive index of the Metamaterial is given by $n = \sqrt{\mu_m \varepsilon_m}$, where μ_m is the magnetic permeability and ε_m is the electric permittivity of the material. In general the magnetic permeability does play an important role in the optical regime. In the present thesis, we have shown that the higher order magnetic susceptibility plays an important role in the optical regime. In brief, we discuss about it in chapter four.

Plan of Thesis

In this thesis, we address the above mentioned points and proposed various designs incorporating the drawbacks at optical frequency region. We also made estimations with realistic situations where suitable materials are identified for the fabrication of such structures.

The thesis introduces the topic of research in **Chapter 1**. In this chapter, we summarize the motivation, objectives of this research work as well as a comprehensive review of the research work going on linear and nonlinear properties of conventional Split Ring Resonator (SRR), which is an important element of conventional Metamaterial.

The Chapter 2, Adopting the standard model proposed by Pendry et al, we incorporated the role of Fermi energy on effective permeability of the composite structure. A blue shift in the resonance frequency of SRR is observed by choosing the metal with higher Fermi energy (E_f). SRR behaves like a series inductive-capacitive circuit, if more gaps are introduced in the SRR. Which otherwise leads to blue-shift in resonance. Hence designing SRR with higher number of gaps and by choosing high Fermi energy metal in the ring structure, one can achieve the blue shift in the resonance frequency of SRR structure. While

dimension remains unaltered. It is observed that the SRR structure with two gaps and four gaps are isotropic, since the magnetic dipole moment is dominating over electric dipole moment. Also, even number of gaps in an SRR structure is free from electric resonance and they do not have a cross-polarization effect.

In chapter 3, we can extend the analysis to include scaling down limit and the role of Fermi energy of the materials of SRR in effective permeability.With a decrease in the dimension of SRR, the inertial inductance increase. However, at smaller sizes the materials with larger Fermi energyexhibitslargerenergy dissipation in terms of an increased effective damping factor as well as the low filling factor. The breakthrough we noted, is material with higher Fermi energy shows huge blue shift in resonance frequency at lower dimensions of SRR. This is a promising news for the fabrication of metamaterials structures in the optical frequency region. We also studied the skin depth and plasma frequency analysis for smaller ratio SRR structures. We have simulated the results with two designs each with four sets of dimensions to understand the effect. We conclude the Aluminium could be a good candidate material for such experimental studies.

In chapter 4, we incorporated the idea of varactor loaded Split Ring Resonator(VLSRR)as a nonlinear optical oscillator for the device. The nonlinear optical response of the varactor diode is feed through the SRR gaps.The dc voltage is applied at diode to tune the response of the SRR element. By changing the capacitance of a diode, one can observe a shift in the resonance frequency along with an adjustment in effective magnetic permeability, capacitance of diode is change by altering the width of PN junction by the application of DC voltage to the diode.We analyse that, by choosing metal with high Fermi energy in the ring structure, magnetic response of the VLSRR improves due to drop in inertial inductance, as magnetic response increases, we achieve a blue shift in resonance frequency. We observe huge blue-shifted resonance for higher Fermi energy, metals as a response of the applied field, since it has lower inertia as well as overall inductance, it had been observed that, not only higher Fermi energy metal is having lower inertial inductance. Due to the asymmetry of the system the nonlinear optical response of the medium is found to play a role.

In Chapter 5, we report the results and best design for optical region is proposed. We simulated our results with materials such as gold, silver, bismuth, tin and aluminium

having Fermi energies 6eV, 10eV, 11eV and 12 eV respectively.We report the best SRR structures which can work in the optical region. However, due to limited broadening, we could notice that a single design may not work for the whole optical region.

The conclusion of the research work, possible extension of the work, and summary of work are given in **Chapter 6**.

References

1. **S** Anantha Ramakrishna Rep. Prog. Phys. **68** (2005) 449–521
2. Linden S, Enkrich C, Wegener M, Zhou JF, Koschny T, Soukoulis CM (2004) Magnetic response of metamaterials at 100 terahertz. Science 306:1351–1353O'
3. Chakrabarti, S. & Ramakrishna, S. A. Magnetic response of split-ring resonator metamaterials: From effective medium dispersion to photonic band gaps.*Pramana***78,** 483–492 (2012).
4. Brien S and Pendry J B 2002 J. Phys.: Condens. Matter 14 6383
5. J. Zhou,1 Th. Koschny, M. Kafesaki,E. N. Economou, J. B. Pendry, and C. M. Soukoulis PRL **95,** 223902 (2005) 10.1103/PhysRevLett.95.223902
6. Penciu, R. S. *et al.* Multi-gap individual and coupled split-ring resonator structures. *Optics Express***16,** 18131 (2008).

Magneto-optical transport studies on ultra-low disordered semiconductor quantum wells grown by MOVPE

Subhomoy Haldar

Raja Ramanna Centre for Advanced Technology, Homi Bhabha National Institute, India.

Thesis Summary

Research on the electronic transport of charge carriers under the interaction of electromagnetic radiation in III-V compound semiconductors has provided unprecedented opportunity to develop numerous forms of optoelectronic devices. In particular, ultra-low disordered semiconductors with high mobility of electrons and large radiative recombination efficiency are widely used in light-emitting diodes, lasers, photovoltaics, and fast-communication devices [1-3]. Additionally, the electro-optical property of semiconductors can be enriched by confining the fundamental charge particles in a low-dimensional system, i.e., quantum well, wire and dots. The effects of charge carrier confinement in quantum structures have found far-reaching consequences in many of the presently available semiconductor devices [4-6]. In particular, a nearly lattice-matched GaAs/AlGaAs compound semiconductor, with a large phase coherence length and high spin dephasing time for electrons, is often used to demonstrate novel effects, like induced-superconductivity, excitonic-superfluidity, spin-lasers, single-photon devices, etc. [7-9]. The confinement of charges in a low-dimensional system enhances the many-body interactions, which is responsible for the stability of excitons (i.e., electron-hole pair) and excitonic-complexes [10]. Investigation of the unique property of these quasi-particles and their coupling with photon (i.e., polaritons), is of paramount importance in condensed matter physics and semiconducting devices. However, with an increase in carrier confinement in quantum structures, a significant amount of electron/hole wave function penetrates in the surrounding medium. Therefore, charge carriers become localized at the hetero-interfaces and may decay via non-radiative process. In view of this, critical factors which can control the radiative and non-radiative processes need to be understood by combining advanced techniques that are sensitive to probe the ultra-low defect density. Spectroscopic and charge carrier transport measurements under high magnetic field are two efficient tools that can probe above processes and help in exploring novel quantum phenomena [11-13]. In addition, a sufficiently strong magnetic perturbation can be desirous to surmount the influence of disorders, and therefore, nearly dissipation-less charge transport becomes possible [14,15]. The magnetic perturbation along the different orientations with respect to the confinement direction can also be used to control the recombination and transport property of charge carriers. Therefore, the motivation of the present thesis is to utilize 'magnetic field' as a unique tool to control charge carriers' localization, recombination and their transport property. The thesis dealt with novel methodologies for spectroscopic and transport measurements on ultra-low disordered quantum wells (QWs) grown by metal organic vapor phase epitaxy technique. The usefulness of magnetic perturbation in evaluating the defect density and its role for increasing the device efficiency are also presented. A simple and inexpensive maskless photolithography system is also developed to fabricate semiconductor devices related to this thesis work.

In the beginning, charge carrier localization in QWs and the role of thermal energy on the radiative and non-radiative processes are investigated by two complementary spectroscopic techniques, i.e., photoluminescence (PL) and surface photovoltage. It is shown that atomic irregularities at the hetero-junctions causing fluctuations in QW thickness can be estimated by modeling the PL linewidth as a function of QW thickness. On the other hand, thermionic escape followed drift/diffusion of charges in a multiple-QWs structure is investigated by temperature, excitation power, and chopping frequency-dependent surface photovoltage measurements. A careful study of surface-photovoltage-amplitude and phase spectra has provided crucial information on carrier-carrier interaction in QWs. The various thicknesses of QW that are grown under identical growth conditions, i.e., the multiple-QW structure, is found to be the key recipe in this work [16]. Also, the impact of quantum confinement on the effective mass of excitons is investigated by PL spectroscopy under a high magnetic field (Fig. 1a). It is observed that the effective mass of electrons significantly increases with a decrease in QW thickness, which cannot be explained by the penetration of wave functions into barrier layers that was reported in the literature. The estimated effective mass of electron as a function of QW-thickness is then used to evaluate the non-parabolicity of bands when the energy eigenstate is at different (E, k) in the band dispersion [17].

It is observed that the asymmetric tail in PL spectra, which is contributed by disorder bound-excitons, decreases under a strong magnetic field (Fig. 1b). Such an effect is explained by the magnetic field-driven spatial confinement of excitons; charge

carriers in the QW experience a smaller number of defects due to the magnetic confinement (Fig. 1c). A phenomenological model of magneto-excitons is therefore developed where the magnetic field-driven reduction in bound-exciton PL helps in evaluating the point defect-density in QWs [18]. In addition to this, the role of magnetic perturbation on the radiative and non-radiative processes of thermally activated excitons are probed by magneto-PL and magneto-surface photovoltage measurements. In particular, the emission-based PL spectra helped to realize the impact of magnetic perturbation on the radiative recombination efficiency of excitons at an elevated temperature. At the same time, carrier escape from QWs, followed by the drift or diffusion of charges, is probed by magneto-surface photovoltage measurements. Although the recombination-rate of thermally activated electron-hole pairs in a thick QW increases under a strong magnetic field, a large number of electron and hole may escape from a narrow QW under this magnetic perturbation. A comprehensive understanding of the magnetic field-assisted relaxation, recombination, and carrier escape mechanisms for a quantum structure is developed by a generation recombination based rate equation model [19]. Considering the above processes, the requirement of a minimum QW-width is suggested that would be essential for the magnetic field-driven advanced optoelectronic device operation.

In addition, anisotropic properties of excitons in GaAs QWs are investigated by magneto-optical spectroscopy and magnetization measurements in perpendicular and parallel magnetic field configurations. A dramatic reduction in the diamagnetic energy of excitons is observed under a magnetic field parallel to the QW-plane [20]. It is found that the existing theoretical models could not explain the feeble diamagnetic-energy of excitons and a decrease in PL intensity under a parallel magnetic field. We have derived an analytical relation of diamagnetic energy by considering (a) the coupling of quantum confinement with the diamagnetic energy of excitons, and (b) interplay between the center of mass and relative motion of charge carriers. According to the theoretical framework, it is proposed that the in-plane separation between electron and hole may increase under a parallel magnetic field, which may cause a chiral charge transport across the hetero-interfaces of the QW. As a result of this, charge carriers in a QW become more susceptible for in-plane motion that gives rise to enhancement of photovoltage signal and reduction in PL intensity [20]. On the contrary, a magnetic field perpendicular to the QW plane emphatically confines the exciton and causes substantial enhancement of PL intensity and reduction in lateral photovoltage signal. Furthermore, it is found that a magnetic field along different orientations can control the paramagnetic and diamagnetic behavior of excitons [21]. Therefore, a unique method to control the recombination, transport, and magnetic properties of charge carriers is shown by varying the strength and orientation of an external magnetic field.

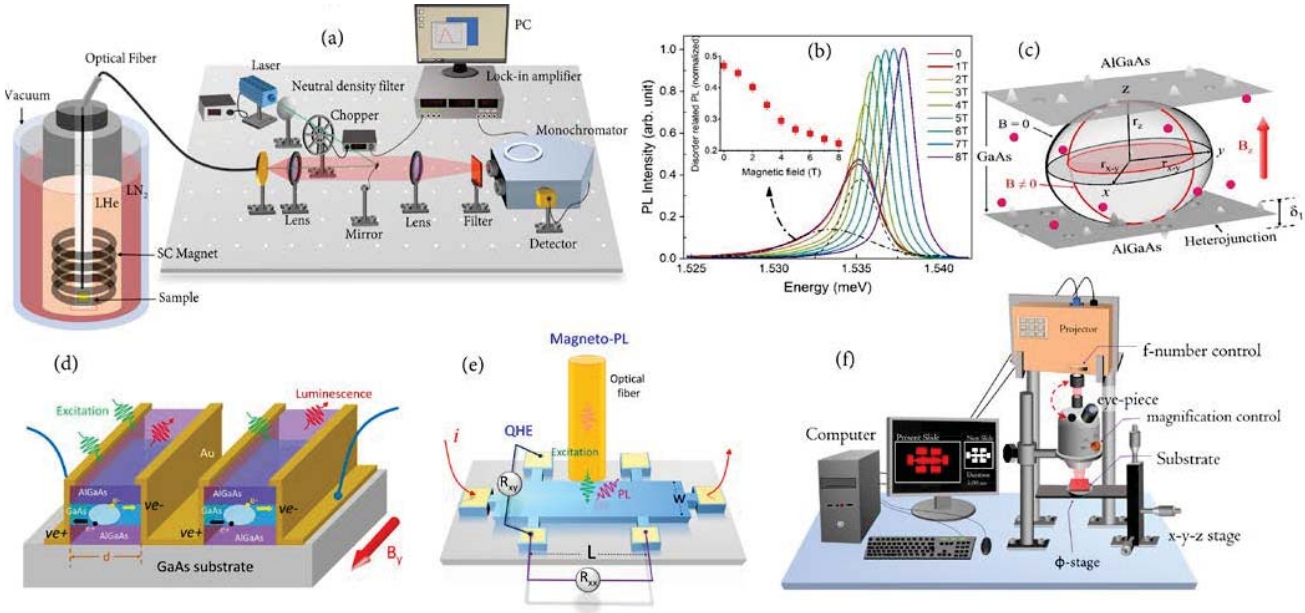

Figure 1 (a) Schematic of the experimental setup for magneto-optical measurements and (b) magneto-PL spectra of a GaAs QW. (c) Magnetic field-driven spatial confinement of excitons in a QW. (d) Measurements of in-plane charge separation under a parallel magnetic field configuration, (e) simultaneous measurement of magneto-PL and quantum Hall, and (f) schematic of the maskless-photolithography setup.

With this understanding of magneto-optical processes, we have investigated the correlation between optical and transport parameters of a quantum structure by the simultaneous measurements of magneto-PL and quantum Hall. (Fig. 1e) [22]. The results obtained by quantum Hall measurements under dark and laser-illuminated conditions helped in realizing the carrier-carrier interactions in a modulation-doped QW, which forces the electrons to move at the hetero-interfaces and scattered by the interface-roughness. It is found that photo-generated holes screen this electron-electron interaction, which enhances the mobility of charge carriers. During the quantum Hall measurements, relaxation of charges among the Landau states and their recombination is probed by magneto-PL spectroscopy on the Hall bar device. The correlation of PL intensity with a rate equation model helped to estimate carrier density in each Landau states, recombination time of excitons, and Fermi energy as a function of the magnetic field. A novel method to investigate magneto-PL intensity oscillations is also presented, which is conceptually similar to the Shubnikov-de Haas oscillations. This new method can be exploited in evaluating the magneto-optical parameters in semiconductor quantum structures without a line-shape fitting procedure.

In order to fabricate semiconductor devices related to this thesis work, a simple and inexpensive maskless-photolithography system is developed by a digital-projector and a stereo-zoom optical-microscope (Fig. 1f) [23]. In this setup, highly divergent light from the projector is focused on a substrate by a 10X eyepiece and an objective lens of a microscope. The projector is equipped with 1920×1080-pixel resolution, 1:13000 contrast ratio, 3500 ANSI Lumens brightness. The 10X eyepiece is placed close to the projector (~ 1 cm), which collimates the light over an aperture area ~1.5×1.5 cm^2. The collimated light is then coupled into the trinocular head of a stereo-zoom microscope (Fig. 1f). The microscope is used for the following reasons- (i) objective lens helps to control exposure area on the substrate, and (ii) eyepiece in the binocular-head helps to check pattern placement and focusing of incident light on the substrate. In this setup, the projector is used to achieve spatial patterning of the light, where the desired image-patterns are drawn in PowerPoint software. The computer software directly controls the intensity and duration of exposure. Note that the hardware configuration of the projector and optical microscope is not affected, and external lenses and mechanical shutters are also not required in the present setup. The wavelength of exposure is indirectly controlled by choosing a suitable color in the PowerPoint image. The entire system development which cost nearly 2 lakh Rs is found to be beneficial to pattern various structures with a minimum feature size of 20 μm.

Finally, to find the validity of our fundamental research on the device performance, semiconductor diode lasers and photo-detectors with QWs are developed. The role of carrier localization on the performance of these devices is understood by operating these devices at a low-temperature and high magnetic field conditions. It is observed that the lasing emission related to defect states decreases under a magnetic field. At the same time, the free-excitonic laser peak increases with the strength of the applied field. Such effects can be explained by the understanding developed in the context of magneto-PL spectroscopy of QWs. On the other hand, the QW embedded in a p-i-n structure of the photodetector traps the background charge carriers, which acts as an artificial localization center to minimize the dark current. Under a high magnetic field, the in-plane diffusion of photo-generated charge carriers is restricted, and therefore, the in-plane migration followed by the carrier localization becomes feeble. As a result of this, the photo-generated charge carriers can only move along the growth direction of the p-i-n structure, which increases the spectral response of the photodetector under a high magnetic field. It is therefore observed that the magnetic field can be used to suppress the impact of defects on the lasing emission and offers a tunability in lasing wavelength, whereas in the case of photo-detectors, magnetic perturbation enhances the spectral response.

In conclusion, the optical, magnetic, and transport properties of charge carriers in ultra-low disordered QWs, with variations in QW-thickness, doping-density, and barrier-composition, are investigated. The results obtained by magneto-optical, magneto-transport, and magnetization measurements helped to develop a detailed understanding of the impact of charge carrier confinement on the electro-optical processes and fundamental parameters of the material system. The magneto-optical measurement is found to be an efficient tool for the quantitative estimation of point defect density in a truly non-invasive manner. A unique method to control recombination, electrical transport, and magnetic behavior of charge carriers by the strength and orientations of a magnetic field is demonstrated by magneto-PL, magneto-photovoltage, and magnetization measurements. The magnetic field induced non-radiative processes that may deteriorate the efficiency of quantum devices is investigated, and a critical dimension of quantum structures that would be essential to suppress those effects is proposed. The results obtained by magneto-transport measurements are correlated with the magneto-optical spectroscopy, which would be beneficial in estimating the electro-optical parameters of quantum structures, especially when a contact-based measurement is not feasible. Therefore, in addition to the fundamental physics of magneto-excitons, the present thesis provides clear guidelines for the magnetic field-assisted advanced electro-optical devices development.

In future, the understanding developed in the present thesis would be beneficial to study the fundamental mechanisms underlying the superfluidity of excitons, dark excitons, light-matter coupling, carrier localization effects in more complex device structures which can be exploited in quantum transport and sensing applications.

1. N. Li, K. Han, W. Spratt, S. Bedell, J. Ott, M. Hopstaken, F. Libsch, Q. Li, and D. Sadana, Nature Photonics 2019, **13**, 588, (2019).
2. G.C. Gardner, S. Fallahi, J.D. Watson, and M.J. Manfra. Journal of Crystal Growth **441**, 71 (2016).
3. V.K. Dixit, A. Marathe, G. Bhatt, S.K. Khamari, K. Rajiv, R. Kumar, C. Mukherjee, C.J. Panchal, T.K. Sharma, and S.M. Oak, Journal of Physics D: Applied Physics **48**, 105102 (2015).
4. F. Bachmann, P. Loosen, and R. Poprawe, "High power diode lasers: technology and applications" 128, Springer 2007.
5. L. Schrottke, X. Lü, G. Rozas, K. Biermann, and H.T. Grahn, Applied Physics Letters **108**, 102102 (2016).
6. R.R. LaPierre, M. Robson, K.M. Azizur-Rahman, and P. Kuyanov. Journal of Physics D: Applied Phys. **50**, 123001 (2017).
7. Z. Wan, U. Kazakov, M.J. Manfra, L.N. Pfeiffer, K.W. West, and L.P. Rokhinson, Nature communications **6**, 7426 (2015).
8. J.A. Seamons, C.P. Morath, J.L. Reno, and M.P. Lilly, Physical Review Letters **102**, 026804 (2009).
9. M. Lindemann, G. Xu, T. Pusch, R. Michalzik, M.R. Hofmann, I. Zutic, and N.C. Gerhardt, Nature **568**, 212 (2019).
10. M.T. Portella-Oberli, V. Ciulin, J.H. Berney, B. Deveaud, M. Kutrowski, & T. Wojtowicz, Phys. Rev. B **69**, 235311 (2004).
11. P. Corfdir, B. Van Hattem, E. Uccelli, S. Conesa-Boj, P. Lefebvre, A.M. Fontcuberta, and R.T. Phillips, Nano letters **13**, 5303 (2013).
12. B. Bansal, M. Hayne, B.M. Arora, and V.V. Moshchalkov, Applied Physics Letters **91**, 251108 (2007).
13. J. Shabani, S.D. Sarma, and C.J. Palmstrøm, Physical Review B **90**, 161303 (2014).
14. R. Sabo, I. Gurman, A. Rosenblatt, F. Lafont, D. Banitt, J. Park, M. Heiblum, Y. Gefen, V. Umansky, and D. Mahalu, Nature Physics **13**, 491 (2017).
15. Z.R. Poux, Wasilewski, K.J. Friedland, R. Hey, K.H. Ploog, R. Airey, P. Plochocka, and D.K. Maude, Physical Review B **94**, 075411 (2016).
16. S. Haldar, S. Kumar, R. Roychowdhury, and V.K. Dixit Physica Status Solidi B **257**, 2000331 (2020).
17. S. Haldar, V.K. Dixit, G. Vashisht, S.K. Khamari, S. Porwal, T.K. Sharma, and S.M. Oak, Scientific Reports **7**, 4905 (2017).
18. S. Haldar, V.K. Dixit, G. Vashisht, S. Porwal, and T.K. Sharma, Journal of Physics D: Applied Physics **50**, 335107 (2017).
19. S. Haldar, V.K. Dixit, G. Vashisht, S. Porwal, and T.K. Sharma, Journal of Applied Physics, **124**, 055704 (2018).
20. S. Haldar, A. Banerjee, G. Vashisht, S. Porwal, T.K. Sharma, and V.K. Dixit, Journal of Luminescence **206**, 342 (2019).
21. S. Haldar, A. Banerjee, K. Kumar, R. Kumar, G. Vashisht, T.K. Sharma, and V.K. Dixit, Superlattices and Microstructures **137**, 106332 (2020).
22. S. Haldar, G. Vashisht, S. Porwal, T.K. Sharma, and V.K. Dixit, Journal of Applied Physics **125**, 205701 (2019).
23. S. Haldar, G. Vashisht, U.K. Ghosh, A.K. Jaiswal, S. Porwal, A. Khakha, T.K. Sharma, and V.K. Dixit, AIP Conf. Proc. **2115**, 030219 (2019).

Ultrafast Molecular Dynamics and Third-order Nonlinear Optical Properties of Novel Organic, Inorganic and Energetic materials

Katturi Naga Krishnakanth

Supervisor: Prof. Soma Venugopal Rao

Advanced Center of Research in High Energy Materials (ACRHEM), University of Hyderabad, Hyderabad 500046, Telangana, India

To probe the decomposition of energetic materials (EMs) at the molecular level and at sub-picosecond time scales is hugely challenging with impediments such as absorption in UV spectral range. The decomposition of EMs can directly be investigated by ultrafast spectroscopic techniques such as femtosecond (fs)/picosecond (ps) CARS and pump-probe techniques. Our main motive at ACRHEM is used to understand the behaviour of EMs upon ultrashort pulse illumination and probing their ultrafast processes at a molecular level; towards this, we have set up the CARS and TAS experiments at our department. We have initiated these studies in simple organic molecules (Porphyrins, Corroles, and phthalocyanines). We have performed extensive studies on their excited state dynamics and NLO properties using TAS (along with global and target analysis), Z-scan, and DFWM experiments. Further, we extend these studies to the EMs on tetrazole molecules.

We have performed broadband NLO studies of both organic and inorganic materials since their applications to lasers, photonic devices and biological applications. The materials possessing fast response and large $\chi^{(3)}$ are prerequisites for all these applications. Several substances of both organic and inorganic counterparts are engineered to meet the required optical properties for different applications. In the case of conjugated organic molecules and their delocalized π electrons plays a crucial role in tailoring NLO properties and excited-state dynamics. Therefore, it is essential to understand the nature of excited states upon photoexcitation in an ultrafast time domain. Where in the case of inorganic materials, we have specifically investigated the NLO properties and excited-state dynamics of perovskite nanocrystals (NCs) and metal nanoparticles (NPs). Recently, perovskite NCs have emerged as a promising material for optoelectronic device applications, possessing strong absorption and emission quantum yields with strong NLO properties (nonlinear absorption and refraction). They have found to exhibits large multi-photon absorption cross-section values, which are useful for biological, optical protection, photonic device applications. In this regard, we have done broadband NLO studies on $CsPbBr_3$ and Cs_4PbBr_6 NCs. The optical properties of perovskite NCs can be tuned by their dimensional reduction (thickness, size, morphology, surroundings/environment, and even preparation method). In the case of metal nanoparticles, the surface plasmon resonance (SPR) plays a vital role in their optical properties, which is use full for photodynamic therapy and optical device applications. The SPR can be tuned by the shape and size of the metal NPs from VIS-NIR range.

The primary outcomes from the thesis are outlined with a brief discussion and graphical abstract as follows:

- The development of state-of-the-art experimental techniques to characterize the light mater interaction upon ultrafast pulse illumination in our lab has been initiated and achieved. To investigate the NLO properties of organic/inorganic/perovskite materials, we have developed single-beam Z-scan and degenerate four-wave mixing (DFWM) techniques. The Z-scan provides both magnitude and sign of the nonlinear absorption and refractive index (n_2), which also contains the intuition into the change of population in their excited states. The DFWM data and analysis provides the true value of $\chi^{(3)}$ (third-order nonlinear susceptibility) as well as the response by performing the time-resolved DFWM experiment. So, both the techniques can be used to find the magnitude of $\chi^{(3)}$, where DFWM avoids the linear contribution and scattering effects that are usually found in Z-scan. Finally, these experimental setups were further implemented to develop the CARS experiment to investigate the ground states' vibrational dynamics of EMs. Apart from this, we have also used a commercial transient absorption spectrometer (HELIOS) to understand the molecular excited state dynamics. Thus, we have performed ground and excited-state dynamics of EMs to understand the decomposition mechanism, which is use full for end-user applications and further implementation of EMs.

- Ultrafast broadband NLO properties of $CsPbBr_3$ NCs this films [1] were performed from 600 – 800 nm wavelength range using 1 kHz 50 fs laser pulses. We have found a large two-photon absorption cross-section values of $\sim 10^5$ GM and n_2 to be $\sim 10^{-13}$ cm^2/W, originating from the quantum confinement effects. At higher input peak intensities, these NCs have shown a switching behaviour from RSA to SA. It was observed that $CsPbBr_3$ NCs and NRs depicted size and thickness dependent NLO properties with increasing saturation intensity at high peak intensities. On the other hand Cs_4PbBr_6 NCs (0D-PRM) have demonstrated large cross-section values compared to $CsPbBr_3$ NCs (The magnitudes of 2PA, 3PA, 4PA cross-sections were

~10^{-43}-10^{-44} cm^4s, ~10^{-75} cm^6s^2 and ~10^{-100} cm^8s^3, respectively) [2]. These higher NLO coefficients and cross-sections are believed to be related to the strong confinement effects with a high dipole moment. DFWM measurements confirmed a fast response (81-92 fs) of the order of input pulse duration, which ensures the pure electronic contribution to the obtained nonlinearity from these NCs and large $\chi^{(3)}$ (~10^{-9} esu). Therefore, the fast response, large $\chi^{(3)}$ and multi-photon absorption capabilities of these NCs are suitable for next-generation bio-imaging and photonic device applications.

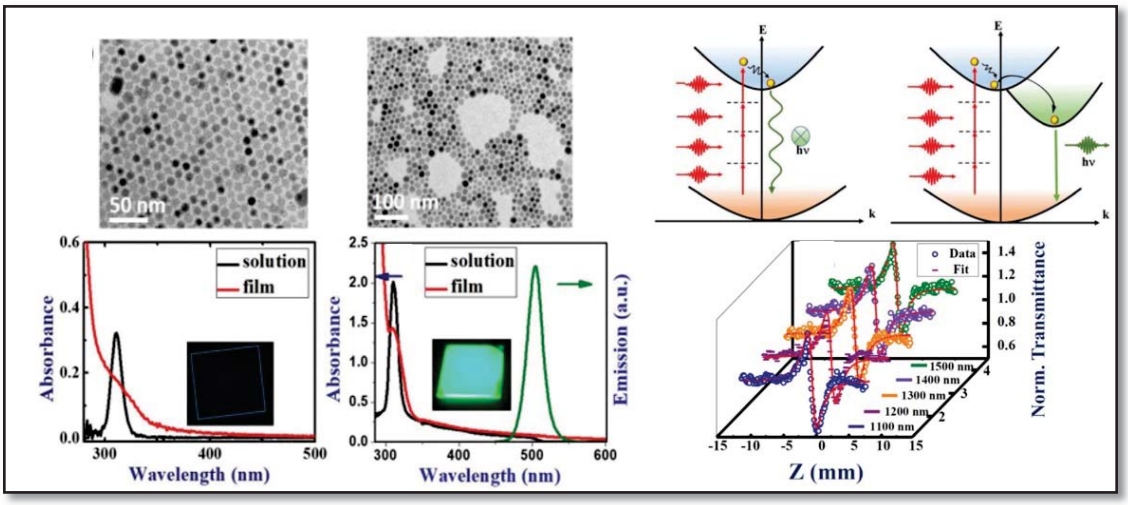

- In the case of metal nanoparticles (NPs), we have successfully synthesized Au and $Au_{50}Ag_{50}$ alloy NPs using femtosecond laser ablation and studied their electron dynamics and NLO properties in aqueous medium using TAS and Z-scan methods [3]. The $Au_{50}Ag_{50}$ alloy NPs has shown a fast response and possessed strong NLO coefficients. The obtained $\chi^{(3)}$ values were smaller compared to perovskite NCs which shows the superiority of perovskite NCs over metal NPs, along with their poor stability. The tunability of the plasmonic band and the fast response of these NPs are prerequisites in optical switching devices and biological applications.
- Phenothiazine-porphyrin-phenothiazine (D-π-D) base porphyrins (HPHT, CPPHT, ZPPHT) molecules were synthesised and their ultrafast photophysical, third-order NLO properties were investigated in solution form [4]. It was observed that these porphyrins have depicted sizeable two-photon absorption cross-section values (~10^3 GM). We have also found that the TPA was the dominant mechanism contributing to the $\chi^{(3)}$. From the transient absorption studies, and with the help of global and target analysis, we have estimated the different rate constants corresponding to various photophysical processes. The copper and zinc-based porphyrin molecules have demonstrated faster internal conversion and vibrational relaxation compared to free-base porphyrin. This could be attributed to either a higher triplet quantum yield through intersystem crossing or reduction in the radiative lifetime in the case of ZPPHT due to the incorporation of Zinc in HPPHT. The TR-DFWM measurements confirmed the real electronic contribution to the obtained $\chi^{(3)}$.

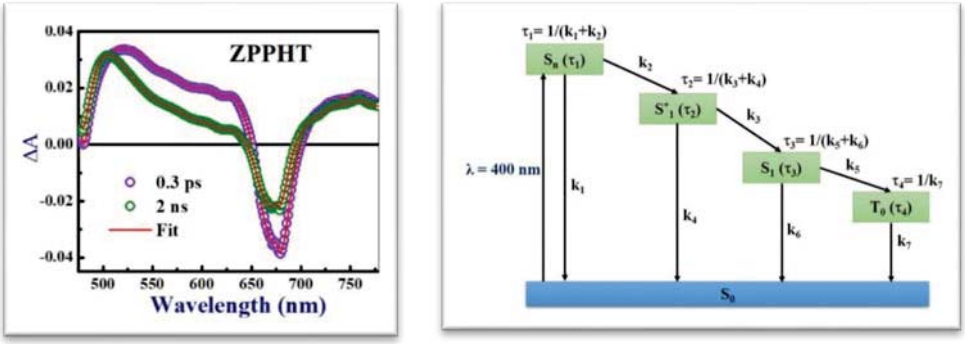

- In the case of corroles, through the transient absorption experiments, and along with global and target analysis, we have found that the phosphorous corrole demonstrated faster internal conversion and vibrational also radiative and triplet relaxation compared to free-base corrole molecule [5]. From the Z-scan measurements, the Phosphorus corrole exhibited a strong two-photon absorption coefficient (4.6×10^{-13}cm/W) compared to free base corrole. This confirmed the effect of phosphorous ion due to its strong

electron-withdrawing nature from the pentafluorophenyl group and possibly a strong intramolecular charge transfer between phosphorus and pentafluorophenyl group which creates the significant dipole moments. Also, the DFWM measurements confirm the slightly higher $\chi(3)$ value for phosphorous corrole with instantaneous response.

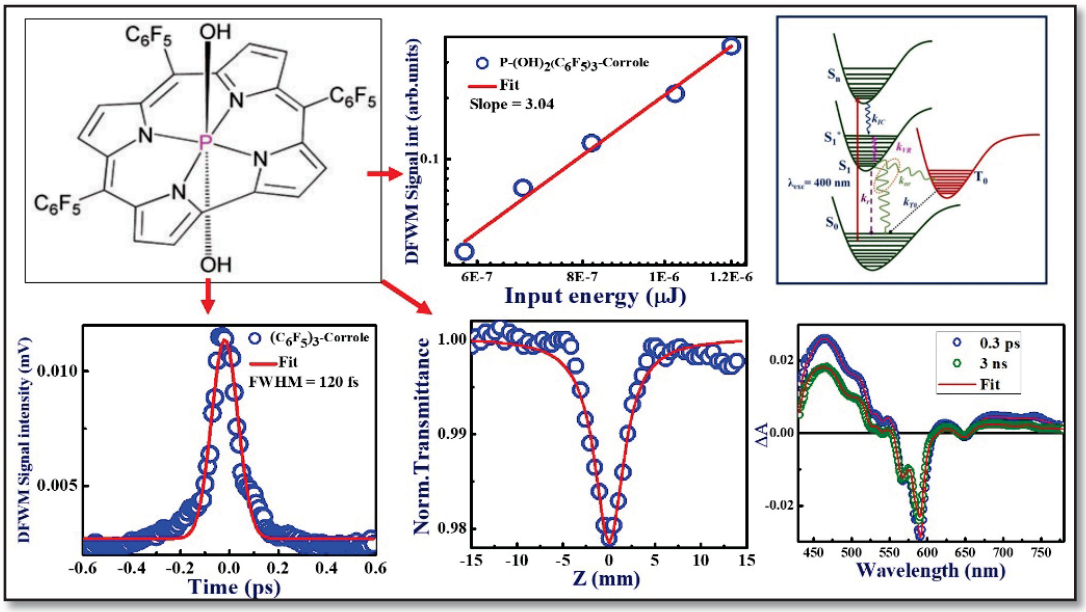

- Finally, we have extensively investigated the new tetrazole-N-(hetero)aryl derivatives (AT and NT) for understanding their potential in energetic applications. We have applied fs TR-CARS and transient absorption techniques to comprehend the ground state vibrational dynamics and excited-state dynamics occurring in the sub-ps timescales. The TR-CARS experiment deliberates the possible IVR mechanism and phase relaxation (dephasing) of vibrational modes [6]. From the CARS experimental data, we observed that the nitro substituted tetrazole demonstrated a faster dephasing time compared to an amino-substituted tetrazole. The transient absorption at 400 nm photoexcitation revealed that the nitro substituted tetrazole has a faster vibrational relaxation (S_1-S_1^*) and a faster intersystem crossing (S_1-T_0). This data confirmed the nitrogen-rich nitro substituted tetrazole demonstrated a faster relaxation due to its high nitrogen content with possible formation of nonradiative relaxation pathways. The time-resolved photoluminescence experiment proves the phosphorescence from T_0-S_0 nearly similar time scales (1 μs).

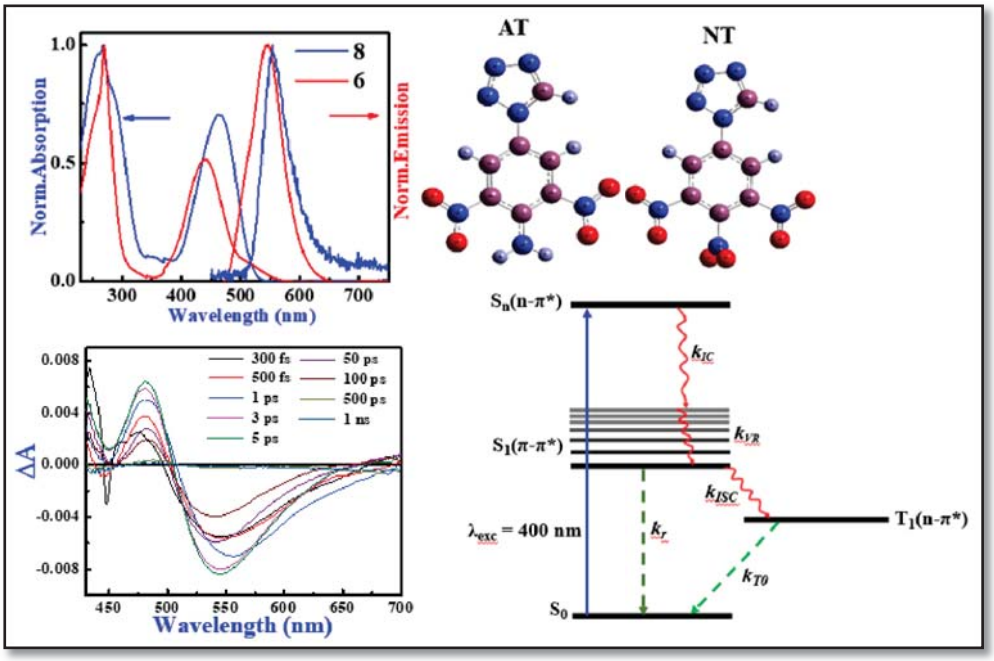

References

1. **K.atturi Naga Krishnakanth,** S. Seth, A. Samanta, and S. Venugopal Rao. "Broadband femtosecond nonlinear optical properties of $CsPbBr_3$ perovskite nanocrystals." *Opt. Lett.* **43** (2018) 603-606.
2. **Katturi Naga Krishnakanth,** Sudipta Seth, Anunay Samanta, and S. Venugopal Rao. "Broadband ultrafast nonlinear optical studies revealing exciting multi-photon absorption coefficients in phase pure zero-dimensional Cs_4PbBr_6 perovskite films." *Nanoscale* **11(3**) (2019) 945-954.
3. **Katturi Naga Krishnakanth,** Byram Chandu, M. S. S. Bharathi, Sai Santhosh Kumar Raavi, and S. VenugopalRao. "Ultrafast excited state dynamics and femtosecond nonlinear optical properties of laser fabricated Au and Ag50Au50 nanoparticles." *Optical Materials* **95** (2019) 109239.
4. **Katturi, Naga Krishnakanth**, Govind Reddy, Chinmoy Biswas, Sai Santosh Kumar Raavi, Lingamallu Giribabu, and Venugopal Rao Soma. "Ultrafast nonlinear optical properties and excited-state dynamics of Soretband excited D-π-D porphyrins." *Optical Materials* **107** (2020) 110041.
5. **Katturi, Naga Krishnakanth**, S. A. Balahoju, A. R. Ramya, C. Biswas, S. S. K. Raavi, Lingamallu Giribabu, and Venugopal Rao Soma. "Ultrafast photophysical and nonlinear optical properties of novel free base and axially substituted phosphorus (V) corroles." *Journal of Molecular Liquids* **311** (2020) 113308.
6. **Naga Krishnakanth Katturi**, Sarang Dev G, Nagarjuna Kommu, G. K. Podagatlapalli, Venugopal Rao Soma, Ultrafast Coherent Anti-Stokes Raman Spectroscopic Studies of Nitro/Nitrogen Rich Aryl-Tetrazole Derivatives, *Chemical Physics Letters* 756 (2020) 137843.

Rigid, Flexible SERS Substrates Fabricated using Femtosecond Laser Pulses for Explosives Detection

Moram Sree Satya Bharati

Supervisor: Prof. Soma Venugopal Rao

Advanced Center for Research in High Energy Materials (ACRHEM),

University of Hyderabad, Telangana, 500046, India

Email: mssbharathi@uohyd.ac.in, soma_venu@uohyd.ac.in

This thesis explores the possibilities of preparing various surface-enhanced Raman scattering (SERS) substrates (colloidal, hybrid, flexible) towards the detection of hazardous materials (mainly explosives) in pure and mixture form using a portable Raman spectrometer (see schematic shown in figure 1). In the last two decades, the usage of explosive devices in terrorist attacks has been dramatically increased. The detection of high energy materials/explosive materials is necessary to ensure the safety and security of the civilian population. One of the best spectroscopic methods, i.e., "Surface-enhanced Raman spectroscopy (SERS)," has recently perceived humongous interest from the scientific community and has become an imperative analytical tool in recent years.[1-2] The on-site sample detection is possible with the development/availability of portable/hand-held Raman spectrometer and the versatile SERS substrates. SERS technique has been extensively applied in various fields such as biological sensing[3], food analysis[4-5], and explosive detection[6-7] because of its abundant fingerprint ability with higher sensitivity. Various new methodologies have to be used to prepare the SERS substrate for on-site molecule detection because of its numerous advantages such as outstanding sensitivity, non-destructive, and finger-print nature. The motivation is from an interest in developing various rigid and flexible SERS substrates for the quick detection and identification of high energy materials (explosives)/dyes/pesticides in pure and mixture form using a simple, portable Raman spectrometer. The combination permits a user to carry the spectrometer to the point of interest and perform the measurements. There are many challenges in developing novel SERS substrates over the last two decades, such as sensitivity, stability, reproducibility, low-cost, and accessible sample collection. To achieve this, highly stable metal NPs were fabricated using femtosecond (fs) laser ablation in liquid (LAL) technique. It is a versatile technique to synthesize the various (semiconductor/metal/ alloy) NPs [8], providing the advantages to synthesize pure colloidal NPs without any chemical precursors and stabilizing agents with high yield (several grams per hour), simple procedure to prepare both NPs (as colloids) and NSs (on solid substrates) in one exposure.

- Synthesized plasmonic metal and alloy NPs using fs LAL and irradiation techniques.
- Hybrid Si micro-squared arrays prepared using femtosecond pulses in conjunction with alloy NPs (obtained using fs LAL).

Rigid and planar substrates are proven to be efficient SERS sensors in terms of sensitivity and reproducibility. To fulfill the point-of-care diagnostic applications, flexible SERS substrates have been envisaged and are demonstrated. These flexible SERS sensors are widely adapted/accepted because of their economical fabrication cost and the direct easy sample collection.[9-11] Therefore, motivated to develop the three different

flexible substrates to overcome the rigid substrate's disadvantages. Flexible substrates achieved using LAL prepared NPs impregnated into filter paper (FP) and electrospun nanofibers.

- Other strategies followed for producing high-density hot-spots by the FP with the salt-induced aggregation of NPs, fabricating anisotropic gold (Au) NPs by chemical method, and polymer nanofibers by electrospinning technique.
- Furthermore, COMSOL Multiphysics simulations were performed to investigate and visualize the near field distributions of metal NPs configurations.

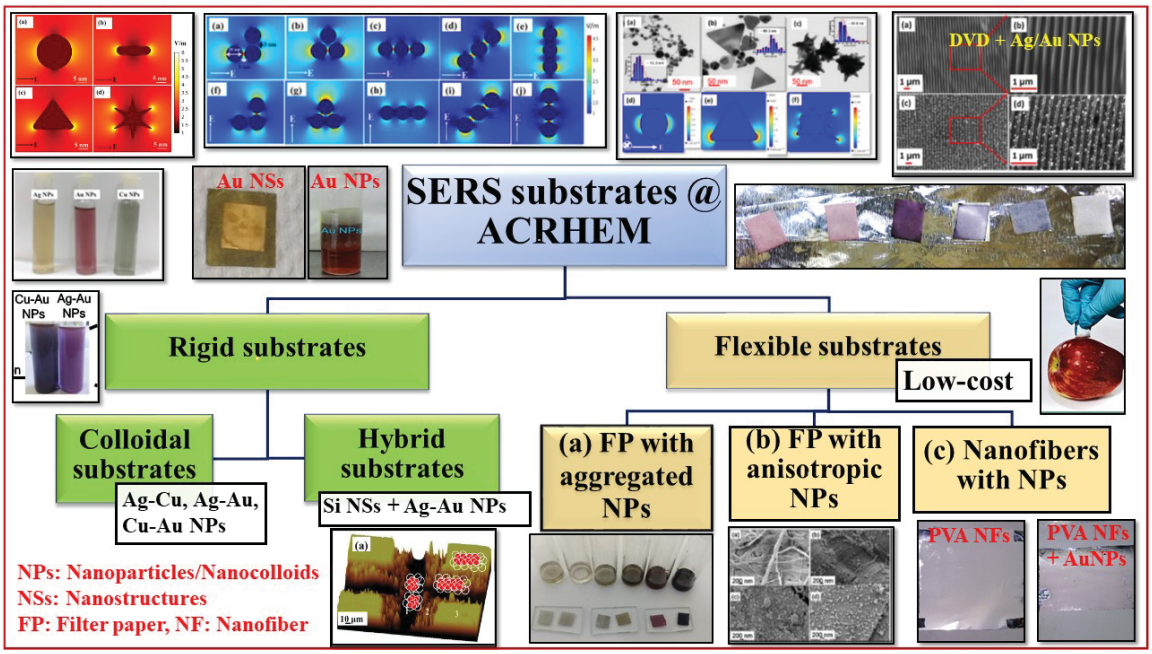

Figure 1 A schematic of all the SERS substrates fabricated at ACRHEM and presented in this thesis.

Colloidal substrates were fabricated by depositing alloy NPs on the plain silicon. Various metal alloy NPs, i.e., Ag-Cu, Ag-Au, and Cu-Au, were fabricated using fs (with ~50 fs pulses at 800 nm) LAL technique. Ag-Cu alloy NPs are prepared via mixing and irradiation of already prepared Ag and Cu NPs. Ag-Au and Cu-Au alloy NPs are prepared by the laser ablation of Ag and Cu targets in the $HAuCl_4$ solution. The formation of alloy NPs was confirmed by different characterization techniques such as UV-Visible absorption spectra, TEM, XRD, and FESEM-mapping. The SERS performance of Ag, Cu, and Ag-Cu alloy NPs were investigated with a dye molecule viz. Methylene blue (MB). The alloy NPs exhibit better SERS signals (1.3 times EF) compared to pure metal NPs (Ag or Cu). Further, Ag-Cu alloy NPs were utilized for the detection of MB (5 nM), explosive molecules PA (5 µM) and AN (5 µM) with enhancement factor (EF) ~3×10^7, 2.8×10^4 and 3.3×10^4 respectively. Moreover, Ag-Au and Cu-Au alloy NPs were utilized for the detection of MB -5 nM and PA-5 µM, and 2,4 di-nitro-toluene (DNT)-1 µM and obtained EFs were in the order of ~10^4, ~10^5 and ~10^7 for PA, DNT, and MB respectively. The reproducibility of three alloys NPs verified, and the obtained RSD as >10% for Ag-Cu and Ag-Au alloy NPs; and >12% for Au-Cu alloy NPs. Among these alloy NPs, Ag-Au alloy NPs were observed to be superior SERS substrates.

Hybrid SERS substrates were fabricated for the improvement in the SERS performance of Ag-Au alloy NPs by changing the base/support from plain silicon to laser textured silicon. The base morphology effect on SERS was examined with MB using a micro-Raman spectrometer, and noticed the maximum SERS signal was

observed from the edges of micro square arrays (MSA) because of the micro-protrusions and/or nanocavities originating from the redistribution of ablated mass. Therefore, MSA was fabricated on Si using fs laser ablation of silicon in the air at different energies 10, 20, 30, 50, and 100 μJ. The SERS performance on base morphology/roughness was examined with MB-5nM and observed the Si MSA substrate fabricated at 30 μJ, coated with Ag-Au alloy NPs had demonstrated the best SERS enhancement, including plain Si. The optimized substrate Si MSA (30 μJ) with Ag-Au alloy NPs able to detect MB- 10 pM with RSD >13%. Consequently, this superior substrate was then used to probe the explosive molecules (PA, RDX) in pure form, and the achieved EFs were ~10^{10} for MB, ~10^{6} for PA, and ~for RDX it was 10^{4}. The estimated LOD values for the MB, PA, and RDX were ~5 pM, ~36 nM, and ~400 nM, respectively. The SERS studies continued with mixture form, i.e., dye-explosive mixture (PA-MB, DNT-MB), and explosive-explosive mixture (PA-DNT) with various concentrations. The repeatability and reproducibility also confirm the efficiency of the SERS substrate. The strength of the rigid substrate was verified with the commercially available substrate [Ag deposited ITO] provided by the SERSitive (Polish) company with MB-5 nM and PA-50 μM.

Next, low cost and flexible SERS substrates were discussed in three different sections. The first section discusses the fabrication of flexible filter paper (FP) with aggregated Ag/Au NPs. The aggregated Ag/Au NPs are achieved by mixing different concentrations (1 mM to 1 M) of NaCl to the prior fs laser-ablated Ag and Au NPs. Colloidal Ag/Au NPs were characterized by UV−visible absorption and TEM. The morphologies of the FP loaded with aggregated NPs were investigated using FESEM. The optimization of NaCl concentration was obtained by performing SERS measurement for a dye molecule (MB) on the aggregated Ag/Au NPs loaded FP substrates. The Ag/Au NPs mixed for an optimum concentration of 50 mM NaCl was used to detect various molecules such as MB-5 nM with EF ~3.4×10^{7} and ~7.9×10^{6} for FP with aggregated Ag and Au NPs, respectively. Further explosive detection was performed PA-5 μM, DNT-1 μM, and NTO-10 μM with EF in the order of ~10^{4}, and the RSD >16%. The stability studies were conducted on FP with Ag and Au NPs in the detection of dye (MB – 5 μM) and pesticide (Thiram-10 μM) molecules. The SERS signal intensity dropped by ~89 % and ~40 % for Ag and Au substrates in 15 days. Because of the high plasmonic nature, Ag demonstrated better SERS signal in the early days compared to Au based substrate. From the stability studies, we observed a ~ 90% drop of SERS intensity in ~30 days for FP with Ag NPs and a ~55 % drop in 45 days for FP with Au NPs. Therefore, we believe that Au NPs loaded FP substrates have exhibited consistent SERS performance.

The second section describes the intriguing SERS performance of FP with anisotropic Au NPs. Three different shapes, i.e., spherical, triangular, and star shapes, are used to study the shape effect in SERS efficiency. Spherical Au NPs were synthesized using fs LAL; triangular and star-shaped Au NPs were prepared by colloidal chemical methods. The shape of the NPs and the distribution of NPs on the FP were characterized by TEM and FESEM. The superior signals SERS were observed from the star-shaped Au NPs than the triangle and spherical Au NPs using a dye molecule Nile blue (NB). FP with star-shaped Au NPs proved to be capable of detecting 10 pM NB, and the estimated EF was ~3.7×10^{10}. Further, a computational [COMSOL Multiphysics] method is presented that investigates the near field distributions of these Au NPs, and as expected, the strongly enhanced near-field intensity at the sharp features was observed. Moreover, this section continues with the comparison of the aggregation of spherical Au NPs with optimized NaCl concentration (50 mM), with the star shape NPs. In this case, the possible hot-spot locations are the aggregated spherical NPs junctions and sharp tips of the star-

shaped NPs. Two probe molecules NB-5 nM and PA -5 µM, are considered to evaluate the SERS performance of both FP with aggregated spherical and star Au NPs. Both the substrates were found to exhibit the same order of enhancement ~10^8 for NB and ~10^4 for PA.

The third section introduces other flexible substrates, i.e., polymer nanofiber mat, which are fabricated by electrospinning technique. The fabrication of poly-vinyl alcohol (PVA) nanofiber was initiated to synthesize by varying the concentration of the PVA (5, 10, and 30 wt%) at a fixed nozzle-collector distance (15 cm) and the applied electric potential (16 kV). The nanofiber's morphology and size were characterized by FESEM. Picosecond laser (~30 ps, 1064 nm, 10 Hz) fabricated Au NPs in distilled water were added to PVA before the electrospinning process. The characterization of the polymer nanofiber with and without NPs was performed using FESEM, TEM, and XRD techniques. Au NPs loaded to the PVA nanofiber were utilized for detecting MB and methyl salicylate. The efficacy of flexible substrates compared with the commercially available flexible substrates [Ag/Au loaded FP] provided by the Metrohm company with MB-5 µM and crystal violet (CV)-5µM. The obtained EF's were 2.54×10^4 and 1.46×10^4 for MB; 8.6×10^3 and 2.2×10^3 for CV using Ag and Au based FP substrates, respectively. Commercially available DVD's were used as SERS substrates. The polycarbonate film on DVD was peeled off and cleaned in ethanol, performed ultrasonic bath. The periodic pattern with a metal film on DVD (blank and written) SERS substrate performance was verified with other base materials such as silicon and glass using NB 500 nM as a probe molecule. Fs LAL fabricated Au NPs deposited DVD -written substrate utilized to detect R6g-5µM, MB-50 nM, NB-50 nM, and CV-50 nM. The intensity of the Raman signal was increased by ~3 times in the presence of Au NPs on the DVD substrate compared to DVD without NPs. The written DVD with Au NPs was able to detect 1 nM NB along with an intensity variation of ~10.46% (RSD) was observed.

The summary of all the SERS substrates investigated in this thesis shown in the table below.

S. No	SERS	Substrate material	Active medium (NPs)	Sensitivity (EF)		Reproducibility	Stability (days)
				Dye	Explosive		
1	Rigid	Silicon (Si)	Ag-Cu	3×10^7	3×10^4	<12% ✓	-
			Ag-Au	3×10^7	8×10^4		-
			Cu-Au	1×10^7	4×10^4		-
2		Si MSA	Ag-Au	1×10^{10} ✓	2×10^6 ✓	<15%	-
3	Flexible	Filter paper	Ag	3×10^7	2×10^4	<15%	15
			Au	8×10^6	1×10^4	<16%	45 ✓
4			Star Au	3×10^{10} ✓	4×10^4	<18%	-
5		Polymer NF	Au	1×10^7	-	-	
6		DVD	Au	1×10^9	-	<11% ✓	

References

1. M. Moskovits, *Rev. Mod. Phys.,* **57**, 783 (1985).
2. J. Langer, et al , *ACS nano*, (2019).
3. E. Petryayeva, and U. J. Krull, *Anal.chim. acta,* **706**, 8-24 (2011).
4. Y. Yu, P. Zeng, C. Yang, J. Gong, R. Liang, Q. Ou, and S. Zhang, *ACS Appl. Nano Mater.,* **2**, 598-606 (2019).
5. D. Kim, Y. Ko, G. Kwon, Y.-M. Choo, and J. You, *Sensors and Actuators B: Chemical,* **274**, 30-36 (2018).
6. A. Hakonen, P. O. Andersson, M. S. Schmidt, T. Rindzevicius, and M. Käll, *Anal. Chim. Acta,* **893**, 1-13 (2015).

7. A. Chou, E. Jaatinen, R. Buividas, G. Seniutinas, S. Juodkazis, E. L. Izake, and P. M. Fredericks, *Nanoscale,* **4**, 7419-7424 (2012).
8. S. Barcikowski, V. Amendola, G. Marzun, C. Rehbock, S. Reichenberger, D. Zhang, and B. Gökce, *DuEPublico, Essen*, (2016).
9. S. M. Restaino, and I. M. White, *Anal. Chim. Acta,* **1060**, 17-29 (2019).
10. C. H. Lee, L. Tian, and S. Singamaneni, *ACS Appl. Mater. & Interf.,* **2**, 3429-3435 (2010).
11. Y. Ma, Y. Wang, Y. Luo, H. Duan, D. Li, H. Xu, and E. K. Fodjo, *Anal. Methods,* **10**, 4655-4664 (2018).

Dynamics of Confined Laser Induced/Ablative Plasmas and Shock Waves

Nagaraju Guthikonda
Advanced Centre of Research in High Energy Materials (ACRHEM), School of Physics
University of Hyderabad, Prof. C.R. Rao road, Hyderabad, Telangana, India-500046.
*Email: naga.gk@uohyd.ac.in

Thesis Summary:

This thesis discusses the dynamics of the confined laser induced/ablative plasmas and shock waves visualized through shadowgraphy technique to understand and develop a nano-second laser based milli-meter (mm) sized shock tube. The downscaling of the shock wave effects such as pressure, velocity attenuation during propagation, laminar and turbulence flow from macroscopic to mm or micro range, requires a proper extensive study to balance the interplay between the down scaling of the shock waves to mm size and maintaining the shock wave properties. This can be achieved by studying the enhancement of the plasma and shock wave properties in different confined geometries. Based on the experimental geometry used for plasma confinement, the confinement methods can be divided into two categories, (a) axial confinement (b) lateral or spatial confinement w.r.t. laser axis. In axial confinement, the plasma source is confined by a fluid (liquid/plasma/gas) or solid (glass) confining layer along laser propagation axis. The collision dynamics of the two counter propagating laser induced plasmas (S1 and S2) and shock waves in ambient air revealed the effect of the separation distance (d) between the confining plasma and confining medium (another plasma as fluid confinement). Here, the plasma source S2 is used as the temporally expanding fluid confining medium, which confines the plasma source S1 generated with 25 mJ laser energy. This study also helps to understand the effect of the relative impedance of the confining plasma and fluid confining medium with different impedances ($Z=\rho U_{sw}$) along with the effect of separation distance between two plasma sources (S1 and S2).

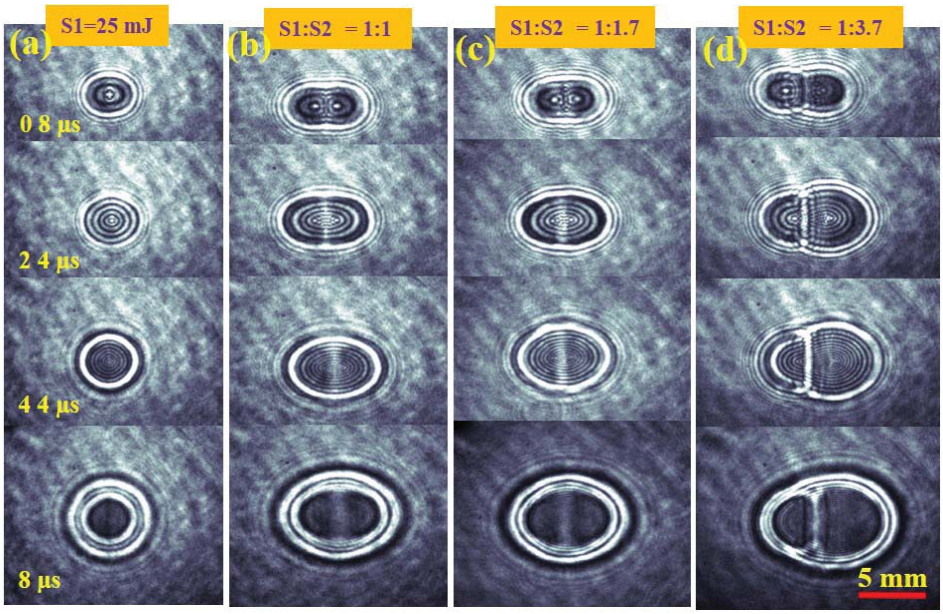

Figure 1. Shadowgrams of the temporal evolution of the (a) single plasma S1 evolution; colliding plasma sources of (b) equal and (c-d) unequal energy ratios with d=1 mm.

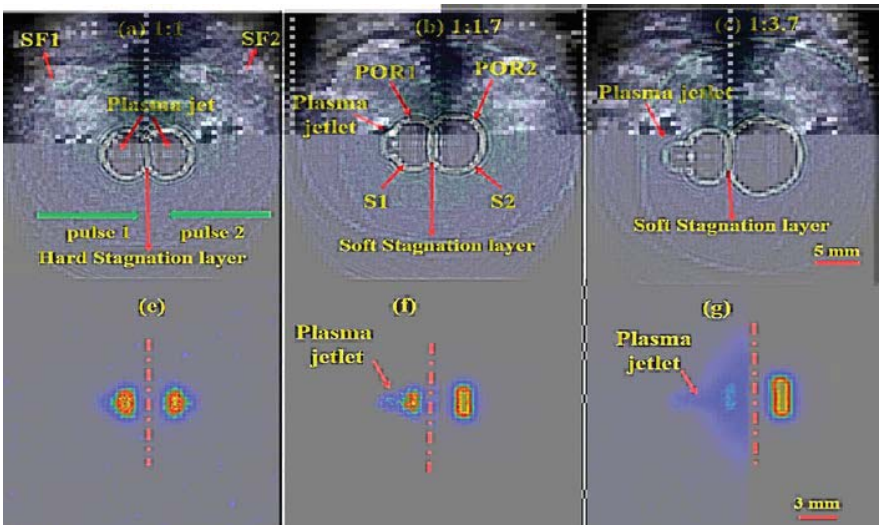

Figure 2. Shadowgrams of two counter propagating laser induced plasma shockwaves for d=4mm, at t=30 µs with different energy/impedance ratios of (a) 1:1, (b) 1:1.7, and (c) 1:3.7. The vertical lines in Figure 2(e-g) represent d=0.

The results showed that, when the two laser pulses are focused with d < 2 mm separation distance, both the plasma sources were merged into a single colliding plasma source which lead to the increment in plasma and shock wave properties as shown in figure 1. For separation distance d ≥ 2 mm, we have observed the plasma jetlet formation in the source S1 due to the impedance mismatch between S1 and S2 plasma sources, along with a stagnation layer at the interaction zone as shown in figure 2.

The evolution dynamics of the laser induced blow off shock waves (LIBO SWs) in ambient air from metal films (Al, Cu, Ti) and polymer films (PVA, Au doped PVA) confined with glass (BK-7) substrate, revealed that the efficient

blow off the shock waves can be achieved for optimal laser input energy by varying focusing conditions. This has resulted in the efficient coupling of the laser energy to the target material.

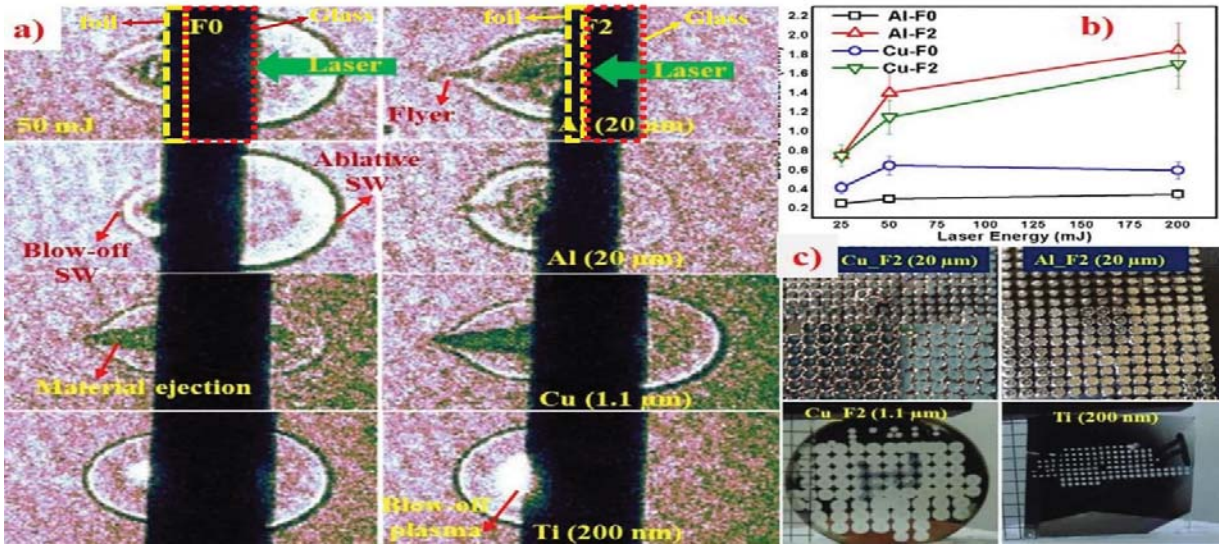

Figure 3. LIBO studies of different samples (a) shadowgrams at 3.05 μs (b) energy dependence behavior of blow off diameter of Al (20 μm) and Cu (20 μm) foils (c) samples after experiment.

In this study, we have shown that the efficient laser energy coupling to the target material can be achieved by precisely shifting the laser focal plane around the interface as shown in figure 3. This study also useful in understanding the effect of the relative impedance between target and confining metal layer on the blow off shock wave properties. The results showed that the PVA and AuPVA polymers gave higher LIBO SWs than Al (20 μm), Cu (20 μm) foils by shifting the focal plane to F2 (2 mm) focusing condition with an optimal 50 mJ laser input energy.

The study of the spatial confinement of the air plasma inside mm size tubes (with 4.7 to 13 mm tube diameters) revealed the inter-dependency and interaction of the plasma and shock waves, which highly depend on the input laser energy and tube aspect ratio (L/D). In spatial confinement of air plasma, the reflected radial/transverse shock waves compression increased the plasma properties such as plasma length, plasma life time, plasma number density and plasma temperature. The squeezing of the air plasma forced out the plasma mass density which increased the axial shock wave position i.e., its velocity as shown in figure 4. This study also helped us to understand the air plasma generated shock wave propagation inside mm sized tubes and the effect of spatial confinement on axial shock wave propagation.

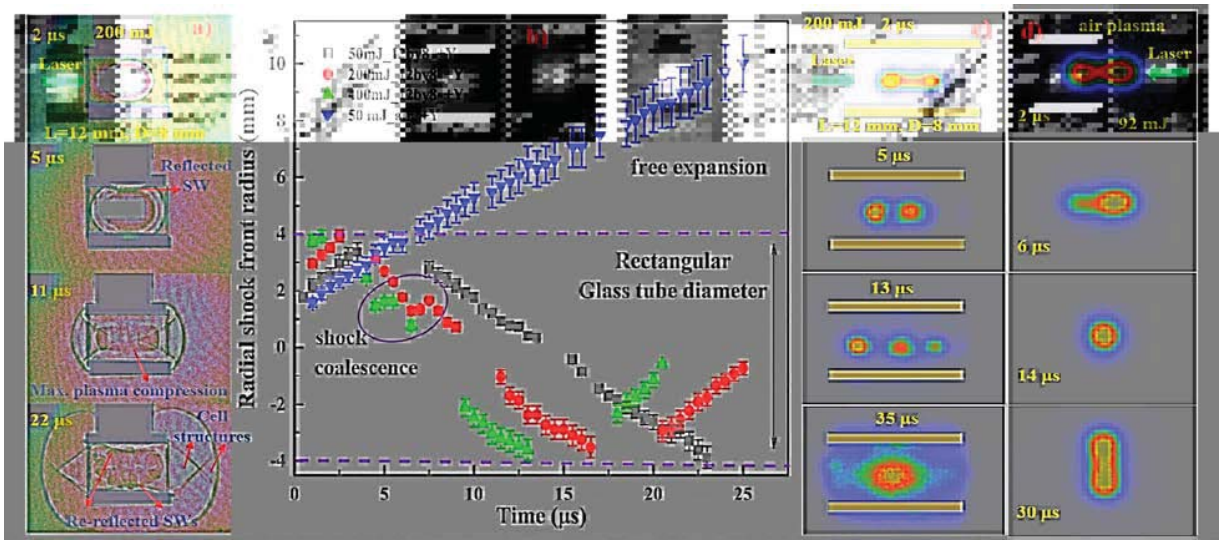

Figure 4. Temporal evolution of (a) shadowgrams of plasma and shock waves (b) radial shock waves along +Y direction, plasma self-emission images of (c) spatially confined 200 mJ air plasma inside glass tube with L/D=1.5 (d) ambient air plasma with 92 mJ energy.

Finally, this work also investigated the shock wave propagation inside transparent solid material, which will be helpful to understand the Laser Shock Peening (LSP) process. The dynamics of the temporal evolution of the laser induced/ablative shock waves inside a transparent dielectric material, BK-7 glass slab is used to understand the effects of both the axial confinement and spatial confinement on the shock wave propagating inside a transparent solid material. The axial confinement of shock waves is achieved using an overlay of 20 µm Al/Cu foils, while the dimensions of BK-7 glass have provided the spatial confinement to shock waves launched and propagated inside BK-7 glass slab as shown in figure 5.

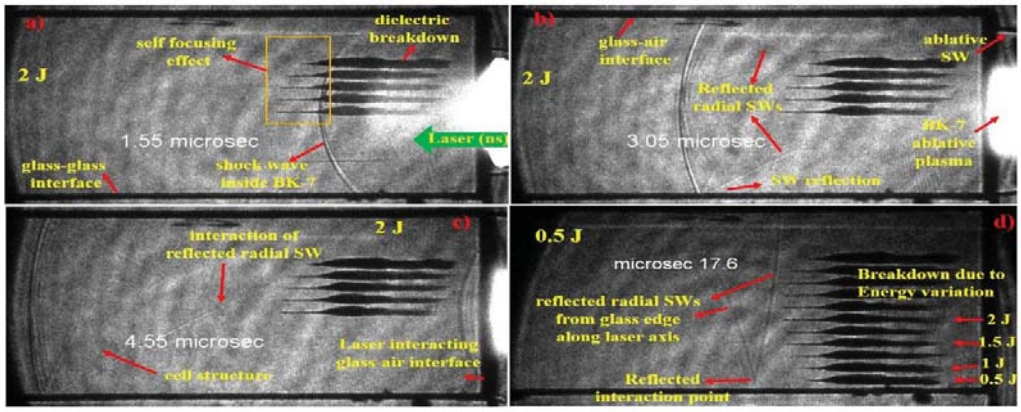

Figure 5. Dielectric breakdown of BK-7 glass slab for laser energies (a-c) 2 J (d) 0.5 J in direct ablation geometry

The results showed that, the shifting of the laser beam focal plane from F0 to F2 (6 mm) focusing condition enhanced (around 0.6 - 2.2 km/s) the shock wave velocities inside the BK-7 glass due to the 20 µm Al foil confinement of the BK-7 glass, but it has not affected for the 20 µm Cu foil confinement of the BK-7 glass. The energy dependence study on the shock wave propagation inside BK-7 glass revealed that, the enhancement of the

shock wave inside BK-7 glass greatly depends on the relative acoustic impedance of the confining layer (20 µm Al and Cu thin foils) and BK-7 glass as well as on the laser energy density in the focal volume at the interface. Future roadmap for the development of nano-second laser based micro shock tubes with optimal input laser energies, better laser focusing conditions, selection of confining layer material and aspect ratio (L/D) of the tube based on the thesis is proposed. The experimental set up used for the initial data from mm sized shock tube is shown in figure 6.

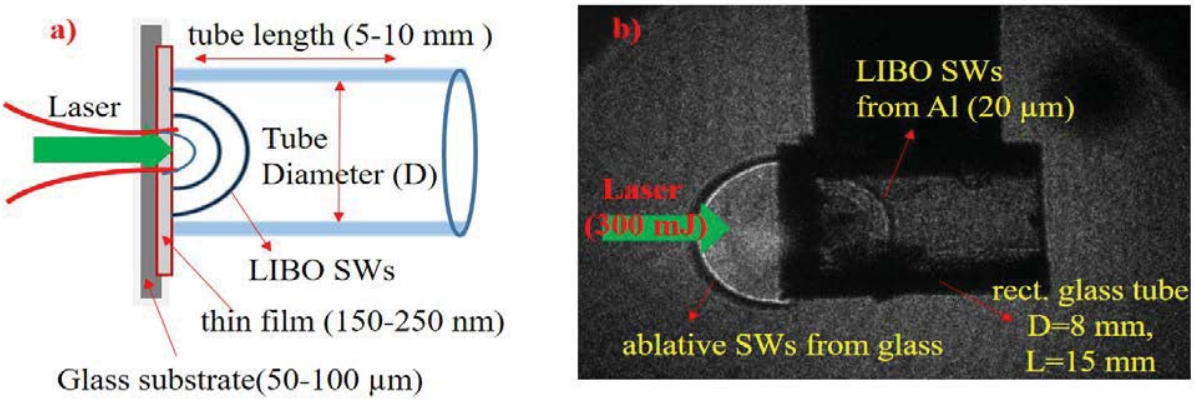

Figure 6. (a) Schematic used for the LIBO SWs propagation inside the mm sized tubes (b) experimental visualization of ns laser shock tube using rectangular tube geometry.

Linear and Nonlinear Optical Exciton Probing in Inorganic-Organic Hybrid Semiconductors

Mohammad Adnan

Nanophotonics Lab, Department of Physics, Indian Institute of Technology Delhi, Hauz Khas, New Delhi-110016, India

Email: mohdadnan898@gmail.com

Abstract: The thesis motive is to demonstrate the influence of structure and laser-matter interactions on the strong room-temperature optical exciton energies of the novel inorganic-organic (IO) semiconducting hybrids. The synthesis and optical properties of varieties of IO hybrids are systematically explored to understand the excitons dynamic and static behaviour in the linear and nonlinear excitation domains. High intense IR ultrashort pulse optical probing provide information of sample deeper depths and reveal several underlying structural perturbations and also information about new excited states. The study of transient absorption and time-resolved photoluminescence studies highlight the excitation and de-activation mechanisms of various excitons involved.

Introduction: Hybrid materials, incorporating both organic and inorganic constituents into a single molecular level composite, are emerging as effective and promising new materials due to the diverse, but complementary properties of different classes. These crystallographically two-dimensional (2D) IO hybrid van der Waals materials are represented by the general formula $(R\text{-}NH_3)_2PbX_4$, having alternative stacks of corner-shared PbX_6 octahedral network, separated by wider bandgap organic moieties forming natural multiple quantum wells (MQWs) structures[1, 2]. In these MQWs, the molecular layers of inorganic behave as *'wells'* and mono/bi organic spacer layers act as *'barriers'*. These MQWs show strong room-temperature Mott-type exciton properties due to quantum confinement and the reduced dielectric screening effects[3]. These Mott-type excitons are confined within the lowest inorganic bandgap and the exciton binding energies are manifold enhanced (~200-250 meV) compared to the parent PbI_2 (~23 meV). Thus, these room-temperature exciton optical features have thermal stability[3, 4] even up to 200 °C.

Among various 2D IO hybrids, the alkylammonium ($C_nH_{2n+1}NH_2$) based hybrids are special because of their distinctly different organic moiety conformation behavior. Long alkylamine organic moiety ($C_nH_{2n+1}NH_2$; n>3 and upto as long as 22) interaction with PbI_2 results into typical 2D crystal packing of $(C_nH_{2n+1}NH_3)_2PbI_4$ [5, 6, 7]. Most interesting in their crystal packing is that they show strong reversible phase transitions within the reachable temperatures[6, 7]. During phase transitions, the corner shared PbI_6 octahedra can be either staggered or in eclipsed arrangements which often adopts orthorhombic and monoclinic crystal packing respectively[8]. These phase transitions are pronounced with temperature, thickness and aging effects[6, 8]. On the contrary, the small alkylamine organic moieties ($CH_3NH_2^+$ and $C_2H_5NH_2^+$ for n=1, 2) result into a true 3D AMX_3 type perovskite structure with small exciton binding energy, where the corner-sharing MX_6 octahedra are inter-connected and the organic cation is located at larger 12-fold coordinated voids[9].

In general, when laser light interacts with semiconductors, the optical processes witness from simple linear processes (optical excitation etc.) to a wide range of nonlinear processes depending upon various laser

parameters such as wavelength and incident laser intensities[10]. From continuous wave (CW) resonant excitation (in the absorbing region, $\hbar\omega \geq Eg$), along with typical linear band-to-band electron excitation, the irradiation further causes local heating and ablation effects[11]. Highly intense ultrashort laser-matter interactions generally produce wide range of nonlinear optical phenomena such as two-photon (or multi-photon) absorption[12], excited state absorption, exciton-exciton annihilation[13] and ultrafast charge carrier dynamics[13]. Two-photon (2PA) absorption is an interesting Kerr type third-order nonlinear process in which electrons in the valence band can absorb two low energy photons ($2\hbar\omega \geq Eg$) simultaneously and make an electronic transition to the conduction band and subsequently relaxation of the electron resulting in the emission of a photon with frequency greater than that of absorbed photons[14]. The advantages of two-photon absorption induced photoluminescence (2PA-PL) is that it has larger penetration depth, three dimensional resolution, stronger spatial confinement and most importantly reduced background fluorescence[15]. A careful comparative study of one-photon (1PA) and two-photon (2PA) absorption induced photoluminescence reveal many interesting surface and bulk photo-physics, and convoluted information such as defects, coexisting photo-excited species etc.[16]. The fast transient dynamics of optically excited carriers and their population dynamics can be further visualized from femtosecond transient absorption pump-probe spectroscopy[16]. Thus, the advances in the wide range of recently available laser technologies, the study of laser-matter interactions in 2D and 3D IO hybrids are of special importance, especially, the high intense linear and nonlinear probing, transient absorption and PL studies

Section I: Synthesis, structural and optical properties of structurally slightly different layered IO hybrid single crystals

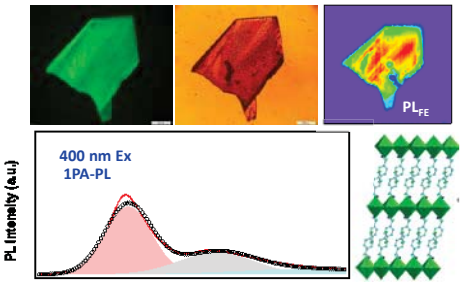

In this work we report the synthesis protocol and optical properties of two-dimensional layered structurally slightly different inorganic-organic (IO) hybrid semiconductors (R-$C_6H_4C_2H_4NH_3)_2PbI_4$ (R=CH_3, Cl). As thin film, both IO hybrids are perfectly oriented along the *(l00)* direction. Both single crystals and thin films show strong room-temperature Mott-type exciton features and such features are highly sensitive to the self-assembly and crystal packing. The exciton photoluminescence imaging and spectral spatial mapping provide a deeper insight into the layered re-arrangement, structural crumpling due to organic conformation. Their structural and photoluminescence aspects are successfully presented with a proper correlation that emphasizes differences in physical and optical properties associated between these novel IO hybrids. {*Adnan et al. ACS Omega, 4 (2019) 19565-19572*}

Section II: **Linear and nonlinear optical probing of various excitons and their PL dynamics in 2D IO hybrid semiconductors**

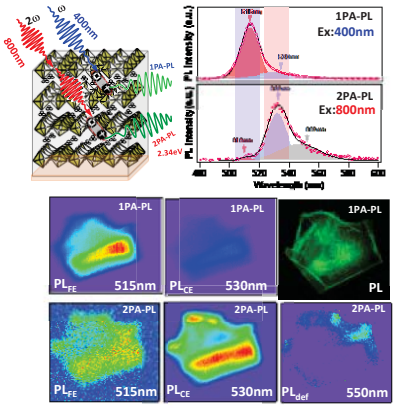

Nonlinear optical properties, such as two-(or multi-) photon absorption (2PA) are of special interest for technologically important applications in fast optical switching, *in vivo* imaging and so on. Highly intense infrared ultrashort pulses probe deep into samples and reveal several underlying structural perturbations such as inter-layer

distortions, intra-layer crumpling and provide information about new excited states and their relaxation. Strongly confined excitons show distinctly different one- and two-photon excited photoluminescence energies: from free-excitons coupled to the perfectly aligned MQWs and from energy down-shifted excitons that originate from the locally crumpled layered architecture. The nonlinear behavior of one-photon absorption induced PL (1PA-PL) suggests the saturation of absorption and exciton-exciton annihilation characteristic features. Both 1PA- and 2PA-PL spatial mappings over large areas of single crystal platelets demonstrate the co-existence of both free- and deep-level crumpled excitons with some traces of defect-induced trap state emission. This study paves a way to tailor the nonlinear properties of many 2D material classes. Our results thus open new avenues for exploring fundamental phenomena and novel optoelectronic applications using layered inorganic-organic and other metal-organic frameworks. {*Adnan et al. Nature Scientific Reports, 10 (2020) 2615*}

Section III: Real-time dynamic evolution monitoring of laser-induced exciton phase flips in long-alkylamine based 2D IO hybrid semiconductors

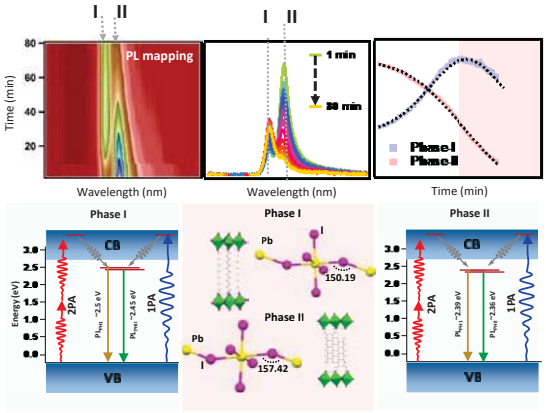

Here we demonstrate the real-time monitoring of laser-induced exciton phase flips in two-dimensional IO hybrid semiconductors when irradiated with ultrafast laser excitation (Ultraviolet and infrared). UV excitation based one-photon absorption induced PL is influenced by localized heating, ablation effects, and third-order nonlinear effects such as saturation of linear absorption and exciton-exciton annihilation. However, during two-photon excitation, the near infrared laser excitation reveals the red-shifted crumpled excitons from the deeper depth of the sample, which are induced by multi-photon absorption and avalanche ionization. {*Adnan et al. Journal of Applied Physics, 128 (2020) 023104*}

Section IV: Laser-induced inter-ion migration phase stabilities in long alkylammonium halide functionalized mixed halide 3D IO hybrid colloidal nanoparticles

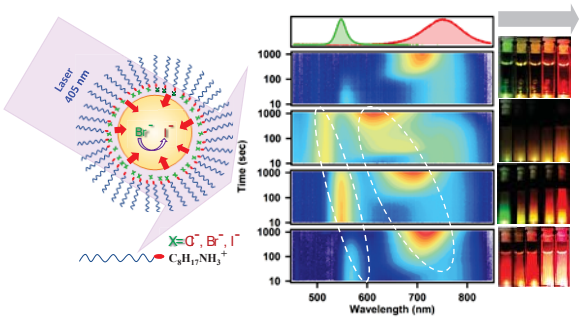

Here we present laser-induced phase segregation effect and dynamic evolution of room-temperature photoluminescence (PL) from mixed halide colloidal 3D perovskite nanoparticles. UV laser-assisted compositional changes are observed when the nanoparticles are surface-functionalized with different halide based long alkylammonium moieties ($C_8H_{17}NH_3X$; X=Cl, Br or I). The results are direct evidence of laser-assisted reversible phase segregation, halide ion diffusion from surface ligand to nanoparticles, and the effect of surface functionalization on photo-assisted bandgap engineering. {*Adnan et al. Applied Surface Science, 526 (2020) 146789*}

Section V: Study of surface and bulk recombination kinetics of 2D IO hybrid semiconductors under linear and nonlinear femtosecond transient absorption analysis

Here, photo-generated charge carrier dynamics in two-dimensional inorganic-organic (IO) hybrid semiconductors have been presented using linear and nonlinear femtosecond transient absorption spectroscopy. Linear and nonlinear excitations reveal surface and bulk excitons dynamics in these layered materials. Fluence dependent studies clearly demonstrate the hot phonon bottleneck effect at higher fluences. The results presented here are important to understand the nature of photo-generated charge carriers at the exciton energy level for developing advanced optoelectronic applications. {*Adnan et al. (under communication)*}

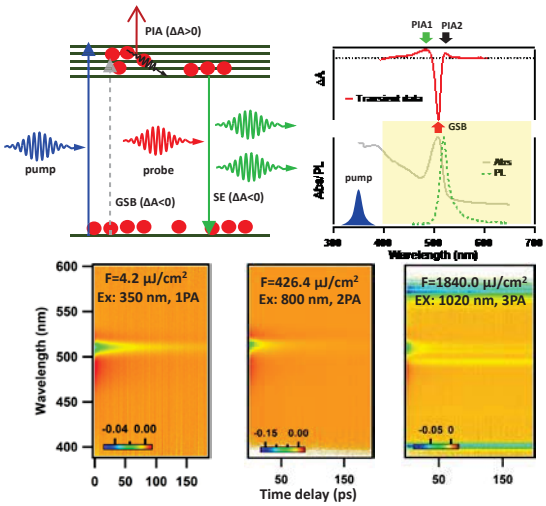

References:

1. S. Ahmad, J. J. Baumberg, and G. Vijaya Prakash, *J. Appl. Phys.* **114**, 233511 (2013).
2. K. Pradeesh, J. J. Baumberg, and G. Vijaya Prakash, *Opt. Express* **17**, 22171 (2009).
3. D. B. Mitzi, *Chem. Mater.* **8**, 791 (1996).
4. T. Ishihara, J. Takahashi, and T. Goto, *Solid State Commun.* **69**, 933 (1989).
5. G. C. Papavassiliou and I. B. Koutselas, *Synth. Metals.* **71**, 1713 (1995).
6. S. Barman, N. V. Venkataraman, S. Vasudevan, and R. Seshadri, *J. Phys. Chem. B.* **107**, 1875 (2003).
7. A. Lemmerer and D. G. Billing, *Dalton. Trans.* **41**, 1146 (2012).
8. K. Pradeesh, J. J. Baumberg, and G. Vijaya Prakash, *J. Appl. Phys.* **111**, 013511 (2012).
9. M. Mittal, A. Jana, S. Sarkar, P. Mahadevan, and S. Sapra, *J. Phys. Chem. Lett.* **7**, 3270 (2016).
10. P. K. Kanaujia, A. Bulbul, V. Parmar, and G. Vijaya Prakash, *Appl. Sur. Sci.* **420**, 63 (2017).
11. P. K. Kanaujia and G. Vijaya Prakash, *Phys. Chem. Chem. Phys.* **18**, 9666 (2016).
12. H. S. Quah, W. Chen, M. K. Schreyer, H. Yang, M. W. Wong, W. Ji, and J. J. Vittal, *Nature Commun.* **6**, 7954 (2015).
13. G. Delport et al. *J. Phys. Chem. Lett.* **10**, 5153 (2019).
14. W. Liu, J. Xing, J. Zhao, X. Wen, K. Wang, P. Lu, and Q. Xiong, *Adv. Opt. Mater.* **5**, 1601045 (2017).
15. M. Drobizhev, N. S. Makarov, S. E. Tillo, T. E. Hughes, and A. Rebane, *Nat. Methods.* **8**, 393 (2011).
16. B. Wu, H. T. Nguyen, Z. Ku, G. Han, D. Giovanni, N. Mathews, H. J. Fan, and T. C. Sum, *Adv. Energy Mater.* **6**, 1600551 (2016).

Studies on electromagnetically induced transparency in ^{87}Rb atoms

Charu Mishra

[1]*Laser Physics Applications Section, Raja Ramanna Centre for Advanced Technology, Indore 452013,India*

[2]*Homi Bhabha National Institute, Training School Complex, Anushakti Nagar, Mumbai-400094, India*

Email: charu.physics91@gmail.com

The thesis is devoted to the extensive study of electromagnetically induced transparency (EIT) in ^{87}Rb atoms in vapor cell and in magneto-optical trap (MOT). EIT is an effect where an opaque medium becomes transparent for a probe field in presence of a strong coupling field. The interesting feature of EIT is that the probe transmission can exhibit very narrow linewidth, *i.e.* an order of subnatural linewidth of the excited state of atomic system. This makes the EIT medium suitable for precision spectroscopy[1], high resolution spectroscopy[2] and tight laser frequency locking[3]. The Λ-system is an interesting choice for investigating EIT effects for several reasons[4]. In the begining of the thesis work , two Λ-systems in D_2 line of ^{87}Rb atom are investigated in various conditions and results are compared. Thereafter, two N-systems prepared in cold atom cloud trapped in MOT are investigated which have shown interconversion of absorption and transparency with detuning of control fields. Finally, a more complex system, modified inverted-Y system, with larger number of coupling fields is then studied theoretically beyond rotating wave approximation.

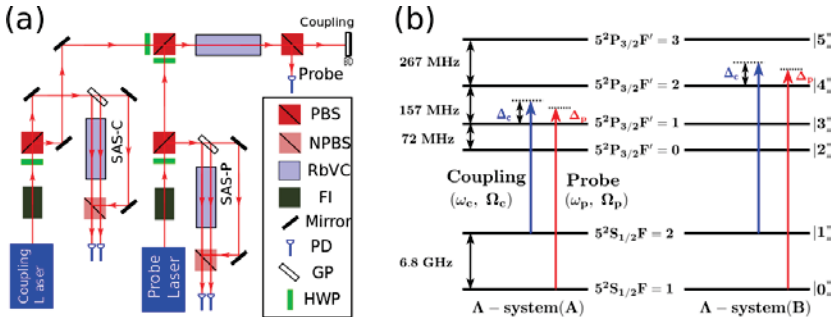

Figure 1:(a) The schematic diagram of experimental setup. (b) The two Λ-systems created by probe and coupling beams in D_2-line transition of Rb atom.

The thesis work includes both theoretical and experimental studies. The work begins with investigating EIT in two Λ-systems in D_2-line transition of ^{87}Rb atom in vapor cell. The schematic diagram of experimental setup is in fig1 (a) and two Λ-systems are shown in fig 1 (b). To study the Λ-systems experimentally, two different external cavity diode lasers of wavelength 780 nm and linewidth less than 1 MHz were used. The independent SAS (SAS-P and SAS-C) for both the lasers have been used to control their corresponding frequencies. The probe beam frequency was kept fixed corresponding to transitions $5^2S_{1/2}$ F=1 to $5^2P_{3/2}$ F'=1 for Λ-system (A) and $5^2S_{1/2}$ F=1 to $5^2P_{3/2}$ F'=2 for Λ-system (B), whereas, the frequency of the coupling beam was scanned across the transition $5^2S_{1/2}$ F=2 to $5^2P_{3/2}$ F'=2. The Rb vapor cell was kept inside a current carrying coil used for creating a longitudinal magnetic field. The polarization of two beams were linear and orthogonal to each other

so that they got separated using polarizing beam splitter (PBS) and half-wave plate (HWP) after Rb vapor cell and only probe beam was collected over photodiode.

The measurements for two Λ-systems are made in absence and in presence of a longitudinal magnetic field. In absence of the magnetic field, the EIT signal is observed at resonance condition. With the presence of the longitudinal magnetic field, the EIT splits into three peaks, shown in fig 2(I). The increase in coupling beam power increased the strength and asymmetry of the single EIT peak (in absence of the magnetic field) and the slope of the central EIT peak (in the presence of the magnetic field). On comparing the two Λ-systems, the system (B) exhibits more strong and symmetric EIT signal in absence of the magnetic field and steeper slope of central EIT peak in presence of the magnetic field. This study is also carried out theoretically where six-level model and thirteen-level model is considered for the case of absence and presence of magnetic field respectively. The experimental and theoretical results are shown in fig 2(I) and (II) respectively.

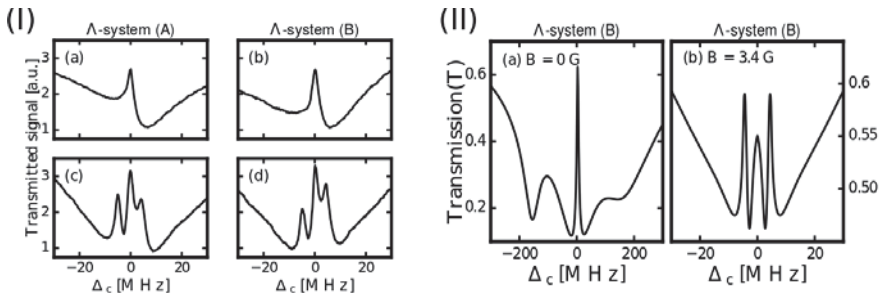

Figure 2: (I) The experimentally observed probe transmission spectrum for Λ-system (A) (left column) and Λ-system (B) (right column). Upper and lower rows corresponds to spectrum in absence and in presence of the longitudinal magnetic field respectively. (II) Graphs show the calculated probe transmission for system-B in absence (a) and presence (b) of the magnetic field.

The Λ-system (B) has been explored with standing wave coupling beam, where at resonance, instead of EIT, an enhanced absorption signal is observed. Due to its subnatural linewidth, it is named as EIA. The EIA also has higher slope at high coupling beam power. The slope of the three signals *i.e.* the single EIT in the absence of the magnetic field, the central EIT peak in presence of the magnetic field and the EIA with the standing wave coupling beam is obtained at different coupling powers. The EIA signal exhibits larger slope for all coupling power, which makes this signal more suitable for applications like tight laser frequency locking.

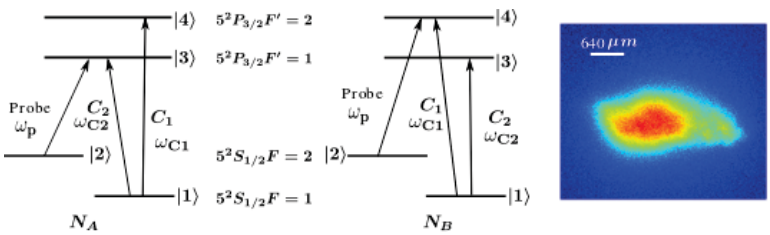

Figure 3: N-systems formed by probe and beams C_1 and C_2. Right figure is fluorescence image of ^{87}Rb atoms.

Thereafter, EIT is explored in an extension of Λ-system, which is N-system. This study is carried out in cold ^{87}Rb atoms trapped in MOT. The cold atom offers reduced Doppler effect and low collisional dephasing rate. The N-systems can be created by applying a control beam to a Λ-system. In our case, a drive beam, named as

$C_{1,}$ is used as a control beam in previously mentioned Λ-system (A) to form system N_A, and another drive beam, named as $C_{2,}$ is used as a control beam in previously mentioned Λ-system (B) to form system $N_{B.}$ These N-systems are shown in fig 3.

The probe spectrum for N-system shows three transmission dips which are explainable from dressed-state approach. The variation in probe spectrum due to variation in strength and detuning of coupling and control beam are measured. The numerical calculations are done by solving Liouvelli master equation using matrix method. The experimental and numerical results are shown in fig 4.

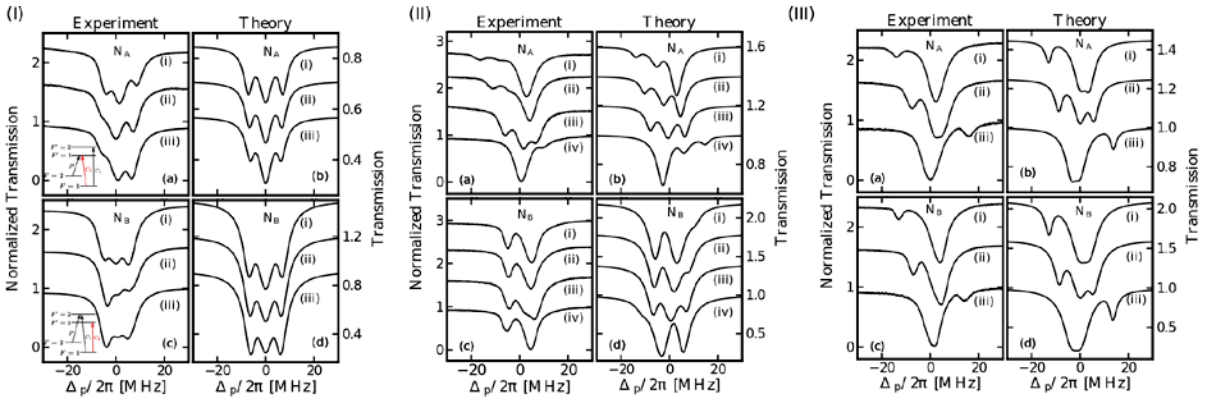

Figure 4: The experimental and numerical probe transmission spectrum with variation in beams strengths and detuning. (I) The power in C2 beam (i) 12 mW, (ii) 10 mW, and (iii) 8 mW. (II) The detuning in C_2 beam (i)$-2\pi \times 9$ MHz, (ii)$-2\pi \times 3$ MHz, (iii)$2\pi \times 10$ MHz. (III) The detuning in C_1 and C_2 beams are (i)$-2\pi \times 8$ MHz, (ii) $-2\pi \times 4$ MHz, (iii) $2\pi \times 1$ MHz, (iv) $2\pi \times 9$ MHz.

In fig 4(I), the strength of beam C_2 is varied and the probe transmission is measured. The beam C_2 acts as a coupling beam for system N_A and control beam for system N_B. Thus, the effect of coupling and control beam's strength on the probe transmission can be obtained by observing the spectrum for system N_A and N_B respectively. The system N_A shows that the strength of the side transmission dips are reducing with decrease in power of C_2 beam (fig 4(I)(a,b)). Similar dependence is observable for central dip in system N_B. This shows that side transmission dips are more affected by coupling beam and central transmission dip is depending on control beam of N-system. In fig 4(II), the detuning of beam C_2 is varied and the systems N_A and N_B show the effect of coupling and control beam detuning on N-system respectively. When coupling beam is detuned the three transmission dips become asymmetric and change its position. When control beam is detuned, the system begins to behave like Λ-system with some perturbation. At last, the detuning of both the beams C_1 and C_2 is varied and observed results are plotted in fig 4(III). In this case, both the systems has shown similar feature which is alike of the detuned Λ-system. This study reveals that depending on control beam detuning inter-conversion of absorption and transmission can be obtained.

Next, probe absorption characteristics of a modified inverted-Y (IY^+) system, is investigated theoretically beyond rotating wave approximation (RWA). The IY^+-system is shown in fig 5(I). This study is carried out using a numerical matrix propagation (NMP) method, where a complete density matrix has been propagated through time in order to obtain the transient characteristics as well as the steady state condition for a probe field

absorption. The motivation behind the IY^{+}-system is that this system is comprised of basic systems like Λ, ladder, vee, N and inverted-Y system. The spectral characteristics of IY^{+}-system can give the interdependence of basic systems on each other. The detuning dependent study is shown in fig 5(II). Plots (a) and (c) corresponds to detuning Δ_{04}. The large detuning in field Δ_{04} results in sharp transparency which could be due to no constructive interfernce from vee system. The strength (Ω_{23}) dependent results are shown in fig 5(III). For weak Ω_{23}, system behaves like N-system with some perturbation which explains the three peaks with asymmetry. For strong Ω_{23}, the obtained absorption peaks can be explained from doubly-dressed approach. Fig 5 (III) shows primary dressed states and fig 5 (III) shows secondary dressed states. The transitions between dressed states explain the obtained results for this case. Similar study is carried out with other parameters as well where inter-conversion of absorption and transparency, splitting and shifting of transparency are obtained.

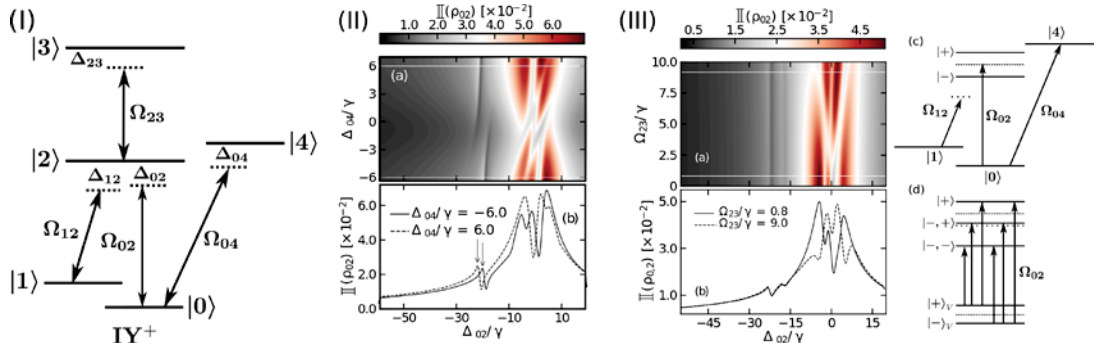

Figure 5: (I) shows the level diagram of IY^{+}-system. (II) shows the amulgamated spectrum in plots (a) and individual spectrum corresponding to white lines drawn in plots (a) is in plots (b). (III) shows the spectrum with variation in strength Ω_{23}. Level schemes (c) and (d) show primary and secondary dressed states respectively.

In summary, the EIT signal has been investigated and compared in two Λ-systems in D_2-line of ^{87}Rb atoms in vapor cell at different conditions. In this study, central EIT peak in presence of the longitudinal magnetic field and enhanced absorption signal with standing wave coupling field are noteworthy observations which may find applications in precision spectroscopy and tight frequency locking. An extension of Λ-system, *i.e.* N-system, is investigated in cold ^{87}Rb atom cloud trapped in MOT. Further, a more complex atomic system (IY+) with multiple levels involved has been investigated theoretically beyond RWA. With increase in the number of coupling fields, degrees of freedom to control probe transmission spectrum are increased alongwith some complexities involved in the experiments . With larger number of fields, a larger control over spectrum has been shown. The obtained key results in the studies are interchange of absorption and transparency and splitting in transparency with variation in coupling field parameters. The features can be exploited application in optical switching and multi-channel optical communication.

References:

1. Iftiquar, S *Opt. Commun.* **281**, 4951 (2008)
2. Y.B. kale, S.R. Mishra, V. B. Tiwari, S. Singh, H. S. Rawat, *Phys. Rev. A* **91**, 053852 (2015).
3. S. C. Bell, D. M. Heywood, J. D. White, J. D. Close, R. E. Scholten, *App. Phys. Lett.*, **90** (17), 171120 (2007).
4. D. J. Fulton, S. Shephard, R. R. Moseley, B. D. Sinclair, and M. H. Dunn, *Phys. Rev. A* **52**, 2302 (1995)

STUDY AND CHARACTERIZATION OF LASER BASED PARTICLE ASSISTED SURFACE NANOSTRUCTURING AND CLEANING

Bijoy Sugathan

Department of Optoelectronics, University of Kerala, Kariavattom, Thiruvananthapuram, Kerala-6955881

Laser and Plasma Technology Division, BARC, Mumbai-400085

E-mail: bijoysugathan@gmail.com

There is a growing interest among the research fraternity in this age of miniaturization to fabricate nanostructures for applications in nano devices. Therefore, nanostructuring finds applications in diverse disciplines ranging from optics, biosensors, tissue engineering, data storage, to wettability improvement etc. Laser based lithography is a non-contact technique that can generate nanostructures at low cost, maintaining at the same time, a high throughput. However, in the case of far field optics, diffraction will set a limit on the focusabilty of laser beam and in turn affect the minimum achievable spot size. One of the effective ways of overcoming this limitation due to diffraction is to adopt particle assisted approach, that relies on near field enhancement as a result of focusing of the light beam as it traverses through micron or sub-micron sized particle. In this work, an attempt has been made to study fabrication and characterization of nanostructures on both metallic (such as stainless steel) as well as dielectric (such as like Si and GaAs) substrates by adopting particle assisted near field lithography. The thesis consists of eight chapters organized as follows.

Chapter 1 introduces laser assisted surface cleaning and various nanostructuring methods with an emphasis on near field approach. An introduction to particle assisted near field method for fabrication of nanostructures and review of previous works is the principal focus of this chapter. Various characterization tools and an introduction to the simulation of the particle assisted focusing effect leading to the formation of photonic nanojet is also a part of this chapter.

Chapter 2 discusses experimental results on field enhanced surface absorption during laser assisted removal of

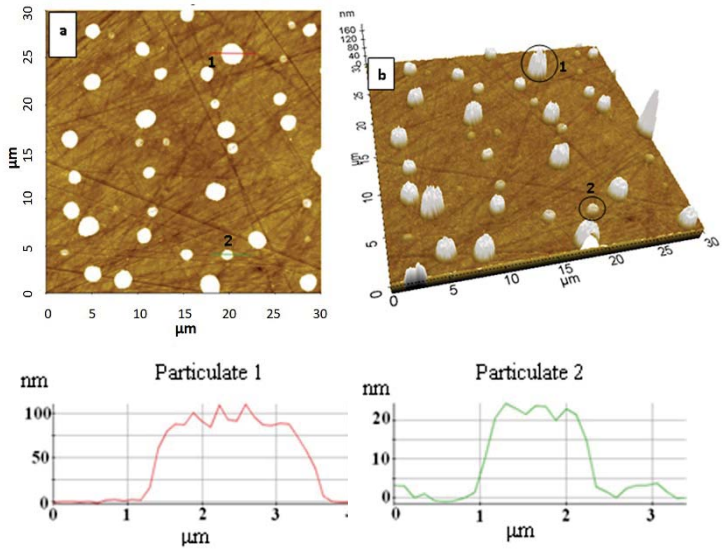

Fig. 1. AFM micrograph of the SS surface simulated with Cs contamination showing a typical distribution of particulates in 2D and 3D views (Fig. a and b respectively). The insets show the surface topography of two randomly chosen particulates 1 and 2 that have also been identified in the AFM images.

translucent particulates of ellipsoidal geometry from a metallic substrate surface. Fig. 1 depicts AFM micrograph of the SS surface simulated with Cs contamination showing a typical distribution of ellipsoidal particles. The surface pitting caused due to this effect has been experimentally probed as a function of the ratio of minor to major axis of the ellipsoid and the behavioural trend has been theoretically interpreted by invoking the principle of geometrical optics. Fig. 2 depicts effect of focusing of the incident light by the ellipsoidal particulate on the substrate surface as a function of 'a' viz., the ratio of minor to major axis. The study also includes the effect of fluence and wavelength of the incident coherent radiation on the surface pitting. Probing of the surface topography has helped gain insight into the formation of multiple pits by a single particulate following its removal post laser exposure.

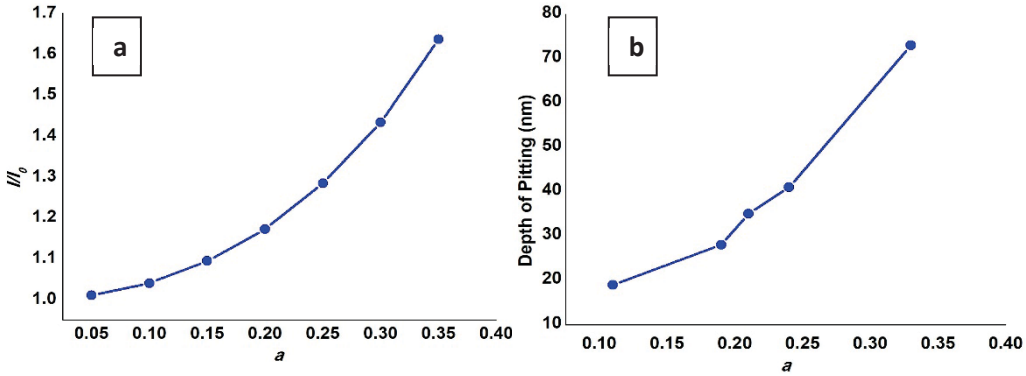

Fig. 2. The effect of focusing of the incident light by the ellipsoidal particulate on the substrate surface as a function of 'a' viz., the ratio of minor to major axis. a. Enhanced intensity as a result of focusing obtained theoretically b. experimentally measured pit depth, a direct consequence of enhanced intensity.

Chapter 3 describes the experimental study on particle assisted structuring on a stainless steel by using polystyrene microspheres as the particles. The surface structuring was characterized for various conditions such as particle size < wavelength, particle size ≈ wavelength, and particle size > wavelength. While the

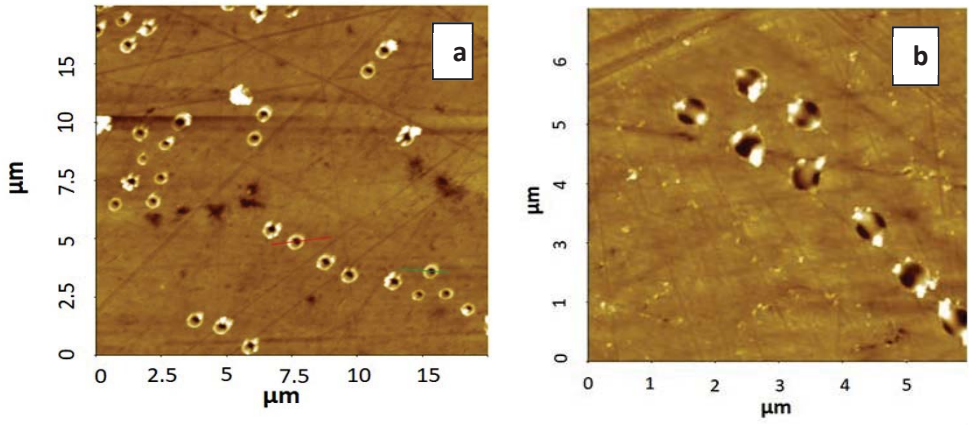

Fig. 3. AFM micrographs formed on SS substrate using PS particles of 1 µm diameter on irradiation of a. typical single pits with 1064 nm laser wavelength at a laser fluence of ~ 65 mJ/cm^2 b. typical double pits when irradiated by laser radiation of wavelength 532 nm at laser fluence of 75 mJ/cm^2.

experimentally measured fluence values for the onset of pitting are in agreement with the analytically estimated field enhancement factors in the former two cases, there is a strong departure noted in the latter case. Percentile absorption of the incident radiation by the SS substrates as measured by an integrating sphere bore testimony to this anomalous behaviour. Towards gaining a deeper insight into this phenomenon, AFM based topographic analysis of the laser exposed surface was undertaken. This study clearly reveals formation of double pits underneath the particulate when its size exceeds the wavelength of exposure thus pointing to the fact that the incident energy is being redistributed giving rise to the observed anomaly.

Chapter 4 discusses the generation of nanostructures on an n-doped silicon substrate through particle assisted dry laser exposure technique. Of particular interest is the formation of nano rings in case of Silicon substrate following exposure with sub nano-second laser pulse at 532 nm wavelength. Usage of such a laser pulse enabled us to realise a condition wherein the dominating thermo-capillary force allowed the formation of nano rings. With gradual increase in the laser fluence the nano rings gave way to formation of nano bumps and nano holes.

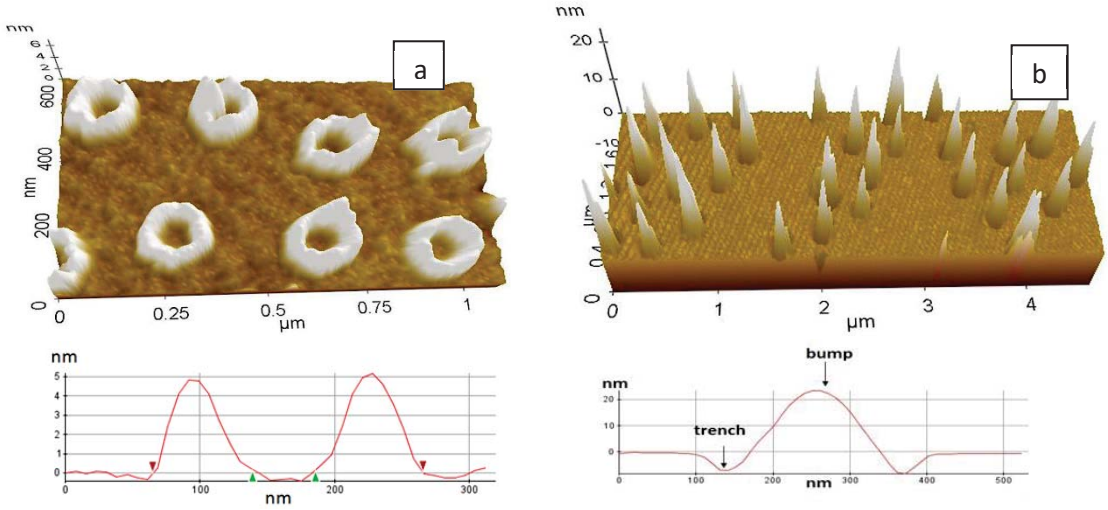

Fig. 4.a. Typical nano rings formed on Si substrate when polystyrene particulate diameter: 300 nm, wavelength of irradiation 532 nm, laser fluence: 55 mJ/cm^2. b. nano bumps formed at a laser fluence of 95 mJ/cm^2

Chapter 5 discusses the experimental results of nanostructuring on GaAs substrate surface by particle assisted near field enhancement method has been presented. A double ring structure, nano holes and nanoring structures

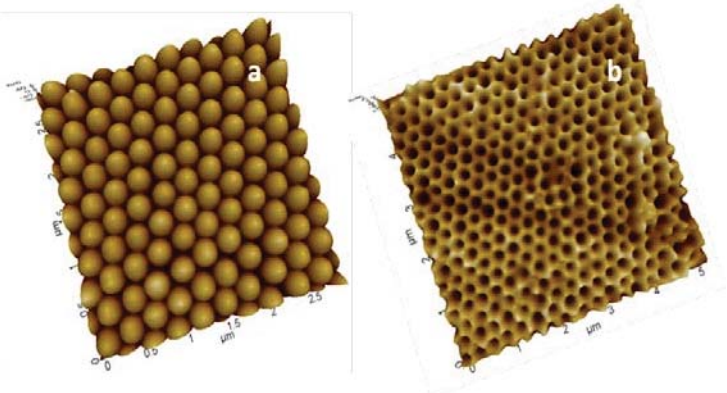

Fig. 5. AFM micrograph of a. perfectly close packed PS particles before exposure b. honeycomb structures formed when exposed at a fluence of 48.3 mJ/cm^2.

were fabricated on GaAs surface by varying particle size and laser parameters. Modifications in the Micro Raman spectra in accordance with different structures were studied.

Chapter 6 discusses the simulation study using Comsol Multiphysics 3.4, of photonic nanojet for particles with spherical and ellipsoidal geometry. Enhancement factors and FWHM of the photonic nanojets were compared for particles different dimensions. It was observed that particles with ellipsoidal geometry are suitable for generation of ultra-elongated nanojets compared to that with particles of spherical geometry.

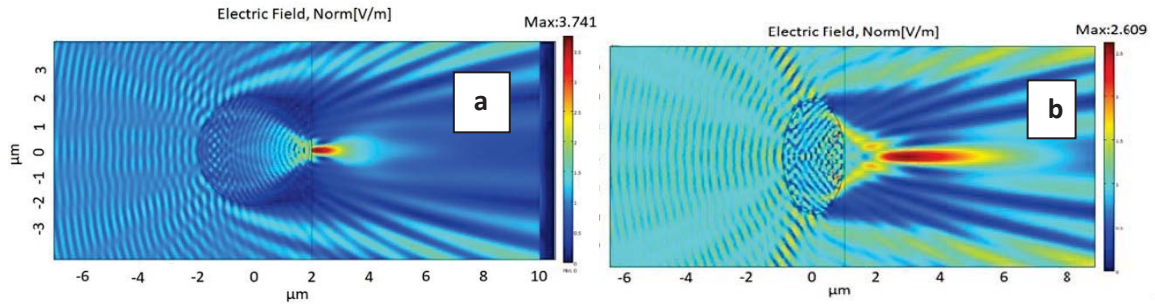

Fig. 6. Electric field Intensity distribution of photonic nanojet by a particle with different minor to major ratios. a. ***a*** *=1* b. ***a*** *= 0.5*

Chapter 7 discusses experimental studies on laser assisted removal of fixed alpha contamination from D9 stainless steel by ablation and the thickness removed was quantified by the sensitive method of thin layer activation analysis technique. The percentage of remaining activity after the removal of certain depth of material is computed by integration technique. Thus, the calibration curve (CC) using the ^{56}Co isotope for D9 SS material is as shown in Fig. The laser erosion of D9 S.S. sample was accomplished by employing an electro optically Q-switched Nd-YAG laser operating at 1064 nm and capable of delivering a maximum energy of ~180 mJ at 10 Hz repetition rate with a pulse duration of 300 pS. Fixed contamination over a thickness of 90 µm depth of D9 material was removed for a total deposited laser energy of ~20kJ.

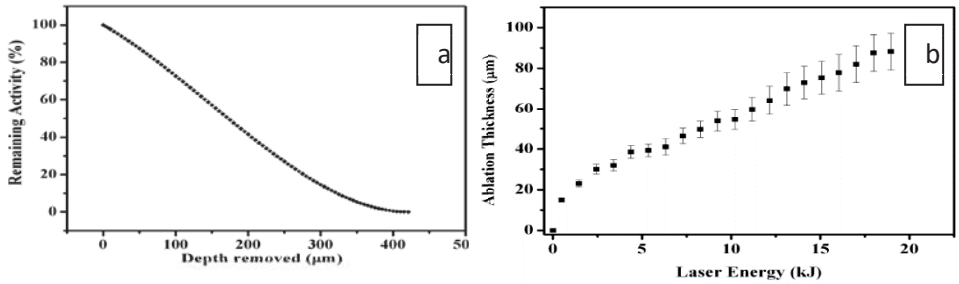

Fig. 7.a. Calibration curve for S.S. 316 foils for ^{56}Co isotope b. Surface erosion *of D9 S.S. material during laser ablation measured by TLA technique.*

Chapter 8: Discusses conclusions and future scope of the work.

Acknowledgements:

The author would like to thank his mentors Dr. V.P. Mahadevan Pillai, Dr. D.J. Biswas and Dr. J. Padma Nilaya for their encouragement, continuous guidance during this doctoral work. The author also acknowledges UGC, Government of India for providing research fellowship.

Structural and Optical Characterization of Pulsed Laser Deposited MoS_2 and WS_2 Layered Thin Films and Quantum Dots

Gobinda Pradhan
Indian Institute of Technology Guwahati
Email: p.gobinda@iitg.ac.in

In the present thesis, growth of monolayer to multilayer MoS_2 and WS_2 film were studied on various substrates like SiO_2/Si, Corning glass, Si by varying the deposition time, laser fluence, substrate temperature in PLD. 2H-1T mixed-phase mono and few-layered MoS_2 films have been obtained by PLD in a very short time span of only 20 sec at various deposition temperatures. The tunability of the ratio of the two phases with deposition temperature as well as deposition time has been investigated extensively. The surface morphology evolution of MoS_2 and WS2 thin films from a few layered to bulk like structure, grown by the PLD technique, has been studied based on generic scaling theory using AFM images of the films. A detail study on structural and linear and nonlinear optical characteristics of the MoS_2 and WS_2 films was performed. Along with layered thin films, MoS_2 and WS_2 QDs of various sizes were also synthesized by tuning the nanosecond pulsed laser fluence and ablation time. Further, the MoS_2 and WS_2 thin films and QDs were efficiently used as a catalyst for hydrogen evolution reaction (HER).

For depositing MoS_2 and WS_2 thin films, sintered MoS_2 and WS_2 pellets were prepared from highly pure MoS_2 and WS_2 powder. The sintered pellets were used as the target in be employed PLD system. A high power Nd: YAG laser (Quanta-Ray INDI, λ = 355 nm, repetition rate 10 Hz with the pulse width of 8 ns) was focused on the MoS_2 target. Experiments were performed at various optimized conditions like deposition times, Ar gas pressures, substrate temperatures and laser fluences to synthesis films of desired properties. The crystallinity of the deposited films was analyzed by recording X-ray diffraction pattern at 3 degrees/mins scanning speed with a step size of 0.03°. Raman and photoluminescence spectra were recorded in the backscattering geometry using an excitation wavelength of 488 nm. The exciting laser was focused onto the sample with the 100X objective lens. Atomic force microscope was used in the non-contact mode to image the surface morphology. Transmission electron microscopy was performed to analyze the particle size and crystallinity of the deposited film. The SE measurements were carried out over the spectral range of 1.32–3.50 eV using Variable Angle Spectroscopic Ellipsometer (*Semilab SOPRA: GES-5E*) equipped with goniometer at incident angles of 65°, 70°, and 75°. The nonlinear optical behavior of the films was studied using *Z*-scan setup. He-Ne laser of wavelength 632.8 nm was used as the laser source which was focused onto the film surface using a bi-convex lens of focal length of 5 cm.

Mono- and a few layered MoS_2 films were deposited on SiO_2/Si substrate (300 nm/0.38 mm) using PLD technique. The layered numbers were controlled by applying different number of laser pulses. Raman spectroscopy and AFM height profile were used to determine MoS_2 layered structure. The *as*-grown films show highly crystalline (002) plane oriented epitaxial growth. The deposited MoS_2 films showed an epitaxial compression due to its adhesion to the substrate. XRD and Raman analysis confirmed that crystalline properties of deposited MoS_2 films reduce with an increase in the number of monolayers. The two Raman active modes

A_{1g} and E^1_{2g} of the layered MoS_2 films showed strain-induced blue-shifted spectra. TEM measurement demonstrated layered MoS_2 formation as well as nanocrystallite quantum dot formation. Similar experiment was also performed to synthesize monolayer to multilayered WS_2 thin films where the laser fluence was varied and other deposition parameters were kept constant.

An efficient way to deposit mixed-phase mono and a few layered MoS_2 thin films for a very short span of time of 20 sec was realized by pulsed laser deposition. The 1T/2H phase ratio in monolayer to a few layered MoS_2 films was modulated by altering the substrate temperature. Irrespective of deposition temperature all the films showed a mixed-phase structure while the 2H to 1T phase ratio increased from 66 to 84% with an increase in deposition temperature from 400 to 720 °C. The presence of 1T-2H mixed-phase MoS_2 layers was confirmed and their structural and optical properties were analyzed in nano (TEM), micro (Raman, AFM) and macro (ellipsometer) scale. The ellipsometer analysis demonstrated the two excitonic absorption peaks, denoted as *A*/*B* and *C*/*D*, corresponding to 2H phase while the presence of 1T phase caused excess semimetal like charge density of the order of ~10^{20} cm^{-3}. Hence, stable 1T/2H mixed phase MoS_2 films, strongly adhered to the substrate were obtained in a single step bottom-up growth process. The highly crystalline 1T Phase MoS_2 films could be used as an efficient electrocatalyst.

An experimental investigation was carried out to identify the scaling behavior as well as growth mechanism of 2D MoS_2 thin films, grown on glass substrates by PLD at different deposition time durations, using atomic force microscopy images. Growth dynamics of thin films expressed by scaling theory is a useful tool to quantify statistical properties of surface morphology of the thin films. The growth of MoS_2 films evolved from layer-by-layer to layer plus island with the increase in deposition time from 20 sec to 15 min. The film surface exhibited anisotropic growth dynamics in vertical and lateral direction where RMS roughness varied with deposition time as, $w \sim t^{\beta}$ with growth exponent, $\beta = 0.85 \pm 0.11$ while lateral correlation length ξ, as $\xi = t^{1/z}$ with dynamic scaling exponent, $1/z = 0.49 \pm 0.09$. The films showed local roughness exponent $\alpha_{loc} = 0.89 \pm 0.01$, global roughness exponent $\alpha = 1.72 \pm 0.14$ and spectral roughness exponent, $\alpha_s = 0.85 \pm 0.03$, suggesting the growth of MoS_2 thin films followed intrinsic anomalous scaling behavior ($\alpha_s < 1$, $\alpha_{loc} = \alpha_s \neq \alpha$). Shadowing owing to conical incoming particle flux distribution towards substrate during deposition has been attributed to the anomalous growth mode. Optical properties of the films, extracted from ellipsometric analysis, were also correlated with RMS roughness and cluster size variation which unveiled the important role played by surface roughness and film density. Similar work extended to WS_2 films deposited onto corning glass and SiO_2/Si substrate as well.

Multilayered-to-bulk like MoS_2 and WS_2 films were deposited by pulsed laser deposition at various argon gas deposition pressure. A significantly large reverse saturation absorption and positive nonlinear refraction response were observed in all the films, as measured by the open and closed aperture *Z*-scan experiment under He-Ne laser at 632.8 nm. In addition, third-order non-linear optical susceptibility of the thin films was found to be of the order of 10^{-2} esu as measured from *Z*-scan experiment. The anomalously high nonlinear optical response of the film was attributed to the continuous-wave laser-induced thermal nonlinearity

dominance over optical nonlinearity. Optical limiting was also observed in the WS_2 thin films where optical limiting thresholds were found to increase with increasing nonlinear absorption coefficient.

MoS_2 QDs were synthesized with great efficient by multilevel photo-exfoliation of solid MoS_2 target using pulsed laser ablation in distilled water. It is a single step, chemical-free simple physical process. Highly pure MoS_2 quantum dots (QDs) of average sizes 4, 2.91 and 6.13 nm were obtained by applying a fixed laser energy of 40 mJ at ablation time of 5, 10 and 20 min while for the fixed ablation time of 5 min the average QDs size were 2.91, 3.57 and 4 nm at the laser energy of 10, 20 and 40 mJ, respectively. The wide size distribution of the QDs resulted in a broad luminescence in the visible region. The MoS_2 QDs solution showed excitation-dependent luminescence emission which shifted to longer wavelength by varying the excitation wavelength from 290 to 390 nm. EDX, XRD and SAED pattern, zeta potential analysis demonstrated the formation of stoichiometric, highly crystalline, stable MoS_2 QDs. In Raman spectroscopy, the peaks corresponding to the A_{1g} and E^1_{2g} phonon modes of MoS_2 were clearly observed, indicating crystalline MoS_2 QDs formation. The colloidal MoS_2 QDs solution showed an absorption edge ~ 310 nm. The blue-shift in optical absorption of the as-prepared MoS_2 QDs was attributed to the quantum confinement. The following work can be extended to other transitional metal dichalcogenides to effectively synthesis their QDs counterpart.

As an application, MoS_2 and WS_2 films of various thicknesses deposited onto the FTO substrate and MoS_2 QDs drop casted onto GCE were used as an active electrocatalyst for HER. The overpotential @-10mA/cm^2 current density was 0.472 -0.580 V, and Tafel slope in between 83-108 mV/decade for various MoS_2 and WS_2 films. The overpotential @-10mA/cm^2 current density was 0.529, 0.536 and 0.534 V for the MoS_2 QDs, synthesized at 20, 10 and 5 min ablation time. Tafel slope of the QDs at ablation time of 20, 10 and 5 min were 57, 83 and 92 mV/dec. These results suggest an excellent efficiency of the thin films and QDs as HER catalyst.

Study of Spectral Beam Combination Techniques for High Power, Pulsed, Dye Laser Applications

Paramjit Rana[1,2,*]

[1]Homi Bhabha National Institute, Anushaktinagar, Mumbai – 94 INDIA

[2]Beam Technology Development Group

Bhabha Atomic Research Centre, Mumbai – 85 INDIA

*Email: paramjit@barc.gov.in

1. Introduction:

Differential Absorption Lidar (DIAL), Remote sensing, Laser Spectroscopy, non linear frequency mixing and trace analysis etc., requires a composite tunable laser beam of multiple wavelengths. Several beam combination techniques such as side by side, spectral and coherent combinations are used to generate composite laser beam as per the desired beam parameters and the type of lasers employed. Narrowband, widely tunable dye lasers in visible to near infrared spectrum are suitable for such applications. High repetition rate and power scalability extends its application regime to large scale industrial as well as commercial use such as laser isotope separation of medical isotopes. DIAL based environmental and remote sensing applications require closely separated (<10nm) multi-wavelength tunable dye lasers with suitable power level. Therefore, studies on spectral beam combination techniques for closer wavelengths, high power, pulsed dye lasers were taken up for the present research work.

Motivation behind this elaborated study was to advance the knowledge of spectral beam combination techniques for high power dye lasers and its associated technologies. We could achieve narrowband, multi-wavelength, high power, high repetition rate, pulsed dye laser using three spectral beam combination techniques. Intra-cavity and external cavity beam combination techniques along with its associated important elements (high power pump laser and dye laser gain medium) were studied in this thesis work.

Many researchers have studied various aspects of spectral beam combination to generate multi-wavelength dye lasers for different applications. In this thesis, some of the unexplored areas in the field of spectral beam combination techniques and multi-wavelength dye laser generation were studied in detail. The important aspects of intra-cavity and external cavity beam combination techniques for multi-wavelength (separated by less than 10 nm) dye lasers were explored during current course of study. In the intra-cavity spectral beam combination technique, cascaded grating sub-cavities in a resonator for generating four to five wavelengths in a single dye laser has been studied, which was not explored yet. Tuning characteristics of all the cascaded grating sub-cavities were established in order to simultaneously operate four wavelengths from a single dye laser cavity. Co-amplification based spectral beam combination technique for high power, closely separated wavelength was found to be less explored in the literature for oscillator-amplifier configuration. This was studied in detail in order to generate high power (~8W), high repetition rate (~10 kHz), dual wavelength (<10 nm separated) dye laser. The co-amplification of closely separated wavelengths proved to be an efficient approach over individually amplified dye laser beams for high power generation using oscillator-amplifier configuration. Gain competition among the closely separated wavelengths was studied in the dye common amplifier. In both of these spectral beam combination techniques, gain competition among closer wavelengths limit the individual optimization of the participating laser wavelengths with added complexity of intensity control. Therefore, gain competition free spectral beam combination technique was required to be studied. Hence, development of

spectral beam combining element suitable for closer wavelength combination was taken up as the third spectral beam combination technique.

Efficient spectral beam combination of multiple dye laser beams could not be realized without a beam combining optical device. Multilayer dielectric coated beam combiner was selected for studies among other beam combining elements such as grating, prism etc., due to its ease of handling wide wavelength tunability and high power. The thin film Fabry Perot (FP) filter was chosen as a spectral beam combiner due to its capability of combining closely separated wavelengths (<10nm). Single cavity FP filter (19 layers, TiO_2, SiO_2) based beam combiner was designed, fabricated and tested with dye laser beam. FP beam combiner was characterized in terms of transmission spectrum (spectrophotometer), surface roughness (atomic force microscopy) and damage threshold (laser induced damage threshold). This FP beam combiner was successfully tested for spectral beam combination of two dye laser beams with closely separated wavelengths of less than 10 nm as well as widely separated wavelengths of 30 nm. FP beam combiner was found to be an efficient device for closer wavelength beam combination as compared to conventional broadband beam splitter based combination. This FP beam combiner served dual purpose of spectral beam combiner as well as amplified spontaneous emission (ASE) filter. ASE filtering was advantageous for combining the dye laser beams operated at the end of the tuning range as ASE in the laser beam is relatively higher while tuned to the end of tuning range. A novel mechanism for varying the FP transmission peak along with dye laser wavelength tuning was established using a combination of precision rotation and translation stage. The thesis is organized as follows:

2. Spectral Beam Combination Techniques:

Intra-cavity beam combined multi-wavelength dye laser configurations are described in this chapter. Linear cascaded resonator without intra-cavity beam expansion was chosen to configure the cavity to generate two to five wavelengths in a single composite output laser beam. Single laser beam consisting of four wavelengths were generated from the linear cascaded grazing incidence grating configuration (CGIG, fig.1).

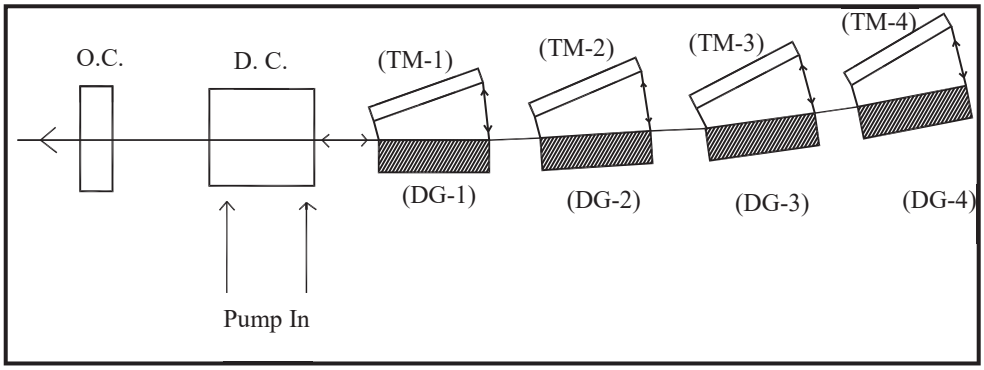

Figure.1 Intra-cavity Beam combination (Cascaded Grazing Incidence Grating Cavity)

This configuration was studied in order to achieve the tuning range for simultaneous four wavelength operation. A hybrid cavity configuration (HCGIG) consisting of three GIG cavities and one Littrow cavity was studied to understand the effect of sub-cavity on the overall emission characteristics. Characteristics of these intra-cavity beam combined CGIG and HCGIG cavities are discussed in the fourth chapter of the thesis.

High power, dual wavelength laser beam generation is elaborated in the chapter-5 of this thesis. MOPA configurations were employed for enhancing the power of the dye laser beams. High power generation using external cavity beam combination was investigated using two techniques i.e. spectral beam combination post amplification of the individual laser beams and co-amplification of the composite (spectral beam combined) dye

laser beam. Both these methods of high power, multi-wavelength dye laser generation are presented in this chapter.

Studies on amplification includes narrow band grazing incidence grating (GIG) oscillator (CVL and Diode Pumped Solid State Laser pumped oscillators) for individual dye laser beam generation and its amplification using transverse pumped amplifiers. Effect of pump power and dye concentration on amplifier extraction efficiency is presented here. Common amplifier of DCM pumped by CVL for closely spaced wavelength (<10nm) was studied. Gain competition in common amplifier (fig.2) was characterized by varying individual input intensities as well as pump power. This efficient spectral beam combination technique is described in detail.

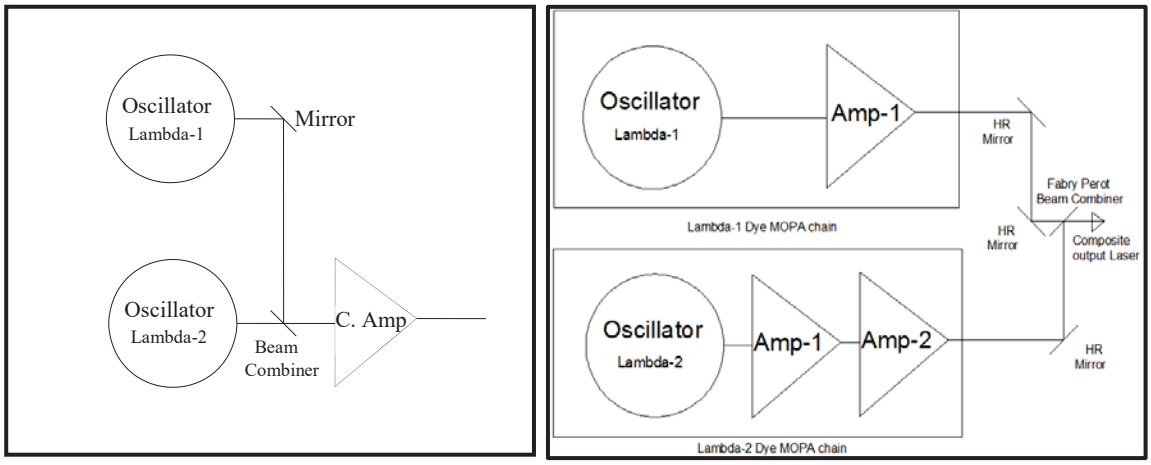

Figure.2 External Cavity Beam Combination (Co-amplification and Fabry-Perot Beam Combiner)

Efficient, gain competition free and effective combination of two or more laser beams requires a beam combining element. A single cavity FP filter was designed using 19 layers of TiO_2 and SiO_2. It was fabricated using ion-assisted e-beam evaporation technique. The filter was characterized using spectrophotometer, atomic force microscopy (AFM) and laser induced damage threshold (LIDT). This filter was used for laser beam combination of high power (~8W) dye laser beams of closely separated wavelength. This combiner was also utilized (fig.2) for filtering the amplified spontaneous emission (ASE) present in the dye laser beam. The tuning mechanism to match the dye laser wavelength tunability was established. Design, development, characterization and implementation of this FP beam combiner are elaborated in this chapter.

3. Associated Studies:

Pump laser plays a key role in the high power dye laser generation. An indigenously developed copper vapor laser (CVL) was thoroughly characterized in order to pump the dye lasers. One of the objectives of this current study was to generate high power pump laser for generating high power multi-wavelength dye laser beam for spectral beam combination. The high pump power was generated by six CVLs configured in one oscillator followed by five amplifiers in a Master Oscillator Power Amplifier (MOPA) configuration. Various MOPA configurations were theoretically analyzed using an individual CVL as an amplifier, whereas amplifying capabilities has been experimentally established. Thermal lensing was found to be a key factor to maximize the power extraction from a CVL in the longer MOPA chain. A novel technique was established to measure the effective thermal focal length of amplifier using oscillator beam as the probe beam. The compensation techniques were theoretically analyzed in order to minimize its impact on a longer MOPA chain of eight modules.

The dye laser was chosen for spectral beam combination experiments due to its versatile capabilities. Fluorescent laser dye, dye cell, dye solvent are crucial components for any narrowband dye laser system. Study of beam combination techniques for multi-wavelength dye laser needs these elements to be utilized to their best possible capabilities. Use of different solvents, their mixture, for shifting the absorption and emission characteristics of a laser dye is used for obtaining desired wavelength. Mixing two or more laser dyes notably widens the wavelength tunability range and also shifts the emission peak wavelength. These areas were not explored much, especially for multi-wavelength dye laser systems. We have studied these aspects of the dye gain medium during this thesis work: effect of pH on photo-physical characteristics of Rh 101 dye, measurement of thermo-optic coefficient of dye solvents and their mixtures, characterization of SRh 101 dye in water-ethanol binary solvent and extension of tuning range for three wavelength dye laser using binary dye mixture.

Several spectral beam combination techniques for multi-wavelength dye laser generation are discussed in chapter-1. Laser beam combination techniques used for various applications and experiments are summarized in this chapter. The classes of laser beam combination schemes i.e. side by side beam combination; coherent beam combination and spectral beam combination are presented in detail. An elaborate literature survey on multiple wavelength dye laser generation using various beam combination techniques is presented and the review of existing knowledge in the field of spectral beam combination is presented.

Copper vapor laser (CVL) is the most suitable pump laser source for pumping the dye lasers in order to generate high power and high repetition rate. We have studied and characterized the indigenously developed CVL system operating at 9 kHz pulse repetition rate in MOPA configuration. Analysis of several MOPA configuration designs is discussed in chapter-2 of this thesis. Thermal lensing in the CVL plays a significant role in the output beam size management, divergence and power extraction capability in longer MOPA chain. The thermal lensing of the CVL amplifier system was experimentally measured using a collimated CVL oscillator probe beam in an oscillator-amplifier configuration. Effect of neon buffer gas pressure and input electrical power on the resultant thermal focal length of the CVL system was studied. Various compensation techniques were theoretically analyzed for CVL MOPA chain, which are elaborated here in this chapter.

The dye gain medium is responsible for a versatile, tunable, multi-wavelength dye laser system, which is described in this chapter- 3. Possibility of spectral tailoring of photo-physical properties of the gain medium by simple techniques adds the versatility and application potential of the dye laser. The effects of various solvent environments such as pH variation, binary solvent, polar and non-polar solvents on the photo-physical properties of few of the laser dyes of interest for spectral beam combination experiments were studied. The photo-physical properties of Rh 101 and SRh 101 dyes were studied in detail. Thermo-optic coefficient of solvents plays a significant role in high power operation of the dye lasers, which was measured using the Michelson interferometer based technique for commonly used dye solvents and their mixture. Broadening of wavelength tuning range of three wavelength dye laser was achieved using DCM and PM 567 binary dye mixture with optimized concentration. Studies on the dye gain medium properties are presented in this chapter in detail.

4. Conclusions and Future Directions:

An elaborated study on spectral beam combination techniques for high power, pulsed, dye laser is presented in the thesis. The important conclusions drawn from the current thesis work are described in this chapter, which are as follows:

- ✓ Three laser beam combination techniques namely intra-cavity beam combination, co-amplification based external cavity combination and multilayer dielectric coated Fabry Perot beam combiner were studied in detail for combining laser beams with closely separated wavelengths (<10nm). Spectral beam combination using FP beam combiner proved to be efficient and gain competition free technique as compared to other two techniques.
- ✓ CGIG and HCGIG based intra-cavity beam combined configurations were characterized in detail to determine simultaneous multi-wavelength operation. These techniques were found to be suitable for generation of four to five, narrow band wavelengths in a compact resonator cavity.
- ✓ Laser beam combination after amplification was suitable for widely separated wavelengths whereas co-amplification of combined beam was proved to be more efficient for closely spaced wavelengths.
- ✓ Tailoring of the dye emission spectrum could be achieved by changing the solvent pH environment and ethanol-water binary solvent. Widening of the tuning range from 40 nm to 82 nm in a three wavelength dye laser using concentration optimized binary dye mixture of PM567and DCM demonstrated.
- ✓ Multilayer thin film FP based filter was designed, fabricated and used as a beam combiner. It was characterized for transmission spectrum, surface morphology and damage threshold using spectrophotometer, AFM and LIDT techniques respectively.
- ✓ This beam combiner was successfully tested for combination of laser beams wavelength separated by less than 10 nm, which was proved to be more efficient as compared to beam splitter based combiner with added advantage of ASE filter for the transmitted laser beam operating at the end of its tuning range. A tuning mechanism for the FP beam combiner for widely tunable laser systems was successfully established for combining closely as well as widely separated wavelength.
- ✓ An indigenously developed copper vapor laser MOPA configurations were characterized and optimized to generate maximum possible pump power. Theoretically studied thermal lensing compensation techniques seem to be effective for maximum power extraction using longer CVL MOPA chains.

In future, remotely operable, optical fiber pumped, intra-cavity beam combined dual wavelength system will be developed. Application of multi-wavelength dye laser in trace analysis and environmental application will be explored. Remote gas sensing based exploration will be an important work towards environmental monitoring and control.

OPTICAL SPECTROSCOPY BASED URINE ANALYSIS FOR DISEASE DIAGNOSIS

Surjendu Bikash Dutta
Discipline of Physics, Indian Institute of Technology, Indore

Urine is a clinically important and easily accessible body-fluid having extensive diagnostic information about the health status of an individual. Human urine specimen has been subjected to analysis for different disease diagnosis since ancient times. In general, urine consists of more than 95% water, several nonprotein nitrogenous compounds (NPNs) such as urea, creatinine, uric acid, *etc*. trace amounts of proteins, hormones, enzymes, bacteria, metabolites, and some inorganic ions such as chloride, sodium, potassium, *etc*. The varying concentration of different constituents or metabolites present in urine identifies a wide range of disorders in their early stages such as kidney disorders, urinary tract infections (UTI), liver diseases, diabetes, cancers, *etc*. In current medical practice, different analytical methods such as high-performance liquid chromatography, liquid chromatography-mass spectrometry/mass spectroscopy, gas chromatography, capillary zone electrophoresis, *etc*. have been widely used to estimate the concentration changes of metabolites present in urine. However, all these methods follow sequences of sample preparation steps, need multiple reagents, and specialized training. Further, these methods require sophisticated, bulky, and expensive instruments for urine analysis. Therefore, there is a need for an alternate approach that is rapid, reliable, inexpensive, and does not require any special sample preparation.

Recently, optical techniques such as Raman and fluorescence spectroscopy, have shown immense potential for rapid urinalysis by overcoming the limitations. These techniques are able to correlate specific biochemical changes of the analytes present in urine with their normal and disease conditions. The simple instrumentation, cost-effectiveness, and molecular sensitivity of these techniques make them as suitable analytical tools for human health monitoring. Despite the promising developments, the clinical applications of optical techniques are limited due to the poor signal collection and lack of reproducibility in the measured signal intensities from the analytes present in biofluids including urine. These limitations could be addressed by incorporating nanotechnology and improved optical signal detection strategies.

The goal of the present thesis is to investigate the use of optical spectroscopy in urine analysis for rapid and reliable disease diagnosis. In this regard, an attempt has been made for the quantitative determination of trace amounts of analytes present in urine using drop coating deposition Raman spectroscopy (DCDRS) and Nano-Trap Enhanced Raman Spectroscopy (NTERS). DCDRS is a comparatively new variant of Raman spectroscopy in which analytes or molecules get deposited in ring shape pattern on an appropriate substrate due to the coffee-ring effect and improves the sensitivity of Raman signal measurement from analytes. NTERS is a new Raman signal enhancement technique in which nanoclusters of metallic nanoparticles are formed at the focus of the excitation laser beam due to optical trapping. The analytes get trapped within these nanoclusters at the peripheral region of the dried drop of solution where maximum deposition of the solute has occurred. The

Raman signals measured from these analytes trapped within the nanoclusters get highly enhanced due to both surface plasmon and coffee ring effects. In the subsequence of these studies, the fluorescence photo-bleaching dynamics of urine samples have been studied and used for oral cancer diagnosis.

This thesis is divided into six chapters and the chapter-wise organization is summarized below.

Chapter 1 provides the general overview of urine analysis including the currently used analytical techniques in clinical settings and their major drawbacks. This is followed by the comprehensive review of the applications of optical spectroscopy, with a special focus on Raman and fluorescence spectroscopy, for urine analysis. Further, the motivation and specific aims of the thesis are introduced. This chapter is concluded with a summary of the current findings and future directions of the present thesis work.

Chapter 2 describes the materials and methods used to carry out this research work. The details of sample preparations, experimental arrangements, and data processing are explained in this chapter.

Chapter 3 demonstrates the applicability of drop coating deposition Raman spectroscopy (DCDRS) for the quantitative determination of creatinine present in urine. The elevated level of urinary creatinine is the indicator of kidney diseases and other muscle diseases like muscular poliomyelitis, muscular dystrophy, hyperthyroidism, *etc.* In order to find the potentiality of the DCDRS technique over other commonly used Raman techniques, the first normal Raman spectra were measured from the aqueous solutions of creatinine as well as the artificial urine samples prepared with varying concentrations of creatinine. Then the normal Raman spectra were compared with the corresponding DCDRS spectra measured from the dried-up drops of these samples. It was observed that the measured DCDRS signal of creatinine has significantly higher intensity as compared to the Raman signal measured from its aqueous solution. Further, the possibility of the use of surface-enhanced Raman spectroscopy (SERS) was evaluated for the detection of trace quantity of creatinine present in artificial urine samples and described in detail in this chapter. SERS is a frequently used Raman signal enhancement technique based on the surface plasmon resonance (SPR) of metallic nanoparticles. Although the measured SERS signal intensity of creatinine was higher as compared with the measured DCDRS signal, the repeatability for DCDRS measurement was considerably greater than the corresponding SERS measurement. Following, the varying concentrations of creatinine present in artificial urine samples were quantified using a multivariate chemometric algorithm based on partial least square (PLS) in the recorded DCDRS spectra and the results are presented. Finally, the ability of the DCDRS technique has been evaluated in detecting the analytes in human urine samples.

In spite of the promising potential of the DCDRS technique, the detection of Raman signal of analytes present in bio-fluids in millimolar (mM) to nanomolar (nM) concentration range is limited. Therefore, the sensitive and accurate detection of disease-specific analytes present in urine is highly desired. **Chapter 4** elaborates on the design and development of Nano-Trap enhanced Raman spectroscopy (NTERS). NTERS is a new Raman signal enhancement technique in which two phenomena are happening simultaneously (i) the maximum deposition of the solute at the periphery due to coffee ring effect during drying up of the solution drop, and (ii) the formation of nanoparticles clusters at the laser beam focus due to optical trapping. Thus, in NTERS, when the laser beam is focussed at the peripheral region, it leads to the formation of nanoparticle aggregates at the region of the maximum deposition of the solute thereby causing the maximum enhancement of

the backscattered Raman signal. The performance of this technique for both qualitative and quantitative determination of analytes present in urine samples has been assessed and discussed in this chapter.

Photo-stability of urine is important for the optical spectroscopy-based diagnosis of any disease where urine is used as a sample of choice. It has been observed that urine samples go through a photo-bleaching process upon optical irradiation. In this chapter (**Chapter 5**) fluorescence photo-bleaching dynamics of urine samples have been used for disease diagnosis. This chapter evaluates the applicability of photo-bleaching characteristics of urine for discriminating patients with oral cancer from healthy volunteers. A classification algorithm based on the nearest-mean classifier (NMC) has been developed and applied to the photo-bleaching decay constants obtained from the fluorescence spectra of urine samples to discriminate the two categories. NMC is a classification model that considers the least Euclidean distance of the test data from the means of the prototype data of the corresponding classes in the training set as the classification criterion.

This thesis is concluded with **Chapter 6** by summarizing the major findings followed by the possible future directions of this work in clinical applications.

Raman and Time-Domain Photoacoustic and Terahertz Spectroscopy of some Inorganic, Organic and High Energy Materials

Archana Kumari

University of Hyderabad, Hyderabad - 500046

Thesis Summary

This thesis is designed with the strategy to explore the wide range of electromagnetic spectra between UV-Vis-NIR and far IR regions. In this thesis, we have selected different laser-based spectroscopic techniques such as the use of visible (532 nm) nanosecond laser for photoacoustic spectroscopy, use of CW laser (532nm and 785nm) for Raman spectroscopy, use of femtosecond laser for generation and detection of Terahertz using non-linear CdTe crystal and use of FTIR and Raman spectroscopy to establish the new results obtained. We have also concentrated on the temperature-dependent properties of CdTe and have explained how the properties change when subjected to femtosecond laser pulses using a modified temperature-based spectrometer. The region between UV-Vis-NIR covers different aspects of molecular spectroscopy such as electronic transition based vibronic and vibrational modes, vibrational-rotation and weak vibrational-rotation bands along with Raman scattering. An attempt has been made to use these techniques without any chemical treatment and in a non-destructive way so that the samples can be reused again. One of the advantages of photoacoustic spectroscopy is that it can be performed on all phases of matter. In one section of this thesis, the emphasis has been given on pulsed photoacoustic technique using 532 nm wavelength (visible) of pulsed laser for the study of conducting polymers like PEDOT and its role as an optode for detection of solid explosives. such as RDX, TNT, HMX, CL20. Also, it is extended to study the physical properties of different types of natural rubber added with organic and inorganic fillers.

By the use of Raman Spectroscopy, our ultimate aim is to provide a post and pre blast application of explosives using PEDOT polymer. In addition, Raman spectroscopic studies are potentially useful sources of information concerning the composition, structure, and stability of coordination compounds. It is also used for investigating organic and inorganic systems. Also, Raman spectra tend to be less cluttered with peaks as compared to infra-red spectra, and hence, as a consequence, peak overlap in mixtures is less likely, and quantitative measurements are simpler. Besides, the advantage of this technique includes the small sample requirement, minimal sensitivity towards interference by water, spectral detail, and environmental sensitivity. Therefore, technique is also employed for cross verifications of results of antibiotic drugs as well.

The range of time domain spectroscopy is further extended to THz domain. This technique finds great application in physical, chemical and biological fields such as its use for studying biological tissues, their imaging, calculation of the percentage of water content within tissues, etc. Recently terahertz carrier waves have also found an application in wireless technology.

We have used Terahertz Spectroscopy to study the temperature-dependent properties such as energy of the band gap, determination of Urbach-tail and non-linear absorption introduced by the femtosecond laser pulses along with generation of terahertz using the non-linear CdTe crystal. We have also studied the changes in the physical properties of CdTe in terms of its refractive index, coherence length and energy band gap when it is exposed to heating due to femtosecond laser pulses for a long period of time. THz-TDS has also been used to study an anti-biotic medicine, commonly known as Cefixime in this thesis. Various physical properties including absorbance strength, absorption coefficient along with a method for quality check have been provided for Cefixime.

The chapter on Photoacoustic spectroscopy discusses the use of photoacoustic spectroscopy as a spectroscopic tool to study different samples based on their physical and chemical parameters.

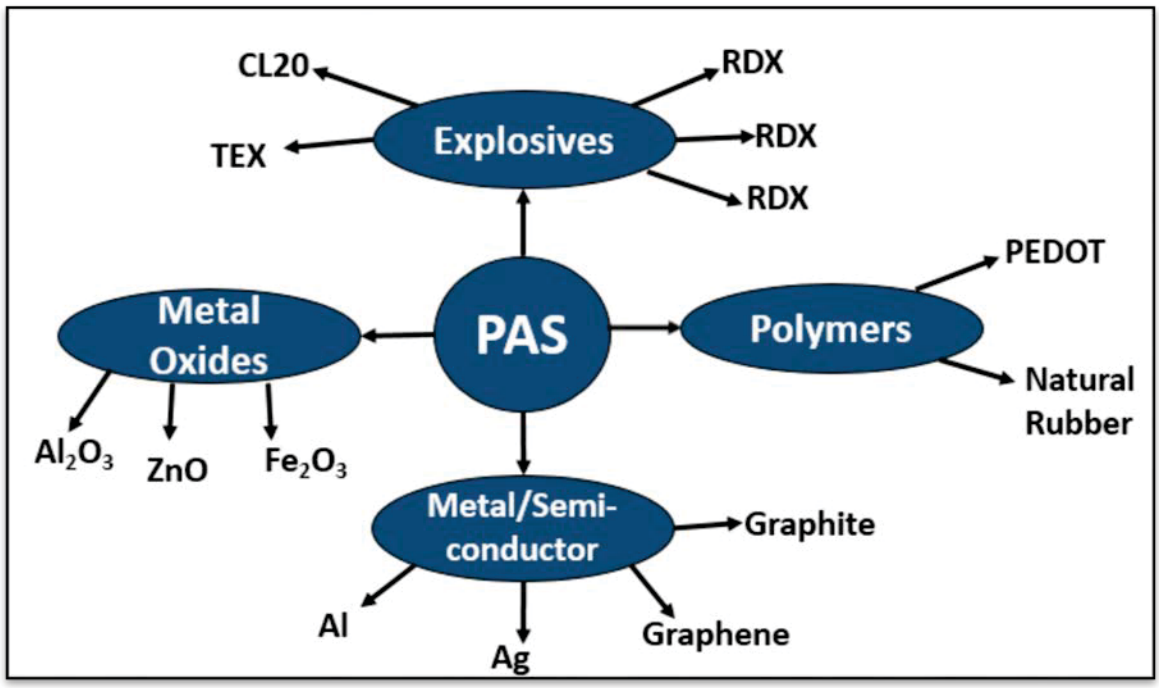

Fig: 1 shows the samples under various categories that were considered for study under photoacoustic spectroscopy(PAS)

This chapter discusses the fingerprint photoacoustic spectra of the above mentioned samples The chapter then discusses the natural rubber polymer where it describes the effect of carbon and inorganic fillers in different proportions in natural rubber(NR) /chloro butyl rubber (CIIR) blends in terms of absorption, thermal diffusion and penetration depth using time-domain pulsed photoacoustic technique. A 532nm wavelength of 7nS pulse obtained from Q-switched Nd: YAG laser at 10 Hz repetition rate was used for recording the time-domain spectra of rubber sheet in the indigenously designed solid PA cell made of aluminium. The values of the absorption coefficient were found between 39-89 cm^{-1} range, whereas thermal diffusion length and penetration depth are of the order of 0.1-0.625 $x10^{-6}m^2/s$ and 0.1-7.9 microns. This chapter also establishes poly (3,4-ethylene dioxythiophene), commonly known as PEDOT polymer, as an optode sensor for high energy materials/explosives such as RDX, HMX, TNT, CL20, and TEX. This chapter discusses the use of the redox nature of PEDOT as a tool for the detection of high energy materials (HEMs) in the visible region using pulsed photoacoustic spectroscopic (PAS) technique at 532 nm wavelength. The sensitivity of the detector is also evaluated to find the minimum amount of sample i.e. the minimum detection limit that can be detected by the PEDOT sensor.

Major Objectives:

The outline of major objectives of the thesis are as follows:

- To develop a cost-effective, reliable, and highly sensitive sensor for the low level detection of solid explosives like RDX, HMX, TNT, CL-20, etc.
- To study the role of PEDOT polymer as a sensing medium for explosives using visible 532 nm wavelength of laser
- To study the effects of fillers used as reinforcements to increase the durability and strength of the rubber polymer
- To study the temperature-dependent properties of CdTe to explain the changes in properties of the crystal when it is subjected to femtosecond laser pulses for a long duration of time as well as its use for THz generation
- To study the temperature-dependent properties such as energy of the band gap, determination of Urbach-tail and non-linear absorption with the help of a self-modified temperature-dependent spectrometer

- To use time-domain terahertz spectroscopy for characterization of an antibiotic Cefixime drug obtained from the different origin along with an assessment of their quality
- To find an alternative method for the detection of explosives using Raman Spectroscopy using the study of the role of PEDOT polymer

Ultimately, this thesis aims to unify various spectroscopic techniques used above as explained in the flowchart shown in Fig.2.

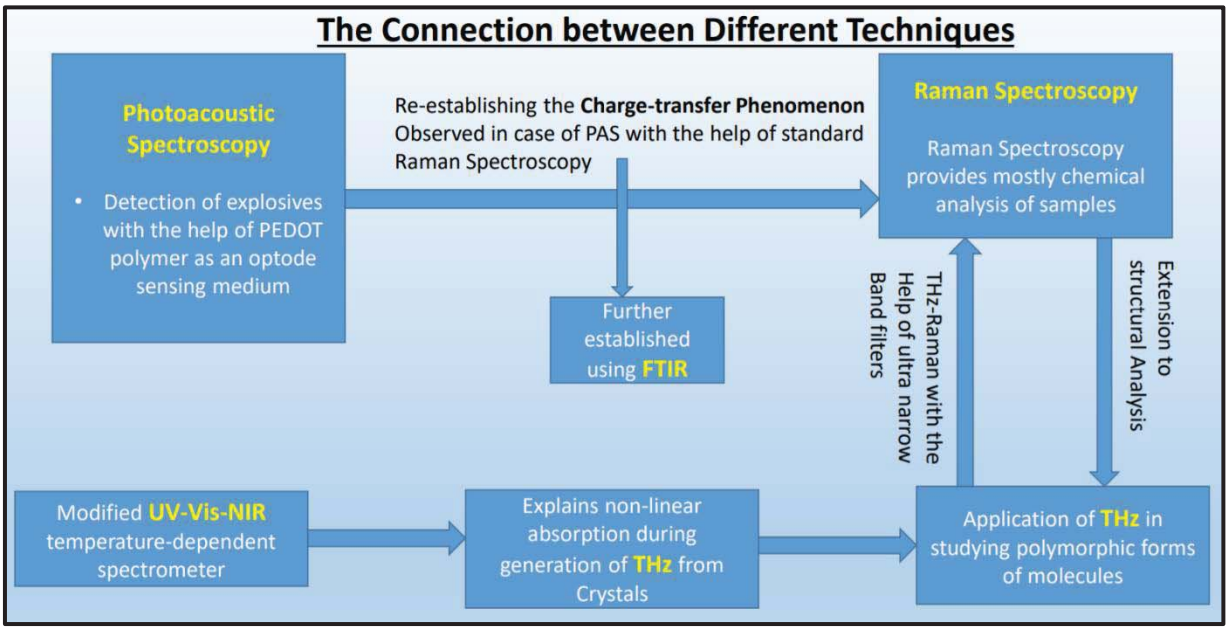

Future Scope:

(a) Photoacoustic Spectroscopy

- **In Spectroscopy:**

➢ Storing of PEDOT conjugated polymer in liquid form in spray bottles keeping in mind its easy use on the field, cost, and availability. It has already been tested by our group that liquid PEDOT polymer has a characteristic fingerprint spectrum in Photoacoustic Spectroscopy.

➢ Use of picosecond and tunable Quantum Cascade Laser (QCL) in the visible to the mid-IR range to further broaden the range of detection of explosive molecules.

➢ Design and use of liquid photoacoustic cell for studying liquid solvents and detection of explosives dissolved in water and other solvents.

➢ Photoacoustic imaging of various solid samples along with explosives and High Energy Materials.

- **In Medicine and Biophysics:**
  - **Based on Solid Cell Photoacoustic Spectroscopy**

➢ Using PAS in the food/drug industry for optical characterization of fruits, vegetables, condiments, grains, legumes, flours, etc. to evaluate adulterated, irradiated, and contaminated food and their quality assessment.

  - **Based on Solid Cell Photoacoustic Spectroscopy**

➢ Study of optical properties of Cancerous tissues and cells

➢ Blood cells can be imaged at a single wavelength in the visible range because of their high optical absorption contrast compared to surrounding tissues.

➢ To detect oxygen saturation in blood vessels

(b) Terahertz Spectroscopy and Raman Spectroscopy:

In medicine, various polymorphs of different drugs and drugs are often confused due to similar-sounding names. THz spectroscopy can play a significant role in differentiating such polymorphs, thereby proving to be an essential part of the food and drug industry. Further, bulk molecules can be analyzed in more critical details, and the information about the vibration of molecules even lower than 50 cm^{-1} can be determined using THz-Raman Spectroscopy. Various other future scopes exist, some of which are listed below:

- Generation of efficient Terahertz radiations using nonlinear crystals other than CdTe, such as ZnTe, $ZnGeP_2$, etc. coupled with bandpass filters and gratings to record the pulsed PA spectra of HEMs. This will help us combine the two well established spectroscopic techniques; Photoacoustic and Terahertz.

- Most of the HEMs possess several rotational lines. Therefore, THz spectroscopy helps us to record the fingerprint spectra of these compounds.

- The time-domain THz spectroscopy, as well as PA Spectroscopy, can help us to build a library database for the detection of HEMs.

- Development of optical parametric oscillator (OPO) using the DFG technique for efficient generation of tunable THz radiation.

An Insight into the Optical Nonlinearities of Certain Au/Ag Based Metal-Metal/Organic Core Shell Nanostructures and Nanohybrids

E. Shiju

National Institute of Technology Calicut, Kozhikode 673601, Kerala, India.

Ph.D.Thesis Summary

In this thesis work, thrust is on the synthesis as well as investigation of the third order nonlinear optical properties of certain Au/Ag based metal- metal/organic core shell nanostructures and nanohybrids by Z- scan technique under nanosecond pulse excitation regime.

Chapter 1 is devoted to present the formal description of the fundamental aspects of nonlinear optics, and a brief summary about the motivation and present work. The basic mathematical description of NLO using Maxwell's equations that leads to nonlinear polarization is explained in detail. A brief overview of the nonlinear optical processes and associated phenomena, with relevant theory is also presented in this chapter. Finally, various mechanisms responsible for the NLO behavior of materials, previous reported studies on the same area and a brief description about the materials under present study are included at the end section of this chapter.

An overview on the common experimental techniques and equipment used for the synthesis and characterization of the samples and their working principles has been concisely given in chapter 2. It includes the details of liquid phase pulsed laser ablation technique, UV-Visible spectrophotometer, fluorometer, transmission electron microscopy, and Fourier transform infrared spectroscopy. Third-order nonlinear optical properties investigated by means of single beam Z-scan technique and its experimental details are described along with relevant theory.

In chapter 3, we include the nonlinear optical studies of Au@Ag core shell nanostructures of different shell thickness under ns laser pulse excitation. Core shell structures have been attaining tremendous research interest due to their tunable multifunctional properties induced as a result of the co-occurrence of more than one nano-structured phase of various proportions with one forming shell on the outer surface of the other. The diameter of nanostructures is found to be systematically increased from 31 nm (t = 7.5 nm) to 61 nm (t = 22.5 nm) when the volume of $AgNO_3$ is increased from 0.1 to 0.8 ml. A significant blue shift from 519 nm to 411 nm in surface plasmon maxima is observed upon forming Ag shell over Au nanoparticles and a slight red shift (411 nm to 425 nm) is observed as the shell thickness increases. All the samples showed RSA behavior and negative nonlinearity under ns excitation and the extent of nonlinearity enhances on increasing the shell thickness. Improved nonlinear optical activity is due to enhanced local field effect and scattering effect, which was later confirmed from the FDTD simulation analysis. The limiting threshold (output transmittance falls 50 % input value) of Au@Ag core shell with highest shell thickness is 2.4 J/cm^2 and it is better than many of the similar systems studied. The good nonlinear optical properties of Au@Ag core shell structures, ensures its potential for future nonlinear optical applications.

Next, we studied the NLO properties of Au@graphite and Ag@graphite core shell structures. Here we adopted a comparatively easy method to prepare core shell nanostructures of Au and Ag with graphite where we didn't use any graphitic substrate. That is, we have ablated Au and Ag targets in toluene, a mono substituted benzene derivative from which graphite has evolved. The prepared nanostructures have been characterized and analyzed by UV -Vis spectroscopy, Raman spectroscopy and transmission electron microscopy (TEM). Also the theoretical simulations of the core shells have been done by FDTD solutions software. The quenching of SPR in case of both Au and Ag NPs by the graphitic layer was prominent from these studies. Though the preparation of nanohybrids with graphite and metal nanoparticles especially core shell structures has already been discussed in few recent reports mentioned above, the interesting fact to be noted is that, plasmon absorption is weakened by graphitic layer, which is another light absorbing material. In other words, calculations showed that coupling plasmonic NPs with graphitic multilayers is an efficient way to dramatically change the optical density in the SPR region, without acting directly or irreversibly on the metal nanostructure. A drastic enhancement in the NLA on nanohybrid formation could be due to the interplay between the intermediate energy states of metal which extends up to the conduction band of graphite in case of metal graphite nanocomposite. Enhanced defect formation modifies electronic structre of graphite as a result of core shell formation. This modification leads to the accessibility of dopant state within the bandgap which results in an enhanced NLA through free carrier absorption (FCA)and ESA. Also the photo-generated charge carriers in the conduction bands of Au/Ag or the increase in defect states during the formation of core shells might also contribute to ESA and thus the enhancement in NLA. The optical limiting threshold value is found to be one of the best (0.38 J/cm^2 for Au@graphite and 0.33 J/cm^2 for Ag@graphite) and it is better than few benchmark results under similar study reported in the area. Since the integration of Ag and Au NPs with graphitic layer is frequently sought for the realization of hybrid materials with optical, photoelectric and photocatalytic applications, these results are useful to guide characterization and for monitoring the synthesis of similar nanostructures, as well as for the development of nanohybrids with desired optical properties.

Materials with large and quick nonlinear optical response, excellent photo thermal stability, cost effectiveness and off resonant NLA are essential requirements for a good OL. Among them, organic systems and π conjugated polymers are getting special interest due to their flexibility in structural modification which leads to the tuning of optical and electronic properties which is suitable for working under large band width. The next set of studies was based on organic- inorganic hybrid systems. The first organic system taken was certain set of BODIPYs with different substitution at the para and meta- positions. All the compounds exhibit good RSA behavior and negative nonlinear refraction property. One of the BODIPY was chosen to prepare nanohybrids with Au/Ag NPs, as it was the best NLO materials among the studied compounds due to slightly better charge separation as a result of substitution of aldehyde group at para position. A significant enhancement in NLO property was observed on hybrid system formation. The optical limiting threshold of that compound (5.2 J/cm^2) is reduced to 1 J/cm^2 on hybrid system formation with Au NPs and this limiting threshold value is comparable to the bench mark OL materials like C_{60}. The mechanism behind the NLA is found to be the combination of ESA and two photon absorption (TPA). Energy / charge transfer as well as local field effect of nanoparticles plays a crucial role in the improved NLO properties of the samples. Enhancement in nonlinear optical property is found to be stronger in hybrid system with Au NPs and is due to the resonant charge transfer and intense local field

effect on exciting with 532 nm pulse compared to that of Ag NPs. The improved NLA and OL property of hybrid system guarantees successful usage of the strategy in optical limiting applications.

Phenothiazine–gold/silver nanocomposite was synthesized by ablating Au/Ag target in PTZ-dimethyl formamide (DMF) solution using Q- switched Nd: YAG laser delivering 7 ns pulses at 532 nm. The production of nanoparticles by ablation and their reduction as well as stabilization by photo-ionized PTZ molecules are simultaneously carried out within the same setup. Presence of NPs in the composite was evident from the absorption studies and TEM analysis and composite formation is confirmed from absorption studies and FTIR analysis. A noticeable reduction in photoluminescence intensity was observed in both PTZ- Au and PTZ-Ag composites material, indicating the electron/energy transfer between the constituents. A significant enhancement (~ 67 times for PTZ-Au and 100 times for PTZ-Ag) in NLA coefficient was observed in the hybrid system compared to that of PTZ and the reason behind the enhancement could be attributed to both local field effect and electron/energy transfer. It is observed that the NLA mechanism for pure PTZ is TPA whereas in hybrid system, it is a combination of TPA and ESA. Optical limiting threshold values of the hybrid system are comparable or better than that of many reported values of nanocomposites. Self-defocusing nature of both the composite and pristine compounds was explored from the closed aperture Z-scan studies. The adopted strategy is found to be worth useful for designing novel materials with potential applications in photonics

In order to overcome the limitations posed by electronic devices, and to fulfill the need for optical elements in integrated photonic circuits, it is crucial to develop an optical analogue of an electronic diode which is one of the most basic elements of electronic circuits. Finally, we studied theoretical investigation as well as consequent experimental realization of a nonlinear thin-film multilayer device that exhibits passive anisotropic optical transmission, an optical analogue of electronic diode. The variation of optical diode action on changing the parameters such as linear transmittance, nonlinear absorption coefficients and saturation intensity are theoretically simulated to understand how the forward and reverse direction transmittances change with the parameters. The experimental demonstration of the diode activity has been accomplished using single beam open aperture Z-scan technique at an on-axis input intensity of ~ 0.27 GW/cm^2, where the saturable absorber was Ag nanoparticles prepared by liquid phase laser ablation technique and the reverse saturable absorber was PTZ-Ag hybrid system. The system exhibited good non-reciprocity in the range 0.14- 0.42 GW/cm^2 and the observed non-reciprocity factor at 0.27 GW/cm^2 on-axis input intensity is around 3. Due to the large bandwidth, good chemical and thermal stability, cost-effectiveness and large-scale integration with existing fabrication technologies, this optical diode based on axial asymmetry in nonlinear absorption is a good candidate for future all optical device fabrication and computing.

Day 1: Friday, 12th February 2021

Time	Topic	
	Session 1 (Live Telecast from Auditorium SVVV, Indore)	
10:30-12:15	**Inaugural Session** (Online joining after 10:00) Conference Portal: https://nls-29.webconevents.com/	
10:30-11:10	Inaugural function and addresses by dignitaries ILA Perspective for NLS-29 **Shri S.V. Nakhe,** President, ILA Presidential address: Prof. Upinder Dhar, VC, SVVV, Indore Address by "Special Guest: **Shri Purushottamdas Pasari,** Chancellor, SVVV, Indore Address by "Special Guest: **Shri Debashis Das,** Director, RRCAT, Indore	
11:10-11:30	Address by Chief Guest: **Dr. G. Satheesh Reddy,** Chairman DRDO	
11:35-12:15	Keynote Address: **Prof. Raman Kashyap,** Montreal, Canada Photonics Gone Rogue	
12:15-13:00	**Lunch Break**	
	Session 2 Advanced Laser Technologies & Applications Session Coordinator: **Dr B N Upadhyaya** Session Chair: **Dr. Alok Ray**	
13:00-13:30	**Prof. Philippe Grelu,** Uni. Bourgogne, France Pulses and patterns in ultrafast fiber lasers: The dissipative soliton approach	IT-01
13:30-14:00	**Dr. Shaju K. Albert,** IGCAR, India Laser Welding in Fabrication of FBR fuel pins: Metallurgical Considerations	IT-02
14:00-14:30	**Prof. Michalis N. Zervas,** Uni. Southampton, UK Power Scaling Limits in High Power Fibre Lasers	IT-03
	Session 3 Oral Presentation of Paper (3 min + 2 min)	
14:30-16:45	**OPP-1A (24 nos.)** **Category 1:Physics & Technology of Lasers** Refer Annexure OPP-1A	
16:45-17:00	**Break**	
	Session 4 Lasers in Fiber based Instrumentation Session Coordinator: **Dr. Om Prakash** Session Chair: **Shri Viraj P. Bhanage**	
17:00-17:30	**Dr. Umesh Tiwari,** CSIO, Chandigarh Optical Fiber Biosensors: Principles and Applications	IT-04
17:30-18:00	**Prof. Sanjeev Raghuvanshi,** IIT, ISM (Dhanbad) Advancement of Speciality Fibre Optic sensors for In Situ monitoring	IT-05
18:00-18:30	**Dr. Aseem Singh Rawat,** BARC, Mumbai Laser based measurements and perimeter intrusion detection	IT-06
18:30-19:00	**Break** (End of the day)	

Day 1: Friday, 12th February 2021
Parallel Session

	Session 3 Oral Presentation of Paper (3 min + 2 min)	
14:30-16:45	**OPP-1B (25 nos.)** **Category 9: Laser Spectroscopy & Application** Refer Annexure OPP-1B	

Day 2: Saturday, 13th February 2021
Auditorium

Time	Topic	
	Session 5A Ultra Short, Ultra Intense Laser Plasma Interaction Session Coordinator: **Dr. A. Moorti** Session Chair: **Prof. R P Sharma**	
10:00-10:30	**Prof. Donald Umstadter,** University of Nebraska, Lincoln, USA Physics and Applications of Scattering with Extreme Light	IT-07
10:30-11:00	**Prof. Chan Joshi,** UCLA, USA Plasma Acceleration- What were we thinking in those early days and where are we headed?	IT-09
11:00-11:30	**Prof. G. Ravindra Kumar,** TIFR, India Spatiotemporal Dynamics of Relativistically Hot Plasmas	IT-11
11:30-11:45	**Break**	
	Session 6A Non-linear Optics **Session Coordinator: Dr. J. Jayabalan** **Session Chair: Prof. D. N. Rao**	
11:45-12:15	**Dr. Sai Santosh Kumar Raavi,** IIT Hyderabad Novel multifunctional organic chromophores for non-linear optical applications	IT-13
12:15-12:45	**Prof. K. V. Adarsh,** IISER, Bhopal Flatland Nonlinear Optics	IT-15
12:45-13:45	**Lunch Break**	
	Session 7 Oral Presentation of Paper (3 min + 2 min)	
13:45-16:15	**OPP-2A (29 nos.)** **Category 3: Laser Materials, Devices and Components (14 nos.)** **Category 6: Lasers in Material Science (15 nos.)** Refer Annexure OPP-2A	
16:15-16:45	**Tea Break**	
16:45-18:00	**Break**	
	Session 8 Ultrafast Lasers Session Coordinator: **Dr. P. K. Mukhopadhyay** Session Chair: **Dr. K. S.Bindra**	
18:00-18:30	**Prof. F. Ömer Ilday,** Uni. Bilkent, Ankara, Turkey Multi-GHz Burst-Mode Fiber Lasers	IT-17
18:30-19:00	**Prof. Ruediger Paschotta,** RP Photonics, Germany Solid-state Lasers for Ultrashort Pulse Generation	IT-18
19:00-19:30	**Prof. Frank W. Wise,** Cornell University, Ithaca, NY, USA Spatiotemporal Mode-Locking in Fiber Lasers	IT-19

Day 2: Saturday, 13th February 2021
Parallel Session

Time	Topic	
	Session 5B Applications of laser in Chemistry, Biology and Materials Coordinator: **Dr. J Jayabalan** Session Chair: **Dr. Anindya Datta**	
10:00-10:30	**Dr. Mohammed Ahmed,** RIKEN, Japan Probing Ultrafast Dynamics of Water at Aqueous Interfaces with Femtosecond Two-Dimensional Heterodyne-Detected VSFG Spectroscopy	IT-08
10:30-11:00	**Prof. Sachin Dev Verma,** IISER, Bhopal Visualization of charge separation at the in-plane organic heterojunctions using pump-probe microscopy	IT-10
11:00-11:30	**Prof. S. K. Sarkar,** BARC & SP Pune Univesity Making the Stories Come True: Molecular Laser Isotope Separation to Coherent Control	IT-12
11:30-11:45	**Break**	
	Session 6B Quantum and Atom Optics Session Coordinator: **Dr. Sunil Verma** Session Chair: **Dr. S R Mishra**	
11:45-12:15	**Dr. Harshawardhan Wanare,** IIT Kanpur, Kanpur, India Quantum Interference based approach to Nonlinear Optics	IT-14
12:15-12:45	**Dr. Y. B. Kale,** Uni. of Bermingham, UK A quantum of science' for the future technologies	IT-16
12:45-13:45	**Lunch Break**	
	Session 7 Oral Presentation of Paper (3 min + 2 min)	
13:45-16:15	**OPP-2B (28 nos.)** **Category 2: Lasers in Nuclear Science & Technology (4 nos.)** **Category 7: Lasers Plasma Interaction (10 nos.)** **Category 8: Lasers in Industry and Defence (2 nos.)** **Category 10: Lasers in Chemistry, Biology & Medicine (12 nos.)** Refer Annexure OPP-2B	
	Session 9 Lasers Additive Manufacturing Session Coordinator: **Dr C. P Paul** Session Chair: **Dr. U. Chandra Sekar**	
19:30-20:00	**Prof. Ehsan Toyserkani,** University of Waterloo, Canada Advancement in Monitoring and Quality Assurance Paradigms for Laser Powder-Bed Fusion	IT-20
20:00-20:30	**Prof. Andrew Pinkerton,** Uni. Lancaster, UK Towards a Predictive Model of Direct Metal Deposition	IT-21
20:30-21:00	**Prof. J. Ram Kumar,** IIT Kanpur, Kanpur Post processing of LAM components	IT-22
	Break (End of the day)	

Day 3 : Sunday, 14th February 2021

Time	Topic	

Auditorium

Session 10 Ph. D. Thesis Presentations

10:00-11:30 **ThP - A (6 nos.)**
Session Coordinator: **S. G. Nakhate**
Refer Annexure ThP-A

11:30-11:45 **Thesis presentation (2 nos.)** (3 min + 2 min)
Refer Annexure ThP-C

11:45-12:00 Break

Session 11 Presentations from Industries
Coordinators: **Shri P. Saxena & Dr. C. P. Paul**

12:00-13:00
1. Presentation of Incubation Centre, RRCAT (10 min.)
2. Presentations of M/S ATOS Instruments, Banglore (15 min)
3. Presentations of M/S Light Guide Optics Pvt. Ltd. (10 mins)
4. Presentations of M/S Research India, Bhopal (10 min)
5. Presentations of M/S New Age Instruments, Gurugram (10 min)

13:00-14:00 Lunch

Session 12 Oral Presentation of Paper (3 min + 2 min)

14:00-16:15 **OPP-3A (27 nos.)**
Category 11: Lasers & Fiber based Instrumentation (12 nos.)
Category 12: Electronics and Instrumentation for Lasers(15 nos.)
Refer Annexure OPP-3A

16:15-16:30 Break

Session 13 Laser applications in Chemistry, Biology and Medicine
Session Coordinator: **Dr S. K. Majumder**
Session Chair: **Prof. N. Ghosh**

16:30-17:00 **Prof. Igor Meglinski,** Aston Uni. UK — IT-23
Functional brain diagnosis with dynamic light scattering imaging approach at broken ergodicity conditions

17:00-17:30 **Prof. Martin Leahy,** National Uni. of Ireland — IT-24
Lasers and Nanotechnology in Regenerative Medicine

17:30-18:00 **Prof. Alex Vitkin,** Uni. Toronto — IT-25
Shedding light on radiotherapy: functional optical coherence tomography for radiobiological micro vascular imaging

18:00-18:15 Break

Day 3 : Sunday, 14th February 2021

Time	Topic	
	Session 14 Special Evening Talk	
18:15-19:15	**Prof. Martin Olivier,** Swiss Federal Institute of Technology Lausanne (EPFL) Plasmonic technologies for alloyed and hybrid metasurfaces Coordinator: **Dr. S K Majumdar** Introducer: **Prof. N. Ghosh**	ST-01
19:15-20:00	**Break**	
20:00-21:00	**Prof. Rainer Weiss,** MIT, USA (Physics Nobel Laureate 2017) The beginnings of gravitational wave astronomy: current state and future Coordinator: **Dr. Sendhil Raja** Introducer: **Prof. Somak Raychaudhary,** Director, IUCAA	ST-02
	Break (End of the day)	

Day 3 : Sunday, 14th February 2021
Parallel Session

	Session 10 Ph. D. Thesis Presentations	
10:00-11:30	**ThP – B (6 nos.)** Session Coordinator **Dr S. K. Majumder** **Refer Annexure ThP-B**	
11:30-11:45	**Thesis presentation (3 nos.)** (3 min + 2 min) **Refer Annexure ThP-D**	
11:45-12:00	**Break**	
	Session 12 Oral Presentation of Paper (3 min + 2 min)	
14:00-16:15	**OPP-3B (28 nos.)** **Category 4: Non linear, Quantum and Atom Optics (19 nos.)** **Category 5: Ultrafast lasers & Applications (9 nos.)** Refer Annexure OPP-3B	
16:15-16:30	**Break**	

Day 4: Monday, 15th February 2021
Auditorium

Time	Topic	
	15A Laser materials and devices Session Coordinator: **Dr Sunil Verma** Session Chair: **Dr D K Aswal**	
10:00-10:30	**Prof. Binay Kumar,** Univ. of Delhi, Delhi Growth of Single Crystals by Various Techniques for Optical, Piezoelectric and Communication Applications	IT-26
10:30-11:00	**Dr. Muthu Senthil Pandian,** SSN Institution, Chennai Development of High Quality Nonlinear Optical (NLO) Single Crystals for Second Harmonic Generation (SHG) Applications	IT-28
11:00-11:30	**Dr. N. Vijayan,** NPL, New Delhi Growth of Potential Nonlinear Optical Single Crystals by Melt and Solution Growth Techniques	IT-30
11:30-11:45	**Break**	
	Session 16 Laser Spectroscopy & Applications Session Coordinator: **Dr V B Tiwari,** Session Chair: **Dr S G Nakhate**	
11:45-12:15	**Dr. B. K. Sahoo,** PRL, Ahmedabad Atomic probe of nuclear properties	IT-32
12:15-12:45	**Prof. Ashok Mohapatra**, NISER, Bhuvaneshwar Dynamical phase transition in mirrorless optical parametric oscillator	IT-33
12:45-13:15	**Prof. Alika Khare,** IIT Guwahati Some of the Applications of Laser Induced Breakdown	IT-34
13:15-14:15	**Lunch**	
	Session 17 LIGO Science and Technologies Session Coordinator: **Dr Sendhil Raja** Session Chair: **Dr. Shashank Chaturvedi,** Director, IPR	
14:15-14:45	**Dr. David H. Reitze,** Caltech, USA The Advanced LIGO Gravitational-wave Detector: A Discovery Machine	IT-35
14:45-15:15	**Prof. Rana Adhikari,** Caltech, USA Future of Gravitational Wave Detection Technology	IT-36
15:15-15:30	**Break**	
15:30-16:30	**Session 18 Award Presentation and Closing Ceremony**	
16:30-17:00	(Closure of NLS-29)	
17:00-18:00	**ILA General Body Meeting**	

Day 4: Monday, 15th February 2021
Parallel Hall

Time	Topic	
	15 B Laser applications in Chemistry, Biology and Medicine Session Coordinator: **Dr S. K. Majumder** Session Chair: **Prof. Renu John**	
10:00-10:30	**Prof. Jessica Ramella,** Florida International University , USA Design of wearable devices for underserved populations	IT-27
10:30-11:00	**Prof. Dalip Singh Mehta,** Indian Institute of Technology Delhi, New Delhi Quantitative phase microscopy and nanoscopy using partially spatially coherent laser light: Improvement on image sharpness, phase noise, resolution and speckle free imaging	IT-29
11:00-11:30	**Dr. Kamal Kant Sharma,** NUS, Singapore Investigation of Dengue infectivity and dynamics using Förster Resonance Energy Transfer (FRET)	IT-31
11:30-11:45	**Break**	

ILA Best Thesis Awards NLS-29

(*Awards Sponsored by M/s Laser Spectra, Bengaluru*)

S.No.	Thesis Title	Name	Affiliation
1	Optical Spectroscopy Based Urine Analysis for Disease Diagnosis	**Surjendu Bikash Dutta**	*IIT, Indore*
2	Study of Spectral Beam Combination Techniques for High Power Pulsed Dye Laser Applications	**Paramjit Rana**	*BARC & HBNI, Mumbai*
3	Laser Drilling and Welding of Advanced Engineering Materials: An Experimental Investigation	**Suman Chatterjee**	*NIT, Rourkela*
4	Studies on Electromagnetically Induced Transparency in ^{87}Rb atoms	**Charu Mishra**	*HBNI, RRCAT, Indore*
5	Magneto-Optical Transport Studies on Ultra-Low Disordered Semiconductor Quantum Wells Grown by MOVPE	**Subhomoy Haldar**	*HBNI, RRCAT, Indore*

ILA Best Poster Awards NLS-29

(Awards Sponsored by Indian Laser Association)

S.No.	Paper Title	Name	Affiliation
1	A Compact Intensity Auto-Correlator for Ultra-Short Laser Pulse Width Measurement	**Deepak Dahiya, R. K. Patidar, S. W. Amalraj, A. Moorti, M. P. Kamath, Sushil Kumar Sharma, N. S. Benerji, K. S. Bindra**	*RRCAT, Indore*
2	Trace Elemental Detection in Liquid Sample using Laser Induced Breakdown Spectroscopy and Its Application in Environmental Field	**Keerthi K., Anish Kumar Warrier, Sajan D. George, Suresh D. Kulkarni, Santhosh C., Unnikrishnan V. K.**	*Manipal Academy of Higher Education, Manipal*
3	THz- TDS As a Diagnostic Tool for Monitoring the Water Content in Different Coloured Indian Almond (Catappa) Leaves	**Nagaraju Menchu, Chandan Ghorui, Ganesh Damarla, Anil Kumar Chaudhary**	*University of Hyderabad, Hyderabad*
4	Growth of Bulk Size Organic Single Crystal by a Novel Immersing Ampoule Sankaranarayanan-Ramasamy (ISR) Method for NLO Applications	**P. Karuppasamy, T. Kamalesh, Muthu Senthil Pandian, P. Ramasamy, Sunil Verma, A. K. Karnal**	*SSN College of Engineering, Chennai*
5	Study of Laser Polarization Dependent J×B Acceleration in Relativistic Ultrashort Laser Foil Interaction	**Tirtha Mandal,V. Arora, A. Moorti, A. Uphadhyay, J. A. Chakera**	*RRCAT & HBNI, Indore*
6	Raman Spectroscopy for Dissolution Testing of Paracetamol Tablets: An Exploratory Study	**V. Kumar, R. Shrivastava, J. Kumawat, N. Kumar, S. Maru, S. K. Majumder**	*RRCAT, Indore*
7	Development of Control Software for Cold Atom Interferometry Experiments	**Ayukt Kumar Pathak, Shradha Tiwari, P. P. Deshpande, Viraj Bhanage**	*RRCAT, Indore*
8	Studies on Optimization of Optical Pumping of Cold ^{87}Rb Atoms Using Stern-Gerlach (SG) Technique	**Vivek Singh, V. B. Tiwari, S. R. Mishra**	*RRCAT & HBNI, Indore*
9	Broadband Nonlinear Optical Studies of a Novel Phthalocyanine Using MHz and kHz Femtosecond Pulses	**Dipanjan Banerjee, K. S. Srivishnu, Jagannath Rathod, L. Giribabu, S. Venugopal Rao**	*University of Hyderabad, Hyderabad*
10	$^{98/100}$Mo Enrichment by Infrared Multi-Photon Dissociation of MoF_6	**M. B. Sai Prasad, A. Ghosh, R. C. Das, T. Dwivedi, G. Chakraborty, D. J. Biswas, J. P. Nilaya**	*BARC, Mumbai*

List of ILA Exhibiters

Applied Optical Technologies, Mumbai	https://appliedoptical.in
Anatech Lasers, Mumbai	http://www.anatechlaser.com
ATOS Instruments Marketing Services, Bengaluru	https://www.atosindia.com
Laser Science Services (I) Pvt. Ltd., Mumbai	http://www.laserscience.co.in
Laser Spectra Services India Pvt Ltd, Bengaluru	http://www.laser-spectra.com
Light Guide Optics, Indore	http://lightguide.org
New Age Instruments & Materials, Gurgaon	http://newagein.com
NS Scientific, Indore	https://nsscientific.in
PG Tech Pvt. Ltd. & Research Institute, Indore	http://www.pgtech.in
Research India, Bhopal	https://www.research-india.co.in
RTK Meditech India	https://www.meditech-india.com
Specialize Instruments Marketing Company, Mumbai	http://simc.co.in
Sinsil International, Mumbai	https://www.sinsilinternational.com
Sandvic Component, Delhi	http://sandviccomponents.com
Scientific Mes Technik, Indore	https://www.scientificindia.com

National Advisory Committee

Aswal, D. K.
NPL, New Delhi
Banerjee, S.
HBNI, Mumbai
Bhaduri, A. K.
IGCAR, Kalpakkam
Bhawalkar, D. D.
Indore
Chaturvedi, S.
IPR, Gandhinagar
Das, B. K.
IRDE, Dehradun
Das, D.
RRCAT, Indore
Dhar, U.
SVVV, Indore
Gupta, P. D.
Indore
Gupta, P. K.
Indore
Lionel , B.
DIC, New Delhi
Mohanty, A. K.
BARC, Mumbai
Naik, P. A.
ITS-Pilani, Goa
Nath, A. K.
IIT Kharagpur, Kharagpur
Nayak, J.
CHESS, DRDO, Hyderabad
Padmanabham, G.
ARCI, Hyderabad
Rao, D. N.
University of Hyderabad, Hyderabad
Ravindra Kumar, G.
TIFR, Mumbai
Sarkar, S. K.
SPPU, Pune
Sharma, S. K.
NPCIL, Mumbai
Singh, B. P.
IIT Bombay, Mumbai
Som, S.
VECC, Kolkata
Sood, A. K.
IISc, Bengaluru
Sriram, K.V
LEOS, ISRO, Bengaluru
Srivastava, H. B.
LASTEC, DRDO, New Delhi
Vasudev Rao, P. R.
HBNI, Mumbai
Vinayak, S. SSPL,
DRDO, New Delhi
Vyas, K. N.
DAE, Mumbai

Symposium Organizing Committee

Arya, R.
RRCAT, Indore
Bhanage, V. P.
RRCAT, Indore
Bindra, K. S.
RRCAT, Indore
Bisht, P. B.
IIT Madras,Chennai
Chakera, J. A.
RRCAT, Indore
Datta, A.
IIT Bombay, Mumbai
Datta, P. K.
IIT Kharagpur, Kharagpur
Dixit, S. K. RRCAT,
Indore
Guruprasad, K. N.
SVVV, Indore
John, R.
IIT Hyderabad, Hyderabad
Joseph, J.
IIT Delhi, New Delhi
Khare, A.
IIT Guwahati, Guwahati
Krishnamurthy, M.
TIFR, Hyderabad
Kundu, S.
BARC, Mumbai
Majumder, S. K.
RRCAT, Indore
Moorthy Babu, S.
Anna University, Chennai
Rajawat, A.
SVVV, Indore
Rapol, U. D.
IISER, Pune
Ray, A.
BARC, Mumbai
Razdan, A. K.
LASTEC, New Delhi
Sanyal, D. N.
NPCIL, New Delhi
Sharma, A.
BARC, Mumbai
Tata, B.V.R.
University of Hyderabad, Hyderabad
Nakhe S V
Chairman, NLS-29, RRCAT, Indore
Mishra S R
Convener, NLS-29, RRCAT, Indore
Sharma U
Co-Convener, NLS-29, SVVV, Indore
Agrawal, P. K.
Secretary, NLS-29, RRCAT, Indore
Katariya, N.
Co-Secretary, NLS-29, SVVV, Indore
Saxena, P.
General Secretary, ILA
Upadhyay, A.
Webmaster, NLS-29, RRCAT, Indore

Local Organizing Committee

Patrons

Shri Purushottamdas Pasari
Chancellor, SVVV, Indore

Shri Debashis Das
Director, RRCAT, Indore

Prof. (Dr.) Upinder Dhar
Vice Chancellor,SVVV, Indore

Members

Dave, I. A.
RRCAT, Indore

Dubey, J.
SVVV, Indore

Jain, P.
SVVV, Indore

Khan, M.P.
SVVV, Indore

Narwat, D.
RRCAT, Indore

Patel, S.
SVVV, Indore

Ram, S. P.
RRCAT, Indore

Rawat, R.
SVVV, Indore

Sheikh, S.
SVVV, Indore

Talwar, S.
RRCAT, Indore

Telang, S.
SVVV, Indore

Thakur, S.
SVVV, IndoreC

Dr. Santosh Dhar
Dean- Faculty of Doctoral Studies & Research, SVVV, Indore

Agrawal, P. K.
Secretary, NLS-29, RRCAT, Indore

Saxena, P.
Secretary, ILA, RRCAT, Indore

Upadhyay, A.
Web-master, NLS-29, RRCAT, Indore

Misra, P.
Treasurer ILA, RRCAT, Indore

Agrawal, S. K.
Treasurer, NLS-29, RRCAT, Indore

Local Organizing Sub-committees

Technical / Infrastructure development

From RRCAT

Dr. Ajit Upadhyay (Overall Coordinator)

Hall 1	Hall 2
Dr. Ajit Upadhyay	Shri Sandeep Talwar
Shri Sarthak Gupta	Shri Ishant A. Dave
Shri Dhruvdeep Narwat	Shri Sachin Agrawal
Shri Hitendra S. Chouhan	Dr. S. P. Ram

Shri J.S. Ganapathi, Shri H.Chitre and Shri V.S. Tiwari

From SVVV

Dr. Jigyasu Dubey (Coordinator)
Shri Srikant Telang
Shri Mohd. Parvej
Shri Shadab Sheikh
Shri Alok Malviya

E-Publication

Shri Sandeep Talwar (Coordinator)
Shri Ishant A. Dave
Shri T. Sivananda Reddy
Shri R. K. Mishra
Shri D.V.S. Raju
Shri Manoj Barwe and Smt. Rejina S. Mathews (office support)

Accounts

Shri Sachin Agrawal (Coordinator)

Refreshments, Tea, Snacks & Food

Dr. Manoj K. Saxena (Coordinator)
Shri Inderjeet Singh
Shri Dheeraj Shukla

Dr. Navita Khatri (Coordinator)
Prof. Rupali Goud, SVVV
Dr. Ravi Vanshpal
Shri Vishal Shrivastava
Shri Ankit Chouhan

Exhibition

Shri Piyush Saxena (Coordinator)
Dr. Pankaj Misra (Coordinator)

Transport

Shri Rajesh Kumar Patidar (Coordinator)
Shri Vivek Singh (Co-Coordinator)

Dr. Uttam Sharma (Coordinator)

SVVV Auditorium Management

Dr. Uttam Sharma (Coordinator)
Dr. Shweta Mishra
Dr. Aarti Sharma
Dr. Pragya Palod
Shri Vishal Shrivastava
Shri Ankit Chouhan

NLS - 29

Addresses for Correspondence

Dr. S. R. Mishra
Convener, NLS-29
Head, LPAS
R & D Block-A,
RRCAT, Indore
Phone : 0731-248 8377
e-mail : nls@ila.org.in

Dr. Uttam Sharma
Co-Convener, NLS-29
Professor & HOD
Shri Vaishnav Institute of Science,
SVVV, Indore
Phone : 0731-272 9071
e-mail : uttamsharma@svvv.edu.in

Shri Praveen Kumar Agrawal
Secretary, NLS-29
Head, CVLEL , LPSD,
RRCAT, Indore
Phone : 0731- 244 2419
e-mail : nls@ila.org.in

Dr. Nitu Katariya
Co-Secretary, NLS-29
Asstt. Professor.
SVVV, Indore.
Phone : 0731-272 9071
e-mail : nitukatariya@svvv.edu.in

For ILA courses

Shri Piyush Saxena
General Secretary, ILA
RRCAT, Indore
Phone : 0731-244 2422
e-mail : secretary@ila.org.in

For NLS information on web

Dr. Ajit Upadhyay
Plasma Simulation Activity
LTD, RRCAT, Indore
Phone : 0731-2442007
e-mail : admin@ila.org.in

For more details kindly visit: **www.ila.org.in/nls29**